

Proceedings ICSBM 2019

Citation for published version (APA):

Caprai, V., & Brouwers, J. (Eds.) (2019). *Proceedings ICSBM 2019: 2nd international conference of sustainable building materials*. Technische Universiteit Eindhoven.

Document status and date:

Published: 01/11/2019

Document Version:

Publisher's PDF, also known as Version of Record (includes final page, issue and volume numbers)

Please check the document version of this publication:

- A submitted manuscript is the version of the article upon submission and before peer-review. There can be important differences between the submitted version and the official published version of record. People interested in the research are advised to contact the author for the final version of the publication, or visit the DOI to the publisher's website.
- The final author version and the galley proof are versions of the publication after peer review.
- The final published version features the final layout of the paper including the volume, issue and page numbers.

[Link to publication](#)

General rights

Copyright and moral rights for the publications made accessible in the public portal are retained by the authors and/or other copyright owners and it is a condition of accessing publications that users recognise and abide by the legal requirements associated with these rights.

- Users may download and print one copy of any publication from the public portal for the purpose of private study or research.
- You may not further distribute the material or use it for any profit-making activity or commercial gain
- You may freely distribute the URL identifying the publication in the public portal.

If the publication is distributed under the terms of Article 25fa of the Dutch Copyright Act, indicated by the "Taverne" license above, please follow below link for the End User Agreement:

www.tue.nl/taverne

Take down policy

If you believe that this document breaches copyright please contact us at:

openaccess@tue.nl

providing details and we will investigate your claim.



Organized by
**Eindhoven University
of Technology**

TU/e

In cooperation with
**Wuhan University
of Technology**

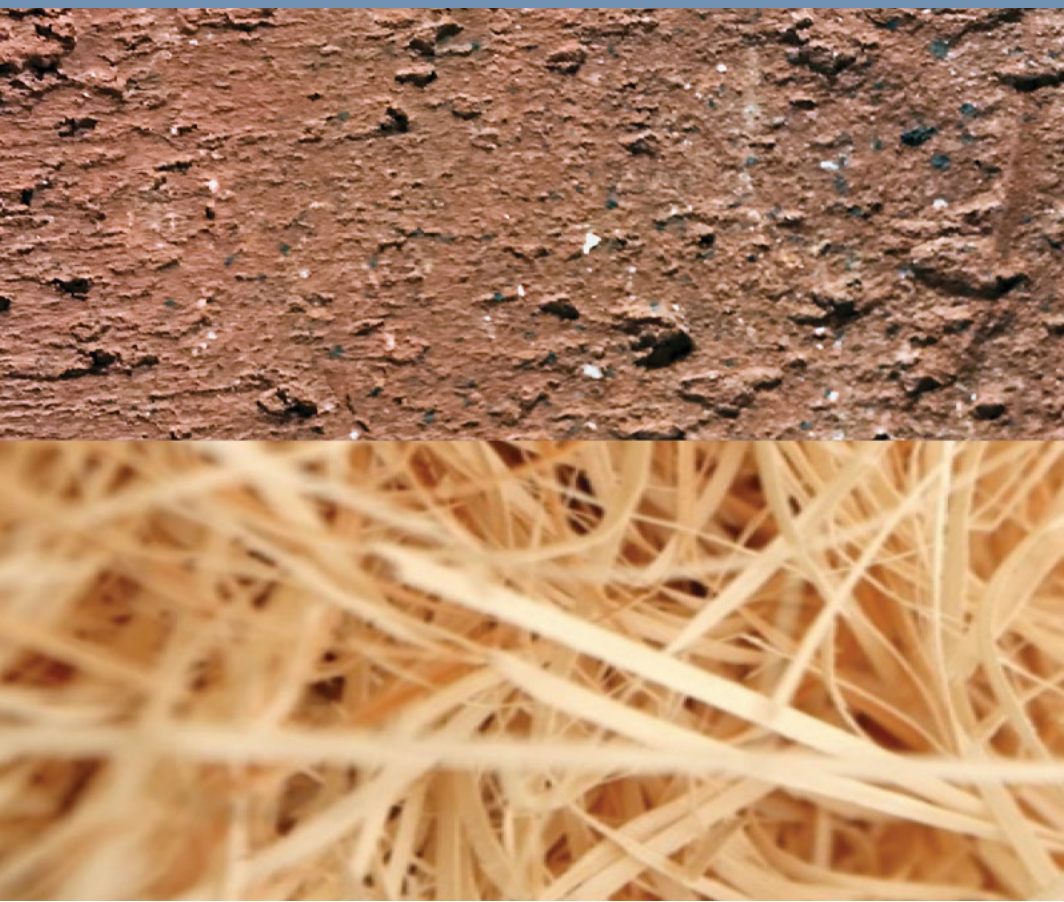


PROCEEDINGS ICSBM 2019

2nd International Conference on Sustainable Building Materials

August 12-15, 2019 - Eindhoven, The Netherlands

Editors: V. Caprai and H.J.H. Brouwers



and supported by





Organized by
**Eindhoven University
of Technology**

TU/e

In cooperation with
**Wuhan University
of Technology**



PROCEEDINGS ICSBM 2019

VOLUME 1 - Keynote speakers session

2nd International Conference on Sustainable Building Materials

August 12-15, 2019 - Eindhoven, The Netherlands
Editors: V. Caprai and H.J.H. Brouwers



and supported by



ICSBM 2019, Conference proceedings

A catalogue record is available from the Eindhoven University of Technology Library

ISBN of the volumes set: 978-90-386-4898-9

ISBN of Volume 1: 978-90-386-4910-8

Sponsored by: CRH, Eltomation - Wood cement board plant, Tata Steel Europe (Gold sponsors), VDZ, PCA (Bronze Sponsors).

Front page image: V. Caprai

Editors: V. Caprai and H.J.H. Brouwers

Organizing committee:

Conference Chairman: Prof. H.J.H. (Jos) Brouwers, Eindhoven

Conference Co-Chairman: Prof. Wen Chen, Wuhan

Conference Secretary: Mrs V. (Veronica) Caprai and Dr. M.V.A. (Miruna) Florea, Eindhoven

Dr. Qiu Li, Wuhan

Dr. Bo Yuan, Wuhan

Dr. Q. Yu, Eindhoven

Dr. F. Gauvin, Eindhoven

Dr. K. Schollbach, Eindhoven

Mr. Y. Chen, Eindhoven

Mrs. L.T.J. Harmsen, Eindhoven

Mrs. N.L. Rombley, Eindhoven

Table of Contents

Hydration of Portland cement	
K. Scrivener.....	6
Application of new concrete processes and materials	
Z. Li, G. Sun, R. Liang, B. Chen.....	9
Performance of SCMs – Chemical and Physical Principles	
H. Justnes.....	10
On the setting and hardening control of alkali-activated slag cements	
C. Shi	11
Biobased building materials	
J.E.G. van Dam, M.J.A. van den Oever	12
Techniques for analyzing microstructures	
S. Igarashi.....	13
Natural and artificial Pozzolanes - Industrial residues and natural supplementary materials	
P. Herbert.....	14
Use of Supplementary Cementitious Materials to Manufacture High Performance Concrete	
Y. Peiyu	16
Bio-based admixtures	
W. Schmidt	17
Cementitious materials for marine structures - Specification of building materials for in service durability	
C. Gehlen, C. Thiel	20
Portland cement – SCM blends: insights from solid-state NMR spectroscopy	
J. Skibsted.....	21
Functional coatings for building materials	
A. van Herk, S. Jana	22
Utilization of waste and residues in building materials	
M. Illikainen	23
Natural fibers in building materials	
M. Sonebi	24
Energy efficiency of building materials	
M. Tyrer	25

Volume 1

Keynote speaker session

Hydration of Portland cement

K. Scrivener

Laboratory of Construction Materials, EPFL STI IMX LMC, Station 12, 1015 Lausanne, Switzerland

Abstract - The latest thinking on the mechanisms of hydration is outlined.

Keywords: Hydration, induction period, main hydration peak, C-S-H.

1. Introduction

The resources of the earth mean that almost all cement will continue to be based on Portland cement clinker. The most realistic way to continue to reduce environmental impact is to replace part of this clinker by supplementary cementitious materials. Nevertheless, the early properties are dominated by the hydration of the Portland clinker component.

- The hydrations reactions can be broken down into three stages:
- Up to the end of the induction period;
- The main hydration peak;
- Later hydration after the main peak.

2. Up to the end of the induction period

Initially cement reacts rapidly and then after only a few minutes the reaction slows to a low rate: the so called “induction period”, lasting a few hours. This pattern of reaction is very important from a practical standpoint as it gives time from concrete to be mixed and transported to site. For many years the most widely believed hypothesis for this initial slow down and the induction period was the formation of a layer of hydrates around the cement grains which inhibited further reaction. Work over the past few years has shown that this is certainly incorrect.

Instead the induction period can be simply attributed to the build up of ions in solution which lower the undersaturation. It is well known from studies in geochemistry that minerals show a similar behaviour. When they first come into contact with water the undersaturation is very high and this provides the energy to increase the surface area with dissolution at many sites and formation of a rough surface. As dissolution proceeds the undersaturation decreases and so the energy to form new surfaces, progressively dissolution becomes localised at defects. Then there is a dramatic fall in dissolution rate which corresponds to a switch to dissolution only at steps. This fall in dissolution rate may occur when the solution is still many orders of magnitude more dilute than saturation. Experiments with alite immersed in water and then in saturated lime solution [1] demonstrate that this transition also occurs for alite and can explain the rapid fall in reaction rate and the onset of the induction period. The hypothesis has been well validated by theory [1], experiment [2] and modelling [3]. Furthermore, unlike the inhibiting membrane hypothesis, it can explain all experimental observations.

Calcium silicate hydrate precipitates very soon after the addition of water. This C-S-H has a much lower Ca/Si ratio than alite and so the Ca/Si ratio of the solution increases during the induction period

During the induction period reaction continues at a slow rate. Eventually the precipitation of calcium hydroxide occurs. This leads to an increase in the undersaturation and so to an increase in the rate of dissolution. Changes may also occur in the C-S-H precipitates which lead to the onset of rapid growth of both C-S-H and CH.

3. Main hydration peak

The main hydration peak is characterised by the rapid growth of C-S-H and CH. Most C-S-H grows from the surface of the cement grains, but will also take place on other surfaces, such as SCMs. CH growth is concentrated in the pore space. During this period there is first an acceleration in the rate of reaction and then a deceleration, such that the reaction has again dropped to a low rate by the end of the first day (at 20°C). The two main mechanisms proposed to explain this pattern of reaction have been impingement of hydration products or onset of diffusion control through a layer of hydrates. Careful quantitative study of the reaction kinetics through experiment and modelling have clearly shown both these hypotheses are wrong. At the maximum of the peak, the amount of hydrates formed is much less than that needed for impingement to be the factor slowing down hydration. There are also many arguments against diffusion through a hydrate layer being the mechanism:

- It does not fit quantitative models;
- there is no “layer” – in places the alite surface is still visible
- there is a gap between the grain and hydrate shell
- there is no change in activation energy.

Study of a large number of parameters (particle size, water to cement ratio and ion doping) clearly indicates that the kinetics in this period are controlled by the growth of C-S-H needles. This “needle” hypothesis has been demonstrated to well match the experimental data, with no fitting – taking its parameters only from experimental observations.

4. After the main hydration peak

Unfortunately, this period has received far less attention than the previous two periods. Despite the fact that at one day the degree of reaction is around 50% and the mechanical strength around 25% of its final value. Another month is needed to reach around 80% hydration and 80% of mechanical strength. Careful study of the cumulative heat of hydration [4] clearly indicates that the amount of space available plays a critical role. After a few days it is observed by ¹H NMR relaxation and by MIP that the water filled pores decrease to a certain critical size and then do not decrease further. This suggests that after this point the pores are too small to allow classical crystal growth. At the point when this limiting pore size is reached not only does the rate of the clinker reaction slow dramatically, but also the reaction rate of SCMs such as slag and calcined clay. In systems with additions of calcined clay and limestone it is also seen that the carboaluminate phases no longer form and alumina from the continuing reaction of the calcined clay goes into the C-S-H phase instead.

After this limiting critical pore size is reached, the rate of reaction, again slows dramatically, but does continue. The mechanisms controlling reaction at this stage are far from clear, but probably involve densification of the C-S-H phase.

4.1 Why do we get a gap between the hydrating cement grain and the hydrate shell

It has long been a mystery as to why a gap opens up between the shell of hydrates (mainly C-S-H) formed during the main hydration peak. From our present understanding of the hydration mechanisms it now

appears that this is a consequence of the growth rates of outer and inner C-S-H. During the main hydration peak, the growth rate of the C-S-H needles is rapid and it is favourable for growth to occur on the outer surface of the hydrate shell. As the rate of growth of the outer C-S-H slows down it becomes similar to the rate of growth of inner C-S-H so it becomes equally favourable for growth to occur on the grain surface and at the ends of the needles. Gradually the gap fills in of about a week. Thereafter the growth of the outer and inner product is closely linked a growth of outer product is needed to allow more dissolution of the anhydrous grain and so more space for inner product.

5. Outstanding Questions

Despite the considerable progress in understanding hydration mechanisms in recent year, many questions remain. Most of these concern growth of C-S-H:

- Why is it slow during the induction period and is the increase in rate at the end of the induction period only linked to the precipitation of calcium hydroxide or is there also some structural change which facilitates growth?
- Why to the needles grow rapidly to a certain length and then their growth rate slows dramatically?
- What are the changes occurring after the limiting pore size is reached?

More knowledge about C-S-H growth is important to increase the efficiency of the hydration of Portland cement which would facilitate greater levels of clinker substitution and further reduction of its environmental footprint.

6. References

- [1] P. Juilland, E. Gallucci, R. Flatt, K. Scrivener, Dissolution theory applied to the induction period in alite hydration, *Cem. Concr. Res.* 40 (2010) 831–844. doi:10.1016/j.cemconres.2010.01.012.
- [2] L. Nicoleau, M.A. Bertolim, Analytical Model for the Alite (C3S) Dissolution Topography, *J. Am. Ceram. Soc.* 99 (2016) 773–786. doi:10.1111/jace.13647.
- [3] A. Kumar, S. Bishnoi, K.L. Scrivener, Modelling early age hydration kinetics of alite, *Cem. Concr. Res.* 42 (2012) 903–918. doi:10.1016/j.cemconres.2012.03.003.
- [4] E. Berodier, K.L. Scrivener, Understanding the Filler Effect on the Nucleation and Growth of C-S-H, *J. Am. Ceram. Soc.* 97 (2014) 3764–3773.

Application of new concrete processes and materials

Z. Li¹, G. Sun¹, R. Liang², B. Chen²

¹ University of Macao

² The Hong Kong University of Science and technology

Abstract

In this talk, the application of new process and materials to produce high modulus concrete and high bending resistance cement-based composites will be introduced. Along this line, the ultrasonic technique has been adopted in concrete mixing to improve the interface density for high modulus concrete development. The high modulus concrete developed through the ultrasonic vibration and addition of nano particles will be introduced on its optimization in materials formulation, dimension stability behavior and structural performance. Moreover, 3D printing process has been applied to produce sophisticated cement-based architectural and decoration products. The application of both selective reaction and direct deposition techniques will be introduced.

Recently, it becomes popular to achieve enhanced mechanical properties of cement-based materials through incorporation of nano particles. In this presentation, advanced cement-based materials through application of nanotechnology will be introduced. One example is to use cement to generate 5 nm nanoparticles which is utilized to enhance the mechanical properties of hydrogel. By adding 5-nm inorganic particles in organic matrix, hydrogels with the best all-round performance in the world has been successfully developed in aspects of strength, elastic recovery and ultimate stretch ratio. In addition, by adding organic or inorganic nano particles into cement based materials, the flexural strength of the cement-based materials increased significantly. For cement paste, bending strength is increased by three times without lowering the compressive strength. Finally, newly developed inorganic-organic integrated nano particles for lowering hydration heat will be explained on their mechanism and effect.

Performance of SCMs – Chemical and Physical Principles

H. Justnes

SINTEF Building and Infrastructure, Trondheim, Norway. E-mail: harald.justnes@sintef.no

Abstract

The influence of supplementary cementing materials (SCMs) on the hydration and durability of blended cement has been evaluated using chemical and physical principles. Similarities and differences between various SCMs have been considered grouping them into latent hydraulic or pozzolanic with sub-division into siliceous, aluminous, carbonaceous etc. Synergy between SCMs producing calcium aluminate hydrate and calcium carbonate maximize water binding leading to reduced porosity and increased strength by forming calcium monocarboaluminate hydrate. Any magnesium content in the carbonate leads to hydrotalcite formation in the presence of aluminates.

The interaction of SCMs with plasticizers and use of hydration accelerators are also treated.

The influence of SCMs on durability issues like chloride ingress, carbonation, alkali aggregate reactions, sulphate resistance and freeze-thaw resistance is discussed as well. Generally speaking SCMs improve the resistance of blended cements to most degradation mechanisms at equal w/c, except for carbonation resistance that can be improved by reducing w/c.

Keywords: Supplementary cementing material, hydration, durability, microstructure, porosity.

The unabridged version of this article can be found in Volume 2 - New cementitious binder, page 2.

On the setting and hardening control of alkali-activated slag cements

C. Shi

Key Laboratory for Green & Advanced Civil Engineering Materials and Application Technology of Hunan Province, College of Civil Engineering, Hunan University, Changsha 410082, China

Abstract

Sodium silicate activated slag often gives high early strength but sets too rapid. Commercial retarders for Portland cement and replacement with other cementing components have been proven little effective. This study investigated the approach of controlling setting by alter activator ion composition and silica polymer status. The roles of activators during the alkali-activation process were studied via pore solution chemistry analysis and microstructural analysis of hydration products. The addition of Na_2CO_3 does not, but NaOH does alter the polymerization of silicate ion groups in sodium silicate solution due to the increase in pH and Na_2O concentration. The specific effect of Na_2CO_3 on the setting of alkali-activated slag depends on the relatively contents of NaOH and $\text{Na}_2\text{O} \cdot n\text{SiO}_2$ in alkaline solution. The reaction degree of AAS is dependent on activator composition, which governs the kinetics of formation and intrinsic characteristics of the hydration product calcium aluminosilicate hydrate. The setting and strength development of sodium silicate-activated slag can be controlled by manipulating the composition of Na_2CO_3 - NaOH - $\text{Na}_2\text{O} \cdot n\text{SiO}_2$.

Biobased building materials

J. E.G. van Dam and M.J.A. van den Oever

Wageningen Food and Biobased Research, Wageningen UR, POB17, 6700AA Wageningen, The Netherlands

Abstract

Construction industries are expanding worldwide, and so does demand for building materials and resources as a result. With a share of 36% of CO₂ emissions in EU, the construction sector contributes significantly to greenhouse gas emissions. The industry must therefore play a key role in the EU policy targets for a low carbon economy by 2050. Energy saving in the production of building materials and increased thermal insulation of buildings does not suffice for the transition. Therefore shift towards more CO₂ neutral resources will be needed and the options for circular and bioeconomic solutions were explored in the building and construction industry. A focus of R&D and innovations is on the increased use of renewable and recyclable raw materials. Besides the use of traditional timber and wood derived materials, fibre crops such as flax and hemp play a key role in this regard. Polymer and mineral composite materials can be produced with these lignocellulosic fibres. Composites based on bioresins and bioplastics are tested at lab and applied in demonstration building projects. For biobased materials an environmentally safe protection against decay is important for extension of the durability. The use of various other natural biopolymer derived components with anti-microbial properties or uv protection properties are explored in coatings and adhesives. Other innovations in the building and construction sector that are aimed at reducing the ecological impact include the design of light weight constructions, tiny houses and reusable elements. An overview of the current state of the art and new trends for green and circular building will be presented.

Keywords: biobased products, lignocellulose, CO₂ neutral, circular building

Techniques for analyzing microstructures

S. Igarashi

Department of Civil and Environmental Engineering, Kanazawa University

Abstract

Microscope examination is classical and the easiest way for understanding and explaining microstructure. Looking back on its history, there was a pioneering work by Scrivener and Platt as a milestone in cement microscopy. Their work using BSE image analysis had introduced a new perspective of quantification into evaluation for microstructure. Then the development of IT and AV utilization has achieved the sophistication of image analysis. Nowadays, image analysis for microstructure is a quite common tool for not only research fields but also practical evaluations of concrete structures. In this presentation, image analysis techniques for microstructure in concrete is briefly reviewed with a focus on what we've been evaluating. Furthermore, a new direction which is aiming at an evaluation of spatial structure, not a simple quantity is also introduced. A quantity of a phase of interest is simply evaluated through a binary segmentation and tallying pixels. Once a threshold value for the segmentation is determined, quantification of a phase is instantaneously done with image analysis software. Thresholding is generally based on grayscale values in images. These days, various types of images are used in image analysis. For example, pseudo-color images of EPMA mapping for an element is used for evaluating supplementary cementitious materials. The background of this process is the fundamental stereology, Delesse's rule ($A_A = V_V$). Combining the evaluated quantity with simple cement chemistry or kinetics model such as the Powers model, capillary pore structure that is the most important in determining properties of concrete is evaluated with regard to volume changes in the hydration of cement. However, it should be noted that whether the presence of finer pores smaller than the resolution is ignored or taken into account affects the interpretation of microstructure and relevant properties in concrete.

Another important approach to the analysis of microstructure is to evaluate spatial distribution, not a quantity. In the early stage of the image analysis from the 80s to 90s, it was difficult to evaluate it in the complicated and inhomogeneous microstructure. Nowadays, spatial statistics functions have been actively introduced into random heterogeneous microstructure like concrete. This trend is greatly attributable to the availability of reliable software. Some are downloadable as free software. For example, densification of concrete microstructure with time is well known as a decrease in porosity. However, using those functions, the evolution of pore structure is understood as changes in spatial structure, which includes not only the porosity but also continuity and connectedness of pores. In particular importance, this evaluation of structure gives characteristic length parameters that are significant in the interpretation of many transport phenomena in concrete. For example, to discuss durability such as permeability or frost resistance of concrete, depth from a surface or spacing between air bubbles are key issues. Some approaches to these issues using the spatial statistics functions are described. They lead to future research of simulation of 3D microstructure in concrete.

Keywords: image analysis, stereology, spatial statistics, second-order function

Natural and artificial Pozzolanes - Industrial residues and natural supplementary materials

P. Herbert

Mineralogy and geochemistry department, University of Halle.

Due to the necessary reduction of CO₂ during the production of cement clinkers several possibilities exist to reduce the contents of volatile gases during the different production stages. As the amount of industrial residues is not sufficient for producing all type of composite cements other natural and artificial mineral products may be applied. The different strategies for CO₂-reduction producing cementitious materials can be summarized :

- Replacement of cement clinker by addition of different other raw materials to produce
- composite cements
- Replacement of limestone by CO₂-free natural/industrial raw materials
- Increase of reactivity of clinker minerals leads to a reduced amount of cement materials in
- cement application
- Reductions in process conditions (reduced temperatures, other phases, mineralizers,
- grinding aids, the total efficiency of processes)
- Clinker minerals with reduced CO₂-output-different compositions
- Activation of slowly reacting cements by introducing highly reactive clinker minerals
- Production of clinker minerals with increased specific surface and increased reactivity
- Activation of clinker minerals
- Cement clinkering using mineralizers
- Hydration reaction replaced by the carbonation process

Therefore different materials coming from natural and artificial sources are used in these strategies. Different origins of the materials result in many varying compositions. Many different industrial residues and natural materials can be used under this aspect to produce composite cements. In this context the focus lies on the usage of industrial residues (fly ashes, slags, thermally optimized mineral mixtures, leaching residues, plant ashes) and also natural sources with volcanic or sedimentary origin (pyroclastics, altered and weathered rocks, altered clays, clastic rocks). The use of calcium-poor chemical compositions of pozzolans can lead to a substantial reduction of CO₂, despite combined with excellent qualities of these cementitious materials. Different materials, qualities and measurement methods combined with essential details of the varying compositions of these different materials will be given.

As the supply from industrial residues is not sufficient, also natural products like volcanic ashes and thermally pre-treated clay materials are discussed.

Keywords: pozzolane, industrial residue, CO₂-reduction, supplementary material, cement

Use of Supplementary Cementitious Materials to Manufacture High Performance Concrete

Y. Peiyu

Department of Civil Engineering, Tsinghua University, Beijing, China

Abstract - Supplementary cementitious materials (SCMs) are very valuable and indispensable for the manufacture of high performance concrete. Use of SCM is necessary for the recycle of solid waste and to produce green and sustainable concrete. The using situation of CSMs in China is shortly reviewed. Fly ash and ground granule blast furnace slag are the most important mineral admixture in Chinese cement and concrete industry. Silica fume is used only for high strength concrete. New kinds of mineral admixture from metallurgical slag is now explored. 20%-40% of binder is SCM in ready-mix concrete for both normal and high strength classes. Even higher dosage of SCM is used to prepare massive concrete or the concrete with high durability. The properties of complex binder containing different kinds and different dosage of mineral admixture are evaluated. Some examples are given to show the performance of high volume mineral admixture concrete and how to use it in the building construction.

Keywords: Supplementary cementitious material; high performance concrete; high volume mineral admixture concrete; fly ash; ground granule blast furnace slag

Bio-based admixtures

W. Schmidt

Bundesanstalt für Materialforschung und -prüfung, Division: Technology of Construction Materials.

Abstract

Due to the high carbon emissions linked to concrete production and a rapidly increasing demand for cementitious materials, particularly in the global South, it is inevitable to use cement in concrete more efficiently. This can be achieved best by minimising the Portland cement content in the binder and by developing concrete mixtures with low water to cement ratios. For both approaches, chemical admixtures are required to cope with the negative rheological influences of supplementary cementitious materials that are often observed, and the higher solid volume fraction, respectively.

However, particularly in the growing economies of the Southern hemisphere, where a massive part of the future construction activities will take place, the supply chains are often poor with regard to performance enhancing chemical admixtures, and local production facilities are lacking today. This paper presents case studies of polysaccharide based alternative admixtures such as acacia gum, cassava starch and the gum of the bark of *Triumfetta pendrata* A. Rich, which can be used effectively as superplasticizer, robustness enhancer, and thixotropy incorporating agent, respectively. Their modes of operation are discussed based on their zeta potentials and hydrodynamic diameters in the presence of calcium ions. Eventually, local value chains are discussed for bio-based by products on the example of cassava peels wastes.

Keywords: admixtures, concrete, cassava, acacia gum, *Triumfetta pendrata* A. Rich.

The unabridged version of this article can be found in Volume 5 - Biogenic and functionalized materials, page 2.

Cementitious materials for marine structures

Z. Shui

Wuhan University of Technology, China

Keywords: Please insert a maximum of 5 keywords.

Abstract - With the continuous exploitation of the ocean, the scale of infrastructure construction in the marine environment is experiencing a booming increase. Concrete is the main material for marine infrastructure construction due to its high reliability and low cost. However, in such an environment rich in aggressive components such as chloride, sulfate and magnesium ions, the concrete structures suffer a faster damaging than that in the mainland. Concerning that, it is of great significance to investigate the damage behaviors and relevant mechanisms of concrete structure in the marine environment and provide some effective methods to prolong the service life of the concrete. In recent years, the research group of the reporter devoted to studying the damage of concrete in the marine environment. Some of the research findings are reported here for concrete serving in the marine environment including several aspects:

1. Performance and microstructure degradation

To obtain reliable information on the long-term behaviors of concrete under real marine conditions, this part aims to identify the mechanisms of degradation in Portland cement mortar exposed to simulated seawater attack under drying-wetting cycle conditions. Hardened mortar mixtures with different supplementary cementitious materials (SCMs) are exposed to NaCl, NaCl+MgCl₂, NaCl+Na₂SO₄ and NaCl+Na₂SO₄+MgCl₂ solutions with a fixed chloride concentration. The results show that the degradation process of mortar samples in single and composite solution coupled with drying-wetting includes three stages, 1) performance enhancement stage; 2) stable stage and 3) performance deterioration stage. The samples exposed to the NaCl+Na₂SO₄ solutions show higher mass and dynamic modulus of elasticity changes compared to the single NaCl solution, and the NaCl+Na₂SO₄+MgCl₂ solution reveals severe performance degradation. The phase composition highlights that the presence of SO₄²⁻+Mg²⁺ in chloride environment increases consumption of portlandite at the surface and causes the decalcification of C-S-H, thus aggravates the degradations of mortar. Microstructure analysis shows that the presence of SO₄²⁻ in chloride solution changes the pore structure and results in an increase of porosity. The SO₄²⁻+Mg²⁺ in chloride environment further increases the harmful pore volume, which accelerates the ingress of corrosive ions in the mortar matrix. The ability to resistance aggressive solution attack can be significantly improved with the utilization of SCMs.

2. Chloride binding and hydration product conversion

Chloride binding is considered to be a process that can restrain the free chloride diffusion and therefore benefit the chloride corrosion resistance of the concrete structure. This part is aimed to identify the key factors affecting the chloride binding capacity of cement-based materials. Several cementing systems including, mineral admixture (MA)-Portland cement, MA-C₃S and MA-lime system are employed here.

The MA used here are pozzolanic materials (FA, MK, SG) and aluminum compounds (Al_2O_3 , $\text{Al}(\text{OH})_3$, $\text{A}(\text{OH})_3$). Sodium chloride is added in either exposure solution or mixing water. Results show alumina-rich pozzolans (ARP) can improve the chloride binding capacity of cement-based materials and MK performs the best. For a give ARP, chloride binding capacity is depended on the incorporation level, and the optimal chloride binding capacity is achieved at $\text{CaO}/\text{Al}_2\text{O}_3$ ratio between 3 and 6. For a given $\text{CaO}/\text{Al}_2\text{O}_3$ of the system, the chloride binding capacity decreases with the increase of $\text{SiO}_2/\text{Al}_2\text{O}_3$ ratio. That means the potential of ARP to improve the chloride binding capacity of cementitious materials can be limited by the high amount of amorphous silica in ARP. The silicate in cementitious materials restrains chloride binding due to two negative effects: 1) dilute the total mass of $\text{CaO}+\text{Al}_2\text{O}_3$; 2) its hydration reduces the portlandite available for chloroaluminate formation. As for aluminum compounds, very higher potential to improve chloride binding capacity of cement-based materials is observed due to no silica contained in aluminum compound, therefore more portlandite can be involve in the formation of chloroaluminate.

Chloroaluminate in hardened samples exposed to sodium chloride is mainly formed from other AFm phases such as carboaluminate, stratlingite and monosulfoaluminate and OH-AFm. The transformation of these phases to chloroaluminate can improve the alkali in pore solution, reduce portlandite and increase chemically bound water in matrix. Besides, chloride exposure also promotes delayed ettringite formation in hardened cement, because the sulfates in monosulfoaluminate are replaced by chlorides and the released sulfates react with monosulfoaluminate to form delayed ettringite in return. In the presence of admixed chloride, the reaction of calcite is restrained. When sulfates are coupled with chlorides in mixing water, the chloride binding capacity is reduced because sulfates can compete with chloride to insert into the interlayer of AFm. During carbonation, the chloride previously bound in chloroaluminate can reverse to free chloride. This indicates that, for the concrete contaminated with chloride, the carbonation of matrix results in the neutralization of pore solution as well as improvement of free chloride solution, which can be expected to significantly accelerate steel corrosion.

3. Chloride diffusion behavior

The chloride diffusion induced reinforcement corrosion seriously threatens the durability of concrete construction in the marine environment. This part investigates the effects of sulfate and magnesium ion in simulated seawater on the chloride diffusion behavior of Portland cement mortar with continuous full immersion and drying-wetting cycle. Results indicate that the samples exposed to $\text{NaCl} + \text{MgCl}_2$ solutions show the highest chloride content at the outmost layer (0–5 mm). The presence of SO_4^{2-} in the composite solution decreases the chloride ingress and reduces the apparent chloride diffusion coefficient at 60 days of exposure, while the opposition is observed at later exposure period. The $\text{SO}_4^{2-}+\text{Mg}^{2+}$ in chloride salt accelerates chloride ingress and increase apparent chloride diffusion coefficient. The drying-wetting cycle further accelerates chloride ingress. Nevertheless, the addition of SCMs significantly improves the resistance to chloride ingress into mortar specimens.

The above findings help a better understanding of the damaging behaviors and mechanisms of cementitious materials used in marine environment, and provide some guidance for the design of cementitious materials suitable for marine environment and concrete with chloride-containing ingredients. In the upcoming researches, the group of the reporter will also focus on the use of marine sand in concrete structure modified with design cementitious materials, aiming to improve the stability of marine sand concrete structure.

Specification of building materials for in service durability

C. Gehlen¹, C. Thiel¹

¹Department of Civil, Geo and Environmental Engineering, Technical University of Munich.

Abstract

To assess whether a structural element made of a given building material can withstand the expected mechanical load and environmental exposure in service, designers need information on the material resistances and loads as well as the local conditions. The durability of a building material in the structure can only be assessed if these factors are taken into account. Usually, the material resistances are obtained from laboratory tests. However, the performance of materials under standardized laboratory conditions differs from those occurring in the field. This paper considers this assessment problem and develops a solution strategy based on carbonation-induced corrosion as an example.

Keywords: durability design, concrete, reinforcement, material resistances, modeling.

The unabridged version of this article can be found in Volume 2- New cementitious binders, page 25.

Portland cement – SCM blends: insights from solid-state NMR spectroscopy

J. Skibsted

Department of Chemistry and Interdisciplinary Nanoscience Center (iNANO), Aarhus University.

Abstract

Society's increasing demands for new construction materials with low embodied CO₂ emission promote research in new binders and cement blends where a significant part of traditional cement is replaced by a supplementary cementitious material (SCM). These materials comprise generally industrial waste products, natural pozzolans and activated minerals that exhibit either hydraulic or pozzolanic properties. As separate materials and in contact with water, most SCMs will not show any significant hydraulic reactions of cementitious value. However, as fine powders and under alkaline aqueous conditions or in contact with calcium hydroxide they will react chemically, *i.e.* 'the pozzolanic reaction', and form hydration products similar to those of cementitious systems. Typical SCMs used by the cement industry are limestone and by-products such as fly ashes, blast furnace slags, silica fume, and rice husk ashes. However, the availability of some of these materials varies regionally and they will not be able to cover the global needs for SCMs in the future. In particular, the amounts of fly ashes are decreasing since coal-fired power plants are being phased out for environmental protection purposes in several countries. Thus, there is an urgent need for developments of new SCMs that are comparable or superior to fly ashes and slags. In this context, limestone and clays represent important types of material available in large deposits all over the world.

This presentation focusses on the development of binary and ternary Portland cement – SCMs incorporating calcined clays, glasses and limestone as SCM's and targeting cement replacement levels of 30 – 50 wt%. The glasses exhibit pozzolanic properties similar to fly ashes and slags and they may be synthesized from minerals and clays with a low CO₂ footprint compared to Portland cement. Moreover, thermal activation of clay minerals results in dehydroxylation of the aluminate and silicate species of the layered structure and the formation of disordered structural sites with high pozzolanic activity. Solid-state NMR spectroscopy represents a strong tool for characterization, quantitation, and structural analysis at the nanoscale of a wide range of diamagnetic, inorganic materials. Main advantages of the method are the nuclear-spin selectivity where one nuclear spin-isotope (*e.g.* ¹H, ¹¹B, ¹³C, ¹⁹F, ²³Na, ²⁷Al, ²⁹Si ...) is detected at a time and the equal observation of crystalline and amorphous phases. Thus, rather simple NMR spectra can often be achieved for complex materials, for example reflecting minor constituent phases or guest-ion incorporation. These features will be illustrated in the presentation by quantification of glasses and calcined clays in Portland cement blends, providing kinetic information about their pozzolanic reactivity. Moreover, focus will be paid to the impact of SCM's on the structure and composition of the C-A-S-H phase, the principal binding component, in blended cements.

Keywords: Supplementary cementitious materials, calcined clays, glasses, C-A-S-H phase, NMR spectroscopy

Functional coatings for building materials

A. van Herk, S. Jana

Institute of Chemical and Engineering Sciences, A*Star, division functional molecules and polymers, 1
Pesek Road, Jurong Island, 627833 Singapore

Abstract

New developments in coatings for buildings often rely on nanotechnology developments. Properties like hiding power, colour and even total solar reflectance (for cool coatings) depend on the level of dispersion and spacing of the pigment particles. Dispersants play a key role in this; a relatively unexplored option is to coat the pigment particles with polymer to force a minimum spacing of the particles. Surface properties like dirt pick-up of the coatings film depend on surface tension and surface roughness. Both superhydrophilic and superhydrophobic coatings have been explored. Creating hydrophobic surfaces by utilization of fluorinated polymers seems like an expensive option, again through utilization of nanotechnology the amount of expensive fluorinated polymer can be minimized still obtaining desired effects.

Other developments in the area of coatings for building materials are low VOC coatings to even completely plasticizer free coatings and the use of reactive plasticizers. A*Star is conducting a program called NoSOC (no small organic compounds) that is targeting to reduce and eliminate small organic molecules leaking out of coatings for example. For the purpose of measuring the emission of small organic molecules from coatings and new device has been developed which can detect very small amounts, the so-called “sniffer”.

In the keynote presentation several approaches to create nanostructured particles will be presented and examples of potential applications in coatings and construction materials will be shown.

Keywords: Coatings, anti-fouling, solar reflectance, nanotechnology, emulsion polymerization

Utilization of waste and residues in building materials

M. Illikainen

Fibre and particle engineering research unit, University of Oulu, P.O. Box 4300, 90014 University of Oulu, Finland

Abstract

Millions of tons of inorganic waste materials and residues are produced annually in Europe. Metal production, energy industry, mining activities and construction and demolition are the main sources of high-volume secondary materials. Some of these secondary materials are utilized but still large amounts of material end up to landfills. Based on the principles of circular economy, materials and their value should remain in the society as long as possible, and virgin raw materials should be used only if there are no recycled materials available. Industrial residues typically consist chiefly of oxides of the most abundant elements of the planet: Si, Al, Fe and Ca. These are also the main elements forming the base of different inorganic binders, such as alkali-activated cements. From the chemical composition point of view, industrial residues are thus interesting raw materials for building materials. Most of the industrial residues have gone through several processing steps such as mechanical and thermal treatments, which improves their properties and therefore their utilization potential. High-potential waste materials that currently are not utilized include e.g. mineral wool waste, crystalline slags from metallurgical industry as well as fly ash from biomass combustion. Some challenges remain in waste and industrial residues' utilization due to high variation in waste material quality, need for local production and utilization, as well as competition against cheap and robust cement-based materials. Despite the challenges, there is a growing interest towards the more sustainable production and use of waste materials in new construction products.

Keywords: inorganic waste, industrial residue, alkali-activated material, building material

Natural fibers in building materials

M. Sonebi

Queen's University Belfast, School of Natural and Built Environment, Belfast, UK

Abstract

Construction remains a significant consumer of raw materials, specifically non-renewable resources derived from the extractive industries. In addition, construction is a significant contributor to the emission of global warming gases, both through its dependence on the extractive industries, and its consumption of energy during and after construction. Natural fibres have gained interest as reinforcing materials in the composite industry for low-cost housings. Their advantages have been increasingly recognised as a major motivation to be more environmental friendly, cost-efficiency, renewable, and good thermal conductivity and acoustic. The building industry has thus been called to account for its role in the massive use of mineral raw materials and environmental pollution. One solution comes from the bio-building sector which draws on unlimited sources of natural materials such as natural fibres, which is a recyclable carbon sequestrator. The natural fibres can be sourced from plants or animals. From part of the plant where the fibres are sourced, the fibres can be classified into bast fibres (okra, flax, hemp, roselle, jute, kudzu, ramie), leaf fibres (agave, banana, palm, sisal, and pineapple), seed fibres (cotton, coir and kapok), core fibres (hemp, kenaf, jute), grass and reed (wheat, corn and rice), and other types of fibres. Fibbers from animals are for example wool (Sheep) and feathers have been used. Traditionally, natural fibres have been cultivated and used extensively for non-structural applications in rural developing countries for multipurpose such as rope, bag, broom, fish net and filters. The fibres have also been used for applications in housing as roof material and wall insulation. Natural fibre used for insulation can often be used as replacements for mineral- or petrochemical-based insulation. When used appropriately, natural fibre insulation materials can deliver thermal and acoustic insulation comparable to other insulation materials, but with a lower or potentially negative carbon footprint and fewer health issues during the installation of these materials. They can create more energy-efficient buildings. They can also assist in regulating relative humidity, and can provide a vapour permeable system and improve indoor quality. This multi-functionality should be borne in mind when specifying natural fibre insulations in order to ensure maximum value and benefits. A large variation is found in the properties of natural fibres. The properties are affected by several factors such as type of fibres, moisture content and form of fibres. Moreover, the properties are also affected by the place where the fibres are grown, cultivation condition, the part of the plant they are harvested from which region/country, growing period (year) and retting or extracting process. The mechanical performance, conductivity, weathering and carbonation of bio-based building materials made with hemp and rapeseed are discussed.

Keywords: Carbonation, conductivity, fibres, mechanical performance, weathering.

Energy efficiency of building materials

M. Tyrer

Centre for Research in the Built and Natural Environment Coventry University, Coventry, CV1 5FB,
United Kingdom.

Abstract

The energy efficiency of building materials divides into two distinct areas; the inherent ‘passive’ savings in energy and embodied CO₂ of modern building materials and ‘active’ materials whose function is to conserve or moderate energy transfer in the built environment or harvest energy such as solar radiation.

Examples of the first group are widespread as the search for ever-lower energy materials continues. The efficiency of Portland cement production has increased markedly over the last 30 years, such that a modern cement kiln operates at only a little above the thermodynamic (theoretical) minimum of ~2.8 GJ/ tonne of cement. Globally, the energy efficiency has continued to increase as dry-process kilns (including staged preheaters and precalciners) replace wet-process kilns, and as more efficient grinding equipment is deployed. Overall, the thermal energy intensity of clinker was estimated at 3.4 GJ/t on average in 2017. This is a remarkable manufacturing success and greatly exceeds the efficiency of other materials (i.e. steel, glass, pharmaceuticals, or plastics) and generates no solid or liquid waste. It does however, liberate carbon dioxide both from fossil fuel use and decarbonating limestone in the kiln. Cement is made of a vast scale (4.1 Gt in 2018) so its production contributes over 5% of anthropogenic CO₂. Indirect emissions from burning fossil fuels to heat the kiln can be reduced by burning alternative fuels, including natural gas, biomass and waste-derived fuels such as tyres, sewage sludge and municipal solid wastes. These less carbon-intensive fuels might reduce overall cement emissions by 18-24 percent from 2006 levels by 2050 but efficiency gains in cement production are incremental and yield diminishing returns.

Practically, the greatest saving is to be made through reducing the amount of cement clinker used in concrete production. Numerous supplementary cementitious materials (SCMs) exist and some have been in use for many years, whilst new materials are developed regularly. Through the use of blended cements we have a range of Portland-SCM binders, some of which offer strength or durability advantages over Portland cement concrete. Focus in recent years has turned to non-Portland cement binders, such as Magnesia Cements, Celitement, Alinite Cement, Calcium sulfoaluminate systems, and Alkali Activated Systems / Geopolymers and each has a role to play in the future of construction. The practicality of such alternatives must be assessed at many levels; the fiscal and environmental impact must be balanced against the long-term security of supply and performance of the materials in service. One thing is certain however, the enormity of the existing Portland cement industry will not change rapidly but evolve to accommodate new ideas and new opportunities.

Finally, it is important to consider ‘active’ materials in the built environment. A modern office block, for example, may be clad with a decorative façade. Recent trends in energy harvesting have seen both solar heat collection and photovoltaic panels incorporated in building cladding, whilst energy generation by thermoelectric glass is an attractive technology allowing electricity to be generated from near-transparent

glass. The incorporation of hydrogels in porous ceramics allows the inner layer of a building façade to offer evaporative cooling, much like sweat cooling mammalian skin. The water in this case is replenished at night, when the air cools to below the dew point. To conclude, it is important to consider the use of phase change materials in regulating heating and cooling needs.



Organized by
**Eindhoven University
of Technology**

TU/e

In cooperation with
**Wuhan University
of Technology**



PROCEEDINGS ICSBM 2019

VOLUME 2 - New cementitious binders

2nd International Conference on Sustainable Building Materials

August 12-15, 2019 - Eindhoven, The Netherlands
Editors: V. Caprai and H.J.H. Brouwers



and supported by



ICSBM 2019, Conference proceedings

A catalogue record is available from the Eindhoven University of Technology Library

ISBN of the volumes set: 978-90-386-4898-9

ISBN of Volume 2: 978-90-386-4911-5

Sponsored by: CRH, Eltomation - Wood cement board plant, Tata Steel Europe (Gold sponsors), VDZ, PCA (Bronze Sponsors).

Front page image: V. Caprai

Editors: V. Caprai and H.J.H. Brouwers

Organizing committee:

Conference Chairman: Prof. H.J.H. (Jos) Brouwers, Eindhoven

Conference Co-Chairman: Prof. Wen Chen, Wuhan

Conference Secretary: Mrs V. (Veronica) Caprai and Dr. M.V.A. (Miruna) Florea, Eindhoven

Dr. Qiu Li, Wuhan

Dr. Bo Yuan, Wuhan

Dr. Q. Yu, Eindhoven

Dr. F. Gauvin, Eindhoven

Dr. K. Schollbach, Eindhoven

Mr. Y. Chen, Eindhoven

Mrs. L.T.J. Harmsen, Eindhoven

Mrs. N.L. Rombley, Eindhoven

Table of Contents

Performance of SCMs – Chemical and Physical Principles

H. Justnes	8
------------------	---

Specification of building materials for in service durability

C. Gehlen, C. Thiel.....	31
--------------------------	----

Design of reinforced concrete slabs with consideration of the construction joints

V. Kurochkina, I. Yakovleva, A. Deineko, A. Starostin	42
-------------------------------------------------------------	----

Eco-efficiency in cement use analysed by the concept of distance among particles in concrete phases

M. F. L. Menezes, R.G. Pileggi, M. Rebmann, C. Massucato.....	57
---------------------------------------------------------------	----

HYDCEM: A new cement hydration model

N. Holmes, D. Kelliher and M. Tyrer	66
-------------------------------------------	----

Chloride Ingress and Degradation of Portland Cement Mortar Exposed to Seawater Attack Coupling with Drying-wetting Cycle

S. Cheng, Z. Shui, T. Sun, X. Gao.....	75
----------------------------------------	----

Locally available material (manufactured sands) impacts on properties for an Ultra-High Performance Concrete (UHPC)

R. Yang, R. Yu, Z. Shui, C. Guo, S. Wu, X. Gao	88
------------------------------------------------------	----

Application of Krstulovic-Dabic model on early hydration analysis of Portland cement under Mg²⁺ influence

X.S. Li, Z.H. Shui, X. Gao	101
----------------------------------	-----

Recent Sustainable Development of Ultra-High Performance Concrete (UHPC)

R. Yu, Z. Liu, X. Wang, Q. Song, Z. Shui, C. Hao	110
--------------------------------------------------------	-----

Influence of External Water Introducing by Coral Sand on Autogenous Shrinkage and Microstructure of Ultra-High Performance Concrete (UHPC)

K. Liu, Z. Shui, R. Yu, S. Yi	119
-------------------------------------	-----

Neutron radiography to study water ingress via the interlayer of 3D printed cementitious materials

J. Van Der Putten, M. Azima, P. Van den Heede, T. Van Mullem, G. De Schutter and K. Van Tittelboom	130
----------------------------------------------------------------------------------------------------------	-----

Influence of heat treatment and mechanical activation on reactivity of natural pozzolan for geopolymer synthesis

R. Firdous, D. Stephan	138
------------------------------	-----

Effect of calcium hydroxide on the hydration of sulphoaluminate cement with high concentration of borate solution	
Q. Li, H. Ma, X. Ling, B. Yuan, W. Chen	156
The effect of MgO on the structure and chemical composition of C-S-H gels	
Y. Tang, W. Chen.....	167
Impact of steel fibre content on the fibre network structure of ultra-high performance fibre reinforced concrete (UHPFRC)	
Q. Song, Z. Shui, R. Yu, S. Rao	176
Investigation of the zonation of thermally treated ultra high performance concrete	
M. Voigt, J. von Werder, B. Meng.....	185
Role of Mg²⁺ stabilized amorphous calcium carbonate on the early reaction of sodium carbonate activated slag	
B. Yuan, Q.L. Yu, W. Chen, H.J.H. Brouwers.....	194
Pozzolanic reactivity of size-classified siliceous fly ashes	
R. Snellings, H. Kamyab, S. Joseph, P. Nielsen, M. Loots, L. Van den Abeele	199
Evaluation of calcined dredged sediments as supplementary cementitious materials	
H. Kazemi-Kamyab, L. Van den Abeele, M. Henry, L. Haouche, R. Snellings	214
The Effects of Epoxy Resin as Partial Cement Replacement on the Mechanical Properties of Concrete	
G.A. Jokhio, Y. Gul, A. Abu-Tair, G. S. Wei	224
Polycarboxylate Superplasticizer Modified Fly Ash: Its Effects on Fluidity and Mechanical Properties of Cement Paste	
P. Liu, M. Qu, F. Wang, G. Hu, L. Yang, W. Zhang	232
Understanding Hydrogen Bonding in Calcium Silicate Hydrates	
B. Li ¹ , H.J.H. Brouwers, Q. Yu, W. Chen.....	233
Concrete with High-purity Volcanic Glass Powder Manufactured from Pyroclastic Deposit through Dry Gravity Classification and Pulverization	
T. Noguchi, A. Tomoyose, K. Sodeyama and K. Higashi	244
Manufacturing high-performance supplementary cementitious materials from pyroclastic deposit through dry gravity classification and pulverization	
A. Tomoyose, T. Noguchi, K. Sodeyama, K. Higashi.....	256
Early hydration of C₂S doped with combination of S and Li	
M. Boháč, T. Staněk, A. Rybová, A. Zezulová, F. Bellmann, H.-M. Ludwig.....	269
Safe Use of Sustainable Building Materials: A reappraisal of Adobe	
T. Li Piani, J. Weerheijm, L. Koene and L. J. Sluys	278

Microstructural changes in porosity due to carbonation of fly ash blended pastes assessed by dynamic vapour sorption	
Y. Villagrán-Zaccardi, N. Alderete, N. De Belie.....	297
Isothermal Calorimetric Study on Heat Evolution and of Apparent Activation Energy of Alkali-activated Slag/Fly ash Pastes	
S. Zhang, Y. Zuo, Z. Li, G. Ye	304
Uncovering strength developing regularities of ultra-high performance concrete cured under high temperature	
Z. Liu, Z. Shui, R. Yu, Q. Song.....	312
Depth of penetration for steel-tube-confined concrete targets penetrated by rigid sharp-nosed projectiles	
Q. Tan, D. Song, Z. Jiang.....	320
Ballistic performances of multi-layered Ultra-high Performance Fibre Reinforced Concrete	
Y.Y.Y. Cao, M. Sluijsmans, Q.L. Yu , H.J.H. Brouwers	337
Effect of MgO, nitrate intercalated LDH and Calcined-LDH on chloride resistance of alkali-activated fly ash /slag mortar	
T. Liu, Y. Chen, Q.L.Yu, H.J.H. Brouwers	344
Recent development on sustainable ultra-high performance concrete design with low cement consumption: a review	
P.P. Li, Q.L. Yu, H.J.H. Brouwers	353
Suitability of phenolphthalein indicator method for alkali activated concrete	
O.O. Ojedokun, P.S. Mangat	363
Activation of binary binder containing fly ash and cement with red mud as alkali source and application in controlled low strength materials	
B. Yuan, S. Yuan, C. Straub, W. Chen	373

Volume 2

New cementitious binders

Performance of SCMs

– Chemical and Physical Principles

H. Justnes

SINTEF Building and Infrastructure, Trondheim, Norway. E-mail: harald.justnes@sintef.no

Abstract

The influence of supplementary cementing materials (SCMs) on the hydration and durability of blended cement has been evaluated using chemical and physical principles. Similarities and differences between various SCMs have been considered grouping them into latent hydraulic or pozzolanic with sub-division into siliceous, aluminous, carbonaceous etc. Synergy between SCMs producing calcium aluminate hydrate and calcium carbonate maximize water binding leading to reduced porosity and increased strength by forming calcium monocarboaluminate hydrate. Any magnesium content in the carbonate leads to hydrotalcite formation in the presence of aluminates.

The interaction of SCMs with plasticizers and use of hydration accelerators are also treated.

The influence of SCMs on durability issues like chloride ingress, carbonation, alkali aggregate reactions, sulphate resistance and freeze-thaw resistance is discussed as well. Generally speaking SCMs improve the resistance of blended cements to most degradation mechanisms at equal w/c, except for carbonation resistance that can be improved by reducing w/c.

Keywords: Supplementary cementing material, hydration, durability, microstructure, porosity.

1. Introduction

1.1 Reason for extended use of SCMs

The cement industry world-wide is calculated to bring about 5-8% of the total global anthropogenic carbon dioxide (CO₂) emissions. The general estimate is about 1 tonne of CO₂ emission per tonne clinker produced, if fossil fuel is used and no measures are taken to reduce it. The 3rd rank after heating/cooling of buildings and transport is not because cement is such a bad material with respect to CO₂ emissions, but owing to the fact that it is so widely used to construct the infrastructure and buildings of modern society as we know it. Concrete is actually among the more environmentally friendly materials since it is composed in general of about 1 part cement, 0.5 parts water and 5-6 parts of sand and gravel (i.e. aggregate). The world's cement production was roughly 4 billion tonnes in 2013, meaning roughly 24 billion tonnes concrete or 1·10¹⁰ m³ concrete. This quantity can be translated into making a concrete cylinder of about ϕ 20 cm reaching the moon and back to earth every day or building a solid concrete block with 1 km² base reaching higher (10 000 m) than Mount Everest (8 848 m) in a year!

A lot is done by cement producers to reduce the global carbon footprint, in particular to replace coal with waste having a calorific value equivalent to (fossil) fuel and by making blended cement where parts of the clinker is replaced with supplementary cementing materials (SCMs). However, cement is a bulk product that should cover a wide range of applications and serve different customers, giving limitations on clinker

replacements.

Concrete, on the other hand, is the end product where the performance criteria are already specified and depending on application more can be done to increase its sustainability. As pointed out by Justnes [1] the shortest route to make cement and concrete more sustainable, is to replace clinker in cement or cement in concrete by supplementary cementing materials (SCMs). This paper discusses how SCMs affect cement and concrete principally in chemical and physical ways and what this means in terms of durability.

Classes of SCMs

One can divide SCMs into *latent hydraulic* and *pozzolanic*. Latent hydraulic SCMs are inorganic additives that only need an activator to react with water and form a cementitious binder. Examples are ground, granulated blast furnace slag (GGBS), synthetic calcium aluminate glasses and to some extent high calcium fly ash. Pozzolanic SCMs are mineral additives that form cementitious binders in reaction with calcium hydroxides. Pozzolanic SCMs can be sub-divided by their major oxides like silicas (e.g. silica fume, nano-silica, rice husk ash, hydrothermal silica and diatomaceous earth or kieselgur), aluminosilicates (e.g. siliceous fly ash, calcined clays like metakaolin, burnt shale and natural pozzolana of volcanic origin like trass, scoria etc) and alumina (e.g. nano-alumina). Lothenbach *et al* [2] have given an overview of the performance of the most common SCMs (i.e. silica fume, fly ash and GGBS) in blended cements, while Thomas [3] published a book on SCMs in concrete. Carbonates as SCM are in a class by itself since they need aluminate hydrates to react with and they were for a long time considered inert, or at best accelerating the cement setting acting as nucleation sites, since there were relatively little aluminate in cement clinker not tied up by sulphates to ettringite and thereby the carbonate reactivity was difficult to observe. However, the reactivity of calcium carbonate becomes first observable on a macro level in ternary systems with fly ash producing extra calcium aluminate hydrates in its pozzolanic reaction (De Weerd and Justnes [4]) and recently the strength increase of fly ash blended cement with dolomite versus limestone was found to be due to hydrotalcite formation also requiring aluminates (Zajac *et al* [5]).

1.1.1 Physical Principles

The physical principles include particle packing, pore refinement and connectivity of pores reducing the transport of aggressives into the concrete. The two latter points are actually indirectly chemical since they are a consequence of hydration and depend on how much liquid water is transferred into solid hydrates. The effect improves as a function of time.

1.1.2 Chemical Principles

The chemical principles involve the chemical nature of the hydration products and how they interact with aggressives forming new products.

2. Physical effects of SCMs

2.1 Initial particle packing

SCMs have often higher surface and consist of smaller particles than portland cement and also lower density. Hence, in the practical approach of just replacing cement with SCM by mass, there will be an increased volume of binder (cement + SCM + water) relative to the aggregate. The same goes for *adding* SCM to cement instead of *replacing* cement, which is common in many former studies, in particular for silica fume. In more scientific studies it is therefore recommended to use *volume replacement* of cement by SCM in order to sort out the physical and chemical effects of the SCM compared to cement.

If one considers a portland cement with average particle size $d_{50} \approx 20 \mu\text{m}$, it still has a particle size distribution

(psd) allowing smaller particles to pack in between the larger particles. For a particle with radius r to fit into a tetrahedral hole created by 4 spheres of $20\text{ }\mu\text{m}$ diameter (radius $R = 10\text{ }\mu\text{m}$); $r < (\sqrt{3}/2 - 1)R = 2.25\text{ }\mu\text{m}$, and to fit in an octahedral hole of 6 spheres of diameter $20\text{ }\mu\text{m}$; $r < (\sqrt{2}-1)R = 4.14\text{ }\mu\text{m}$. An individual silica fume particle of $0.15\text{ }\mu\text{m}$ can then even fit into a tetrahedral hole of cement particles as small as $1.33\text{ }\mu\text{m}$ in diameter, while calcined clay particles with a typical diameter of $5\text{ }\mu\text{m}$ only can pack in between coarser cement particles and compete with cement grains of similar size.

The simplest SCM example is silica fume (Justnes [6]) consisting of basically spherical individual particles with an average diameter of $0.15\text{ }\mu\text{m}$, although usually occurring as aggregation of fused particles. As comparison, the irregular grains of a portland cement have typical average diameter of $15\text{--}20\text{ }\mu\text{m}$. The chemical composition of silica fume (SF) is also rather simple as it usually contains more than 90% SiO_2 with a range of 85 to 99%. Because of its small particle size, SF will pack in the cavities formed by the irregular shaped cement grains until a certain dosage when the SF will disperse cement grains or its agglomerates in the fresh state. The result is a considerable void size refinement from the start.

Reduced permeability during setting, or shortly thereafter, is important for durability of concrete (for instance in marine environment) when made by slip forming or when demoulded early. Ingress of aggressive ions like water-borne chlorides can be very rapid during early exposure, in particular due to suction created by the under pressure in contraction pores formed as a consequence of hydration.

2.2 Increased volume of solids

Hydration reactions lead normally to an increased volume of solids as liquid water is transformed into hydrates. The strength increase after initial contact between the particles is mainly a consequence of reduced porosity, even though the mechanical properties of the formed compounds matters as well. One can use alite hydration as an example as illustrated in Eq. 1 where the increase in volume of solids during hydration is $(0.300+0.217)-0.317= 0.200\text{ ml/g C}_3\text{S}$ corresponding to an increase of 63 vol%.

$2\text{ C}_3\text{S}$	+	6 H	=	$\text{C}_3\text{S}_2\text{H}_3$	+	3 CH	(1)
$m=1.00\text{g}$		0.237		0.750		0.487	
$M=228.32\text{g/mol}$		18.02		342.46		74.09	
$n = 4.38\text{ mmol}$		13.14		2.19		6.57	
$\rho = 3.15\text{ g/ml}$		0.998		2.50		2.24	
$V=0.317\text{ml}$		0.237		0.300		0.217	

3. Chemical effects of SCMs

Scrivener *et al* [7] published a state of the art on methods to determine the degree of reaction of SCMs. The chemical effects of different SCMs are treated in the following:

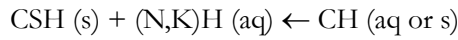
3.1 Silica

Using the cement chemist's notation the pozzolanic reaction of silica fume can be written:



A mixture of silica fume and pure lime needs weeks to harden properly. The acceleration of the pozzolanic reaction by alkalis creating high pH in the pore water was confirmed by Justnes [8] following the strength development for mortars with lime/silica fume cementitious materials. The presence of alkalis seems to

serve as a catalyst for a rapid pozzolanic reaction of silica fume (aq = aqueous, s = solid):



The nature of the CSH-gel from the pozzolanic reaction is different than the CSH gel formed by cement hydration. The two different gels coming from the cement hydration and the pozzolanic reaction, respectively, can be interwoven. The calcium silicate hydrate amorphous gel can exist in a wide range of compositions. The general difference between CSH from pozzolanic reaction and from cement hydration is that the former CSH has longer linear polysilicate anions and lower C/S-ratio than the latter (Justnes [9]).

In Fig. 1 (Justnes [10]) the relative compressive strength of mortar with lime/SF cementitious material (corresponding to C/S = 1.11, water-to-solid = 0.70 and alkalis of K/Na = 2 to pH = 13) is plotted versus curing time. In the same figure the degree of reaction of SF as measured by ²⁹Si MAS NMR versus curing time is plotted as well with a nearly identical trend indicating linearity between SF conversion and strength.

Justnes *et al* [11, 12] used ²⁹Si MAS NMR to study the influence of silica fume on the hydration rate of the silicate phases (sum of alite and belite) in ordinary and high strength cement, as well as the rate of silica fume reaction in such blends and the overall composition of the CSH gel under sealed conditions. Justnes *et al* [12] and Sellevold *et al* [13] showed that for low w/(c+s), the silica fume reacted faster than cement and left cement grains as micro-aggregate embedded in the CSH-gel. However, this is not necessarily negative for strength as cement grains are quite hard particles. Furthermore, some unreacted cement has potential in contributing to self-healing of microcracks during the service life of concrete.

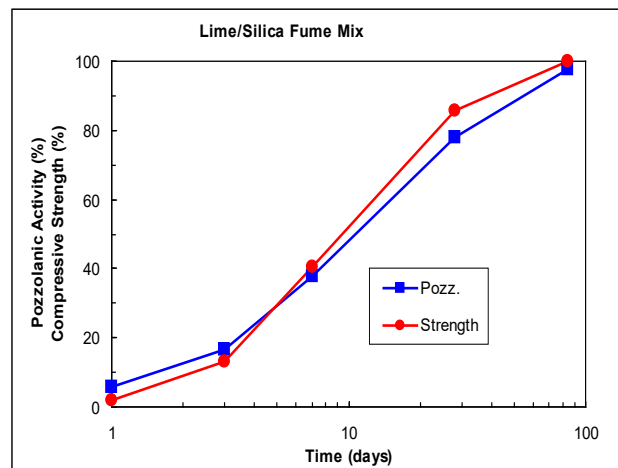


Figure 1: Comparison of compressive strength (100% = 63.9 MPa at 84 days) development of mortar with reactivity of silica fume in the cementitious material lime /SF with C/S = 1.11 and water-to-solid ratio 0.70 after Justnes [10].

3.2 Alumina and aluminosilicates

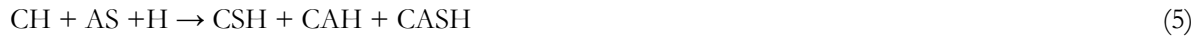
The chemical reaction of alumina, as in for instance nano-alumina (e.g. Barbhuiya *et al* [14]) or simply $\gamma\text{-Al}_2\text{O}_3$, is equally simple as for silica in reaction (2);



C_3AH_6 is the stable end-product in an isolated system of finely divided alumina and lime in spite of a number of metastable calcium aluminate hydrates (CAH_{10} , C_4AH_{19} etc). As for silica in reaction (3), alkalis will also

here play a catalytic role with soluble aluminum hydroxide ions like $\text{Al}(\text{OH})_4^-$ as the likely intermediate product. The difference is that the CAH products in general are crystalline rather than amorphous.

The pozzolanic reaction of the aluminosilicate (AS) glass phase in fly ash and the distorted aluminosilicate layers in calcined clays is complex but can be written in a non-balanced way;



A representative for calcium aluminate hydrate (CAH) will be C_3AH_6 and the mixed product CASH can be Strätlingite; C_2ASH_8 . In addition to that, it is typical that the CSH-gel will contain more aluminate than when it is formed by cement hydration only.

Ground blast-furnace slag (GGBS) contains sufficient calcium to react by itself when activated by alkalis. GGBS has a typical composition of 47% $\text{CaO}+\text{MgO}$, 35% SiO_2 and 12% Al_2O_3 . When activated with gypsum together with cement, the hydration products of slag are generally the same as for ordinary Portland cement (OPC); CSH-gel, Ettringite and monosulphate (Smocsyk [15] and Uchikawa [16]). The formation of Strätlingite (C_2ASH_8) is only to be expected if alkali hydroxide is added to the slag cement according to Richartz [17] or if the blast furnace slag is activated with alkali hydroxide (Regourd [18] and Forss [19]). Like fly ash, GGBS has a somewhat variable composition and it may not be entirely true that it does not consume calcium hydroxide during its reaction (Hinrichs and Odler [20]), which may depend on its content of CaO relative to SiO_2 and Al_2O_3 . The introduction of more calcium aluminate hydrate in the system by GGBS will destabilize ettringite (AFt) and form more calcium monosulphate hydrate (AFm), as for fly ash (Fig. 2).

3.3 Carbonates

Carbonates need CAH to react with. The combination of limestone together with an aluminate containing pozzolan (e.g. fly ash) makes calcium carbonate react more since it is too little CAH available from the clinker. This synergistic reaction lead to more bound water, reduced porosity and thereby higher strength has been documented by De Weerd and Justnes [4, 21] and De Weerd *et al* [22-26].

The synergetic effect between fly ash and limestone powder is attributed to the impact of CaCO_3 on the AFm phases which has been documented for pure OPC (Lothenbach *et al* [27]). AFm can in general be written $[\text{Ca}_2(\text{Al},\text{Fe})(\text{OH})_6]\text{X}\cdot x\text{H}_2\text{O}$ where X denotes one formula unit of a singly charged anion or half a formula unit of a doubly charged anion (e.g. OH^- , SO_4^{2-} or CO_3^{2-} often referred to as OH-AFm, SO_4 -AFm and CO_3 -AFm. The impact of limestone powder is amplified as fly ash provides additional aluminates to the system by its pozzolanic reaction with calcium hydroxide from the cement hydration. The effect is demonstrated by Eqs. 6 and 7 showing the increased volume of the hydration phases in the reactions. The remains and original boundary of a partial reacted limestone grain in a cement-fly ash-limestone blend is shown in Fig. 2.

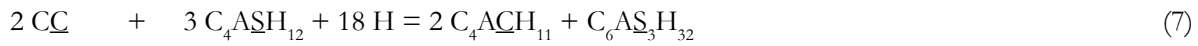
It is beneficial to blend calcium carbonate with something forming either more C_3AH_6 or sulphate-AFm that can react with calcium carbonate to bind more water and increase volume;



m = 1.00 g	3.78	0.90	5.68
M = 100.09 g/mol	378.29	18.02	568.50
n = 9.99 mmol	9.99	49.95	9.99
ρ = 2.67 g/ml	2.52	0.998	2.17

V = 0.375 ml 1.500 0.902 2.618

According to the reaction in Eq. 6, 100 g calcium carbonate (≈ 1 mol) would bind 90 g (≈ 5 mol) extra water. The total increase in volume of solids will then be $(2.618 - (0.375 + 1.500)) \cdot 100 \text{ vol\%} / (0.375 + 1.500) = 39.6 \text{ vol\%}$. So with a lot of C_3AH_6 produced, this will matter. Alternatively, the reaction with sulphate AFm will be as follows;



m = 1.00 g	9.33	1.62	5.68	6.27
M = 100.09 g/mol	622.52	8.02	568.50	1255.11
n = 9.99 mmol	14.99	9.91	9.99	5.00
$\rho = 2.67 \text{ g/ml}$	2.015	0.998	2.17	1.778
V = 0.375 ml	4.630	1.623	2.618	3.526

According to the reaction in Eq. 7, 100 g calcium carbonate (≈ 1 mol) would bind 162 g (≈ 9 mol) extra water. The total increase in volume of solids will then be $((3.526 + 2.618) - (0.375 + 4.630)) \cdot 100 \text{ vol\%} / (0.375 + 4.630) = 22.8 \text{ vol\%}$. This is just above half the volume increase compared to limestone reacting directly with C_3AH_6 in Eq. 6.

Small additions of limestone powder result in the formation of calcium hemicarboaluminate hydrate (“hemicarbonate”) instead of calcium monosulphoaluminate hydrate (“monosulphate”) and thereby stabilizing ettringite. Larger limestone additions lead to the formation of calcium monocarboaluminate hydrate (“monocarbonate”). Due to the difference in specific volume of these phases, and higher amount of hydrate water in ettringite or AFt (32 mole) vs. AFm (12 mole), an increase in the total volume of hydration phases can be observed. This will in turn lead to a reduction in porosity and consequently to an increase in strength. Segments of XRD profiles of paste showing how phases shift for different mixes of cement, cement with fly ash (FA), cement with limestone (L) and cement with limestone and fly ash (FA/L) are plotted in Fig. 2. The validity of the synergistic effect of limestone/fly ash for different clinker types and fly ash types was documented by De Weerd *et al* [28].

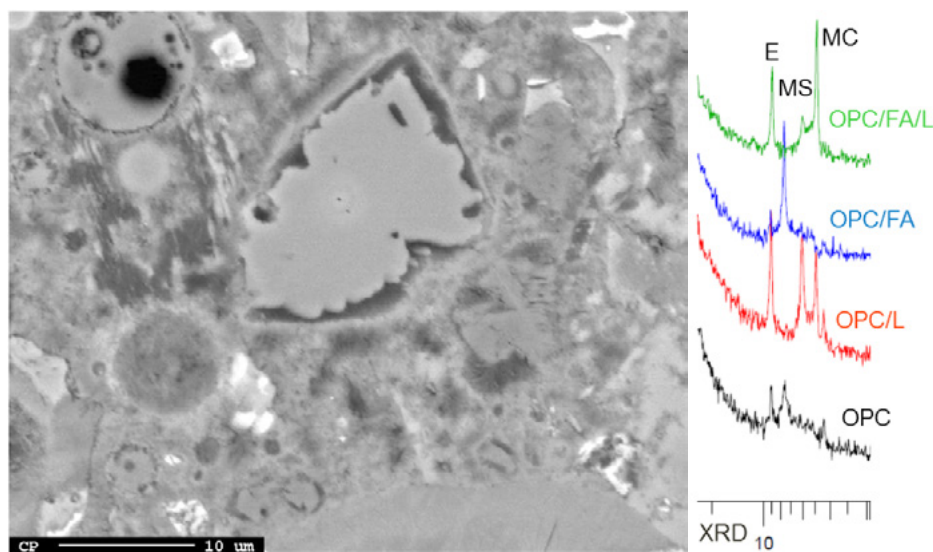


Figure 2: Left; BSE of paste consisting of cement/fly ash/limestone showing boundaries of a partly

reacted limestone in the centre and a circular fly ash particle in the upper left. Right; Segments of XRD profiles for OPC with combinations of fly ash (FA) and limestone (L). OPC alone gives a mixture of ettringite (E) and monosulphate (MS). OPC/L stabilises E and form hemicarboxate and monocarbonate (MC). OPC/FA destabilises E and form MS. OPC/FA/L stabilises E and forms mainly MC.

It is of course not only fly ash that will form aluminates having a synergistic reaction with limestone, but also GGBS and calcined clay (Antoni *et al* [29]) or marl. Fig. 3 (photo to the left) shows a BSE image of a mortar where 35% of cement has been replaced with calcined marl, and the formation of CAH in the centre of the image. A wave length dispersive spectrum (WDS) revealed the composition 16.5 Ca, 8.3 Al and 0.4 Fe in atom% (mark of electron beam can be seen), giving $\text{Ca}/\text{Al} = 2.0$, so it is $\text{C}_4\text{ACH}_{11}$. (Justnes and Østnor [30]). The segment of XRD to the right in Fig. 3 reveals the formation of $\text{C}_4\text{ACH}_{11}$, calcium carboaluminate hydrate, in a mixture of calcined marl and calcium hydroxide (Justnes and Østnor [31]).

Neither is it necessary to use limestone, CaCO_3 , as carbonate source, since dolomite, $\text{CaMg}(\text{CO}_3)_2$, will function as well and even lead to higher strength through formation of voluminous hydrotalcite; $\text{Mg}_6\text{Al}_2(\text{CO}_3)(\text{OH})_{16} \cdot 4\text{H}_2\text{O}$, according to Zajac *et al* [5].

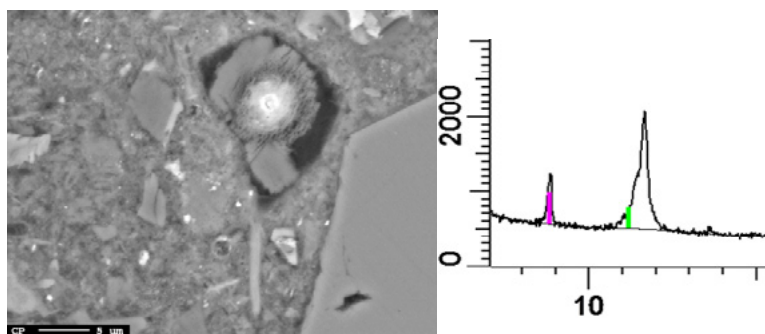


Figure 3: Left; BSE image of mortar where 35% cement is replaced with calcined marl and a CAH is formed in a void (Justnes and Østnor [30]). Right; XRD segment of a paste of calcined marl mixed with lime showing an illite peak (clay mineral) at $2\theta \approx 8.7^\circ$ and a peak from calcium monocarboaluminate hydrate at $2\theta \approx 11.7^\circ$ (Justnes and Østnor [31]).

4. Increasing reactivity of blended cements by accelerators

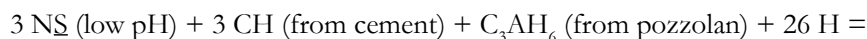
SCMs react in general slower than cement. Both GGBS and FA are activated by increased pH, but while GGBS is a latent hydraulic material, FA is a pozzolanic material consuming calcium hydroxide in producing hydraulic binder.

One advantage of using common potassium carbonate (K_2CO_3 or KC in short) or sodium carbonate (Na_2CO_3 or NC in short) as fly ash or slag activator, is that they are safe to handle and will form high pH *in situ* by reaction with calcium hydroxide from cement hydration;



and at the same time form calcium carbonate with high surface area that probably is faster reactive with calcium aluminate hydrates than limestone powder. Such *in situ* forming accelerators were utilized by Justnes [8] making lime-pozzolan mortars with high early strength. The disadvantage may be that alkali carbonates may retard the setting of cement and/or give somewhat lower long-term strength depending on total alkali content.

Sodium sulphate is also a good accelerator for aluminate containing pozzolana and slag involving in situ formation of NaOH (short hand notation NH) for further acceleration and formation of solid ettringite and/or monosulphate with increased water binding;



Shi and Day [32-25] studied the effect of Na_2SO_4 and CaCl_2 as chemical activators on the strength of lime-fly ash pastes. ASTM type C and F fly ashes were used in the 20% hydrated lime and 80% fly ash mixes (no cement) and the chemical activators were added in dosages up to 5% of the lime-fly ash mass. The pastes were prepared with a water/solid ratio of 0.35 for type F or 0.375 for type C fly ashes and cured moist at 50°C. Both Na_2SO_4 and CaCl_2 clearly increased the compressive strength of the mortars, but sodium sulphate was superior with respect to the 1 day strength. Unfortunately, are many chemical activation experiments performed at elevated temperatures being irrelevant for ready mix concrete, but still applicable for precast concreting.

Shi and Day [32] used X-ray diffraction (XRD) and scanning electron microscopy (SEM) to examine pastes with and without activators. The low lime fly ash (ASTM type F) without any activator had a CSH-like phase as principal hydration product, and the second major hydration product was found to be C_4AH_{13} . Minor products detected were ettringite (Aft) at early age and C_2ASH_8 at later age. The addition of sodium sulphate resulted in an increase of the Aft phase and a decrease in the C_4AH_{13} phase, which is in line with reaction 9. Calcium chloride activator led to formation of the solid solution $\text{C}_4\text{AH}_{13}\text{-C}_3\text{A}\cdot\text{CaCl}_2\cdot 10\text{H}_2\text{O}$.

Qian *et al* [36] compared the effect of grinding for 30 minutes in a ball mill and chemical activation through the addition of 3-4% Na_2SO_4 . They found that chemical activation was more efficient than ordinary grinding. Chemical activation increased the 3 and 7 day-strength of cement replaced with 30% fly ash by 5-10 MPa.

Lee *et al* [37] studied the strength and microstructure of fly ash-cement systems containing the accelerators Na_2SO_4 , K_2SO_4 and triethanolamine. The accelerators increased the amount of ettringite at early ages. The authors concluded that accelerators were a viable solution to increase early compressive strength of concrete with high amounts of fly ash.

High dosages of alkaline salts as accelerators may give lower long-term strengths and may also be negative in terms of alkali-aggregate reactions (AAR). Another approach is to boost the cement reactivity rather than the SCM reactivity. Hoang [38] investigated accelerators for mortars where cement was replaced with 30% fly ash. He arrived at a ternary accelerator based on 0.2% sodium thiocyanate (NaSCN), 0.1% diethanolamine (DEA) and 0.05% glycerol and showed that a 0.35% dosage of this ternary accelerator gave same improved strength after 2 days at 5°C (41°F) as 4% sodium sulphate (Na_2SO_4) + 0.4% NaSCN (total 4.4%, more than 12x increased dosage), but the 28 days strength was higher for the low dosage of ternary accelerator. The ternary accelerator also fulfilled the requirements to a hardening accelerator according to EN 934-2 [39] at a 0.35% dosage with +60% 2 day strength at 5°C and +30% 1 day strength at 20°C relative to reference and was patented (Hoang *et al* [40]).

5. Rheology of blended cements

Cement blended with SCMs with substantially higher specific surface than cement, and in particular irregular particles shapes with voids, leads to inferior rheology compared to ordinary cement. Justnes and Ng [41] published a review on the influence of all components of a concrete matrix (i.e. cement type, SCMs and mineral fillers). Some information for the individual SCMs are repeated in the respective sub-sections.

4.1 Silica fume

Vikan and Justnes [42] made cement pastes with a constant total particle volume of 0.442 corresponding to w/c about 0.40 as basis, while the amount of silica fume (SF) was replacing cement in volume increments of 0.01 from 0.00 to 0.06. They concluded that the influence of SF replacement on the flow resistance (FR) depended on the plasticizer type: FR increased with increasing SF replacement when naphthalene sulphonated – formaldehyde condensate (NSF) was added as a plasticizer and decreased when polycarboxylic ether (PCE) was added. Increased FR and gel strength with SF replacement using SNF may be caused by early gel formation due to water binding by SF or the ionization of SF surface due to the high pH and possible bridging with polyvalent cations like calcium. Decreased FR with increasing SF replacement using PCE was explained by the dispersing power of PCE coupled with SF packing between cement grains displacing water or by a ball-bearing effect of silica spheres.

4.2 Fly ash

Ng and Justnes [43] studied cementitious paste where OPC were replaced by siliceous fly ash (FA) in increments of 20 to 60% by mass and with a constant water-to-powder ratio of 0.36. They investigated the effect of 5 plasticizers; lignosulfonate (LS), NSF and 3 PCEs. Some results are presented here, but Ng and Justnes [44] have presented detailed results for one PCE. The flow resistance (FR) decreased steadily with increasing replacement of OPC by FA as shown in Fig. 4 in spite of increased total volume of solids since the density of FA is lower than OPC. The decrease in FR is due to the spherical nature of FA and the low reactivity of the glass phase at this early stage. Furthermore, there is much lower interaction of the plasticizers with FA than with cement, so the effective plasticizer-to-cement ratio is increasing and thereby also the retardation of the cement as illustrated in Fig. 5 for NSF.

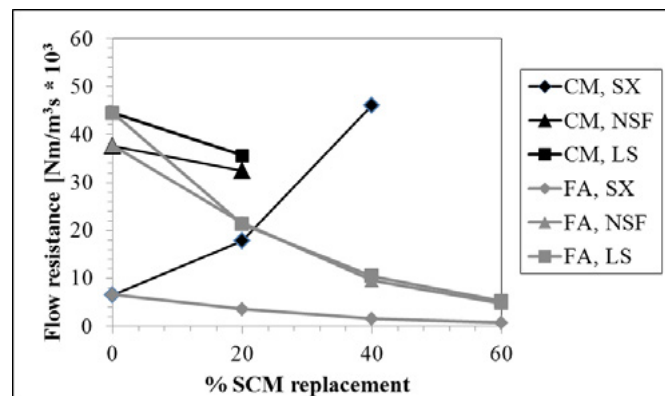


Figure 4: Flow resistance as a function of OPC replacement by SCM, fly ash (FA) or calcined marl (CM) with 0.2% dry plasticizer LS, NSF and a PCE named SX) of powder mass.

4.3 Blast furnace slag

Investigations on admixture interactions with cement blended with ground blast furnace slag are limited. Blast furnace slag consists of a glass phase with in the order of 40% CaO. The surface is believed to have calcium-sites capable of coordinating with plasticizers unlike the glassy phase of siliceous fly ash, but still to a smaller extent than for OPC.

Palacios *et al* [45] studied the effect of a number of plasticizers on the yield stress and plastic viscosity of alkali activated slag (AAS) and OPC pastes. They concluded that the adsorption of the plasticizers on AAS pastes was independent of the pH of the alkaline solutions used and lower than on OPC pastes. However, the effect of the admixtures on the rheological parameters depended directly on the type and dosage of plasticizer as well as of the binder used and, in the case of the AAS, on the pH of the alkaline activator solution. In 11.7-pH NaOH-AAS pastes the dosages of plasticizers required to attain similar reduction in

the yield stress were ten-fold lower than for Portland cement. For this pH the plasticizers showed a fluidizing effect considerably higher than in OPC pastes. In 13.6-pH NaOH-AAS pastes, the only plasticizer to affect the rheological parameters was NSF due to its higher chemical stability in such extremely alkaline media.

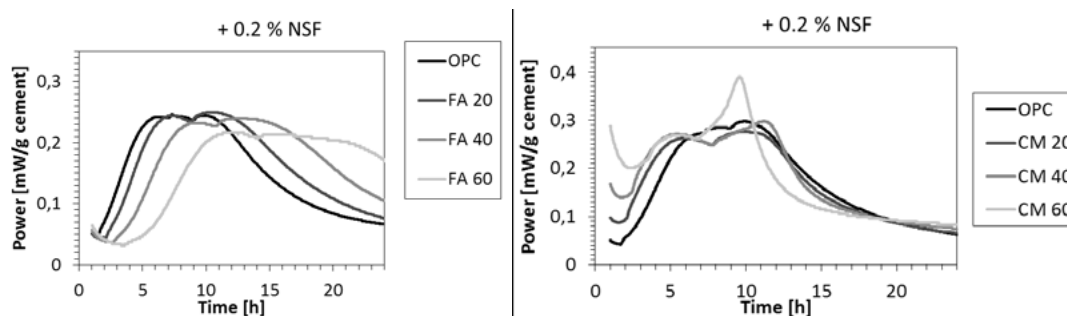


Figure 5: Heat of hydration (Power) evolution per cement mass for cementitious pastes with 0 (OPC), 20 (FA20), 40 (FA40) and 60% (FA60) replacement of OPC with FA to the left and with 0 (OPC), 20 (CM20), 40 (CM40) and 60% (CM60) replacement of OPC with CM to the right. All pastes are plasticized by 0.2% dry NSF of powder mass.

4.4 Calcined clay

Ng and Justnes [43] studied also cementitious paste where OPC were replaced by calcined marl (CM) in increments of 20 to 60% by mass and with a constant water-to-powder ratio of 0.36. They investigated the effect of the same 5 plasticizers; LS, NSF and 3 PCEs as for fly ash. The flow resistance (FR) plotted in Fig. 4 shows that it decreased slightly from 0 to 20% OPC replacement by CM and 0.2% addition of dry plasticizer for LS and NSF. Workable mixes were not attained for these plasticizers at a 0.2% dosage for higher CM replacements. For 0.2% PCE (SX) addition, FR increased with increasing OPC replacement by CM until 40%, while the 60% was not workable at this PCE dosage. Reasons for lower workability when OPC is replaced by CM are higher volume of solid due to lower density, higher water absorption by its porous nature and less reactive surface with less calcium sites than OPC. CM surface is assumed to be more reactive and have more Ca-sites than siliceous fly ash (FA) and adsorb more plasticizer. This is also reflected in the heat of hydration evolution curves when OPC is replaced with CM using NSF leading to acceleration rather than retardation for the FA replacement as seen in Fig. 5. This indicates that the effective plasticizer-to-cement ratio is less in the case of CM replacement than for FA replacement.

5. Influence of SCMs on durability of blended cements

5.1 General

There is a general dilemma in all accelerated durability testing: How can the exposure be sufficiently accelerated in order to give in a relative short time the same environmental load as a long-term natural exposure? This is usually sought achieved by increasing the exposure temperature (e.g. alkali aggregate reactions) or by increasing the concentration of the aggressive component (e.g. carbonation).

Increased temperature prior to exposure is also often used to achieve a more mature cementitious binder since SCMs often react much slower than the cement hydrate at ambient temperature and many of the degradation mechanisms happens slowly over years. However, it is important to not raise the temperature so high that changes occur in the binder that will not happen in practice. For instance it is well known, that the CSH gel becomes coarser and more porous already at 50°C (Kjellsen *et al* [46-48]) and fly ash/lime mixes might have a phase change when cured at 38°C relative to 20°C (De Weerd and Justnes [21]). Another example is paste where cement is partly replaced by calcined clay as SCM and cured at 38°C (Danner [49]) where dense areas of the hydrogarnet katoite formed and not seen at 20°C.

5.2 Chloride ingress

Chloride ingress is not detrimental to the binder itself but may induce corrosion of reinforcement steel in spite of high pH when exceeding a certain threshold value of chloride at the steel surface. The required total chloride content at the rebar to initiate corrosion is often taken as 0.1% Cl of concrete mass irrespectively of the binder type. Chloride binding is not taken into account even though it is the chlorides in the pore water next to the steel that are destabilizing the protective oxide layer created by the high pH. Many refer to a certain Cl⁻/OH⁻ ratio in order to initiate steel corrosion, but the values scatter. The following conclusions were made from a state-of-the-art report on critical chloride level (Angst and Vennesland [50]); “A lot of studies have been undertaken in the context of critical chloride content and the published results scatter in a wide range. The reported results span from 0.02 to 3.08% total chloride by weight of binder and thus over two orders of magnitude. Published Cl⁻/OH⁻ ratios even range from 0.03 to 45 and thus over three orders of magnitude.”

Even though pozzolanic SCMs consume calcium hydroxide (CH), the remaining CH will buffer pH to 12.5, albeit it may be reduced from pH 13.2 given by the alkali hydroxides as long as SCM prevails. Alumina containing SCMs may in addition form CAH that will lead to increased chemical binding of chlorides as Friedel’s salt; $\text{Ca}_3\text{Al}_2\text{O}_6 \cdot \text{CaCl}_2 \cdot 12\text{H}_2\text{O}$, as well as increased adsorption on CSH-gel as more gel is formed on the expense of CH in the pozzolanic reaction. Thus, it is difficult to judge how SCMs will affect the Cl⁻/OH⁻ ratio. If properly dispersed, SCMs will in general also refine the porosity of the binder and reduce the diffusion rate of aggressives as chloride.

An example of chloride ingress profiles in mortars with increasingly volume replacement of cement by calcined marl is shown in Fig. 6 (Justnes and Østnor [30]) revealing that chloride ingress is substantially reduced up to a cement replacement of 50 vol%. Such profiles of *total* chloride content is often erroneously (Justnes and Geiker [51]) used to be fitted to solutions of Fick’s 2nd law of diffusion to yield a surface concentration of chlorides and an apparent diffusion coefficient that is further used in service life modelling of concrete structures, even though it is only the *free* chlorides that are moving. Another benefit of SCMs is increased electrical resistivity as exemplified in Fig. 7 for the same mortars as in Fig. 6. A high electrical resistivity brought about by a combination of porosity segmentation and reduced ion activity (i.e. hydroxyl ions are the most important charge carriers) in the pore fluid, may also reduce corrosion rate of steel once it is initiated.

Fidjestøl and Justnes [52] investigated the chloride profiles in a quay structure in Gothenburg harbor after 24 years of service. The water in the harbor is partly brackish with an average chloride concentration of 1.4% as opposed to 1.9% in Atlantic waters. The quay was cast with different segments of concrete with 5% silica fume and without, and if the chloride profiles are fitted to the solution of Fick’s 2nd law of diffusion it resulted in apparent diffusion coefficients of 0.32 and $0.90 \cdot 10^{-12} \text{m}^2/\text{s}$ for 5% and 0% silica fume, respectively.

Thomas and Bamforth [53] investigated the effect of cement replacement by 30% fly ash or 70% GGBS on chloride ingress in concrete blocks naturally exposed to seawater spray over a period of several years with the objective of finding the decay coefficient (m) of the apparent diffusion coefficient in Eq. 10;

$$D_t = D_{\text{ref}} \cdot (t_{\text{ref}}/t)^m \quad (10)$$

where

D_t = apparent diffusion coefficient at time t

D_{ref} = apparent diffusion coefficient at a given reference time, e.g. 28 days

m = decay coefficient

Thomas and Bamforth [53] found $D_{28d} = 8, 6$ and $25 \cdot 10^{-12} \text{m}^2/\text{s}$ for reference, 30 FA and 70% GGBS, respectively, with corresponding values $m = 0.1, 0.7$ and 1.2 . In spite of higher D_{28d} , the accumulated chloride ingress in concrete with 30% fly ash or 70% GGBS was about equal but much lower than reference after 2 years and onwards to 8 years. This illustrates the importance of mature samples with high dosages of SCMs prior to accelerated exposure.

Sometimes ternary mixes are beneficial, as shown by Thomas *et al* [54] where cement replaced by 25% FA and 8% SF resulted in lower chloride ingress than either component alone, probably by a combination of improved particle packing and increased reactivity.

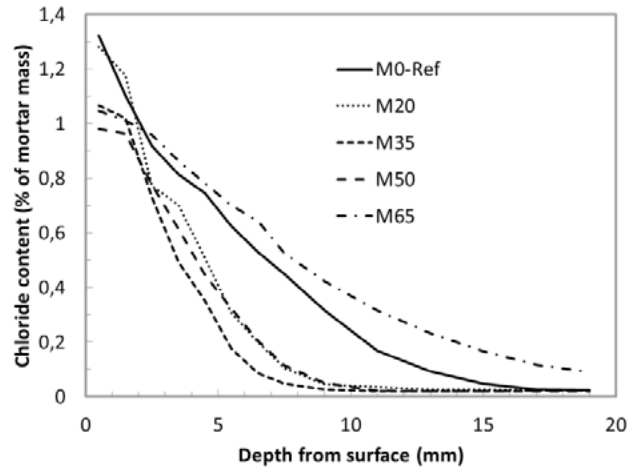


Figure 6: Chloride ingress in mortars where cement is replaced with 0 (M0), 20 (M20), 35 (M35), 50 (M50) and 65 (M65) vol% calcined marl after exposure for 35 days to 165 g NaCl/liter (Justnes and Østnor [30]).

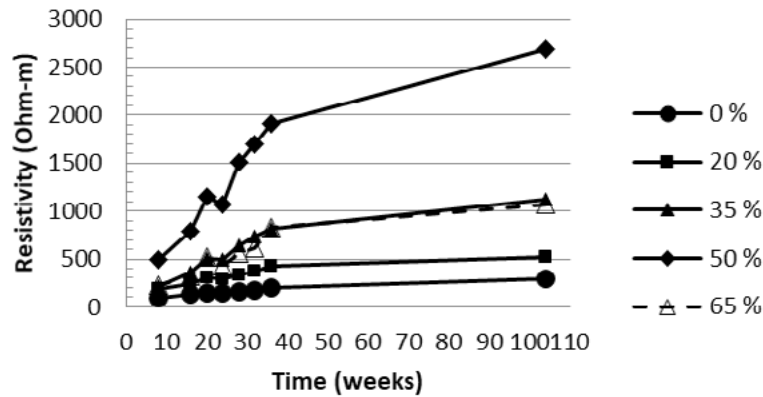
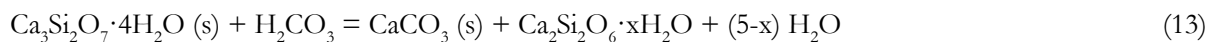


Figure 7: Resistivity of mortars where cement is replaced with calcined marl from 0-65 vol% as a function of time.

5.3 Carbonation

Carbonation is actually a neutralization reaction between carbonic acid, H_2CO_3 (i.e. CO_2 dissolved in water) and alkaline components in the blended cement;



According to Engelsen and Justnes [55], all hydrates formed by cement will carbonate, but CSH will probably only carbonate down to a Ca/Si of about 1. Based on stoichiometric considerations they calculated that about 72% of all CaO in an ordinary portland cement will carbonate. Visser [56] recently reviewed carbonation mechanisms and consequences of elevated CO₂ concentrations for accelerated testing. Carbonation reduces pH of the pore water from about 13 to around 9 and the carbonation front inwards is easily detected by spraying an indicator like phenolphthalein on a broken surface since it is colorless for pH <10 and pink above. The carbonation front is also believed to be relatively steep.

There are basically 2 reasons why cements blended with SCMs are more prone to carbonation than ordinary portland cements; 1) the physical thinning effect since there is less cement per volume unit to produce calcium hydroxide and 2) the chemical pozzolanic effect of some SCMs consuming calcium hydroxide. The question is whether or not their hydration products will carbonate as they tend to produce CSH of low C/S less prone to carbonation under natural conditions ($\approx 0.04\%$ CO₂) even though they might carbonate at $\geq 1\%$ CO₂.

The water-to-cement ratio (w/c) together with the amount and volume of hydration products determines the connectivity of pores and also the carbonation depth as shown in Fig. 8 for mortar where OPC is replaced by FA and GGBS as function of w/c and compared to OPC. It can be seen that a mortar with 17% replacement of cement by FA carbonates only slightly faster than for cement replaced with 48% GGBS at the same w/c. Thus, it seems to be controlled by total CaO in the system which is about 52% for both.

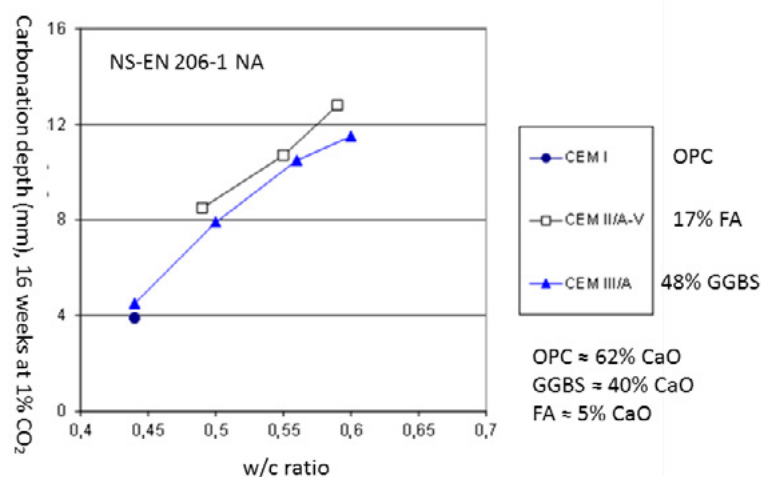


Figure 8: Carbonation depth (mm) of mortar where cement has been replaced with 17% fly ash containing $\approx 5\%$ CaO or 48% GGBS containing $\approx 40\%$ CaO as a function of w/c and compared to OPC (CEM I) containing $\approx 62\%$ CaO after exposure for 16 weeks to 1% CO₂ at 60% RH and 20°C. Samples preconditioned 28 d in water and 14 d at 50% RH.

Justnes and Østnor [30] tested the carbonation rate of mortars with increasing volume replacement of cement by calcined marl and constant water-binder ratio for carbonation depth versus square root of time. Such a plot is expected to be linear if diffusion controlled, but in this case it is curved for replacement levels ≥ 35 vol%. This might be due to formation of increasing amount of AFt (stabilized by carbonate) and AFm rich in crystal water. When these phases carbonate, they form calcium carbonate and gibbsite while the crystal water goes back to liquid, which leads to increased porosity forming pathways for increased carbonation rate. Calcined clay/marl reacts much faster than for instance fly ash.

Generally speaking, the carbonation rate will increase with increasing SCM at constant w/c and curing time. However, when the concrete is proportioned to give same 28 days strength, the carbonation rate

seems to be similar irrespectively of SCM according to Thomas [3]. Studies that employ enriched CO₂ to accelerate carbonation tend to overestimate the carbonation rate in concrete with SCMs (Thomas *et al* [57]). Concluding from short-term tests (< 5 years) may overestimate the negative impact of fly ash on carbonation rates in concrete (Hobbs [58]).

5.4 Alkali aggregate reactions (AAR)

Alkali aggregate reactions (AAR) are most often caused by dissolution of reactive silica in the aggregate by alkali hydroxides in the pore solution, which turn into a viscous, swelling gel when it meets the paste binder and alkalis partly ion exchange with calcium.

Replacing cement with SCMs generally reduce expansion due to AAR (Thomas [59]). This has in general been thought to be caused by a reduction in pH (i.e. hydroxyl concentration) of pore water and a lower content of calcium hydroxide. In the author's opinion, the reduction in pH will be the case as long as the alkalis are busy in dissolving SCM in the catalytic way outlined in Eq. 3, but the implication is that this may cause only a delay of AAR until the SF has reacted totally. Bérubé and Duchesne [60] showed indeed that SF merely postpones expansion due to AAR. Nevertheless, SF as a preventative against AAR, together with other improvements in construction procedures, has found its application in Iceland where all cement has been interground with 7-8 % SF to combat the problem (Asgeirsson [61]). Fournier *et al* [62] also showed that >7% SF was able to control ASR.

According to Thomas [3] the level of cement replacement by SCM required to control AAR expansion increases as 1) SiO₂ content of SCM decreases, 2) CaO of SCM increases, 3) alkali content of SCM increases, 4) alkali availability in the concrete increases and 5) reactivity of the aggregate increases. Shehata and Thomas [63] showed that low calcium fly ashes (ASTM Class F) are much more effective in reducing AAR expansion (typical cement replacement level >20%) than high calcium fly ashes (ASTM class C). Shehata and Thomas [64] demonstrated that the required level of low calcium fly ash could be reduced to 10% when combined with 5% SF as a ternary blend. Thomas and Innis [65] found that North American GGBS at a cement replacement level of > 40% was able to control expansion caused by AAR. Bleszynski *et al* [66] showed that GGBS in combination with SF as a ternary blend including cement was better than GGBS replacement alone in reducing AAR expansion. Ramlochan *et al* [67] proved that highly reactive metakaolin at a cement replacement level > 10% was able to combat expansion due to AAR.

Some have suggested that the presence of alumina in SCMs contributes to prevent the release of alkali back to the pore solution by binding in the hydration products. However, Chappex and Scrivener [68] showed that this effect is extremely small, and instead it was found that alumina is an inhibitor of silica dissolution (Chappex and Scrivener [69, 70]) in their system with metakaoline as SCM. Favier *et al* [71] showed that AAR is prevented by calcined clay mixed with limestone as well.

5.5 Sulphate attack

There are 2 forms of sulphate attack; 1) external where sulphates from the surroundings are penetrating the hardened concrete forming expanding ettringite and 2) internal that can be caused by decomposition of ettringite during hot curing exceeding 70°C and later reformation and expansion after cooling (i.e. delayed ettringite formation shortened DEF). A special form of external sulphate attack can occur at low temperatures (<15°C) if the concrete contains limestone, namely the formation of thaumasite; Ca₃Si(OH)₆(CO₃)(SO₄)·2H₂O, that can take silicate from the CSH and turn it into a non-binding mush (Irassar [72]). A special form of internal sulphate attack is from aggregate containing iron sulfides that may oxidize to sulphates (Duchesne [73]).

The good performance of concrete with SCMs in a sulfate environment can be attributed to several

factors of which the most important are likely to be i) the refined pore structure and thus reduced mobility of harmful ions and ii) the lower calcium hydroxide content by thinning or pozzolanic reaction and iii) formation of more CAH that will at least delay formation of AFt since AFm must form first. The second factor leads to reduced formation of expansive gypsum (Eq. 14) and later ettringite from, for instance, calcium aluminate hydrates (Eq. 15) or monosulphate, AFm (Eq. 16), found in the hydrated concrete binder.



Based on molar volumes, it can be calculated that the reaction in Eq. 14 leads to 124% expansion of the solid (s). The reaction in Eq. 15 leads to 371% increase relative to the C_3AH_6 crystal (localized growth) or 89% relative to both C_3AH_6 and gypsum, while the reaction in Eq. 16 leads to 128 % expansion relative to the AFm phase only (localized growth) or 54 % expansion relative to both AFm and gypsum. These expansive reactions result in cracking and spalling if the stress exceeds the tensile strength of the binder. Scrivener [74] pointed out that ettringite needs to be supersaturated in order to create a pressure leading to expansion. Müllauer *et al* [75] studied sulfate attack mechanisms in detail.

When SF is used together with GGBS or FA as cement replacement (Carlsen and Vennesland [76] and Fidjestøl and Frearson [77]) these ternary mixtures have been found to be more resistant to sulfate attack than special sulfate resisting cements.

Kunther *et al* [78] showed an improvement of the sulphate resistance (50 g Na_2SO_4 /liter) for a cement with 70% GGBS relative to an OPC, and also that the expansion due to sulphate attack was substantially reduced when bicarbonate was present simultaneously (50 g Na_2SO_4 + 30 g NaHCO_3 /liter). They explained the latter effect by ettringite and gypsum becoming unstable in presence of bicarbonate and that the ettringite could not build up the crystallization pressure required to create expansion. An alternative explanation is that CO_3 -AFm is more stable than SO_4 -AFm and would prevent AFt formation.

Dehwah [79] exposed concrete specimen to 5% NaCl and sodium sulphate of concentrations 1, 2.5 and 4% solutions for up to 4 years. The concretes were based on two types of cement (ASTM C150 type I and V), as well as cement type I replaced by 10% silica fume, 20% fly ash or 70% GGBS. None of the concretes showed any deterioration after 4 years, indicating that Friedel's salt (Cl-AFm) may be more stable than monosulphate (SO_4 -AFm) at the experimental conditions.

Ghafoori *et al* [80] evaluated the sulfate resistance of concrete based on ASTM type V cement of different cement contents (and thereby w/c) when replaced with 0, 15, 20, 25 and 30% ASTM class F (siliceous) fly ash. They found that the improvement in sulfate resistance was only modest (15%) and that the required FA replacement increased with increasing cementitious content of the concrete.

Hossack and Thomas [81] studied the sulfate resistance at both 5 (41) and 23°C for mortars based on cements with limestone content varying from 4-22%. In their series cement was partly replaced with fly ash (ASTM types C and F), blast furnace slag, silica fume or metakaolin, as well as some ternary blends thereof. They found that SCMs greatly improved the sulfate resistance at 23°C, but higher SCM levels may be required when limestone is present. The greatest degree of resistance to sulphate attack was found with ternary mixes of silica fume with fly ash or blast furnace slag, as well as for high replacement levels of metakaolin. Ettringite, thaumasite and gypsum were found in all samples exposed to Na_2SO_4 at 5°C indicating a mixed form of sulfate attack. Abdalkader *et al* [82] investigated sulphate attack on mortars based on cement and cement blended with 10% limestone exposed for combined action of chloride (0,

0.5, 1 or 2% Cl and sulfate (0.6% SO_4^{2-}) for 630 days at 5°C. All specimens suffered from the thaumasite form of sulfate attack, with the exception of the combination of sulfate with 2% Cl. The degradation was more severe for samples with limestone. The better performance in combination with the highest chloride concentration was explained by increased Friedel's salt formation, possibly preventing ettringite formation that many consider a prerequisite for the formation of the isostructural thaumasite. Even though chloride may prohibit thaumasite formation it was still found in concrete with limestone filler exposed to sea water (0.27% SO_4^{2-} and 1.9% Cl) for 10 years outside Trondheim, Norway (De Weerd *et al* [83]).

When it comes to the effect of SCMs on internal sulphate attack, Rønne *et al* [84] published the effect of SF on expansion due to delayed ettringite formation (DEF), and the measurements for 2 years are plotted in Fig. 9 for OPC with 0 and 8% SF and $w/(c+SF) = 0.40$. The concrete was resting for 6 hours before being heated to the set temperature of 20, 70 or 85 °C with a rate of 12°C/h in a water bath that thereafter cooled down slowly to the ambient temperature of 20°C to mimic the temperature evolution in a massive structure driven by heat of hydration. The rest of the curing time was at 20°C and the volume of the specimens was monitored by weighing in water and air according to the principle of Archimedes. SEM confirmed ettringite formation in aggregate interfaces and cracks for the expanding specimens.

Ramlochan *et al* [85, 86] initial cured mortar samples at 95°C followed by storage in limewater at 23°C up to 1500 days. They found that 25% replacement of cement by SCMs containing alumina; such as fly ash (both ASTM class C and F), blast furnace slag and metakaolin, was able to prevent DEF while 8% silica fume only had limited effect (expansion reached 1.0% compared to reference expanding 2.8%).

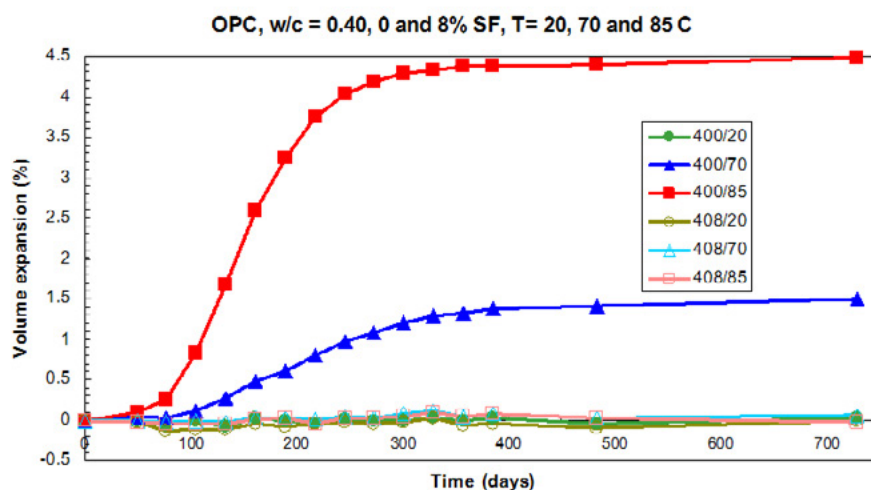


Figure 9: Volume changes of OPC concrete with $w/cm = 0.40$ with 0% (legend 400) and 8% (legend 408) SF initial cured at 20, 70 and 85°C followed by 20°C water curing > 2 years (Rønne *et al* [84]).

5.6 Freeze-thaw resistance

Concrete with a high degree of capillary saturation with water (>92%) can be damaged by repetitive freezing and thawing cycles (fatigue) since water expands 9% upon freezing and can create a hydraulic pressure forcing unfrozen water into smaller pores leading to cracking. This is usually mitigated by entraining small air bubbles with the help of appropriate admixtures. These well distributed air bubbles are empty and will function as pressure relief chambers upon freezing. Concrete with SCMs is believed to be equal resistant to freeze-thaw as concrete with ordinary portland cement providing that a good air void system is obtained by the aid of air entraining agents and that the concrete is well cured. SCMs react slower than OPC and concrete with SCM is thus more sensitive to improper workmanship.

There are indications that blended cement may be more sensitive to freeze-thaw under the influence of

thawing salts like sodium chloride (NaCl), and an interaction with aluminates forming Friedel's salt can not be ruled out. Residual carbon in fly ash is known to create a problem by adsorbing air entraining agents leading to the need of higher dosages to obtain a good air void system. This can also be omitted by adding sacrificial agents that will preferentially adsorb to the free carbon (Jolicoeur *et al* [87]). There have also been reports on concrete with high blast furnace slag content that become more prone to freeze-thaw damage under influence of thawing salts (Panesar and Chidiac [88], Giergiczny *et al* [89]), and in particular when carbonated (Utgenannt [90]). A possible remedy against the inferior freeze-thaw resistance of concrete with GGBS seems to be surface treatment with sodium monofluorophosphate (Sisomphon *et al* [91]).

7. Conclusions

Concrete based on cement blended with SCMs, or where ordinary cement is partly replaced with SCMs, is more durable in general than concrete based on ordinary portland cement at equal water-to-binder ratio, when well cured and when the SCM is properly dispersed. The main reasons are a denser microstructure either due to improved particle packing initially or more binder (CSH or CAH) formed on the expense of calcium hydroxide (CH) either due to displacement of cement or pozzolanic reaction.

The exception is carbonation resistance which is increasing with increasing cement replacement by SCMs at equal water-to-binder ratio due to less CH, even though most calcium containing components will carbonate in the end. However, the increased carbonation rate can be counteracted by reducing the water-to-binder ratio, but if this is achieved by increasing the binder content the positive effect of using SCM_s for the sake of environment will be reduced.

Limestone can also be considered as a SCM, in particular in combination with other SCMs producing CAH that can be a reactant for a synergic reaction binding even more water that will help densifying the porosity of the binder.

The resistance to ingress of chemicals depends largely on the AFm phases in the binder and which one is the most stable. For instance, the binding of chlorides is improved by the presence of CAH forming Friedel's salt and ingress is delayed.

8. References

1. Justnes, H., "How to make concrete more sustainable", *1st International Conference on Concrete Sustainability*, May 27-29, 2013, Tokyo, Japan, Paper S1-1-2, 92-99 (ISBN 978-4-86384-041-6-C3050).
2. Lothenbach, B.; Scrivener, K. and Hooton, R.D., "Supplementary cementing materials". *Cement and Concrete Research*, V. 41, 2011, pp. 1244-1256.
3. Thomas, M., *Supplementary Cementing Materials in Concrete*. 1st Ed. CRC Press, Taylor & Francis Group, 2013, 190 pp. (ISBN 978-1-4665-7298-0).
4. De Weerd, K. and Justnes, H., "Synergic Reactions in Triple Blended Cements", *11th NCB International Seminar on Cement and Building Materials*, 17-20 November, 2009, New Delhi, India, pp. 257-261.
5. Zajac, M.; Bremseth, S.K.; Whitehead, M. and Ben Haha, M., "Effect of CaMg(CO₃)₂ on hydrate assemblages and mechanical properties of hydrated cement pastes at 40°C and 60°C", *Cement and Concrete Research*, V. 65, 2014, pp. 21 -29.
6. Justnes, H., "Silica Fume in High-Quality Concrete - A Review of Mechanism and Performance", *9th CANMET/ACI International Conference on Fly Ash, Silica Fume, Slag and Natural Pozzolans in Concrete*, ACI SP-242, Ed. Mohan Malhotra, Warszawa, Poland, 21-25th May, 2007, SP-242-6, 63-78.

7. Scrivener, K.L.; Lothenbach, B.; De Belie, N.; Gruyaert, E.; Skibsted, J.; Snellings, R. and Vollpracht, A., “RILEM TC 238-SCM: hydration and microstructure of concrete with SCMs”, *Materials and Structures*, 2015, DOI 10.1617/s11527-015-0527-4.
8. Justnes, H., “Accelerated Hardening of Mortars with Hydraulic Binders of Silica Fume/Lime”, *Nordic Concrete Research*, Publication No. 17, 2/1995, pp. 30-41.
9. Justnes, H., “Hydraulic binders based on condensed silica fume and slaked lime”, *9th International Congress on the Chemistry of Cement*, New Delhi, India, 23-28 November, 1992, V. III, pp. 284-290.
10. Justnes, H., “Kinetics of Reaction in Cementitious Pastes Containing Silica Fume as Studied by ²⁹Si MAS NMR”, in *Nuclear Magnetic Resonance Spectroscopy of Cement-based Materials* (Eds. P. Colombet, A.-R. Grimmer, H. Zanni and P. Sozzani), Springer Verlag, Berlin, 1998, pp. 245-268.
11. Justnes, H.; Meland, I.; Bjørgum, J.O. and Krane, J., «A ²⁹Si MAS NMR Study of the Pozzolanic Activity of Condensed Silica Fume and the Hydration of Di- and Tricalcium Silicate”, *Advances in Cement Research*, V. 3, 1990, pp. 111-116.
12. Justnes, H.; Sellevold, E.J. and Lundevall, G., “High Strength Concrete Binders. Part A: Reactivity and Composition of Cement Pastes with and without Condensed Silica Fume”, *4th ACI International Conference on Fly Ash, Silica Fume, Slag and Natural Pozzolana in Concrete*, Ed.: V.M. Malhotra, Istanbul, May 3-8, 1992, CANMET/ACI SP 132-47, V. 2, pp. 873-889.
13. Sellevold, E.J. and Justnes, H., “High-Strength Concrete Binders. Part B: Non-evaporable Water, Self-desiccation and Porosity of Cement Pastes with and without Condensed Silica Fume”, *4th CANMET/ACI International Conference on Fly Ash, Silica Fume, Slag and Natural Pozzolana in Concrete*, Ed.: V.M. Malhotra, Istanbul, May 3-8, 1992, CANMET/ACI SP 132-48, V. 2, pp. 891-902.
14. Barbhuiya, S.; Mukherjee, S. and Nikraz, H., “Effects of nano-Al₂O₃ on early-age microstructural properties of cement paste”, *Construction and Building Materials*, V. 52, 2014, pp. 189-193.
15. Smolczyk, H.-G., “The hydration products of cements with high contents of blast furnace slag”, *Zement-Kalk-Gips International*, V. 18, 1965, pp. 238-246.
16. Uchikawa, H., “Effect of blending components on hydration and structure formation”, *8th International Congress on the Chemistry of Cement*, Rio de Janeiro, V. 1, 1986, pp. 249-280.
17. Richartz, W., “On the formation of the aluminous hydrate phases during setting of cement”, *Tonind.-Ztg.*, V. 90, 1966, pp. 449-457.
18. Regourd, M., “Structure and behaviour of slag Portland cement hydrates”, *7th International Congress on the Chemistry of Cement*, Paris, 1980, Vol. I, pp. III-2/10-III-2/26.
19. Forss, B., “F-cement, a new low-porosity slag cement”, *Sil. Ind.* V. 48, 1983, pp. 79-82.
20. Hinrichs, W. and Odler, I., “Investigation of the hydration of Portland blast furnace slag cement: hydration kinetics”, *Advances in Cement Research*, V. 2, 1989, pp. 15-20.
21. De Weerd, K. and Justnes, H., “Microstructure of Binder from the Pozzolanic Reaction between Lime and Siliceous Fly Ash, and the Effect of Limestone Addition”, *1st International Conference on Microstructure Related Durability of Cementitious Composites*, 13-15 October, 2008, Nanjing, China, RILEM Proceeding PRO 61, pp. 107-116.
22. De Weerd, K.; Justnes, H.; Kjellsen, K.O. and Sellevold, E.J., «Fly Ash-Limestone Ternary Composite Cements: Synergy Effect at 28 days”, *Nordic Concrete Research*, Publication No. 42, 2/2010, pp. 51-70 (ISBN: 978-82-8208-023-1).

23. De Weerd, K.; Kjellsen, K.O.; Sellevold, E.J. and Justnes, H., "Synergy between Fly Ash and Limestone Powder in Ternary Cements", *Cement and Concrete Composites*, V. 33, 2011, pp. 30-38.
24. De Weerd, K.; Ben Ha-Ha, M.; Le Saout, G.; Kjellsen, K.O.; Justnes, H. and Lothenbach, B., "Hydration mechanism of ternary Portland cements containing limestone powder and fly ash", *Cement and Concrete Research*, V. 41, 2011, pp. 279-291.
25. De Weerd, K.; Sellevold, E.J.; Kjellsen, K.O. and Justnes, H., "Fly ash – Limestone Ternary Cements – Effect of Component Fineness", *Advances in Cement Research*, V. 23, 2011, pp. 203-214.
26. De Weerd, K.; Justnes, H. and Kjellsen, K.O., "Synergic Effect between Fly Ash and Limestone Powder in Portland Composite Cements", XXI Nordic Concrete Research Symposium, Hämeenlinna, Finland, May 2011, *Nordic Concrete Research Publication No. 43*, pp. 297-300.
27. Lothenbach, B.; Le Saout, G.; Gallucci, E. and Scrivener, K., "Influence of limestone on the hydration of Portland cements", *Cement and Concrete Research*, V. 38, 2008, pp. 848-860.
28. De Weerd, K.; Østnor, T.A.; Justnes, H.; Ben Haha, M. and Kjellsen, K.O., "Fly ash - limestone synergy in triple cement", *1st International Conference on Concrete Sustainability*, May 27-29, 2013, Tokyo, Japan, Paper S2-2-4, 510-515 (ISBN 978-4-86384-041-6-C3050).
29. Antoni, M.; Rossen, J.; Martirena, F and Scrivener, K., "Cement substitution by a combination of metakaolin and limestone", *Cement and Concrete Research*, V. 42, 201, pp. 1579-1589.
30. Justnes, H. and Østnor, T.A., "Durability and microstructure of mortar with calcined marl as supplementary cementing material", *XIII conference on Durability of Building Materials and Components (DBMC)*, Sao Paulo, Brazil, September 3-5, 2014, pp. 771-780
31. Justnes, H. and Østnor, T.A., "Designing Alternative Binders Utilizing Synergic Reactions", *5th International Conference on Non-traditional Cement and Concrete (NTCC2014)*, Edited by V. Bilek and Z. Keršner, 16-19 June, 2014, Brno, Czech Republic, 101-104 (ISBN 978-80-214-4867-4).
32. Shi, C., and Day, L.R., "Acceleration of the reactivity of fly ash by chemical activation", *Cement and Concrete Research*, V. 25, 1995, pp. 15-21.
33. Shi, C. and Day, L.R., "Pozzolanic reaction in the presence of chemical activators, Part I. Reaction kinetics", *Cement and Concrete Research*, V. 30, 2000, pp. 51-58.
34. Shi, C. and Day, L.R., "Pozzolanic reaction in the presence of chemical activators, Part II. Reaction products and mechanisms", *Cement and Concrete Research*, V. 30, 2000, pp. 607-613.
35. Shi, C. and Day, L.R., "Comparison of different methods for enhancing reactivity of pozzolans", *Cement and Concrete Research*, V. 31, 2001, pp. 813-818.
36. Qian, J., Shi, C. and Wang, Z., "Activation of blended cements containing fly ash", *Cement and Concrete Research*, V. 31, 2001, pp. 1121-1127.
37. Lee, C.Y., Lee, H.K. and Lee, K.M., "Strength and microstructural characteristics of chemically activated fly ash-cement systems", *Cement and Concrete Research*, V. 33, 2003, pp. 425-431.
38. Hoang, K. D., "Hardening Accelerator for Fly Ash Blended Cement", Thesis (PhD) at NTNU (Norwegian University of Science and Technology) 2012:336, 195 pp.
39. EN 934-2:2009. "European Standard: Admixtures for Concrete, Mortar and Grout. Part 2: Concrete Admixtures – Definitions, Requirements, Conformity and Labelling", *CEN (European Committee for Standardization)*, 28 pp.

40. Hoang K.D.; Geiker, M.R.; Justnes, H.; Rudberg, E. and Myrdal, R., “Hardening-Accelerator and a Method for Accelerating the Hardening of Hydraulic Binders and Mixtures Thereof”, WO2013066192 (A1) — 2013-05-10.
41. Justnes, H. and Ng, S., “Concrete Admixtures – Interactions with Cement, Supplementary Cementing Materials and Fillers”, *3rd International Symposium on Design, Performance and Use of Self-Consolidating Concrete, SCC’2014-China*, June 5-8, 2014, Xiamen, China, RILEM Proceedings PRO 93, 2014, p. 138 (ISBN 978-2-35158-143-8, e-ISBN 978-2-35158-144-5).
42. Vikan, H. and Justnes, H., “Rheology of cementitious paste with silica fume and limestone”, *Cement and Concrete Research*, V. 37, 2007, pp. 1512-1517.
43. Ng, S. and Justnes, H., “A Comparison on the Roles of Plasticizers in the Rheology and Hydration of Blended Cements”, *6th International Conference of the Asian Concrete Federation (ACF)*, 21-24 September, 2014, Seoul, South Korea, pp. 614-618.
44. Ng, S. and Justnes, H., “Rheological Properties and Early Hydration of Blended Cement Pastes with PCE Plasticizers”, *3rd International Symposium on Design, Performance and Use of Self-Consolidating Concrete, SCC’2014-China*, June 5-8, 2014, Xiamen, China, RILEM Proceedings PRO 93, pp. 162-169 (ISBN 978-2-35158-143-8, e-ISBN 978-2-35158-144-5).
45. Palacios, M.; Houst, Y.F.; Bowen, P. and Puertas, F., “Adsorption of superplasticizer admixtures on alkali-activated slag pastes”, *Cement and Concrete Research*, V. 39, 2009, pp. 670–677.
46. Kjellsen, K.O.; Detwiler, R.J. and Gjrv, O.D., ”Back scattered electron imaging of cement pastes hydrated at different temperatures”, *Cement and Concrete Research*, V. 20, 1990, pp. 308-311.
47. Kjellsen, K.O.; Detwiler, R.J. and Gjrv, O.D., ”Pore structure of plain cement pastes hydrated at different temperatures”, *Cement and Concrete Research*, V. 20, 1990, pp. 927-933.
48. Kjellsen, K.O.; Detwiler, R.J. and Gjrv, O.D., “Development of microstructure in plain cement pastes hydrated at different temperatures”, *Cement and Concrete Research*, V. 21, 1991, pp. 179-189.
49. Danner, T., “Reactivity of Calcined Clays”, Thesis (PhD) at NTNU (Norwegian University of Science and Technology), 2013:218, 229 pp.
50. Angst, U. and Vennesland, Ø., “COIN P4: Operational Service Life Design, SP 4.2: Critical chloride content. State-of-the-Art”, *SINTEF Report SBF BK A07037*, 2007-12-17, 54 pp. (downloadable from www.coinweb.no)
51. Justnes, H. and Geiker, M.R., “A Critical View on Service Life Predictions based on Chloride Induced Corrosion”, *2nd International Conference on “Microdurability” (Microstructure Related Durability of Cementitious Composites)*. Amsterdam, the Netherlands, 11-13 April, 2012, 13 pp.
52. Fidjestl, P. and Justnes, H., “Long Term Experience with Microsilica Concrete in a Marine Environment”, *Nordic Concrete Research*, Publication No. 31, 1/2004, pp. 30-39.
53. Thomas, M.D.A. and Bamforth, P.B., “Modelling chloride diffusion in concrete - Effect of fly ash and slag”, *Cement and Concrete Research*, V. 29, 1999, pp. 487-495.
54. Thomas, M.D.A.; Shehata, M.H.; Shashiprakash, S.G.; Hopkins, D.S. and Cail, K., “Use of ternary cementitious systems containing silica fume and fly ash in concrete”, *Cement and Concrete Research*, 29, 1999, pp. 1207-1214.

55. Engelsens, C.J. and Justnes, H., “CO₂-Binding by Concrete Structures during Life Cycle”, *2nd International Congress on Durability of Concrete (2nd ICDC)*, 4-6 December 2014, New Delhi, India, Paper 65, 10 pp.
56. Visser, J.H.M., “Influence of the carbon dioxide concentration on the resistance to carbonation of concrete”, *Construction and Building Materials*, V. 67, 2014, pp. 8-13.
57. Thomas, M.D.A.; Matthews, J.D. and Haynes, C.A., “Carbonation of fly ash concrete”, *4th CANMET/ACI International Conference on Durability of Concrete*, 2000, ACI SP-192, V. 1, pp. 539-556.
58. Hobbs, D.W., “Carbonation of concrete containing pfa”, *Magazine of Concrete Research*, V. 40, 1986, p. 143.
59. Thomas, M.D.A., “The effect of supplementary cementing materials on alkali silica reaction: A review”, *Cement and Concrete Research*, V. 41, 2011, pp. 1224-1231.
60. Bérubé, M.-A. and Duchesne, J., “Does Silica Fume merely postpone Expansion due to Alkali-Aggregate Reactivity?”, *9th International Conference on Alkali-Aggregate Reaction in Concrete*, 27-31 July, 1992, London, 71-80.
61. Asgeirsson, H., “Silica Fume in Cement and Silane for counteracting of Alkali-Silica Reactions in Iceland”, *Cement and Concrete Research*, V. 16, 1986, pp. 423-428.
62. Fournier, B.; Nkinamubanzi, P.C. and Chevrier, R., “Comparative field and laboratory investigations on the use of supplementary cementing materials to control alkali-silica reactions in concrete”, *12th International Conference on Alkali-Aggregate Reaction in Concrete* (ed. T. Mingshu and D. Min), V. 1, 2004, pp. 528-537.
63. Shehata, M.H. and Thomas, M.D.A., “The effect of fly ash composition on the expansion of concrete due to alkali silica reaction”, *Cement and Concrete Research*, V. 30, 2000, pp. 1063-1072.
64. Shehata, M.H. and Thomas, M.D.A., “Use of ternary blends containing silica fume and fly ash to suppress expansion due to ASR in concrete”, *Cement and Concrete Research*, V. 32, 2002, pp. 341-349.
65. Thomas, M.D.A. and Innes, F.A., “Effect of slag on expansion due to alkali aggregate reaction in concrete”, *ACI Materials Journal*, V. 95 (6), 1998
66. Bleszynski, R.; Hooton, R.D.; Thomas, M.D.A. and Rogers, C.A., “Durability of ternary blend concrete with silica fume and blast-furnace slag: Laboratory and exposure site studies”, *ACI Materials Journal*, V. 99, 2002, pp. 499-508.
67. Ramlochan, T.; Thomas, M.D.A. and Gruber, K.A., “The effect of metakaolin on alkali-silica reaction in concrete”, *Cement and Concrete Research*, V. 30, 2000, pp. 339-344.
68. Chappex, T. and Scrivener, K.L., “Alkali fixation of C-S-H in blended cement pastes and its relation to alkali silica reaction”, *Cement and Concrete Research*, V. 42, 2012, pp. 1049-1054.
69. Chappex, T. and Scrivener, K.L., “The influence of aluminum on the dissolution of amorphous silica and its relation to alkali silica reaction”, *Cement and Concrete Research*, V. 42, 2012, pp. 1645-1649.
70. Chappex, T. and Scrivener, K.L., “The Effect of Aluminum in Solution on the Dissolution of Amorphous Silica and its Relation to Cementitious Systems”, *J. Am. Ceram. Soc.*, V. 96, 2013, pp. 592-597.
71. Favier, A.R.; Dunant, C.F. and Scrivener, K.L., “Alkali silica reaction mitigation properties of ternary

blended cements with calcined clay and limestone”, 2nd *International Congress on Durability of Concrete (2nd ICDC)*, 4-6 December 2014, New Delhi, India, Paper 11, 7 pp.

72. Irassar, E.F., “Sulfate attack on cementitious materials containing limestone filler – A review”, *Cement and Concrete Research*, V. 39, 2009, pp. 241-254.
73. Duchesne, J., “Deterioration of concrete by the oxidation of sulphide minerals in the aggregate”, 1st *International Congress on Durability of Concrete (1st ICDC)*, Trondheim, Norway, 18-21 June, 2012 (ISBN 978-82-8208-031-6).
74. Scrivener, K.L., “Understanding and establishing sulfate resistance of cementitious materials”, 1st *International Congress on Durability of Concrete (1st ICDC)*, Trondheim, Norway, 18-21 June, 2012 (ISBN 978-82-8208-031-6). KN2, 8 pp.
75. Müllauer, W.; Beddoe, R.E.; Hilbig, H. and Heinz, D., “Mechanisms of sulfate attack for plain and fly ash cements at different storage temperatures and sulfate concentrations”, 1st *International Congress on Durability of Concrete (1st ICDC)*, Trondheim, Norway, 18-21 June, PP3, 12 pp.
76. Carlsen, R. and Vennesland, Ø., “Sulfate and sea water durability of concrete” (In Norwegian), *SINTEF Report STF65 F82010*, 1982.
77. Fidjestøl, P. and Frearson, J., “High-performance concrete using blended and triple blended binders”, *ACI International Conference on High Performance Concrete*, Singapore, ACI SP-149, 1994.
78. Kunther, W.; Lothenbach, B. and Scrivener, K.L., “Influence of bicarbonate ions on the deterioration of mortar bars in sulfate solutions”, *Cement and Concrete Research*, V. 44, 2013, pp. 77-86.
79. Dehwah, H.A.F., “Effect of sulfate concentration and associated cation type on concrete deterioration and morphology changes in cement hydrates”, *Construction and Building Materials*, V. 21, 2007, pp. 29-39.
80. Ghafoori, N.; Najimi, M.; Diawara, H. and Islam, M.S., “Effects of class F fly ash on sulphate resistance of Type V Portland cement concretes under continuous and interrupted sulfate exposures”, *Construction and Building Materials*, V. 78, 2015, pp. 85-91.
81. Hossack, A.M. and Thomas, M.D.A., “Varying fly ash and slag contents in Portland limestone cement mortars exposed to external sulfates”, *Construction and Building Materials*, V. 78, 2015, pp. 333-341.
82. Abdalkader, A.H.M.; Lynsdale, C.J. and Cripps, J.C., “The effect of chloride on cement mortar subjected to sulfate exposure at low temperature”, *Construction and Building Materials*, V. 78, 2015, pp. 102-111.
83. De Weerd, K.; Justnes, H. and Geiker, M.R., “Changes in the phase assemblage of concrete exposed to sea water”, *Cement and Concrete Composites*, V. 47, 2014, pp. 53-63
84. Rønne, M.; Hammer, T.A.; Justnes, H.; Meland, I.S. and Jensen, V., «Chemical Stability of LWAC Exposed to High Hydration Generated Temperatures», *International Symposium on Structural Lightweight Aggregate Concrete*, Sandefjord, Norway, 20-24 June, 1995, pp. 505-516.
85. Ramlochan, T.; Zacarias, P.; Thomas, M.D.A. and Hooton, R.D., “The effect of pozzolans and slag on expansion of mortars cured at elevated temperature. Part I. Expansive behavior”, *Cement and Concrete Research*, V. 33, 2003, pp. 807-814.
86. Ramlochan, T.; Thomas, M.D.A. and Hooton, R.D., “The effect of pozzolans and slag on expansion of mortars cured at elevated temperature. Part II. Microstructural and microchemical investigations”, *Cement and Concrete Research*, V. 34, 2004, pp. 1341-1356.

-
87. Jolicoeur C.; To T.C.; Benoît, É.; Hill, R.; Zhang, Z. and Pagé, M., “Fly Ash Carbon Effects on Air-Entrainment: Fundamental Studies on their Origin and Chemical Mitigation”, *World of Coal Ash (WOCA)*, May 4-7, 2009, Lexington, KY, USA, 23 pp.
 88. Panesar, D.K. and Chidiac, S.E., “Multi-variable statistical analysis for scaling resistance of concrete containing GGBFS”, *Cement & Concrete Composites*, V. 29, 2007, pp. 39-48.
 89. Giergiczny, Z.; Glinicki, M.A.; Sokolowski, M. and Zielinski, M., “Air void system and frost-salt scaling of concrete containing slag-blended cement”, *Construction and Building Materials*, V. 23, 2009, pp. 2451-2456.
 90. Utgennant, P., “The influence of ageing on the salt-frost resistance of concrete”, Thesis (PhD) 2004, Report TVBM-1021, Division of Building Materials, Lund Institute of Technology, Lund University, Sweden, 346 pp (ISBN 91-628-6000-3).
 91. Sisomphon, K.; Copuroglu, O. and Fraaij, A.L.A., “Development of blast furnace slag mixtures against frost salt attack”, *Cement & Concrete Composites*, V. 32, 2010, pp. 630-638.

Specification of building materials for in service durability

C. Gehlen, C. Thiel

Department of Civil, Geo and Environmental Engineering, Technical University of Munich.

Abstract

To assess whether a structural element made of a given building material can withstand the expected mechanical load and environmental exposure in service, designers need information on the material resistances and loads as well as the local conditions. The durability of a building material in the structure can only be assessed if these factors are taken into account. Usually, the material resistances are obtained from laboratory tests. However, the performance of materials under standardized laboratory conditions differs from those occurring in the field. This paper considers this assessment problem and develops a solution strategy based on carbonation-induced corrosion as an example.

Keywords: durability design, concrete, reinforcement, material resistances, modeling.

1. Introduction

Infrastructure made of structural concrete is an essential part of our modern built environment. Supply of goods and services, individual and public transport, all services are very dependent on the technical reliability of concrete structures.

Not only is the preservation of the existing built infrastructure a tremendous task, but also the resource-saving construction of new, permanent infrastructure. The current high degree of worldwide construction activity is driven mainly by the population explosion and the dramatically increasing urbanization. More than 1.7 billion people in the world are under 20 years old, and in future most of them will move to the rapidly growing urban centres. There, all these people will require housing and infrastructure, offices and production facilities, food, consumables, water and energy supplies, as well as schools, universities and hospitals. In just a few years, a construction volume will be required which amounts to more than the total volume created over 150 years since 1800.

Sustainable construction and economical preservation of structures are required to ensure the availability of infrastructure at the high level needed. Premature failure or unexpectedly high maintenance costs can result in economic expenditure amounting to billions of Euros.

Structural elements are generally subjected to mechanical loads and the action of the service environment. Mechanical, thermal, chemical and hygric actions always occur together and affect the serviceability, structural capacity, deformation, and the building-physics of structural elements over time, Figure 1. Consequently, the design and dimensioning of each structural element must take the provision of adequate durability into account.

The underlying interactions between simultaneous chemical and physical processes in the micro-structure of mineral and metallic building materials are not fully understood. In view of the importance of this, there is an urgent need for research: how does the material behave regarding effects which limit durability. What

are the decisive factors affecting and limiting durability? How should the material be designed in future? How can the material be characterized by fair standard tests and qualified for particular applications? How can sufficient durability be proven? How can the durability of reinforced structures be assessed as a whole? How can existing structures be efficiently protected against damaging influences or repaired?

At present, the durability of the majority of civil engineering structures is ensured by approximate prescriptive rules based on experience in field practice. The disadvantage of this approach is that new materials cannot be taken into account, as well as the effect of changing exposure conditions or load during service cannot be estimated (e.g. conversion of buildings, increasing heavy goods traffic, climate change).



Figure 1: Mechanically loaded concrete column, affected by chloride in de-icing salts which has induced corrosion of rebar and freeze-thaw scaling, photo Gehlen

Moreover, studies have shown that classical durability design concepts, in which requirements on concrete composition and cover are based on decades of experience, lead, depending on the exposure class, to uneconomic solutions or solutions which are uncertain, [1]. This approach stifles innovation, [2], and is hard to verify in the field. It is almost impossible to estimate how deviations from the requirements affect the actual component behaviour.

On the contrary, performance-based durability design provides a justified calculation of the time-dependent behaviour of structural components taking statistical uncertainties into account, [3].

For these alternative, probabilistic-based approaches, a probability of occurrence of an unwanted structural condition (failure) p_f remains below a given target probability p_{target} within the prescribed service life (Eq. 1). The occurrence of an unwanted structural condition (failure) is defined when a limiting state is exceeded, i.e. the stress S exceeds the resistance R , Eq. 1.

$$p_f = p\{R - S < 0\} \leq p_{target} \quad (1)$$

The implementation and fulfilment of Eq. 1 is illustrated in Fig. 2.

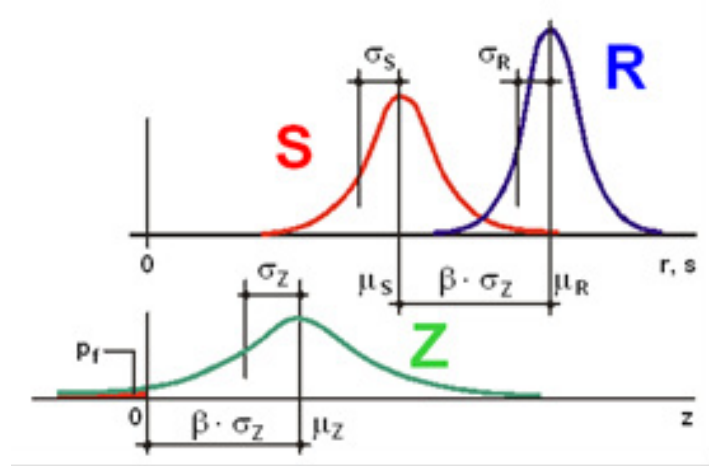


Figure 2: Definition of the probability of occurrence (failure) p_f (μ : mean; σ : standard deviation, β : reliability index) [4].

Since both, S and R , are distributed variables, the result Z is also a distributed variable. The probability of occurrence (failure) is defined by the region of Z for negative values. However, rather than the probability of failure, the reliability index β is commonly used. The reliability index is the factor by which the standard deviation of the variable Z is multiplied to yield the distance of the mean value from zero. The probability of failure p_f and the reliability index β may be calculated for normal distributions of R and S by using Eq. 2 and the mathematical definition of the standard normal distribution Φ .

$$p_f = \Phi\left(-\frac{\mu_Z}{\sigma_Z}\right) = \Phi(-\beta) \quad (2)$$

In the case of a full probabilistic calculation in accordance with Eqs 1 and 2, all the parameters in the stress and resistance models must be defined as statistical parameters each with mean value, standard deviation and distribution type (e.g. [4]).

In field practice, however, the probabilistic analysis is only required in special cases. Usually, the full probabilistic calculation is adapted thereby becoming semi-probabilistic. In this case, stress and resistance are introduced as characteristic variables and the scatter taken into account by partial safety factors, Eq. 3.

$$\frac{R_k}{\gamma_M} - S_k \cdot \gamma_E \geq 0 \quad (3)$$

Here R_k is the characteristic value for resistance, S_k the characteristic value for stress, γ_M is the partial safety factor for the material resistance and γ_E the partial safety factor for the environmental stress.

Often, complex models with different parameters are required. In case of carbonation or chloride-induced corrosion, transport models are generally used for the time until depassivation (initiation phase) and afterwards deterioration models for the propagation phase. Both these phases must be taken into account for the computation of the limiting load-bearing capacity. Eq. (4) can be used to prove that the chosen design provides the target service life, [4].

$$t_{SL} = t_{ini} + t_{prop} \geq t_{SL,target} \quad (4)$$

Here t_{SL} is the service life of structural member, $t_{SL,target}$ the target service life, t_{ini} the time to depassivation and t_{prop} the corrosion period to the ultimately acceptable service condition.

An important advantage of probabilistic durability design compared to prescriptive design is that the service life prediction can be significantly improved during the actual service of the structure, thus becoming more

accurate. The distribution of concrete cover and the penetration of depassivating substances in concrete (for example CO_2) can be determined by measurements on the structure during service. Thus as time passes, the prognosis of service life or the reliability index expected at the end of the target service life can be calculated with increasing accuracy. Moreover, a fundamental basis is available for expert decisions regarding economical concepts for tailored maintenance and repair throughout the target service life of the structure.

In the following, carbonation-induced corrosion is used to demonstrate the diffusion/chemical and electrochemical mechanisms (transport- and deterioration models) and the corresponding models for durability design.

2. Mechanisms

The evolution of the carbonation process is summarized schematically in Fig. 3.

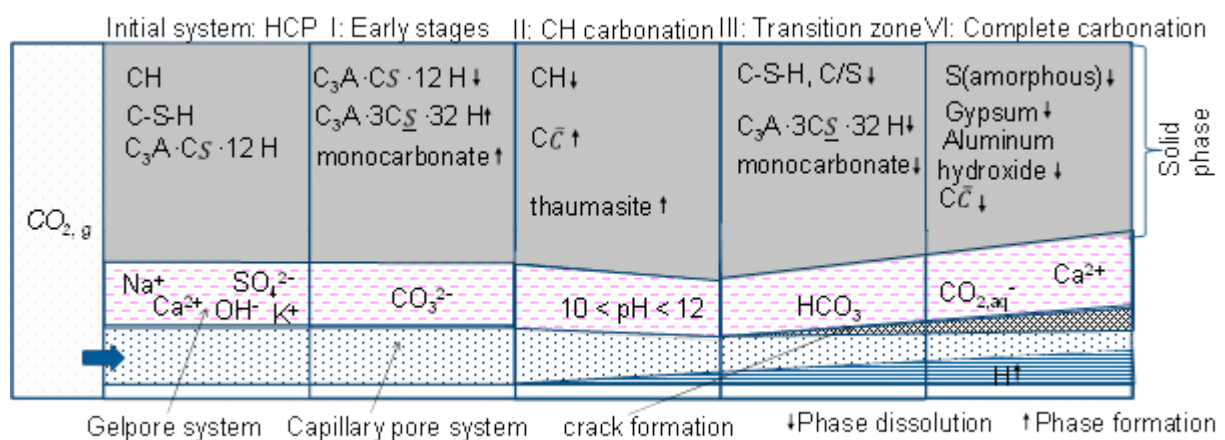


Figure 3: Phase transformations during carbonation according to [5]

Gaseous CO_2 diffuses through the pores in the hardened cement paste (HCP) matrix and dissolves in the pore solution forming carbonic acid. Consequently, dissolved calcium in the alkaline pore solution reacts to form calcium carbonate. The carbonation reactions continue as long as sufficient calcium is available in the pore solution. This is maintained by the dissolution of, in particular, portlandite and the C-S-H phases. Other phases in the hardened cement paste matrix also undergo carbonation. During carbonation the C/S ratio of the C-S-H phases progressively decreases owing to decalcification until ultimately complete degradation occurs. In addition, other phases in HCP carbonate as well. Phases such as monocarbonate, strätlingite and thaumasite can form as intermediate products which are finally followed by calcite, $\text{Al}(\text{OH})_3$, gypsum and an amorphous SiO_2 gel.

The carbonation kinetics of hcp depends on concrete moisture content as well as the concentration and the pressure of CO_2 . The material resistance itself mainly depends on the pore structure of the HCP matrix and the amount components that can carbonate [6]. Concrete with water-saturated pores carbonates very slowly because the pore water inhibits the penetration of CO_2 gas into the concrete [7]. Concrete carbonation at ambient relative humidities below about 30% is very slow because a water film is not available for the dissolution of CO_2 . The most rapid carbonation of concrete occurs at a relative humidity near 50% [8].

After the carbonation front has reached the reinforcement corrosion can be initiated. The corrosion process takes place in two sub-processes: At the anode, iron ions pass into solution, separating from the electrons. They are converted into rust products in further reactions. At the cathode, electrons, water and oxygen are converted into hydroxyl ions. The cathodic process does not cause any deterioration of the steel.

These hydroxyl ions transport the negative charge in the electrolyte through the electrical field created between the anode and the cathode, towards the direction of the anode. Near the anode, they react with the iron ions in solution. Depending on moisture and aeration conditions, this intermediate product may continue to react, producing the final corrosion products. The individual processes are in fact much more complicated.

- In order for the corrosion process to take place, a number of preconditions for the anodic and cathodic process and for the electrolytic process must be satisfied simultaneously:
- There must be differences in potential between anodes and cathodes. The preconditions for sufficiently large differences in potential are, however, usually met.
- Anodic and cathodic surface zones of the steel must be connected electrically and electrolytically, i.e. a flow of electrons and ions between them must be possible. The metallic connection necessary for an electron flow from the anode to the cathode is provided by the reinforcement system in the reinforced concrete. The electrolytic connection is represented by the concrete. This must, however, be sufficiently moist, since otherwise there can be virtually no migration of ions. In dry interior situations, for example, the electrolytic conductivity of the concrete is too low to permit corrosion of the reinforcement, even if the carbonation front reaches the reinforcement, leading to loss of alkaline protection.
- Anodic dissolution of iron must be possible due to depassivation of the steel surface. The cathodic process can, however, take place even in zones with a passive steel surface.

Sufficient oxygen must be available at the cathode. There must be continuous diffusion of oxygen from the surface of the concrete to the steel surface acting as the cathode. There is therefore practically no risk of corrosion to reinforced concrete components which are permanently and completely immersed in (deep) water.

If all conditions for corrosion are fulfilled simultaneously, the reinforcement will corrode. If only one of the conditions can be eliminated, corrosion can be prevented or halted. Fundamental repair principles may be deduced from this knowledge.

If depassivation is caused by carbonation of the concrete generally uniform corrosion takes place. This leads to the formation of micro-corrosion-cells, consisting of pairs of immediately adjacent anodes and cathodes. These are microscopic in size, so that externally they appear to produce uniform removal of the steel.

3. Models

In [9] it was proposed to describe mathematically the evolution of carbonation depth $x_c(t)$ vs time t by utilizing a Fick's law diffusion model, Eq. 5,

$$x_c(t) = k_{NAC} \cdot \sqrt{k_e \cdot k_c \cdot k_a} \cdot \sqrt{t} \cdot W(t) \text{ with } k_a = \frac{c_a}{c_t} \quad (5)$$

where $x_c(t)$ [mm] is the carbonation depth at time t , k_{NAC} [$\sqrt{\text{mm}^2/\text{year}}$] the carbonation rate measured under standard laboratory test conditions on specimens exposed to a standard climate at atmospheric pressure, k_e [-] a function accounting for the environmental effect of relative humidity (RH_a) on carbonation, k_c [-] a function for the effect of curing/execution on the carbonation, k_a [-] a function describing the effect of CO_2 -concentration in the ambient air on carbonation, C_a [kg/m^3] the CO_2 concentration in the ambient air, C_t [kg/m^3] the CO_2 concentration during the concrete test, t [year] the exposure time, $W(t)$ [-] a function describing the effect of wetting events which partly block CO_2 transport. The last parameter becomes more relevant with increasing carbonation depth and therefore with increasing time. More details on the

functions can be found in [9].

If $x_c(t)$ equals the concrete cover, depassivation of rebar takes place and initiation period t_{ini} is over. Corrosion of reinforcement can then occur, i.e. propagation starts. If a certain degree of propagation is acceptable (for example until the concrete cover cracks), a propagation model is needed. An example of a simple one is given in Eq. (6).

$$x_{corr}(t_{prop}) = V_{corr} \cdot t_{prop} \quad (6)$$

Here $x_{corr}(t_{prop})$ [mm] is the uniform corrosion penetration depth, V_{corr} [$\mu\text{m}/\text{year}$] the corrosion rate and t_{prop} [year] the propagation period, i.e. the time period after depassivation during which the rebar can corrode.

Depending on the specifically chosen design criteria, i.e. depending on the structural condition, the designer wants to avoid unwanted structural conditions. Possible unwanted conditions are, for example: Rebars located in carbonated concrete (limit state: depassivation) or corrosion attack on rebars with depths larger than $x_{corr,max} = 100 \mu\text{m}$.

5. Material tests

Material testing plays a central role in the verification of the durability of building materials which means that material compliance tests must be performed. Compliance tests are used to determine reliably the performance of the material, e.g. strength, or carbonation resistance. A compliance test must fulfil the following requirements:

1. Accurate and precise; every measurement method produces errors which are, in general, systematic or random. Systematic errors can be minimized by appropriate calibration, choice of equipment and careful measurement. Unavoidable systematic errors due to variations in experimental conditions or inaccurate measuring equipment can be taken into account by suitable correction factors or equations [4]. In addition, the results of measurements scatter around a true value. Although such random errors cannot be avoided, their effect can be calculated. In this case, the precision of the test method is decisive. The real difference between two materials or a material from a specified limiting value can be determined, [10]. The decisive factor here is the precision of reproducibility as determined in round robin tests.
2. Reliable results consistent with observations in-field practice; a procedure is only suitable as a compliance test if its results agree with the corresponding observations in the field, i.e. the transferability of the results to field practice should not be worsened by acceleration factors which do not occur in service. A compromise must be found between testing on the safe side and the consideration of the real, highly scattered parameters.
3. Fast and easy to perform; a robust test procedure should be performed easily by appropriately trained laboratory staff. In addition, time is crucial in construction practice. To minimize disruption of the production process, the test should be as fast as possible and commercially available.
4. Cost-effective; in order to increase the acceptance of a compliance test, the cost should also be kept as low as possible.

Generally, direct or indirect test methods may be applied. Direct test methods reproduce the real, almost unmodified behaviour of the material in field practice for given boundary conditions (production, storage conditions, test procedure). Natural conditions are simulated over a long time period or accelerated in a compliance test by using extreme conditions (e.g. simulation of extreme freeze-thaw variations with high minimum temperature and constant moisture supply for the determination of freeze-thaw resistance).

In the case of indirect test methods, a property A of the material is measured which is then used to determine a different property B which is not (directly) measured. This is only possible if a mathematical relationship between the two quantities A and B is known. For example, the freeze-thaw resistance of hardened concrete can be determined from the amount of entrained air measured in the fresh concrete or the resistance of concrete to chloride diffusion determined from the measurement of the chloride migration coefficient. The DuraCrete project drew up the state-of-the-art of compliance testing in 1997 [11] and analysed suitable test methods with regard to duration, reproducibility, simplicity and commercial availability [12]. Standard committee CEN TC51(CEN TC 104)/WG12/TG5 created a series of technical specifications prEN 12390-XX in which generally accepted test procedures are described for the measurement of material resistances against various forms of environmental attack. The tests measure the relevant resistances directly or indirectly, and are performed either under natural or accelerated conditions.

DIN EN 12390-10 [13] can be applied for the direct determination of carbonation resistance under natural conditions. The results obtained from this laboratory test can be transferred into a carbonation rate k_{NAC} . In [14], the measurement and subsequent classification of concrete material according to test specification [13] is described in detail.

6. Transfer methods

For design purposes, the laboratory performance must be transferred to field performance. By utilizing models, outlined in Section 3 and described more in detail in [9], and introducing (partial) safety factors, Eq. (3), Greve-Dierfeld and Gehlen [15] developed and proposed a design chart. In this chart material laboratory performance is first transferred into the corresponding field performance and then related to the minimum concrete cover necessary to avoid unwanted structural conditions during a specified period of service. By using this chart, the depassivation of steel in structural members due to carbonation can to be avoided for a targeted reliability level of $\beta = 1.5$, Fig. 4, which corresponds to a probability of occurrence of approximately 7%.

This semi-probabilistic based design starts with information on the mean material resistance (in this case mean carbonation rate) k_{NAC} measured in the laboratory. In addition, information is required on the mean specified curing time t_c [d], the expected mean relative humidity of ambient air RH_a [% RH] at the location of the structure, the expected mean amount of precipitation expressed by the weather function, i.e. the expected time of wetness ToW and probability of driving rain p_{dr} on location, and the targeted design service life which can range between 10 to 100 years. The chart yields the minimum concrete cover which is needed to achieve the targeted design service life with material and execution selected at a reliability level of $\beta = 1.5$. As an example, the following specific design situation is considered.

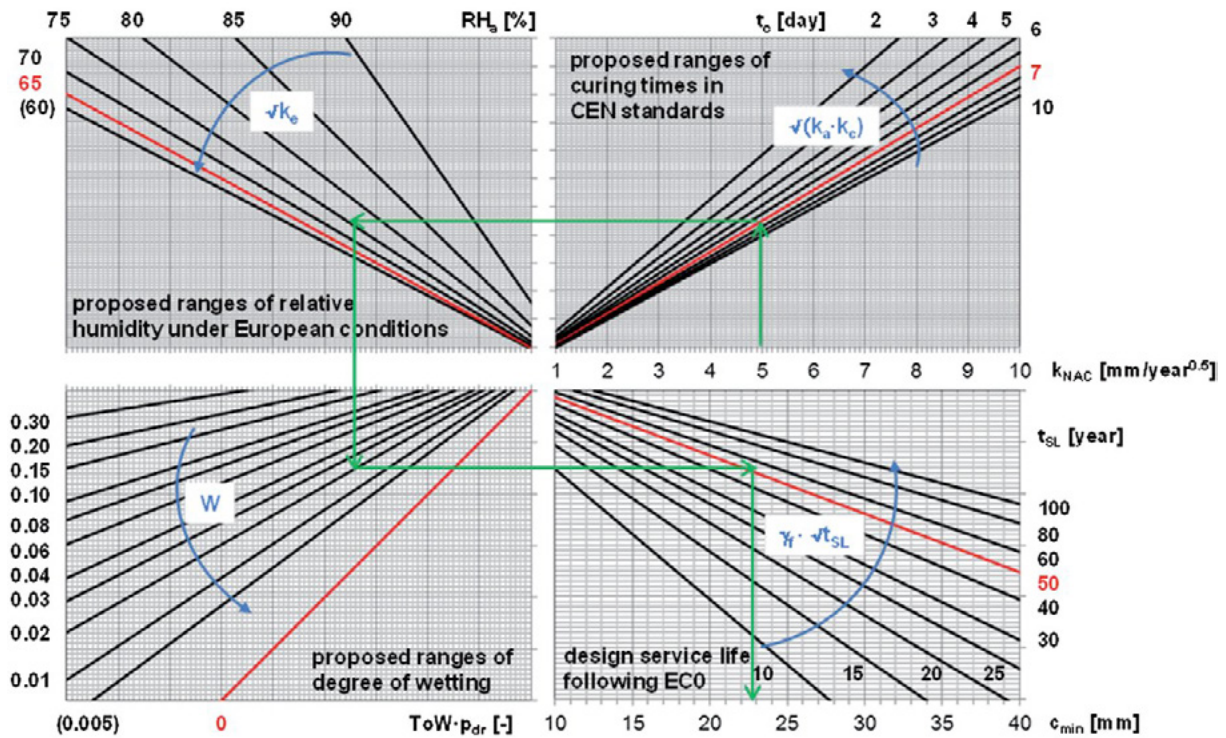


Figure 4: Design chart for carbonation of structural concrete members, target reliability level $\beta = 1.5$, according to [15]

7. Field study

The subject of this study is a reinforced concrete pillar which has already been damaged by carbonation-induced reinforcement corrosion, Fig. 5. Based on the apparent corrosion damage, the remaining service life (before repair) was rated as “expired”. The investor wanted an “extension of the remaining service life” by 50 years, i.e. the quality and thickness the concrete replacement was to be designed for a total of 50 years.

The repair material, whose composition was unknown (trade secret), was subjected to a standardized carbonation test according to DIN EN 12390-10 [13] which yielded a mean carbonation rate of $k_{NAC} = 5.0 \text{ mm}/\sqrt{a}$.

In this case, the curing time t_c was specified at 7 days by an expert planner. According to data provided by the weather service, the average ambient humidity RH_a expected at the location is 75% RH, the expected mean probability of driving rain (north exposure) p_{dr} is 12%, and the expected average rain frequency ToW (proportion of days in the year with precipitation $h_{rain} \geq 2.5 \text{ mm}$) is 17%. The required minimum layer thickness of the replacement concrete was then determined from this data using a design nomogram, Fig. 4. The input values for the nomogram must always be mean values. The safety (by means of partial safety factors) is included by changing the slope of the parameter curves, in order that the required minimum layer thickness of the replacement concrete is obtained.

In the present example, the required minimum layer thickness $d_{c,min}$ is 23 mm, see Figure 4. In order that the minimum layer thickness, like the minimum concrete cover, is defined as a quantile value (usually 95%) a tolerance must be allowed for; fulfilled by 95 % of all cases on the construction site. The tolerance for layer thickness depends on the substrate and the type of execution and is usually between 10 mm and 15 mm.

According to the expert planning described above, the executing company has to use a product of specifically tested performance ($k_{NAC} \leq 5.0 \text{ mm}/\sqrt{a}$). It should be noted that the requirements regarding curing time ($t_c \geq 7 \text{ d}$) and minimum layer thickness ($d_{c,min} = 23 \text{ mm}$) specified by the designer are to be met and an

adequately tolerance taken into account. In this specific case a nominal cover of 35 mm was appropriate.



Figure 5: Reinforced concrete pillar, photo Gehlen

8. References

- [1] Gehlen, C.; Schießl, P.; Schießl-Pecka, A. (2008): Hintergrundinformationen zum Positionspapier des DAfStb zur Umsetzung des Konzepts von leistungsbezogenen Entwurfsverfahren unter Berücksichtigung von DIN EN 206-1, Anhang J für dauerhaftigkeitsrelevante Problemstellungen. Beton- und Stahlbetonbau, 103, 12 (in German).
- [2] Bickley, J.A.; Hooton, D.; Hover, K.C. (2006): Performance specifications for durable concrete, Concrete International 28(9): 51-57
- [3] Bunte, D. (1994): Zum karbonatisierungsbedingten Verlust der Dauerhaftigkeit von Außenbauteilen aus Stahlbeton, PhD-Thesis, Technische Universität Braunschweig (in German).
- [4] Gehlen, C. (2000): Probabilistische Lebensdauerbemessung von Stahlbetonbauwerken – Zuverlässigkeitsberechnungen zur wirksamen Vermeidung von Bewehrungskorrosion, Deutscher Ausschuss für Stahlbeton, Heft 510, Beuth-Verlag, Berlin (in German).
- [5] Glasser, F. P., Matschei, T. (2007): Interactions between Portland Cement and Carbon Dioxide. 12th Int. Cong. on the Chem. of Cem., Montreal, Canada, 8-13 July 2007.
- [6] Papadakis, V.G.; Vayenas, C. G.; Fardis, M. N. (1991): Fundamental modeling and experimental investigation of concrete carbonation, ACI Material Journal, 1, pp 363-373.
- [7] Verbeck, G. J. (1958): Carbonation of Hydrated Portland Cement. In: ASTM Special Technical Publication No. 205 pp. 17-36.
- [8] Papadakis, V.G.; Fardis, M. N., Vayenas, C. G. (1992): Effect of composition, environmental factors and

cement-lime mortar coating on concrete carbonation, *Materials and Structures*, 25, pp. 293-304

[9] Greve-Dierfeld v., S.; Gehlen, C. (2016): Performance based durability design, carbonation part 1 - Benchmarking of European present design rules. *Structural Concrete*, 17: 309-328. DOI: 10.1002/suco.201600066

[10] DIN ISO 5725-2 (2002): Accuracy of measurement methods and results - Part 2: Basic method for the determination of repeatability and reproducibility of a standard measurement method, Beuth Verlag, Berlin.

[11] DuraCrete (1997): Summary and Suitability of Existing Compliance Tests. Brussels: European Union – Brite EuRam, 1997. - Project BE95-1347, Document BE95-1347/R6, 1

[12] Gehlen, C.; Ludwig, H.M. (1999): Compliance Testing for Probabilistic Design Purposes. Brussels: European Union – Brite EuRam, 1999. - Project BE95-1347, Document BE95-1347/R8,

[13] DIN EN 12390-10 (2019): Determination of the carbonation resistance of concrete at atmospheric levels of carbon dioxide, Beuth Verlag, Berlin.

[14] Greve-Dierfeld v., S.; Gehlen, C. (2016), Performance-based durability design, carbonation part 2 – Classification of concrete. *Structural Concrete*, 17: 523–532. DOI: 10.1002/suco.201600067

[15] Greve-Dierfeld v., S.; Gehlen, C. (2016), Performance-based durability design, carbonation, part 3: PSF approach and a proposal for the revision of deemed-to-satisfy rules. *Structural Concrete*, 17: 718–728. DOI: 10.1002/suco.201600085

Parallel session contributions ○

Design of reinforced concrete slabs with consideration of the construction joints

V. Kurochkina¹, I. Yakovleva², A. Deineko³, A. Starostin⁴

¹Dr., Associate Professor, , Department of Engineering Survey and Geoecology, National Research Moscow State University of Civil Engineering, 26, Yaroslavskoe shosse, Moscow, 129337 Russia, kurochkina@mgsu.ru

²Ph.D. Student, Senior Lecturer, , Department of Engineering Survey and Geoecology, National Research Moscow State University of Civil Engineering, 26, Yaroslavskoe shosse, Moscow, 129337 Russia, YakovlevaIYU@mgsu.ru

³Deputy Director for Science and Technology, Spectrum Group of Companies, Building 15, Complex 29, Academica Tupoleva Embankment, Moscow, 105005, Russia, deineko@spgr.ru

⁴Head of Architectural and Civil Engineering Group, Spectrum Group of Companies, Building 76, Letter "A", 7th Line of Vasilievskiy Island, St. Petersburg, 199178, Russia, Starostin@spgr.ru.

Abstract When erecting monolithic reinforced concrete slabs, construction joints have to be installed. Construction joints are the area of weakness of the construction. The evidence from construction practice shows that the compliance with the correct technology of the installation of the construction joint according to the regulations is not a sufficient condition to ensure the strength balance of reinforced concrete slabs. The article considers approaches to calculations of monolithic reinforced concrete slabs taking into account construction joints. The relevance of the task is determined by the fact that the correct calculation of construction joints determines the conformity of design and actual characteristics of the in-situ reinforced concrete constructions as a whole. The problem of the monolithic slabs construction joints was considered in one of the residential buildings under construction. In course of construction, pre-construction land surveys were carried out in the areas of the construction joints installation. Calculations of reinforced concrete structures using finite element method were also performed. As a result of the study, the actual deflections of the floor slabs in the areas of the construction joints were measured, and calculations were made using the finite element method of the same floor slabs, both those erected only a short time ago and those erected in stages, considering the construction joints. The difference between the calculated and actual deflections is conditioned upon the inaccurate conformity of the design diagram (mathematical model) of the real reinforced concrete construction, and its erection and operation conditions. It should be noted that the deflection of horizontal reinforced concrete constructions is only one of the parameters of the stress-strain state, which is best measured. It is shown that if the deflection of a real reinforced concrete construction does not correspond to the estimates, the other parameters of the stress-strain state will also differ from the estimates. The field data shows that the vertical construction concrete joints in the slabs weaken their solidity. However, the installation of joints is necessary due to organization and techniques issues. What is more, their location can be predicted at the stage of development of the project documentation.

Keywords: construction concrete joints, reinforced concrete constructions, framed buildings, concrete slabs deflections, deformations, finite element method, solid compositional modelling of reinforced

concrete.

1. Introduction

Currently, monolithic buildings are very common. The use of in-situ reinforced concrete constructions allow to construct a building of almost any configuration and height (Fig. 1). The frame of the building is often made of in-situ reinforced concrete constructions, consisting, as a rule, of walls, columns and concrete floors.

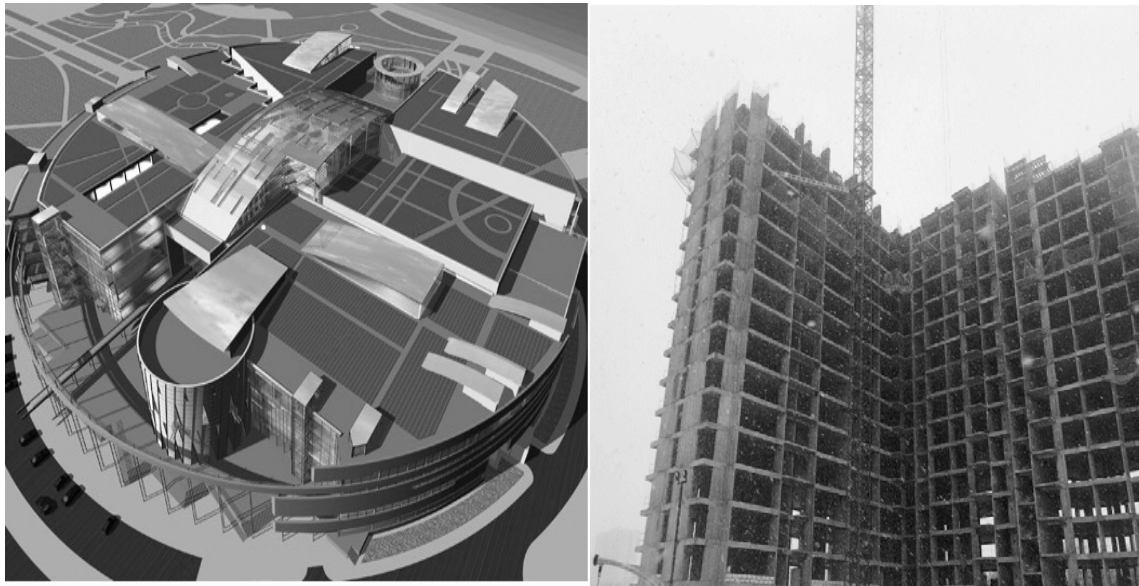


Figure 1: Monolithic frame buildings.

Wherein, it is impossible to install all monolithic constructions at the same time, therefore, construction is carried out in a specific sequence. As a rule, the foundation comes first, then vertical basement structures (walls, columns, piers), then the concrete floor of the basement, the walls of the next floor, and so on. As a result, it is necessary to install horizontal and vertical joints. At the same time, if the installation of horizontal construction joints [1] is often provided by the project, then vertical construction joints arise unplanned, directly during in-situ floor slabs concrete works.

According to common standard 70.13330.2012, installation of construction joints has requirements. The surface of construction joints, installed when pouring concrete intermittently, shall be perpendicular to the axis of the concreted columns and beams, the surface of the slabs and walls. It is allowed to keep pouring concrete when it reaches strength of at least 1.5 MPa. It is allowed to install construction joints in coordination with the design contractor when pouring concrete:

- in columns and piers – at the elevation of the top of the foundation, the bottom of the sills, beams and crane cantilevers, the top of the crane beams, the bottom of the column's beds;
- large beams, integrally connected to the floor slabs – 20–30 mm below the elevation of the lower surface of the slab, and if there are capitals in the slab – at the lower elevation of the capitals of the slab; - flat slabs – in any place parallel to the smaller side of the slab;
- ribbed coatings – in the direction parallel to the secondary girders;
- separate beams – within the middle third of the span of the beams, in the direction parallel to the main beams (girders) within two middle quarters of the span of the girders and slabs;

- bulk concrete, arches, vaults, tanks, bunkers, hydraulic structures, bridges and other complex engineering structures and constructions – in the places specified in the project.

In practice, the design contractors recommend installing construction joints in $1/3-1/4$ of the span, which does not contradict common standard 70.13330.2012. The design of the construction joint (Fig. 2) shall be given in the work production plan.

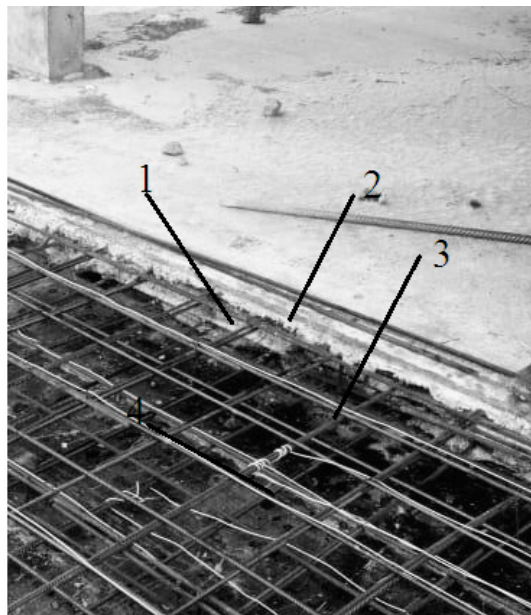


Figure 2: Construction joint structure: 1 - metal grid; 2 - protective concrete layer; 3 - top reinforcement; 4 - bottom reinforcement.

Many authors [2–11] consider the construction joint installation procedure. In their works, they emphasize that the joint shall be cleaned of dirt and garbage, rinsed with water and dried with a stream of air. Also, the authors cite laboratory studies of various constructions that confirm the reduction in strength and stiffness characteristics, as a result, deformations occur in places where the joints are made. The authors also note that when designing a monolithic building, it is calculated as a complete monolithic one.

Authors [8,9], describing the structure of construction joints in the base plates, come to the conclusion that “the ideal position of the concrete joint shall coincide with the position of the zero transverse force of the structure, i.e. the joint is installed in the place where the transverse force is minimal, and better where it is equal to zero. This is determined by the results of the calculation, namely, by the diagram of transverse forces”. The authors [2–12] concur that this issue is poorly studied and the regulatory framework does not give unambiguous answers on how to properly install construction joints. However, they note that construction joints are a weak point and can adversely affect the load bearing capacity of the structure as a whole.

The authors [2, 8, 9] consider one of the reasons for the negative impact of concrete joints to be that they cannot foresee at the design stage the actual places where concrete construction joints will be installed. At the same time, according to common standard 70.13330.2012, the in-situ structures shall provide the structural strength, taking into account the concrete construction joints. To minimize the effect of construction joints on the load bearing capacity of constructions, this paper considers the possibility of construction joints accounting at the design stage

2. Methodology

Consider the vertical concrete construction joints in in-situ reinforced concrete slabs on one of the residential buildings under construction with a height of up to 20 floors. The locations of the construction joints were selected on the basis of the planned average daily volume of concrete or from the shipping length of the reinforcement bars, equal to 11.70 m. During the construction process, preconstruction geodetic surveys were performed at the joint's installation sites. The survey was performed with the Sokkia CX 105 total station. Also, calculations of reinforced concrete structures by the finite element method (FEM) were carried out [13–15].

FEM is the most common method used in practice for numerical (mathematical, computer) simulation of building structures and is used in most specialized design programs. The principle of the method as applied to the calculations of in-situ reinforced concrete structures consists in the approximation of structures by laminar (shell) and beam (bar) bending finite elements (FE) with 6 nodal degrees of freedom (3 degrees of freedom in displacements, 3 degrees of freedom in turns). From the point of view of geometric simulation, planes and segments, that do not have their own volume, are constructed, and they are assigned the geometric characteristics of the section (cross-sectional area A , moment resistance W , moment of inertia I). This allows you to reproduce the stress-strain state (SSS) of an elastic isotropic body with a similar cross-section shape. Bending structure SSS is conveniently represented in the form of internal forces: bending moment M , axial force N , transverse force Q , and also torque, if necessary. To determine the required number of longitudinal reinforcement, internal forces are decomposed into a couple of forces using semi-empirical engineering formulas: the compressive force from the compressed zone of the concrete (as well as in the compressive reinforcement, if any) and the tensile force in the tensile reinforcement. Concrete tensile strength is assumed to be equal to zero. A similar approach is used to determine the required amount of transverse reinforcement and the crack opening width.

Note that the representation of SSS by internal forces involves the postulation of a linear diagram of the distribution of normal stresses σ over the thickness of the structure, while the extreme values of the stresses are determined by formula:

$$\sigma_{\max}^{\min} = \frac{N}{A} \pm \frac{M}{W} \quad (1)$$

The tangential stresses τ in this case are distributed along a parabolic diagram according to the D. I. Zhuravskii formula. For the particular case of a cross-section, the maximum tangential stresses on the neutral axis are:

$$\tau_{\max} = \frac{3}{2} \cdot \frac{Q}{A} \quad (2)$$

The use of internal forces in a solid isotropic bending body to represent the SSS in reinforced concrete structures is due to the need to ensure the compatibility of the results of numerical calculations with semi-empirical engineering techniques given in regulatory documents. The accuracy of this approach is limited by two main conditions:

- rather high (not specified in regulatory documents) ratio of the length of the structure to the characteristic dimension of the cross section, which allows considering the structure as a slab or beam, and not as a volumetric body of arbitrary configuration;
- the stress state is close to the limit state, since otherwise SSS decomposition on the forces in the concrete and reinforcement will not be accurate.

The above approach is called classical theory of reinforced concrete.

A promising alternative to it is the volumetric compositional simulation of reinforced concrete with the reproduction of concrete and reinforcement as independent materials, taking into account their real physical and mechanical properties and mutual spatial arrangement. The main advantage of this approach is its versatility, i.e. in the possibility of calculating reinforced concrete structures of arbitrary configuration with any reinforcement layout in terms of any SSS.

Engineering semi-empirical formulas of regulatory documents are not used in the framework of volumetric compositional simulation of reinforced concrete, since all SSS parameters (concrete stresses, reinforcement stresses, deflection, crack opening width) are clearly determined as a result of numerical simulation.

The SSS calculation in the FEM framework is based on the generalized Hooke's law, which makes the connection between normal σ and tangential τ stress, linear ϵ and shear γ relative deformations

$$\{\sigma\} = [D]\{\epsilon\} \quad (3)$$

$$\begin{Bmatrix} \sigma_x \\ \sigma_y \\ \sigma_z \\ \tau_{xy} \\ \tau_{yz} \\ \tau_{xz} \end{Bmatrix} = \frac{E}{(1+\nu)(1-2\nu)} \begin{bmatrix} \nu & 1-\nu & \nu & 0 & 0 & 0 \\ \nu & \nu & 1-\nu & 0 & 0 & 0 \\ 0 & 0 & 0 & \frac{1-2\nu}{2} & 0 & 0 \\ 0 & 0 & 0 & 0 & \frac{1-2\nu}{2} & 0 \\ 0 & 0 & 0 & 0 & 0 & \frac{1-2\nu}{2} \end{bmatrix} \begin{Bmatrix} \epsilon_x \\ \epsilon_y \\ \epsilon_z \\ \gamma_{xy} \\ \gamma_{yz} \\ \gamma_{xz} \end{Bmatrix} \quad (4)$$

where $[D]$ is a stiffness matrix; $\{\sigma\}$ is a stress vector; $\{\epsilon\}$ is a relative deformations vector.

Each element of the stiffness matrix D_{ij} characterizes the stress arising in the i -th direction from the deformation in the j -th direction, here i and j , respectively, are lines and columns indexes corresponding to the indexes of the $\{\sigma\}$ and $\{\epsilon\}$ column members.

In the framework of statical calculations, the resolving equation of the FEM is a static equilibrium equation:

$$\{F\} = [K]\{u\} \quad (5)$$

where $[K]$ is the global stiffness matrix; $\{F\}$ is a global load vector; $\{u\}$ is a global displacement vector.

The global stiffness matrix is obtained by combining local stiffness matrices of each FE. The total number of lines is equal to the number of nodal degrees of freedom of the finite element model. Due to the application of boundary conditions (loads and supporting fixtures), some members become known, which allows us to calculate unknown members by solving a system of linear algebraic equations.

In the general case, the FEM resolving equation becomes more complicated and is the equation of motion:

$$\{F\} = [M]\{\ddot{u}\} + [C]\{\dot{u}\} + [K]\{u\} \quad (6)$$

where $[M]$ is a mass matrix, $[C]$ is a damping matrix, $\{\dot{u}\}$ is a nodal speed vector; $\{u\}$ is a nodal displacement vector.

A key tool for improving the accuracy of calculations is taking into account nonlinearity (Fig. 3).

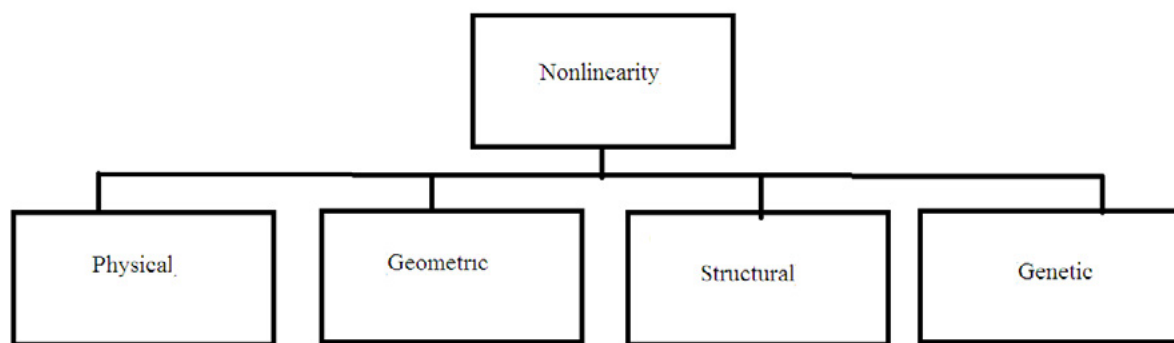


Figure 3. Nonlinear analysis.

Physical nonlinearity is dependence of the nature of the material deformation on the magnitude of stresses accounting, for example, the ability of reinforcement to plastic deformations, and concrete to cracking and creep.

Geometric nonlinearity is a consideration of the influence of the deformation of the model on the spatial distribution of forces, for example, on the eccentricity of the applied load or the span length. Design nonlinearity is taking into account changes in the design diagram depending on the loading conditions, for example, contact closing and opening. Genetic nonlinearity is a phased change in the design diagram accounting by activating and deactivating finite elements. From a computational viewpoint, nonlinearity accounting is a modification of the matrices $[K]$, $[C]$, $[M]$, which occurs automatically depending on the values $\{F\}$, $\{u\}$, $\{\dot{u}\}$, $\{\ddot{u}\}$. The above FEM principles are universal. However, the possibility of their implementation depends on the topology of the finite element model. The stress state represented by volumetric (SOLID) and bending plate (SHELL) FE is outlined in Fig. 4.

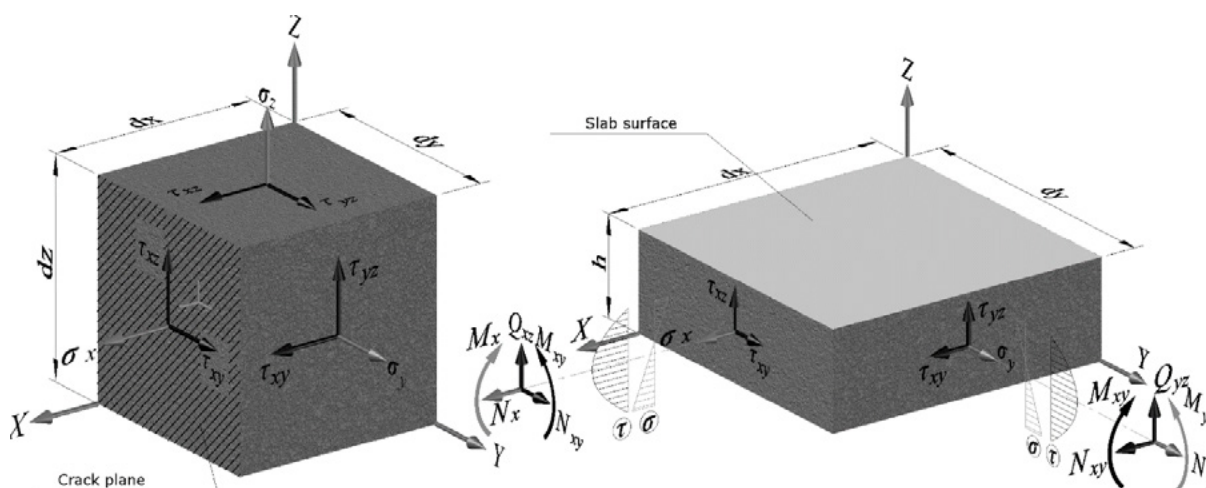


Figure 4. Stress state diagram for solid and thick shell finite elements.

In volumetric FE (SOLID), each integration point reproduces elementary volume with a full stress tensor. In FE (SHELL) plate, each integration point reproduces a volume with a certain size in the Z direction equal to the plate thickness. There are no normal and tangential stresses on the edges of the slab in the XOY plane. Stresses σ_x and σ_y are distributed over the thickness of the slab along a linear diagram and

reach extreme values on the edges of the slab. Stresses τ_{yz} and τ_{xz} are distributed over the thickness of the slab along a parabolic diagram and reach zero values on the edges of the slab. Thus, volumetric FE makes it possible to reproduce the stress state in detail (as compared with plate, as well as beam FE). Consequently, volumetric compositional simulation of reinforced concrete provides the greatest opportunities for accounting for all sorts of manifestations of nonlinearity. For example, consider crack formation in YOZ plane, perpendicular to X-axis, as shown in Fig. 4a. Crack formation can be interpreted as the cessation of the effect of stresses σ_y and σ_z on stress σ_x , with simultaneous σ_x stress relief and lowering τ_{xy} and τ_{xz} tangential stresses (depending on the crack roughness). Stiffness matrix takes shape:

$$[D]_{crack.YOZ} \sim \begin{bmatrix} \rightarrow 0 & 0 & 0 & 0 & 0 & 0 \\ 0 & \dots & \dots & 0 & 0 & 0 \\ 0 & \dots & \dots & 0 & 0 & 0 \\ 0 & 0 & 0 & \dots & 0 & 0 \\ 0 & 0 & 0 & 0 & x & 0 \\ 0 & 0 & 0 & 0 & 0 & \dots \end{bmatrix} \quad (7)$$

where “ $\rightarrow 0$ ” is a member of the matrix characterizing σ_x stress relief, “ \dots ” are nonzero members of the matrix, requiring transformations within the applicable nonlinear model of reinforced concrete [16]; “ x ” is a member of the matrix that does not require conversions.

In particular, such transformations of the stiffness matrix are implemented in FE like SOLID65 of the ANSYS software package. The specified FE is based on the Willam-Warnke [17] concrete strength criterion and allows taking into account up to three reinforcement directions. The reinforcement is an evenly distributed throughout the volume of the FE. Therefore, to simulate the main longitudinal working reinforcement of slabs, the surface layer of the final elements shall be located along the axis of the reinforcement bars and have a size equal to twice the protective layer of concrete (counting from the centre of gravity of the reinforcement bar). SOLID65, apparently, is the most well-known and widely used tool for volumetric composite simulation of reinforced concrete for solving a wide range of practical problems [18–22].

Currently, the use of universal FE reinforcement is being expanded, which allows flexible positioning of reinforcement inside volumetric FE of concrete. This increases opportunities for the development of effective mesh approximations of reinforced concrete structures.

The topology of the finite element model is chosen in accordance with the objectives of the calculation and the adopted design diagram. Consider the main approaches in the framework of the volumetric compositional simulation of reinforced concrete.

1. The reinforcement and concrete are reproduced together (by one FE, or by several geometrically coinciding FE, when one FE reproduces concrete, and the rest are reinforcement in it, possibly made of different materials and with different spatial orientation).

- 1a. Reinforcement is evenly distributed over the FE volume. The reinforcement diagram is reproduced by combining volumetric FE with different reinforcement percentage, provided that FE dimensions are accurately determined. Changing the reinforcement diagram requires FE mesh redesign.

- 1b. Reinforcement is arbitrarily positioned in volumetric FE. Changing the reinforcement diagram does not require FE mesh redesign.

2. Reinforcement and concrete are reproduced separately by non-intersecting volumetric FE, i.e. inside the volume of concrete there are cavities that are filled with reinforcement. Changing the reinforcement

diagram requires FE mesh redesign.

2a. Reinforcement is modelled in a simplified way, down to a rectangular cross-sectional shape reproducible by a single volumetric FE.

2b. Reinforcement is modelled in detail, up to periodic profile of the reinforcement and the reproduction of the “concrete-steel” contact with the possibility of slipping reinforcement accounting.

3. Reinforcement and concrete are reproduced separately by intersecting FE, and the concrete is reproduced by volumetric finite elements, and the reinforcement is reproduced by bar torque-free (LINK), bending beam (BEAM), shell torque free or bending plate FE (SHELL). The change in reinforcement does not require FE mesh complete redesign, since mesh approximations of reinforcement and concrete are independent of each other. Connection of reinforcement with concrete is carried out by assigning links of degrees of freedom by displacements of the FE nodes of concrete and FE of reinforcement.

From the point of view of practical engineering calculations, options 1b and 3 are most preferable, which allow changing the reinforcement diagram without redesigning the FE mesh, which makes it possible to perform optimization calculations with sufficient efficiency. In general, composite simulation of reinforced concrete is advisable to apply for design substantiation of structures that, for one reason or another, fall outside the limits of applicability of semi-empirical engineering techniques:

- check calculations of the actual work of the structure for all types of beyond design SSS;
- strengthening calculations, including overlaid reinforcement;
- calculations of structures with internal cavities, for example, from embedded ductwork in flat slabs;
- calculations of structures with non-metallic reinforcement with nonstandard physical and mechanical characteristics;
- calculations of any nonstandard configuration designs.

Concrete construction joint is a structural imperfection in the form of a layer of concrete decompaction, in which the strength and deformation characteristics are lowered. This layer in the compressed zone of concrete at the initial stage of the construction of the structure causes additional deformations similar to the joint closure, which lead to an increase in the deflection of the structure. Within the framework of composite concrete simulation, the concrete construction joint can be considered as a preliminary open joint, the closure of which under load introduces additional deformation into the compressed zone of concrete with a corresponding additional deflection of the structure. The specified imperfection in the finite element model can be reproduced by the introduction of a contact FE with preliminary disclosure, where the width of the disclosure is a parameter of the FE and can be selected from the field data without FE mesh redesign.

The longitudinal reinforcement crosses concrete construction joint without weakening, which can be reproduced by simulation of the reinforcement with torque-less bar FE (LINK) passing through volumetric FE and contact FE. The transition of the reinforcement through the joint is optimally performed with one FE, in which the ends are located on both sides of the joint. This simulation technique corresponds to the above option 3. It is advisable to reproduce transverse reinforcement, if available, together with concrete reinforcing FE. Depending on the uniform distribution of transverse reinforcement according to the reinforcement diagram, transverse reinforcement can be considered evenly distributed over the slab area, or positioned precisely. This simulation technique corresponds to the above 1b option. The basic diagram of the corresponding finite element approximation of the floor plate is shown in Fig. 5.

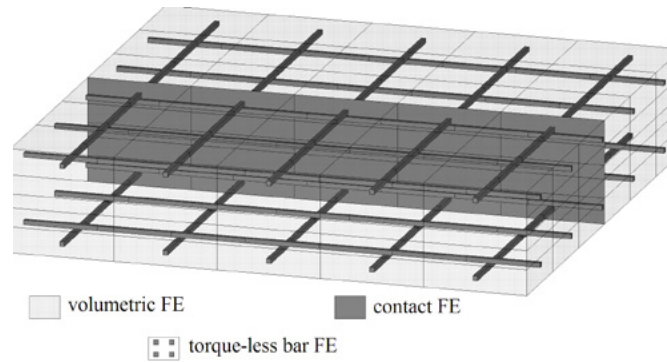


Figure. 5. Schematic finite element mesh of a monolithic reinforced concrete slab with a construction joint.

A practical difficulty in the implementation of volumetric compositional simulation of reinforced concrete is the limited initial data on the physical and mechanical characteristics of concrete for nonlinear simulation, which are specified in the regulatory documents. The available data in common standards 70.13330.2012 and 52-103-2007 are focused on the application of the classical theory of reinforced concrete according to the calculation of slabs and beams in combination with engineering approaches to taking into account nonlinearity, which consists in lowering the effective modulus of deformation of reinforced concrete in accordance with the concrete state diagrams and in accordance with a creep coefficient of concrete. When using modern computational programs, this allows in finite element models of plate and beam FEs to adjust the stiffness individually in each FE with the construction of the corresponding isofields or stiffness diagrams [23, 24]. At the same time, from the point of view of the FEM, the final design diagram continues to remain linear with the effective moduli of deformation of reinforced concrete specified for each FE.

Volumetric compositional simulation of reinforced concrete is based on the use of a universal nonlinear material model, which involves building a yield surface (in the general case, also a loading surface taking into account the material strengthening) in the main stress space, representing the state of the material for any combination of stress and strain tensor components. For this, additional data are needed, which are not included in regulatory documents, for example, concrete strength under a flat (biaxial) stressed state, as well as the dilatancy of concrete under compression and tension.

Practical implementations of concrete models in universal software and computing suites of numerical simulation, as a rule, provide for the possibility of accounting the minimum amount of input data, assuming the rest of the data automatically as default. For example, in the above-mentioned type SOLID65, the concrete adopted for biaxial compression is adopted by default 20% higher than the uniaxial compression strength. Due to the fact that, as a rule, volumetric compositional simulation of reinforced concrete is applied to nonstandard working conditions of structures, the initial data taken automatically require compliance monitoring with the actually considered SSS. Also, when using foreign programs and methods, differences in the designation of the standard strength of concrete in different countries, interconnected with the standardized method of testing samples of different shapes and sizes, shall be taken into account.

3. Results and discussion

As a result of executive geodetic surveys of 6 floors, floor slabs deflections were obtained at the construction joints locations. Magnitudes and location of the deflections are similar on all floors. Therefore, the 10th floor was adopted for a more detailed analysis. As built drawing of which is given in Fig. 6.

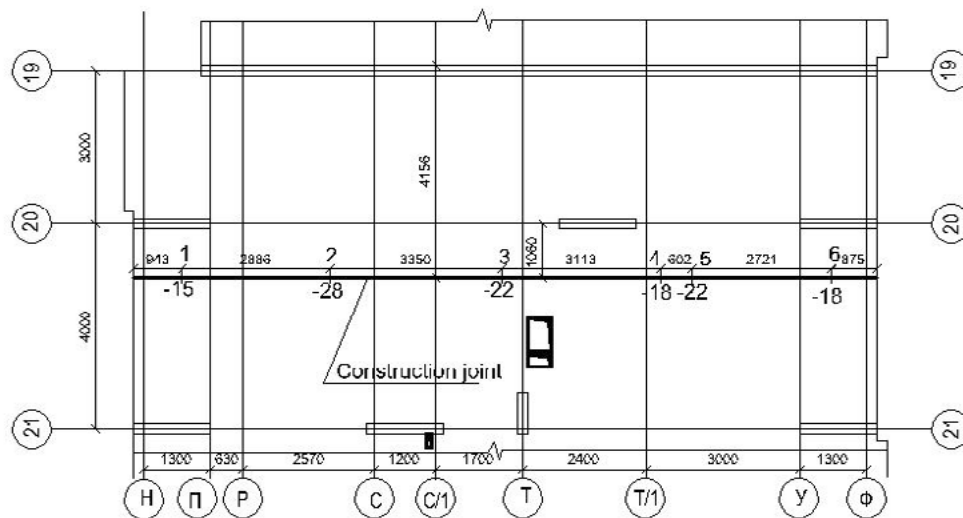


Figure 6. Scheme for the definition of deflections of concrete in the places of the construction joint (10 floor).

Factual measured data of deformations in the construction joint are presented in Table 1.

Table 1: Factual data of deformations in the construction joint.

Stage	Description	Vertical displacement at the check point, mm					
		1	2	3	4	5	6
	Actual deformation measurements	15	28	22	18	22	18

During the calculation using the finite element method, a section of the 10th floor slab was modelled at three stages of construction in accordance with present day practice of performing mass calculations using engineering nonlinearity accounting methods.

1. The initial stage of the slab installation on one pour, while the pattern of the static slab structural behaviour is based on three sides.
2. Topping up the slab to the design dimensions, while the pattern of the static work of the slab is a four-side support.
3. Slab loading with a useful standard load after the strength gain.

For the first and second stage, reduced values of concrete strength and deformation modulus were taken, thus the guidance of common standard 70.13330.2012 on the minimum strength of concrete when stripping unloaded slabs was considered. At each stage of the calculation, a reduction factor was determined for the concrete deformation modulus, taking into account the properties of concrete under load, as well as the presence of cracks in the finished structure and the actual reinforcement. During the calculations, the deformations were analyzed at the check points of the construction joint zone. The calculation results are given in Table 2.

Table 2: The results of the calculation of deformations in the construction joint.

Stage	Description	The strength of concrete is relative to the design strength	The value of the reduction factor to the concrete deformation modulus	Vertical displacement at the check point, mm					
				1	2	3	4	5	6
1	Initial stage	70%	0.118	0.59	19.76	4.89	0.74	1.32	0.30
2	Topping up the slab to the design dimensions	70%	0.354	0.37	1.42	0.65	1.15	1.27	0.39
3	Loading the slab with a useful design load.	100%	0.203	0.21	1.75	0.59	0.63	0.77	0.18
Total deformations taking into account the formation of a construction joint				1.17	22.93	6.13	2.52	3.36	0.87
	Calculation without taking into account the phased construction	100%	0.203	0.86	7.02	1.95	2.97	3.09	0.74

After analyzing the factual measured data in table 1 and the results of the calculation in table 2, we can note the following:

1. Actual deflections exceed the calculated deflections obtained without taking into account the phasing of the construction. At the same time, at the point of maximum deflection, the actual deflections are 4 times higher than the calculated deflections.
2. Actual deflections exceed the calculated deflections obtained taking into account the phasing of the construction. At the same time, at the point of maximum deflection, the actual deformations are 1.3 times higher than the calculated deflections.
3. Calculated deflections, obtained with consideration of the stage of installation, are much closer to the actual deflections.

Based on the above stated, it should be assumed that, in practice, the difference between the calculated deflection of a reinforced concrete structure and the actual one is due to inaccurate correspondence of the design diagram (mathematical model) to a real reinforced concrete structure, the conditions of its installation and operation. It is important to stress that the deflection of horizontal reinforced concrete structures is only one of the parameters of the SSS, which is best measured. Deflection, i.e. the difference in vertical displacements of the structure in the span and on the supports is interconnected with other SSS parameters, such as stresses in concrete and reinforcement, relative deformations of concrete and reinforcement, crack opening width. Thus, if the actual deflection of the reinforced concrete structure does not correspond to the design estimate, then other SSS parameters will also differ from the design estimate, although this is usually not fixed during construction, since full scale measurements of the relevant SSS parameters are not made.

Any calculation operates with a mathematical model that is an idealized reflection of a real building structure. In practice, mathematical models with a limited account of nonlinearity, or fully linear mathematical models, are often used. The linear model uses the principle of superposition (independence of action of forces), which is an extremely important practical advantage of linear models. This allows you to combine the results of the static calculations for different loads, generating results for combinations of these loads without solving the FEM equation (3) for each new combination.

In the linear model, the deformations are directly proportional to the loads; the strength of the material is infinite; displacements, deformations and stresses are not limited. Linear models do not reproduce the limits of the construction work, i.e. allow you to get in the SSS calculation, which cannot be in reality (assessment of the performance of the structure is carried out analytically according to engineering criteria,

such as the calculated strength of materials, permissible structural deflections, adequacy of the required reinforcement).

The above facts convincingly demonstrate that the most significant differences between the estimated and actual SSS are accumulated at the stage of formwork removal before the construction is put into operation. Thus, the conditions of construction with the introduction of imperfections in the form of concrete construction joints, as well as the conditions of loading the structure up to the set of design strength with its own weight and temporary loads of technological nature in the partial removal of formwork with the redistribution of the load on the posts of crossover, and then with the complete removal of formwork have a significant impact on the subsequent SSS in the operation of the structure.

In terms of design, these processes are a phased construction and structural loading, coordinated with the concrete strength. This characterizes the genetic nonlinearity of the floor slab.

The concrete construction joint is a structural imperfection, which can be represented as the ability of compressive zone of the concrete to a limited increment of deformations at the initial loading stage, which can be interpreted as a certain crack closing before concrete begins to perceive compression. Thus, as the load increases, the workflow changes, which is characterized by the structural nonlinearity of the floor slab operation.

Deformation of the structure leads to a change in the distances between the application of loads parts and supporting fixtures, to a change in the characteristic spans, lengths and eccentricities. This characterizes the geometric nonlinearity. With regard to slabs of civic buildings, the influence of geometric nonlinearity should be expected from the influence of other structures in the calculation of the supporting system of the building as a whole.

The nonlinear relationship between stresses and deformations is a physical nonlinearity. The nature of the physically nonlinear work of the materials, from which reinforced concrete (concrete steel reinforcement, non-metallic reinforcement) is made, differs, which requires the use of various mathematical models of materials that can be taken into account in the framework of volumetric composite modelling of reinforced concrete. The engineering approach is to account for the reduced effective modulus of elasticity of reinforced concrete, which is used in the framework of the classical modelling of reinforced concrete with plate and beam FE (finite elements).

Engineering approaches to the accounting of nonlinearity make it possible to consider various types of nonlinearity together. For example, structural nonlinearity can be taken into account by lowering the effective modulus of deformation of reinforced concrete, i.e. methods of accounting for physical nonlinearity. In this case, it is assumed that the distribution of internal forces in the elements of the bearing system of a building depends mainly not on the value but on the ratio of the stiffness of these elements. Accordingly, the accuracy of the calculation depends on the representativeness of the adopted stiffness ratios within the framework of the calculation of the carrier system of the building as a whole.

4. Conclusions

1. The installation of vertical concrete construction joints in floor slabs that were not originally provided by the project documentation is necessary due to a number of organizational and technical reasons related to the limitations of the possibility of continuous concrete supply and the duration of work shifts.
2. The location of vertical concrete construction joints is predictable based on the basic organizational and technical indicators of construction (number of work shifts, number and performance of cranes and concrete pumps). Therefore, concrete construction joints can reasonably be assigned in the development

of project documentation and taken into account when carrying out calculations of reinforced concrete structures.

3. The field studies data show that the concrete construction joints in the floor slabs, installed in accordance with common standard 70.13330.2012, weaken the solidity of the structure. The results of calculations carried out without taking into account the concrete construction joints do not accurately predict the actual SSS of the structure.

4. The effect of concrete construction joints can be taken into account when using common calculation programs that implement FEM, while explicitly taking into account the phasing of the construction of the structure by pours, using engineering approaches to taking into account nonlinearity based on the introduction of reduction factors to the effective modulus of elasticity of reinforced concrete, calculated taking into account the degree of strength and characteristic intermediate operation schemes of construction work during the construction period. Geometrical nonlinearity shall be taken into account, especially when calculating the spatial formulation of the full model of the building's carrier system.

5. The greatest accounting opportunities for all possible manifestations of nonlinearity are provided by volumetric compositional simulation of reinforced concrete, which is advisable to use for calculations of structures that for one reason or another go beyond the limits of the applicability of semiempirical engineering techniques, in particular, for check calculations and calculations of the reinforcement of structures that have switched to no design SSS as a result of beyond-design opening of concrete construction joints.

6. It is advisable to supplement the regulatory and technical documentation with basic data for the bulk composite modelling of reinforced concrete, in particular, with data on the strength of concrete for biaxial compression and dilatancy under compression and tension.

5. References

- [1] Biswajit Roy, Aminul Islam Laskar 2018 Cyclic Performance of Beam-Column Subassemblies with Construction Joint in Column Retrofitted with GFRP // Structures. Vol. 14. Pp. 290-300. <https://doi.org/10.1016/j.istruc.2018.04.002>
- [2] Koyankin A.A., Beletskaya V.I., Guzhevskaya A.I. 2014 The influence of concrete joints on the structural behavior // Vestnik MGSU [Proceedings of Moscow State University of Civil Engineering]. №. 3, pp. 76—81.
- [3] Nagib N. Gerges, Camille A. Issa, Samer Fawaz 2016 The effect of construction joints on the flexural bending capacity of singly reinforced beams // Case Studies in Construction Materials Vol. 5 Pp. 112-123. <http://dx.doi.org/10.1016/j.cscm.2016.09.004>
- [4] Nagib N. Gergesa, Camille A. Issab, Samer Fawaza 2015 Effect of construction joints on the splitting tensile strength of concrete// Case Studies in Construction Materials Vol. 3. Pp. 83-91 <http://dx.doi.org/10.1016/j.cscm.2015.07.001>
- [5] Camille A. Issaa, Nagib N.Gergesb, SamerFawaz 2014 The effect of concrete vertical construction joints on the modulus of rupture // Case Studies in Construction Materials. Vol. 1 Pp. 25-32. <https://doi.org/10.1016/j.cscm.2013.12.001>
- [6] Hyun-O Jang, Han-Seung Lee, Keunhee Cho, Jinkyu Kim 2017 Experimental study on shear performance of plain construction joints integrated with ultra-high performance concrete (UHPC) Construction and Building Materials. Vol. 152 pp.16-23. <http://dx.doi.org/10.1016/j.conbuildmat.2017.06.156>

- [7] Smoljago G.A., Krjuchkov A.A., Dronova A.V., Drokin C.V. 2011 Results of the experimental studies of bearing capacity, crack resistance and deformability of the precast-monolithic and monolithic overlaps // Proceedings of the south-west state university № 5-2 (38) Pp. 105-109.
- [8] Shpilevskaya N., Shvedov A. 2018 Peculiarities of normative support for designing organization and production of works by working sewing device concreting // Electronic collection of articles of the international scientific conference dedicated to the 50th anniversary of Polotsk State University Novopolotsk, 5-6 april 2018 (electronic materials) ed. A. A. Bakatovich, L.M. Parfenova. Pp. 311-315.
- [9] Shvedau A., Shpilevskaya N. 2018 Development of organizational-technological documentation on concreting of massive fundamental slabs // VESTNIK OF PSU №8. Pp. 49-55. (In Russian)
- [10] Wujun Zhou, Pangil Choi, Sureel Saraf, Sung Woo Ryu, Moon C. Won 2014 Premature distresses at transverse construction joints (TCJs) in continuously reinforced concrete pavements // Construction and Building Materials Vol. 55. Pp. 212-219. <https://doi.org/10.1016/j.conbuildmat.2014.01.042>
- [11] Keun-Hyeok Yang, Ju-Hyun Mun, Yong-Ha Hwang, Jin-Kyu Song 2017 Cyclic tests on slip resistance of squat heavyweight concrete shear walls with construction joints // Engineering Structures Vol. 141 Pp. 596-606. <https://doi.org/10.1016/j.engstruct.2017.03.0354>
- [12] Pikin D. Y., Kondrashkova V. A. 2016 The study of various approaches to the determination of the relative deformations of reinforced concrete structures // Youth and XXI century. Materials of the VI International Youth Scientific Conference (Kursk, 25-26 February 2016 r): in 4 volumes. Ed. Gorokhov A.A. Vol. 3 Pp.289-293
- [13] Manakhov P.V., Fedoseev O.B. 2008 On an alternative method of calculating the accumulated plastic strain in plastic problems using the finite element method // Bulletin of the Samara University. Natural Science Series №3(62). pp. 262-271
- [14] Karan Kumar Pradhan 2019 Chapter Four - Finite Element Method // Computational Structural Mechanics Static and Dynamic Behaviors Pp. 25-28. <https://doi.org/10.1016/B978-0-12-815492-2.00010-1>
- [15] Antipov I.V., Balagurov A.V. 2016 Analytical solution of the problem for generation of element stiffness matrix in FE-analysis // Proceedings of Republican Academic Research and Design Institute of Mining Geology, Geomechanics, Geophysics and Surveying №: 1 (16). Pp. 146-156
- [16] R. Raveendra Babua, Gurmail S. Benipala, Arbind K. Singhb 2005 Constitutive Modelling of Concrete: an Overview // Asian Journal of Civil Engineering (Building and Housing) Vol. 6, No. 4. Pp. 211–246.
- [17] K.J. Willam, E.D. Warnke 1975 Constitutive Model for the Triaxial Behavior of Concrete // Proceedings, International Association for Bridge and Structural Engineering Vol. 19. ISMES. Bergamo, Italy. Pp. 1-30.
- [18] A.S. Zalesov, A.A. Pashchanin 2011 Strength calculation for ferroconcrete beams using volume finite elements within a framework of development of ferroconcrete beams design standards// Structural Mechanics and Analysis of Constructions №4. Pp. 66–71. (In Russian)
- [19] Piskunov A.A., Zinnurov T.A., Berezhnoi D.V., Umarov B.Sh., Volter A.R. 2018 Experimental and numerical studies of stress-strain state of concrete structures reinforced with polymer-composite reinforcement // Russian journal of transport engineering №2 (5). Pp. 1-18.
- [20] Shirko A.V., Kamlyuk A.N., Plevoda I.I., Zainudinova N.V. 2014 Strength calculation of reinforced concrete slabs in case of fire using ANSYS software environment // Bulletin of the Command Engineering

Institute of the Republic of Belarus № 1 (19). Pp. 45–58.

[21] Radaikin O.V., Sharafutdinov L.A. 2017 By evaluating the strength, hardness and fracture toughness of bent reinforced-concrete elements, strengthened concrete of steel fiber «jacket» on the basis of computer modeling in PC «ANSYS» // News KSUAE № 1 (39). Pp. 111–120.

[22] Mihub A., Polish P.P., Mailyan D.R., Blyagoz A.M. 2012 Comparison of experimental and theoretical strength of reinforced concrete beams strengthened with composite materials using different calculation methods. New technologies № 4. C. 101–110.

[23] Gorodetsky A.S., Barabash M.S. 2016 Nonlinear behavior of reinforced concrete in Lira-SAPR software. Nonlinear engineering method // International Journal for Computational Civil and Structural Engineering № 2. Pp. 92–98

[24] Ivanova E.I., Kotov A.A. 2019 The stiffness of reinforced concrete beams in finite element analysis models of prefabricated buildings. // Modern Construction and Architecture № 1 (13). Pp 19–25. DOI: <https://doi.org/10.18454/mca.2019.13.4>

Eco-efficiency in cement use analysed by the concept of distance among particles in concrete phases

M. F. L. Menezes^{1,2}, R.G. Pileggi¹, M. Rebmann¹, C. Massucato²

¹Universidade de São Paulo, São Paulo, Brazil.

²InterCement, São Paulo, Brazil.

Abstract

Concrete greenhouse gas emissions are mostly from cement. A relevant strategy for the concrete greenhouse gas emissions abatement is the increase of the efficiency in binder usage. For this, it is important to understand the packing and the distance of concrete particles and their effects on its rheological behaviour in the fresh state and its mechanical properties in the hardened state. Currently, mix design methods are empirical, as opposed to this experimental optimization, computational optimization emerges, based on predictive models. Thus, the objective of this study is to use a model based on particle distance in phases to predict the rheological behaviour of concrete. The method consisted in the following steps: characterization of raw materials; eco-efficiency analysis of 120 formulations of a concrete plant with two different material sets using the binder intensity concept; and a parameter estimation for a descriptive model of the slump in function of particle distance variables. These concrete binder intensities were between 7.5 and 10.5 kg/m³/MPa, in which the rise of specified f_{ck} and maximum aggregate size have a positive impact on this index, while the specified slump growth has a negative effect. For these concretes, the distance variable MPT (Maximum Paste Thickness) for f_{ck} showed good correlations with the specified slump (R^2 0.97 and 0.98), as well as the model presented a good adjustment to the data (R^2 0.91). These results allow an improvement in the mix design methodology – using computational optimization –, which can lead to an increase in concrete eco-efficiency.

Keywords: Particle packing, interparticle separation distance, slump, rheological behaviour.

1. Introduction

Greenhouse gas emissions from concrete are mostly from cement, with the cement industry accounting for approximately 7% of global CO₂ emissions [1]. The levers for reducing these emissions are increasing energy efficiency, using alternative fuels, increasing clinker replacement and using innovative technologies such as carbon capture and storage [1]. In the concrete field, a relevant strategy is to increase the efficiency in binder use, that is, to achieve better properties with lower binder consumption [2]. Besides, because the binder represents the most significant fraction of the concrete cost, increasing efficiency is also a cost-saving solution.

To increase the efficiency of concrete binders, it is necessary to understand the structure of this material and its consequences on the concrete properties, both in the fresh and hardened state. For this, it is important to understand packing and distance among particles of concrete particles and their effects on the material rheological behaviour in the fresh state and on the mechanical properties in the hardened state, a theme that has already been widely discussed by several concrete researchers [3-17].

The concrete can be divided into two phases: the paste and the aggregates. The paste consists of the fine particles and the fluid that moves them away: the water. In this context, the predominant forces are the surface forces. In aggregates, the fluid that moves them away is the paste, and the most relevant forces in this context are the mass forces. Thus, the diameter of 100 μ m is defined as the border between the fine and coarse particle – and the phases – since this diameter is in the region of transition between the predominance of each type of force [4], [12].

Seeking a better concrete eco-efficiency, using different materials, the concrete mix design was evaluated from the perspective of packing and particle distance concepts. Currently, mix design methods are empirical, that is, based on experience from concrete operations over years and experiments results [18]. In contrast to experimental optimization, computational optimization emerges, in which an optimization problem is used based on a model to point out the best solution, which is verified experimentally. In the literature, several types of models are available for predicting concrete properties, including linear, statistical, automatic and physical combinations [19].

The present work was developed using materials and formulations of a concrete plant in São Paulo, Brazil, with the objective of using a model based on particle distance in the phases to predict the rheological behaviour of concrete to improve the current mix design methodology.

2. Methodology

2.1 Materials

Two material sets were collected at a concrete plant in São Paulo, Brazil, to be used in this study. The aggregates of the Material Set 1 were granitic and the ones of the Material Set 2 were calcitic. Particle size distribution was determined by laser granulometry, using Helos equipment from Sympatec, and dynamic image analysis, using Camsizer equipment from Retsch and Qicpic made by Sympatec, density by helium pycnometry, using a Multipycnometer of Quantachrome, and specific area by BET method, using a Belsorp produced by Bel Japan. The Material Set 1 characterization is presented in Table 1 and Figure 1, and the Material Set 2 characterization is presented in Table 2 and Figure 2. Cement and Natural Sand are the same for both Material Sets.

Table 1: Material Set 1 Characteristics

Characteristic	19mm Gravel	9.5mm Gravel	Artificial Sand	Natural Sand	Cement
Density (kg/m ³)	2.71	2.70	2.70	2.65	3.06
Granulometric					
Volumetric Area (m ² /	7.8 x 10 ⁻³	4.0 x 10 ⁻³	8.2 x 10 ⁻²	4.2 x 10 ⁻²	1.17
BET Specific Area (m ² /g)	0.01	0.01	0.26	0.30	1.48
Median Aspect Ratio	0.65	0.63	0.62	0.74	0.75

(1) Granulometric volumetric area was calculated from particle size distribution assuming spherical particles

Comparing the two Material Set, it can be noticed that Artificial Sand from Material Set 1 shows a lower amount of fines (below 100 μ m) than the one from Material 2. Material Set 1 presents a finer 19mm Gravel than Material Set 2, though the other materials are coarser, this impacts on packing porosity and, also, on volumetric granulometric area, that is higher for Material Set 1 19mm Gravel and lower for Material Set 1 9.5mm Gravel and Artificial Sand. Besides, the granulometric curves from Material Set 2 are broader than the Material Set 1's.

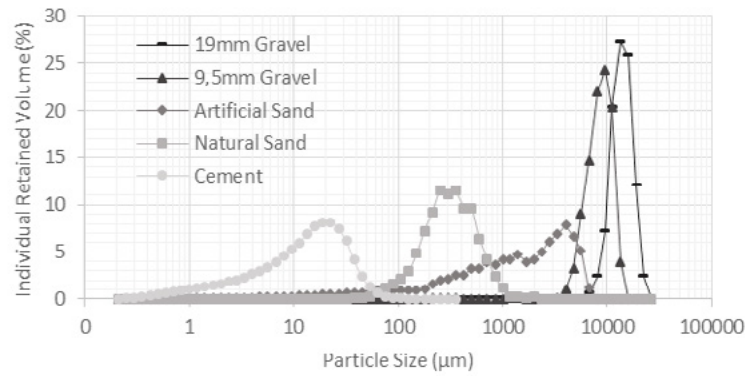


Figure 1: Material Set 1 Particle Size Distribution

Table 2: Material Set 2 Characteristics

Characteristic	19mm Gravel	9.5mm Gravel	Artificial Sand	Natural Sand	Cement
Density (kg/m ³)	2.66	2.65	2.86	2.65	3.06
Granulometric					
Volumetric Area (m ² /cm ³)	6.9x10 ⁻³	4.6x10 ⁻³	0.12	4.2 x 10 ⁻²	1.17
BET Specific Area (m ² /g)	0.02	0.02	0.23	0.30	1.48
Median Aspect Ratio	0.70	0.67	0.68	0.74	0.75

(1) Granulometric volumetric area was calculated from particle size distribution assuming spherical particles

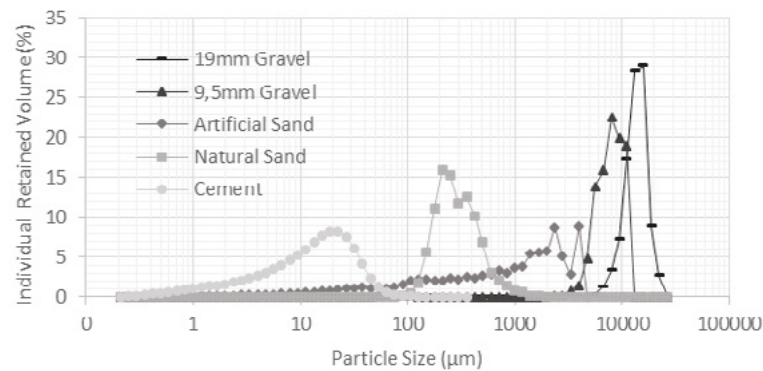


Figure 2: Material Set 2 Particle Size Distribution

In order to understand the current logic of mixture design, data were obtained from conventional concrete formulations of a concrete operation in São Paulo/Brazil. This concrete plant has 60 base formulations for each Material Set (Formulation Set). These concretes have specified compressive strength (f_{ck}) ranging from 20 to 40MPa, slump between 90 and 200mm and maximum aggregate size 19mm or 9.5mm. In concrete operation, the way to adjust the specified slump after all the materials are mixed is adding more water.

2.2 Methods

With this data, the concrete binder intensities (Equation 1) were evaluated to understand their eco-efficiency. In order to elucidate the observed trends, the models of packing and distance between particles were used to evaluate the formulations. In this study, the packing porosity was calculated by the Compressive Packing

Model [8] and mean distances between particles (Equation 2) were calculated: IPS (Interparticle Separation Distance, for the particles finer than 100 μm) and MPT (Maximum Paste Thickness, for the particles greater than 100 μm) [20]. These two variables were correlated with the fresh concrete property, slump, and a model was adjusted.

$$BI = \frac{b}{pr} \quad (1)$$

BI is Binder Intensity ($\text{kg}/\text{m}^3/\text{MPa}$)

b is binder content (kg/m^3)

pr is performance requirement, adopted as cylindrical compressive strength at 28 days (MPa)

$$D = \frac{2}{V_{SA}} \left[\frac{1}{V_{sol}} - \left(\frac{1}{1-\epsilon} \right) \right] \quad (2)$$

D is Distance between particles - IPS for fine or MPT for coarse (μm)

VSA is volumetric surface area (m^2/cm^3)

V_{sol} is solids volumetric fraction

ϵ is packing porosity

For the IPS, the VSA used was the one obtained by BET method. For MPT, the VSA was evaluated based on the granulometric volumetric area, using its sphericity and aspect ratio.

3. Results and discussion

3.1 Binder intensity evaluation

Concrete eco-efficiency can be first analysed by binder intensity since clinker is the most intense source of CO_2 emissions in concrete. So, for concrete using the same binder and produced at the same place, the lower is its binder intensity, the higher is its eco-efficiency.

Looking at the change of binder intensity in function of f_{ck} for the Formulation Set 1, as shown in Figure 3, it is possible to notice that there is a decrease of this index between 20 and 30MPa, but, from 30 to 35MPa the intensity stagnates and grows slightly when reaching 40MPa. Comparing the results with Daminelli [21], the intensities of the evaluated concretes are in the same experimental region of concretes mapped by him, however with binder intensities well above the best-found intensities, which are below $5\text{kg}/\text{m}^3/\text{MPa}$. The name of each series was given using the following pattern: it starts with “form1” for the Formulation Set 1 or “form2” for the Formulation Set 2, followed by the maximum aggregate size (“b1” for 19mm and “b0” for 9.5mm), and then the slump (ex. 140).

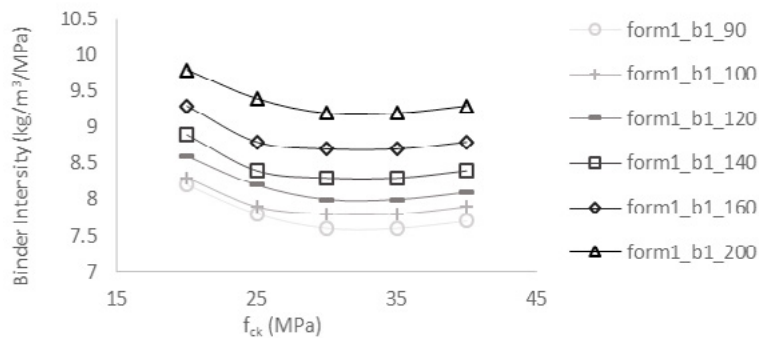


Figure 3: Binder intensity per f_{ck} for different slumps

For a given strength, concretes with the lowest binder intensity are those with maximum aggregate size 19mm and lower slump: about 7.5 to 8 kg/m³/MPa. The concretes with the lowest eco-efficiency are those with a maximum aggregate size 9.5mm and higher slump, reaching values between 9 and 10kg/m³/MPa.

Analysing the mix design strategy, Figure 3 shows the negative effect on binder intensity by the specified slump raise, while a broader particle size distribution, allowed by increasing maximum aggregate size, has a positive impact (Figure 4a). Figure 4b shows that concretes from Formulation Set 2 have a slightly lower binder intensity than those from Formulation Set 1.

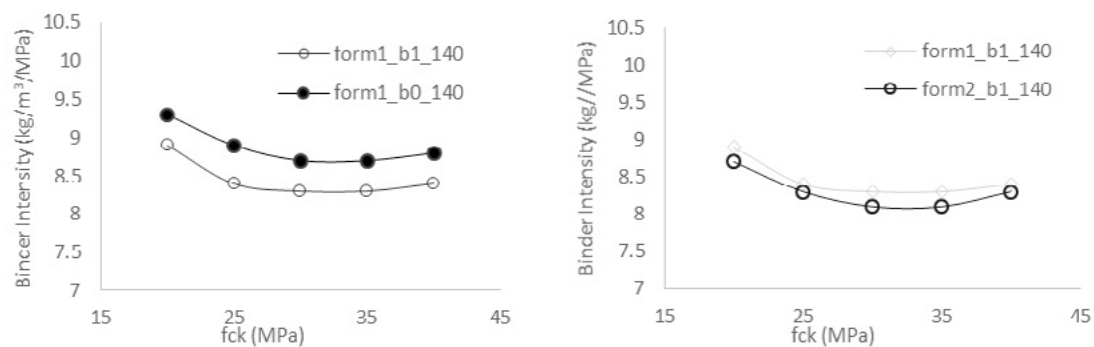


Figure 4: Binder intensity per f_{ck} (a) for different maximum aggregate sizes and (b) for different Formulation Sets

3.2 Distance among particles

In order to understand concrete flowability, coarse packing porosity, MPT and IPS, as defined by Equation 2, were calculated. First, concretes for different f_{ck} – consequently different paste compositions - were analysed plotting the slump as a function of the coarse packing porosity (Figure 5). With these results, it is not possible to find a correlation between the slump and coarse packing porosity. Different concretes with the same slump present different porosities. It can be noticed that for each specified compressive strength that is two groups of data, one with coarse porosity between 16,8% and 17,5% and another one starting from 18,0%. These two groups are the ones with maximum aggregate size 19mm and 9,5mm. The group with 19mm maximum size achieves a lower coarse packing porosity because it has a broader particle size distribution than the 9,5mm.

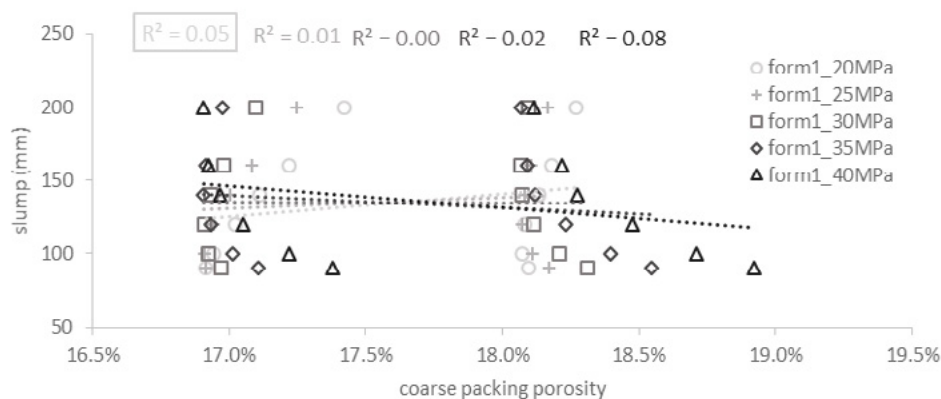


Figure 5: Slump in function of coarse packing porosity per f_{ck}

Porosity is a property of the granular size distribution and does not comprehend the pasta volume either the superficial area, so, in different concretes with the same slump, different material proportions are used,

but also a different paste content, which is not addressed by the porosity.

MPT considers the paste volume and the area as well. Thus, the slump was plotted as a function of MPT (Figure 6) for both Formulation Sets. A high correlation between MPT and slump was observed, with the coefficient of correlation of the adjusted linear regression (R^2) between 0.97 and 0.98, given a paste composition. That is, formulations that use different types of paste (in the graph represented by f_{ck}) do not present the same MPT for a slump, because of the different rheological behaviour of these pastes. But if this variable (paste) is fixed, slump varies linearly with MPT.

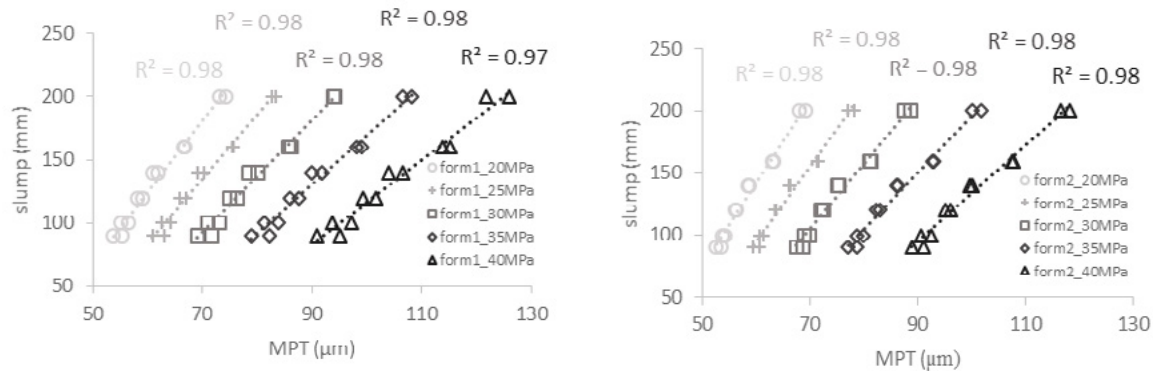


Figure 6: Slump in function of MPT per f_{ck} for (a) Formulation Set 1 (a)Formulation Set 2

The second distance parameter refers to the distance between fine particles (IPS). A high correlation (R^2 0,98), with f_{ck} , for both Formulation Sets, were observed (Figure 7). The cause for this negative correlation is that the strategy to increase f_{ck} is to reduce the water/cement ratio, which leads to less fluid to separate the particles, diminishing the IPS. For concretes without other fine particles rather than cement and aggregates fines, this trend is likely to be repeated.

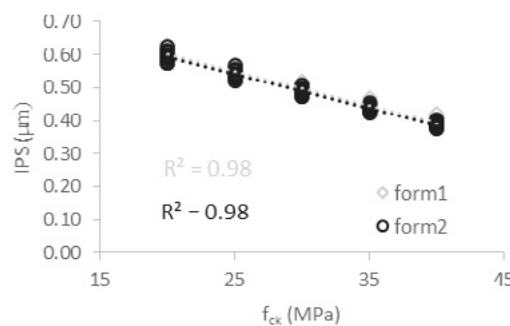


Figure 7: Correlation between IPS and f_{ck}

3.3 Descriptive model

The previous section showed the impact of two distance variables (IPS and MPT) on concrete flowability. Based on the hypothesis that these two variables could describe slump, a linear model was adjusted (Equation 3) to predict slump.

The estimated parameters are shown in Table 3. Figure 8 shows how well expected slump fits to model slump. For an individual Formulation Set, R^2 are between 0.97 and 0.98. When both Formulation Sets are considered together a lower value, but still good, correlation (R^2 0.91) was achieved.

$$s = a + b \times IPS + c \times MPT + d \times IPS * MPT \quad (3)$$

Table 3: Estimated parameters

Parameter	Formulation Set 1	Formulation Set 2	Formulation Set 1 and 2
a	-210.4	-229.5	-197.26
b	124.7	111.8	115.05
c	-0.189	-0.260	-0.175
d	7.58	8.89	7.56

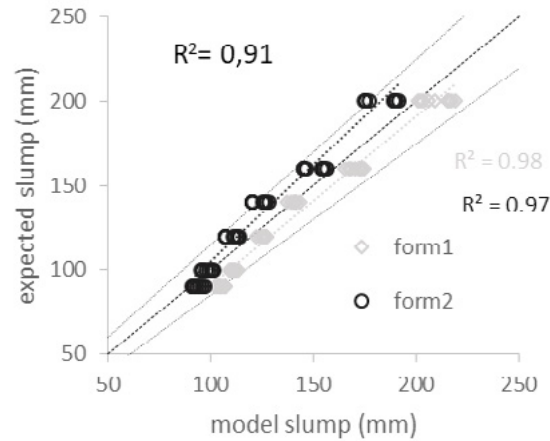


Figure 8: Correlation between the expected slump and model slump

This model is able to describe the slump for two different material sets and 120 concretes. This high correlation can be explained because the distance between particles in phases governs the concrete rheological behaviour, the correlation shows that its three variables present relevance on the physical phenomenon and its equation can quantitatively describe the slump.

This realization allows the creation of a concrete design strategy. The water/cement ratio governs the IPS and, consequently, the viscosity of the paste in this experimental region. As the water/cement ratio is determined by the specified compressive strength, the gain in binder efficiency should be obtained by reducing paste consumption, that is, increasing the coarse solid fraction in the formulation. Thus, for a specified concrete (f_{ck} , slump and maximum aggregate size), it is desired to increase the coarse solid fraction keeping a fixed MPT by reducing the coarse packing porosity. Computational optimization can minimize the coarse packing porosity keeping the specified slump, strategy that will reduce the concrete paste and binder intensity, increasing eco-efficiency.

4. Conclusions

This study analysed eco-efficiency of concrete produced by a concrete plant in São Paulo/Brazil, through binder intensity. For a given strength, concretes with the lowest binder intensity are those with maximum aggregate size 19mm and lower slump, reaching 7.5 to 8 kg/m³/MPa. The lowest eco-efficiency was obtained by those with a maximum aggregate size of 9.5mm and higher slump, reaching values between 9 and 10kg/m³/MPa. The Material Set 2 led to a slightly lower binder intensity than the Material Set 1.

For the concrete rheological behaviour, there is a high correlation between the MPT and the slump, with the correlation coefficient of the adjusted linear curve (R^2) between 0.97 and 0.98, for both Formulation

Set, given a paste composition and a f_{ck} . Based on that, a descriptive model of the slump in function of MPT and IPS was adjusted getting R^2 0.91 between the expected slump and the model slump when both Formulation Set are considered together. This high correlation shows that these three variables used to evaluate particle distance present relevance on the physical phenomenon and its equation can quantitatively describe the slump.

This model can be used by computational optimization of mixture design, in order to reduce the paste volume and increase concrete eco-efficiency.

5. Acknowledgment

This research was partially supported by InterCement. We thank InterCement technical team who provided materials, data, insight and expertise that greatly assisted the research.

6. Reference

- [1] IEA and WBCSD, 2018, Technology Roadmap: Low-Carbon Transition in the Cement Industry.
- [2] R. J. Flatt, N. Roussel, and C. R. Cheeseman, 2012, Concrete: An eco material that needs to be improved, *J. Eur. Ceram. Soc.*, vol. 32, no. 11, pp. 2787–2798.
- [3] T. C. Powers, 1968, The properties of fresh concrete, 1st ed. Michigan.
- [4] R. G. Pileggi, 2001, Ferramentas para o estudo e desenvolvimento de concretos refratários, São Carlos, UFSCar.
- [5] B. L. Damineli, V. M. John, B. Lagerblad, and R. G. Pileggi, 2016, Viscosity prediction of cement-filler suspensions using interference model: A route for binder efficiency enhancement, *Cem. Concr. Res.*, vol. 84, pp. 8–19.
- [6] N. Roussel, A. Lemaître, R. J. Flatt, and P. Coussot, 2010, Steady state flow of cement suspensions: A micromechanical state of the art, *Cem. Concr. Res.*, vol. 40, no. 1, pp. 77–84.
- [7] H. Hafid, G. Ovarlez, F. Toussaint, P. H. Jezequel, and N. Roussel, 2016, Effect of particle morphological parameters on sand grains packing properties and rheology of model mortars, *Cem. Concr. Res.*, vol. 80, pp. 44–51.
- [8] F. de Larrard, Concrete mixture proportioning a scientific approach, 1999, 1st ed. London: E & FN Spon.
- [9] F. Larrard and T. Sedran, 1994, Optimization of ultra-high-performance concrete by the use of a packing model, *Cem. Concr. Res.*, vol. 24, no. 6, pp. 997–1009.
- [10] O. H. Wallevik and J. E. Wallevik, 2011, Rheology as a tool in concrete science: The use of rheographs and workability boxes, *Cem. Concr. Res.*, vol. 41, no. 12, pp. 1279–1288.
- [11] R. J. Flatt and P. Bowen, 2006, Yodel: A Yield Stress Model for Suspensions, *J. Am. Ceram. Soc.*, vol. 89, no. 4, pp. 1244–1256.
- [12] R. J. Flatt, 2004, Towards a prediction of superplasticized concrete rheology, *Mater. Struct.*, vol. 37, no. 5, pp. 289–300.
- [13] A. Arora et al., 2018, Microstructural packing- and rheology-based binder selection and characterization for Ultra-high Performance Concrete (UHPC), *Cem. Concr. Res.*, vol. 103, pp. 179–190.

-
- [14] S. T. Erdoğan, A. M. Forster, P. E. Stutzman, and E. J. Garboczi, 2017, Particle-based characterization of Ottawa sand: Shape, size, mineralogy, and elastic moduli, *Cem. Concr. Compos.*, vol. 83, pp. 36–44.
- [15] K. Sobolev and A. Amirjanov, 2010, Application of genetic algorithm for modeling of dense packing of concrete aggregates, *Constr. Build. Mater.*, vol. 24, no. 8, pp. 1449–1455.
- [16] A. Dörr, A. Sadiki, and A. Mehdizadeh, 2013, A discrete model for the apparent viscosity of polydisperse suspensions including maximum packing fraction, *J. Rheol. (N. Y. N. Y.)*, vol. 57, no. 3, pp. 743–765.
- [17] I. Mehdipour and K. H. Khayat, 2017, Effect of particle-size distribution and specific surface area of different binder systems on packing density and flow characteristics of cement paste, *Cem. Concr. Compos.*, vol. 78, pp. 120–131.
- [18] B. F. Tutikian and P. Helene, 2011, Dosagem dos Concretos de Cimento Portland, in *Concreto: Ciência e Tecnologia*, 1st ed., no. 1927, G. C. ISAIA, Ed. São Paulo, IBRACON, pp. 439–471.
- [19] M. A. DeRousseau, J. R. Kasprzyk, and W. V. Srubar, 2018, Computational design optimization of concrete mixtures: A review, *Cem. Concr. Res.*, vol. 109, pp. 42–53.
- [20] F. Larrard and T. Sedran, 2002, Mixture-proportioning of high-performance concrete, *Cem. Concr. Res.*, vol. 32, no. 11, pp. 1699–1704.
- [21] B. L. Damineli, 2013, Conceitos para formulação de concretos com baixo consumo de ligantes: controle reológico, empacotamento e dispersão de partículas. São Paulo, Universidade de São Paulo.

HYDCEM: A new cement hydration model

N. Holmes¹, D. Kelliher² and M. Tyrer³

¹School of Civil & Structural Engineering, Technological University Dublin, Ireland

²School of Civil, Structural & Environmental Engineering, University College Cork, Ireland;

³Centre for research in the built and natural environment, Coventry University, UK

Abstract

Hydration models are useful to predict, understand and describe the behaviour of different cementitious-based systems. They are indispensable for undertaking long-term performance and service life predictions for existing and new products for generating quantitative data in the move towards more sustainable cements while optimising natural resources. One such application is the development of cement-based thermoelectric applications.

HYDCEM is a new model to predict the phase assemblage, degree of hydration, heat release and changes in pore solution chemistry over time for cements undergoing hydration for any w/c ratio and curing temperatures up to 45°C. HYDCEM, written in MATLAB, is aimed at complementing more sophisticated thermodynamic models to predict these properties over time using user-customisable inputs. A number of functions based on up to date cement hydration behaviour from the literature are hard-wired into the code along with user-changeable inputs such as the cement chemical (oxide) composition, cement phase densities, element molar mass, phase and product densities and heat of hydration enthalpies. HYDCEM uses this input to predict the cement phase and gypsum proportions, volume stoichiometries and dissolution and growth of hydration products from the silicates, aluminates and ferrites, including C-S-H, calcium hydroxide, hydrogarnet (if applicable) ettringite and monosulphate. A number of comparisons are made with published experimental and thermodynamic model results and HYDCEM predictions to assess its accuracy and usefulness.

The results show that HYDCEM can reasonably accurately predict phase assemblages in terms of volume change and behaviour for a range of cements and curing temperatures. It is proposed that HYCEM can complement more sophisticated thermodynamic models to give users a reasonable prediction of cement behaviour over time.

Keywords: Cement; Hydration; microstructure; model; MATLAB

1. Introduction

Cement hydration and microstructure development is a complex process. However, the advances in computing power and range of programmable software in recent years has made the modelling of cement hydration achievable. A comprehensive review of other cement hydration and microstructure models over the past 45 years including single particle models, mathematical nucleation and growth models and vector and lattice-based approaches to simulating microstructure development can be found at [1]. While computer modelling should never completely replace experimental analysis, it does provide valuable insights into the process particularly with the increased use of supplementary cementitious and other sustainable materials [2]. Model outputs here are based on the cements chemical (oxide) composition and element molar masses

to calculate phase proportions (based on modified Bogue equations [3]) and volume stoichiometries to improve the accuracy of the predictions. Previous work to compare simulation and measured properties have been presented [3-6] but, in order to accelerate the acceptance of prediction models, direct comparisons are best [8].

Cement particles at the micro-scale are made up of four main phases, namely tri-calcium silicate (C_3S)¹, di-calcium silicate (C_2S), tri-calcium aluminate (C_3A) and tetra-calcium aluminate ferrite (C_4AF) with particle size distributions ranging from 60-100 μ m to less than 1 μ m. Of the four phases above, C_3S is by far the most influential in terms of chemical reactivity and contribution to long term strength gain making up approximately 65-70% of overall cement content. It is no surprise therefore that the hydration of C_3S alone has been the focus of several numerical models [1,9] due to its influence and relative straightforward reaction and product development. Upon reaction with water, C_3S produces calcium silicate hydrate (written as C-S-H) and calcium hydroxide (CH)². However, in order for a full prediction of the hydration of a cement, it is important that all cement phases are included in any analysis.

One way of predicting the performance of a hydrating cement is by thermodynamic modelling which provides, amongst others, phase assemblage and pore concentration predictions. Such hydration predictions allow cement scientists assess the performance, troubleshoot short and long-term problems and even help design new cement-based materials. Despite significant effort and progress, the ability to perform such a complete simulation has not been developed, mainly because cement hydration is one of the more complex phenomena in engineering science.

This paper presents a new model, HYDCEM, written in MATLAB to undertake cement hydration analysis to predict phase assemblage, degree of hydration, heat release and pore solution chemistry over time for any w/c ratio and curing temperatures up to 45°C. HYDCEM is aimed to complement the more sophisticated thermodynamic models giving users an accurate prediction of how their Portland cement will perform by demonstrating cement phase and gypsum dissolution and the development of hydration products over time.

All input parameters required by the model are fully defined by the user including the cement chemical (oxide) composition, element molar mass, cement phase densities, phase and product densities and heat of hydration enthalpies. It uses this information to calculate the unhydrated cement proportions, gypsum content and magnesium and volume stoichiometries, which in turn determines the volumes of silicates, aluminates and ferrites hydration products namely, C-S-H, calcium hydroxide, hydrogarnet, ettringite, monosulphate and hydrotalcite. The model employs the empirical-based Parrot and Killoh [10] approach for the degree of hydration for the cement phases with an input file read in that includes the Blaine surface area of the cement, temperature, phases activation energies and the constants developed by Lothenbach [11,12] for the three reaction regimes, namely nucleation and growth, shell formation and diffusion.

The initial design of the model is presented along with worked examples to compare HYDCEM phase assemblage predictions with results from the literature. Phase assemblage predictions provide a much better insight how the microstructure is developing. MATLAB is particularly well suited to this type of analysis due to its 'engineering-like' architecture both in terms of coding language and background calculations. Also, the significant amount of help available for MATLAB programmers online make writing and understanding the code very straightforward.

1 Conventional cement chemistry notation: C=CaO, S=SiO₂, A=Al₂O₃, F=Fe₂O₃, and H=H₂O.

2 H = water; CH = Calcium Hydroxide; CAH = Hydrogarnet; GYP = Gypsum; ETTR = Ettringite; MONO = Monosulphate; FH = Iron Oxide

2. Model Design

2.1 Input files

HYDCEM was developed with the user in mind by providing clearly laid out and easy to change flat text input files. The analysis/calculation flow for HYDCEM is shown in Figure 1. As may be seen, when the input data files are read into the model, the analysis follows a well-structured methodology by using multiple functions within the main HYDCEM script along with pre-allocation of single precision outputs for quicker analysis. The data is stored within predefined single column vectors with the number of rows equal to the number of hourly time steps. There is an expected increase in analysis time with the duration of hydration (Figure 2) with 10,000 hourly time steps analysed in less than ½ second.

2.2 Chemical Properties

Using four customisable input files (oxide_proportions.txt, densities.txt, molar_mass.txt & molar_mass_reaction.txt) as shown in Figure 1, the four cement phase and gypsum proportions are determined using the Bogue equations [3] shown in Equations 1-5 below. The volume stoichiometries are calculated based on the molar mass reaction of the cement phase, the molar mass of the phase (C3S, etc.)

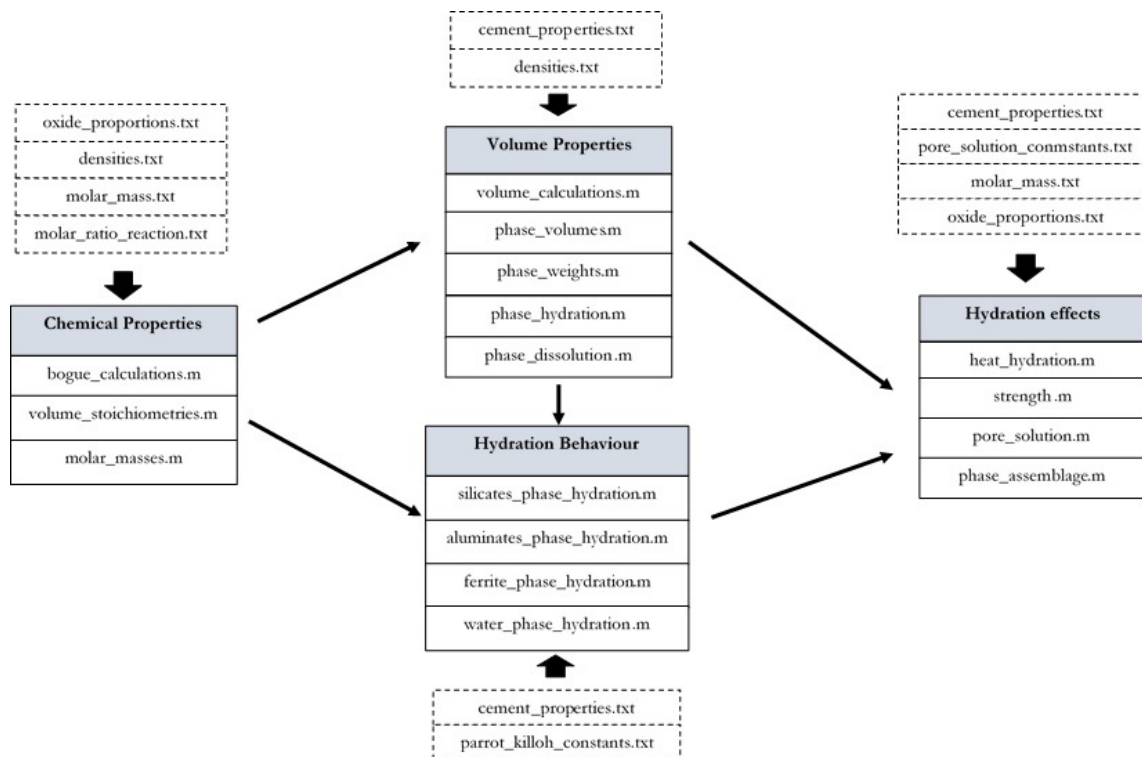


Figure 1: Diagram of HYDCEM's Matlab functions (*.m) and customisable input text files (*.txt)

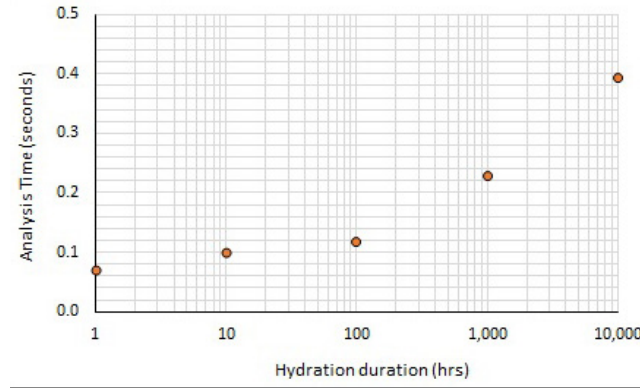


Figure 2: Analysis time for increasing hydration durations

$$C_3S = (4.071C_aO) - (7.600S_iO_2) - (6.718Al_2O_3) - (1.430Fe_2O_3) - (2.852SO_3) \quad (1)$$

$$C_2S = (2.867S_iO_2) - (0.7544C_3S) \quad (2)$$

$$C_3A = (2.65Al_2O_3) - (1.692Fe_2O_3) \quad (3)$$

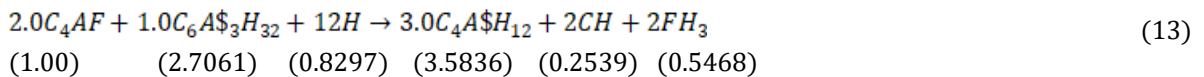
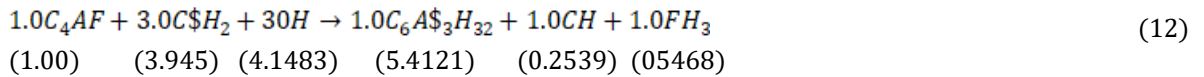
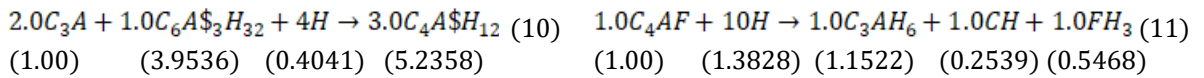
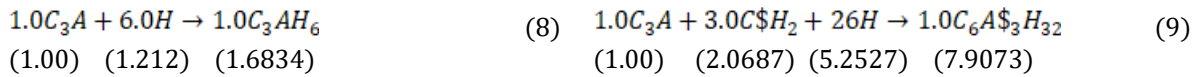
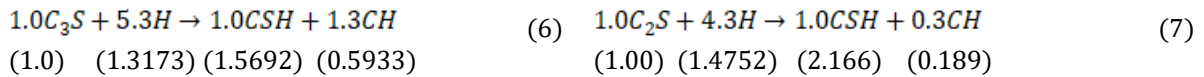
$$C_4AF = (3.043Fe_2O_3) \quad (4)$$

$$Gypsum = (1.7SO_3) \quad (5)$$

or hydration product (C-S-H, etc.) and the density, all of which are customisable by the user. The molar mass reaction for the four cement phases and magnesium (Mg) are shown in Equations 6-14 with their calculated volume stoichiometries shown in brackets below.

2.3 Dissolution of cement phases

The dissolution of the four cement phases are calculated in HYDCEM using the approach presented by Parrot and Killoh [10] that uses a set of empirical expressions to estimate the degree of hydration of each phase as a function of time. The dissolution of each phase is determined using Equations 15 to 17 where the lowest hydration rate R_t is taken as the rate-controlling value.



The degree of hydration (α) is expressed as $\alpha_t = \alpha_{t-1} + \Delta_t \cdot R_{t-1}$. The K, N and H values used for the three phases are those proposed by Lothenbach *et al* [11,12]. The influence of the surface area on the initial hydration are included as well as the influence of w/c ($= (1 + 3.333 (H * w/c - \alpha_v))^4$; for $\alpha_t > H * w/c$).

$$R_t = \frac{K}{N} (1 - \alpha_t) (-\ln(1 - \alpha_t))^{(1-N)} \quad (15)$$

$$R_t = \frac{K(1 - \alpha_t)^{\frac{2}{3}}}{1 - (1 - \alpha_t)^{\frac{1}{3}}} \quad (16)$$

$$R_t = K(1 - \alpha_t)^N \quad (17)$$

2.4 Hydration Behaviour

The change in volume of cement phases, gypsum, hydration products and water are calculated using the volume stoichiometries calculated from the molar ratios in reactions (Equations 6-14) within using a series of programming operations. HYDCEM has implemented well accepted cement hydration behaviour found in the literature as shown Figure 3, for example where the growth in monosulfate (for limestone free cements) begins after gypsum has been depleted [12,13] with increased ettringite volume until all gypsum is depleted [11,13]. The following section presents a worked example to show HYDCEM predictions of hydration behaviour over time.

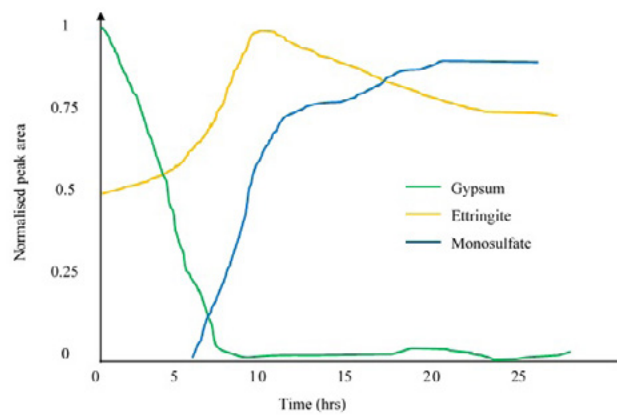


Figure 3: Kinetics of aluminate hydration for limestone-free cements (after Scrivener, 1984 [13])

3. Worked Example

The worked example is based on work by Lothenbach *et al* [11] with the cement properties shown in Table 1. The published phase assemblages or thermodynamic modelling shown here to compare the HYDCEM output with were carried out using the Gibbs free energy minimization program GEMS [14,15]. GEMS is a broad-purpose geochemical modelling code which computes equilibrium phase assemblage and speciation in a complex chemical system from its total bulk elemental composition. A detailed description of GEMS can be found elsewhere in the literature [14-17].

Table 1: Sample of input for worked example

Cement composition [11]		Enthalpy (J/g) [2]		Parameters for degree of hydration analysis [11]				
CaO	63.9	C3S	517	Parameter	C3S	C2S	C3A	C4AF
SiO ₂	20.2	C2S	262	K1	1.5	0.5	1.0	0.37
Al ₂ O ₃	4.9	C3A	1144	N1	0.7	1.0	0.85	0.7
Fe ₂ O ₃	3.2	C4AF	725	K2	0.05	0.02	0.04	0.015
CaO(free)	0.93			K3	1.1	0.7	1.0	0.4
MgO	1.8			N3	3.3	5.0	3.2	3.7
K ₂ O	0.78			H	1.8	1.35	1.6	1.45
Na ₂ O	0.42							
CO ₂	0.26			Blaine surface area (m ² /kg)			413	
SO ₃	2.29			w/c ratio	0.4			
K ₂ O (soluble)	0.72			Temperature (°C)		20		
Na ₂ O (soluble)	0.09							

The (a) HYDCEM predicted and (b) published cement dissolution of the four phases are shown in Figure 4. As may be seen, there is close agreement between the measured and predicted phase dissolution values.

Figure 5 shows (a) the HYDCEM and (b) published phase assemblage diagrams [11] for the cement described in Table 1. Figure 5(b) shows small quantities of monocarbonate, brucite and hemihydrate that are not included in the HYDCEM model. Despite this, the HYDCEM predictions are very close to the measured phase assemblage with the products of hydration forming at a similar rate over time. Also, the dissolution of gypsum is very similar with both predictions showing it completely depleted within 10 hours. As expected, both show similar reductions in the volume of ettringite with increasing monosulfate volume over time. Figure 6 shows the modelled aluminates products of hydration over time. Again, there is a reasonably close agreement between both.

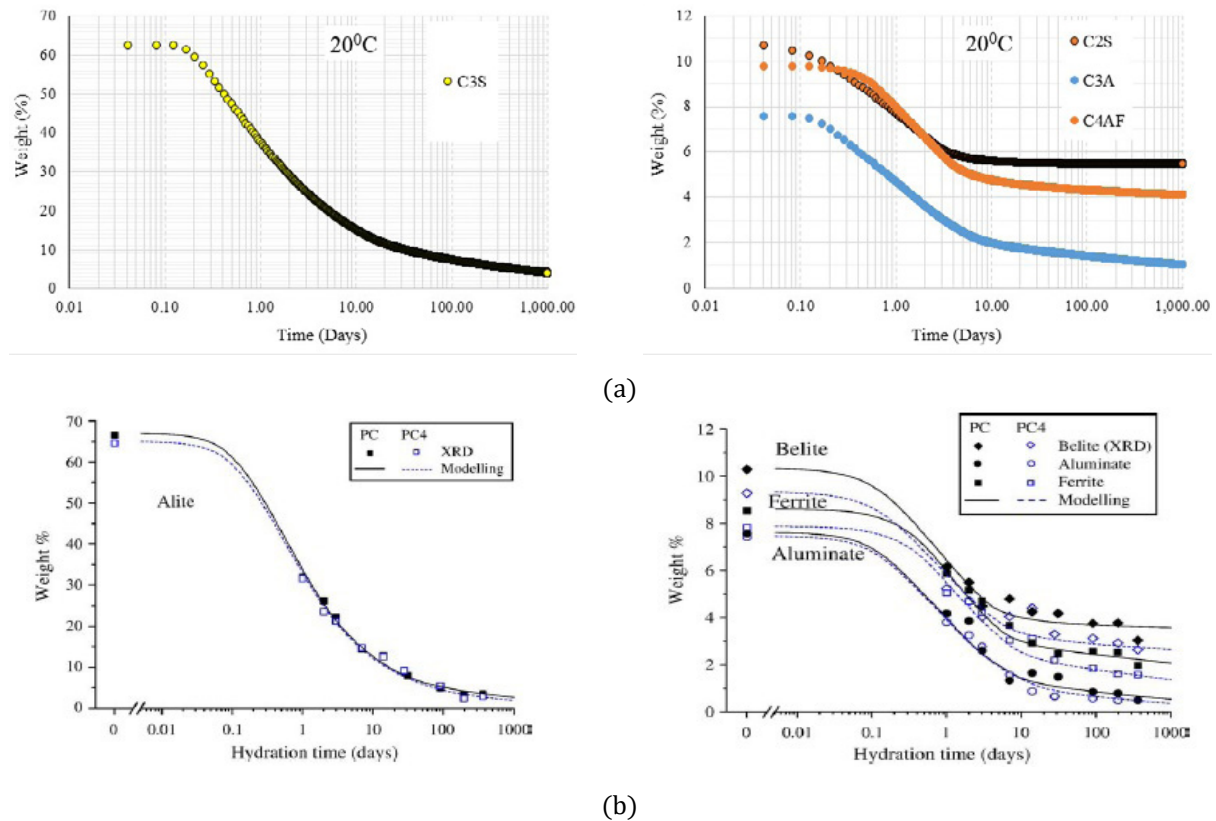


Figure 4: (a) Predicted (HYDCEM) and (b) published [11] cement phase dissolution at 20°C.

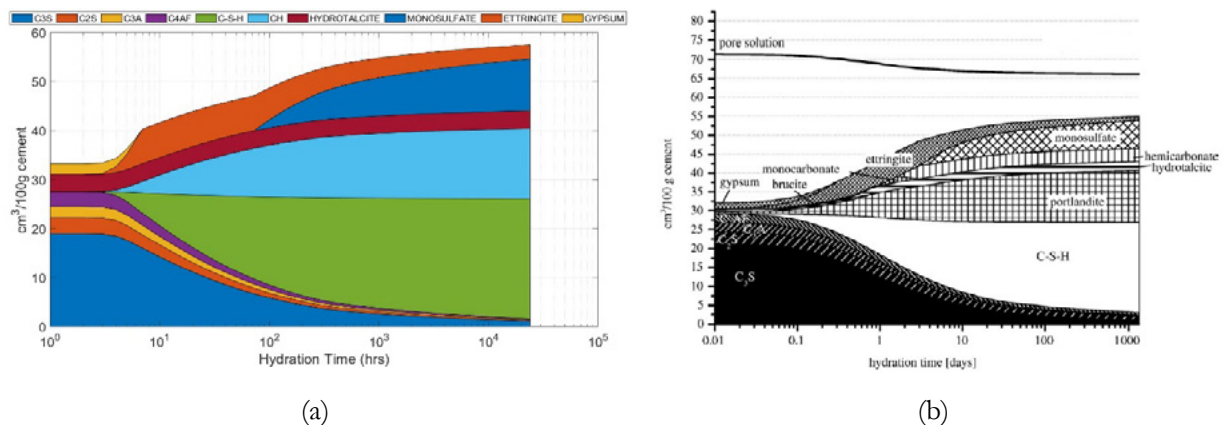


Figure 5: (a) Predicted (HYDCEM) and (b) GEMS modelled phase assemblages [11] at 20°C.

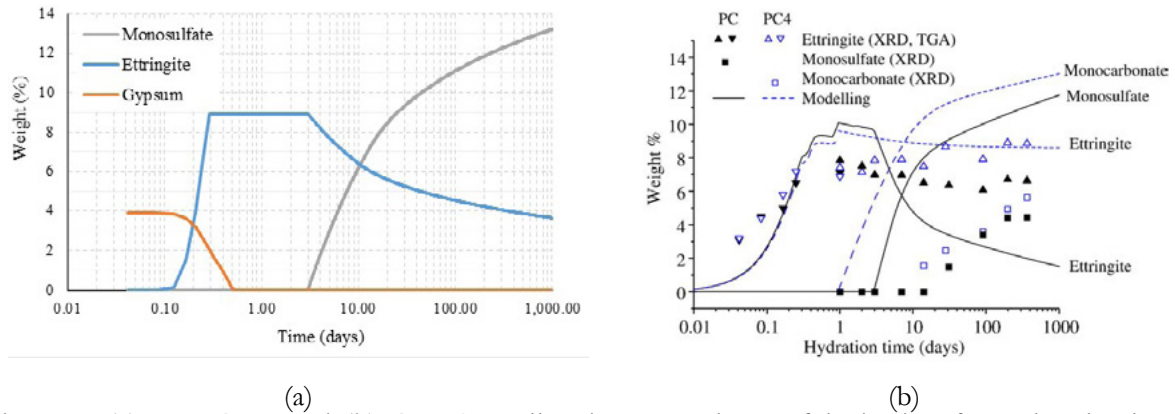


Figure 6: (a) HYDCEM and (b) GEMS predicted [11] products of hydration from the aluminate phase.

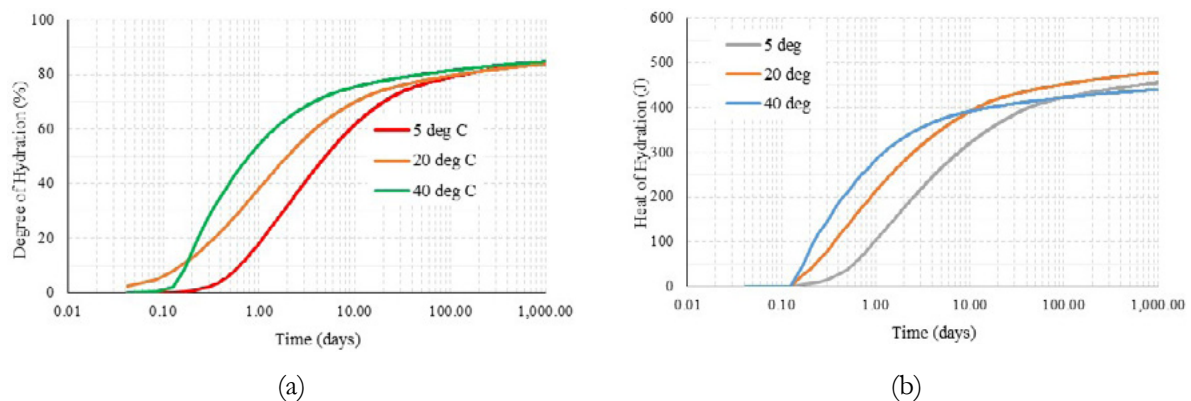


Figure 7: HYDCEM predicted (a) degree of hydration and (b) heat of hydration at (a) 5°C, 20°C and 40°C over time.

Figure 7 shows a suite of HYDCEM predictions of the (a) degrees of hydration and (b) heat release over time for curing temperatures of 5, 20 and 40°C. Lower curing temperatures cause hydration to start very slowly allowing the dissolved ions more time to diffuse prior to precipitation of hydrates along with the slower dissolution of gypsum [18]. This leads to a less dense C-S-H, a more even distribution of hydration products and a less coarse porosity [18-22]. The effect of the higher temperature can be observed with an initially fast dissolution of the four cement phases and a more rapid precipitation of hydration products early on. This is responsible for the early strength development observed at higher temperatures along with a more heterogeneous distribution of hydration products in and around the clinker particles [20]. The effect of the higher temperature demonstrates a much more rapid rate of hydration, as discussed above. The predicted degree of hydration (Figure 7(a)) at the three temperatures are as expected. At 5°C, the degree of hydration is slower whereas at 40°C, it is more rapid early on quickly slowing down over time. For instance, after 10 hours of hydration, the overall degree of hydration at 5°C, 20°C and 40°C is 7, 18 and 36% respectively. However, after 100 hours of hydration, the overall degree of hydration at the three temperatures is 47, 61 and 71% respectively, which clearly shows the effect of curing temperature as discussed above.

4. Conclusions

The HYDCEM model has been found to simulate the hydration and microstructure development of Portland cements. Using cement composition and reaction relationships, the cement phase and products of hydration are determined in volumetric terms over time for any w/c ratio and curing temperatures up to 45°C. Results presented here have shown good agreement with published hydration behaviour. HYDCEM can therefore become a useful tool for the initial prediction of cement hydration and microstructure

behaviour before the use of more sophisticated thermodynamic models. Development of the model is ongoing with additional features being added to include limestone and predictions of the pore solution chemistry by coupling with the PHREEQC geochemical model [23]. Future developments also include predictions of electrical and thermal conductivities to better understand the potential of cement based thermoelectric materials.

5. Acknowledgement

The authors would like to thank the financial assistance provided by Science Foundation Ireland as part of the ThermoConc research project.

6. References

- [1] Thomas, J.J., Biernacki, J.J., Bullard, J.W., Bishnoi, S., Dolado, J.S., Scherer, G.W. and Luttge, A. (2011) Modeling and simulation of cement hydration kinetics and microstructure development, *Cement and Concrete Research* 41, pp. 1257–1278.
- [2] Garbozi, E.J., Bentz, D.P. and Frohnsdorff, G.J (2000) The Past, Present, and Future of Computational Materials Science of Concrete, *Materials Science of Concrete Workshop*, Centre for Advanced-Cement-Based Materials, April 27-29, Lake Shelbyville, IL, 10 pages.
- [3] ASTM C150-09, standard specification for portland cement. *Annual Book of ASTM Standards*, ASTM International, West Conshocken, PA, 4.
- [4] D.P. Bentz, Three-dimensional computer simulation of Portland cement hydration and microstructure development, *J. Am. Ceram. Soc.* 80 (1) (1997) 3– 21.
- [5] D.P. Bentz, E.J. Garboczi, C.J. Haecker, O.M. Jensen, Effects of cement particle size distribution on performance properties of cement-based materials, *Cem. Concr. Res.* 29 (1999) 1663–1671.
- [6] C.J. Haecker, D.P. Bentz, X.P. Feng, P.E. Stutzman, Prediction of cement physical properties by virtual testing, *Cem. Int.* 1 (3) (2003) 86– 92.
- [7] A. Princigallo, P. Lura, K. van Breugel, G. Levita, Early development of properties in a cement paste: a numerical and experimental study, *Cem. Concr. Res.* 33 (2003) 1013– 1020.
- [8] Bentz, D.P (2006) Quantitative comparison of real and CEMHYD3D model microstructures using correlation functions, *Cement and Concrete Research* 36, pp. 259 – 263.
- [9] Holmes, N., Griffin, A., Enright, B. and Kelliher, D (2018) Introducing a new cement hydration and microstructure model, *Civil Engineering Research in Ireland (CERI) conference*, UCD Ireland, Editors Vikram Pakrashi and Jennifer Keenahan, pp. 202-207.
- [10] L.J. Parrot, D.C. Kiloh, Prediction of cement hydration, *Br. Ceram. Proc.* 35 (1984) 41–53.
- [11] Lothenbach, B., Le Saout, G., Gallucci, E. and Scrivener, K. (2008) Influence of limestone on the hydration of Portland cements, *Cement and Concrete Research* 38 pp. 848–860.
- [12] Lothenbach, B., Winnefeld, F., Alder, C., Wieland, E., and Lunk, P. (2007) Effect of temperature on the pore solution, microstructure and hydration products of Portland cement pastes, *Cement and Concrete Research* 37 (4) pp. 483–491.
- [13] Scrivener, K.L and Pratt, P.L (1984) Microstructural studies of the hydration of C3A and C4AF independently and in cement paste, *The Chemistry and Chemically related properties of cement*, Edited

by F.P. Glaser, Proceedings of the British Ceramic Society, Vol. 35, pp. 207-20.

- [14] D. Kulik, GEMS-PSI 2.1, 2007, available at <http://gems.web.psi.ch/>, PSI-Villigen, Switzerland.
- [15] T. Thoenen, D. Kulik, Nagra/PSI chemical thermodynamic database 01/01 for the GEM-Selektor (V.2-PSI) geochemical modeling code, PSI, Villigen, 2003, available at <http://gems.web.psi.ch/doc/pdf/TM-44-03-04-web.pdf>.
- [16] W. Hummel, U. Berner, E. Curti, F.J. Pearson, T. Thoenen, Nagra/PSI chemical thermodynamic data base 01/01, Universal Publishers/uPUBLISH.com, USA, also published as Nagra Technical Report NTB02-16, Wettingen, Switzerland, 2002.
- [17] B. Lothenbach, T. Matschei, G. Möschner, F.P. Glasser, Thermodynamic modelling of the effect of temperature on the hydration and porosity of Portland cement Cement and Concrete Research 38 (1) (2008) 1–18.
- [18] Lothenbach, B. Thermodynamic modelling of the effect of temperature on the hydration of Portland cement, International RILEM Symposium on Concrete Modelling – CONMOD 2008, 26-28 May, Delft, The Netherlands.
- [19] Kjellsen, K.O., Detwiler, R.J., (1992) Reaction-kinetics of Portland-cement mortars hydrated at different temperatures, Cement & Concrete Research 22 (1), pp. 112-120.
- [20] Escalante-Garcia, J.I., Sharp, J.H. (1998) Effect of temperature on the hydration of the main clinker phases in Portland cements: Part I, neat cements, Cement & Concrete Research 28 (9), pp. 1245-1257.
- [21] Komonen, J., Penttala, V. (2003) Effects of high temperatures on the pore structure and strength of plain and polypropylene fiber reinforced cement pastes, Fire Technol 39 (1), pp. 23-34.
- [22] Thomas, J.J., Rothstein, D., Jennings, H.M., Christensen, B.J. (2003), Effect of hydration temperatures on the solubility behaviour of Ca-, S-, Al- and Al- and Si- bearing solid phases in Portland cement pastes, Cement & Concrete Research 33 (12), pp. 2037-2047.
- [23] David L. Parkhurst and C.A.J. Appelo (2013) Description of input and examples for PHREEQC version 3: a computer program for speciation, batch-reaction, one-dimensional transport, and inverse geochemical calculations, Techniques and Methods 6-A43, Chapter 43, Section A.

Chloride Ingress and Degradation of Portland Cement Mortar Exposed to Seawater Attack Coupling with Drying-wetting Cycle

S. Cheng¹, Z. Shui¹, T. Sun^{1,2}, X. Gao^{1,2}

¹State Key Laboratory of Silicate Materials for Architectures, Wuhan University of Technology, Wuhan 430070, China.

²School of Civil Engineering and Architecture, Wuhan University of Technology, Wuhan 430070, China.

Abstract

The chloride, sulphate and magnesium ion attack usually occur together in marine environment. The corrosion of concrete in seawater is mainly caused by the chloride induced reinforcement corrosion, the exfoliation of magnesium salt and the volume expansion due to sulphate attack. In addition to ions attack, the drying-wetting cycles always cause a severe deterioration of concrete structures. This study aims to identify the chloride ingress and mechanisms of degradation in Portland cement mortar exposed to simulated seawater attack under drying-wetting cycle conditions. Mortar mixtures are prepared and exposed to NaCl, NaCl+MgCl₂, NaCl+Na₂SO₄ and NaCl+Na₂SO₄+MgCl₂ solutions with a fixed chloride concentration. Chloride transportation and binding capacity of Portland cement based mortars are investigated by titration. In order to identify phase assemblages and microstructural evolutions under exposure, samples are examined by applying XRD, TGA, SEM-EDS and MIP. The analysis of the physical aspect reveal that after 90 days of drying-wetting, the outmost layer (0-5mm) is enriched in sulphate and magnesium ion, and present the highest chloride ion content when exposed to NaCl+MgCl₂ solutions. Moreover, the presence of Mg²⁺ and Mg²⁺+SO₄²⁻ in chloride solution accelerates the chloride ingress, increases the apparent chloride diffusion coefficient and reduces the chloride binding capacity. However, the presence of SO₄²⁻ in NaCl solution retards the chloride ingress and enhances the chloride binding capacity. On the other hand, the chemical composition analysis highlights the conspicuous consumption of portlandite in the outmost layer, the decalcification of C-S-H, and the ettringite (AFt) formation from AFm and aluminium phases. The microstructure analysis shows a refined pore size and significant micro-cracking formation in the sulphate and chloride conditions due to formation of AFt. These phase changes are generally agreed with the predictions of a thermodynamic model.

Keywords: Chloride ingress; Sulfate; Magnesium; Drying-wetting cycle; Thermodynamic model.

1. Introduction

Reinforced concrete is an important construction material for marine exposed structures due to its ability to withstand the harsh marine environment. However, the service life of reinforced concrete structures can be limited by several deterioration mechanisms. Concerning the chemical attacks, the chloride induced reinforcement corrosion is one of the main degradations of concrete, and the simultaneous presence

of corrosive ions such as chloride, sulfate and magnesium in seawater even shows a combined effect on chemical corrosion [1-4]. On the other hand, the physical degradation of concrete under marine environment is non-ignorable factor that can accelerate the chemical attacks. Typical physical degradations such as leaching, wave erosion, repeated dry and wet usually leads to the dissolution of hydrated products and increases the porosity [5-7], and then the concrete matrix is more vulnerable to ingress of aggressive ions and results in surface crack.

The tidal zone is the most serious damage area of concrete structures in marine environment, where usually presents the most complicated degradations including both physical and chemical attacks. However, the degradation mechanisms of cementitious materials under multiple ions attack and drying-wetting cycles have not been studied in detail. This work highlights the degradation mechanisms of Portland cement mortar by multiple corrosive ions under the drying-wetting zone. First of all, the degradation behaviors including mass changes and relative dynamic modulus of elasticity of samples exposed to simulated seawater and the impacts of sulfate and magnesium ions on the chloride ion ingress are investigated. Then, the multiple corrosive ion induced phase changes under drying-wetting cycles are presented. Furthermore, the phase changes are compared with the predictions of a thermodynamic model. Lastly, the microstructure characteristics of mortar samples under different corrosive environments are identified by scanning electron microscopy-energy dispersive spectrometer (SEM-EDS) and mercury intrusion porosimetry (MIP).

2. Methodology

2.1 Materials

The Portland cement type CEM I (strength class 42.5) was used to produce the mortar specimens according to European standard EN 197-1, the chemical composition of cement was determined by X-ray fluorescence (XRF) and shown in Table 1. The analytical reagents sodium chloride, hexahydrate magnesium chloride and anhydrous sodium sulfate were utilized to simulate the major elements in seawater.

Table 1: Chemical composition of ordinary Portland cement by X-ray fluorescence.

Constituents	SiO ₂	Al ₂ O ₃	CaO	MgO	Fe ₂ O ₃	K ₂ O	Na ₂ O	SO ₃	LOI
wt. %	21.76	5.83	62.69	1.72	3.41	1.22	0.07	1.09	1.11

2.2 Sample preparation and exposed to corrosive solution

According to Chinese standard GB/T 29756-2013, mortar mixtures with water to cement ratio of 0.5 and sand to binder ratio of 3 were prepared. Samples were cast in steel molds of 40×40×160 mm³, and then demould after 1 day and cured under the condition of 20±2°C and 98±2% relative humidity for 7 days. Mortar samples were also prepared and filled into 50 mL centrifuge tube, then stored in standard curing chamber. The cement pastes with the same w/c ratio were produced for microstructure analysis.

Table 2: Detailed composition of the exposure solutions.

Conc. (M)	NaCl	MgCl ₂	Na ₂ SO ₄	Cl conc. (M)
NaCl	0.56	-	-	0.56
NaCl+MgCl₂	0.46	0.05	-	0.56
NaCl+Na₂SO₄	0.56	-	0.028	0.56
NaCl+MgCl₂+Na₂SO₄	0.56	0.05	0.028	0.56

The physical and chemical degradation of samples in the ocean tidal zone was simulated by using a self-made drying-wetting cycle test chamber. The corrosion solutions were used: NaCl solution (N), NaCl+MgCl₂ solution (N+M), NaCl+Na₂SO₄ solution (N+S) and NaCl+MgCl₂+Na₂SO₄ solution

(N+M+S). Compared with the seawater, the detailed composite of each corrosive solution were presented in Table 2. All solutions were having a fixed chloride concentration of 0.56 mol/L, and then they were stored in four self-regulating polymethyl methacrylate boxes.

The drying-wetting cycle was set as follows: Firstly, samples were immersed in corrosive solution for 18 h, and then dried for 0.5 h in the air. Afterwards, the samples were dried for 5 h at a temperature of 60°C and followed by cooling down at the room temperature for 0.5 h. Thus, the 24 h represent one drying-wetting cycle. The schematic of drying-wetting cycle box is shown in the Fig. 1. In order to maintain concentration stability of all ions, the exposed solutions were replaced every two weeks.

2.3 Methods

2.3.1 Chloride diffusion

The specimens in the centrifuge tubes were analyzed after 30, 60, 90 and 120 days of exposure. The exposed surfaces were used for profile grinding according to the following intervals: 0-5, 5-10, 10-15 and 15-20 mm. Then, the ground samples were stored in plastic sample sack and placed in a desiccator until analysis. According to the technical specification for chloride ion content test in concrete (JGJ/T 322-2013), the specimen was grinding and passed through a 0.15mm square hole. Then, the collected powder was dried at 105 °C for 2 h, followed by taking about 5 g and mixing the powder with about 50 mL (V₃) diluted nitric acid (water: nitric acid=15:85), and then shocked for 1~2 minutes and stored for 24 h. Afterwards, 10 mL of the supernatant was taken by pipette and placed in a conical flask, and added with 10 mL silver nitrate solution. Finally, the mixtures were titrated with potassium thiocyanate. The total chloride content of specimen can be calculated by Eq. (1).

$$P = \frac{0.3545(C \times V - C' \times V_1)}{G \times \frac{V_2}{V_3}} \times 100\% \quad (1)$$

where P denotes the total chloride content (%); C is the concentration of silver nitrate solution (mol/L); C' is the potassium thiocyanate solution (mol/L); V and V₁ respectively denotes the volume of the added silver nitrate solution and the consumed volume of potassium thiocyanate solution at each test (mL); G is the sample mass of exposed mortar (g); V₂ and V₃ are the selected amount for titration and the amount of dilute nitric acid for dissolved sample (mL).

The apparent chloride ion diffusion coefficient (D_a) is an important index which can be used to characterize the speed of chloride ingress. The apparent chloride diffusion coefficient and the concentration at the surface of sample are determined by fitting experimental data using the solution of Fick's second law fitting Eq. (2).

$$C_{x,t} = C_s [1 - \operatorname{erf} \left(\frac{x}{2\sqrt{D_a t}} \right)] \quad (2)$$

where C_{x,t} is the free chloride content at depth x (m) and exposure time t (s), C_s is the chloride content at the surface and D_a is the apparent diffusion coefficient. The chloride content at the surface (C_s) and apparent diffusion coefficient (D_a) were obtained from the best fit by least squares.

2.3.2 Degradation performance

The mass change measurements after different exposure times can be used to characterize the surface changes of specimen, which can be regarded as an indicator of physical degradation. The mass change of specimen at different exposure time can be calculated by Eq. (3), according to the China standard GB/T50082-2009.

$$\Delta W = \frac{G_t - G_0}{G_0} \times 100\% \quad (3)$$

where ΔW is mass change rate of specimens after corrosion (%); G_0 is the mass of specimen after erosion (g); G_t is the mass of specimen before erosion (g).

A nonmetal ultrasonic analyzer was used to determine the modulus of elasticity of mortar samples at different erosion cycles. The measurement length in this study is 160 mm. The acoustic time value is converted into the relative dynamic modulus of elasticity by Eq. (4).

$$E_{rd} = \frac{E_{dn}}{E_{do}} = \frac{V_n^2}{V_o^2} = \frac{t_o^2}{t_n^2} \quad (4)$$

where E_d and E_{rd} are the dynamic modulus of elasticity (GPa) and the relative dynamic modulus of elasticity, respectively; V represents the ultrasonic velocity of specimen (m/s); ρ denotes the density of specimen (kg/m^3); ν is the Poisson's ratio; V_o is initial ultrasonic velocity of specimen before erosion (m/s); V_n is the ultrasonic velocity of specimen after erosion (m/s); t_o denotes the initial ultrasonic time of specimen before erosion (μs); t_n represents the ultrasonic time of specimen after erosion (μs).

2.3.3 Microstructure characterization

Cement paste from the exposure surface (0-5mm) was characterized by X-Ray diffraction (XRD). The Empyrean X-ray diffractometer produced by PANalytical B.V. (Netherlands) was performed for the test experiment using $\text{Cu K}\alpha = 1.5406 \text{ \AA}$, step size of 0.019° , measuring time 141.804 s/step , start position 5° and end position 70° . The thermogravimetric analysis (TG) was applied by using a Netzsch STA449F3. The samples were heated from 30°C to 1000°C at a rate of 10°C/min while the oven was purged under an inert atmosphere with N_2 flow of 30 mL/min . The exposed surface of mortar sample was further characterized by QUANTA FEG 450 field emission environment scanning electron microscopy (SEM) with energy dispersive spectrometer (EDS). The specimens were coated by epoxy resin and further polished with diamond polishing machine. The point analysis was used to identify the composites of matrix. The effective capillary pore volume and pore size distribution of mortar samples were measured by mercury intrusion porosimetry (MIP), which were conducted on the polished mortars with an age of 90 days exposure. MIP analysis was carried out by using a micromeritics mercury porosimeter (Auto Pore IV-9500, pore size 6 nm - $360 \text{ }\mu\text{m}$). About $1\sim 2$ grams specimen were prepared and soaked in acetone, and then they were dried in a vacuum atmosphere at $60 \pm 2^\circ\text{C}$ for 8 h.

2.3.2 Thermodynamic modelling

Gibbs free energy minimisation program (GEMS 3.3) was utilized to simulate the changes in phase assemblage of binder. The default databases were obtained from the CEMDATA14 database, which contains solubility products of solids relevant for cementitious systems. The data-set includes thermodynamic data for common cement minerals such as ettringite (AFt) and alumina-ferric monophases (AFm), hydrotalcite, hydrogarnet and C-S-H phases. The following simplifications of equilibrium system were conducted: (i) assumed that 10% cement was not reacted; (ii) there were not containing Fe-AFm and Fe-AFt phases in equilibrium system.

3. Results and discussion

3.1 Chloride diffusion behaviour

3.1.1 Chloride content

Fig. 1 shows the total chloride profiles of mortar specimens exposed to different solutions under drying-wetting cycles. With the increase of mortar depths, the total chloride content decreases, and the total chloride content exhibits a distinctive increase with the increase of exposure time. In contrast to the N solution, samples exposed to the N+M and N+M+S solution show higher total chloride content. However, the total chloride content for samples exposed to the N+S solutions is lower than the N solution with

increasing exposure time. It can be revealed that the presence of sulfate ion in chloride solution obstructs the chloride ingress into mortar. This phenomenon can be attributed to two aspects: 1) According to the charges-equilibrium and mass-equilibrium principle, the diffusion rate of sulfate and chloride ion for mortar exposed to the combined solution is less than their single diffusion. 2) The formation of ettringite refines the pore structure and leads to a densification of the matrix, which block the channels of chloride ion penetration [8]. It is clear that the simultaneous presences of sulfate and magnesium ion in NaCl solution exhibit higher chloride ingress. This is because the magnesium ion can react with hydroxyl ions and result in a reduction pH in the pore solution, promoting the chloride ingress based on the charges-equilibrium [9].

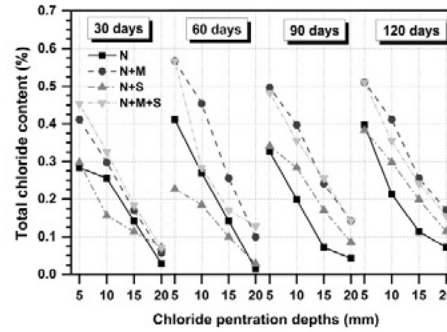


Figure 1: Chloride content of mortar specimens after different exposure time under corrosive solution and drying-wetting cycles.

3.1.2 Apparent chloride diffusion coefficient

The apparent chloride diffusion coefficient (D_{app}) of mortar samples exposed different solutions under drying-wetting cycles are presented in Fig. 2. With increasing of exposure time, the D_{app} exhibits a distinct reduction correspondingly. It is clear that the samples exposed to the N+M solution shows the highest D_{app} regardless of exposure time. The D_{app} of samples in the N+M+S solution is higher than the N solution. It is also found that the N+S solution seems decrease the D_{app} at 60 and 90 days exposure, while it increase the D_{app} after 120 days exposure. Overall, the D_{app} of samples follows $N+M > N+M+S > N+S > N$. It indicates the SO_4^{2-} and Mg^{2+} has different impacts on the D_{app} . Namely, the presence of SO_4^{2-} firstly reduces but later increases the D_{app} of mortar in chloride solution, whereas the $SO_4^{2-} + Mg^{2+}$ in NaCl solution lead to an increase in the D_{app} . The results are in accordance with previous studies, which reveal that the SO_4^{2-} can refine the pore structure of matrix and reduce the D_{app} of mortar when exposed to the combined NaCl and Na_2SO_4 solution at the short exposure time [10]. However, the formation of expansion corrosive product will generate crack occurrence and thereby promote the chloride diffusion. The presence of $SO_4^{2-} + Mg^{2+}$ increases the D_{app} significantly. This may be attributed to the fact that the degradation caused by $SO_4^{2-} + Mg^{2+}$, which aggravates the chloride ingress.

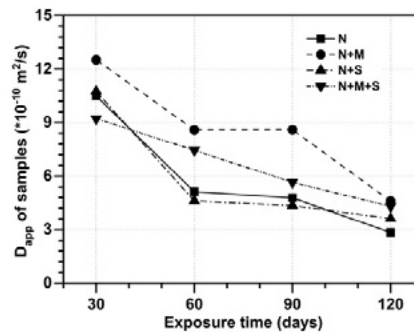


Figure 2: D_{app} of samples after different exposure time under corrosive solution and drying-wetting cycles.

3.2 Magnesium and sulfur profiles

Fig. 3 shows the elemental concentration of magnesium (Mg) and sulfur (S) determined by ICP-OES for the exposed mortar samples at different exposure time. Since the NaCl solution does not contains sulfur and magnesium, samples exposed to solutions of N+M, N+S and N+M+S are selected for analysis. It can be observed that the magnesium content in the outermost layer for mortar exposed to the N+M+S solution is increased with increasing exposure time. The outermost layers (0-5 mm) of the mortar specimens exposed to the N+M+S solution are enriched in magnesium. As for the sulfate ion, although the sulfur content shows a variation between 30 and 120 days of exposure, there is no increase in sulfur content at the outmost layer for the samples exposed to the N+M+S solution. The magnesium profiles in the mortar samples exposed to the N+M reveal that there is no clear increase in the magnesium content at the outermost layer except for 120 days of exposure. For samples exposed to the N+S, the sulfur content also does not further increase at the outmost layer. Compared with the chloride ingress (Fig. 1), it is clear evident that the penetration depths of magnesium ion and sulfate ion are much smaller. The precipitation of brucite occurs at higher pH values ($pH > 10$) and reduces the magnesium concentrations, resulting in limited mobility of magnesium in cementitious systems [11]. Indeed, the formation of brucite is observed on the surface of mortar but its content in the mortar does not increase with the increasing of exposure time. Similar as the results presented in, the magnesium and sulfur were enriched in the outmost section (0-1 mm) [12].

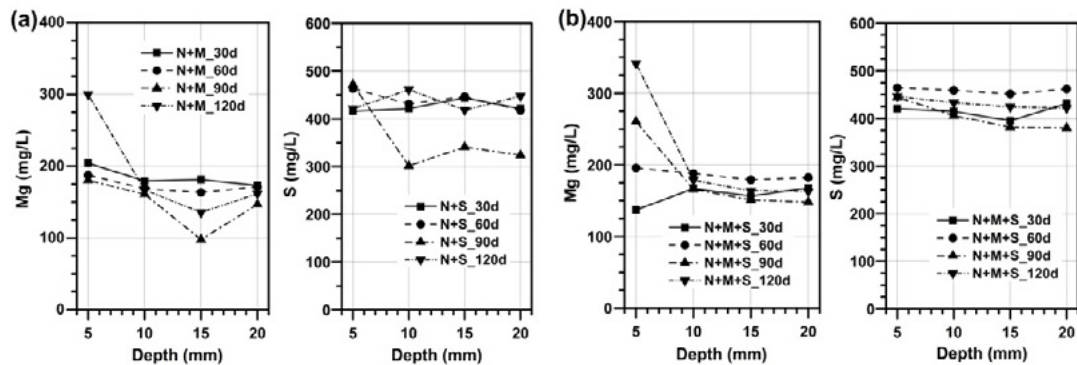


Figure 3: Total magnesium (Mg) and sulfur (S) content determined by ICP-MS for profile ground mortar samples.

3.3 Degradation progress

3.3.1 Mass change

Fig. 4 shows the mass change of mortar specimens exposed to different corrosive solutions under drying-wetting cycle. It is clear that the mass changes of samples exposed to the N solution are increased with the increasing of exposure age. However, for the samples exposed to the N+M solutions, the mass changes show an increase and reach the maximum until the exposure age of 90 days. Afterwards, it shows a decrease after 120 days of exposure. It is also obvious that the mass changes curves of samples exposed to the N+S and N+S+M solution are similar to the group of N+M. The specimens exposed to the N solution show the maximum mass gain of 1.10%, while the mass gains of samples exposed to the combined solution N+M, N+S, and N+M+S reach the maximum of 2.74, 2.34% and 2.51%, respectively. The combined solutions exhibit greater mass changes than those exposed to the N solution under drying-wetting cycles. Initially, the mass of specimens in the N+M solution under drying-wetting cycles increases to 2.74% until 90 days and follows by a slight decrease down to 2.68%. The mass changes of samples exposed to the N+S and N+S+M solutions show a similar tendency. When exposed to corrosive solutions, the presence

of sulfate and magnesium ion in the chloride environment leads to a higher mass gain than the sodium chloride solution. This may be caused by the precipitation of brucite and AFt, which could adhere on the surface of pore walls and inside the pore space in cement matrix. Moreover, it is clear that the solution with sulfate, magnesium and chloride ions results in larger mass change than that with sulfate and chloride. The results in accordance with a previous finding, which revealed that the ordinary Portland concrete immersed in the magnesium sulfate plus sodium chloride solution showed a larger mass decrease than the magnesium sulfate solution [13]. The magnesium ion does not cause obvious mass loss in the chloride solution, this can be attributed to magnesium ion attack, which only reacts with hydroxyl ions at the outmost surface and limit internal erosion, resulting in indistinctive degradation of mortar.

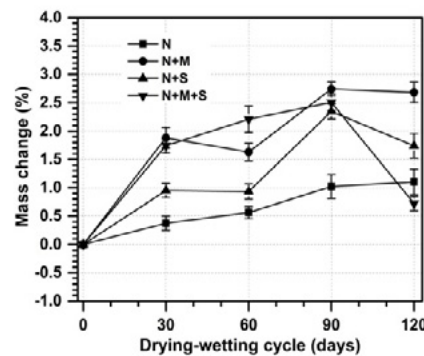


Figure 4: Mass change vs. time for mortar specimens exposed to different solution under drying-wetting cycles.

3.3.2 Dynamic of modulus of elasticity

The dynamic modulus of elasticity for mortar exposed to different exposure solutions under drying-wetting cycles are presented in Fig. 5. It can be noticed that the curves of relative dynamic modulus of elasticity (E_{rd}) is increased with the increasing of exposure age when exposed to the N, N+M and N+S solution, respectively. .

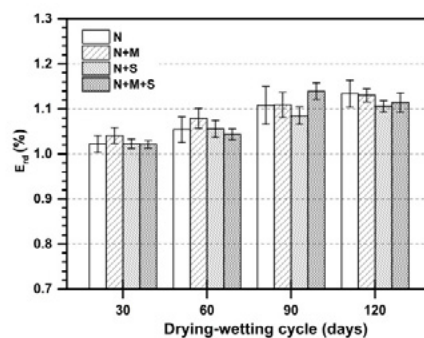


Figure 5: Variation of dynamic modulus of elasticity vs. time for mortar specimens exposed to different solution under drying-wetting cycles

While the E_{rd} of mortars in the N+M+S solution firstly increases until 90 days of exposure and then slightly decreases after 120 days. After 90 days of exposure, the E_{rd} for the mortar exposed to the N+M+S solution reaches the maximum. It can be seen that the presence of sulfate and magnesium in chloride environment has impacts on the variation of E_{rd} , which also proves that the presence of sulfate ion in chloride solution reduces the damage of mortar under drying-wetting cycles. However, the coexistence of sulfate, magnesium and chloride ion intensifies the degradation of mortar. This may indicates that when exposed to sulfate and chloride attack, the generated corrosion products such as ettringite and Friedel's salt (Fig. 6) fill the pore walls and densify the cement matrix. At the early stage of seawater attack, the corrosion

products also refines the pore structure, however, the attacks of multiple corrosive ions lead to corrosion intensification at later stages of exposure

3.4 Phase assemblage

3.4.1 Phase composition

The hydration products and corrosion products of cement paste in different solution after 120 days of exposure are analyzed by XRD and the results are illustrated in Fig. 6. The patterns show that the hydrated products contain hemicarboxonate (Hc) and monocarboxonate (Mc) before exposure and Friedel's salt (Fs) is observed in all samples after exposed to corrosive solutions. Actually, both Hc and Mc could directly convert to Fs with high chloride concentrations. The TGA analysis of exposed hydrated cement for 120 days of exposure (0-5 mm) shows that the phase assemblages contain C-S-H, ettringite (AFt), portlandite (CH) as well as calcium carbonate (Cc), as shown in Fig. 7. It is suggested that the peak ranges from 230~410°C is referred to the decomposition of Fs and the interval of 410-500°C is mainly ascribed to the dehydration of portlandite.

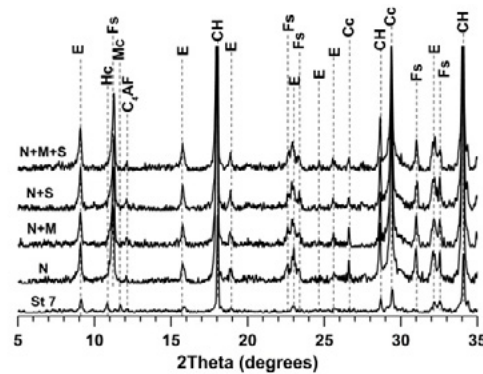


Figure 6: XRD patterns for cement paste samples exposed to different solutions after 120 days drying-wetting cycles

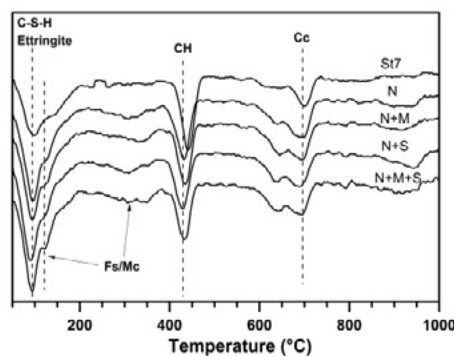


Figure 7: DTG curves for cement paste samples exposed to different solutions after 120 days drying-wetting cycles.

The amount of CH and Fs are determined by DTG and the results are presented in Fig. 8. In contrast to sample exposed to N solution, the amount of Fs decreases in the one exposed to N+S solution, indicating that the formation of Fs is limited by sulfate ions. This is attributed to the fact that C-S-H gels can absorb more sulfates instead of chlorides when exposed to the sulfate + chloride solution. The sulfate presented in combined solution (N+S) reduces the chloride binding and part of Fs converted to Ettringite as a result. Similarly, the presence of $\text{SO}_4^{2-} + \text{Mg}^{2+}$ in chloride solution declines the content of Fs, which suggests that the combined $\text{SO}_4^{2-} + \text{Mg}^{2+}$ decreased the chloride uptake in the C-S-H and induce increased formation of corrosion products [14]. Moreover, it is obvious that the CH content in the N+M+S solution is lower than that exposed to the N solution. The precipitation of brucite reduced the content of CH. Previous study

also indicated that the $\text{SO}_4^{2-} + \text{Mg}^{2+}$ in chloride solution reduce the formation of Fs at the outmost layer.

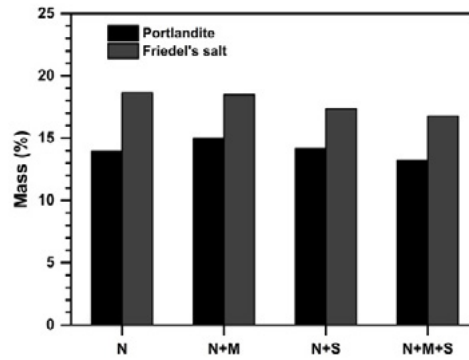


Figure 8: Portlandite and Friedel's salt determined by DTG in the cement paste samples exposed to different solution after 120 days drying-wetting cycles

3.4.2 Modelling of phase change

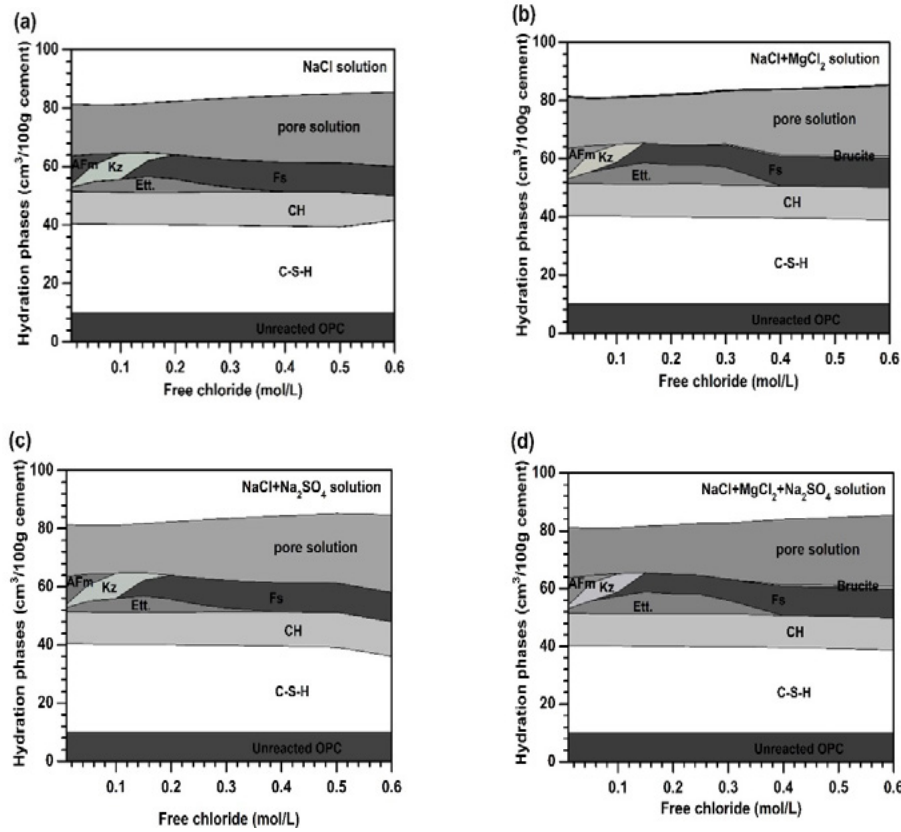


Figure 9: Hydration phases vs. the free chloride concentration for different exposure solutions by GEMS modelling.

Fig. 9 illustrates changes of predicted hydration phases vs. the free chloride present exposed to different solution by GEMS modelling. It is clear that the free chloride concentrations have significant impacts on the phase assemblage of cement. The phase assemblages include C-S-H gel, portlandite, ettringite, monosulphate (AFm) and Kuzel's salt (Ks) in the exposure solutions at low chloride concentrations[15]. However, at high chloride concentration levels, The Fs is the only AFm phase. The results indicate that, with the increasing chloride concentration, the presence of magnesium ion in chloride solution forms to brucite and hence cause a decrease in calcium hydroxide, which is also confirmed by TGA analysis.

Similarly, the changes in hydration phases exposed to N+M+S solutions appear to formation of brucite at high chloride concentration (Fig. 9d). Additionally, it is clear that the content of ettringite is increased when sulfate ion presence in chloride solutions. Thus, GEMS model can predict the hydration phases formed in equilibrium system.

3.5 Microstructure

3.5.1 SEM-EDS

To determine the influence of exposed solutions on the microstructure, mortar matrixes are characterized at 120 days using a Scanning Electron Microscope (SEM) so as to observe their morphology. Fig. 10 shows that the region of SEM observation in mortar matrix generates micro cracking and pores. There are more micro cracking and pores in mortar exposed to the chloride and sulfate solutions (Fig. 10c). However, Mg^{2+} and $SO_4^{2-}+Mg^{2+}$ ion in chloride solution show not significant micro cracking in SEM observation (Fig. 10b and Fig. 10d). This may be attributed to ettringite crystals and resulted in micro cracking occurrence. Fig. 11 shows the SEM-EDS plots for the selected specimens immersed in simulated solutions. The SEM-EDS measurements indicate that, compared with the NaCl solution, the Si/Ca ratios the sample exposed to N+M solutions are decreased. The cloud of points which represent C-S-H gel shifts to left as shown in Fig. 11. This might lead to an increase in the absorption of hydroxyl ions and results in lower pH values. Additionally, the cloud of points of specimens exposed to NaCl+Na₂SO₄ solutions shows higher Si/Ca ratios than the NaCl solution. The change of AFm phases in the composition of the C-S-H can also be observed in the SEM-EDS plots, which are confirmed from XRD spectra and TG curves.

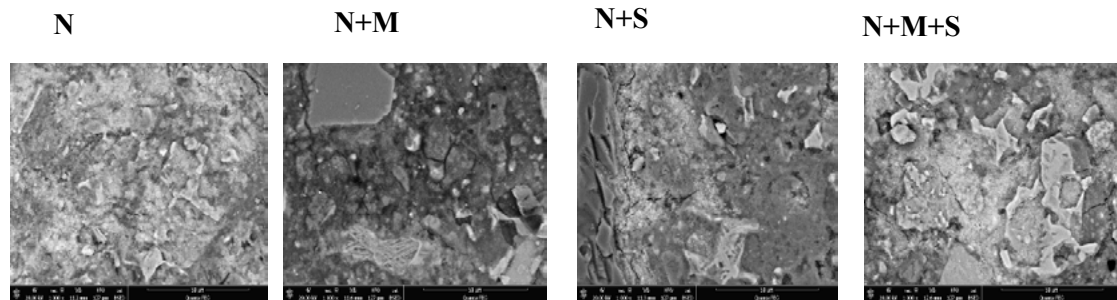


Figure 10: SEM observations of mortar matrices exposed to different solutions after 120 days exposure.

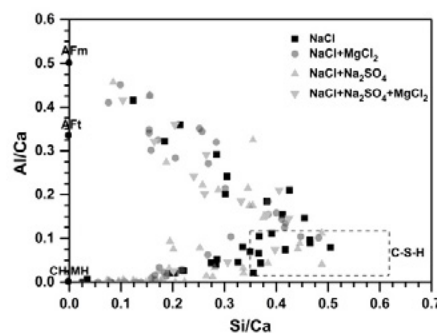


Figure 11: SEM-EDS plots for the mortar specimens exposed to different simulated solutions after 120 days exposure

3.5.2 Pore structure

The MIP analysis is conducted to clearly clarify the pore characteristics. The detailed pore parameters and pore size distribution for samples exposed to different solutions are illustrated Fig. 10. It can be observed that the incremental intrusion follows a similar pattern and there are two main incremental intrusion

distribution peaks in the exposed mortar samples. One peak is ranged from 10 to 50 nm, which is usually considered as less harmful pore (20-50 nm). For the samples in N+S solutions, the pore volume (<20 nm) is higher than that exposed to the N solution, while the volume of pore size between 100 and 200 nm are lower. The pore size volume (<20 nm) of samples exposed to the N+M+S solutions is less than the N solution, whereas the pore size volume (>200 nm) are higher. The results demonstrate that the presence of sulfate ion in chloride solution decrease less harmful pore size, while the presences of sulfate and magnesium ion in NaCl solution increase the harmful pore size. The formation of AFt by sulfate ion precipitates inside the pores and refines the pores size, which declines the chloride penetration channels and retards the chloride ingress. However, the degradations caused by magnesium and sulfate result in increase of porosity and harmful pore size and thus promote the chloride ingress.

Table 3: Detailed composition of the exposure solutions.

Exposure solution	Pore structure information				
	<20 nm volume (%)	20-100 nm volume (%)	100-200 nm volume (%)	>200 nm volume (%)	Porosity (%)
N	55.606	22.564	6.519	15.310	12.977
N+M	57.308	25.267	6.368	11.057	9.006
N+S	58.391	22.819	5.965	12.825	13.681
N+M+S	51.797	21.212	5.987	21.004	13.031

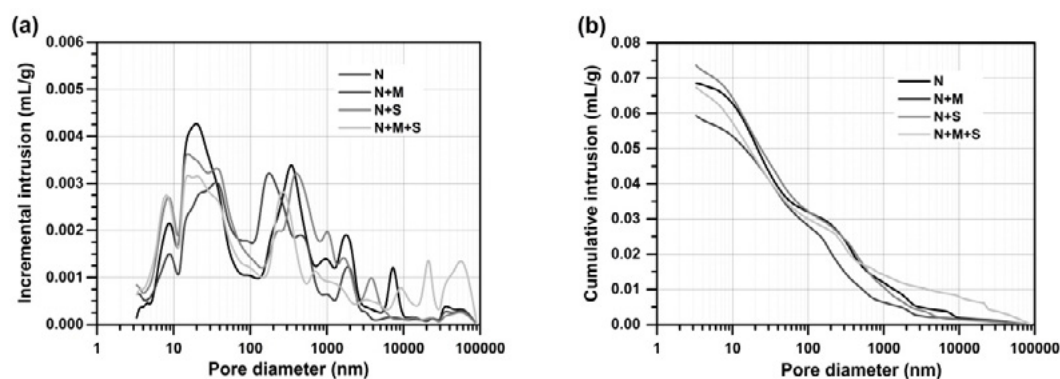


Figure 12: Pore size distribution for mortar samples exposed to different solutions after 120 days drying-wetting cycles.

4. Conclusions

- (1) The presence of sulfate ion in the chloride solution inhibits the chloride ingress, while the $\text{SO}_4^{2-} + \text{Mg}^{2+}$ in chloride ion environment increase the chloride ingress of mortar. In addition, the ingress of magnesium and sulfate ion is limited to the outmost (0-5mm) at the surface.
- (2) The combined corrosive ions have significant effects on the mass loss and relative dynamic modulus of elasticity of Portland cement mortar. The presence of SO_4^{2-} in the chloride solution decreases the mass loss and the dynamic modulus of elasticity change of mortar. However, the simultaneous presences of $\text{SO}_4^{2-} + \text{Mg}^{2+}$ in NaCl solution aggravate the damages of mortar. The SO_4^{2-} in chloride environment reduced the content of Friedel's salt and CH. The presence of sulfate and magnesium ion in chloride solution can further declines the content of Fs and CH and causes decalcification of C-S-H.
- (3) The synergy effects of SO_4^{2-} in chloride environment refine the pore structure and decrease the total

porosity. The coexisting of $\text{SO}_4^{2-} + \text{Mg}^{2+}$ in chloride solution increases the porosity and harmful pore volume, and thus aggravates the ingress of corrosive ions into the matrix.

5. Acknowledgements

This study was financially supported by the National Natural Science Foundation Project of China (No. 51679179) and National Key Research and Development Program of China (No. 2017YFB0310905).

6. References

- [1] M. Maaga, S. Helland, J.E. Cafilan, Exposure to marine environment of chloride penetration of high performance concrete, Science Press, Beijing, 1998.
- [2] M. Santhanam, M. Otieno, 5 - Deterioration of concrete in the marine environment, in: M.G. Alexander (Ed.) Marine Concrete Structures, Woodhead Publishing 2016, pp. 137-149.
- [3] S.-J. Kwon, H.-S. Lee, S. Karthick, V. Saraswathy, H.-M. Yang, Long-term corrosion performance of blended cement concrete in the marine environment – A real-time study, Contribution and Building Materials, 154 (2017) 349-360.
- [4] F.P. Glasser, J. Marchand, E. Samson, Durability of concrete - Degradation phenomena involving detrimental chemical reactions, Cement and Concrete Research, 38 (2008) 226-246.
- [5] T. Simčič, S. Pejovnik, G. De Schutter, V.B. Bosiljkov, Chloride ion penetration into fly ash modified concrete during wetting–drying cycles, Contribution and Building Materials, 93 (2015) 1216-1223.
- [6] Y. Chen, J. Gao, L. Tang, X. Li, Resistance of concrete against combined attack of chloride and sulfate under drying–wetting cycles, Contribution and Building Materials, 106 (2016) 650-658.
- [7] J. Yuan, Y. Liu, Z. Tan, B. Zhang, Investigating the failure process of concrete under the coupled actions between sulfate attack and drying–wetting cycles by using X-ray CT, Contribution and Building Materials, 108 (2016) 129-138.
- [8] M. Zhang, J. Chen, Y. Lv, D. Wang, J. Ye, Study on the expansion of concrete under attack of sulfate and sulfate–chloride ions, Contribution and Building Materials, 39 (2013) 26-32.
- [9] S. Cheng, Z. Shui, T. Sun, X. Gao, C. Guo, Effects of sulfate and magnesium ion on the chloride transportation behavior and binding capacity of Portland cement mortar, Contribution and Building Materials, 204 (2019) 265-275.
- [10] J. Zuquan, S. Wei, Z. Yunsheng, J. Jinyang, L. Jianzhong, Interaction between sulfate and chloride solution attack of concretes with and without fly ash, Cement and Concrete Research, 37 (2007) 1223-1232.
- [11] N.R. Buenfeld, J.B. Newman, The development and stability of surface layers on concrete exposed to sea-water, Cement and Concrete Research, 16 (1986) 721-732.
- [12] K. De Weerd, B. Lothenbach, M.R. Geiker, Comparing chloride ingress from seawater and NaCl solution in Portland cement mortar, Cement and Concrete Research, 115 (2019) 80-89.
- [13] M. Maes, N. De Belie, Influence of chlorides on magnesium sulphate attack for mortars with Portland cement and slag based binders, Contribution and Building Materials, 155 (2017) 630-642.
- [14] K. De Weerd, D. Orsáková, M.R. Geiker, The impact of sulphate and magnesium on chloride binding in Portland cement paste, Cement and Concrete Research, 65 (2014) 30-40.

- [15] Z. Shi, M.R. Geiker, B. Lothenbach, K. De Weerd, S.F. Garzón, K. Enemark-Rasmussen, J. Skibsted, Friedel's salt profiles from thermogravimetric analysis and thermodynamic modelling of Portland cement-based mortars exposed to sodium chloride solution, *Cement Concrete Composites*, 78 (2017) 73-83.

Locally available material (manufactured sands) impacts on properties for an Ultra-High Performance Concrete (UHPC)

R. Yang^{1,2}, R. Yu^{1,4*}, Z. Shui^{1,4}, C. Guo^{1,2}, S. Wu¹, X. Gao³

¹State Key Laboratory of Silicate Materials for Architectures, Wuhan University of Technology, Wuhan 430070, China

²School of Materials Science and Engineering, Wuhan University of Technology, Wuhan 430070, China

³School of Civil Engineering and Architecture, Wuhan University of Technology, Wuhan, 430070, China

⁴Wuhan University of Technology Advanced Engineering Technology Research Institute of Zhongshan City, Zhongshan, 528400, China.

Abstract

In this paper, the physical and chemical characteristics of local material (manufactured sands) impacts on properties for Ultra-High Performance Concrete (UHPC) are studied. Based on the modified Andersen & Andresen (MAA) model, the natural river sand (RS) is partially replaced by manufactured sand (MS) to design UHPC. Then, the properties of the developed UHPC are evaluated. The obtained results show that the particle packing model of UHPC can be disturbed by the addition of MS. Moreover, the flowability and volume stability of the developed UHPC can also be negatively affected by the inclusion of MS. Additionally, based on the chemical reaction and microstructure development points of view, the addition of MS has limited influence on the hydration process and pore size distribution of UHPC, the SEM measurements show that the connection of cementitious matrix with MS is more compact than that with RS, which should be attributed to the typical surface characteristics of the utilized MS particles.

Keywords: Ultra-High Performance Concrete (UHPC), Physical and chemical characteristics, Manufactured sands, Microstructures, Local material.

1. Introduction

Ultra High Performance Concrete (UHPC) is one of the most advanced cement-based construction material. It has outstanding mechanical and durability properties, such as compressive strength [1,2], malleability [3,4], impact resistance [5], chloride penetration resistance and freezing-thawing resistance[6-8]. Compared with other building material (e.g, high performance concrete (HPC)), UHPC can extend service cycle and requires less maintenance costs during their service time, which is fit for structures in harsh working environment, where the durability performance is a primary demand [9]. A representative UHPC mixture proportion consist of binders (cement, fly ash , and silica fume), aggregate (fine sand, quartz or glass power), chemical admixtures, steel fiber, and a small amount of water[10-15]. For UHPC, the aggregate plays an important role in UHPC that occupies about 50% be weight [16-19], which directly influences the cost and mechanical properties of UHPC. Natural river sand has been widely used for producing concrete [20-23]. However, one alarming fact, which should never be ignored, is that the natural river sand (RS) is non-renewable resource. In some regions, RS has already been exceedingly exploited,

which has threatened the safety of bridges and the stability of river banks, and creating environmental problems [24-26]. In addition, the natural river sand is also a typical local material, for instance, there is no RS in Guizhou, China. It must be transported by car from a distance of 1000 kilometers, if this place prepare UHPC use RS which will be generated transportation cost. However, there are a lot of mechanical sand which employed to concrete[27-29]. Therefore, the development of UHPC employing mechanical sand can create additional opportunities for the UHPC applications. The use of mechanical sand not only decreases the cost of UHPC but also eliminates the time in Guizhou. Thus, there is a need to development using mechanical sand which help engineers to use UHPC when necessary without enhances in cost.

Manufactured sand (MS) is a kind of artificial fine aggregates from natural stone based on a series of breaking and grinding techniques. Due to the difference among mother rock composition during crushing, and the reduction ratio, the produced MS grains normally show distinctive particle shapes compared to natural river sand [30-32]. The crushing process tends to produce sharp edged, and angular particles. Compared with more rounded natural sands, the rough-angular particles yield a granular critical state friction angle [33-36]. To clearly understand the influence of MS on the properties of concrete, many investigations have been executed and shown in available literature [37-42]. For instance, Shen et al [43] studied the characterization of MS, for example, surface properties, particle shape, and behavior in concrete. Prakash et al [44] studied the mechanical properties of MS concrete and RS concrete. The experimental results show that the mechanical properties of MS concrete are better than RS concrete. Donza et al [45] investigated the effect of MS on the mechanical properties of concrete. The results show that the shape and physical properties of MS could increase the interlocking between paste and aggregate, thus improving the compressive strength of the concrete. Sahu.Sunil Kumar et al [46] studied the properties of the concrete with RS and MS simultaneously. The results show that the concrete working performance could be reduced by the addition of MS. Li et al [47] studied the influence of MS characteristics on the abrasion resistance and mechanical properties of pavement concrete, and the effect of limestone filler content in MS on durability of different class of concrete. The obtained results indicate that the MS is comparable with RS, and a certain stone powder content in MS can contribute to the strength development, abrasion resistance and durability of the concrete. In general, it can be noticed that, in most cases, the MS is applied in the production of normal or normal strength concrete. With an increase of the requirements on concrete properties from construction industry, it is needed to clarify whether the MS is also suitable to be utilized in producing advanced concrete (e.g. UHPC).

Based on the premises mentioned above, the object of this study is to clarify the physical and chemical characteristics of manufactured sands induced impacts on properties for UHPC. The MS is utilized to partial replace RS by 10-50% in producing UHPC. Then, the macro and micro properties of the developed UHPC are evaluated, such as flowability, mechanical properties, micro-hardness, pore structure and microstructure development.

2. Methodology

2.1 Materials

CEM II, fly ash, and silica fume are used as binding materials in this study. Their chemical constitution is displayed in Table 1. Two types of natural aggregates (0–0.6 mm and 0.6-1.25 mm natural river sand) and two manufactured fine sand (0–0.6 mm and 0.6-1.25 mm manufactured sand). A Polycarboxylic ether based superplasticizer is used to adjust the workability of UHPC.

Table 1: Chemical composition of the used powders in this study (wt. %)

Compositions	Na ₂ O	MgO	Al ₂ O ₃	SiO ₂	P ₂ O ₅	SO ₃	K ₂ O	CaO	Fe ₂ O ₃	LOI
C	0.09	1.61	4.18	19.2	0.09	3.35	0.78	64.93	3.32	2.49
SF	0.13	0.47	0.25	94.65	0.17	0.69	0.84	0.36	0.15	2.29
FA	0.33	0.23	38.01	46.44	0.06	0.69	0.88	7.5	3.12	2.79

(C: Cement, SF: Silica Fume, FA: Fly Ash,)

X-ray diffraction (XRD) patterns of fine aggregates are showed in Fig. 1. As can be seen in figure, their composition is different from each other. The main ingredients of RS are SiO₂, however, the main components of MS are CaCO₃. Fig. 2 shows Scanning Electron Microscopic (SEM) images of particles of RS and MS. The RS grain has round appearance, whose surface is smooth, and the particle has good regularity. Compared with RS, the MS grain has surface asperities, sharp edges and corners.

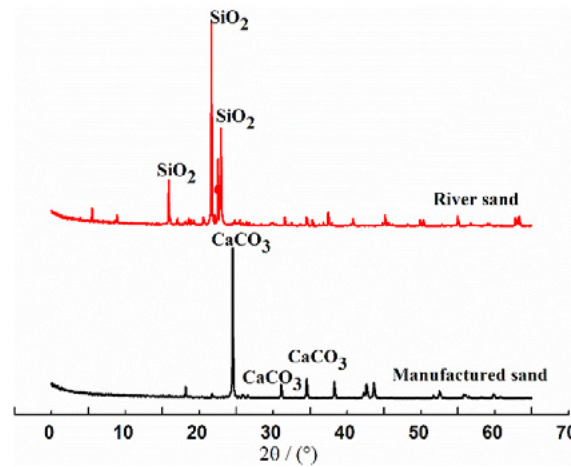


Fig.1 X-Ray diffraction (XRD) patterns of RS and MS

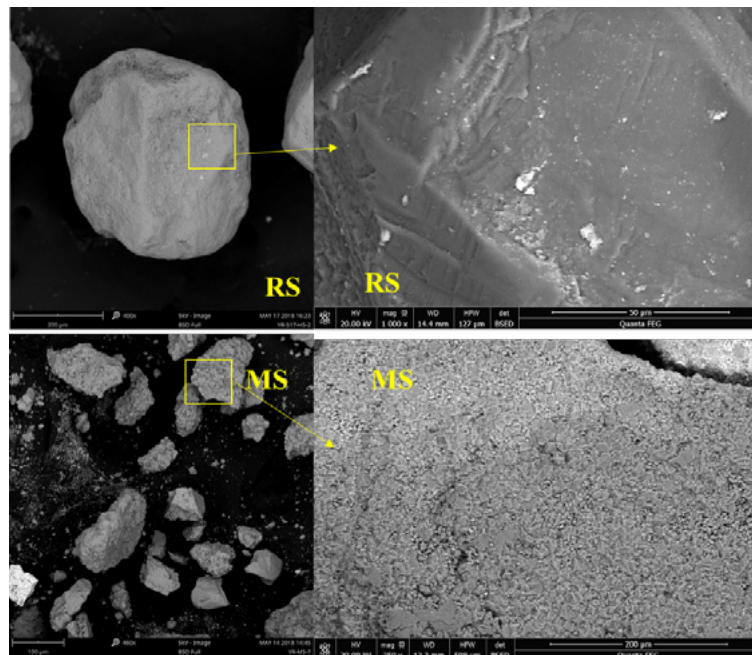


Fig.2 SEM images of NS and MS

2.2 Methods

2.2.1 Mix design

Particle packing theory is used for design the UHPC mixtures in this study. Modified Andreasen & Andersen model was used which is shown in Eq. (1).

$$P(D) = \frac{D^q - D_{min}^q}{D_{max}^q - D_{min}^q} \quad (1)$$

Where $P(D)$ is represented the cumulative percent finer than size D by volume, D is the particle size, D_{min} represent to the minimum particle size, D_{max} is the maximum particle size, and q is coefficient, in this paper, the value of q is set 0.23. The target function play an important role in the optimization of the composition of mixture modified Andreasen & Andersen model. By adjusting the proportion of various materials, an optimum solution is closest to the target curve based on the Least Squares Method (LSM), the result in Eq.(2)

$$RSS = \sum_{i=1}^n \left(P_{mix}(D_i^{i+1}) - P_{tar}(D_i^{i+1}) \right)^2 \quad (2)$$

Where RSS is the sum of the squares of the residuals (RSS), P_{mix} represents the composed mix and the P_{tar} represents the target grading calculated form Eq.(1). When the deviation between the target curve and the calculated curve is minimized, the concrete design is considered to be the best one. In this paper, UHPC which replace RS according to MS is list in table.2. Compared with the reference samples, 10%, 20%, 30%, 40% and 50% of RS (by mass) are replaced by MS in the mixture, four examples of integral gradation curves are given in the figure.3 (due to the fact that the PSD of all the used substitutive are similar). The smaller the integral gradation curve deviates from the target curve, the closer the real accumulation of particles is to the ideal accumulation; the greater the deviation from the target curve, the greater the deviation from the ideal accumulation, and the greater the porosity in the UHPC system. The mixture of RS50-2 is closer to the target curve than the reference RS100, the mixture of RS50-1, RS50-3 deviates from the target curve. This indicates that the particle accumulation of the mixture of RS50-2 is better than that as the reference sample of the mixture of RS100, the MS (0.6-1.25) replaced RS with the same particle size can make the compactness of solid particles pile up maximum. When the MS (0-0.6mm) substitutive to the RS of the same size, the piling between particles becomes worse. The MS (0-1.25mm) replaces the worst stacking between RS particles of the same size

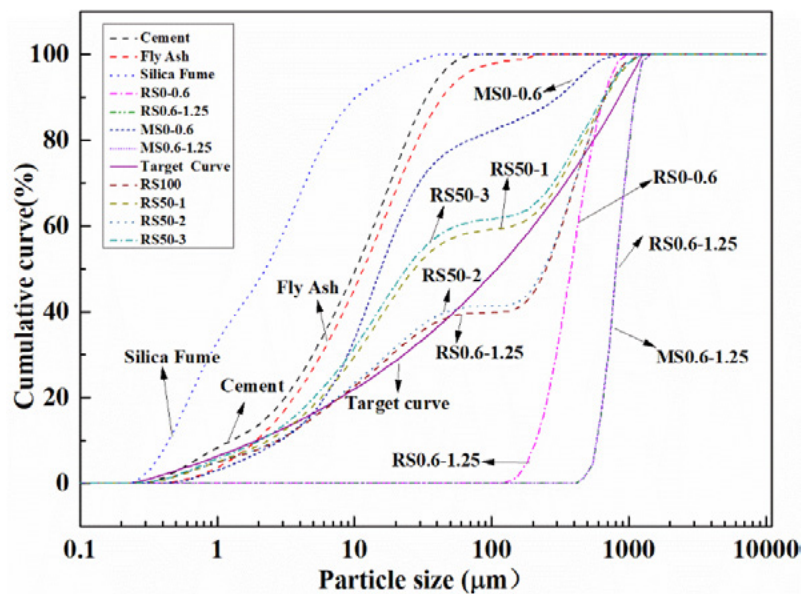


Fig .3 Particle size distribution of the solid constituents and optimized grading curves of different

mixtures.

Table.2 Mix proportion of UHPC

Mixture	C	SF	F	RS _{0-0.6}	RS _{0.6-1.25}	MS _{0-0.6}	MS _{0.6-1.25}	W	SP
RS100	1	0.192	0.267	1.027	0.293	0	0	0.28	0.41
RS10-1	1	0.192	0.267	0.924	0.293	0.103	0	0.28	0.41
RS10-2	1	0.192	0.267	1.027	0.264	0	0.029	0.28	0.41
RS10-3	1	0.192	0.267	0.924	0.264	0.1037	0.029	0.28	0.41
RS20-1	1	0.192	0.267	0.821	0.293	0.235	0	0.28	0.41
RS20-2	1	0.192	0.267	1.027	0.234	0	0.059	0.28	0.41
RS20-3	1	0.192	0.267	0.827	0.235	0.235	0.059	0.28	0.41
RS30-1	1	0.192	0.267	0.719	0.293	0.308	0	0.28	0.41
RS30-2	1	0.192	0.267	1.027	0.205	0	0.088	0.28	0.41
RS30-3	1	0.192	0.267	0.719	0.205	0.308	0.088	0.28	0.41
RS40-1	1	0.192	0.267	0.616	0.293	0.411	0	0.28	0.41
RS40-2	1	0.192	0.267	1.027	0.176	0	0.117	0.28	0.41
RS40-3	1	0.192	0.267	0.616	0.176	0.411	0.117	0.28	0.41
RS50-1	1	0.192	0.267	0.513	0.293	0.513	0	0.28	0.41
RS50-2	1	0.192	0.267	1.027	0.147	0	0.147	0.28	0.41
RS50-3	1	0.192	0.267	0.513	0.147	0.513	0.147	0.28	0.41

(C: cement, F: fly ash, SF: silica fume, RS_{0-0.6} and RS_{0.6-1.25}: natural river sand 0-0.6 mm and 0.6-1.25mm, MS_{0-0.6} and MS_{0.6-1.25}: manufactured sand 0-0.6 mm and 0.6-1.25mm, W: water, SP: superplasticizer)

2.2.2 Flowability test

To evaluate the fresh behavior of the developed UHPC, EN1015-3 is applied in this research. Two diameters perpendicular to each other are measured. Their mean value is used as the slump flow of the designed UHPC.

2.2.3 Mechanical properties test

All the fresh concrete is cast in moulds with the sizes of 40 × 40 × 160 mm, the block are demold about 24h, after place and cured in standard maintenance room, after curing 3,7,28 days, the flexural and compressive strength are tested according to the standard- EN196-1.

2.2.4 Hydration kinetics test

To understand the influence of fine particles (≤ 0.125 mm) of MS on the hydration process of cement, a heat flow calorimetry test is employed. The isothermal heat of each sample was measured by ATM AIR isothermal calorimeter at 25 °C. When the mortar is made, put 24.75g into the volumetric flask, mechanically seal, the container was placed into the calorimeter. The heat evolution and total heat released of the sample was continuously monitored for the first 7 days of hydration.

2.2.5 Microstructure analysis

To clearly understand the effect of the MS on the microstructure development of the design UHPC, three test methods are applied. The pore (pore size distribution and total porosity) of the UHPC measured

by a Micromeritics mercury Porosimeter (namely AutoPore IV-9500, pore size range: 6 nm-360 μ m). The pore structure was test on 7 days and 28 days respectively. The Scanning Electron microscopy (SEM) is characterized the microstructure of UHPC in Backscattered electron mode.

3. Results and discussion

3.1 Fresh behavior of the developed UHPC with manufactured sand

The flowability of UHPC in this research is shown in Fig.4. It is clear that the fluidity is continuously reduced with the increase of the substitution rate of the MS. Compared with reference sample, the fluidity decreased 35mm when the replacement(0-1.25mm) rate is 50% and the fluidity only decreased 15mm when the substitute ratios(0.6-1.25mm) is 50%. This indicated the MS impact on flowability, and then the MS (0-1.25mm) has greater effect than MS (0.6-1.25mm). The main reason is caused by the surface properties of the MS and the particle size distribution. Firstly, the surface of MS is rough, multi-ridges. The increase of internal friction between the paste and the MS in UHPC, result in the slurry flow needs to be overcome greater resistance. Secondly, the accumulation of MS is worse than that of RS, led to the free water reduction of UHPC.

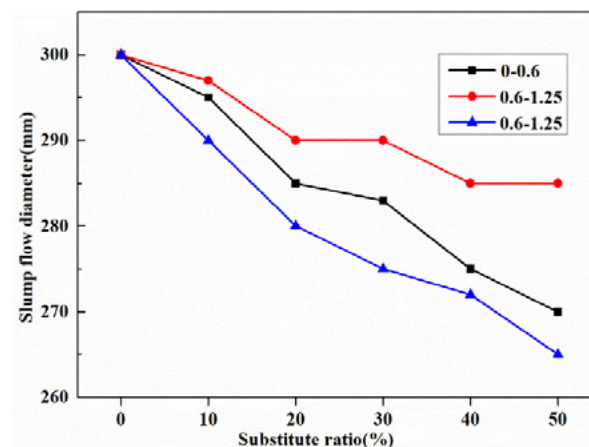


Fig .4 Results of slump flow test

3.2 Mechanical properties of the developed UHPC with manufactured sand

Fig. 5 shows the compressive strength when the different particle size of RS are replaced by MS in designed UHPC matrix at 3, 7, and 28 days, respectively. It can be noticed that the compressive strength increased, when the RS is replaced by the MS (0-0.6 mm and 0-1.25 mm, respectively). The increased value of compressive strength is 0.2-16.8 MPa. When the substitution rate is less than 30%, the compressive strength is not noticeably. When the substitution rate is more than 40%, the value of compressive strength increase more than 10 MPa. The maximum compressive strength increasement is 16.8MPa when the RS substitution ratio is 40% and the 0-1.25 mm. The compressive strength does not increase significantly when the RS is replaced by the MS (0.6-1.25 mm).

Based on appropriate application of modified Andreasen & Andersen particle packing model. Firstly, good stacking generate better mechanical properties in UHPC. Although the strength should be the highest because the MS (0.6-1.25 mm) are the best substitute for stacking. However, the experimental showed opposite result. When MS (0-0.6 mm and 0~ 1.25 mm) are replaced by the same particle size RS, the strength of RS is improved, especially when the substituted rate is considerable, the strength increase is more obvious. Secondly, when the RS is replaced by the MS, there are interlockings between slurry and aggregate in MS UHPC, which would increase the coupling force between slurry and aggregate because

of the edge-angle of the MS particle. Compared with RS, the surface of MS is rough, and the effect of UHPC matrix and aggregate is enhanced by rough surface. In addition, the rough surface makes the C-S-H gel grow nondirective, thus increasing the ratio of crystal to gel. In summary, the compressive strength is determined by the particle accumulation and the surface properties of aggregate in UHPC system.

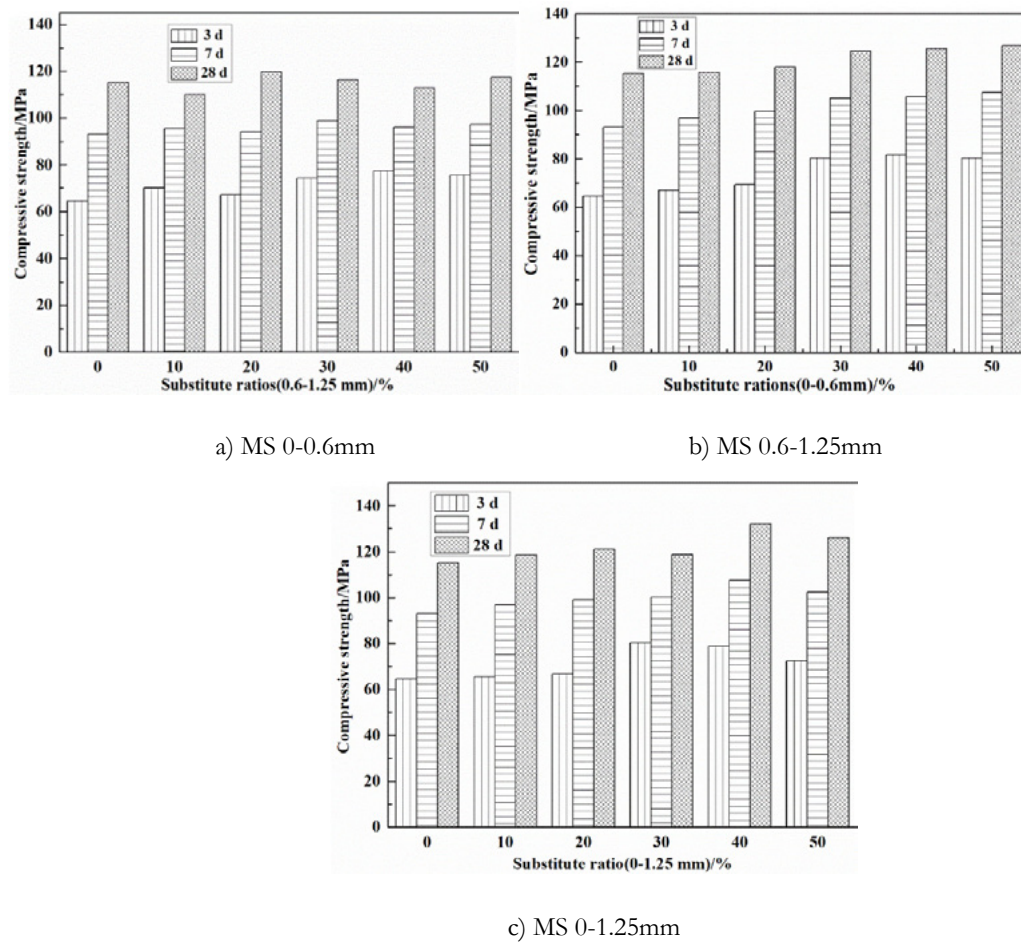


Fig. 5: Results of compressive strength

3.3 Pores structure of the developed UHPC with manufactured sand

To clearly understand the influence of MS on the microstructure development of UHPC, the MIP is used to evaluate the development of UHPC pore structures. The results are shown Fig.6. It can be seen from the figure that the pore size of UHPC is mainly between 5-20 nm at 7days, with the increase of age, the cement continues to hydrate and fill the void between particles. At 28days of age, the pore size of UHPC is mainly are in 3-11nm. The critical pore size is decreasing, the density of concrete increasing. The reason for this phenomenon is that there are more MS particles which less than 125 μ m, and the grain surface is rough, which can be better combined with cement paste. The ITZ can be improved and the density of the ITZ can be increased, the porosity of ITZ is reduced. In addition, the composition of MS is CaCO₃, it can be react with cement hydration product and improve the connection between MS and slurry, therefore the ITZ becoming denser.

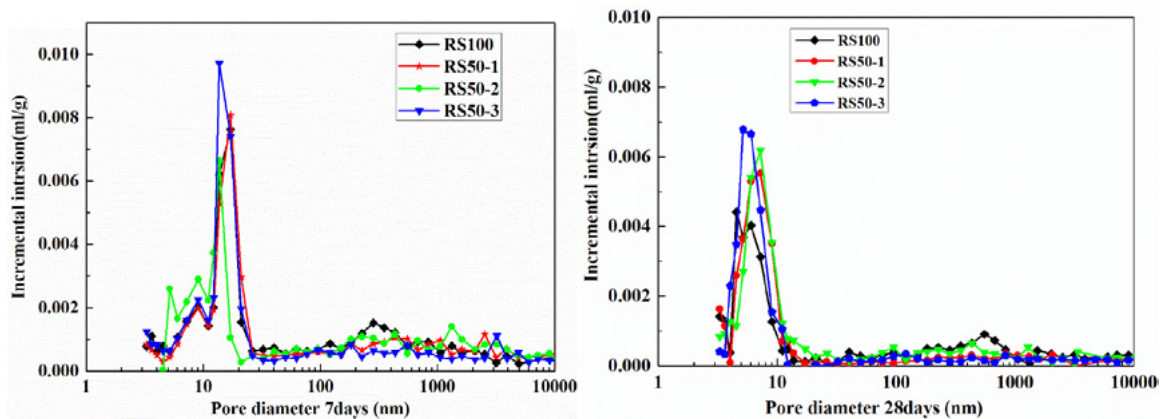


Fig .6 Pore structure analysis results of the UHPC

3.4 Isothermal calorimetry

To clearly understand the impact of these sand particles on cement hydration in UHPC. The hydration heat test was carried out in cement hydration process in UHPC, the results are shown in Fig. 7 (hydration heat release rate curve). The as seen in figure, this results in a slightly different looking the RS100 than the RS50-3 in hydration heat release curve and cumulative heat release curve, this is consistent with previous research. This indicates those grain do not affect the hydration process in cement, or has weakness nucleation effect. Therefore, they have very limited influence on cement hydration and most likely act as filler in the developed UHPC.

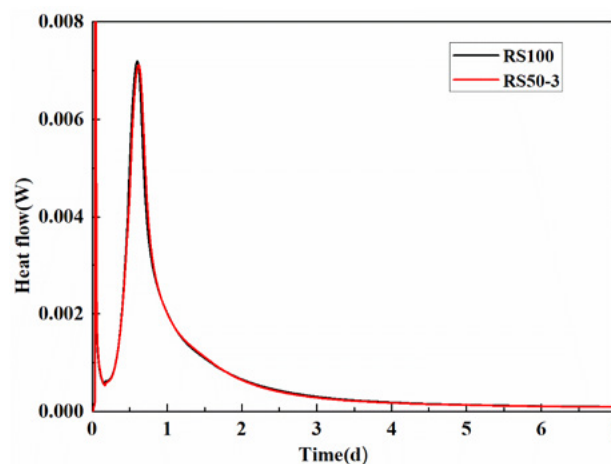


Fig.7 Effect of different sand on the hydration kinetics of the UHPC cementitious system

3.5 Microstructure development and ITZ analysis

To observe the ITZ between aggregate and cement paste, the backsacatter scanning electron was used to study the ITZ. The results are shown in Fig. 8. As can be seen from the figure, there are obvious cracks in the ITZ between RS and paste, but the cracks were not found in ITZ of MS. The reason is mainly due to the nature of the surface properties and particles shape of aggregate. Fig. 2 shows that the surface of RS is smooth, the particles are regular, but the grain of MS is multi-angled and the surface is rough. When the cement is hydrated, the contact area between the rough surface and cement paste increases, which can be better combined with the paste. In addition, the MS particles have edge-angles, there are interlocks between MS and the cement paste. In the complex process of cement hydration, it is difficult to slip the cement paste and the MS. Therefore, compared with the RS, the MS can be better combined with the cement paste and restrain the slippage of the slurry on the surface of the aggregate during the cement hydration process,

forming a denser ITZ.

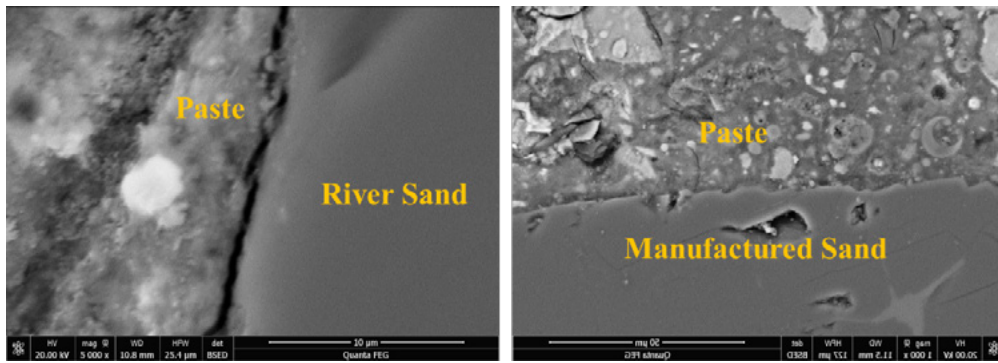


Fig .8 BSE/SEM images for the mixture at 28 days

Fig. 9 shows the relationship between the porosity and strength of UHPC at 28days. In generally, the strength of concrete decrease with the increase of porosity, the strength concrete increase with the decrease porosity. It can be seen from the Fig. 9, the mixture of RS100 has the highest porosity, and the lowest corresponding strength, the macro-porosity of the mixture of RS50-1 and RS50-3 is equivalent and the strength is also equivalent. The reason is mainly caused by the surface characteristics and composition of the MS. The main component of MS is CaCO_3 , it could have a weak chemical reaction with the cement paste, the interface between aggregate and paste is closely connected, in addition, the surface of the MS is rough, compared with the volume of the MS and RS, its specific surface area is large, and it can be better combined with the slurry. The MS particles have multiple edges and corners, thus the interlockings exist between the cement pastes. The results are in good agreement with the results of BES. There is no obvious crack between the MS and the slurry, but it can be found between the RS and the slurry.

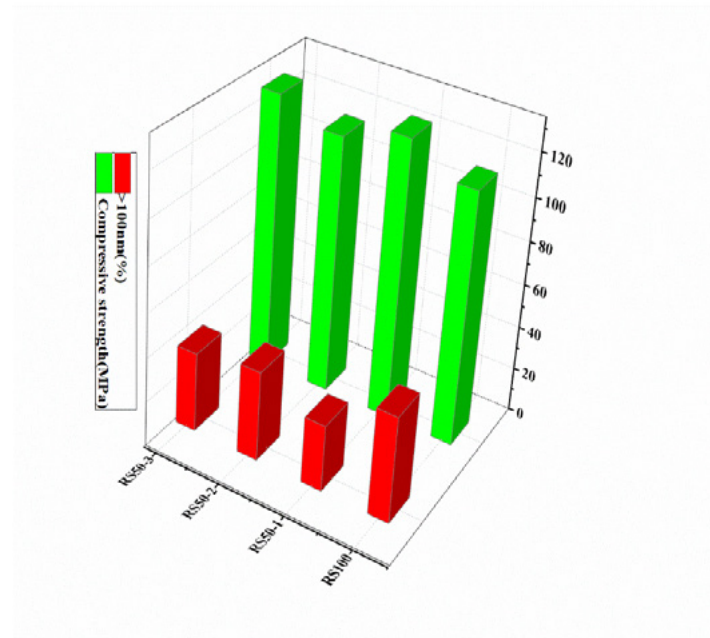


Fig.9 Compressive strength and Macro-porous percentage

4. Conclusions

Based on closest packing theory, a study on the replacement of RS by limestone MS is carried out. The properties of MS UHPC are analyzed in terms of fluidity, mechanical properties, and 2.2.5

Microstructure analysis. The key survey and findings of this research can be summarized as follows:

1. The MS has great influence on fluidity, the UHPC which is made up of MS has worse fluidity;
2. Under certain conditions, particle accumulation determining the mechanical properties of UHPC. The surface properties of aggregate also affect the mechanical properties of UHPC. Namely, the mechanical properties of UHPC are determined by particle packing, aggregate morphology and surface properties;
3. Based on the chemical reaction point of view, the included fine particles from MS have limited effect on the cement hydration kinetics of UHPC. However, the typical physical characteristics of MS (rough surface, multi-edges, and interlocks) are the key factor to obtain UHPC with advanced mechanical properties and optimized microstructure (e.g. ITZ of UHPC)

5. Acknowledgment

The authors acknowledge the financial supports of National Nature Science Foundation Project of China (51608409), Major science and technology project in Zhongshan city, Guangdong province (2017A1021), Yang Fan plan of Guangdong Province (201312C12), Science and Technology Program of Guangdong Province in 2016 (2016A090924002), Science and Technology Program of Guangdong Province in 2017 (2017B090907009), Late-model Research Institute Development Program of Zhongshan in 2016: Subsidy for Major Research Platform Construction (2016F2FC0008), and open research project of Advanced Engineering Technology Research Institute of Wuhan University of technology in Zhongshan city (WUT201802).

6. References

- [1] K. Wille, A.E. Naaman, G.J. Parra-Montesinos, Ultra-high performance concrete with compressive strength exceeding 150 MPa (22 ksi): a simpler way, *ACI Mater. J.*108 (1) (2011) 46–54.
- [2] De Larrard F, Sedran T. Optimization of ultra-high-performance concrete by the use of a packing model. *Cem. Concr. Res.* 24(6) (1994) 997-1009.
- [3] Pyo S, Wille K, El-Tawil S, Naaman AE. Strain rate dependent properties of ultra high performance fiber reinforced concrete (UHP-FRC) under tension. *Cem. Concr. Compos.* 56 (2015) 15–24.
- [4] Yoo D-Y, Banthia N. Mechanical properties of ultra-high-performance fiber-reinforced concrete: A review. *Cem. Concr. Compos.*73 (2016) 267-80.
- [5] Tran NT, Tran TK, Jeon JK, Park JK, Kim DJ. Fracture energy of ultra-high-performance fiber-reinforced concrete at high strain rates. *Cem. Concr. Res.* 79 (2016) 169–184.
- [6] Shi C, Wu Z, Xiao J, Wang D, Huang Z, Fang Z. A review on ultra high performance concrete: Part I. Raw materials and mixture design. *Constr. Build. Mater.* 101 (2015) 741-51.
- [7] Hooton R, Titherington M. Chloride resistance of high-performance concretes subjected to accelerated curing. *Cem. Concr. Res.*34 (2004)1561–1567.
- [8] Abbas S, Soliman AM, Nehdi ML. Exploring mechanical and durability properties of ultra-high performance concrete incorporating various steel fiber lengths and dosages. *Constr. Build. Mater.* 75 (2015) 429-41.
- [9] Kono K, Musha H, Kawaguchi T, Eriguchi A, Tanaka S, Kobayashi T, et al. Durability study of the first PC bridge constructed with ultra high strength fiber reinforced concrete in Japan. *Proceedings of the RILEM-fib-AFGC International Symposium on Ultra-High Performance Fibre-Reinforced Concrete*2013,

239-48.

[10] Kim H, Koh T, Pyo S. Enhancing flowability and sustainability of ultra high performance concrete incorporating high replacement levels of industrial slags. *Constr. Build. Mater.* 123 (2016) 153-160.

[11] Wu Z, Khayat KH, Shi C. Effect of nano-SiO₂ particles and curing time on development of fiber-matrix bond properties and microstructure of ultra-high strength concrete. *Cem. Concr. Res.* 95 (2017) 247-56.

[12] Ngo TT, Park JK, Pyo S, Kim DJ. Shear resistance of ultra-high-performance fiber-reinforced concrete. *Constr. Build. Mater.* 151 (2017) 246-257.

[13] Meng W, Khayat KH. Improving flexural performance of ultra-high-performance concrete by rheology control of suspending mortar. *Composites Part B*, 117 (2017) 26-34.

[14] Richard P, Cheyrezy M. Composition of reactive powder concretes. *Cem. Concr. Res.* 25(7) (1995) 1501-1511.

[15] Yu R, Spiesz P, Brouwers H. Mix design and properties assessment of ultra-high performance fibre reinforced concrete (UHPFRC). *Cem. Concr. Res.* 56 (2014) 29-39.

[16] Lee Y, Kang S-T, Kim J-K. Pullout behavior of inclined steel fiber in an ultra-high strength cementitious matrix. *Constr. Build. Mater.* 24(10) (2010) 2030-2041.

[17] Ghafari E, Ghahari SA, Costa H, Júlio E, Portugal A, Durães L. Effect of supplementary cementitious materials on autogenous shrinkage of ultra-high performance concrete. *Constr. Build. Mater.* 127 (2016) 43-48.

[18] Yu R, Spiesz P, Brouwers H. Development of an eco-friendly Ultra-High Performance Concrete (UHPC) with efficient cement and mineral admixtures uses *Cem. Concr. Compos.* 55 (2015) 383-394.

[19] Alsalman A, Dang CN, Hale WM. Development of ultra-high performance concrete with locally available materials. *Constr. Build. Mater.* 133 (2017) 135-145.

[20] Wang X, Yu R, Shui Z, Song Q, Zhang Z. Mix design and characteristics evaluation of an eco-friendly Ultra-High Performance Concrete incorporating recycled coral based materials. *J Clean Prod*, 165 (2017) 70-80.

[21] Chen Y, Yu R, Wang X, Chen J, Shui Z. Evaluation and optimization of Ultra-High Performance Concrete (UHPC) subjected to harsh ocean environment: Towards an application of Layered Double Hydroxides (LDHs). *Constr. Build. Mater.* 177 (2018) 51-62.

[22] Song Q, Yu R, Shui Z, Wang X, Rao S, Lin Z. Optimization of fibre orientation and distribution for a sustainable Ultra-High Performance Fibre Reinforced Concrete (UHPFRC): Experiments and mechanism analysis. *Constr. Build. Mater.* 169 (2018) 8-19.

[23] Su Y, Wu C, Li J, Li Z-X, Li W. Development of novel ultra-high performance concrete: From material to structure. *Constr. Build. Mater.* 135 (2017) 517-528.

[24] Raman SN, Ngo T, Mendis P, Mahmud H. High-strength rice husk ash concrete incorporating quarry dust as a partial substitute for sand. *Constr. Build. Mater.* 25 (2011) 3123–3130.

[25] Manning D, Vetterlein J. Exploitation and Use of Quarry Fines; Report No: 087. MIST2/DACM/01; Mineral Solutions Limited: Manchester, UK; March; 2004; pp. 1–60. Available online: <http://www.>

sustainableaggregates.com/library/docs/mist/10066_ma_2_4_003.pdf (accessed on 5 August 2015).

- [26] Thomas T, Dumitru I, van Koeverden M, West G, Basford G, Lucas G, et al. Manufactured Sand. National Test Methods and Specification Values Available online: http://www.ccaa.com.au/imis_prod/documents/Library%20Documents/CCAA%20Reports/ManSand.pdf (accessed on 7 April 2016).
- [27] Singh S, Nagar R, Agrawal V. A review on Properties of Sustainable Concrete using granite dust as replacement for river sand. *J CLEAN PROD*, 126 (2016) 74-87.
- [28] Joudi-Bahri I, Lecomte A, Ouezdou MB, Achour T. Use of limestone sands and fillers in concrete without superplasticizer. *Cem. Concr. Compos.* 34(6) (2012) 771-780.
- [29] Shen W, Li X, Gan G, et al. Experimental investigation on shrinkage and water desorption of the paste in high performance concrete[J]. *Constr. Build. Mater.* 114(2016): 618-624.
- [30] Chi C, Wu Y, Riefler C. The use of crushed dust production of self-consolidating concrete (SCC), Recycling Concrete and other materials for sustainable development, Editors Tony C. Liu Christian Meyer. ACI International SP-219. 2004.
- [31] Kenai S, Benna Y, Menadi B. The effect of fines in crushed calcareous sand on properties of mortar and concrete. *Infrastructure regeneration and rehabilitation improving the quality of life through better construction International conference1999*: 253-261.
- [32] F.L. Li, C.J. Liu, L.Y. Pan, C.Y. Li, *Machine-Made Sand Concrete*, China Water Power Press, Beijing, China, 2013 (in Chinese with English content).
- [33] Ji T, Chen C-Y, Zhuang Y-Z, Chen J-F. A mix proportion design method of manufactured sand concrete based on minimum paste theory. *Constr. Build. Mater.* 44 (2013) 422-426.
- [34] Zhao S, Ding X, Zhao M, Li C, Pei S. Experimental study on tensile strength development of concrete with manufactured sand. *Constr. Build. Mater.* 138 (2017) 247-253.
- [35] Cepuritis R, Wigum B, Garboczi E, Mørtzell E, Jacobsen S. Filler from crushed aggregate for concrete: Pore structure, specific surface, particle shape and size distribution. *Cem. Concr. Compos.* 54 (2014) 2-16.
- [36] Cepuritis R, Jacobsen S, Smeplass S, Mørtzell E, Wigum BJ, Ng S. Influence of crushed aggregate fines with micro-proportioned particle size distributions on rheology of cement paste. *Cem. Concr. Compos.* 80 (2017) 64-79.
- [37] Donza H, Cabrera O, Irassar E. High-strength concrete with different fine aggregate. *Cem. Concr. Res.* 32(11) (2002) 1755-1761.
- [38] Cortes D, Kim H-K, Palomino A, Santamarina J. Rheological and mechanical properties of mortars prepared with natural and manufactured sands. *Cem. Concr. Res.* 38(10) (2008) 1142-1147.
- [39] Shen W, Liu Y, Cao L, Huo X, Yang Z, Zhou C, et al. Mixing design and microstructure of ultra high strength concrete with manufactured sand. *Constr. Build. Mater.* 143 (2017) 312-321.
- [40] Nanthagopalan P, Santhanam M. Fresh and hardened properties of self-compacting concrete produced with manufactured sand. *Cem. Concr. Compos.* 33(3) (2011) 353-358.
- [41] Li H, Huang F, Cheng G, Xie Y, Tan Y, Li L, et al. Effect of granite dust on mechanical and some durability properties of manufactured sand concrete. *Constr. Build. Mater.* 109 (2016) 41-46.

-
- [42] Cepuritis R, Jacobsen S, Pedersen B, Mørtzell E. Crushed sand in concrete—effect of particle shape in different fractions and filler properties on rheology. *Cem. Concr. Compos.* 71 (2016) 26-41.
- [43] Shen W, Yang Z, Cao L, Cao L, Liu Y, Yang H, et al. Characterization of manufactured sand: Particle shape, surface texture and behavior in concrete. *Constr. Build. Mater.* 114 (2016) 595-601.
- [44] Prakash Rao D, Giridhar Kumar V. Investigations on concrete with stone crusher dust as fine aggregate. *The Indian Concrete Journal*, July, 2004.45-50.
- [45] Bonavetti V, Donza H, Rahhal V, Irassar E. High-strength concrete with limestone filler cements. *Special Publication.* 186 (1999) 567-80.
- [46] Sahu A, Kumar S, Sachan A. Crushed stone waste as fine aggregate for concrete.. *The Indian Concrete Journal*, January, 2003.845-848.
- [47] Li B, Ke G, Zhou M. Influence of manufactured sand characteristics on strength and abrasion resistance of pavement cement concrete. *Constr. Build. Mater.* 25(10) (2011) 3849-3853.

Application of Krstulovic-Dabic model on early hydration analysis of Portland cement under Mg^{2+} influence

X.S. Li ^{1,2}, Z.H. Shui ¹, X. Gao ³

¹ State Key Laboratory of Silicate Materials for Architectures, Wuhan University of Technology, Wuhan 430070, China

² School of Materials Science and Engineering, Wuhan University of Technology, Wuhan 430070, China

³ School of Civil Engineering and Architecture, Wuhan University of Technology, Wuhan 430070, China

Abstract - Fresh water is the natural resource for human survival, and it is widely used in human life and production. Due to the increasing scarcity of freshwater resources, more and more freshwater applications need to find alternatives to other substances. Concrete production needs a large amount of fresh water. Processes including mixing and maintenance all require massive fresh water. In coastal areas far from the interior, sea water is used to produce concrete. However, there are still many problems to be verified during seawater mixing, one of which is Mg^{2+} interaction with matrix. In this study, the effect of Mg^{2+} on early hydration of Portland cement is discussed. Heat flow calorimetry is employed to characterize influence of Mg^{2+} on early hydration of cement. The obtained results reveal that hydration during induction and acceleration periods is significantly influenced after incorporation of Mg^{2+} . Mg^{2+} induces hydration inhibition during deceleration and stabilization period. The results from this study can provide more supporting materials for verification on seawater mixing.

Keywords: Mg^{2+} ; calorimetry; Krstulovic-Dabic model; C_3S dissolution

1. Introduction

With the growing shortage of drinking water and constantly increasing on global population, insufficient supply of freshwater has become a severe problem in the front of human races [1]. It is predicted that half of global population will be lack of freshwater at the end of 2025 [2]. Development of concrete industry requests huge consumption of freshwater. In the year of 2016, the whole production amount of cement worldwide was 4.2 billion tons [3]. It is estimated that over 3.0 tons of freshwater has consumed in concrete mixing and curing in one year. In coastal areas far from continent, seawater is considered to be an alternative of freshwater and it is concluded that seawater can be employed in concrete structures without reinforced rebars [4-6]. However, there are still many problems to be solved concerning about safe utilization of seawater mixing, one of which is concerns about interactions of Mg^{2+} from seawater with cement-based materials.

Mixing with Mg^{2+} solutions could induce significant hydration delay in cement system. Reddy et al incorporate $MgCl_2$ with different concentrations into ordinary Portland cement system and find that both initial and final setting time are prolonged. More importantly, the elongation degree increases with increase on $MgCl_2$ concentrations [7]. Thomas et al apply seawater in the peninsular area of Sierra Leone as mixing water in ordinary Portland cement system and conclude that seawater in Goderich, Sussex, Bawbaw and No. 2 River significantly delay setting time of cement [8].

In previous study, research about internal corrosion of Mg^{2+} mainly analysis with calorimetry analysis [9-12]. However, effect of Mg^{2+} on cement hydration should be further carried out. Discussion on this part requires more comprehensive understanding on hydration process.

In this study, research is concentrated on Mg^{2+} induced influences on early age cement hydration. Heat flow calorimetry is employed to characterize influence of Mg^{2+} on early hydration of cement. Hydration kinetics analysis is carried out with Krstulovic-Dabic model. The results from this study can provide more supporting materials for verification on seawater mixing.

2. Methodology

2.1 Materials

P I 52.5 Portland cement is used in this study. Chemically pure magnesium nitrate is applied to provide magnesium into hydration system. The chemical composition of P I 52.5 Portland cement is presented in Table 1.

Table 1: Chemical composition of main materials (wt. %).

Material	SiO ₂	Al ₂ O ₃	CaO	Fe ₂ O ₃	SO ₃	MgO	Na ₂ O	K ₂ O	P ₂ O ₅	LOI
PC	20.04	5.27	63.19	3.24	2.59	1.59	0.17	0.83	0.06	2.06

2.2 Methods

The w/c ratio of cement paste is fixed at 0.3. 0.055 mol/L (M1 group), 0.110 mol/L (M2 group) and 0.22 mol/L (M3 group) magnesium nitrate solution are prepared to introduce different concentration of magnesium during mixing. The group (R group) without magnesium added is employed as reference.

Hydration heat test is carried out with TAM AIR microcalorimeter from TA instruments, USA. Based on consistence on specific heat with reference, 15 g paste is prepared and examined. The heating rate is fixed from 0.1 - 2.0 °C/min.

3. Results and discussion

3.1 Hydration heat release

The heat flow of Portland cement with different Mg^{2+} concentration is presented in Figure 1. It can be seen the heat release during induction period is promoted after Mg^{2+} incorporation. The improvement degree is proportional to the concentration of Mg^{2+} , especially when concentration of Mg^{2+} reaches 0.22 mol/L. In terms of acceleration period, it can be seen from Figure 1 that heat release presented limited difference when Mg^{2+} concentration is below 0.11 mol/L. While significant promotion on heat evolution is observed when concentration of Mg^{2+} reaches 0.22 mol/L. The lowest heat flow during induction period is 0.75 mW/g, 0.85 mW/g, 0.92 mW/g and 1.14 mW/g for R, M1, M2 and M3, respectively. The enhancement on heat release is inherited from induction period to acceleration period. As the heat release between 1 and 12 h of Portland cement is mainly brought by reaction of C_3S and to C-S-H and $Ca(OH)_2$ as presented by Jansen et al, it can be seen that incorporation of Mg^{2+} could somehow influence C_3S reaction, especially under high concentrations [13]. More importantly, it can be seen that Mg^{2+} also induces regular decline on maximum heat flow and advance on time of maximum heat flow. This will be further discussed in the following part. The maximum heat flow is also considered to be controlled by C_3S hydration [13-14].

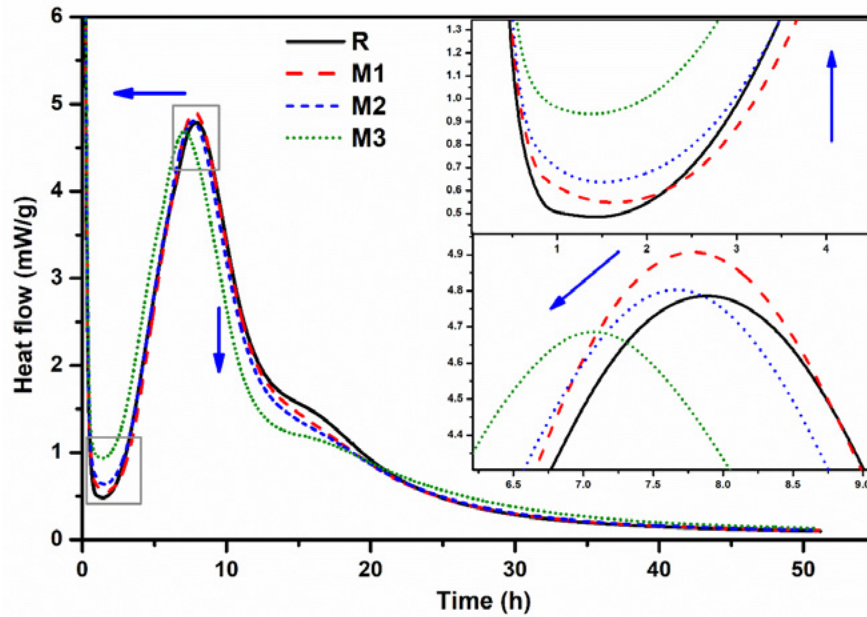


Figure 1: Heat flow of Portland cement with different Mg^{2+} concentration.

Figure 2 presents heat of Portland cement with different Mg^{2+} concentration. As all groups possess the same mix proportion, the heat released is in consistent with hydration degree. It can be seen when Mg^{2+} concentration is below 0.11 mol/L, influence from Mg^{2+} is not obvious in first 12 hs. However, when Mg^{2+} concentration is reaches 0.22 mol/L, significant hydration promotion is exhibited in first 12 hs. The reaction from C_3S to C-S-H and $Ca(OH)_2$ during acceleration period is more significant in M3 group and that in reference group. The promotion on heat evolution should be attributed to changes on pore solution environment [15-17].

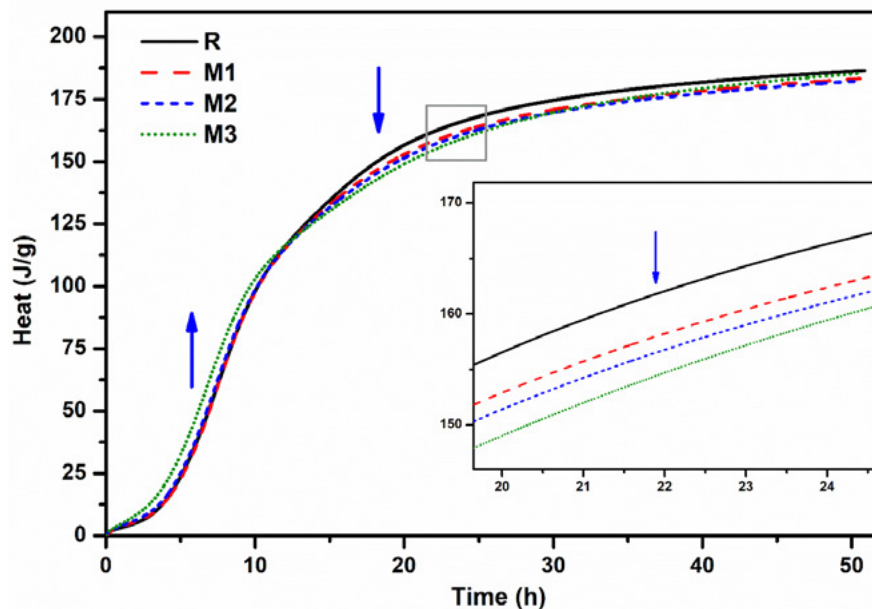


Figure 2: Heat of Portland cement with different Mg^{2+} concentration.

However, after hydrated for 12 hs, the decrease on heat release is presented in groups with Mg^{2+} incorporated. This is consistent with research from Agatzini et al [18-20]. The M3 group also exhibits some specific characteristics. Except for acceleration during acceleration period and inhibition during deacceleration period, decreased difference between R and M3 groups during stabilization period is observed.

Furthermore, the main information of heat release characteristics of Portland cement with different Mg^{2+} concentration is presented in Table 2. Mg^{2+} increases maximum heat flow when Mg^{2+} concentration is 0.055 mol/L and 0.110 mol/L but decreases maximum heat flow when Mg^{2+} concentration is 0.220 mol/L. Meanwhile, Mg^{2+} decreases time of maximum heat flow. The time of maximum heat flow of R, M1, M2 and M3 is 7.88 h, 7.78 h, 7.66 h and 7.07 h, respectively. The onset of acceleration period of R, M1, M2 and M3 are 2.28 h, 2.92 h, 2.87 h and 2.54 h, respectively. More importantly, the delay degree decreases with increase on Mg^{2+} added. Simultaneously, Mg^{2+} decreases hydration heat after hydrated for 24 h. As presented in Table 2, the heat release at 24 h of R, M1, M2 and M3 is 166.3 J/g, 162.4 J/g, 161.0 J/g and 159.5 J/g, respectively. The inhibition effect is proportional to Mg^{2+} addition. However, after hydrated for 48 h, the heat release of R, M1, M2 and M3 is 185.5 J/g, 182.2 J/g, 181.3 J/g and 184.1 J/g, respectively. The M3 group does not exhibit the most significant inhibition.

Table 2: Heat release characteristics of Portland cement with different Mg^{2+} concentration.

	R	M1	M2	M3
maximum heat flow [mW/g]	4.76	4.91	4.80	4.69
time of maximum heat flow [h]	7.88	7.78	7.66	7.07
Onset of acceleration period [h]	2.28	2.92	2.87	2.54
24 h heat release [J/g]	166.3	162.4	161.0	159.5
48 h heat release [J/g]	185.5	182.2	181.3	184.1

3.2 Hydration kinetics analysis

Krstulovic-Dabic model is employed to analyze the hydration kinetics analysis of Portland cement [21]. Based on Krstulovic-Dabic model, hydration of cement should be divided into three stages, including nucleation and growth process (NG), phase boundary process (I), diffusion process (D) [22-23]. Determination of kinetic factors from linear regression and fitting curves of hydration rate are presented in Figure 3, Figure 4, Figure 5 and Figure 6. It can be seen R^2 during linear fitting are all above 0.9950, indicating the fitting is credible.

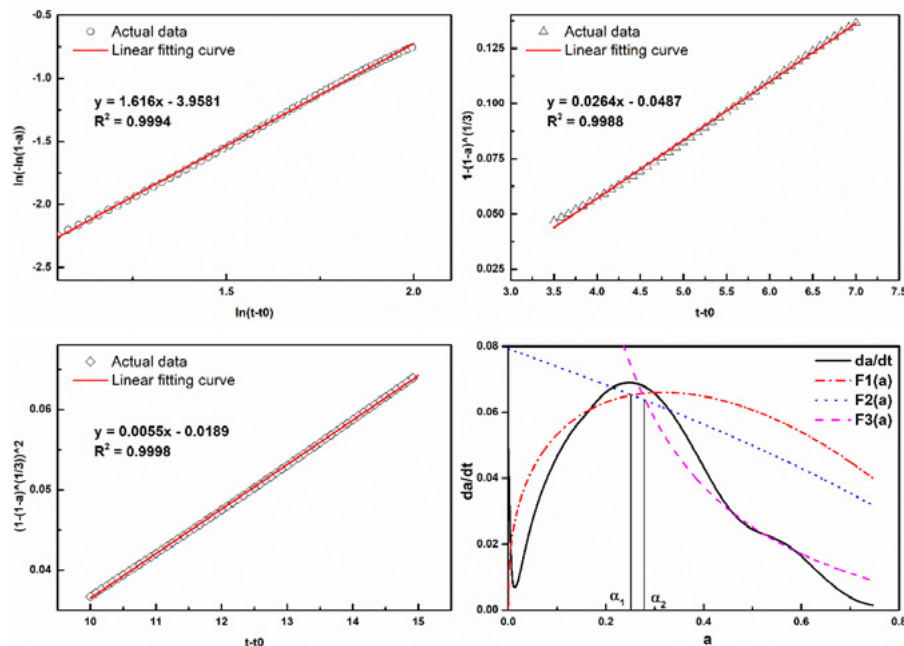


Figure 3: Determination of kinetic factors from linear regression for R group.

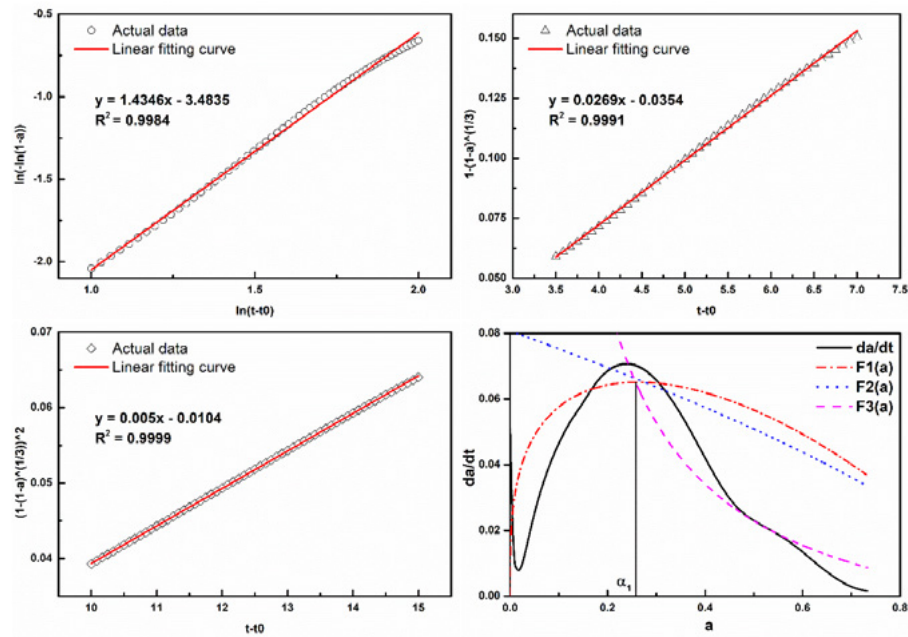


Figure 4: Determination of kinetic factors from linear regression for M1 group.

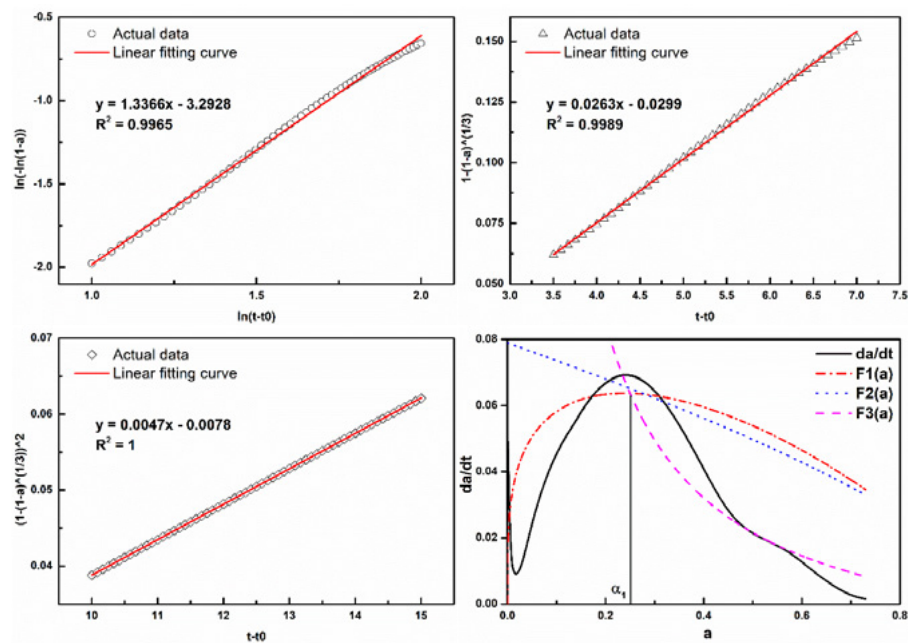


Figure 5: Determination of kinetic factors from linear regression for M2 group.

Furthermore, the kinetic parameters determined by Krstulovic-Dabic model are presented in Table 3. The n value of R, M1, M2 and M3 is 1.6160, 1.4346, 1.3724 and 1.2666, respectively.

The hydration rate during D process of R, M1, M2 and M3 is 0.005, 0.0050, 0.0047 and 0.0041, respectively. It is proposed by Zheng et al that brucite precipitates on cement particles in micro-crystalline size and form a “protective layer”, which hinders the further cement hydration [19]. Moreover, it can be seen hydration mechanism in group without Mg^{2+} is NG-I-D. Addition of Mg^{2+} limits development of I process and makes hydration mechanism become NG-D.

The hydration degree during NG process of R, M1, M2 and M3 is 0.2463, 0.2533, 0.2466 and 0.2267,

respectively. Decreased hydration degree is observed when Mg^{2+} concentration increases from 0.055 mol/L to 0.220 mol/L.

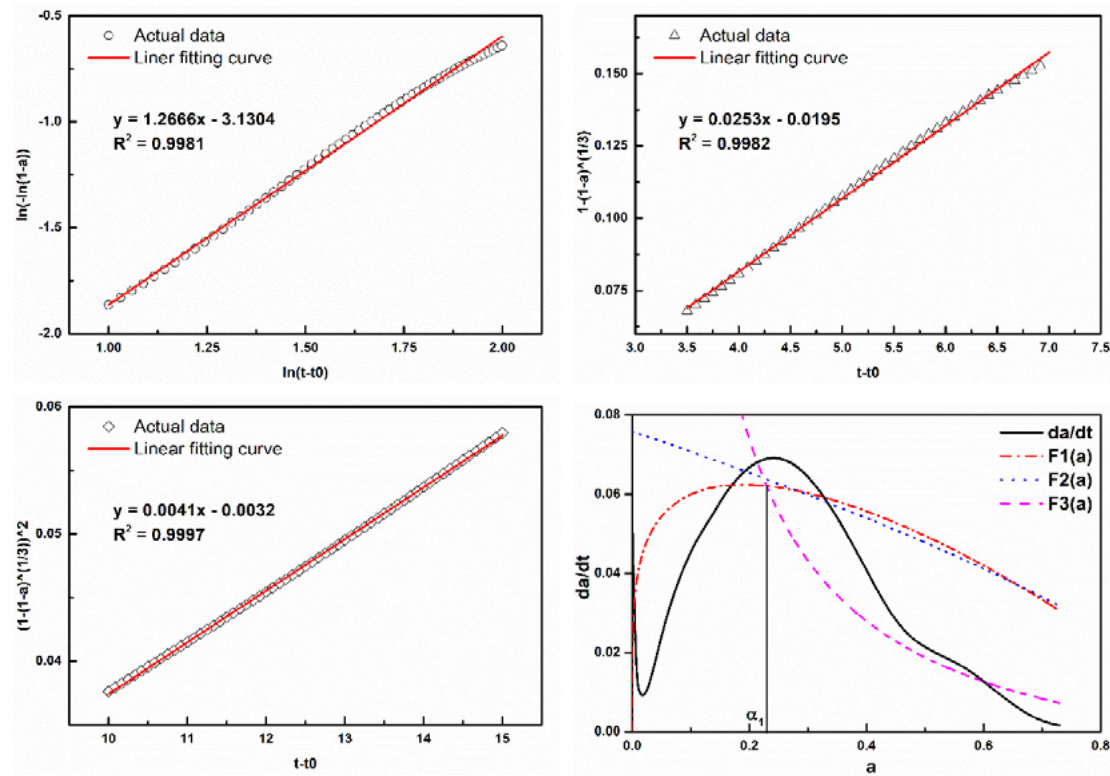


Figure 6: Determination of kinetic factors from linear regression for M3 group.

Table 3: Kinetic parameters determined by Krstulovic-Dabic model.

	n	K_{NG} [h^{-1}]	K_I [$\mu m \cdot h^{-1}$]	K_D [$\mu m^2 \cdot h^{-1}$]	hydration mechanism	α_1	α_2	$\alpha_1 - \alpha_2$
R	1.6160	0.0864	0.0264	0.0055	NG-I-D	0.2463	0.2470	0.0007
M1	1.4346	0.0882	0.0269	0.0050	NG-D	0.2533	0.2533	0
M2	1.3724	0.0893	0.0263	0.0047	NG-D	0.2466	0.2466	0
M3	1.2666	0.0907	0.0253	0.0041	NG-D	0.2267	0.2267	0

Table 4: Share of individual processes up to 48 h of hydration /h.

Sample	Induction period	NG	I	D
R	2.28	5.28	0.01	40.43
M1	2.92	4.76	0	40.32
M2	2.87	4.57	0	40.56
M3	2.54	4.05	0	41.41

Share of individual processes up to 48 h of hydration is presented in Table 4. It can be seen the duration of induction period R, M1, M2 and M3 is 2.28 h, 2.92 h, 2.87 h and 2.54 h, respectively. The most significant extension is presented when Mg^{2+} concentration is 0.055 mol/L. The duration of NG process decreases regularly as increase on Mg^{2+} added from 0 mol/L to 0.22 mol/L. The duration of R, M1, M2 and M3 is 5.28 h, 4.76 h, 4.57 h and 4.05 h, respectively. Within 48 h hydration, the share of D process of R, M1, M2 and M3 is 40.43 h, 40.32 h, 40.56 h and 41.41 h, respectively.

4. Conclusions

In this study, effect of Mg^{2+} on early hydration of Portland cement is discussed. Based on calorimetry test and hydration kinetic analysis, the following conclusions can be drawn:

1. Mg^{2+} increases heat release during induction and acceleration period, especially under high Mg^{2+} concentrations.
2. Mg^{2+} induces hydration inhibition during deacceleration and stabilization period.

5. Acknowledgment

This research has been financially supported by the National Natural Science Foundation of China (No. 51679179), National Nature Science Foundation Project of China (No. 51608409), Major science and technology project in Zhongshan city, Guangdong province (2017A1021), Yang Fan plan of Guangdong Province (201312C12), Open research project of Advanced Engineering Technology Research Institute of Wuhan University of technology in Zhongshan city (WUT201802).

1 References

1. T. Nishida, N. Otsuki, H. Ohara, Z.M. Garba-Say, T. Nagata, Some Considerations for Applicability of Seawater as Mixing Water in Concrete, *J. Mater. Civ. Eng.* 27 (2015) B4014004.
2. Nobuaki, Otsuki, Tsuyoshi, Saito, Yutaka, Tadokoro, Possibility of Sea Water as Mixing Water in Concrete, *J. Civ. Eng. Arch.* 6 (2012) 1273-1279.
3. <https://www.statista.com/statistics/219343/cement-production-worldwide/>
4. S.K. Kaushik, S. Islam, Suitability of sea water for mixing structural concrete exposed to a marine environment, *Cem. Concr. Comp.* 17 (1995) 177-185.
5. O.O. Akinkurolere, C. Jiang, O.M. Shobola, The Influence of Salt Water on the Compressive Strength of Concrete, *J Eng Appl Sci*, 2 (2012) 412-415.
6. W.J. McCoy, Water for mixing and curing concrete. In *Significance of Test and Properties of Concrete and Concrete Aggregates*, ASTM STP. 169 (1956) 352-357.
7. V.V. Reddy, N.V. Ramana, K. Gnaneswar, C. Sashidhar, Effect of magnesium chloride ($MgCl_2$) on ordinary Portland cement concrete, *Indian J. Sci. Technol.* 4 (2011) 643-645.
8. K. Thomas, W.E.A. Lisk, Effect of sea water from tropical areas on setting times of cements, *Mater. Struct.* 3 (1970) 101-105.
9. P.K. Mehta, J.M. Monteiro, *Concrete Microstructure Properties and Materials*, McGraw-Hill Professional, 2006 (Third Edition).
10. A. Tangen, W. Lund, J. Frederiksen, J. Determination of Na^+ , K^+ , Mg^{2+} , and Ca^{2+} in mixtures of seawater and formation water by capillary electrophoresis, *J. Chromatogr. A.* 767 (1997) 311-317.
11. L. Shan, Y. Wang, J. Li, H. Li, X. Wu, J. Chen, Tribological behaviours of PVD TiN and TiCN coatings in artificial seawater, *Surf. Coat. Technol.* 226 (2013) 40-50.
12. J. Olek, M. Cohen, M. Santhanam, Differentiating seawater and groundwater sulfate attack in Portland cement mortars, *Cem. Concr. Res.* 36 (2006) 2132-2137.
13. D. Jansen, F. Götz-Neunhoeffler, B. Lothenbach, J. Neubauer, The early hydration of Ordinary Portland Cement (OPC): an approach comparing measured heat flow with calculated heat flow from QXRD, *Cem. Concr. Res.* 42 (2012) 134-138.
14. C. Hesse, F. Götz-Neunhoeffler, J. Neubauer, A new approach in quantitative in-situ XRD of cement pastes: correlation of heat flow curves with early hadration reactions, *Cem. Concr. Res.* 41 (2011) 123-128.
15. J.W. Bullard, G.W. Scherer, J.J. Thomas, Time dependent driving forces and the kinetics of tricalcium silicate hydration, *Cem. Concr. Res.* 74 (2015) 26-34.
16. G. Sandrine, B. Tanja, N. André, Formation of the C-S-H Layer during early hydration of tricalcium silicate grains with different sizes, *J. Phys. Chem. B* 110(1) (2006) 270.
17. P. Juilland, E. Gallucci, R. Flatt, K. Scrivener, Dissolution theory applied to the induction period in alite hydration, *Cem. Concr. Res.* 40(6) (2010) 831-844.
18. G.C. Edwards, R.L. Angstadt, The effect of some soluble inorganic admixtures on the early hydration

- of Portland cement, J. Appl. Chem. 16 (1966) 166-168.
19. L. Zheng, X. Cui, M. Tang, Hydration and setting time of MgO-type expansive cement, Cem. Concr. Res. 22(1) (1992) 1-5.
 20. S Agatzini-Leonardou, Karidakis T, Tsakiridis P E. Use of gypsum/brucite mixed precipitate instead of gypsum in Portland cement[J]. J. Chem. Technol. Biotechnol. 2005, 80(3):5.
 21. KRSTULOVIC, DABIC, A conceptual model of the cement hydration process, Cem. Concr. Res. 30(5) (2000) 693-698.
 22. W. Teng, Y. Xue, Z. Min, L. Yi, Y. Chen, S. Wu, H. Hou, Hydration kinetics, freeze-thaw resistance, leaching behavior of blended cement containing co-combustion ash of sewage sludge and rice husk, Constr. Build. Mater. 131(Complete) (2017) 361-370.
 23. X. Chang, X. Yang, W. Zhou, G. Xie, S. Liu, Influence of glass powder on hydration kinetics of composite cementitious materials, Adv. Mater. Sci. Eng. 2015 (2015).

Recent Sustainable Development of Ultra-High Performance Concrete (UHPC)

R. Yu^{1*}, Z. Liu^{1,2}, X. Wang^{1,2}, Q. Song^{1,2}, Z. Shui¹, C. Hao³

¹State Key Laboratory of Silicate Materials for Architectures, Wuhan University of Technology, Wuhan 430070, China;

² School of Materials Science and Engineering, Wuhan University of Technology, Wuhan 430070, China

³ Zhonganruibao Construction Group CO., LTD, East Huizhan road 1, 528400, Zhongshan, Guangdong, China

Abstract

Ultra-high performance concrete (UHPC) is a relatively new building materials, which has superior durability, ductility and strengths in comparison with Normal Strength Concrete (NSC) and Fiber Reinforced Concrete (FRC) due to its extremely low porosity, dense matrix, high homogeneous system and the inclusion of various fibres. However, in recent years, due to the fact that more and more attentions have been paid on sustainable development and cleaner products, the high materials cost and high environmental impact of UHRC seem to be the main disadvantages that restrict its further development and application. Hence, to solve the problem mentioned above, a series of approaches have been proposed. In this study, based on the investigation by the authors, several key methods for developing eco-friendly UHPC are presented: 1) optimized design of UHPC particle packing skeleton; 2) appropriate application of cementitious materials; 3) appropriate application of aggregates; 4) effective increase of steel fibre efficiency. Moreover, some detailed mechanism for the properties and microstructure development in the developed sustainable UHPC are also discussed. At last, based on a large amount of experimental results and analysis, the development trend for sustainable UHPC in near future is suggested.

Keywords: Ultra-High Performance Concrete (UHPC), Sustainable development, optimized design, efficient application, mechanism analysis

1. Introduction

Nowadays, the sector of building materials (mainly cement based materials, as concrete) is the third largest CO₂ emitting industrial sector world-wide [1]. Therefore, to achieve a sustainable development of concrete industry, one of the promising approaches is to design and produce a type of concrete with less clinker [2-4], inducing lower CO₂ emissions than traditional ones [5], while providing the same or better reliability and durability [6].

Ultra-High Performance Fibre Reinforced Concrete (UHPFRC) is a relatively new construction material [7]. Considering the successful application of UHPFRC in practice (e.g. Mediterranean Culture Museum in Marseille of France, Gärtnerplatz bridge build in Kassel of Germany), UHPFRC seems to be one of the most suitable candidates to reduce the global warming impact of construction materials [8]. Due to the advanced mechanical properties and durability, the structure made of UHPFRC can be much more slender compared to normal concrete structure. However, the disadvantage of UHPFRC in reducing its environmental impacts can also be noticed. This can mainly attributed into following three aspects: 1) the

cement/binder amount in the production of UHPFRC is relatively high, and the cement/binder efficiency is relatively low; 2) the application of recycled materials or industry by products needs theoretical support; 3) the utilization of steel fibres can be treated as a black box, and the fibre efficiency is relatively low. Although, in available literature, many researchers have contributed a lot of experimental and theoretical results in developing sustainable UHPFRC, this field still needs further investigation and effort.

In general, based on these premises mentioned above, to promote the sustainable development of UHPFRC, its matrix and used fibres efficiencies should be optimized. Therefore, in this study, three strategies are mainly employed: 1) optimized design of the UHPFRC matrix based on modified Andreasen & Andersen particle packing model and appropriate application of substitutive materials; 2) appropriate utilization of recycled materials based on close packing theory; 3) efficient improve the fibre efficiency based on an optimized casting method.

2. Methodology

2.1 Materials

The cement used in this study is Ordinary Portland Cement (52.5). A polycarboxylic ether based superplasticizer is used to adjust the workability of concrete. Several supplementary cementing materials (SCM), such as fly ash (FA), ground granulated blastfurnace slag (GGBS) and silica particles (S-P) in slurry, are used as pozzolanic materials to replace cement. Limestone powder (LP) is treated as filler in this study. Four types of sand are used: micro-sand, sand (0-0.6), sand (0.6-1.25) and sand (0-2). The addition of construction and demolition wastes is used to reduce energy consumption. The particle size distribution, shape and texture of river sand and construction and demolition wastes have been compared and the detailed information is presented in Figures 1. The water absorption of construction and demolition wastes and river sand has also been measured (19.60% for construction and demolition wastes and 2.9% for river sand). Additionally, one type of steel fibres is utilized: length = 13 mm, diameter = 0.2 mm.

Based on the modified Andreasen & Andersen particle packing model, the optimized UHPFRC matrix is firstly designed (as shown in Table 1). Compared to the reference sample, about 30% of Portland cement (by mass) is replaced by FA, GGBS or LP in the mixtures. One of the resulting integral grading curves are shown in Figure 2.

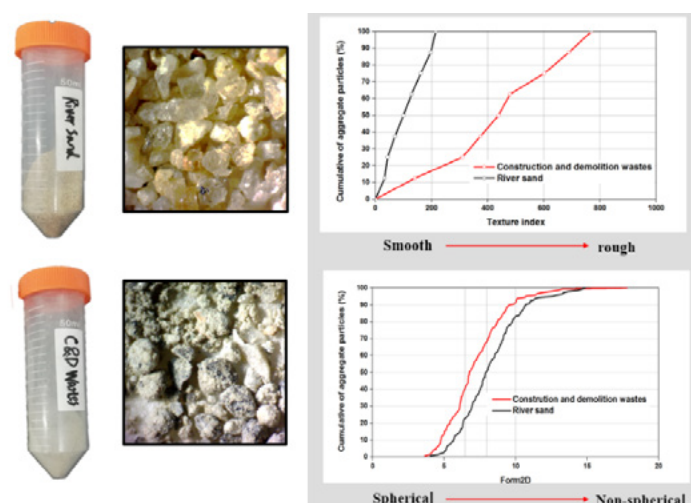


Figure 1: Properties of C&D (construction and demolition wastes) and river sand

Table 1: Mix recipes of the designed UHPFRC matrix (kg/m³ concrete)

NO.	C (kg/m ³)	FA (kg/m ³)	GGBS (kg/m ³)	LP (kg/m ³)	S (kg/m ³)	MS (kg/m ³)	S-P (kg/m ³)	W (kg/m ³)	SP (kg/m ³)
1	591.9	264.3	0	0	1057.0	220.2	24.7	159.3	44.0
2	606.4	0	270.7	0	1082.9	225.6	25.3	163.2	45.1
3	602.8	0	0	269.1	1076.5	224.3	25.1	162.2	44.9
Ref.	883.9	0	0	0	1091.2	227.3	25.5	164.4	45.5

(C: Cement, FA: Fly ash, GGBS: Ground granulated blast-furnace slag, LP: Limestone powder, S: sand, MS: Microsand, S-P: Silica particle, W: Water, SP: Superplasticizer, W/B: water to binder ratio, Ref.: reference samples without industry by-products, #: LP is considered as a binder in the calculation)

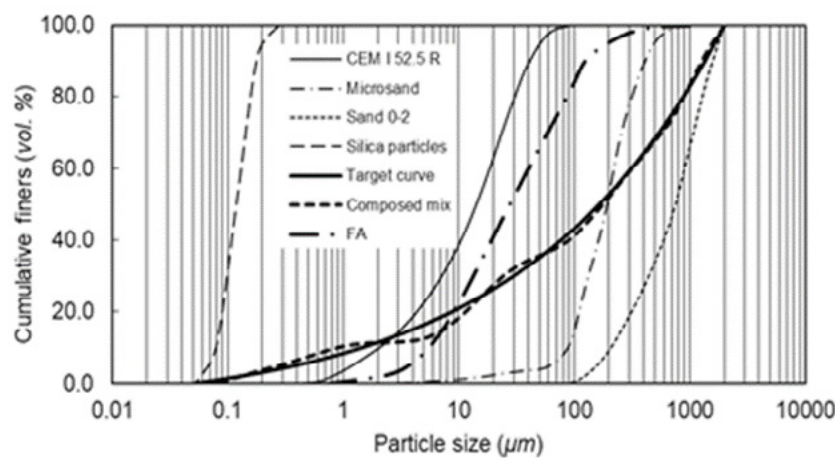


Figure 2: PSDs of the involved ingredients, the target and optimized grading curves of the developed UHPFRC matrix

After that, construction and demolition wastes with maximum size of 0.6mm are utilized to replace cement and natural river sand. The influence of the replacement by construction and demolition wastes on the solid particle system is illustrated in Figure 3 and results further confirm the feasibility. The mixing design and binder composition of UHPC mixtures including construction and demolition wastes are shown in table 2.

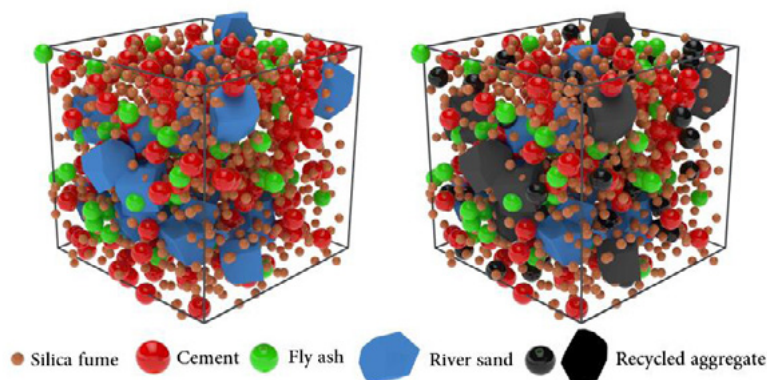


Figure 3: the replacement of cement and river sand by construction and demolition wastes on the packing system of UHPC

Table 2: Recipe of UHPFRC with different compounded high-active powders (kg/m³)

	C&D	C	SF	FA	S	Water	Sp	R ₁	R ₂
REF	0	670	188	200	990	210	30	0	0
C&D 215	215	536	188	200	904	210	30	25	8.7
C&D 430	430	402	188	200	818	210	30	50	17.4

(C: Cement, FA: Fly Ash, SF: Silica Fume, C&D: construction and demolition wastes; R₁: Volume replacement ratio of cement by construction and demolition wastes; R₂: Volume replacement ratio of river sand by construction and demolition wastes; S: river sand with particle size of 0-0.6 mm; Sp: superplasticizer.)

Thirdly, to efficiently improve the fibre orientation and fibre efficiency, two cast methods (as shown in Figure 4) are used in this study: 1) A: cast at one side of the mould with flowing process (optimized casting); 2) B: cast randomly without flowing process (non-optimized casting).

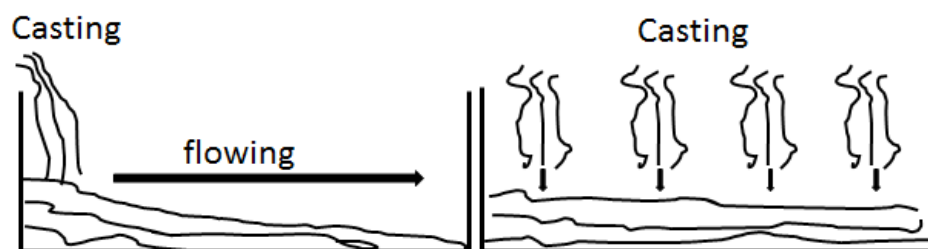


Figure 4: Employed casting methods: (a) cast at one side of the mould with flowing process (optimized casting); (b) cast randomly without flowing process (non-optimized casting)

3. Results and discussion

3.1 Properties evaluation of UHPFRC skeleton with low cement/binder amount

Figure 5 presents the compressive strength of the designed UHPFRC matrix (without fibres) at 28 and 91 days. It can be noticed that the reference sample always has the highest compressive strengths at both 28 and 91 days, which can be attributed to its high cement content. When the cement is partly replaced by industry by-products, it can be found here the mixture with GGBS has superior mechanical properties at both 28 and 91 day, while that the strengths of the mixtures with FA or LP are similar to each other. According to the compressive strength results obtained in this study, it can be summarized that based on appropriate application of modified Andreasen and Andersen particle packing model, a dense packed UHPFRC matrix skeleton can be obtained. When the unhydrated cement particles in this dense packed skeleton are replaced by industry by-products, the utilized cement amount can be reduced by about 30%, and the concrete mechanical properties are still acceptable.

To evaluate the eco properties of the designed UHPFRC matrix, the concept of embedded CO₂ emission is employed in this study, which focus on the amount of materials required for 1 m³ of compacted concrete. Based on the embodied CO₂ values for each components of concrete [9], the embedded CO₂ emissions of the designed UHPFRC matrix in this study are calculated and shown in Figure 6. It is obvious that the reference sample has the highest embedded CO₂ emission, while that value for the mixture with industry by-products are much lower (about 30% less) and similar to each other. This can be attributed to the large cement amount in reference sample and the relatively high environmental impact of cement material. Therefore, appropriately replace the cement by industry by-products is a promising method to promote the sustainable development of UHPFRC.

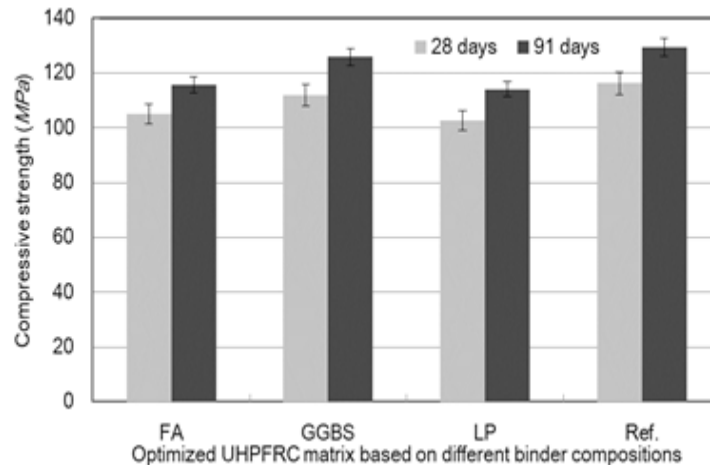


Figure 5: Compressive strengths of the designed UHPFRC matrix with different mineral admixtures

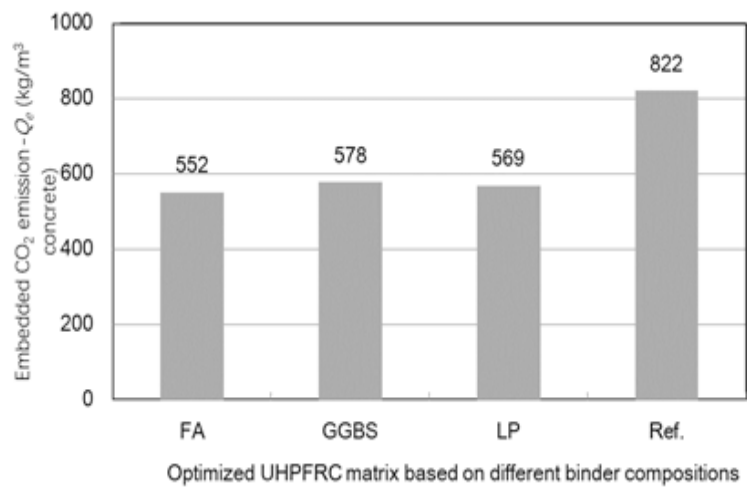


Figure 6: Comparison of embedded CO₂ emission (Q_e) for the optimized UHPFRC matrix based on different binder compositions

3.2 Appropriate application of recycled materials in UHPFRC

The compressive strength for the UHPC mixtures are presented in Figure 7. It can be noticed that with increase amount of C&D wastes, the 1d compressive strength of UHPC including construction and demolition wastes obvious decrease. However, it is important to notice that the addition of C&D wastes have limited effect on the compressive strength development of UHPC at 7 and 28 days. For instance, the maximum compressive strength for the UHPC produced is about 127 MPa (at 28 days), while the value for UHPC including 448kg/m³ C&D is around 116 MPa (at 28 days). Compared with other eco-efficient UHPC, it can be concluded that the compressive strength per cement is higher. This also highlights the advantage of substitution strategy based on maintaining the close packing system of UHPC. To evaluate the environmental contribution of UHPC mixtures including C&D wastes, the ecological indexes are calculated based on 1m³ designed materials. As shown in Figure 8, it is clear that the ecological overload can be significantly reduced with the addition of C&D wastes. For instance, C&D 448 (mixtures replacing 40% cement and 18.2% river sand) shows a significant reduction in environmental categories: about 39%, 20%, 33%, 11% and 16% reduction in renewable energy input, non-renewable energy input, global warming potential, nitrification potential and acidification potential, respectively, compared to that of reference specimens (REF). Hence, based on the obtained experimental results, it can be summarized that the outcome of this research can not only benefit for solving the landfill problem caused by C&D waste, but also provide UHPC with low environmental burden [10].

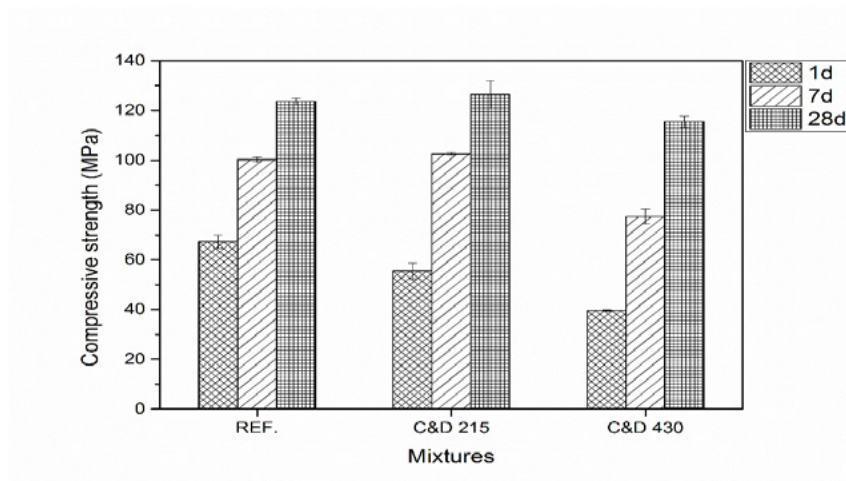


Figure 7: Compressive strengths for the UHPC with and without C&D wastes

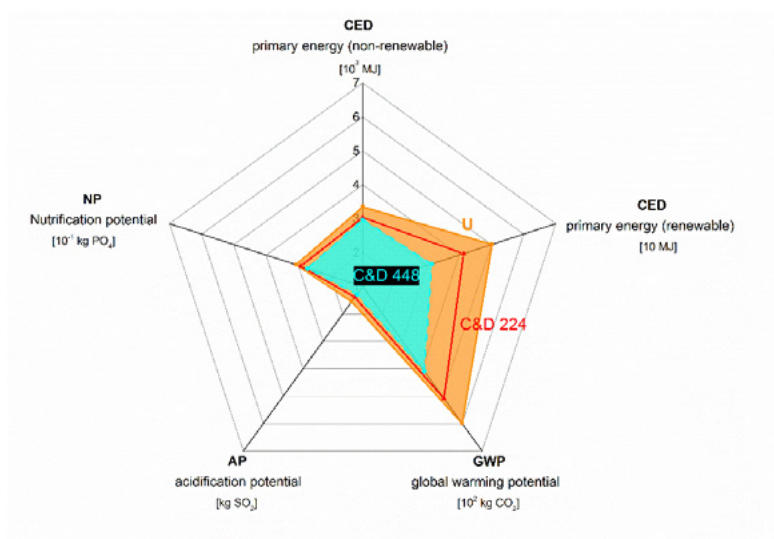


Figure 8: Comparison of the ecological characteristics of UHPC with different C&D wastes dosages

3.3 Improvement of fibre efficiency of UHPFRC based on optimized casting method

Figure 9 illustrates the flexural strength variation of the UHPFRC with different steel fibre content. The two curves represent the 28d flexural strength of UHPFRC based on optimized casting method (with flowing process) and non-optimized casting method (without flowing process). It is found that with an increase of the steel fibre content, the flexural strengths simultaneously increase. Moreover, it is important to notice that the UHPFRC produced based on optimized casting method always has higher flexural strength than that of the one produced based on non-optimized casting method, which proves that the UHPFRC cast at one side of the mould has higher flexural strength than randomly casting samples.

These difference flexural strength results obtained from two casting methods can be attributed to the influence of fibre orientation in UHPFRC. As commonly known, the fibre orientation has close relationship with the flexural strength of concrete. When a large amount of steel fibres are perpendicular to the flexural force direction, the steel fibres can significantly resist the cracks generation and growth, which is helpful for improving the concrete flexural strength. Hence, in this study, it can be predicted that in the UHPFRC produced based on the optimized casting method has more fibres perpendicular to the flexural force direction [11-12].

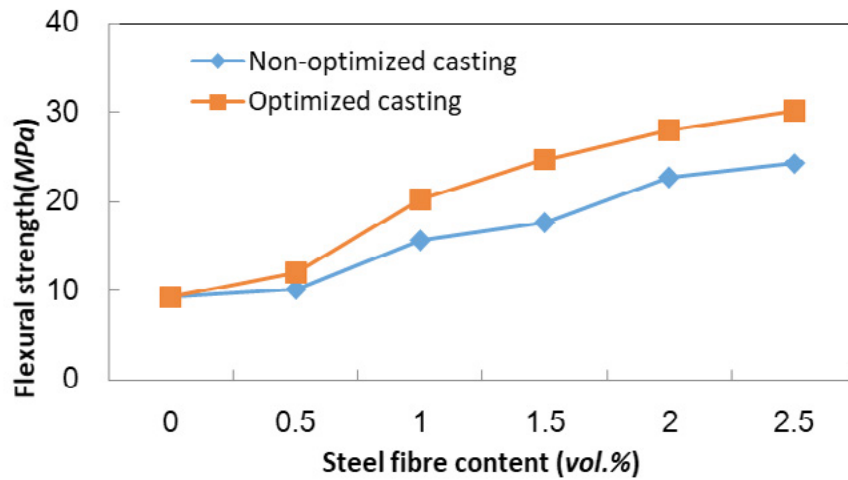


Figure 9: Flexural strength variation of the UHPFRC produced based on different casting methods

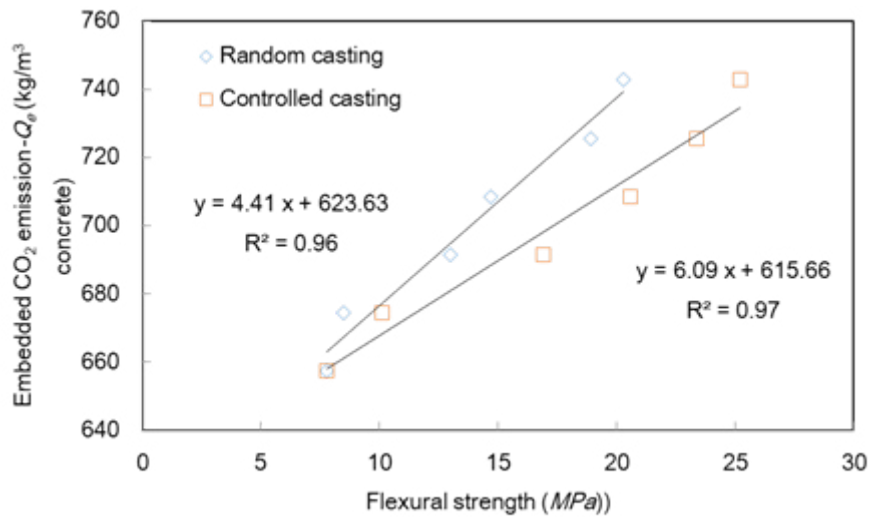


Figure 10: Comparison of embedded CO₂ emission (Q_e) for the designed UHPFRC based on different casting methods

As shown in previous sections, the concept of embedded CO₂ emission (EN ISO 14040 and 14044) is also employed to evaluate the eco properties of the optimized UHPFRC based on different casting methods (as presented in Figure 10). It is obvious that with almost the same flexural strength, the designed UHPFRC based on controlled casting method presents low environmental impact. For instance, when the flexural strength is about 20 MPa, the embedded CO₂ emissions are about 700 and 750 kg/m³ for the UHPFRC based on controlled casting and random casting. This further demonstrates the controlled casting method can effectively promote the sustainable development of UHPFRC for a cleaner production [13].

4. Conclusions

Based on the experimental investigations shown in this study, the following conclusions can be drawn:

- 1) Based on appropriate application of modified Andreasen and Andersen (A&A) particle packing model, a dense packed UHPFRC matrix skeleton can be obtained, which has relatively higher binder efficiency.
- 2) C&D wastes with maximum size of 0.6mm can be treated as mixture blending of cement and natural sand and the reasonable substitution of cement and sand has no negative effect on the deviation between mixtures and target curve calculated by modified A&A model.

- 3) When the developed UHPFRC cast at one side of the mould (optimized casting method), the fibres orientation can be well optimized, which is beneficial for improving the fibre efficiency and producing sustainable UHPFRC.

5. Acknowledgment

The authors acknowledge the financial supports of National Nature Science Foundation Project of China (No. 51608409), National Nature Science Foundation Project of China (51679179), Major science and technology project in Zhongshan city, Guangdong province (2017A1021), Yang Fan plan of Guangdong Province (201312C12), Open research project of Advanced Engineering Technology Research Institute of Wuhan University of technology in Zhongshan city (WUT201802).

6. References

- [1] UNSTATS, 2010. Greenhouse gas emissions by sector (absolute values).United Nation Statistical Division: Springer.
- [2] Yu, R., Spiesz, P., Brouwers, H.J.H., 2015. Development of an eco-friendly Ultra-High Performance Concrete (UHPC) with efficient cement and mineral admixtures uses. *Cem. Concr. Comp.*, 55, 383-394.
- [3] Yu R., Spiesz P., Brouwers H.J.H., Mix design and properties assessment of Ultra- High Performance Fibre Reinforced Concrete (UHPFRC), *Cement and Concrete Research*, 2014, 56: 29-39.
- [4] Yu R., Spiesz P., Brouwers H.J.H., Effect of nanosilica on the hydration and microstructure development of Ultra-High Performance Concrete (UHPC) with a low binder amount. *Construction and Building Materials*, 2014; 65: 140-150.
- [5] Igliński, B., Buczkowski, R., 2017. Development of cement industry in Poland – History, current state, ecological aspects. A review. *J. Clean. Prod.*, 141, 702-720.
- [6] Mohammadhosseini, H., Yatim, J.M., Sam, A.R.M., Abdul Awal, A.S.M., 2017. Durability performance of green concrete composites containing waste carpet fibers and palm oil fuel ash. *J. Clean. Prod.*, 144, 448-458.
- [7] Richard P., Cheyrezy M., Composition of reactive powder concretes, *Cement and Concrete Research*, 1995; 25 (7): 1501-1511.
- [8] Habert, G., Arribe, D., Dehove, T., Espinasse, L., Le Roy, R., 2012. Reducing environmental impact by increasing the strength of concrete: quantification of the improvement to concrete bridges. *J. Clean. Prod.*, 35, 250-262.
- [9] Randl N., Steiner T., Ofner S., Baumgartner E., Mészöly T., Development of UHPC mixtures from an ecological point of view. *Construction and Building Materials*, 2014; 67: 373-378.
- [10] Wang X.P., Yu R., Shui Z.H., Song Q.L., Liu Z., Bao M., Liu Z.J., Wu S., Optimized treatment of recycled construction and demolition waste in developing sustainable ultra-high performance concrete. *Journal of Cleaner Production*, 2019, 221: 805-816.
- [11] Song Q.L., Yu R., Shui Z.H., Wang X.P., Rao S.D., Lin Z.W., Optimization of fibre orientation and distribution for a sustainable Ultra-High Performance Fibre Reinforced Concrete (UHPFRC): Experiments and mechanism analysis. *Construction and Building Materials*, 2018, 169: 8-19.
- [12] Song Q.L., Yu R.*, Shui Z.H., Wang X.P., Rao S.D., Lin Z.W., Wang Z., Key parameters in optimizing fibres orientation and distribution for Ultra-High Performance Fibre Reinforced Concrete (UHPFRC). *Construction and Building Materials*, 2018, 188: 17-27.

- [13] Yu R., Song Q.L., Wang X.P., Zhang Z.H., Shui Z.H., Brouwers H.J.H., Sustainable development of Ultra-High Performance Fibre Reinforced Concrete (UHPFRC): Towards to an optimized concrete matrix and efficient fibre application. *Journal of Cleaner Production*, 2017, 162: 220-233.

Influence of External Water Introducing by Coral Sand on Autogenous Shrinkage and Microstructure of Ultra-High Performance Concrete (UHPC)

K. Liu^{1,2}, Z. Shui¹, R. Yu¹, S. Yi²

¹ State Key Laboratory of Silicate Materials for Architectures, Wuhan University of Technology, Wuhan 430070, China;

² School of Materials Science and Engineering, Wuhan University of Technology, Wuhan 430070, China

Abstract

Ultra-High Performance Concrete (UHPC) is a new cement-based material with high strength, toughness and durability, which has broad application prospects in marine engineering. The biggest disadvantage of UHPC is large early autogenous shrinkage and cracking risk. Coral sand as an internal curing agent employed in UHPC can effectively inhibit the self-desiccation inside the concrete and reduce its autogenous shrinkage. In this paper, 0-0.6 mm river sand was replaced by the same size of pre-wetting coral sand (water absorption rate of 19.0%, 24.7% and 31.2%, respectively) by a certain volume fraction (10%, 20% and 30%, respectively), and the early autogenous shrinkage and development of microstructure of UHPC were evaluated. The experimental results show that the introduction of wet coral sand improves the fluidity of UHPC fresh slurry and prolong the setting time. Meanwhile, the development of mechanical properties and early autogenous shrinkage of UHPC hardened paste are inhibited as a whole. The optimum mixture design is that 20% (vol. %) of river sand is replaced by coral sand with 19.0% (wt. %) water absorption rate, and UHPC fluidity increases by 43.2%, 28 d compressive strength increases by 1.3%, 28 d flexural strength decreases by 4.8%, 7 d autogenous shrinkage decreases by 42.2%. Image analysis of pore structure presents that the porosity of micron-scale coarse pores in UHPC increase, and that porosity of millimeter-scale stomata decreases. Environmental Scanning Electron Microscope and Electron Backscattered Diffraction photomicrographs show that Interfacial Transition Zone (ITZ) of damp coral sand and matrix becomes homogenized and densified, and micro-cracks are more difficult to initiate and propagate.

Keywords: ultra-high performance concrete (UHPC), coral sand, water absorption, autogenous shrinkage, microstructure

1. Introduction

Ultra-high Performance Concrete (UHPC), as a new type of cement-based material, is designed based on the tightest accumulation of component particles at low water/binder ratio ($w/b < 0.2$) [1-3]. Compared with ordinary concrete, UHPC has excellent performance such as ultra-high strength, toughness and durability, leading to wide application prospect and development potential in construction and restoration engineering fields [4,5]. However, due to the low water/binder ratio of UHPC, the early autogenous shrinkage caused by the self-desiccation phenomenon is extremely large, which makes the concrete have poor volume stability and cracking risk. Therefore, how to effectively reduce the early contraction of UHPC is particularly important.

The commonly method for controlling of the early autogenous shrinkage of concrete is adding expansion agent, shrinkage reducing agent and introduce internal curing agent. However, the action time of expansive agents and the scale of expansion are quite difficult to control [6-8]. Shrinkage reducing agent can inhibit the early strength development of concrete, and it is easy to interact with admixtures, resulting in further degradation of performance [8-10]. Internal curing can radically solve the problem of self-shrinkage by compensating the internal humidity of concrete through the water slow-release effect of the medium and delay the self-desiccation. Recent research on super absorbent polymer (SAP) and porous mineral materials are the main internal curing media studied. SAP has a good internal curing effect, which can completely eliminate self-shrinkage and even cause the matrix to slightly expand [11-14]. However, the holes caused by SAP after water release will reduce the density of concrete matrix, resulting in a decrease in the mechanical properties and durability. Therefore, the use of porous mineral materials as internal curing agent is an effective way to reduce the early autogenous shrinkage of UHPC.

Nowadays, the research on using porous mineral materials as internal curing agent in UHPC is still at initial stage. Meng et al. [15,16] designed UHPC by replacing river sand with saturated expansion shale and light sand respectively. The results showed that the compressive strength of UHPC introducing saturated expansion shale (25%, vol. %) increased from 130 MPa to 158 MPa after 28 days, and the corresponding self-shrinking deformation decreased from 489 $\mu\text{m}/\text{m}$ to 365 $\mu\text{m}/\text{m}$. When saturated light sand replaced river sand, UHPC 28 d compressive strength increased from 145 MPa to 160 MPa, 28 d self-shrinking deformation decreased from 406 $\mu\text{m}/\text{m}$ to 72 $\mu\text{m}/\text{m}$. Liu et al. [17] used saturated coral sand as internal curing agent in UHPC, and revealed that the early self-shrinking deformation of UHPC decreased with the increase of coral sand. When the content of saturated coral sand exceeded 35% (vol. %), the micro-expansion began to appear. Meanwhile, the strength of UHPC decreased, as well as the degree of reduction was positively correlated with the content of that saturated coral sand. When the dosage reached 35% (vol. %), the compressive strength decreased by 19.6% on the 28th day. Wang et al. [18] not only prepared the ecological UHPC by using saturated micro-coral powder and coral sand to replace cement and river sand respectively, but also evaluated its early self-shrinking development. The results indicated that saturated coral sand had significant internal curing effect, and the content of 30% (vol. %) saturated coral sand reduced the 7 d self-shrinkage of UHPC from 1175 $\mu\text{m}/\text{m}$ to 617 $\mu\text{m}/\text{m}$. At the same time, under the condition that saturated coral sand replaced river sand at a lower level, mechanical properties of UHPC would not be significantly degraded, or even improved to a certain extent ($< 20\%$, vol. %). However, it has not systematically studied about the water absorption rate of porous mineral materials curing agent and the total amount of water introduced on the internal curing effect in UHPC.

In this paper, UHPC was prepared using water-absorbing coral sand with different water absorption rates to replace river sand with a certain volume fraction, and its influence on the performance of UHPC was studied. The macroscopic properties of UHPC such as working performance, mechanical properties and early autogenous shrinking were characterized according to relevant standards. Besides, the pore structure and microstructure development of UHPC were evaluated.

2. Methodology

2.1 Materials

Cementitious materials used in the experiment include OPC 52.5 cement, fly ash (FA), silica fume (SF). Fine aggregates include two particle sizes of natural river sand (0-0.6 mm and 0.6-1.25 mm) and coral sand (0-0.6 mm) from south China sea. The XRF analysis results of cementitious materials and coral sand (CS) are shown in Table 1. Admixture is a polycarboxylic ether based superplasticizer (SP) with a solid content of 20% and water reduction rate of 40%.

Table 1 Chemical compositions of cementitious materials and coral sand (wt. %)

Compositions	Na ₂ O	MgO	Al ₂ O ₃	SiO ₂	P ₂ O ₅	SO ₃	K ₂ O	CaO	Fe ₂ O ₃	LOI
Cement	0.09	1.61	4.18	19.20	0.09	3.35	0.78	64.93	3.32	2.49
SF	0.13	0.47	0.25	94.65	0.17	0.69	0.84	0.36	0.15	2.29
FA	0.33	0.23	38.01	46.44	0.06	0.69	0.88	7.50	3.12	2.79
CS	0.38	2.00	0.25	0.98	0.07	0.74	0.03	50.42	0.09	44.32

The apparent densities of 0-0.6 mm natural river sand and crushed coral sand are 2.66 kg/m³ and 2.57 kg/m³ respectively, and their particle morphology is shown in Figure 1. As a naturally formed porous mineral material, the SEM photomicrograph of coral sand is shown in Figure 2. The saturated water absorption rate of 0-0.6 mm coral sand is 31.2% (wt. %) [19].

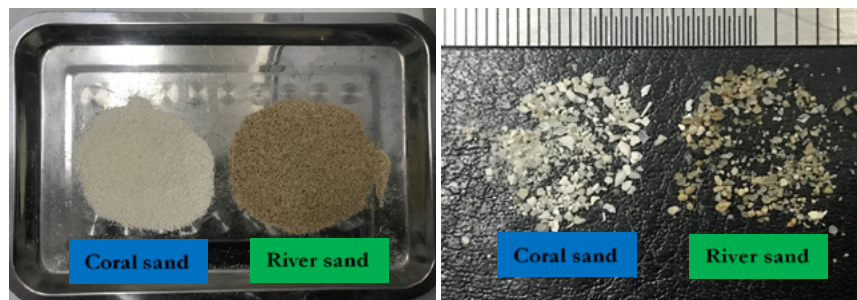


Figure 1 Images of 0-0.6 mm nature river sand and broken coral sand particles

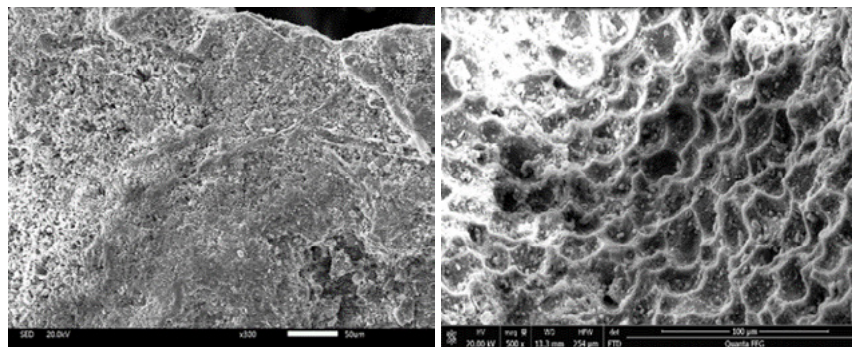


Figure 2 SEM photomicrographs of coral sand

2.2 Methods

2.2.1 UHPC mix design method

The modified Andreasen-Andersen (A&A) model is the most widely used mix design method for UHPC, as shown in equation (1). Where, $P(D)$ represents the total amount of particles under sieve (%), D is the current particle size (μm), D_{\min} and D_{\max} represent the minimum and maximum particle size (μm), q is the distribution modulus. In this paper, the q value is 0.23 [18,20,21].

$$P(D) = \frac{D^q - D_{\min}^q}{D_{\max}^q - D_{\min}^q} \quad (1)$$

According to the particle size distribution of cement, fly ash, silica fume, river sand and coral sand, the least square method is used to evaluate the packing state between particles of each component, as shown

in equation (2). Among them, the D_i^{i+1} represents particles of a certain level of distribution scope, n represents the number of particles selected, P_{mix} and P_{tar} represent the actual accumulation curve and target curve between particles respectively. RSS represents the sum of squares of residuals. The smaller the value of RSS is, the smaller the error between the actual accumulation curve and the target curve will be.

$$RSS = \frac{\sum_{i=1}^n (P_{mix}(D_i^{i+1}) - P_{tar}(D_i^{i+1}))^2}{n} \quad (2)$$

According to the cementitious materials (cement, fly ash and silica fume) and the fine aggregates (river sand and coral sand) particle size distributions to adjust their volume fractions, the mix proportion of UHPC system was designed. The closer the actual accumulation curve and the target curve was, UHPC components between particles reached the more compact packing. The mix design of UHPC was prepared with 0-0.6 mm coral sand particles with different water absorption rates (19.0%, 24.7% and 31.2%, wt. %) instead of a certain amount (10%, 20% and 30%, vol. %) of same size river sand. The mix design is shown in Table 2 and the accumulation curve is shown in Figure 3. The results showed that although the gradation of coral sand particles in the same size range was not completely the same as that of river sand, the actual accumulation curve of each substitution ratio was in good agreement with the target curve. It meant that the particles accumulation form of UHPC components mixed with coral sand was not obviously destroyed, and the matrix was still in a compact packing state.

Table 2 Mix design of UHPC combined with pre-wetting coral sand (kg/m³)

Group	Cement	FA	SF	River sand		Pre-wetting coral sand		Water	SP
				0-0.6 mm	0.6-1.25 mm	Drying coral sand	Extra water		
RE	750	200	144	770	220	0	0	175	31
C1	750	200	144	693	220	74.33	14.12	175	31
C2	750	200	144	616	220	148.66	28.25	175	31
C3	750	200	144	539	220	222.99	42.37	175	31
C4	750	200	144	693	220	74.33	18.36	175	31
C5	750	200	144	616	220	148.66	36.72	175	31
C6	750	200	144	539	220	222.99	55.08	175	31
C7	750	200	144	693	220	74.33	23.19	175	31
C8	750	200	144	616	220	148.66	46.38	175	31
C9	750	200	144	539	220	222.99	69.57	175	31

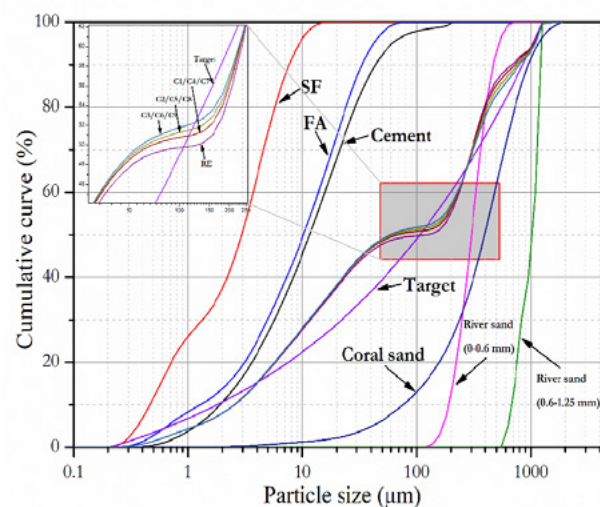


Figure 3 Particle accumulation curve of UHPC raw materials

2.2.2 Fluidity

The fluidity of UHPC slurry was tested according to the related Chinese standard GB/T 2419-2005.

2.2.3 Setting time

The setting time of UHPC slurry was tested according to the related Chinese standard JGJ/T 70-2009.

2.2.4 Mechanical properties

The compressive and flexural strength of UHPC samples were tested according to the related Chinese standard GB/T 17671-1999. The sample size was 40 mm×40 mm×160 mm and cured in water ($20\pm2^\circ$).

2.2.5 Autogenous shrinkage

The Autogenous shrinkage of UHPC was tested according to the related Chinese standard GB/T 50082-2009, and the device was shown in Figure 4. The temperature and humidity of deposited surrounding were $20\pm2^\circ$ and $60\pm5\%$, respectively, and setting time was the beginning of the test.



Figure 4 UHPC autogenous shrinkage testing device

2.2.6 Pore structure

The pore structure of UHPC was evaluated by Image J software with image analysis on cross-sectional morphology of matrix.

2.2.7 Microstructure

The development of microstructure of UHPC was evaluated by image analysis of SEM and EBSD (Electron BackScattered Diffraction). SEM and EBSD were used to observe the structure of ITZ and the development of microcrack in matrix, respectively.

3. Results and discussion

3.1 Fresh behavior

Figure 5 shows the fluidity and setting time of fresh UHPC slurry with different mixing ratios. The fluidity of C1~C9 was 115.3%, 143.2%, 148.6%, 147.0%, 170.0%, 174.3%, 105.5%, 157.4% and 168.9% of the reference group, respectively. The results show that the fluidity of UHPC fresh slurry can be improved by adding wet coral sand, and the growth is positively correlated with the total amount of introducing water as a whole. This is because during mixing process of UHPC, the water introduced by water-absorbing coral sand breaks away under the action of rotor centrifugal force and enters into the slurry, which increases the free water in the system. As more free water can participate in the lubrication between particles, the fluidity of the paste increases. The fluidity of C7 group was not significantly improved compared with the reference group, because the content of water-absorbing coral sand was relatively high, which increased

the contact opportunities with the cementitious material, so that part of free water released by wet coral sand was adsorbed on the surface of cementitious material particles. The amount of water introduced into effective lubrication was limited, and the fluidity of slurry was not significantly increased.

The setting time of C1~C9 was 75.0%, 150.0%, 168.8%, 156.3%, 164.6%, 187.5%, 158.3%, 187.5% and 187.5% of the reference group. The results show that the addition of water-absorbing coral sand will lead to prolonged setting time of UHPC slurry. The setting time of UHPC mortar is directly proportional to the total amount of introduced water. This is because the moisture released by the wet coral sand promotes the hydration of cement and generates more hydration products, which thickens the film layer of hydration products covering cement particles, and delays the formation of the gel network and prolongs the setting time. However, the shortened setting time of group C1 is due to the fact that the coral sand with low water absorption rate and content will continuously absorb free water out from the system, so as to thin the film of hydration product encapsulating cement particles, accelerating the continuous hydration of cement particles and the formation of cementitious structure network.

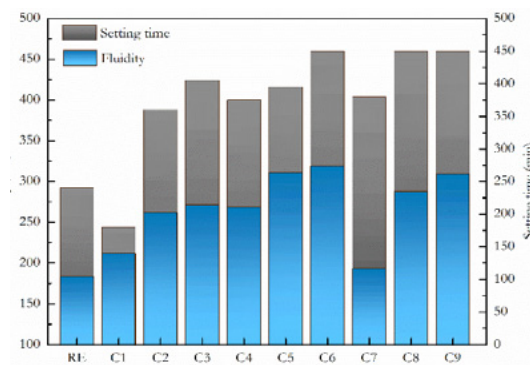


Figure 5 Fluidity and setting time of UHPC fresh slurry with different mixture ratios

3.2 Mechanical properties

The development of compressive and flexural strength of UHPC with different mixing ratios is shown in Figure 6 and 7 respectively. The compressive strength of C1~C9 on the 28th day was 105.6%, 101.3%, 96.1%, 93.9%, 90.1%, 87.8%, 91.0%, 77.3% and 68.5% of the reference group respectively. The results showed that the introduction of water-absorbing coral sand could inhibit the development of early compressive strength of UHPC. As the total amount of introduced water was low, UHPC had a significant strength compensation development after 7 days, and the compressive strength of 28 days would exceed that of the reference group (C1 and C2). This is because the introduction of water-absorbing coral sand has positive and negative effects on the development of mechanical properties of UHPC. The negative effect is mainly due to the fact that the water introduced by the wet coral sand increases the actual water-binder ratio of the UHPC system, increasing the porosity of the hardened paste and decreasing the mechanical properties. The positive effect is that the water released from the water-absorbing coral sand can continuously promote the hydration of cement and the secondary hydration of active mineral admixtures (SF and FA), and improve the hydration rate of the cementitious system and promote the development of UHPC strength, especially in the later stage. The development of compressive strength of UHPC is the result of these two effects.

The 28 d flexural strength of C1~C9 was 112.5%, 95.2%, 85.6%, 87.5%, 82.7%, 73.1%, 83.7%, 71.2% and 68.3% of the reference group. The results show that, except for group C1, the addition of water-absorbing coral sand not only leads to the reduction of the flexural strength of UHPC, but also the flexural strength will retract obviously with the extension of age. This is because the coral sand is more porous than river sand, which easily leads to stress concentration and micro cracks [22]. With the extension of age,

the continuous expansion of micro-cracks causes more defects and the bending strength of UHPC matrix decreases.

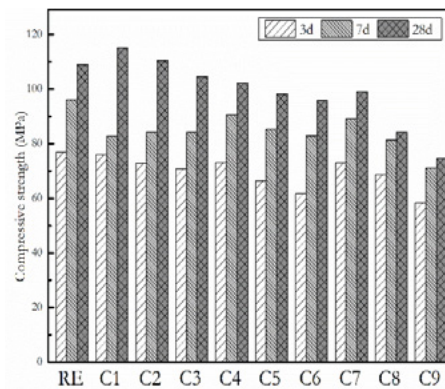


Figure 6 Development of compressive strength of UHPC with different mixture ratios

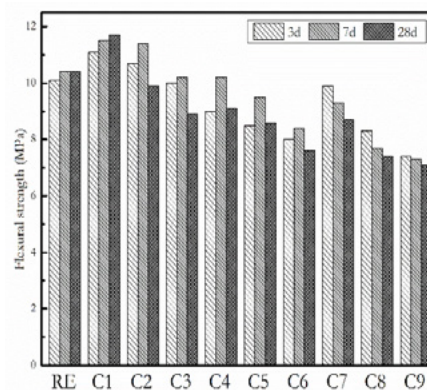


Figure 7 Development of flexural strength of UHPC with different mixture ratios

3.3 Autogenous shrinkage

The development of early autogenous shrinking of UHPC with different mix ratios is shown in Figure 8. The self-shrinking evolution of UHPC could be divided into three stages: rapid growth, callback and stable growth. The contraction of UHPC increased rapidly within 12 h after hardening, and the shrinkage accounts for more than 40% of the total shrinkage deformation at 7 d, which is the most important stage determining the volume stability of UHPC matrix [23].

Compared with the reference group, the total amount of 7 d autogenous shrinking deformation of C1~C9 decreased by -16.1%, 42.2%, 59.1%, 20.3%, 30.2%, 35.5%, 24.4%, 47.2% and 47.9%. The results show that the water-absorbing coral sand has good internal curing effect, and the shrinkage reducing efficiency is proportional to the amount of water introduced. This is because the slow-release effect of moisture from wet coral sand can compensate for the decline of relative humidity in UHPC, delaying the self-desiccation and inhibiting the early self-shrinking development of UHPC matrix.

Compared with the reference group, the autogenous shrinkage of group C1 increased by 16.1%. The water-absorbing coral sand did not reach the state of saturation, and the total amount of introduced water was too low. Hence, the coral sand would continue to absorb water from the system, which aggravated the decrease of relative humidity inside the matrix and caused the contraction to increase. Consequently, the water absorption rate of wet coral sand and the total amount of water introduced have a great influence on its internal curing effect. Too little water will lead to the increase of UHPC autogenous shrinkage. If

excessive water is introduced, the mechanical properties of UHPC will decrease significantly. The optimal mix ratio given in this experiment was C2, the fluidity of UHPC increased by 43.2%, the 28 d compressive strength increased by 1.3%, the 28 d flexural strength decreased by 4.8%, and the total autogenous shrinkage deformation within 7 d decreased by 42.2%.

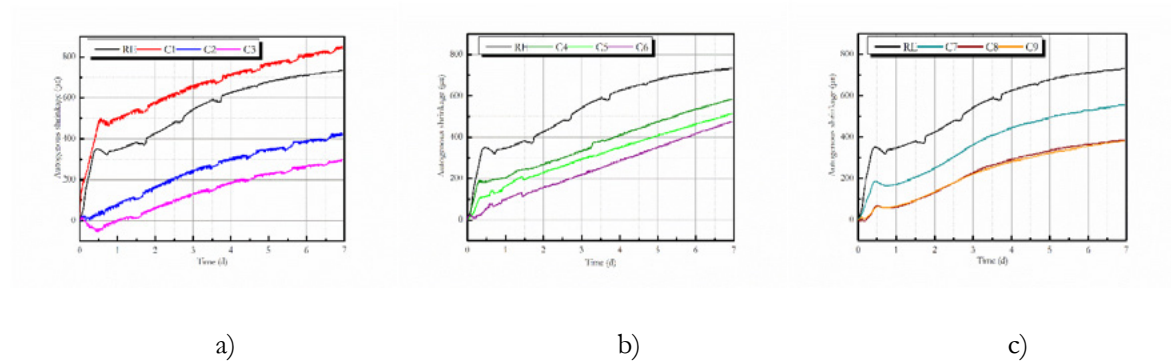


Figure 8 Early autogenous shrinkage development of UHPC with different mixture ratios:

a) C1~C3; b) C4~C6; c) C7~C9;

3.4 Pore structure

Due to the porous structure of coral sand particles, it is not accurate to characterize pore structure of UHPC hardened paste mixed with coral sand by means of mercury intrusion porosimetry, which is difficult to eliminate the disturbance of pores of coral sand. Therefore, this paper intends to evaluate the pore structure of UHPC matrix by image analysis on cross-sectional morphology.

Figure 9 shows the image analysis on cross-sectional morphology of representative UHPC specimens after 28 d curing, such as RE, C2, C5 and C8 groups. The pore of micron size is coarse pore, the hole of millimeter size is stomata. The results of pore structure analysis are shown in Table 3. The results show that the porosity of UHPC matrix mixed with water-absorbing coral sand is proportional to the total amount of water introduced. The higher the porosity of coarse pore, the lower the compressive strength of UHPC hardened paste. The higher the porosity of stomata, the lower the fluidity of UHPC fresh slurry. The results of pore structure analysis are completely consistent with the preceding performance of UHPC.

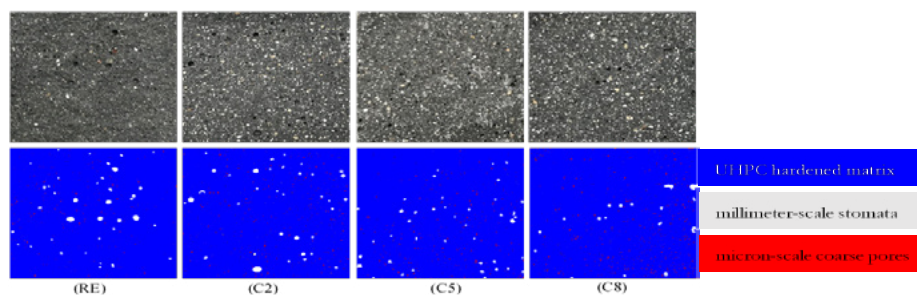


Figure 9 Cross-sectional image analysis of UHPC specimens

Table 3 Cross-sectional pore structure of UHPC specimens (area. %)

Code	RE	C2	C5	C8
Coarse pore	2.178	2.421	2.948	3.751
Stomata	1.247	1.224	1.042	0.732
Total porosity	3.425	3.645	3.990	4.483

3.5 Microstructure

The morphological characteristics of ITZ structure between river sand/coral sand and paste in hardened UHPC after 28 d curing are shown in Figure 10 and Figure 11. Figure 10 photomicrographs display that compared with the ITZ between river sand and paste, the ITZ boundary between coral sand and that paste is not obvious, and the structure is more uniform and dense. Figure 11 images exhibit that micro-cracks around the ITZ region between coral sand and paste are more difficult to initiate and expand under stress conditions compared with that ITZ structure between river sand and paste. It can be summarized that the ITZ structure between fine aggregate and paste is significantly improved and optimized in UHPC mixed with wet coral sand. Main reasons can be concluded as follow: (1) The slow release of water from the wet coral sand can promote the hydration of ITZ reaction layer. (2) The shape of coral sand is irregular (the river sand is spherical), increasing the contact area with paste, and the mechanical meshing force between fine aggregate and paste is strengthened. (3) The moisture released from wet tank promotes secondary hydration of FA and SF, consuming flaky $\text{Ca}(\text{OH})_2$ crystal and inhibiting its directional distribution near ITZ. The optimization of ITZ between fine aggregate and paste also contributes positively to mechanical properties of UHPC.

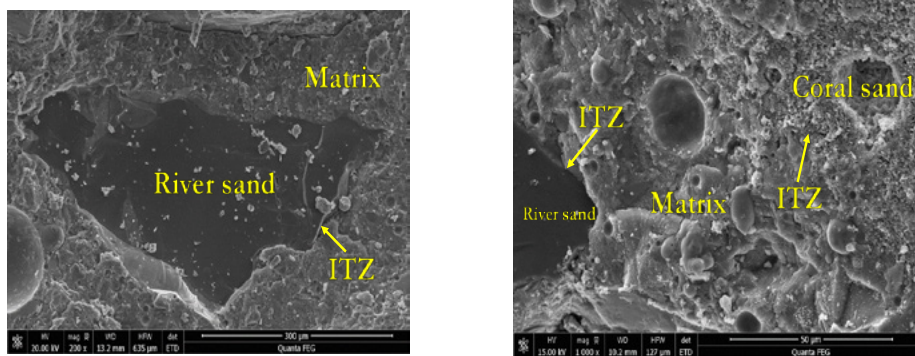


Figure 10 SEM photomicrographs of river sand/coral sand and paste ITZ structure

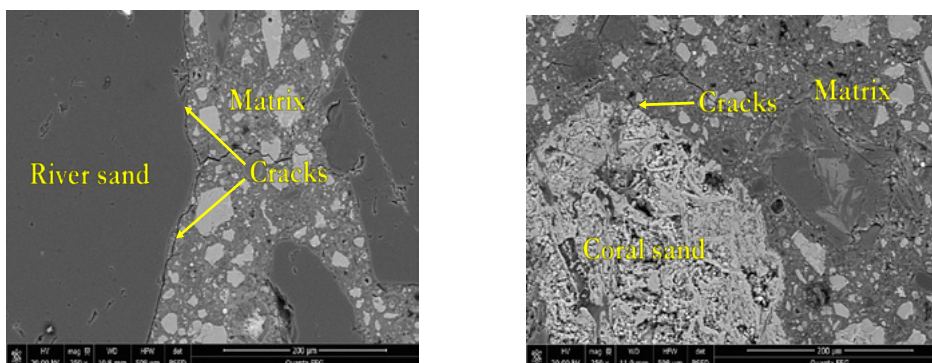


Figure 11 EBSD photomicrographs of river sand/coral sand and paste ITZ structure

4. Conclusions

- (1) UHPC is prepared by mixing with water-absorbing coral sand, the fluidity of fresh slurry is increased and the setting time is prolonged. The fluidity and setting time of UHPC fresh slurry are positively correlated with the total amount of water introduced by wet coral sand as a whole.
- (2) The addition of damp coral sand inhibits the development of mechanical properties of UHPC, especially during the early strength. Coral sand with a low water absorption rate (19.0%, wt. %) replaces river sand at a low level (< 20%, vol. %), there is a significant strength compensation development of

UHPC after 7 days, and the compressive strength at 28 days will exceed that of the reference group. At the same time, the introduction of water-absorbing coral sand will lead to a retraction of the flexural strength of UHPC.

3. (3) Water-absorbing coral sand has significant internal curing effect, and the shrinkage reducing efficiency is proportional to the amount of water introduced in the mass. Under substitution system of unsaturated coral sand with low content ($< 10\%$, vol. %), the early autogenous shrinkage of UHPC will be increased.
4. (4) The optimal conditions for water-absorbing coral sand to be used as internal curing agent for UHPC are: replacing 20% (vol. %) river sand with 19.0% (wt. %) water absorption rate coral sand, the fluidity of UHPC increases by 43.2%, the 28 d compressive strength increases by 1.3%, the 28 d flexural strength decreases by 4.8%, and the autogenous shrinking deformation decreases by 42.2% within 7 d.
5. (5) The introduction of wet coral sand will lead to an increase in the porosity of micron-scale coarse pores in UHPC matrix, and that porosity of millimeter-scale stomata will decrease.
6. (6) The ITZ structure of damp coral sand and matrix is more uniform and dense, and micro-cracks are more difficult to initiate and expand.

5. Acknowledgment

The authors acknowledge the financial supports of National Nature Science Foundation Project of China (51608409), Major science and technology project in Zhongshan city, Guangdong province (2017A1021), Yang Fan plan of Guangdong Province (201312C12), Science and Technology Program of Guangdong Province in 2016 (2016A090924002), Science and Technology Program of Guangdong Province in 2017 (2017B090907009), Late-model Research Institute Development Program of Zhongshan in 2016: Subsidy for Major Research Platform Construction (2016F2FC0008), and open research project of Advanced Engineering Technology Research Institute of Wuhan University of technology in Zhongshan city (WUT201802).

6. References

- [1] Richard P, Cheyrezy M., Composition of reactive powder concretes, *Cem Concr Res*, 1995, 25(7): 1501-1511.
- [2] Shi C, Wu Z, Xiao J, et al., A review on ultra high performance concrete: Part I. Raw materials and mixture design, *Constr Build Mater*, 2015, 101: 741-751.
- [3] Wang D, Shi C, Wu Z, et al., A review on ultra high performance concrete: Part II. Hydration, microstructure and properties, *Constr Build Mater*, 2015, 96: 368-377.
- [4] Yoo D Y; Yoon Y S., A Review on Structural Behavior, Design, and Application of Ultra-High-Performance Fiber-Reinforced Concrete, *Int J Concr Struct Mater*, 2016, 10(2): 125-142.
- [5] Zhou M.; Lu W.; Song J W. et al., Application of Ultra-High Performance Concrete in bridge engineering, *Constr Build Mater*, 2018, 186: 1256-1267.
- [6] Sun W, Chen H, Luo X, et al., The effect of hybrid fibers and expansive agent on the shrinkage and permeability of high-performance concrete, *Cem Concr Res*, 2001, 31(4): 595-601.
- [7] Corinaldesi V, Nardinocchi A, Donnini J., The influence of expansive agent on the performance of fibre

reinforced cement-based composites, *Constr Build Mater*, 2015, 91: 171-179.

[8] Yoo D Y, Kim S W, Yoon Y S, et al., Benefits of using expansive and shrinkage-reducing agents in UHPC for volume stability, *Mag Concr Res*, 2014, 66(14): 745-750.

[9] Yoo D Y, Banthia N, Yoon Y S., Effectiveness of shrinkage-reducing admixture in reducing autogenous shrinkage stress of ultra-high-performance fiber-reinforced concrete, *Cem Concr Comp*, 2015, 64: 27-36.

[10] Rajabipour F; Sant G.; Weiss J., Interactions between shrinkage reducing admixtures (SRA) and cement paste's pore solution, *Cem Concr Res*, 2008, 38(5): 606-615.

[11] Craeye B, Geirnaert M, Schutter G., Super absorbing polymers as an internal curing agent for mitigation of early-age cracking of high-performance concrete bridge decks, *Constr Build Mater*, 2011, 25(1):1-13.

[12] Soliman A M, Nehdi M L., Effect of partially hydrated cementitious materials and superabsorbent polymer on early-age shrinkage of UHPC, *Constr Build Mater*, 2013, 41(41): 270-275.

[13] Justs J, Wyrzykowski M, Bajare D, et al., Internal curing by superabsorbent polymers in ultra-high performance concrete, *Cem Concr Res*, 2015, 76: 82-90.

[14] Kang S H.; Hong S G.; Moon J., Shrinkage characteristics of heat-treated ultra-high performance concrete and its mitigation using superabsorbent polymer based internal curing method, *Cem Concr Comp*, 2018, 89: 130-138.

[15] Meng W, Khayat K., Effects of saturated lightweight sand content on key characteristics of ultra-high-performance concrete, *Cem Concr Res*, 2017, 101: 46-54.

[16] Meng W, Samaranayake V, Khayat K., Factorial Design and Optimization of Ultra-High-Performance Concrete with Lightweight Sand, *ACI Mater J*, 2018, 115(1):129-138.

[17] Liu J, Ou Z, Mo J, et al., Effectiveness of Saturated Coral Aggregate and Shrinkage Reducing Admixture on the Autogenous Shrinkage of Ultrahigh Performance Concrete, *Adv Mater Sci Eng*, 2017, 2017(4): 1-11.

[18] Wang X, Yu R, Shui Z, et al., Mix design and characteristics evaluation of an eco-friendly Ultra-High Performance Concrete incorporating recycled coral based materials, *J Cleaner Prod*, 2017, 165: 70-80.

[19] ASTM Committee C09, C1761: Standard Specification for Lightweight Aggregate for Internal Curing of Concrete, ASTM, 2013.

[20] Yu R, Spiesz P, Brouwers H J H., Mix design and properties assessment of Ultra- High Performance Fibre Reinforced Concrete (UHPFRC), *Cem Concr Res*, 2014, 56: 29-39.

[21] Liu K, Yu R, Shui Z, et al., Effects of Pumice-Based Porous Material on Hydration Characteristics and Persistent Shrinkage of Ultra-High Performance Concrete (UHPC), *Materials*, 2019;12(1):11.

[22] Cheng S, Shui Z, Yu R, et al., Multiple influences of internal curing and supplementary cementitious materials on the shrinkage and microstructure development of reefs aggregate concrete, *Constr Build Mater*, 2017, 155(30): 522-530.

[23] Liu K, Yu R, Shui Z, et al., Optimization of autogenous shrinkage and microstructure for Ultra-High Performance Concrete (UHPC) based on appropriate application of porous pumice, *Constr Build Mater*, doi: [10.1016/j.conbuildmat.2019.04.089](https://doi.org/10.1016/j.conbuildmat.2019.04.089).

Neutron radiography to study water ingress via the interlayer of 3D printed cementitious materials

J. Van Der Putten ¹, M. Azima ¹, P. Van den Heede ¹, T. Van Mullem ¹, G. De Schutter¹ and K. Van Tittelboom ^{1*}

¹Magnel Laboratory for Concrete Research, Department of Structural Engineering, Faculty of Engineering and Architecture, Ghent University, Tech Lane Ghent Science Park/Campus A, Technologiepark-Zwijnaarde 60, 9052 Ghent, Belgium

*Corresponding author: Kim.VanTittelboom@UGent.be

Abstract

3D printing of cementitious materials is a newly developing technology in which structural elements are built via a layer-by-layer process. Among the many advantages of this technique, it is also expected to lead to more sustainable structures due to a reduced waste generation and more efficient structural design, placing materials only where needed. However, the result of this technique is a layered and anisotropic specimen, creating weak interlayers which will not only endanger the structural behaviour, but also affect the durability as they form a preferential path for the ingress of aggressive substances. For that reason, this research study focuses on the transport of water through printed elements, fabricated with different print velocities (i.e. 1.7 cm/s and 3.0 cm/s) and with special attention for the interlayer interface. Water transport was visualised by means of neutron radiography, performed at the Paul Sherrer institute in Villigen. The effect of an increased print velocity is investigated through qualitative and quantitative analyses of the obtained radiographs. First qualitative results showed that for samples printed with a lower printing speed, the water uptake occurs in a more uniform way compared to specimens printed with a higher velocity. In case of a higher printing speed, the water ingress starts more at the sides and this effect becomes more and more pronounced due to the non-uniform distribution of sand particles through the sample. These results are confirmed by representing the water profile at the interface in a quantitative way. Calculation of the amount of water in a specified zone at the interface shows that, independently from the water distribution, the water uptake after 60 minutes of exposure is higher in case of a low printing speed.

Keywords: 3D printing, cementitious materials, interlayer, water ingress, neutron radiography

1. Introduction

3D printing of cementitious materials enlarges the possibilities in construction, especially in terms of geometrical freedom and flexibility. This newly developing technique not only reduces construction time, it also leads to more sustainable structures due to a reduced waste generation and more efficient structural design. Notwithstanding the many advantages, this technique includes a layer-by-layer deposition of the material, introducing an additional amount of voids. These voids will create a weak interface between two super positioned layers and deteriorate the mechanical performance of the printed element. Due to the absence of moulding, also drying shrinkage will become more pronounced when comparing 3D printing with traditional casting, creating cracks all over the printed specimens. The combination of an increased

amount of voids and cracks will endanger the durability as both result in capillary suction of aggressive liquids from the concrete surface to the interior.

Visual impressions of several existing 3D-printed elements have already disclosed that there is a preferential water uptake via the interlayer [1]. However, further research on the transport properties on the meso- and microscale has not been performed yet and a lot of parameters in this research field are still unknown. Therefore, the current study aims at further developing the correlation between the print process parameters and the transport properties of a printed element. In particular, the effect of an increased printing speed has been investigated and neutron radiography was used to visualise and quantify the capillary sorption behaviour of 3D printed cementitious materials along the interface at different times after water exposure. Prior to neutron radiography testing, basic capillary sorption tests were performed in order to select the maximal exposure time.

2. Methodology

2.1 Materials and mix compositions

Ordinary Portland Cement (CEM I 52.5 N) was combined with standardized sand ($D_{\max} = 2 \text{ mm}$) and a water to cement ratio equal to 0.35 was applied. To increase the flowability of the mix composition, a polycarboxylic ether (PCE) with a molecular weight of approximately 4000 g/mol and 35% solids was used as superplasticizer. The exact mix composition can be found in Table 1.

Table 1: Mix composition

Mix component [-]	Amount [kg/m ³]
CEM I 52.5 N	620.5
Sand 0/2	1241.0
Water	226.5
PCE	0.15% [WOC]

The printability of the cementitious material was evaluated based on three different parameters: extrudability, buildability and workability. To classify the mixture as extrudable, it was mandatory that one layer with a total length of 300 mm could be expelled without blocking or segregation and that the deformation after extrusion was limited to 10%. Buildability was obtained when at least 5 layers could be printed on top of each other and a general conclusion about the workability was made by performing VICAT tests in an automated way.

2.2 Sample preparation

An in house developed apparatus was used to simulate the 3D printing process. The extrusion-based system is capable of printing up to 300 mm long specimens at different speeds and different interlayer time intervals between the depositions of two layers. For the purpose of this research, two different printing speeds were applied (1.7 cm/s and 3.0 cm/s, respectively). The height of each layer is manually adjustable and to ensure the same print quality in both cases, layer heights of respectively 15 mm and 20 mm were selected for both printing speeds. The nozzle of the print equipment was elliptical shaped (28 mm x 18 mm), creating layers with an average width of 30 mm. Consequently, a different printing speed and layer height introduce a different flow rate. In case of a low printing speed, the flow rate is equal to 0.028 m³/h, a higher printing speed induces a flow rate of 0.065 m³/h.

Sample preparation consists of filling the equipment and extruding the material through the nozzle with a constant speed. A base layer ($l = 300 \text{ mm}$) was extruded for each specimen and the second layer was

immediately deposited on top of the previous one. Due to the zero minute time gap, both layers were printed from the same batch of material in order to induce layers with the same rheological behaviour. After changing the height of the nozzle, the second layer was printed at the same position to create a similar time gap at every position. After printing, the specimens were stored during 28 days in a standardized environment ($20 \pm 3^\circ\text{C}$, 60% RH) and saw-cut to a thickness of maximum 20 mm (Figure 1). Afterwards, the specimens were placed in an oven. Based on previous research [2], a temperature of 35°C was selected in order to minimize microstructural damage. After two days, the specimens were removed from the oven and sample dimensions were determined. Due to the very irregular shape of the specimens (Figure 1 and Figure 2) and in order to create unidirectional water uptake, lateral surfaces were not sealed by self-adhesive aluminium tape in order to simulate real life printing conditions as much as possible.

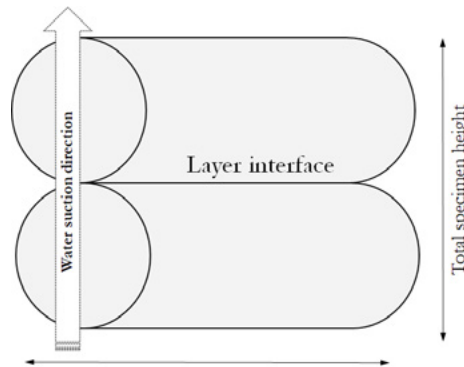


Figure 1: Schematic representation of a printed specimen, saw-cut from an original printed element, used for visualizing the capillary water uptake based on neutron radiography

2.3 Capillary water sorption

Capillary water sorption tests were performed on three cylindrical specimens with a diameter equal to 14 mm. These specimens were drilled out of an original printed specimen, stored in standardized conditions ($20 \pm 3^\circ\text{C}$, 60% RH) until the age of 28 days and dried in a ventilated oven at $35 \pm 5^\circ\text{C}$ for 7 days. A capillary sorption test was performed by placing the cylinders on circular rods in a small water bath, locating the water level at 2 ± 1 mm above the bottom side of the specimens. After wiping them with a towel, capillary sorption was measured by weighing the specimens with a Kern Electronic balance (accuracy 0.01 g) at different times (1, 3, 4, 24 and 72 hours).

2.4 Neutron radiography

Visualisation of the moisture distribution and quantification of the water content was done by using neutron radiography. The measuring principle consists of recording the radiation passing through an object by a position sensitive detector. The beam used for performing these measurements was the neutron beam line at the measuring station NEUTRA. This beam line is situated at the thermal neutron radiographic institute at the Swiss spallation source SINQ of the Paul Scherrer Institute (PSI). Measurements resulted in a radiograph consisting out of an array of grey level intensity values.

Before starting the test, specimens were weighted with a Sartorius BP 3100 S balance (accuracy 0.01 g) and afterwards placed on line supports into a water basin mounted on a support frame (Figure 2). Before the water basins were filled with water, reference images of the samples were taken in dry state. Subsequently, water was added manually 3 min before the actual start of neutron radiography measurements. The samples were approximately 4 mm immersed in the liquid. Subsequent radiographs were made every 20 seconds for a total measurement time of 6 hours. In this way, the water penetration through capillary suction could be followed as a function of time. After the 6 hours test, the wet mass was determined using the same

mass scale and the total amount of absorbed moisture was quantified and compared to the values obtained by post-processing the neutron radiographs. After 24 hours of water suction, the mass of the specimen was measured again and a last neutron radiograph was made to correlate with the other specimens in a qualitative way.

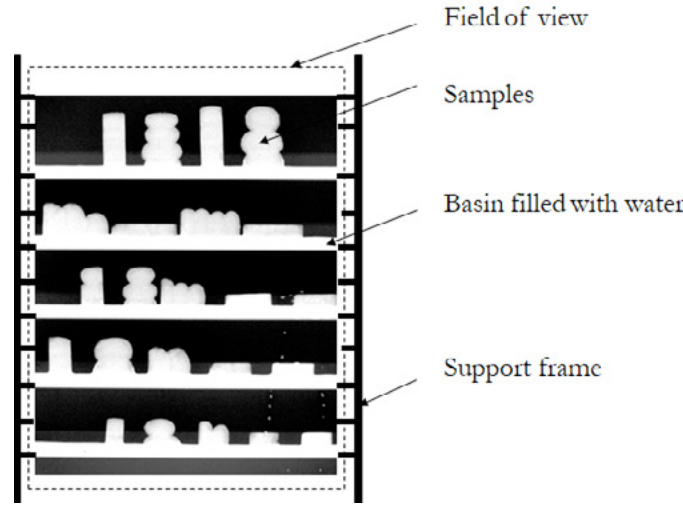


Figure 2: Test setup for neutron radiography testing

Based on previous research [1, 3, 4], a comparison was made by calculating the water content W [kg/m^3] at different time steps by comparing the wet and dry radiographs (Eq. [1]).

$$W = -\frac{\rho_w}{\sum_w \cdot d} \cdot \ln\left(\frac{I_w}{I_{\text{dry}}}\right) \quad [1]$$

Where ρ_w [kg/m^3] is the density of water, \sum_w [m^{-1}] the attenuation coefficient of water (3.64 cm^{-1}), d [m] the thickness of the specimen, I_w [$\text{cm}^{-2} \cdot \text{s}^{-1} \cdot \mu\text{A}^{-1}$] the flux through wet material and I_{dry} [$\text{cm}^{-2} \cdot \text{s}^{-1} \cdot \mu\text{A}^{-1}$] the flux through dry material. More in depth information about the before mentioned parameters can be found in [3, 4].

For qualitative information, each image obtained with neutron radiography needed to be filtered with the image correction tool “Quantitative Neutron Imaging (QNI)”, provided and developed at the PSI institute. The reason for this processing is that the exponential law of attenuation is influenced by several deviations. The images were corrected using the dark current, the open beam (flat field) and the black body radiographs with and without samples. These separate radiographs were made before every new test series. All corrections were based on an average of five radiographs per correction factor, to further optimize the obtained results. After post-processing of these radiographs, all further image operations were performed using ImageJ. Within this software, a distinct water content profile along a rectangular zone (Figure 3) at the interlayer of the printed specimen was calculated using a grey-level profile plot. In case of a low printing speed, the rectangular zone had a width of 12 mm and a height equal to 0.1 mm. In case of a higher printing speed, the width and height of this zone of interest were respectively 15 mm and 0.1 mm. In this way, the water uptake over time could be studied and visualized in detail. The profiles were made and a precise calculation of the water amount in this interlayer zone was done after 5 min, 60 min and 360 min of water exposure.

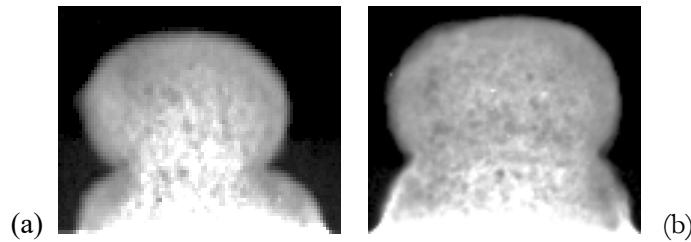


Figure 3: Representation of the rectangular zone used for calculation of the capillary water uptake in case of specimens printed on (a) low speed and (b) high speed.

3. Results and discussion

3.1 Capillary water sorption

Figure 4(a) shows the capillary water sorption capacity of a specimen, fabricated with a low printing speed. Based on this, one can conclude that the highest water uptake occurs within the first 4 hours. For that reason, a water exposure time equal to 6 hours is selected for neutron radiography and the relevance of the selected exposure time is confirmed by measurements with neutron radiography (Figure 4(b)).

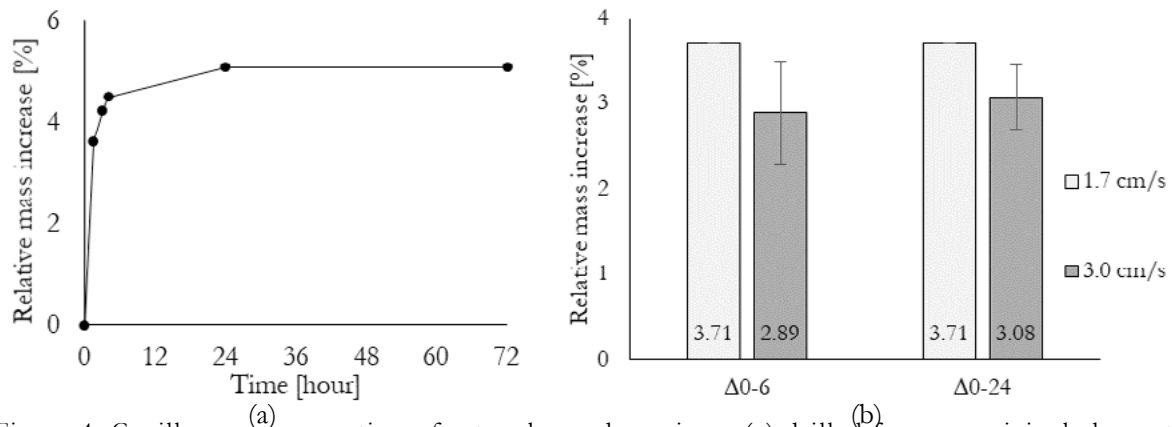


Figure 4: Capillary water sorption of a two layered specimen (a) drilled from an original element and measured in standardized conditions, (b) saw-cut from an original printed element and measured by using neutron radiography (error bars represent standard deviation)

3.2 Neutron radiography

3.2.1 Qualitative analysis

Figure 5 visualizes the capillary water uptake of specimens, fabricated with different print velocities, after different water exposure times. In case of elements fabricated with a low printing speed, the water front (white region) rises in a very consistent way through the material. Immediately after being placed in contact with water (0 minutes), one can see that the water uptake is most pronounced in the central part of the specimen. With an increased exposure time, the water front rises gradually and reaches the interface between the two super positioned layers around 60 minutes. After crossing this weak zone, the water front rises in the same way. After 24 hours, the specimen is almost completely saturated.

Increasing the printing speed of the element introduced a change in water front behaviour. Within the first minutes after exposure, the water amount is higher at the sides compared to the bulk material. This effect becomes more pronounced with an increased exposure time (Figure 5). After 30 minutes, the water front at the sides reaches, but even after 360 minutes the water front in the bulk material did not yet completely cross the interface. After 24 hours, the water front looks similar as the one of the sample printed at low printing speed.

This different water front behaviour can be explained based on previous research [5]. Within this research,

it was observed that a higher printing speed introduces a lower surface roughness. This lower roughness could be explained by a higher kinetic energy working on the sand particles, forcing them deeper into the layer. Consequently, the bulk material of layers printed with a higher velocity will contain a higher sand fraction and be more compacted compared with the interface, limiting the water ingress and creating a non-uniform water front. In case of a low printing speed, the composition of the bulk material and the interface are more or less comparable, resulting in an uniform water ingress over the whole specimen.

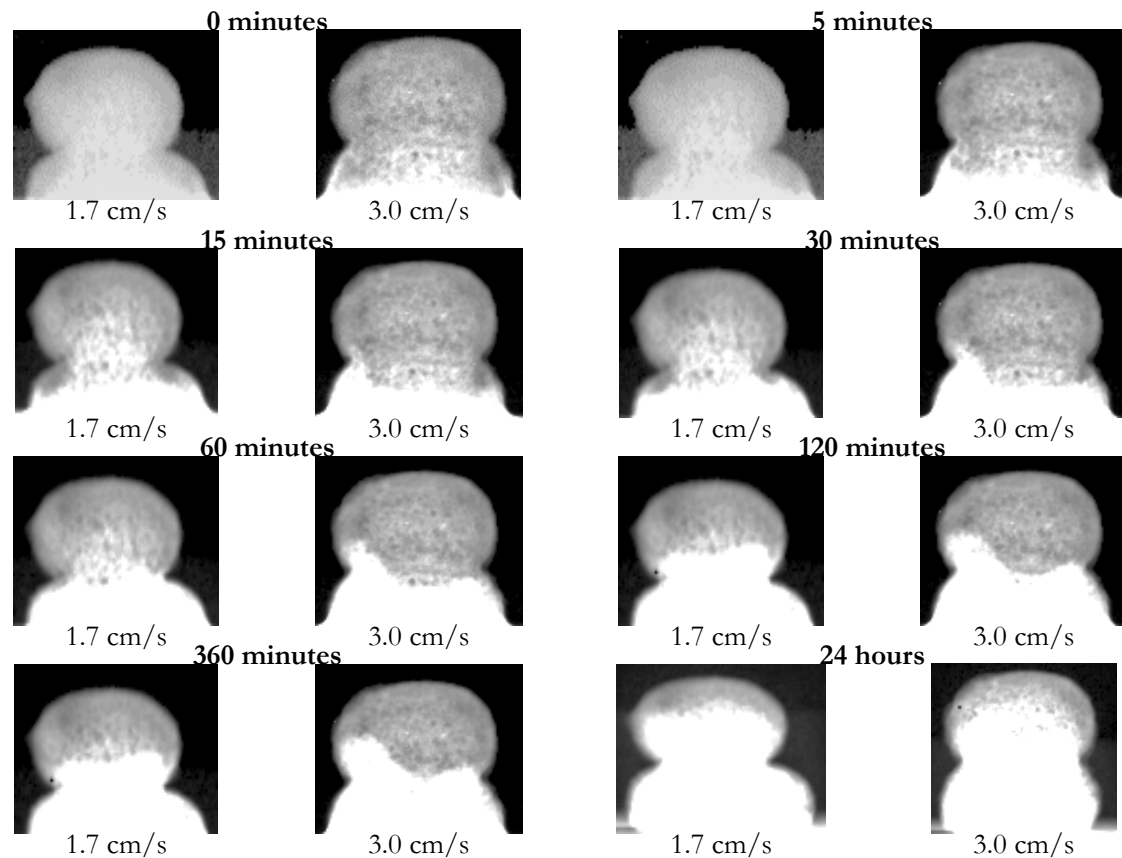


Figure 5: Qualitative comparison of the capillary water uptake capacity at different water exposure times of specimens fabricated with different printing speeds. For each test series, a representative sample is pictured.

3.2.2 Quantitative analysis

Based on Eq. [1], the exact amount of water in a specified region (Figure 3) can be calculated and these results are represented in Table 2. One can conclude that after 5 minutes of water exposure, the amount of water calculated based on the obtained grey levels in ImageJ is almost zero in case of specimens printed with a low velocity.

Comparing the samples after an exposure time of 60 minutes, one can see that the water amount is higher in case of a low printing speed, indicating that a higher amount of water was able to reach the interlayer zone. This phenomenon can be explained by the microstructural change induced by a higher print velocity. As mentioned before, the sand fraction in the bulk material is higher, creating a denser structure in the bulk of the printed specimen, limiting the water uptake capacity, introducing a lower amount of water at the interface. After 360 minutes (6 hours), the water amount in the interface region is higher in case of a higher printing speed.

Figure 6 shows the water amount at the interlayer on different positions in the horizontal direction. These results confirm in a qualitative way the results showed in Figure 5. After 5 minutes of water exposure, the

amount of water in the interface is zero in case of a low printing speed. In case of an increased printing speed, some of the water already reached the interface at the left side of the specimen. With an increased exposure time, one can see that the water amount is more equally distributed in case of a lower printing speed. After 60 minutes, the water amount through the interface region is comparable, while in case of a higher printing speed, the water uptake at the sides of the element is more pronounced. One can also see that in both cases, after 60 minutes of water exposure, the water has not completely reached the interlayer.

Table 2: Calculated amount of water at the interface region after different exposure times

Exposure time [minutes]	Water amount [g/cm ³]	
	1.7 cm/s	3.0 cm/s
5 minutes	0.00001	0.00011
60 minutes	0.00073	0.00041
360 minutes	0.00101	0.00121

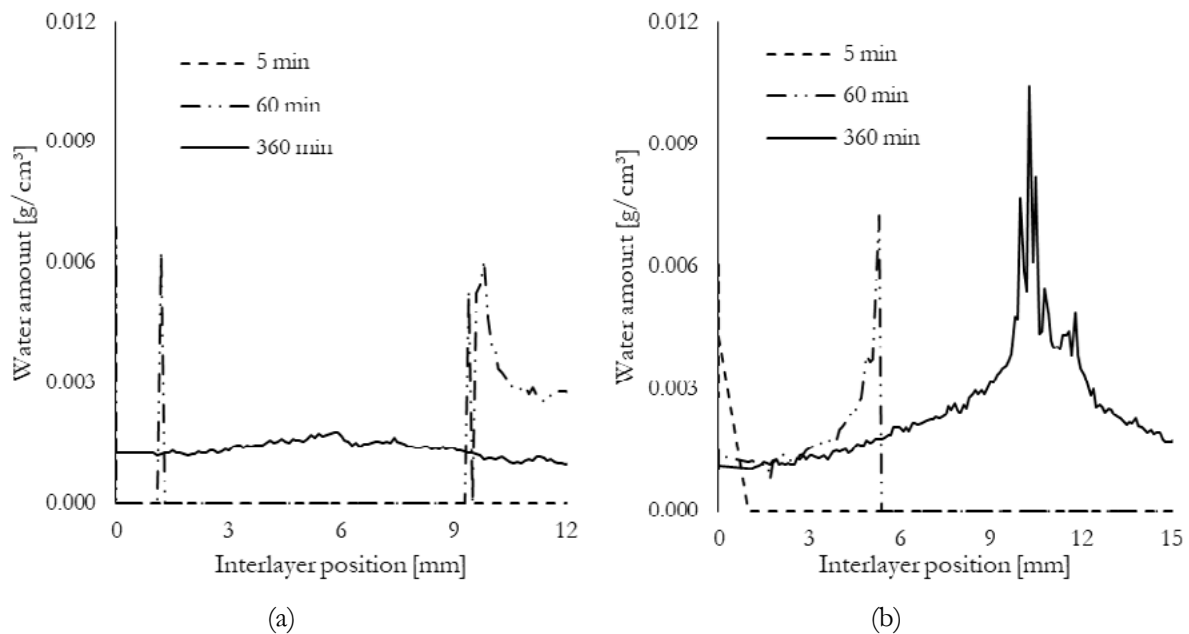


Figure 6: Water absorption at the interlayer at different exposure times for samples printed on (a) 1.7 cm/s and (b) 3.0 cm/s

4. Conclusions

The effect of an increased print velocity on the water uptake of printed specimens was investigated in this research. Visualisation of the moisture distribution and quantification of the water content was done by using neutron radiography and image analysis. From this study, the following conclusions can be drawn:

- Capillary water absorption measurements, performed under standardized circumstances, showed that the highest amount of water is absorbed during the first 4 – 6 hours of exposure. These results were confirmed by measurements performed by neutron radiography and therefore, a total exposure time of 6 hours was selected;
- In case of a low printing speed (1.7 cm/s), the water ingress occurs in a more uniform way compared to specimens fabricated with a higher velocity;

- Increasing the printing speed to 3.0 cm/s will induce a higher amount of water at the sides due to the non-uniform distribution of sand particles through the sample;
- After a water exposure time of 60 minutes, the water front did not reach the predefined interlayer zone completely. This phenomenon could be observed in case of both a low and high printing speed;
- After a water exposure time of 360 minutes, the samples were not completely saturated;
- The water amount at the interlayer is higher in case of an increased printing speed.

5. Acknowledgements

The authors would like to thank the Neutron Image and Activation Group of Paul-Scherrer-Institute (PSI Switzerland), and especially Mr. J. Hovind, for experimental support and useful discussions during operation of neutron radiography. J. Van Der Putten would like to acknowledge the support by EFRO for the C3PO-project (B/15100/01). T. Van Mullem also acknowledges the support of the grant (19SCIP-B103706-05) from the Construction Technology Research Program funded by the Ministry of Land, Infrastructure and Transport of the Korean government and P. Van den Heede is a postdoctoral fellow of Research Foundation-Flanders (FWO) (project No. 3E013917) and acknowledges its supports.

6. References

1. Schröfl, C., V.N. Nerella, and V. Mechtcherine. *Capillary Water Intake by 3D-Printed Concrete Visualised and Quantified by Neutron Radiography*. 2019. Cham: Springer International Publishing.
2. Brew, D.R.M., et al., *Water transport through cement-based barriers—A preliminary study using neutron radiography and tomography*. Nuclear Instruments and Methods in Physics Research Section A: Accelerators, Spectrometers, Detectors and Associated Equipment, 2009. **605**(1): p. 163-166.
3. Van Tittelboom, K., et al., *Use of neutron radiography and tomography to visualize the autonomous crack sealing efficiency in cementitious materials*. Materials and Structures, 2013. **46**(1): p. 105-121.
4. Snoeck, D., et al., *Visualization of water penetration in cementitious materials with superabsorbent polymers by means of neutron radiography*. Cement and Concrete Research, 2012. **42**(8): p. 1113-1121.
5. Van Der Putten, J., et al., *Microstructural characterization of 3D printed cementitious materials*. In preparation, 2019

Influence of heat treatment and mechanical activation on reactivity of natural pozzolan for geopolymer synthesis

R. Firdous¹, D. Stephan^{1*}

¹Technische Universität Berlin, Department of Civil Engineering, Building Materials and Construction Chemistry, Gustav-Meyer-Allee 25, 13355 Berlin, Germany

*Corresponding author E-mail: stephan@tu-berlin.de

Abstract

Natural pozzolans are suitable raw material for geopolymer synthesis as they are a tremendous source of silica and alumina with ease of mining and transportation accompanying lesser cost and lower environmental footprint than for artificial precursors. In this research study, a natural pozzolan formed as a result of meteorite impact has been used for the production of geopolymers. A comparative study has been made between heat treatment and mechanical activation as reactivity alteration methods. The geopolymer samples have been synthesised using raw and altered pozzolans. Several silica moduli of the alkaline solution and curing at ambient conditions were used. Results show that the heat treatment is more suitable as a reactivity alteration method compared to the mechanical activation as indicated by higher compressive strength and accelerated geopolymer reaction. Based on these results, microstructural characteristics have been studied for the geopolymer samples made with raw natural pozzolan and heat-treated pozzolan. Findings indicate that the heat-treated pozzolan has higher reactivity because of partial conversion of calcite to lime. A shift of optimum silica modulus to higher value in order to achieve maximum compressive strength has also been observed. Results of ATR-FTIR show the shift of various bands with the time due to uptake of Al into the structure. On the one hand, broadening of the band corresponding to Al/Si-O-Si indicates disorder introduced by initial geopolymerization. On the other hand, sharpening of this band denotes an increase in order with the age of geopolymer. TGA gives insight about the changes occurred during geopolymerization and shows the formation of C-S-H gel in geopolymer of heat-treated natural pozzolan. Results of XRD and SEM reveal that geopolymer gel is nevertheless mainly a mixture of N-A-S-H and (C)-N-A-S-H phase with the incorporation of Mg, Fe and K as charge-balancing cations.

Keywords: Geopolymer, natural pozzolan, compressive strength, alkaline solution, heat treatment.

1. Introduction

Global warming is the increase in the average atmospheric temperature over long-time, and it is one of the major issues which the world is facing currently. Scientists around the globe are thriving to find ways to reduce the green-house gas emissions. Building industry is one of the major contributors to global warming because of high production and consumption of cement [1]. Hence, there is a need to develop building materials with comparatively low CO₂ emissions for specific applications in order to cut short the use of cement. In this context, geopolymers have gained a lot of interest in recent decades. Comparatively low green-house gas emission, good mechanical and durability properties make them a foreseeable material for specific applications [1–3]. Geopolymers are a class of inorganic binders which possess a polymeric

Si-O-Al framework structure and can be synthesised by reaction of aluminosilicate source material with a concentrated alkaline solution [2, 4, 5]. Several aluminosilicate sources including natural and artificial pozzolans can be used as geopolymer precursor. Studies conducted till to date show that the natural pozzolans of volcanic origin can be used for geopolymer synthesis [6–13]. However, there is limited published data on the usability of other natural pozzolans for geopolymer synthesis which include diatomaceous earths, opaline cherts, shales, pumicites and materials formed by meteorite impact. This research study focusses on the use of natural pozzolan formed as a result of meteorite impact for geopolymer synthesis. The material named as breccia Suevite or Bavarian trass was formed approx. 14.5 million years ago when a meteorite hit the earth in a region later called the Nördlinger Ries, Germany [14].

Studies show that natural pozzolans have lower reactivity in alkaline medium in comparison to artificial pozzolans such as fly ash and metakaolin [8, 15]. Several methods have been applied to improve their reactivity including mechanical activation, heat treatment, partial replacement by secondary cementitious materials and alkali fusion [8, 16–19]. Bondar et al. applied heat treatment by calcinating four different natural pozzolans at different temperatures. Results showed that the calcination can have positive and negative effects on the reactivity of natural pozzolan depending on the mineralogy of the raw sample [18]. Djobo et al. investigated the effect of mechanical activation on Cameroonian volcanic ash and found that mechanical activation helps in improving the reactivity, however, excess milling beyond a certain limit can have adverse effect on the reactivity of volcanic ash [16]. Alkali fusion includes calcination in the presence of alkali hydroxides. Tchakoute et al. applied the alkali fusion technique on Cameroonian volcanic ash using NaOH pellets and burning at 550 °C for 1 h. Geopolymer samples synthesised using this fused volcanic ash and metakaolin showed good mechanical properties, short setting time and low shrinkage [19]. Several materials such as kaolinite, metakaolin, bauxite, calcined oyster shell and slag have been used as partial replacement of natural pozzolan for geopolymer synthesis [17, 20–22]. Results pointed out that the addition of kaolinite give similar compressive strength has no appreciable effect on the improvement of compressive strength [17]. Whereas, replacement by slag and metakaolin improves the properties of resultant geopolymer [21, 22]. The inclusion of bauxite has been found a promising way to reduce efflorescence while the addition of calcined oyster shell helps in reduction of setting time [20].

However, there are limited published studies available on the comparison of different reactivity enhancement methods and their effect on the properties of the geopolymer product. This research study aims to compare two reactivity alteration methods, i.e. heat treatment and mechanical activation and to study their effect on final geopolymer product. Geopolymer samples have been obtained by mixing raw natural pozzolan, heat-treated or mechanical activated natural pozzolan with an alkaline solution. For the purpose, three different silica moduli of alkaline solution have been used. Based on the results of compressive strength and reaction kinetics, one reactivity enhancement method has been chosen to study its effect on the microstructural properties of final geopolymer made with several silica moduli at various ages. TGA, XRD, ATR-FTIR and SEM have been used to study the microstructural characteristics.

2. Materials and methods

2.1 Materials and characterization

2.1.1 Pozzolans

Natural pozzolan from Germany named as Bavarian trass (BT) has been used in this study. Bavarian trass was supplied by Märker Zement GmbH, Germany. Chemical composition was determined by XRF analysis using PW 2400, PHILIPS and is given in Table 1. Bavarian trass (BT) was subjected to heat treatment and mechanical activation. Heat treatment was conducted by calcining the sample at 700 °C for 3 h, followed by cooling to room temperature in a desiccator with silica gel. While, the mechanical activation was performed

by milling in a planetary ball mill (PULVERISETTE 5 classic line, Fritsch GmbH, Germany) at a speed of 200 rpm for 5 min or 10 min with media to material ratio of 1:0.16.

Table 1: Chemical composition of all natural pozzolans.

Sample / wt. %	Total	LOI	SiO ₂	Al ₂ O ₃	Fe ₂ O ₃	MnO	MgO	CaO	Na ₂ O	K ₂ O	TiO ₂	P ₂ O ₅	SO ₃
BT	100.25	11.24	52.35	12.25	4.15	0.09	0.91	13.85	1.67	2.44	0.61	0.22	0.47

The grinding bowl made of hardened steel consisting of 125 ml capacity was filled with 80 g of pozzolan sample. 15 grinding balls made of hardened steel of 20 mm diameter were used for milling. The calcined Bavarian trass has been named as BTC and milled Bavarian trass for 5 and 10 min has been named as BT5 and BT10, respectively. It should be noted here that applying reactivity alteration methods add additional cost to the production of the building material. Therefore, from economical and industrial perspective more practical methodology was adopted. Specific surface area as measured by Blaine fineness according to EN 196-6 [23] was recorded as 6746 cm²/g for BT sample. For BTC as a result of heat treatment specific surface area increased to 7141 cm²/g. While for BT5 and BT10 the specific surface area was recorded as 7018 cm²/g and 11721 cm²/g. Figure 1a presents the particle size distributions of BT, BTC, BT5 and BT10 samples measured using Mastersizer 2000 of Malvern Instruments and Figure 1b shows the d₅₀ particle size for BT, BT5 and BT10 samples. With the applied mechanical activation method, a reduction of 23% and 43% in d₅₀ has occurred for BT5 and BT10, respectively. X-ray diffraction analysis was performed on BT, BTC, BT5 and BT10 using the method as described in section 2.2. Figure 2 presents the X-ray diffractograms of all pozzolans with the mineralogical phases. The mineralogical phases were determined in accordance with the literature [24–29]. In addition to mentioned crystalline phases, BT sample also contain a glass phase. Due to heat treatment, some amount of calcite has been found to decompose (calcite peaks reduced in height) and formation of lime has been observed in XRD in BTC sample (as shown in Figure 2). Partially crystalline phases present in BT which may correspond to the presence of clay and zeolite minerals also decomposed as a result of heat treatment. XRD detects entirely no differences between BT, BT5 and BT10.

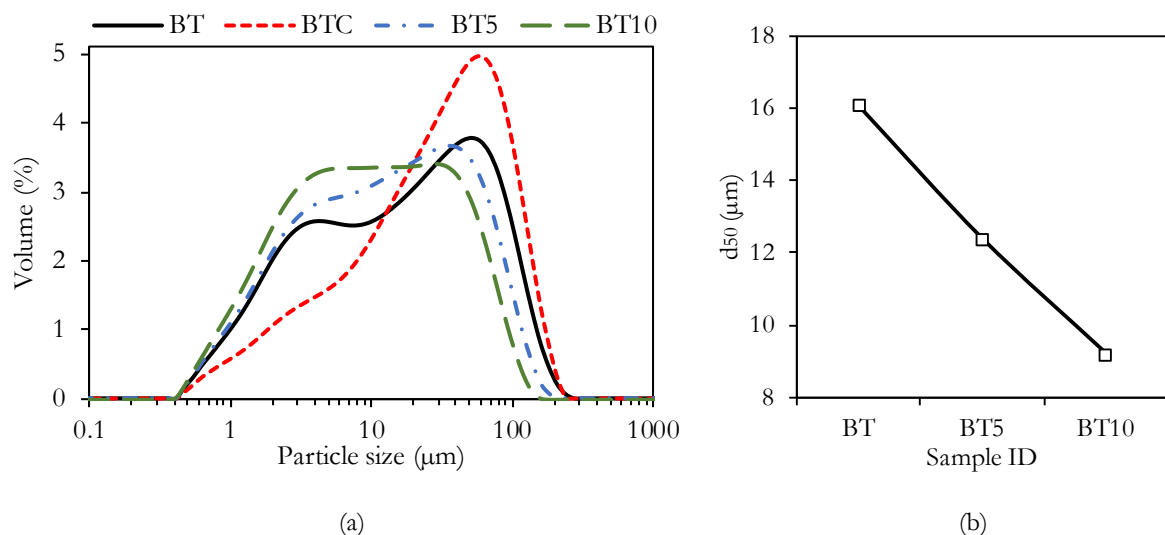


Figure 1: (a) Particle size distribution for BT, BTC, BT5 and BT10 samples, (b) d₅₀ for BT, BT5 and BT10 samples.

2.1.2 Alkaline activator

Alkaline activator consisting of combinations of sodium hydroxide (NaOH) and sodium silicate solutions (Na₂SiO₃) were used. NaOH of 99 wt.% purity was obtained from VWR International GmbH in pellets.

NaOH solutions were prepared by dissolving NaOH pellets in deionized water at least 24 h before use. Sodium silicate solution (Betol 52T) was obtained from Woellner GmbH with silica modulus of 2.12. The NaOH solution and Na₂SiO₃ solution were mixed in different fractions to obtain the alkaline solutions of desired silica modulus. Three silica moduli of alkaline solution of 0.707 (H₂O/Na₂O molar ratio = 9.7), 0.797 (H₂O/Na₂O molar ratio = 11.4) and 1.061 (H₂O/Na₂O molar ratio = 10.5) were used for BT and BTC geopolymers, while silica modulus of 0.707 was used for BT5 and BT10 geopolymer samples.

2.2 Experimental methodology

The geopolymer paste samples were prepared using a laboratory hand mixer with a mixing time of 3 min. In-between break of 30 s was taken after mixing the sample for 90 s to collect all the sample in the centre of the bowl for homogeneous mixing. After complete mixing, the paste was poured in 20 mm cubic molds and was compacted using vibration table for 2 min. Samples were sealed using plastic foil from all sides and were cured at 21 ± 1 °C and 100% relative humidity till test age. Alkaline solution to solid ratio was kept equal to 0.75 for all geopolymer samples to achieve good workability.

The compressive strength of cubic samples was determined at 7, 28, 90 and 180 d age. Pieces of broken samples were collected at 7, 28 and 90 d age and geopolymer reaction was stopped for examination by TGA, XRD, ATR-FTIR and SEM-EDX. The reaction was stopped by solvent exchange using isopropanol. Samples were submerged in isopropanol for 24 h followed freeze-drying for 7 d. Afterwards, samples were ground by hand in mortar and pestle to a size <125 µm. In the case of storing, the samples were stored in a desiccator with sodium hydroxide (on support) obtained from Merck, KGaA, Germany to avoid environmental carbonation.

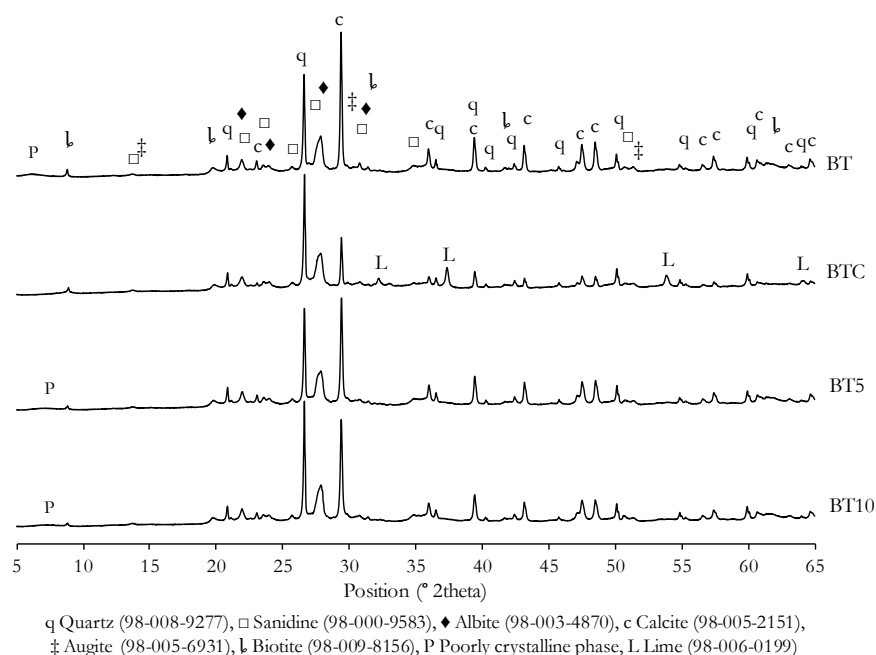


Figure 2: X-ray diffractograms of BT, BTC, BT5 and BT10 samples.

Isothermal conduction calorimetry was performed to understand the reaction kinetics and to study the effect of heat treatment and grinding on the reactivity of natural pozzolan. For the calorimetric study, device MC-CAL 100P, C3 Prozess- und Analysentechnik GmbH, Germany was used. Samples were mixed outside the device for 45 s each with vortexer. Therefore, zero in the calorimetric curves is the point when samples were placed inside the device.

Thermogravimetric analysis (TGA) was performed using TG 209, Tarsus F3, Netzsch Instruments under a nitrogen atmosphere at a flow rate of 250 mL/min. For each test, 10 ± 1 mg of sample was used. The sample was first held at 25 °C for 20 min, and then heated from 25 °C to 850 °C at a heating rate of 10 °C/min.

Fourier transform infrared spectroscopy (FTIR) was performed on raw natural pozzolan and respective geopolymer samples using Spectrum Two of PerkinElmer fitted with diamond crystal via the attenuated total reflection (ATR) method. IR spectra were obtained between 4000 to 400 cm^{-1} with a resolution of 1 cm^{-1} .

X-ray diffraction analysis (XRD) was performed using an Empyrean PANalytical diffractometer with Ni filter and $\text{CuK}\alpha$ radiation ($k = 1.540598 \text{ \AA}$), operating at 40 kV and 40 mA in continuous mode with a resolution of 0.0131° and speed of $0.0176^\circ/\text{s}$ for a range of 5° to 65° for 1 h. The phase evaluation was performed using HighScore Plus software with ICDD and ICSD.

Polished freeze-dried samples were impregnated in epoxy resin to study the microstructure and elemental distribution. For the purpose, scanning electron microscopy fitted with energy-dispersive X-ray spectrometer (SEM-EDX) was performed using device GeminiSEM500, ZEISS operated at 15 kV.

Throughout the manuscript, the geopolymer samples made with BT, BTC, BT5 and BT10 are labelled with the respective raw sample, silica modulus used to prepare each geopolymer and the age of the sample.

3. Results and discussion

3.1 Effect of heat treatment on compressive strength

Figure 3 presents the compressive strength development of BT and BTC geopolymer samples. Results indicate that heat treatment of BT improved the reactivity as found by an increase of compressive strength in BTC geopolymer samples. An increase of 32% and 45% in compressive strength has been observed at 90 d age for samples BTC-0.797 and BTC-1.061, in comparison to corresponding BT samples. While for sample BTC-0.707, 7- and 28-d compressive strength was improved and thereafter, no significant improvement in compressive strength has been observed. Considering the BT geopolymer, the optimum silica modulus to achieve highest compressive strength was recorded as 0.707, while for BTC geopolymers it is found as 0.797. Thus, the optimum silica modulus shifted to higher silica modulus for BTC geopolymers in comparison to BT geopolymers. This confirms the improvement in reactivity of this natural pozzolan and a reduction in the alkali concentration of the solution used, which is beneficial from both economic and environmental perspective.

Table 2 presents the visual observation of BT and BTC samples prepared with various silica moduli at 90 d. The pictures presented in Table 2 show that for sample BTC-0.707, efflorescence formation increased in comparison to sample BT-0.707. While for sample BTC-0.797 and BTC-1.061, the formation of efflorescence decreased in comparison to samples BT-0.797 and BT-1.061. The formation of efflorescence is because of an excess of free alkalis in geopolymer matrix which react with carbon dioxide from the environment and produce sodium carbonate which precipitates at the surface or in pores of geopolymer matrix.

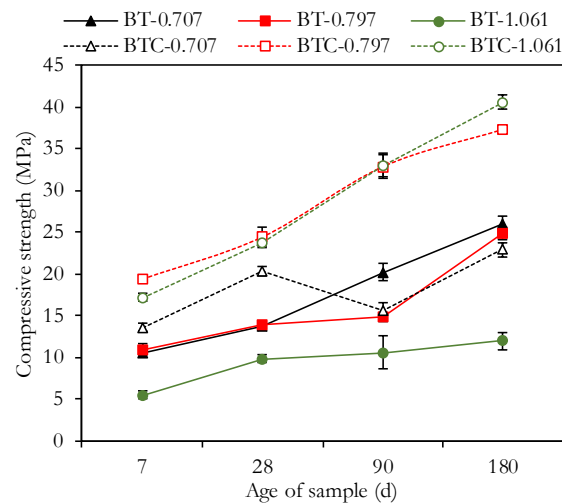








Figure 3: Compressive strength of BT and BTC geopolymer at different ages.

Table 2: Visual observation of BT and BTC sample at 90 d age.

Silica modulus	0.707	0.797	1.061
BT			
BTC			

3.2 Effect of mechanical activation on compressive strength

The effect of mechanical activation as the reactivity alteration process has also been studied by compressive strength and the results are presented in Figure 4.

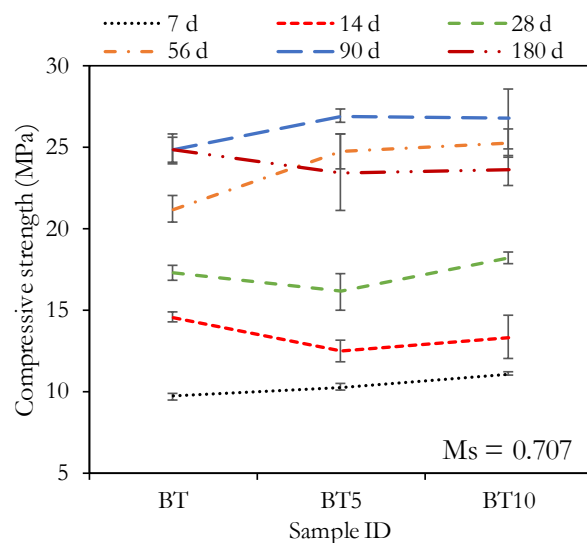


Figure 4: Effect of mechanical activation on the compressive strength of BT sample.

A slight improvement in strength with grinding has been found. However, no significant improvement in strength has been observed at all ages of the sample, and the values are mostly within the range of standard deviation.

3.3 Effect of heat treatment on reaction kinetics

Figure 5 presents the calorimetric curves for BTC compared to BT samples. Results show that geopolymer reaction for BT geopolymer samples is characterised by two exothermic peaks. The initial peak occurs when natural pozzolan and alkaline solution come in contact and is therefore attributed to wetting and dissolution of reactive phases. This peak is followed by deceleration which is associated with polycondensation thus the amount of heat released decreases. Thereafter, a second exothermic peak has been observed which is assigned to a delayed dissolution of some phases. Delayed dissolution of calcium-rich phases leading to a second exothermic peak was observed by Gebregziabihier et al. [30]. The formation of early product in alkali-activated system depletes the alkalis and the relative silica concentration increases, which in turn retards the dissolution of calcium phases [30]. For samples BT-0.707, BT-0.797 and BT-1.061, second exothermic peak was observed at 11 h, 12.6 h and 28.3 h with a maximum at approx. 12.5 h, 14.5 h and 34.7 h, respectively.

Comparing BT and BTC geopolymer samples, the rate of reaction increased for all calcinated samples in comparison to BT samples indicated by higher heat evolved over 168 h, higher heat flow in first hours and shift of second exothermic peak to an earlier time or complete disappearance. For sample BTC-0.797 and BTC-1.061 this peak was not observed at all. For BTC-0.707 sample, this peak moved to approx. 8 h and appears only as a slight hump (Figure 5). These findings are in accordance with the results of compressive strength, as for sample BTC-0.707 compressive strength is also lower than for sample BTC-0.797 and BTC-1.061 which can be described by the delayed dissolution and therefore, lack in a gain of compressive strength. Comparing BTC-0.707, BTC-0.797 and BTC-1.061 to each other, the rate of dissolution increases with the decrease of silica modulus.

The improvement of pozzolanic reactivity as a result of calcination for this natural pozzolan has also been reported by [25], however the authors found that a possible reason of such improvement was presence of smectite minerals. In the current research, this mineral group has not been identified. Therefore, the reason for such improvement in reactivity as a result of the heat treatment is most likely the conversion of calcite to lime which imparts higher reactivity [31]. This is because the reaction of lime with water leads to a rise in the pH of the system which enhances the dissolution of aluminosilicate species [32]. Thus, the rate of reaction increases and 2nd exothermic peak shifts to earlier times. Henceforth, the increase in dissolution rate results in a higher amount of precipitated geopolymer gel associated with an increase of compressive strength in most cases (Figure 3) and heat evolved over 168 h (Figure 5) of calcinated samples in comparison to BT samples. This finding also enables to explain the alteration of efflorescence development depicted in Table 2. The samples with silica moduli 0.797 and 1.061 precipitate enough geopolymer gel to incorporate most of the alkalis of activator solution. Therefore, lower efflorescence product is formed. On the other hand, the alkaline concentration in sample BTC-0.707 is too high and most of it has not been incorporated in geopolymer gel and thus it leads to formation of higher amount of efflorescence (as seen in Table 2).

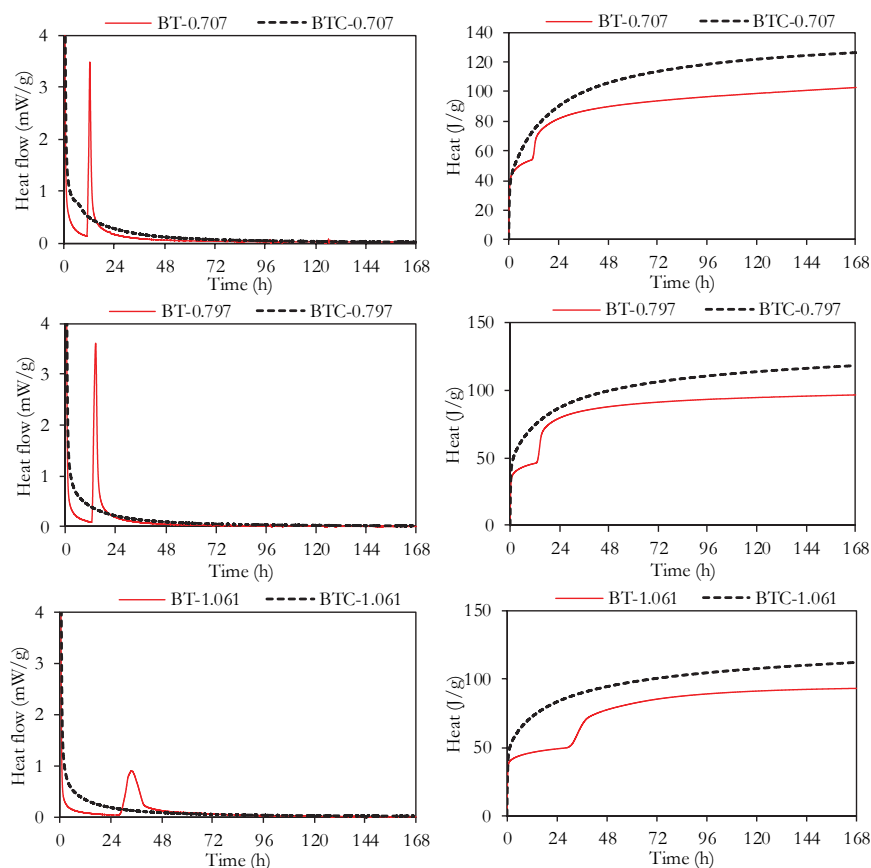


Figure 5: Heat evolution curves for BT and BTC geopolymers.

3.4 Effect of mechanical activation on reaction kinetics

To study the influence of mechanical activation on reaction kinetics, isothermal conduction calorimetry was conducted. Firstly, BT, BT5 and BT10 raw samples were separated in two fractions by a 40 μm sieve, afterwards, calorimetry was conducted on these separated fractions. The fractions of material were separated to understand the effectiveness of mechanical activation on the fine and coarse fractions of the sample, such that the first hump of bimodal particle size distribution was separated (Figure 1). Geopolymer samples were prepared with silica modulus of 0.707 for each fineness and are labelled as BT-0.707, BT5-0.707 and BT10-0.707. The results of the calorimetric study are presented in Figure 6 for both fractions of samples.

Results indicate that the fraction <40 μm exhibits higher reactivity than fraction >40 μm . Mechanical activation in the ball mill is more effective in reducing the size of larger particles. The calorimetry curves of BT samples show that the part of sample <40 μm develops approx. twice as much hydration heat after 168 h as that >40 μm . Total heat slightly increases with increasing fineness of sample (from BT over BT5 to BT10) for fraction <40 μm . While for the fraction >40 μm , total heat released stays nearly unchanged from BT to BT5 but increases significantly for BT10-0.707.

It is important to note here that the second exothermic peak occurs only for fraction <40 μm for sample BT-0.707 and BT5-0.707. While for sample BT10-0.707, it occurs for both fractions. By increasing the overall fineness of sample (from BT over BT5 to BT10), this reaction triggers to earlier time and heat flow value decreases but time span over which reaction occurs is increased. These observations indicate that with the increase in fineness the reaction degree is increasing at a lower rate; therefore, only a slight improvement in compressive strength has been observed. However, to see a significant impact of mechanical activation,

sample may be milled for a longer time, but care must be taken while choosing a reactivity alteration method and its economic advantages.

XRD analysis was performed on the separated fractions of BT, BT5 and BT10 as shown in Figure 7 to understand calorimetric analysis. The results show that the fractions $<40\ \mu\text{m}$ have excess amount of calcite while the fractions $>40\ \mu\text{m}$ are enriched in minerals such as quartz, sanidine and albite which have higher Mohs scale hardness. Further the fraction BT $<40\ \mu\text{m}$ has highest amount of calcite while as a result of milling the calcite content is slightly decreasing in BT5 $<40\ \mu\text{m}$ and BT10 $<40\ \mu\text{m}$. Therefore, as a result in calorimetric analysis the height of 2nd exothermic peak is decreasing with increasing milling time.

With increasing milling time, the calcite content in fraction $>40\ \mu\text{m}$ is consequently increasing. This is because of possible agglomeration of soft and small calcite particles during milling. In BT10 geopolymers samples both fractions exhibit the 2nd exothermic peak. This can be because of sufficiently high content of calcite in both fractions. The agglomeration leads also in coarse fraction to a sufficient amount of calcite content to develop the 2nd peak. While the hard minerals are not much effected by grinding and therefore, doesn't exhibit any appreciable differences in their reactivity.

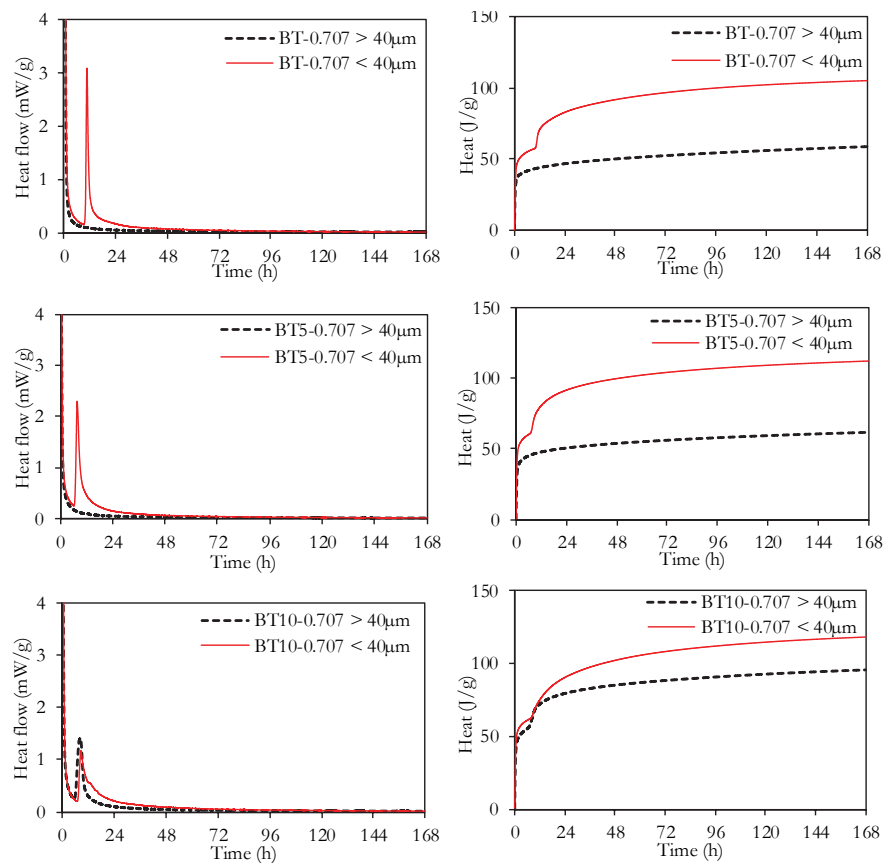


Figure 6: Heat evolution curves for BT, BT5 and BT10 geopolymers.

Comparing both reactivity alteration methods, the effect of heat treatment is more prominent than reduced particle size. Looking at Figure 1, BTC sample has a higher fraction of coarser particles in comparison to BT5 and BT10 samples. But the inclusion of more reactive phases such as lime imparts higher reactivity than reduced size of particles. Based on these results, heat treatment has a higher influence on the reactivity of BT. Therefore, further detailed microstructural analysis has been made only on BT- and BTC-based geopolymers in following sections.

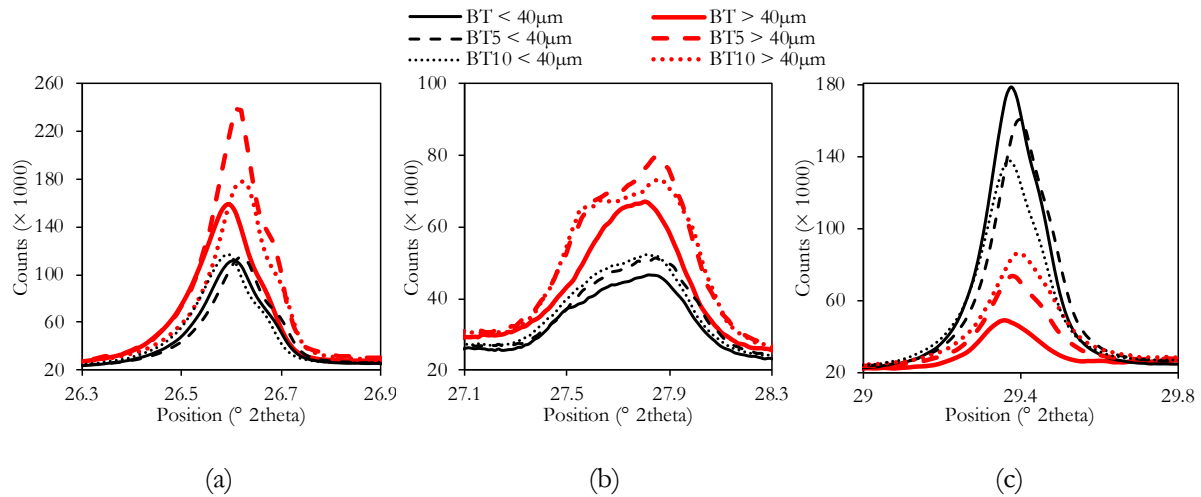


Figure 7: Diffractograms of BT, BT5 and BT10 fractions below and above 40 μm showing reflexes for (a) quartz (b) sanidine and albite (c) calcite.

4. Microstructural characteristics

4.1 Thermogravimetric analysis (TGA)

Thermogravimetric analysis was performed on BT and BTC geopolymer samples at the age of 7, 28 and 90 d. Results for the sample prepared with silica modulus of 0.797 for both pozzolans are presented in Figure 8.

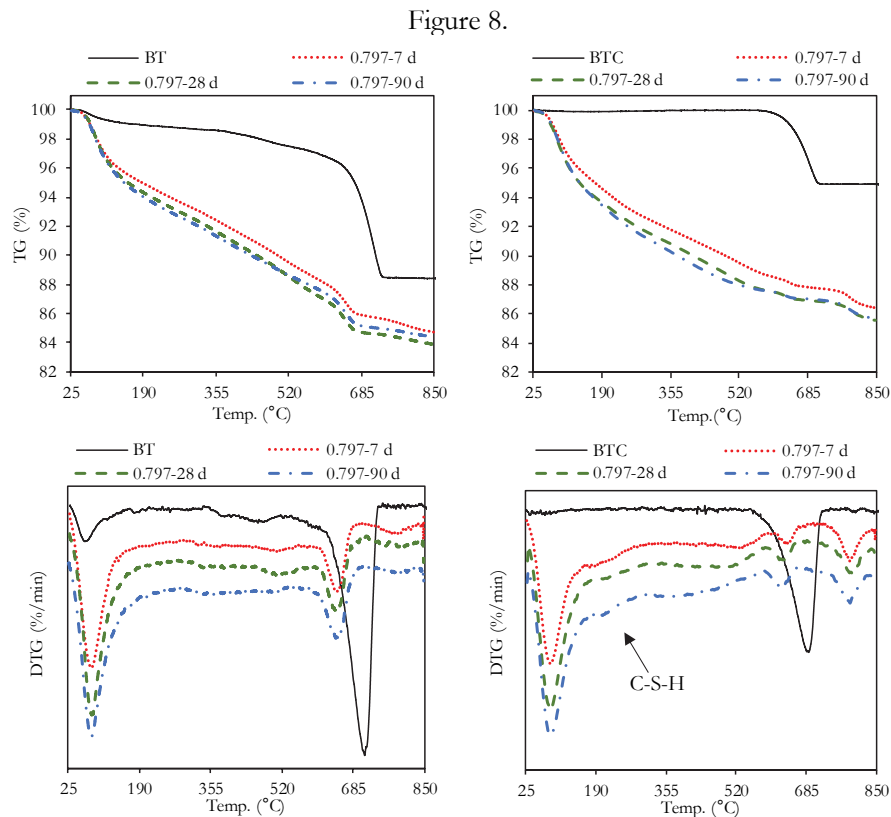


Figure 8: TG and DTG curves of BT and BTC samples at 7, 28 and 90 d age.

The overall mass loss for BT and BTC geopolymers prepared with silica modulus of 0.797 is higher at all ages than in raw pozzolans. Similar behaviour has been also observed for BT and BTC geopolymer samples prepared with silica modulus of 0.707 and 1.061 which are not shown here. The overall mass loss seems to increase with the age of sample slightly. This increase in the mass loss is attributed to geopolymerization

reaction. Mass loss till approx. 150 °C is considered as the liberation of loosely bound water. Mass loss from 150 – 600 °C is attributed to liberation of stronger chemically bound water. As a result of geopolymerization, bound water is introduced in the system as a part of geopolymer gel which is formed due to dissolution and subsequent precipitation of aluminate and silicate species. This mass loss in the range of 30 – 600 °C can be correlated to the amount of reaction product formed [33]. Results presented in Table 3 show that dehydration in the temperature range of 30 – 600 °C is affected by the change of silica modulus of alkaline solution used and the age of the sample. For samples BTC-0.797 and BTC-1.061, the mass loss in mentioned temperature range increases with age while for all others it initially increases from 7 to 28 d and then decreases till 90 d. Such a reduction in water content with the age can be caused by efflorescence formation in these samples with age [34]. The last stage in TG refers to decarbonization (600 – 850 °C) and shows that the carbonate content of samples is reduced as a result of geopolymerization [35, 36].

Table 3: Mass losses in the temperature range of 30 – 600 °C for BT and BTC geopolymer samples at various ages.

Age of sample	Mass loss (wt.%)					
	BT-0.707	BT-0.797	BT-1.061	BTC-0.707	BTC-0.797	BTC-1.061
7 d	11.87	11.88	10.76	11.44	11.40	10.38
28 d	13.25	12.98	12.38	11.74	12.40	10.98
90 d	13.00	12.48	12.17	11.43	12.77	11.40

The effects mentioned above are observed in both BT and BTC geopolymers. Additionally, for BTC geopolymers, two other peaks in DTG have also been found, i.e. a diffuse peak in the temperature range of 160 – 300 °C with its centre at approx. 200 °C and a sharp peak above 790 °C with a maximum at approx. 795 °C. The first peak is attributed to dehydration of C-S-H gel which has been observed to form in case of availability of reactive calcium [35, 36]. This peak has been observed in all BTC geopolymer samples but in none of the BT geopolymer samples. This shows that as a result of calcination, calcite converts to lime which imparts more reactive calcium. After that, the second peak observed only in BTC geopolymer samples is attributed to the decomposition of C-S-H to wollastonite; such decomposition has been also observed in the literature and was also confirmed here by conducting XRD on the decomposed residue [36, 37].

4.2 X-ray diffraction analysis (XRD)

Figures 9 and 10 show the XRD diffractograms of BT and BTC geopolymers at the age of 7, 28 and 90 d prepared with silica modulus of 0.797, respectively. XRD analysis was made on all samples, but for easy understanding selected samples have been shown here.

In raw BT and BT geopolymer samples, two amorphous humps were recorded ranging approx. 5° – 8° and 24° – 34°. While in raw BTC and BTC geopolymer samples only the second hump mentioned above has been recorded. The first hump in raw BT and BT-based geopolymers was not identifiable, but it may correspond to the presence of clay or zeolite minerals. As a result of geopolymerization the shape of this amorphous hump changed indicated by the shift of the centre of the hump. This may be due to the formation of aluminosilicate gel phase.

In both raw pozzolans, the centre of the second amorphous hump was recorded at 27°. While in both pozzolan-based geopolymer samples the centre of the second amorphous hump shifted to higher 2 theta values i.e. 31°. Such a shift has been described to occur due to the formation of geopolymeric gel [38–40]. Further, in BT geopolymer sample made with silica modulus of 0.707 at 7 d and in BTC geopolymer samples made with silica modulus of 1.061 at 28 d a new reflex has been observed to form at approx. 27°. This reflex has not been observed in all other samples. It is attributed to the formation of aragonite (98-028-0991) which is a polymorph of calcium carbonate and may form under high alkaline conditions [41, 42]. However, the lower stability of this phase is the reason that it has been not observed in other samples.

As seen earlier, efflorescence formation was observed for BT and BTC geopolymer samples. XRD results reveal that efflorescence is caused by precipitation of natrite ($\gamma\text{-Na}_2\text{CO}_3$, 98-009-5549). This is formed because of the reaction of excess free alkalis in the geopolymer system with environmental carbon dioxide. Looking at Figures 9 and 10, the participation of calcite and lime in geopolymer reaction can be clearly observed as indicated by the reduction of reflex height of calcite while reflexes of lime are completely absent in geopolymer samples.

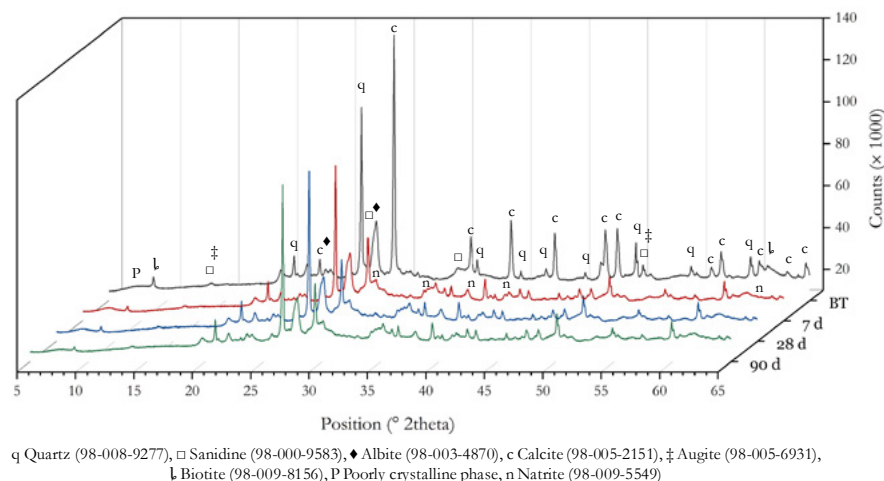


Figure 9: Comparison of raw BT and BT geopolymer sample at the age of 7, 28 and 90 d for geopolymer sample prepared with silica modulus of 0.797.

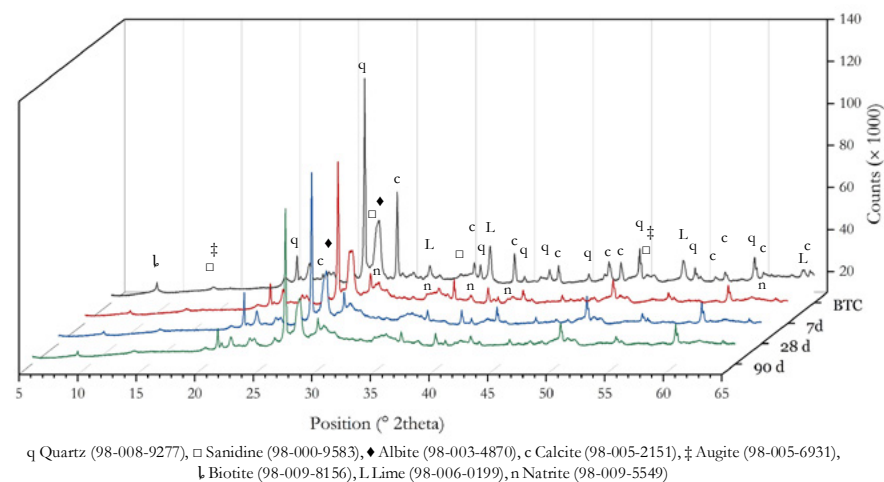


Figure 10: Comparison of raw BTC and BTC geopolymer sample at the age of 7, 28 and 90 d for geopolymer sample prepared with silica modulus of 0.797.

This confirms the previous finding that lime imparts higher reactivity than calcite as indicated by its complete participation in geopolymer reaction. Other crystalline phases may be participating in geopolymer reaction include biotite and sanidine, as indicated by slight changes in the reflexes for these minerals.

4.3 Fourier transform infrared spectroscopy (FTIR)

ATR-FTIR spectra were collected for the BT and BTC raw samples and their respective geopolymer samples at 7, 28 and 90 d ages. Results have been presented in Figure 11. FTIR analysis was made on all geopolymer samples and they showed comparable characteristics; therefore, for the easy understanding sample prepared with silica modulus of 0.707 has been shown here. The major characteristic peaks have been observed in region 1600 to 400 cm^{-1} . In region 4000 to 1600 cm^{-1} only one broad hump around 3100

cm⁻¹ has been observed which indicates the OH stretching vibration.

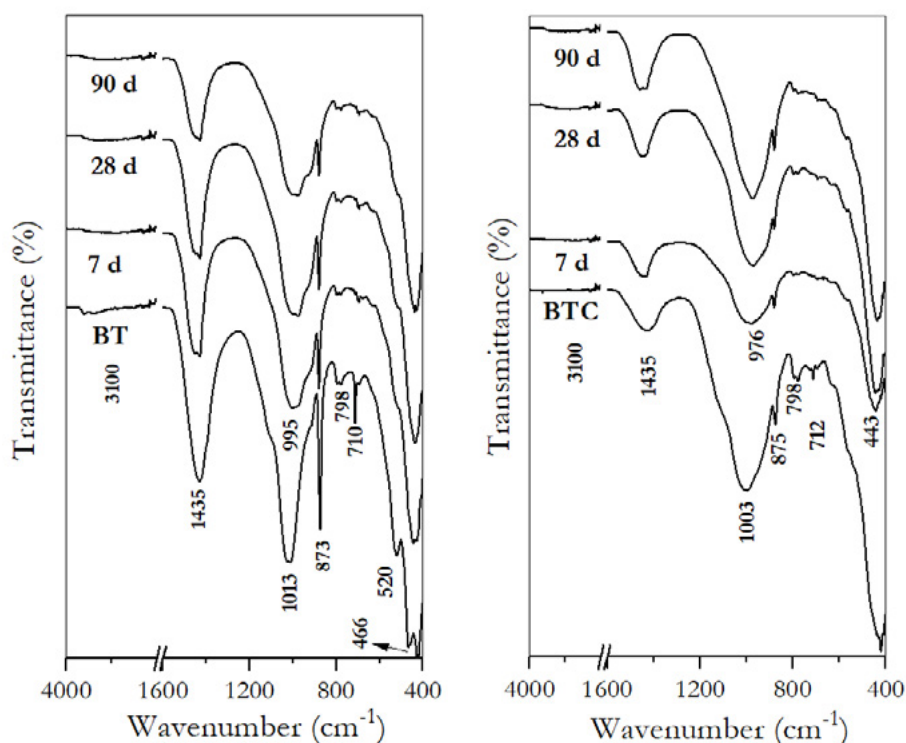


Figure 11: ATR-FTIR spectra of raw BT and BTC samples and BT and BTC geopolymer samples prepared with silica modulus of 0.707 at 7, 28 and 90 d age.

An intense band in raw BT and raw BTC samples at 1013 and 1003 cm⁻¹, respectively, attributed to asymmetric stretching of Al/Si-O-Si has been found to move to lower wavenumber i.e. 995 and 976 cm⁻¹ in respective geopolymer samples. This is significant of changes that occurred as a result of the dissolution of the raw sample to form Al-rich geopolymer gel. As the SiO₄ tetrahedra of silica-rich network of the raw sample are broken and precipitates take AlO₄ tetrahedra up [9, 43]. Further, broadening of bands observed at 995 and 976 cm⁻¹ in comparison to respective raw sample has been observed. This broadening is significant of structural disorder with the addition of water in structure [44]. Moreover, in BTC geopolymers the band present at 976 cm⁻¹ is sharpening with age, which indicates the increasing order in the phase [43].

Another significant change observed between raw BT and BTC samples is the reduction of the carbonate group as a result of heat treatment. As the stretching bands of O-C-O observed at 1435, 873 and 710 cm⁻¹ in raw BT sample and at 1435, 875 and 712 cm⁻¹ in raw BTC sample reduced in intensity while comparing BT and BTC samples to each other. Moreover, comparing the BT and BTC geopolymer samples, a clear reduction in this band has been observed as a result of geopolymerization. This indicates the participation of carbonates in geopolymer reaction. Further, a characteristic band corresponding to symmetrical stretching of Si-O-Si has been observed in both geopolymer samples at 798 and 520 cm⁻¹. Bending vibration band of Si-O-Si has been observed at 466 cm⁻¹ in BT geopolymers and at 420 cm⁻¹ in BTC geopolymers. This shift from higher to lower wavenumber is significant of incorporation of Al in gel structure [43].

4.4 Scanning electron microscopic (SEM) analysis coupled with energy dispersive X-ray spectroscopy (EDX)

Figures 12 and 13 show the scanning electron microscope micrographs and elemental maps of same region of the selected samples obtained for BT and BTC geopolymers, respectively. The microstructure illustrates a heterogeneous morphology, while elemental maps show a nonhomogeneous distribution of

several elements. Looking at the micrographs of BT geopolymers, three different zones in microstructure labelled as 1, 2 and 3 and microcracks are visible (Figure 12). The microcracks may appear as a result of the sample preparation method. Zone 1 in the micrograph shows a sponge-like structure which corresponds to Na-rich aluminosilicate geopolymer gel as indicated by the presence of Na, Al, Si and O in this zone from elemental maps. In addition to Na, the presence of Mg and Fe has also been recorded in this zone. While the elemental maps of K and Ca show that there is a small amount of K present while no Ca has been observed. Comparison of Si and Al elemental maps in this zone shows that the reaction product is richer in Al. Thus, it signifies that zone 1 potentially consists of N-A-S-H geopolymer gel incorporating Mg and Fe cations.

Zone 2 shows a natural pozzolan particle under alkali attack and dissolution of the particle. The particle has broken to small fragments under alkaline solution attack. Meanwhile, the reaction product is precipitated in cavities as indicated by the elemental map. Further, the elemental maps show that K and Ca are non-uniformly distributed in gel structure in contrast to zone 1. Zone 3 shows an unreacted particle of natural pozzolan which is rich in Si and O, and can be a quartz particle.

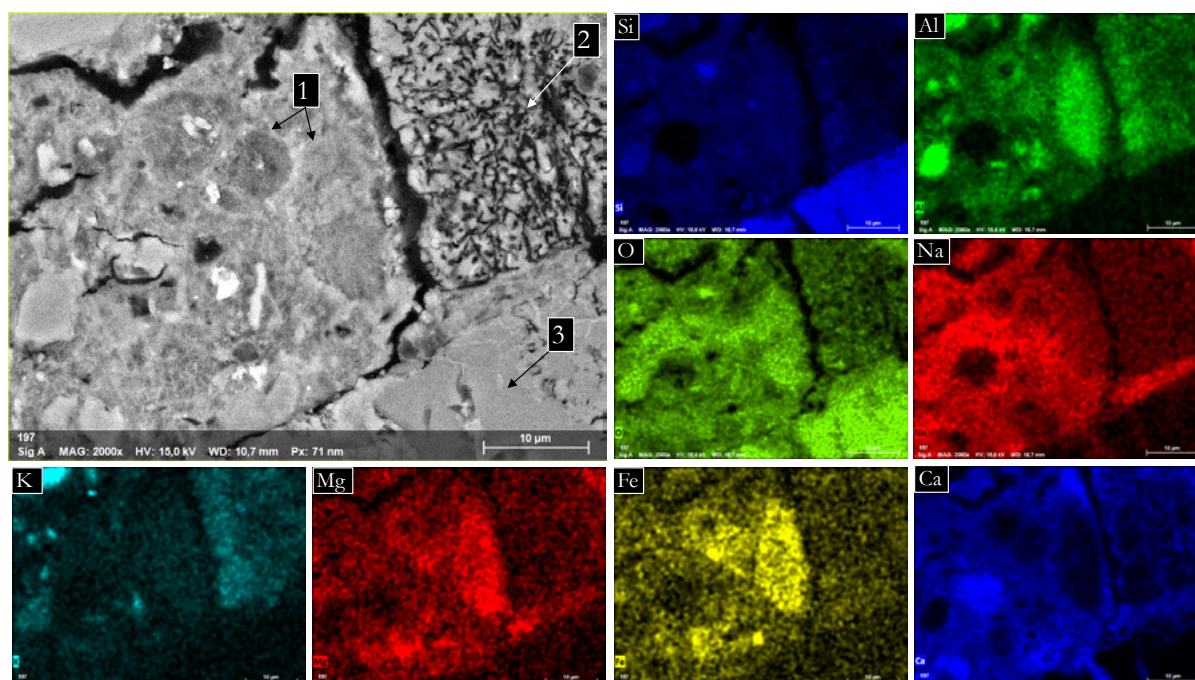


Figure 12: SEM image and elemental maps of BT geopolymer made with silica modulus of 0.707 at 7 d age.

Figure 13 presents a micrograph and elemental maps for BTC geopolymer sample. At least two types of gel phases can be seen marked as 1 and 2. The micrograph of the BTC geopolymer sample depicts a more homogeneous and compact microstructure with a more uniform distribution of several elements than the BT geopolymer. Like BT geopolymers, zone 1 shows Na-rich aluminosilicate gel, with an absence of Ca and the presence of Mg and Fe cations. As seen in BT geopolymers, this gel also has sponge-like structure. Zone 2 is characterized by a heterogeneous morphology with a compact gel structure where Na- and Ca-rich regions are overlapping each other. Further, in BTC micrograph a clear reduction in the size of unreacted particles of natural pozzolan can be seen in comparison to BT geopolymer sample. The geopolymer binder strongly binds the unreacted particles present. Comparing the elemental maps of Si and Al, the geopolymer gel in BTC geopolymers is rich in Si. This justifies the higher reactivity of BTC and higher compressive strength as Si-O bonds are stronger than corresponding Al-O bonds [2]. Combining the results of BT and BTC geopolymers, it is obvious that the geopolymer binder is heterogeneous in nature and consists majorly

of N-A-S-H, within cooperation of Mg, K, Fe and Ca.

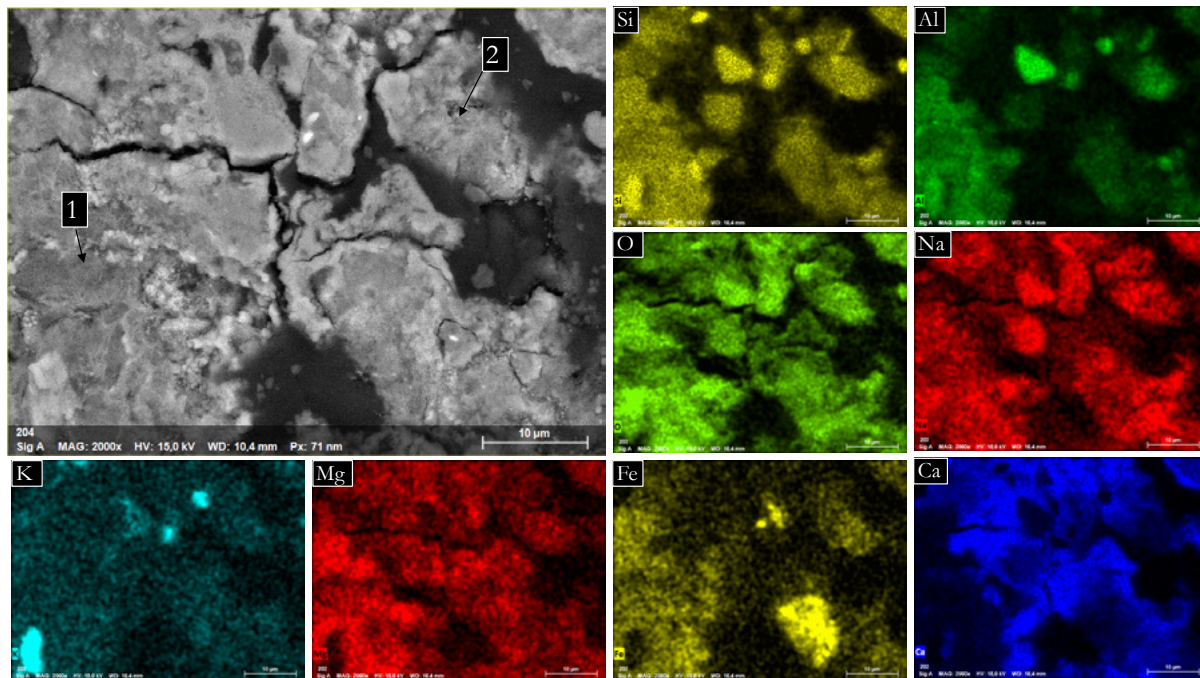


Figure 13: SEM image and elemental maps of BTC geopolymers made with silica modulus of 0.707 at 7 d age.

5. Conclusions

In this work, the natural pozzolan Bavarian trass obtained from Germany has been subjected to heat treatment and mechanical activation as reactivity enhancement methods. Results show that pozzolans in their natural state and after implementation of reactivity enhancement methods can be used as a precursor for geopolymer synthesis. The chemical composition, particle size and mineralogical phase composition of natural pozzolan effects the properties of resultant geopolymer product. The calcite-rich natural pozzolans can be used as geopolymer precursor by heat treatment, as the conversion of calcite to lime imparts higher reactivity and thus, an increase in compressive strength. An economical mechanical activation method was applied as reactivity enhancement method. However, no significant improvement in compressive strength has been observed as a result of mechanical activation. The calorimetric study showed that the fine fraction of natural pozzolan largely contributes to the reactivity. While mechanical activation helps majorly in reducing the size of coarser fraction thus only a slight improvement in reactivity has been observed. Comparing both reactivity enhancements methods, it is seen that the effect of calcination is more prominent than the reduced particle size.

For geopolymer samples prepared with calcined Bavarian trass (BTC), less amount of efflorescence was observed in comparison to BT samples for high silica modulus samples. As a result of heat treatment, an increase in the optimum silica modulus required to achieve higher compressive strength has also been observed. Therefore, the choice of reactivity enhancement method should be made depending on the properties, economic and environmental advantages. The second exothermic peak observed in the calorimetric study of BT geopolymers is assigned to the delayed dissolution of some phase(s) likely calcium rich phases. This delayed dissolution shifted to an earlier time for BTC geopolymers because of higher reactivity of BTC. The chemically bound water in the geopolymer structure gives insight about the dependence of the rate of reaction on silica modulus and age of the sample. Crystalline mineral phases such as calcite, lime, biotite and sanidine participate in geopolymer reaction by either complete or partial

dissolution in alkaline medium. Phase composition of geopolymer gel shows that it consists of N-A-S-H and (C)-N-A-S-H with the incorporation of Mg, Fe and K in the structure for both BT and BTC geopolymers.

6. Acknowledgements

The support of German Academic Exchange Service (DAAD) and Higher Education Commission of Pakistan (HEC) under funding programme “Faculty Development for PhD Candidates (Balochistan), 2016 (Programme ID: 57245990)” is acknowledged. The authors are thankful to Dr. Christian Lehmann for performing SEM-EDX experiment.

7. References

1. Robayo-Salazar R, Mejía-Arcila J, Mejía de Gutiérrez R et al. (2018) Life cycle assessment (LCA) of an alkali-activated binary concrete based on natural volcanic pozzolan: A comparative analysis to OPC concrete. *Constr. Build. Mater.* 176: 103–111. doi: 10.1016/j.conbuildmat.2018.05.017
2. Pacheco-Torgal F, Labrincha JA, Leonelli C et al. (eds) (2012) *Handbook of Alkali-activated Cements, Mortars and Concretes*. Woodhead Publishing in materials. Woodhead Publishing, Cambridge, Philadelphia, PA
3. Duxson P, Fernández-Jiménez A, Provis JL et al. (2007) Geopolymer technology: The current state of the art. *J. Mater. Sci.* 42(9): 2917–2933. doi: 10.1007/s10853-006-0637-z
4. Provis JL, van Deventer JSJ (eds) (2009) *Geopolymers - Structure, processing, properties and industrial applications*. Woodhead Publishing Limited
5. Provis JL, van Deventer JSJ (2014) *Alkali Activated Materials, State-of-the-Art Report*, RILEM TC 224-AAM. Springer, Dordrecht, Heidelberg, New York, London
6. Firdous R, Stephan D, Jin Y (2018) Investigation of Rhenish and Bavarian Trass as Geopolymer Precursor. 20th International Conference of Building Materials - Ibausil 2018, 12 – 14 September 2018, Weimar, Germany (Book 2): 617–624.
7. Firdous R, Stephan D (2019) Effect of silica modulus on the geopolymerization activity of natural pozzolans. *Constr. Build. Mater.* 219: 31–43. doi: 10.1016/j.conbuildmat.2019.05.161
8. Firdous R, Stephan D, Djobo JNY (2018) Natural pozzolan based geopolymers: A review on mechanical, microstructural and durability characteristics. *Constr. Build. Mater.* 190: 1251–1263. doi: 10.1016/j.conbuildmat.2018.09.191
9. Djobo JNY, Elimbi A, Tchakouté HK et al. (2016) Reactivity of volcanic ash in alkaline medium, microstructural and strength characteristics of resulting geopolymers under different synthesis conditions. *J. Mater. Sci.* 51(22): 10301–10317. doi: 10.1007/s10853-016-0257-1
10. Allahverdi A, Mehrpour K, Kani EN (2008) Investigating the possibility of utilizing pumice-type natural pozzolan in production of geopolymer cement. *Ceram. – Silik.* 52(1): 16–23
11. Bondar D, Lynsdale CJ, Milestone NB et al. (2011) Effect of type, form, and dosage of activators on strength of alkali-activated natural pozzolans. *Cem. Concr. Compos.* 33(2): 251–260. doi: 10.1016/j.cemconcomp.2010.10.021
12. Ghafoori N, Najimi M, Radke B (2016) Natural pozzolan-based geopolymers for sustainable construction. *Environ. Earth Sci.* 75:1110(14): 1–16. doi: 10.1007/s12665-016-5898-5
13. Haddad RH, Alshbuol O (2016) Production of geopolymer concrete using natural pozzolan: A

parametric study. *Constr. Build. Mater.* 114: 699–707. doi: 10.1016/j.conbuildmat.2016.04.011

14. Hewlett PC (ed) (1988) *Lea's Chemistry of Cement and Concrete*, 4th edn. Elsevier Ltd.
15. Djobo JNY, Elimbi A, Tchakouté HK et al. (2017) Volcanic ash-based geopolymer cements/concretes: The current state of the art and perspectives. *Environ. Sci. Pollut. Res.* 24(5): 4433–4446. doi: 10.1007/s11356-016-8230-8
16. Djobo JNY, Elimbi A, Tchakouté HK et al. (2016) Mechanical activation of volcanic ash for geopolymer synthesis: Effect on reaction kinetics, gel characteristics, physical and mechanical properties. *R. Soc. Chem. (RSC Adv.)* 6(45): 39106–39117. doi: 10.1039/C6RA03667H
17. Bondar D, Lynsdale CJ, Milestone NB et al. (2011) Effect of adding mineral additives to alkali-activated natural pozzolan paste. *Constr. Build. Mater.* 25(6): 2906–2910. doi: 10.1016/j.conbuildmat.2010.12.031
18. Bondar D, Lynsdale CJ, Milestone NB et al. (2011) Effect of heat treatment on reactivity-strength of alkali-activated natural pozzolans. *Constr. Build. Mater.* 25(10): 4065–4071. doi: 10.1016/j.conbuildmat.2011.04.044
19. Tchakoute HK, Mbey JA, Elimbi A et al. (2013) Synthesis of volcanic ash-based geopolymer mortars by fusion method: Effects of adding metakaolin to fused volcanic ash. *Ceram. Int.* 39(2): 1613–1621. doi: 10.1016/j.ceramint.2012.08.003
20. Djobo YJN, Elimbi A, Dika Manga J et al. (2016) Partial replacement of volcanic ash by bauxite and calcined oyster shell in the synthesis of volcanic ash-based geopolymers. *Constr. Build. Mater.* 113: 673–681. doi: 10.1016/j.conbuildmat.2016.03.104
21. Robayo RA, Mejía de Gutiérrez R, Gordillo M (2016) Natural pozzolan-and granulated blast furnace slag-based binary geopolymers. *Mater. Constr.* 66(321): e077. doi: 10.3989/mc.2016.03615
22. Djobo JNY, Tchadjié LN, Tchakoute HK et al. (2014) Synthesis of geopolymer composites from a mixture of volcanic scoria and metakaolin. *J. Asian Ceram. Soc.* 2(4): 387–398. doi: 10.1016/j.jascer.2014.08.003
23. EN 196-6 (2010) *Methods of testing cement – Part 6: Determination of fineness*
24. Schwiete H-E, Ludwig U, Wigger K-H (1961) *Die Konstitution einiger rheinischer und bayrischer Trasse*. Westdeutscher Verlag, Köln Opladen
25. Liebig E, Althaus E (1998) Pozzolanic activity of volcanic tuff and suevite: effects of calcination. *Cem. Concr. Res.* 28 (4): 567–575
26. Chukanov NV, Chervonnyi AD (2016) *Infrared spectroscopy of minerals and related compounds*. Springer Berlin Heidelberg
27. Ludwig U, Schwiete HE (1963) *Untersuchungen an Deutschen Trassen*. *Silicates Ind.*: 439–447
28. Fleischer M (1965) New mineral names. *Am. Miner.* 50: 2096–2111
29. Stark J, Wicht B (2000) *Zement und Kalk: Der Baustoff als Werkstoff*. Springer Berlin Heidelberg
30. Gebregziabihier BS, Thomas RJ, Peethamparan S (2016) Temperature and activator effect on early-age reaction kinetics of alkali-activated slag binders. *Constr. Build. Mater.* 113: 783–793. doi: 10.1016/j.conbuildmat.2016.03.098
31. Triantafyllou G, Christidis G, Markopoulos T (2003) Influence of porosity and grain size of carbonate rocks in the reactivity of lime. *Mineral Exploration and Sustainable Development*, Eliopoulos et al., eds. Millpress, Rotterdam: 931–934

32. Černý R, Rovnaníková P (2002) Transport processes in concrete. Spon Press, Taylor & Francis Group, London
33. Ben Haha M, Le Saout G, Winnefeld F et al. (2011) Influence of activator type on hydration kinetics, hydrate assemblage and microstructural development of alkali activated blast-furnace slags. *Cem. Concr. Res.* 41(3): 301–310. doi: 10.1016/j.cemconres.2010.11.016
34. Zhang Z, Provis JL, Reid A et al. (2014) Fly ash-based geopolymers: The relationship between composition, pore structure and efflorescence. *Cem. Concr. Res.* 64: 30–41. doi: 10.1016/j.cemconres.2014.06.004
35. Djobo JNY, Tchakouté HK, Ranjbar N et al. (2016) Gel Composition and Strength Properties of Alkali-Activated Oyster Shell-Volcanic Ash: Effect of Synthesis Conditions. *J. Am. Ceram. Soc.* 99(9): 3159–3166. doi: 10.1111/jace.14332
36. Scrivener K, Snellings R, Lothenbach B (eds) (2016) A Practical Guide to Microstructural Analysis of Cementitious Materials. Taylor & Francis Group
37. Tajuelo Rodriguez E, Garbev K, Merz D et al. (2017) Thermal stability of C-S-H phases and applicability of Richardson and Groves' and Richardson C-(A)-S-H(I) models to synthetic C-S-H. *Cem. Concr. Res.* 93: 45–56. doi: 10.1016/j.cemconres.2016.12.005
38. Zhang Z, Provis JL, Wang H et al. (2013) Quantitative kinetic and structural analysis of geopolymers. Part 2. Thermodynamics of sodium silicate activation of metakaolin. *Thermochim. Acta* 565: 163–171. doi: 10.1016/j.tca.2013.01.040
39. Sun Z, Vollpracht A (2018) Isothermal calorimetry and in-situ XRD study of the NaOH activated fly ash, metakaolin and slag. *Cem. Concr. Res.* 103: 110–122. doi: 10.1016/j.cemconres.2017.10.004
40. Lecomte I, Henrist C, Liégeois M et al. (2006) (Micro)-structural comparison between geopolymers, alkali-activated slag cement and Portland cement. *J. Eur. Ceram. Soc.* 26(16): 3789–3797. doi: 10.1016/j.jeurceramsoc.2005.12.021
41. van Deventer JSJ, San Nicolas R, Ismail I et al. (2015) Microstructure and durability of alkali-activated materials as key parameters for standardization. *J. Sustain. Cem. Mater.* 4(2): 116–128. doi: 10.1080/21650373.2014.979265
42. Komnitsas K, Zaharaki D, Perdikatsis V (2007) Geopolymerisation of low calcium ferronickel slags. *J. Mater. Sci.* 42(9): 3073–3082. doi: 10.1007/s10853-006-0529-2
43. Walkley B, San Nicolas R, Sani M-A et al. (2016) Phase evolution of C-(N)-A-S-H/N-A-S-H gel blends investigated via alkali-activation of synthetic calcium aluminosilicate precursors. *Cem. Concr. Res.* 89: 120–135. doi: 10.1016/j.cemconres.2016.08.010
44. Baykara H, Cornejo MH, Murillo R et al. (2017) Preparation, characterization and reaction kinetics of green cement: Ecuadorian natural mordenite-based geopolymers. *Mater. Struct.* 50: 188. doi: 10.1617/s11527-017-1057-z

Effect of calcium hydroxide on the hydration of sulphoaluminate cement with high concentration of borate solution

Q. Li¹, H. Ma², X. Ling², B. Yuan², W. Chen^{1*}

¹ State Key Laboratory of Silicate Materials for Architectures, Wuhan University of Technology, 430070 Wuhan, P.R. China

² School of Material Science and Engineering, Wuhan University of Technology, 430070 Wuhan, P.R. China

Abstract

The effect of calcium hydroxide on the hydration of CSA cement with high concentration of borate solution were investigated by a range of analytical techniques, aiming to accelerate the hydration of CSA cement and prevent the retardation by borate solution. The results indicate that the hydration of CSA cement was severely retarded by borate solution through formation of dense layer of amorphous ulexite on the surface of cement particles, preventing further dissolution of anhydrous cement particles. No hydration product was identified by up to 28 days. The amorphous ulexite transformed into crystalline ulexite by 56 days of hydration in borate solution. By addition of sodium hydroxide, the hydration of CSA cement in borate solution accelerated through formation of foil-like hexahydroborite and borate-incorporating ettringite, resulting in the prevention of formation of ulexite. The main hydration products for CSA cement in borate solution with sodium hydroxide addition were ettringite, AFm and hexahydroborite.

Keywords: Ulexite, Hexahydroborite, Borate solution, Sulphoaluminate cement, Borate-incorporating ettringite.

1. Introduction

Radioactive waste is produced from nuclear power plant, scientific research and medicine industry[1], which is classified into four levels according to radioactivity, namely high-level waste (HLW), intermediate-level waste (ILW), low-level waste (LLW) and very low-level waste (VLLW)[2]. The latter three types of radioactive waste take up approximately 99% in volume globally, but with lower radioactive content[3]. With long decays period of radionuclides in the radioactive waste, ionized radiation severely harms humans and the environment[4].

The radioactive waste liquid is mainly produced from cooling system of nuclear power plants, and usually contains high concentration of boron [5]. Borate compound or boric acid is used to control the rate of nuclear reaction in a pressurized water reactor (PWR)[6]. Borate compound is well known as set retarder during the hydration of cement [7-10], which will affect the effectively consolidation of radioactive waste liquid during the successful disposal of ILW and LLW. Several types of calcium borate ($2\text{CaO} \cdot 3\text{B}_2\text{O}_3 \cdot 8\text{H}_2\text{O}$, $\text{CaO} \cdot \text{B}_2\text{O}_3 \cdot 6\text{H}_2\text{O}$ [11, 12]) were identified during the hydration of cement in borate solution under various pH values, resulting in the retardation of hydration. Using alkaline additive to react with borate acid was suggested to solve the retardation of hydration[13]. Retardation phases still formed after addition of alkaline additives. More effective method could be to decompose unstable calcium hexahydroborite[14].

Calcium sulphoaluminate (CSA) cement is manufactured by calcining gypsum, bauxite and limestone at 1300°C, with less energy consumption and less carbon footprint[15-17]. CSA cement is widely used in applications such as fast construction, fast repair[18] and permeability resistance project[19, 20] due to its high early-age strength and short setting time. CSA cement is a potential candidate to consolidate the radioactive waste with high concentration of borate because borate ions demonstrated less effect on the hydration of CSA cement than Portland cement[21-23]. The hydration of CSA cement has been intensively studied by many researchers. Ettringite and monosulphate are identified as main hydration products (Eq. 1 and 2)[24]. High-density and low-porosity microstructure are obtained during the early age hydration due to the formation of ettringite, monosulphate and alumina hydrate, resulting in the high early strength and short setting time[19].



Previous study on the hydration of CSA cement in 1M borate solution under pH of 11 indicates that the hydration is retarded by 15 hours, comparing to that in deionized water, due to the formation of poorly-crystallized borate compound (ulexite, $NaCaB_5O_6(OH)_6 \cdot 5H_2O$)[25], although no direct observation of the compound. Ulexite, a crystalline borate mineral containing three borate tetrahedra and two borate triangular groups, is fibrous. There is little literature reporting the formation of poorly crystalline ulexite. Potential methods to prevent the retardation during the hydration of CSA cement with high concentration boron solution are to avoid the ulexite formation or accelerate the phase transformation of ulexite to other minerals.

In this study, the effects of calcium hydroxide on the hydration of CSA cement with high concentration of borate solution were investigated by a range of analytical techniques, aiming to accelerate the hydration of CSA cement and prevent the retardation by borate solution, and to provide feasible solution to improve the hydration and properties of CSA cement on radioactive waste liquid solidification in the future.

2. Methodology

2.1 Materials

Sulphoaluminate cement and sulphoaluminate cement clinker from Anda Special Cement Ltd. (Yicheng, Hubei, China) were used. Chemical composition of CSA clinker and CSA cement are shown in Table 1, which were quantitatively analysed by X-ray fluorescence spectroscopy (XRF, PANalytical Axios advanced, Netherlands). Solid sodium hydroxide (NaOH, Sinopharm, AR grade, CAS code:1310-73-2), boric acid (H_3BO_3 , Sinopharm, AR grade, CAS code:10043-35-3), calcium hydroxide ($Ca(OH)_2$, Sinopharm, AR grade, CAS code:1305-62-0) and deionized water were used for simulated highly-concentrated borate liquid waste and paste specimens. Zeolite with specific surface area of 740 m²/g was used during the paste specimen preparation.

Table 1 Chemical composition of CSA clinker and CSA cement determined by XRF (wt%)

Oxides	SiO ₂	Al ₂ O ₃	Fe ₂ O ₃	CaO	SO ₃	TiO ₂	MgO	Na ₂ O	K ₂ O	SrO	LOI*
C S A clinker	12.92	25.99	8.38	39.83	7.82	1.93	1.26	0.30	0.20	0.12	1.25
C S A cement	10.67	13.99	5.60	36.98	20.92	1.12	1.76	0.24	0.40	0.23	8.09

*Loss on ignition at 1000 °C.

2.2 Specimen preparation

Simulated liquid waste with high concentration of borate was prepared as follows. Boric acid solution of 0.5M was used as the boron solution. After dissolution of boric acid in deionized water, sodium hydroxide was added in the solution to modify the pH value to 7, which is the pH value specified by LLW and ILW effluent produced from PWR nuclear plants in China.

To investigate the effect of calcium hydroxide on the properties of CSA cement with high concentration borate solution, the water/cement (w/c) ratio was set at 0.6, which could prevent the potential early age bleeding and the stop of hydration resulted from the lack of water[25]. Calcium hydroxide was added as the mole ratio of borate, namely 0, 0.22, 0.44, 0.66, 0.88, 1.10, 1.32, 1.44 and 1.56. Paste specimens were cast in cylinder moulds of 50 mm in diameter and 50 mm in height. After demoulded at 1 day, the cylinder specimens were cured at temperature of 20 °C and relative humidity of 98%.

To characterize the effects of borate on the hydration of main mineral phases of CSA cement, the powder of CSA clinker was mixed with 0.5 M borate solution at a w/c ratio of 25, where 500 g of borate solution of 0.5 M were mixed with 20 g powder of CSA clinker in a sealed container stirring by a magnetic stirrer. The hydration of CSA clinker powder was stopped at 0, 1, 3, 6, 10, 18, 24 hours, and 3, 7 and 28 days, respectively, by immersing the clinker powder in ethanol and drying at room temperature (20±2 °C). Similarly, the effects of calcium hydroxide on the hydration of CSA cement in the borate solution were characterized. CSA cement was mixed with calcium hydroxide under the ratio of 1:1 and hydrated in 0.5 M borate solution at w/c of 25. The hydration was stopped at 5, 15, 30 and 45 min, and 1, 2, 18, 24 and 72 hours by immersing the paste in ethanol and drying at room temperature.

2.3 Analytical techniques

2.3.1 Calorimetry

The heat evolved during the hydration of CSA cement in borate solution with and without calcium hydroxide was measured by Thermometric TAM Air under isothermal conditions at 20 °C. 10 g of CSA cement and 6 g of 0.5 M borate solution with or without calcium hydroxide were mixed in a flask. After stirring for 1 min, the paste was sealed with cap in the container and transferred into the calorimeter for 72 hours. The heat evolved from specimens during the first hour was excluded due to the external mixing. The total evolved heat during hydration was calculated by integration of heat flow rate excluding those from the first hour.

2.3.2 X-ray powder diffraction (XRD)

XRD was performed to characterize the phase assemblage in the specimens with w/c of 25 by a Bruker D8 Advance diffractometer with Cu K α radiation (1.5406Å), under conditions of step size of 0.02° 2 θ /step, measuring time of 0.24 s/step, start position 5° (2 θ) and end position 60° (2 θ). After stopping hydration at various ages, approximately 1 g of paste was finely ground until passing 0.063 mm sieve. The fine powder was backfilled in the sample holder before being transferred for characterization. The XRD patterns obtained were analysed and the mineral phases were identified by PANalytical Highscore Plus with PDF 2004 database.

2.3.3 Thermal analysis

Thermal analysis was conducted on the specimens by a Netzsch STA 499 simultaneous thermal analyser under N₂ atmosphere with flow rate of 50 ml/min on approximately 15 mg of fresh finely-ground specimen at a heating rate of 10 K/min up to 1000 °C. Differential thermogravity (DTG) results were calculated from thermogravity (TG).

2.3.4 Fourier-transform infrared spectroscopy

Fourier-transform infrared (FTIR) spectroscopy was performed to identify the bonding in the mineral phases in the specimens with w/c of 25. Thermo Nicolet Nexus FTIR spectroscopy was employed under attenuated total reflectance (ATR) mode in the wavenumber range of 4000–400 cm⁻¹ under 4 cm⁻¹ resolution. Specimens were freshly finely ground to powder before transferred for analysis.

2.3.5 Scanning electron microscopy (SEM)

The development of microstructure of specimens was characterized by FEI Quanta 450FEG Environmental SEM under the conditions of spot size 5, accelerating voltage 20 kV. The specimens were coated with Pt before transferred to the vacuum chamber of SEM. Images were taken under secondary electron mode.

2.3.6 Electron probe micro-analysis (EPMA)

The morphology and elements distribution on the surface of specimens were characterized by JEOL JXA-8230 electron probe microanalyser equipped with Oxford Instruments INCA X-Act energy dispersive spectrometer (EDS). The specimens were coated with carbon before transferred for analysis.

3. Results and discussion

3.1 Hydration kinetics

The mineral phases of CSA clinker and CSA cement used in this study were identified by XRD and shown in Figure 1. The main mineral phases in the clinker were ye'elimite and belite, with minor minerals, namely perovskite and calcite. Anhydrite was identified in the CSA cement together with those minerals identified in the CSA clinker.

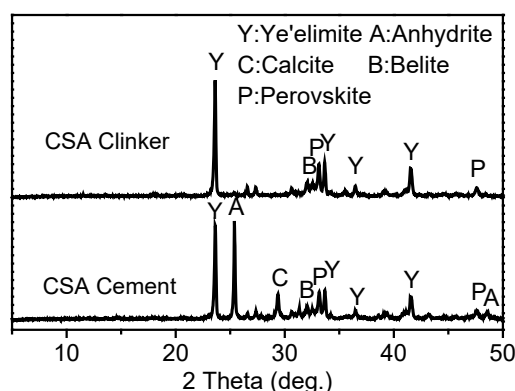


Figure 1 XRD patterns of CSA clinker and CSA cement.

The heat evolution rate and cumulative heat in the first 72 hours of hydration of CSA cement in deionized water and borate solution were characterized (Figure 2(a)). For CSA cement hydrating with deionized water, a dormant period of approximately 1.2 h was noted before the initial peak, which indicated the reaction of $C_4A_3\bar{S}$ with $C\bar{S}$. The second main hydration peak was at 3.2 h, due to the rapid dissolution of $C_4A_3\bar{S}$ after sulphates in solution were depleted. The total heat in the first 72 hours was approximately 149 J/g.

No peak was observed by up to 72 hours of hydration for CSA cement hydrated with 0.5 M borate solution, indicating that the hydration of CSA cement is greatly retarded. Borate solution retarded the hydration of both ordinary Portland cement and CSA cement. Borate anions reacted with calcium component in CSA cement by formation of various borate compounds. The retardation mechanism and chemical composition of borate compound will be discussed in the following sections.

Addition of calcium hydroxide accelerated the hydration of CSA cement with borate solution (Figure 2(b))

and (c)). The time of maximum heat evolution rate decreased with the increase of content of calcium hydroxide, indicating that the hydration of CSA cement was effectively accelerated by calcium hydroxide, possibly by formation of different borate mineral comparing to that in CSA cement with borate solution.

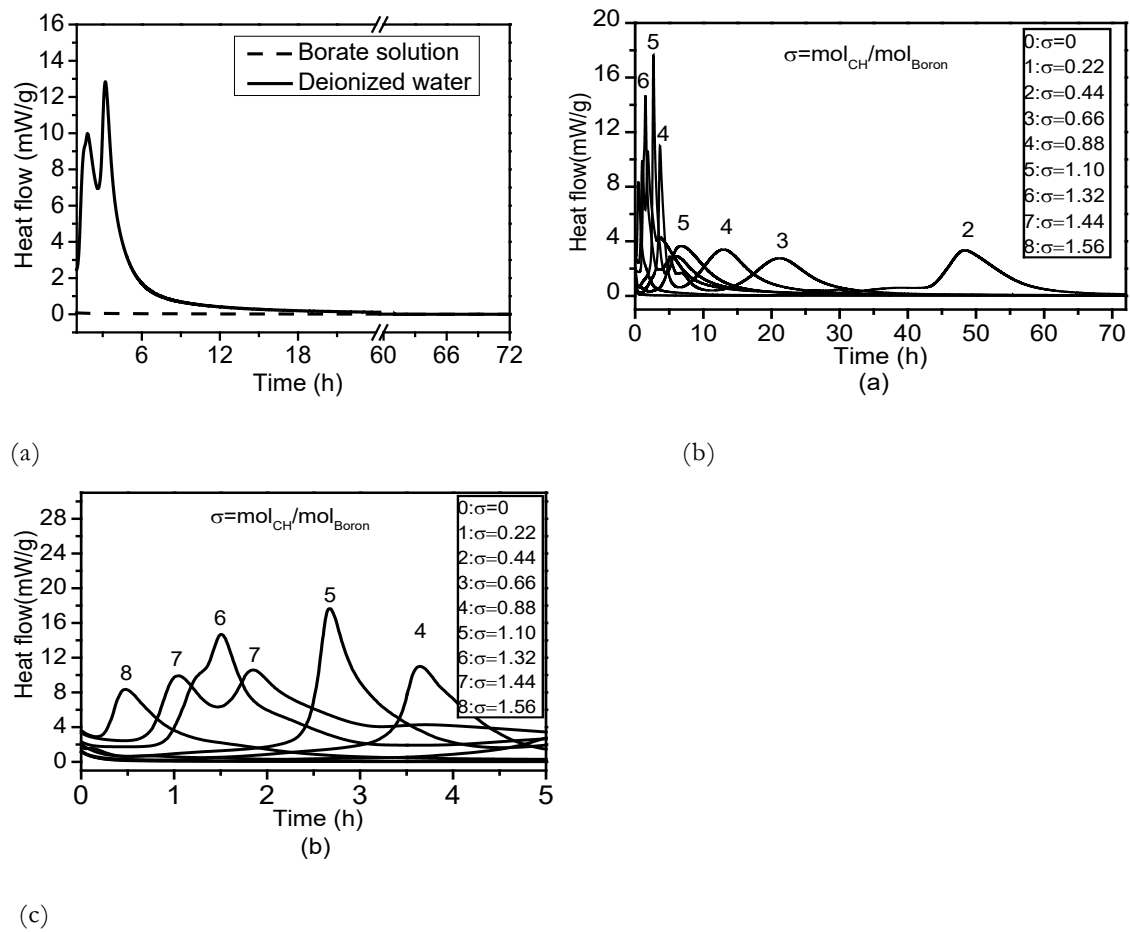


Figure 2 Heat evolution rate of (a) CSA cement hydrated with deionized water and borate solution (break from 24 h to 60 h) and (b) CSA cement hydrated in borate solution with various content of $\text{Ca}(\text{OH})_2$ in 72 h, and (c) first 5 h in (b).

3.2 Phase assemblage

The phase assemblage of CSA cement hydrated in borate solution for 28 d, together with anhydrous CSA cement is shown in Figure 3(a). According to these results, there was hardly any hydration products formed after 28 day of hydration in borate solution, indicating strong retardation of CSA cement hydration by borate. After 56 days of hydration in borate solution (Figure 3(b)), crystalline ulexite ($\text{NaCaB}_5\text{O}_8(\text{OH})_6 \cdot 5\text{H}_2\text{O}$) was identified as the main hydration products. By addition of the same amount of calcium hydroxide as CSA cement, the hydration of CSA cement in borate solution was accelerated and the hydration products were formed, namely hexahydroborite ($\text{Ca}[\text{B}(\text{OH})_4]_2 \cdot 2\text{H}_2\text{O}$) and ettringite as seen in Figure 3(c). By hydration of 5 min, most of CSA cement hydrated due to the high amount of calcium hydroxide addition. The main peak of ettringite shifted to the left (Figure 3(d)), indicating the increase of space of (001) plane due to the incorporation of boron in the ettringite crystal structure in the form of $\text{B}(\text{OH})_4^-$ [9, 25]. These results agree well with those from calorimetry.

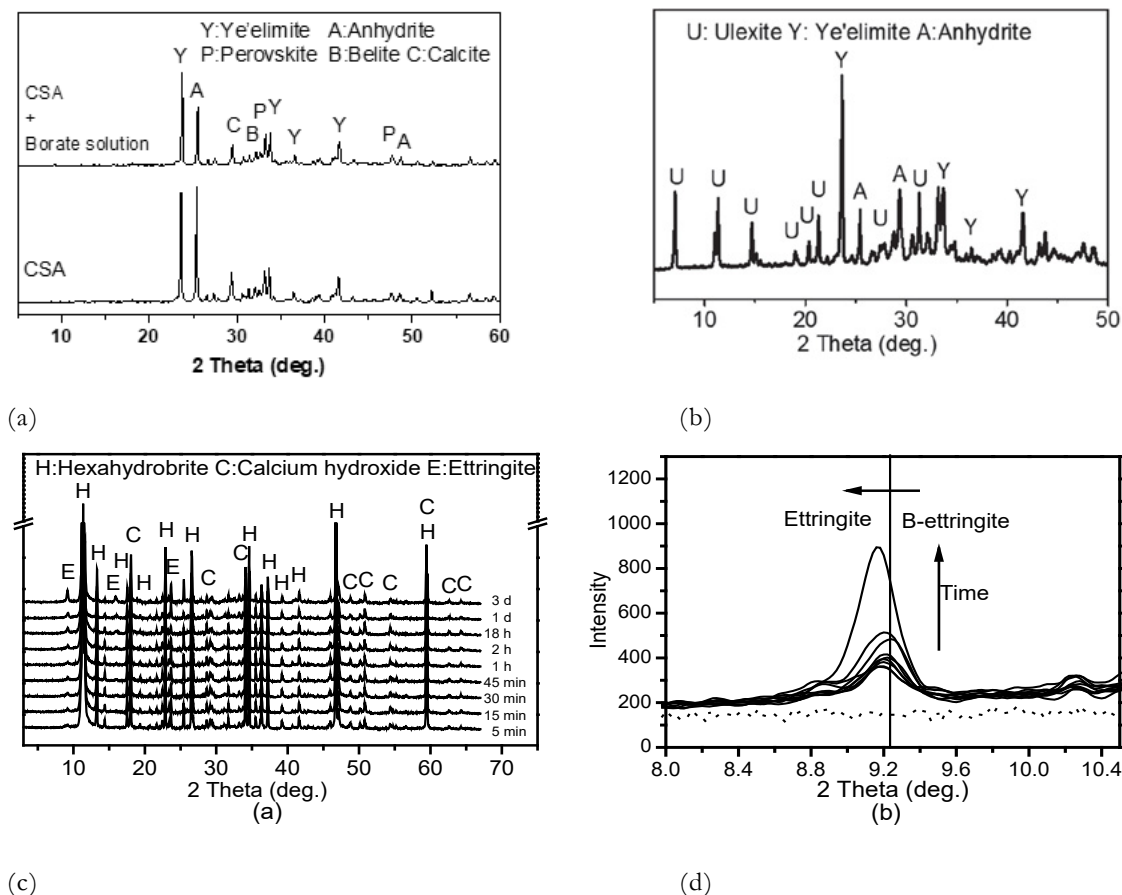
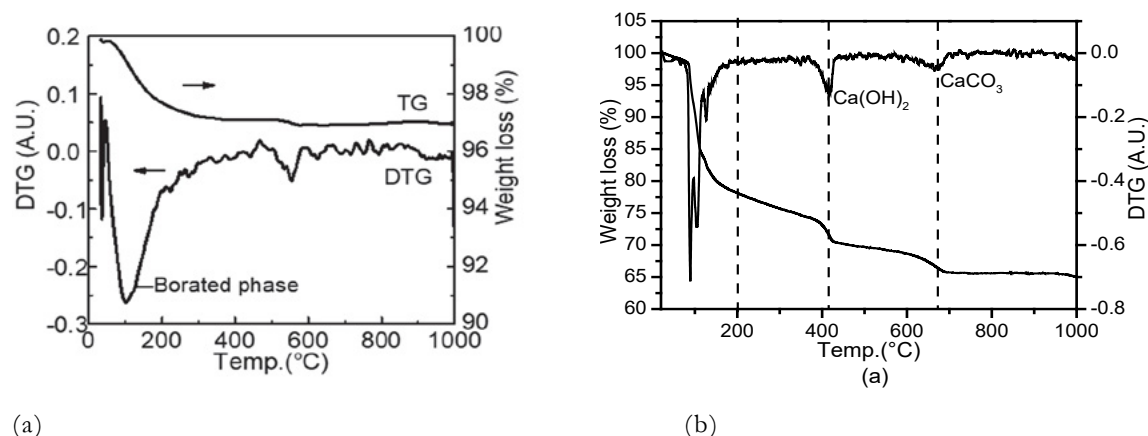
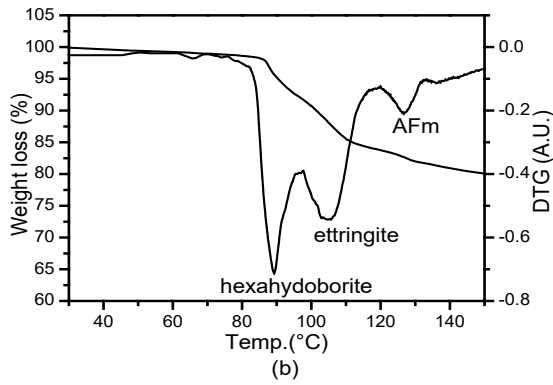


Figure 3 XRD results of CSA cement hydrated with borate solution at (a) 28 d and anhydrous CSA cement, (b) at 56 d, (c) CSA cement hydrated in borate solution with the same amount of $\text{Ca}(\text{OH})_2$ at various ages, and (d) first 5 h in (c).

Although there was no crystalline phase identified in CSA cement hydrated in borate solution for 28 days according to XRD results, amorphous borate phase was identified from TG/DTG results as weight loss at 100 °C [25] (Figure 4(a)), due to the dehydration of borate related phases. After addition of the same amount of calcium hydroxide, the formation of hexahydroborite, ettringite, AFm and calcite were confirmed from TG/DTG results after 3 days of hydration, together with residue calcium hydroxide (Figure 4(b) and (c)). These results well agree with those from XRD, confirming the accelerated hydration of CSA cement in borate solution after calcium hydroxide addition by formation of hexahydroborite, ettringite and AFm phases.



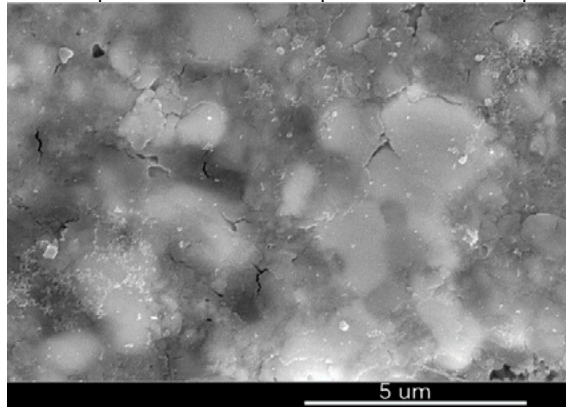


(c)

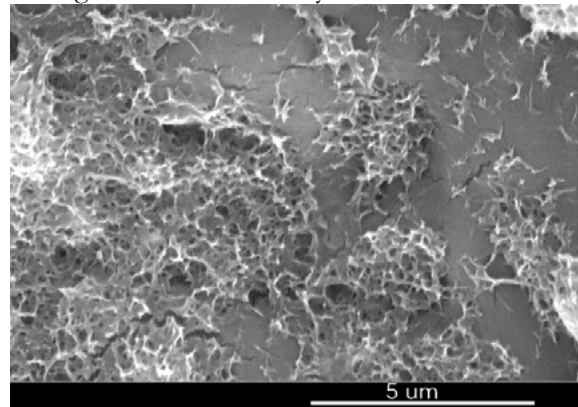
Figure 4 TG/DTG results of (a) CSA cement hydrated with borate solution at 28 d, (b) CSA cement hydrated in borate solution with the same amount of Ca(OH)_2 at 3 d, and (c) 30-150 °C in (b).

3.3 Microstructure

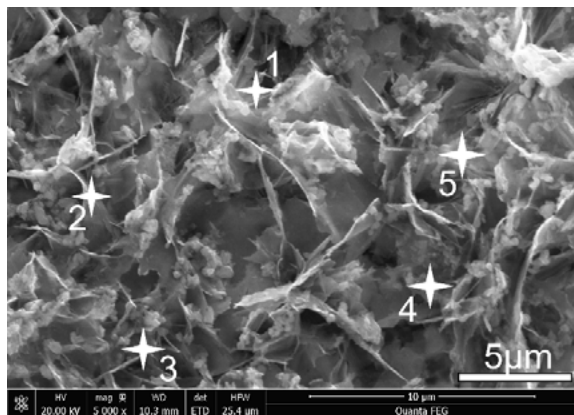
After hydrated in borate solution for 3 days, a dense layer of hydration products fully covered the surface of CSA cement particles (Figure 5(a)), preventing further dissolution of anhydrous phases and resulting in strong retardation of CSA cement hydration. While for CSA cement hydrated in the deionized water for 3 days (Figure 5(b)), foil-like hydration products formed on the surface of CSA cement particles with most part of surface exposed, resulting in the continuous hydration of CSA cement.



(a)



(b)



(c)

Figure 5 Microstructure of (a) CSA cement hydrated with borate solution at 3 days, (b) CSA cement hydrated in deionized water at 3 days, and (c) CSA cement hydrated in borate solution with the same amount of Ca(OH)_2 at 1 day.

After addition of calcium hydroxide in the CSA cement with borate solution (Figure 5(c)), foil-like hydration products were observed after 1 day of hydration. Chemical composition of hydration products of CSA cement with addition of calcium hydroxide in borate solution was characterized by energy-dispersive X-ray spectroscopy (EDX). The average Ca/Al ratio in five positions was 4.38 (Table 2), indicating the hydration products were hexahydroborate and ettringite, which intermixed with residue calcium hydroxide.

Table 2 Chemical composition of points in Figure 5(c). (atom%)

	1	2	3	4	5	Ca/Al
Ca	24.6	27.1	26.9	24.5	28.6	4.38
O	69.6	64.7	64	64.3	66.2	
Al	5.7	8.2	9.1	4.2	5.2	

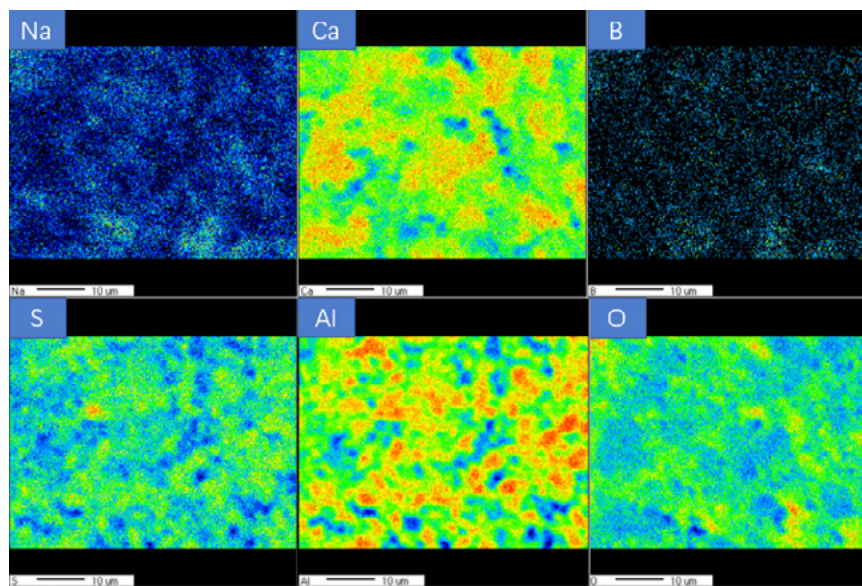


Figure 6 Element mapping of CSA cement hydrated with borate solution for 3 days

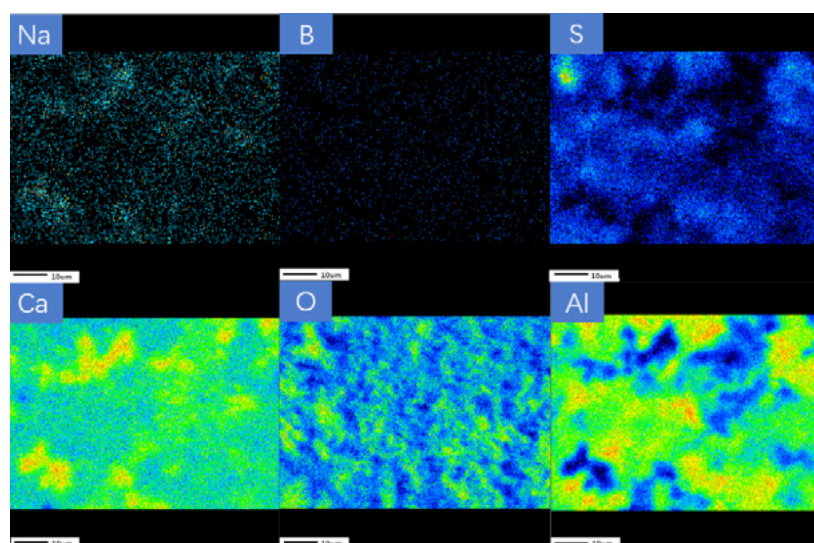


Figure 7 Element mapping of CSA cement hydrated in borate solution with addition of the same amount of $\text{Ca}(\text{OH})_2$ at 1 day.

EPMA was performed on the CSA cement hydrated with borate solution for 3 days and CSA cement hydrated in borate solution with calcium hydroxide addition for 1 day, to characterized the chemical composition of hydration products. For CSA cement hydrated in borate solution for 3 days (Figure 6), the distributions of boron and sodium were similar, indicating the formation of borate mineral, which was ulexite according to XRD results. For CSA cement hydrated in borate solution with sodium hydroxide addition (Figure 7), there was hardly any boron on the surface of cement particles. The distribution of sulphur and aluminium were similar, indicating the formation of ettringite.

4. Conclusions

The effects of calcium hydroxide on the hydration of CSA cement with high concentration of borate solution were investigated by a range of analytical techniques. The hydration kinetics, phase assemblage and microstructure of CSA cement hydrated in borate solution with or without sodium hydroxide addition were characterized. According to the results obtained, the following conclusions can be drawn.

High concentration of borate severely retarded the hydration of CSA cement by formation of a dense layer of amorphous ulexite on the surface of cement particles, preventing further dissolution of anhydrous cement particles. The amorphous ulexite transformed into crystalline ulexite by 56 days of hydration.

Addition of sodium hydroxide accelerated the hydration of CSA cement in borate solution by formation of hexahydroborite and incorporation of borate in ettringite to prevent the formation of ulexite layer on the surface of cement particles. The main hydration products for CSA cement in borate solution with sodium hydroxide addition were ettringite, AFm and hexahydroborite.

5. Acknowledgment

This research was financially supported by the National Natural Science Foundation of China (grant numbers 51672199, 51611530545); the Fundamental Research Funds for the Central Universities (grant number WUT: 2017-YB-008) and the National Key Research and Development Program of China (grant number 2016YFB0303501, BY115J004).

6. Reference

- [1] W.E. Lee, M.I. Ojovan, Fundamentals of Radioactive Waste (RAW): Science, Sources, Classification and Management Strategies, Radioactive Waste Management and Contaminated Site Clean-Up, Woodhead Publishing 2013, pp. 3-50.
- [2] R. Burcl, Radioactive Waste (RAW) Categories, Characterization and Processing Route Selection, Radioactive Waste Management and Contaminated Site Clean-Up, Woodhead Publishing 2013, pp. 50-72.
- [3] IAEA, Status and Trends in Spent Fuel and Radioactive Waste Management, IAEA Nuclear Energy Series, International Atomic Energy Agency (IAEA), 2018, pp. 1-57.
- [4] IAEA, Strategy and Methodology for Radioactive Waste Characterization, 2007.
- [5] R. Ishihara, K. Fujiwara, T. Harayama, Removal of Cesium Using Cobalt-Ferrocyanide-Impregnated Polymer-Chain-Grafted Fibers, Journal of Nuclear Science and Technology, 48 (2011) 1281–1284.
- [6] P. Demirçivi, G. Nasün-saygılı, Removal of Boron from Waste Waters by Ion- Exchange in a Batch System, World Academy of Science, Engineering and Technology, 2 (2008) 95-98.
- [7] I.S. Bell, P.V. Coveney, Molecular Modelling of the Mechanism of Action of Borate Retarders on Hydrating Cements at High Temperature, Molecular Simulation, 20 (1998) 331-356.

- [8] L.J. Cseteyi, F.P. Glasser, Borate Retardation of Cement Set and Phase Relations in the System Na₂O—CaO—B₂O₃—H₂O, *Advances in Cement Research*, 7 (1995) 13-19.
- [9] J. Bensted, I.C. Callaghan, A. Lepre, Comparative Study of the Efficiency of Various Borate Compounds as Set-Retarders of Class G Oilwell Cement, *Cement and Concrete Research*, 125 (1991) 2384–2395.
- [10] Y. Hu, W. Li, S. Ma, X. Shen, Influence of borax and citric acid on the hydration of calcium sulfoaluminate cement, *Chemical Papers*, 71 (2017) 1909-1919.
- [11] S. Hernandez, A. Guerrero, S. Goni, Leaching of borate waste cement matrices: pore solution and solid phase characterization, *Advances in Cement Research*, 12 (2000) 1-8.
- [12] A. Guerrero, S. Goni, Efficiency of a blast furnace slag cement for immobilizing simulated borate radioactive liquid waste, *Waste Management*, 22 (2002) 831-836.
- [13] O. Gorbunova, Cementation of liquid radioactive waste with high content of borate salts, *J Radioanal Nucl Ch*, 304 (2015) 361-370.
- [14] B. Florence, F. Fabien, L. Sylvie, C.-d.-C. Céline, *Cement-Based Materials for Nuclear Waste Storage*, 2013.
- [15] E. Gartner, Industrially interesting approaches to “low-CO₂” cements, *Cement and Concrete Research*, 34 (2004) 1489-1498.
- [16] M.C.G. Juenger, F. Winnefeld, J.L. Provis, J.H. Ideker, *Advances in alternative cementitious binders*, *Cement and Concrete Research*, 41 (2011) 1232-1243.
- [17] D. Gastaldi, G. Paul, L. Marchese, S. Irico, E. Boccaleri, S. Mutke, L. Buzzi, F. Canonico, Hydration products in sulfoaluminate cements: Evaluation of amorphous phases by XRD/solid-state NMR, *Cement and Concrete Research*, 90 (2016) 162-173.
- [18] J. Qian, C. You, Q. Wang, H. Wang, X. Jia, A method for assessing bond performance of cement-based repair materials, *Construction and Building Materials*, 68 (2014) 307-313.
- [19] T. Kuryatnyk, M. Chabannet, J. Ambroise, J. Pera, Leaching behaviour of mixtures containing plaster of Paris and calcium sulphoaluminate clinker, *Cement and Concrete Research*, 40 (2010) 1149-1156.
- [20] K. Quillin, Performance of belite-sulfoaluminate cements, *Cement and Concrete Research*, 31 (2001) 1341-1349.
- [21] C.C.D. Coumes, S. Courtois, S. Peysson, J. Ambroise, J. Pera, Calcium sulfoaluminate cement blended with OPC: A potential binder to encapsulate low-level radioactive slurries of complex chemistry, *Cement and Concrete Research*, 39 (2009) 740-747.
- [22] J. Pera, J. Ambroise, New applications of calcium sulfoaluminate cement, *Cement and Concrete Research*, 34 (2004) 671-676.
- [23] Q. Sun, J. Li, J. Wang, Effect of borate concentration on solidification of radioactive wastes by different cements, *Nuclear Engineering and Design*, 241 (2011) 4341-4345.
- [24] F. Winnefeld, B. Lothenbach, Hydration of calcium sulfoaluminate cements - Experimental findings and thermodynamic modelling, *Cement and Concrete Research*, 40 (2010) 1239-1247.
- [25] J.-B. Champenois, M. Dhoury, C.C.D. Coumes, C. Mercier, B. Revel, P. Le Bescop, D. Damidot,

Influence of sodium borate on the early age hydration of calcium sulfoaluminate cement, Cement and Concrete Research, 70 (2015) 83-93.

The effect of MgO on the structure and chemical composition of C-S-H gels

Y. Tang^{1,2}, W. Chen¹

¹ School of Material Science and Engineering, Wuhan University of Technology, Wuhan 430070, China.

² State Key Laboratory of Silicate Materials for Architectures, Wuhan University of Technology, Wuhan 430070, China.

Abstract

As the amount of high-grade limestone decreases rapidly, limestone containing high amount of MgO could be applied as the supplement in the production of Portland cement clinker. This paper aims to study the effect of MgO on the structure and chemical composition of calcium silicate hydrates (C-S-H) gels during early stage hydration, which is the main product of Portland cement hydration. Magnesium oxide (MgO), silica fume (SiO₂) and calcium oxide (CaO) were used in the preparation of MgO modified C-S-H with (Ca + Mg)/Si ratio=0.8. A high water to solid ratio (around 10) and elevated temperature (60 C) were applied in order to ensure the sufficient water for reaction, promoting the ions diffusion and accelerating the reaction. The obtained solids were characterized by SEM, TEM-EDS, XRD, FT-IR and TG-DSC. The results show that the pure magnesium silicate hydrates (M-S-H) gels exhibit significantly different structure and chemical composition from C-S-H. The addition of MgO could retard the reaction of the entire MgO-CaO-SiO₂ system. The prepared MgO modified C-S-H gels have a poorly crystalline structure, which are similar to the synthesized pure C-S-H gels. The increasing initial amount of MgO lead to the formation of M-S-H gels and the possible formation of a new phase magnesium calcium silicate hydrates (M-C-S-H), showing the homogenous distribution of Mg, Si and Ca elements which was observed by TEM-EDS. The structure and chemical composition of reaction products is highly depending on the input molar ratio of Mg to Ca. However, the detailed reaction process still requires further investigations.

Keywords: magnesium silicate hydrates, calcium silicate hydrates, hydration, modification

1. Introduction

Cement remains the most used building materials and it will continue for a quite long time[1]. As the annual cement production is continuously increasing and high-grade limestone is not sufficiently available around the world, more low-grade limestone containing high magnesium content would be applied into the cement industry[2]. Some researchers have shown great interests in the effect of magnesium on calcium silicate hydrates[3–7]. Calcium silicate hydrate(C-S-H) gels are the primary hydration product and binding phase of Portland cement paste. It has a poor crystalline structure and variable composition controlled by initial Ca : Si ratio and the calcium ions content [8–10]. By mixing appropriate quantities of magnesium oxide, calcium oxide and silica fume, two sperate phases C-S-H and M-S-H (magnesium silicate hydrates) were observed by Bernard[4]. The structure of C-S-H which is based on single silica chains is clearly different from the sheet like structure of M-S-H. Although both phases are poorly crystalline, have loosely bound water and a variable chemical composition, M-S-H has higher silica polymerization degree than C-S-H[10–14]. In M-S-H, Q³ silicate tetrahedrons are present as the main silica network while C-S-H has mainly Q¹, Q²

silicate tetrahedrons corresponding to the single chain-like structure. As Chiang[15] reported before, the primary units of C-S-H gels are polydisperse multilayer disks while the M-S-H globules can be modelled as polydisperse spheres at nanoscale. As a result, the interaction between C-S-H and M-S-H is negligible.

With magnesium addition into $\text{CaO-SiO}_2\text{-H}_2\text{O}$ system, the decomposition of C-S-H is possibly happened and the calcium concentration in the solution is increased. Magnesium facilitates the formation of brucite or reacts with dissolved silicon ions and leads to the formation of M-S-H[16]. The formation of M-S-H is a slow process at ambient temperature ($20\sim 25^\circ\text{C}$), which could continuous for a quite long time to consume the unreacted silica. At early age, only a small amount of M-S-H would be formed. Magnesium and silica exist as brucite and amorphous silica respectively. Therefore, in the mixed $\text{MgO-CaO-SiO}_2\text{-H}_2\text{O}$ system, the formation of C-S-H and brucite is faster than that of M-S-H at room temperature[4,16]. The limited concentration of magnesium in the solution makes it difficult to be incorporated into the structure of C-S-H or form a single phase magnesium calcium silicate hydrates (M-C-S-H)[3,7]. However, under hydrothermal conditions, G. Qian[6] has confirmed the incorporation of magnesium into tobermorite and xonotlite. Brucite disappears with the increasing time and temperature. The possible presence of magnesium into C-S-H structure was also identified by L. Fernandez[17,18]. The magnesium might be incorporated into the octahedral sites in the interlayer space of dreierketten or the gap of $\text{Q}^{3\text{p}}$ silicon tetrahedron as tetrahedral magnesium, which depends largely on Ca/Si ratio. The addition of magnesium can also increase crystallinity of C-S-H and the polymerization of silicate chains[19]. Elevating the reaction temperature in $\text{MgO-SiO}_2\text{-H}_2\text{O}$ system has been claimed to have great influence of temperature on hydration behavior[20]. The samples with the same initial Mg/Si cured at different temperature shows quite different results. More brucite was observed in the XRD pattern from the sample cured at ambient temperature than these samples cured at elevated temperature, which shows more formation of M-S-H. The effect of magnesium on the chemical composition and structure of C-S-H is still unclear, which depends on the reaction temperature, the magnesium source and water/solid ratio etc. At present research, the $\text{MgO-CaO-SiO}_2\text{-H}_2\text{O}$ system was investigated via mixing calcium oxide, silica fume and magnesium oxide at 60°C for 72h to obtain the products. The obtained solids were characterized by TEM/EDS, SEM, XRD, FT-IR and TG-DSC. The morphology, chemical composition and structure characteristics of the synthesized phase M-C-S-H would be discussed and compared to that of C-S-H and M-S-H gel.

2. Methodology

2.1 Materials

Pure C-S-H, M-S-H and MgO modified C-S-H gels were synthesized by mixing magnesium oxide (MgO), calcium hydroxide (CaO) and silica fume (SiO_2) at 60°C . Different Ca/Si molar ratios (0, 0.2, 0.4, 0.5, 0.6 and 0.8) were used in the preparation of M-C-S-H with a total $(\text{Mg}+\text{Ca})/\text{Si} = 0.8$. The samples are labelled according to the prepared Mg/Si atomic ratio, i.e. 0.8M, 0.6M, 0.4M, 0.3M, 0.2M and 0M, respectively, as shown in Table 1.

Table 1: Mix proportions.

Sample	CaO	SiO ₂	MgO	Water
	g	g	g	g
0.8M	0.00	10.00	5.33	153.33
0.6M	1.87	10.00	4.00	158.67
0.4M	3.73	10.00	2.67	164.00
0.3M	4.67	10.00	2.00	166.67
0.2M	5.60	10.00	1.33	169.33
0M	7.47	10.00	0.00	174.67

2.2 Methods

All samples were prepared in conical flasks sealed with plastic foils with a water/solid ratio of 10 in order to minimize CO₂ contamination. A high water/solid ratio of 10 was used to ensure sufficient water for dissolution and reaction. The samples were matured in a water bath at 60°C for 3d and then filtered with 0.45 µm Nylon filter. The residues were rinsed first with 50 mL of 1:1 water–ethanol solution and then flashed with 50 mL 94% ethanol solution. The obtained solids were freeze dried for 2d, and ground in an agate mortar before stored in desiccators using sodium hydroxide pellets as CO₂ trap until analysis[4].

XRD measurement was carried out on a D8 Advance X-ray diffractometer using CuKα radiation. The samples were scanned between 5° and 60° 2θ with the scanning speed of 5°/min. TG-DSC experiment was performed with sample mass of 30 to 40mg using a STA449F3 TG-DSC with a heating rate of 20°C/min from 50 to 980 °C. FT-IR spectra were recorded on a Nicolet 6700 FT-IR spectrometer using the attenuated total reflection (ATR) method. The investigated frequency range was from 400 to 4000 cm⁻¹ with a resolution of 1 cm⁻¹. SEM investigations were carried out with a JSM-IT300 SEM and TEM investigations were done with a JEM-2100F microscope.

3. Results and discussion

3.1 XRD

Figure 1 shows the XRD patterns of samples M-S-H, C-S-H and MgO modified C-S-H samples, respectively. As can be seen, the pure M-S-H (Mg/Si = 0.8) has a semi-crystalline structure indicated by the broad Bragg reflections at 20.1, 35.1 and 59.9° (2θ). The result is in good agreement with previous finding about the crystalline structure of M-S-H[21–23]. Besides, the existence of silica fume is clearly shown by the broad peak of about 20° 2θ[12]. The reflection peaks of pure C-S-H (Ca/Si = 0.8) at 16.3, 29.3, 32.0, 43.0, 49.7 and 55.1 °2θ is attributed to a poorly-ordered 14Å tobermorite (5CaO·6SiO₂·9H₂O, PDF 00-029-0331). The XRD patterns of samples containing Mg and Ca show the Bragg reflections both shown in M-S-H and C-S-H, and the changes on Mg/Ca ratio makes no big difference. Besides, for the samples with higher initial Ca/Si ratio, the formation of brucite is also found. Furthermore, it can be seen that the intensity of M-S-H gel, magnesium hydroxide and unreacted silica fume gradually decreases with the decrease of Mg/Si ratio. For instance, the reflections of sample 0.4M at 20.1, 35.1 and 59.9° 2θ almost disappear. However, the intensity of C-S-H gel is gradually increased with the decrease of Mg/Si ratio, especially for the reflection located at 29.3 °2θ.

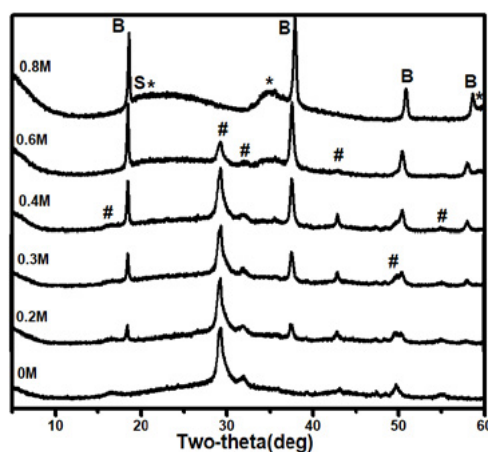


Figure 1: XRD patterns of the synthesized samples (S=silica fume, B=brucite, *=M-S-H, #=C-S-H).

3.2 FTIR

Figure 2 shows FT-IR spectra of six samples. The pure C-S-H ($\text{Ca/Si} = 0.8$) shows a OH stretching vibrations at 3442 cm^{-1} and H-OH bending vibrations of molecular water at 1639 cm^{-1} . Furthermore, the spectrum contains an Si-O-Si bending band at 662 cm^{-1} and Si-O stretching vibration bands at 971 cm^{-1} (Q^2 tetrahedra) and 876 cm^{-1} (Q^1 tetrahedra)[24]. The pure M-S-H ($\text{Mg/Si} = 0.8$) shows Mg-OH stretching vibrations at 3692 cm^{-1} and other OH vibrations at 3439 cm^{-1} together with H-OH bending vibrations of non-structural water at 1637 cm^{-1} . Besides, the sample also shows a Si-O-Si bending band at 899 cm^{-1} and Si-O stretching vibration bands at 798 cm^{-1} (unreacted silica fume), 1017 cm^{-1} (Q^3) [21]. The bands in the range of $1400\text{--}1500\text{ cm}^{-1}$ correspond to the asymmetric stretching of CO_3^{2-} . It is difficult to prevent carbonation when the sample is exposed to air. 0.6M sample shows the similar spectra to that of 0.8M sample. It shows a Si-O-Si bending band at 899 cm^{-1} and Si-O stretching vibration bands at 798 cm^{-1} (unreacted silica fume), 1017 cm^{-1} (Q^3), indicating that M-S-H gel remains the major reaction product at higher Mg-Si ratios and the amount of unreacted silica fume decreases. The presence of magnesium (0.4M, 0.3M, 0.2M) does not further influence the position of the C-S-H band, but decreases its relative intensity. The disappearance of the Si-O stretching vibration bands at 798 cm^{-1} is in consistence with the XRD results that silica fume is completely consumed. It can be concluded that the formation of C-S-H is faster than that of M-S-H, which is in line with previous findings that the formation of M-S-H is extremely slow that equilibrium has not yet been reached even after 1 year[4]. The constant position of the bands in the presence of varying fractions of C-S-H and M-S-H is in consistence with the presence of two different phases.

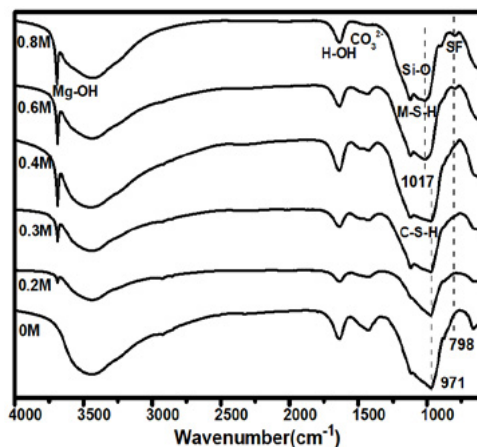


Figure 2: FT-IR spectra of the synthetic M-C-S-H samples

3.3 TG-DSC

Figure 3 shows the TG/DTG data of M-C-S-H sample. In general, the results can be classified into two stages [12]: the loss of loosely bound interlayer water between 50 and $250\text{ }^{\circ}\text{C}$; weight loss between $250\text{ }^{\circ}\text{C}$ and $800\text{ }^{\circ}\text{C}$ associated with the dehydroxylation of magnesium hydroxide and silanol groups. The pure C-S-H ($\text{Ca/Si} = 0.8$) gel shows a main water loss between 50 and $250\text{ }^{\circ}\text{C}$, which can be attributed to the dehydration of interlayer water. No weight loss is observed at $400\text{ }^{\circ}\text{C}$ in the pure C-S-H gel, indicating that calcium hydroxide is absent and all calcium is incorporated in C-S-H. The TG-DTG data is in line with the differential scanning calorimeter (DSC) results (shown in Figure 4), and the peaks at $850\text{ }^{\circ}\text{C}$ indicates a distinct exothermic transition, which can be attributed to the decomposition of wollastonite or enstatite [4,25]. The existence of brucite in

the sample containing magnesium indicates that C-S-H is more stable than M-S-H or alternatively that the formation of M-S-H is much slower than that of C-S-H, which is in line with the FT-IR data. The weight loss of interlayer water in samples containing magnesium shows no difference, while that of C-S-H is significantly larger. It indicates that more water molecules are incorporated into the structure of C-S-H and the transformation from SiO_2 to C-S-H is easier at high pH, consuming more water molecules to enhance the reaction.

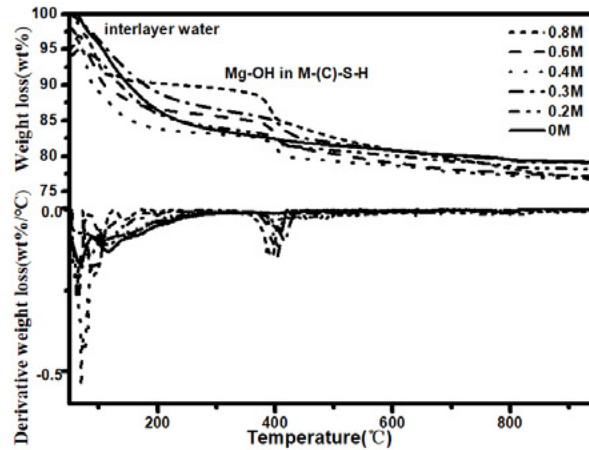


Figure 3: Weight loss determined by thermogravimetric analysis and 1st derivative of M-C-S-H samples

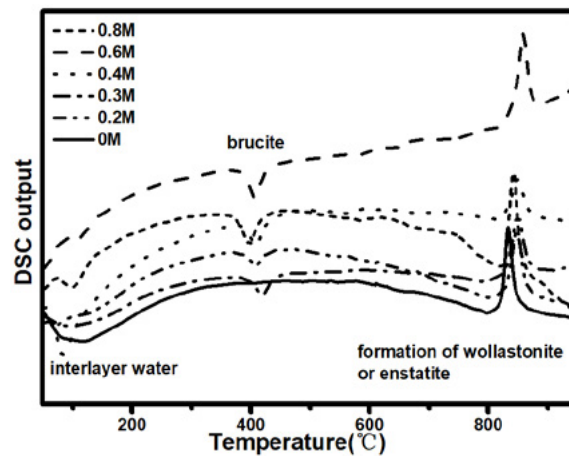


Figure 4: DSC curves of M-C-S-H samples

3.4 Microscopic analysis (SEM/TEM)

Fig. 5 shows the morphology of the pure C-S-H, M-S-H and MgO modified C-S-H gel obtained by SEM. Figure 5a) evidences an irregular porosity between interconnected and densely packed spherical particles at the micron level in M-S-H[26]. However, the morphology of pure C-S-H shows great difference from M-S-H. Figure 5c) exhibits foil-like objects arranging in a dense, laminar pattern. 0.4M Sample (shown in Figure 5b)) is similar in morphology to pure C-S-H. However, the foils are more distinct in a less extended network structure. The addition of MgO changes the microstructure of C-S-H and M-S-H more or less. Obviously, the formation of C-S-H play a dominant role in MgO-CaO-SiO₂ system.

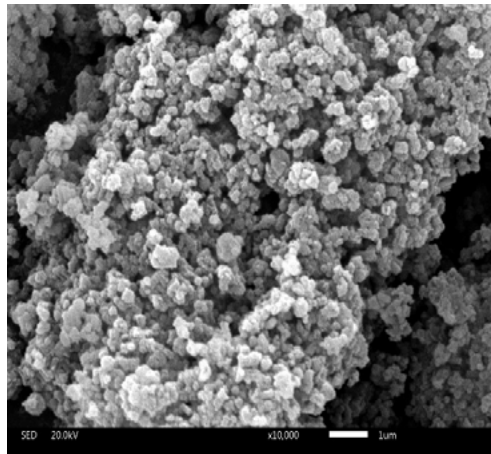


Figure 5a): SEM image of 0.8M sample

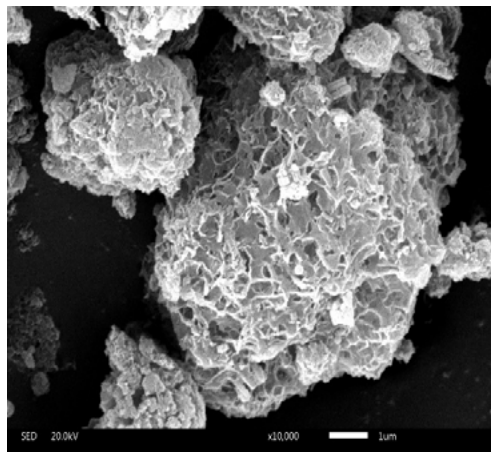


Figure 5b): SEM image of 0.4M sample

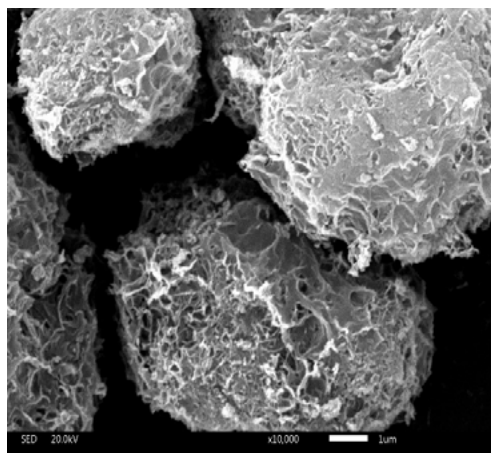


Figure 5c): SEM image of 0M sample

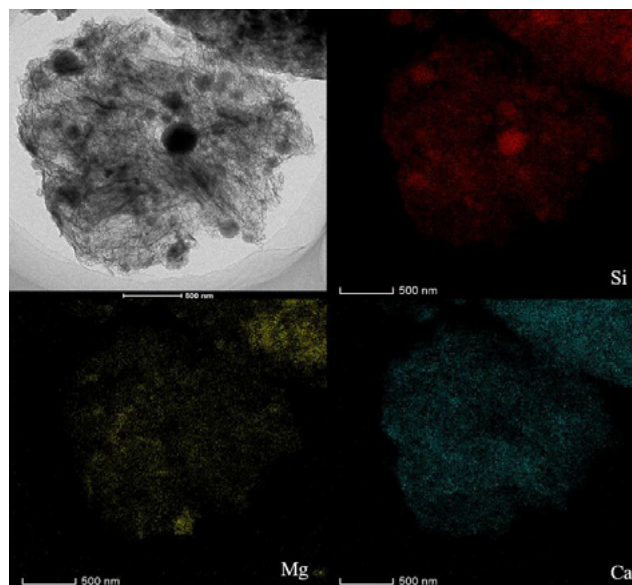


Figure 6: TEM characterizations of the 0.4M-0.4-C-S-H sample and EDS mappings of magnesium, calcium and silicon

The TEM picture of 0.4M sample in Figure 6 illustrates that MgO modified C-S-H gel exhibits a layered texture characteristic. This area is homogeneous and the SiO_2 grain is also shown, revealing that the formation of M-C-S-H gel is a process of dissolution, diffusion and precipitation, and the reaction starts on the surface of SiO_2 particles. The EDS data confirms the existence of an evenly distributed phase where the calcium and magnesium elements are distributed homogeneously, indicating the presence of large amounts of calcium in M-S-H or magnesium in C-S-H phase and the possible formation of the new phase M-C-S-H.

4. Conclusions

By mixing MgO, CaO with silica fume and water at 60°C for 3d, pure C-S-H, M-S-H and MgO modified C-S-H gels were successfully prepared. The structure and properties were confirmed by FT-IR, XRD, TG-DSC, SEM and TEM-EDS. Based on the results discussed above, the following conclusions can be drawn:

1. The hydration products in MgO-CaO- SiO_2 system are mainly brucite, M-S-H gel and C-S-H gel. The formation of C-S-H is faster than that of M-S-H under the same conditions, probably due to the higher dissolution of portlandite than brucite, strongly limiting the concentration of magnesium in the solution.
2. Increasing Ca/Si ratio in MgO-CaO- SiO_2 system benefits the reaction among silica fume, magnesium oxide and calcium oxide, which contributes to a more extended network structure.
3. The microstructure of M-S-H is different from that of C-S-H. In MgO-CaO- SiO_2 system, the hydration products show more similarities to C-S-H.
4. The possible formation of a new phase M-C-S-H where magnesium, calcium and silicon elements distribute homogeneously in a nanoscale was observed by TEM-EDS. However, the formation process of the new phases remains unclear, which requires further investigation.

5. Acknowledgment

This research has been financially supported by the National Natural Science Foundation of China (grant

numbers 51672199); the Fundamental Research Funds for the Central Universities (grant number WUT: 2017-YB-008□ 2019III018GX); and the 111 Project (No. B18038)

6. References

- [1] M. Schneider, M. Romer, M. Tschudin, H. Bolio, Sustainable cement production-present and future, *Cem. Concr. Res.* 41 (2011) 642–650. doi:10.1016/j.cemconres.2011.03.019.
- [2] A. Machner, M. Zajac, M. Ben Haha, K.O. Kjellsen, M.R. Geiker, K. De Weerd, Limitations of the hydrotalcite formation in Portland composite cement pastes containing dolomite and metakaolin, *Cem. Concr. Res.* 89 (2018) 89–106. doi:10.1016/j.cemconcomp.2018.02.013.
- [3] E. Bernard, B. Lothenbach, C. Cau-Dit-Coumes, C. Chlique, A. Dauzères, I. Pochard, Magnesium and calcium silicate hydrates, Part I: Investigation of the possible magnesium incorporation in calcium silicate hydrate (C-S-H) and of the calcium in magnesium silicate hydrate (M-S-H), *Appl. Geochemistry*. 89 (2018) 229–242. doi:10.1016/j.apgeochem.2017.12.005.
- [4] B. Lothenbach, D. Nied, E. L'Hôpital, G. Achiedo, A. Dauzères, Magnesium and calcium silicate hydrates, *Cem. Concr. Res.* 77 (2015) 60–68. doi:10.1016/j.cemconres.2015.06.007.
- [5] O.P. Shrivastava, S. Komarneni, E. Breval, Mg²⁺ uptake by synthetic tobermorite and xonotlite, *Cem. Concr. Res.* 21 (1991) 83–90. doi:10.1016/0008-8846(91)90034-F.
- [6] G. Qian, G. Xu, H. Li, A. Li, Mg-Xonotlite and its coexisting phases, *Cem. Concr. Res.* 27 (1997) 315–320. doi:10.1016/S0008-8846(97)00018-5.
- [7] E. Bernard, A. Dauzères, B. Lothenbach, Magnesium and calcium silicate hydrates, Part II: Mg-exchange at the interface “low-pH” cement and magnesium environment studied in a C-S-H and M-S-H model system, *Appl. Geochemistry*. 89 (2018) 210–218. doi:10.1016/j.apgeochem.2017.12.006.
- [8] H.F.W. Taylor, *Cement chemistry*. 2nd ed., Acad. Press. (1997). doi:10.1016/S0958-9465(98)00023-7.
- [9] A.J. Allen, J.J. Thomas, H.M. Jennings, Composition and density of nanoscale calcium-silicate-hydrate in cement, *Nat. Mater.* 6 (2007) 311–316. doi:10.1038/nmat1871.
- [10] I.G. Richardson, The calcium silicate hydrates, *Cem. Concr. Res.* 38 (2008) 137–158. doi:10.1016/j.cemconres.2007.11.005.
- [11] A. Hartmann, D. Schulenberg, J.-C. Buhl, Synthesis and Structural Characterization of CSH-Phases in the Range of C/S = 0.41 - 1.66 at Temperatures of the Tobermorite Xonotlite Crossover, *J. Mater. Sci. Chem. Eng.* 3 (2015) 39–55. doi:10.4236/msce.2015.311006.
- [12] E. Bernard, B. Lothenbach, D. Rentsch, I. Pochard, A. Dauzères, Formation of magnesium silicate hydrates (M-S-H), *Phys. Chem. Earth*. 99 (2017) 142–157. doi:10.1016/j.pce.2017.02.005.
- [13] D.A. Kulik, Improving the structural consistency of C-S-H solid solution thermodynamic models, *Cem. Concr. Res.* 41 (2011) 477–495. doi:10.1016/j.cemconres.2011.01.012.
- [14] D. Nied, K. Enemark-Rasmussen, E. L'Hôpital, J. Skibsted, B. Lothenbach, Properties of magnesium silicate hydrates (M-S-H), *Cem. Concr. Res.* 79 (2016) 323–332. doi:10.1016/j.cemconres.2015.10.003.
- [15] W. Chiang, G. Ferraro, E. Fratini, F. Ridi, Y. Yeh, U. Jeng, S. Chen, P. Baglioni, Multiscale structure of calcium- and magnesium-silicate-hydrate gels, *J. Mater. Chem. A Mater. Energy Sustain.* 2 (2014) 12991–

12998. doi:10.1039/C4TA02479F.

- [16] E. Bernard, B. Lothenbach, F. Le Goff, I. Pochard, A. Dauzères, Effect of magnesium on calcium silicate hydrate (C-S-H), *Cem. Concr. Res.* 97 (2017) 61–72. doi:10.1016/j.cemconres.2017.03.012.
- [17] L. Fernandez, C. Alonso, A. Hidalgo, C. Andrade, The role of magnesium during the hydration of C3S and C-S-H formation. Scanning electron microscopy and mid-infrared studies, *Adv. Cem. Res.* 17 (2005) 9–21. doi:10.1680/adcr.2005.17.1.9.
- [18] L. Fernandez, C. Alonso, C. Andrade, A. Hidalgo, The interaction of magnesium in hydration of C3S and CSH formation using ²⁹Si MAS-NMR, *J. Mater. Sci.* 43 (2008) 5772–5783. doi:10.1007/s10853-008-2889-2.
- [19] N.Y. Mostafa, E.A. Kishar, S.A. Abo-El-Enin, FTIR study and cation exchange capacity of Fe³⁺- and Mg²⁺-substituted calcium silicate hydrates, *J. Alloys Compd.* 473 (2009) 538–542. doi:10.1016/j.jallcom.2008.06.029.
- [20] J. Szczerba, R. Prorok, E. Snie, D. Madej, K. Ma, Influence of time and temperature on ageing and phases synthesis in the MgO–SiO₂–H₂O system, *Thermochim. Acta.* 567 (2013) 57–64. doi:10.1016/j.tca.2013.01.018.
- [21] D.R.M. Brew, F.P. Glasser, Synthesis and characterisation of magnesium silicate hydrate gels, *Cem. Concr. Res.* 35 (2005) 85–98. doi:10.1016/j.cemconres.2004.06.022.
- [22] A.A.-T. Fei Jin, Strength and hydration products of reactive MgO–silica pastes, *Cem. Concr. Compos.* 37 (2008) 1285–1288. doi:10.1016/j.cemconcomp.2014.04.003.
- [23] T. Zhang, C.R. Cheeseman, L.J. Vandeperre, Development of low pH cement systems forming magnesium silicate hydrate (M-S-H), *Cem. Concr. Res.* 41 (2011) 439–442. doi:10.1016/j.cemconres.2011.01.016.
- [24] P. Yu, R.J. Kirkpatrick, B. Poe, P.F. McMillan, X. Cong, Structure of Calcium Silicate Hydrate (C-S-H): Near-, Mid-, and Far-Infrared Spectroscopy, *J. Am. Ceram. Soc.* 82 (1999) 742–748. doi:10.1111/j.1151-2916.1999.tb01826.x.
- [25] Y. Wei, W. Yao, X. Xing, M. Wu, Quantitative evaluation of hydrated cement modified by silica fume using QXRD, ²⁷Al MAS NMR, TG-DSC and selective dissolution techniques, *Constr. Build. Mater.* 36 (2012) 925–932. doi:10.1016/j.conbuildmat.2012.06.075.
- [26] W.S. Chiang, G. Ferraro, E. Fratini, F. Ridi, Y.Q. Yeh, U.S. Jeng, S.H. Chen, P. Baglioni, Multiscale structure of calcium- and magnesium-silicate-hydrate gels, *J. Mater. Chem. A.* 2 (2014) 12991–12998. doi:10.1039/c4ta02479f.
- [27] H.M. Jennings, J.J. Thomas, J.J. Chen, D. Rothstein, Cement Paste as a Porous Material, *Handb. Porous Solids.* (2002) 2971–3028. doi:10.1002/9783527618286.

Impact of steel fibre content on the fibre network structure of ultra-high performance fibre reinforced concrete (UHPFRC)

Q. Song^{1,2}, Z. Shui¹, R. Yu^{1*}, S. Rao^{1,2}

¹State Key Laboratory of Silicate Materials for Architectures, Wuhan University of Technology, Wuhan 430070, China;

²School of Materials Science and Engineering, Wuhan University of Technology, Wuhan 430070, China

Abstract

This paper address the impact of steel fibre content on the fibre network structure of ultra-high performance fibre reinforced concrete (UHPFRC). Firstly, the design of the concrete mixtures is based on the aim to achieve a densely compacted cementitious matrix, employing the modified Andreasen & Andersen particle packing model. And, six fibre content, including 0, 0.5, 1, 1.5, 2, 2.5 and 3 vol.% are used in this study. Then, the effect of fibre content on the properties of UHPFRC is analysed, including the fresh properties and mechanics properties. Moreover, the X-ray CT is employed to evaluate the fibres distribution and directions in hardened UHPFRC. The obtained results show that with an increase of steel fibre content, the fresh properties of the UHPFRC and the fibre efficiency of mechanics properties improvement decrease. The X-ray CT results imply that with an increase of fibre content, the fibre connected probability will be increased and the 2 vol. % is a break point.

Keywords: Ultra-high performance fibre reinforced concrete (UHPFRC), fibre content, hybrid fibre, fibre network structure

1. Introduction

Ultra-High Performance Fibre Reinforced Concrete (UHPFRC) is a new kind of cement based composite material, which exhibits advanced mechanical properties, excellent durability, and high toughness. The main differences between UHPFRC and normal concrete (NC) or high-performance concrete (HPC) are high content of cementitious materials, low water to binder ratio (W/B), and high content of superplasticizer [1-11]. Moreover, to improve its ductility, toughness, flexural and shear strengths, steel fibres are normally used in the production of UHPFRC, since the utilized fibres can bridge cracks and prevent the cracks extended in the concrete [12-16]. Many studies have reported the positive influence of steel fibre on the UHPFRC, including the fibre content, fibre shape and fibre physical parameters (length, diameter etc.) [17-24]. However, in most cases, the fibres are added into the concrete directly and randomly, and the fibre network structure in the concrete are not clear, which is equal to a black box treatment. Based on available literatures [25-27], it can be concluded that the statement of fibre are important factors for improving concrete properties and fibre efficiency in fibre reinforced concrete. For example, the anisotropic properties of fibre reinforced concrete are caused by the orientation distribution of fibres [25, 26] and Bensaid et al. investigated the flexural behavior of steel fibre-reinforced concrete, it fund that the flexural behavior are significantly improved by the fibre orientation [27]. Hence, to effectively improve the fibre efficiency in

UHPFRC, the fibre network structure should be optimized.

In fact, the statement of fibres have been studied in normal concrete system and some achievements have already been obtained [28-35]. For instance, the distribution and orientation of steel fibres in the concrete can be adjusted by magnetic field, since the steel fibres are ferromagnetic. For instance, Torrents et al. [28] and Al-Mattarneh [29] investigated the effect of magnetic field on steel fibres distribution and orientation. It was found that the used magnetic field is beneficial for optimizing the fibre orientation. Nevertheless, due to the fact that the used steel fibres in concrete can also be magnetized and attracted to each other in the magnetic field, the homogeneity of the fibre distribution may be significantly disturbed, which cause that the mechanical properties of the fibre reinforced concrete are also decreased. Hence, it is logical to find other methods to control the fibre orientations and distributions.

As commonly known, the added steel fibres content in UHPFRC are much higher (2-6% by volume) than the normally steel reinforced concrete, which means there is a high chance for the fibres to connect/tough each other. When the amount of interconnected fibre is relatively large, a potential steel fibres network structure can be generated. Therefore, if one point of this potential steel fibres network structure is attacked by the harmful irons (e.g. Cl-) in the marine environment, the whole UHPFRC structure can be seriously corroded and damaged. In this case, the steel fibres network structure can be treated as a steel re-bar or other metal conductors that buried in the concrete materials without safe protection layer. Generally, the fibre interconnection induce corrosion problem in common concrete has not attracted enough attentions, since the added steel fibre amount is relatively low (about 0.5% vol.) in normal steel fibre reinforced concrete (SFRC), and very limited data can be found in available literature. Therefore, it is necessary and important to study the impact of fibre content on the fibre network of the UHPFRC.

Based on the entire premise listed above, the impact of steel fibres content on the fibre network of UHPFRC is investigated in this study. First of all, to obtain a densely packed concrete skeleton, the modified Andersen & Andreasen model is employed. Then, the properties of the UHPFRC with different fibre amount are evaluated, including flowability, mechanical. Lastly, X-ray computed tomography (X-ray CT) is utilized to detailed clarify the fibres network structure in hardened UHPFRC.

2. Methodology

2.1 Materials

PC 52.5 cement, fly ash, silica fume, metakaolin are treated as cementitious materials in this study, and their chemical compositions are shown in Table 1. Two types of fine aggregates (0–0.6mm and 0.6-1.25 mm natural river sand) are utilized. A polycarboxylic ether based superplasticizer is employed to meet the flowability requirements for the designed UHPFRC. Additionally steel fibre (13 mm length and 0.2 mm diameter) is also included in the UHPFRC production

Table 1: Chemical composition of the used powders in this study (wt. %)

Compositions	Na ₂ O	MgO	Al ₂ O ₃	SiO ₂	P ₂ O ₅	SO ₃	K ₂ O	CaO	Fe ₂ O ₃	LOI
Cement	0.09	1.61	4.18	19.2	0.09	3.35	0.78	64.93	3.32	2.49
Silica fume	0.13	0.47	0.25	94.65	0.17	0.69	0.84	0.36	0.15	2.29
Fly ash	0.33	0.23	38.01	46.44	0.06	0.69	0.88	7.5	3.12	2.79

In this research, the mixtures of the UHPFRC are presented in Table 2. It can be found that the fibres amount added in the UHPFRC are 0.5%, 1.0%, 1.5%, 2.0%, 2.5% and 3.0%(vol.), respectively. In addition, the particle size of materials and the derived comparison between the optimized and target grading curves of the UHPFRC matrix are presented in Figure 1.

Table 2: Recipe of the designed UHPFRC with different steel fibres dosage

	C (kg/m ³)	FA (kg/m ³)	SF (kg/m ³)	Sand-1 (kg/m ³)	Sand-2 (kg/m ³)	Water (kg/m ³)	Sp (kg/m ³)	SSF (vol.%)
1	750	200	144	770	220	190	30	0.0
2	750	200	144	770	220	190	30	0.5
3	750	200	144	770	220	190	30	1.0
4	750	200	144	770	220	190	30	1.5
5	750	200	144	770	220	190	30	2.0
6	750	200	144	770	220	190	30	2.5
7	750	200	144	770	220	190	30	3.0

(C: Cement, FA: Fly Ash, SF: Silica Fume, Sand-1: sand 0-0.6 mm, Sand-2: sand 0.6-1.25 mm, Sp: superplasticizer, SSF: straight steel fibres)

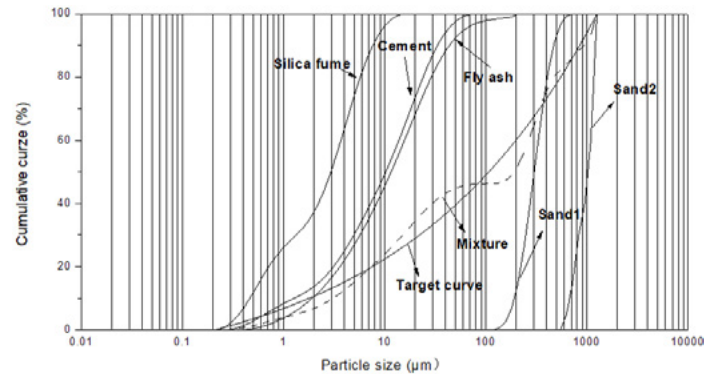


Figure 1: Particle size distributions (PSDs) of the involved ingredients, the target and optimized grading curves of the UHPFRC mixtures

2.2 Methods

After mixing, the flowability of the designed fresh UHPFRC is measured in accordance with the GB/T 2419-2005. Firstly, the mixtures are filled in a conical cone with the form of a frustum, respectively. Secondly, the molds are lifted vertically so as to allow a free flow for the paste without any jolting. Eventually, two diameters perpendicular to each other are measured, and their mean value is treated as the slump flow of the developed UHPFRC. The mechanical properties of concrete are tested according to EN 196-1(2005). Flexural strength tests are carried out at 28 days.

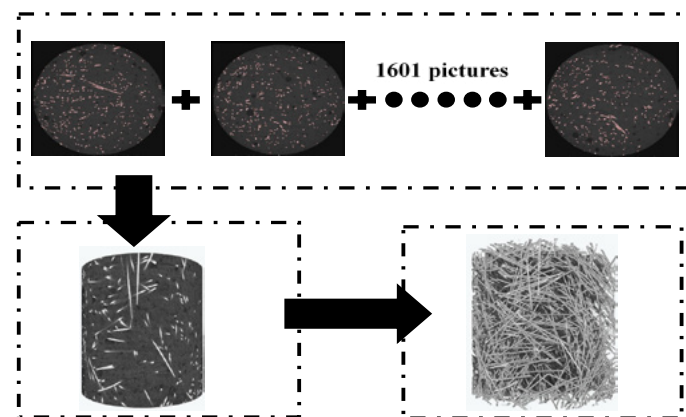


Figure 2: The rebuilt process of the designed UHPFRC 3D structure

The distribution of steel fibres is analyzed by the system of Zeiss Xradia 510 versa X-ray CT in this experiment. The general principle of this test can be summarized as follows: 1) The density of the fiber and the UHPFRC matrix is different; 2) Therefore, when the X ray passes through the specimen, different greyscale could be observed; 3) The utilized steel fibres have the largest density in the designed UHPFRC, so its gray value expressed should be also the largest, which cause that the steel fibres displayed in the

CT images are relatively white [30]. The X-ray CT system is composed by the X-ray source, detector and sample table. The three-dimensional structure information inside the sample can be obtained by rotating the sample in the range of 360 degrees. In order to clearly understand the network structure of steel fibres in UHPFRC, the sample size is 40mm×40mm×100mm and a total of 1601 sequential scan 2D-images are captured, which is 2048×2048 pixel². Then, the 3D structure of designed UHPFRC can be rebuilt with the soft of object research system (ORS) visual SI (as shown in Figure 2).

3. Results and discussion

3.1 Fresh properties of the designed UHPFRC

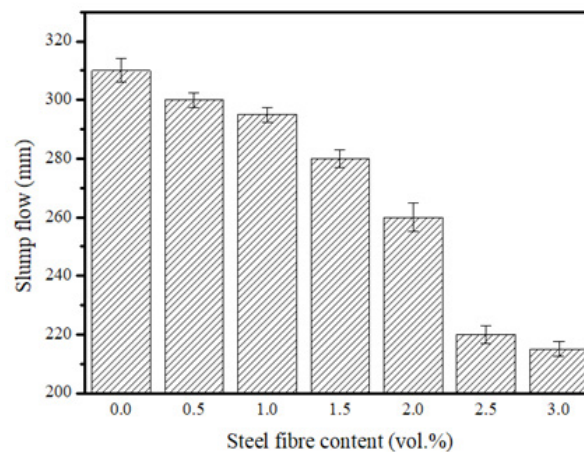


Figure 3: Flowability of the designed UHPFRC with different steel fibre amount

Figure 3 shows the flowability of the UHPFRC with different fibre amounts (0%~3%). It can be found that the flowability of the UHPFRC decreases with an increase of fibres amount. In general, the variation of the tested UHPFRC with different fibres content can be divided into three periods: Firstly, the decline of UHPFRC flowability is relatively slow (from 315mm to 260mm) with the increase of fibres amount increases from 0.5% to 2.0%; Then, the decline of UHPFRC flowability becomes quick (from 260mm to 220mm) when the added fibre is enhanced from 2.0% to 2.5%. Lastly, if the added steel fibre amount is further increased from 2.5% to 3.0%, the flowability of designed UHPFRC almost keeps stable (about 220mm).

These phenomena mentioned above may be caused by the formation of fibres network structure in UHPFRC, which could significantly enhance the flowing resistance for the tested fresh UHPFRC. Similar as the results presented in [31], the negative influence of fibres “skeleton” on the flowability of UHPFRC has already been investigated. Additionally, the three periods for the UHPFRC flowing process with different content of steel fibres can be explained by the relationship between the steel fibre numbers and the sample volume. For example, when the steel fibres content is relatively low (less than 2%), due to the activity space for steel fibres inside the UHPFRC is enough, very limited amount of fibres join the network formation, which simultaneously causes that the decreasing rate of the UHPFRC flowability is relatively small. However, when the added steel fibres content increases from 2.0% to 2.5%, the free activity space for the steel fibres is decreasing, and more fibres could connect to each other, which could significantly resistant the fibres movement and UHPFRC flowing. When the steel fibres content is further enhanced to about 3%, the fibres network structure could be further strengthened and improved, and the activity space for fibres is still very limited. Hence, the UHPFRC flowability still keeps at a relatively low level. In general, based on the fresh behavior of the designed UHPFRC, it can be summarized that the 2% (vol.) is a critical fibres amount to design UHPFRC with great flowability, with which the interconnection between fibres may be effectively limited.

3.2 Mechanical properties of the designed UHPFRC

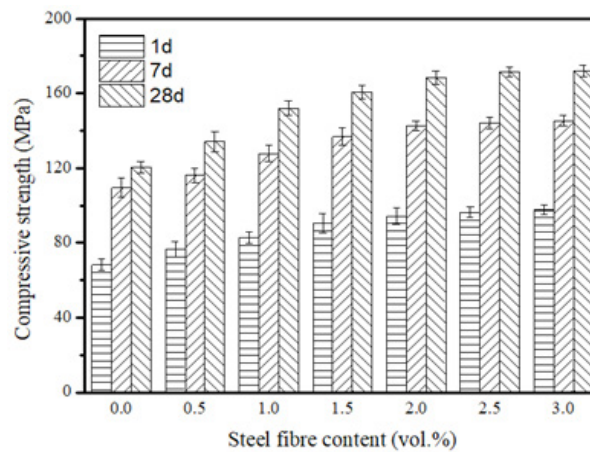


Figure 4: Compressive strength of the designed UHPFRC with different steel fibre amount at 1d, 7d, 28d

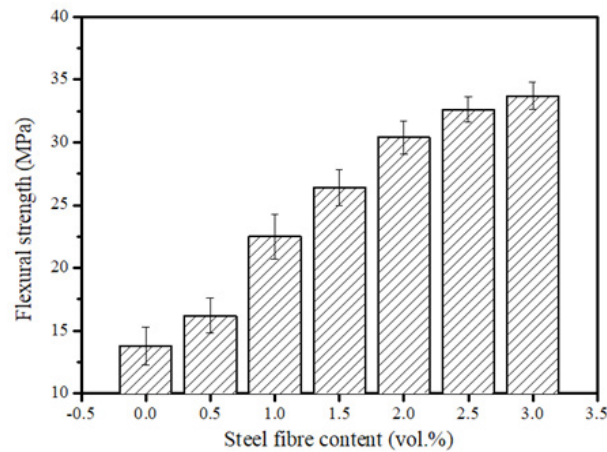


Figure 5: Flexural strengths of the designed UHPFRC with different steel fibre amount at 28d

The compressive strength of the developed UHPFRC are presented in Figure 4. It can be noticed that the compressive strength of the UHPFRC can be gradually enhanced with an increase of the fibres amount, which is similar as that presented in available literature [32]. Here, the compressive strength of the designed UHPFRC with 2% steel fibres can reach to about 168MPa at 28d, which can be explained by the role of high active powders and optimized particle packing model (as shown in [33]). However, when the fibres amount increased from 2.0% to 3.0%, the compressive strength improvement for the designed UHPFRC is limited. Furthermore, the flexural strength of the UHPFRC is presented in Figure 5. As it shown, the flexural strength of the UHPFRC significantly increases with the fibres amount increased. But, when the fibres amount increases from 2.0% to 2.5% or 2.5% to 3.0%, the flexural strength increasing rate is reduced, which implies that more steel fibres are connected to each other and the fibres efficiency is decreasing. Hence, it can be predicted that 2.0% (vol.) is an appropriate steel fibres content in UHPFRC produced.

Generally, based on the mechanical properties of the designed UHPFRC, it can be summarized that the 2% (vol.) is a critical steel fibres amount to effectively improve the fibres efficiency in UHPFRC, since the interconnection between fibres may be effectively limited in this case.

3.3 The 3D structure of the designed UHPFRC

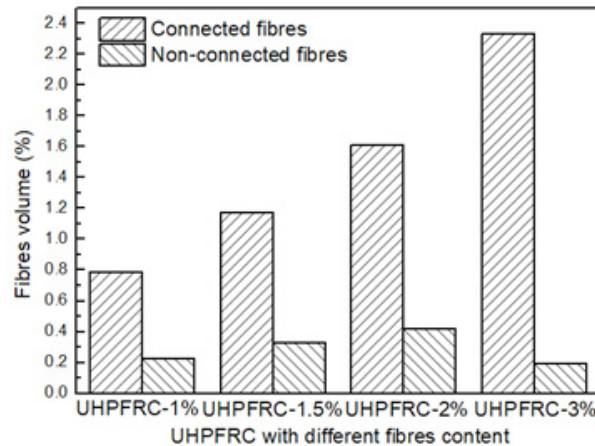


Figure 6: Results of the connected and non-connected steel fibres in the developed UHPFRC

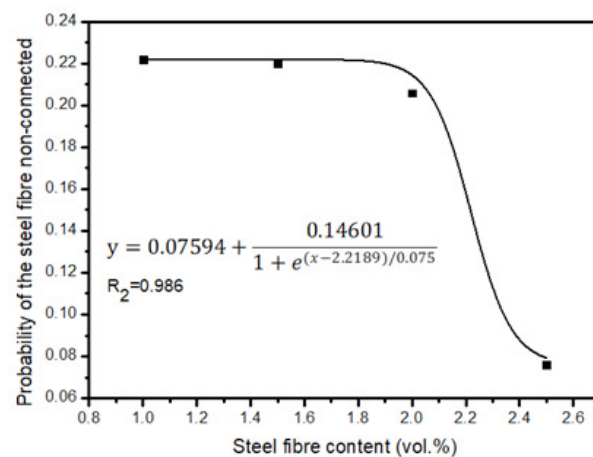


Figure 7: The probability for the steel fibres connecting to each other in the designed UHPFRC with different fibre amount

All the above shown experimental results imply the generation of steel fibres network structure in the developed UHPFRC. To more directly clarify the existence of the steel fibres network structure, the X-ray CT method is employed in this research. Figure 6 present the connected and non-connected steel fibres in the designed UHPFRC with 1.0%, 1.5%, 2.0% and 2.5% (vol.) steel fibres, respectively. Here, based on the obtained X-ray CT results, the total steel fibres amount can be measured by the software of object research system (ORS) visual SI, which is quite similar as the experimental addition. This also proves that the obtained X-ray CT results and relative software are reliable. Moreover, it is important to notice that the connected steel fibres volume increases (from about 0.79% to 2.33%) with an enhancement of the added steel fibres amount (from 1.0% to 2.5%, vol.). Nevertheless, different from the connected fibres amount variation trend, the non-connected steel fibres content is increased at first and then gradually decline. For example, when the added steel fibres content increases from 1.0% to 2.0% (vol.), the non-connected steel fibres volume also increases from about 0.23% to 0.42%. Meanwhile, when the added steel fibres content increases from 2.0% to 2.5% (vol.), the non-connected steel fibres volume decreases to only about 0.19%.

In general, these phenomena mentioned above could be attributed to the relationship between the steel fibres number and the UHPFRC internal space. To be specific, when the steel fibres content is relatively low (less than 2.0% vol.), there is enough space for the fibres movement inside the UHPFRC sample. Therefore, the originally added steel fibres can be easily divided into two parts: connected steel fibres and non-connected steel fibres. When the added steel fibres amount is increased from 1.0% to 2.0% (vol.), the connected steel fibres volume and non-connected steel fibres volume could be simultaneously enhanced.

However, when the steel fibres content is relatively high (more than 2.5% vol.), the remaining space for fibres movement inside the UHPFRC specimen is quite limited, which could cause a corresponding decline of the non-connected steel fibres volume. Similar as shown in Figure 7, the probability for the steel fibres connecting to each other will generally increase with an enhancement of the added total steel fibres amount. During this process, a great improvement of the probability can be observed when the steel fibres content is increased from 2.0% to 2.5% (vol.).

Based on the X-ray CT results, the interconnection of the steel fibres in UHPFRC is carefully clarified. It is important to notice that 2% (vol.) steel fibres can be treated as a critical value in restricting the fibres interconnection, which could also be used to explain the phenomena observed in Sections 3.1-3.2 (fresh behaviour and mechanical properties of the developed UHPFRC).

4. Conclusions

This research addresses the impact of steel fibre content on the fibre network structure of ultra-high performance fibre reinforced concrete (UHPFRC). Based on the experiment results, the following conclusions can be obtained:

- 1) As the fibres content increased, the flowability of the fresh UHPFRC gradually decreases. This UHPFRC flowability decline can be explained by the steel fibres interconnection in the UHPFRC. Additionally, the 2% (vol.) is a critical steel fibres amount to produce UHPFRC with great flowability, with which the interconnection between fibres may be effectively limited.
- 2) The compressive and flexural strengths could be improved by an increasing of added steel fibres content. Similar as the flowability test results, the 2% (vol.) is a critical steel fibres amount to effectively improve the fibres efficiency in UHPFRC, since the interconnection between fibres may be effectively limited in this case.
- 3) The X-ray CT method could be suitably used in investigating the fibres distribution in the hardened UHPFRC. It is important to found that, with an increase of the total added fibres amount, the non-connected steel fibres content is increased at first and then gradually decline. The 2% (vol.) steel fibres can be treated as a critical value in restricting the fibres interconnection.

5. Acknowledgment

The authors acknowledge the financial supports of National Nature Science Foundation Project of China (No. 51608409), National Nature Science Foundation Project of China (51679179), Major science and technology project in Zhongshan city, Guangdong province (2017A1021), Yang Fan plan of Guangdong Province (201312C12), Open research project of Advanced Engineering Technology Research Institute of Wuhan University of technology in Zhongshan city (WUT201802).

6. References

- [1] Richard P., Cheyrezy M., Composition of reactive powder concretes, *Cement and Concrete Research*, 1995; 25 (7): 1501-1511.
- [2] Habel K., Viviani M., Denarié E., et al. Development of the mechanical properties of an Ultra-High Performance Fibre Reinforced Concrete (UHPFRC). *Cement and Concrete Research*, 2006; 36:1362–1370.
- [3] Yu R., Spiesz P., Brouwers H.J.H., Mix design and properties assessment of Ultra- High Performance Fibre Reinforced Concrete (UHPFRC), *Cement and Concrete Research*, 2014; 56: 29-39.

- [4] N.V. Tuan, G. Ye, K.V. Breugel, et al. Hydration and microstructure of ultra-high performance concrete incorporating rice husk ash. *Cement and Concrete Research*, 2011; 41: 1104–1111.
- [5] Máca P., Sovják R., Konvalinka P., Mix design of UHPFRC and its response to projectile impact. *International Journal of Impact Engineering*, 2014; 63: 158-163.
- [6] Yu R., Spiesz P., Brouwers H.J.H., Effect of nanosilica on the hydration and microstructure development of Ultra-High Performance Concrete (UHPC) with a low binder amount. *Construction and Building Materials*, 2014; 65: 140-150.
- [7] Wu Z., Khayat K. H., Shi C., Effect of nano-SiO₂ particles and curing time on development of fiber-matrix bond properties and microstructure of ultra-high strength concrete. *Cement and Concrete Research*, 2017; 95: 247–256.
- [8] Yu R., Spiesz P., Brouwers H.J.H., Development of an eco-friendly Ultra-High Performance Concrete (UHPC) with efficient cement and mineral admixtures uses. *Cement and Concrete Composites*, 2015, 55: 383-394.
- [9] Yang S.L., Millard S.G., Soutsos M.N., Barnett S.J., Le T.T., Influence of aggregate and curing regime on the mechanical properties of ultra-high performance fibre reinforced concrete (UHPFRC). *Construction and Building Materials*, 2009; 23: 2291-2298.
- [10] Fehling E., Bunje K., Schmidt M., Schreiber W. (2008) The “Gärtnerplatzbrücke”: Design of First Hybrid UHPC-Steel Bridge across the River Fulda in Kassel, Germany. 2nd International Symposium on Ultra High Performance Concrete, March 05-07, Kassel, Germany, 581-588.
- [11] Wang X.P., Yu R.*, Shui Z.H., Song Q.L., Zhang Z.H., Mix design and characteristics evaluation of an eco-friendly Ultra-High Performance Concrete incorporating recycled coral based materials. *Journal of Cleaner Production*, 2017, 165: 70-80.
- [12] Randl N., Steiner T., Ofner S., Baumgartner E., Mészöly T., Development of UHPC mixtures from an ecological point of view. *Construction and Building Materials*, 2014; 67: 373-378.
- [13] Habel K., Gauvreau P., Response of ultra-high performance fibre reinforced concrete (UHPFRC) to impact and static loading. *Cement and Concrete Composites*, 2008; 30(10): 938-946.
- [14] Hassan A.M.T., Jones S.W., Mahmud G.H., Experimental test methods to determine the uniaxial tensile and compressive behaviour of ultra-high performance fibre reinforced concrete (UHPFRC). *Construction and Building Materials*, 2012; 37: 874-882.
- [15] Yoo D.Y., Banthia N., Kang S.T., et al. Size effect in ultra-high-performance concrete beams, *Engineering Fracture Mechanics*, 2016; 157:86–106.
- [16] Yu R., Spiesz P., Brouwers H.J.H., Development of Ultra-High Performance Fibre Reinforced Concrete (UHPFRC): towards an efficient application of binders and fibres. *Construction and Building Materials*, 2015, 79: 273-282.
- [17] Yoo D.Y., Yoon Y.S., Banthia N., Flexural response of steel-fibre-reinforced concrete beams: effects of strength, fibre content, and strain-rate. *Cement and Concrete Composites*, 2015; 64:84–92.
- [18] Wu Z., Shi C., He W., et al. Effects of steel fibre content and shape on mechanical properties of ultra-high performance concrete. *Construction and Building Materials*, 2016; 103: 8-14.
- [19] Yoo D.Y., Kang S.T., Yoon Y.S., Effect of fiber length and placement method on flexural behaviour,

tension-softening curve, and fiber distribution characteristics of UHPFRC. *Construction and Building Materials*, 2014; 64: 67-81.

[20] Kang S.T., Lee Y., Park Y.D., et al. Tensile fracture properties of an ultra-high performance fibre reinforced concrete (UHPFRC) with steel fibre, *Composite Structures*, 2010; 92 (1): 61–71.

[21] Park S.H., Kim D.J., Ryu G.S., et al. Tensile behavior of ultra-high performance hybrid fibre reinforced concrete, *Cement and Concrete Composites*, 2012; 34 (2):172–184.

[22] Yu R., Spiesz P., Brouwers H.J.H., Static and impact resistance of a green Ultra-High Performance Hybrid Fibre Reinforced Concrete (UHPHFRC): experiments and modeling. *Construction and Building Materials*, 2014, 68: 158-171.

[23] Wang W., Liu J., Agostini F., Davy C.A., Skoczylas F., Corvez D., Durability of an Ultra High Performance Fibre Reinforced Concrete (UHPFRC) under progressive aging. *Cement and Concrete Research*, 2014; 55: 1-13.

[24] Song Q.L., Yu R., Wang X.P., Rao S.D., Shui Z.H., A novel Self-Compacting Ultra-High Performance Fibre Reinforced Concrete (SCUHPFRC) derived from compounded high-active powders. *Construction and Building Materials*, 2018, 158: 883-893.

[25] Boulekbache B., Hamrat M., Chemrouk M., et al. Flexural behavior of steel fibre-reinforced concrete under cyclic loading. *Construction and Building Materials*, 2016; 126: 253-262.

[26] Martine L., Roussel N., Simple tools for fibre orientation prediction in industrial practice. *Cement and Concrete Research*, 2011; 41: 993-1000.

[27] Eik M., Puttonen J., Herrmann H., An orthotropic material model for steel fibre reinforced concrete based on the orientation distribution of fibres. *Composite Structures*, 2015; 121: 324-336.

[28] Torrents J.M., Blanco A., Pujadas P., et al. Inductive method for assessing the amount and orientation of steel fibres in concrete. *Materials and Structures*, 2012; 45:1577-1592.

[29] Al-Mattarneh H., Electromagnetic quality control of steel fibre concrete. *Construction and Building Materials*, 2014; 73:350-356.

[30] Z. Wu, C.J. Shi, W. He, et al. Effects of steel fibre content and shape on mechanical properties of ultra-high performance concrete. *Construction and Building Materials*, 2016; 103:8-14.

[31] R. Wang, X.J. Gao, J.Y. Zhang, et al. Spatial distribution of steel fibers and air bubbles in UHPC cylinder determined by X-ray CT method. *Construction and Building Materials*, 2018; 160:39-47.

[32] B. Boulekbache, M. Hamrat, M. Chemrouk, et al. Flowability of fibre reinforced concrete and its effect on the mechanical properties of the material. *Construction and Building Materials*, 2010; 24 (9): 1664–1671.

[33] D.X. Xuan, Z.H. Shui, S.P. Wu. Influence of silica fume on the interfacial bond between aggregate and matrix in near-surface layer of concrete. *Construction and Building Materials*, 2009; 23(7): 2631-2635.

Investigation of the zonation of thermally treated ultra high performance concrete

M. Voigt¹, J. von Werder¹, B. Meng¹

¹Bundesanstalt für Materialforschung und -prüfung, Unter den Eichen 87, 12205 Berlin, Germany

Abstract

Ultra high performance concrete (UHPC) is characterised by its high compressive strength of more than 150 MPa and its high durability. Due to thermal treatment at 90°C a strength comparable to the 28-days-strength can be achieved immediately after the treatment and in some cases can be even further increased up to 30 %. The explanations for the increase in strength are the accelerated hydration of the clinker minerals and the intensified pozzolanic reaction contributing to a denser microstructure and hence, a high performance in compressive strength.

Former research shows that thermal treatment can lead to inhomogeneities in form of a visible zonation within the cross-section. The width of the margin increases with shorter pre-storage time before the thermal treatment and with omitting protective measures against desiccation during the treatment. Specimens exhibiting a zonation typically show a lower compressive strength compared to the undisturbed reference whereas changes in chemistry, mineral content and microstructure were not reported in detail.

In this study the zonation of thermally treated UHPC is investigated with respect to its chemistry, mineral composition and microstructure to allow predictions on durability and strength development. Measurements show a change in pore sizes, minerals phase composition and element distribution leading to the visible zonation and weaker bending tensile strength compared to the reference.

Keywords: UHPC, thermal treatment, zonation, desiccation, microstructure, durability

1. Introduction

In 1994 the term ultra high performance concrete (UHPC) was introduced by [1]. It characterizes concrete with an exceptional compressive strength which was accomplished by optimizing the packing density and viscosity using a low water/binder ratio and moderate thermal treatment. In the last decades the term UHPC is used for concrete with a characteristic compressive strength over 150 MPa and high durability. These characteristics derive from the low water/binder ratio of < 0.3 and the high viscosity of the fresh concrete and thus a self-compacting behaviour facilitated by a superplasticizer. By its well-tuned mixture based on assorted additives UHPC obtains its typical high packing density, low porosity and homogeneous microstructure.

In the production of precast UHPC elements thermal treatment became a common practice to shorten fabrication times, as the 28-days-strength of UHPC specimens is achieved after 24h of thermal treatment up to 90 °C [2, 3]. The thermal treatment accelerates and intensifies the hydration process and the pozzolanic reaction so that shrinkage [4] is largely completed after the treatment. For the early and rapid precipitation of hydration products during exposure to higher temperatures [5] the presence of water is crucial. Thus, some guidelines like the German regulation [6] propose a protection from desiccation but do not clearly specify to which degree. To evaluate the impact of the lacking definition three different measures against

desiccation of UHPC during thermal treatment were investigated by [7]. In the study of [7] a zonation was observed in foil covered and unprotected UHPC samples after 90 °C thermal treatment (as in Figure 1). After optical assessment of the dimension of the zonation from high resolution scans of cross sections of standard prisms (4x4x16 cm³) it could be detected that the dimension of the zonation varied with the time span between demoulding and thermal treatment (pre-treatment time), the duration of the thermal treatment time (thermal-treatment time) and the level of protection against desiccation. Compressive strength is one of the key parameters defining concrete. Thermal treatment of UHPC in general was found not to be detrimental for the further strength development but on the contrary the compressive strength of later age was even increased [8, 9]. Specimens, however, which were treated at 90 °C in the oven without any protection performed inferior to the water cured reference samples at all times [7, 10].

This study focuses on the analysis of the microstructure of the zonation and aims to provide an insight into the processes leading to the diminished strength performance.

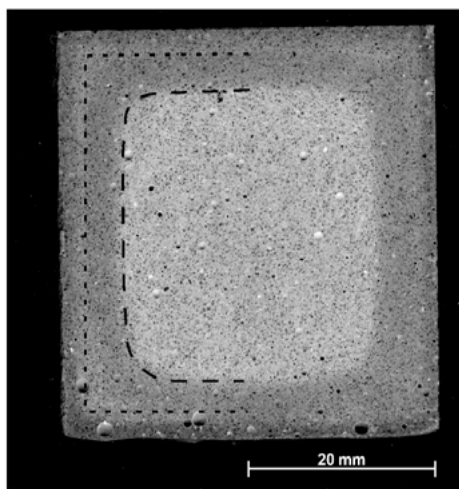


Figure 1: High resolution scan of a UHPC standard prism treated 6 days at 90 °C under dry conditions comparable to [7]. The zonation shows an inner lighter part and an outer darker part. At the rim there is a slim darker zone visible. The image was modified for better visibility of the zonation.

2. Methodology

2.1 Materials

To investigate the formation of the zonation during thermal treatment a well-established (M2Q) UHPC mixture design after [7, 11] was selected. The mixture is based on mainly SiO₂ containing components and CEM I 52,5 R as shown in table 1. The addition of fibres was omitted as the focus of the study lies on microstructure and mineral phase analysis.

The mixing was conducted in an Eirich intensive mixer with a volume of 10 l within 11 minutes. The homogenisation and mixing of the dry components were followed by the addition of water and the first half of the PCE superplasticizer. The remaining superplasticizer was added 5 minutes after the water admixture resulting in a flow spread of 30 cm.

Standard prisms of 4 x 4 x 16 cm³ were cast, prestored under water for one day at 23 °C, thermally treated in an oven with full circulation at 90 °C for six days (no protection from desiccation) and afterwards kept under water at 23 °C till strength testing after 28 days. These conditions for the thermal treatment were chosen after [7] to establish a “worst-case scenario” and ensure a strongly developed zonation of the cross section. The reference samples were immersed in water at 23 °C until testing after 28 days.

Table 1: Components of the UHPC mixture.

Components	Mass
	kg/m ³
CEM I 52,5 R	832
Microsilica	135
Quartz Powder	207
Quartz Sand	975
Superplasticizer(PCE)	25
Water	209

2.2 Methods

2.2.1 Strength testing

The prisms were tested after 28 days according to DIN EN 196-1 with a three-point bending-test set up in a universal testing machine. The bending test was followed by a compressive strength test according to DIN EN 196-1 with an area of 40 x 40 mm² using the two split halves of the prisms.

2.2.2 Pore Size Distribution

For the mercury intrusion porosity testing (MIP) the outer zone of the samples was cut off and parts of the rim and the inner zone were broken into 2-5 mm cubes so that the inner and outer parts of the samples could be measured individually. Before measuring the samples were dried at 40 °C under vacuum to avoid further hydration. The pressure applied was 410 MPa and a contact angle of 140 ° reaching a resolution of 3.6 nm as the finest pore diameter.

2.2.3 X-Ray diffraction (XRD)

The samples for the XRD measurements were prepared in the same way as for MIP so that the outer zonation and the inner part of the prisms could be analysed separately. After drying the samples were ground in an agate mortar and scanned in the 2theta range 5-65 ° with a step size of 0.02 ° and a speed of 0.5 °/min with a conventional XRD (CuK α radiation, 40 mA, 40 kV).

2.2.4 Micro X-Ray Fluorescence (μ XRF)

For μ XRF measurements cross sections of the prisms were polished with water and dried at 40 °C under vacuum to stop hydration. The measurements were conducted with 40 kV, 300 μ A and a spot size of 150 μ m.

2.2.5 Scanning Electron Microscope (SEM)

For the SEM analysis smaller cross sections of 20 x 20 mm² were embedded in epoxy resin and polished to perform qualitative and semi quantitative analysis on back scattered electron images and energy dispersive X-ray analysis (EDX). The samples for the SEM analysis represent a quarter of the overall cross section of the prisms and were selected corresponding to the outer and inner part of the sample. To recognize changes in microstructure punctual EDX mappings and backscattered electron (BSE) images were taken along a 10 mm linear line from the surface towards the core of the sample.

3. Results and discussion

3.1 Strength testing

The compressive strength of the prisms is shown in figure 2a and does not indicate a dependency on the thermal treatment after 28 days. As noted in [7] the compressive strength loss in standard prisms which are thermally treated without protection compared to thermally treated prisms immersed in water is marginal

compared to smaller sample sizes due to the basically intact core. Hence, the prisms tested after 28 days for compressive strength exhibit similar strength independent of the unprotected treatment. The bending strength however displays unambiguous lower strength values in thermally treated samples compared to the reference (Figure 2b). The reduction in bending tensile strength and compressive strength of samples cured at room temperature exposed to air compared to samples cured in water is a well-known phenomenon and due to the shrinkage stress during dry curing [12]. The resulting crack formation is likely to be increased by thermal stress arising from a temperature gradient during thermal treatment [13]. As the zonation is dependent on the degree of protection against desiccation during thermal treatment the loss in strength seems to be the logical consequence of an excessive drying process.

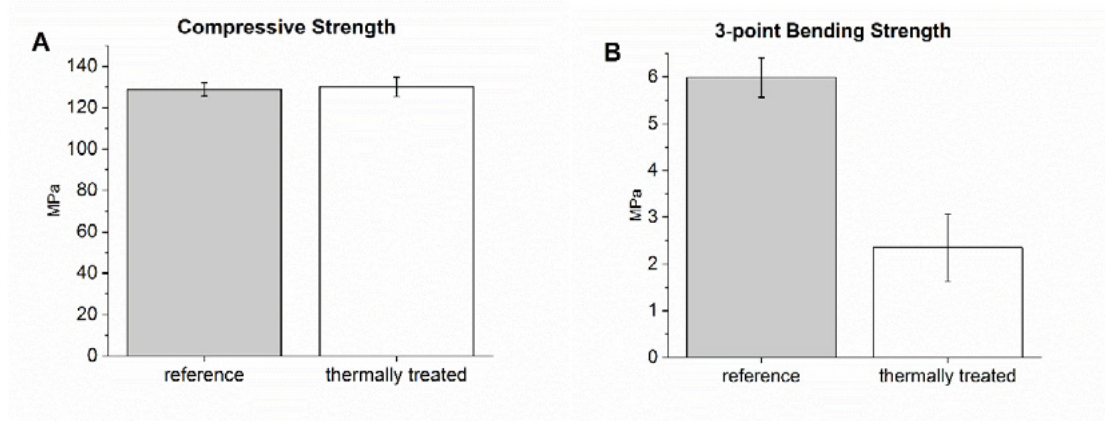


Figure 2: Test results of the compressive strength (a) and bending tensile strength (b).

3.2 Pore Size Distribution

In figure 3 the porosities of the inner and outer part of the thermally treated samples are shown in comparison to the reference sample cured in the water bath. As shown in figure 3a the outer part has a median pore size diameter of 12,5 nm, the inner part of 29 nm while the median pore size diameter of the reference lies in the middle and measures 24 nm. Figure 3b shows the cumulative intrusion and thus represents the total porosity which is comparable for the reference sample and the inner part with an average value of 10.2 Vol.-%. For the outer part, however, a noticeably smaller porosity of 8.9 Vol.-% was measured.

It is known [5] that cement matrix, exposed to elevated temperatures early during the hardening process, develops a more heterogeneous microstructure as the hydration products precipitate rapidly in a dense structure around the clinker minerals and lead to a coarser porosity. The coarser median pore diameter of the inner part of the thermally treated sample compared to the reference can therefore be explained with the thermal treatment. The fact that the outer part is mainly not characterized by a coarser but on the contrary by a finer porous structure is possibly due to the water storage after thermal treatment. In the water bath additional water is provided so that the remaining clinker phases can hydrate and thus reduce the pore size towards the surface. The weak bending tensile strength could be explained by possible microcracks occurring in the large pore size region due to the thermal stresses during thermal treatment. The lack of evidence for an accumulation of microcracks by the measurements is probably concealed by the self-healing taking place during the subsequent water storage to the thermal treatment and is matter of further research.

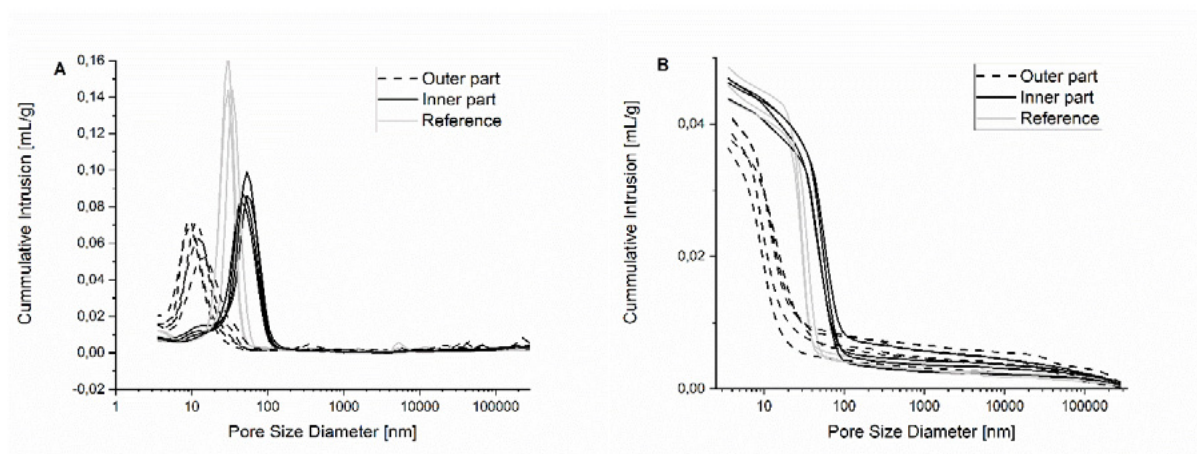


Figure 3: Pore size distribution of thermally treated and water cured (reference) UHPC at 28 days: (a) Log differential intrusions and (b) cumulative pore volume.

3.3 X-Ray diffraction

The diffraction patterns pictured in figure 4 show in general the same peak positions for the reference as well as the inner and the outer part of then thermally treated sample and therefore a similar composition of the crystalline phases. As it is typical for UHPC with a low w/c ratio alite peaks are observed as well as aluminate peaks as the remaining clinker phases besides the sharp quartz peaks from the aggregates. Focusing on the clinker mineral peaks of alite at 32.2 and $32.6^{\circ}2\theta$ it seems that in the outer part of the zonation peak intensities decrease compared to the reference and the inner part. In the detailed frame of figure 4 the AFm phase peak at $10.9^{\circ}2\theta$ is displayed to emphasize the decrease in the outer part of the zonation whereas the reference and the inner part show a distinct peak of lower intensity at this position. The peak position matches data from [14] and seems to represent a partly carbonated AFm phase like Hemicarboaluminate.

Even though the changes seem marginal it indicates that the clinker consumption at the rim of the thermally treated sample is slightly higher and hence, points to a continued hydration after thermal treatment via the renewed water influx during water storage. The change of the crystallinity of the AFm phase towards the rim is evidence for ongoing carbonatization even though it is not comprehensible from the calcite peak at $29.5^{\circ}2\theta$ as it is superimposed by alite and belite peaks.

3.4 Micro X-Ray Fluorescence

The mapping of the μ XRF in figure 5a shows an enriched potassium concentration in the outer zone and a depletion in the core. The sulphur content distribution is exactly diametrical to the potassium enrichment (Figure 5b). Thus, it is decreasing from the rim towards the outer zone followed by a sharp increase towards the core where it slightly declines in the thermally treated sample. The reference sample shows no distinct zonation in the potassium (Figure 5e) or sulphur distribution (Figure 5f) even though the distribution seems not entirely homogeneous. Especially in the case of the potassium a depletion in the concentration around the air pores is visible.

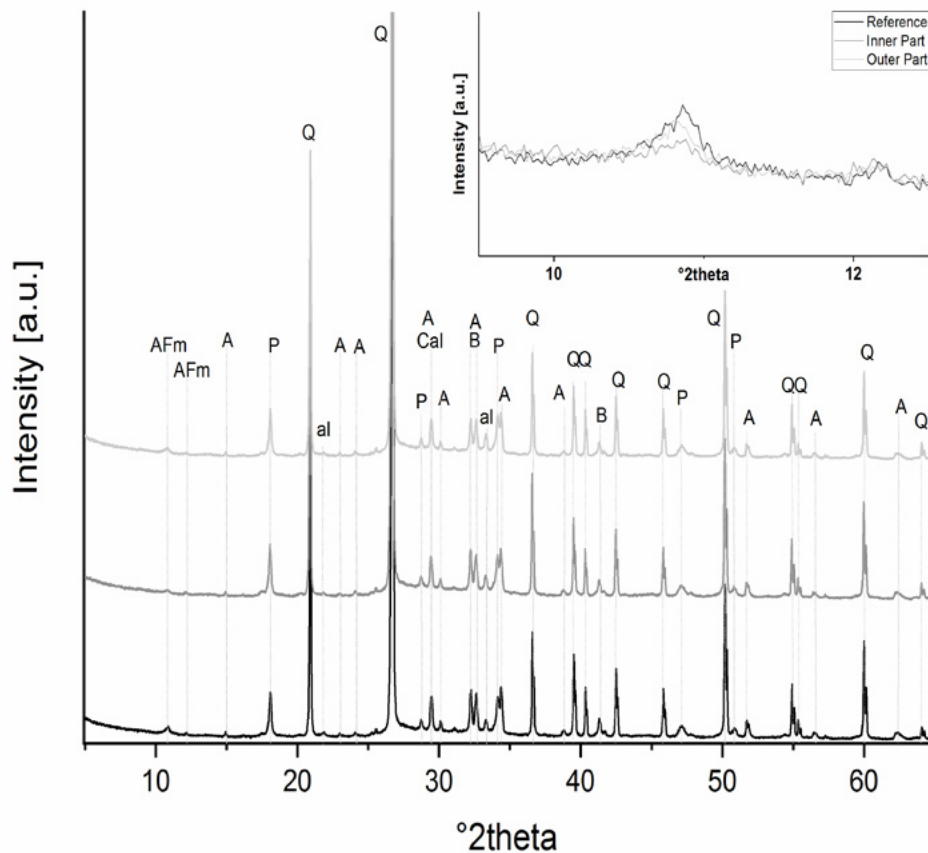


Figure 4: XRD patterns of UHPC at 28 days: q-quartz, a-alite, b-belite, p- portlandite, al-aluminates AFm-AFm phases, cal-calcite

Other elemental mappings e.g. Ca or Si in figure 5 c and d, do not exhibit any measurable shifts in element concentration across the cross-section due to the high intensities of either the chosen SiO₂-rich aggregates or the typical mineral phases expected in a Portland cement.

The low potassium content at the rim of the outer zone is probably caused by leaching during water storage subsequent to the thermal treatment. The depletion in the core, however could be assigned to the capillary transport of the K-rich pore solution from the inner core driven by the gradient in capillary pressure during thermal treatment.

The varying potassium and sulphur contents can be related to plural transport mechanisms through the capillary pores and diffusion during thermal treatment and subsequent storage in water. For more detailed insights of the element distribution the effects of the thermal treatment should be investigated separately without water storage.

3.5 Scanning Electron Microscope

The punctual EDX mappings of the cement matrix confirm the trends seen in the μ XRF analysis. Qualitative it can be recognized that less clinker phases are found in the inner part of the thermal treated sample (Figure 6a) compared to the rim (Figure 6b) and the reference. For the thermally treated as well as the water cured sample clinker phases seem both diminished at the rim of the cross section and suggest an

external water influx and subsequent further hydration during water storage.

Portlandite crystals (Figure 7) appearing as stacks and agglomerates of crystals are found in all parts of the thermally treated sample and the reference sample. The composition is validated via EDX measurements where the Wt.% of Ca is noticeable increased whereas the C value is smaller compared to the mappings of the cement matrix.

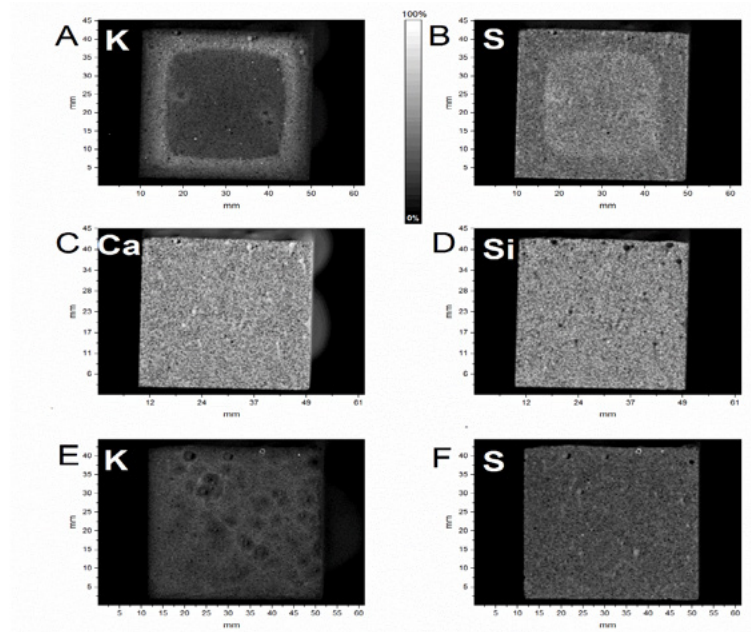


Figure 5: The μ XRF mappings of the potassium (a), the sulphur (b), the calcium (c) and the silicium (d) distribution of the thermally treated sample in comparison to the potassium (e) and sulphur (f) concentrations of the water immersed reference sample.

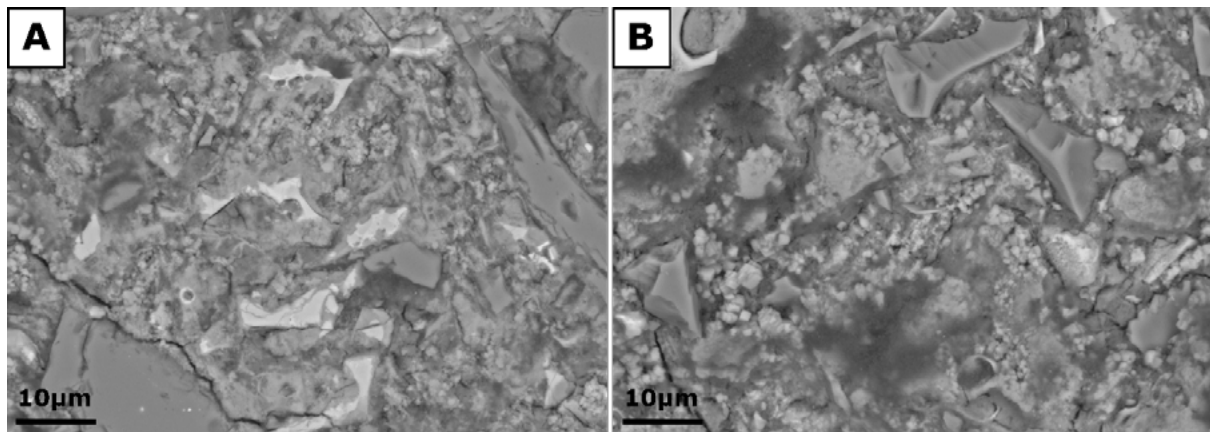


Figure 6: BSE images (4000x magnification) of the thermally treated sample of the core (a) and the outer zone (b).

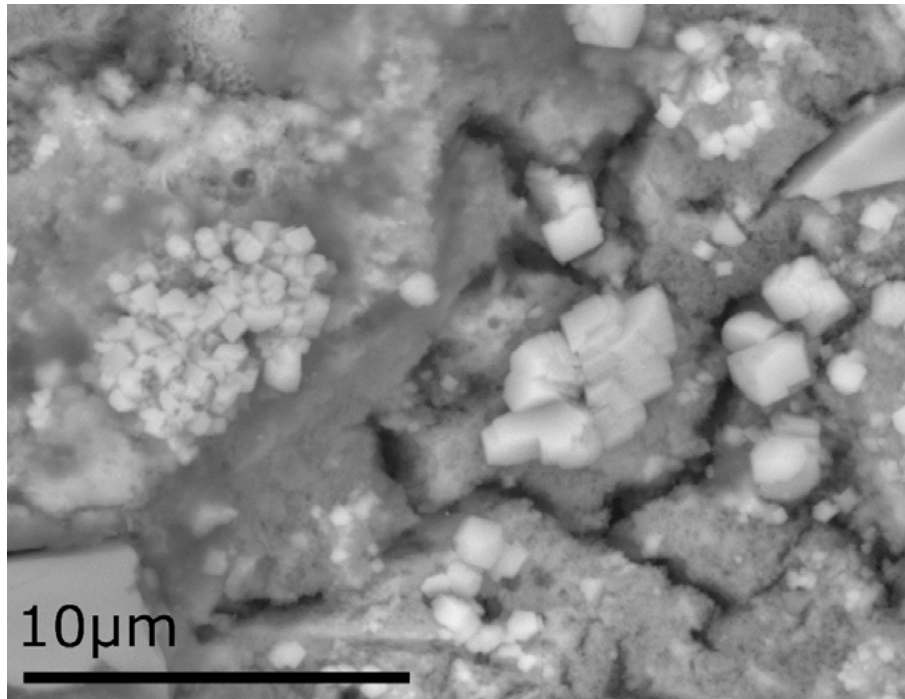


Figure 7: BSE image (8000x magnification) of the portlandite stacks and agglomerates of different crystal sizes in a water immersed reference sample.

4. Conclusions

The microstructure of the depth dependent zonation of unprotected, thermally treated UHPC was investigated. The results exhibited a different microstructure in the core of the thermally treated UHPC sample compared to the outer zone.

The dehydration effects near the surface during the thermal treatment appears to be responsible for the measured weaker bending tensile strength in that zone. For the outer zone, additionally the appearance of partly carbonated AFm points to ingress and reaction of CO₂ during the unprotected exposition.

The microstructure of the outer zone displayed consistently that the water storage following the treatment resulted in ongoing hydration effects, densifying the structure and consuming clinker minerals. Accordingly, the core of the thermal treated sample showed a larger median pore diameter and more remaining clinker minerals compared to the water immersed reference sample.

Additionally, the drying and wetting processes in the outer zone seem to provoke migration effects of ions mobilised with the pore solution. Such effects, which could not be explained in detail so far, were indicated by μ XRF mappings, indicating a depletion of potassium in the core und an enrichment towards the rim and an opposing sulphur distribution. Further research is needed to explain the interrelationships between element distributions and the transport mechanisms.

Also, the other zonation effects mentioned above desire a deepening investigation of dehydration and rehydration processes caused by treatment and storage parameters, because this knowledge is essential for durability performance of thermally treated UHPC.

5. Acknowledgment

The authors would like to thank P. Drabetzki, A. Gardei and S. Simon from BAM for assistance with XRD, XRF, MIP measurements, strength testing and stimulating discussions.

6. References

1. 1. De Larrad, F. and T. Sedran, *Optimization of ultra-high-performance concrete by the use of a packing model*. Cement and Concrete Research, 1994. **24**(6): p. 997-1009.
2. 2. NPCA, *Ultra High Performance Concrete (UHPC): Guide to Manufacturing Architectural Precast UHPC Elements*. 2013: Carmel, IN, USA.
3. 3. Kang, S., et al., *Microstructural Investigation of Heat-treated Ultra-High performance Concrete for Optimum Production*. Materials, 2017. **10**(1106): p. 1-13.
4. 4. Heinz, D. and H.-M. Ludwig, *Heat Treatment and the Risk of DEF Delayed Ettringite Formation in UHPC*, in *Proceedings of the International Symposium on Ultra High Performance Concrete*, M. Schmidt, E. Fehling, and C. Geisenhanslüke, Editors. 2004, Kassel University Press: Kassel. p. 717-730.
5. 5. Lothenbach, B., et al., *Effect of temperature on the pore solution, microstructure and hydration products of Portland cement pastes*. Cement & Concrete Research, 2007. **37**: p. 483-491.
6. 6. DAfStb, *Sachstandsbericht Ultrahochfester Beton*. DAfStb-Heft, ed. Deutscher Ausschuss für Stahlbeton. Vol. 561. 2008, Berlin: Beuth Verlag GmbH. 126.
7. 7. Selleng, C., et al., *Influencing factors for the effectivity of heat treatment of ultra-high performance concrete (UHPC)*. Beton- und Stahlbetonbau, 2017. **112**(1): p. 12-21.
8. 8. Schmidt, M., et al., *The German Guideline for ultra-high performance concrete*, in *AFGC-ACI-fib-RILEM Int. Symposium on Ultra-High Performance Fibre-Reinforced Concrete, Volume II*. 2017: Montpellier, Franca. p. 545-555.
9. 9. Schachinger, A.I., H. Hilbig, and T. Stengel, *Effect of Curing Temperature at an Early Age on the Long-Term Strength Development of UHPC*, in *2nd International Symposium on Ultra High Performance Concrete*, E. Fehling, M. Schmidt, and S. Stürwald, Editors. 2008, Kassel University Press: Kassel, Germany. p. 205-212.
10. 10. Gröger, K., et al., *Effect of 90 °C Thermal Treatment on Ultra High Performance Concrete*, in *GeoBerlin 2015 - Dynamic Earth from Alfred Wegener to today and beyond*, J. Wagner and K. Elger, Editors. 2015, GFZ German Research Centre for Geosciences: Berlin. p. 162.
11. 11. Bornemann, R., et al., *Ultra High Performance Concrete UHPC - Composition, Properties and Applications*. Beton- und Stahlbetonbau, 2001. **96**(7): p. 458-467.
12. 12. Graf, O. and K. Walz, *Vergleichende Prüfungen von Straßenbauelementen in der Versuchsanstalt und in der Straße*. Zement, 1939. **28**: p. 445-505.
13. 13. Ma, Q., et al., *Mechanical properties of concrete at high temperature—A review*. Construction and Building Materials, 2015. **93**: p. 371-383.
14. 14. Baquerizo, L., T. Matschei, and K.L. Scrivener, *Impact of water activity on the stability of systems containing ettringite*, in *19. ibausil*. 2015, F. A. Finger-Institut für Baustoffkunde: Weimar, Germany. p. 556-560.

Role of Mg^{2+} stabilized amorphous calcium carbonate on the early reaction of sodium carbonate activated slag

B. Yuan^{1,2}, Q.L. Yu³, W. Chen¹, H.J.H. Brouwers^{1,3}

¹State Key Lab of Silicate Materials for Architectures, Wuhan University of Technology, Wuhan 430070, PR China;

²School of Material Science and Engineering, Wuhan University of Technology, Wuhan 430070, PR China

³Department of the Built Environment, Eindhoven University of Technology, P.O. Box 513, 5600 MB Eindhoven, The Netherlands

Abstract

Amorphous calcium carbonate (ACC) is the least stable phase of calcium carbonate, and will quickly transfer to more stable phases, e.g. aragonite, vaterite and calcite, the phases of which are widely reported in sodium carbonate activated slag (SCAS). However, the existence of ACC was not reported in SCAS yet, probably because of its extreme instability at ambient condition. Mg^{2+} ion is known as an effective inorganic ion that increases the stability of ACC. In order to study the effect of ACC on the early age reaction of SCAS, Mg^{2+} ion is added to the SCAS system to increase the stability of ACC in order to evaluate the effect of ACC on the early age reaction. The results show that the reaction rate, reaction intensity and reaction products depend on the dosage of Mg^{2+} , providing that Mg^{2+} -stabilized ACC plays an important role on the early age reaction of SCAS. Due to the presence of Mg^{2+} , the precipitation of reaction product is clearly identified at different reaction stages as classified by the reaction kinetic results. The precipitation of calcium carbonate starts when the solids mix with the sodium carbonate solution, and the first reaction peak in the heat release curve assigns to the precipitation of gaylussite. The existence of ACC is observed by SEM. Furthermore, the role of ACC or Mg^{2+} -stabilized ACC on the early age reaction of sodium carbonate activated slag is discussed and a model is proposed.

Keywords: Sodium carbonate activated slag, amorphous calcium carbonate, Magnesium stabilization, early age reaction.

1. Introduction

Applying near neutral salts, e.g. sodium carbonate, as activator for alkali activated materials has received increased attention because of its good properties, low price and environmental benefits [1–4]. However, slow reaction of sodium carbonate activated slag (SCAS) are often reported, while current understandings about the long dormant period are still limited to the effect of CO_3^{2-} anion in controlling the Ca^{2+} ion at the early age reaction [5,6]. There 3 out of 4 polymorphous of calcium carbonate are widely reported as the secondary products of SCAS at the early stages, i.e. aragonite, vaterite and calcite. While the least stable phase of calcium carbonate, ACC, is not reported yet. It is known that high pH value and Mg^{2+} ion can

stabilize ACC [7,8], which indicates that the other three phases of CaCO_3 are originally converted from ACC. Considering the pore solution environment, ACC can potentially plays an important role on the early age reaction of SCAS.

This study aims to investigate the effect of Mg^{2+} ion on the early age reaction of SCAS. MgCl_2 is used as the Mg^{2+} ion source. The reaction kinetics and reaction products of the samples containing different amounts of Mg^{2+} ion are characterized with isothermal calorimeter, X-ray diffraction (XRD) and scanning electron microscope (SEM). Based on the results, the role of Mg^{2+} -stabilized ACC on the early age reaction of SCAS is discussed.

2. Materials and experiments

2.1 Materials

Ground granulated blast furnace slag (GGBS) was used in this study (supplied by ENCI B.V, the Netherlands). The elemental composition and particle size distribution of the slag were determined by X-ray fluorescence (XRF) using a PANalytical Epsilon3 analyzer and the results are shown in Table 1, respectively. Sodium carbonate (powder, analytical grade) was applied as the activator in this study with different concentrations. The designed Na_2CO_3 concentrations (Table 2) were firstly mixed/dissolved in water followed by cooling down to room temperature (20 ± 1 °C) prior to further actions. MgCl_2 (powder, analytical grade) was used as the source of Mg^{2+} ion and mixed with the prepared Na_2CO_3 solutions about ≈ 20 s using a vibrator (ensuring the completed reaction of Mg^{2+} and CO_3^{2-}) before mixing with the slag powders.

Table 1 Chemical composition of GGBS.

Oxidations (%)	SiO_2	CaO	Al_2O_3	MgO	Fe_2O_3	SO_3	K_2O	Cl	L.O.I
Slag	30.24	40.68	12.67	9.05	0.64	3.53	0.38	0.05	-0.36

Table 2 Mix proportions of specimens.

Items	Na_2CO_3 dosage	MgCl_2 dosage	W/S
Unit	[Na_2O wt.%]	[Na_2O wt.%]*	
Reference	4.00		0.4
Mg/Ca 1/9	4.44	0.44	
Mg/Ca 2/8	5.00	1.00	
Mg/Ca 3/7	5.71	1.71	

*means that the MgCl_2 dosage is calculated by the same mole of Na_2CO_3 and shown as the dosage of equivalent Na_2O wt.% by mass of slag. Due to the reaction of $\text{MgCl}_2 + \text{Na}_2\text{CO}_3 = \text{MgCO}_3 + 2\text{NaCl}$, the Na_2CO_3 dosage keeps the same to be 4.00 Na_2O wt.% for all the mixtures.

2.2 Experiments

The reaction kinetic of the samples with different amount of Mg^{2+} ion content is investigated using an isothermal calorimeter, set at 20 °C (TAM AIR Calorimeter). The microscopic analysis is performed using a JSM-IT100 InTouchScope™ Scanning Electron Microscope (SEM).

3. Results and discussion

3.1 Reaction kinetics

Fig. 1 shows the heat release of sodium carbonate activated slag with different dosage of Mg^{2+} ion. It is clear that the reaction process can generally be classified into five stages, and the duration of each stage is highly depending on the dosage of the Mg^{2+} ion. The reference sample shows a similar reaction pattern to previous studies [5,9], but with a shortened dormant period. This is explained by the fineness of the applied slag [10]. It is reported that the CO_3^{2-} anions concentration in the pore solution controls the reaction of

sodium carbonate activated slag [5]. In this case, more Ca^{2+} ions are dissolved from finer slag particles and precipitated with CO_3^{2-} anions, which consequently lead to a faster reaction.

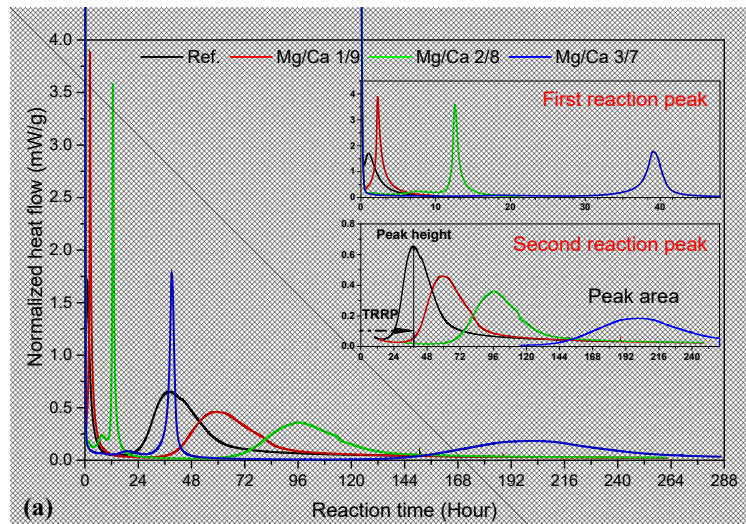


Fig. 1 Heat evolutions of sodium carbonate activated slag with different Mg^{2+} ion dosages. (TTRP is time to reach the reaction peak).

Table 3 Summarized results of TTRP (time to reach reaction peak), peak height (intensities), and peak area (identified in Fig. 1)

Items	Peak height	TTRP	Peak area
Reference	0.65	36.81	78.30
Mg/Ca 1/9	0.46	58.96	70.03
Mg/Ca 2/8	0.36	95.93	61.33
Mg/Ca 3/7	0.18	201.49	53.78*

*the value is relatively low because the main reaction (second reaction peak) is not finished yet.

After dosing a small amount of Mg^{2+} ion, the first peak on the heat release curve is slightly delayed by about 1 h (from 1 h to ≈ 2 h), as shown in Fig. 2. However, further increasing the Mg^{2+} ion dosage leads to a significant delay up to 12 h (mixture Mg/Ca 2/8) and 39 h (mixture Mg/Ca 3/7), respectively. The time to reach the second peak (i.e. the main reaction peak) is also significantly extended. Besides, the peak height of the samples decreases with the increase of Mg^{2+} ion content. The total heat release during the main reaction is estimated, as shown in Table 3. It is seen that the intensity of the second reaction peak decreases with the increasing content of Mg^{2+} ion, the total heat release of the mixtures is slightly reduced. It is obvious that the incorporated Mg^{2+} ion dominates the reaction kinetics of SCAS.

3.2 Role of Mg^{2+} stabilized ACC

Fig. 2 presents the SEM picture of the reference sample after 6 h of reaction. As can be seen, two distinguishable products are clearly identified, i.e. calcite with hexagonal crystalline structure and many clusters of irregular micro-particles. The sample is washed with distilled water and left dried on a silica plate. Considering the chemical reaction involved in the early reaction of SCAS, the micro-particles can be assigned to ACC, which is known as the least stable polymorphous structure of calcium carbonate. In most cases, ACC will quickly convert to more stable products, e.g. aragonite, vaterite and/or calcite. However, methods such as increasing the pH [11] or dosing stabilization agent [12] delay the process and improve the stability of ACC.

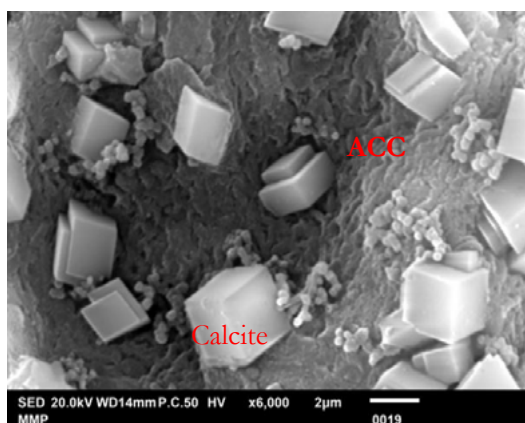


Fig. 2 SEM picture of the mixture Mg/Ca 2/8 after 7 h of curing (washed with water and then left dry).

It is clear that the incorporation of Mg^{2+} ion stabilizes ACC, which is responsible for the delayed initial precipitation peak of gaylussite. Why the main reaction peak, i.e. precipitation of C-(A)-S-H gel is significantly prolonged, however, is not clear understood yet. In theory, when the pH of the pore solution rises over 10.52, $MgCO_3$ will turn to a less soluble product $Mg(OH)_2$, and its ability in stabilizing ACC will not be prominent. In which case, the stabilization effect could be the synergetic effect of Mg, pH and SiO_3^{2-} that requires further study.

Fig. 4 presents the carbonate consumption routine of the samples after incorporating Mg^{2+} ion as an stabilization agent. If the initial precipitated ACC is not stabilized, it will quickly react with Na_2CO_3 forming gaylussite, or convert to other more thermodynamic stable polymorphous of $CaCO_3$, e.g. aragonite, vaterite and/or calcite. In which case, the reaction in stage 1 and stage 3 happens simultaneously. However, when the initially precipitated ACC is stabilized by Mg^{2+} ion (stage 2), the formation of gaylussite is delayed, as shown in Fig. 3. The duration of this stage is highly depending on the dosage of Mg^{2+} , which can vary from a few hours to days. The mechanism behind this phenomenon still requires further investigations.

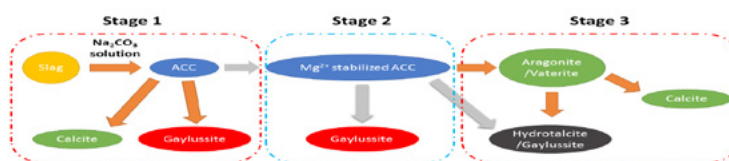


Fig. 3 Scheme of role of Mg^{2+} ion stabilized ACC on sodium carbonate activated slag.

4. Conclusions

The effect of Mg^{2+} -stabilized ACC on the reaction of sodium carbonate activated slag (SCAS). The results demonstrate that Mg^{2+} -stabilized ACC plays a significant role on the early age reaction of SCAS. The first reaction peak of SCAS is assigned to the precipitation of gaylussite, while the second reaction peak is attributed to the precipitation of C-A-S-H gel together with the generation of hydrotalcite-like structures.

5. Acknowledgment

Acknowledgments of people, grants, funds, etc. should be placed in a separate section before the reference list. The names of funding organizations should be written in full.

6. References

- [1] S.A. Bernal, Advances in near-neutral salts activation of blast furnace slags, RILEM Tech. Lett. (2016) 39–44.
- [2] A.F. Abdalqader, F. Jin, A. Al-Tabbaa, Development of greener alkali-activated cement: utilisation of sodium carbonate for activating slag and fly ash mixtures, J. Clean. Prod. 113 (2015) 66–75. doi:10.1016/j.jclepro.2015.12.010.
- [3] B. Yuan, C. Straub, S. Segers, Q.L.L. Yu, H.J. J.H. Brouwers, Sodium carbonate activated slag as cement replacement in autoclaved aerated concrete, Ceram. Int. 43 (2017) 6039–6047. doi:10.1016/j.ceramint.2017.01.144.
- [4] A.J. Moseson, D.E. Moseson, M.W. Barsoum, High volume limestone alkali-activated cement developed by design of experiment, Cem. Concr. Compos. 34 (2012) 328–336. doi:10.1016/j.cemconcomp.2011.11.004.
- [5] S.A. Bernal, J.L. Provis, R.J. Myers, R. San Nicolas, J.S.J. van Deventer, Role of carbonates in the chemical evolution of sodium carbonate-activated slag binders, Mater. Struct. 48 (2014) 517–529. doi:10.1617/s11527-014-0412-6.
- [6] M. Kovtun, E.P. Kearsley, J. Shekhovtsova, Chemical acceleration of a neutral granulated blast-furnace slag activated by sodium carbonate, Cem. Concr. Res. 72 (2015) 1–9. doi:10.1016/j.cemconres.2015.02.014.
- [7] J.D. Rodriguez-Blanco, S. Shaw, P. Bots, T. Roncal-Herrero, L.G. Benning, The role of pH and Mg on the stability and crystallization of amorphous calcium carbonate, J. Alloys Compd. 536 (2012) S477–S479. doi:10.1016/j.jallcom.2011.11.057.
- [8] J.D. Rodriguez-Blanco, S. Shaw, P. Bots, T. Roncal-Herrero, L.G. Benning, The role of Mg in the crystallization of monohydrocalcite, Geochim. Cosmochim. Acta. 127 (2014) 204–220. doi:10.1016/j.gca.2013.11.034.
- [9] B. Yuan, Q.L.L. Yu, H.J.H. J.H. Brouwers, Time-dependent characterization of Na₂CO₃ activated slag, Cem. Concr. Compos. 84 (2017) 188–197. doi:10.1016/j.cemconcomp.2017.09.005.
- [10] B. Yuan, Q.L. Yu, H.J.H. Brouwers, Evaluation of slag characteristics on the reaction kinetics and mechanical properties of Na₂CO₃ activated slag, Constr. Build. Mater. 131 (2017) 334–346. doi:10.1016/j.conbuildmat.2016.11.074.
- [11] N. Koga, Y. Nakagoe, H. Tanaka, Crystallization of amorphous calcium carbonate, Thermochim. Acta. 318 (1998) 239–244. doi:10.1016/S0040-6031(98)00348-7.
- [12] J. Ihli, W.C. Wong, E.H. Noel, Y.-Y. Kim, A.N. Kulak, H.K. Christenson, M.J. Duer, F.C. Meldrum, Dehydration and crystallization of amorphous calcium carbonate in solution and in air, Nat. Commun. 5 (2014) 3169. doi:10.1038/ncomms4169.

Pozzolanic reactivity of size-classified siliceous fly ashes

R. Snellings¹, H. Kamyab¹, S. Joseph², P. Nielsen¹, M. Loots³, L. Van den Abeele¹

¹Sustainable Materials, Flemish Institute of Technological Research (VITO), Boeretang 200, B-2400 Mol, Belgium

²Department of Civil Engineering, KU Leuven, Kasteelpark Arenberg 40/2448, B-3001 Heverlee, Belgium

³Value Ash Technologies NV, Centrum-Zuid 1111, B-3530 Houthalen-Helchteren, Belgium

Email of the corresponding author: ruben.snellings@vito.be

Abstract

High grade mineral powders are essential as high-quality supplementary cementitious materials and fillers for low carbon, high performance cement and concrete. In the FLAME project a new technology for size classification of mineral powders is upscaled from lab to pilot prototype. The new size classification technique operates on dry powders in a closed circuit. The pilot prototype was tested on a number of mineral powders, amongst which coal combustion ashes, and generated ultrafine (d_{50} of 2-3 μm), very fine (d_{50} of 4-5 μm), medium (d_{50} of 15-20 μm), and coarse (d_{50} >20 μm) size fractions.

This contribution reports on the physico-chemical properties and the pozzolanic reactivity of the size-separated siliceous coal combustion ashes. The particle size distribution, specific surface area, density and chemical, mineralogical composition were measured for all size fractions. Quartz, iron oxide and unburnt carbon were found to be concentrated in the coarser fractions, amorphous phases and trace elements were more abundant in the finer fractions.

The R3 heat release test for measuring chemical reactivity as supplementary cementitious material showed a strong dependence of reactivity on particle size. The finest fractions were found to be twice as reactive as the initial fly ash, the coarse fraction only half. The reactivity-particle size relationship was further investigated using a microstructure based kinetic model to calculate the intrinsic volumetric reaction rate of the fly ash. The model simulations confirm the first order impact of particle size on reactivity, however they indicate that also secondary effects such as density variations should be included to fully explain the reactivity measurements.

The impact of the very fine and medium fly ash size fractions on cement hydration was investigated on cement blends using isothermal calorimetry and X-ray diffraction. The effect on compressive strength development was measured on mortar bars with 30% replacement of Portland cement (CEM I 42.5 R) by fly ash. The results confirm the higher reactivity of the very fine fly ash by showing higher heat release, more portlandite consumption and more rapid and greater strength development.

Keywords: Coal combustion fly ash, Pozzolan, Reactivity, Hydration, Blended cement

1. Introduction

To keep the global temperature rise well below 2°C above pre-industrial levels, global anthropogenic greenhouse gas emissions will need to be drastically reduced on the short term [1, 2]. Already by 2030, the EU commits to a reduction of at least 40% of the 1990 emissions to avoid the far-reaching impacts of climate change [3]. To accomplish such drastic cuts at the short term, all greenhouse gas emitting human activities will need to be concerned and undergo intensive changes. Energy-efficiency measures need to find widespread adoption in appliances, buildings and industrial processes, while shifts towards low-carbon technologies in energy generation and transport gain impetus. Simultaneously also the global warming impact of the composing materials will need to be tackled by a transition to a more circular economy that makes more efficient use of materials that require carbon or energy intensive production processes [4].

In response to rising global demands for housing and transport infrastructure, the production of building materials such as concrete has increased strongly over the last decades, predominantly in rapidly developing countries such as China and India, reaching a global estimate of 30-40 Gt/y of produced concrete in 2017 [5]. In conventional concrete products the Portland cement binder is responsible for about 75-80% of the embodied CO₂ [6]. Pure Portland cement consists of 95% clinker and minor additives, mostly calcium sulphates. The production of Portland clinker from (impure) limestone and corrective raw meal additions emits about 0.9 tonne of CO₂ per tonne of clinker [7]. Since modern clinker production processes are nearing the thermodynamic energy efficiency limit, the most appropriate approach to reducing the global warming impact of concrete is by making efficient use of Portland clinker [8]. This approach can be adopted by various actors along the value chain. Cement producers blend in supplementary cementitious materials (SCMs) to partially substitute clinker in composite cements. Also concrete producers add in SCMs at the concrete mixing stage to replace clinker. Concrete producers can minimise clinker levels in their concrete design, e.g. by optimising the concrete particle size grading or by using microfillers. Finally designers and end-users may opt for low-impact high-performance products containing high-grade microfillers or SCMs and as such reduce material volumes as well as clinker volumes [9].

As such, high grade mineral powders suitable for use in concrete are essential in achieving substantial CO₂ emission savings in the clinker efficiency approach. In terms of fine mineral additions for concrete a distinction is made between inert and reactive materials. Largely inert materials comprise quartz dust or finely ground limestone and contribute to the properties mainly through physical interactions, such as improving particle packing. Reactive powders contribute to the concrete properties by undergoing a chemical reaction with the hydrating Portland cement. A distinction among reactive materials is generally made between (latent) hydraulic and pozzolanic materials. Latent hydraulic materials do not require a source of soluble Ca but will spontaneously hydrate when contacted with water and, if need be, small amounts of (alkali) activator to initiate the hydration. Pozzolanic materials, on the other hand, require a soluble source of Ca to form typical cement hydrates and trigger a continuous hydration reaction [10]. Blast furnace slag generated in the smelting of iron ore to pig iron behaves typically as a latent hydraulic material, fly ash generated during combustion of hard coal for electricity production typically behaves as a pozzolanic material. Given the scale of production of Portland clinker (3.2 Gt/y) it is obvious that large volumes of SCMs and fillers need to be available for substitution [5, 11]. In this respect, blast furnace slag supplies are practically exhausted by their use in cement in concrete and other materials are needed. Considerable research efforts are therefore directed towards extending supplies of SCMs. Different approaches are followed. Next to exploring the behaviour of materials for which little experience exists in terms of use as SCM, ternary blends of common SCMs, including limestone, and clinker have been thoroughly investigated to establish viable combinations and formulation boundaries [12-14]. This paper treats new SCMs that were obtained by post-processing of candidate SCMs, in this case coal combustion fly ashes. Post-processing is

generally applied to improve material quality, i.e. it can transform off-spec materials into candidate SCMs that comply to standard specifications, or it can generate SCMs that have superior properties to regular products. In view of enhancing clinker efficiency, processing of mineral powders can enable more dense particle packing and can increase SCM reactivity to obtain a denser and more durable microstructure of low-clinker cements.

Coal combustion fly ashes are globally one of the most used SCMs. Based on global coal consumption for electricity generation about 1 Gt/y of fly ashes are generated, of which an estimated third is used in cement and concrete applications [5, 11]. The rate of use is highly variable by region, depending partly on logistics and local incentives to accommodate reuse, but is also determined to a large extent by the actual material properties and associated quality as SCM. Coal quality, precombustion treatment, combustion conditions and fly ash collection technology all impact ash properties [15, 16]. Most common ash deficiencies are the content of unburnt carbon, excessive sulphate contents, free lime in calcareous fly ashes, and low reactivity for siliceous fly ashes. Low reactivity is generally related to large fractions of inert materials such as quartz, mullite or coarse particles [17]. To recover usable materials from low reactivity fly ashes or to tailor fly ash fineness, screening, classification and/or comminution treatments can be applied. Earlier work has shown clear positive effects of finer fly ash on reactivity with cement, and concrete properties such as strength development, pore structure and durability [18-20]. This paper describes how fly ash quality varies for a range of classified size fractions obtained from a dry powder classification device under development. Material properties of the classified fractions are characterised, including pozzolanic reactivity measured by the R3 calorimetry test, and the impact of the fly ash on the hydration kinetics and hydrate assemblage of composite cements are reported. Finally microstructure-based kinetic modelling is applied to quantitatively assign the impact of particle size on reactivity.

2. Methodology

2.1 Materials

The starting materials in this study were a siliceous fly ash and a pure Portland cement of type CEM I 42.5 R. The siliceous fly ash was classified by a proprietary prototype device into 4 fractions of different particle size distribution, henceforth they will be designated as ultrafine, very fine, medium, and coarse fraction. The prototype was developed and tested in the FLAME project, in the device fly ashes are separated based on size in a dry, closed system. For the pozzolanic reactivity test material replicates resulting from different classification runs on the same starting material were included.

The impact of fly ash fineness and processing on cement hydration was assessed for two different fractions, i.e. the very fine fraction and the medium fraction obtained through classification. A Portland cement replacement level of 30 wt.% was used. Thus, including the reference Portland cement, the hydration of a total of 3 cements was studied.

2.2 Methods

The bulk chemistry, mineralogy and physical properties of the starting materials as well as the classified fly ashes were measured. The chemical composition was measured by X-ray Fluorescence (XRF) spectroscopy on beads. Loss on Ignition (LOI) and Total Organic Carbon (TOC) were determined according to EN 196-2 and EN 15936. To investigate the distribution of trace elements acid digestates of the different size fractions were analysed by Inductively Coupled Plasma – Optical Emission Spectrometry (ICP-OES). The mineralogical composition was determined using Rietveld analysis of X-ray powder diffraction (XRD) scans. The amorphous phase was quantified using the external standard method applied to the Rietveld fitting results. Rietveld analysis was based on the procedure and starting crystal structures given by [21].

The particle size distribution of the materials was measured by a Microtrac s3500 laser diffractometer on samples dispersed in isopropanol suspensions using ultrasonication. The specific surface area was measured using BET analysis of N₂ sorption data of samples off-gassed at 40 °C overnight. The specific gravity of the samples was measured by He pycnometry. Scanning electron microscopy (FEI FEG NanoSEM) was applied on Pd-coated powder stubs for imaging of the size, shape and surface texture of the different size fractions.

The pozzolanic reactivity of the fly ashes was evaluated using the R3 calorimetry test [22]. This test measures the heat release of a model mixture of the SCM, Ca(OH)₂, H₂O and small additions of reagent grade CaCO₃, K₂SO₄ and KOH. The model system simulates the reaction environment of the SCM in a hydrating Portland cement, by eliminating the Portland cement component itself the reaction of the SCM can be measured directly. The test protocol is described in more detail in [23]. The isothermal calorimetry measurements were made using a TAM Air calorimeter calibrated at 40°C, heat flow data were recorded until 7 days after mixing.

The reaction kinetics for the different particle fractions of fly ash from the R3 test is modelled using CemRS assuming particles to be spherical [24]. The model uses the uniform reactive thickness concept [25] which assumes that the depth of dissolution is constant irrespective of the size of the particle. While most models use a time dependent variation in the reactive thickness [26, 27], the CemRS model uses a constant reactive thickness. Such a model assumes that the reaction is controlled by isotropic dissolution of the fly ash particles.

The impact of the classified fly ashes on the hydration and performance of blended cements was carried on the paste and mortar level. The cement replacement level by fly ash was 30 wt.% on a solids base. For the pastes a water to binder of 0.4 was used for all mixes. The solids were premixed by hand, and all materials were equilibrated at room temperature before mixing. About 120 g of cement paste was mixed at 1600 rpm during 2 min using an overhead mixer. 15 g of paste was immediately transferred to calorimeter flasks, closed, and introduced into the measurement channel for recording of the heat flow. Isothermal calorimetry measurements were made at 20°C for 28 days. The remainder of the paste was cast into HDPE containers, sealed air-tight using wax paper, and left to cure at 20 °C until the sampling time. After 1, 2, 7, 14, 28 and 90 days disks of the hardened paste were cut. The slices were slightly polished on sandpaper, flushed with water to remove polishing residue and superficially dried and subsequently measured by XRD as a “fresh” disk to study the hydration product assemblage.

Mortar bars of the reference and composite cements were prepared according to EN 196-1, the strength development was measured accordingly at 2, 7 and 28 days.

3. Results and discussion

3.1 Characterisation of the starting materials

The chemical and mineralogical composition of the fly ash and cement starting materials are reported in Table 1. The fly ash has a chemical composition typical for a siliceous fly ash, the amorphous content is relatively high, which could be indicative for above average reactivity. The Portland cement composition is normal for a good quality CEM I, the alite (C₃S M3) content is relatively high, C₃A and C₄AF are balanced. Limestone was to be added as minor constituent, but is below the 5% limit for CEM I. The physical properties of each are summarized in Table 2. The initial fly ash has a relatively broad particle size distribution, with a significant fraction under 3 µm. This makes the fly ash an interesting candidate material for further classification treatment. The Portland cement had a d₅₀ of 14 µm, this slightly coarse PSD is in line with the declared cement strength class of 42.5 R.

3.2 Characterisation of size-classified fly ashes

The classification device generated 4 different fractions of fly ash. The particle size distribution curves of these fractions and the initial fly ash are given in Figure 1. The classification mass balance, i.e. the mass fraction of each classified fly ash, and the particle size grading and physical properties of the fly ash fractions are summarized in Table 3. The ultrafine and very fine fractions are close in terms of physical properties; also the medium and coarse fractions are similar.

The ultrafine and very fine fractions represent the bulk of the fraction smaller than 10 µm in the initial fly ash, the recovery yield being 76 % based on the initial fly ash particle size distribution. It should be noted that a compilation of the different fly ash fractions results in a reconstituted particle size distribution which is considerably finer than the initial fly ash. This indicates that the classification treatment leads to particle refinement, either through particle deagglomeration or milling of fly ash particles.

Table 1. Chemical and mineralogical composition of the starting materials – siliceous fly ash and Portland cement

	Raw fly ash	Portland cement		Raw fly ash	Portland cement
	Wt.%	Wt.%		Wt.%	Wt.%
Al ₂ O ₃	22.7	5.2	Quartz	8.1	0.9
SiO ₂	54.4	20.8	Mullite	6.7	-
CaO	3.0	62.1	Magnetite	2.3	-
MgO	1.6	2.0	Hematite	1.4	-
K ₂ O	2.7	1.2	Calcite	0.7	4.8
Na ₂ O	1.1	0.2	Anhydrite	0.6	0.4
Fe ₂ O ₃	8.7	1.9	C ₃ S M3	-	65.7
Mn ₂ O ₃	0.1	-	β C ₂ S	-	13.1
TiO ₂	0.9	0.2	C ₃ A cubic	-	4.2
P ₂ O ₅	0.2	0.3	C ₄ AF	-	6.7
SO ₃	0.3	2.7	Periclase	-	0.9
LOI	4.2	2.4	Gypsum	-	1.8
TOC	3.9	-	Bassanite	-	0.7
			Aphthalite	-	1.0
			Amorphous	80.1	-

Table 2. Physical properties of the starting materials of this study – siliceous fly ash and Portland cement

Sample	Specific surface area	Specific gravity	Particle size distribution		
	m ² /g	g/cm ³	d ₁₀ (µm)	d ₅₀ (µm)	d ₉₀ (µm)
Raw fly ash	4.6	2.40	3.0	21	88
Portland cement	1.2	3.13	2.4	14	42

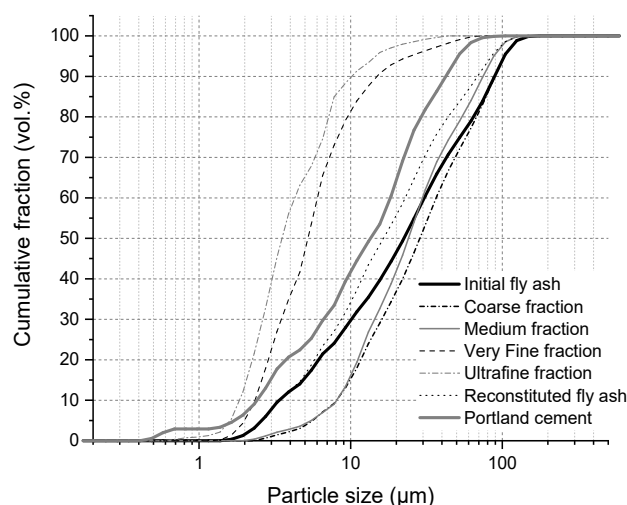


Figure 1. Particle size distribution of the initial and classified fly ashes measured by laser diffractometry.

The main oxide chemical composition of the classified fly ash fractions is given in Table 4. The trace element composition of the respective fractions is reported in Table 5. A distinction between the ultrafine and very fine fractions on the one hand, and the medium and coarse fraction is apparent. The fine fractions are enriched in Al_2O_3 , and to a lesser extent in alkalis and sulphate than the initial fly ash. In exchange the coarser fractions show higher SiO_2 , CaO and Fe_2O_3 than the feed material. A more pronounced repartitioning is noted for the trace element composition. The finer fractions show strong enrichment in As, Cd, Cr, Cu, Hg, Mo, Ni, Pb, V and Zn. Previous studies reported that these hazardous volatile elements (HVEs) metals are captured as condensates sorbed on or encapsulated in nanoparticles such as nano-sulphates, iron nano-hydroxides and residual carbonaceous materials [28].

Table 3. Physical properties of the classified fly ash fractions

Property	Ultrafine fraction	Very fine fraction	Medium fraction	Coarse fraction
Classification mass balance (wt.%)	2.6	25	61.2	11.2
d_{10} (μm)	1.6	2.2	6.8	6.9
d_{50} (μm)	3.0	5.0	22	27
d_{90} (μm)	9.3	12.5	73	90
Specific surface area (m^2/g)	7.1	6.9	4.4	3.6
Specific gravity (g/cm^3)	2.55	2.50	2.32	2.28

Table 4. Major element composition, expressed as oxides, of the classified fly ash fractions

Oxide	Ultrafine fraction	Very fine fraction	Medium fraction	Coarse fraction
	Wt.%	Wt.%	Wt.%	Wt.%
Al_2O_3	26.0	25.5	21.6	21.9
SiO_2	51.9	52.3	55.2	55.5
CaO	2.2	2.3	3.3	3.2
MgO	1.8	1.7	1.6	1.6
K_2O	3.4	3.3	2.5	2.6
Na_2O	1.4	1.4	1.0	1.0
Fe_2O_3	7.7	7.6	9.1	9.1
Mn_2O_3	0.09	0.08	0.11	0.10
TiO_2	1.0	1.0	0.9	0.9
P_2O_5	0.3	0.3	0.2	0.2
SO_3	0.5	0.5	0.2	0.2
LOI	4.3	4.5	4.1	4.7
TOC	3.2	3.7	3.9	4.7

The phase composition measured by XRD-Rietveld analysis of the classified fly ashes is shown in Table 6. The repartitioning of phases over the different fractions is in line with the observed contrasts in chemical composition and earlier characterisation studies on classified fly ash [29]. The enrichment of SiO_2 in the coarser fractions is largely explained by higher quartz and mullite levels. Also the concentration of Fe_2O_3 in the coarser fractions is clarified by an enrichment in crystalline iron oxides such as magnetite and hematite. In the finer fractions, anhydrite is slightly enriched in line with the higher SO_3 levels. Most important in terms of reactivity, however, is the significantly higher amorphous content of the finer fractions. A visual impression of particle size and shape was obtained through SEM imaging. Representative SEM pictures of the ultrafine and the medium size fractions are given in Figure 2. The ultrafine and very fine fractions consist predominantly of spherical particles, with a large fraction of spheres below 5 μm . The medium fly ash fraction is generally more coarse and contains more irregularly shaped particles, such as flaky or angular particles. Still, spherical particles smaller than 5 μm are clearly present in the medium fraction. Part of these particles occur in agglomerates or are partially welded onto the surface of large particles.

Table 5. Trace element composition of the classified fly ash fractions

Element	Ultrafine fraction	Very fine fraction	Medium fraction	Coarse fraction
	mg/kg	mg/kg	mg/kg	mg/kg
<i>As</i>	133	107	35.2	32.9
<i>Ba</i>	1670	1570	1350	1350
<i>Be</i>	10.2	9.8	6.7	6.5
<i>Cd</i>	4.88	3.97	1.46	1.36
<i>Co</i>	45.7	42.7	33.2	32.6
<i>Cr</i>	234	188	112	115
<i>Cu</i>	137	123	72	72
<i>Hg</i>	0.93	0.91	0.25	0.3
<i>Mo</i>	47.1	41.4	18.8	18.4
<i>Ni</i>	173	146	93.8	92.1
<i>Pb</i>	151	135	53	50
<i>Sr</i>	495	501	484	477
<i>V</i>	342	309	216	220
<i>Zn</i>	527	434	153	152
<i>Zr</i>	118	121	126	126

Table 6. Phase composition of the classified fly ash fractions

Phase	Ultrafine fraction	Very fine fraction	Medium fraction	Coarse fraction
	Wt. %	Wt. %	Wt. %	Wt. %
<i>Quartz</i>	3.1	3.6	9.8	9.7
<i>Mullite</i>	5.4	5.7	7	7.5
<i>Hematite</i>	0.6	0.8	1.7	1.6
<i>Magnetite</i>	0.6	0.8	2.8	2.8
<i>Anhydrite</i>	0.8	0.8	0.5	0.7
<i>Calcite</i>	0.8	0.7	0.7	0.9
<i>Amorphous</i>	88.7	87.5	77.5	76.8

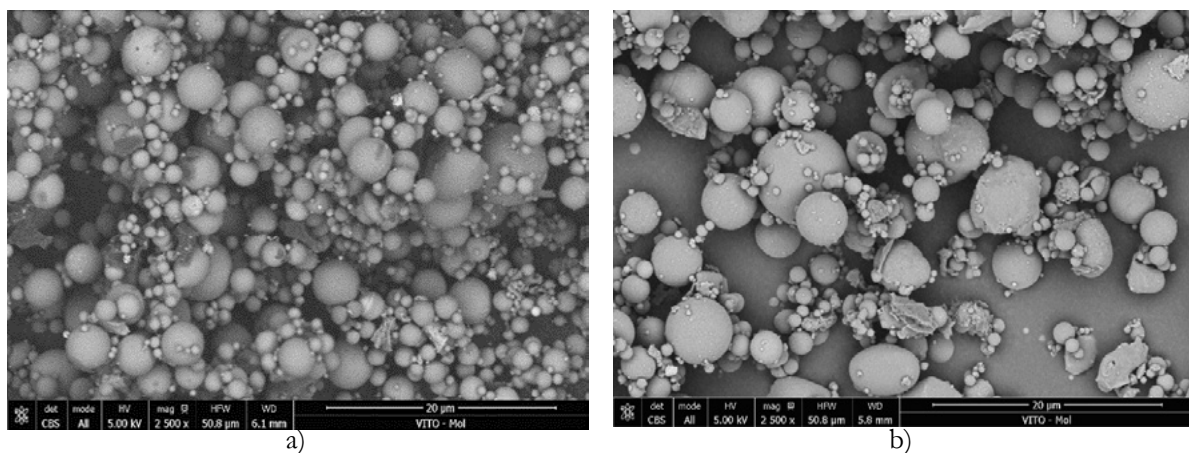


Figure 2. SEM pictures of a) ultrafine fly ash and b) medium size fly ash obtained through classification.

3.3 Reactivity of size-classified fly ashes

The R3 SCM reactivity test is used to measure the chemical (pozzolanic and hydraulic) reactivity of the fly ash fractions obtained by classification. For the ultrafine and very fine fractions, samples from different classification runs performed under different operating conditions were included to increase the number of different results. The particle size distribution of the tested materials is shown in Figure 3. The heat release by the hydration reaction of the fly ash fraction in combination with water, calcium hydroxide, calcium carbonate and small amounts of KOH and K_2SO_4 was measured by isothermal calorimetry at 40 °C. The cumulated heat results until 7 days of reaction are given in Figure 4.

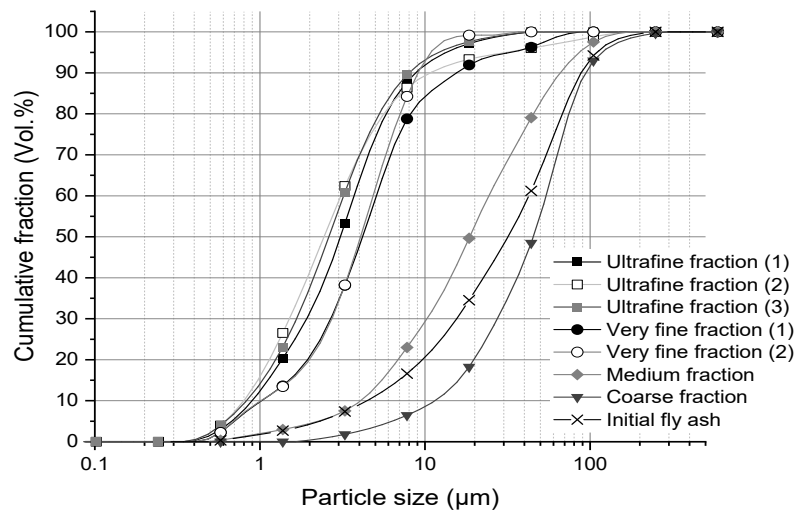


Figure 3. Particle size distribution of all fly ash fractions tested by the R3 reactivity test. The number in brackets indicates that the material was obtained by replicate classification runs.

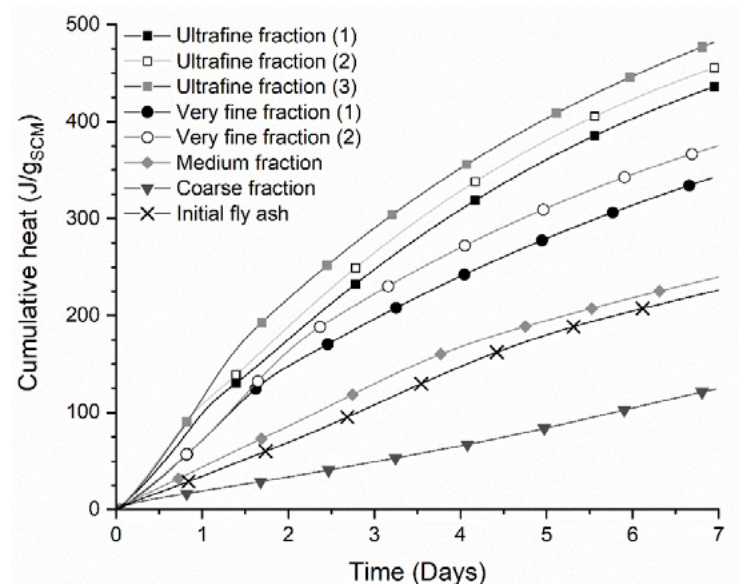


Figure 4. Fly ash reactivity as measured by the R3 calorimetry test. The cumulative heat released by the reaction of the fly ashes over time is a proxy for reactivity. The number in brackets indicates that the material was obtained by a replicate classification run.

The heat release at isothermal conditions can be related directly to the enthalpy difference between products and starting materials. Previous research has shown that the heat release is directly related to the water

bound [23], which is supported by the enthalpy calculations for common cement hydration reactions [30]. More than assessing pozzolanic reactivity, the test results relate to hydration reactivity of the SCM directly and thus avoid issues in determining portlandite consumption rates.

In case of the classified fly ashes, the test results clearly show that the reactivity increases with decreasing particle size. The initial fly ash and the medium fraction show similar heat release and are moderately reactive. The coarser fraction clearly shows reduced reactivity. The very fine and ultrafine fractions clearly show enhanced reactivity in order of decreasing particle size distribution.

To verify whether differences in particle size of the different fraction can explain the noted differences in reactivity microstructure based kinetic modelling was carried out using the particle size distributions from Figure 3. Figure 5 compares the cumulative heat release measured from the isothermal calorimeter and numerical simulations. Based on thermodynamic calculations the simulations assumed the enthalpy of reaction to be 600 J/g. The rate of dissolution was fitted to the experimental data. For both the ultrafine and very fine fractions good fits were obtained using 0.003 $\mu\text{m}/\text{h}$. For the medium and coarse fraction 0.006 $\mu\text{m}/\text{h}$ was obtained. For the initial fly ash 0.008 $\mu\text{m}/\text{h}$ was used. There can be different ways to explain the higher dissolution rates for the coarser fractions. On the one hand, a larger fraction of hollow particles in the coarser fractions (which were found to have significantly lower specific gravity) could positively affect the reaction rate by exposing additional reactive surface once the outer shell is partially consumed. On the other hand experimental effects such as agglomeration of fly ash particles could reduce the reaction rates for the finer fractions. It should also be noted that the simplified approach for modelling presumed isotropic dissolution which was constant over time which may conflict with experimental evidence. The reasons for the discrepancy in dissolution rates will be further investigated in the future.

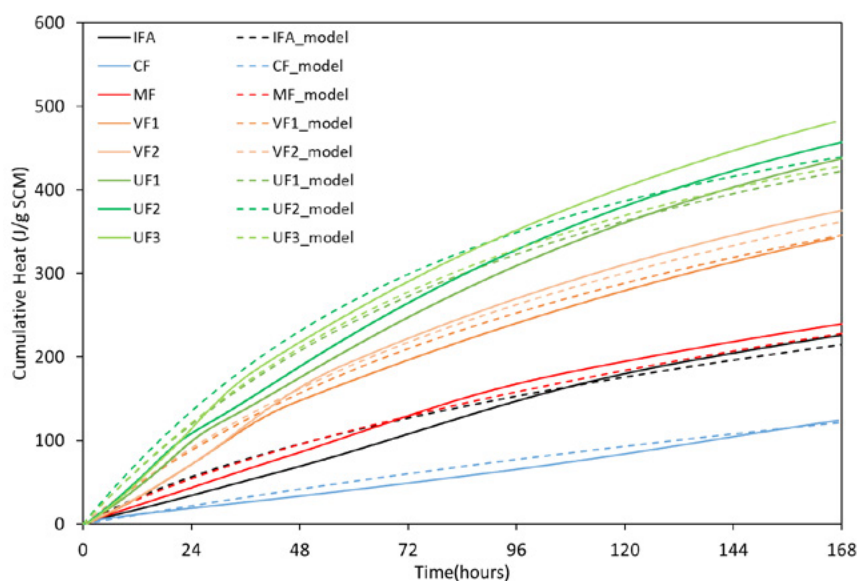


Figure 5 Comparison of experimental heat release from the R3 test (solid line) and simulations (dashed line).

3.4 Impact of fly ash fineness on cement hydration

The replacement of Portland cement by SCMs affects the hydration kinetics and hydration product assemblage. In return, also the strength of the cement changes. In this study the impact of fly ash fineness on cement hydration kinetics was evaluated through measurement of the hydration heat flow by isothermal calorimetry. During hydration the cements were kept at 20°C inside the calorimeter. The heat flow over the first seven days of hydration is shown in Figure 5. A comparison is made between the pure Portland

cement, and the composite cements in which 30 wt.% of the Portland cement is substituted by siliceous fly ash of different fineness, i.e. the very fine and the medium fractions obtained through classification. The calorimetry measurements did not show noticeable changes in the acceleration period of the main hydration peak. The duration of the main hydration peak is lengthened in the composite cements, in particular in case of Portland cement replacement by very fine fly ash. Even more clear is the delay and extension of the heat release peak (shoulder) in the deceleration period, usually explained as an increase in hydration of calcium aluminates upon depletion of solid sulphates. Possibly the presence of some anhydrite in the fly ashes may lead to the delay and extension of the peak.

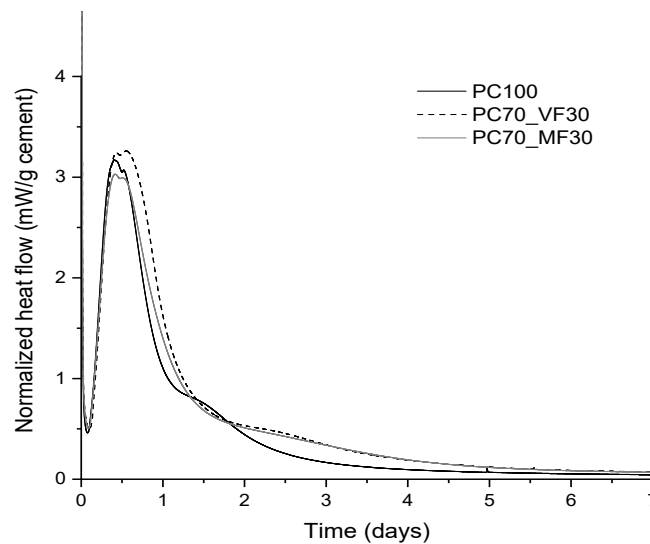


Figure 6. Heat flow measured by isothermal (20°C) calorimetry for the reference Portland cement paste (PC100), and composite cements in which 30% of Portland cement is replaced by the very fine (PC70_VF30) and the medium (PC70_MF30) particle size fractions of the classified fly ash. The heat flow data are normalised per gram of Portland cement.

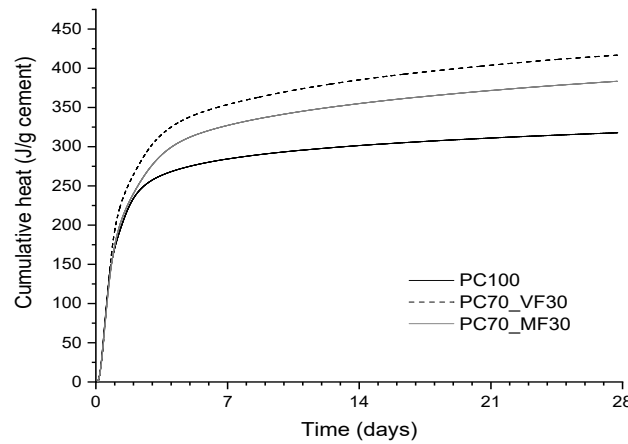


Figure 7. Cumulative heat measured by isothermal calorimetry for the reference Portland cement paste (PC100), and composite cements in which 30% of Portland cement is replaced by the very fine (PC70_VF30) and the medium (PC70_MF30) particle size fractions of the classified fly ash. The data are normalised per gram of Portland cement.

The shoulder peak in the composite cements between 2 to 5 days of hydration leads to a strong increase in cumulative heat signals of the composite cements compared to the reference cement in Figure 6. This overall increase in cumulative heat (normalised to Portland cement content) in composite cements is related to on the one hand additional reaction of the Portland cement also referred to as the filler effect, and on the other hand the reaction of the fly ash. The composite cement with the very fine fly ash shows, at the same

30 wt.% level, higher heat than the medium sized fly ash cement.

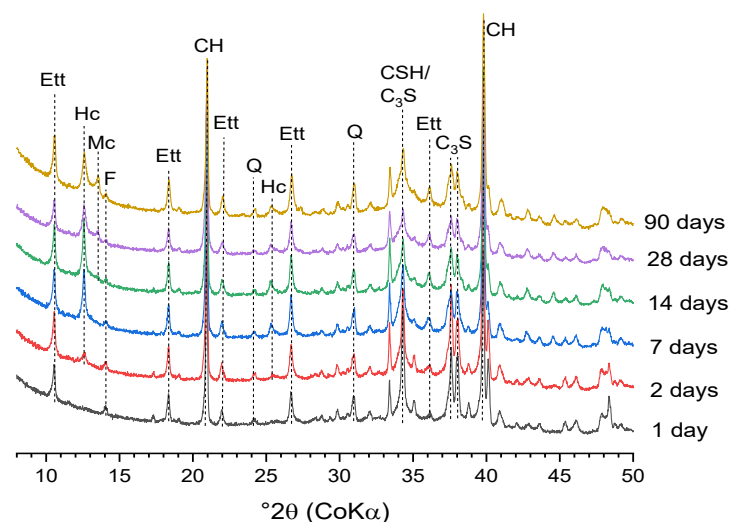


Figure 8. XRD scans of the hydrated composite cement with very fine fly ash (PC70_VF30). The development of the cement hydrate assemblage is shown for selected hydration ages. The main XRD peaks are labelled; Ett stands for ettringite, Hc for hemicarboaluminate, Mc for Monocarboaluminate; F for ferrite, CH for portlandite, Q for quartz, C₃S for alite and CSH for C-S-H.

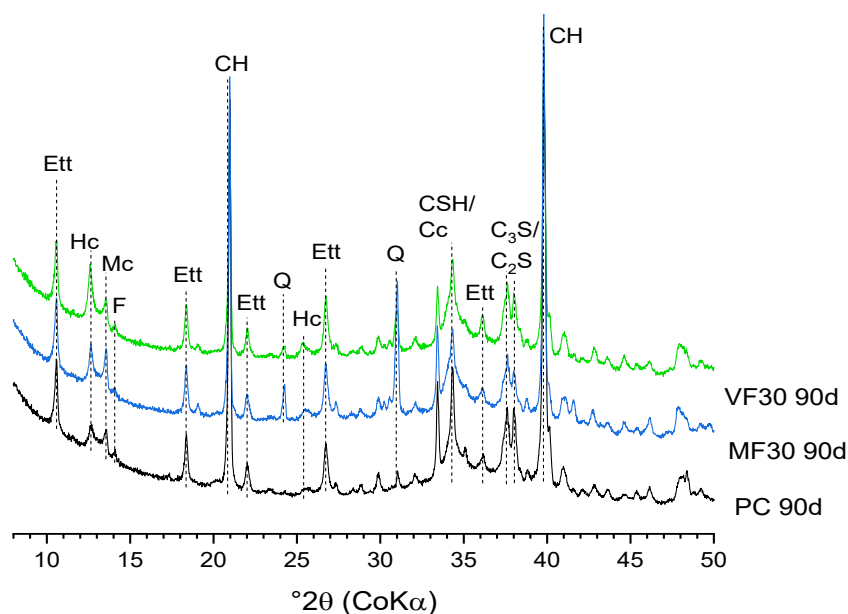


Figure 9. XRD scans of the studied cements at 90 days of hydration. The main XRD peaks are labelled; Ett stands for ettringite, Hc for hemicarboaluminate, Mc for Monocarboaluminate; F for ferrite, CH for portlandite, Q for quartz, C₃S for alite, C₂S for belite, Cc for calcite and CSH for C-S-H.

This implies that part of the additional heat is generated by the reaction of the fly ash, even at early ages of 1 to 2 days of hydration. Thus, it is apparent that the 2-5 days heat flow signal is not only related to renewed hydration of aluminate (C₃A), but also to the reaction of fly ash. In an extended study the reaction degree of the clinker phases and the fly ash will be quantified by Rietveld-PONKCS analysis of XRD data.

The formation of the cement hydration product assemblage was studied by qualitative XRD. XRD measurements on freshly cut disks were made up to 90 days of hydration. A representative time series is shown in Figure 7 for the composite cement containing very fine fly ash. At 1 day of hydration, ettringite is the main calcium aluminate hydrate product. C-S-H is present as well, but difficult to observe as broad

peak overlapping with the alite peaks. During further hydration the typical AFm phases appear. From 2 days onwards hemicarboaluminate can be discerned. Around 14 days, and more conspicuously at 28 days, moncarboaluminate appears. The formation of AFm-carbonate instead of monosulfoaluminate phases is caused by the presence of calcite in the Portland cement. A comparison of the XRD scans of the hydrated cements at 90 days of hydration in Figure 8 learns that the addition of fly ash did not result in important changes in types of products formed. However the fly ash composite cements do show higher peaks for the calcium aluminate hydration products and clearly reduced portlandite peaks, both are indicative for the pozzolanic reaction of the fly ash. The reduction in portlandite peak heights was greater for the very fine fly ash, in line with the higher reactivity measured by the R3 test.

The reactivity study was complemented with compressive strength data for mortar bars containing the reference and composite cements. The data compiled in Figure 9 show that the compressive strength development in the composite cements is slower than for the reference. The very fine fly ash composite cement catches up with the Portland cement by 28 days, the medium fly ash cement stays significantly below the Portland cement at all tested ages. The increased strength gain for the very fine fly ash can be largely related to the additional pozzolanic reaction, although an improved particle packing can also be expected to contribute to the higher strength.

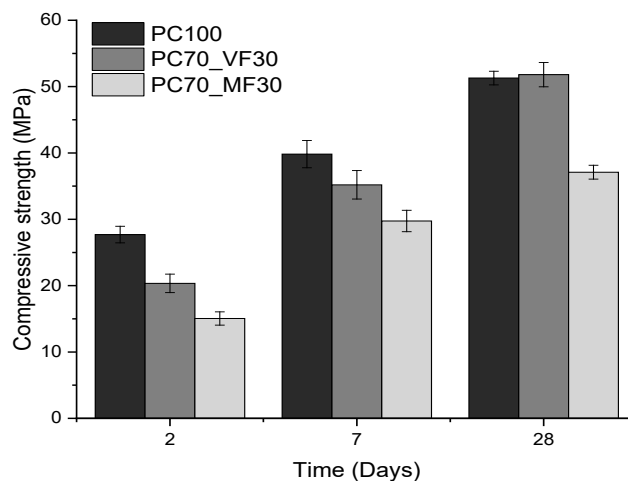


Figure 10. Mortar bar (EN 196-1) compressive strength results up to 28 days of hydration for the studied cements.

4. Conclusions

This paper described the physical properties and the chemical and mineralogical composition of fly ash fractions classified by an innovative, dry, closed-circuit classification device. The classification treatment produced four main fractions: i.e. an ultrafine fraction, a very fine fraction, a medium fraction and a coarse fraction. The ultrafine and very fine fractions had a d_{50} of 3 and 5 μm , the medium and coarse fraction 22 and 27 μm , respectively. As expected, the BET specific surface area was higher for the finer fractions; in contrast their specific gravity was higher, indicating less internal porosity or hollow cores. In terms of chemical composition the finer fractions were enriched in Al_2O_3 and depleted in SiO_2 and Fe_2O_3 , mainly reflecting concentration of quartz and iron oxide particles in the coarser fractions. In exchange the finer fractions contained higher amounts of amorphous material. The TOC increased with median particle size. Hazardous volatile elements on the other hand were considerably enriched in the finer fractions reflecting condensation on smaller particles.

The pozzolanic reactivity of the fly ash fractions measured using the R3 heat release test showed a

predominant effect of particle size. The finer the fraction, the higher the reactivity. The ultrafine fraction was about two times more reactive than the initial, non-classified fly ash. The coarse fraction was only half as reactive. Kinetic modelling indicated that secondary factors such as particle geometry need to be taken into account to fully explain the differences in reactivity. Hydration studies of cement and mortar containing the classified fly ashes confirmed the beneficial effect of fly ash fineness on reactivity by showing a.o. increased $\text{Ca}(\text{OH})_2$ consumption and strength development for finer fly ash.

4. Acknowledgments

RS, HK, ML, PN and LV gratefully acknowledge funding support by the European Institute of Innovation and Technology (EIT) RawMaterials received under PA 16390 FLAME – FLy Ash to valuable MinErals.

5. References

- [1] United Nations Framework Convention on Climate Change 2015. The Paris Agreement, Secretary-General of the United Nations, New York City, United States.
- [2] International Panel on Climate Change, 2014. Climate Change 2014: Synthesis Report. Contribution of Working Groups I, II and III to the Fifth Assessment Report of the Intergovernmental Panel on Climate Change, in: R.K. Pachauri, L.A. Meyer (Eds.), IPCC, Geneva, Switzerland.
- [3] European Commission, 2014. A policy framework for climate and energy in the period from 2020 to 2030, European Commission, Brussels, Belgium.
- [4] European Commission, 2018. A Clean Planet for all - A European strategic long-term vision for a prosperous, modern, competitive and climate neutral economy, European Commission, Brussels, Belgium.
- [5] K.L. Scrivener, V.M. John, E.M. Gartner, 2016. Eco-efficient cements: Potential economically viable solutions for a low- CO_2 cement-based materials industry, UNEP report, 64 pp.
- [6] M. De Schepper, P. Van den Heede, I. Van Driessche, N. De Belie, 2014. Life cycle assessment of completely recyclable concrete, *Materials*, 7, 6010-6027.
- [7] J.S. Damtoft, J. Lukasik, D. Herfort, D. Sorrentino, E.M. Gartner, 2008. Sustainable development and climate change initiatives, *Cement and Concrete Research*, 38, 115-127.
- [8] K.L. Scrivener, 2014. Options for the future of cement. *Indian Concrete Journal*, 88, 11-21.
- [9] A. Favier, C. De Wolf, K. Scrivener, G. Habert, 2018. A Sustainable Future for the European Cement and Concrete Industry - Technology assessment for the full decarbonisation of the industry by 2050, European Climate Foundation, Brussels, Belgium.
- [10] R. Snellings, G. Mertens, J. Elsen, 2012. Supplementary cementitious materials, *Reviews in Mineralogy and Geochemistry*, 74, 211-278.
- [11] R. Snellings, 2016. Assessing, understanding and unlocking supplementary cementitious materials, *RILEM Technical Letters*, 1, 50-55.
- [12] M. Antoni, J. Rossen, F. Martirena, K. Scrivener, 2012. Cement substitution by a combination of metakaolin and limestone, *Cement and Concrete Research*, 42, 1579-1589.
- [13] S. Adu-Amankwah, M. Zajac, C. Stabler, B. Lothenbach, L. Black, 2017. Influence of limestone on the hydration of ternary slag cements, *Cement and Concrete Research*, 100, 96-109.

- [14] K. De Weerd, M.B. Haha, G. Le Saout, K.O. Kjellsen, H. Justnes, B. Lothenbach, 2011. Hydration mechanisms of ternary Portland cements containing limestone powder and fly ash, *Cement and Concrete Research*, 41, 279-291.
- [15] K. Sideris, H. Justnes, M. Soutsos, T. Sui, 2018. Fly Ash, In: De Belie, N., Soutsos, M., Gruyaert, E. (eds.), *Properties of Fresh and Hardened Concrete Containing Supplementary Cementitious Materials*, Springer, pp. 55-98.
- [16] H.S. Pietersen, A.L. Fraay, J.M. Bijen, 1989. Reactivity of fly ash at high pH, *MRS Online Proceedings Library Archive*, 178.
- [17] Z. Yao, X. Ji, P. Sarker, J. Tang, L. Ge, M. Xia, Y. Xi, 2015. A comprehensive review on the applications of coal fly ash, *Earth-Science Reviews*, 141, 105-121.
- [18] K.H. Obla, R.L. Hill, M.D. Thomas, S.G. Shashiprakash, O. Perebatova, 2003. Properties of concrete containing ultra-fine fly ash, *ACI materials journal*, 100, 426-433.
- [19] P. Chindaprasirt, S. Homwuttiwong, V. Sirivivatnanon, 2004. Influence of fly ash fineness on strength, drying shrinkage and sulfate resistance of blended cement mortar, *Cement and Concrete Research*, 34, 1087-1092.
- [20] P. Chindaprasirt, C. Jaturapitakkul, T. Sinsiri, 2007. Effect of fly ash fineness on microstructure of blended cement paste, *Construction and Building Materials*, 21, 1534-1541.
- [21] R. Snellings, 2016. X-ray powder diffraction applied to cement, in: Scrivener, K.L., Snellings, R., Lothenbach, B.L. (eds.) *A practical guide to microstructural analysis of cementitious materials*. CRC Press, Boca Raton, pp. 107-176.
- [22] X. Li, R. Snellings, M. Antoni, N.M. Alderete, M.B. Haha, S. Bishnoi, Ö. Cizer, M. Cyr, K. De Weerd, Y. Dhandapani, 2018. Reactivity tests for supplementary cementitious materials: RILEM TC 267-TRM phase 1, *Materials and Structures*, 51, 151.
- [23] F. Avet, R. Snellings, A.A. Diaz, M.B. Haha, K. Scrivener, 2016. Development of a new rapid, relevant and reliable (R3) test method to evaluate the pozzolanic reactivity of calcined kaolinitic clays, *Cement and Concrete Research*, 85, 1-11.
- [24] S. Joseph, K. Van Balen, S. Bishnoi, Ö. Cizer, CemRS: fast and efficient modelling platform for the simulation of cementitious systems, 2016. *International RILEM Conference Materials Systems and Structures in Civil Engineering 2016 (MSSCE 2016) on Service Life of Cement-Based Materials and Structures*, pp. 573-579.
- [25] P. Termkhajornkit, R. Barbarulo, 2012. Modeling the coupled effects of temperature and fineness of Portland cement on the hydration kinetics in cement paste, *Cement and Concrete Research*, 42, 526-538.
- [26] S. Bishnoi, K.L. Scrivener, µic, 2009. A new platform for modelling the hydration of cements, *Cement and Concrete Research*, 39, 266-274.
- [27] K. Van Breugel, 1995. Numerical simulation of hydration and microstructural development in hardening cement-based materials (I) theory, *Cement and Concrete Research*, 25, 319-331.
- [28] M.L. Oliveira, F. Marostega, S.R. Taffarel, B.K. Saikia, F.B. Waanders, K. DaBoit, B.P. Baruah, L.F. Silva, 2014. Nano-mineralogical investigation of coal and fly ashes from coal-based captive power plant (India): an introduction of occupational health hazards, *Science of the Total Environment*, 468, 1128-1137.

- [29] M. Jones, A. McCarthy, A. Booth, 2006. Characteristics of the ultrafine component of fly ash, Fuel, 85, 2250-2259.
- [30] R. Snellings, X. Li, F. Avet, K. Scrivener, 2019. A rapid, robust and relevant R3 reactivity test for supplementary cementitious materials, ACI Materials.

Evaluation of calcined dredged sediments as supplementary cementitious materials

H. Kazemi-Kamyab¹, L. Van den Abeele¹, M. Henry², L. Haouche³, R. Snellings¹

¹ Sustainable Materials, Flemish Institute of Technological Research (VITO), Boeretang 200, B-2400 Mol, Belgium

² Centre Terre et Pierre (CTP), Chaussée d'Antoine 55, 7500 Tournai, Belgium

³ Institut Scientifique de Service Publique (ISSEP), Rue de la Platinerie 12/Z, 7340 Colfontaine, Belgium

Email of the corresponding author: hadi.kamyab@vito.be

Abstract

Valorisation of the dredging sediments has gained a lot of attention over the recent years. An application route that has attracted considerable interest is the use of calcined dredged sediments as Supplementary Cementitious Material (SCM) in composite cements to replace clinker.

The present study investigates the valorisation potential of sediments dredged from three different inland waterway locations in the Belgian – French cross-border region as part of the Interreg V France-Wallonie-Vlaanderen VALSE project. The objective is to evaluate the optimum calcination temperature of the sediments at which the calcined sediments would be most reactive as SCMs. The sediment filter cake (raw) from each location was calcined at 500 °C, 600 °C, 700 °C and 800 °C. Physical and chemical characteristics were evaluated as a function of the calcination temperature.

The results show that the optimum calcination temperature was at 800°C for Brussels-Charleroi (BC) and Lens (L), and 700°C for Gent-Terneuzen (GT). The optimum calcination resulted in degradation of organic matter, which along with densification of particles and sintering, decreased the specific surface area and increased the particle size; furthermore the optimum calcination resulted in activation of clay minerals, and dissolution of CaCO₃. The R³ test method confirmed the optimum calcination temperature for each sediment to have the highest pozzolanic reactivity in the model system. Furthermore it was seen from the R³ test that all calcined sediments had comparable or even better reactivity as regular siliceous fly ashes.

Keywords: Dredged sediments, Supplementary cementitious materials, Calcination, Pozzolanic activity

1. Introduction

The buildup of sediments in ports, channels, reservoirs and dams can significantly alter their foreseen designed functionalities. In Europe the disposal of the dredged sediment by landfilling has become already an inferior option due to unwanted ecological effects, cost of landfilling, and scarcity of suitable landfilling sites. That is why valorization of the dredging sediments are of paramount importance and have gained a lot of attention.

Valorization routes for dredged sediments that have been considered include use in large-scale civil engineering works such as hydraulic or road works, use as raw material in the production of fired bricks or light-weight aggregates or use as raw material in the production of Portland clinker [1]. An application route that has received considerable recent attention is the use of calcined dredged sediments as Supplementary

Cementitious Material (SCM) in composite cements to replace clinker [2-4]. As such it could contribute to reducing the CO₂ impact of cement production. In addition careful selection and preparation of SCMs and their replacement levels can improve the rheological, mechanical and durability of concrete [5-7].

However due to the heterogeneity of the dredged sediments and different sources of contaminants such as heavy metals, and organics, most studies carried out are site specific. In order to be able to have a holistic approach toward their utilizations as an SCM, a broader investigation needs to be undertaken on a regional level. Characterizing the dredged sediments of several specific sites within a region provides the necessary information to gain better understanding of important parameters influencing their reactivity as SCMs. In this context the present study investigates the valorisation potential of sediments dredged from inland waterways in the Belgian – French cross-border region as part of the Interreg V France-Wallonie-Vlaanderen VALSE project. This region has experienced strong (historic) industrial activity resulting in increased concentrations of heavy metals and organic contamination in some areas. Dredged sediments with different composition and varying heavy metal and organic material contamination from three different locations were considered: Brussels-Charleroi (BC) channel, Gent-Terneuzen (GT) channel and Lens (SO) channel sediment.

The outcome will be to use the results obtained in the regional scale to assist in framing guidelines on influential parameters that can affect the pozzolanic activity of the calcined sediments as a SCM and also how to deal with contaminations.

2. Materials & Methods

Dredged sediments from three different locations were considered: Brussels-Charleroi (BC) channel, Gent-Terneuzen (GT) channel and Lens (SO) channel sediment. Herein for each sediment before calcination the sand fraction (>63 µm) was removed and the remaining fine fraction was dewatered using a pilot filter press. The obtained sediment filter cake (here defined as raw) was calcined for 1 hour in a box furnace under static conditions at the following temperatures 500 °C, 600 °C, 700 °C and 800 °C, in air. The following material designation is used herein:

1. For raw filter cakes: “Location-Raw”. For instance BC-Raw means the raw filter cake from Brussels-Charleroi (BC) channel.
2. Associated calcinated temperatures: “Location-Temperature.” For instance BC-500 °C means the BC raw filter cake calcined at 500 °C.

The chemical composition of the raw sediments were obtained using VARIAN Vista MPX Radial inductively coupled plasma (ICP). A sediment sample was attacked with regia water under reflux for 4 hours. After filtration, the residue undergoes alkaline fusion (in a crucible, under a Bunsen nozzle and in the presence of fluxes [NaOH and Na₂O₂]). The result of the alkaline fusion and the filtrate of the regia water attack are then analysed by inductively coupled plasma - optical emission spectrometry (ICP-OES).

Physical and chemical characteristics were evaluated as a function of the calcination temperature by means of BET N₂ sorption, laser diffraction particle size analysis, helium pycnometry, thermogravimetric analysis (TG), X-ray powder diffraction (XRD), Total Inorganic Carbon (TIC) and Total Organic Carbon (TOC) analysis, and bomb calorimetry to measure the sample calorific value.

The specific surface areas were measured using a Quantachrome Nova 3000 instrument with Brunauer–Emmett–Teller (BET) N₂ sorption method; the materials were pre-treated by degassing at 40 °C under N₂ atmosphere for 16 h.

Particle size distributions (PSD) were evaluated using a Microtrac S3500 laser diffraction setup. The powders were first pre-treated by dispersing them in distilled water and ammonium polyacrylate, followed by external ultrasonication at 270 W for 2 min.

The density of the powders was evaluated using a Micromeritics Accupyc II 1340 Helium pycnometer. Approximately 1.5 to 2 g of powders are used to carry out the analysis.

Thermogravimetric analysis (TGA) on the powders was carried out using a Netzsch STA449 F3 Jupiter. Approximately 50 mg of powders was analysed from 30 °C to 1050 °C with a heating rate of 10 °C/min under N₂ flow of 50 mL/min.

Changes in the crystalline phases were identified using X-ray powder diffraction (XRD). The XRD patterns were acquired on a X'Pert PRO diffractometer from PanAnalytical with CoK α tube operating at 40 kV and 45 mA. Diffraction scans were recorded from 3 to 120 °2 θ , with accumulated dwell time of 59.6 s, and step size of 0.013 °2 θ .

The R³ test method was used to evaluate pozzolanic reactivity of the raw and calcined sediments. In this method the SCM under investigation was mixed with excess portlandite, and water; calcite, potassium sulphate and potassium hydroxide were also added. The paste simulates the environment in which the SCM reacts in hydrating cement without the complexity of simultaneous reactions of clinker phases. The reaction of the SCM in this model environment was measured by isothermal calorimetry at 40 °C for 7 days. The heat flow of the model paste was used to obtain the cumulative heat release up to 7 days. Complementary X-ray diffraction (XRD) and TG data were used to identify reaction products and portlandite consumption. More information about this method can be found in [8, 9].

3. Results and discussion

3.1 Dredging sediment characterisation

Table 1 shows the chemical composition of the raw sediments obtained by ICP. Furthermore the total carbon and total inorganic carbon are also tabulated. It can be seen the main oxides are SiO₂, followed by Al₂O₃, Fe₂O₃, and CaO. Note that the amount of CaO in SO is two times more than BC and GT.

Table 1 - Chemical composition of the raw sediments.

Raw Sediment	Chemical composition (wt.%)											
	SiO ₂	Al ₂ O ₃	Fe ₂ O ₃	CaO	MgO	K ₂ O	Na ₂ O	SO ₃	P ₂ O ₅	LOI	TC	TOC
BC	40.8	13.9	10.0	2.6	1.1	2.1	0.5	1.0	1.1		13.18	11.97
GT	61.8	9.9	4.1	5.5	1.3	1.4	<0.7			13.3	4.50	3.62
SO	32.2	8.2	4.3	10.8	0.9	1.6	1.9	4.0	1.4		13.79	10.35

Figure 1, shows the X-ray diffraction patterns of the three raw sediments. It can be seen that all have notable presence of quartz, in descending order of signal intensity, being GT>SO>BC. All sediments also contained carbonates. The amount of calcite in BC was small while in case of SO the amount was very significant; the presence of calcite in descending order of signal intensity is as follows SO>GT>BC.

Depending on the sediment, there is more or less of the clay minerals (Clinochlore, kaolinite, and illite) and feldspar minerals (albite and microcline). However it can be seen that all have a noticeable presence of kaolinite which is well-known to transform into a reactive SCM upon calcination at the appropriate temperature [10]. The combined presence of calcite and potentially less-reactive clay minerals is also considered promising as they may react during calcination to form a reactive amorphous Ca-enriched aluminosilicate compound [4].

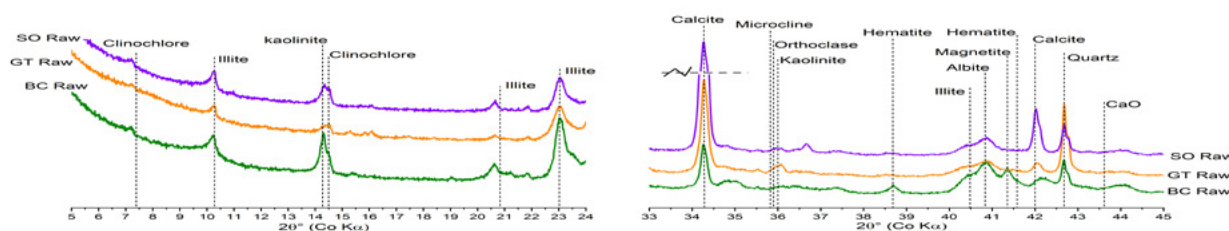


Figure 1- X-ray diffraction patterns of the raw sediments.

Table 2 shows the trace elements in the raw sediments, measured by ICP-OES. In addition the maximum allowable content values and safety limit values set by Wallonia, Flanders and France have also been tabulated. For each sediment if the value of the trace elements is below the maximum allowable content set by any of the legislations, the sediment is safe to be used in any application. However the approach of the legislations somewhat differs if one or more trace elements exceed the maximum allowable content:

1. In case of Flanders: if one or more trace elements exceed the maximum allowable content but not the safety limit, the sediment can be used in soil/bound and unbound construction applications. However if one or more trace elements exceed also the safety limit values, then leaching tests according to EN 12457-2 need to be carried out. If none of elements exceed the maximum allowable leaching limits put into effect by the legislation, then the sediment can still be used in soil/bound and unbound construction applications.
2. In case of Wallonia and France: if one or more trace elements exceed the maximum allowable content but not the safety limit, the sediment can be used in soil/bound and unbound construction applications. However if one or more trace elements exceed also the safety limit values, then leaching tests according to EN 12457-2 need to be carried out but even if none of elements exceed the maximum allowable leaching limits put into effect by legislations, extra actions need to be taken before the sediment is allowed to be used in soil/bound and unbound construction applications.
3. In case of France: For road applications, SETRA (2011) which is a guide dedicated to the valorization of alternative materials is used [11]. Note that in the absence of other standards, this guide is also used in other fields. In case of immersion of the marine sediment, a common approach for conducting a screening sediment risk assessment is to compare available chemical data on sediments with Sediment Quality Guidelines (SQGs). At the French level, SQGs are available for management of contaminated dredged sediments for several chemicals. These regulatory SQGs, named levels N1 and N2, are defined for metals and some organic compounds. Dredged sediment dispersal is permitted offshore when pollutant concentrations are lower than level 1 (N1). Dredged sediments considered as contaminated for marine environment ($> N1$) cannot be discharged into the sea without further ecotoxicological assessment according to GEODRISK framework [12]. Above the level N2, dredged sediments must be managed on land and are considered as wastes.

Table 2 - Trace elements concentrations in the raw sediments (units are in mg/kg of dry matter).

	Raw Sediment	As	Cd	Co	Cr _{total}	Cu	Hg	Ni	Pb	Zn	F ⁻	CN ⁻
	BC	54.9	126.7	< 10	268.4	269.1	1.45	149.9	813.5	4790.5	437.0	109.1
	GT	12	5	11	82	76.9	3.7	26	116	591	5.41	-
	SO	21.2	< 10	14.6	125.8	855.5	1.74	61.0	480	2023.8	346.1	7.7
Wallonia	Maximum allowable content	50	6	25	200	150	1,5	75	250	1200	250	5
	Safety Limit	100	30	100	460	420	15	300	1500	2400	500	25
	Maximum allowable leaching limits	0.5	0.1	0.5	0.5	2	0.02	0.5	0.5	2.0	20.0	0.1
Flanders	Maximum allowable content	30	2	19	70	74	2.9	48	200	200	55	-
	Safety Limit	267	30	-	880	500	11	530	1250	1250	-	5
	Maximum allowable leaching limits	0.3	0.02	-	0.1	0.6	0	0.2	0.3	1.00	-	-
France	Maximum allowable content (N1)	25	1.2	-	90	45	0.4	37	100	276	-	-
	Safety Limit (N2)	50	2.4	-	180	90	0.8	74	200	552	-	-
	Maximum allowable leaching limits	0.5	0.04	-	0.5	2	0.01	0.4	0.5	4.0	10.0	-

There are significant differences on the pollutant concentrations, contained in the three raw sediments. The BC-Raw sediment surpasses the local (Wallonia) safety limit for Cd, Cr_{total}, Cu, Zn, fluoride (F⁻) and cyanide (CN⁻), while the SO-raw surpasses the local (French) safety limit for Cu, Zn, and fluoride. Table 2 shows that none of the raw sediments pass the maximum allowable content criteria set by any of the legislations. However it can be seen that while sediments BC and SO exceed the safety limit values set by the three legislations, the GT sediment passes the safety limit values set by Wallonia and Flanders, but not the French legislation. It can therefore be concluded that leaching test on final products need to be carried out to evaluate compliance to environmental legislation for cement and concrete containing (treated) BC and SO sediments.

In order to interpret the changes in physical properties such as specific gravity, specific surface area, and PSD as function of calcination temperature (Figure 2) following the alteration in the chemical characteristics of sediments as function of temperature (Figure 3) is necessary.

Figure 2.a shows the total carbon (TC) and total organic carbon (TOC) as function of calcination temperature. Note that in case of SO sediment calcinated at 500 °C and 700 °C, the measurements were

not carried out at the time of writing. Furthermore the bomb calorimetry results carried out on the three raw sediments are also shown as a 2nd y-axis in Figure 2.a. It can be seen that GT sediment has three times smaller TC and TOC compared to BC and SO which corresponds well with the calorific value of GT-raw that is approximately 3 to 4 times smaller. It can be observed that already at 500 °C, most organic matter has been decomposed and values of TC and TOC have decreased significantly; this trend continues and by 800 °C the TC and TOC values in case of BC and GT are negligible. However in case of SO, the rate of degradation of organic matter is lower with increasing calcination temperature compared to the other two sediments and it persisted up to 600 °C, and even at 800 °C but again the values of TC and TOC are very small at this heat treatment temperature. Rock-Eval pyrolysis can be carried out to better understand the source of the organic carbon in case of SO sediment [13].

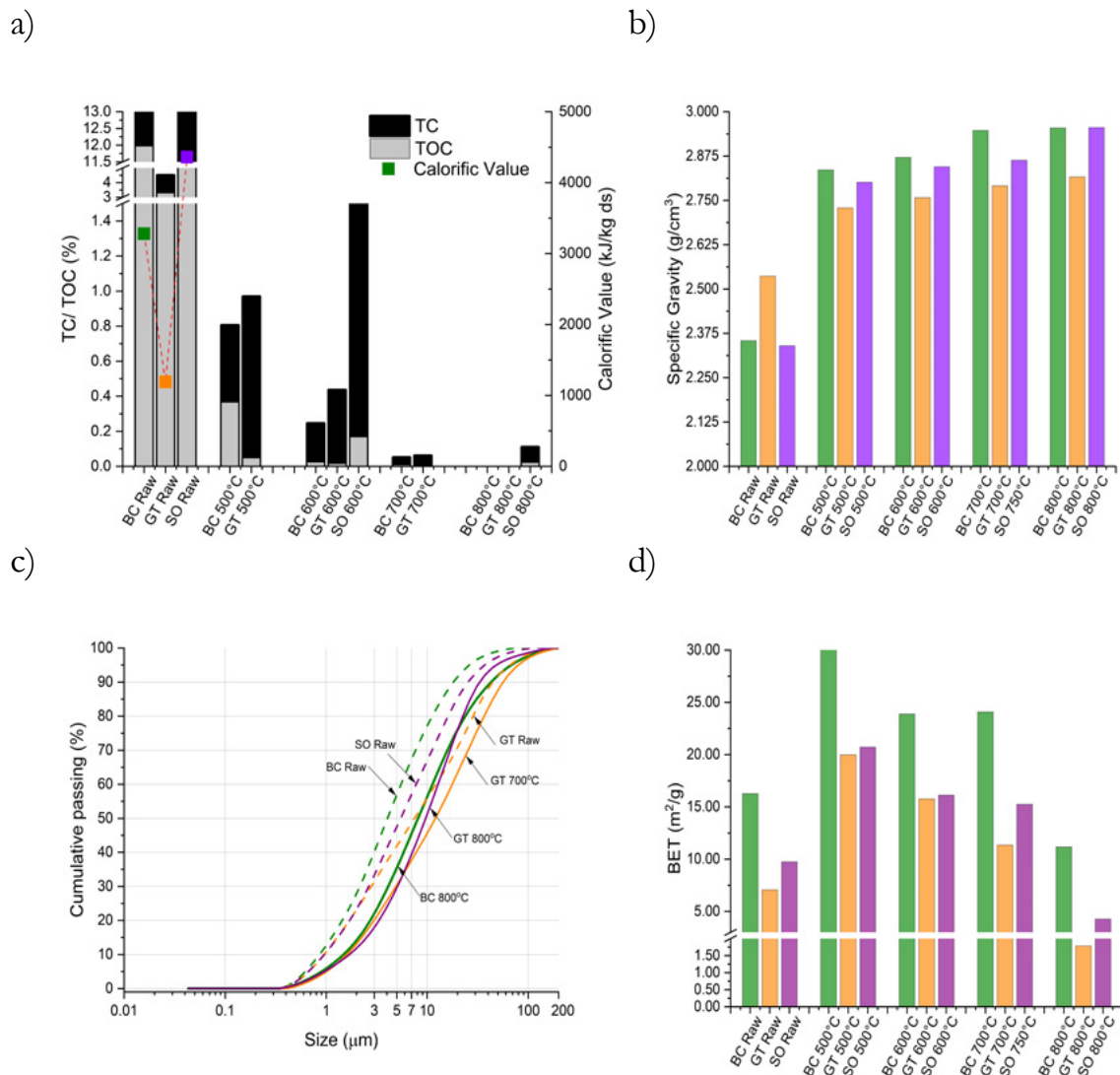


Figure 2 - Physical & chemical characterization of the sediments as function of calcinated temperature: a) Total carbon (TC), total organic carbon (TOC), and calorific value from bomb calorimetry . b) Specific gravity c) Particle size distribution (PSD) d) BET specific surface area.

Figure 2.b,c, and d show respectively the specific gravity, PSD, and specific surface area of the sediments as function of calcination temperature. It can be seen that in case of all sediments there is an increase of the specific surface at 500 °C, and thereafter they continuously decrease. In addition, the PSD shifts to coarser size with increasing calcination temperature. The specific gravity of all sediments increases with increasing calcination temperature and reaches a constant value around 700 °C to 800 °C. The abovementioned observation can be explained as following: degradation of the coarse organic matter increases the specific

surface area and specific gravity at 550 °C. Although there might be some agglomeration of particles which leads to having a small increase in the PSD, this influence is small at 500 °C. Calcination at higher temperatures leads to densification of particles due to partial sintering and formation of high temperature phases such as albite and hematite. This is also reflected in a coarser PSD, and lower specific surface area. In addition to densification and partial sintering, decomposition of organics and decarbonation of limestone are the main reasons increasing the specific gravity from 500 °C to 800 °C in all sediments.

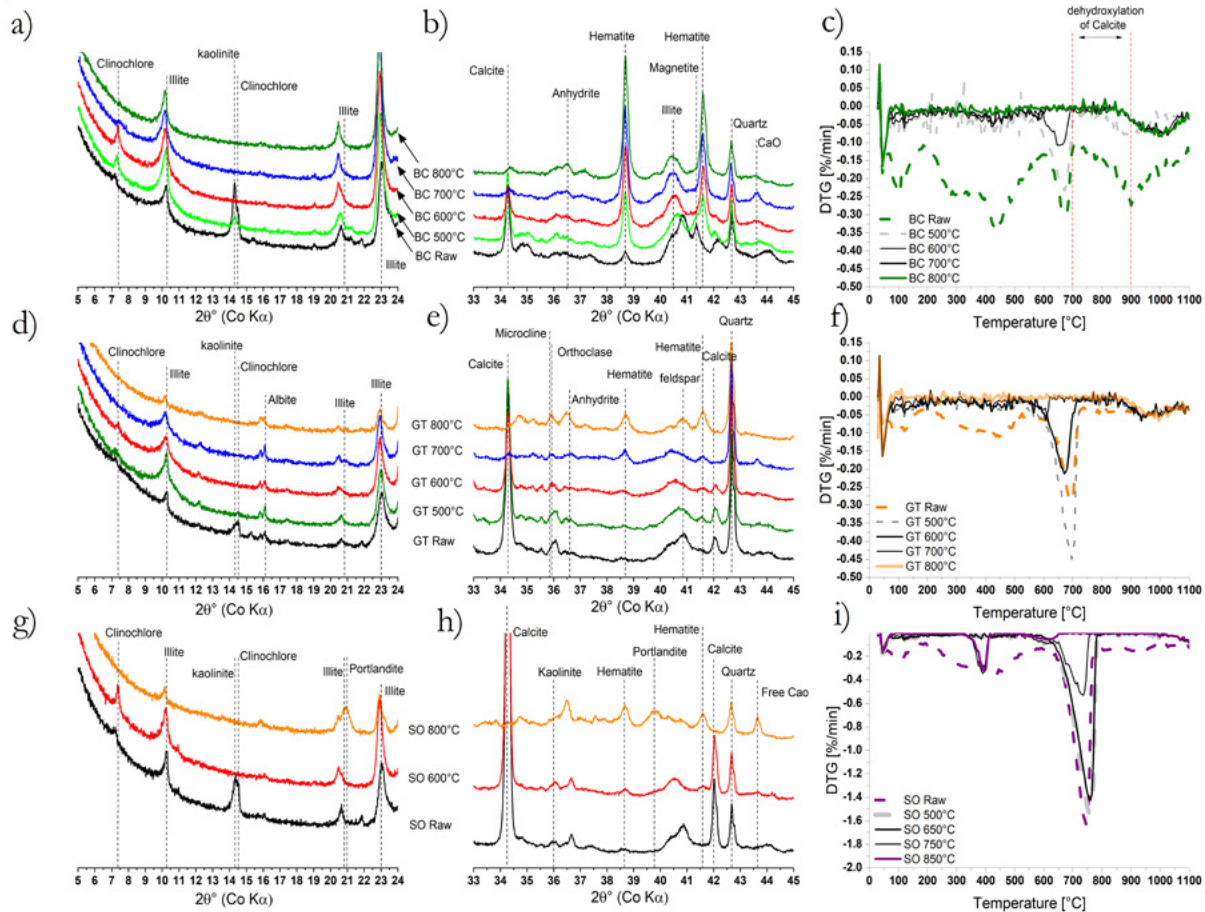


Figure 3 - Chemical characterization of sediments as function of calcination temperature.

Figure 3 shows the XRD patterns and derivative thermogravimetry (DTG) results of the sediments as function of the calcination temperature. The heat treatment has caused a mineralogical modification of clay fractions which led to reflection of some clays such as kaolinite and Illite to disappear or weaken making the sediment more amorphous. In addition both from the XRD patterns and DTG, it is clear that in all sediments calcined at 700 °C and 800 °C the calcite originally present was decomposed. In case of the SO sediment, decarbonation of the calcite was accompanied with formation of portlandite and free CaO.

3.2 R³ test

Based on the physical and chemical characterization carried out as function of temperature in the previous section, it can be inferred that the optimum calcination temperatures should be at the higher temperature range. However it is not clear what specific temperature investigated is the optimum calcination temperature in terms of pozzolanic reactivity for the calcined sediments. Therefore R³ reactivity tests were carried out on all three dredging sediments at various calcination temperatures.

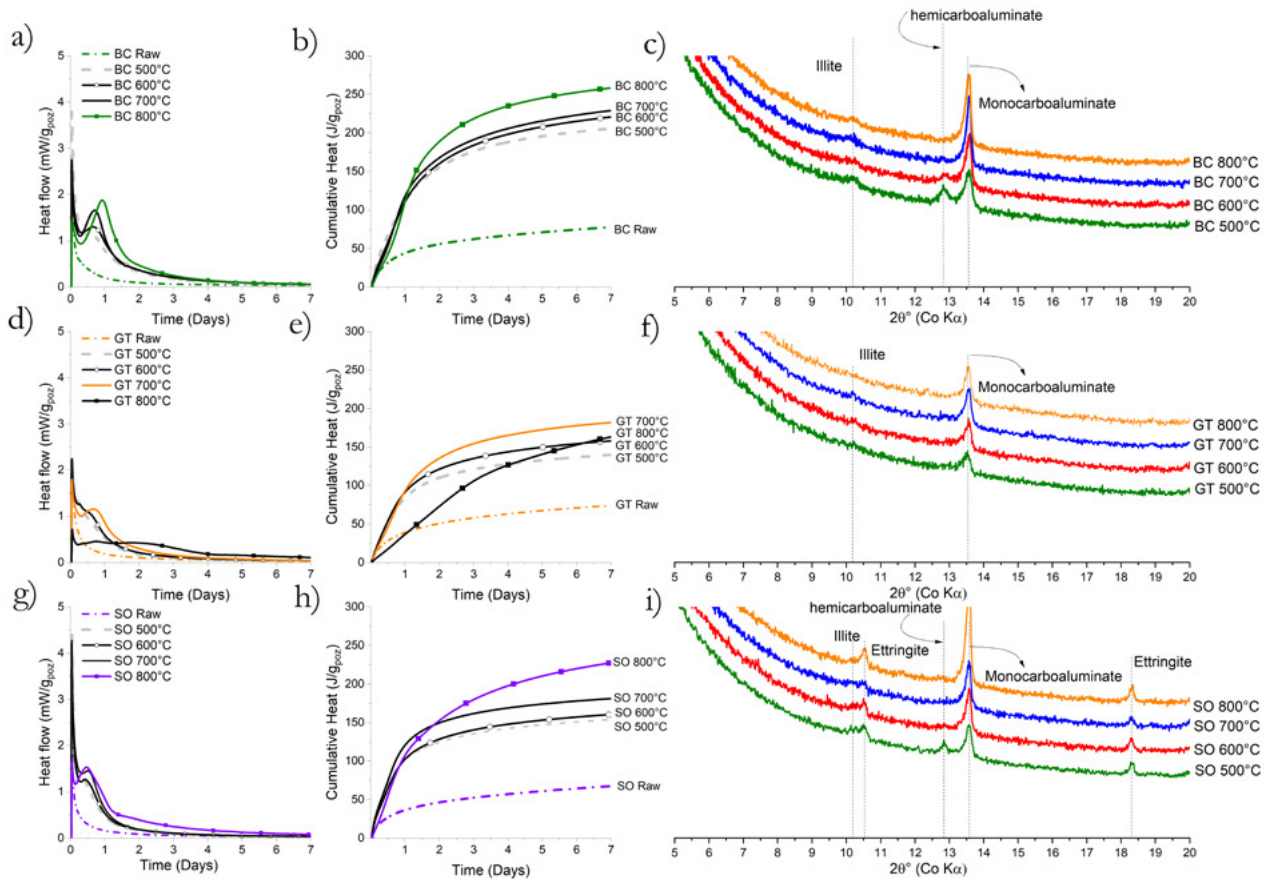


Figure 4 - R³ test results of the three calcined dredging sediment fine fractions as function of calcination temperature: a&b) heat flow and cumulative heat from the isothermal calorimetry at 40°C of the BC sediment c) XRD pattern of the BC samples after 7 days of hydration/reaction at 40°C. d&e) heat flow and cumulative heat from the isothermal calorimetry at 40°C of the GT sediment f) XRD pattern of the GT samples after 7 days of hydration/reaction at 40°C g&h) heat flow and cumulative heat from the isothermal calorimetry at 40°C of the SO sediment i) XRD pattern of the SO samples after 7 days of hydration/reaction at 40°C.

Figure 4 shows the results of the R³ test on the dredging sediments as a function of calcination temperature. It can be seen from the R³ tests, that the optimum calcination temperature for BC and SO is around 800 °C while in case of GT is around 700 °C. In case of GT calcined at 800 °C the decrease in reactivity can be linked with a recrystallization and formation of high temperate phases and thus decrease in the amorphous content coming from the clay content. The XRD measurements of the R³ pastes hydrated for 7 days at 40 °C in Figure 4 show hydration product forming; monocarboaluminate and hemicarboaluminate form in all sediments and in case of SO, ettringite is also formed. All sediments show promising pozzolanic activity at their optimum calcination temperatures. The R³ test shows that if the sediments are calcined at their optimum temperature, they are potentially more or at least as reactive as a commercial siliceous fly ash which in a R³ test shows cumulative heat in the range of 100 to 200 J/g_{poz} by the age of 7 days.

4. Conclusion

The valorisation as supplementary cementitious material of inland waterway dredged sediments from the Belgian-French cross border region was studied. To this purpose, the fine (<63 µm) fraction of sediments from the Brussels-Charleroi (BC), Lens (SO), and Gent-Terneuzen (GT) channels was recovered and calcined at 500 °C, 600 °C, 700 °C and 800 °C. The chemical and physical characterization of the raw and calcined sediments showed that thermal treatment at 500 °C to 800 °C led to distinct physical and chemical changes in the materials. These changes are summarized by calcination temperature interval as follows:

- It was seen that at 500 °C, organic matter was largely decomposed. The specific surface area increased, while the specific gravity increased and the PSD coarsened mainly due to decomposition of most of the organic matter at 500 °C. At 500 °C, the heat treatment did not cause decomposition of kaolinite and chlorite clay minerals.
- At 600 °C and higher, the decrease in organic content observed at 500 °C continued and by 800 °C it was very small. The PSD further coarsened with increasing calcination temperature, likewise the specific gravity of all sediments increased with increasing calcination temperature. Conversely, the specific surface area decreased. The main reason for the physical changes observed herein were due to decomposition of calcite, partial sintering and formation of high temperature phases such as feldspars and hematite.

The R3 SCM reactivity test was used to evaluate the optimal calcination temperature for the dredging sediments. The R3 test results clearly demonstrated that the optimum calcination temperature of Brussels-Charleroi, Lens sediments were at 800 °C and for the Gent-Terneuzen channel sediment was 700 °C.

5. Acknowledgments

The authors like to thank the financial support of the Interreg V France-Wallonie-Vlaanderen VALSE project.

6. References

- [1] S. Rakshith, D. Singh, Utilization of dredged sediments: contemporary issues, Journal of Waterway, Port, Coastal, and Ocean Engineering, 143 (2016) 04016025.
- [2] T.A. Dang, S. Kamali-Bernard, W.A. Prince, Design of new blended cement based on marine dredged sediment, Construction and Building Materials, 41 (2013) 602-611.
- [3] B. Beckstrom, D. R. Leavitt, M. C. Mesinger, B. Cutler, A. Hendricks, R. Fabricant, E. Peck, E. Stern, Thermal Treatment for Reclamation and Beneficial Use of Contaminated Sediments, 2014.
- [4] R. Snellings, Ö. Cizer, L. Horckmans, P.T. Durdziński, P. Dierckx, P. Nielsen, K. Van Balen, L. Vandewalle, Properties and pozzolanic reactivity of flash calcined dredging sediments, Applied Clay Science, 129 (2016) 35-39.
- [5] R. Snellings, L. Horckmans, C. Van Bunderen, L. Vandewalle, Ö. Cizer, Flash-calcined dredging sediment blended cements: effect on cement hydration and properties, Materials and Structures, 50 (2017) 241.
- [6] H. Du, S.D. Pang, Value-added utilization of marine clay as cement replacement for sustainable concrete production, Journal of Cleaner Production, 198 (2018) 867-873.
- [7] C. Van Bunderen, R. Snellings, L. Vandewalle, Ö. Cizer, Early-age hydration and autogenous deformation of cement paste containing flash calcined dredging sediments, Construction and Building Materials, 200 (2019) 104-115.
- [8] F. Avet, R. Snellings, A.A. Diaz, M.B. Haha, K. Scrivener, Development of a new rapid, relevant and reliable (R3) test method to evaluate the pozzolanic reactivity of calcined kaolinitic clays, Cement and Concrete Research, 85 (2016) 1-11.
- [9] X. Li, R. Snellings, M. Antoni, N.M. Alderete, M.B. Haha, S. Bishnoi, Ö. Cizer, M. Cyr, K. De Weerd, Y. Dhandapani, Reactivity tests for supplementary cementitious materials: RILEM TC 267-TRM phase 1, Materials and Structures, 51 (2018) 151.

-
- [10] R. Fernandez, F. Martirena, K.L. Scrivener, The origin of the pozzolanic activity of calcined clay minerals: A comparison between kaolinite, illite and montmorillonite, *Cement and Concrete Research*, 41 (2011) 113-122.
- [11] L. Chateau, P. Vaillant, F. Leray, A. Orsini, S. Cavellec, J. Crosnier, D. Guyonnet, G. Bellenfant, P. Piantone, B. Hazebrouck, Guide méthodologique-Acceptabilité de matériaux alternatifs en technique routière-Evaluation environnementale, in, SÉTRA. <http://www.setra.equipement.gouv.fr/Acceptabilite-de-materiaux.html>, 2011.
- [12] C. Alzieu, F. Quiniou, Géodrisk—La démarche d’analyse des risques liés à l’immersion des boues de dragage des ports maritimes, CD-ROM Geodrisk «Logiciel d’évaluation des risques liés à l’immersion des déblais de dragages des ports maritimes», Coord. C. Alzieu, Ed. Ifremer, (2001).
- [13] D. Sebag, J.R. Disnar, B. Guillet, C. Di Giovanni, E.P. Verrecchia, A. Durand, Monitoring organic matter dynamics in soil profiles by ‘Rock-Eval pyrolysis’: bulk characterization and quantification of degradation, *European Journal of Soil Science*, 57 (2006) 344-355.

The Effects of Epoxy Resin as Partial Cement Replacement on the Mechanical Properties of Concrete

G.A. Jokhio, Y. Gul, A. Abu-Tair, G. S. Wei

¹Assistant Professor, Faculty of Engineering & IT, The British University in Dubai, United Arab Emirates.

²Assistant Professor, Department of Architectural Engineering, Prince Mugrin University, AlMadina, Saudi Arabia.

³Professor, Faculty of Engineering & IT, The British University in Dubai, United Arab Emirates.

⁴Student, Faculty of Civil Engineering and Earth Resources, University Malaysia Pahang, Malaysia

Abstract

Plain concrete has low tensile strength, therefore, it is reinforced with steel for structural use. Both the production of concrete and the manufacture of steel adversely affect the environment. This can be addressed partially by increasing the efficiency of these materials in terms of their mechanical properties. The present study is exploratory in nature in that it is breaking new ground by incorporating epoxy resin as fine aggregate replacement in concrete. It was hypothesized that an increase specially in the tensile strength of concrete by the incorporation of epoxy resin will reduce the requirement of reinforcing steel. To test this hypothesis, a total of 72 concrete cubes and cylinders were made with 0%, 10%, 20%, and 30% of cement replaced by epoxy resin. These samples were tested at the curing ages of 3, 7, and 28 days. The results show that for lower values of cement replacement with epoxy, both the compressive and the tensile strength were reduced. However, when the epoxy proportion was increased, a positive change was noticed in the mechanical properties, especially the tensile strength. While the results obtained in the present study are not comprehensive, this research is a significant step towards further exploration in this area.

Keywords: Epoxy resin, cement replacement, silica, aggregate replacement, sustainable materials.

1. Introduction

Cement concrete is the most widely used material in the construction of contemporary buildings. The production of concrete is an energy intensive process that also consumes a great amount of natural resources [1]. It is stipulated that the production of cement alone is a major contributor to the emission of CO₂ gases in the atmosphere [2]. Several attempts have been made over the recent years to improve the sustainability of the construction industry with respect to the production of concrete. A significant number of these attempts have been at incorporating agricultural and industrial wastes as partial or full replacement of concrete ingredients including cement, fine aggregate, and coarse aggregate [3, 4, 5]. The most recent notable contributions in this regard have been the use of nano palm oil fuel ash and nano fly ash in concrete [6]. Some attempts have also been made at replacing concrete in less structurally intensive situations by alternative materials such as adobe [7, 8].

The manufacture of reinforcing steel is another energy intensive and environmentally expensive process.

Additionally, more often than not, it requires transportation over large distances, which adds to its adverse environmental impact. The use of reinforcing steel in concrete is necessary because concrete is generally weak at taking tensile stresses. To improve the tensile capacity of concrete and to reduce the use of reinforcing steel, several alternative reinforcement strategies have been used over recent years. Some of these strategies include the use of steel wire mesh [9], which additionally helps prevent excessive cracking; and the use of additional fibres such as kenaf [10]. These recent developments towards improving the sustainability of reinforced concrete notwithstanding, there is still great potential of the use of alternative materials and techniques in order to make this industry more environment friendly. A novel technique in this regard is the use of epoxy resin as a binding material in concrete.

Epoxy resins are petroleum derived materials. These have been used to produce, among other applications, strong coatings. Some epoxy-bonded fibre-composite materials have also been used in structural applications such as strengthening of RC beams [11]. However, no evidence was found in the literature by the authors of this paper on the use of epoxy resin as a binder replacement in the preparation of cement concrete. The present study, therefore, aims to test the hypothesis that including epoxy resin as a binder replacement will increase the tensile strength of cement concrete. It is expected that such an increase in the tensile strength without significantly compromising on the compressive strength can potentially reduce the use of cement, but more importantly, the reinforcing steel. The above hypothesis was tested experimentally. For this purpose, an experimental program was designed and carried out. The methodology adopted, the results obtained, and the conclusions drawn have been provided in the following sections.

2. Methodology

The methodology of the present study has been divided into two parts; materials, and methods.

2.1 Materials

The materials used in the present study consisted of Ordinary Portland Cement (OPC), a 50-50 mixture of common river sand and silica sand as fine aggregate, ordinary crushed stone as coarse aggregate, and epoxy resin as partial binder replacement. A total of 72 specimens were prepared. Out of the 72, 36 were cubes of 100 mm side length and the other 36 were cylinders of 150 mm diameter and 300 mm height. The cubes were used for testing the compressive strength whereas the cylinder specimens were used to test the splitting tensile strength. 4 proportions of the replacement of binder with epoxy resin were used i.e. 0%, 10%, 20%, and 30%. This yielded 18 specimens for each proportion, 9 cylinders and 9 cubes. For each proportion under investigation, 3 cylinders and 3 cubes each were tested after 3, 7, and 28 days after casting. Two sizes of coarse aggregate i.e. 10mm and 20mm were used. Table 1 presents the mix proportions used for cubes and Table 2 presents the same for cylinders.

Table 1: Details of the mix proportions used for cube samples (All quantities are in kg).

Epoxy Proportion	Cement	Epoxy Resin	Water	Fine Aggregate	Coarse Aggregate 10mm	Coarse Aggregate 20mm
0%	0.32	0	0.205	0.801	0.337	0.673
10%	0.288	0.032	0.205	0.801	0.337	0.673
20%	0.256	0.062	0.205	0.801	0.337	0.673
30%	0.224	0.096	0.205	0.801	0.337	0.673

Table 2: Details of the mix proportions used for cylinder samples (All quantities are in kg).

Epoxy Proportion	Cement	Epoxy Resin	Water	Fine Aggregate	Coarse Aggregate 10mm	Coarse Aggregate 20mm
0%	0.512	0	0.328	1.283	0.539	1.077
10%	0.461	0.0512	0.328	1.283	0.539	1.077
20%	0.41	0.102	0.328	1.283	0.539	1.077
30%	0.358	0.154	0.328	1.283	0.539	1.077

2.2 Methods

The testing methods used in the present study consisted of the compressive strength test as per ASTM C39 and the tensile splitting test as per ASTM 496. The details of the method used for specimen preparation and the testing methods used have been provided in the following subsections:

2.2.1 Specimen Preparation

For the preparation of cube as well as cylinder samples, the ingredients were mixed together in a concrete mixer. First, dry ingredients were mixed for 3 minutes and then the water was added. The concrete was mixed for another 3 minutes after the addition of water. Epoxy resin, mixed with a hardener and where applicable, was added after the addition of water and further mixed for 3 minutes.

2.2.2 Compressive Strength Test

The compressive strength of the cubic specimens was measured using the Universal Testing Machine by adopting the ASTM C39 testing standard. The compressive load was applied to the specimens at a rate of 0.25 MPa per second until failure. Figure 1 shows a specimen under compressive strength test.



Figure 1: A cubic specimen under compressive strength test.

2.2.3 Splitting Tensile Strength Test

The splitting tensile strength of the cylinder specimens was also measured using the Universal Testing Machine. For this purpose, the ASTM C496 testing standard was adopted. The standard recommends a load rate of 0.7 to 1.4 MPa per minutes. In the present study, a load rate of about 1 MPa per minute was used until the specimen failed. Figure 2 shows a specimen being subjected to the splitting tensile strength test.



Figure 2: A cylinder specimen under splitting tensile strength test.

3. Results and Discussion

The results of the compressive strength test and the splitting tensile strength along with the relevant discussion have been presented in the following subsections.

3.1 Compressive Strength Test Results

The results of the compressive strength test carried out on the cube specimens with various proportions of epoxy resin at 3, 7, and 28 days of curing age are presented in Tables 4, 5, and 6.

Table 4: Results of compressive strength test at 3 days of curing (All strength values are in MPa).

Epoxy Proportion	Sample 1	Sample 2	Sample 3	Average	Standard Deviation
0%	12.93	16.62	15.21	14.92	1.86
10%	4.02	3.62	3.04	3.56	0.49
20%	2.78	2.46	2.88	2.71	0.22
30%	15.56	15.4	15.33	15.43	0.12

Table 5: Results of compressive strength test at 7 days of curing (All strength values are in MPa).

Epoxy Proportion	Sample 1	Sample 2	Sample 3	Average	Standard Deviation
0%	20.22	17.59	19.02	18.94	1.32
10%	4.82	5.12	4.13	4.69	0.51
20%	3.81	3.76	3.82	3.8	0.03
30%	17.49	17.57	17.63	17.56	0.07

Table 6: Results of compressive strength test at 28 days of curing (All strength values are in MPa).

Epoxy Proportion	Sample 1	Sample 2	Sample 3	Average	Standard Deviation
0%	28.61	32.12	27.46	29.4	2.43
10%	4.82	4.92	5.12	4.92	0.15
20%	3.88	3.5	3.92	3.77	0.23
30%	18.78	18.56	19.41	18.9	0.44

The average compressive strength for the different epoxy resin proportions at different curing ages have been plotted in Figure 3.

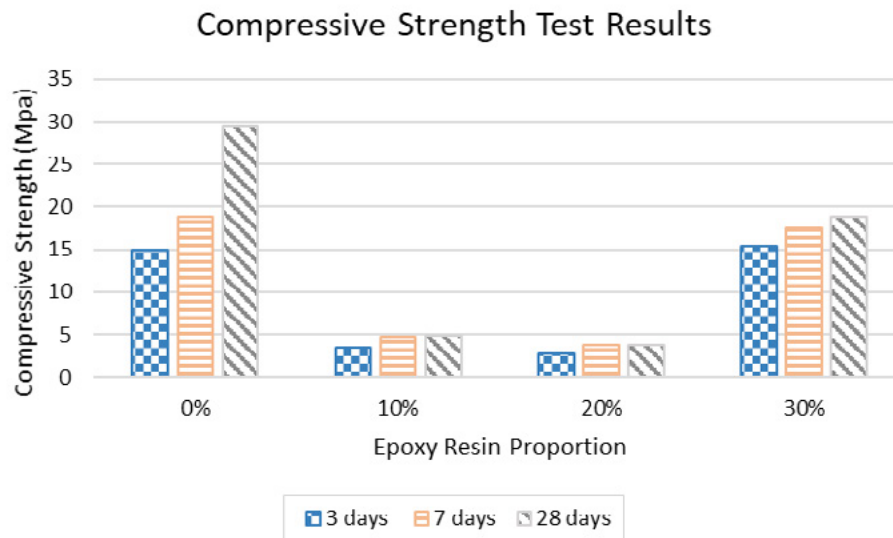


Figure 3: Average compressive strength test results.

It can be observed in Figure 3 that the compressive strength drops as epoxy resin is added in lower portions. The average compressive strength at 28 days for 10% epoxy resin is only 16.74% of that with no epoxy resin. This further drops to 12.83% when 20% epoxy resin was used. However, for epoxy resin proportion of 30%, the compressive strength seems to have bounced back to reach 64.3% of that of the control specimen. It is stipulated that the addition of epoxy resin adversely affects the effectiveness of cement as a binder and the low amount of epoxy does not produce enough of its own binding force. For larger proportion, the increase in the compressive strength may be attributed to epoxy resin. This hypothesis, however, requires further investigation to be validated.

3.2 Splitting Tensile Strength Test Results

The results of the splitting tensile strength test carried out on the cylinder specimens with various proportions of epoxy resin at 3, 7, and 28 days of curing age are presented in Tables 7, 8, and 9.

Table 7: Results of splitting tensile strength test at 3 days of curing (All strength values are in MPa).

Epoxy Proportion	Sample 1	Sample 2	Sample 3	Average	Standard Deviation
0%	0.87	0.95	1.06	0.95	0.095
10%	0.04	0.06	0.07	0.06	0.015
20%	0.11	0.19	0.23	0.18	0.061
30%	1.1	1.12	1.21	1.14	0.059

Table 5: Results of compressive strength test at 7 days of curing (All strength values are in MPa).

Epoxy Proportion	Sample 1	Sample 2	Sample 3	Average	Standard Deviation
0%	1.39	1.34	1.42	1.38	0.040
10%	0.12	0.28	0.32	0.24	0.106
20%	0.24	0.25	0.27	0.25	0.015
30%	1.65	1.48	1.73	1.62	0.128

Table 6: Results of compressive strength test at 28 days of curing (All strength values are in MPa).

Epoxy Proportion	Sample 1	Sample 2	Sample 3	Average	Standard Deviation
0%	2.25	2.21	2.28	2.25	0.035
10%	0.52	0.59	0.63	0.56	0.056
20%	0.65	0.69	0.77	0.7	0.061
30%	2.33	2.34	2.39	2.35	0.032

The average splitting tensile strength for the different epoxy resin proportions at different curing ages have been plotted in Figure 4.

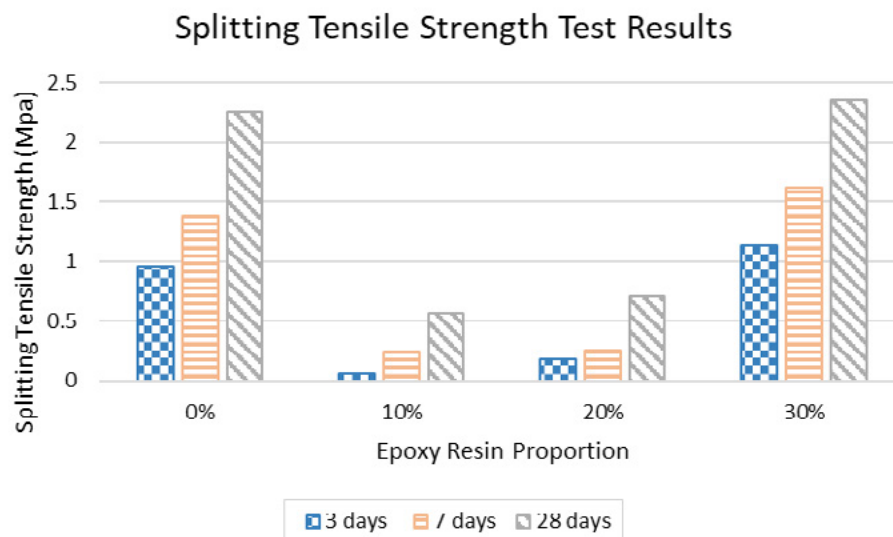


Figure 4: Average compressive strength test results.

A similar trend for the splitting tensile strength to that of the compressive strength can be observed in Figure 4. However, the drop in the tensile strength is slightly less as it drops to about 25% and 31% of the splitting tensile strength of the control specimen for the epoxy proportions of 10% and 20%, respectively. While the compressive strength for 20% epoxy proportion was less than that for 10%, the splitting tensile strength is higher for 20% epoxy proportion. More importantly, the tensile strength for the epoxy resin proportion of 30% went higher than the control specimen by about 4%. It is stipulated that a higher proportion of epoxy resin may further increase the tensile strength of concrete.

4. Conclusions

The present study was a relatively small study where only 4 proportions of epoxy resins were used. The conclusions drawn from the observed results are as follows:

The compressive strength of concrete dropped to about one-sixth of that of the control specimen when 10% cement was replaced by epoxy resin

The compressive strength of concrete dropped further to about one-eighth of that of the control specimen when 20% cement was replaced by epoxy resin

The compressive strength of concrete bounced back to about two-thirds of that of the control specimen for a higher proportion of epoxy resin replacing 30% of cement

The splitting tensile strength of concrete dropped to about one-fourth of that of the control specimen when 10% cement was replaced by epoxy resin

The splitting tensile strength of concrete slightly increased to about one-third of that of the control specimen when 20% cement was replaced by epoxy resin as compared to 10%

The splitting tensile strength of concrete went slightly higher than that of the control specimen for a higher proportion of epoxy resin replacing 30% cement

The above conclusions are based on the small size of data observed in the present study. It is recommended that further investigation in this regard be carried out to ascertain the validity of these conclusions. It would especially be of interest to find out how the higher proportions than those used in the present study may affect the compressive and the splitting tensile strength of concrete. Furthermore, the present study did not investigate the economic or environmental aspects of the use of epoxy resin in concrete. Future research in these areas is also recommended.

5. References

- [1] H. M. Hamada, G. A. Jokhio, F. M. Yahaya, A. M. Humada and Y. Gul, "The present state of the use of Palm Oil Fuel Ash (POFA) in concrete," *Construction and Building Materials*, vol. 175, pp. 26-40, 2018.
- [2] C. Meyer, "The greening of the concrete industry," *Cement and Concrete Composites*, vol. 31, no. 8, pp. 601-605, 2009.
- [3] B. H. Nagaratnam, M. E. Rahman, A. K. Mirasa, M. A. Mannan and S. O. Lame, "Workability and heat of hydration of self-compacting concrete incorporating agro-industrial waste," *Journal of Cleaner Production*, vol. 112, no. 1, pp. 882-894, 2016.
- [4] W. Tangchirapat, T. Saeting, C. Jaturapitakkul, K. Kiattikomol and A. Siripanichgorn, "Use of waste ash from palm oil industry in concrete," *Waste Management*, vol. 27, no. 1, pp. 81-88, 2007.
- [5] E. Khankahje, M. W. Hussin, J. Mirza, M. Rafeizonooz, M. R. Salim, H. C. Siong and M. N. Warid, "On blended cement and geopolymer concretes containing palm oil fuel ash," *Materials & Design*, vol. 89, pp. 385-398, 2016.
- [6] H. M. Hamada, G. A. Jokhio, F. M. Yahaya and A. M. Humada, "Applications of nano palm oil fuel ash and nano fly ash in concrete," *IOP Conference series: Materials Science and Engineering*, vol. 342, no. 1, p. 012068, 2018.
- [7] G. A. Jokhio, F. M. Saad, Y. Gul, S. M. S. Mohsin and N. I. Ramli, "Uniaxial compression and tensile splitting tests on adobe with embedded steel wire reinforcement," *Construction and Building Materials*, vol. 176, pp. 383-393, July 2018.
- [8] G. A. Jokhio, Y. M. Y. Al-Tawil, S. M. S. Mohsin, Y. Gul and N. I. Ramli, "Compressive and flexural tests on adobe samples reinforced with wire mesh," *IOP Conference Series: Materials Science and Engineering*, vol. 318, no. 1, p. 012030, 2018.

- [9] S. H. Lodi, S. F. A. Rafeeqi and G. A. Jokhio, "Ferrocement constitutive model and experimental validation," *NED University Journal of Research*, vol. 7, no. 2, pp. 137-151, 2010.
- [10] S. M. S. Mohsin, A. O. Baarimah and G. A. Jokhio, "Effect of kenaf fiber in reinforced concrete slab," *IOP Conference Series: Materials Science and Engineering*, vol. 342, no. 1, p. 012104, 2018.
- [11] T. C. Triantafillou and N. Plevris, "Strengthening of RC beams with epoxy-bonded fibre-composite materials," *Materials and Structures*, vol. 25, no. 4, pp. 201-211, 1992.

Polycarboxylate Superplasticizer Modified Fly Ash: Its Effects on Fluidity and Mechanical Properties of Cement Paste

P. Liu^{a,b}, M. Qu^b, F. Wang^{a,*}, G. Hu^c, L. Yang^a, W. Zhang^a

^a State Key Laboratory of Silicate Materials for Architectures, Wuhan University of Technology, Wuhan 430070, PR China

^b School of chemistry, chemical engineering and life science, Wuhan University of Technology, Wuhan 430070, PR China

^c Laboratory of Reactions and Process Engineering (LRPG, UMR 7274), Université de Lorraine - CNRS, 1 rue Grandville, BP 20451, 54001 Nancy, France

*Corresponding author: Prof. Fazhou Wang, State Key Laboratory of Silicate Materials for Architectures, Wuhan University of Technology, Email: fzhwang@whut.edu.cn

Abstract

A polycarboxylate superplasticizer (PC) which contained PEG side chain, carboxylic groups and hydroxysilane ones, was synthesized by free radical copolymerization. It was subsequently grafted onto fly ash (FA) beads. The Si–OH groups on the surface of alkali-activated FA beads were connected to the PC molecules via covalent hydroxysilane linkage. In the PC-modified FA beads, new IR peaks appeared at 2900 and 1100 cm⁻¹ and were assigned to the vibration of C–H and C–O–C groups. A peak shift in ²⁹Si NMR from –80 to –86 ppm also confirmed the successful grafting of the PC molecules onto the FA beads. Thermal analyses indicated that the PC moieties accounted for 2.1 wt.% of the modified FA beads. Compared with the crude FA and the alkali-activated one, the PC-modified FA significantly improved the workability of the cement paste, and enhanced the mechanical properties of the cement after hydration for seven days. Thus, the PC modified FA composite could serve as a promising additive for cementitious materials.

Keywords: water reducing; fly ash; alkali activation; fluidity; workability

Understanding Hydrogen Bonding in Calcium Silicate Hydrates

B. Li^{1,2}, H.J.H. Brouwers³, Q. Yu³, W. Chen^{1*}

¹State Key Laboratory of Silicate Materials for Architectures, Wuhan University of Technology, Wuhan, PR China

²School of Material Science and Engineering, Wuhan University of Technology, Wuhan, PR China

³Department of the Built Environment, Eindhoven University of Technology, Eindhoven, The Netherlands

Email of the corresponding author: chen.wei@whut.edu.cn

Abstract

The hydrogen bonding mechanisms and atomic interactions in C-S-H gels are investigated by combining ²⁹Si, ¹H solid state NMR and first principle calculation. Five distinct peaks of protons were observed in the ¹H MAS NMR spectra for C-S-H gels. The interactions between protons and silicate species are discussed in detail with well-defined first principle calculations. Amorphous portlandite and strong hydrogen bonded protons are identified. The strong hydrogen bonded protons are favored in C-S-H with high Ca/Si ratios, which is associated with Q¹ sites in the termination of silicate chains. The stronger atomic interactions between Q¹ species or silanols and water in C-S-H gel with higher Ca/Si ratio are presented than Q² species in C-S-H gel with Ca/Si ratio of 1.0. The stronger hydrogen bonds in the interlayer are expected to be an interpretation for the decrease of interlayer spacing with the Ca/Si ratio. The results are expected to pave the way to develop new components of cement with stronger hydrogen bonding features.

Keywords: calcium silicate hydrate, Ca/Si ratio, H₂O/Si ratio, hydrogen bonds, first principle calculation

1. Introduction

Hydrated Portland cement paste is a porous matrix consisting of crystals embedded in a poorly crystalline phase, the calcium-silicate-hydrate (C-S-H) gel [1]. C-S-H gel is the most abundant hydration product of Portland cement, accounting for about 50–60% by volume of hardened cement paste and making it one of the most common substances of the modern world [2]. It is also the primary binding component in cementitious materials.

C-S-H gel has a layered structure and shows similarities to 14 Å tobermorite (Ca₅Si₆O₁₆(OH)₂·4H₂O) [3, 4]. The structure of tobermorite contains layers of calcium ions linked on both sides to linear silicate chains with the ‘dreierkette’ form in such a way as to repeat a kinked pattern after every three tetrahedra [5]. Two of the three tetrahedra, named pairing tetrahedra (Q²_p), are linked together and share O-O edges with the central Ca-O part of the layer. The third tetrahedron, named bridging tetrahedron (Q²_b), shares an oxygen atom at the pyramidal apex of a calcium polyhedron and connects the dimers of pairing tetrahedra. C-S-H gel can be considered as defective tobermorite-like structure whose molar ratio of calcium to silicon varies between 0.66 and 2.0.

The local chemical environments and atomic arrangements in C-S-H gel are probed with Solid-state Nuclear

Magnetic Resonance (NMR) spectroscopy [6, 7]. The ^{29}Si NMR peaks are assigned with the assumption that chemical shifts of silicon atoms decrease with the condensation degree of (SiO_4) units, structures of which transform from isolated monomers to tetrahedrally coordinated chains [8]. The ^{29}Si NMR results show that C-S-H gel contains silicate chains with limited lengths with a 2, 5, 8... $(3n-1)$ ($n=1, 2, \dots$) chain length sequence [4].

Hydrogen atoms in C-S-H exist in the form of silanols, hydroxyl groups and water molecule which play an important role in atomic interactions between protons and silicate chains with hydrogen bonding. Hydrogen bonding is a special type of atomic interactions between a hydrogen atom covalently bonded to a very electronegative atom such as N, O, or F atom and another very electronegative atom, whose strengths range from 4 to 50 kJ per mole of hydrogen bonds [9]. The hydrogen bonding between hydrogen-containing species and oxygen atoms has a wide range of bond length and bond strength which contributes to the internal cohesion in the C-S-H [10].

The mechanism of hydrogen bonding in C-S-H gel or hydrated cements are not sufficiently clarified, yet. Efforts have been made to study the hydrogen bonding and interactions between different silicate and hydrogen-containing species in cement hydrates or synthetic C-S-H gels [11-14]. The nanopore space in the C-S-H gel is hydrophilic because of the nonbridging oxygen atoms on the disordered silicate chains which serve as hydrogen-bond acceptor sites, based on the classical molecular simulations [13]. Glassy nature of hydrogen bonds between interlayer water and silicate chains is demonstrated because of the heterogeneity in the distribution of hydrogen bond strengths and multi-range structure [13]. ^1H - ^{29}Si Heteronuclear nuclear chemical shift correlation provides information about the distance of protons to silicon atoms and interactions between protons and silicate moieties. The results from ^1H - ^{29}Si Heteronuclear nuclear chemical shift correlation establishes strong interactions of the Q^1 species with water molecular [11, 12, 14].

Understanding on the mechanism of hydrogen bonds in C-S-H gels is lacking because the correlation between experimental results and underlying complex structure is lacking. A method to reveal the mechanism of hydrogen bonds in maltose anomers and C-S-H gel is proposed by a combination of first principle calculation and NMR tests [14, 15].

First principle calculations based on the Density Functional Theory (DFT) with the Gauge Including Projector Augmented Wave (GIPAW) algorithm enable the calculation of chemical shielding, which establishes a clear link between the observed spectra and underlying atomic structure [15, 16]. The mechanisms of hydrogen bonding between various silicate moieties and hydrogen groups in C-S-H can be determined by using combination of ^1H NMR and first principle calculations. Understanding the mechanisms of hydrogen bonding provides great possibilities for developing C-S-H gel with strong cohesive performance [10].

In this paper, three types of C-S-H gels with Ca/Si ratios of 1.0, 1.4 and 1.5 are synthesized. First principle calculations for ^1H chemical shifts are used to correlate the observed ^1H NMR spectra with structure of the hydrogen bonding between different silicon moieties and hydrogen groups in the C-S-H gels. The effect of Ca/Si ratios on the chemical environment of hydrogen bonds is studied.

2. Experiments

2.1 Experiments

C-S-H gels are synthesized by using pozzolanic reaction between calcium oxide and amorphous silica fume [17]. C-S-H gels with Ca/Si molar ratios of 1.0, 1.4 and 1.5 are synthesized according to the mix designs in Table 1. Calcium oxide is prepared with decomposition of calcium carbonate (AR grade, Sinopharm) at 1000°C for 10h. Amorphous silica fume (99.6% SiO_2 , Shenzhen Anmisco) with a specific area of 250 m²/g

is used as silicon sources. Deionized water is mixed with calcium oxide and silica fume and the water/powder mass ratio is 50. The resulting slurry is stirred under nitrogen protection for 7d at 30°C followed by filtration. The filtrates are analyzed with Inductively Coupled Plasma (ICP, Model Optima 4300DV) to determine the Ca/Si molar ratio of the filtrate. Each test is performed three times with test error smaller than 0.01mM and the mean value of the results is recorded.

The powders are washed with deionized water. No portlandite is detected in X-ray diffraction pattern (XRD, Model Rigaku MiniFlex600, Cu K α = 1.5406 Å, step size of 0.02° from 5° to 50°) after three times washing. C-S-H gels are freeze dried at 2Pa, -50°C for 24 h. The XRD patterns of the C-S-H gels are analysed (Figure 1).

The Ca/Si ratio in C-S-H is determined in two ways, including calculations from the elemental concentrations of calcium and silicon in the filtrate and measurements with X fluorescence spectrometer (XRF, Model Axios Advanced) of the C-S-H solids. The H₂O/Si molar ratios are calculated with the weight loss after calcination 1000°C for 12h. The results of Ca/Si ratios and H₂O/Si molar ratios are listed in Table 1.

Table 1 Mix design for synthesizing C-S-H and compositions of C-S-H gel

Samples	C-S-H1.0	C-S-H1.4	C-S-H1.5
Mix design			
CaO (g)	4.96	4.14	3.31
SiO ₂ (g)	5.04	6	6.69
Water (ml)		500	
Analysis of filtrate (volume 500ml)*			
Ca in filtrate (mM)	6.7	14.6	22.4
Si in filtrate (mM)	0.08	0.01	0.01
Composition of C-S-H			
Calculated Ca/Si ratio ^{&}	0.98	1.42	1.57
Measured Ca/Si ratio [#]	0.98	1.44	1.52
Measured H ₂ O/Si ratio	1.66	1.83	2.08

Note: * Determined with ICP-OES.

& Calculated from the moles of Ca and Si in the filtrates.

Determined with XRF of the powders.

¹H MAS NMR spectra are recorded on an Agilent 600 DD2 spectrometer, equipped with a 14.1T magnet, operating at a Larmor frequency of 600MHz. A 4.0mm probe is used for ¹H NMR with a spinning speed of 25.0kHz, a $\pi/2$ pulse length of 5ms, a relaxation delay of 20s and 200 scans. Tetramethylsilane is used as the reference for ¹H tests.

2.2 First principles calculation

The first principle calculations on NMR results are performed with CASTEP (Accelrys, Material Studio17.2) using DFT theory [16]. The calculation is executed in three steps, including geometry optimization, energy calculation and chemical shielding calculation. Geometry optimization and energy calculation are carried out within CASTEP using a k point grip of 4×2×1 equal to 0.04 1/Å and cut off energy of 400eV. The core-valence interactions are described with ultrasoft pseudopotentials. Little changes of unit cell and atomic positions are allowed during geometry optimization. ¹H chemical

shielding calculation is performed in the crystal frame. All-electron wave function in the presence of a magnetic field is reconstructed with the gauge including projector augmented wave (GIPAW) algorithm. The chemical shifts δ_{cal} are obtained from chemical shielding σ_{cal} with the relation

$$\delta_{\text{cal}} = \sigma_{\text{ref}} - \sigma_{\text{cal}} \quad (1)$$

Where σ_{ref} is 30.09ppm.

3. Results and discussion

3.1 XRD analysis of C-S-H gels

The XRD patterns of the three types of C-S-H gels are shown in Figure 1, which shows a typical tobermorite-like structure. Poorly resolved XRD patterns demonstrate the prominent features of heavy defects and poor long range order in C-S-H structures. No secondary calcic phases such as portlandite are observed in all C-S-H gels, indicating that crystalline portlandite is sufficiently removed by washing with deionized water.

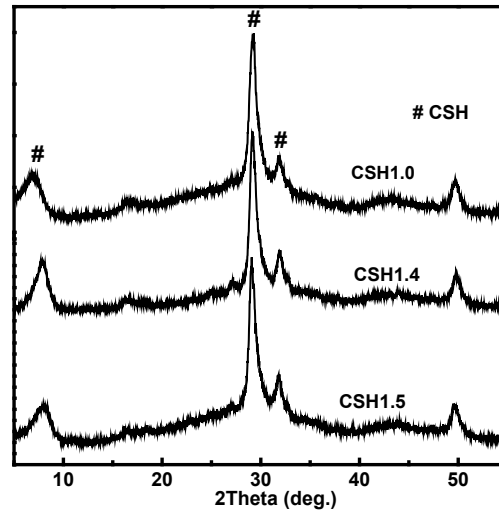


Figure 1 XRD patterns of three types of C-S-H gels after freeze drying

The position of the first diffraction peak ((020) about $2\theta=7^\circ$) shows the basal spacing of the tobermorite-like structure. The basal spacing of C-S-H1.0 is about 13\AA ($2\theta=6.78^\circ$), while the basal spacing decreases to 11.3\AA ($2\theta=7.81^\circ$) and 11\AA ($2\theta=8.02^\circ$) for C-S-H1.4 and C-S-H1.5, respectively. The change of basal spacing with Ca/Si ratio of C-S-H observed in the experiments agrees with the findings in the study of Renaudin et al [5] corresponding to about 20% contraction of the unit cell volume. The basal spacing is determined by the amount of water and the coordination requirements of the interlayer calcium ions. Removal of interlayer water and calcium ions will thus decrease the basal spacing of C-S-H. According to model proposed by Richardson, C-S-H gels with Ca/Si ratio greater than 1.4 consist of C-S-H(I) with constant basal spacing and a Ca-rich phase intermixed with C-S-H(I) [3].

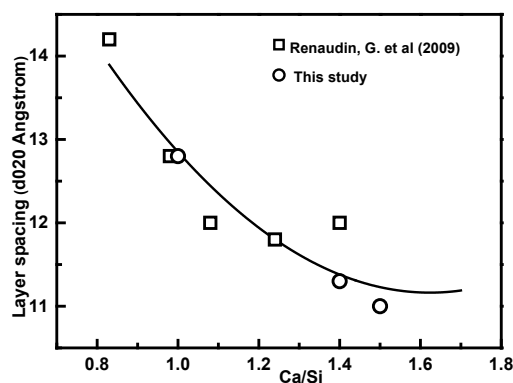


Fig. 2 Relationship between basal spacing and Ca/Si ratio of C-S-H gel plotted together with the results of [3]

3.2 ¹H NMR of C-S-H gels

Information obtained in the ¹H NMR analysis helps probing the molecular structure of C-S-H gels and the atomic interactions between hydrogen groups and silicate moieties (Figure 3). Five distinct peaks of protons are observed in the ¹H NMR spectra of C-S-H gels. The first peak at about -0.3 ppm corresponding to the hydroxyl proton in the ¹H MAS SSNMR spectra suggests the formation of portlandite in C-S-H with a Ca/Si ratio of 1.4 or 1.5. It is previously reported that portlandite is formed after excessive drying of C-S-H gels with Ca/Si ratios up to 1.5 [18]. No peaks of crystalline portlandite in the XRD patterns of C-S-H are observed (Figure 1). The hydroxyl protons identified in ¹H NMR spectra in C-S-H gels with Ca/Si ratios of 1.4 and 1.5 exist most likely in portlandite in an amorphous state. Amorphous portlandite in C-S-H gels is also traced in other studies by using nanoindentation and high energy X-ray tests [19, 20].

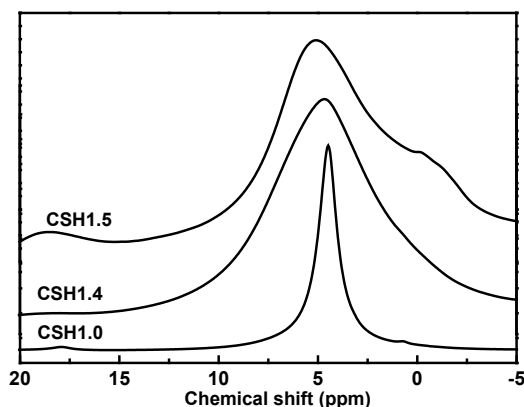


Figure 3 ¹H NMR spectra of C-S-H gels

The chemical shifts of proton species in Ca-OH, and Al-OH are between 0 and 3ppm, and those of the protons in water are between 3 and 6ppm, based on ¹H NMR studies on crystalline silicates and aluminosilicate minerals [21]. The chemical shifts of protons in Si-OH groups of silicates extend to the range between 6 and 18ppm [21].

The ¹H NMR spectrum of C-S-H gel with the Ca/Si ratio of 1.0 shows a sharp resonance peak at 4.4ppm, indicating that most protons exist as absorbed water in the interlayer, which is consistent with the observation of tobermorite. A broad and overlapped peak shifts to 5.2 and 5.6ppm in the ¹H NMR spectra of C-S-H gels with Ca/Si ratios of 1.4 and 1.5, respectively, which indicates that the protons in these C-S-H gels exist in more complex environment than those in C-S-H with a Ca/Si ratio of 1.0. Resonance peaks of the Si-

OH groups between 6-10 ppm are observed in the C-S-H gels with Ca/Si ratio of 1.4 and 1.5, whereas the peaks are absent in C-S-H gels with a Ca/Si ratio of 1.0. The deconvolution of ¹H NMR spectra of C-S-H gels with different Ca/Si ratios based on the assignment of the peaks described above is shown in Figure 4 and Table 2. The resonance peak assigned to absorbed water represents about 40-80% of the total ¹H population in all C-S-H gels with different Ca/Si ratio, which decreases with increasing Ca/Si ratio. The resonance peaks of Si-OH groups between 6-10ppm and Ca-OH in the C-S-H at about 2.5ppm is observed in C-S-H gels with Ca/Si ratios higher than 1.0. The relative fractions of Si-OH groups and Ca-OH in the C-S-H increase with the Ca/Si ratio.

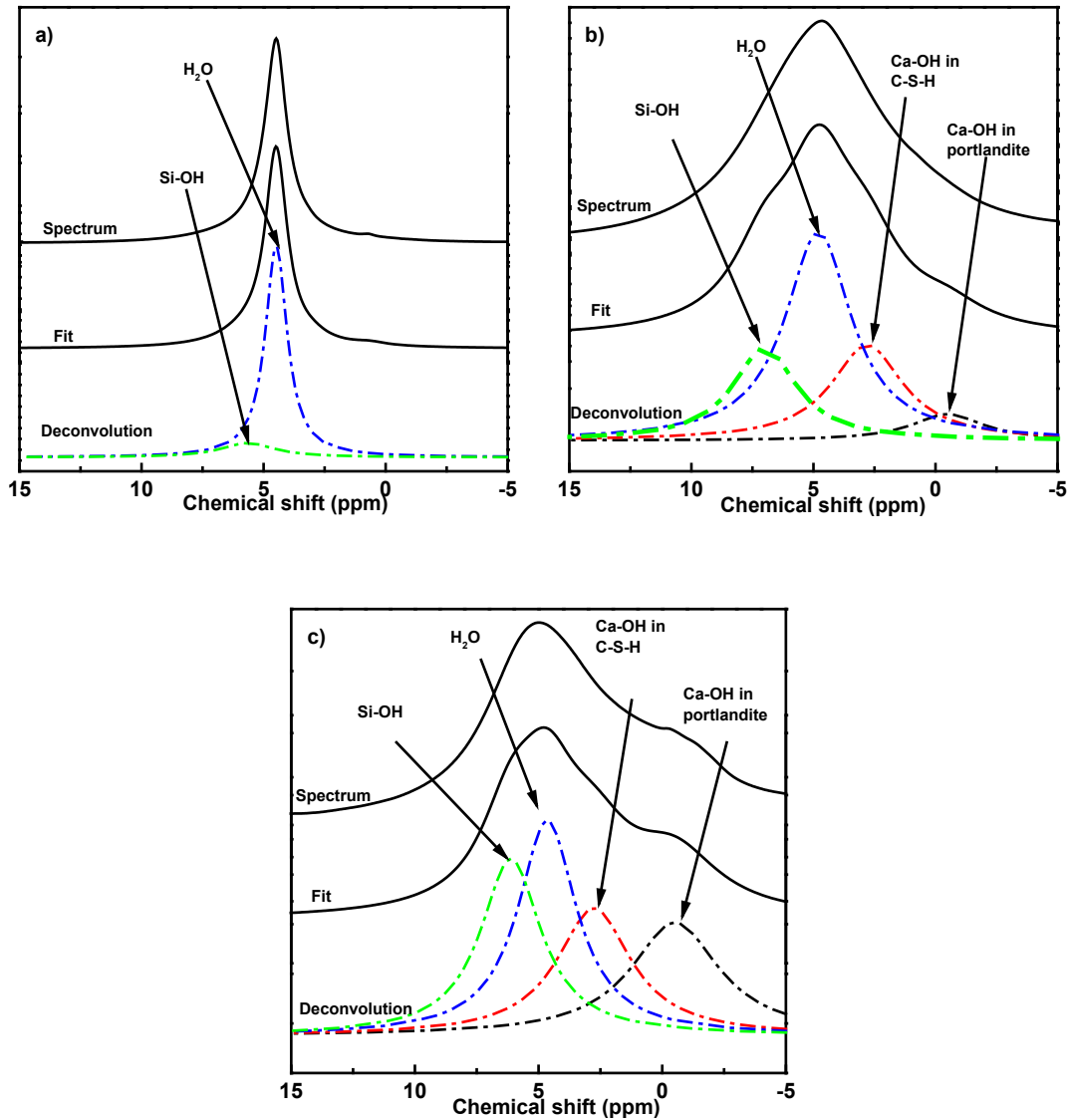


Figure 4 Deconvolution of ¹H NMR spectra of C-S-H gels. a) C-S-H1.0, b) C-S-H1.4, c) C-S-H1.5

Table 4 Quantitative results of fractions of hydrogen groups via deconvolution of ¹H NMR spectra

Samples	Si-OH	H ₂ O	Ca-OH in
	6-15 ppm	3-6 ppm	C-S-H gel 0-3 ppm
C-S-H1.0 (%)	13.8	84	3.2
C-S-H1.4 (%)	23	52	25
C-S-H1.5 (%)	33	38	29

3.3 First principle calculation of ¹H chemical shifts

The mechanism of hydrogen bonding especially the chemical environment of protons and the interactions between hydrogen containing groups and silicate chains are not known, yet. The chemical environment of protons and the distribution of hydrogen bonding between hydrogen containing groups and silicate chains are essential for establishing the structural model of C-S-H. The observed ¹H NMR results are linked to the underlying structure of hydrogen bonds with the help of first principle calculation rooting in DFT-GIPAW methods.

The structural model of C-S-H gel used in calculating the chemical shifts of protons is based on tobermorite-14 Å provided by Crystallography Open Database (as shown in Figure 5a). The protons in the tobermorite-14 Å exist in the interlayer water and silanols bonded with bridging tetrahedral silicates (Q^2_B -OH).

A structural model of C-S-H gel consisting of dimers and pentamers is constructed by modifying the infinite silicate chain model following the literature [8]. The dimers and pentamers are obtained by removing some bridging tetrahedral silicates (Q^2_B -OH) in the infinite chains in the structure of tobermorite. The local negative charge is compensated with H^+ , Ca^{2+} or $Ca(OH)^+$ ions, forming the defective sites and increasing the Ca/Si ratios [14]. After removing a bridging silicate tetrahedron, the unbalanced charge is compensated by either adding two protons forming two silanols bonded with terminal tetrahedral silicates or adding a bridging Ca^{2+} to connect terminal tetrahedral silicates. Additional interlayer water molecular, interlayer $Ca(OH)^+$ ions and $Ca(OH)_2$ are used to connect the defect sites through the interlayer spaces. Three types of calcium ions are distinguished in the model of C-S-H as calcium ions in main layer (Ca_M), calcium ions in interlayer (Ca_I) and calcium ions in bridging sites (Ca_B). Four proton environments are distinguished as interlayer water molecular (H_2O), silanols bonded with bridging tetrahedral silicates (Q^2_B -OH), silanols bonded with terminal tetrahedron silicates (Q^1 -OH) and hydroxyl associated with Ca ions (OH⁻). The constructed structure are geometry and energy optimized with CASTEP based on DFT theory. The optimized structure of the C-S-H model with the mean chemical formula of $C_{1.2}SH_{1.8}$ and various proton environments are shown in Figure 9b).

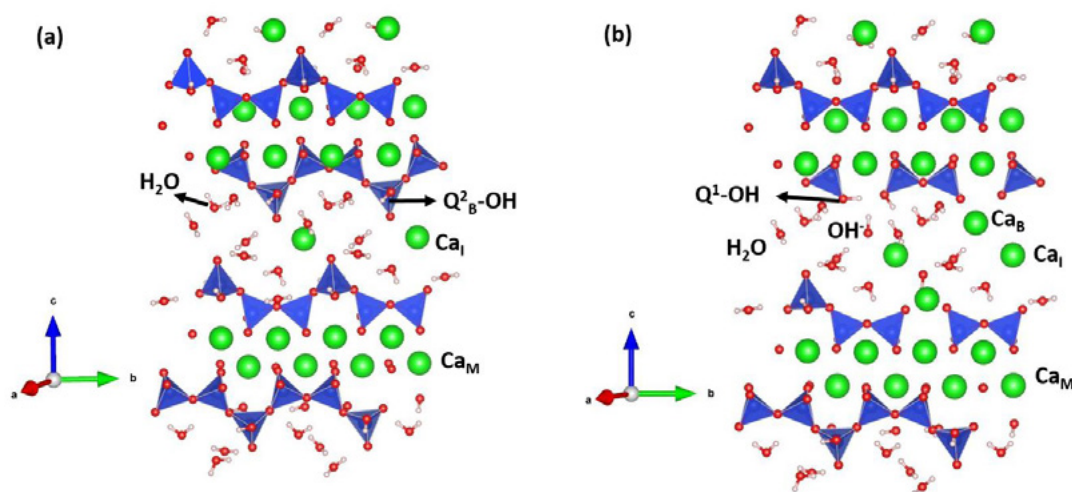


Figure 5 Geometry structures of tobermorite-14Å minerals and $C_{1.2}SH_{1.8}$ gel. a) tobermorite-14Å and various proton environments, b) $C_{1.2}SH_{1.8}$ gel and various proton environments

Protons in different chemical environments exist in the structure of tobermorite-14Å and constructed model of C-S-H gel. The hydrogen bonds are classified into three types according to the donors in the

bond. Three different structure units containing protons and oxygen atoms are labeled as TH (silanols bonded with tetrahedral silicates (T)), W (water molecular) and OH (hydroxyl groups bonded with calcium ions). Nine different hydrogen bonds involving the different donators and acceptors are named as W---W, W---T(Q²) and W---T(TH)(Q¹) etc.

The observed NMR chemical shifts are compared with the calculated values, aiming to correlate the underlying structure of hydrogen containing groups which are shown in the C-S-H model to the observed spectra. Hydrogen bonds affect greatly the isotropic ¹H chemical shifts. A well-established linear relationship between ¹H isotropic chemical shifts and distance of hydrogen bonds ($d_{O-H\cdots O}$) has been reported by experiment if the proton is bonded to oxygen atoms [6, 21]. The accurate values of $d_{O-H\cdots O}$ are calculated from the C-S-H model used in the calculation, with which the correlation between ¹H isotropic chemical shifts and hydrogen bonds are established. The linear relationship between the calculated ¹H chemical shift and values of $d_{O-H\cdots O}$ is shown in Figure 6.

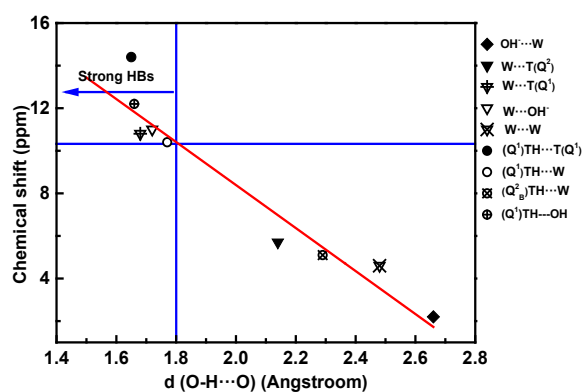


Figure 6 Relationship between calculated ¹H chemical shift and value of $d_{O-H\cdots O}$ (HBs: Hydrogen Bonds)

The comparison between the observed ¹H chemical shifts and the calculated values shows much higher overlapped ranges of protons in water and silanols groups than that indicated from the literatures [12]. Protons in water molecule resonate from 3 to 11ppm, while peaks of protons in silanols bonded with tetrahedral silicates ranges between 10 and 14ppm, leading to broaden and overlapped peaks observed in the ¹H NMR spectra of C-S-H gels with the Ca/Si ratio of 1.4 and 1.5. The highly overlapped ranges of protons are due to the different distance and strength of hydrogen bonds which influence shielded effect to protons. Thus, the hydrogen bonds should be taken into consideration to reasonably analyze the ¹H NMR of C-S-H or cement based materials.

There is a linear correlation between the calculated ¹H chemical shift and the values of $d_{O-H\cdots O}$: $\delta_{iso} = 28.587 - 10.10 d_{O-H\cdots O}$ with δ_{iso} in ppm and $d_{O-H\cdots O}$ in Å (Figure 6). The protons in Ca-OH involved in the hydrogen bond labeled as OH---W resonate at about 2.5ppm, suggesting an average $d_{O-H\cdots O}$ value of about 2.7Å and rather weak hydrogen bonds. Protons in hydroxyl groups serves as a weak donator in hydrogen bonds. Most protons in C-S-H gels exit in water whose ¹H chemical shifts spread in a wide range and has various values of $d_{O-H\cdots O}$. The protons resonating at 4.6ppm is involved in hydrogen bond named as W---W and have an average $d_{O-H\cdots O}$ value of 2.37Å, which is the dominant chemical environment of protons in C-S-H with Ca/Si ratio of 1.0. The protons in water forming the hydrogen bonds with Q¹ sites (W---T(TH) (Q¹)) show higher chemical shifts at 10ppm than those with Q² sites (W---T (Q²)) and have an average value of $d_{O-H\cdots O}$ about 1.84Å. The observation suggests stronger hydrogen bonding between water and Q¹ sites than those with Q² site in the silicate chains, which agrees with the ranking of strength of hydrogen bonds proposed in the literature [13]. Nonbridging oxygen atoms in Q¹ sites serve as stronger hydrogen-bond acceptor

sites than bridging oxygen atoms in Q² sites. The protons in forming hydrogen bonds with water show similar observation that hydrogen bonding between Si-OH groups in Q¹ sites and water ((Q¹)TH---W) are stronger than those between Si-OH groups in Q²_B sites ((Q²_B)TH---W) with water. In conclusion, the Q¹ sites enhance the internal cohesions with water and hydrophilicity of the silicate main chain.

Hydrogen bonds whose the average value of d_{O-H...O} is lower 1.8Å are defined as strong hydrogen bonds (shown in Figure 10). The strong hydrogen bonding are dominated by (Q¹)T-H---T(Q¹), (Q¹)T-H---W, W---OH, W---T(Q¹) and (Q¹)TH---OH. Strong hydrogen bonding between terminal silanol and terminal silicate sites shows the internal cohesions between the parallel chains, which are present in the minerals suolunite and acts as the major interactions between dimes in the structure [10]. The hydroxyl groups bonded with calcium ions serve as strong acceptors for hydrogen bonds, which forms the strong bonding with water (W---OH) and terminal silanol ((Q¹)TH---OH). The strong hydrogen bonding between terminal silanol and hydroxyl acts as the interlayer affinity in the structure of C-S-H gel.

4. Conclusions

The observed ¹H NMR results are correlated with the underlying structure of hydrogen bonds, aiming to reveal the mechanism of hydrogen bonding. The main conclusions can be drawn as followings.

1. Amorphous portlandite exists in C-S-H gels with high Ca/Si ratios.
2. Chemical shifts of protons in C-S-H gel are affected greatly by the hydrogen bonds. Protons in water and silanol resonate in a highly overlapped range. Hydrogen bonds should be taken into consideration to reasonably analyze the ¹H NMR of C-S-H or cement based materials.
3. Strong hydrogen bonding between water and terminal silicate sites or silanol are revealed, which enhance the hydrophilicity of silicate chains in the C-S-H gel.
4. The strong hydrogen bonding between terminal silanol and hydroxyl bonded with calcium ions in C-S-H gel with high Ca/Si ratio is observed, which acts as the affinity in the interlayer space of C-S-H gel, and consequently decreased basal spacing with increasing Ca/Si ratio.

5. Acknowledgment

This research has been financially supported by the National Natural Science Foundation of China (grant numbers 51672199); the Fundamental Research Funds for the Central Universities (grant number WUT: 2017-YB-008□2019III018GX); and the 111 Project (No. B18038).

6. References

- [1] B. Lothenbach, A. Nonat, Calcium silicate hydrates: Solid and liquid phase composition, *Cem Concr Res*, 78 (2015) 57-70. <https://doi.org/10.1016/j.cemconres.2015.03.019>.
- [2] H.F.W. Taylor, *Cement Chemistry*, 2nd ed., Thomas Telford, London, 1997.
- [3] I.G. Richardson, Model structures for C-(A)-S-H(I), *Acta crystallographica Section B, Structural science, crystal engineering and materials*, 70 (2014) 903-923. <https://doi.org/10.1107/S2052520614021982>.
- [4] I.G. Richardson, Tobermorite/jennite- and tobermorite/calcium hydroxide-based models for the structure of C-S-H: applicability to hardened pastes of tricalcium silicate, β-dicalcium silicate, Portland cement, and blends of Portland cement with blast-furnace slag, metakaolin, or silica fume, *Cem Concr Res*, 34 (2004) 1733-1777. <https://doi.org/10.1016/j.cemconres.2004.05.034>.
- [5] G. Renaudin, J. Russias, F. Leroux, F. Frizon, C. Cau-dit-Coumes, Structural characterization of C-S-H

and C–A–S–H samples—Part I: Long-range order investigated by Rietveld analyses, *J Solid State Chem*, 182 (2009) 3312-3319. <https://doi.org/10.1016/j.jssc.2009.09.026>.

[6] G. Renaudin, J. Russias, F. Leroux, C. Cau-dit-Coumes, F. Frizon, Structural characterization of C–S–H and C–A–S–H samples—Part II: Local environment investigated by spectroscopic analyses, *J Solid State Chem*, 182 (2009) 3320-3329. <https://doi.org/10.1016/j.jssc.2009.09.024>.

[7] X. Pardal, F. Brunet, T. Charpentier, I. Pochard, A. Nonat, ²⁷Al and ²⁹Si solid-state NMR characterization of calcium-aluminosilicate-hydrate, *Inorganic chemistry*, 51 (2012) 1827-1836. <https://doi.org/10.1021/ic202124x>.

[8] P. Rejmak, J.S. Dolado, M.J. Stott, A. Ayuela, ²⁹Si NMR in Cement: A Theoretical Study on Calcium Silicate Hydrates, *J Chem Phys C*, 116 (2012) 9755-9761. <https://doi.org/10.1021/jp302218j>.

[9] G.A. Jeffrey, *An introduction to hydrogen bonding*, Oxford university press, New York, 1997.

[10] C. Dharmawardhana, M. Bakare, A. Misra, W.-Y. Ching, J. Bullard, Nature of Interatomic Bonding in Controlling the Mechanical Properties of Calcium Silicate Hydrates, *J Am Ceram Soc*, 99 (2016) 2120-2130. <https://doi.org/10.1111/jace.14214>.

[11] F. Brunet, P. Bertani, T. Charpentier, A. Nonat, J. Virlet, Application of ²⁹Si Homonuclear and ¹H-²⁹Si Heteronuclear NMR Correlation to Structural Studies of Calcium Silicate Hydrates, *J Phys Chem B*, 108 (2004) 15494-15502. <https://doi.org/10.1021/jp031174g>.

[12] A. Rawal, B.J. Smith, G.L. Athens, C.L. Edwards, L. Roberts, V. Gupta, B.F. Chmelka, Molecular Silicate and Aluminate Species in Anhydrous and Hydrated Cements, *J Am Chem Soc*, 132 (2010) 7321-7337. <https://doi.org/10.1021/ja908146m>.

[13] M. Youssef, R.J.M. Pellenq, B. Yildiz, Glassy Nature of Water in an Ultraconfining Disordered Material: The Case of Calcium–Silicate–Hydrate, *J Am Chem Soc*, 133 (2011) 2499-2510. <https://doi.org/10.1021/ja107003a>.

[14] A. Kumar, B.J. Walder, A. Kunhi Mohamed, A. Hofstetter, B. Srinivasan, A.J. Rossini, K. Scrivener, L. Emsley, P. Bowen, The Atomic-Level Structure of Cementitious Calcium Silicate Hydrate, *J Phys Chem C*, 121 (2017) 17188-17196. <https://doi.org/10.1021/acs.jpcc.7b02439>.

[15] J.R. Yates, T.N. Pham, C.J. Pickard, F. Mauri, A.M. Amado, A.M. Gil, S.P. Brown, An Investigation of Weak CH...O Hydrogen Bonds in Maltose Anomers by a Combination of Calculation and Experimental Solid-State NMR Spectroscopy, *J Am Chem Soc* 127 (2005) 10216-10220.

[16] M. Profeta, F. Mauri, C.J. Pickard, Accurate First Principles Prediction of ¹⁷O NMR Parameters in SiO₂ Assignment of the Zeolite Ferrierite Spectrum, *J Am Chem Soc*, 125 (2003) 541-548.

[17] X. Pardal, I. Pochard, A. Nonat, Experimental study of Si–Al substitution in calcium-silicate-hydrate (C-S-H) prepared under equilibrium conditions, *Cem Concr Res*, 39 (2009) 637-643. <https://doi.org/10.1016/j.cemconres.2009.05.001>.

[18] E. Pustovgar, R.P. Sangodkar, A.S. Andreev, M. Palacios, B.F. Chmelka, R.J. Flatt, J.B. d'Espinose de Lacaillerie, Understanding silicate hydration from quantitative analyses of hydrating tricalcium silicates, *Nature communications*, 7 (2016) 10952. <https://doi.org/10.1038/ncomms10952>.

[19] F. Puertas, M. Palacios, H. Manzano, J.S. Dolado, A. Rico, J. Rodríguez, A model for the C-A-S-H gel formed in alkali-activated slag cements, *J Eur Chem Soc*, 31 (2011) 2043-2056. <https://doi.org/10.1016/j>.

jeurceramsoc.2011.04.036.

[20] S. Grangeon, A. Fernandez-Martinez, A. Baronnet, N. Marty, A. Poulain, E. Elkaim, C. Roos, S. Gaboreau, P. Henocq, F. Claret, Quantitative X-ray pair distribution function analysis of nanocrystalline calcium silicate hydrates: a contribution to the understanding of cement chemistry, *Journal of applied crystallography*, 50 (2017) 14-21. <https://doi.org/10.1107/S1600576716017404>.

[21] J.P. Yesinowski, H. Eckert, G.R. Rossman, Characterization of Hydrous Species in Minerals by High-Speed MAS-NMR, *J Am Chem Soc*, 110 (1988) 11367-11375. <https://doi.org/10.1021/ja00213a007>.

Concrete with High-purity Volcanic Glass Powder Manufactured from Pyroclastic Deposit through Dry Gravity Classification and Pulverization

T. Noguchi¹, A. Tomoyose¹, K. Sodeyama² and K. Higashi³

¹Department of Architecture, The University of Tokyo, 7-3-1 Hongo, Bunkyo-ku, Tokyo, Japan

²Kagoshima Prefectural Institute of Industrial Technology, 1445-1 Oda, Hayato-cho, Kirishima-shi, Kagoshima, Japan

³Principle Co., Ltd., 1-17-8 Kamoike, Kagoshima-shi, Kagoshima, Japan

Abstract

Utilization of natural pozzolan such as volcano-related materials in concrete as a supplementary cementitious material can contribute to establishment of low-carbon society and resource circulation society. Volcanic-related materials generally comprise not only glass but also crystal mineral and clay mineral, which may cause undesirable properties in concrete. The authors developed the technology for dividing volcanic-related materials into crystalline mineral, pumice, high-purity volcanic glass, and clay fraction toward total utilization of volcanic-related materials as construction materials. In this study, concrete containing high-purity volcanic glass powders with different fineness are investigated regarding fresh properties, strength development, chloride ion penetration and CO₂ reduction. Experimental works were conducted using 7 types of volcanic glass powders with replacement ratios of 5%, 10% and 20% in concrete with water-to-binder ratios of 20% and 50% for the investigation of fresh properties and strength development. Another experiment on chloride ion penetration in concrete was also conducted using concrete with water-binder ratio of 60% containing volcanic glass powders with replacement ratios of 20%. As a result, it was found that volcanic glass powders gave excellent contribution to the improvement of flowability like fly ash, the enhancement of strength like silica fume, and the restraint of chloride ion penetration like ground granulated blast-furnace-slag. Volcanic glass powders can also contribute to the reduction of CO₂ emission because the content of portland cement can be largely reduced to obtain the same strength in concrete with 100% portland cement.

Keywords: Volcanic glass powder, Supplementary cementitious material, Strength development, Chloride ion diffusion, CO₂ reduction

1. Introduction

Ancient concrete used in the Pantheon in Rome contains volcanic ejecta, which is known as pozzolana. One popular technique to reduce CO₂ emissions stemming from concrete production and construction involves the use of these natural pozzolans as supplementary cementitious materials (SCMs) [1]. Volcanic activity is common in Japan, and one of the earliest researches to use volcanic ejecta as SCM began more than 110 years ago in Hokkaido, the northern part of Japan [2, 3]. Subsequently, many studies were done on the applications of domestic natural pozzolan as SCM, and have been recently reviewed by Cai et

al. [4]. Although concrete made with volcano-related materials had been manufactured practically until 1960's, artificial materials have been chosen as a replacement. The reaction of natural pozzolans is due to volcanic siliceous glass [5], but volcanic ejecta generally comprises not only glass but also crystal mineral and clay mineral in their natural conditions [6], which may lead to typical undesirable properties of natural pozzolans; large variety, variability, and high water demand [7].

In the previous researches [8-11] on the total utilization of pyroclastic flow deposits as construction materials, the authors clarified that dry gravity classification is effective in dividing Ito-shirasu into crystalline mineral, pumice, high-purity volcanic glass, and clay fraction. Through a separating machine made by combining a gravity separator with a winnowing sorter, the amorphous content of volcanic glass increased to 88% when that of raw material is about 60%. As the mechanism of the machine is shown in Figure 1, winnowing with the action of the vibration fluid bed can sort particles by density, particle size, and terminal velocity with low energy consumption.

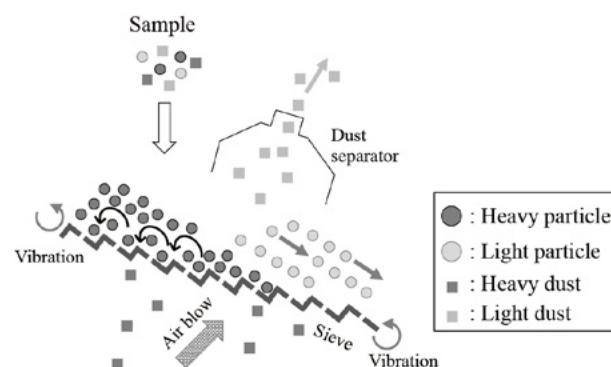


Figure 1: The mechanism of the separating machine for dividing Ito-shirasu.

We have also reported earlier that, when using this material pulverized to a BET specific surface of 15m²/g by a jet mill as a SCM, a replacement ratio of 10% in high strength concrete with a water-to-binder ratio (W/B) of 0.2 leads to fresh properties (microfiller effect) and strength development comparable to those of silica fume. In normal concrete with a W/B of 0.6, a replacement ratio of 5% to 20% leads to strengths higher than that of concrete with no SCM beginning from an age of 7 days, and the strength increases as the replacement ratio increases. Immersion tests in saltwater revealed that the apparent diffusion coefficient decreases to as low as 15% and 10% with replacement ratios of 10% and 20%, respectively, when compared with those of concrete with no replacement. Volcanic glass powder (VGP) was thus found to provide excellent resistance to chloride ion penetration. Furthermore, a replacement ratio of up to 20% does not impair the carbonation resistance. The long-term strength development and durability have also been investigated with a replacement ratio of 20%.

In this study, concrete containing volcanic glass powders with different fineness are investigated from a more practical aspect.

2. Experimental program

2.1 Manufacturing process of VGP

Ito-shirasu used in this investigation was delivered from Kanoya-city, Kagoshima Prefecture in Japan by a mine operator without any pretreatment as shown in Figure 2. The mineral composition of particle size fractions and the chemical composition of the raw material reported in the previous research [12] are presented in Figure 3. As to mineral components, the fraction over 2.4g/cm³ is defined as crystalline, under 2.4g/cm³ defined as amorphous, and in particular under 1.5g/cm³ as pumice in this figure. After sieving Ito-shirasu to under 5mm, Ito-shirasu is divided into five substances by a dry gravity separator. Volcanic

glass powder was manufactured through dry gravity classification and pulverization as shown in Figure 4. First, classified volcanic glass is crushed by a roller mill to a mean particle size of 5.1 μ m. This was then pulverized and classified using three devices, namely, a jet mill, an air classifier, and a cyclone, with the resulting coarse and fine powders being recovered by cyclones and dust collectors, respectively.

2.2 Properties of VGP

The basic properties of seven VGPs are shown in Table 1; the BET specific surface area measured by N₂-adsorption, amorphous content based on heavy liquid separation using zinc bromide ($\rho=2.4\text{g/cm}^3$), and chemical composition by fluorescent X-ray analysis.

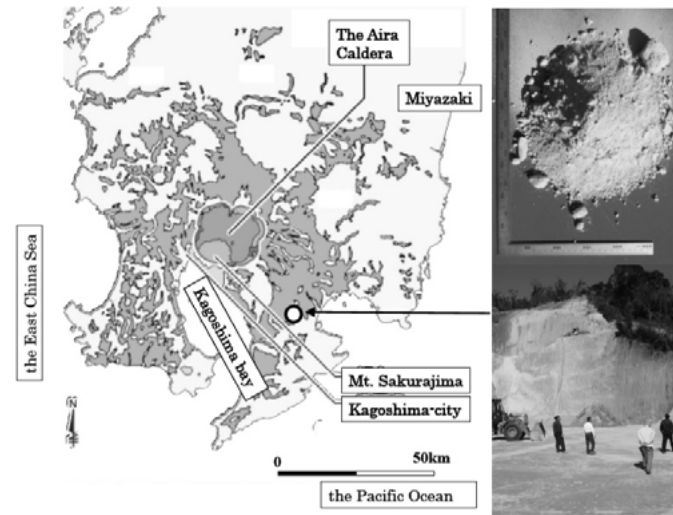


Figure 1: Distribution of shirasu and location of sampling site.

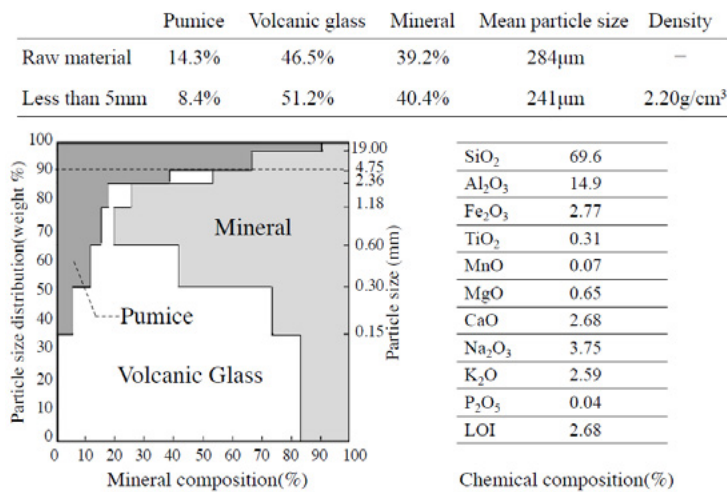


Figure 3: Mineral composition of particle size fractions and chemical composition of Ito-shirasu.

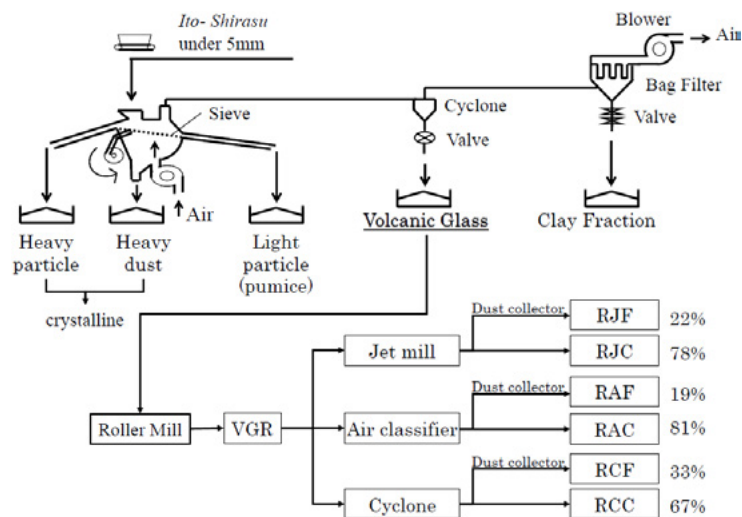


Figure 4: Dry gravity classification and pulverization for manufacturing volcanic glass powder.

Table 1: Basic properties of VGPs.

Marks	VGR	RJF	RJC	RAF	RAC	RCF	RCC
SiO ₂	73.9	72.4	74.3	72.6	74.2	73.0	74.3
TiO ₂	0.20	0.21	0.20	0.21	0.20	0.21	0.19
Al ₂ O ₃	12.8	13.3	12.6	13.2	12.7	13.1	12.6
Fe ₂ O ₃	1.89	2.33	1.76	2.26	1.83	2.38	1.78
MnO	0.05	0.06	0.05	0.06	0.05	0.06	0.05
MgO	0.30	0.37	0.26	0.34	0.29	0.32	0.28
CaO	1.44	1.56	1.40	1.55	1.42	1.51	1.39
Na ₂ O	3.78	3.57	3.91	3.60	3.71	3.59	3.75
K ₂ O	3.34	3.36	3.38	3.30	3.37	3.32	3.35
P ₂ O ₅	0.03	0.04	0.03	0.04	0.03	0.04	0.03
LOI	2.25	2.81	2.02	2.84	2.14	2.47	2.25
BET surface area (m ² /g)	6.4	16.1	4.2	15.2	5.1	12.0	3.6
Glass content (%)	85.7	88.6	87.4				

Table 2: Materials used.

Material	Properties	Marks
Binder	Cement	Normal portland cement, density: 3.24 g/cm ³
		Low-heat portland cement, density: 3.24 g/cm ³
	SCM	VGP, SF, FA
Fine aggregate		Crushed lime, density: 2.67g/cm ³
		Crushed tight sand, density: 2.62 g/cm ³
Coarse aggregate		Crushed tight sand, density: 2.64 g/cm ³
		Crushed lime, density: 2.70 g/cm ³
Chemical admixture		High-range water-reducing admixture
		Air-entraining and high-range water-reducing admixture
		Air-entraining and water reducing admixture
		Air-entraining admixture

Table 3: Factors and level, mixing proportions.

Series	W/B	Cement	W (kg/m ³)	SCM/B (%)	S1:S2	s/a (%)	SCM used	Chemical admixture used	Target air content (%)	Target slump (cm)
I	0.20	L	160	10	4:6	45.2	SF + 6 VGP	SP1	2.0±1.0	Slump flow 65±10
II	0.50	N	167	25	2.5:7.5	42.8	FA + 6 VGP	SP2+AE	5.0±1.0	Slump 18±2.5
III	0.60	N	183	5 10 20	2.5:7.5	50.8	RF RC VGR	SP3 + AE	5.0 ± 1.5	Slump 18±2.5

2.3 Mix proportion and test method

The experimental program for three types of VGP was divided into four series, and tests were conducted on concrete mixtures. A forced-action double-axis mixer was used for mixing. Referring to the JIS test method for the activity indices for silica fume (SF) and fly ash (FA), the W/B and replacement ratio were set at 20% and 10%, respectively, in Series 1, whereas they were set at 50% and 25% in Series 2, respectively. The materials and mixture proportions are listed in Tables 2 and 3, respectively. The reference SCM for Series 1 (W/B=20%) was SF. Its target air content and slump flow were 2.0±1.0% and 65±10cm, respectively. The reference SCM for Series 2 (W/B=50%) was FA. Its target air content and slump were 5.0±1.5% and 18±2.5cm, respectively. The chemical admixture dosage was adjusted to achieve the target air content and slump. Compression specimens (φ100×200mm cylinders) were fabricated after testing the fresh properties, namely, the slump (only for Series 2), slump flow, air content, concrete temperature, time to 50cm flow, and time to end-of-flow (only for Series 1). Compression tests were conducted at standard curing ages of 1, 4, and 13 weeks.

In Series III, the influence of VGP on the chloride diffusion of concrete was experimentally examined. Tests were performed on concrete specimens (W/B=60%) of three different sizes of VGP (RF, RC and VGR) with a replacement ratio of 20% and OPC for reference, according to the JSCE standard “Test method for apparent diffusion coefficient of chloride ion in concrete by submergence in salt water”. After cutting off 25mm slices from the top and bottom ends of each cylinder, concrete specimens were cured in a water bath at 20°C. The curing period was 28 days. Specimens were coated with epoxy excepting the circular placing surface and immersed in a 10% NaCl solution at 20°C for 42 weeks. The total chloride ion profile was determined by cutting four 10 mm slices from each cylinder so that the centers of the slices would be the points at depths of 5, 20, 35, 50 and 65 mm from the uncoated surface. These were crushed to less than 150 μm and subjected to ion chromatography to quantify chloride ions in accordance with JIS A 1154 (Method of test for chloride ion content in hardened concrete).

In Series IV, the relational expressions between the binder-water ratio (B/W) and the 28-day compressive strength were experimentally determined to evaluate the environmental performance of concrete containing VGP on a practical basis. Tests were conducted at a ready-mixed concrete plant with actual shipping experience. All materials excepting VGP were the same as those normally shipped from the plant. Trial mixtures of RF, RC, and VGR were prepared with a fixed replacement ratio and three levels of W/Bs. Table 4 tabulates the test levels, proportioning factors, and fresh test results. The replacement ratio was 20% for RF, RC and VGR. RF was also tested with replacement ratios of 5% and 10%. The target slump and air content were 18±3cm and 4.5±1.5%, respectively, for all mixtures. Compression tests were conducted at 28 days after standard curing.

Table 4: Test levels, proportioning factors and fresh test results.

SCM-replacement	W/B (%)	W (kg/m ³)	SP dosage (B*wt%)	AE dosage (B*wt%)	Slump (cm)	Air (%)
RF-20%	60	172	0.80	0.3	19.0	5.9
	50	170	0.90	0.0	19.0	5.7
	35	174	0.90	0.0	19.0	5.9
VGR-20%	60	172	0.65	0.2	19.0	5.9
	50	170	0.65	0.1	19.0	4.6
	35	174	0.80	0.0	20.0	3.4
RC-20%	60	172	0.65	0.0	20.0	5.4
	50	170	0.60	0.1	20.0	4.9
	35	174	0.95	0.1	20.0	3.7
RF-5%	60	172	0.70	0.0	18.5	5.8
	50	170	0.90	0.0	20.5	4.8
	40	172	0.70	0.0	19.0	3.5
RF-10%	60	172	0.70	0.0	18.0	5.2
	50	170	0.90	0.0	20.0	5.4
	40	172	0.85	0.0	21.0	4.0

3. Experimental results

3.1 Fresh properties

Table 5 gives the fresh properties immediately after mixing and chemical admixture dosage of Series I. All VGPs are found to provide slump flows equal to or greater than SF with smaller chemical admixture dosages. In comparison with SF with a mean diameter of 0.1 μ m, the size of VGP is large. It is therefore presumed that agglomerations are prone to be dispersed due to the small van der Waals forces, requiring a small chemical admixture dosage. The time to 50-cm flow of the coarse powders is longer than that of fine powders, with substantial viscosity and dilatancy to cause resistance to shoveling with a cement shovel. Though the time to 50-cm flow with the three fine powders is longer than that with SF, the consistency was sufficiently practicable. Powders with a BET specific surface of 12m²/g or greater contain sufficient amounts of fine particles to fill the spaces between cement particles, increasing the packing factor of the binder. This presumably achieves a microfiller effect comparable to SF. Based on these results, it is judged that, in fresh concrete with a W/B of around 20%, fine powders with a BET specific surface of 12m²/g or more provide a flowability-improving effect, while the effect is less evident with coarse powders with a BET specific surface of 5m²/g or less.

However, it can be said that VGP is a supplementary cementitious material that is expected to produce a sufficient effect of improving the workability of low W/B mixtures as demonstrated in the present results, provided that its physical properties including grading are rectified during the process of crushing and classification and that impurities including clay minerals are removed.

Table 6 gives the fresh properties and chemical admixture dosage of Series II. The mixing time was the same for all VGPs. The dosage of the high-performance air-entraining and water-reducing admixture for fine powders to achieve the target slump is higher than FA, whereas the admixture dosage to achieve the target slump and air content with coarse powders was the same as SF. The use of VGP reduces the slump flow by 15%, leading to fresh concrete with a high yield value. This is presumably due to the effect of the angular shape of crushed VGP particles in contrast to spherical FA particles. However, coarse powders with a BET specific surface of 5m²/g or less show sufficiently practicable viscosity comparable to FA. It can therefore be said, from these results, that the target slump and air content were achievable in fresh concrete with a W/B of around 50% by using the same dosage of a chemical admixture as FA, which is effective in improving the concrete flowability.

Table 5: Fresh properties and chemical admixture dosage of Series 1.

Type pf SCM /BET surface area (m ² /g)	Slump flow (cm)	Air (%)	Time to 500mm flow (sec)	Time to end-of-flow (sec)	SP1 dosage (B*wt%)
RJF/16.1	74.0×74.8	2.1	5.3	97	1.40
RAF/15.2	73.2×75.0	2.1	5.8	118	1.40
RGF/12.0	73.8×72.2	1.8	5.5	92	1.40
RJC/4.2	74.0×73.8	1.8	6.3	95	1.30
RAC/5.1	72.4×71.1	1.9	6.8	102	1.20
RGC/3.6	69.8×68.2	1.9	8.3	103	1.20
SF/17.7	69.0×68.0	2.9	4.3	79	1.60

Table 6: fresh properties and chemical admixture dosage of Series II.

Type pf SCM /BET surface area (m ² /g)	Slump (cm)	Air □ % □	SP2 Dosage (B*wt%)	AE dosage (B*wt%)
RJF/16.1	18.5	5.8	1.10	0.40
RAF/15.2	19.5	5.8	1.10	0.40
RGF/12.0	19.0	5.6	1.10	0.40
RJC/4.2	19.5	5.8	0.83	0.40
RAC/5.1	19.0	5.7	0.83	0.40
RGC/3.6	18.0	5.5	0.83	0.40
FA/1.4	20.0	5.9	0.83	0.40

3.2 Strength development

Figure 5 shows the compressive strength with a W/B of 20%. At an age of 4 weeks, the strength with VGPs is equal to or higher than with SF. At 13 weeks, the strength is equal to or lower than SF. It has been reported that, if the W/B is constant, then a 1% increase in the air content reduces the strength by 4% to 6%. The air content with SF is higher than that with VGP by around 1% in a fresh state. It follows that, even if the strength with VGP is reduced by 5%, it can be regarded as roughly comparable to SF up to 4 weeks. Figure 6 shows the compressive strength with W/B=50%. The strength with fine powders is approximately 20% higher than with FA, while that with coarse powders is equivalent to that with FA, at all ages.

Figure 7 shows the strength development. With W/B=20%, the strength gains with SF from 4 to 13 weeks are greater than with any of the VGPs, but the slopes from 7 to 28 days are similar for all specimens. With W/B=50%, similar tendencies are found in the strength development over time in both cases of FA and VGP.

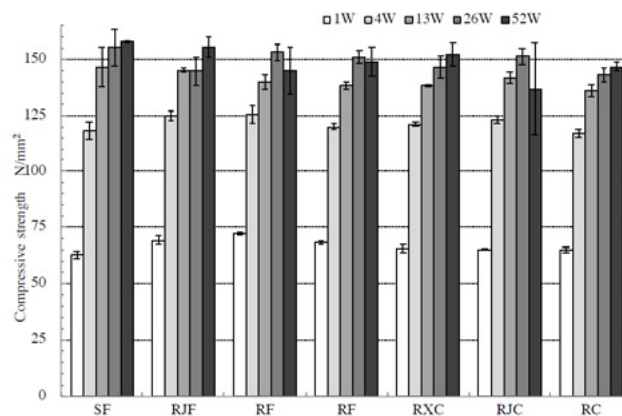


Figure 5: Compressive strength with a W/B of 20% in Series I.

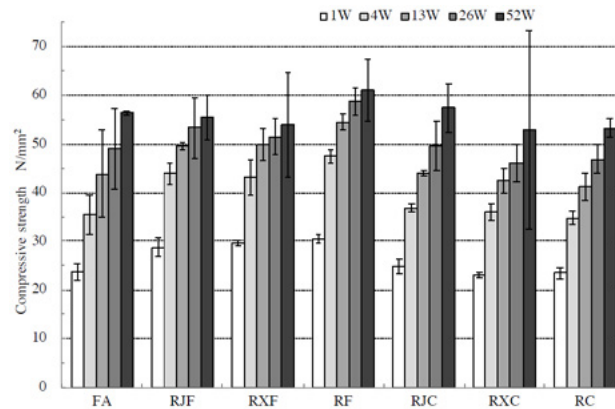


Figure 6: Compressive strength with a W/B of 50% in Series II.

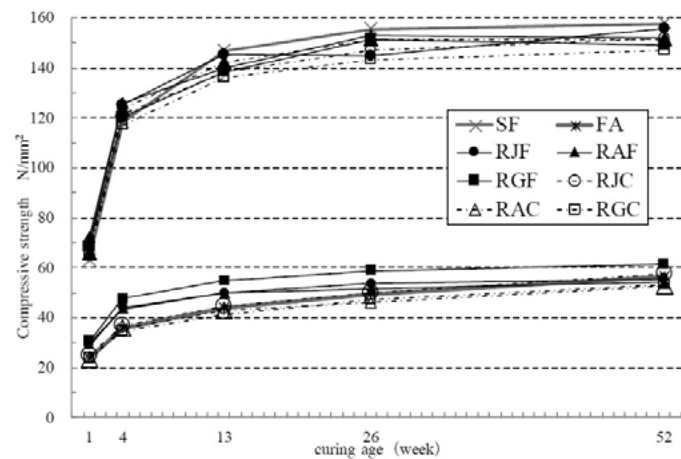


Figure 7: Strength development.

Figure 8 shows VGP's BET specific surface and the relative strength ratio to SF at W/B=20%. The strongest correlation between the relative strength ratio and the BET specific surface is observed at 1 week, with the strength being equivalent with SF even at a BET specific surface of 3m²/g. With a BET specific surface of 12m²/g or greater, the strength is equal to or higher than with SF. However, both the slope of the approximate lines and the correlation coefficients decrease over time, ending up with a strength equivalent to that with SF with all specific surfaces at 4 weeks and a strength equal to or lower than that with SF even with 15m²/g or more at 13 weeks. The reaction rate of SF in place of 10% of cement in a paste with W/B=22% is reported to rapidly increase up to 7 days and slows down thereafter. Though the strength development mechanism of VGP can slightly differ from that of SF due to the different glass percentage and chemical composition, it is presumed that the strength test results of VGP correlate well with the BET specific surface at 1 week and delayed reaction of particles with smaller BET specific surfaces proceeds thereafter. However, the results that strength ratio to SF is 100% or higher up to 4 weeks but is less than SF at 13 weeks imply the effects of factors other than reactions, such as void percentage. Elucidation of strength development related to age remains a subject for future research.

Figure 9 shows the relative strength ratio to FA with W/B=50%. A closer correlation than 20% W/B is observed between VGP's BET specific surface and strength ratio to FA, though with a slight scatter at 13 weeks. According to a former research on pastes with a replacement ratio of 20% and a W/B of 40%, the

reaction ratio of Type II fly ash specified in JIS A 6201 is around 10% at 7 days and 42% to 53% at 555 days, being affected by the amount, chemical composition, and fineness of the glass phase. Since the only difference among the six types of VGPs in the present study is fineness, the obtained strength development presumably corresponds with the BET specific surface, which is closely related to fineness. However, the slightly low strength ratio to FA at 13 weeks requires further observation of long-term strength to elucidate the strength development mechanism.

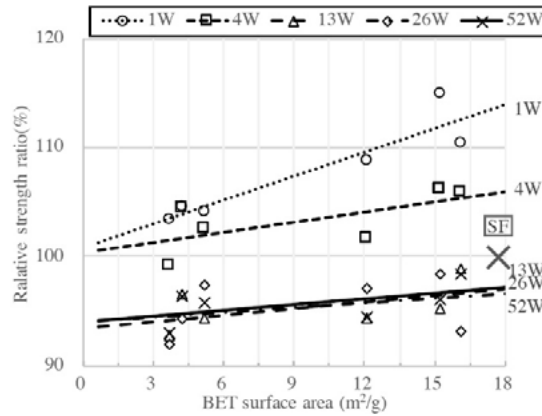


Figure 8: VGP's BET specific surface and the relative strength ratio to SF at W/B=20%.

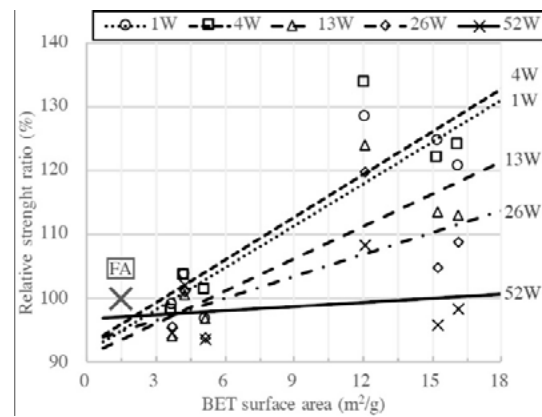


Figure 9: VGP's BET specific surface and the relative strength ratio to FA at W/B=50%.

Resistance to chloride ion penetration

Figure 10 shows the results of immersion tests on concrete specimens in 10% saltwater for 42 weeks after 4-week water curing. The concretes with W/B=60% were OPC and concretes containing RF, VGR, and RC in place of 20% of cement. The chloride contents in the surfaces and deeper inward of concrete containing VGPs are significantly lower than those of OPC. Concrete containing RF or VGR not only shields the penetration of chlorides at a depth of 20mm but also inhibits its penetration at 10mm. Even concrete containing RC with the smallest BET specific surface is found to shield chloride ion penetration at 35mm. Though the shielding effect of RC is weaker than those of RF and VGR, it significantly improves the chloride ion resistance of concrete when compared with OPC. The apparent diffusion coefficients of OPC, RF, VGR, and RC regarding all chloride ions are 4.00, 0.16, 0.20, and 0.60cm²/year, respectively. VGPs with a larger BET specific surface show a smaller apparent diffusion coefficient of chloride ions. In the case of a replacement ratio of 20%, even the apparent diffusion coefficient of RC with a BET specific surface of approximately 3m²/g is less than 20% of that of OPC. The diffusion coefficients of VGR and RF with BET specific surfaces of approximately 7m²/g and 11m²/g, respectively, are less than 20% and less than 10%, respectively, of that of OPC.

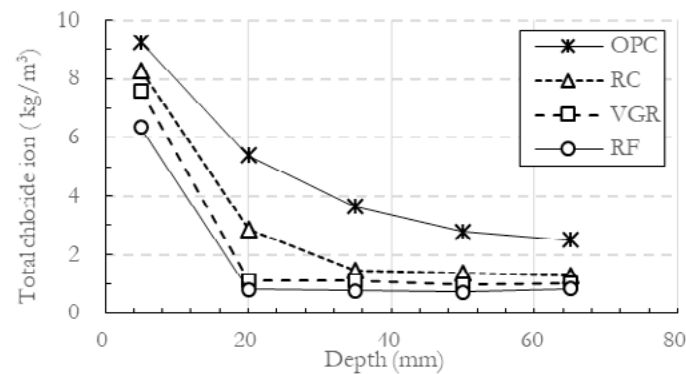


Figure 10: Chloride ion penetration in 10% saltwater for 42 weeks.

3.3 W/B-strength relation and contribution to CO2 reduction

Figure 11 shows the approximate lines calculated from the compression test results and the B/W-strength relational expressions. The relational expression for OPC in the figure is the expression adopted for the actual ready-mixed concrete made of the same materials and shipped by the plant. Due to approximation of trial mixtures with three levels by $n=1$, the scatter of the results of 20%-replaced RF is wider than that of OPC approximated by $n=4$. RF with a BET specific surface of 11m²/g shows a higher strength than OPC with the same B/W even with a replacement ratio of 5%, and the effect remains up to a replacement ratio of 20%. The strength of VGR with a BET specific surface of 7m²/g is slightly higher than OPC. That of RC with a BET specific surface of 3m²/g is slightly lower than OPC. In Series 2, the strength development is comparable to fly ash with a W/B of 50% and replacement ratio of 25%. It can therefore be regarded as equivalent to general fly ash of JIS Type II, which is available on the market in Japan. A higher strength at 91 days is therefore expected.

Figure 12 shows the unit cement reduction determined from calculation by the relational expression for proportioning to achieve compressive strengths of 30, 40, and 50MPa. The unit water content of OPC proportioning for general slump control is assumed to be 180kg/m³, whereas the unit water content in the flow control using VGP is assumed to be 170kg/m³. By assuming the proportioning control strength as 50MPa, the cement content can be reduced by more than 100kg even with a replacement ratio of 10% at which the carbonation rate coefficient decreases. With a 20% replacement, the cement content can be reduced by 150kg. Also, with RC, the B/W-strength relational expression of which is lower than cement, the cement demand to obtain the same strength becomes smaller, as the replacement ratio is 20%. Reductions of more than 50kg are therefore achieved at all strength levels.

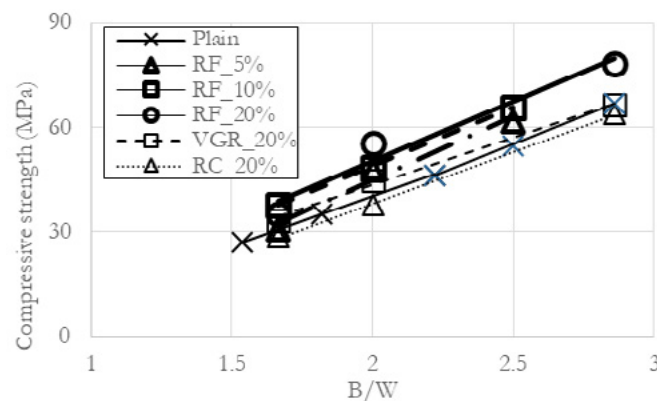


Figure 11: B/W-compressive strength relation

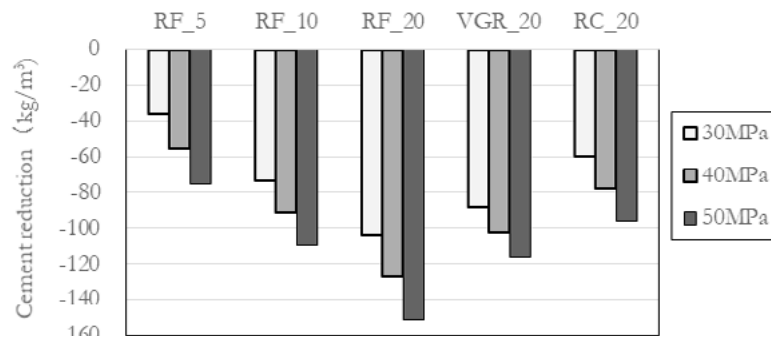


Figure 12: Unit cement reduction to achieve compressive strengths of 30, 40 and 50MPa.

4. Conclusions

The findings regarding concrete made using volcanic glass powder obtained in this study include the following:

(1) Fresh properties

With a W/B of around 20%, VGP powder with a BET specific surface of 12m²/g or more has a flowability-improving effect, while such an effect is judged as being weak with a BET specific surface of 5m²/g or less. With a W/B of around 50% or more, a replacement ratio exceeding 10% of VGP with a BET specific surface of 12m²/g or more increases the chemical admixture demand for achieving the target slump increases. With a BET specific surface of 5m²/g or less, however, the target slump and air content can be achieved with a chemical admixture dosage equivalent to JIS Type II fly ash with a replacement ratio of 25%.

(2) Strength properties

With a W/B of around 20%, the BET specific surface of VGP correlates with the strength, demonstrating the strength-developing performance equivalent to SF with a BET specific surface of around 5m²/g, and that equal to or higher than SF with a BET specific surface of 12m²/g. At four weeks, the correlation between the BET specific surface and strength becomes weak, demonstrating a strength-developing performance equivalent to SF. At an age of 13 weeks, the correlation becomes even weaker, with the strength being equivalent or lower than SF. With a W/B of around 50% or more, a strength equivalent to JIS Type II fly ash is obtained with a BET specific surface of around 3m²/g. The strength becomes 20% higher than fly ash with a BET specific surface of 12m²/g or more, with correlation between the BET specific surface and the strength being observed up to 91 days.

(3) Durability and CO₂ reduction

The use of VGP with a BET specific surface of around 3m²/g at a replacement ratio of 20% provides sufficient resistance to chloride ion penetration, being sufficiently effective in reducing the amount of portland cement consumption.

5. Acknowledgment

This research is supported by JSPS Grant-in-Aid for Scientific Research (A) with No. 18H03803 entitled “Carbon-minus Recyclable High-performance Concrete”.

6. Reference

- [1] K. Kupwade-Patil, C. de Wolf, S. Chin, J. Ochsendorf, AE. Hajiah, A. Al-Mumin, O. Büyüköztürk,

Impact of Embodied Energy on materials/buildings with partial replacement of ordinary Portland Cement (OPC) by natural Pozzolan volcanic Ash, *J Clean Prod* (2018) 177: 547-554. <https://doi.org/10.1016/j.jclepro.2017.12.234>

[2] I. Hiroi, The Preparation and Use of concrete Blocks for Harbour Works, *Transactions, ASCE* (1904) LIV. Part A (10): 211-220

[3] I. Hiroi, On Long-time Tests of Portland Cement, Hydraulic Lime, and Volcanic Ashes, *J College Engrg, Tokyo Imperial Univ* (1920) X (7): 155-172

[4] G. Cai, T. Noguchi, H. Degée, J. Zhao, R. Kitagaki, Volcano-related materials in concretes: a comprehensive review, *Environ Sci Pollut Res* (2016) 23 (8): 7720-7243, <https://doi.org/10.1007/s11356-016-6161-z>

[5] R. Snellings, G. Mertens, J. Elsen, Supplementary Cementitious Materials. *Rev Mineral Geochem* (2012) 74 (1): 211-278, <https://doi.org/10.2138/rmg.2012.74.6>

[6] S. Shipley, A. M. Sama-Wojcicki, Maps Showing Distribution, Thickness, and Mass of Late Pleistocene and Holocene Tephra from Major Volcanoes in the Pacific Northwest of the United States; a Preliminary Assessment of Hazards from Volcanic Ejecta to Nuclear Reactors in the Pacific Northwest (1983), USGS, MF-1435, <https://doi.org/10.3133/mf1435>

[7] R. Snellings, Assessing, Understanding and Unlocking Supplementary Cementitious Materials, *RILEM Tech Lett* (2016) 1 (1): 50-55, <https://doi.org/10.21809/rilemtechlett.2016.12>

[8] A. Tomoyose, T. Noguchi, K. Sodeyama, K. Higashi, Experimental study on using differentiated shirasu by gravity concentration and classification as concrete material, *CAJ Proc Cem Concr* (2016) 70 (1): 580-587, <https://doi.org/10.14250/cement.70.580>

[9] A. Tomoyose, T. Noguchi, K. Sodeyama, K. Higashi, Stability of volcanic silicate powder for concrete manufactured from shirasu through gravity classification and pulverization, *CAJ Proc Cem and Concr* (2017) 71 (1): 674-681, <https://doi.org/10.14250/cement.71.674>

[10] K. Sodeyama, A. Tomoyose, T. Noguchi and K. Higashi, Total Utilization of Shirasu as Construction Materials through Dry Gravity Classification and Pulverization, *J Soc Mat Sci, Japan* (2017) 66 (8): 574-581, <https://doi.org/10.2472/jsms.66.574>

[11] A. Tomoyose, T. Noguchi, K. Sodeyama and K. Higashi, Fundamental study about volcanic glass classified from Ito-shirasu by gravity classification, *Proc Jpn Concr Ins* (2017) 38 (1): 151-156

[12] Tomoyose, A. et al.: Utilization of volcanic ejecta as a high-performance supplementary cementitious material by gravity classification and pulverization, *RILEM technical letters*, Vol.3, pp.66-74, 2018.12, <https://doi.org/10.21809/rilemtechlett.2018.66>

Manufacturing high-performance supplementary cementitious materials from pyroclastic deposit through dry gravity classification and pulverization

A. Tomoyose¹, T. Noguchi¹, K. Sodeyama², K. Higashi³

¹Department of Architecture, The University of Tokyo, 7-3-1 Hongo, Bunkyo-ku, Tokyo, Japan

²Kagoshima Prefectural Institute of Industrial Technology, 1445-1 Oda, Hayato-cho, Kirishima-shi, Kagoshima, Japan

³Principle Co., Ltd., 1-17-8 Kamoike, Kagoshima-shi, Kagoshima, Japan

Abstract

Volcanic ejecta and deposits, which are pozzolanically reactive, have long been known to improve the durability of concrete. Nevertheless, it has also been pointed out that the use of a natural pozzolan as a supplementary cementitious material (SCM) can pose problems of low workability and slow strength development. Also, in addition to the low performance as a natural SCM, its composition and physical properties are widely variable and significantly scattered when compared with industrial by-products. The authors have been conducting studies on the total utilization of volcanic deposits for applications suitable for respective properties by classifying them by floating speed difference and particle diameter. Pyroclastic flow deposits called “Ito-Shirasu” which erupted out in 29,000 years ago covers an area of about 3,427 km², and it forms extensive pyroclastic plateaus with a layer about 10 meters to 200 meters thick in the southern regions of Kyushu, Japan. The amount of sediments of Ito-Shirasu is estimated to have a volume of 75 billion m³. It includes a crystal mineral and an amorphous silicate and so on, therefore it has the properties of both a fine aggregate and a SCM owing to its pozzolanic reaction. They reported that sorting out particles less than 2.4 g/cm³ by dry gravity classification and removal of smaller clay fraction by bag filter is technically effective to recover high purity volcanic glass from Ito-shirasu.

This study provides a possibility to produce high performance SCMs in volcanic regions worldwide from volcanic ejecta, which have been regarded as a low performance SCM, by sorting out a high purity volcanic glass by the same method using an air table.

Keywords: Volcanic glass, natural pozzolan, supplementary cementitious material, dry gravity classification

1. Introduction

A quest for supplementary cementitious materials (SCMs) with a reactivity allowing them to be used as a replacement for Portland cement has been under way worldwide, with industrial byproducts including ground-granulated blast-furnace slag and fly ash being globally applied to actual construction. However, an expected reduction in the output of such materials, particularly fly ash, was pointed out already in 2007 [1], amid the trend to cope with the environmental problems. Then in December 2015, the Paris Agreement

was adopted to urge the world to take measures against greenhouse gas emissions, edging out coal-fired power generation.

Though the term “pozzolan” is widely used today to describe a reactive material for concrete regardless of whether it is natural or artificial, it is derived from “pozzolana,” natural volcanic ejecta, which was used as a material for concrete in the Roman era. Volcanic ejecta and deposits, which are pozzolanically reactive, have long been known to improve the durability of concrete. No standard has been available for these materials due to their being no industrial products, with their physical properties widely varying. Volcanic ejecta and deposits have therefore not been actively employed for construction under the circumstances where laws and regulations require engineers to refer to standards. However, with a shift from specification codes to performance-based codes in sight, active use of natural resources in the future of north America has been highlighted [2].

Nevertheless, it has also been pointed out that the use of a natural pozzolan as a supplementary cementitious material can pose problems of low workability and slow strength development [3]. Also, in addition to the low performance as a natural SCM, its composition and physical properties are widely variable [4] and significantly scattered [5] when compared with industrial byproducts.

The wide variety of natural pozzolans are classified by their origins as shown in Figure 1. They are broadly divided into two categories: primary volcanic and sedimentary. Diatomaceous earth and white earth fall in the sedimentary category due to their undergoing hydrothermal action during the depositional process. The volcanic category includes zeolitised tuff, or volcanic tuff, which is also altered by diagenetic processes. Though zeolite is a sedimentary rock diagenetically crystallized after being ejected and deposited, it shows reactivity with lime when finely pulverized by a base-change reaction. Excepting the group of diatomaceous earth, all natural pozzolans are derived from volcanic rock and volcanic minerals [6]. All these natural pozzolans contain such impurities as quartz and feldspar, along with amorphous silica (volcanic glass, VG), which causes reactivity. However, in many cases these are studied and used as they are, through the processes of pulverization and classification (mostly into a particle smaller than 45 µm)[6].

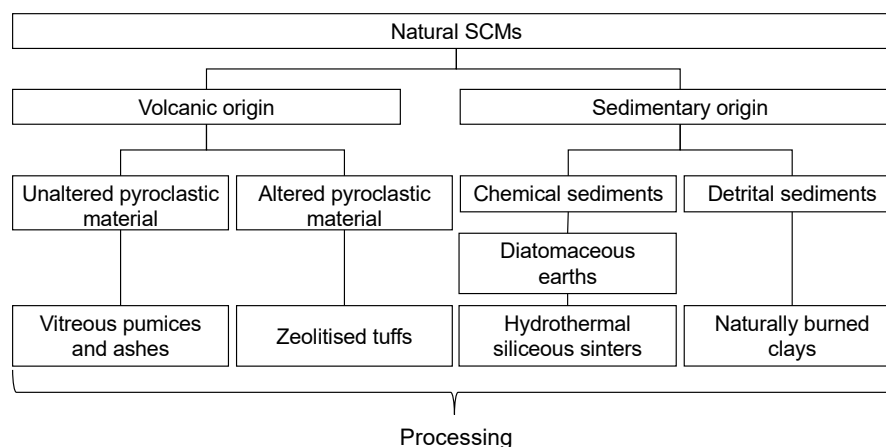


Figure 1: General classification scheme of natural supplementary materials. Processing usually involves crushing grinding, and size separation, mostly under 45 µm

The authors have been conducting studies on the total utilization of volcanic deposits for applications suitable for respective properties by classifying them by floating speed difference and particle diameter. This is done by using equipment referred to as an air table, which is based on a principle shown in figure 2. We have already blended the heavy particle and heavy dust fractions dry-classified by the air table from pyroclastic flow deposits (Ito-Shirasu), which is categorized as unaltered matter of volcanic origin, and

found that the blend can be used as fine aggregate in the same manner as crushed sand [7]. Furthermore, based on the analysis of the mineral composition and amorphous content of classified light dust, sorting out particles less than 2.4 g/cm³ by dry gravity concentration and removal of smaller clay fraction by bag filter is technically effective to recover high purity VG from raw material. The authors demonstrated that, by pulverizing this VG to around 1 µm, a slump flow and 7-day and later strength equal to or greater than silica fume can be obtained when used for concrete at W/B = 0.2 even with smaller dosages of chemical admixtures. When used at W/B = 0.6, the concrete demonstrated excellent strength development from an age of 7 days even when up to 20% of normal Portland cement was replaced with VG. That concrete also showed no reduction in the carbonation rate coefficient, indicating extremely high resistance to chloride ion penetration [8].

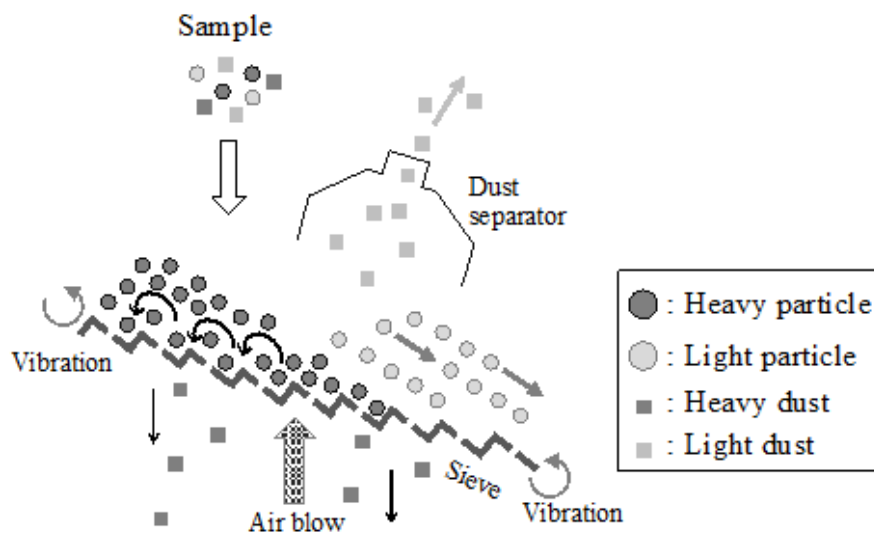


Figure 2: Mechanism of air table; dry gravity classification. The particles are almost classified according to the density and diameter.

This study aims to verify whether the effect of dry classification of volcanic deposits by an air table is limited only to Ito-Shirasu, which spreads over Southern Kyushu of Japan, or whether it is more universal, by analyzing its deposition principle and powder properties.

2. Test materials and procedures

2.1 Method of producing volcanic glass powder

Similarly to a former report [9], unprocessed Ito-Shirasu was obtained from a mining firm in Kagoshima Prefecture. The test material was prepared by drying the part passing a 5 mm sieve to a water content of 1% or less. Figure 3 shows details of the classifier used. This equipment consisting of an air table along with a cyclone and dust collector classifies the material into five components. The classifying conditions include the material feed, pore size of the sieve, concavo-convex shape, inclination angle, rotation frequency, vibration amplitude, and air flow. The density and size of each component can be adjusted by setting these conditions [9]. The particles are classified according to the density and mean size as listed in Table 1 along with the recovery rate. Most crystal minerals are recovered as heavy particles 1 mm or more in diameter and heavy dust less than 1 mm in diameter, while pumice is recovered as light particles. Among the light dust, fine particles recovered by the cyclone include high purity VG. The super fine part not recovered at the cyclone is recovered by the dust collector as the clay fraction (CF).

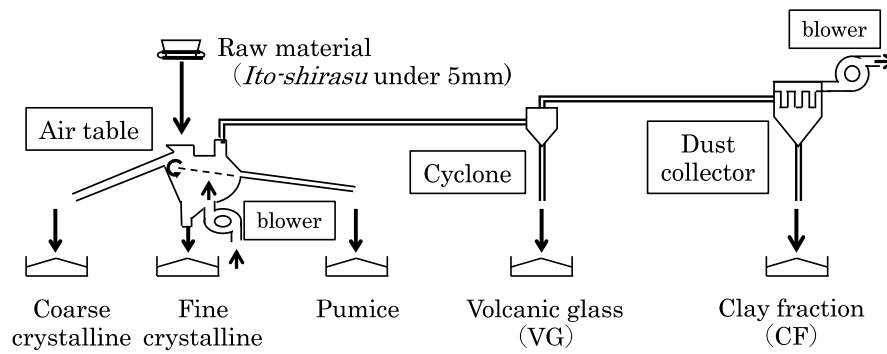


Figure 3: the dry classifier used. An air table along with cyclone and dust collector classifies Ito-shirasu into five elements.

Table 1: Recovery rate, density and mean size of components

	Coarse crystalline	Fine crystalline	Pumice	VG	CF
Recovery rate (%)	12	21	19	46	2
Density (g/cm ³)	2.63	2.66	1.81	2.36	2.37
Particle mean size (μm)	1137	330	742	83.5	4.1

Figure 4 shows the size distributions of VG recovered by the cyclone and CF recovered by the dust collector measured by a laser diffractometer. The mean size of the fraction recovered by the dust collector is 4 μm, representing the fine particle fraction slightly contained in the ore, though the two curves partly overlap due to dry classification.

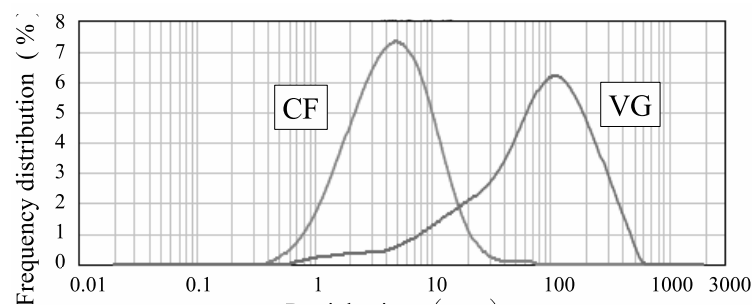


Figure 4: Particle size distribution of VG and CF

The sorted VG and CF were crushed and classified as shown in figure 5. Volcanic glass primary-crushed by a roller mill into a powder (VGR) is pulverized and classified using three devices: a jet mill, air classifier, and cyclone. The fractions recovered by the dust collector (RJF, RAF, and RCF) are referred to as fine powder. The fractions recovered by the cyclone (RJC, RAC, and RCC) are referred to as coarse powder. These fractions, including the primary-crushed VGR, are referred to as volcanic glass powder (VGP). Also, the CF, including its crushing, are collectively referred to as clay powder.

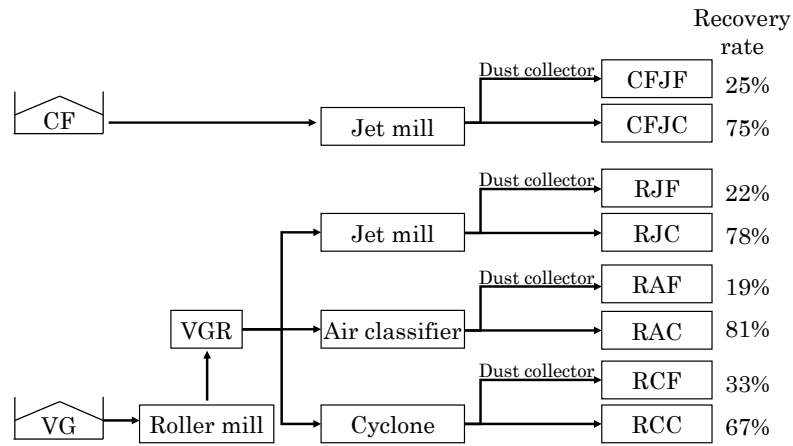


Figure 5: Manufacturing process of volcanic glass powder and clay powder

2.2 Chemical composition and ignition loss

Calibration curves of the standard minerals were prepared by the glass bead method for VGP and clay powder using lithium tetraborate as the flux, and their chemical compositions were measured by XRF. The ignition loss was calculated from the loss values obtained from samples dried for more than 12 h at 105°C and then ignited at 1,000°C for 1 h.

2.3 Thermogravimetric analysis, water vapor adsorption, BET specific surface

Prior to heating, measurement samples for thermogravimetric analysis 20 to 30 mg in mass were vacuum-dried for more than 12 h to eliminate the effect of adsorption water in the atmosphere. These were then heated from the room temperature (approximately 20°C) to 1,100°C at a rate of 10°C/min with measurement intervals of 30 sec.

The water vapor adsorption isotherm was measured at 25°C using an automatic vapor adsorption meter. The specific surface was then determined by the BET method. The measurement cell containing the sample was vacuumed and dried for 3 h at 105°C to eliminate the effect of adsorption water.

2.4 MB adsorption

Adsorption of methylene blue (MB) was determined in accordance with JCAS I-61: 2008 (Test method for methylene blue adsorption of fly ash). Based on the preliminary test results, a MB solution was added to samples weighed to between 0.05 and 0.10 g, and the absorbance was measured by suction filtration. The MB adsorption of samples was calculated by preparing calibration curves from the absorbance by blank tests. Six types of VGP and three types of clay powder were used as the materials.

3. Results and discussion

3.1 Chemical composition and ignition loss

Table 2 tabulates the results of chemical composition and ignition loss measurements. As shown in figure 6, the SiO₂ content of both VGP and clay powder negatively correlate with the ignition loss. The SiO₂ content and ignition loss of VGP are more than 72% and less than 3%, respectively, but after pulverization and classification, the SiO₂ content tends to slightly decrease in the fine powder fraction and slightly increase in the coarse powder fraction, with the difference being around 2 percentage points. As for clay powder, the SiO₂ content and ignition loss of CF are 65% and 4.5%, respectively, but the difference between those of the fine powder fraction (CFJF) and coarse powder fraction (CFJC) after pulverization and recovery are greater than those of VGP, being around 10 percentage points for SiO₂ content and around 3 percentage

points for ignition loss.

Table 2: Chemical composition and LOI of the materials

Sample	VGR	RJF	RJC	RAF	RAC	RCF	RCC	CF	CFJF	CFJC
SiO ₂	73.9	72.4	74.3	72.6	74.2	73.0	74.3	64.4	60.5	69.2
TiO ₂	0.20	0.21	0.20	0.21	0.20	0.21	0.19	0.30	0.33	0.24
Al ₂ O ₃	12.8	13.3	12.6	13.2	12.7	13.1	12.6	16.0	16.9	13.7
Fe ₂ O ₃	1.89	2.33	1.76	2.26	1.83	2.38	1.78	7.03	8.26	5.07
MnO	0.05	0.06	0.05	0.06	0.05	0.06	0.05	0.07	0.08	0.06
MgO	0.30	0.37	0.26	0.34	0.29	0.32	0.28	0.75	1.09	0.52
CaO	1.44	1.56	1.40	1.55	1.42	1.51	1.39	1.47	1.62	1.45
Na ₂ O	3.78	3.57	3.91	3.60	3.71	3.59	3.75	2.22	1.75	2.59
K ₂ O	3.34	3.36	3.38	3.30	3.37	3.32	3.35	3.21	3.05	3.76
P ₂ O ₅	0.03	0.04	0.03	0.04	0.03	0.04	0.03	0.03	0.04	0.03
LOI	2.25	2.81	2.02	2.84	2.14	2.47	2.25	4.47	6.37	3.44

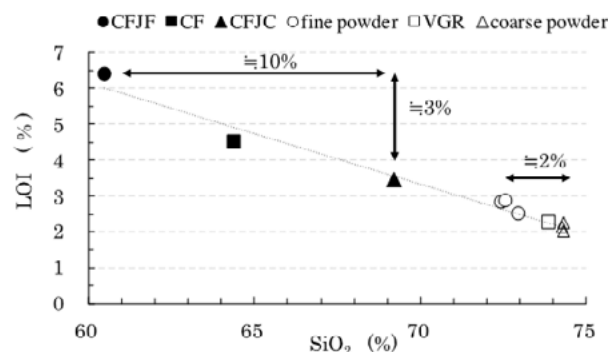


Figure 6: Relation between SiO₂ and LOI

Volcanic glass is subjected to weathering action of water, undergoing hydration and elution, and follows a weathering sequence shown in Fig. 7, ultimately being modified to a clay mineral (halloysite)[10]. SiO₂ is prone to elution through chemical changes, leaving compositions rich in H₂O and Al₂O₃. Clay powder can therefore be regarded as being in a later stage of weathering in terms of chemical composition than VGP. In either case, fine powder shows a composition at a later stage of weathering than coarse powder, with the difference between fine and coarse powders of clay powder being greater.

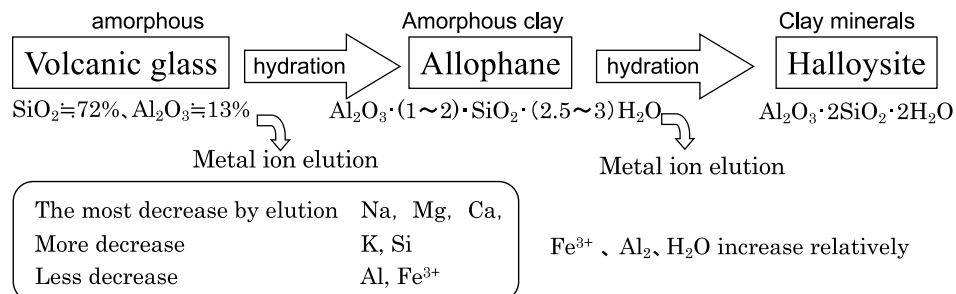


Figure 7: Weathering sequence of volcanic glass

3.2 Properties of adsorbed water

Figure 8 shows the thermogravimetric curves of three types of clay powder and three types of VGP from

among the results of thermogravimetric analysis tests. The mass losses of CFJF and CF are significant, being 8% and 6%, respectively. Those of CFJC and RJF are similar at around 4%, but their ignition losses differed at 3.4% and 2.8%, respectively. This is presumably because the mass loss of RJF during drying at 105°C for pretreatment before ignition loss measurement is greater as shown in the different low temperature ranges of their TG curves. The mass losses of RJC and VGR are both below 3%, demonstrating similar trends to the ignition loss results. Since volcanic glass derived from magma is reported to contain moisture equivalent to ignition loss [11], the losses in the TG curves are considered to be attributable to reduction in the moisture content, but the differential thermogravimetric curves shown in figure 9 demonstrate different trends of the peak temperatures of dehydration. One peak is found at around 250°C for VGP including those not shown in the figure. This is a typical peak of volcanic glass [12]. The shift of this temperature toward a lower temperature as the sample is crushed to smaller particles was also confirmed in the tests [12]. For clay powder, peaks are found at less than 100°C, around 250°C, and 450°C. The large peak at less than 100°C is a tendency observed in allophane, an amorphous clay of weathered volcanic glass, indicating the presence of physical adsorbed water or interlayer water, which result from weathering-induced hydration and are not dehydrated by vacuum drying. Similar water is also found to be present in CF and CFJF.

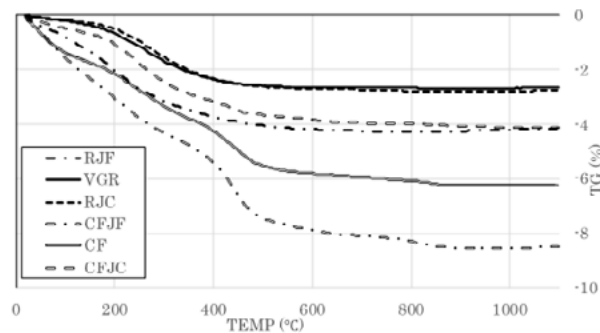


Figure 8: Thermogravimetric curves of VGP and clay powder

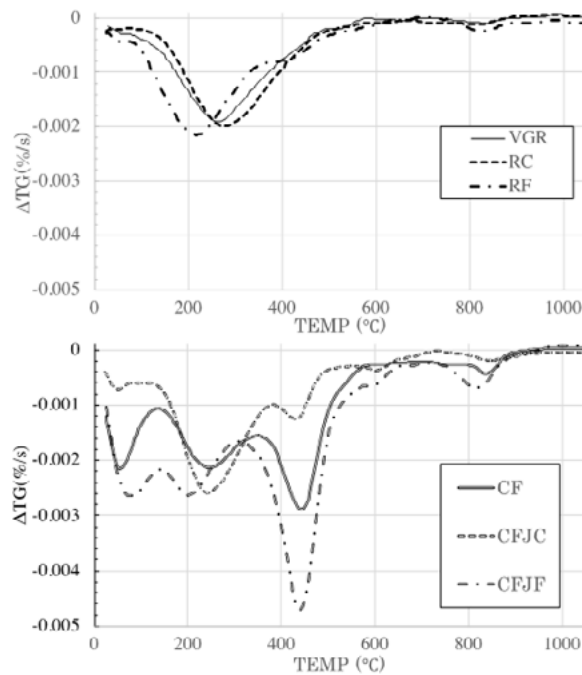


Figure 9: Differential thermogravimetric curves of VGP and clay powder

At the peaks of 450°C, slight endothermic shoulders are observed in all clay powders and in DTA as well. These are considered to be the dehydration of water bound by further hydration or of structural water

(hydroxyl), suggesting an indication of clay mineralization [10].

Figure 10 shows part of the obtained water vapor adsorption isotherms. The adsorption and desorption curves of RJF are separated, being hysteretic similar to Type II or Type H4 that suggest the presence of slit-shaped pores and micropores according to the classification by IUPAC [13]. CF shows hysteretic curves close to Type III or Type V, with adsorption being small in low pressure ranges less than 0.1, which demonstrates that adsorption does not occur while the interaction between vapors is greater. The total adsorption of CF is high, though its hydrophily can be low, with the difference between adsorption and desorption being large. Therefore, once water is adsorbed, it tends to be hard to be desorbed. Regarding TG curves for which the pretreatment is vacuum drying, CF shows a dehydration peak of ΔTG at less than 100°C. Therefore, the adsorbed water is mostly not desorbed at normal temperatures and low pressure, demonstrating properties close to allophane, which is used as a desiccant-adsorbent. Table 3 shows the BET specific surface determined from the water vapor adsorption at a pretreatment temperature of 105°C and the nitrogen gas adsorption at a pretreatment temperature of 300°C. CF was incalculable, as no linearity in the plots was found in the relative pressure range of 0.05 to 0.35. In contrast to SF, VGP and FA show BET specific surfaces by water vapor adsorption greater than that by nitrogen adsorption. In vapor adsorption, water is adsorbed selectively by hydrophilic sites, whereas nitrogen is an adsorbate that covers the entire powder surfaces uniformly. The surface physical properties can therefore be discussed by using different adsorbates. Since the BET specific surface is calculated in the relative pressure range of 0.05 to 0.35, the amount of water vapor adsorption of VGP in the low pressure range turned out to be great due to its high hydrophily.

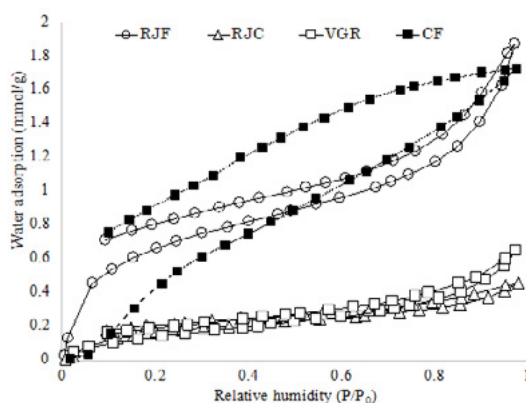


Figure 10: Thermogravimetric curves of VGP and clay powder

Table 3: BET surface area determined from water and nitrogen

Sample	VGR	RJF	RJC	RAF	RAC	RCF	RCC	CF	SF	FA
Water adsorption BET (m ² /g)	10.0	41.9	11.2	23.6	8.4	18.6	6.4	-	14.4	7.1
Nitrogen adsorption BET (m ² /g)	7.1	16.1	4.2	12.4	5.1	10.7	3.7	31.4	20.2	1.5

3.3 BET specific surface area and adsorption

Figure 11 shows the relationship between the mean particle size and the BET specific surface. The BET specific surface of VGP increases as the mean size decreases. On the other hand, clay powder shows no particular trend between the mean particle size and the BET specific surface. The BET specific surfaces of CF and CFJF are particularly large, being twice as large as that of VGP with similar mean size. The state of

particle surfaces can differ from that of VGP.

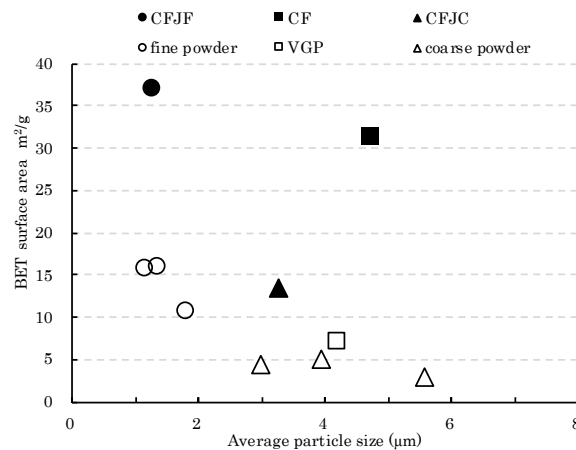


Figure 11: Relationship between mean particle size and BET surface area of VGP and Clay powder

Figure 12 shows the relationship between the BET specific surface and the MB adsorption. The BET specific surface and MB adsorption of VGP are closely correlated, with all sizes meeting the requirement to be not more than 1.20 g/100 g (12.0 mg/g) by EN 197-1: 2000 for the MB adsorption of limestone as a cement component. On the other hand, clay powders exceed this limit, with the adsorption tending to be above the approximate line for VGP.

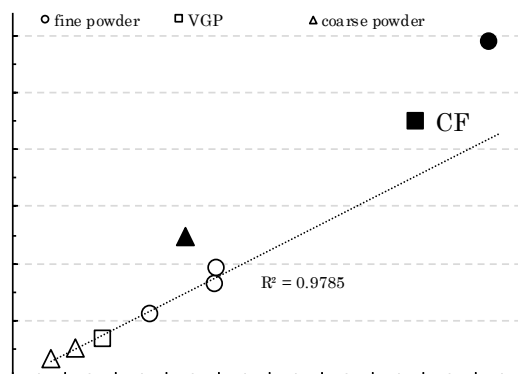


Figure 12: Relationship between BET surface area and MB adsorption of VGP and Clay powder

Focusing on the fact that silica is lost during the process of weathering, leaving alumina, the ratio of SiO₂ to Al₂O₃ (silica-alumina ratio) has been proposed as a most simple index to the degree of weathering [14]. Figure 13 shows the relationship between the silica-alumina ratio and the MB adsorption per unit BET specific surface. The chemical compositions of CFJF and CF represent particularly high degrees of weathering among the clay powders. Their MB adsorption is also 30% greater than that of VGP. When compared with CFJF and CF, the degree of weathering of CFJC is closer to that of VGP, but the value of adsorption is nearly twice as large as that of VGP. As for VGP, the degree of weathering of fine powder is slightly higher than coarse powder in terms of chemical composition, but their MB adsorptions can be regarded as being on the same level from their respective mean values and standard deviations. The adsorption of a polycarboxylate-based dispersant per unit area of powders of the same types (i.e., powders with the same compositions) is reported to be constant [18]. If this applies to MB, then fine and coarse powders of VGP can be regarded as the same powder from the aspect of dispersant adsorption, but clay powder cannot be regarded as the same type as VGPs. Also, the unit adsorption of CFJC is the largest,

though its degree of weathering is not as high as CF and CFJF.

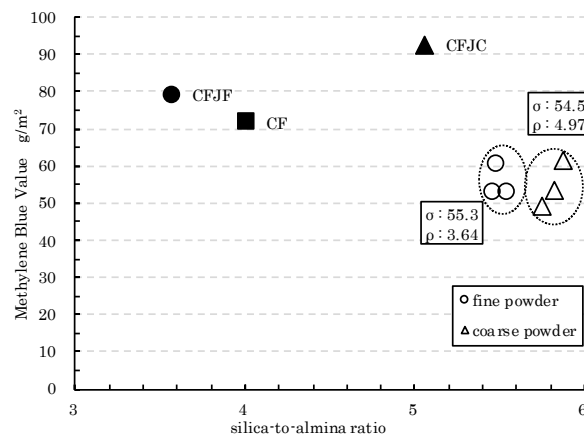


Figure 12: Relationship between BET surface area and MB adsorption of VGP and Clay powder

4. Discussion

In the field of natural disaster science, the refractive index of volcanic glass is used as an index to the progress of weathering of a cliff, as it increases under the effect of hydration. Also, the particle structure of a glass shard is explained as a structure consisting of a non-hydrated core surrounded by a hydrated rim, since the refractive index of crushed glass shards is widened toward the lower side [15]. Volcanic glass is a most weatherable material, and the smaller the particle, the faster the weathering proceeds, changing to a different soft material under chemical weathering action [16]. In view of these findings and the results of the present study, figure 14 shows the particle properties and process of crushing/classification.

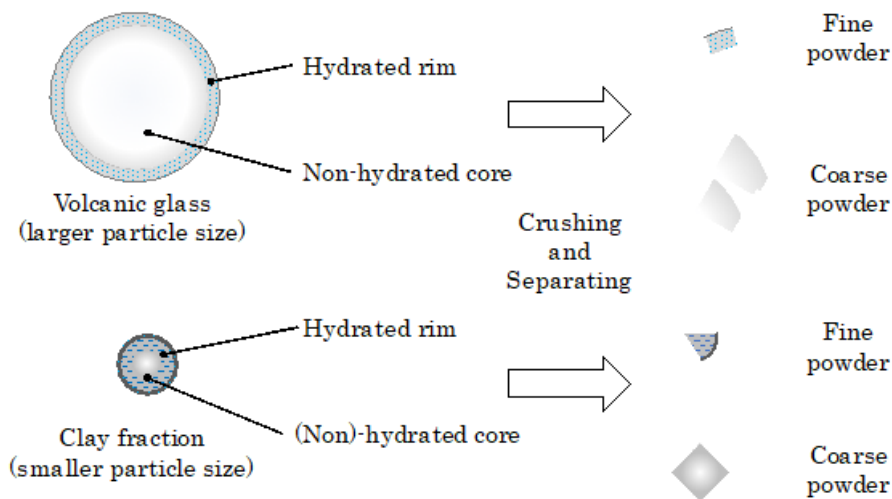


Figure 14: Particle contained in volcanic ejecta and deposits and their crushing process

Both VG and CF have a structure with a hydrated rim on the surfaces, and layers closer to the surface are softer and more prone to be pulverized during the crushing process, tending to be recovered by a dust collector. This agrees with the fact that fine and coarse powders have different chemical compositions and ignition losses. Based on the adsorption per unit area and the results of thermoanalysis of CFJC, it is considered that CF with a smaller particle size with hydration proceeding more to the core layer leads to a thicker hydrated surface rim. CFJF in particular has a concentrate of highly weathered surface layer. In other words, crushing after removing heavily weathered fine particles is effective in manufacturing unweathered high purity VGP, which is a high performance SCM, from volcanic deposits.

Whereas basaltic magma with low viscosity causes moderate volcanic activity, rhyolitic magma is generally said to cause violent and explosive eruption. In other words, magma with a large SiO₂ content is said to cause explosive eruption. The deposits of volcanic materials excepting gasses are classified into three types: pyroclastic fall deposit, pyroclastic flow deposit, and lava. Pyroclastic fall deposit results from a Plinian eruption shown in figure 15, whereas pyroclastic flow deposit results from a pyroclastic flow.

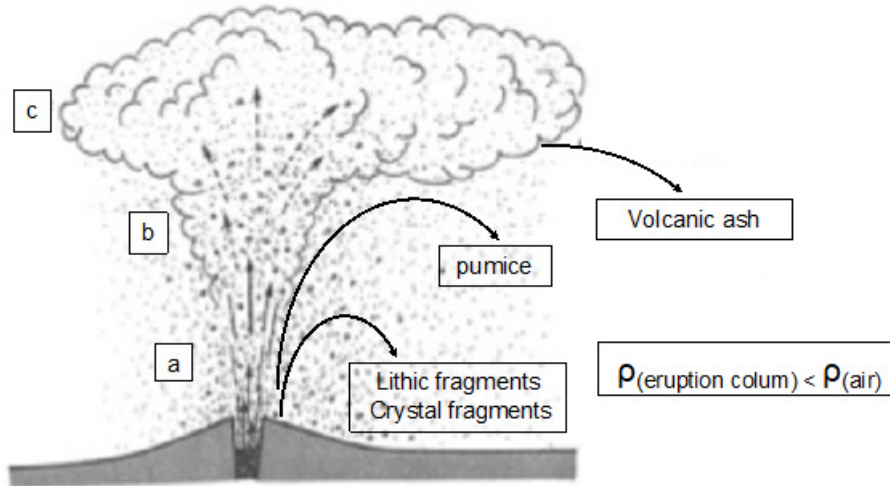


Figure 15: Diagram of Plinian eruption

A Plinian eruption, an explosive one represented by the eruption of Mount Vesuvius in 79 AD, forms an eruptive column made of gases, magma and rocks crushed to pieces, and fragments of minerals directly above the crater for half an hour to several days. The temperatures of this column higher than the surrounding atmosphere cause convection (b in the figure). The top of the eruptive column is formed where the density of the column equals the surroundings (c) and spreads horizontally. Low-density particles including volcanic ash and pumice are horizontally blown by the wind out of the regions of b and c and begin to fall when their speed decreases to the point of equilibrium between air resistance and gravity; 'terminal speed'. Since smaller particles are carried farther away due to their lower terminal speed, they are subjected to classification while flying. The material deposited near the crater is referred to as fall pumice. The material 2 mm or less in size is referred to as volcanic fall ash. Both are uniform in size and contain little crystal minerals or lithic fragments. There can be a case where weathered materials subjected to hydration are included, but high purity volcanic glass can be sorted out by the cyclone and dust collector of the present device for air classification. Collapse of an eruptive column leads to a so-called pyroclastic flow. A large-scale flow is formed by gravitational collapse of an eruptive column, which is regarded as a phenomenon of a rapid outflow of unclassified pumice, volcanic ash, and rock fragments with volcanic gases as shown in figure 16. A theoretical calculation has shown that, when an eruptive column of 2 to 3 km in height collapses, the resulting pyroclastic flow runs over a distance of 20 to 30 km, traversing ridges with a relative elevation of 200 to 300 m. Coarse particles tend to be entrapped among fine particles due to the weak classifying action.

Though such ejecta, which is also referred to as tephra, is derived from magma, it also includes 'accessory' materials derived from the old volcanic body near the magma reservoir and conduit and 'accidental' materials, which are fragments of the basement rock. Their quantitative ratios vary depending on the scale and pattern of eruption and distance from the eruption source. After deposition, extraneous materials from the surrounding ground can be normally included during various stages of turning into soil. In view of the use as a SCM in the field of concrete, pyroclastic deposits resulting from explosive eruption of magma with a high SiO₂ content are advantageous from the aspect of the amount of resources, but they simultaneously

entail abundant impurities other than pozzolanically reactive volcanic glass.

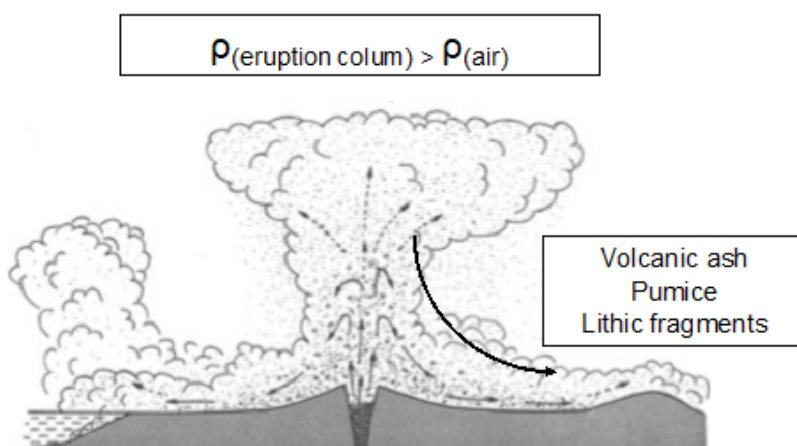


Figure 16: Diagram of Pyroclastic eruption

Ito-Shirasu presently under study is a large-scale pyroclastic flow sedimentation with an estimated reserve of 75 billion m³, but amorphous materials including pumice were reported to account for around 60%, while crystal minerals were approximately 40%. Also, the fine fraction of CF with a recovery ratio of 2% showed indications of weathering. According to the results of research into volcanic glass and other minerals contained in volcanic ejecta from Cascade Range in North America [17], the densities of pumice, glass shards, and lithic fragments were 0.7 to 1.2 g/cm³, 2.35 to 2.45 g/cm³, and 2.7 to 3.2 g/cm³, respectively. That of crystalline materials and crystal fragments was 2.6 to 5.2 g/cm³. Therefore, our findings from volcanic deposits in Japan that volcanic glass can be perfectly sorted out both with a density limit of 2.4 g/cm³ and with a diameter limit of around 5 μm can be applicable to volcanic ejecta from Cascade Range. Physical densities of particles should, even beyond national borders, fall in constant ranges when considering the mechanisms acting on volcanic ejecta -- eruption of volcanic glass onto the ground and rapid cooling thereafter, crystallization within the underground magma, rocks present on the ground, weathering after deposition, and so on. In that sense, this study provides a possibility to produce high performance SCMs in volcanic regions worldwide from volcanic ejecta, which have been regarded as a low performance material, by sorting out a high purity volcanic glass by the same method using an air table.

5. Acknowledgment

This research is supported by JSPS Grant-in-Aid for Scientific Research (A) with No. 18H03803 entitled "Carbon-minus Recyclable High-performance Concrete".

6. Reference

- [1] K. L. Scrivener, R. J. Kirkpatrick, 2008, Innovation in use and research on cementitious material, Cement and Concrete Research, Vol.38, pp.128-136, <https://doi.org/10.1016/j.cemconres.2007.09.025>
- [2] R. D. Hooton, 2008, Bridging the gap between research and standard, Cement and Concrete Research, Vol.38, pp.247-258, <https://doi.org/10.1016/j.cemconres.2007.09.012>
- [3] J. S. Damtoft, J. Lukasik, D. Herfort, D. Sorrentino, E. M. Gartner, 2008, Sustainable development and climate change initiatives, Cement and Concrete Research, Vol.38, pp.115-127, <https://doi.org/10.1016/j.cemconres.2007.09.008>
- [4] R. Snellings, G. Mertens, J. Elsen, 2012, Supplementary Cementitious Materials, Reviews in Mineralogy and Geochemistry, Vol.74 (1), pp.211-278, <https://doi.org/10.2138/rmg.2012.74.6>

- [5] R. Snellings, 2016, Assessing, Understanding and Unlocking Supplementary Cementitious Materials, RILEM Technical Letters 1, pp.50-55, <https://doi.org/10.21809/rilemtechlett.2016.12>
- [6] P. K. Mehta, P. J. M. Monteiro, 2006, CONCRETE Microstructure, properties, and Materials third edition, McGraw-Hill Companies, pp.295-315
- [7] A. Tomoyose, T. Noguchi, K. Sodeyama, K. Higashi, 2018, Total utilization of pyroclastic flow deposits as construction materials through dry gravity classification and pulverization, Proceedings of the 8th International Concrete of Asian Concrete Federation, Vol.1, pp.475-481
- [8] A. Tomoyose, T. Noguchi, K. Sodeyama, K. Higashi, 2018, Utilization of volcanic ejecta as a high-performance supplementary cementitious material by dry gravity classification and pulverization, RILEM Technical Letters, Vol.3, pp.66-74, <https://doi.org/10.21809/rilemtechlett.2018.66>
- [9] K. Sodeyama, A. Tomoyose, T. Noguchi and K. Higashi, 2017, Total Utilization of Shirasu as Construction Materials through Dry Gravity Classification and Pulverization, Journal of the Society of Materials Science, Japan, Vol. 66, Issue 8, pp. 574-581, <https://doi.org/10.2472/jsms.66.574>
- [10] S. Iwao, 1985, Nendo no Jiten, Asakura Publishing Co. Ltd, ISBN 4254162286 (in Japanese)
- [11] H. Taniguchi, 1972, Studies on Si⁴⁺ ion, Al³⁺ ion and H₂O(+) in volcanic glasses by means of infrared absorption and other methods, the journal of the Japanese association of Mineralogists, Petrologists and economic geologists, Vol. 67, Issue 9, pp.291-300, <https://doi.org/10.2465/ganko1941.67.291> (in Japanese)
- [12] H. Tateyama, K. Kimura, K. Jinnai, K. Tsunematsu, 1982, Changes on bloating properties of volcanic glass by weathering, Journal of the clay society of Japan, Vol.22, Issue 1, pp.1-10, <https://doi.org/10.11362/jcssjnendokagaku1961.22.1>(in Japanese)
- [13] K. S. W. Sing, D. H. Everett, R. A. W. Haul, L. Moscou, R. A. Pierotti, J. Rouquerol, T. Siemieniowska, 1985, Reporting physisorption data for gas/solid systems with special reference to the determination of surface area and porosity, Pure and applied chemistry, Vol.57, No.4, pp.603-619, <https://doi.org/10.1351/pac198557040603>
- [14] B. P. Ruxton, 1968, Measures of the degree of chemical weathering of rocks, the journal of geology, vol. 76, No. 5, pp.518-527, DOI: [10.1086/627357](https://doi.org/10.1086/627357)
- [15] T. Yamashita, T. Danhara, 1995, Problem in measuring refractive indices of younger tephra glass shards: effect of thin hydration layer, the geological society of Japan the 102nd annual meeting, p.112, https://doi.org/10.14863/geosocabst.1995.0_112_2 (in Japanese)
- [16] H. Tsukamoto, S. Mizutani, 1988, Clay Minerals in Weathering Process and Their Transformation, Journal of the Japan Society of Engineering Geology, Vol.29, Issue 3, pp.231-241, <https://doi.org/10.5110/jjseg.29.231> (in Japanese)
- [17] S. Shipley, A. M. Sama-Wojcicki, 1983, Maps Showing Distribution, Thickness, and Mass of Late Pleistocene and Holocene Tephra from Major Volcanoes in the Pacific Northwest of the United States; a Preliminary Assessment of Hazards from Volcanic Ejecta to Nuclear Reactors in the Pacific Northwest, USGS, MF-1435, <https://doi.org/10.3133/mf1435>
- [18] A. Ohta, T. Uomoto, 1999, A Study of the Dispersing Effects of Polycarboxylate-Based Dispersant on Fine Particles, Concrete research and technology, Vol.10, Issue 2, pp.131-140, https://doi.org/10.3151/crt1990.10.2_131

Early hydration of C₂S doped with combination of S and Li

M. Boháč¹, T. Staněk¹, A. Rybová¹, A. Zezulová¹, F. Bellmann², H.-M. Ludwig²

¹Physical Chemistry Dep., Research Institute for Building Materials, 62400 Brno, Czech Republic

²F.A. Finger-Institute of Building Materials Science, Bauhaus University Weimar, 99423 Weimar, Germany

Abstract

Production of low-energy cements would result in energy saving and lower CO₂ emissions related to reduced consumption of fuel and high-grade limestone as a raw material. Belite rich clinker, made more reactive by doping with combination of S and Li, could possibly be one of the low-energy alternatives for Portland cement clinker. Paper describes the preparation of doped belite and deals with its early hydration and reactivity. Belite rich clinkers were prepared in laboratory in high-temperature solid state synthesis. Pure substances were used for the preparation of raw meal and clinker. Early hydration heat flow development of cement pastes was monitored by isothermal calorimetry, changes in phase composition by “in-situ” X-ray diffraction and TGA/DTA and microstructure by SEM-SE. Heat flow exotherms were correlated with quantified phase composition at given time. Heat related to C₃S hydration measured by isothermal calorimetry is proportional to its content and the position of its peak and maximum changes with increased Li content. Doping of the C₂S by the S or the combination of S and Li significantly increases the reactivity of the C₂S-rich cement. The formation of C-S-H products is a continuous process that depends mainly on C₃S during first 6 hours and then is supported by slow reaction of β-C₂S. The reactivity of C₂S is affected by the timing of the hydration of other clinker phases. Two generations of portlandite formation detectable as a double endotherm on TGA/DTA can be attributed to hydration of C₃S and β-C₂S.

Keywords: belite clinker, S, Li, doping, early hydration

1. Introduction

The manufacture and use of concrete produce a wide range of environmental and social consequences. The cement industry is together with the energy production and transportation industries one of the three primary producers of carbon dioxide, a major greenhouse gas. The share of cement production in total anthropogenic CO₂ emissions has been rising steadily and is now estimated by some sources to be around 10% [1], or about 6% of the total anthropogenic greenhouse gases [2].

Although energy use and release of CO₂ are closely related in the usual cement manufacturing industry, it is the release of CO₂ to the atmosphere rather than the consumption of energy which is of chief concern. Decarbonation of limestone (CaCO₃) results in the release of CO₂ and, since natural limestone and chalk are the only large-scale sources of calcium available to the cement industry, this CO₂ release is only reducible by changing the chemical composition of the cement [3].

Clinker is the main constituent of the cement. The clinker is mixed with a few per cent of gypsum and finely ground to make the cement. The clinker typically has a composition in the region of 67% CaO, 22% SiO₂, 5% Al₂O₃, 3% Fe₂O₃ and 3% of other components, and normally contains four major phases,

called alite (C_3S , Ca_3SiO_5), belite (C_2S , Ca_2SiO_4), aluminate phase (C_3A , $Ca_3Al_2O_6$) and ferrite phase (C_4AF , Ca_2AlFeO_5). Several other phases, such as alkali sulfates and calcium oxide, are normally present in minor amounts [4].

Recently, there are four classes of alternative clinker system that deserve serious attention with respect to global reductions in concrete-related CO₂ emissions [5]; reactive belite-rich Portland cement clinkers (RBPC), belite-ye'elinite-ferrite clinkers, carbonatable calcium silicate clinkers, magnesium oxides derived from magnesium silicates.

RBPC belong to the same family as ordinary Portland cement (OPC) in terms of clinker mineralogy, i.e. they are in the C_2S - C_3S - C_3A - C_4AF system. The difference in clinker composition between RBPC and OPC lies mainly in the belite/alite ratio. For RBPC the belite content is more than 40 % and alite normally less than 35 %, making belite the most abundant phase in RBPC, as opposed to alite in OPC. The manufacture of RBPC therefore leads to lower specific energy consumption and CO₂ emissions, and also has the additional practical advantage of requiring less high-grade (low-silica) limestone as a raw material [5]. The ideal clinkering temperature for RBPC is usually close to 1350 °C, which is about 100 °C lower than the average for OPC, which can lead to somewhat lower kiln heat consumption and permit more use of low-grade kiln fuels.

Physical or chemical activation, e.g. rapid clinker cooling or minor element doping may be needed in some cases to make the belite sufficiently reactive. As an example, the use of 0.5–1.0% SO₃ in the raw meal combined with rapid clinker cooling can lead to the formation of reactive belite in the clinker. Staněk and Sulovský [6] reported the principle of activation during preparation of belite-rich clinkers with an increased Ca:Si ratio in the structure of dicalcium silicate and partial substitution of SiO₄⁴⁻ by SO₄²⁻. Activation was realized by the addition of sulfate ions, which in the structure of belite substitute SiO₄, caused an increased entry of Al₂O₃ into the belite and increased the CaO:SiO₂ in belite. The sulfur addition to the clinker also stabilized the hydraulically more active monoclinic alite M1 modification. The clinker for its preparation, contained only around 20 wt.% of alite, was burned at a temperature of 1350 °C and was activated by the addition of about 5% SO₃ (related to the bulk clinker weight). It contained a small proportion of anhydrite.

Specific kiln fuel requirements and CO₂ emissions of RBPC are typically about 10 % below those for OPC. Lower emissions of NO_x and SO_x are commonly observed when making RBPC, due mainly to the lower burning temperature. On the other hand, it requires about 5 % more electric power to grind RBPC to the same fineness as OPC, due to the greater hardness of belite relative to alite [5].

Pure C₂S exhibits five polymorphic forms, depending on temperature and pressure during formation [7], all are metastable except the γ (orthorhombic) form. In Portland cement the equilibrium temperature between α (hexagonal) and α' is 1280 °C and the conversion reaches a maximum rate at 1100 °C. With decreasing cooling rate, the $\alpha'H$ (orthorhombic) phase tends to dominate, and finally the belite is composed entirely of this form, which transforms into β -C₂S (monoclinic) after passing through the $\alpha'L$ (orthorhombic) form [8].

Belite is a major phase in active belite cements and is chiefly present in the α and α' modifications, stabilized either by rapid cooling in the temperature range 1300-900 °C [8], or by the use of higher alkali levels [9]. It has been suggested that the hydraulic activity of β -C₂S is related to the calculated strength of the Ca-O ionic bond [10]. A study of the relationship between crystal structure and hydraulic activity, including synthetic β -C₂S and samples separated from Portland cement, indicates that the electric field strength at the site of the Ca²⁺ ions in the crystal lattice determines the hydraulic activity [11].

Paper deals with reactive C₂S-rich clinkers doped with a combination of S and Li. Early hydration properties of cements prepared from the clinkers were monitored by isothermal calorimetry, XRD-in situ and inner standard method, DTA-DTG and SEM-SE. Paper brings comparison of reactivity and phase development during early hydration of S and Li doped belite clinkers and undoped belite clinker.

2. Methodology

2.1 Materials

Belite clinkers, prepared by high-temperature solid state synthesis, were doped with S and combination of S and 2 % or 4 % of Li in form of CaSO₄·2H₂O and LiCO₃. Pure compounds were used to prepare the clinkers. The composition of the raw meal constituents was calculated on the composition of belite. The raw meal composition and phase composition of burned clinkers are given in Table 1 and 2. Clinker tablets were prepared from raw meal which was homogenized for 2.5 hours. Clinkers were burned in Kanthal furnace at 1400 °C with 12 hours of soaking time. Thereafter, the clinkers were quickly cooled in the air when they were placed on a metal substrate after being removed from the furnace. For isothermal calorimetry, X-ray and DTA testing, clinkers were ground in a vibratory mill for 1 minute.

Table 1: Raw meal composition for clinker preparation

	C ₂ S	C ₂ S S	C ₂ S S 2Li	C ₂ S S 4Li
	wt. %			
CaCO ₃	75.41	74.98	72.34	69.70
SiO ₂	24.59	21.16	21.16	21.16
LiCO ₃	-	-	3.66	7.32
CaSO ₄ ·2H ₂ O	-	3.86	3.86	3.86

2.2 Methods

The development of heat flow and total hydration heat was monitored by isothermal calorimetry (TAM Air – TA Instruments) on samples of cements prepared from synthesized clinkers. Calorimetric measurements were performed at 25 °C for 7 days on cement pastes with w/c = 0.4 when 5 grams of cement was used for individual test. Samples were stored under laboratory conditions at 25 °C for 24 hours prior to the experiment. Before inserting the ampoules pastes into the calorimeter, each cement sample was mixed with water and stirred at 2 rpm for 1 minute outside the calorimeter. The measurement itself started 1 minute after the addition of the mixing water.

The in-situ X-ray diffraction analysis was performed on Bruker D8 Advance apparatus with Cu anode ($\lambda K\alpha = 1.54184 \text{ \AA}$) and variable divergence slits at Θ - Θ reflection Bragg-Brentano para focusing geometry, scan range 7-50 2 Θ , scan step size 0.039°. Data were processed using EVA software. The duration of individual scans was approximately 20 minutes; duration of the whole experiment was 24 hours. The paste (w/c=0.4) was placed in a sample holder and covered with kapton foil to prevent carbonation. In case of C₂S S 2Li sample, the phase composition over time (0, 45, 90, 360, 720, and 2880 minutes) was monitored using the inner standard method. As a standard, 20 wt.% fluorite was used. After each time interval the hydration was stopped by isopropyl alcohol and acetone. The phase composition of burned clinkers was determined using Rietveld refinement. Since the inner standard method was used the amorphous content was not quantified.

The sample C₂S S 2Li was investigated by thermal analysis. The samples were prepared following the same procedure as for XRD. The hydration process of the paste was stopped by isopropyl alcohol and acetone after 45, 90, 360, 720 and 2880 min of hydration. Combined TGA/DTA data were obtained using STA 449 F3 Jupiter (by Netzsch). The samples were tested in Pt crucibles at a heating rate 10 °C/min, from 35 °C to 1000 °C. The sample atmosphere was synthetic air (50 ml/min, ratio N₂/O₂ was 80/20).

Development of microstructure at 45, 90, 360, 720, and 2880 minutes of hydration of the sample C2S S 2Li was observed by scanning electron microscope ZEISS EVO LS10 in secondary electrons (SE). SE micrographs were taken at 100x, 500x, 1000x, 2000x and 5000x magnification, EHT 15 kV, WD 12 mm and I probe 80pA. Samples were sputtered with gold before SEM SE analyses.

Table 2: Phase composition of burned clinkers

	C ₂ S	C ₂ S S	C ₂ S S 2Li	C ₂ S S 4Li
	wt. %			
β-C ₂ S	27.1	42.5	80.7	82.5
γ-C ₂ S	72.7	27.3	1.0	1.1
C ₃ S	-	27.7	9.9	2.9
CaO free	0.2	2.5	7.7	10.0
anhydrite	-	-	0.7	3.5

3. Results and discussion

3.1 Isothermal calorimetry

Early hydration exothermic reactions were monitored by isothermal calorimetry during 7 days of hydration (Figure 1). Exothermic reactions are related to dissolution of amorphous and crystalline phases (Table 2), growth, nucleation and precipitation, complexation and adsorption processes. Main contributors of the evolved heat during hydration are portlandite - Ca(OH)₂ (CH) and C-S-H. These phases are hydration products of clinker phases C₃S and C₂S and CaO. Understanding the mechanism of cement hydration involve the study of the kinetics of individual mechanistic steps [12].

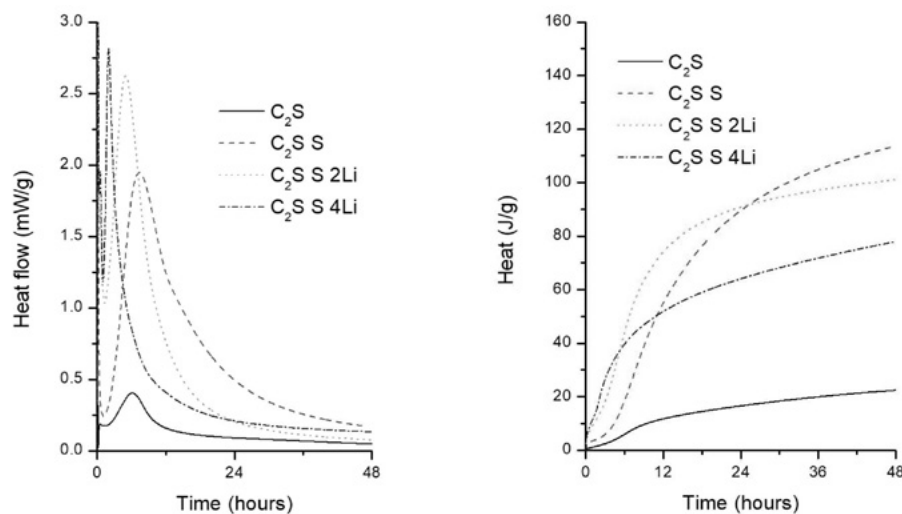


Figure 1: Heat flow and total heat development during 48 hours of hydration

When in contact with water, the initial reactions' exotherms include wetting and dissolution/dissociation of molecular units from the surface of a solid. Despite the fact that the measurement started after 1 min after water addition, the first exotherm is still controlled by CaO content in the sample. Total heat evolved in the time interval between 1st and 60th min of hydration is proportional to CaO content in the samples (Table 2): C2S – 1.1 J/g, C2S S – 3.4 J/g, C2S S 2Li – 9.2 J/g, C2S S 4Li – 11.4 J/g. The CaO reaction during initial period of hydration exhibits large signal overshadowing other reactions. Samples with Li contains also anhydrite which is also expected to react during the initial period of hydration. Despite considerably lower solubility of anhydrite comparing to gypsum, anhydrite still serves in the presence of alkali solvent as a retarder of the setting forming ettringite (AFt) during the initial reactions contributing to total heat.

Anhydrite in this belite rich system deserves further research since it plays an important role in terms of hydration mechanism and performance of hardened material in systems with OPC and CSA [13].

Period of slow reactions is followed by acceleration period which is characterized by the main peak related to hydration of C3S. Despite the fact that the heat related to C3S hydration is proportional to its content, the position of the peak and its maximum changes with increased Li content. With higher Li contents the temperature of the maximum increases and the position moves to earlier times. Total heat development during 7 days of hydration show that doping of the belite with the S and the combination of S and Li dramatically increases the reactivity of the resulting cement (Figure 1). The combination of S and Li accelerates the heat evolution during first days compared to doping with the S only.

C2S hydration is very slow and heat contribution is considerably lower. C2S reactions are represented by minute peaks in deceleration period where diffusion is the controlling process of hydration. In principle, it is claimed that both hydraulically highly active and nearly inactive forms may be possible for all belite modifications and the measured strength generation depends on the experimental conditions like burning temperature, cooling rate, foreign oxide content, etc. [14]. The reactivity of C2S is affected by the timing of the clinker phases hydration. Since the hydration of C2S take part mainly in deceleration period, the lack of water, space and smaller number of fine and more reactive particles are parameters affecting C2S hydration kinetics.

3.2 Phase analysis

From results of phase composition of burned clunkers, it can be stated that the enhancement of β -polymorph of dicalcium silicate is the criteria of doping with S and combination of S and Li. Vice versa the content of γ -polymorph of dicalcium silicate decreases with the doping (Table 2). C3S formation is significantly suppressed with increasing Li content. Recent study [15] clarifies this effect of Li by significant reduction in the temperature of the clinker melt formation and a decrease in its viscosity. Lithium causes a partial to complete decomposition of the alite into microcrystalline mixture of belite and free CaO depending on Li₂O content and cooling rate.

The phase composition was monitored by XRD hydration in situ during 24 hours of hydration. Sample C2S contains mainly γ -C2S with a small amount of β -C2S and a minimum of CH (CH peak is overlapped with peaks of C2S and a slight amorphous hump). In the course of 24 hours the phase composition does not change considerably. Sample C2S S contains β -C2S and γ -C2S, C3S and CH. Although the raw material composition was designed so that the resulting CaO : SiO₂ + SO₃ ratio would match belite, relatively high amount of C3S is probably caused due to release of a part of SO₃ during synthesis. At the beginning, amorphous hump and intensity of CH peaks are increasing. From 160 min on, there is no longer a hump and CH peaks are clearly visible and their intensities increase. After 800 min., there is no change. Sample C2S S 2Li contains β -C2S, C3S and CH. CH peaks appear right at the beginning and gradually increase their intensity reaching their maximum at around 360 min (Figure 2).

β -C2S intensities have a very slight decrease at the beginning, otherwise unchanging. C3S intensities also decrease from the start. Sample C2S S 4Li contains β -C2S, C3S, CH and anhydrite. At the beginning, a pronounced amorphous hump disappears around 200 min. From 200 min, anhydrite is visible and then its signal stays invariant. CH grows from 80 to 1200, then its intensities stay unchanged. Detailed XRD and DTA analyses were done on sample C2S S 2Li. Hydration of the sample was stopped after 0, 45, 90, 360, 720 and 2880 minutes. Phase composition including amorphous phase was determined. CaO reacts completely within first minutes of hydration, which is demonstrated as a large exothermic signal in isothermal experiments (Figure 1). C3S content decrease and increase of amorphous content and

CH content are in good correlation with the main calorimetric peak. β -C2S reacts very slowly showing continuous content decrease (Figure 3).

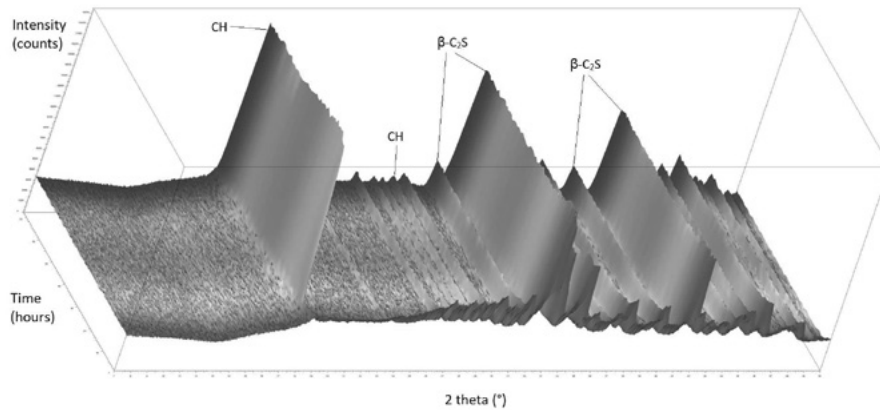


Figure 2: XRD, hydration in situ, sample C2S S 2Li, 24 hours

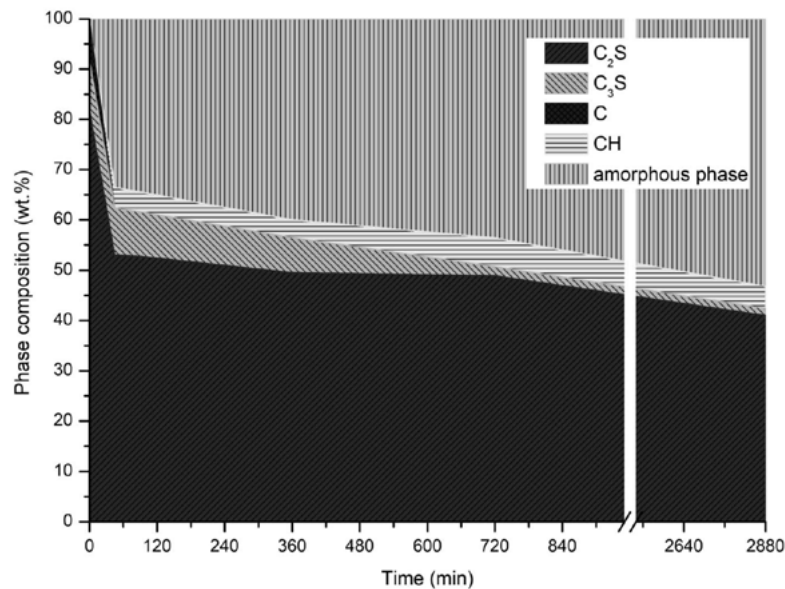


Figure 3: XRD, inner standard method, phase composition during 2 days of hydration, sample C2S S 2Li

Quantitative analysis of effluent fluids with calculation of phases for single processes was done by DTA-TGA on sample C2S S 2Li. The phase composition of the sample was determined after 45, 90, 360, 720 and 2880 minutes of hydration. Position and intensity of main endotherms were monitored at selected time intervals during hydration (Figure 3, Tables 3 and 4). Processes of H₂O release from C-S-H and AFt overlap each other. Taking in account recrystallization of AFt, continuous increase of C-S-H content can be seen on endotherm which changes its position from 76-127 °C during 48 hours of hydration. CH endotherm moves its minimum as the crystal size increases. From 720th minute on, double endotherm of CH is visible. This double endotherm can be explained as a second generation of CH, which might indicate the presence of another source. From the results of calorimetry and XRD, it is obvious that this source is β -C2S which starts to react later than C3S. Furthermore, the C3S content stays the same after 720 minutes of hydration (Figure 3). Based on the intensities and positions of endotherms, it is likely that two generations of CH differing in crystal size are formed. Second generation, that is detectable from about 6 hours of hydration onwards, grows simultaneously with first generation.

Table 3: Quantification of effluent gases or phases* from thermographs (wt. %), sample C2S S 2Li

	45	90	360	720	2880
	min				
H ₂ O; C-S-H, AFt	0.21	0.18	0.47	1.22	1.72
H ₂ O; CH	1.5	1.56	1.36	1.84	2.07
CH*	6.17	6.42	5.59	7.57	8.51
CO ₂ ; calcite* (minor peak)	0.15	0.16	0.4	-	0.14
CO ₂ ; calcite* (larger peak)	0.71	0.41	1.07	1.19	1.47
CO ₂ ; calcite* (sum)	0.86	0.57	1.47	1.19	1.61
calcite*	1.96	1.30	3.34	2.71	3.66

Table 4: Position of endotherms (°C), sample C2S S 2Li

	45	90	360	720	2880
	min				
C-S-H, AFt	76	96	99	116	127
CH	443	441	451	441, 468	474, 489
calcite (main peak)	762	739	777	774	788

3.3 Microstructure

Development of the structure during hydration of C2S S 2Li cement paste was observed by SEM in secondary electrons. The microstructure after 45 min, 90 min, 360 min, 720 min and 2880 min is given in Figure 4. A study [16] that has discussed the microstructure of a similar system after 90 and 180 days of hydration revealed similar C-S-H fibrous structures, that was transformed into dense aggregates of globular morphology at later ages (180 days). The studied structure shows platy larger CH crystals with undergrowth of fine fibrous C-S-H after 45 min and 90 min of hydration and continuous recrystallization of CH and densification of C-S-H on the surface of the particles after 2880 min of hydration. Based on SEM-SE, it is not possible to distinguish C-S-H formed from C3S and C2S hydration, yet it is the goal of further microstructural studies. Nevertheless, the densification of C-S-H from 720 min on, taking into account the phase analyses, can be supported by C2S hydration.

4. Conclusions

Heat related to C3S hydration measured by isothermal calorimetry is proportional to its content and the position and maximum of heat flow peak changes with increased Li content. The reactivity of β -C2S is affected by the timing of the hydration of other clinker phases. Based on heat development, the formation of C-S-H products is a continuous process that relates mainly to C3S hydration during first 6 hours which is then supported also by slow reaction of β -C2S. Results of thermal analyses show the presence of double portlandite endotherm in DTA curves revealing two generations of portlandite attributed to C3S and C2S hydration. This finding is in agreement with changes in phase composition and position of exotherms determined by XRD-in situ and inner standard method, isothermal calorimetry and densification of C-S-H on the surface of the anhydrous particles studied by SEM.

5. Acknowledgment

Thanks are due to project No. 19-05762S financed by the Czech Science Foundation.

6. References

- [1] Boden, T, Andres, B, Marland, G 2016 Global CO₂ Emissions from Fossil-Fuel Burning, Cement Manufacture, and Gas Flaring: 1751–2013, Oak Ridge National Laboratory, Oak Ridge
- [2] IEA, WBCSD, Cement Technology Road-map 2009 Carbon Emissions Reductions up to 2050, OECD/IEA.; WBCSD, Paris.; Conches-Geneva, Switzerland, 2009
- [3] Lea, F M, & Hewlett, PC (2004). *Lea's chemistry of cement and concrete*. New York: Elsevier Butterworth-Heinmann.
- [4] Taylor, HFW. *Cement Chemistry*, 2nd Edition. Thomas Telford, London, 1997.
- [5] Gartner, E, Sui, T (2017). Alternative cement clinkers. *Cement and Concrete Research*, <http://dx.doi.org/10.1016/j.cemconres.2017.02.002>
- [6] Staněk, T, Sulovský, P (2015). Active low-energy belite cement. *Cement and Concrete Research* 68 203–210.
- [7] Hanic, F, Kamarad, J, Stracelsky, J, Kapralik, J (1987). The p-T diagram of Ca₂SiO₄. *British Ceramic Society Transactions and Journal* 86: 194-198.
- [8] Sahu, S (1994). Developments in low energy clinkers. *Ceramics-Silikáty* 38: 191-200.
- [9] Stark, J, Müller, A (1988). International development trends in low-energy cements. *Zement-Kalk-Gips* 41: 162-164.
- [10] Xiuji F, Xinmin M, Congxi T (1994). Study on the structure and characteristic of dicalcium silicate with quantum chemistry calculations. *Cement and Concrete Research* 24: 1311-1316.
- [11] Tsurumi, T, Hirano, Y, Kato, H, Kamiya, T, Daimon, M (1994). Crystal structure and hydration of belite. *Cement Technology* (The American Ceramic Society) 19-25.
- [12] Bullard, JW, Jennings, HM, Livingston, RA, Nonat, A, Scherer, GW, Schweitzer, JS, Scrivener, KL, Thomas, JJ (2011). Mechanism of cement hydration. *Cement and Concrete Research* 41: 1208–1223.
- [13] Pelletier, L, Winnefeld, F, Lothenbach, B (2010). The ternary system Portland cement–calcium sulphoaluminate clinker–anhydrite: Hydration mechanism and mortar properties. *Cement and Concrete Composites* 32: 497–507
- [14] von Lampe, F, Seydel, R (1989). On a new form of β-belite. *Cement and Concrete Research* 19: 509-18
- [15] Staněk, T, Rybová, S, Zezulová, A, Boháč, M (2019). Formation of clinker containing lithium. *Materials Science Forum* 955: 50-55
- [16] Goni, S, Guerrero, A (2007). SEM/EDX Characterization of the Hydration Products of Belite Cements from Class C Coal Fly Ash. *Journal of the American Society* 90, 12, 3915-3922

Safe Use of Sustainable Building Materials: A reappraisal of Adobe

T. Li Piani^{1,2,3}, J. Weerheijm^{1,2}, L. Koene³ and L. J. Sluys¹

¹ Technical University of Delft (TU Delft), Computational Mechanics, Civil Engineering Faculty, Delft, The Netherlands

² TNO, Defence, Safety and Security, The Hague, The Netherlands

³ Netherlands Defence Academy (NLDA), Den Helder, The Netherlands

Abstract

Adobe is a sustainable masonry made of sundried earthen bricks and mortar. A critical analysis of the normative bodies currently available for the material characterization of adobe is addressed in this paper. Guidelines, prescriptions and requirements related to test methods, materials selection and properties contained in the available building codes for adobe around the world are discussed in this study. The physical and mechanical properties of adobe presented in literature are addressed, with particular attention to the most recent scientific findings produced by the authors over the last five years of research. These have been assessed in several experimental campaigns as well as corresponding numerical simulations aimed at physically-mechanically characterizing the behaviour of various soil mixtures, adobe bricks and mortar under different environmental (humidity content and temperature) and loading conditions (in tension and compression) in the static and dynamic regimes. On the basis of these findings, some issues have been identified in relation to the knowledge currently condensed in the prescriptions, requirements and procedures of the available norms for the material characterization of adobe. A final series of guidelines is aimed at orienting future research on adobe as well as fostering the process of updating its current normative body. The importance of a normative update for adobe is cogent in relation to the need for a sustainable conversion of the current product and production processes inherent to building industry in order to satisfy requirements for safety and sustainability to structural design.

Keywords: adobe; material; properties; standardization; characterization.

1. Introduction

Goal number 11 of the UN urban agenda is concerned with making cities inclusive, safe, resilient and sustainable. The introduction of the concept of sustainability in the building construction industry is urgent because of its current impact on the increasing threats inherent to natural material scarcity and global pollution. Construction industry nowadays influences up to half of the total anthropogenic emissions of dioxin in the atmosphere and is responsible for more than one third of the total energy and water use. A relevant portion of these contributions regards only the material production phase [1]. Thus, sustainable alternatives to current building practices are cogent priorities and researches aimed at reducing the environmental impact of building materials while respecting performance requirements have been recently started around the world. For example, biological fibers have been recently tested as sustainable alternatives

to steel in reinforced concrete and natural binders or aggregates have been partially replacing Portland cement in concrete [2]. Alternatives to baking processes such as air drying procedures are studied for baked clay bricks [3]. Most of the aforementioned practices, despite being applied to new materials, are far from being new. In particular, they belong to the tradition of adobe. In adobe masonry, bricks are made of soil mixed with natural fibers locally available in the field. Mixtures are then cast in moulds and sundried without baking [4]. Fiber inclusion as well as air drying contribute to the eco-sustainability of adobe as a material. Adobe is fully disposable and recyclable. It causes almost null carbon footprint and ensures also higher acoustical and thermal performance than classical modern materials. Therefore, this material has recently gained renovated attention also in Europe within trends of sustainable architecture [5]. Unfortunately, the effects inherent to air drying and fiber inclusion as well as other sustainable practices tied to adobe tradition on its mechanical performance have not been addressed yet. In fact, use of adobe decayed in industrialized societies in favour of artificial building materials with higher performance and standardized production methods [6]. As a result, most of the adobe buildings in the world are currently not designed according to any standard. However, more than two billion people still live in earthen dwellings spread mainly in regions of developing countries involved into military operations or prone to severe earthquakes and building heritage of adobe can be encountered in Europe as well [7]. Thus, in the specific case of adobe, sustainability is intertwined with other global urgencies inherent to safety and housing affordability tasks [8]. As a result, a comprehensive characterization of earthen material is of paramount importance nowadays. Normative efforts for the material characterization of adobe have started about fifty years ago in different areas of the world. The first attempts to characterize earthen materials for constructions relate to standards in Germany [9], [10] and in New Zealand [11] and the most widely used reference nowadays according to literature studies is the Australian earth building handbook [12]. Other guidelines can be found in different areas of the world, including Mexico, Peru, California and Spain [13]–[15]. In codes for adobe, indications about material selection and characterization test requirements are often lacking, scarce or not consistent among the different guidelines. This occurs also because adobe is a site dependent material whose properties vary based on the local resources availability and building traditions, that prevented an uniform treatment of the subject. Nevertheless, it has been the lack of definite knowledge on the mechanical properties of earthen mixtures that mostly prevented a shared standardization process of adobe similarly to modern building materials. Comprehensive studies on the mineralogical, physical and mechanical properties of adobe are still rare in literature: if this is true in statics, literature production on the dynamic performance of adobe is almost null [16]. However, research efforts toward the mechanical characterization of adobe have been focusing in the last decades [17]–[19]. Over the last five years, research by the authors has been devoted to comprehensively studying the properties of adobe. Earthen bricks and mortar with different soil and fiber proportions have been physically as well as mechanically studied at different humidity contents [20]. In particular, the role of fibers and water content have been experimentally studied also in the dynamic regime, in ranges of strain rates which cover earthquakes and ballistic impacts [21]. These studies resulted in theories, analytical models and numerical frameworks developed to assess the material performance of adobe from statics to dynamics, including to address the effects of its mineralogical composition at a meso-scale on the material response [21]–[23]. In this paper, the resulting updated knowledge gained on its physical-mechanical performance serves as a critical normative review on the material characterization of adobe. Normative guidelines, prescriptions and requirements condensed in the heterogeneous normative production currently available around the world have been confronted against the recent physical evidences collected for adobe. In the following paragraphs, a review of characterization norms is presented into three subjects: soil selection, sample testing and material requirements. From the normative-experimental, analytical and numerical comparison, issues and knowledge gaps have been identified in some existing prescriptions, requirements and procedures currently available for the material characterization of adobe.

Therefore, final recommendations are meant to support the development of a normative framework/body for adobe as well as give a perspective on future research.-

2. Material Characterization of Adobe in three steps

Material standardization derives from a shared definition of soil selection, test methods and product performance. In the following paragraphs, a normative review is based on the analysis of these three main subjects.

2.1 Material Selection

Traditional adobe bricks result from mixtures of clay, silt, sand, water and air. In most cases, bricks' soil is mixed with natural fibers while mortar contains limited or no fiber amounts. Despite already back in the 90's scientific papers in literature recommended a proper characterization of the soil granulometry, plasticity and compaction properties of adobe with building purposes, importance on the selection and identification practices of soil mixtures for earthen building applications is still not reflected in current design codes [24]. All codes for adobe currently available agree in selecting soils with no organic content and avoiding soluble salts above 0.5-2% [11], [12], [14]. Thus, top soil shall not be used. Potable water is recommended for mixing soil. Granulometry ranges are the most common recommendation contained in current building codes for adobe as indications of the cohesion properties of the final product [12], [14]. Guidelines mainly focus on the quantitative evaluation of clay amount in the mixture. In fact clay is the binder for the cohesionless granular fraction of the soil and is responsible for providing strength to the dried material [20], [25]. All codes agree that a minimum of 10% by weight of clay should be present in the mixture [12]. However, recommended ranges vary also significantly around the different normative bodies, including in experimental characterization campaigns found in literature [20]. As a result, maximum recommended clay percentage and foremost relative proportions with the larger size aggregates are still not defined neither agreed [4], [12]. For instance, maximum aggregate size recommended can range between 5 mm to 25mm [12]–[14]. This uncertainty happens because the adopted mixture is dependent on local availability of raw resources and an optimal clay amount is also determined by its mineralogical family and mutual proportions with the larger particles of the soil mixture. Expansive clay such as smectite or montmorillonite are highly cohesive but also cause shrinkage cracks in the resulting adobe bricks [25]. In this regards the use of expansive soil (i.e. "black earth") is sometimes discouraged in codes [11], but studies in literature reveal that an optimum balance between expandable and non expandable soil is possible and desired to ensure adequate strength to the brick [26]. Permitted ranges of soil components in the different codes are resumed in Figure 1. As a result of the possible combinations available in literature, consistency in the normative assessment of the optimal ranges of soil particles for earthen building purposes is lacking. The (loose) ranges contained in the Australian standard include the best quantitative soil mixture compositions for building purposes identified by the authors for adobe in [20] from a literature survey. Besides availability of raw materials, quantity of clay as well as other soil elements and including mixing water depend on a vernacular building practice typical for adobe. It consists of mixing soil with natural fibers. This practice is tied to earthen architecture and dates back to ancient Egypt [6]. It takes roots in the need for limiting shrinkage cracks naturally forming in the brick during curing process under sun [19]. In fact, fibers ensure better drainage systems [27]. Recommended materials are e.g. rice, barley, maize, wheat and including animal hair. Obviously, inclusion of fibers necessarily influences the initial mineralogical composition and the mixing water content and has an impact also on the physical-mechanical behaviour of the final product. However, despite a consolidated practice, the assessment of the mixture properties after fiber inclusion is currently not regulated by characterization standards for adobe. Instead, judgment of its opportunity in soil mixtures in codes is deputized again to the user and regulated only by not defined limits of not "*excessive use*" [12].

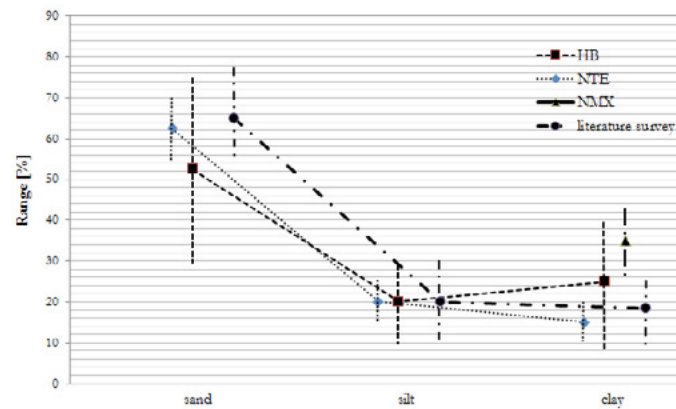


Figure 1: Granulometry ranges for soil mixtures of adobe for building purposes according to Australian (HB), Peru (NTE) and New Mexico (NMX) codes compared with the results of a survey by the authors from literature.

Actually, fiber inclusion in adobe guidelines is often considered as a stabilization technique of otherwise unsuitable soil compositions and suggested as an alternative to the introduction of cementitious bituminous binders recommended for highly clayey soils [11]–[13]. In this regard, fibers are suggested to improve the mechanical properties in hardness and strength, especially in tension [11]. The current interpretation on the role of fibers in many building codes for adobe is instead in contradiction with the main experimental trends recently observed for fibrous adobe in the field [20], [21].

The most common effect described in literature when adding natural fibers to soil mixtures is a decay of the initial mechanical properties of the resulting brick, namely strength and elastic modulus [19], [20]. This is valid both for flexure and compression and at different loading rates in the static and dynamic regimes [21]. According to [20], higher amounts of clay were needed to partially recover the initial brick strength of a given soil mixture, if mixed with fibers, at the expenses of cracking problems after curing due to large clay amounts (Figure 2). These effects on the mechanical performance of adobe have been interpreted by the authors as the consequence of a loss of cohesion in the meso-structure of the soil mixture after fibers insertion. Particles can be separated by fibers and interaction between clay floccules to bind the cohesion less fraction of the mixture is less effective [21]. This particularly happens for fiber amounts above 10% b.w. However, also cases in which fibers strengthen the soil mixture can be encountered in literature [28], [29]. This happens because cohesion of the brick's macro-structure results from the mineralogical properties and relative proportions of the soil and by the material, quality and quantity of the added fibers, including their mutual interactions with clay binders at the meso-scale. This interpretation suggests that an optimum mixture of fiber and soil elements capable of reducing shrinkage and enhancing the mechanical performance exists. However, only a few codes currently prescribe cohesion tests for characterization purposes and they all require them to be performed only on the soil before fiber mixing [12]. Laboratory tests are recommended only in very few standard [9], [12]. In most of the cases, they imply the evaluation of Atterberg limits but only few quantitative indications are found, despite in broad ranges (16-30 for the plastic index and 30-50 for the liquid index) [12]. Quantitative evaluations inherent to soil plasticity as indication of soil consistency (without fibers) in standard are instead more commonly related to simple in field tests such as the Ribbon test, with an acceptance rate of 60-120mm for the broken pieces [12].

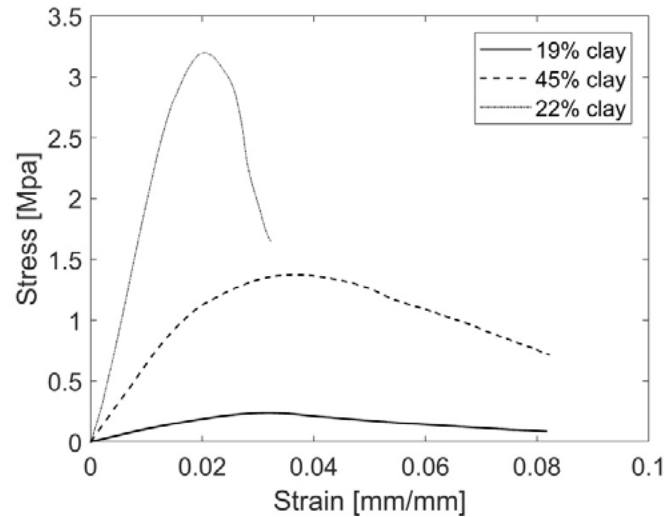


Figure 2: Experimental stress-strain curves of two adobe bricks containing about the same fiber content ($\cong 30\%$ b.w.) and different percentages in clay ($\cong 20\%$ and $\cong 45\%$) and one brick containing only clay (22%) tested statically (rate of 1mm/min) in compression at laboratory conditions [20].

2.2 Material Testing

As emerged in the material selection phase, test methods and requirements inherent to the characterization of adobe components are not comprehensively neither consistently registered among the available codes [9]-[15]. A representative list of characterization tests required according to three different normative bodies on adobe is provided in Table 1. In adobe building codes, in-field tests are still considered as acceptable alternatives to more rigorous laboratory test methods. In-field tests are recommended provided the presence of the persons responsible for final construction, despite most of earthen dwellings in the world are still designed and fabricated by owners themselves, often without the necessary specialist technical competences [30]. Also the level of sophistication of the testing procedures and requirements rely on the user judgement on the importance of the building project [11]. Some characterization tests in codes are even fully sensorial, such as the smell test to verify the presence of organic matter in soil mixtures [12]. The most widely used test to determine the grading of a soil mixture is the sedimentation bottle test, in which the shaking of a jar containing loose soil is aimed at ascertaining approximate fine and sand particles [12]. Instead, sieving and hydrometer tests are strictly recommended only in few norms [9]. In 2017, granulometry tests were performed by the authors using the BS 1377-2 norm for classification methods on soils for civil engineering purposes (Figure 3a-b) [31]. In fact, this code also includes the preliminary treatment of soil mixtures with natural fibers. Tests were performed starting from cured bricks of several mineralogical compositions.

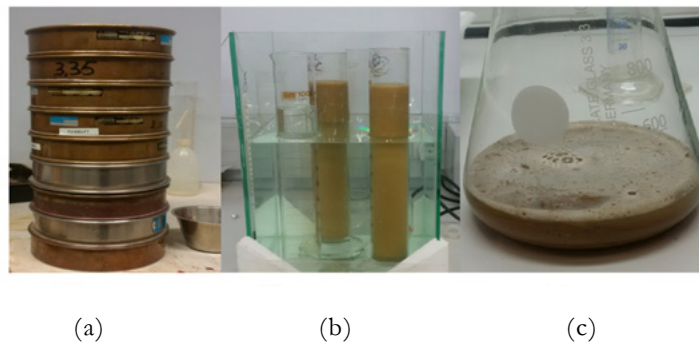


Figure 3: Sieving (a) and hydrometer (b) test, with preliminary chemical treatment of fibers (c) in [20]

This implied the preliminary desegregation of the product into its original soil mixture. Later, organic

content was excluded using mechanical and chemical treatments (Figure 3c). Dissolution was accomplished using hydrogen peroxide. In case of soil mixed with significant amounts and large sized fibers, this process required more cycles of chemical treatment.

Also the mechanical characterization of adobe is not solely prescribed according to laboratory standards but in-field compressive and flexural tests are often possible and still preferred [11]–[14]. However, mechanical properties can be rigorously derived from the standard commonly used for modern materials such as concrete. Compression tests on adobe samples were performed in [20] using UNI EN 772-1 for modern masonry materials [32]. Required levels of plane parallelisms for testing purposes were achieved using mechanical rectification procedures which did not cause visible damage and achieved precisions included in standard tolerance (Figure 4 a-b). The interposition of layers of materials of significantly different properties like cement mortar is not recommended for plane parallelism purposes for adobe.



Figure 4: Sanding paper (a) and machine (b) used for rectification purposes and wooden strip interposition between steel rolls in a three point bending test (c) [20], [21]

Static three point bending tests were performed by the authors according to UNI EN 12390-5 [33]. In this case, no indentation occurred when wooden stripes between adobe surfaces and steel rolls were interposed (Figure 4c). Literature studies and norms for adobe indicate that applied deformation rates above 5 mm/min may be not adequate for testing soft earthen materials. This limit is generally respected in literature studies and suggested by the authors. Displacement controlled tests at velocities of 1-2 mm/min are suggested especially for soft adobe tested in compression and tension [20]. Higher values are discouraged also because the mechanical properties of adobe have been recently found to be sensitive to the applied loading rate [21].

Table 1: List of main tests required for the characterization of adobe components according to the Australian (HB), New Zealand (NZS) and Mexico (NMX) codes, distinguishing in-field test (*in italic*) from laboratory tests and denoting with * tests without quantitative requirement limits

Property	HB	NZS	NMX
Grading	Bottle test Sieving/sedimentation	*	*
Organic content	Smell test*	*	*
Plasticity	Casagrande test Ribbon test Touch test	*	*
Durability&Erosion	Water retention test* Water absorption test* Spray test*	Wet/dry test* Spray test*	Water retention test*
Shrinkage	Box test	Box test*	*
Density	Oven drying*		*
Compression	Uniaxial test Drop test	Uniaxial test Drop test	Uniaxial test
Tension	Bending test Flexure test	Flexure test*	Flexure test*

If methods of investigation are uncertain, material performance requirements in codes are controversial

as well. As shown in Table 1, prescribed values for important physical and mechanical properties are often lacking or incomplete. Not strictly quantitative recommendations that rely on the arbitrary judgment of the user according to the specific need and destination of the product are often encountered in codes for the assessment of many parameters [11], [12]. This is the case for instance for the smell or the wet/dry in-field tests. When not lacking, test limits are often not uniform among different sources. Most of the quantitative requirements normed in codes for adobe nowadays focus on the assessment of minimum strength values in compression and tension. However, there is often no agreement about the minimum required performance and the assessment of other important mechanical parameters for masonry design is missing.

2.3 Material Performance

2.3.1 Physical Properties

Mixtures of adobe are casted in moulds and dried under the sun for a minimum of 28 days in an exterior environment before testing [11], [12]. Both literature references and current standard for adobe recommend to protect bricks from wind and rain during drying [11]. It is known that natural fibers explicate their role during this phase. They fasten this process facilitating draining through cavities and prevent the formation of severe shrinkage cracks [34]. Shrinkage is abundant during drying of earthen materials and is allowed also according to codes, provided that shrinkage cracks do not jeopardize the material properties of the product [11], [13]. Caution is recommended in [11] if short fine cracks spread randomly at the surface of the brick are observed. In [12], it is preferred to exclude products with crack lengths above 7 cm. Only [10] recommends quantitative limits of 2% for the property of linear shrinkage. Shrinkage cracks represent a significant issue especially in case of high amounts of expandable clays in soil mixtures or in absence of fibers. Therefore, it can represent a threat especially for mud mortar. Characterization of mud mortar receives very little attention in codes and it is treated only in [9], [11]. Despite its importance on the overall performance of adobe walls is recognized in literature, physical tests on mortar are usually prescribed only if different soil materials than for the bricks is used. This implies neglecting the influence of fibers during production of material and life cycle of the structure. Different shrinkage rates between bricks and mortar can be responsible for initial loss of adherence and de-cohesion issues which may soon affect structural integrity. Unfortunately, also scientific studies on the material characterization of adobe mortar are lacking and only two references concerning the physical mechanical assessment of mud mortar have been found in literature [20], [35]. In [20] physical tests for the determination of density and moisture content were performed on various types of bricks and mortar for the same curing conditions. They confirmed that mortar is denser and characterized by higher shrinkage rates than fibrous bricks (Figure 5).



Figure 5: Picture of mortar just casted(a) and after five days since pouring(b): volumetric shrinkage of about 18%[22]

Even if the same soil is used for bricks and mortar, also the corresponding values for the property of density are different after 28 days of curing. Density in adobe is significantly influenced by fiber addition and its inclusion in the mixture significantly reduces the density of the resulting brick. This is a common trend observed in literature and quantified in [21]. Density was determined on two types of bricks with the same mineralogical composition but with only one mixed with 18%b.w. of fibers. Tests showed that average

density of the fibrous samples was more than 30% lower than the fiber free homologous bricks. As a result of different compositions, density values among different bricks also greatly vary in literature. They usually range between 800 kg/m³ for fibrous mixtures to 1800 kg/m³ for clayey bricks [20], [21]. This range is close to the one recommended in standards for adobe (1200 kg/m³ – 2000 kg/m³) [12]. Tested mortar in [20] showed a density of 1400 kg/m³ whereas the one in [35] was almost 2000 kg/m³.

In codes, durability performance of cured adobe is addressed mainly using in-field tests. The most common property evaluated (without specific restrictions) is erosion against water simulating raining conditions or dry/wet cycles to which adobe walls may be exposed to during its life cycle [11]-[12]. Instead, the assessment of the moisture content at 28 days of drying before wall fabrication is not required by codes. It is generally assumed that water content after curing is lower than 4% [11]. This is not always the case and actually depends on the internal composition of the product. This was inferred in [20] during an experimental campaign aimed at testing the mechanical performance of bricks and mortar made with different clay and fiber percentages. Bricks mixed with 30%b.w. of fiber and containing 45%b.w. of clay contained more than 6% of water after 28 days of curing, whereas the same fiber amount in a mixture with half of the clay almost halved its initial moisture level for the same environmental conditions (Figure 6). This suggests that 28 days are not always sufficient to ensure a fully dried product. Furthermore, presence of fibers in the mixture has been found to have a relatively minor influence on the final level of water content at cured conditions of bricks [21], [23], [36]. In particular, for certain amount of fibers, it is found that water content increases significantly with the increment of the clay proportion in the mixture. This is interpreted as a consequence of the fact that the areas of the mixtures surrounding fibers are fully dried after 28 days. Thus, the final water content depend on the spatial distribution of the fibers in the mixture, with particular concern to concentrations of clay. In fact, water can still be retained by floccules of clay due to its affinity toward water: it swells in its presence and it shrinks in its absence [25].

Finally, the eco-efficiency of the material in terms of physical properties such as thermal resistance are not contemplated by codes, with the exception of [12] where a typical range of the expected performance is included between 0.25-0.6 m²K/W.

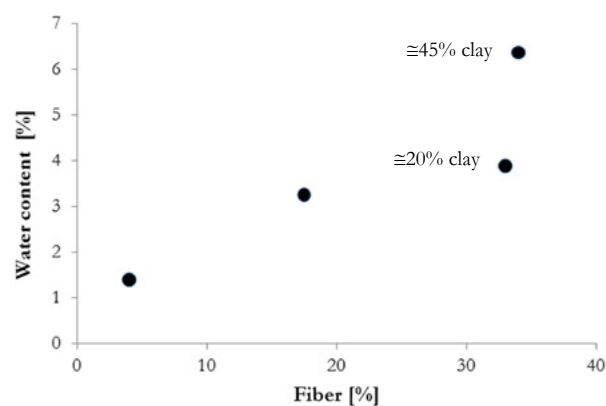


Figure 6: Water content at 28 days of curing for four different adobe bricks as a function of the mixing fibers: focus on the moisture content for two bricks with similar amount of fiber but different clay percentages [20].

2.3.2 Mechanical Properties in Compression

For adobe, assessing the interstitial water content of earthen components prior to construction is of paramount importance. Not only it is already known that water affects the durability performance of the structure due to erosion phenomena during the life cycle of the structure [4] but it also directly influences the nominal strength of the bricks and mortar and thus of the overall walls. Guidelines consider adobe

bricks as fully dried after 28 days of curing, when the water content is expected to be lower than 4% [11]. However, also water levels below 2% are sufficient to determine a significant decrement in the parameters in strength, whereas a minor influence is exerted in deformation. This has been experimentally found testing different types of adobe bricks at different induced moisture levels (including oven drying the samples) [20], [21]. Tests revealed an increment in strength for progressively lower water contents in the bricks. This trend has been observed for all the tests performed, both in static and dynamic regimes and also when mixtures contain fibers (Figure 7).

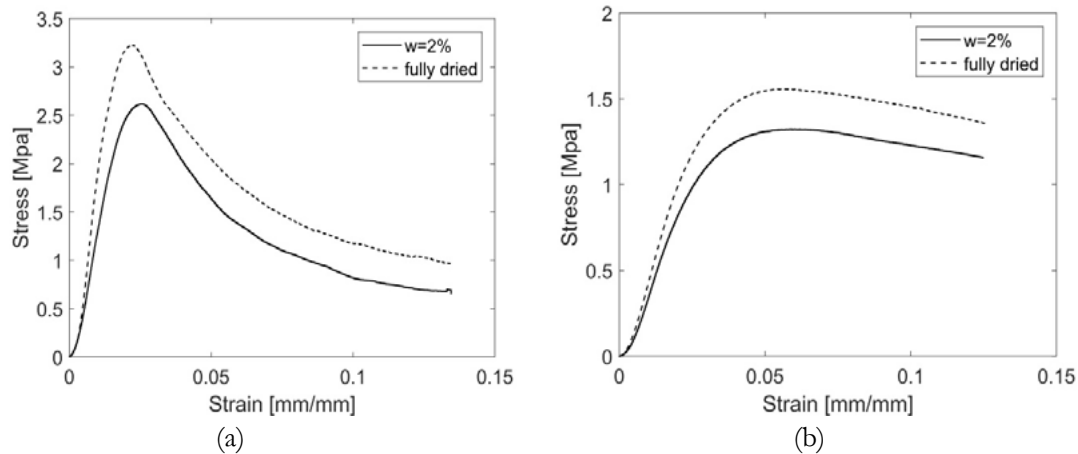


Figure 7: Stress-Strain curves in compression for fiber free adobe bricks (a) and fibrous bricks (b) air dried at laboratory conditions ($w \cong 2\%$) and dried in the oven (reduction of about 20% in strength)[21]

However, the rate of decay of the strength of adobe due to interstitial water has been quantified in [20] as a function of the mineralogical composition of the mixture. By testing samples with different clay and fibers at certain drying conditions, it was revealed that the mineralogical composition of adobe can accelerate or decrease the loss of the mechanical property. In particular, statistical regression of experimental data on adobe resulted in the law of eq.1 for the prediction of strength at a given humidity as a function of its internal composition, namely fiber, clay and water contents [16]:

$$f_b \sim \frac{\text{clay}}{\text{fiber}} w^{-\frac{\text{clay}}{\text{fiber}}} \quad (1)$$

Where w stands for water and all variables are expressed in volumetric percentages. Examples of these laws are shown in Figure 8 for one type of brick and mortar experimentally tested. The shape of the law in eq. 1 recalls the trend previously derived for baked clay bricks in [3], where the rate of decay increased for higher clay contents. As expected from the formulation in eq.1, the rate of strength decay experimentally derived for adobe mortar (with low or no fiber content) is in general higher than for adobe bricks and it is found to be similar to one of the slopes determined in [3] for only clay bricks.

The mechanical testing procedures and prescribed values in compression of the brick after curing are covered the best by current standards. Table 2 summarises the quantitative requirements in strength prescribed by four different codes for adobe. Recommendations in the different sources are not fully consistent in the prescribed test setup as well as in the required performance levels. However, the minimum values for strength prescribed by codes after aspect ratio correction are in average consistent with the values usually found for adobe bricks and mortar in literature, although lower values than prescribed requirements can also be encountered in the field [6]. Figure 9a shows the nominal strength distribution for adobe after elaboration of a database collecting more than 150 static characterization tests in literature supplemented with authors data [20]. Most common values for adobe range between 0.8MPa and 2MPa. The average

value of strength is found to be about 1.28 MPa, with 0.95 percentile of about 0.29 MPa.

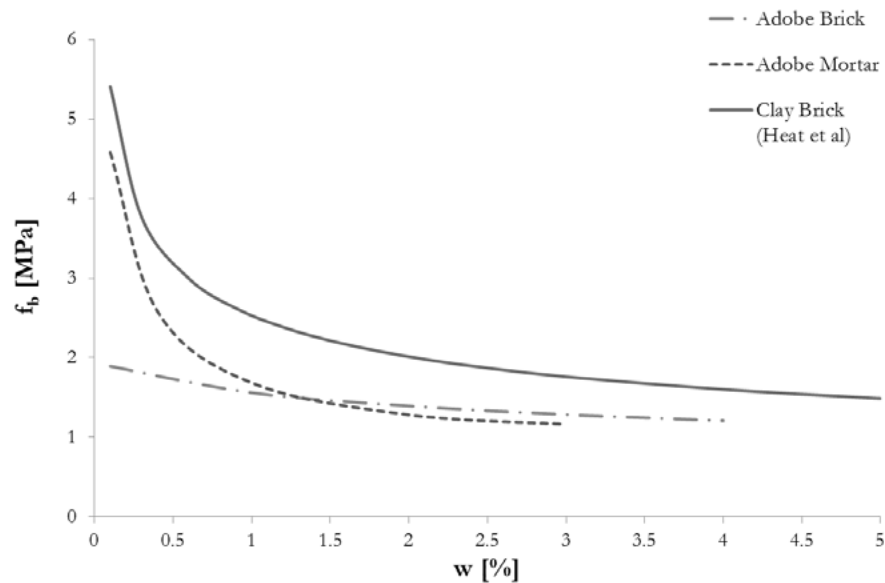
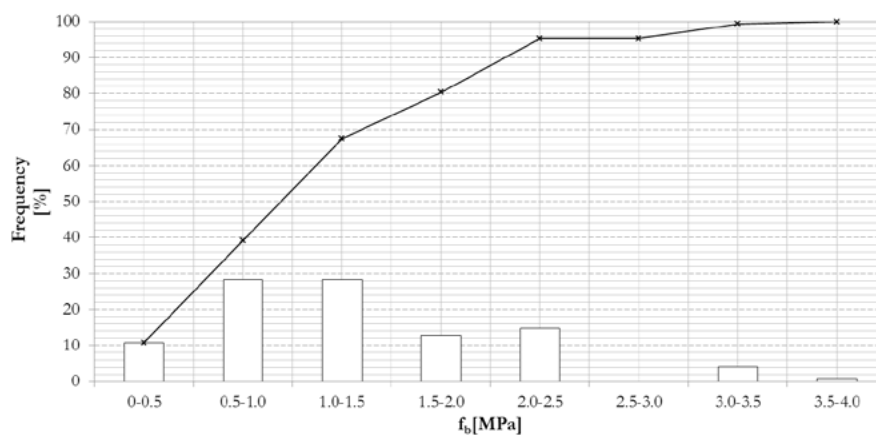


Figure 8: Compressive strength law for adobe dependent on water content. Examples of predicted trends for one type of adobe brick and one type of adobe mortar using eq.1, compared with law derived in [3] for clay bricks

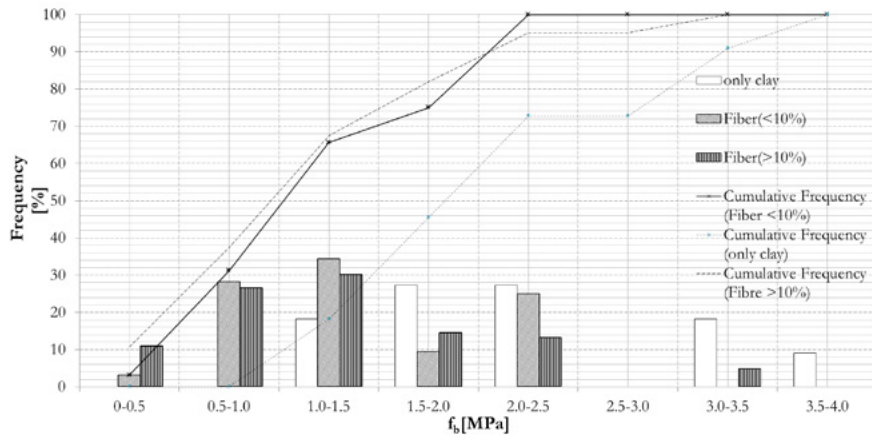
On the other hand, in almost 40% of the test cases, strength of adobe bricks was lower than 1 MPa. The unconfined values of strength are usually determined in literature using the aspect correlation factors commonly prescribed for concrete [37]. Instead, codes in [12] and [11] prescribe a more conservative law for adobe and recommend slenderness's of 3-5 as representative of the unconfined strength (Figure 10). Applying this law to the available tests in the database, the average strength is equal to 1.19 MPa, with 0.95 fractile of about 0.2 MPa.

Table 2: Prescribed strengths (and additional indications) for four building codes on adobe

Standard	Requirement	Indication
NZS	Minimum > 0.9 MPa	after aspect ratio correction (Figure 10)
NTE	80% fractile > 0.85 Mpa	after aspect ratio correction
NMX	Average > 2 MPa	on flat direction/no geometry info
HB	Average > 1 MPa	after aspect ratio correction (Figure 10)



(a)



(b)

Figure 9: Relative frequency (histogram) and cumulative frequency (line) for the unconfined strength of adobe in literature (including data from authors) considering all data (a) or disaggregating data according to fiber ratios in the mixtures (b)

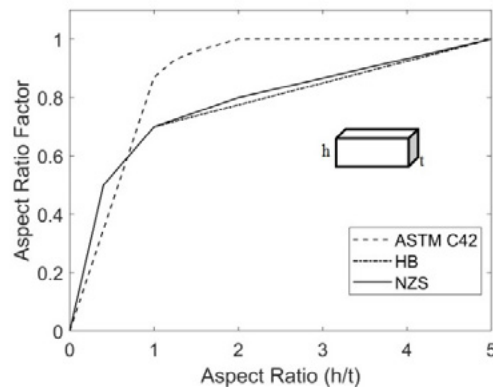


Figure 10: Aspect ratio correction law in strength for concrete compared with the laws proposed in the Australian and New Zealand code for adobe

Despite the specific shape of the curves in Figure 9, there are almost no systematic studies publicly available in literature on the size and shape dependencies of adobe [38]. Preliminary size dependence studies by the authors reveal a significant sensitivity to sample dimensions in the response in strength and deformation (Figure 11a). However, derived values for nominal strength are consistent with the aspect ratio laws depicted for adobe in Figure 10.

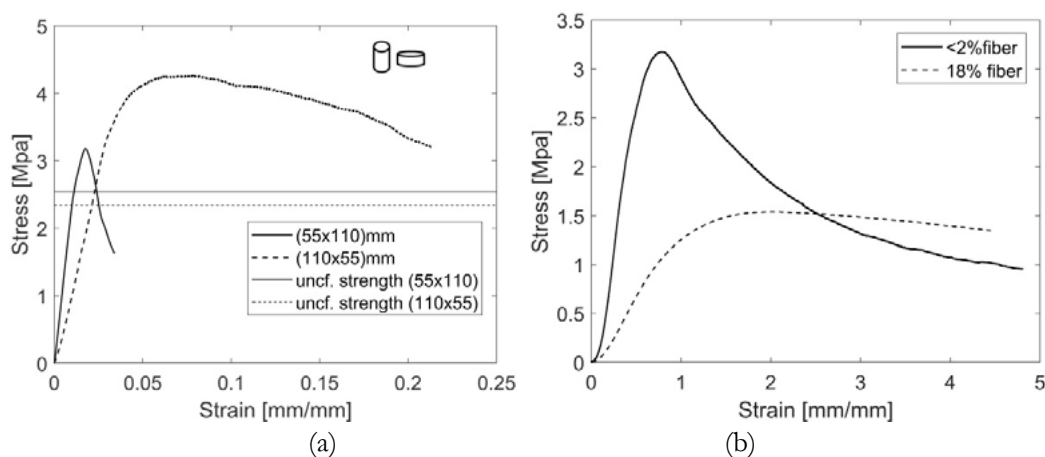


Figure 11: Stress - strain curves and unconfined strength values after aspect ratio correction in HB (Figure 10) for two adobe cylinders with same soil and fiber compositions but different slenderness

(a) or with the same geometry but different fiber percentages (b) tested in uniaxial compression at laboratory conditions in [21]

As for shape dependence, in [38] a correlation between tests on cylinders and cubes was found with a slope of 0.94. Furthermore, aside the role of water content, the mechanical characterization of adobe in standards does not address the influence of fiber content on strength, despite that most common trends in literature relate fiber in soil mixtures to a decay of the mechanical parameters of the material (Par. 2.1). However, recognizing this role is not always easy in literature. In Figure 9b, the same data plotted in Figure 9a are disaggregated according to the relative presence of fibers in the mixture, organized in three categories: fiber free (<2 b.w.%), low fiber ratio (<10%b.w) and high fiber ratios (>10 % b.w). From Figure 9b, fiber free samples do not possess strength values lower than 1 MPa, whereas fibrous bricks have a significant statistical incidence in the 0.5-1MPa and 1.0-1.5 MPa ranges. However, fibers can confer to the brick also values of strength above 3MPa. As explained in Par. 2.1. the outcome of fiber inclusion depends also on the specific characteristics of the applied soil. However, there are only few systematic studies aimed at quantitatively addressing the role of fibers in adobe bricks [39]. Tests by the authors [21] showed that parameters in strength and stiffness are significantly affected by fibers whereas their inclusion is always accompanied by an enhanced ductility and retarded failure (Figure 11b). The major contribution associated to the presence of fibres in the mixture on the mechanical performance of adobe is indeed related to the material ductility. Fibers allow the bridging of the stress through cracks, limiting their entity and holding together the vital cores of the matrix until large deformation stages.

Indications on the elastic stiffness of adobe bricks are not provided in standards. Data in literature reveal a significant scatter in values, with ranges between 10 MPa and 2500 MPa. However, most common values lie between 50 MPa and 200 MPa (Figure 12). The only reference to this parameter in standards relates to the stiffness of the adobe wall, which should be designed as 300 times the corresponding strength in [11]. Calculating E as a ratio of the strength reduces the scatter in value associated to stiffness, since strength and stiffness are found to react in a similar manner to clay, fiber and water contents in the mixture [21]. However the recommended value in standards is lower than the ratios commonly encountered for adobe bricks. Considering only data set in [20], $E=60-80f_b$, whereas considering data in literature $E=120-180f_b$ [40].

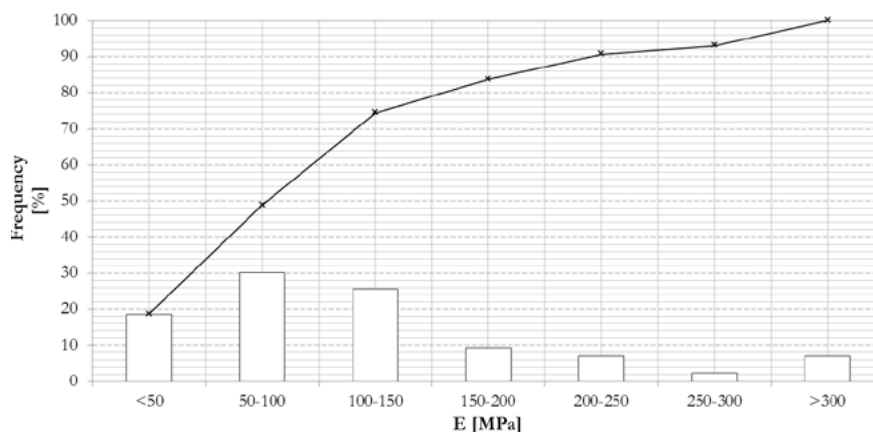


Figure 12: Relative frequency (histogram) and cumulative frequency (line) of the elastic stiffness of adobe

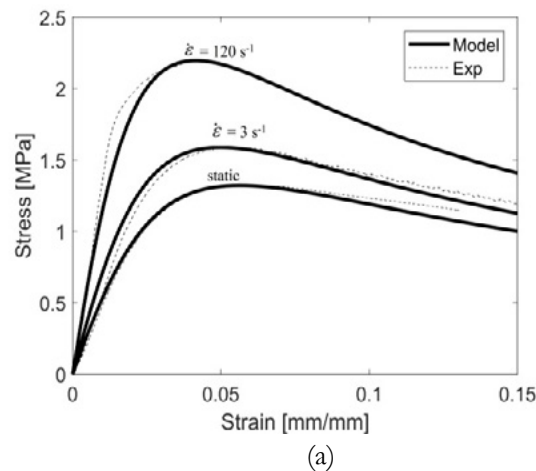
Besides the assessment of the mechanical parameters in compression, the definition of the entire curve in compression is of paramount importance for masonry materials. In fact, deformation curves can be used to develop constitutive models for non linear analyses [41]. Research has revealed that constitutive models originally developed for concrete can be used to address the curve of response of bricks and mortar of

adobe. In [21] a constitutive model has been developed to assess the stress-strain plots of adobe bricks made of different mineralogical composition and water content and subjected to various loading rates, from statics to dynamic impact (Figure 13a). The law recalled in eq. 2 takes roots from the Popovics' model developed for cement geo-pastes in statics [42]. It properly addresses the typical non linearity observed in the curves of response of adobe in compression, characterized by micro-cracking processes starting in the pre-peak phase of the curve and in the final quasi-brittle softening behaviour [18], [43]. Parameter n in eq. 2 controls the amount of non linearity in the uniaxial response and calibration with experimental data in [17] makes the parameter a function of fiber content (n ranges between about 1.5 and 3.5 in adobe and decreases with increasing fiber amounts). Furthermore, the model in eq. 2 modifies the original formulation in [42] implementing rate dependent functions of logarithmic shape $f(\text{DIF})$ for the uniaxial assessment of adobe in dynamics [21] (Figure 13b).

$$\sigma = f(\text{DIF}) E \left(\frac{\epsilon}{\epsilon_0} \right)^{\frac{n}{n-1 + \left(\frac{f(\text{DIF})}{f_0} \right)^n}} \quad (2)$$

In fact, the response of adobe at high strain rate loadings has been recently experimentally assessed [21]. Strain rates in the order of 120 s^{-1} were achieved using Hopkinson bar tests. Tests revealed that adobe is a material sensitive to the deformation rate. The dynamic increase factor of the mechanical property of strength for adobe lies in the lower boundary of the cloud of data usually associated to concrete (Figure 13b) [44]. From the same Figure it is shown that if soil mixtures are provided with fibers, rate sensitivity of adobe decays. This is consistent with interpreting a reduction of cohesion after fiber inclusion. Instead water content in the mixture enhances sensitivity to the deformation rate for a physical principle of viscosity called Stefan effect (Figure 13b) [21].

The scarcity of constitutive models describing the non linear response in compression up to failure for adobe is reflected in the lack of numerical models for the material simulation of bricks and mortar [45]. Constitutive models as in eq. 2 can be implemented in numerical frameworks, together with the definition of damage or plasticity surfaces. In [22], a smoothed Mohr Coloumb damage surface implemented in a finite element isotropic damage model with exponential softening damage evolution laws was suitable for interpreting the damage process of soil based masonry materials loaded in compression. This constitutive law has been validated against a wide range of loading conditions, including impact penetration tests on adobe walls [23].



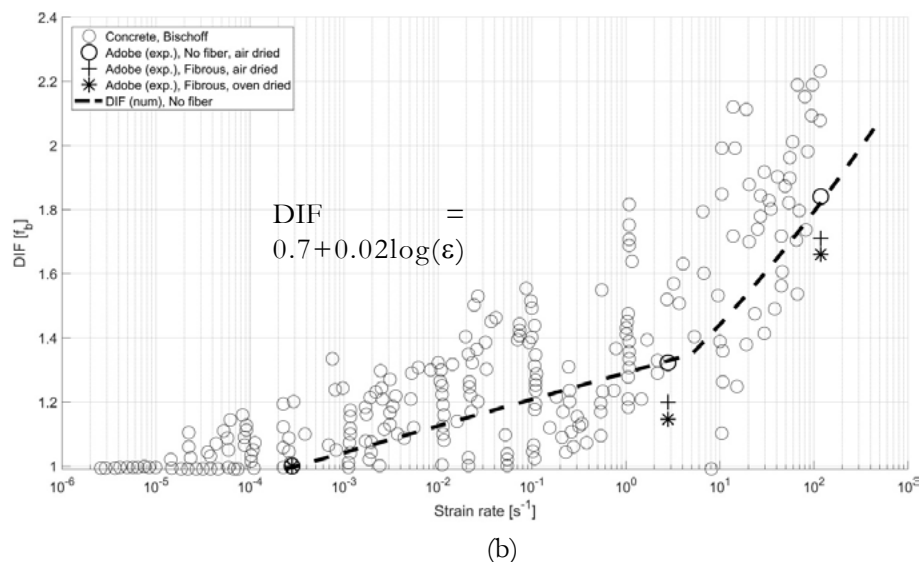


Figure 13: Experimental-numerical stress strain curves in compression for a fibrous adobe ($n=1.7$) compressed at three different loading rates from statics to high velocity impacts using eq. 2 (a) equipped with dynamic increase factor functions (DIF) experimentally derived in [21] (b)

2.3.3 Mechanical Properties in Tension

As for many quasi brittle materials used in masonry, correctly addressing the response of adobe in tension is very important. The mechanical characterization of adobe in tension in current codes mainly concerns the evaluation of its strength parameter. Quantitative values are evaluated mainly from flexural tests, despite literature studies suggest that splitting tests better reproduce the uniaxial tensile state [38]. Experimental data available for adobe in tension in literature and including tests in [20] is shown in Figure 14 similarly to Par. 2.3.1. Averages and 0.95 percentile values respectively are about 0.4 MPa and 0.15 MPa. According to codes, average values for strength of 0.34 MPa is prescribed in [13], while a minimum of 0.25 MPa is requested in [9]-[11]. This requirement is met by 65% of the experimental data for adobe in tension available in literature (Figure 14).

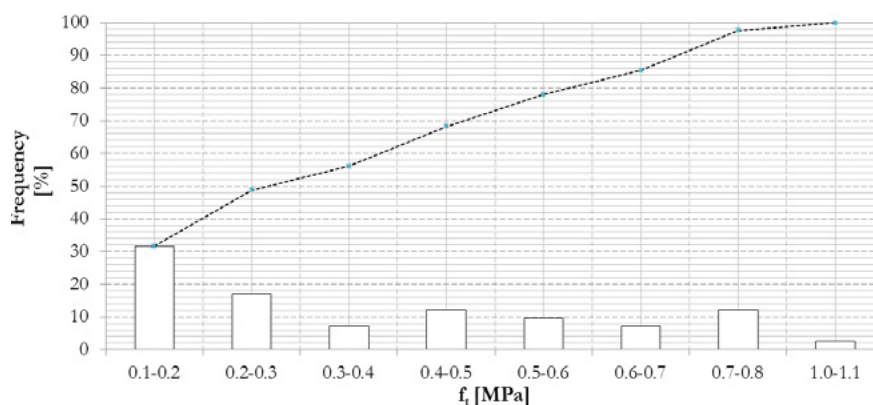


Figure 14: Relative frequency (histogram) and cumulative frequency (line) for the tensile strength for adobe using data in literature (including authors')

Disaggregating data in tension according to the possible presence of fibers in the mixture as in Par. 2.3.1., also in tension mixing soil with fibers statistically results to a lower strength performance in average (Figure 15a). In [45], bending tests at the same laboratory conditions have revealed an enhancement of ductility in the response of adobe when fibers are added to the mixture (Figure 15b). With a value of 0.7 MPa, adobe mortar (fiber free) tested in [20] possesses one of the highest values of tensile strength encountered in literature for adobe.

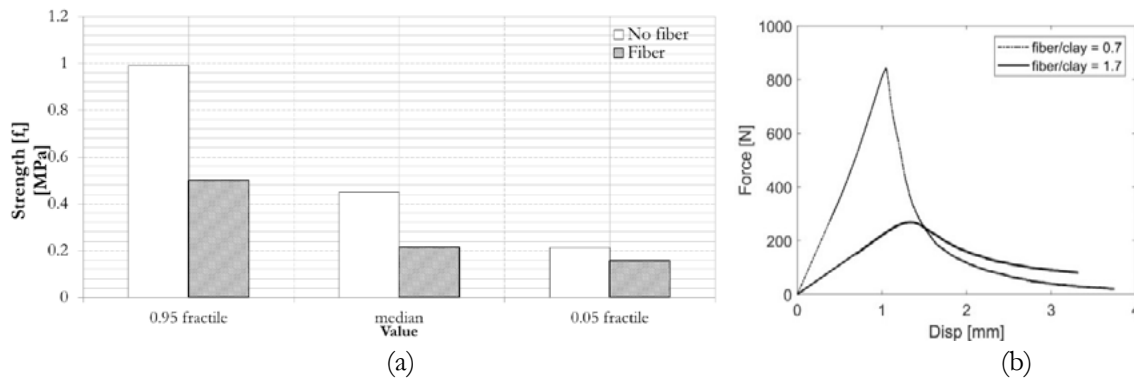


Figure 15: Relative frequency for the tensile strength of adobe bricks disaggregated for fiber free and fibrous adobe samples (a) and Force – displacement plots in bending tests in [16] on two adobe bricks with different fiber proportion ratios (b).

Tensile strength relates to the parameter in compression in ranges between $0.18f_b$ [6] and $0.4f_b$ [28]. In [16], this ratio ranges between $0.3f_b$ and $0.7f_b$, with a median equal to $0.57f_b$. These values are in general higher than the minimum levels suggested in [11], included between 10% and 20% of the compressive strength [11]. The failure process of adobe in tension is typically more brittle than in compression. A localized failure has characterized bricks and mortar subjected to bending tests in [20], independently from water content and fiber inclusion in the mixture. Typical curves of response are characterized by an elastic phase followed by softening with exponential shape (Figure 15b). In [22], numerical simulations of bending tests on adobe using a local damage finite element model recently developed for the simulation of bricks and mortar at various loading conditions showed that a constitutive law in RILEM TC 162 [46] originally prescribed for steel fiber reinforced concrete is suitable to numerically assess the localized damage failure experimentally observed in adobe in flexure (Figure 16). The adopted constitutive model in tension is linear elastic with an elastic modulus being the same as in compression until the attainment of the stress level associated to the first crack in bending, which anticipates softening.

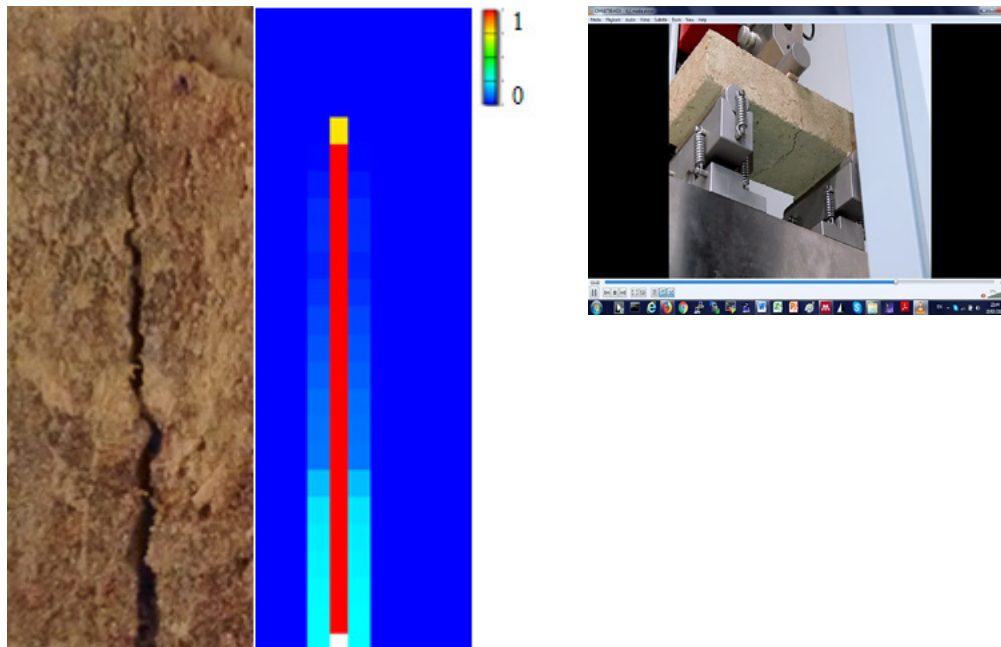


Figure 16: Experimental crack and numerical damage (using RILEM TC) localized in the middle of a brick subjected to bending test using the *adobe delta damage model* in [22], a finite element model for the simulation of adobe bricks

3. Final Recommendations and Conclusions

A review of the codes currently available for the material characterization of adobe bricks and mortar is reported in this study. The prescriptions provided by the normative bodies for adobe around the world related to test methods, soil selection and material properties have been critically addressed. They have been compared with the most recent scientific findings produced for adobe regarding the assessment and interpretation of its physical-mechanical properties. To this end, the experimental data, theoretical interpretations and numerical elaborations produced by the authors over the last years on adobe have been used as main reference. From the analysis, lack of knowledge, consistency and completeness in the current normative body stand out and a normative and knowledge update is needed. Among others, two areas of improvement are deemed as priority:

- Definition of a shared set of identifying properties for the physical-mechanical performance of adobe components, both bricks and mortar. The assessment of the drying conditions preliminary to tests on samples is a priority and the set of maximum moisture levels before mechanical characterization is necessary. The influence of moisture on the mechanical performance must be integrated both at an experimental characterization and at a material design level. Moisture content dependent strength laws should be considered when designing for the life cycle of the structure. Required properties should not solely relate to the characterization of the mechanical parameters of the resulting brick but rather to the evaluation of its original soil. If the minimum requirements in strengths by codes are generally consistent with mean experimental values found in literature, soil particle distributions tests are not sufficient to certify suitability of adobe as a building material. Assessment of fiber properties and amounts in the brick before mechanical characterization in codes is necessary. A comprehensive physical study on the mixture is needed, with particular reference to the plasticity and cohesive property assessment. These must not only be determined on the raw soil, but also directly on the final mixture used to produce the brick, namely including the assessment of fiber-soil mixtures properties. At a research level, the identification of the materials, quantity and orientation of mixing fibers which ensures durability, ductility and strength to bricks and mortar of given mineralogical compositions is a priority task.
- Homogenization of test procedures, methods and requirements for each targeted property. Simplistic identification tests in the field must be preferably substituted by laboratory tests because they are often not sufficient to determine exhaustive information of fundamental properties for adobe. Standard methods can be adapted from codes for modern building materials for masonry applications. Furthermore, for each property, acceptable ranges of values or minimum requirements should be carefully defined to ensure prescribed levels of safety. These values should concern the properties in strength and deformation of the brick as well as the physical properties of the mixture. Given the site dependency inherent to soil selection, prescriptions are expected in terms of ranges for the soil distribution properties and in terms of strict minimum requirements for cohesion, durability and plasticity properties. At a research level, new building production and construction processes capable of removing randomness in the manual production of adobe bricks can help to ensure safety in contexts of scarcity.

4. References

- [1] Transitieteam Bouw, "Circulaire Bouweconomie," p. 38, 2018.
- [2] J. Reis, "Fracture and flexural characterization of natural fiber-reinforced polymer concrete," *Constr. Build. Mater.*, vol. 20, no. 9, 2006.

- [3] A. Heath, P. Walker, C. Fourie, and M. Lawrence, "Compressive strength of extruded unfired clay masonry units," *Proc. Inst. Civ. Eng. Constr. Mater.* 162 3, vol. 162, no. 3, pp. 105–112, 2009.
- [4] R. Coffman, N. Agnew, G. Austin, and E. Doehne, "Adobe mineralogy: characterization of adobes from around the world," *6th Int. Conf. Conserv. Earthen Archit. Las Cruces, New Mex. U.S.A., Oct. 14-19, 1990*, vol. 1, no. May, pp. 424–429, 1990.
- [5] G. Minke, "Building with earth: Design and Technology of a sustainable architecture," *Birkhauser*, 2009.
- [6] D. Silveira and et al., "Mechanical properties of adobe bricks in ancient constructions," *Constr. Build. Mater.*, vol. 28, no. 1, pp. 36–44, 2012.
- [7] "Centre de recherche et d'application en terre <http://craterre.org/>."
- [8] G. R. Wekerle and P. S. B. Jackson, "Urbanizing the security agenda," *City*, vol. 9, no. 1, pp. 33–49, 2005.
- [9] "DIN 18952: Methods of test for earth (1956), 2008."
- [10] "Lehmbau Regeln. Begriffe; Baustoffe; Bauteile. Braunschweig/Wiesbaden, Germany: Friedr. Vieweg & Sohn Verlagsgesellschaft mbH, 1999."
- [11] NZS 4298, "NZS 4298 (1998): Materials and workmanship for earth buildings," *New Zeal. Tech. Committee*, vol. 4298, p. 91, 1998.
- [12] HB 195 - 2002 *The Australian earth building handbook-Standards Australia International, NSW 2001*. 2001.
- [13] *New Mexico Earthen Building Materials Code - Title 14, Chapter 7 (Part 4), 2004*. New Mexico.
- [14] *Sencico Norma Tecnica Edificacion, NTE E 0.8 Adobe, 2000*. .
- [15] "California Code of Regulations for Adobe in New Constructions, Title 24, Part 10." 2011.
- [16] M. Larcher *et al.*, "Dynamic Increase Factor of Masonry Materials: Experimental Investigations," in *ISIEMS, International Symposium for the Interaction of Munitions with Structures*, 2013, p. 10.
- [17] H. Varum, A. Costa, D. Silveira, H. Pereira, J. Almeida, and T. Martins, "Structural Behaviour Assessment and Material Characterization of Traditional Adobe Constructions," *AdobeUSA 2007, El Rito, NM, USA* , no. January, 2007.
- [18] R. Illampas, I. Ioannou, and D. C. Charmpis, "Adobe bricks under compression : Experimental investigation and derivation of stress – strain equation," *Constr. Build. Mater.*, vol. 53, pp. 83–90, 2014.
- [19] S. Yetgin, O. Cavdar, and A. Cavdar, "The effects of the fiber contents on the mechanic properties of the adobes," *Constr. Build. Mater.*, vol. 22, no. 222–227, 2006.
- [20] T. Li Piani, D. Krabbenborg, J. Weerheijm, L. Koene, and L. J. Sluys, "The Mechanical Performance of Traditional Adobe Masonry Components: An experimental-analytical characterization of soil bricks and mud mortar," *J. green Build.*, vol. 13, no. 3, pp. 17–44, 2018.
- [21] T. Li Piani, J. Weerheijm, M. Peroni, L. Koene, G. Solomos, and L. J. Sluys, "Dynamic Characterization of Adobe in compression: The effect of fibres with soil binders," in *FraMCoS-X : Fracture Mechanics of Concrete and Concrete Structures*, 2019.

- [22] T. Li Piani, J. Weerheijm, L. Koene, and L. J. Sluys, "The Adobe delta damage model: A locally regularized rate-dependent model for the static assessment of soil masonry bricks and mortar," *Eng. Fract. Mech.*, vol. 206, pp. 114–130, 2019.
- [23] T. Li Piani, J. Weerheijm, and L. J. Sluys, "Ballistic model for the prediction of penetration depth and residual velocity in Adobe: A new interpretation of the ballistic resistance of earthen masonry," *Def. Technol.*, vol. 14, no. 5, pp. 4–8, 2018.
- [24] H. Houben and H. Guillaud, *Earth construction: a comprehensive guide*. ITDG Publishing, 1994.
- [25] E. W. Smith, "Adobe bricks in New Mexico, Circular 188, New Mexico Bureau of Mines and Mineral Resources." p. 89, 1982.
- [26] G. S. Austin, "Adobe as a building material," *New Mex. Bur. Mines Miner. Resour. Socorro*, pp. 69–71, 1984.
- [27] E. Quagliarini, S. Lenci, and M. Iorio, "Mechanical properties of adobe walls in a Roman Republican domus at Suasa," *J. Cult. Herit.*, vol. 11, no. 2, pp. 130–137, 2010.
- [28] A. Caporale, F. Parisi, D. Asprone, R. Luciano, and A. Prota, "Comparative micromechanical assessment of adobe and clay brick masonry assemblages based on experimental data sets," *Compos. Struct.*, vol. 120, pp. 208–220, 2015.
- [29] E. Quagliarini and S. Lenci, "The influence of natural stabilizers and natural fibres on the mechanical properties of ancient Roman adobe bricks," *J. Cult. Herit.*, vol. 11, no. 3, pp. 309–314, 2010.
- [30] A. A. Hammond, "Prolonging the life of earth buildings in the tropics," *Build. Res. Pract.*, vol. 1, no. 3, pp. 154–163, 1973.
- [31] *BS 1377-2: 1990, Methods of test for soils for civil engineering purposes, Classification tests.* .
- [32] *UNI EN 772-1:2015 "Test Methods for masonry elements". Title 1: Determination of compressive strength".* .
- [33] "UNI EN 12390-5: "Tests on hardened concrete. Title 5: Bending tests on concrete specimens", 2009."
- [34] A. Agarwal, "Mud as a Traditional Building Material," *Chang. Rural Habitat; Ed. by Brian Brace Taylor. Singapore Concept Media/ Aga Khan Award Archit.*, vol. 1, pp. 137–146, 1975.
- [35] R. Aguilar, M. Montesinos, and S. Uceda, "Mechanical characterization of the structural components of Pre-Columbian earthen monuments: Analysis of bricks and mortar from Huaca de la Luna in Peru," *Case Stud. Constr. Mater.*, vol. 6, pp. 16–28, 2017.
- [36] T. Li Piani, L. Koene, J. Weerheijm, and L. J. Sluys, "The Ballistic Performance of Adobe Masonry: An analytical model for penetration in soil bricks and mortar," in *International Symposium on Ballistics Impacts on Structures (17th ISIEMS)*, 2017.
- [37] "ASTM C42: Standard Test Method for Obtaining and Testing Drilled Cores and Sawed Beams of Concrete."
- [38] D. Silveira, H. Varum, and A. Costa, "Influence of the testing procedures in the mechanical characterization of adobe bricks," *Constr. Build. Mater.*, vol. 40, no. March, pp. 719–728, 2013.
- [39] Ş. Yetgin, Ö. Çavdar, and A. Çavdar, "The effects of the fiber contents on the mechanic properties

of the adobes,” *Constr. Build. Mater.*, vol. 22, no. 3, pp. 222–227, 2008.

[40] A. Caporale, F. Parisi, D. Asprone, R. Luciano, and A. Prota, “Critical surfaces for adobe masonry: Micromechanical approach,” *Compos. Part B Eng.*, vol. 56, no. January, pp. 790–796, 2014.

[41] J. Ingham, D. Biggs, and L. R., “Uniaxial Compressive Strength and Stiffness of Field-Extracted and Laboratory-Constructed Masonry Prisms,” *J. Mater. Civ. Eng.*, vol. 26, no. 4, pp. 567–575, 2014.

[42] Popovics, “A numerical approach to the complete stress strain curve of concrete,” *Cem. Concr. Res.*, vol. 3, pp. 583–599, 1973.

[43] T. Li Piani, J. Weerheijm, L. Koene, and L. J. Sluys, “Modelling the mechanical response of Adobe components under uniaxial loadings,” in *European Conference on Computational Mechanics (ECCM 6)*, 2018.

[44] P. H. Bischoff and S. H. Perry, “Compressive behaviour of concrete at high strain rates,” *Mater. Struct.*, vol. 24, no. 6, pp. 425–450, 1991.

[45] T. Li Piani, J. Weerheijm, L. Koene, and L. J. Sluys, “Modelling the Mechanical Response of Adobe Components under Uniaxial Loading,” *Key Eng. Mater.*, vol. 774, pp. 650–657, 2018.

[46] “RILEM TC 162-TDF: Test and design methods for steel fibre reinforced concrete. Sigma-epsilon design method. Final Recommendation,” 2003.

Microstructural changes in porosity due to carbonation of fly ash blended pastes assessed by dynamic vapour sorption

Y. Villagrán-Zaccardi ^{1,2}, N. Alderete ¹, N. De Belie ¹

¹ Magnel Laboratory for Concrete Research, Department of Structural Engineering, Faculty of Engineering and Architecture, Ghent University, Tech Lane Ghent Science Park, Campus A, Technologiepark Zwijnaarde 60, B-9052 Ghent, Belgium

² LEMIT, CONICET, 52 entre 121 y 122 s/n, 1900 La Plata, Argentina

Abstract

Blended cement pastes are usually reported to carbonate faster than ordinary Portland cement (OPC) pastes due to the reduced portlandite content caused by the pozzolanic action. Moreover, the effect of carbonation on the pore structure of hydrated cement paste may be variable depending on the binder. On the one hand, calcium carbonate precipitates and clogs the pore network. On the other hand, decalcification of C-S-H may cause shrinkage, and potentially microcracking that increases pore connectivity. When fly ash is included in the system, the situation becomes quite different from ordinary Portland cement paste. As the pozzolanic reaction consumes portlandite, carbonation is more likely to progress by decalcifying C-S-H. Blended cement pastes are therefore more susceptible to microstructural changes due to carbonation. In this paper, we assessed the overall effect of carbonation on the porosity of well-cured fly ash blended cement paste by dynamic vapour sorption (DVS). This technique allows determining the pore structure from the quantification of water uptake by condensation of water vapour at different relative humidities. The Barrett, Joyner and Halenda (BJH) method, based on the Kelvin model, was applied for computing the volume of mesopores (0.002-0.05 μm). The Dubinin–Radushkevich (DR) equation was used to calculate the volume of micropores ($<0.002 \mu\text{m}$). Samples with 20, 30, and 40% replacement ratios of OPC by fly ash were prepared and cured for one year before carbonating them in an accelerated chamber with 1% CO_2 . Despite the advanced age of the pastes, considerable reductions due to carbonation in the volume of mesopores and micropores were registered.

Keywords: fly ash, carbonation, porosity, DVS

1. Introduction

The dynamic vapour sorption (DVS) test helps in the description of the pore structure of cementitious materials by measuring the equilibrium between the mass water content of the sample and the relative humidity (RH), at a constant temperature. Water molecules are relatively smaller than those of gases CO_2 or N_2 [1], and this advantage allows water molecules to penetrate smaller pores and ink-bottle pores as well. Also, it is very convenient that no degassing process of the sample prior to the measurements is necessary, hence possible microstructural damage is avoided. Furthermore, the test can be performed at room temperature, which is a practical and realistic approach for most applications. The sorption isotherms obtained from the test are used afterwards to calculate specific surface area and pore size distributions (PSDs) of samples.

The most applied theories of adsorption that mathematically describe the results are the Barrett, Joyner and Halenda (BJH) method [2] for the calculation of the pore size distribution in the mesopore range, and the Dubinin–Radushkevich (DR) equation [3] for the calculation of the pore size distribution in the micropore range. These models include a number of simplifications that should be considered. For instance, for the computation of the specific surface, a monolayer of adsorbate is assumed to be uniformly distributed on pore walls, but this surface is never completely covered until the saturated vapour pressure is reached [4]. Another important aspect is that calculations of the pore size distribution consider cylindrical pore shapes for the distribution [2].

Changes in pore structure of carbonating blended cementitious mixes occur over time and in relation to the reaction degree of the supplementary cementitious material and the affectation of hydration products by their reaction with carbon dioxide. Even developing at a relatively slow pace, when fly ash is added to concrete there is normally an improvement in durability-related properties of the cementitious material [5-8]. Nevertheless, the carbonation of fly ash blended mixes has particular implications. The consumption of calcium hydroxide by the pozzolanic reaction of the fly ash and the dilution effect of the portland cement reduce the alkaline reserve of the material that offers resistance to carbonation. As a result, the carbonation front progresses more rapidly than in unblended mixes with the same porosity. Moreover, the relative amounts of calcium hydroxide and C-S-H suffering carbonation are modified with the inclusion of fly ash [9-10], and the effect of carbonation on porosity differs from the case of plain Portland cement pastes. Whereas carbonation of calcium hydroxide partially contributes in clogging the pore structure, carbonation of C-S-H causes the opposite effect when increasing porosity.

Previous studies have dealt with the effect of carbonation on the pore structure of fly ash blended cement pastes. Techniques such as mercury intrusion porosimetry, scanning electron microscopy and the X-ray attenuation method have been applied for describing the changes in the microstructure. These techniques are effective in describing the total porosity, but they are imperfect for connecting these changes to different pore size ranges due to the potential affectation of the microstructure caused by the procedure or the preconditioning required. Results from DVS tests can complement previous descriptions of carbonated fly ash blended paste, in relation to the particular capabilities of the method, which requires no preconditioning.

2. Methodology

2.1 Materials

The mineralogical and chemical compositions, and particle size distribution of the Class F fly ash and ordinary Portland cement (OPC, CEM I, 42.5 N) used in this study are presented in Tables 1, 2 and 3, respectively. The mineralogical compositions were determined by Rietveld analysis of the X-ray diffraction patterns. These analyses were performed by adding 10% w/w of internal standard (zincite) to apply the PONKCS method and determine the content of amorphous phases as well. The particle size distributions were measured by laser diffractometry. The values of the refractive/absorption indexes considered in this analysis were 1.73/0.1 and 1.56/1 for the OPC and fly ash, respectively.

Pastes were prepared with 20, 30, and 40 % w/w replacement ratios of OPC by fly ash. The water to binder was 0.40 in all cases. These samples were cured in a conditioned room at $(20 \pm 2) ^\circ\text{C}$ and $(95 \pm 5) \% \text{RH}$ for 360 days for assuring nearly the maximum possible reaction degree of the fly ash.

Table 1. Mineralogical composition of the fly ash and OPC, determined by XRD/Rietveld analysis (and PONKCS method for the amorphous content) (%).

Material	C ₃ S	C ₂ S	C ₃ A	C ₄ AF	Gypsum	Quartz	Magnetite	Calcite	Amorphous
OPC	60.2	22.0	10.8	2.7	4.2	nd	nd	0.04	nd
Fly ash	nd	nd	nd	nd	nd	5.9	1.2	nd	91.9

nd = not determined

Table 2. XRF chemical compositions of raw materials (%).

Material	Na ₂ O	MgO	Al ₂ O ₃	SiO ₂	SO ₃	K ₂ O	CaO	Fe ₂ O ₃	Free CaO
OPC	0.27	0.95	4.91	20.74	2.96	0.77	64.67	1.52	0.2
Fly ash	1.08	1.92	23.50	54.19	0.94	3.38	3.02	7.92	0.1

Table 3. Particle size distribution of OPC and fly ash (μm).

Material	d10	d50	d90
OPC	3.1	16.3	57.9
Fly ash	2.1	15.0	89.3

2.2 Methods

After the curing period, samples were ground and sieved between 500–1000 μm. This range of particle size for the samples was considered as a good compromise between DVS test duration and practicality [11]. Portions of the samples were immediately conditioned by removing free water by solvent exchange with isopropanol for 15 min and dried under vacuum afterwards. Then, approximately 5 mg was tested for DVS. The device was set at 20 °C, with a $dm/dt < 0.002$ wt. %/min as a detection limit to continue to the following RH level. The RH levels at which samples were subsequently equilibrated included 5-10-20-30-40-50-60-70-80-90-98 % RH. Since these samples were predried under vacuum, they were first increasingly tested for adsorption up to 98 % RH and then a complete desorption process was performed. Other portions of the samples were put in a carbonation chamber (60 % RH, 1 % CO₂) for six weeks to allow them to carbonate. Afterwards, small fractions of the samples were crushed and sprayed with phenolphthalein solution to confirm full carbonation by no colour change. Then, portions of the samples were conditioned and tested for DVS with the previously described set-up. Each DVS test demanded approximately 7 days to be completed.

The BJH method [2] was used for the calculation of the pore size distribution in the mesopore range (0.002-0.05 μm [12]). This method, based on the Kelvin model, considers that capillary and adsorbed water phases exist in cylindrical pores and calculations of the pore size distribution are made by step-by-step iterative calculations [1]. The DR equation [3] was used to calculate the pore size distribution in the micropore range (<0.002μm). The method is based on the assumptions of a change in potential energy between the gas and adsorbed phases.

3. Results and discussion

Figure 1 presents the DVS isotherms. Carbonated pastes are drawn with dashed lines, and uncarbonated pastes are drawn with continuous lines. Small increases in the mass water contents for each RH are noted as the content of fly ash increases. This effect of fly ash is showing an increased overall porosity due to a dilution effect of the OPC [5]. An exception should be made for 20 and 30 % uncarbonated samples, as between these two the paste with the 30 % fly ash content showed the lowest water content. However, the difference between these two series is very small, and it can be therefore considered within the variability of the test. In general, a significant variation in the desorption branches between 40 and 30 % RH is observed.

This change is produced near the RH generally considered key for separating free water from interlayer water [1]. The device required a much more extended stabilization period during the step from 40 to 30 % RH, and a steeper desorption curve is presented in this particular range. Further analyses for this situation are possible, but they have no implications for the comparative study aimed in this work. More significant hysteresis is also noted for uncarbonated samples. Hysteresis commonly points at the presence of ink-bottle effects, and the observed attenuation suggests a reduction in the tortuosity caused by an increased accessibility of all pores when samples are carbonated.

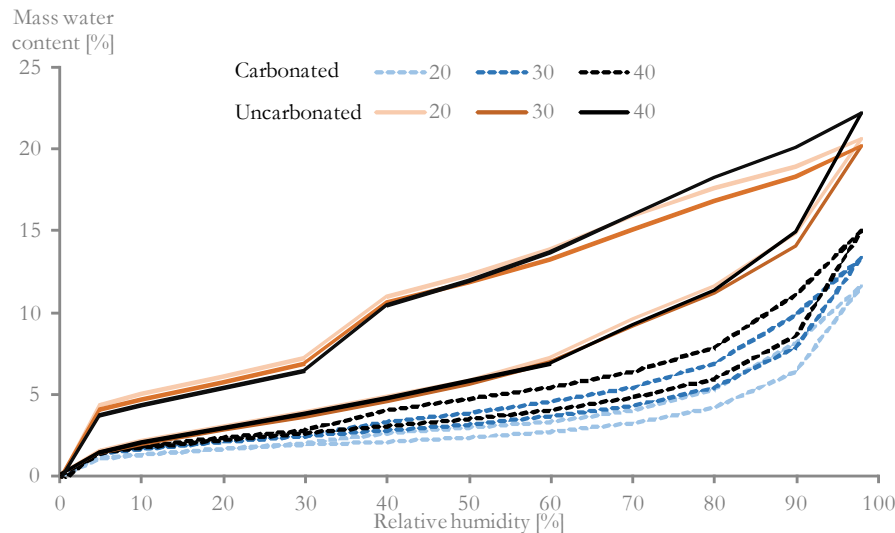


Figure 1: Sorption isotherms of the samples.

Figure 2 presents the pore volume and pore specific surface area of samples calculated from the DVS isotherms data. The replacement ratio of OPC by fly ash did not cause significant differences in the micro and meso pore volumes or the specific surface area of the pore structure. The long curing period promoted a reaction degree very close to the maximum possible in the mixes, and compared to the 20% paste, the higher dilution effect in the 40% paste seems to be compensated by the reaction of the fly ash. In this case, uncarbonated 40% paste must have had a significantly lower content of calcium hydroxide than the 30 and 20% pastes, and this is certainly defining the effect of carbonation on the pore structure depending on the replacement ratio. Accelerated carbonation produced a notorious decrease in the volume of micro and meso pores in the mixtures. The decrease is smaller with a higher replacement ratio, showing the connection between the pore volume reduction due to carbonation and the initial content of calcium hydroxide in the samples. Several authors [13-16] have indicated that carbonation of calcium hydroxide contributes to the clogging of the pore structure, whereas carbonation of C-S-H produces a detrimental effect instead. In relative terms, similar reductions due to carbonation were found for the mesopore and micropore size ranges. Accelerated carbonation also caused the specific surface to decrease. The relative reduction due to carbonation in the specific surface area is greater than the reduction in pore volume. However the number of tests is insufficient and this outcome requires to be confirmed by additional testing, this indication is also in agreement with the reduced hysteresis. When the comparative analysis is made on the basis of the same porosity, a slight coarsening of the pore structure caused by carbonation is suggested by the decreased pore specific surface area. Overall, the relative pore size distribution seems to remain the same, so the effect of carbonation would be homogeneous over the whole pore size range. The suggested coarsening might be explained by microcracking, which typically has a totally different structure than innate porosity. As during carbonation the previous consumption of portlandite by the fly ash promotes decalcification of C-S-H, the microcracking may be associated to 'carbonation shrinkage'. Additional results from other experimental techniques would be valuable for assessing the complete pore size range in the pastes (i.e. covering also

larger pores) and confirming this hypothesis.

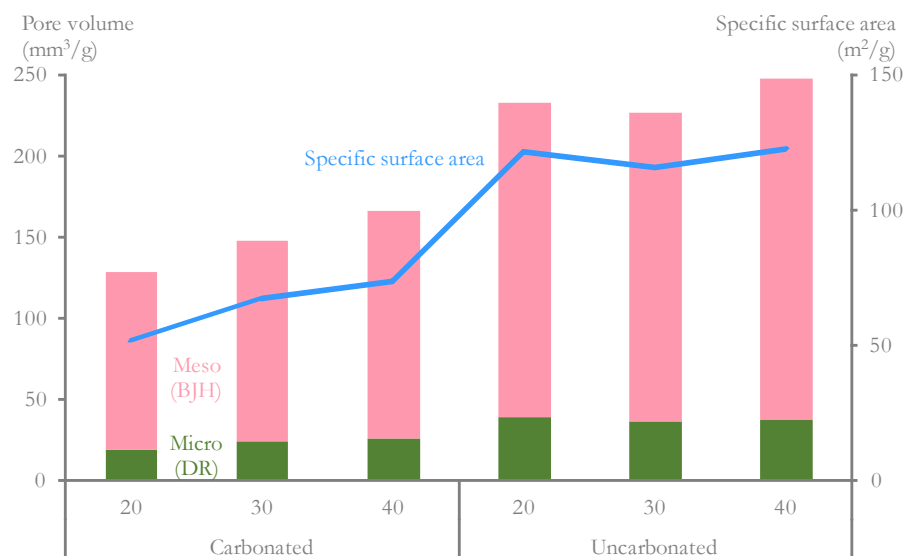


Figure 2: Computed pore volume and specific surface area.

The results in the present study differ from the findings from Wu and Ye [9], where increased porosity in fly ash blended pastes was registered by mercury intrusion porosimetry, and Cui et al [17], where similar results were found by the extended X-ray attenuation method (XRAM), for fly ash contents of 30, 50 % or higher. These studies attributed the increase in porosity to carbonation of C-S-H, which is probably enhanced when they apply accelerated carbonation at 3 % CO₂. In agreement, a previous study considering accelerated carbonation at 10 % CO₂ [18] also found a decrease in capillary porosity due to carbonation with 35 and 50 % fly ash, whereas an increase in capillary porosity was detected for 67 % fly ash. In the present study the CO₂ concentration was only one-third and one-tenth of the values in previous works (i.e., a closer value to natural exposure), and clogging of the pore structure seems to be the main effect. Moreover, no high fly ash contents were included in the present study, so our analysis is limited to 40 % fly ash at the most, and it is possible that the situation is different for higher fly ash contents. For example, Shah et al [19] suggest that reductions in porosity are to be expected whenever high replacement ratios, with a consequent full consumption of portlandite, are applied. Conversely, with replacement ratios of up to 40 %, Chindaprasirt and Rukzon [20] found similar results to those presented in the present work. It is therefore clear that significant attention should be put on the replacement ratio and the CO₂ concentration when assessing the impact of carbonation on fly ash blended paste.

4. Conclusions

- A small increase in porosity was measured in fly ash blended pastes, in connection with a dilution effect due to a limited reactivity of the fly ash, even after 1 year of curing.
- Significant reductions in the volumes of micro and mesopores due to accelerated carbonation (1 % CO₂) of fly ash blended cement pastes were detected by dynamic vapour sorption tests. This reduction was registered for replacement ratios between 20 and 40 % w/w of OPC by fly ash.
- The reduction in the pore specific surface area of fly ash blended pastes due to the carbonation seems more significant in relative terms than the reduction in pore volume. The contrast between both parameters can be interpreted as a suggestion of a slight coarsening of the meso/micro pore structure due to carbonation, probably due to the development of carbonation shrinkage caused by the reduced portlandite content as a result of the pozzolanic reaction. This hypothesis is supported by a concurrent reduction in the tortuosity of pastes due to carbonation. Confirmation studies including tests with other

techniques that assess larger pores are necessary.

5. Acknowledgement

The participation of Yury Villagrán-Zaccardi in this publication is possible thanks to partial funding received from ANPCyT through PICT 2017-0091 Prest BID.

6. References

- [1] Baroghel-Bouny V., (2007), Water vapor sorption experiments on hardened cementitious materials. Part I: Essential tool for analysis of hygral behavior and its relation to pore structure, *Cement and Concrete Research* 37, 414-437.
- [2] Barret E., Joyner L., Halenda P., (1951), The determination of pore volume and area distributions in porous substances - computations from nitrogen isotherms, *Journal of the American Chemical Society* 73, 373-380.
- [3] Dubinin M., (1975), Physical adsorption of gases and vapors in micropores, *Progress in Surface and Membrane Science* 9, 1–70.
- [4] Dollimore D., Spooner P., Turner A., (1976), The BET method of analysis of gas adsorption data and its relevance to the calculation of surface areas, *Surface Technology* 4, 121-160.
- [5] Van den Heede P., Gruyaert E., De Belie N. (2010), Transport properties of high-volume fly ash concrete: Capillary water sorption, water sorption under vacuum and gas permeability. *Cement and Concrete Composites* 32, 749–756.
- [6] Saha A. K. (2018), Effect of class F fly ash on the durability properties of concrete. *Sustainable Environment Research* 28, 25–31.
- [7] Bijen J. (1996), Benefits of slag and fly ash. *Construction and Building Materials*, 10(5), 309–314.
- [8] Chindaprasirt P., Jaturapitakkul C., Sinsiri T. (2005), Effect of fly ash fineness on compressive strength and pore size of blended cement paste. *Cement and Concrete Composites*, 27(4), 425–428.
- [9] Wu B., Ye G. (2017), Development of porosity of cement paste blended with supplementary cementitious materials after carbonation, *Construction and Building Materials* 145, 52–61.
- [10] Van den Heede P., De Schepper M., De Belie N. (2019), Accelerated and natural carbonation of concrete with high volumes of fly ash: chemical, mineralogical and microstructural effects, *Royal Society Open Science* 6, 181665.
- [11] Snoeck D., Velasco L.F., Mignon A., Van Vlierberghe S., Dubruel P., Lodewyckx P., De Belie N., (2014), The influence of different drying techniques on the water sorption properties of cement-based materials, *Cement and Concrete Research* 64, 54–62.
- [12] IUPAC (1972), Manual of symbols and terminology. Appendix 2. Pt. 1. Colloid and surface chemistry, *Pure Applied Chemistry*.
- [13] Borges P., Costa J., Milestone N., Lynsdale C., Streatfield R. (2010), Carbonation of CH and C-S-H in composite cement pastes containing high amounts of BFS, *Cement and Concrete Research* 40, 284–292.
- [14] De Belie N., Kratky J., Van Vlierberghe S. (2010), Influence of pozzolans and slag on the microstructure of partially carbonated cement paste by means of water vapour and nitrogen sorption experiments and

BET calculations, *Cement and Concrete Research* 40, 1723–1733.

[15] Gruyaert E., Van den Heede P., De Belie N. (2013), Carbonation of slag concrete: Effect of the cement replacement level and curing on the carbonation coefficient – Effect of carbonation on the pore structure, *Cement & Concrete Composites* 35, 39–48.

[16] Groves G., Rodway D., Richardson I. (1990), The carbonation of hardened cement pastes, *Advances in Cement Research* 3, 117–125.

[17] Cui D., Banthia N., Wang Q., Sun W. (2019), Investigation on porosity of partly carbonated paste specimens blended with fly ash through dual CT scans, *Construction and Building Materials* 196, 692–702.

[18] Lammertijn S. and De Belie N. (2008) Porosity, gas permeability, carbonation and their interaction in high-volume fly ash concrete, *Magazine of Concrete Research* 60 (7), 535–545.

[19] Shah V., Scrivener K., Bhattacharjee B., Bishnoi S. (2018) Changes in microstructure characteristics of cement paste on carbonation, *Cement and Concrete Research* 109, 184–197.

[20] Chindapasirt P. and Rukzon S. (2009) Pore Structure Changes of Blended Cement Pastes Containing Fly Ash, Rice Husk Ash, and Palm Oil Fuel Ash Caused by Carbonation, *Journal of Materials in Civil Engineering* 21 (11), 666–671.

Isothermal Calorimetric Study on Heat Evolution and of Apparent Activation Energy of Alkali-activated Slag/Fly ash Pastes

S. Zhang¹, Y. Zuo¹, Z. Li¹, G. Ye^{1,*}

¹Microlab, Section Materials and Environment, Faculty of Civil Engineering and Geosciences, Delft University of Technology, Stevinweg 1, 2628 CN, Delft, The Netherlands

*G.Ye@tudelft.nl

Abstract - Alkali-activated slag/fly ash (AASF), as an environmental-friendly binder system for construction materials, has recently attracted great attention from both academic and industrial communities. Towards its wider engineering application, it is crucial to have a better understanding of the temperature induced effects by different curing regimes and the temperature sensitivity on the thermal properties of this system, for instance the apparent activation energy. However, the available information on the apparent activation energy of AASF system is still quite limited.

The present study is aimed at investigating the role of alkali activator (AA) chemistry on the reaction kinetics of AASF at early age. The binder is made of 50 wt.% blast furnace slag and 50 wt.% fly ash. Four AA moduli ($\text{SiO}_2/\text{Na}_2\text{O}$ ratio = 0.8, 1.0, 1.2 and 1.5) were used for the mixture preparation. The effect of AA modulus on the heat evolution was studied by performing isothermal calorimetry test up to 160 h at ambient temperature. The total heat release was studied through curve fitting using exponential model. Furthermore, the apparent activation energy of AASF pastes was determined using incremental methods and its variation over wide range of early age reaction was studied. It was found that the AA modulus evidently influences the heat evolution of AASF. The cumulative heat release reached the maximum value at AA modulus of 1.0, followed by at 0.8, 1.2 and 1.5. This trend is well in line with the changes of the apparent activation energy of AASF mixtures. In addition, it was confirmed that the apparent activation energy of AASF was not only related to the chemistry of reactants but also reaction-stage dependent. Particularly it varied significantly at the very early age of reaction.

Keywords: Activation energy; alkali-activation; isothermal calorimetry; Slag; Fly ash

1. General introductions

Alkali activated materials (AAMs), derived by the reaction of an alkali metal source (solid or dissolved) with a solid (alumino)silicate powder [1, 2], are considered as an environmental friendly binder and one of the best alternatives for ordinary Portland cement (OPC). These materials show comparable or even better performances and less energy consumption at the same time when compared to the traditional cementitious binders. Furthermore, concrete made of alkali activated materials also provide added advantage regarding the greenhouse gas emission, i.e. an reduction of up to 80% compared with concrete made of OPC [3]. Up till now, the most intensively studied system of AAMs is based on blast furnace slag and class F fly ash. This is mainly due to their large quantity of annual production as well as their relatively stable chemical composition. Previous studies on AASF have focused on microstructure development,

nature of reaction products and mechanical properties [4-6]. However, few studies have paid attention to the heat evolution related properties especially the apparent activation energy of AASF. As an important parameter for engineering predictions and applications of AASF with regards to different temperature curing regime, the knowledge of the apparent activation energy of AASF binder system is crucial.

Compared to that within traditional cementitious systems, the data concerning the apparent activation energy of AASF is currently still scarce. Most previous results were related to alkali-activated slag (AAS). For instance, Fernandez et al [7] determined apparent activation energy to be 57.6 kJ/mol in AAS system activated by sodium hydroxide and sodium silicate. Zhou [8] studied the kinetics of hydration of AAS and the apparent activation energy was determined to be 53.63 kJ/mol. Only one work related to apparent activation energy in AASF was found [9] and the value calculated was 53.1 kJ/mol.

Therefore, this work aims to further investigate the influence of mixture parameters, especially the AA modulus, on the heat evolution and to determine the apparent activation energy of AASF systems by isothermal calorimetry testing.

2. Experimental program

2.1 Materials and mix design

The solid precursors used in this study were ground granulated blast furnace slag (GGBS) and Class F fly ash (FA) according to ASTM 618. Material density is 2890 kg/m³ for slag and 2440 kg/m³ for fly ash. The d₅₀ particle size is 17.88 µm for slag and 33.19 µm for fly ash. The chemical compositions deduced from X-ray Fluorescence along with other properties of the precursors (including LOI at 950 °C and fineness passing 45 µm) are shown in Table 1.

Table 1. Chemical compositions and properties of raw materials

Oxide (wt %)	SiO ₂	Al ₂ O ₃	Fe ₂ O ₃	CaO	MgO	SO ₃	Na ₂ O	K ₂ O	LOI	Fineness, % passing 45µm
Slag	32.91	11.84	0.46	40.96	9.23	1.60	-	0.33	1.15	95
Fly ash	52.90	26.96	6.60	4.36	1.50	0.73	0.17	-	3.37	81

As reported previously by the authors [10], the major crystalline phases in fly ash are quartz, mullite and hematite, while the blast furnace slag contains mainly amorphous phases. The reactivity of slag could be indicated by its abundant amorphous content (over 98%). On the other hand, the reactivity of fly ash is reflected by its reactive silica content of 43.04% and reactive alumina content of 15.51%. Sound mechanical properties have been achieved using both solid precursors.

To study the heat evolution of AASF, three levels of alkali activator (AA) moduli (ratio of SiO₂ wt. % / Na₂O wt. % within AA) were considered for preparation of AASF pastes with fixed binder combination of 50 wt. % blast furnace slag and 50 wt. % Class F fly ash. The detailed mixture designs are shown in Table 2. Na₂O wt. % content (in alkali activator with respect to total binder mass) was kept constant to be 4 wt. %. In addition, the water to binder (w/b) ratio was chosen to be 0.32 to maintain adequate workability for all the paste mixtures. The mixtures were named M0.8, M1.0, M1.2 and M1.5 accordingly, with the number representing the AA modulus.

Table 2 Mixture design of AASF

Mixture	Slag (wt.%)	Fly ash (wt.%)	w/b ratio	Na ₂ O (wt.%)	Modulus
M0.8	50	50	0.32	4.0	0.8
M1.0					1.0
M1.2					1.2
M1.5					1.5

The alkaline activator was prepared by dissolving NaOH pellets (analytical grade, purity ≥ 98%) and sodium silicate (Na₂O: 8.25 wt.%, SiO₂: 27.50 wt.%) in distilled water. The activator was cooled down to room temperature prior to mixture preparation.

2.2 Isothermal calorimetry

Isothermal calorimetry was conducted using a TAM-Air-314 isothermal conduction calorimeter. Calibration of the heat flow channels was carried out prior to measurements. The solid precursors were firstly hand mixed for 5 min. Afterwards, the alkaline activator solution was added and the batches were mixed for additional 2 min using a head-mixer with speed of 1600 rpm. Approximately 5g of freshly mixed paste was introduced into a small glass ampoule and was immediately loaded into the heat flow channels along with the reference ampoule. Two replicates for each mixture were measured. Heat release was recorded for a period of 160 h. For the tests carried out at 40 °C, the solid precursors, alkali activator and reference ampoules were stored in 40 °C oven before the tests. Extra caution has been paid to minimize the decrease of temperature during mixing and sample transfer.

2.3 Ultimate total heat and global reaction degree through curve fitting

The global reaction degree of AASF is also calculated using cumulative heat release data by the aid of curve fitting using exponential model shown in Equation 5.

$$Q(t) = Q_{max} \exp\left(\frac{-t}{\tau}\right)^{\beta} \quad (5)$$

where Q_{max} corresponds to the ultimate total heat at completion of reaction; τ and β are parameters associated with time and shape in the exponential model. This model along with Knudsen linear dispersion model, have been proven somewhat adequate for Q_{max} prediction and has been previously used in alkali-activated systems [11, 12], especially when the data before the induction period is neglected. Finally, the reaction degree $\alpha(t)$ could be then calculated by Equation 6

$$\alpha(t) = \frac{Q(t)}{Q_{max}} \quad (6)$$

where $\alpha(t)$ was determined for all AASF mixtures reacted under 20 °C and 40 °C for later calculation of apparent activation energy using incremental method.

2.4 Apparent activation energy determination

Arrhenius's theory as shown in Equation 1 has been proven to be an effective tool to study the temperature related effects and combined rate sensitivity of hydration reactions in cementitious systems. The Arrhenius equation is written as:

$$k(T) = A \exp\left(\frac{-E_a}{RT}\right) \quad (1)$$

where k is the temperature sensitivity rate constant, T is the absolute temperature (K). A is a constant (pre-exponential factor that varies for different chemical reaction), E_a is the activation energy (kJ/mol), R is the

universal gas constant (J/(mol.K)).

Arrhenius equation could be rewritten using two sets of rates constants at different temperature:

$$k(T_1) = k(T_2) \exp \left[\frac{-E_a}{RT} \left(\frac{1}{T_1} - \frac{1}{T_2} \right) \right] \quad (2)$$

This study used the incremental method or 'rates' method to determine the apparent activation energy E_a of AASF as has been previously used for OPC pastes [13, 14]. Assuming the calorimeter is calibrated properly, the rate constant k equals to the power of heat flow measured for a given reaction degree α and reaction temperature T :

$$k(T) = P(\alpha, T) \quad (3)$$

Therefore, in order to calculate E_a , two sets of heat flow data were used which enables calculation of E_a as a function of reaction degree α continuously.

$$E_a = R \left[\frac{T_1 T_2}{T_1 - T_2} \ln \left(\frac{P_{\alpha_0}^{T_1}}{P_{\alpha_0}^{T_2}} \right) \right] \quad (4)$$

It is worth noting that a huge simplification is made here to use E_a for the entire alkali activation and geopolymerization processes. Evidently, E_a is also sensitive to different reaction stages as the microstructure changes with elapse of time. However, considering the great difficulties to distinguish the different individual reactions within geopolymerization, E_a acquired in this way can still give further insights on temperature dependent reaction kinetics of the global reaction.

3. Results and discussions

3.1 Heat evolution and reaction degree

The heat flow curves of mixture M0.8-M1.5 under the temperature of 20 °C and 40 °C are shown in Figure 1. In general, the heat flow curve is characterized by two calorimetric peaks, The first peak is due to the wetting and dissolution of precursors particles and the second broader peak corresponds to the formation of reaction products. Compared to the heat flow at 20 °C, an evident increase of heat flow intensity could be found at 40 °C. In addition, the intensity and the time of appearance of the second peak are positively correlated and both of them change with increasing AA modulus. More specifically, with increasing AA modulus, both the intensity and time of appearance of the second peak first increase and then decline after reaching the maximum when AA modulus is 1.2. This trend indicates AA modulus has a significant influence over the early age of heat evolution, and therefore the early age reaction kinetics of AASF. It is commonly acknowledged that the early age reaction kinetics of AASF is dominated by two processes, i.e. the dissolution of Ca, Si, Al species from the solid precursor and Si oligomer dissociation presented in AA, and the geopolymerization of useful?? species to form various reaction products. Previous studies by ²⁹Si NMR and FTIR proved that higher amount of silica species with low polymerization degree (monomers) is favoured at lower AA modulus [15, 16], A lower polymerization degree of silica species can promote the gel formation. However, by lowering the AA modulus, the total amount of available species within AA is also reduced, which might have negative impact over the very early geopolymerization process. The experimental data and corresponding curve fitting using exponential model were presented in Figure 2 (a) and (b). For the calculation of total reaction heat, it is worth noting that the initial data related to the heat flow of first peak was not taken into consideration. The reason is to avoid the testing error induced during the mixing and transferring of the AASF mixtures. This is in accord with previous studies [7, 17, 18].

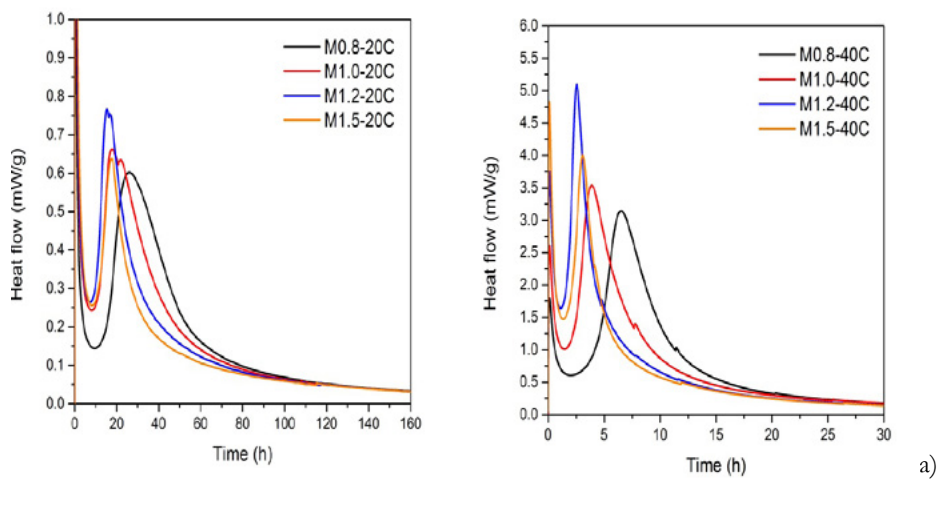


Figure 1 Heat flow of AASF mixtures at different temperature: (a) 20°C; (b) 40°C.

As expected, the cumulative heat for AASF at 40 °C were evidently higher than that at 20 °C due to the facilitating effect on reaction kinetics induced by a higher temperature. At 7d, M1.0 has the highest cumulative heat release followed by M0.8, M1.2 and M1.5. This trend is not consistent with the trend of the heat flow of the main reaction peak, which reached maximum when AA is 1.0. Therefore, it seems that a faster early age reaction is neither necessary nor sufficient for a higher reaction cumulative heat of AASF. In this study, the higher cumulative heat release of certain AA modulus could be related to the early age dissolution of species and the following-up geopolymerization process. With increasing AA modulus, the pH of AA drops [16]. Although in this way the early age dissolution is slowed down, higher AA modulus also increase the total amount of available species for geopolymerization in the liquids. Hence, an optimum activating conditions for overall reaction would exist which is favoured by its higher total heat release and higher amount of main reaction products.

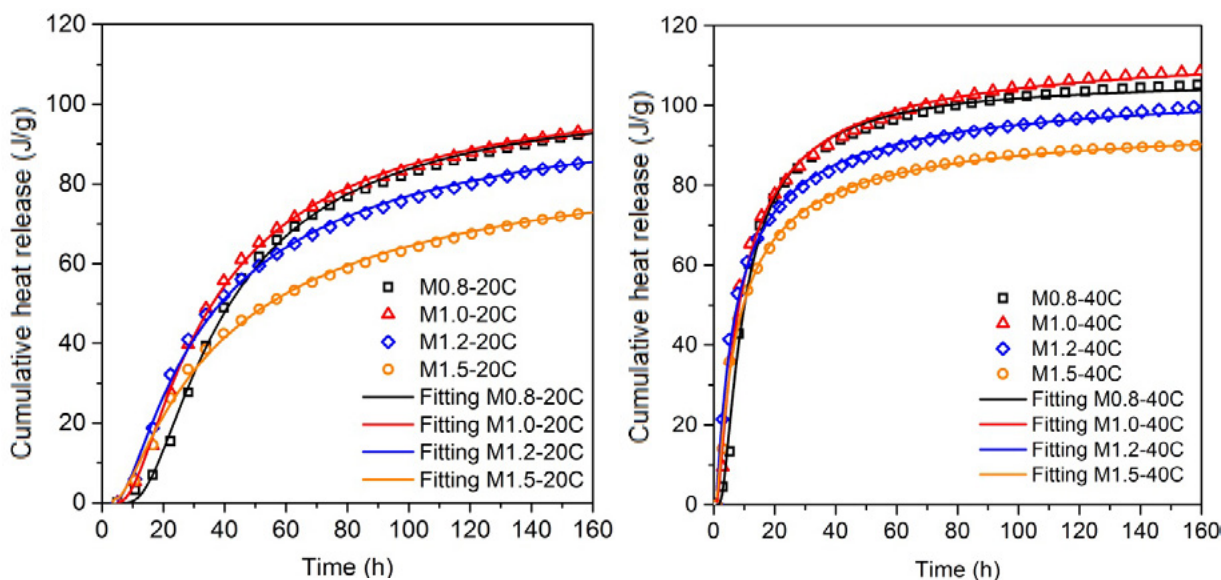


Figure 2 Cumulative heat release of AASF mixtures and curve fitting using the exponential model: (a) 20°C; (b) 40°C

The fitted parameters of exponential model for Q_{\max} are presented in Table 3. As could be seen in Table 3, the accuracy of fitting (Adjusted R-Square) is rather satisfactory, implying the effectiveness of using exponential model for total heat fitting in AASF. In addition, the Q_{\max} obtained exhibit identical trend with

increasing AA modulus when comparing with corresponding total heat release Q_{160h} of AASF up to 160h.

Table 3 Fitted parameters of exponential model for maximum total heat

Mixture		M0.8		M1.0		M1.2		M1.5	
		20 °C	40 °C	20 °C	40 °C	20 °C	40 °C	20 °C	40 °C
Total heat at 160h	Q_{160h}	92.8	105.1	93.6	108.5	85.7	99.8	73.1	89.9
	Q_{max}	103.55	106.65	107.46	114.95	103.30	106.80	94.47	97.24
Fitting parameters	τ	33.33	8.03	28.49	6.73	27.53	5.27	31.70	5.79
	β	1.41	1.22	1.14	0.86	0.95	0.73	0.84	0.78
Adjusted R-Square	r^2	0.998	0.996	0.999	0.996	0.998	0.996	0.997	0.997

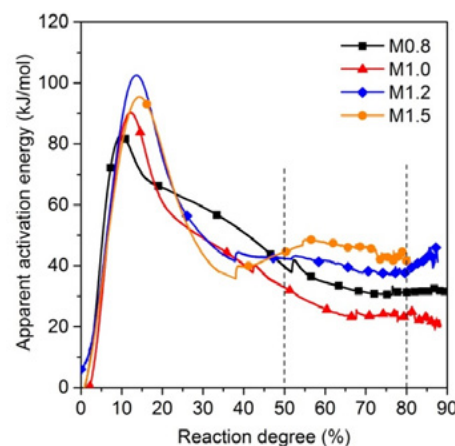


Figure 3 Apparent activation energy E_a as a function of reaction degree

According to previous studies of E_a of alkali-activated systems, comparison of related results is made and is shown in Table 4. It could be found that E_a determined in AASF is in general lower than those determined in AAS systems and close to the value determined in AASF systems. However, it is crucial to notice that by changing AA modulus, the global chemical reaction is already changed. E_a as one of its reflections, therefore, cannot be directly used to compare the chemical nature and ultimate total heat release of different AASF systems.

Table 4 Apparent activation energy E_a for different alkali-activated systems

E_a	Solid precursor	Activator (Liquids)	Reference
57.6	GGBS	NaOH+Na ₂ SiO ₃ (Na20% = 4%)	Fernandez et al [7].
53.6	GGBS	NaOH+Na ₂ SiO ₃	Zhou et al [8].
48.2 ± 2.9	GGBS	9M NaOH	Sun & Vollpracht [20]
48.2 ± 5.9	80%GGBS+20%FA	8M NaOH+Na ₂ SiO ₃	Joseph et al [9].
24.6 ~ 46.4	50%GGBS+50%FA	NaOH+Na ₂ SiO ₃ (Na20% = 4%)	Present study

4. Conclusions

The present study is aimed at investigating the role of alkali activator (AA) chemistry on the early age reaction kinetics of AASF made of 50 wt.% blast furnace slag and 50 wt.% fly ash. The effect of AA modulus on the heat evolution and cumulative reaction heat release was studied. Additionally, the apparent activation energy was determined using the incremental method and its variation over wide range of early age reaction was studied.

It was found that the AA modulus evidently influences the heat evolution of AASF. The cumulative heat release at 160h reached the maximum value at AA modulus of 1.0, followed by at 0.8, 1.2 and 1.5. This trend

is inversely related to the changes of the apparent activation energy E_a of AASF mixtures. Disagreement of the trend of early age heat flow and that of total reaction heat implies that a faster early age reaction does not necessarily result in a higher reaction total heat of AASF. The calculated E_a varies from 24.6 to 46.4 kJ/mol, which is in generally close to the values reported for GGBS based alkali activated systems. Furthermore, this study confirmed that the apparent activation energy of AASF was not only related to the chemistry of reactants but also reaction-stage dependent. Particularly it varied significantly at the very early age of reaction.

5. Acknowledgements

This research is carried out in Microlab, Delft University of Technology and supported by the Netherlands Organisation for Scientific Research (NWO), Grant No.729.001.013 and National Natural Science Foundation of China (NSFC), Grant No. 5151101050. Additionally, the second and third author would like to thank the financial support from China Scholarship Council (CSC).

7. References

1. Shi, C., D. Roy, and P. Krivenko, Alkali-activated cements and concretes. 2006: CRC press.
2. Davidovits, J., Geopolymers. *Journal of Thermal Analysis and Calorimetry*, 1991. 37(8): p. 1633-1656.
3. Duxson, P., et al., The role of inorganic polymer technology in the development of 'green concrete'. *Cement and Concrete Research*, 2007. 37(12): p. 1590-1597.
4. Ismail, I., et al., Modification of phase evolution in alkali-activated blast furnace slag by the incorporation of fly ash. *Cement and Concrete Composites*, 2014. 45: p. 125-135.
5. Puertas, F. and A. Fernández-Jiménez, Mineralogical and microstructural characterisation of alkali-activated fly ash/slag pastes. *Cement and Concrete composites*, 2003. 25(3): p. 287-292.
6. Lee, N.K. and H.K. Lee, Reactivity and reaction products of alkali-activated, fly ash/slag paste. *Construction and Building Materials*, 2015. 81: p. 303-312.
7. Fernández-Jiménez, A. and F. Puertas, Alkali-activated slag cements: kinetic studies. *Cement and concrete research*, 1997. 27(3): p. 359-368.
8. Huanhai, Z., et al., Kinetic study on hydration of alkali-activated slag. *Cement and Concrete Research*, 1993. 23(6): p. 1253-1258.
9. Joseph, S., S. Uppalapati, and O. Cizer, Instantaneous activation energy of alkali activated materials. *RILEM Technical Letters*, 2018. 3: p. 121-123.
10. Zhang, S., et al., Waste glass as partial mineral precursor in alkali-activated slag/fly ash system. *Cement and Concrete Research*, 2017. 102: p. 29-40.
11. Chithiraputhiran, S. and N. Neithalath, Isothermal reaction kinetics and temperature dependence of alkali activation of slag, fly ash and their blends. *Construction and Building Materials*, 2013. 45(0): p. 233-242.
12. Ravikumar, D. and N. Neithalath, Reaction kinetics in sodium silicate powder and liquid activated slag binders evaluated using isothermal calorimetry. *Thermochimica Acta*, 2012. 546(0): p. 32-43.
13. Poole, J.L., et al., Methods for calculating activation energy for Portland cement. *ACI Materials*

Journal, 2007. 104(1): p. 303-311.

14. Broda, M., E. Wirquin, and B. Duthoit, Conception of an isothermal calorimeter for concrete—Determination of the apparent activation energy. *Materials and Structures*, 2002. 35(7): p. 389-394.
15. Criado, M., et al., Effect of the $\text{SiO}_2/\text{Na}_2\text{O}$ ratio on the alkali activation of fly ash. Part II: ^{29}Si MAS-NMR Survey. *Microporous and Mesoporous Materials*, 2008. 109(1): p. 525-534.
16. Jansson, H., D. Bernin, and K. Ramser, Silicate species of water glass and insights for alkali-activated green cement. *Aip Advances*, 2015. 5(6): p. 067167.
17. Fernández-Jiménez, A., F. Puertas, and A. Arteaga, *Determination of kinetic equations of alkaline activation of blast furnace slag by means of calorimetric data*. *Journal of thermal analysis and calorimetry*, 1998. 52(3): p. 945-955.
18. Carette, J. and S. Staquet, Monitoring and modelling the early age and hardening behaviour of eco-concrete through continuous non-destructive measurements: Part I. Hydration and apparent activation energy. *Cement and Concrete Composites*, 2016. 73: p. 10-18.
19. Kada-Benameur, H., E. Wirquin, and B. Duthoit, Determination of apparent activation energy of concrete by isothermal calorimetry. *Cement and concrete research*, 2000. 30(2): p. 301-305.
20. Sun, Z. and A. Vollpracht, Isothermal calorimetry and in-situ XRD study of the NaOH activated fly ash, metakaolin and slag. *Cement and Concrete Research*, 2018. 103: p. 110-122.

Uncovering strength developing regularities of ultra-high performance concrete cured under high temperature

Z. Liu^{1,3}, Z. Shui¹, R. Yu^{1*}, Q. Song^{1,2}

¹State Key Laboratory of Silicate Materials for Architectures, Wuhan University of Technology, Wuhan 430070, China;

²School of Materials Science and Engineering, Wuhan University of Technology, Wuhan 430070, China.

³International School of Materials Science and Engineering, Wuhan University of Technology, Wuhan 430070, China

Abstract

Early studies suggested that fly ash has low volcanic ash activity and is an inert material in the early stage of hydration. It only acts as a filling agent and does not react with other substances. In fact, the activity of volcanic ash depends on factors such as the volcanic ash activity of the fly ash and the maintenance system. In addition to its pozzolanic activity, fly ash can also act as a micro-aggregate in the slurry to improve the microstructure and macroscopic properties of UHPC. To study the influence of different curing conditions on the mechanical properties of UHPC replacing parts of cement with fly ash, the current work replaced 20% of the cement content for fly ash to obtain a UHPC sample. The compressive strength, flexural strength and pore structure of Ultra High Performance Concrete under steam curing and hot water curing conditions were studied. The results of strength test reveal that the compressive strength can be improved by heated curing, especially hot water curing, which allowed the highest strength to reach 139 MPa after 48 hours. The results of the pore structure indicate that the cumulative pore volume of UHPC decreases with increasing curing time. And the cumulative pore size of hot water curing is lower than that of steam curing.

Keywords: Ultra-High Performance Concrete(UHPC), Fly ash, Curing system, pore structure

1. Introduction

In 1994, Larrard applied the concept of high packing density to concrete technology and first proposed the concept of Ultra-high Performance Concrete (UHPC) [1]. UHPC is defined as a cementitious composite with a compressive strength of more than 150 MPa and good ductility and durability[2, 3]. Typical UHPC includes very high levels of cement, silica fume, quartz powder, quartz sand, steel fibers and superplasticizers [4]. UHPC is characterized by extremely low porosity and extremely high bulk density. It is because UHPC contains a great quantity of particles with low diameter and extremely low W/B[5]. Due to the addition of fibers, UHPC has a flexural strength of 15 MPa and an elastic modulus of 45 GPa [6]. At the International Conference on Ultra-High Performance Fiber Reinforced Concrete (UHPRFC) held in Marseille, France in 2009, the experts hold that UHPRFC is low-carbon, environmentally friendly and has excellent performance. It can be used to build low-carbon concretes structures and will be developed in the future.

As various mineral admixtures are increasingly used in cement-based materials, fly ash has also begun to be used in the preparation of UHPC. Ultra-high performance concrete with different content of fly ash has

different degrees of mechanical strength improvement, and reduces the porosity of UHPC samples and the content of calcium hydroxide in uhpc samples[7]. Therefore, the use of cement-fly ash-silica ash as a cementitious material for the preparation of UHPC has become more common.

The macro performance and microstructure of UHPC are closely related to the maintenance system. The best curing technique for UHPC was found to be heat curing[8]. Thermal curing can significantly promote cement hydration and pozzolanic reactions, thereby improving the mechanical properties of UHPC. Different curing conditions and curing time will also affect the performance of UHPC[9].

Based on this, the mechanical properties of UHPC for 95C steam curing and 95C hot water curing were studied. First, the modified Andersen & Andreasen model [10, 11] was used to obtain a densely packed concrete skeleton. Then, the properties of the UHPC cured at different systems are evaluated.

2. Methodology

2.1 Materials

In this study, the cementitious materials are Portland cement type 2 (52.5), fly ash and silica fume, and their chemical compositions are evaluated by X-ray fluorescence (XRF) as shown in Table 1. Fine aggregates are natural river sand with particle size of 0-0.6mm and apparent density of 2.6g/cm³. A polycarboxylic ether-based superplasticizer is used to adjust the workability of the UHPC.

Table 1: The chemical composition of cementitious materials(%)

Compound	Na ₂ O	MgO	Al ₂ O ₃	SiO ₂	P ₂ O ₅	SO ₃	K ₂ O	CaO	Fe ₂ O ₃	LOI
Cement	0.09	1.61	4.18	19.2	0.09	3.35	0.78	64.93	3.32	2.49
SF	0.13	0.47	0.25	94.65	0.17	0.69	0.84	0.36	0.15	2.29
FA	0.33	0.23	38.01	46.44	0.06	0.69	0.88	7.5	3.12	2.79

2.2 Methods

2.2.1 Mix design of UHPC

In this study, the modified Andreasen and Andersen model[10, 11] is used to design a dense particle packing skeleton, to improving the overall performance of the UHPC. The modified A & A model acts as a target function, as show in Eq.(1)

$$P(D) = \frac{D^q - D_{min}^q}{D_{max}^q - D_{min}^q}$$

Where $P(D)$ represents the percentage of particles smaller than size D to the total, D is the particle size (μm), D_{max} means the maximum particle size(μm); D_{min} means the minimum particle size(μm) and q is dispersion coefficient. In this study, the q value is fixed at 0.23.

By adjusting the composition of the raw materials, the optimized grading curve is approximated to the target curve calculated by the modified A & A model. In addition, the recipe of designed UHPC is shown in Table 2 and the particle size distributions of the ingredients, target and optimized grading curves of UHPC mixtures are shown in Figure 1.

Table 2: Recipe of the designed UHPC (kg/m³).

	C	FA	SF	Sand	Water	Sp
UHPC	660	200	188	990	195	34

(C: Cement, FA: Fly Ash, SF: Silica Fume, Sand: ϕ :0-0.6 mm; Sp: superplasticizer, solid content=18.2%).

2.2.2 Casting and Curing

First, add powder materials such as cement, silica fume, fly ash and sand to the mixer for 1 min. Second,

mix 90% of the water and superplasticizer and add to the mixer to stir at low speed until it is slurried. Third, add the remaining water and stir at high speed for 2 minutes to mix well. Last, Stir at low speed for 1 min to make the bubbles slowly dispatched. The fresh UHPC was cast in the moulds with the size of 40mm*40mm*160mm and were vibrated on the shaking table for 4 min[12].

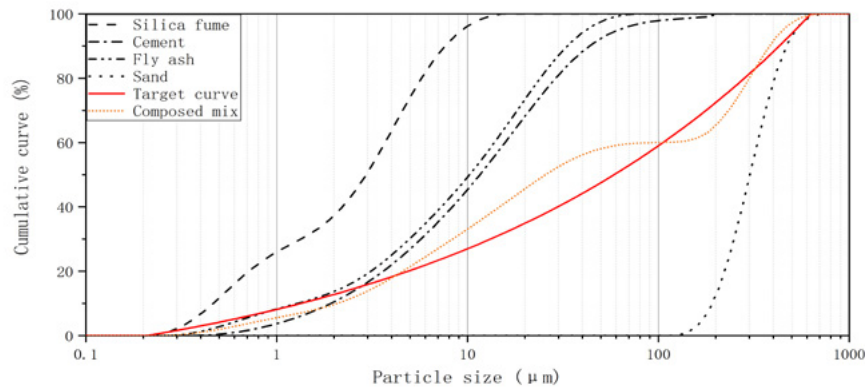


Figure 1: Particle size distributions of the ingredients, target and optimized grading curves of UHPC mixtures.

After 20 hours of standard curing in the curing room, the moulds were removed for hot water curing and steam curing respectively. The curing box heats up at a rate of 10℃ per hour. When temperature reaches 95℃, the timing starts.

2.2.3 Mechanical properties

After high temperature for 6, 12, 18, 24, 48, 72, 96 and 120 hours, the compressive strength of the specimens are tested according to Chinese standards GB17671-1999. At least three specimens are tested for each batch.

2.2.4 Pore structure analysis

The pore structure (total porosity and pore size distribution) of the UHPC is measured by a micromeritics mercury porosimeter (named AutoPore IV-9500, pore size range: 3 nm-360 μm). Specimen is soaked in acetone firstly, and then dried in a vacuum atmosphere at 65 ± 2 °C for 4 h[13].

2.2.5 Hydration heat test

The hydration heat test was carried out using a TAM Air eight-channel isothermal microcalorimeter. The hydration heat test was carried out using a mortar having the same water-cement ratio (water-cement ratio = 0.21) as the concrete, and the quality of the test sample was determined according to the same total specific heat capacity as the inert reference sample. In this test, water was used as a reference sample, and the specific heat capacity of water was 4.2×10^3 J/(kg·°C).

3. Results and discussion

3.1 Mechanical properties

Figure 2 and figure 3 shows the test results of UHPC compressive and flexible strength under different curing systems and different time. As can be seen from the figure, after steam curing at 95 °C or hot water curing at 95 °C for 48h, the compressive strength reaches 136MPa and 139MPa respectively. The flexible strength reached the highest after 18h of curing. We can also find that whether cured at steam or cured at hot water 24 h can be considered to be a stage boundary. In the earlier stage(0-24h), the compressive strength and flexible strength of UHPC is growing quickly. In the later stage(24-120h), there was no significant increase of the strength of UHPC. The strength of hot water curing is slightly higher

than that of steam curing.

The above phenomenon may be caused by changes in the microstructure of the concrete. In the earlier stage, as the hydration reaction proceeds rapidly, the hydration products continue to increase, the capillary pores continue to decrease, and the compressive strength and flexural strength increase rapidly. In the later stage, as the hydration proceeds further, the newly formed hydration product exceeds the volume of the capillary pores, and the micro-cracks in the concrete continuously generate and disappear. The strength is generally unchanged, but exhibits fluctuations[14-16]. The strength of the test piece for hot water curing is slightly higher than that of the same age test piece for steam curing[8, 17, 18]. This may be due to the difference between steaming and hot water curing heat transfer media, which are condensed water and hot water, respectively.

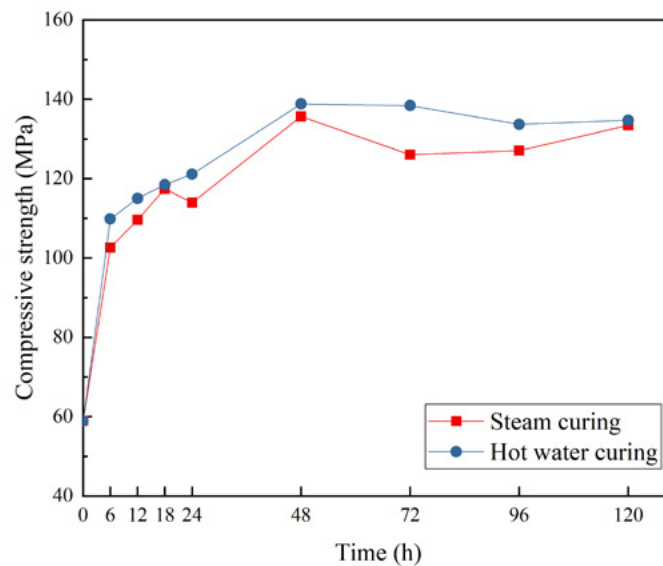


Figure 2: Compressive strength of UHPC cured at different systems (Steam curing, Hot water curing)

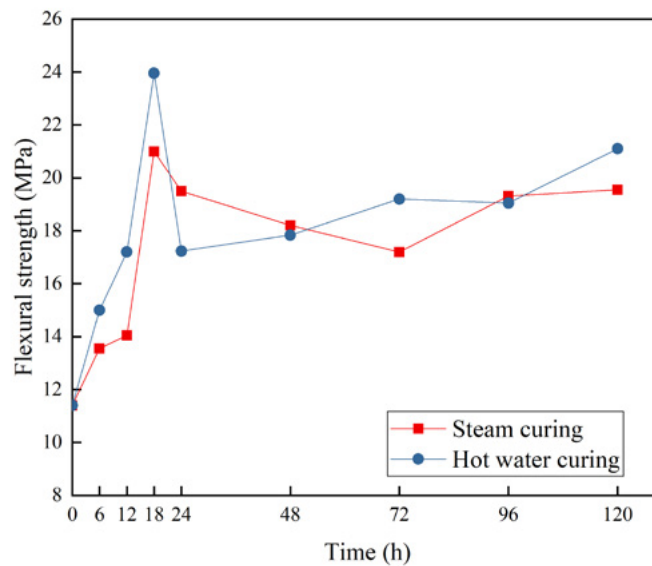


Figure 3: Flexible strength of UHPC cured at different systems (Steam curing, Hot water curing)

At the beginning of the heating, the steaming mainly passes steam and radiates heat. When steam first

meets the surface of a cold concrete, it immediately condenses into water, releasing a large amount of heat. Because the temperature gradient is too large, the thermal conductivity of concrete is small, resulting in large temperature stress, which has a great destructive effect on the concrete structure. In contrast, the heat transfer rate of hot water curing is relatively constant, because the concrete is immersed in water, and the water temperature rises slowly, and the damage to the concrete structure is small. During the constant temperature, due to the hydration reaction, the internal temperature of the concrete is higher than the external temperature, and the external heat is radiated, and the internal moisture is evaporated outward. While curing at steam, the moisture in the UHPC is easily vaporized, transferred, and forms a directional channel that affects UHPC strength[19].

3.2 Effect of curing condition on UHPC pore structure

The pore size distribution and cumulative pore volume of UHPC with different curing systems curing for 18h, 48h, 120h are illustrated in Figs.4.

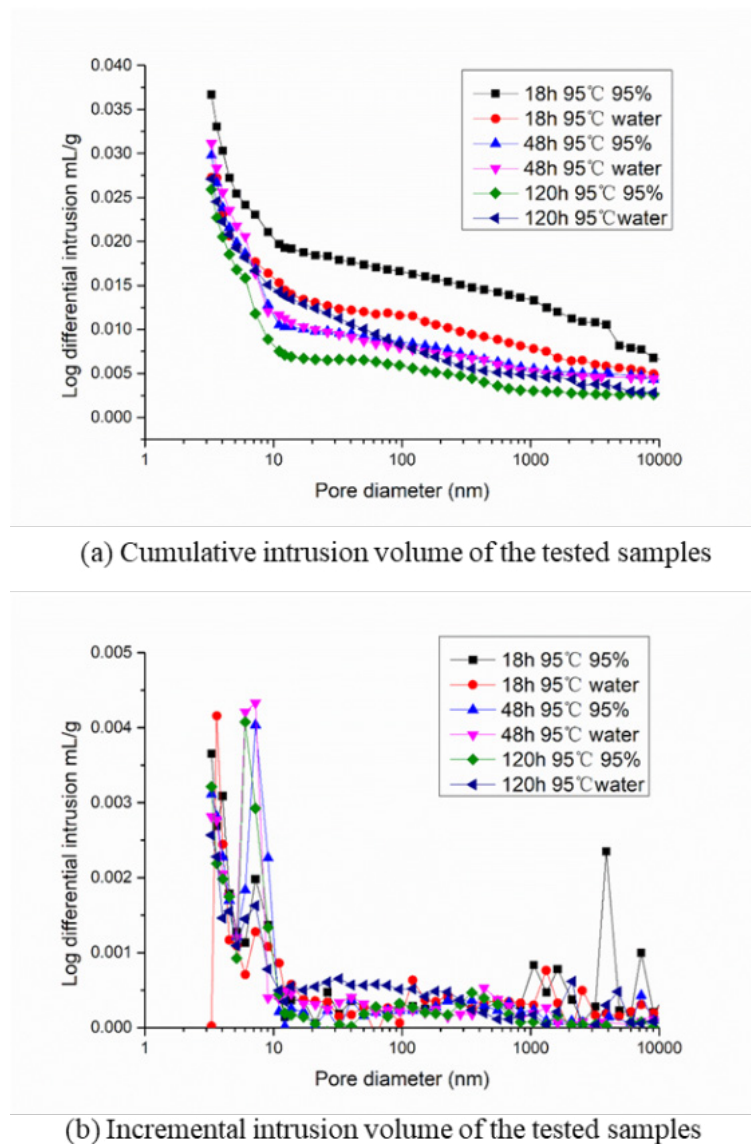


Figure 4: Pore size distributions of UHPC with different curing systems curing for 18h, 48h, 120h

It can be seen that as the curing time is extended, the cumulative pore volume of the UHPC is continuously reduced. And the cumulative pore size of hot water curing is lower than that of steam curing. This also

confirms the assumption that steam curing will form a directional channel inside the UHPC.

It can be seen from Figure 4 that most of the pore diameter is less than 30 nm, and it is known that pores within 30 nm are harmless or less harmful[20]. This means that this part of the pores has little negative impact on UHPC properties, while those close to 100 nm can significantly reduce concrete performance. It can also be found that as the curing time increases, the large pores are constantly changing into small holes. This is consistent with the findings of other researchers[21-23].

3.3 Hydration heat test

Fig.5 is the hydration exotherm of the slurry of the UHPC at room temperature. The hydration heat release curve can be divided into three stages. The first stage: slow hydration stage, the cumulative heat release of cement is less, the chemical reaction is slow, and the time of this stage is prolonged due to the addition of fly ash. In the second stage, the hydration heat is rapidly accumulating, and a severe hydration reaction occurs at this stage, releasing a large amount of heat, and the hydration heat curve is suddenly increased. In the third stage, the slow hydration stage, in which the hydration heat release rate is slowed down and the hydration heat release is less.

In the slow hydration stage (0-6h), the hydration heat release is only 6.4% of the final hydration heat release, the degree of reaction of the cement is still very low, and the concrete strength is at a lower level. In the second stage (6-48h), the hydration heat release is 80.3% of the final hydration heat release. With the rapid progress of hydration, the mechanical properties of concrete also increase rapidly. In the slow hydration stage, the hydration heat release is about 13.3% of the final hydration heat release, and the concrete strength does not increase significantly at this stage, but the internal structure is improved.

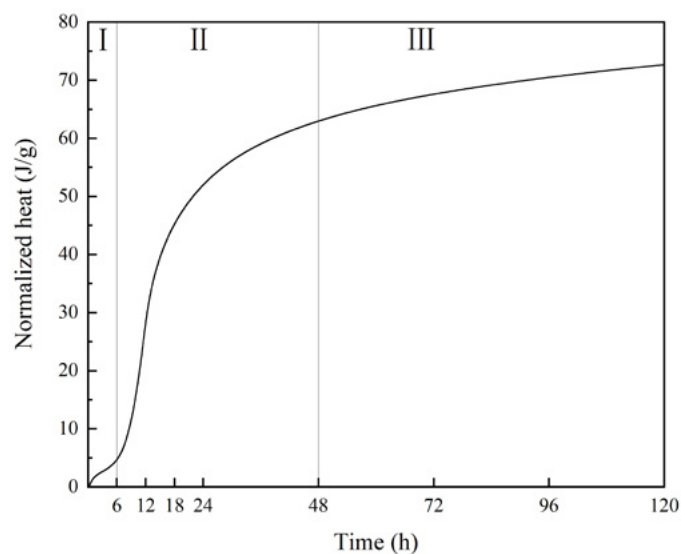


Figure 5: Hydration heat emission of cement pastes

4. Conclusions

This study explored the effects of curing systems on the development of mechanical strength and microstructure of concrete. According to the experimental results, the following conclusions can be drawn:

1. At the same temperature, the hot water curing strength is slightly higher than the steam curing. This is due to the difference in heat transfer medium. Due to the small thermal conductivity of concrete, the instability of steam heat transfer leads to large temperature stress inside the concrete, which has a great destructive effect on the concrete microstructure.

2. Under high temperature curing conditions, concrete strength rises rapidly in the early stage, and high temperature curing after peaking causes fluctuations in strength. This is because high temperature promotes hydration to generate more hydration products and microcracks are continuously generated and repaired.

5. Acknowledgment

The authors acknowledge the financial supports of National Nature Science Foundation Project of China (No. 51608409), National Nature Science Foundation Project of China (51679179), Major science and technology project in Zhongshan city, Guangdong province (2017A1021), Yang Fan plan of Guangdong Province (201312C12), Open research project of Advanced Engineering Technology Research Institute of Wuhan University of technology in Zhongshan city (WUT201802).

6. References

1. Larrard, F.o.d., *Concrete mixture proportioning : a scientific approach*. Modern concrete technology. 1999, London ; New York: E & FN Spon. xvii, 421 p.
2. Li, Y., K.H. Tan, and E.-H. Yang, *Influence of aggregate size and inclusion of polypropylene and steel fibers on the hot permeability of ultra-high performance concrete (UHPC) at elevated temperature*. Construction and Building Materials, 2018. **169**: p. 629-637.
3. Schmidt, M. and E. Fehling, *Ultra-high-performance concrete: research, development and application in Europe*. ACI Special publication, 2005. **228**: p. 51-78.
4. Lee, M.J., et al., *The Study of UHPC Precast Concrete Containing Incinerator Fly Ash*. Journal of Testing and Evaluation, 2018. **46**(1): p. 160-167.
5. Xu, Y., et al., *Experimental studies and modeling of creep of UHPC*. Construction and Building Materials, 2018. **175**: p. 643-652.
6. Fehling, E. and S. Sturwald, *Flexural Behaviour of UHPC with Fibres and Rebars*. Fib Symposium Prague 2011: Concrete Engineering for Excellence and Efficiency, Vols 1 and 2, 2011: p. 535-538.
7. Chen, T., X. Gao, and M. Ren, *Effects of autoclave curing and fly ash on mechanical properties of ultra-high performance concrete*. Construction and Building Materials, 2018. **158**: p. 864-872.
8. Prem, P.R., A.R. Murthy, and B.H. Bharatkumar, *Influence of curing regime and steel fibres on the mechanical properties of UHPC*. Magazine Of Concrete Research, 2015. **67**(18).
9. Ng, S., et al., *Effect of storage and curing conditions at elevated temperatures on aerogel-incorporated mortar samples based on UHPC recipe*. Construction And Building Materials, 2016. **106**: p. 640-649.
10. Song, Q., et al., *Steel fibre content and interconnection induced electrochemical corrosion of Ultra-High Performance Fibre Reinforced Concrete (UHPRFC)*. Cement and Concrete Composites, 2018. **94**: p. 191-200.
11. Yu, R., P. Spiesz, and H.J.H. Brouwers, *Mix design and properties assessment of Ultra-High Performance Fibre Reinforced Concrete (UHPRFC)*. Cement and Concrete Research, 2014. **56**: p. 29-39.
12. Huang, H., et al., *Influence of formwork wall effect on fiber orientation of UHPC with two casting methods*. Construction and Building Materials, 2019. **215**: p. 310-320.
13. Wang, X., et al., *Development of a novel cleaner construction product: Ultra-high performance concrete incorporating lead-zinc tailings*. Journal of Cleaner Production, 2018. **196**: p. 172-182.

14. Yu, R., P. Spiesz, and H.J.H. Brouwers, *Effect of nano-silica on the hydration and microstructure development of Ultra-High Performance Concrete (UHPC) with a low binder amount*. Construction and Building Materials, 2014. **65**: p. 140-150.
15. Buck, J.J., D.L. McDowell, and M. Zhou, *Effect of microstructure on load-carrying and energy-dissipation capacities of UHPC*. Cement and Concrete Research, 2013. **43**: p. 34-50.
16. Sadrmomtazi, A., S. Tajasosi, and B. Tahmouresi, *Effect of materials proportion on rheology and mechanical strength and microstructure of ultra-high performance concrete (UHPC)*. Construction and Building Materials, 2018. **187**: p. 1103-1112.
17. Shen, P., et al., *Experimental investigation on the autogenous shrinkage of steam cured ultra-high performance concrete*. Construction and Building Materials, 2018. **162**: p. 512-522.
18. Mosaberpanah, M.A. and O. Eren, *Effect of quartz powder, quartz sand and water curing regimes on mechanical properties of UHPC using response surface modelling*. Advances in Concrete Construction, 2017. **5**(5): p. 481-492.
19. Du, H., S. Du, and X. Liu, *Durability performances of concrete with nano-silica*. Construction and Building Materials, 2014. **73**: p. 705-712.
20. Fan, Y.-f. and H.-y. Luan, *Pore structure in concrete exposed to acid deposit*. Construction and Building Materials, 2013. **49**: p. 407-416.
21. Wang, Z., et al., *Experimental and numerical investigation of the interfacial properties of non-steam-cured UHPC-steel composite beams*. Construction and Building Materials, 2019. **195**: p. 323-339.
22. Kang, S.-H., S.-G. Hong, and J. Moon, *The effect of superabsorbent polymer on various scale of pore structure in ultra-high performance concrete*. Construction and Building Materials, 2018. **172**: p. 29-40.
23. Lee, N.K., et al., *Microstructural investigation of calcium aluminate cement-based ultra-high performance concrete (UHPC) exposed to high temperatures*. Cement and Concrete Research, 2017. **102**: p. 109-118.

Depth of penetration for steel-tube-confined concrete targets penetrated by rigid sharp-nosed projectiles

Q. Tan¹, D. Song², Z. Jiang²

¹ College of Aerospace Science and Engineering, National University of Defense Technology, Changsha, 410073, P.R. China.

² Undergraduate School, National University of Defense Technology, Changsha, 410072, P.R. China.

Abstract

Steel-tube-confined concrete (STCC) targets have excellent anti-penetration performance as a result of the confinement effect of steel tube to in-filled concrete. Therefore, establishing engineering models to predict depth of penetration (DOP) of STCC targets has application value for the potential application of STCC in protective structures. When the STCC targets are impacted by rigid sharp-nosed projectiles, dynamic cylindrical cavity-expansion model is used to get the approximate solutions of pressure at cavity wall with the inclusion of confinement effect and establish the formulas of DOP for STCC targets in this paper. Firstly, several assumptions including Heok-Brown criterion describing concrete in comminuted region, confinement effect of steel tube to in-filled concrete and incompressibility of concrete etc., are made to establish the basic equations of dynamic cylindrical cavity-expansion model. And then, approximate solutions of pressure at cavity wall are gained under the possible response modes including “elastic-cracked-comminuted”, “cracked-comminuted” and “full-comminuted”. Moreover, the scope of application and procedure of numerical solution are also derived. Lastly, on the basis of approximate solutions of pressure at cavity wall, an engineering model is proposed to predict the DOP of STCC targets normally penetrated by rigid sharp-nosed projectiles, and the existing tests of STCC targets normally penetrated by armor piecing projectile (APP) are used to validate the DOP formulas. The comparison results show that the engineering model in this paper is in good agreement with the results of penetration experiments, which further reveals that the engineering model is applicable to the calculation of DOP of the STCC targets normally penetrated by the rigid sharp-nosed projectiles with an impact velocity less than 830 m/s.

Keywords: Penetration mechanics, depth of penetration (DOP), dynamic cylindrical cavity-expansion; steel-tube-confined concrete (STCC), finite targets.

1. Introduction

With the rapid development of weapons and ammunition, a variety of concrete structures and protective facilities are facing more and more serious threat of projectile impact, such as the concrete protective walls of nuclear power plant and concrete shelters of protective engineering [1, 2]. As concrete is easy to crack or fracture under projectile impact, it has been a critical issue to improve the strength, ductility and toughness of concrete under impact loading [3], in which steel-tube-confined concrete (STCC) is one of the effective ways [4, 5]. STCC targets have excellent penetration resistance in comparisons with unconfined concrete targets. The penetration tests performed by Wan et al. [4] revealed that steel tube could restrict the radial

displacement of the in-filled concrete and development of radial cracks, and the damage was restrained within the element of STCC targets when impacted by projectiles; the depth of penetration (DOP) of STCC targets can be reduced by 10%–20% than that of semi-infinite targets. Therefore, proposing an appropriate DOP model for STCC targets is of significant importance to conveniently and efficiently expand the application of STCC to protective structures.

DOP models based on spherical or cylindrical cavity-expansion approximation have been extensively used [6, 7]. The spherical cavity-expansion (SCE) approximation model is shown to be suitable to deep penetration problems of semi-infinite targets impacted by ogival nose rigid projectiles [8, 9], while the cylindrical cavity-expansion (CCE) approximation model is more applicable to perforation problems with ductile hole-growth and deep penetration problems of semi-infinite targets impacted by rigid conical or other sharp-nosed projectiles or [10–12]. The CCE approximation model has been employed to solve the penetration problems of dry porous rock [13, 14], soil [15] and concrete [16, 17] targets. Mastilovic and Krajcinovic [18] proposed CCE approximation model for semi-infinite targets on the assumption that the target is divided into elastic, process (damaged), crushed (comminuted) and cavity zones, and material in crushed (comminuted) zone yields according to the Mohr–Coulomb (M–C) criterion. Forrestal and Tzou [19] also used M–C criterion to capture the mechanical performance of concrete in the comminuted zone.

Macek and Duffey [20] regarded the targets as incompressible materials, and proposed a finite SCE approximation model for the analysis of rigid ogival-nose projectiles obliquely penetrating into geological medium to consider the effect of free surface at the initial stage. On the basis of incompressible M–C material and the SCE approximation model for semi-infinite targets proposed by Forrestal and Tzou [19], Warren et al. [21, 22] proposed a dynamic finite spherical cavity-expansion (FSCE) approximation model for the targets obliquely impacted by projectiles. With targets treated as incompressible M–C material, Fang et al. [23] constructed a decay function to include the free-surface effect for geological targets by assuming that plastic-cracked-elastic response region exists during the cavity-expansion process. Chen et al. [24] proposed a fast algorithm to predict penetration trajectory in simulation of a rigid steel projectile obliquely penetrating into a limestone target and the effect of cratering and free surface, and separation-reattachment phenomenon were involved. However, the models mentioned above do not include the influence of lateral free boundary and also do not account for the confinement effect of restraints imposed on the target material. Zhen et al. [25] established a finite cylindrical cavity-expansion (FCCE) approximation model for perfect elastic-plastic compressible and incompressible materials with the inclusion of the influence of the lateral free boundary. On the basis of assumptions of incompressible material and the Modified-Griffith (M–G) criterion [26, 27], which shows the same form with Hoek–Brown (H–B) criterion [28, 29], Meng et al. [30] proposed a dynamic FSCE approximation model and DOP model for confined concrete targets normally impacted by rigid projectile. The results showed that under high confinement, the empirical constant m in the M–G criterion was recommended to be above 15 on the basis of triaxial experiments. However, in the practical application to calculation of DOP for armor piercing projectile (APP) with conical core normally penetrating into STCC targets in Ref. [4], the calculated results with m ranged between 6 and 8 agree well with the test results, i.e., the value of m in Ref. [30] is lower than the recommended values. The reason is that under conditions that there is no coarse aggregate within concrete of the targets in Ref. [4] and the penetration resistance is overestimated by the FSCE approximation model. Moreover, the geometric shape of an STCC target with finite lateral dimensions and tunneling cavity response is approximately cylindrical when the STCC target is normally penetrated by rigid conical or other sharp-nosed projectiles, which is close to the FCCE models.

On the basis of the above backgrounds and problems, a dynamic FCCE approximation model is proposed to analyze the stress distribution during the penetration process and predict the DOP of STCC targets

normally impacted by rigid conical or other sharp-nosed projectiles. Firstly, a dynamic FCCE approximation model is established for STCC targets with the H–B criterion and incompressible material, and the equations of stresses and displacements in STCC targets are proposed. Moreover, formula of the DOP for STCC targets based on the dynamic FCCE approximation model is developed and then the relevant penetration tests of STCC targets are employed to validate the DOP model.

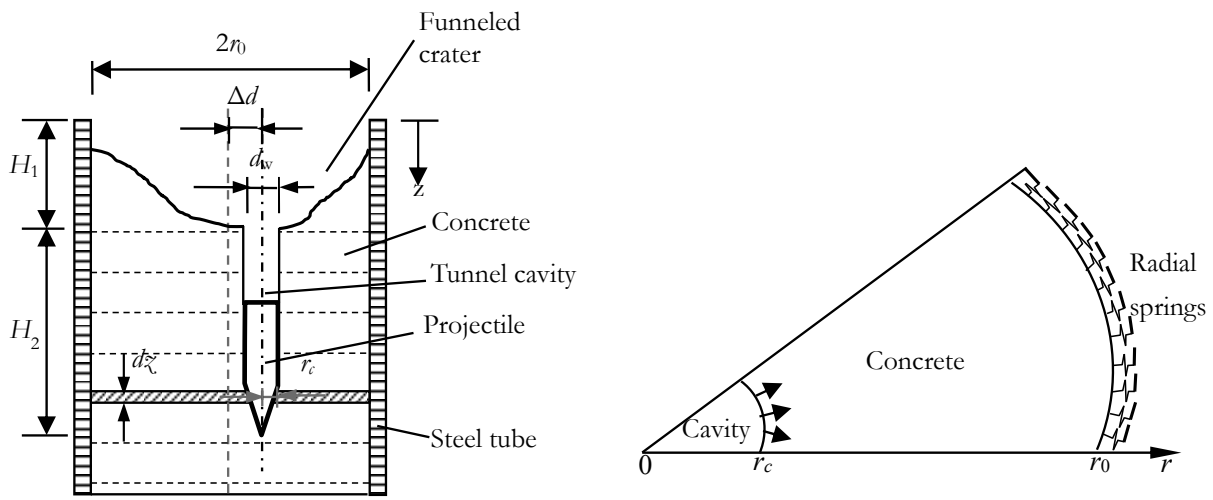
2. Dynamic FCCE model for STCC targets

2.1 Simplification of penetration problems

On the basis of the above backgrounds and problems, a dynamic FCCE approximation model is proposed to analyze the stress distribution during the penetration process and predict the DOP of STCC targets normally impacted by rigid conical or other sharp-nosed projectiles. Firstly, a dynamic FCCE approximation model is established for STCC targets with the H–B criterion and incompressible material, and the equations of stresses and displacements in STCC targets are proposed. Moreover, the key parameters on cavity-expansion process, radial stress at cavity wall and critical cavity radii are also analyzed. Lastly, formula of the DOP for STCC targets based on the dynamic FCCE approximation model is developed and then the relevant penetration tests of STCC targets are employed to validate the DOP model.

The penetration process of projectiles into STCC targets includes the cratering and tunneling stages [4], as shown in Fig. 1 (a). Generally, the DOP in the cratering stage (H_1) is based on empirical formula according to experimental results, while the DOP in the tunneling stage (H_2) is usually calculated by analytical models based on cavity-expansion approximation models. Like the results of cavity-expansion approximation model for semi-infinite targets [8–12], FCCE approximation model is expected to be more applicable to analyze the penetration problem of STCC targets normally penetrated by rigid conical or other sharp-nosed projectiles.

For FCCE approximation model, the STCC targets can be idealized as infinitely thin layers normal to the impacting direction and particles of the target material move in a radial direction during the penetration process shown in Fig. 1 (a). And then the penetration analysis can be simplified to one dimensional problem, as shown in Fig. 1 (b).



1a) Penetration process of STCC target 1b) Diagram for process of cavity expansion

Figure 1: Schematic diagram for FCCE models.

Like the dynamic FSCE approximation model for confined concrete targets proposed by Meng et al. [30], some assumptions are further employed to establish the dynamic FCCE approximation model for STCC targets.

(1) Target concrete is a fully incompressible material with Poisson's ratio $\nu=0.5$. By ignoring the compressibility and strain-softening of concrete, the cavity-expansion pressure would be overestimated; and if shear dilatancy, strain-rate, strain-hardening of concrete are not included, the cavity-expansion pressure would be underestimated. Therefore, under low and medium penetration velocity, the above effects of concrete material generally offset each other, which indicates the incompressible material assumption of target concrete is reasonable [30–32]. Additionally, incompressible material assumption excludes the effect of stress wave and thus greatly simplifies the problem with possible analytical solutions.

(2) Confinement effect of steel tube to concrete is equivalent to a series of linear radial springs with stiffness (K) shown in Fig. 1 (b). As for the circular STCC targets, the equivalent confining stiffness (K) is shown in Eq. (1) [4].

$$K = \frac{E_s \delta}{r_0^2} \quad (1)$$

Where E_s , δ and r_0 are the elastic modulus, thickness and internal radius of steel tube, respectively.

(3) Finite cavity-expansion is assumed as a concentric cylindrical cavity expanding at a constant velocity \dot{r}_c from initial radius zero to the radius of r_0 . Under low and medium penetration velocity, elastic, cracked and comminuted regions generally appear in the STCC targets [30]. A typical finite cavity-expansion process includes three phases, i.e., “elastic-cracked-comminuted” “cracked- comminuted” and “completely comminuted” phases, as shown in Fig. 2. In Fig. 2, r_c , r_{cr} and r_p are the cavity radius, radius of the interface between the elastic and cracked zones and radius of the interface between the cracked and comminuted zones, respectively.

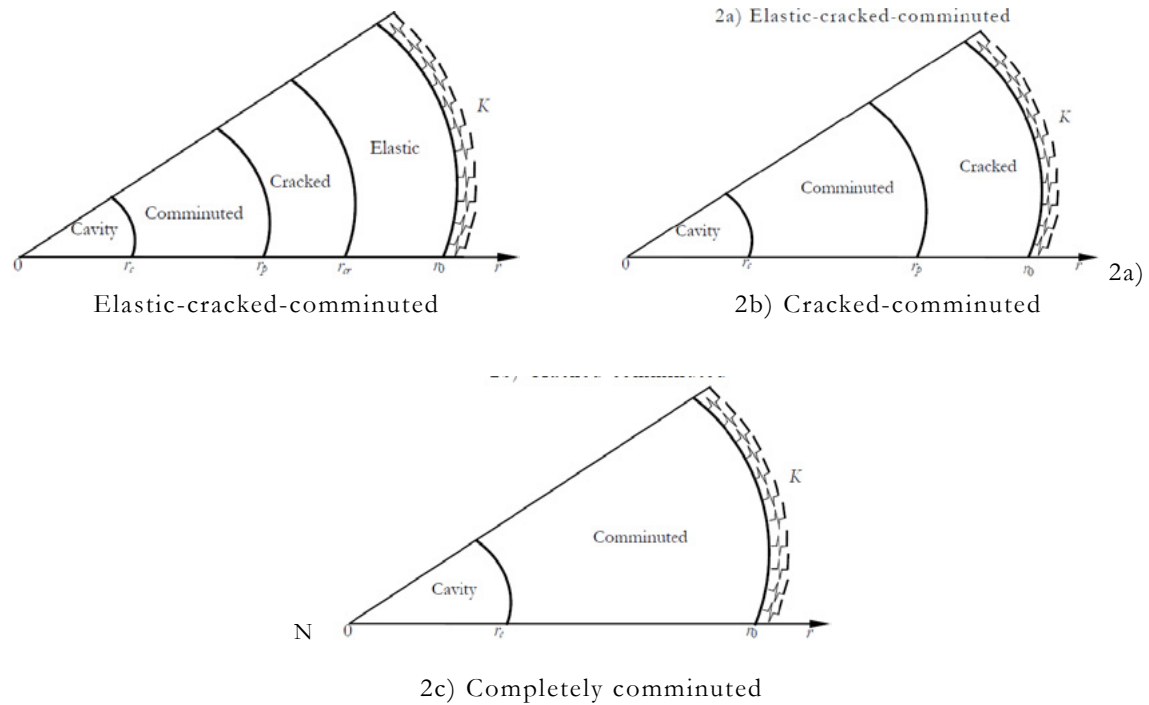


Figure 2: Schematic diagram of a typical cavity-expansion process.

For “elastic-cracked-comminuted” phase shown in Fig. 2 (a), the elastic zone is surrounded by the radius r_0 of core concrete as the outer boundary. When the cracked zone expands to the outer boundary of core concrete ($r_{cr}=r_0$), the elastic zone disappears; and the first phase comes to end ($r_c=r_{cl}$, r_{cl} is a critical cavity radius).

For “cracked-comminuted” phase shown in Fig. 2 (b), the cracked zone takes the radius r_0 of core concrete as the outer boundary, i.e., $r_{cr}=r_0$; when the comminuted zone reaches the outer boundary of the core

concrete, the cracked zone disappears, then the second phase ends ($r_p=r_0$, $r_c=r_{c2}$, r_{c2} is another critical cavity radius and larger than r_{c1}).

For “completely comminuted” phase shown in Fig. 2 (c), the external radius of the comminuted zone is r_0 , i.e., $r_p \equiv r_0$; and the third phase ends when the elastic constraint fails.

Moreover, in cracked zone, the radial stress of the incompressible target concrete is continuous with the circumferential stress $\sigma_\theta=0$, and the radial stress gets to equal the uniaxial compressive strength (σ_u) at the interface between the comminuted and cracked zones. In elastic zone, the circumferential stress is equal to the uniaxial tensile strength (σ_t) at the elastic-cracked interface.

(4) As strength performance of confined concrete is similar to that of the surrounding rock, the nonlinear H–B criterion is used to describe the confined concrete in comminuted region under triaxial compression [30]. The equation of H–B criterion is Eq. (2) for intact rock [28, 29].

$$\frac{\sigma_1}{\sigma_u} = \frac{\sigma_3}{\sigma_u} + \sqrt{m \frac{\sigma_3}{\sigma_u} + 1} \quad (2)$$

Where, σ_u , σ_1 and σ_3 are the uniaxial compressive strength, first and third principal stresses respectively, measured positive in compression; and m is an empirical constant.

For cylindrical coordinate system, equilibrium equation of axial stress (σ_z) is shown in Eq. (3) and further simplified according to assumption (1) ($\nu=0.5$).

$$\sigma_z = \delta(\sigma_r + \sigma_\theta) = \frac{1}{2}(\sigma_r + \sigma_\theta), \quad \sigma_r > \sigma_\theta \quad (3)$$

Where σ_z , σ_r and σ_θ are the axial, radial and circumferential stresses, respectively, and taken positive in compression.

Generally, the three principal stresses in cylindrical coordinate system meet relationship of Eq. (4).

$$\sigma_1 = \sigma_r, \sigma_2 = \sigma_z, \sigma_3 = \sigma_\theta \quad (4)$$

Transforming Eq. (2) into the function of σ_r can give Eq. (5).

$$\frac{\sigma_\theta}{\sigma_u} = \frac{\sigma_r}{\sigma_u} + \frac{m}{2} - \sqrt{m \frac{\sigma_r}{\sigma_u} + n} \quad (5)$$

Where $n = m^2/4 + 1$.

2.2 Basic equations

For solutions of FCCE approximation model, as the density of concrete keeps constant according to assumption (1), the equations of momentum and mass conservation and the relations between particle velocity and displacement in the cylindrical coordinates are as follows [12].

$$\frac{\partial \sigma_r}{\partial r} + \frac{\sigma_r - \sigma_\theta}{r} = -\rho \left(\frac{\partial v}{\partial t} + v \frac{\partial v}{\partial r} \right) \quad (6)$$

$$\frac{\partial(r-u)^2}{\partial r} = 2r \quad (7)$$

Where u and v are displacement and velocity of particle, respectively, with outward motion considered positive; ρ is the density of material.

The particle velocity can be obtained by time derivative of the particle displacement.

$$v = \frac{\partial u}{\partial t} + v \frac{\partial u}{\partial r} \quad (8)$$

At cavity wall ($r=r_0$), the particle displacement (u) is equal to the cavity radius ($r=r_0$), and integral of Eq. (7) would get

$$(r-u)^2 = r^2 - r_c^2 \quad (9)$$

Derivation of time from Eq. (9) gets

$$v = \frac{r_c}{r} \dot{r}_c \quad (10)$$

At the interface between concrete and steel tube ($r=r_0$), the boundary conditions can be expressed as

$$\sigma_r(r=r_0) = Ku_0, \quad u_0 = u(r=r_0) = r_0 - \sqrt{r_0^2 - r_c^2} \quad (11)$$

According to assumption (3) about the elastic-cracked and cracked-comminuted interfaces, the stresses at the interfaces are

$$\sigma_\theta(r=r_c^+) = -|\sigma_r| \quad (12)$$

$$\sigma_r(r=r_p^-) = \sigma_u \quad (13)$$

On the basis of assumption (3) with a constant cavity-expansion velocity (\dot{r}_c), integrating Eq. (10) with Eq. (6) obtains

$$\frac{d\sigma_r}{dr} + \frac{\sigma_r - \sigma_\theta}{r} = -\rho \dot{r}_c^2 \left(\frac{1}{r} - \frac{2r_c^2}{r^3} \right) \quad (14)$$

Furthermore, when compressibility of concrete is ignored according to assumption (1), the continuous conditions at interface are obtained as follows [19].

$$u_2 = u_1, v_2 = v_1, \sigma_{r2} = \sigma_{r1} \quad (15)$$

Where figure subscripts (1 and 2) represent the front and rear of the interfaces, respectively.

2.3 Solutions of concrete responses

2.3.1 Elastic-cracked-comminuted phase ($r_c < r < r_0$)

In the elastic region ($r_c \leq r \leq r_0$, $r_c < r$), relationships between strain and displacement can be described with Eq. (16) under the conditions of small deformation.

$$\varepsilon_r = -\frac{\partial u}{\partial r}, \quad \varepsilon_\theta = -\frac{u}{r} \quad (16)$$

Derivative of r for Eq. (9) and in combination with Eq. (16) could gain the relationship between strain and displacement.

$$\varepsilon_r - \varepsilon_\theta = -\left(\frac{\partial u}{\partial r} - \frac{u}{r} \right) = \left(\frac{r_c}{r} \right)^2 \left(1 - \frac{r_c^2}{r^2} \right)^{-\frac{1}{2}}$$

(17)

Using the Hooke law with assumption (1) ($\nu=0.5$) and ignoring the high-order terms of Eq. (17) get

$$\sigma_r - \sigma_\theta = \frac{2E}{3} \left(\frac{r_c}{r} \right)^2 \quad (18)$$

At the elastic-cracked interface ($r=r_c$), substituting Eq. (12) into Eq. (18) gets

$$\sigma_r = \frac{2E}{3} \frac{r_c^2}{r_c^2} - |\sigma_t| \quad (19)$$

Combining Eq.(14) with Eq. (18) can obtain

$$\frac{d\sigma_r}{dr} = -\frac{2E}{3} \frac{r_c^2}{r^3} - \rho \dot{r}_c^2 \left(\frac{1}{r} - \frac{2r_c^2}{r^3} \right) \quad (20)$$

Integral of Eq. (20) with the boundary conditions of Eq. (11) gains the radial stress (σ_r).

$$\sigma_r = \frac{E}{3} \left(\frac{r_c^2}{r^2} - \frac{r_c^2}{r_0^2} \right) - \rho \dot{r}_c^2 \left(h \frac{r}{r_0} + \frac{r_c^2}{r^2} - \frac{r_c^2}{r_0^2} \right) + K_0 \left[1 - \left(1 - \frac{r_c^2}{r_0^2} \right)^{\frac{1}{2}} \right] \quad (21)$$

The circumferential stress (σ_θ) in elastic region is gotten by combining Eq. (21) and Eq. (18).

$$\sigma_\theta = -\frac{E}{3} \left(\frac{r_c^2}{r^2} + \frac{r_c^2}{r_0^2} \right) - \rho \dot{r}_c^2 \left(h \frac{r}{r_0} + \frac{r_c^2}{r^2} - \frac{r_c^2}{r_0^2} \right) + K_0 \left[1 - \left(1 - \frac{r_c^2}{r_0^2} \right)^{\frac{1}{2}} \right] \quad (22)$$

Combining Eq. (21) with Eq. (19) can gain the equation of interface radius (r_c).

$$\frac{E}{3\sigma_u} \left(\frac{r_c^2}{r_c^2} + \frac{r_c^2}{r_0^2} \right) - \frac{|\sigma_t|}{\sigma_u} = \frac{K_0}{\sigma_u} \left[1 - \left(1 - \frac{r_c^2}{r_0^2} \right)^{\frac{1}{2}} \right] - \frac{\rho \dot{r}_c^2}{\sigma_u} \left(h \frac{r_c}{r_0} + \frac{r_c^2}{r_c^2} - \frac{r_c^2}{r_0^2} \right) \quad (23)$$

The critical cavity radius r_{cl} is gained by definition of $r_c=r_0$ in Eq. (23). The “elastic-cracked-comminuted” phase would come to end if $r_c=r_0$, and then Eq. (23) can be further simplified as

$$\frac{K_0}{\sigma_u} \left[1 - \left(1 - \frac{r_{cl}^2}{r_0^2} \right)^{\frac{1}{2}} \right] + \frac{|\sigma_t|}{\sigma_u} = \frac{2E}{3\sigma_u} \frac{r_{cl}^2}{r_0^2} \quad (24)$$

It can be seen from Eq. (24) that r_{cl}/r_0 is only related to the parameters of the targets (K_0/σ_u , $|\sigma_t|/\sigma_u$ and E/σ_u) but independent of the cavity-expansion velocity.

In the cracked region ($r_p \leq r \leq r_c$), according to assumption (3), there is no circumferential stress, i.e., $\sigma_\theta=0$, and then integral of Eq. (14) gains

$$\sigma_r = \frac{C}{r} - \rho \dot{r}_c^2 \left(1 + 2 \frac{r_c^2}{r^2} \right) \quad (25)$$

Where, C is the integral constant.

Moreover, on the basis of the continuous conditions of the radial stress (σ_r) related to Eq. (15), substituting Eq. (19) into Eq. (25) can provide C as

$$C = r_e \left[\frac{2E}{3} \left(\frac{r_c}{r_e} \right)^2 - |\sigma_t| + \rho \dot{r}_c^2 \left(1 + 2 \frac{r_c^2}{r_e^2} \right) \right] \quad (26)$$

The integral constant (C) can be further simplified by substituting Eq. (13) in to Eq. (25).

$$C = r_p \left[\sigma_u + \rho \dot{r}_c^2 \left(1 + 2 \frac{r_c^2}{r_p^2} \right) \right] \quad (27)$$

Integration of Eqs. (26) and (27) gains the relationship between r_p and r_{cr} , as shown in Eq. (28).

$$r_{cr} \left[\frac{2E}{3} \left(\frac{r_c}{r_{cr}} \right)^2 - |\sigma_t| + \rho \dot{r}_c^2 \left(1 + 2 \frac{r_c^2}{r_{cr}^2} \right) \right] = r_p \left[\sigma_u + \rho \dot{r}_c^2 \left(1 + 2 \frac{r_c^2}{r_p^2} \right) \right] \quad (28)$$

Interface radii r_{cr} and r_p can be solved by combining Eq. (23) and Eq. (28).

If the cracked zone is absent during the FCCE process, by definition of $r_{cr} = r_p$ in Eq. (28), it gets

$$\frac{r_c}{r_e} = \frac{r_c}{r_p} = \sqrt{\frac{3(\sigma_u + |\sigma_t|)}{2E}} \quad (29)$$

Integration of Eqs. (23) and (29) can gain the cavity-expansion velocity ($\dot{r}_{c,max}$) for response mode exchange, i.e., $\dot{r}_{c,max}$ is the maximum cavity-expansion velocity for the “elastic-cracked- comminuted” phase during the FCCE process; and there is no cracked zone in targets at initial expansion if cavity-expansion velocity exceeds $\dot{r}_{c,max}$, which belongs to hypervelocity penetration problems.

$$\dot{r}_{c,max} = \left\{ \frac{\frac{E}{3\sigma_u} \left(\frac{r_c}{r_0} \right)^2 + \frac{\sigma_u - |\sigma_t|}{2\sigma_u} - \frac{K_0}{\sigma_u} \left[1 - \left(1 - \frac{r_c^2}{r_0^2} \right)^{\frac{1}{2}} \right]}{\frac{r_c^2}{r_0^2} - \frac{r_c}{r_0} + \frac{1}{2} \frac{3(\sigma_u + |\sigma_t|)}{2E} - \frac{3(\sigma_u + |\sigma_t|)}{2E}} \frac{\sigma_u}{\rho} \right\}^{\frac{1}{2}} \quad (30)$$

It can be seen from Eq. (30) that $\dot{r}_{c,max}$ is related to the geometric and mechanical parameters of the targets.

Then, combining Eq. (25) with Eq. (26) gets

$$\sigma_r = \frac{r_{cr}}{r} \left[\frac{2E}{3} \left(\frac{r_c}{r_{cr}} \right)^2 - |\sigma_t| + \rho \dot{r}_c^2 \left(1 + 2 \frac{r_c^2}{r_{cr}^2} \right) \right] - \rho \dot{r}_c^2 \left(1 + 2 \frac{r_c^2}{r^2} \right) \quad (31)$$

In the comminuted region ($r_c \leq r \leq r_p$), transformation of Eq. (5) gives

$$\sigma_r - \sigma_\theta = \sigma_u \left(\sqrt{m \frac{\sigma_r}{\sigma_u} + n} - \frac{m}{2} \right) \quad (32)$$

Combining Eq. (32) with Eq. (14) provides

$$\frac{d\sigma_r}{dr} = \frac{\sigma_u \left(\frac{m}{2} - \sqrt{m \frac{\sigma_r}{\sigma_u} + n} \right)}{r} - \rho \dot{r}_c^2 \left(\frac{1}{r} - \frac{2r_c^2}{r^3} \right) \quad (33)$$

Eq. (33) is a nonlinear ordinary differential equation, and could be solved by Runge-Kutta method with the boundary conditions of Eq. (13).

2.3.2 Cracked-comminuted phase ($r_{c1} \leq r_c < r_{c2}$)

In the cracked region ($r_p \leq r \leq r_0$), radial stress (σ_r) can still be obtained by Eqs. (25) and (27). The equation of boundary conditions is still Eq. (11) at $r=r_0$, and then the integral constant C in Eq. (25) can be gained by combination of Eqs. (25) and (11).

$$C = r_0 \left[K_0 \left[1 - \left(1 - \frac{r_c^2}{r_0^2} \right)^{\frac{1}{2}} \right] + \rho \dot{r}_c^2 \left(1 + 2 \frac{r_c^2}{r_0^2} \right) \right] \quad (34)$$

The radial stress (σ_r) can be gained by substituting Eq. (34) into Eq. (25).

$$\sigma_r = \frac{r_0}{r} \left[K_0 \left[1 - \left(1 - \frac{r_c^2}{r_0^2} \right)^{\frac{1}{2}} \right] + \rho \dot{r}_c^2 \left(1 + 2 \frac{r_c^2}{r_0^2} \right) \right] - \rho \dot{r}_c^2 \left(1 + 2 \frac{r_c^2}{r^2} \right) \quad (35)$$

In the comminuted region ($r_c \leq r \leq r_p$), the solution procedure of the control equation Eq. (33) with the boundary conditions of Eq. (13) is similar to that in the “elastic-cracked-comminuted” phase.

At the cracked-comminuted interface, the Eq. (36) is gotten by integrating Eqs. (27) with (34).

$$\frac{Kr_0}{\sigma_u} \left[1 - \left(1 - \frac{r_c^2}{r_0^2} \right)^{\frac{1}{2}} \right] + \frac{\rho \dot{r}_c^2}{\sigma_u} \left(1 + 2 \frac{r_c^2}{r_0^2} \right) = \frac{r_p}{r_0} \left[1 + \frac{\rho \dot{r}_c^2}{\sigma_u} \left(1 + 2 \frac{r_c^2}{r_p^2} \right) \right] \quad (36)$$

When the “cracked-comminuted” phase ends, the comminuted region has just reached the outer boundary of the targets. Therefore, the critical cavity radius (r_{c2}) is obtained by definition of $r_p = r_0$, and then Eq. (36) can be transformed into

$$\left(\frac{r_{c2}}{r_0}\right)^2 = 1 - \left(1 - \frac{\sigma_u}{K_0}\right)^2 \quad (37)$$

It is shown in Eq. (37) that r_{c2}/r_0 is correlated closely with dimensionless confinement stiffness Kr_0/σ_u , which can reflect the confinement effect of the outer tube to concrete to a certain degree. The applicable maximum confinement $(Kr_0)_{\max}$ can be obtained by the substitution of the critical condition $r_{c1}=r_{c2}$ into Eqs. (24) and (37).

$$\frac{\sigma_u}{(Kr_0)_{\max}} = 1 - \sqrt{1 - \frac{3(\sigma_u + |\sigma_t|)}{2E}} \quad (38)$$

There will be no “cracked-comminuted” phase if $Kr_0 > (Kr_0)_{\max}$, and the cavity-expansion process just includes “elastic-cracked-comminuted” and “completely comminuted” phases.

2.3.3 Completely comminuted phase ($r_c \geq r_{c2}$)

In the completely comminuted phase, the comminuted zone has reached the outer boundary of the targets, i.e., $r_p \equiv r_0$. The boundary conditions and control equation would be Eqs. (11) and (33), respectively, and the solution procedure of radial stress σ_r is also similar to the “elastic-cracked-comminuted” phase.

As equations of stresses for the three possible phases of FCCE models are complex, numerical solutions of the radial stress and circumferential stress at the cavity wall can be solved by Runge-Kutta method according to a standardized and classified procedure shown in Fig. 3, which is similar to the procedure for FSCE models reported by Meng et al. [30]. The procedure generally includes five steps: (1) Collecting and defining the initial conditions; (2) Discussing the applicability of the dynamic FCCE model; (3) Calculating the two critical cavity radii; (4) Determination of the response phases; (5) Solving the stresses at cavity wall at different phases, as shown in Fig. 3.

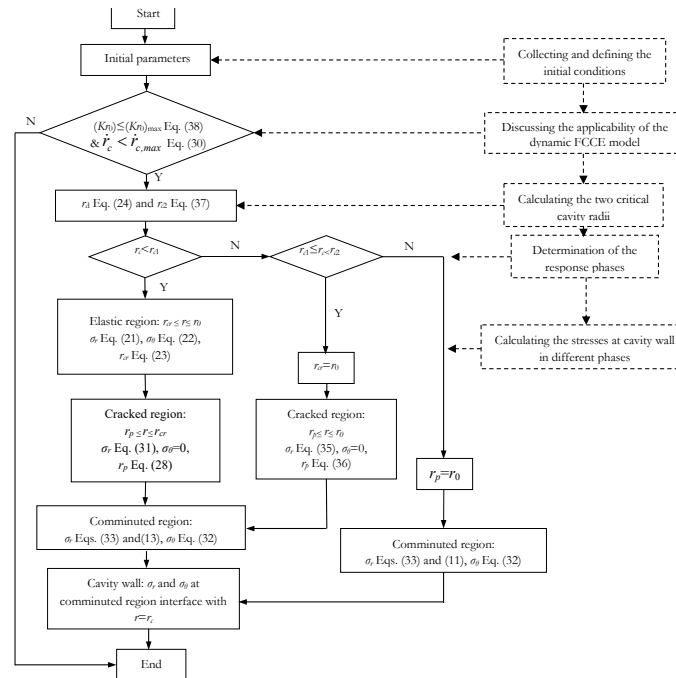


Figure 3: Flowchart and steps for calculation of pressure at cavity wall.

3. DOP model for STCC targets based on the FCCE model

3.1 DOP formula of STCC targets

The penetration process of the STCC targets normally penetrated by rigid projectiles includes the cratering and tunneling stages [4] and the formula of total DOP (H) is

$$H = H_1 + H_2 \quad (39)$$

Where H_1 is the DOP of the cratering stage with $H_1 = kd$, k is an empirical constant and d is the diameter of projectile; H_2 is the DOP of the tunneling stage obtained by the FCCE model.

For the confined concrete targets, the tunneling stage DOP (H_2) can be calculated by Eq. (40) according to Ref. [30]

$$H_2 = \frac{2M}{\pi d^2 \rho N B} \ln \left(1 + \frac{N B \rho V_1^2}{A \sigma_u} \right), \quad V_1^2 = \frac{4M V_0^2 - A k \pi d^3 \sigma_u}{4M + k \pi d^3 \rho N B} \quad (40)$$

Where, N is the shape factor of the projectile nose [34, 35]; V_1 is the velocity of projectile at beginning of the tunneling stage, which can be equal to the impact velocity of projectile (V_0) for APP [30]; A and B are constants, obtained by curve-fitting of the numerical solutions of the dynamic FCCE governing equations with Eq. (41) between a series of σ_{rc} and the given $\dot{\epsilon}_c$.

$$\frac{\sigma_{rc}}{\sigma_u} = A + B \frac{\rho \dot{\epsilon}_c^2}{\sigma_u} \quad (41)$$

Where σ_{rc} is calculated with the FCCE model described above. Therefore, the total DOP (H) is the sum of H_1 and H_2 .

$$H = H_1 + H_2 = k d + \frac{2M}{\pi d^2 \rho N B} \ln \left(1 + \frac{N B \rho V_1^2}{A \sigma_u} \right) \quad (42)$$

3.2 Validation of the DOP model

Penetration tests of STCC targets in Ref. [36] were selected to validate the DOP model in the Section 3.1. In Ref. [36], 9 specimens were designed, as shown in Table 1. All the tubes of the targets had the same dimension and the diameter, wall thickness and length of the tubes were 140 mm, 3.5 mm and 350 mm, respectively. Self-compacting concrete was filled in the steel tube and the unconfined compressive strength and splitting tensile strength of the standard specimens at the time of test (age 35 d) were 56.3 MPa and 5.66 MPa, respectively.

The test set-ups, procedures and methods were also the same as those in Ref. [4]. The damage parameters of the STCC targets were summarized in Table 1. Where, Δd is the distance from the center of ballistic crater to the center of target, r_0 is the radius of confined concrete, as shown in Fig. 1; V_L is the volume of the crater volume, which is measured by sand-filling method; H is the total DOP; H_1 is the depth of the funneled crater and correlated with the diameter of projectile. Based on the tested H_1 , the empirical constant k is deduced by rounding the numbers of the averaged values according to the designed penetration velocity range. The results show that for the 12.7 mm APP, k is related closely to the impact velocity V_0 , approximately, $k=4$ for $V_0 = 820$ m/s–830 m/s, $k=3$ for $V_0 = 700$ m/s–710 m/s and $k=2$ for $V_0 = 600$ m/s–610 m/s.

Table 1: Damage parameters of targets in Ref. [36].

Specimens number	Diameter/ thickness of steel tube (mm)	V_0 (m/s)	Δd (mm)	$\Delta d/r_0$ (%)	V_L (mL)	$H_1=kd$ (mm)	H (mm)	Average value of k	Notes
C140-1	140/3.5	-	-	-	-	-	142*		Perforation of steel tube
C140-2	140/3.5	820.7	6.4	9.1	270	42.0	173.0	4	
C140-3	140/3.5	829.9	13.0	18.6	252	45.5	181.0		
C140-8	140/3.5	-	3.0	4.3	290	45.0	172.1*		Unmeasured velocity
C140-6	140/3.5	703.0	4.0	5.7	235	40.0	126.8	3	
C140-7	140/3.5	710.5	3.0	4.3	190	34.0	129.2		
C140-4	140/3.5	603.0	0	0	195	36.0	92.0		
C140-5	140/3.5	599.3	4.0	5.7	84	29.0	80.6*	2	Unseparated steel sleeve
C140-9	140/3.5	611.8	2.0	2.9	172	26	93.5		

Notes: “-” denotes the unmeasured data; “*” signifies the perforation or the abnormal cases of the concrete or projectiles, which would be considered as invalid during the penetration-depth analysis.

The hard core of 12.7 mm APP can be considered to be rigid during the penetration process and the velocity loss of hard core during the cratering stage can be neglected [4, 36]. Therefore, the parameters of projectile of the DOP model can be replaced by those of the hard core during the tunneling stage, i.e., $d=d_w$ and $V_1=V_0$ in Eq. (40), where d_w is the diameter of hard core. The relevant parameters of the 12.7 mm APP and STCC targets in Ref. [36] are as follows: $d=12.7$ mm, $d_w=7.5$ mm, $M=9.8$ g, $N=0.8$; $E_s=198$ GPa; $K_0/\sigma_u=192$, $\delta=3.5$ mm, $r_0=66.5$ mm, $r_c=d_w/2=3.75$ mm, $\sigma_u=4.3$ MPa, $|\sigma_t|=5.6$ MPa, $E=3375 \times \sqrt{\sigma_u}=24869.9$ MPa, $\rho=2420$ kg/m³; the constant of k is valued according to the deduced results in Table 1.

As m between 8 and 26 is recommended in Ref. [30], $m=10, 15, 20$ and 25 are tentatively selected and the corresponding constant coefficients A and B were fitted with Eq. (41) as described in Section 3.1. One of the fitted results for $m=25$ is shown in Fig. 4, and the fitted parameters A and B are 4.96 and 9.44, respectively, with the correlation coefficient (R^2) 0.998. And then, the tested DOP (the DOP and impact velocity are averaged for the specimens with valid measured results) and calculated DOP are compared as shown in Table 2.

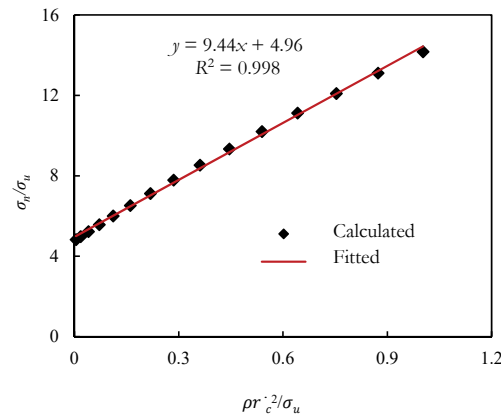


Figure 4: Curve-fitting of coefficients A and B ($m=25$).

The results in Table 2 show that the relative error decreases with the increasing values of m , and the optimal values are gained with $m=25$ where the relative error is about 8% except that of the targets with the impact velocity about 600 m/s (The possible reason is that the projectiles do not completely normally impact the STCC targets under the lower impact velocity [36]).

Table 2: Resistance coefficient and DOP of FCCE model for STCC targets.

r_0/δ (mm)	σ_u (MPa)	r_c/r_0	Kr_0/σ_u	m	A	B	k	V_0 (m/s)	Tested DOP (mm)	Calculated DOP (mm)	Relative error (%)
66.5/3.5	54.3	0.056	192	10	4.53	7.21	4	825.4	177.0	188.6	6.6
							3	706.7	128.0	160.5	25.4
							2	607.4	92.8	133.2	43.6
							4	825.4	177.0	175.9	-0.6
				15	4.75	8.18	3	706.7	128.0	149.4	16.7
							2	607.4	92.8	123.7	33.4
							4	825.4	177.0	168.2	-4.9
							3	706.7	128.0	142.8	11.5
							2	607.4	92.8	118.1	27.3
							4	825.4	177.0	163.1	-7.9
							3	706.7	128.0	138.3	8.1
				25	4.96	9.44	2	607.4	92.8	114.2	23.1

The comparisons of several DOP models for STCC targets including Li–Chen model [34, 35], FSCE model [30] and FCCE model in this paper, are shown in Fig. 5. As for Li–Chen model, in cratering stage, $H_1=2d$, and d is replaced with d_w in tunneling stage; H_2 is calculated by Eq. (40) with $V_1=V_0$, $B=1$, $\sigma_u=f_c$, $A=S$ and $S=72f_c^{-0.5}$. For FSCE model and FCCE model, $m=25$ is selected.

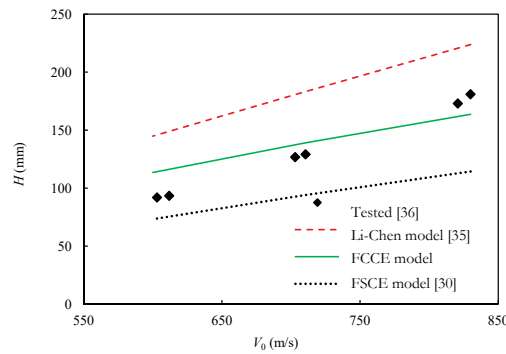


Figure 5: Comparison between the predicted models and tested results in Ref. [36].

As shown in Fig. 5, the results of DOP calculated by Li–Chen model are much larger than those of tests with the relative error as high as 23.7%–57.5%, while the results of DOP calculated by FSCE model are smaller than those of tests with the relative error of 5.9%–25.1%. However, the relative error between the results calculated by Eq. (42) in this paper and the tested data is less than 8 % except that the targets with the impact velocity about 600 m/s. Generally, it is shown that the DOP of STCC targets calculated by engineering model based on H–B criterion and FCCE model is obviously superior to that of the Li–Chen model. It is because that the constraint effect of the steel tube on concrete is not considered in Li–Chen model. It should point out that all the DOP of the engineering models are discrete with the impact velocity about 600 m/s, which may be due to the oblique penetration of the projectiles [36].

In order to further testify the applicability of the DOP model in this paper, Table 3 presents the comparison between the DOP model based on FCCE model and the tests in Ref. [4]. The parameters of penetrators, i.e., 12.7 mm APP, are identical to Ref. [36]. The parameters of STCC targets in Ref. [4] are as follows: $\sigma_u = 35.8$ MPa, $|\sigma_t| = 5.9$ MPa, $E_s = 198$ GPa, $\delta = 3.5$ mm (4.5 mm) and $r_0 = 53.5$ mm (52.5 mm). Since the in-filled concrete of targets was designed without coarse aggregate, the value of m should be smaller than that of concrete with coarse aggregate in Ref. [36]. Therefore, m (10, 15 and 20) is tentatively selected for that concrete without coarse aggregate in Ref. [4]. The tested (the DOP and impact velocity are averaged for the specimens with valid measured results) and calculated DOP data are compared as shown in Table 3.

Table 3: Resistance coefficients and DOP for STCC targets in Ref. [4].

r_0/δ (mm)	σ_u (MPa)	r_c/r_0	Kr_0/σ_u	A	B	m	k	V_0 (m/s)	Tested DOP (mm)	Calculated DOP (mm)	Relative error (%)
53.5/3.5		0.070	362	8.07	4.78	10				216.4	9.6
				8.81	5.44	15		825.9	197.4	199.0	0.8
				9.33	5.94	20				188.3	-4.6
52.5/4.5	35.8	0.071	474	9.69	4.43	10				208.9	10.0
				10.74	5.02	15	4	820.7	189.8	191.7	1.0
				11.48	5.49	20				181.1	-4.6
66.5/3.5		0.056	291	6.15	6.32	10				206.0	-2.4
				6.56	7.23	15		819.0	211.1	190.0	-10.0
				6.87	7.92	20				179.9	-14.8

It can be seen from Table 3 that when $m=15$, the calculated results of the FCCE model are generally consistent with the experimental data in Ref. [4], with the maximum disparity of 10.0 %. And the comparison results further shows that the DOP model based on the dynamic FCCE models can predict the DOP of the STCC targets normally impacted by rigid conical nosed projectile.

Furthermore, the comparisons of DOP models based on the dynamic FSCE model [30] and FCCE model ($m=15$) for STCC targets with $r_0=53.5$ mm and $\delta=3.5$ mm in Ref. [4] normally impacted by 12.7 mm APP ranging from 600 m/s to 830 m/s are shown in Fig. 6.

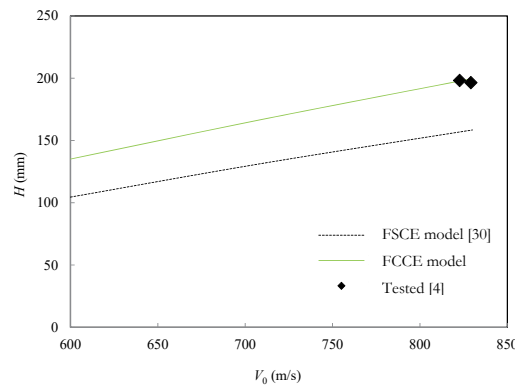


Figure 6: Comparison of the predicted models with tested results in Ref. [4].

It is shown that the DOP obtained by FCCE model are 26%–29% higher than that obtained by FSCE model with impact velocity ranging from 600 m/s to 830 m/s. Especially, for the tested STCC targets (D6#, D7#) in Ref. [4] normally impacted by 12.7 mm APP ranging from 822.7 m/s to 829.1 m/s, the DOP obtained by FCCE model agrees well with tested results with the maximum relative error about 1%, while

the relative error between tested results and the DOP obtained by FSCE model is about -25%. Therefore, the DOP model based the dynamic FCCE model is more applicable to predict the DOP of STCC targets penetrated by rigid conical projectiles with a proper value of m .

4. Conclusions

Based on the assumptions of incompressibility and H-B criterion, a dynamic FCCE model has been developed to analyze the penetrating process and stresses at cavity wall of the STCC targets, followed by a DOP model of STCC targets normally penetrated by rigid sharp-nosed projectiles. And the relevant penetration tests of STCC targets by 12.7 mm APP were used to testify the DOP model based on the FCCE model. The results of DOP for the STCC targets based on the dynamic FCCE model have the optimal consistence with those of the relevant penetration experiments in comparisons with the results based on the dynamic FSCE and Li–Chen models, which shows that under the conditions of a proper m , the DOP model based on the dynamic FCCE model is more applicable to predict the DOP of STCC targets penetrated by rigid conical or other sharp-nosed projectiles with an impact velocity below 830 m/s.

5. Acknowledgment

The research reported in the paper is part of the Natural Science Foundation of Hunan Province, China (No. 2018JJ2470) and the Project supported by National Natural Science Foundation of China (No. 51308539). The financial support is highly appreciated.

6. References

1. Kamal IM, Eltehwewy EM, 2012, Projectile penetration of reinforced concrete blocks: Test and analysis, Theoretical and Applied Fracture Mechanics, 60: 31–37.
2. Bruhl JC, Varma AH, Johnson WH, 2015, Design of composite SC wall to prevent perforation from missile impact, International Journal of Impact Engineering, 75: 75–87.
3. Tai YS, 2009, Flat ended projectile penetrating ultra-high strength concrete plate target, Theoretical and Applied Fracture Mechanics, 51: 117–128.
4. Wan F, Jiang ZG, Tan QH, Cao YYY, 2016, Response of steel-tube-confined concrete targets to projectile impact, International Journal of Impact Engineering, 94: 50–59.
5. Jiang ZG, Wan F, Tan QH, Liu F, 2016, Multi-hit experiments of steel-tube-confined concrete targets, Journal of National University of Defense Technology, 38(3): 117–123. (In Chinese)
6. Ben-Dor G, Dubinsky A, Elperin T, 2015, Analytical engineering models for predicting high speed penetration of hard projectiles into concrete shields: A review, International Journal of Damage Mechanics, 24(1): 76–94.
7. Anderson CE, 2017, Analytical models for penetration mechanics: A Review, International Journal of Impact Engineering, 108: 3–26.
8. Forrestal MJ, Warren TL, 2008, Penetration equations for ogive-nose rods into aluminum targets, International Journal of Impact Engineering, 35: 727–730.
9. Kong XZ, Wu H, Fang Q, Ren GM, 2016, Analyses of rigid projectile penetration into UHPCC target based on an improved dynamic cavity expansion model, Construction and Building Materials, 126: 759–767.
10. Forrestal MJ, Warren TL, 2009, Perforation equations for conical and ogival nose rigid projectiles into

aluminum plate targets, *International Journal of Impact Engineering*, 36: 220-225.

11. Forrestal MJ, Luk VK, Brar NS, 1990, Perforation of aluminum armor plates with conical-nose projectiles, *Mechanics of Materials*, 10: 97-105.
12. Johnsen J, Holmen JK, Warren TL, Børvik T, 2017, Cylindrical cavity expansion approximations using different constitutive models for the target material, *International Journal of Protective Structures*, 1-27.
13. Forrestal MJ, Longcope DB, Norwood FR, 1981, A model to estimate forces on conical penetrators into dry porous rock, *Journal of Applied Mechanics-Transactions of the ASME*, 48(1): 25-29.
14. Forrestal MJ, 1986, Penetration into dry porous rock, *International Journal of Solids and Structures*, 22(12): 1485-1500.
15. Forrestal MJ, Luk VK, 1992, Penetration into soil targets, *International Journal of Impact Engineering*, 21: 427-444.
16. Guo X J, He T, Wen HM, 2013, Cylindrical cavity expansion penetration model for concrete targets with shear dilatancy, *Journal of Engineering Mechanics ASCE*, 139(9): 1260-1267.
17. Yankelevsky DZ, Feldgun VR, Karinski YS, 2017, Rigid projectile penetration into a concrete medium: A new model, *International Journal of Protective Structures*, 8(3): 204141961772154.
18. Mastilovic S, Krajcinovic D, 1999, High-velocity expansion of the cavity within a brittle material, *Journal of the Mechanics and Physics of Solids*, 47: 577-610.
19. Forrestal MJ, Tzou DY, 1997, A spherical cavity-expansion penetration model for concrete targets, *International Journal of Solids and Structures*, 34: 4127-4146.
20. Macek RW. and Duffey AD, 2000, Finite cavity expansion method for near-surface effects and layering during earth penetration, *International Journal of Impact Engineering*, 24: 239-258.
21. Warren TL, Poormon KL, 2001, Penetration of 6061-T6511 aluminum targets by ogive-nosed VAR 4340 steel projectiles at oblique angles: experiments and simulations, *International Journal of Impact Engineering*, 25: 993-1022.
22. Warren TL, Hanchak SJ, Poormon KL, 2004, Penetration of limestone targets by ogive-nosed VAR 4340 steel projectiles at oblique angles: experiments and simulations, *International Journal of Impact Engineering*, 30: 1307-1331.
23. Fang Q, Kong XZ, Hong J, Wu H, 2014, Prediction of projectile penetration and perforation by finite cavity expansion method with the free-surface effect, *Acta Mechanica Solida Sinica*, 27: 597-611.
24. Chen XG, Zhang D, Yao SJ, Lu FY, 2017, Fast algorithm for simulation of normal and oblique penetration into limestone targets, *Applied Mathematics and Mechanics-English Edition*, 38(5): 671-688.
25. Zhen M, Jiang ZG, Song DY, Liu F, 2014, Analytical solutions for finite cylindrical dynamic cavity expansion in compressible elastic-plastic materials, *Applied Mathematics and Mechanics-English Edition*, 35: 1039-1050.
26. Zuo JP, Li HT, Xie HP, Peng SP, 2008, A nonlinear strength criterion for rock-like materials based on fracture mechanics, *International Journal of Rock Mechanics and Mining Sciences*, 45(4): 594-599.

27. Zuo JP, Liu HH, Li HT, 2015, A theoretical derivation of the Hoek-Brown failure criterion for rock materials, *Journal of Rock Mechanics and Geotechnical Engineering*, 7: 361–366.
28. Eberhardt E, 2012, The Hoek-Brown failure criterion, *Rock Mechanics and Rock Engineering*, 45(6): 981–988.
29. Hoek E, Martin CD, 2014, Fracture initiation and propagation in intact rock-A review, *Journal of Rock Mechanics and Geotechnical Engineering*, 6: 287–300.
30. Meng CM, Tan QH, Jiang ZG, Song DY, Liu F, 2018, Approximate solutions of finite dynamic spherical cavity-expansion models for penetration into elastically confined concrete targets, *International Journal of Impact Engineering*, 114: 182–193.
31. Warren TL, Forrestal MJ, 1998, Effect of strain hardening and strain-rate sensitivity on the penetration of aluminum targets with spherical-nosed rods, *International Journal of Solids and Structures*, 35: 3737–3753.
32. He T, Wen HM, Guo XJ, 2011, A spherical cavity expansion model for penetration of ogival-nosed projectiles into concrete targets with shear-dilatancy, *Acta Mechanica Solida Sinica*, 27(6): 1001–1012.
33. Iravani S, 1996, Mechanical properties of high-performance concrete, *ACI Materials Journal*, 93(5): 416–426.
34. Chen XW, Li QM, 2002, Deep penetration of a non-deformable projectile with different geometrical characteristics, *International Journal of Impact Engineering*, 27: 619–637.
35. Li QM, Chen XW, 2003, Dimensionless formula for penetration depth of concrete target impacted by a non-deformable projectile, *International Journal of Impact Engineering*, 28: 93–116.
36. Meng CM, Song DY, Jiang ZG, Liu F, Tan QH, 2018, Experimental research on anti-penetration performance of polygonal steel-tube-confined concrete targets, *Journal of Vibration and Shock*, 37 (13): 3–9. (In Chinese)

Ballistic performances of multi-layered Ultra-high Performance Fibre Reinforced Concrete

Y.Y.Y. Cao ¹, M. Sluijsmans ¹, Q.L. Yu ¹, H.J.H. Brouwers ¹

¹ Department of the Built Environment, Eindhoven University of Technology, the Netherlands

Abstract

The security problem of protective infrastructures is a critical consideration. Ultra-High Performance Fibre Reinforced Concrete (UHPFRC) is a newly-developed material with superior mechanical properties, and excellent damage tolerance. These characteristics make UHPFRC a potential solution for increasing the resistant capacities of the infrastructures subjected to impacts. In this study, a series of high-velocity bullet impact tests are conducted to investigate the ballistic performances of UHPFRC targets consisting of one to three layers, and the influences of the fibre re-arrangement in the layered structure on the ballistic properties are analysed. The in-service 7.62 mm bullets are used in the experiments and the impact velocity is around 830 m/s. The diameter and thickness of the UHPFRC targets are 275 mm and 90 mm, respectively. The tested UHPFRC targets have an identical total fibre content, but different fibre amounts in the individual layers. The experimental results present that steel fibres play a significant role in prohibiting the development of cracks under bullet impact, thus reducing the damage area in the front and back faces of the target. Moreover, the UHPFRC targets with two and three layers show smaller penetration depths than their single-layered counterpart, which indicates the positive effects of the layered structure on enhancing the impact resistance.

Keywords: Ultra-high performance concrete, Layered structure, High-velocity bullet impact

1. Introduction

Ensuring the security of protective infrastructures against weapons is a critical consideration in both civil and military fields. These infrastructures have a high risk of being exposed to bullet impacts generated in terrorist attacks or military activities. To improve the impact resistance of these infrastructures, utilizing Ultra-High Performance Fibre Reinforced Concrete (UHPFRC) is one of the solutions considering its ultra-high strength and outstanding damage tolerance [1–3]. Increasing attentions have been paid to study the response of UHPFRC under penetration. For example, Yu et al. [4] investigated the ballistic performances of UHPFRC targets against 7.62 mm bullets and confirmed the advantageous resistance of UHPFRC material. Sovják et al. [5,6] transportation hubs, protective or defence structures are at exposure risk to extreme load event such as blast loading or direct armed attack. This kind of loading is typical by its rapid increase in release of energy in a very short time. It is believed that emerging cementitious materials such as Engineered Cementitious Composite (ECC and Máca et al. [7] experimentally evaluated the behaviour of UHPFRC under bullet penetration and obtained that the optimal resistance can be achieved by the UHPFRC reinforced with 2% fibres.

When a concrete target is under impact, there are generally three regions in the target, as shown in Figure 1.

(1) The impact region is crushed by the bullet and a crater is generated; the stress waves after many times

of reflections inside the target result in cracks around the crater.

(2) The middle tunnel region is mainly under compression with confining pressure, and a tunnel is formed as the bullet passes by.

(3) At the rear region of the target, the compressive waves reflect to be tensile ones, causing the cracking and scabbing in the rear surface.

Previous studies suggest that adding steel fibres to Ultra-High Performance Concrete (UHPC) matrix can result in a prominent improvement of its tensile strength [8]; however, fibres contribution to the compressive strength of UHPFRC is relatively limited [9,10] limited data is available on the influence of the steel fiber length and dosage on UHPC mechanical and durability performance. Therefore, in this study, a number of UHPC mixtures with varying steel fiber lengths (8 mm (0.31 in. Considering the above two points, i.e. the stress distribution in the concrete target and the effects of fibre on the UHPFRC properties, one can suppose that fibres are not fully utilized when they are distributed in the whole volume of a UHPFRC target. Designing layered target with different fibre amounts at different regions can be one of the approaches to increase the fibre efficiency. Due to the complexity of the casting process, few studies can be found concerning layered concrete target. Among the limited studies, Quek et al. [11] developed a cementitious target containing four layers: the impact and the rear layers are reinforced with hybrid fibres, the second layer is composed of tough aggregates, and the third layer is plain mortar. Their penetration tests presented that the developed layered target has superior ballistic resistance than the plain mortar. With regards to UHPFRC, very few investigation on the penetration resistance of layered UHPFRC targets can be found in the literature. The previous study [12] conducted by the authors confirms the advantages of applying layered structure to UHPFRC under the static bending, however, the dynamic penetration response of layered UHPFRC is not addressed. Lai et al. [13] designed a double-layered UHPFRC composite with an anti-penetration layer (without fibres) and a crack resistance layer (with fibres), the investigation showed that the designed layered composite has an improved impact resistance. But the composite in their study is filled with a large amount of aggregates or fibres in the two layers respectively, i.e. it is not a UHPFRC composite in the strict meaning.

This paper presents the ballistic performances of the layered UHPFRC targets against the in-service 7.62 mm bullet. The penetration depth in UHPFRC targets with one to three layers incorporating different amounts of steel fibres are compared. The results from this paper can promote a better understanding about the effects of fibres and the layered structure on the penetration resistant capacity of UHPFRC.

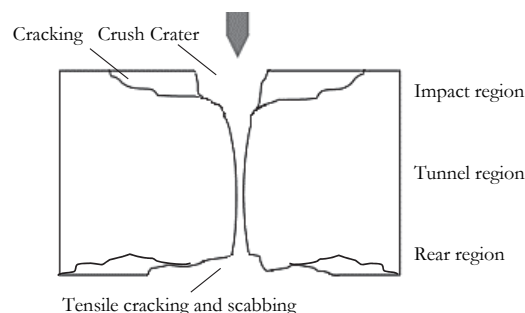


Figure 1: Illustration of a concrete target under penetration.

2. Methodology

2.1 Target design

Cylinder targets with the diameter of 275 mm and thickness of 90 mm were casted. Parameters of the designed targets are listed in Table 1, in which U0 is the plain UHPC target without fibres, UF1-3 are the

layered UHPFRC targets with one to three layers, respectively. Note that UF1-3 have the same total fibre amount, i.e. the equivalent fibre volume fraction for the three targets is 1%.

Table 1: Designed targets in the study.

Target	Layer thickness			Fibre dosage		
	Impact	Middle	Rear	Impact	Middle	Rear
	layer	layer	layer	layer	layer	layer
	mm	%				
U0	90	-	-	0	-	-
UF1	90	-	-	1	-	-
UF2	45	-	45	2	-	0
UF3	30	30	30	1.5	0	1.5

The raw materials and the recipe used for the UHPFRC target are given in Table 2. The fractions of the materials were calculated applying the Brouwers mix design method [14,15] the features of \”Japanese and Chinese Methods\” are discussed, in which the packing of sand and gravel plays a major role. Here, the grading and packing of all solids in the concrete mix serves as a basis for the development of new concrete mixes. Mixes, consisting of slag blended cement, gravel (4-16 mm. Two groups of coarse basalt aggregates were used in the target with size fractions of 2-5 mm and 5-8 mm. The straight steel fibre in the UHPFRC has a length of 13 mm and a diameter of 0.2 mm. The amounts of water and superplasticizer adding into the UHPFRC mixtures are adjusted with the fibre amount to achieve a satisfying flowability.

Table 2 Recipes of the UHP(FR)C: CEM = Portland cement I 52.5 R, LP = limestone powder, mS = micro-silica, S = sand, BA = basalt aggregate, W = water, SF = steel fiber, SP = superplasticizer.

Materials	CEM	LP	mS	S	BA 2-5	BA 5-8	W	SP	SF
	kg/m ³	kg/m ³	kg/m ³	kg/m ³	kg/m ³	kg/m ³	kg/m ³	kg/m ³	%
$V_f = 0\%$							149	9.4	0
$V_f = 1.0\%$	588	156.8	39.2	839.9	413.2	232.3	157	8.5	1.0
$V_f = 1.5\%$							157	12.5	1.5
$V_f = 2.0\%$							157	16.5	2.0

2.2 Mixing and casting

The mixing and casting of the UHP(FR)C were conducted at room temperature (20 ± 1 °C). The mixing procedure of the UHPC and the UHPFRC is given below: dry mixing of all powders and sand for 2 minutes; adding 75% of the water while mixing; after 2 minutes, adding the superplasticizer and the remaining water; mixing for 4 minutes and adding the steel fibres (for UHPFRC); mixing until the mixture is slurred; then adding the basalt aggregates and mixing for 3 minutes.

Cylindrical moulds with a diameter of approximately 275 mm were used for casting the targets. For the layered UHPFRC targets, the time interval between casting each layer is about 45 min, which is determined by considering both the experimental operability and the interfacial bond strength. More information about the casting method can be found in [12]. The cast targets were covered with plastic sheet and demoulded after 24 hours. Then the samples are curing in water at room temperature until the day of testing.

2.3 Testing methods

The experimental set-up and the 7.62 mm armour-piercing incendiary bullet utilized for the penetration tests are shown in Figure 2. The bullet was launched by the system given in Figure 2a and the impact

velocity around is 830 m/s. The target was held by a specially designed fixing frame that constrains the movement of the target, as presented in Figure 2b.

The damage level of the target is assessed by the penetration depth, which is measured as the distance from the impact surface to the deepest point in the target. In order to obtain the accurate penetration depth, the targets were cut along the axial direction by a saw cutting machine after the penetration tests.



(a) Launch system

(b) Fixing frame

(c) 7.62 mm Bullet

Figure 2: Penetration test set-up and the bullet.

3. Results and discussion

3.1 Penetration depth

The compressive strengths of the UHPC and the UHPFRC with 1 to 2% of fibres at the day of the penetration tests are within the range of 149 to 159 MPa, and the difference on the strength is too small to cause significant influences on the impact resistance. The penetration depths of the UHPFRC targets are plotted in Table 3. Note that no penetration depth is collected for U0 as the bullet went through the target, i.e. perforation occurred in the case of U0.

Table 3 Penetration depth.

Target	Velocity	Penetration depth	Note
	m/s	mm	
U0	838.9	-	perforation
UF1	838.5	62	penetration
UF2	838.0	59	penetration
UF3	836.0	54	penetration

As summarized in Table 3, the multi-layered UHPFRC target can provide a superior impact resistance and therefore results in a reduced penetration depth. To be precise, the penetration depths in UF2 and UF3 are 15% and 5% smaller than that in UF1, respectively. These reductions of the penetration depth can be attributed to the re-arrangement of the fibres in the target by the layered structure. Among the tested samples, UF3 with fibres purposefully reinforced in the impact and the rear layers archives the smallest penetration depth. In the impact region of UF3 the concentrated steel fibres, on the one hand, provide a better control of the tensile cracks in the surface and increase the tensile strength of the target; on the other hand, they work as a mesh wire to trap the travelling bullet and slow down its velocity. Moreover, fibres in the rear region of UF3 can contribute to the reduction of the cracking area caused by the tensile waves, as well as help to keep the rear surface remaining intact, which creates an additional restraint to the bullet.

3.2 Failure pattern

The failure pattern of the targets are given in Figures 3 - 6. As can be observed in Figure 3, U0 disintegrated into pieces due to the lack of fibres and the bullet perforated the target with a residual speed. The rear region of U0 is more seriously damaged than the impact region, indicating the stronger reflected tensile waves at the rear surface and a dampened tensile wave at the impact surface. The targets reinforced with steel fibres, viz. UF1-3, remained intact after the penetrations and the bullets were stopped inside the targets. Few cracks are observed in the impact and rear surfaces of UF1 and UF3 thanks to the application of fibres which inhibit the propagation of cracks. The rear surface of UF2 (Figure 5b) has some large cracks as no fibre is added in its rear layer. However, the rear layer of UF2 did not break into several pieces as U0 did, which is attributed to the reduced velocity of the bullet when it arrived at the rear layer and the constraint effects provided by the impact layer on the rear layer.

An important feature shown in Figures 5 and 6 is that cracking exhibited in the side surface of the layered targets along the interface and the crack is more obvious in the double-layered target (UF2) than in its triple-layered counterpart (UF3). As suggested by the previous study [12], the layer interface is the weakest part in the layered composite that the bond strength usually tends to be smaller than the tensile strength of the layer material. When the reflected tensile waves reach to the layer interface, cracking can occur if the amplitude of the tensile wave is higher than the bond strength. Although cracks are observed in the interface, no layer delamination occurs during the penetration tests, reflecting the rationality of the casting method. Moreover, the interface cracking process of the layered target can also promote the energy absorption of the target through the networks of micro-cracks [11], and thus contributes to the reduction of the penetration depth.

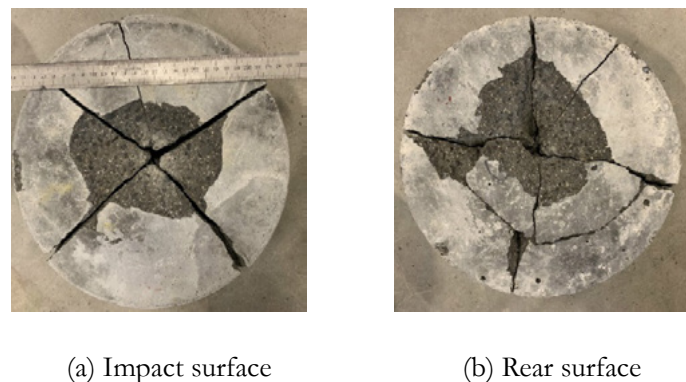


Figure 3: Failure pattern of U0.

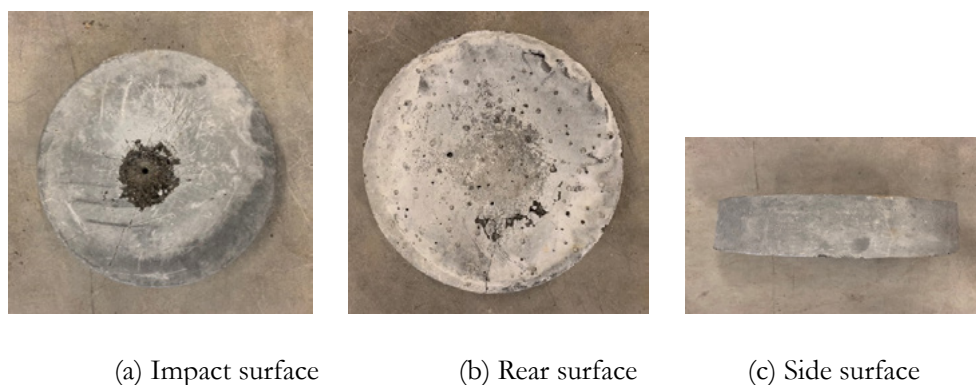


Figure 4: Failure pattern of UF1.

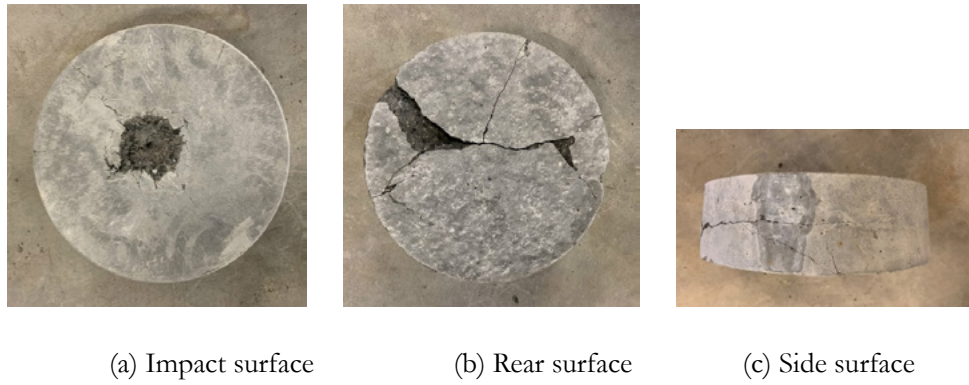


Figure 5: Failure pattern of UF2.

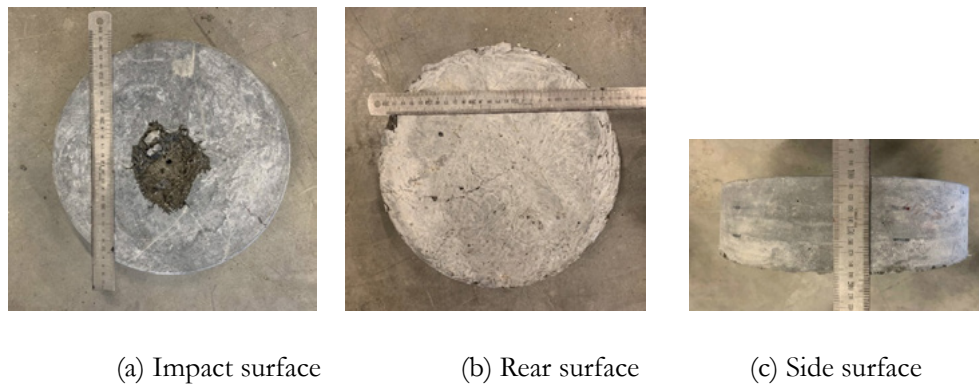


Figure 6: Failure pattern of UF3.

4. Conclusions

This study investigates the ballistic performances of layered UHPFRC targets against 7.62 mm bullet impacting at around 830 m/s. The tested UHPFRC targets have an identical total fibre content, but different fibre amounts in the individual layers. The penetration depth and the failure pattern of the tested targets are analysed in the study. The experimental results show that the UHPC target without fibres disintegrated into several pieces under the impact while the UHPFRC targets remained intact, which indicates the significance of adding fibres in the target. Moreover, the layered structure benefits the impact resistance of the UHPFRC targets, and the penetration depth in the double and triple-layered UHPFRC targets are approximately 13.8% and 8.3% smaller than its single-layered counterpart. This study promotes a better understanding about the fibres effects on the ballistic performance of UHPFRC, benefits the more efficient utilization of steel fibres in UHPFRC target, and contributes to the design of UHPFRC protective structures for both civil and military fields.

5. Acknowledgment

This research was carried out under the funding of China Scholarship Council and Eindhoven University of Technology. Furthermore, the authors wish to express their gratitude to Ing. D. Krabbenborg from the Dutch Defense Academy and the following organizations for conducting the penetration experiments: Ministerie van Defensie, Defensie Materieel Organisatie, Kenniscentrum Wapensystemen en Munitie, and Bureau Kleinkaliber.

6. References

- [1] Yu R. Development of sustainable protective Ultra-High Performance Fibre Reinforced Concrete (UHPFRC). Eindhoven University of Technology, 2015.

- [2] Li PP, Yu QL. Responses and post-impact properties of ultra-high performance fibre reinforced concrete under pendulum impact. *Compos Struct* 2019;208:806–15. doi:10.1016/j.compstruct.2018.10.071.
- [3] Cao YYY, Yu QL, Brouwers HJH, Chen W. Predicting the rate effects on hooked-end fiber pullout performance from Ultra- High Performance Concrete. *Cem Concr Res* 2019;120:164–75. doi:10.1182/blood-2016-03-705590.
- [4] Yu R, Spiesz P, Brouwers HJH. Energy absorption capacity of a sustainable Ultra-High Performance Fibre Reinforced Concrete (UHPFRC) in quasi-static mode and under high velocity projectile impact. *Cem Concr Compos* 2016;68:109–22. doi:10.1016/j.cemconcomp.2016.02.012.
- [5] Sovják R, Vavříník T, Zatloukal J, Máca P, Mičunek T, Frydrýn M. Resistance of slim UHPFRC targets to projectile impact using in-service bullets. *Int J Impact Eng* 2015;76:166–77. doi:10.1016/j.ijimpeng.2014.10.002.
- [6] Sovják R, Vavříník T, Máca P, Zatloukal J, Konvalinka P, Song Y. Experimental investigation of ultra-high performance fiber reinforced concrete slabs subjected to deformable projectile impact. *Procedia Eng* 2013;65:120–5. doi:10.1016/j.proeng.2013.09.021.
- [7] Máca P, Sovják R, Konvalinka P. Mix design of UHPFRC and its response to projectile impact. *Int J Impact Eng* 2014;63:158–63. doi:10.1016/j.ijimpeng.2013.08.003.
- [8] Nguyen DL, Ryu GS, Koh KT, Kim DJ. Size and geometry dependent tensile behavior of ultra-high-performance fiber-reinforced concrete. *Compos Part B Eng* 2014;58:279–92. doi:10.1016/j.compositesb.2013.10.072.
- [9] Abbas S, Soliman AM, Nehdi ML. Exploring mechanical and durability properties of ultra-high performance concrete incorporating various steel fiber lengths and dosages. *Constr Build Mater* 2015;75:429–41. doi:10.1016/j.conbuildmat.2014.11.017.
- [10] Savino V, Lanzoni L, Tarantino AM, Viviani M. Simple and effective models to predict the compressive and tensile strength of HPFRC as the steel fiber content and type changes. *Compos Part B Eng* 2018;137:153–62. doi:10.1016/j.compositesb.2017.11.003.
- [11] Quek ST, Lin VWJ, Maalej M. Development of functionally-graded cementitious panel against high-velocity small projectile impact. *Int J Impact Eng* 2010;37:928–41. doi:10.1016/j.ijimpeng.2010.02.002.
- [12] Cao YYY, Li PP, Brouwers HJH, Sluijsmans M, Yu QL. Enhancing flexural performance of ultra-high performance concrete by an optimized layered-structure concept. *Compos Part B Eng* 2019;171:154–65. doi:10.1016/j.compositesb.2019.04.021.
- [13] Lai J, Wang H, Yang H, Zheng X, Wang Q. Dynamic properties and SPH simulation of functionally graded cementitious composite subjected to repeated penetration. *Constr Build Mater* 2017;146:54–65. doi:10.1016/j.conbuildmat.2017.04.023.
- [14] Brouwers HJH, Radix HJ. Self-compacting concrete: Theoretical and experimental study. *Cem Concr Res* 2005;35:2116–36. doi:10.1016/j.cemconres.2005.06.002.
- [15] Wang X, Wang K, Taylor P, Morcous G. Assessing particle packing based self-consolidating concrete mix design method. *Constr Build Mater* 2014;70:439–52. doi:10.1016/j.conbuildmat.2014.08.002.

Effect of MgO, nitrate intercalated LDH and Calcined-LDH on chloride resistance of alkali-activated fly ash /slag mortar

T. Liu¹, Y. Chen¹, Q.L.Yu¹, H.J.H. Brouwers¹

¹Department of the Built Environment, Eindhoven University of Technology, 5600 MB, Eindhoven, the Netherlands

Abstract

Layered double hydroxides (LDHs) are the major secondary reaction products of alkali activated slag. The formation and absorptive performance of LDHs can be affected by factors such as the amount of magnesium oxide (MgO) and the structure of LDHs, making it possible to absorb the chloride ions Cl^- in alkali activated materials (AAMs). Meanwhile, Calcined layered double hydroxides (CLDHs) have the potential to act as a more effective chloride adsorbent than the original LDHs because of the reconstruction of LDH-like structure in AAMs matrix. The effects of MgO, LDHs- NO_3 and CLDHs on mitigating the chloride penetration in alkali activated fly ash and slag blends (AAFS) were investigated in terms of the chloride ingress in AAMs matrix. The objective is to explore the mechanism of LDHs formation with MgO, LDHs and CLDHs addition in alkali-activated materials. In this research, nitrate intercalated Mg–Al layered double hydroxide (Mg–Al-LDH- NO_3) was successfully synthesized with the co-precipitation method followed by subsequent washing and aging treatment. Calcined Mg–Al layered double hydroxide was obtained by thermal treatment of MgAl-LDH- NO_3 at 500 °C for 3 hours. The results of the rapid chloride migration test (RCM) revealed the ability of the CLDH, LDH and MgO to absorb the chloride ion in mortars. Furthermore, the microstructure of nitrate intercalated LDH and CLDH materials were analyzed by scanning electron microscopy (SEM).

Keywords: Alkali activated materials, LDH, MgO, Chloride penetration, RCM.

1. Introduction

Corrosion of steels by chloride attack plagues the durability of steel reinforced concrete, which often occurs in reinforced concrete structures built in the marine environment and saline regions. Large amounts of military and civil structures are exposed to the marine environment, and the main cause of corrosion in these concrete structures is the chloride ingress [1]. Severe corrosion, which often occurs in reinforced concrete structures, can be due to penetration of chloride ions, causing local destruction of the passive layer and leading to localized corrosion. Consequently, the usability and load bearing capacity are decreased, even leading to the failure of the structure. As a result, approximately 3.4% of the global GDP (\$2.5 Trillion USD) is spent each year to prevent and repair the infrastructure damage caused by chloride-induced corrosion [2].

To address this issue, many protecting methods to prevent chloride ingress have been discussed [3,4], for instance, adding new chemical inhibitors and applied on the surface of reinforcing bars. Layered double hydroxides (LDHs) are the typical reaction product of alkali activated slags [5], and the structure of LDHs makes it possible to adsorb the Cl^- in AAMs. MgO can promote the formation of LDHs in AAMs matrix,

which results in a higher chloride binding capacity of AAMs [6]. A higher MgO dosage (8%) leads to more hydrotalcite-like phase to form [7]. Consequently, the binding ability of chloride ion in AAMs is increased. However, one issue when using MgO in AAMs causes concerns because the hydration product of LDHs is controlled by many factors, e.g. M^{2+}/M^{3+} ratio [8], thus it is not easy to control the LDHs content in AAMs by simply adding MgO. The most common type of LDHs in nature is the mineral hydrotalcite that is a Mg–Al type LDHs intercalated with carbonate ions. The interlayer anions can be exchanged with other anions and the affinity order of anion is demonstrated by Costa et al. [9] as:



Thus, Mg–Al– NO_3 show better chloride binding ability in Ordinary Portland Cement (OPC) due to the higher affinity of chloride than nitrate [10,11]. The Mg–Al– NO_3 LDH was synthesized by Xu et al. [10], which could later exchange NO_3^- with Cl^- , therefore immobilizing chloride ion as an adsorbent. Furthermore, several methods, using LDH-like chemical products, have been developed in cement concrete structure [12]. For instance, the thermal treatment of Mg–Al– CO_3 LDH at 500 °C had been operated by Sato et al. [13]. The calcined layered double hydroxide (CLDH) shows the increased binding capacity of anions because of the reconstruction of LDH-like structure in cementitious matrix, which is shown in Fig. 1 [12].

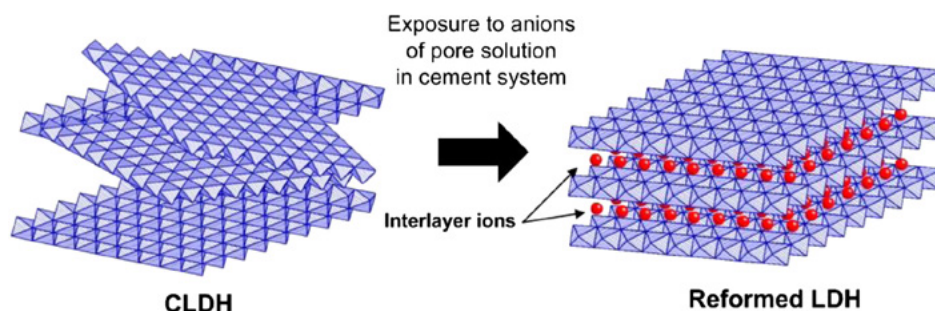


Figure 1 Schematic illustration of reforming layered structure of CLDH by adsorbing anions[12].

Yoon et al. [12] simulated the behavior of CLDHs in hardened Portland cement paste by utilizing the Langmuir's equation and Freundlich's equation. The analytic results showed the CLDHs rebuild the layered structure in a cementitious environment, thereby demonstrating the feasibility of applying CLDHs in concrete. Ke et al. [14,15] reported that the binding ability of CLDHs in sodium carbonate-activated slag pastes and mortars also showed the decreased porosity with the incorporation of 5 wt. % CLDHs, and the lower chloride migration coefficient than the samples without CLDH. In this article, the MgO, synthetic nitrate intercalated LDH and calcined LDH were utilized to replace the mass content of the AAFS binder (defined as FA + GGBS) to investigate their effects on the chloride penetration resistance of the AAFS mortars. The X-ray diffraction was applied to detect the crystalline phases of the AAFS samples. The chloride resistance was revealed by the RCM test, besides, the effects of the dosages of these materials in AAFS samples were discussed.

2. Experimental program

2.1 Materials

Class F fly ash, and ground granulated blast-furnace slag (GGBS) were utilized in this research. The chemical composition of the fly ash and GGBS were measured by X-ray fluorescence (XRF) and are shown in Table 1.

Table 1: Chemical composition of the fly ash and GGBS

Compound	MgO	Al ₂ O ₃	SiO ₂	SO ₃	K ₂ O	CaO	TiO ₂	Fe ₂ O ₃	Cl	LOI* %
Fly Ash	1.137	25.576	53.892	2.905	1.601	5.441	1.503	7.883	0.062	3.79
GGBS	9.023	13.093	31.246	5.15	0.299	39.067	1.4	0.679	0.043	1

*LOI = loss on ignition at 1000 °C

Table 2: Composition of the water glass

	SiO ₂	Na ₂ O	H ₂ O
Wt. %	27.69%	8.39%	63.92%

The activator used in this research was prepared by mixing NaOH solution and sodium silicate solution, and the SiO₂/ Na₂O molar ratio is 1.5. The composition of the water glass is shown in Table 2. MgO (96% purity) was added to replace the AAMs binder at different mass percentage (2 wt. % and 4 wt. %)

Mg-Al-NO₃ LDH was prepared by a co-precipitation method [10]. Solution A containing Mg (NO₃)₂·6H₂O and Al(NO₃)₃·9H₂O with Mg/Al molar ratio of 3.0 ($M[Mg^{2+}] + M[Al^{3+}] = 1.0 \text{ mol/L}$) and solution B containing 1.75 mol/L NaOH and 0.75 mol/L NaNO₃ were simultaneously dripped into 50 ml deionized water in a 500 mL container with magnetic stirring under N₂ atmosphere. The pH value of the mixture was maintained at 10.0±0.5. After this, the resulting suspension was aged at 65 °C for 24 h in a thermostatic bath. The final precipitate was filtered, washed thoroughly, and dried in vacuum at 90 °C for 24 h.

Calcined layered double hydroxide (CLDH) was prepared from the synthesized nitrite intercalated LDH using a heating rate of 5°C /min till 500°C and then kept constant for 3h. Afterwards the material was cooled down naturally in the furnace to 105°C before it was moved to a sealed centrifuge tube and kept in a desiccator under vacuum [14].

2.2 Sample preparation

The alkali activated samples were consisting of GGBS and fly ash, and the MgO, LDH and CLDH replaced 2 wt. % and 4 wt. % by mass of the alkali activated binder. GGBS / FA mass ratio was 7:3 (See the sample ID in Table 3). All the mortar samples were casted in the Ø 100 mm × 200 mm cylindrical moulds.

Table 3: Mix design of the mortars using different additions

Sample ID	Binder (g)					Sand (g)	Na ₂ O/Precursor	W/B*
	Slag	Fly Ash	MgO	LDHs(NO ₃)	CLDHs			
A0	70	30	-	-	-	300	7%	0.4
M2	68.6	29.4	2	-	-	300	7%	0.4
M4	67.2	28.8	4	-	-	300	7%	0.4
L2	68.6	29.4	-	2	-	300	7%	0.4
L4	67.2	28.8	-	4	-	300	7%	0.4
C2	68.6	29.4	-	-	2	300	7%	0.4
C4	67.2	28.8	-	-	4	300	7%	0.4

* W/B = Water/Binder mass ratio (where binder is defined as FA + GGBS)

2.3 Test methods

2.3.1 Scanning electron microscopy

The samples were selected from the synthetic LDH and CLDH powder. The microscopic analysis was performed using a JSM-IT100 InTouchScope™ Scanning Electron Microscope (SEM).

2.3.2 X-ray diffractometry

X-ray diffractometry (XRD) analysis was performed by using a Co tube (40kV, 30mA) with a scanning range from 5° to 90° 2θ, applying a step 0.01° and 1 s/step measuring process. The qualitative analysis was carried out by the Highscore Plus and the PDF database of ICDD.

2.3.3 Non-steady-state migration experiments

The Ø 100×100 mm cast cylinder mortars were used and cut into 50 ± 2 mm thick slice from the central portion. After sawing, brushing and washing away any burrs from the surfaces of the samples, and wiping off the excess water from the surfaces, the cylinder samples were put in the vacuum container for vacuum treatment for 3 hours with the pressure in the range of 10-50 mbar (1-5 kPa), and then immersed in the saturated Ca(OH)₂ solution for 18±2 hours. Subsequently, the non-steady-state migration experiments were tested according to the NT Build 492 [16].

The samples subjected to the accelerated NT Build 492 procedure, AgNO₃ solution was used to reveal the chloride penetration depths.

The non-steady-state migration coefficient is calculated from Equation (2):

$$D_{nssm} = \frac{0.0239(273+T)L}{\pi} \left(\frac{0.0239}{\sqrt{(273+T)L \cdot x_d}} \right) \quad (2)$$

Where:

D_{nssm} : non-steady-state migration coefficient, ×10⁻¹² m²/s;

U : absolute value of the applied voltage, V;

T : average value of the initial and final temperatures in the anolyte solution, °C;

L : thickness of the specimen, mm;

x_d : average value of the penetration depths, mm;

t : test duration, hour.

The RCM test set-up was shown in Fig. 2.



Figure 1: RCM test set-up

3. Results and discussion

3.1 Characterization of the synthetic LDH and CLDH

The X-ray diffraction patterns of the synthetic LDH and CLDH are presented in Fig. 3. Most peaks were consistent with the typical XRD patterns of $\text{Mg}_6\text{Al}_2(\text{OH})_{16}(\text{NO}_3)_2 \cdot 4\text{H}_2\text{O}$, corresponding to hydrotalcite-like phase (PDF 00-089-0460). The characteristic peak of Mg-Al-LDHs was observed at 13.6° , corresponding to crystal plane [003]. Cavani et al. [17] investigated the crystal phase of different anion intercalated hydrotalcite, which exhibited the same XRD pattern. Meanwhile, the characteristic peaks of Mg-Al-CLDH were detected at 41.2° , 51.3° and 75.6° , which were similar with the experimental results reported by Kanezaki et al. [18].

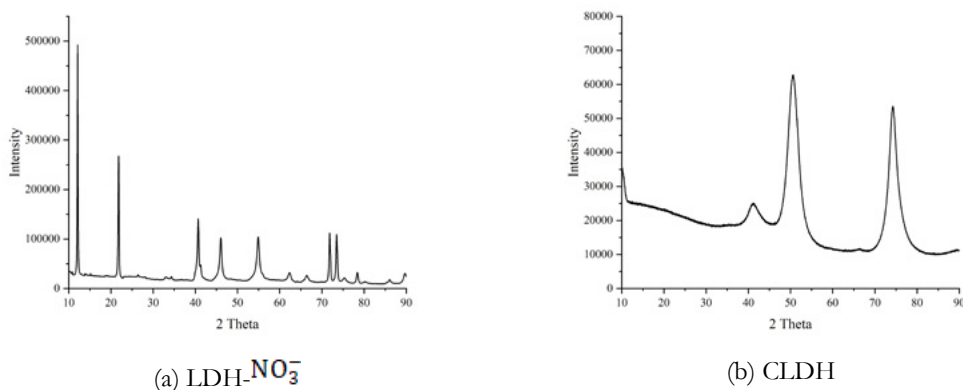


Figure 2: X-ray diffractogram and structure of LDH and CLDH

The layered structure of the LDHs and CLDHs were shown in Fig. 4. The size of the layered products LDH (Fig. 4(a)) is about $1\ \mu\text{m}$ in length, which is in agreement with the previously reported SEM micrographs [19]. The micrographs of CLDH (Fig. 4(b)) showed the layered structure without rules. And the raw CLDH in Fig. 4 (b) has plate-like particles with sharp edges [12]. Due to the non-homogeneity of the CLDHs, the formed LDH particles from reconstruction of CLDHs may not be homogeneous for all particles [12].

3.2 Hydration products of AAFS

The XRD patterns of the samples showed that the primary hydration products of C-S-H, hydrotalcite and Mullite were identified in all AAFS samples.

The main characteristic peak of hydrotalcite was identified at 13.6° . However, Ke et al. [20] reported the main peak of XRD pattern for similar hydrotalcite-like phase after filtration was centered at 11.6° . The shift in the hydrotalcite-like peak is attributed to the partly carbonation of the LDH. As we can see in Fig. 5, the

crystalline phases in the AAFS samples exhibited the same reaction products.

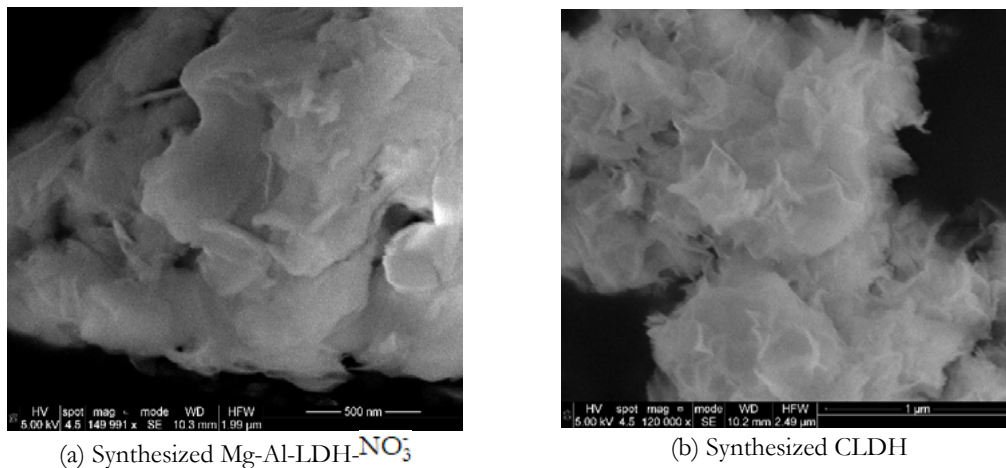


Figure 3: SEM micrographs of LDH and CLDH

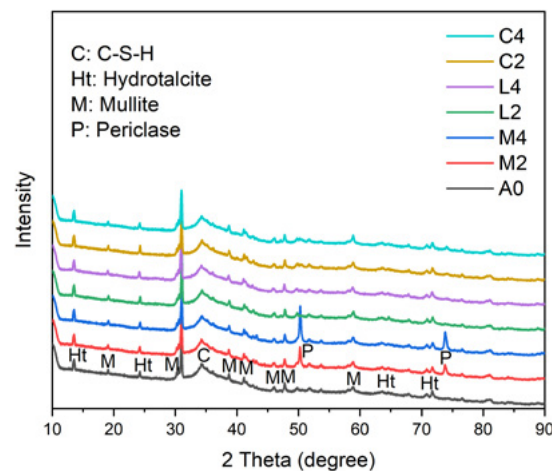


Figure 4: X-ray diffractogram of samples at 28-day curing age

Periclase was identified in specimens prepared with MgO addition (M2 and M4), which indicated that the MgO was not fully reacted with slag to form LDH [6]. However, according to previous study [7], the content of LDH formed from MgO in AAFS environment had the potential to grow over time, due to the solid phase reaction of MgO in alkali-activated cement.

The XRD patterns of L2, L4, C2 and C4 demonstrated almost the same intensity of hydrotalcite. The CLDH phase was not found in the XRD patterns while the emerged peak of hydrotalcite-like phase appeared, which proved that the CLDH completed the reconstruction process in AAFS to form the LDH [21].

3.3 Chloride resistance of AAFS

The penetration depths of the chloride in the AAFS samples confirmed a low degree of the chloride attack (shown in Fig. 6). All the ternary AAFS (M2, M4, L2, L4, C2 and C4) exhibited better chloride penetration resistances than the reference sample A0, reflected by the lower chloride diffusion coefficients of ternary AAFS samples than that of reference sample A0.

The chloride diffusion coefficients of all samples were listed in Table 4 and the chloride penetration depths were marked with the black lines in Fig. 6, where chloride penetration started in each sample from bottom to top. Moreover, the chloride diffusion coefficients (shown in Table 4) of C2 and C4 were $4.11 \times 10^{-12} \text{ m}^2/\text{s}$ and $2.88 \times 10^{-12} \text{ m}^2/\text{s}$, respectively, much lower compared to other samples. The experimental results were in line with the previous study [12], which demonstrated the CLDH in hardened AAFS paste can reduce the chloride content.

The coefficients of M2 and M4 were $4.68 \times 10^{-12} \text{ m}^2/\text{s}$ and $4.55 \times 10^{-12} \text{ m}^2/\text{s}$, respectively. And the coefficients of L2 and L4 were $6.91 \times 10^{-12} \text{ m}^2/\text{s}$ and $4.49 \times 10^{-12} \text{ m}^2/\text{s}$, respectively. It showed that the chloride banding capacity was increased with the increase of the MgO and LDH dosage. Meanwhile, the coefficient of M2 was lower than the L2 at 47.6% while M4 was higher than L4 at 1.3%, which showed that the content of LDH had an obvious influence on chloride resistance in AAFS system.

Combined with XRD results and chloride diffusion coefficients, the M2 and M4 samples had the same level of the chloride resistance with L2 and L4 at 28 days, but the MgO in M2 and M4 would continue forming the LDHs-like phase to absorb the chloride ion. The addition of CLDH in hardened AAFS could mitigate more chloride penetration than the addition of LDH and MgO.

Table 4: Chloride diffusion coefficients calculated from the RCM test in mortar cured for 28 days.

Sample ID	A0	M2	M4	L2	L4	C2	C4
Chloride diffusion coefficient ($\times 10^{-12} \text{ m}^2/\text{s}$)	5.42	4.68	4.55	6.91	4.49	4.11	2.88

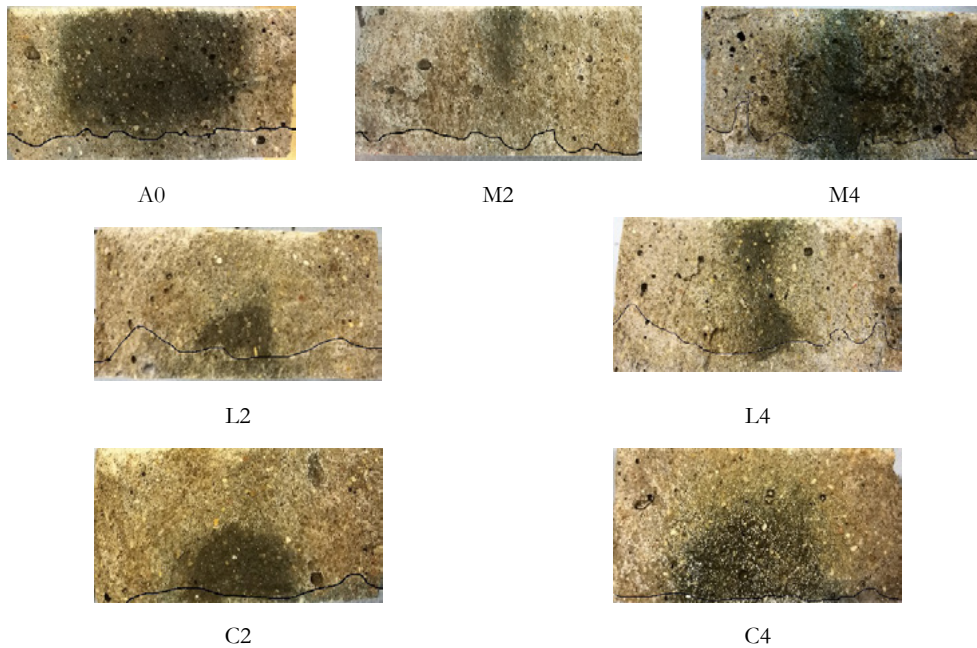


Figure 5: Boundary of chloride penetration in 28-day curing age

4. Conclusions

The effects of MgO, LDH and CLDH additions on the chloride resistance in AAFSs were examined by the XRD, SEM and RCM tests. The experimental data indicated that the ternary AAFS could resist the chloride ingress better than the slag/fly ash blends mortars.

The CLDH could reconstruct the LDH in AAFS system, however the MgO was not fully reacted in AAFS at the age of 28 days and still had potential to form more LDH in AAFS. Based on the results of this study, the MgO and CLDH have potential in preventing the chloride ingress in the AAFS.

5. Acknowledgment

This research was supported by the Department of the Built Environment at Eindhoven University of Technology. Ing. A.C.A. Delsing is acknowledged for the experimental support on analytical analysis.

6. References

- [1] C. Tennakoon, A. Shayan, J.G. Sanjayan, A. Xu, Chloride ingress and steel corrosion in geopolymer concrete based on long term tests, *Mater. Des.* 116 (2017) 287–299. doi:10.1016/j.matdes.2016.12.030.
- [2] J. Osio-Norgaard, J.P. Gevaudan, W. V. Srubar, A review of chloride transport in alkali-activated cement paste, mortar, and concrete, *Constr. Build. Mater.* 186 (2018) 191–206. doi:10.1016/j.conbuildmat.2018.07.119.
- [3] H. Tatematsu, T. Sasaki, Repair materials system for chloride-induced corrosion of reinforcing bars, *Cem. Concr. Compos.* 25 (2003) 123–129. doi:10.1016/S0958-9465(01)00059-2.
- [4] Y. Tian, C. Dong, G. Wang, X. Cheng, X. Li, Zn–Al–NO₂ layered double hydroxide as a controlled-release corrosion inhibitor for steel reinforcements, *Mater. Lett.* 236 (2019) 517–520. doi:10.1016/j.matlet.2018.10.177.
- [5] R.J. Myers, J.S.J. van Deventer, F. Puertas, R. San Nicolas, S.A. Bernal, R. Mejía de Gutiérrez, J.L. Provis, MgO content of slag controls phase evolution and structural changes induced by accelerated carbonation in alkali-activated binders, *Cem. Concr. Res.* 57 (2014) 33–43. doi:10.1016/j.cemconres.2013.12.003.
- [6] H.N. Yoon, S.M. Park, H.K. Lee, Effect of MgO on chloride penetration resistance of alkali-activated binder, *Constr. Build. Mater.* 178 (2018) 584–592. doi:10.1016/j.conbuildmat.2018.05.156.
- [7] M. Ben Haha, B. Lothenbach, G. Le Saout, W. F., Influence of slag chemistry on the hydration of alkali-activated blast-furnace slag — Part I: Effect of MgO, *Cem. Concr. Res.* 41 (2011) 955–963. doi:http://dx.doi.org/10.1016/j.cemconres.2011.05.002.
- [8] Y. Chen, Z. Shui, W. Chen, G. Chen, Chloride binding of synthetic Ca–Al–NO₃ LDHs in hardened cement paste, *Constr. Build. Mater.* 93 (2015) 1051–1058. doi:10.1016/j.conbuildmat.2015.05.047.
- [9] D.G. Costa, A.B. Rocha, W.F. Souza, S. Shirley, X. Chiaro, A.A. Leitão, Comparative Structural, thermodynamic and electronic analyses of ZnAlAn – hydrotalcite-like compounds (An – Cl –, F –, Br –, OH –, CO₃²⁻ or NO₃⁻): An ab initio study *Applied Clay Science Comparative Structural, thermodynamic and electronic analy*, *Appl. Clay Sci.* 56 (2018) 16–22. doi:10.1016/j.clay.2011.11.014.
- [10] J. Xu, Y. Song, Y. Zhao, L. Jiang, Y. Mei, P. Chen, Chloride removal and corrosion inhibitions of nitrate, nitrite-intercalated Mg–Al layered double hydroxides on steel in saturated calcium hydroxide solution, *Appl. Clay Sci.* 163 (2018) 129–136. doi:10.1016/j.clay.2018.07.023.

- [11] H. Ye, Nanoscale attraction between calcium-aluminosilicate-hydrate and Mg-Al layered double hydroxides in alkali-activated slag, *Mater. Charact.* 140 (2018) 95–102. doi:10.1016/j.matchar.2018.03.049.
- [12] S. Yoon, J. Moon, S. Bae, X. Duan, E.P. Giannelis, P.M. Monteiro, Chloride adsorption by calcined layered double hydroxides in hardened Portland cement paste, *Mater. Chem. Phys.* 145 (2014) 376–386. doi:10.1016/j.matchemphys.2014.02.026.
- [13] T. Sato, T. Wakabayashi, M. Shimada, Adsorption of Various Anions by Magnesium Aluminum Oxide, *Am. Chem. Soc.* 25 (1986) 89–92.
- [14] X. Ke, S.A. Bernal, J.L. Provis, Controlling the reaction kinetics of sodium carbonate-activated slag cements using calcined layered double hydroxides, *Cem. Concr. Res.* 81 (2016) 24–37. doi:10.1016/j.cemconres.2015.11.012.
- [15] X. Ke, S.A. Bernal, O.H. Hussein, J.L. Provis, Chloride binding and mobility in sodium carbonate-activated slag pastes and mortars, *Mater. Struct. Constr.* 50 (2017). doi:10.1617/s11527-017-1121-8.
- [16] Nordtest Method, NT Build 492, (1999) 1–8.
- [17] F. Cavani, F. Trifirò, A. Vaccari, Hydrotalcite-type anionic clays: Preparation, properties and applications., *Catal. Today.* 11 (1991) 173–301. doi:10.1016/0920-5861(91)80068-k.
- [18] E. Kanazaki, A thermally induced metastable solid phase of Mg/Al-layered double hydroxides by means of in situ high temperature powder X-ray diffraction, *J. Mater. Sci. Lett.* 17 (1998) 371–374. doi:10.1023/A:1006570730849.
- [19] Y. Chen, Z. Shui, W. Chen, Q. Li, G. Chen, Effect of MgO content of synthetic slag on the formation of Mg-Al LDHs and sulfate resistance of slag-fly ash-clinker binder, *Constr. Build. Mater.* 125 (2016) 766–774. doi:10.1016/j.conbuildmat.2016.08.086.
- [20] X. Ke, S.A. Bernal, J.L. Provis, Uptake of chloride and carbonate by Mg-Al and Ca-Al layered double hydroxides in simulated pore solutions of alkali-activated slag cement, *Cem. Concr. Res.* 100 (2017) 1–13. doi:10.1016/j.cemconres.2017.05.015.
- [21] Y. Lin, Q. Fang, B. Chen, Metal composition of layered double hydroxides (LDHs) regulating ClO₄ adsorption to calcined LDHs via the memory effect and hydrogen bonding, *J. Environ. Sci. (China).* 26 (2014) 493–501. doi:10.1016/S1001-0742(13)60462-3.

Recent development on sustainable ultra-high performance concrete design with low cement consumption: a review

P.P. Li, Q.L. Yu, H.J.H. Brouwers

Department of the Built Environment, Eindhoven University of Technology, 5600 MB, the Netherlands.

Abstract - Ultra-high performance concrete (UHPC) is a relatively new building material with a relatively high consumption of cement compared to the conventional concrete, which causes the economic and environmental burdens. This paper aims to review the recently reported methods on developing sustainable UHPC with low cement consumption. The hybrid replacement by supplementary cementitious materials (SCMs), high-volume substitution by filler powders, inclusion of coarse aggregate, and two-stage casting method have been summarized. Furthermore, the thermal and chemical activation on SCMs, and the mineral plasticization effect of substitute material are discussed. Lastly, further research trends are identified.

Keywords: ultra-high performance concrete, sustainable, low cement, SCMs.

1. Introduction

Ultra-high performance concrete (UHPC) is a relatively novel cementitious construction material with excellent mechanical properties, durability and impact resistance [1]. During the past few decades, it has drawn great attention from both researchers and engineers. Richard et al. developed the reactive powder concrete (RPC) in 1993, which was characterized by a large amount of reactive powder, fine quartz powder without any coarse aggregate, very low water content and high superplasticizer dosage, utilization of steel fibre, special treatment (pre-setting pressurization and heat-treating) [2]. RPC showed a dense microstructure, excellent toughness and ultra-high strength over 150 MPa. A few years later, De Larrard proposed the term of ‘ultra-high performance concrete’ with high packing density [3]. Although, the special mix design methods of UHPC are beneficial for the excellent performance that allows to design thin and light concrete structures with long service life. They also cause problem of high binder or cement consumption, usually more than 900 kg/m² that is about 3 times more than that in conventional concrete. The large amount of cement utilization results in a high energy consumption and increased costs of UHPC material and structure, consequently limiting the engineering applications. Therefore, designing sustainable UHPC with relatively low cement consumption has been attempted by more and more researchers nowadays.

Currently, substitution of partial cement by cheaper and sustainable supplementary cementitious materials (SCMs) has been investigated to develop sustainable UHPC [4], including such as ground granulated blast slag (GGBS), fly ash, bottom ash, silica fume, glass powder etc. Yu et al. developed eco-friendly UHPC with different mineral admixtures uses, which showed better properties than the reference mixture [5]. Kang et al. used 16.5% of rice husk ash as pozzolanic admixture and internal curing agent in UHPC [6]. However, cement reduction by the traditional replacement methods is usually very limited, mostly less than 30%, to avoid sacrifice of too much properties of UHPC due to dilution effect. More efficient measures are needed to achieve much low-cost and eco-friendly UHPC with low cement content, but meanwhile without decreasing too much or even improving the performance of UHPC.

The aim of this review is to summarize the current novel methods to develop the sustainable UHPC with low cement consumption, including using ternary or quaternary SCMs, adding minerals with plasticization effect, activating weak-active binder by thermal and chemical methods, introducing coarse aggregate, casting UHPC by two-stage method. Furthermore, research needs are identified and suggestions are given.

2. Hybrid utilization of SCMs

To develop more sustainable UHPC, higher contents of cheap and eco-friendly substitution materials are desired to be utilized in UHPC system. To overcome or partly compensate the negative effect (e.g. dilution effect of cement) of SCM on the properties of UHPC, hybrid utilization of SCMs is probably a good method rather than blending a single SCM. Kang et al. found that UHPC with ternary binder (63% cement + 17% rice husk ash + 20% GGBS) even showed slightly better properties compared to the binary blends (83% cement + 17% rice husk ash), especially under the thermal curing conditions [6]. As shown in Figure 1, the workability, 28d strength and volume stability were much better, except for the slightly lower early age strength. The positive combination of GGBS and RHA was probably due to the mesoporous amorphous structure of RHA, which absorbed aqueous water at early age and thereafter provided water for further hydration for the GGBS at the later stage. Shi et al. designed UHPC with cement-silica fume-slag binder considering the hydration and microstructure [7]. It revealed that there existed optimum hybrid blending proportions between those three raw materials for the best flowability or compressive strength, as illustrated in Figure 2. They indicated that hybrid utilization of SCMs had some certain positive synergistic effects on hydration and thus improved the performance of UHPC system.

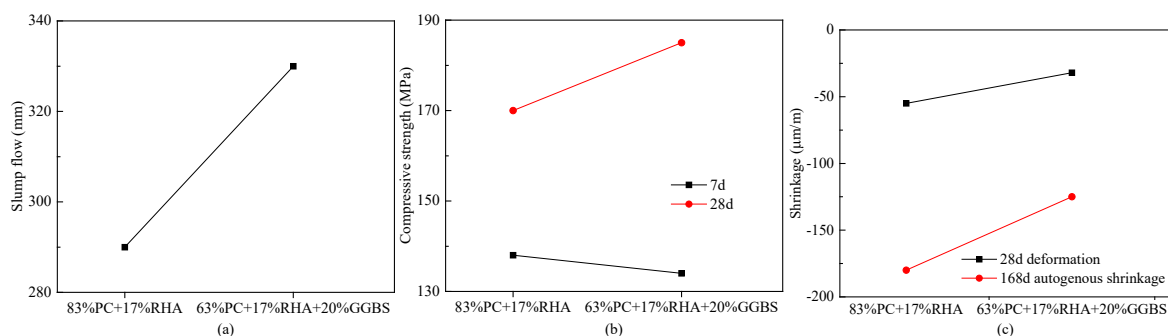


Figure 1: Properties between ternary (PC+RHA+GGBS) and binary (PC+RHA) blends [6].

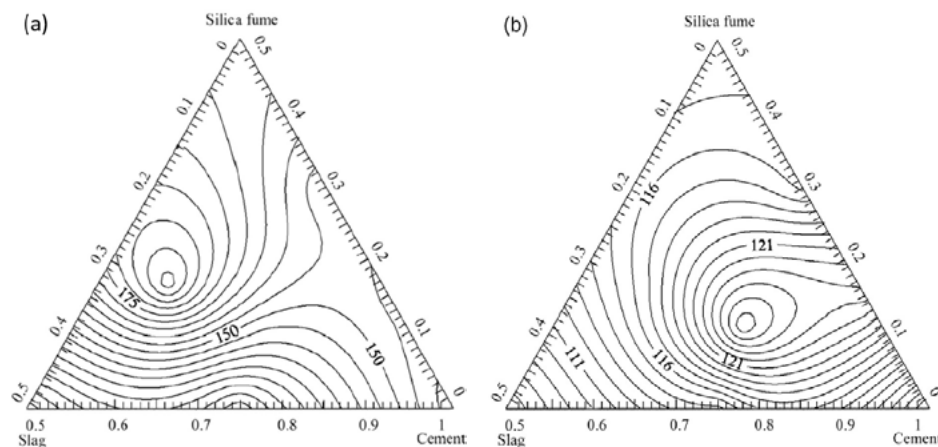


Figure 2: (a) flowability and (b) 56d compressive strength of UHPC with cement-silica fume-slag binder [7].

Arora et al. reported binder phase selection for UHPC from commonly available cement replacement and

fine filler, namely fly ash (F), slag (S), microsilica (M), metakaolin (K) and limestone (L) [8]. The strategies to select optimum binders were mainly based on packing and rheology. As shown in Figures 3, the ternary and quaternary blends, with a total cement replacement of 30%, were selected and suggested for sustainable application, which had better packing densities and rheological properties than pure cement or binary blends. After the optimization, UHPC mixtures with ternary or quaternary binders showed lower cement consumption, but only slightly lower or even higher compressive strength, as shown in Figure 4.

K ₁₀	M ₁₀	M ₂₀	F ₂₀	F ₃₀	S ₂₀	S ₃₀	
F ₁₀ K ₁₀	F ₂₀ K ₁₀	S ₁₀ K ₁₀	S ₂₀ K ₁₀	F ₁₀ M ₁₀	F ₂₀ M ₁₀	S ₁₀ M ₁₀	S ₂₀ M ₁₀
F ₂₀ L _{10a}	F ₂₀ L _{10b}	F ₂₅ L _{5a}	F ₂₅ L _{5c}	S ₂₀ L _{10a}	S ₂₀ L _{10b}	S ₂₅ L _{5a}	S ₂₅ L _{5b}
F _{17.5} K _{7.5} L _{5b}	F _{17.5} K _{7.5} L _{5c}	F _{17.5} M _{7.5} L _{5b}	F _{17.5} M _{7.5} L _{5c}	S _{17.5} K _{7.5} L _{5b}	S _{17.5} K _{7.5} L _{5c}	S _{17.5} M _{7.5} L _{5b}	S _{17.5} M _{7.5} L _{5c}

Figure 3: UHPC matrix selection based on packing and rheology. The subscript numbers represent the % by mass of SCMs replacing cement [8].

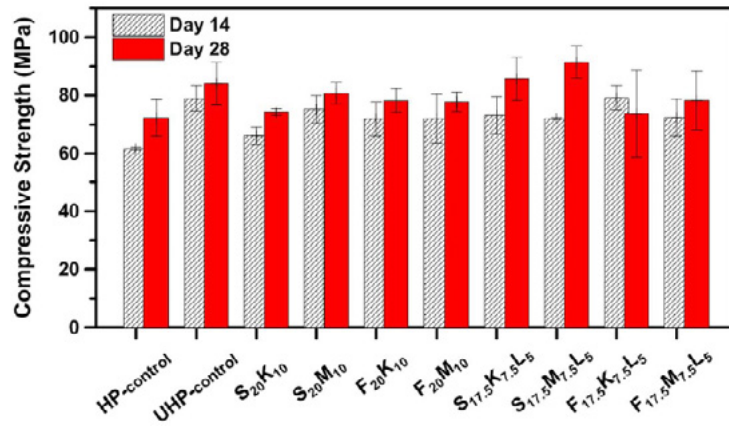


Figure 4: Compressive strength of UHPC with ternary and quaternary blends [8].

To further prove the hybrid benefit of SCMs, our study proposed to evaluate the synergy of quaternary blends (cement-slag-silica-limestone) compared to binary (cement-slag) and ternary binders (cement-silica-limestone),

$$synergy = \frac{(X_{ref} - X_B) + (X_{ref} - X_T)}{X_{ref} - X_Q} - 1 \quad (1)$$

where X represents the properties of UHPC pastes, and subscripts represent the mixtures with reference cement (ref), binary (B), ternary (T) and quaternary (Q) binders. A positive synergy (>0) indicates that quaternary blends have less adverse influence than binary and ternary blends. Normally, positive values of synergy in terms of 28d compressive strength, fibre-to-matrix bond and total free shrinkage were observed in the sustainable UHPC pastes with quaternary binders, as shown in Figure 5. The positive synergy was probably attributed to optimized total particle size distribution and reasonable mineral composition, e.g. Ca/Si ratio.

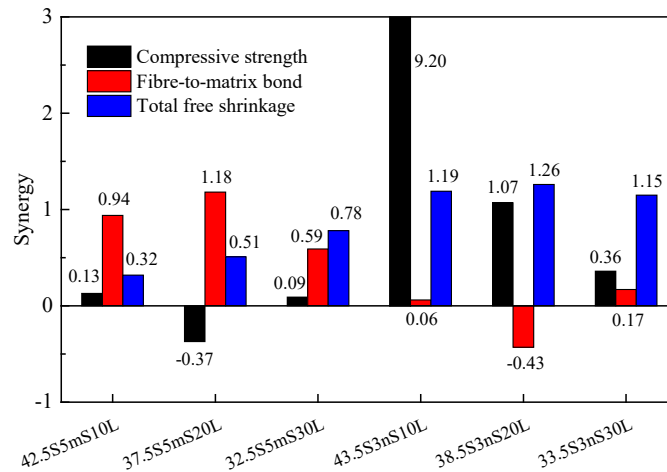


Figure 5: Synergy of quaternary binders compared to binary and ternary ones (S = slag, mS = micro-silica, nS = nano-silica, L = limestone, the number in mixture name means % by mass of SCMs replacing cement).

To sum up, hybrid utilization of SCMs such as ternary and quaternary binders is more appropriate to design sustainable UHPC instead of simple binary blends, due to the positive synergetic effect on hydration kinetics, optimization of mineral composition, whole packing density, rheology behaviour and even internal curing.

3. Mineral additions with plasticization effect

UHPC is characterized as relatively high superplasticizer dosages, in order to decrease the low water amount and the porosity, thus increase the packing density, microstructure and mechanical properties. Therefore, it is potentially desirable to use some mineral additions that possess plasticization effect to replace cement in sustainable UHPC, in order to decrease the water demand and compensate the probable negative dilution effect. Some carbonate fillers, e.g. limestone powder, show good plasticization effect, which can greatly enhance the workability of concrete [9,10]. Even though, limestone powder has negative dilution effect on cement because of its limited solubility and reactivity, the function as a mineral plasticizer can reduce the water demand to obtain a desirable flow ability. A less water utilization tends to a better compactness, which can overcome or partly compensate the negative dilution effect.

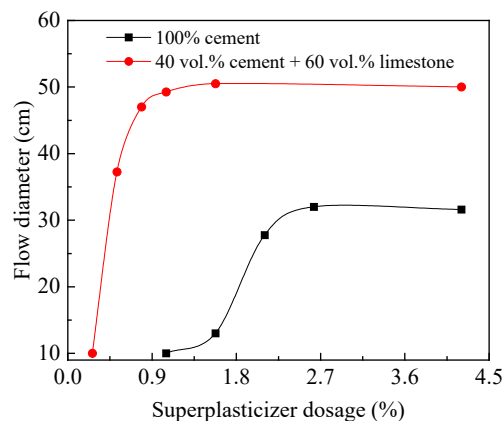


Figure 6: Spread flow of cement-limestone pastes (water = 200 kg/m³).

Figure 6 shows the spread flow of cement-limestone paste with a fixed water content (200 kg/m³). Replacing cement by high-volume limestone fillers, e.g. 60 vol.%, the mini-slump flow was significantly enhanced. In addition, the saturation dosage of superplasticizer was greatly decreased from about 2.3% to 0.7% by the

mass of powder. In other words, high-volume limestone powder substitution could not only decrease the cement consumption, but also improve the compactness by largely reducing both water content and superplasticizer dosage. Furthermore, a lot of cement grains were not completely hydrated due to the very low water-to-cement ratio. Limestone powder addition could increase the hydration degree of cement because of the increased water-to-cement ratio, as proven in Figure 7(a) [11]. The improved compactness and hydration degree contributed to higher compressive strength with 34% and 54% limestone powder, while a slightly lower strength with a further higher amount of limestone powder, e.g. 74%, as shown in Figure 7(b) [11]. It can be concluded that some minimal additions with good plasticization effect can be used to replace high volume of cement in sustainable UHPC.

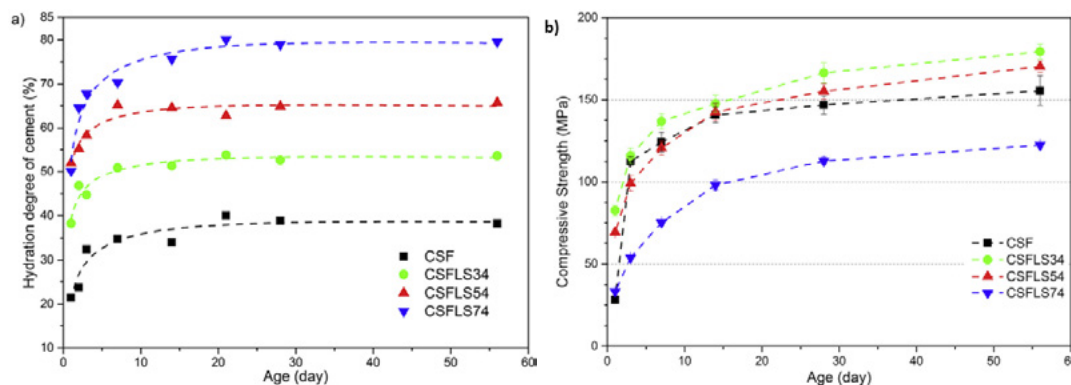


Figure 7: (a) hydration degree and (b) compressive strength of UHPC with limestone powder [11].

4. Thermal and chemical activation

If too much SCM is used, the performance usually tends to decrease. Abdulkareem et al. used GGBS to replace cement with 30%, 50% and 80% by the volume [12,13]. As shown in Figure 8, 50% and 80% volume-substitution rates caused a considerable reduction on compressive strength development. The negative influence was mainly attributed to the dilution of the more reactive cement and alkali environment. Hence, activations on the hydration of SCM and cement by increased thermal and alkaline environments are probably efficient solutions.

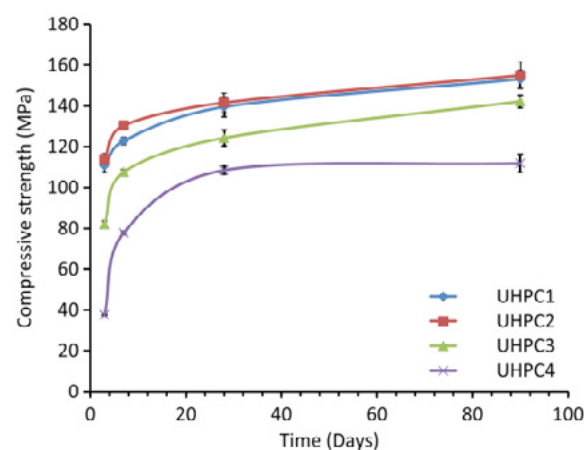


Figure 8: Compressive strength of UHPC with different contents of GGBS, the volume-substitution rates of cement by GGBS are 0, 30%, 50%, 80% for UHPC1, UHPC2, UHPC3 and UHPC4, respectively [13].

When different contents of alkalis (e.g. KOH) were added in UHPC with large amounts of slag, the compressive strength could be improved, especially at early ages, as shown in Figure 9. Slag particles reacted rapidly and promoted the formation of hydrates. More hydration products were generated to fill the

porosity and improve the strength in alkali-activated UHPC. In addition, relatively low content of KOH, namely 3.39 kg/m³, seemed to be enough to activate the combined binders. And further higher contents only showed effect on 3 days strength instead of later strength development.

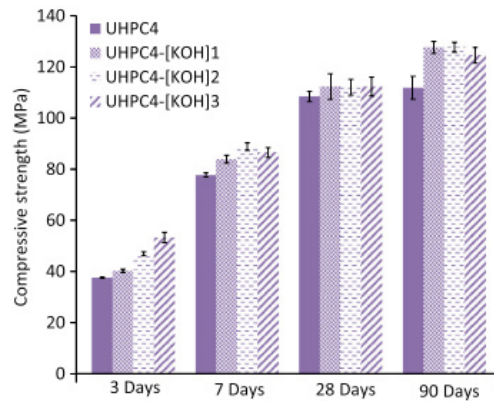


Figure 9: Compressive strength of UHPC with chemical activation, the used concentrations are 3.39 kg/m³, 6.78 kg/m³ and 10.17 kg/m³ for [KOH]₁, [KOH]₂ and [KOH]₃, respectively [13].

The sustainable UHPC incorporating high content of GGBS can also be activated by high temperatures curing. Figure 10 shows the 90 days compressive strength of sustainable UHPC with GGBS, by using a thermal curing with 90 °C from 48 h to 72 h after mixing. Compared to the results in Figure 8, the thermal activation significantly enhanced the compressive strength, attributed to the faster hydration reaction rate of both cement and slag under higher temperatures. Furthermore, the thermal-activated UHPC with a high content of GGBS could even acquire a higher mechanical strength than the reference without any GGBS.

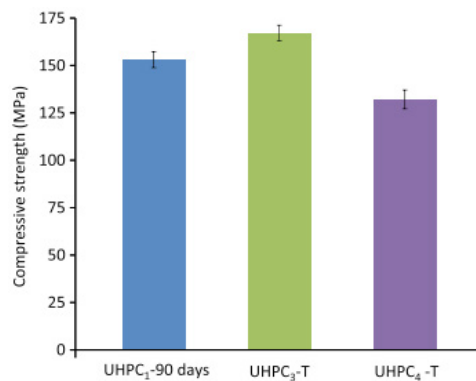


Figure 10: 90 days compressive strength of UHPC with thermal activation, a temperature of 90 °C is applied from 48 h to 72 h after mixing [13].

5. Introducing coarse aggregates

The aggregate-to-powder ratio is another key factor to determine the cement consumption. Traditional UHPC is usually developed without utilizing any coarse aggregate. Recently, coarse aggregates are attempted to be introduced into UHPC system, in order to reduce the powder content, as well as strengthen the impact resistance [14,15] and volume stability [16]. Liu et al. investigated the content effect of coarse aggregate with the particle size between 8 mm to 20 mm on tensile behaviour of UHPC, as shown in Figure 11 [17]. With the increase of coarse aggregate content up to 40%, both first-crack and maximum tensile strength tended to have a decrease. But considering the benefits of coarse aggregate on powder reduction, the strength decrease was tolerable.

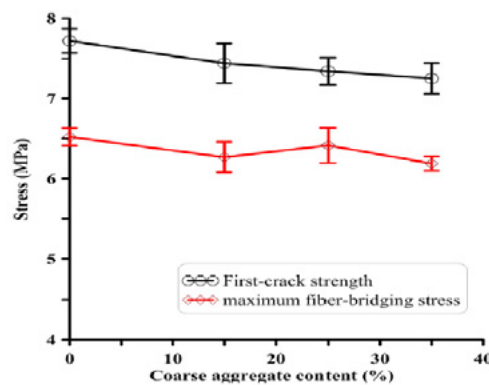


Figure 11: Tensile properties of UHPC on coarse aggregate content [17].

Our previous study investigated the size effect of coarse aggregate on properties of UHPC [18]. The basalt aggregates were selected to match the high-strength of UHPC matrix. As illustrated in Figure 12, the optimum powder content was diminished from 800 kg/m³ to 700 kg/m³, when the maximum basalt aggregates size increased from 8 mm to 16 mm. It revealed that less powder/cement content was demanded for UHPC incorporating coarser aggregates. Although the powder consumption was reduced (Figure 12(b)), the compressive strength was still comparable to the mixture with more powder content and finer aggregates in Figure 12(a). With the inclusion of coarse aggregates, the optimal particle size distribution and compactness could be changed, resulting in less powder demand but comparable strength [18].

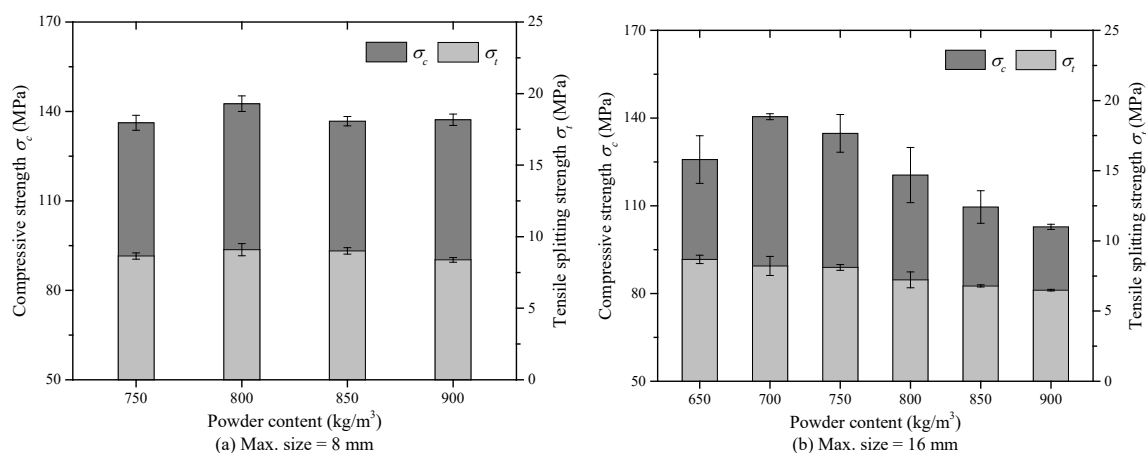


Figure 12: strength of UHPC with different powder contents [18].

6. Two-stage casting method

As analysed above, utilization of coarse aggregates is an efficient way to design sustainable UHPC with low cement consumption. However, the aggregates normally occupy rather limited volume, around 36% of total UHPC mixture [19]. How to increase the granular skeleton volume and decrease the powder content is still an issue in UHPC system. Two-stage concrete (TSC) is a type of concrete that makes full potential to enlarge the volume of aggregate [20]. The coarse aggregates are firstly pre-placed in the concrete mould, then grout is injected into the voids between the aggregates by gravity pressure, as illustrated in Figure 13 [21]. The volume of coarse aggregate skeleton could easily achieve 55% based on the drying packing density of coarse aggregates themselves, which is much higher than that in the conventional UHPC.

Thus, it is of great interest to develop low-cement UHPC by the two-stage casting method. To meet the requirement of high strength in two-stage UHPC, high strength coarse and ultra-high performance grout are needed. Our research showed that the concept of two-stage UHPC was successfully designed with very low cement consumption between 340 kg/m³ and 450 kg/m³, and compressive strength between

120 MPa-150 MPa. Figure 14 shows the binder (mainly cement) efficiency of TS-UHPC that was defined as compressive strength normalized by binder amount. The designed TS-UHPC achieved the advantages of both UHPC (high strength) and TSC (low binder consumption), resulting in a relatively high binder efficiency between 0.19 MPa/(kg/m³) and 0.42 MPa/(kg/m³).

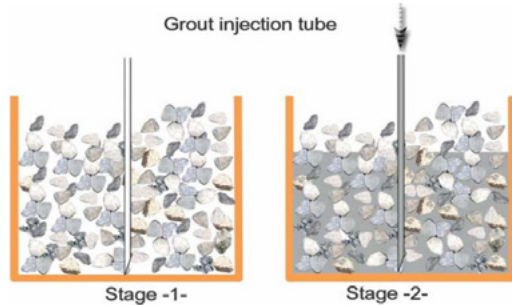


Figure 13: Casting procedure of two-stage concrete [21].

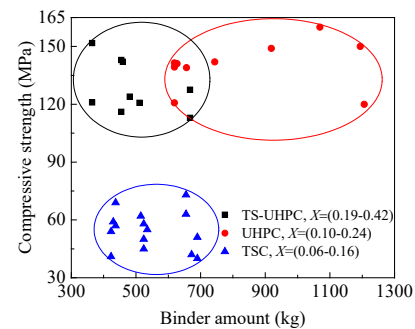


Figure 14: Binder efficiency of TS-UHPC.

7. Conclusions and recommendations

Based on the reviews and discussions above, the following conclusions can be drawn:

1. Appropriate ternary and quaternary blends with SCMs have positive synergistic effect on both fresh and hardened properties of UHPC with low cement, due to improved particle packing, mineral proportion, hydration production and microstructure.
2. Certain minerals possessing plasticization effect, e.g. limestone powder, can be used to replace cement in sustainable UHPC without sacrificing properties, attributed to the less water and superplasticizer demands.
3. Thermal curing and alkalis addition are efficient to activate the hydration and then compensate the negative dilution effect, when a high volume of SCMs is used to partly substitute cement in UHPC.
4. Introducing coarse aggregates in UHPC is an efficient attempt to reduce the powder demand. Although coarser aggregates tend to decrease the mechanical strength of UHPC, appropriate contents and particles sizes would limit the negative influences.
5. The concept of two-stage UHPC is successfully designed with very low cement consumption between 340 kg/m³ and 450 kg/m³, and compressive strength between 120 MPa-150 MPa.

Based on the previous studies, the following researches need to be further investigated to develop sustainable UHPC with low cement consumption:

1. More ternary and quaternary binders for UHPC are needed to be developed for sustainable UHPC, considering not only mechanical strength but also durability.
2. More raw materials possessing mineral plasticization effect should be investigated, under the condition of lower water amount and superplasticizer.
3. The thermal and chemical activations adversely increase the cost and energy consumption. Hence, efficient thermal curing regimes and optimum alkalis contents should be proposed by considering both cost and performance of UHPC, in the cases of different SCMs conditions. And the compatibility between superplasticizer and chemical activation also should be carefully researched.

4. More possible materials for granular skeleton in TS-UHPC need to be researched, such as ceramic or metal to improve some special properties, e.g. impact resistance.

8. Acknowledgment

The research was carried out with funding by the China Scholarship Council and Eindhoven University of Technology.

9. References

- [1] Wang D, Shi C, Wu Z, Xiao J, Huang Z, Fang Z. A review on ultra high performance concrete: Part II. Hydration, microstructure and properties. *Constr Build Mater* 2015;96:368–77.
- [2] Richard P, Cheyrezy M. Composition of reactive powder concretes. *Cem Concr Res* 1995;25:1501–11.
- [3] de Larrard F, Sedran T. Optimization of ultra-high-performance concrete by the use of a packing model. *Cem Concr Res* 1994;24:997–1009.
- [4] Shi C, Wu Z, Xiao J, Wang D, Huang Z, Fang Z. A review on ultra high performance concrete: Part I. Raw materials and mixture design. *Constr Build Mater* 2015;96:368–77.
- [5] Yu R, Spiesz P, Brouwers HJH. Development of an eco-friendly Ultra-High Performance Concrete (UHPC) with efficient cement and mineral admixtures uses. *Cem Concr Compos* 2015;55:383–94.
- [6] Kang SH, Hong SG, Moon J. The use of rice husk ash as reactive filler in ultra-high performance concrete. *Cem Concr Res* 2019;115:389–400.
- [7] Shi C, Wang D, Wu L, Wu Z. The hydration and microstructure of ultra high-strength concrete with cement–silica fume–slag binder. *Cem Concr Compos* 2015;61:44–52.
- [8] Arora A, Aguayo M, Hansen H, Castro C, Federspiel E, Mobasher B, et al. Microstructural packing- and rheology-based binder selection and characterization for Ultra-high Performance Concrete (UHPC). *Cem Concr Res* 2018;103:179–90.
- [9] Bentz DP, Ferraris CF, Jones SZ, Lootens D, Zunino F. Limestone and silica powder replacements for cement: Early-age performance. *Cem Concr Compos* 2017;78:43–56.
- [10] Kang SH, Jeong Y, Tan KH, Moon J. The use of limestone to replace physical filler of quartz powder in UHPFRC. *Cem Concr Compos* 2018;94:238–47.
- [11] Huang W, Kazemi-Kamyab H, Sun W, Scrivener K. Effect of cement substitution by limestone on the hydration and microstructural development of ultra-high performance concrete (UHPC). *Cem Concr Compos* 2017;77:86–101.
- [12] Abdulkareem OM, Ben Fraj A, Bouasker M, Khelidj A. Mixture design and early age investigations of more sustainable UHPC. *Constr Build Mater* 2018;163:235–46.
- [13] Abdulkareem OM, Ben Fraj A, Bouasker M, Khelidj A. Effect of chemical and thermal activation on the microstructural and mechanical properties of more sustainable UHPC. *Constr Build Mater* 2018;169:567–77.
- [14] Peng Y, Wu H, Fang Q, Liu JZ, Gong ZM. Impact resistance of basalt aggregated UHP-SFRC/fabric composite panel against small caliber arm. *Int J Impact Eng* 2016;88:201–13.

-
- [15] Li PP, Yu QL. Responses and post-impact properties of ultra-high performance fibre reinforced concrete under pendulum impact. *Compos Struct* 2019;208:806–15.
- [16] Dittmer T, Beushausen H. The effect of coarse aggregate content and size on the age at cracking of bonded concrete overlays subjected to restrained deformation. *Constr Build Mater* 2014;69:73–82.
- [17] Liu J, Han F, Cui G, Zhang Q, Lv J, Zhang L, et al. Combined effect of coarse aggregate and fiber on tensile behavior of ultra-high performance concrete. *Constr Build Mater* 2016;121:310–8.
- [18] Li PP, Yu QL, Brouwers HJH. Effect of coarse basalt aggregates on the properties of Ultra-high Performance Concrete (UHPC). *Constr Build Mater* 2018;170:649–59.
- [19] Stengel T, Schießl P. Life cycle assessment (LCA) of ultra high performance concrete (UHPC) structures. Woodhead Publishing Limited; 2014.
- [20] Abdelgader HS. How to design concrete produced by a two-stage concreting method. *Cem Concr Res* 1999;29:331–7.
- [21] Abdelgader HS, S E-BA. Investigations on some properties of two-stage (pre-placed aggregate) concrete. NTCC2014 Int. Conf. Non-Traditional Cem. Concr., 2015.

Suitability of phenolphthalein indicator method for alkali activated concrete

O. O. Ojedokun¹, P.S. Mangat¹

¹Centre for Infrastructure Management, Materials and Engineering Research Institute, Sheffield Hallam University, Sheffield S1 1WB, UK.

Abstract

Alkali activated cementitious materials (AACM) concrete is a sustainable alternative to Portland cement PC concrete by reducing CO₂ emitted during the production of PC by 60%. Fundamental investigations on alkali activated concrete (AACM) has been on their engineering properties with less emphasis on the service life and durability properties. The carbonation effect on concrete is crucial for its service life prediction. This paper investigates the suitability of phenolphthalein indicator method to determine the carbonation front in AACM. The geopolymerisation products of AACM are different from the hydration products of PC concrete and consequently, the carbonation process of these two types of concrete is expected to be different. Three mixes of AACM 1, 2, 3 and control PC concrete were produced and cured in water ($20 \pm 2^\circ\text{C}$) for 27 days and then in laboratory air ($20 \pm 2^\circ\text{C}$, 65% R.H) for 42 days. A total of twenty-four cylindrical specimens with 50mm diameter X 60mm depth were produced. All the specimens were exposed to 5% CO₂ inside a carbonation chamber at $20 \pm 2^\circ\text{C}$ and 65% R.H for 327 days. Carbonation depths were determined by phenolphthalein indicator method on twelve specimens. Powder samples were obtained from the carbonated and non-carbonated zones of the other twelve specimens to measure the pH of the carbonated concrete and powder. Results show that the pH of the carbonation in AACM concrete and mortar are above threshold 9 while it was below 9 in PC concrete. This suggests that phenolphthalein indicator method is inappropriate to determine the carbonation of alkali activated cementitious materials (AACM) concrete

Keywords: Alkali activated cementitious materials (AACM) concrete, carbonation depths, phenolphthalein indicator method, carbonated and non-carbonated zones.

1. Introduction

Research findings show attractive attributes of alkali activated cementitious materials (AACM) concrete as a construction material over Portland cement (PC) concrete. These attributes include low CO₂ emission and energy demand during its production [1, 2], superior strength and pore properties [3], lower bound chloride ingress [4]. However, limited knowledge on the durability properties and in-service performance of AACM exists in literature. Field applications of AACM are restricted due to the limited knowledge of its structural behaviour when subjected to exposure to corrosion initiators such as carbonation.

Carbonation in PC concrete reduces the pH of its pore solution to below 9 [5, 6]. This occurs when atmospheric carbon dioxide, CO₂, dissolves in the concrete pore solution to form carbonic acid HCO₃ which then reacts with the main hydration products of concrete, Ca(OH)₂ and C-S-H, to form calcium carbonate CaCO₃ [7, 8]. The hydroxyl ion (OH)₂ within the pore solution is displaced by this reaction thereby depleting the protective passive film around the reinforcing steel in concrete. The progression of these reactions results in carbonation induced corrosion of reinforcement in the presence of oxygen and water.

AACM concrete does not contain calcium hydroxide, $\text{Ca}(\text{OH})_2$, which can react with carbonic acid, HCO_3^- , to produce calcium carbonate CaCO_3 , unlike PC concrete which has calcium hydroxide $\text{Ca}(\text{OH})_2$ as its hydration product. The reaction of atmospheric CO_2 with the geopolymerisation and hydration compounds of AACM and PC concrete respectively is dependent on the amount and type of these compounds.

The carbonated zone of PC concrete is determined by the phenolphthalein indicator test [9]. Spraying phenolphthalein solution on carbonated concrete surfaces indicates the depletion of $\text{Ca}(\text{OH})_2$ within the concrete matrix, which is not present in AACM concrete. Therefore, the use of phenolphthalein indicator method to determine the carbonation front may not give a true extent of carbonation in AACM concrete. The suitability of the phenolphthalein indicator method for AACM concrete will be addressed in this study.

The chemistry of carbonation in PC concrete is fairly well documented while limited knowledge is available for AACM concrete [10]. Like other durability properties, the carbonation of AACM is significantly influenced by its pore chemistry which is significantly different from that of PC concrete. The mechanism of carbonation in PC concrete is represented in equation 1 -3:



Bicarbonate ions are formed when CO_2 reacts with water at the carbonated zone (equation 1). These bicarbonate ions dissociate near the non-carbonated zone within the PC concrete to form carbonate ions due to the high pH of the pore solution (equation 2). The carbonate ions precipitate as calcium carbonate (CaCO_3) crystals when they react with the hydration product of PC concrete ($\text{Ca}(\text{OH})_2$) (equation 3). These crystals are present in PC concrete in two forms: vaterite and calcite, the metastable vaterite turns to calcite over time [11]. This process will continue until all the hydration product, $\text{Ca}(\text{OH})_2$, of PC concrete is consumed by the carbonate ions. The pH of PC concrete drops because of the low calcium ions present in the pore solution due to this process. The phenolphthalein test for PC concrete is suitable for detecting these chemical layers in PC concrete.

The carbonation effect on AACM concrete by using the accelerated testing method may have overestimated its actual degradation in service life [12]. A change in AACM pore solution equilibria may induce accelerated carbonation compared to under natural carbonation giving a higher apparent carbonation rate [12]. Published results on the carbonation of AACM concrete are inconsistent in comparison with PC concrete. For example, high depths of carbonation were recorded for silicate-activated blast furnace slag concrete compared with PC concrete under accelerated carbonation conditions 10-20% CO_2 and 70% R.H. [13, 14]. Other studies show that the depth of carbonation of alkali activated blast furnace slag concrete and mortar is comparable to those of PC concrete or mortar [15]. The author [15] concluded that the refinement of the pore structure of alkali activated blast furnace slag concrete is responsible for its carbonation resistance, however, a high relative humidity of 90% was used for the accelerated carbonation test which would slow the diffusion of CO_2 within the concrete matrix and invalidate the author's results.

The rate of carbonation in concrete is a slow process which sometimes takes years to manifest. Concrete structures in large cities are susceptible to carbonation due to human activities involving high emissions of CO_2 , up to 1% by volume of air [16]. The carbonation chamber used in the laboratory for accelerated testing was maintained at 5% CO_2 concentration, 65% relative humidity and a temperature of $20 \pm 2^\circ\text{C}$ to achieve the optimum rate of carbonation in both AACM and the control PC concrete. The diffusion parameters of the concrete pores have considerable influence on the rate of carbonation. The diffusion

rate of CO₂ within a concrete matrix is four orders of magnitude slower than O₂ when its pores are fully saturated while its diffusion remains inactive when the concrete pores are insufficiently saturated [16–18].

2. Experimental Programme

2.1 Materials and mixes

Details of AACM mixes 1, 2 and 3 and the control PC concrete are given in Table 1. AACM and PC concrete were produced from ground granulated blast furnace slag (GGBS) and ordinary Portland cement CEM 1 of grade 42.5R [19] respectively. 10 mm uncrushed gravel, 6 mm limestone and a medium grade sand of 80% particle size passing 1mm sieve were used as coarse and fine aggregates. The activator dilutions of 0%, 3.88% and 7.76% were used to prepare AACM 1, 2 and 3 mixes respectively. Liquid/binder ratio 0.47 was used for both AACM and PC concrete mixes. AACM mixes contained 2% by binder weight of shrinkage reducing admixtures (SRA) made from Alkyl-ether and 0.75% by binder weight of retarder R42 made from a blend of high grade polyhydroxycarboxylic acid derivatives. The shrinkage reducing admixture also enhances workability while the retarder reduces the setting time of AACM concrete.

Table 1: Composition of AACM 1, 2, 3 and the control PC concrete

Mix	Binder Content (%)	Fine Agg. (%)	Coarse Agg. (%)		Liquid/Binder Ratio	Activator Dilution (%)	R42	SRA
			10mm Gravel	6mm Limestone			(% by weight of binder)	
AACM 1	25	18	29.3	15.7	0.47	0	0.2	0.5
AACM 2	25	18	29.3	15.7	0.47	3.88	0.2	0.5
AACM 3	25	18	29.3	15.7	0.47	7.76	0.2	0.5
Control PC	20	26	28.9	15.5	0.47(w/c)	-	-	-

*R42 is the retarder; SRA is the shrinkage reducing admixture

2.2 Specimen preparation

The concrete specimens were cast in a 0.0625m³ (150kg) capacity Cretangle mixer. AACM and PC concrete specimens were cast in plastic cylinders of 50mm diameter X 60mm depth as shown in Fig. 1 in two layers and compacted on a vibrating table. Self-adhesive bitumen tape was fixed at the bottom of the plastic cylinder moulds before casting to prevent the concrete from pouring out (Fig. 2). The specimens were cured in the laboratory air (20 ± 2°C, 65% R.H.) for 24hrs while covered with polythene sheets. They were left in the moulds to prevent the ingress of CO₂ through the bottom face and circumference of the specimens. The specimens were wet cured for 27days at a temperature of 20 ± 2°C followed by dry curing for 42days at 65% R.H. and a temperature of 20 ± 2°C until the change in their unit weight was less than 0.2% in a 24-hour period to reduce its moisture content. The specimens were then placed inside the carbonation chamber exposed to 5% CO₂ concentration at 65% relative humidity and temperature of 50°C for 327days. After exposure to 5% CO₂ concentration for 327days, the specimens were grouped into two batches. The first batch of AACM and PC concrete specimens were used to determine the depth of carbonation with the phenolphthalein test [9]. Powder samples were collected at the carbonated and non-carbonated zones in the second batch for pH analysis. A total of 24 specimens were produced for both AACM and the control PC concrete, 6 specimens per each mix in Table 1.



Fig. 1: Casting concrete specimens in cylindrical plastic moulds



Fig. 2: Self-adhesive tape fixed at the bottom of cylindrical moulds

2.3 Test Procedure

The cylindrical specimens were removed from the carbonation chamber after 327 days exposure. These specimens were removed from their plastic moulds (sleeves) and split into halves vertically along their depths as shown by section A-A in Fig. 3. The splitting tensile strength procedure was adopted to break the cylinders into two longitudinal halves. The depth of carbonation was determined by spraying phenolphthalein on the exposed (split) surface of one broken half of each cylinder according to standard procedure [9]. However, phenolphthalein was not applied to the surface of the second half of each cylinder.

The depth of carbonation profile obtained from the first half cylinder was marked on the second half of the cylinder that was not sprayed with phenolphthalein. This was carefully chiselled out to obtain concrete chunks of the carbonated and non-carbonated zones. This procedure was performed on six specimens for each AACM and PC concrete to obtain enough concrete chunks for the test. The chunks were ground to powder and passed through a 150 μm sieve to obtain concrete powder for the carbonated and non-carbonated zones (Fig. 4).

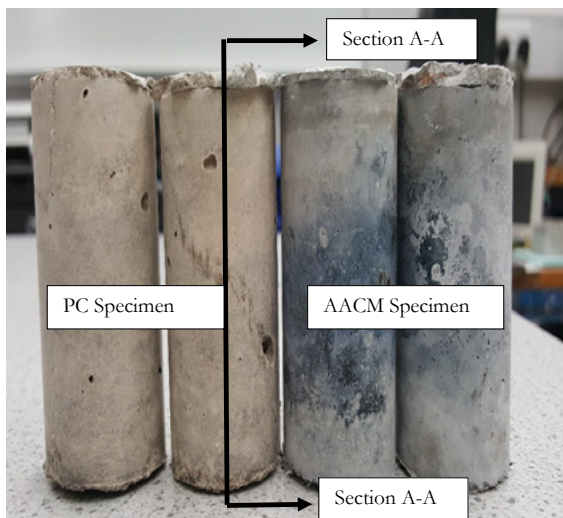


Fig. 3: Demoulded cylinders showing the section A-A of splitting concrete/mortar powder stored in air-proof plastic vials

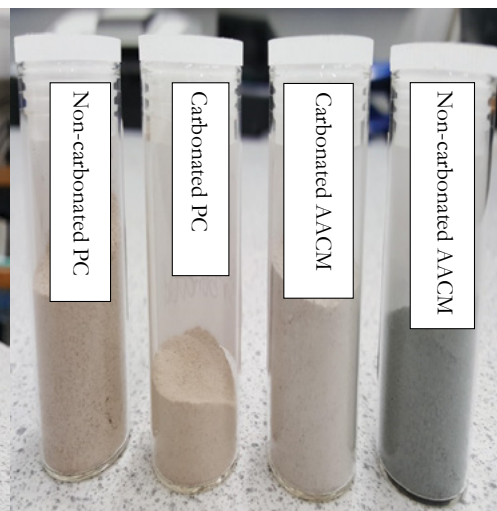


Fig. 4: AACM and OPC

A second set of powder test samples was similarly obtained by removing the coarse aggregate particles from the concrete chunks. The concrete pieces were crushed to separate the coarse aggregate particles from the matrix and they were removed by sieving. The remaining mortar material was ground to obtain mortar powder for the carbonated and non-carbonated zones. pH analysis was performed on these carbonated and non-carbonated powder samples.

2.3.1 pH Analysis

The ex-situ leaching method of concrete [20] was adopted to obtain the solution used for the pH analysis of the concrete and mortar samples. This was carried out by dissolving 5grams of the powder sample in distilled water at a liquid/solid ratio of 1:1 in an air-tight plastic vial. The solution was shaken thoroughly for 2mins to ensure a homogenous mix of the powder. The powder solution in an air-tight plastic vial was left undisturbed for 5hrs to allow for leaching. The concrete powder solution was then filtered to obtain a solution that does not contain powder particles. A double junction electrode connected to a benchtop meter 3-in-1 was dipped inside the filtered solution to measure its pH. This device measures pH ranging from 0.00 to 14.00 and can measure sample volumes as small as 0.2mL with an accuracy of ± 0.01 .

3. Results and discussion

3.1 Depth of carbonation

The carbonation depths of AACM and PC concrete is shown in Fig. 5. The carbonated and non-carbonated zones are marked on the broken faces of both AACM and PC concrete (Fig. 5).

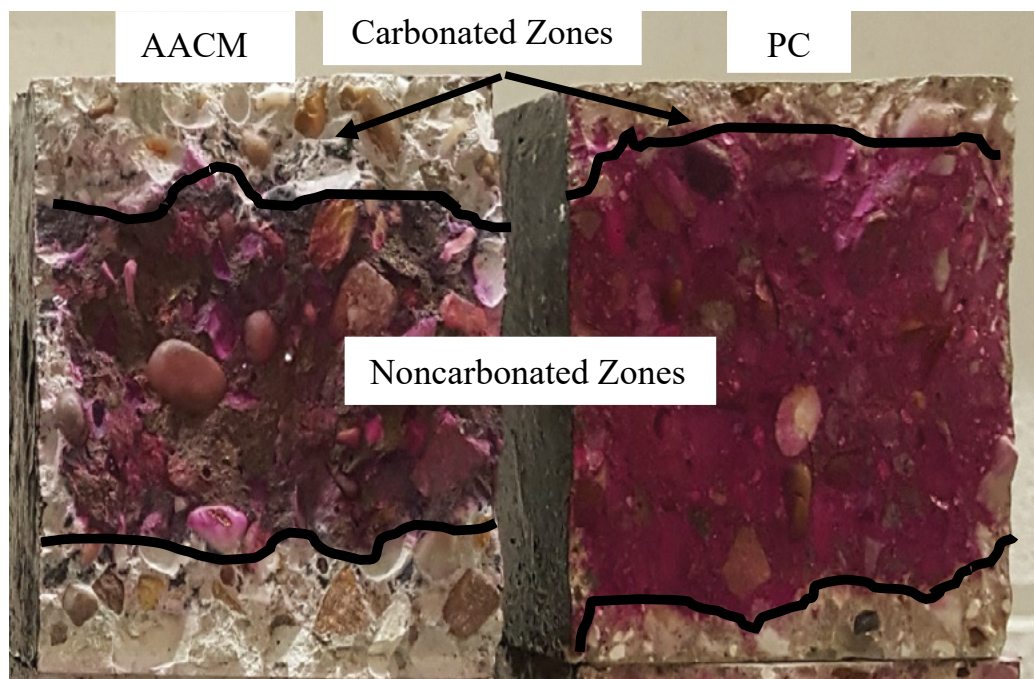


Fig. 5: showing the carbonation and non-carbonated zones in AACM and PC concrete

Fig. 5 shows that the depths of carbonation front which occurred at the two opposite faces exposed to CO_2 while the other opposite two faces coated with bitumen paint have insignificant carbonation front. This shows that the bitumen paint is an effective barrier to CO_2 diffusion in concrete. The presence of optimum moisture content and CO_2 within the concrete matrix resulted in the decalcification of the Ca-rich gel binder within the concrete matrix.

Increase in the depth of carbonation is observed in AACM concrete than the control PC concrete as shown

in Fig. 5. The average carbonation depth in AACM 1, 2 and 3 are 25.19, 26.75 and 29.25mm respectively while it is 14.13mm for PC concrete after 327days exposure.

Increase in the depth of carbonation was observed for water-glass activated slag mortar [21]. The author [21] observed a much deeper and intense carbonation between 28 and 120 days while moderate increase in the carbonation depth was observed between 120 and 240 days. The specimens were cured in a closed chamber containing K_2CO_3 solution, kept at a relative humidity of 43.2%. The chamber was saturated with CO_2 twice daily with unknown concentration of the CO_2 .

3.2 pH of carbonated zone

The pH of the powder solutions extracted from AACM and PC concrete and mortar at the carbonated zones is shown in Fig. 6.

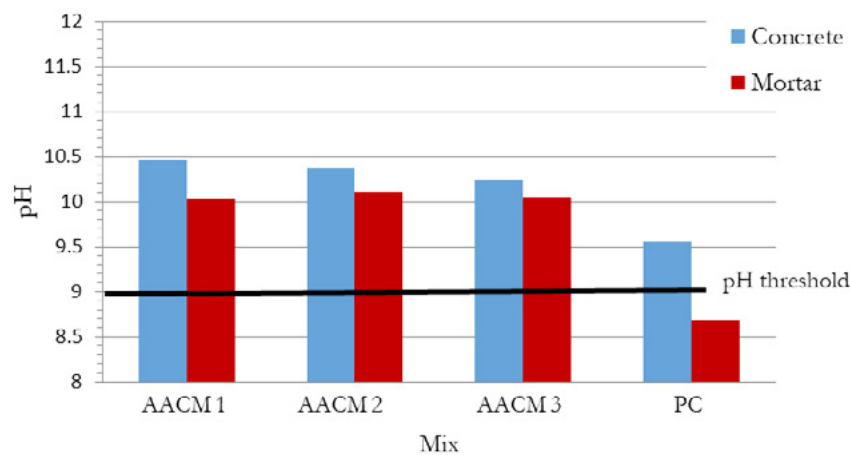


Fig. 6: pH of AACM and PC powder solutions after 327days exposure to 5% CO_2 .

The pH of the concrete powder solutions at the carbonated zones of AACM 1, 2, 3 and PC concrete are above the carbonated threshold of 9 as shown in Fig. 6. The pH values are 10.62, 10.46, 10.37, 10.25 and 9.56 for AACM 1, 2, 3 and PC concrete respectively. The pH of the mortar solution is also greater than the threshold value of 9 for all AACM mixes whereas the PC mortar has a pH value significantly lower than the threshold of 9. The high pH exceeding the carbonation threshold in AACM mortar solution is an indication that the phenolphthalein indicator method fails to detect carbonation in AACM concrete compared with PC concrete having pH of 8.69. The phenolphthalein indicator method produces no colour change when the pH of the pore solution is about 9 for PC concrete at the carbonated zone. However, in the case of AACM the phenolphthalein indicator method show no colour change when the pH of pore solution is above 10 at the carbonated zone (Fig. 6). The colourless change at the carbonated zone indicates the absence of $Ca(OH)_2$ [16]. Since $Ca(OH)_2$ is absent from the AACM pore solution, an alternative method besides using the phenolphthalein indicator method for assessing the carbonation in AACM is required.

The pH of mortar solutions at the carbonated zones for both AACM and PC are lower than that of the concrete. The pH of the mortar solutions of AACM 1, 2, 3 and PC at the carbonated zones are 10.33, 10.02, 10.1, 10.05 and 8.69 respectively. The difference in their solution pH is due to the release of alkaline content by the aggregate present in the concrete. PC concrete which had the highest aggregate content of 70.4% compared with 63% for AACM (Table 1) shows the highest pH difference between the solution extracted from concrete powder and mortar powder. The differences in pH between concrete and mortar for AACM 1, 2, 3 and PC concrete are 4.2%, 2.6%, 1.95% and 9.1% respectively.

3.3 Activator Dilution

The influence of activator dilution on the pH of powder solution from AACM concrete and mortar at the carbonated zones is shown in Fig 7.

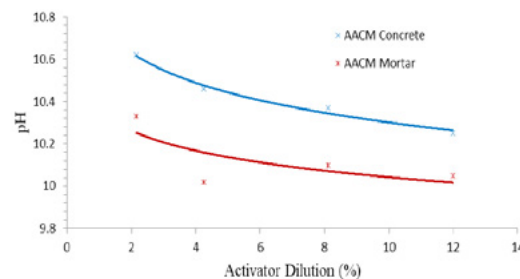


Fig. 7: Influence of activator on the pH of AACM concrete and mortar solutions at carbonated zones

The difference in the pH of solutions extracted from AACM concrete and mortar powder at the carbonated zones is fairly constant at different activator dilution (Fig. 7). This is because the aggregate content of 63% is constant in AACM 1, 2 and 3 mixes are the same (Table 1). The release of alkaline content by the aggregate present in the AACM 1, 2 and 3 accounts for the increase in the pH of solutions extracted from the AACM mortar. On the other hand, carbonation reacts chemically with AACM mortar while the aggregate in the concrete will influence the diffusion rate of CO_2 and moisture due to the interfacial transition zones around the aggregate.

The pH of solutions extracted from AACM concrete and mortar powders is highest at the lowest activator dilution (Fig. 7). The differences in the pH of AACM concrete and mortar solutions for different activator dilution are attributed to their porosity [3] which affected the rate of carbonation. AACM with 0% activator dilution has the lowest porosity of 4.64%, followed by 3.88% activator dilution which has 6.67% porosity while 7.76% activator dilution has the highest porosity of 7.71% under 3days wet curing ($20 \pm 2^\circ\text{C}$) following 24days dry curing ($20 \pm 2^\circ\text{C}$, 65% R.H) [3]. The corresponding pH values of AACM concrete are 10.46, 10.3 and 10.25. The other factor influencing the difference in pH in both AACM concrete and mortar solutions is the aggregate content. Yinghong [22] studied the leaching of alkali content of an open graded recycled coarse aggregate and the adverse effect of carbonation on the pore solution. The author [22] observed an increased pH of the pore solution due to leaching of alkali content from the recycled coarse aggregate. The alkali content of the recycled coarse aggregate is consumed during carbonation. However the release of pH-dependent constituents that cause the drop in pH is delayed by the dense structure of concrete [22]. AACM represented in Fig 7 is denser at 0% activator dilution than at 7.76% activator dilution, which is the reason for the differences between the pH of concrete solution and mortar solution at higher and lower activator dilution.

3.4 Relationship between carbonation depth and porosity

The relationship between carbonation depth at 327days exposure to 5% CO_2 and effective porosity of AACM 1, 2 and 3 mixes at 28 days is shown in Fig 8. Details of the pore properties and the effective porosity of AACM mortar mixes are reported in the authors' previous publication [3]. The following linear relationship is established between the effective porosity and the depth of carbonation with a correlation of 0.98:

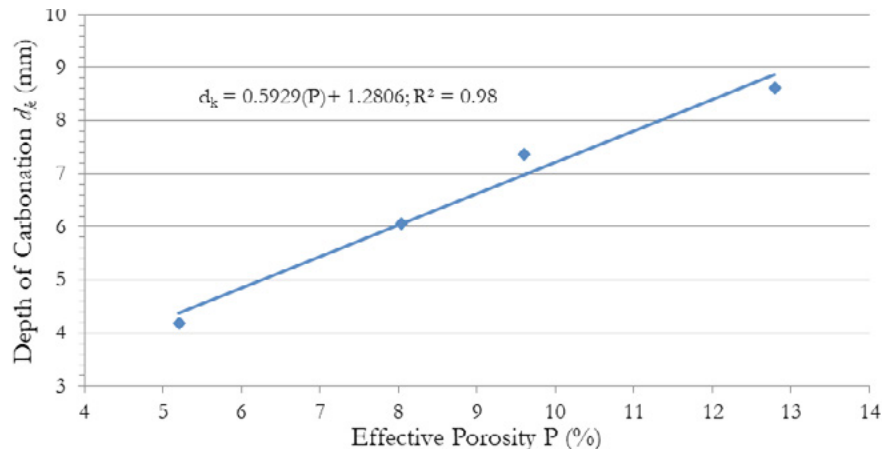


Fig. 8: The relationship between depth of carbonation d_k and effective porosity of AACM concrete

$$d_k = 0.5929(P) + 1.2806 \text{ with } R^2 = 0.98.$$

where; d_k is the depth of carbonation (mm) and P is the effective porosity (%).

The depth of carbonation increases with greater porosity. Concrete diffusivity which is a function of porosity is a major controlling factor for carbonation [16]. The ingress of CO_2 and moisture from the environment into the concrete is inhibited by decreasing porosity. The carbonation process is complicated because it involves the transport of liquid and gas which cannot be represented simply with Fick's law [23]. Lagerblad [11] stated that it is difficult to apply the Fick's law equation because of the simultaneous inward and outward diffusions involving carbonate and calcium ions. The pore structure is altered during the inward and outward diffusions involving carbonate ions and calcium ions by reacting with the concrete matrix. For PC concrete, a dense pore structure evolves as the outward diffusion of CaCO_3 forms precipitates that block the concrete pores. In the case of AACM, the calcium ions from the geopolymerization products disintegrate by a process termed decalcification and diffuse outward into the environment. Whilst the chemical compound (CaCO_3) formed during carbonation in PC concrete blocks the pores, the disintegration of calcium ion due to decalcification in AACM concrete enlarges the pores.

4. Conclusions

This paper investigates the suitability of using phenolphthalein indicator method to determine carbonation front in alkali activated concrete AACM. Twenty-four AACM and PC concrete were produced and cured in water ($20 \pm 2^\circ\text{C}$) for 27 days and then in laboratory air ($20 \pm 2^\circ\text{C}$, 65% R.H) for 42 days. These specimens were exposed to 5% CO_2 inside a carbonation chamber at $20 \pm 2^\circ\text{C}$ and 65% R.H for 327 days. Phenolphthalein indicator method was used to determine carbonation front of the AACM and PC concrete specimens. Powder samples were collected from the carbonated zones and their pH was determined. The following conclusions can be drawn from the study.

- The pH of mortar solutions at the carbonated zones for alkali activated cementitious materials (AACM) concrete is greater than the threshold of 9 while the corresponding PC mortar is below 9. For example, the pH of mortar solutions of AACM 1, 2, 3 and PC at the carbonated zones are 10.33, 10.02, 10.1, 10.05 and 8.69 respectively. This suggests that the application of phenolphthalein solution on faces of AACM produces pH higher than 9. The phenolphthalein method of determining the carbonation in AACM does not give a true representation and may not be an appropriate method for investigating the carbonation depth.
- The release of alkaline content by the coarse aggregate present in the AACM and PC concrete results in higher pH in concrete than the mortar excluding the coarse aggregate particles. The difference is

greater with increasing coarse aggregate content.

- Activator dilution with water increases the pH of carbonated AACMs (mortar and concrete). The porosity of AACMs also increases with activator dilution as they both provides a linear relationship between the two parameters. For example, AACM with 0% dilution has the lowest porosity of 4.64%, followed by 3.88% activator dilution which has 6.67% porosity while 7.76% activator dilution has the highest porosity of 7.71% under 3days wet curing ($20 \pm 2^{\circ}\text{C}$) and 24days dry curing ($20 \pm 2^{\circ}\text{C}$, 65% R.H). The corresponding pHs of AACM are 10.46, 10.3 and 10.25.
- The relationships between porosity and depth of carbonation in AACM concrete is as follows:

$$d_k = 0.5929(P) + 1.2806 \text{ with } R^2 = 0.98.$$

where; d_k is the depth of carbonation (mm) and P is the effective porosity (%).

5. Acknowledgment

The authors gratefully acknowledge the support of the Materials and Engineering Research Institute, Sheffield Hallam University and the funding provided to the second author for postgraduate study by the Tertiary Education Trust Fund, Ministry of Education, Federal Republic of Nigeria. The authors also acknowledge the award by the UK - India Newton - Bhabha programme through funding provided by Innovate UK, EPSRC (EP/P026206/1) and the Government of India for research on alkali activated cementitious materials AACMs.

6. References

1. Scrivener KL, Kirkpatrick RJ (2008) Innovation in use and research on cementitious material. *Cem Concr Res* 38:128–136. <https://doi.org/10.1016/j.cemconres.2007.09.025>
2. Madloul NA, Saidur R, Hossain MS, Rahim NA (2011) A critical review on energy use and savings in the cement industries. *Renew. Sustain. Energy Rev.* 15:2042–2060
3. Mangat PS, Ojedokun OO (2018) Influence of curing on pore properties and strength of alkali activated mortars. *Constr Build Mater* 188:337–348. <https://doi.org/10.1016/j.conbuildmat.2018.07.180>
4. Mangat, P.S. and Ojedokun OO (2019) Bound chloride ingress in alkali activated concrete. *Constr Build Mater* 212:375–387. <https://doi.org/https://doi.org/10.1016/j.conbuildmat.2019.03.302>
5. Ho DWS, Lewis RK (1987) Carbonation of concrete and its prediction. *Cem Concr Res.* [https://doi.org/10.1016/0008-8846\(87\)90012-3](https://doi.org/10.1016/0008-8846(87)90012-3)
6. Papadakis VG, Fardis MN, Vayenas CG (1992) Effect of composition, environmental factors and cement-lime mortar coating on concrete carbonation. *Mater Struct* 25:293–304. <https://doi.org/10.1007/BF02472670>
7. Hobbs DW (2001) Concrete deterioration: causes, diagnosis, and minimising risk. *Int Mater Rev* 46:117–144. <https://doi.org/10.1179/095066001101528420>
8. Johannesson B, Utgenannt P (2001) Microstructural changes caused by carbonation of cement mortar. *Cem Concr Res* 31:925–931. [https://doi.org/10.1016/S0008-8846\(01\)00498-7](https://doi.org/10.1016/S0008-8846(01)00498-7)
9. BS EN 14630 (2006) Products and systems for the protection and repair of concrete structures — Test methods — Determination of carbonation depth in hardened concrete by the phenolphthalein method

10. John L. Provis, Deventer JSJ van (2014) Alkali-Activated Materials State-of-the-Art Report, RILEM TC 224-AAM
11. Lagerblad B (2005) Carbon dioxide uptake during concrete life cycle – State of the art
12. Bernal SA, Provis JL, Brice DG, et al (2012) Accelerated carbonation testing of alkali-activated binders significantly underestimates service life: The role of pore solution chemistry. *Cem Concr Res* 42:1317–1326. <https://doi.org/10.1016/j.cemconres.2012.07.002>
13. Byfors K, Klingstedt G, Lehtonen V, et al (1989) Durability of Concrete Made With Alkali-Activated Slag. In: Third International Conference Proceedings. Fly Ash, Silica Fume, Slag, and Natural Pozzolans in Concrete. pp 1429–1466
14. Bakharev T, Sanjayan JG, Cheng Y-B (2001) Resistance of alkali-activated slag concrete to carbonation. *Cem Concr Res* 31:1277–1283
15. Deja J (2002) Carbonation aspects of alkali activated slag mortars and concretes. *Silic Ind* 37–42
16. Neville AM (2011) Properties of Concrete. Pearson Education Limited
17. Papadakis VG, Vayenas CG, Fardis MN (1991) Experimental Investigation and Mathematical-Modeling of the Concrete Carbonation Problem. *Chem Eng Sci* 46:1333–1338. [https://doi.org/10.1016/0009-2509\(91\)85060-b](https://doi.org/10.1016/0009-2509(91)85060-b)
18. Houst YF (1996) The role of moisture in the carbonation of cementitious materials TT - Bauinstandsetzen und Baudenkmalpflege: eine internationale Zeitschrift. *Restor Build Monum an Int J = Bauinstandsetz und Baudenkmalpfl eine Int Zeitschrift* 2:67–82
19. BS EN 206 (2014) Concrete — Specification, performance, production and conformity. British Standards Institution
20. Plusquellec G, Geiker MR, Lindgard J, et al (2017) Determination of the pH and the free alkali metal content in the pore solution of concrete: Review and experimental comparison. *Cem Concr Res* 96:13–26. <https://doi.org/10.1016/j.cemconres.2017.03.002>
21. Puertas F, Palacios M, Vázquez T (2006) Carbonation process of alkali-activated slag mortars. *J Mater Sci*. <https://doi.org/10.1007/s10853-005-1821-2>
22. Qin Y, Yang H (2015) Carbonation dominates the acid intake of recycled concrete aggregate subjected to intermittent leaching. *Constr Build Mater* 89:110–114. <https://doi.org/10.1016/j.conbuildmat.2015.04.038>
23. Collepardi, M., Marcialis, A, and Turriziani R (1970) The Kinetics of Chloride ions Penetration in Concrete. *II Cem* 67:157–164

Activation of binary binder containing fly ash and cement with red mud as alkali source and application in controlled low strength materials

B. Yuan¹, S. Yuan^{1,2}, C. Straub³, W. Chen^{1,2}

¹ Wuhan University of Technology, 1School of Material Science and Engineering

² State Key Lab of Silicate Materials for Architectures

³ Eindhoven University of Technology, Department of the Built Environment

Email of the corresponding author: chen.wei@whut.edu.cn

Abstract

The feasibility of using red mud as alkali source in alkali-activated fly ash and cement based binary binder for controlled low strength material (CLSM) is investigated. The red mud contains NaOH and Na₂CO₃ that can be used as the alkali source. The incorporation of red mud increases the pH of pore solutions in the mixtures by the direct dissolution of NaOH and the reaction of Na₂CO₃ with portlandite released from the cement hydration. The increased pH accelerates the hydration of the fly ash cement binary binder, contributing to the strength development. The red mud also act as micro-filler that refines the pore structure, reducing the amount of harmful pores. The mechanical performance is promoted after incorporating red mud, which is mainly attributed to the accelerated hydration of the fly ash cement binary binder and the refinement of red mud on the pore structure.

Keywords: Red mud; alkali source; fly ash-cement blends; controlled low strength materials.



Organized by
**Eindhoven University
of Technology**

TU/e

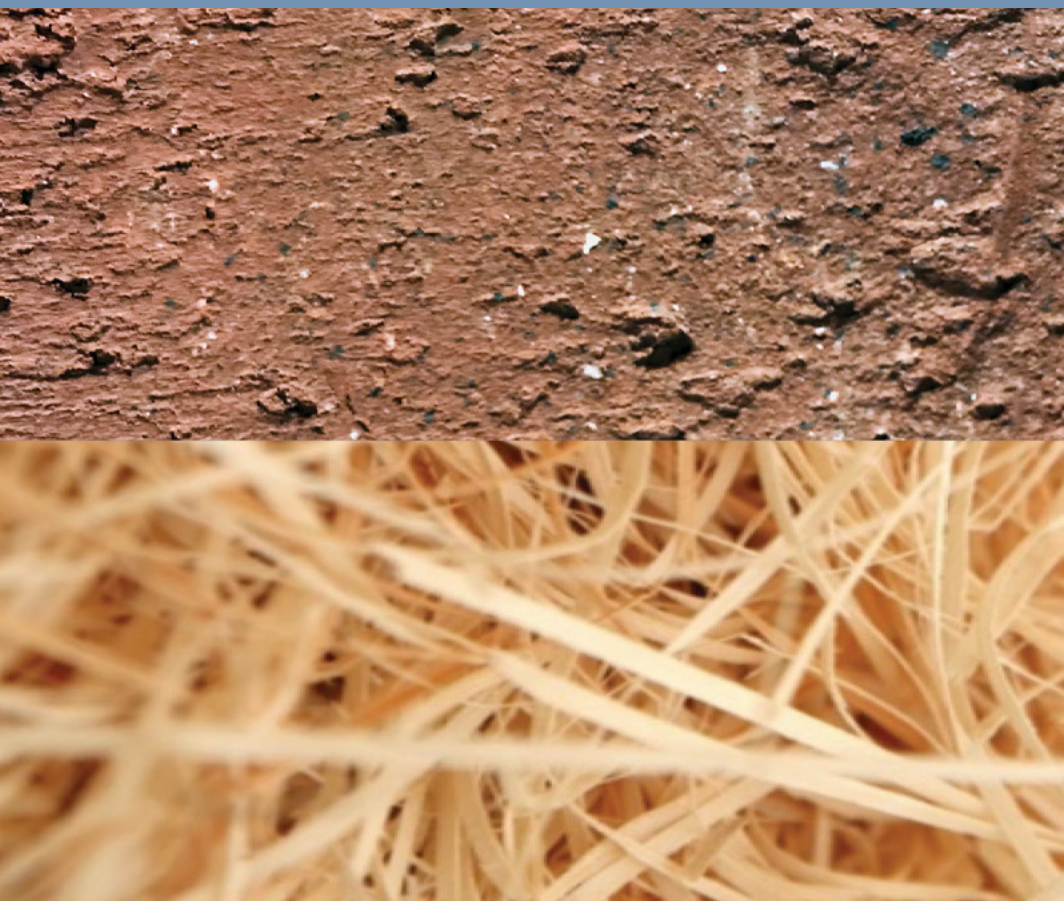
In cooperation with
**Wuhan University
of Technology**



PROCEEDINGS ICSBM 2019 VOLUME 3 - Greened Materials

2nd International Conference on Sustainable Building Materials

August 12-15, 2019 - Eindhoven, The Netherlands
Editors: V. Caprai and H.J.H. Brouwers



and supported by



ICSBM 2019, Conference proceedings

A catalogue record is available from the Eindhoven University of Technology Library

ISBN of the volumes set: 978-90-386-4898-9

ISBN of Volume 3: 978-90-386-4912-2

Sponsored by: CRH, Eltomation - Wood cement board plant, Tata Steel Europe (Gold sponsors), VDZ, PCA (Bronze Sponsors).

Front page image: V. Caprai

Editors: V. Caprai and H.J.H. Brouwers

Organizing committee:

Conference Chairman: Prof. H.J.H. (Jos) Brouwers, Eindhoven

Conference Co-Chairman: Prof. Wen Chen, Wuhan

Conference Secretary: Mrs V. (Veronica) Caprai and Dr. M.V.A. (Miruna) Florea, Eindhoven

Dr. Qiu Li, Wuhan

Dr. Bo Yuan, Wuhan

Dr. Q. Yu, Eindhoven

Dr. F. Gauvin, Eindhoven

Dr. K. Schollbach, Eindhoven

Mr. Y. Chen, Eindhoven

Mrs. L.T.J. Harmsen, Eindhoven

Mrs. N.L. Rombley, Eindhoven

Table of Contents

Sustainability of Durable Concrete Reinforced with Aluminum Metal

H. Justnes 6

Experimental investigation on RC one-way slabs subjected to contact explosion

Y. Hu, D. Song, Z. Jiang, Y. Huang, Z. Wu..... 16

Electrodialytically treated MSWI fly ash use in clay bricks

L. Skevi, L.M. Ottosen, G. M. Kirkelund..... 25

Experimental Studies on Fly Ash Gypsum Slurry

V. Revathi, S. Jayanthi..... 39

Production of bioplastic from CO₂ with light energy by coupling *Cupriavidus necator* with inorganic photocatalysts

T. Zhang, P. Tremblay 48

Study on the preparation of high quality autoclaved aerated concrete made from stone-sawing mud

H. Wan, Y. Hu, G. Liu, J. Liu, Y. Qu 50

Mechanochemically activated clay as a sustainable cementitious binder

I. Tole, K. Habermehl-Cwirzen, A. Cwirzen..... 61

Phase and dimensional stability of volcanic ash-based phosphate geopolymers at elevated temperatures

J.N. Yankwa Djobo, A. Elimbi and D. Stephan..... 68

The Effect of NaOH Concentration on the Mechanical and Physical Properties of Alkali Activated Fly Ash-Based Artificial Lightweight Aggregate

P. Risdanaren, K. Schollbach, J. Wang, N. De Belie 84

Performance evaluation of functional alkali activated lightweight composites produced with an eco-silica source based activator

X. Gao, Q.L. Yu 94

Effect of expansive agent on shrinkage and Long-term Performance of SCC

G. Ling, Z. Shui, T. Sun, X. Gao, X. Li, G. Wang..... 102

Converter slag - ladle slag - gypsum ternary binder – effect of CaO slaking

E.D. Adesanya, K. M. Ohenoja, P. K. Kinnunen, M. H. Illikainen 112

CSA as A Revisited Vernacular Technique for Earth Stabilization

B. Cicek, N. Pires Martins, C.Brumaud G. Habert..... 120

Assessment of mine tailings as precursors for alkali-activated materials for on-site applications

R. Obenaus-Emler, M. Falah, M. Illikainen..... 128

Experimental development of alternative lightweight concretes

D. Zwicky..... 141

Fire resistance of aerated alkali-activated cements

J. Rodriguez-Sanchez, M. Fedorciuc-Onisa, H. Kinoshita, J.L. Provis, S. MacLachlan 154

Durability parameters of self-compacting concrete with binary and ternary combinations of Portland cement, limestone filler and metakaolin

L.R.M. Miranda, V. M. S. Capuzzo..... 161

Eco-synthesis of zeolite from coal fly ash

K.M. Klima, Q.L. Yu, H.J.H. Brouwers..... 171

Influence of Particle Size Distribution and MSWI Bottom Ash Aggregate Replacement in Zero-Slump Concrete

P.M.F. van de Wouw, M.V.A. Florea, H.J.H. Brouwers 172

Influence of the Water- and Foaming Agent Dosage on Hardened Autoclaved Aerated Concrete

C. Straub, M.V.A. Florea, G. Quercia, H.J.H. Brouwers 184

Effect of carbonation on chloride binding behaviors and hydration product formation of metakaolin-ground waste coral blended marine mortars

Y. Wang, Z. Shui, X. Gao, Y. Huang, R. Yu, Q. Song..... 194

Rejuvenators for High RAP Asphalt Mixes and New Preservation Techniques for Open-Graded Pavements

S.N. Nahar, F.B. Elzinga, B.J. Lommerts..... 206

Volume 3

Greened materials

Sustainability of Durable Concrete Reinforced with Aluminum Metal

H. Justnes

SINTEF Building and Infrastructure, Trondheim, Norway. Contact: harald.justnes@sintef.no.

Abstract - Aluminium metal cannot be used to reinforce regular concrete since the high hydroxyl ion concentration will attack the metal and evolve hydrogen gas. However, it has been shown the aluminium metal rods alloyed with 5% magnesium is stable in concrete where 55% of the regular cement is replaced with calcined, natural clay in the concrete mix. Replacing high fraction of clinker burnt at 1450°C, and with high CO₂ emission from decomposition of limestone in the raw meal, with a clay calcined at 850°C obtainable by bio-fuel gives obvious savings in energy and CO₂ emissions. Furthermore, since aluminium can withstand carbonation and chlorides a cover of only 20 mm for mechanical interaction with reinforcement is needed resulting in a smaller volume of concrete. The binder with 55% calcined clay has been shown to be sulphate resistant, and no chance of AAR is expected due to lower pH and no remaining calcium hydroxide in the system. Hence, the only degradation mechanism left, is freeze-thaw action that can be avoided by proper air entrainment. Thus, in theory an infinite service life without maintenance may be at hand for aluminium metal reinforced concrete.

Instead of overshooting strength by making an impermeable concrete to protect steel reinforcement using low w/c, and often excess cement, the design criterion can now be the strength itself with a higher w/c enabling fast carbonation of the concrete guaranteeing a stable reinforcement in the long run. After all, > 80% of the concrete market is covered by a design strength of < 30 MPa in compression.

Aluminium metal is weaker than iron with 1/3 of the E-modulus and 1/4 tensile strength of the pure metals, but density is also 1/3 of iron. However, the tensile strength level of steel can be met by alloying (e.g. 10% Mg). The E-modulus is of the same level of FRP rods used for construction, but the failure is ductile unlike FRP rods with a brittle failure. Ductile failure is important for safety with concrete crack warning. Aluminium metal rods can be made from scrap metal in an electricity powered screw extrusion without heating.

Keywords: Aluminium, calcined clay, durability, reinforcement, sustainability.

1. Introduction

Cement is a key binder component of concrete production in the building industry. It is a complex hydraulic binder, made up of four main clinker components; alite (Ca₃SiO₃), belite (Ca₂SiO₄), tricalcium aluminate (Ca₃Al₂O₆) and ferrite (Ca₂AlFeO₃), which are milled together with gypsum to regulate setting time. In recent years, the production of cement has been identified as the third largest emitters of carbon dioxide (CO₂), accounting for approximately 5 to 8% of the total global anthropogenic emissions, with 60% coming from decomposition of limestone in the raw meal and 40% from fuel to reach clinkerization temperatures of 1450°C for a pure Portland clinker. Four main methods are currently in place to mitigate this challenge; i) switching from fossil fuels to alternative fuels, ii) increase efficiencies in factories, iii) implementation of supplementary cementitious materials (SCMs) replacing cement clinker [1] and iv) carbon capture and

storage (CCS) [2]. Among which, clinker partially replaced by SCMs is the most promising on a short term [1], whereby significant reduction in CO₂ emission could be expected depending on how much emission is associated with the SCM (transport, activation energy etc.). Replacing cement with SCM will also reduce the amount of raw meal needed per unit cement and increase the cement production volume of a cement plant. Most of the cement produced today has clinker replaced with SCMs with an average global clinker factor of 0.65 in 2014 [3], but higher clinker replacement with a greater variety of SCMs is expected in the future. The potential SCMs of the future include combustion ashes, slag, calcined clay and limestone. Fly ash is commonly employed in current cements with replacement of 20% in Norway. Calcined clay and marl are new and upcoming SCMs due to their abundance as increased clinker replacement demands large volumes of available SCMs. Additionally, previous studies displayed that calcined marl is a potential SCM up to a replacement level of 50% in terms of equal 28 day strength according to Justnes [1], but generally it is limited to < 35% replacement if sufficient alkalinity is to be maintained to protect steel from corroding in the long run.

The most common reinforcement for structural concrete is rebars made of steel. At the same time the most common degradation mechanism of reinforced concrete is corrosion of the steel initiated by carbonation (i.e. CO₂ from the air diffuse in and lower the pH by neutralization) or by chlorides exceeding a critical limit in spite of maintained pH. Thus, there is a need for concrete reinforcement that will not corrode, but at the same time being composed of common chemical elements like aluminium (8.1% of earth's crust [4]) since a gross volume of 10¹⁰ m³ concrete is produced annually world-wide. "Stainless steel" exists that will not corrode, but the typical 16-20% chromium (0.014% of earth's crust [4]) and 8-14% nickel (0.009% of earth's crust [4]) content makes it rather pricy. Some efforts have been made to make rebars out of fibre reinforced plastic (FRP), but these tend to have a brittle failure unlike metals being ductile and cannot be bent in place at site. Karlsson [5] made a review and evaluation of alternative concrete reinforcement. Naturally, aluminium was not a part of this evaluation since it will be degraded by the high pH of regular concrete and can only function in a sufficiently low pH concrete.

The main durability design of concrete today is in relation to preventing the steel reinforcement from corroding. The major degradation mechanisms; chloride ingress and carbonation, does not jeopardize the integrity of the concrete binder itself. Steel needs the high pH of conventional concrete to be passive towards corrosion while aluminium metal will be corroded by high pH and develop hydrogen gas. Environmentally friendly concrete is often designed by either using blended cement where maximum 35% of the clinker is replaced by supplementary cementitious materials (SCMs) to secure the presence of calcium hydroxide over time that will buffer a pH of 12.5 passivating steel, or by replacing cement in concrete mixes with corresponding amounts of SCM. In order to secure long service life for steel reinforced concrete, low w/c is used for low permeability often leading to much higher strength and even higher cement content than required. Low w/c can also create complications in the construction phase as lower workability is calling for use of super-plasticizing admixtures. Using more cement to attain low w/c can create higher temperature and subsequent thermal cracking risk generated by hydration heat as well as chemical shrinkage. The required compressive strength for the bulk of concrete today is still in the range of 25-30 MPa (B25).

The new concept is to make environmentally friendly concrete with > 50% cement replacement by a combination of SCMs where some are so pozzolanic active that all calcium hydroxide formed by cement hydration is consumed and the pH is kept so low that the concrete can be reinforced with aluminium metal rods without formation of hydrogen gas. The w/c can then be so high that it is only determined by required compressive strength for construction. Then workability should not be a problem and neither hydration generated heat. Permeability is not important as aluminium metal is resilient to atmospheric CO₂ and chlorides (when alloyed with 5% Mg), and high initial permeability is in fact beneficial for the concrete to

carbonate as fast as possible to reduce the carbon footprint further and lower the pH further for the long run. The concrete cover over the reinforcement can be made much thinner (20 mm) than today (50-70 mm) reducing weight and further improving the carbon footprint by using less concrete. Justnes [6] discussed the options of making a concrete with lower pH than usual ranging from large cement replacement (>50%) to calcium sulphoaluminate-belite cement systems with a smaller content of pozzolana.

2. Methodology

2.1 Materials

The aluminium reinforcement used in the experimental part was alloyed with 5% magnesium. The cement was a CEM I with composition of oxides as listed in Table 1. The cement Blaine value was 388 m²/kg and the equivalent sodium oxide content (Na₂O_{Eq}) was 0.61%. The clay was rich in smectite (53.5%) and contained some calcium carbonate (24.7%), mainly in the form coccolith skeletons due to its marine origin. Other minerals in the raw clay was 8.4% kaolinite, 4.4% illite, 4.3% quartz, 3.3% siderite and 1.4% pyrite. The specific surface of the calcined clay as measured by BET was 32.1 m²/g.

Table 1 – Chemical composition of cement and calcined clay as oxides as obtained by XRF

Oxide (%)	CEM I	Calcined clay
SiO ₂	21.12	43.34
Al ₂ O ₃	4.60	15.99
Fe ₂ O ₃	3.77	8.97
CaO	63.21	10.64
K ₂ O	0.40	2.10
Na ₂ O	0.35	0.85
MgO	1.71	2.39
TiO ₂	0.31	1.00
P ₂ O ₅	0.18	0.18
Mn ₂ O ₃	0.06	0.27
SO ₃	3.39	-

2.2 Mortar and concrete

The mortar mixing was performed according to EN 196-1, however at w/p = 0.6 or 0.7 instead of 0.5 (sand/cementitious powder = 3/1). The basic powder mix was 0.45 parts CEM I and 0.55 parts calcined clay with compositions as in Table 1. The compressive strength and the flexural strength for the mortar prisms were measured according to EN 196-1. A concrete was also made with composition as in Table 2.

Table 2: Concrete composition

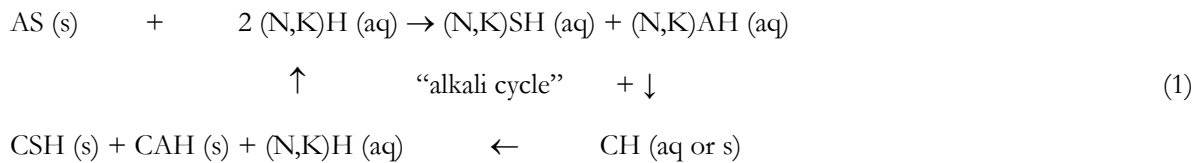
Component	Mass (kg/m ³)
CEM I	143.9
Calcined marl	175.9
Free water	223.9
Adsorbed water	5.7
0-8 mm Granite sand	970.9
8-16 mm Granite gravel	702.4
SIKA Viscocrete RMC-315	1.92

3. Results and discussion

As a proof of concept, two paste mixes with w/c = 0.60 were made with 100% ordinary Portland cement and 50% calcined marl [7] replacing cement. These pastes were poured into a plastic cup and an aluminium plate placed in each of them as shown in Fig. 1. The paste of pure cement separated and after a few minutes

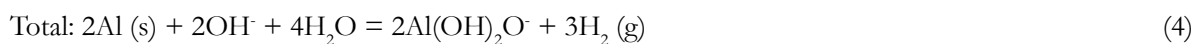
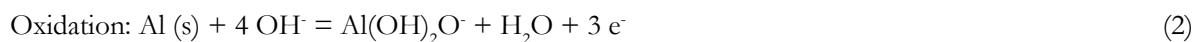
hydrogen gas started to bubble vigorously along the aluminium plate as seen from the top image of Fig. 1, while for the mix with 50% calcined marl some water was added on top for better visualization, but only a few small bubbles were observed. After the pastes had hardened, the samples were split and the imprints of the front and back of the aluminium plates on the pastes showed clearly much more cavities in the OPC sample next to the plate, while only a few small gas voids were seen on the interface for the paste with 50% calcined marl. One cannot rule out that these minor gas voids were due to entrained air by the high shear mixer, and the only way to find out is to capture and measure the evolved hydrogen gas volume [8]. This was done for Al/5%Mg rods placed in paste in plastic cups in confined environment. Fig. 2 shows such rods when the hardened paste is split after 28 days. The rod in the OPC paste had reacted completely to gibbsite while the rod in the OPC/calcined marl paste showed no sign of corrosion.

The purpose of the calcined marl was to consume all calcium hydroxide produced by the cement and render all alkalis as aluminate or silicate and to prevent them for regenerating as hydroxides as outlined in the alkali cycle for catalytic pozzolanic reaction exemplified principally (i.e. not necessarily correct ratio between the different oxides in the compounds) for aluminosilicate (AS) in Eq. 1.



where cement chemist's short hand notation is used; C = CaO, H = H₂O, K = K₂O, N = Na₂O, S = SiO₂ and A = Al₂O₃. The alkali hydroxides dissolves alumina and silica from the aluminosilicate that react with calcium hydroxide (CH) to amorphous calcium silicate hydrate (CSH) gel and crystalline calcium aluminate hydrates (CAH) as binder. After reaction with CH the alkali hydroxides are regenerated, and the cycle continues until all calcium hydroxide is consumed and they end up as alkali silicate and alkali aluminate that in theory should not attack the aluminium metal in the rebars even though they result in a high pH. Justnes et al [7] showed that paste where cement is replaced with 50% calcined marl showed no traces of calcium hydroxide after 2 years by XRD.

Aluminium metal forms a dense layer of Al₂O₃ in contact with air that prevents further oxidation (or corrosion). This layer may dissolve by alkali hydroxides and open up for further corrosion evolving hydrogen gas;



The standard electrochemical potentials of Eqs. 2, 3 and 4 are E⁰ = +2.333 V, E⁰ = -0.828 V and E⁰ = +1.502 V, respectively. According to the total reaction in Eq. 4, there will be a net consumption of one hydroxide ion per aluminium oxidized, or none if gibbsite, Al(OH)₃, is precipitated rather than the dissolved aluminate anion due to lack of water as indicated in the top photo of Fig. 2 with total reaction;

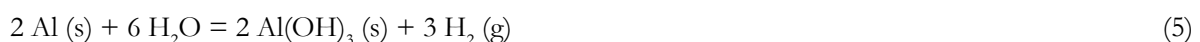




Figure 1: Aluminium metal plate placed in OPC paste (top) evolving gas and in paste where OPC is replaced with 50% calcined marl (bottom).



Figure 2: Al/5% Mg alloy rods placed in OPC paste (top) and totally converted to gibbsite after 28 days curing in moist condition, while same rod placed in paste where OPC is replaced with 55% calcined marl is in pristine condition without any corrosion products in its imprint (bottom).

Concrete was made with composition as given in Table 2, and a soluble magnesium salt (0.57% Mg^{2+} of binder mass) added to lower the initial pH. The compressive strength, splitting tensile strength and static E-modulus of cylinders (Φ 100 mm · 200 mm) was measured after 28 days curing under wet burlap and plastic wrapping to avoid drying, and the results listed in Table 3. The concrete was made in two batches and used to cast 18 cylinders and three 150·250·1100 mm beams reinforced with Φ 10 mm aluminium bars alloyed with 5% magnesium. The beams were tested in a 4-point bending and the crack pattern compared to finite element calculations (not reported here). After the bending test, one of the beams were cut and split to inspect the bars for corrosion. As seen from Fig. 3, there was no sign of corrosion on the bars (top image) and the imprint in the concrete (lower image) was clean without corrosion products. Prior

to these bigger batches, a smaller trial mix was made, and a number of 10 cm cubes cast in steel moulds. The strength evolution for the trial mix versus curing age at 98% RH and 20°C is plotted in Fig. 4, and the temperature evolution in a 3.5 litre Styrofoam mould (10 mm wall thickness) was measured indicating a setting time of 4.5 h (270 min) and giving a maximum temperature increase of 6.5°C from ambient.

Table 3: Mechanical properties of concrete cylinders

Property	No. samples	Value
Density (kg/m ³)	12 from 2 batches	2328±16
Compressive strength (MPa)	8 from 2 batches	22.3±0.9
Splitting tensile strength (MPa)	4 from 2 batches	2.3±0.2
Dynamic E-modulus (GPa)	4 from 2 batches	20.3±0.9

Note that the concrete target strength was around 25 MPa and that it was deliberately made porous with a water-to-binder ratio of 0.7 so it would carbonate quickly and keep pH low over time. It could of course be made stronger by simply lowering the water content and increasing the super-plasticizer dosage a bit from the current 0.6% of binder mass. Justnes et al [9] showed that mortar where cement was replaced with 50% calcined marl and the water-to-binder ratio was 0.55 achieved the same compressive strength as mortar with 100% cement and that the compressive strength continued to increase until the last measurement at 2 years age in spite of no calcium hydroxide present at 28 days age.

The pH evolution of paste similar to the binder of the concrete with and without 6% magnesium nitrate hexahydrate is plotted in Fig. 5. The idea was that this would convert alkali hydroxides to nitrates when precipitating brucite and lower pH to 10.5;



Figure 3: Aluminium alloy round bars and T-bar (top) of beam after chiselling it open and their imprints (bottom) showing no signs of corrosion products after 40 days moist curing at 20°C.

However, as seen from Fig. 5, the pH rises back towards the level of the mix without magnesium nitrate after 7 days. The reason is probably that the nitrate ion exchange with the layered double hydroxide AFm

phases forming $\text{Ca}_3\text{Al}_2\text{O}_6 \cdot \text{Ca}(\text{NO}_3)_2 \cdot 11\text{H}_2\text{O}$.

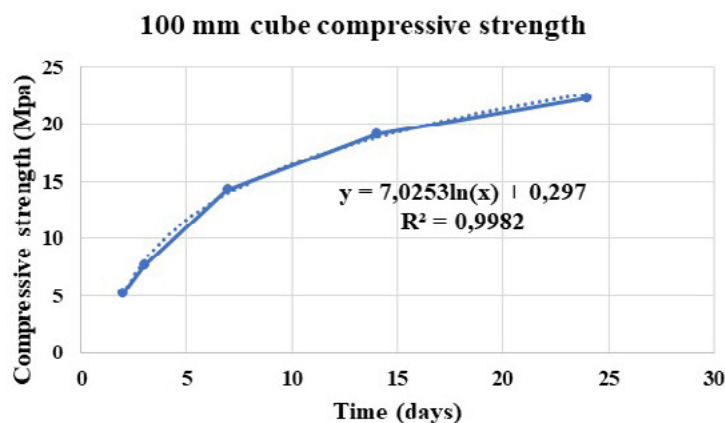


Figure 4: Compressive strength evolution versus time of the concrete cured at 98% RH and 20°C.

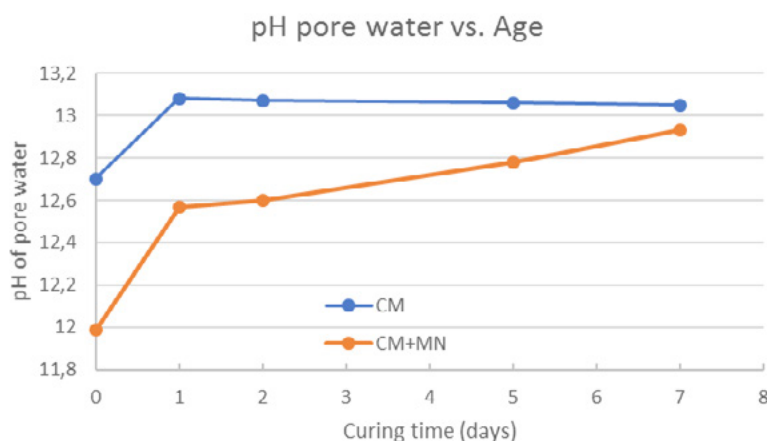
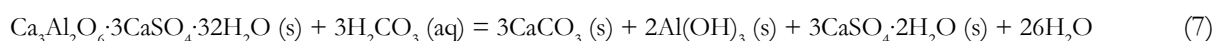


Figure 5: pH evolution as a function of sealed curing age at 20°C. CM = paste with 45% CEM I, 55% calcined marl and w/p = 0.70, while CM+MN is added additional 6% $\text{Mg}(\text{NO}_3)_2 \cdot 6\text{H}_2\text{O}$ of powder mass.

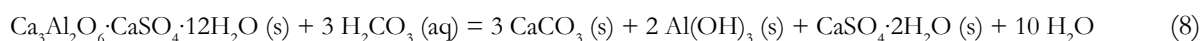
The compressive strength of carbonated mortar versus non-carbonated mortar was measured to 20.2 ± 0.2 and 23.7 ± 0.5 , respectively. The mortar composition was 0.45 parts CEM I, 0.55% calcined clay and w/p = 0.7 cured for 28 days at 90% RH and 20°C for 28 days before one set of 3 prisms were carbonated through in a 5% CO_2 chamber with 60% RH and the other set just stored at 60% RH in a closed box for same length of time. According to Justnes et al [10] the strength reduction is higher for cements blended with alumina containing SCMs than for OPC since the higher amount of calcium aluminate hydrates formed [11] will lead to a porosity increase when they carbonate, unlike calcium hydroxide leading to a volume decrease upon carbonation.

The molar volume change (ΔV_m) for ettringite carbonating to calcite, gibbsite, gypsum and liquid water;



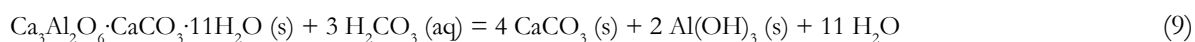
$$\Delta V_m = 3 \cdot 36.93 + 2 \cdot 32.22 + 3 \cdot 74.50 - 705.91 = -307.18 \text{ cm}^3/\text{mol AF}_t$$

For calcium monosulphoaluminate hydrate carbonating to calcite, gibbsite, gypsum and liquid water;



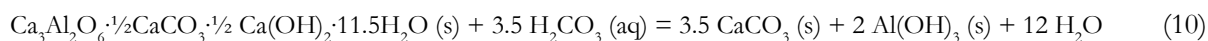
$$\Delta V_m = 3 \cdot 36.93 + 2 \cdot 32.22 + 74.50 - 308.94 = -59.21 \text{ cm}^3/\text{mol AF}_m$$

For calcium monocarboaluminate hydrate carbonating to calcite, gibbsite and liquid water;



$$\Delta V_m = 4 \cdot 36.93 + 2 \cdot 32.22 - 261.28 = -49.12 \text{ cm}^3/\text{mol monocarboaluminate}$$

For calcium hemicarboaluminate hydrate carbonating to calcite, gibbsite and liquid water;



$$\Delta V_m = 3.5 \cdot 36.93 + 2 \cdot 32.22 - 284.36 = -90.67 \text{ cm}^3/\text{mol hemicarboaluminate}$$

For mortars with binders based on 30% siliceous fly ash and 5% limestone stabilizing ettringite cured for 56 days [10], the water vapour diffusion coefficient, k_d ($10^{-12} \text{ kg}/\text{Pa} \cdot \text{m} \cdot \text{s}$), increased upon carbonation (from 0.41 ± 0.09 to 3.06 ± 0.04) unlike mortar based on OPC (changed from 0.76 ± 0.10 to 0.59 ± 0.10).

The aluminium rebars are produced by an extrusion process. The screw extrusion process is patented by Werenskiöld et al [12]. A prototype extruder along with fundamental knowledge of the process have been developed to a level that allows industrial implementation. Compared to the traditional process route based on re-melting and ram extrusion, direct screw extrusion of scrap material represents a significant reduction in energy consumption according to Duflou et al [13]. Moreover, this process is well suited for utilization of swarf material from material removal processes such as cutting, milling and turning that is commonly of less value than other scrap types. This is further contributing to the environmental friendliness of the overall concept of reinforcing with aluminium metal.

The E-modulus of pure aluminium metal (70 GPa) is 1/3 of steel (210 GPa), but the density of aluminium (2.70 kg/l) is also about 1/3 of iron (7.87 kg/l). The ultimate tensile strength of pure aluminium is 110 MPa, while it for steel is 400 MPa, but aluminium can be alloyed to approach steel in tensile strength. Ram extruded aluminium alloyed with 5 and 10% magnesium have tensile strengths of 274 and 395 MPa, respectively, and even higher for screw extruded rods. The challenge is the lower E-modulus, but some of this may be alleviated by designing the aluminium rebars differently. On the other hand, FRP rebars made with glass, basalt or carbon fibres have E-moduli of 45, 60 and 145 GPa and tensile strength of 700, 800 and 2000 MPa, respectively, according to Karlsson [5]. In the SEACON project [14] a bridge was built using FRP rebars demonstrating the feasibility of constructing with rebars with such lower E-modulus than steel.

Another issue is the difference in linear thermal expansion coefficient. Concrete has $6 \cdot 10^{-6} \text{ m}/\text{m} \cdot \text{K}$, while pure iron and pure aluminium exhibits 10 and $22 \cdot 10^{-6} \text{ m}/\text{m} \cdot \text{K}$, respectively. The thermal expansion of aluminium can be reduced by alloying (in particular by silicon). As comparison, glass fibre reinforced polyester has a linear thermal expansion coefficient of $25 \cdot 10^{-6} \text{ m}/\text{m} \cdot \text{K}$. The consequence of difference in thermal dilation between reinforcement and concrete will be an issue for further research.

4. Conclusions

A new concept of durable and environmentally friendly aluminium reinforced concrete is described where cement is replaced by high content (50-55%) of pozzolanic SCM that might lead to;

- No corrosion induced by carbonation or chloride intrusion
- Tolerable microcracks caused by drying shrinkage etc that will not jeopardize reinforcement durability
- Superior sulphate resistance when alumina containing SCMs like calcined marl is used [6]
- Applicability of alkali reactive aggregate due to alkali binding [15] or soluble aluminates from clay inhibiting silica dissolution [16, 17]

- Usability of seawater as mixing water when reinforcement is Al alloyed with e.g. 5% Mg
- Acceptance of the best strength accelerator, calcium chloride, when reinforcement is aluminium alloyed with 5% Mg (sea-water resistant aluminium used for boats)
- Much less need of cover over rebar (save 30 mm in concrete cover), probably only 20 mm needed for proper anchoring of reinforcement with concrete
- Significant lower unit weight of Al-reinforced concrete (reduced “dead-weight”)
- Higher w/c allowed giving more permeable concrete leading to
- Easier to cast concrete with less plasticizers or none
- Faster carbonation leading to binding of CO₂ and further reduction of Carbon-footprint
- Less thermal movements in monolithic concrete

Hence, aluminium metal reinforced concrete may provide a system for extraordinary long service life without maintenance.

5. Acknowledgment

The grant no. 269767 from the Research Council of Norway to establish the research project DARE2C; Durable Aluminium Reinforced Environmentally-friendly Concrete Construction, is greatly appreciated.

6. References

- [1] Justnes, H., 2015. How to Make Concrete More Sustainable. *Journal of Advanced Concrete Technology*. 13:147-154.
- [2] Bosoga, A., Mazek, O., Oakey, J.E., 2009. CO₂ Capture Technologies for Cement Industry. *Energy Procedia*. 1:133-140.
- [3] <https://www.iea.org/publications/freepublications/publication/TechnologyRoadmapLowCarbonTransitionintheCementIndustry.pdf>
- [4] <http://periodictable.com/Properties/A/CrustAbundance.vlog.html>
- [5] Karlsson, J., 2014. Alternative reinforcement approaches – Extended service life of exposed concrete structures. MSc thesis 151, Chalmers University of Technology, Department of Civil and Environmental Engineering, Gothenburg, Sweden, 117 pp.
- [6] Justnes, H., 2017. Durable Aluminium Reinforced Environmentally-friendly Concrete Construction – DARE2C. *Nordic Concrete Research*. 56:71-81.
- [7] Danner, T., Justnes, H., Norden, G., Østnor, T., 2015. Feasibility of calcined marl as alternative pozzolan. *Proc. 1st Int. Conf. Calcined Clays for Sustainable Concrete*, Eds. Karen Scrivener and Aurélie Favier, RILEM Book series 10:67-74. Springer.
- [8] Justnes, H., 2018. Utilizing Pozzolana to Enable Aluminium Reinforced Concrete. 14th Int. Conf. Recent Advances in Concrete Technology and Sustainability Issues, Supplementary paper proceeding, Beijing, October 30-November 2, 2018.
- [9] Justnes, H., Østnor, T.A., Ng, S., 2016. Applicability of Nordic clays as SCM. *Proc. Int. RILEM Conf. on Materials, Systems and Structures in Civil Engineering*, Conference segment on Concrete with

Supplementary Cementitious materials, 22-24 August, Technical University of Denmark, Lyngby, Denmark, RILEM Proceedings 113:331-340.

[10] Justnes, H., Skocek, J., Østnor, T.A, Engelsen, C.J., Skjølsvold, O. 2019. Microstructural changes of hydrated cement blended with fly ash upon carbonation. Reviewed but under revision for Cement and Concrete Research.

[11] De Weerd, K., Ben Ha-Ha, M., Le Saout, G., Kjellsen, K.O., Justnes, H. and Lothenbach, B.: "Hydration mechanism of ternary Portland cements containing limestone powder and fly ash", Cement and Concrete Research, Volume 41, Issue 3, March 2011, pp. 279-291.

[12] Werenskiold, J. C., Auran, L., Roven, H. J., Ryum, N., Reiso, O., 2013. Screw extruder for continuous extrusion of materials with high viscosity. European Patent 2 086 697 B1, 01.05.2013, 8 pp.

[13] Duflou, J. R., Tekkaya, A. E., Haase, M., Welo, T., Vanmeensel, K., Kellens, K., Dewulf, W. and Paraskevas, D., 2015. Environmental assessment of solid-state recycling routes for aluminium alloys: Can solid state processes significantly reduce the environmental impact of aluminium recycling? CIRP Annals - Manufacturing Technology, 64:37–40.

[14] www.infravation.net/projects/SEACON

[15] Chappex, T., Scrivener, K.L., 2012. Alkali fixation of C–S–H in blended cement pastes and its relation to alkali silica reaction. Cement and Concrete Research, 42:1049–1054.

[16] Chappex, T., Scrivener, K.L., 2012. The influence of aluminum on the dissolution of amorphous silica and its relation to alkali silica reaction. Cement and Concrete Research, 42:1645–1649.

[17] Chappex, T., Scrivener, K.L., 2013. The Effect of Aluminum in Solution on the Dissolution of Amorphous Silica and its Relation to Cementitious Systems. J. Am. Ceram. Soc., 96:592–597.

Experimental investigation on RC one-way slabs subjected to contact explosion

Y. Hu¹, D. Song², Z. Jiang², Y. Huang², Z. Wu¹

¹ College of Aerospace Science and Engineering, National University of Defense Technology, Changsha, 410073, P.R. China.

² Undergraduate School, National University of Defense Technology, Changsha, 410072, P.R. China.

Abstract

RC one-way slabs which have been widely used in bridge decks of bridge structures refer to reinforced concrete slabs supported by two pairs of sides or four sides and having a ratio of long side to short side greater than 3. These kinds of engineering structures may suffer from blast loads such as accidental explosions, explosive terrorist attacks, or military strikes throughout their life cycle. In this paper, four RC one-way slabs have been designed and tested under contact explosion, and the effects of charge mass have been investigated. The failure modes and damage parameters of RC one-way slabs were obtained and discussed. The results show that a smaller funneled crater in the front surface of the tested slabs under the contact explosion is observed with cracks around the funneled crater, while a larger funneled crater in the rear surface is also observed; as the amount of charge mass increases, the damage degree of RC one-way slabs also increases; when the amount of charge mass is 150 g, 225 g and 300 g, the range of damage of the front (rear) surface for the slabs is approximately equal, but the depth and the volume of the funneled craters increase; the failure mode of the above three slabs is found to be the combination of the overpressure damage of the front surface and the tensile failure of the rear surface and the slabs is collapsed without any penetration. When the amount of charge mass is 450g, the slab is penetrated under the explosion shock wave, and the failure mode of the slab is found to be punching failure.

Keywords: RC slab, Contact explosion, Failure mode, Funneled crater, Experimental investigation.

1. Introduction

Bridges have strategic significance for the development of national economic and the security of social life as an important joint of public transportation, and they may be subjected to blast loading during their life-cycle as a result of military strike, terrorist attack and accidental explosion accident. In 2007, the Sarafiya Bridge in Baghdad was attacked by a car bomb, causing heavy casualties and leading to panic among the locals, as shown in Figure 1(a) [1]. In 2013, a truck loaded with fireworks exploded in the Yichang Bridge of the Lianhuo Expressway, China, and the bridge surface collapsed immediately, as shown in Figure 1(b) [2]. The above examples show that the damage caused by blast loading may be serious, and it is especially necessary to improve the anti-explosion performance of the bridge.

RC slabs which refer to reinforced concrete slabs are the basic structures or components in building construction and various engineering structures. RC slabs are also widely used in bridge engineering, and a lot of researches were conducted on the explosion of RC slabs. Low and Hao [3-4] simulated the shear failure and bending failure of RC slab under blast loading and studied the reliability of the RC slab. Xu and

Lu [5] considered the strain rate effect of materials, and used the erosion technique to simulate the concrete cracks under different blast loads and structural conditions.



1a) The collapsed Sarafiya Bridge

1b) The collapsed Yichang Bridge

Figure 1: Cases of explosions on bridges

Luccioni et al. [6] conducted experiments and simulations on RC pavement slabs under different blast loads. Ngo et al. [7] carried out the anti-explosion test of high-strength concrete slabs. The results show that the anti-explosion performance of high-strength concrete slabs is better than that of ordinary concrete slabs, but the brittleness is enhanced and the cracking of the slabs is serious. Zhou et al. [8] used dynamic plastic damage model to reproduce the response of RC slabs under blast loading and numerical simulation analysis was also carried out. Schenker et al. [9] studied the dynamic response of concrete slabs under blast loading by field explosion test, and concluded that aluminium foam can effectively reduce the impact load of explosion. Wu et al. [10] analyzed the size of the fragments formed by concrete slabs under blast loading. Petro and Lu [11] analyzed the dynamic response and failure modes of the test-piece by the anti-explosion test of the RC square plate. Pantelides et al. [12] found that RC slabs reinforced with steel fibers have better blast resistance than other types of slabs. Thiagarajan [13] studied the damage behavior and dynamic response of high-strength concrete slabs and ordinary strength concrete slabs under blast loading through explosion test. It is concluded that the use of high-strength materials can improve the protection ability of structures under blast loading. Assadi-Lamouki and Krauthammer [14] used a modified Timoshenko beam formula including nonlinear effects of materials to re-evaluate the damage of RC slabs under blast loading, and the models were validated by 11 tests of RC slabs under blast loading. Kuang and Tsoi [15] based on the rigid plastic model and took the effects of orthotropic steel bars and asymmetric support bending constraints into account; the response and failure modes of RC slabs under blast loading are studied. Li et al. [16] conducted field explosion tests on high-strength self-compacting concrete slabs incorporating steel wire mesh. The results show that the incorporation of steel mesh effectively reduces the propagation of shock waves, and the range of concrete spalling and damage is reduced. Syed et al. [17] studied the effects of explosion pressure distribution and strength on damage and failure modes of RC slabs by far (near) field explosion tests.

In China, Yan et al. [18] used the finite element software ABAQUS to analyze the failure modes of RC slabs under blast loading. The results show that the peak pressure of the explosion is small, and the bending failure mainly occurs when the action time is long; Shear damage occurs mainly when the action time is short. Zhang et al. [19] conducted a contact explosion test on finite-thickness RC slabs, and simulated the dynamic process of plate deformation and failure. Sun [20] conducted an independent explosion test on two identical RC slabs, and studied the failure modes of RC slabs in elastic and plastic regions. Li et al. [21] used the finite element analysis software to establish the analysis method of response and failure of RC slab under blast loading, and fitted the *P-I* curve according to the simulation results, which can be used to evaluate the RC slab after explosion. Wang et al. [22] conducted a near-field explosion test on a square RC slab under unidirectional support conditions, and used the AUTODYN software to numerically

simulate the dynamic response process of the slab. The results show that with the amount of charge increases, the failure mode of the concrete slab changes from bending failure to punching failure. Liu et al. [23] conducted a comparative test of RC two-way slabs under contact blast loading. The results show that improving the strength grade of steel and the reinforcement ratio of steel can effectively improve the anti-explosion performance of RC slabs. Chen et al. [24] experimentally analyzed the effects of steel bar type, reinforcement ratio, peak value of explosive load on the anti-explosion performance of RC slabs. In summary, most of the previous studies are focused on the anti-explosion performance of RC two-way slabs, while the research on RC one-way slabs under contact explosion is still limited. Set against this backgrounds, tests of RC one-way slabs under contact explosion are conducted, and the damage mechanism and failure characteristics of the RC one-way slabs under different blast loadings are also discussed. The test results can not only be used for engineering application of RC one-way slabs but also provide a reference for damage assessment.

2. Specimens design and test methods

2.1 Specimens design

The RC one-way slab was designed according to “Code for Design of Concrete Structures” (GB50010-2010) in China[25]. Four specimens have the same materials and dimensions and the dimensions are 2000mm × 500mm × 100mm. The configurations of the specimens are shown in Figure 2. During the installation, the two short sides were simply supported. Four RC one-way slabs were numbered with P1-P4, and the mass of the charge (Emulsion explosive) was 150g, 225g, 300g and 450g respectively. The design concrete cube strength for pouring the RC one-way slab is 50 MPa.

2.2 Material properties

The designed ingredients and mix proportion of concrete are shown in Table 1. When pouring, the cubic specimens with the size of 150mm×150mm×150mm and the prism specimens of 150mm×150mm×300mm were reserved. After 28 days of natural curing, the cube compressive strength of concrete was measured to be 46.3 MPa, and the tensile strength was 4.0 MPa.

Table 1: Ingredients and mix proportion of concrete (kg/m³).

Cement	Sand	Aggregate	Water	Admixture
440	653	1045	140	142

Using HRB335 steel of $\Phi 8$ mm and $\Phi 6$ mm, the yield strength of reinforcement with ($\Phi 8$ mm) is 554MPa, the ultimate strength is 684MPa, and the reinforcement ratio of RC one-way slab is 0.628%.

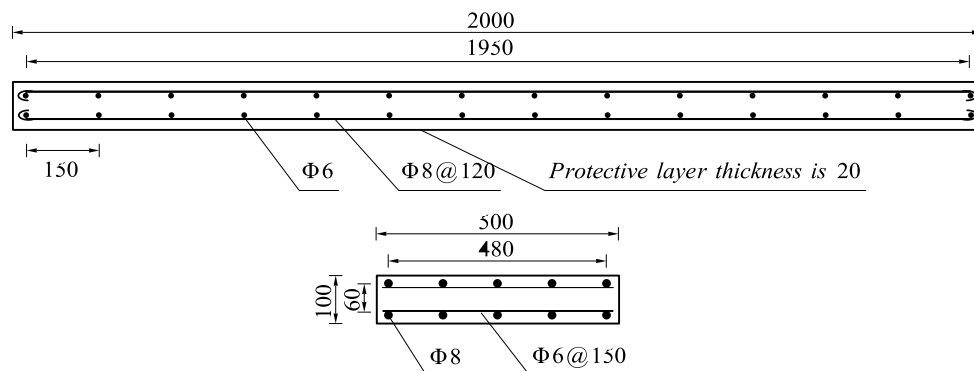


Figure 2: RC one-way slab structure diagram(Units:mm)

2.3 Explosive loading and testing

The explosion test was carried out by means of electric detonator detonating emulsion explosive. A cylindrical charge was 75g and the charge mass of specimens P1-P4 in the test design is composed of several cylindrical charges, as shown in Figure 3 (a). The explosive was placed at the center of the top surface of the slabs with contact explosion. The detonation direction was the width direction of the slabs, as shown in Figure 3(b). During the test, in order to make the bottom surface of the slabs in the free surface, the site was levelled before the test, and the brick support was fixed firmly. The contact parts of the specimens and the support were padded with oil felt to form a simple support structure, and the installation are shown in Figure 3(c). After the test, the macroscopic phenomena such as the failure mode and crack distribution of the RC one-way slabs were observed, and the specific parameters such as the size and depth of the local failure feature were measured to evaluate the damage degree of the RC one-way slabs under blast loading.

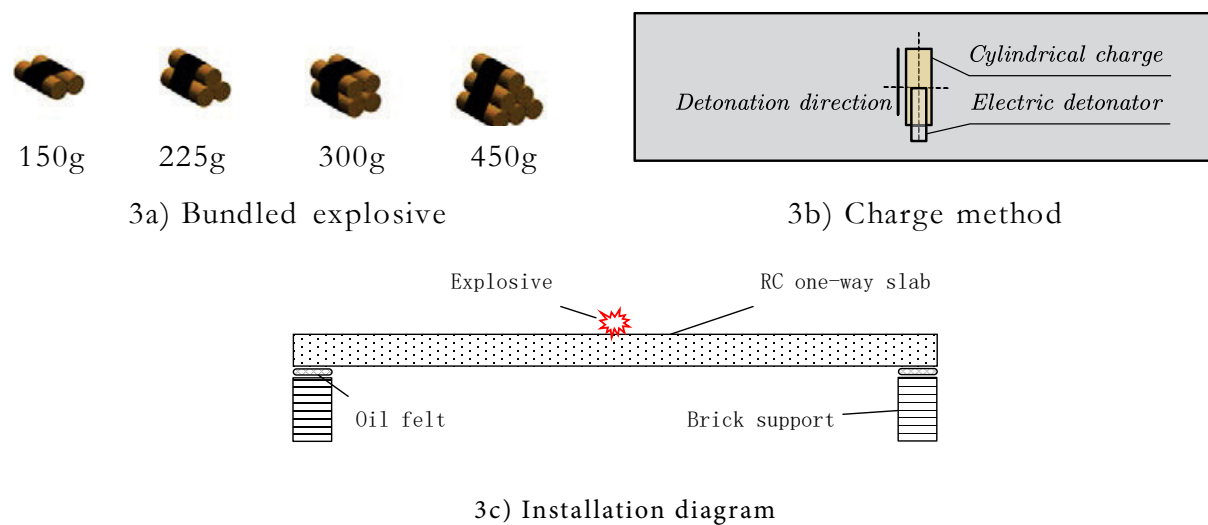


Figure 3: Specimens installation and loading method

3. Test results

According to the specifications of the specimens designed in Section 2.1 and the test conditions proposed in Section 2.3, the anti-explosion tests of the RC one-way slabs were carried out. Figure 4 shows the failure modes of the top and bottom surface of the specimen P1-P4. In order to facilitate the observation of the extent and shape of the specimens after test, the concrete of slabs were divided into 5cm*5cm grids by ink cartridges. After the test, the macroscopic damage phenomena of the blasting concrete on the top surfac and bottom surfaces are listed in Table 2. It can be seen from Fig. 4 that the failure modes of P1, P2 and P3 are similar, there are a small amount of concrete caving on the top surface, and concrete cracking phenomenon of the bottom surface is remarkable, a tensile spalling crater appears on the bottom surface of the slab. The amount of concrete caving increases with the increase of explosive equivalent, the range and depth of the spalling crater increase, and there is a phenomenon that the steel are bare. The failure mode of P4 is that the concrete spalling crater on the bottom surface and the spalling crater on the top surface form a breach, and the bottom surface has the phenomenon of transverse steel fracture. In addition to the concrete caving on the top surface and the spalling crater on the bottom surface, a large number of radial cracks generated near the explosion point and the transverse (longitudinal) cracks away from the explosion point are also the failure modes of the RC one-way slabs.

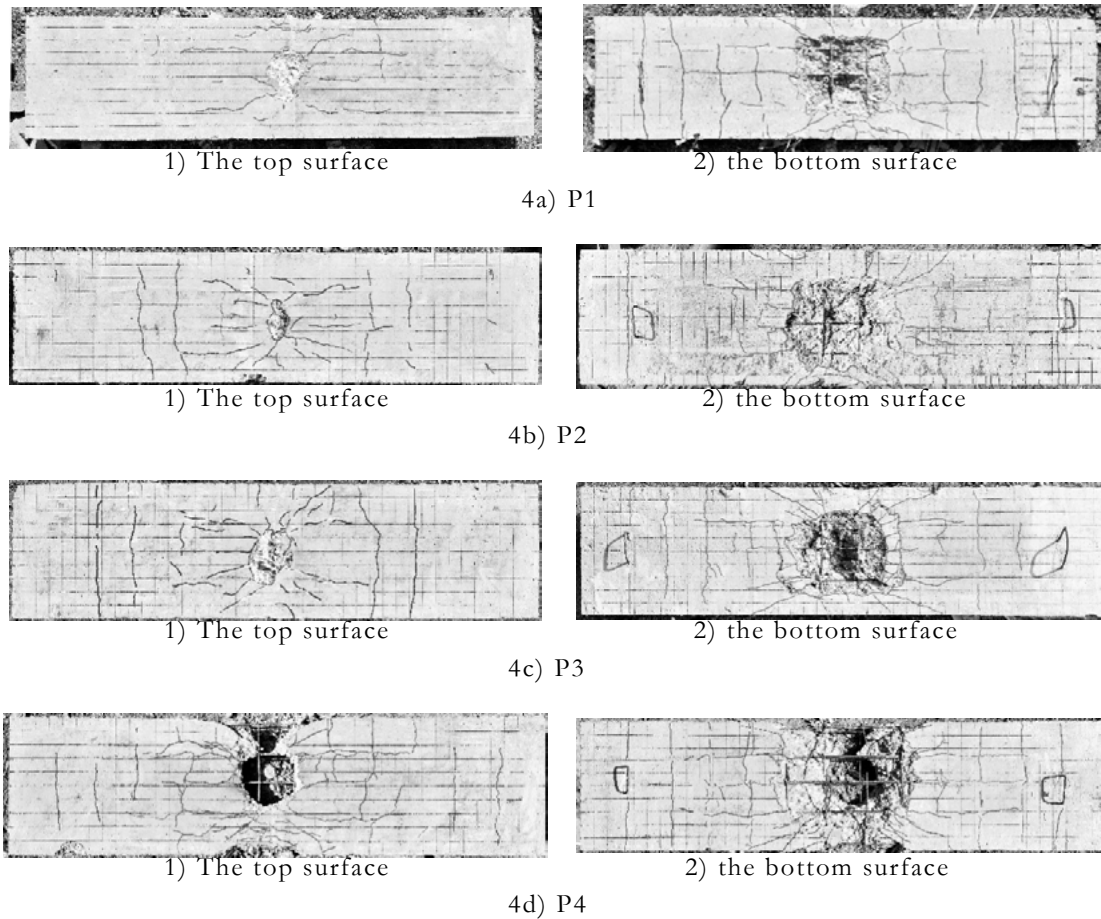


Figure 4: Explosion surface (back explosion surface) damage form

Therefore, the macroscopic characteristics of the RC one-way slabs are: the top surface (the bottom surface) spalling crater + radial cracks at the explosion point + transverse (longitudinal) cracks away from the explosion point. The damage of P4 also includes the collapse of the side concrete, while the concentrated charge and the detonation direction cause the pressure distribution in the concrete to be uneven, furthermore the concrete displacement on the side of the concrete slab is not coordinated, resulting in concrete peeling.

Table 2: RC one-way slab failure mode

Specimens number	Test condition	The top surface damage	The bottom surface damage
P1	150g emulsion explosive	A small amount of concrete collapsed, no steel bare	Tensile spalling crater, 2*2 (Longitudinal * transverse) bare steel exposed
P2	225g emulsion explosive	A small amount of concrete collapsed, no steel bare	Tensile spalling crater, 3*2 (Longitudinal * transverse) bare steel exposed
P3	300g emulsion explosive	A small amount of concrete collapsed, no steel bare	Tensile spalling crater, 3*2 (Longitudinal * transverse) bare steel exposed
P4	450g emulsion explosive	Large concrete collapses, 3*1 (Longitudinal reinforcement * transverse reinforcement) steel bars are exposed	Tensile spalling crater, forming a break with the front funnel pit, 5*4 (Longitudinal * transverse) steel bars, 2 steel bars broken

4. Analysis and discussion

4.1 Damage parameters

The measurement results of the spalling crater including the plane size, depth and volume are shown in

Table 3, where d_1 and d_2 are the length of the damage range along the direction of the longitudinal and transverse reinforcements respectively, h_0 and v_0 are the depth and the volume of the spalling crater; or the bottom surface, D_1 and D_2 are the length of the damage range along the direction of the longitudinal and transverse reinforcements, h_0 and v_0 are the length of the damage range along the direction of the longitudinal and transverse reinforcements. The damage parameters are shown in Fig. 5.

Figure 5: Damage parameter

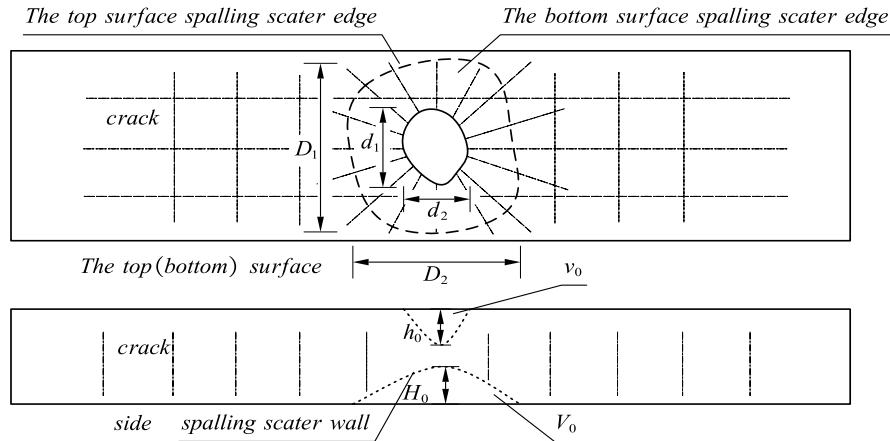


Table 3: Main damage parameters of the specimens

Specimens number	Explosive mass/g	The top surface				The bottom surface			
		d_1 /cm	d_2 /cm	h_0 /cm	v_0 /cm ³	D_1 /cm	D_2 /cm	H_0 /cm	V_0 /cm ³
P1	150	15.38	15.67	1.65	209.24	30.39	37.10	4.54	2400.26
P2	225	12.28	7.08	2.13	273.65	32.76	41.59	6.05	2566.49
P3	300	17.86	12.28	3.04	310.94	32.73	38.94	5.93	3045.79
P4	450	20.18	20.35	3.42	380.32	42.86	53.10	6.58	5676.96

4.2 Influence of parameters

It can be seen from Fig. 4 and Table 2 that the RC one-way slabs generates spalling craters on the top surface and bottom surface under the contact blast loading, and the crater size and depth increase correspondingly with the increase of explosive equivalent. Figure 6 shows the crater volume histogram of the RC one-way slab under different equivalents. It can be seen that with the increase of explosive mass, the volume of the spalling crater increases; compared with P1, the top surfaces of P2, P3 and P4 increased by 31.1%, 48.8% and 81.8%. For the bottom surface, the volume of the spalling crater of P2, P3 and P4 increased by 6.92%, 26.91% and 136.54% in compared with P1, respectively.

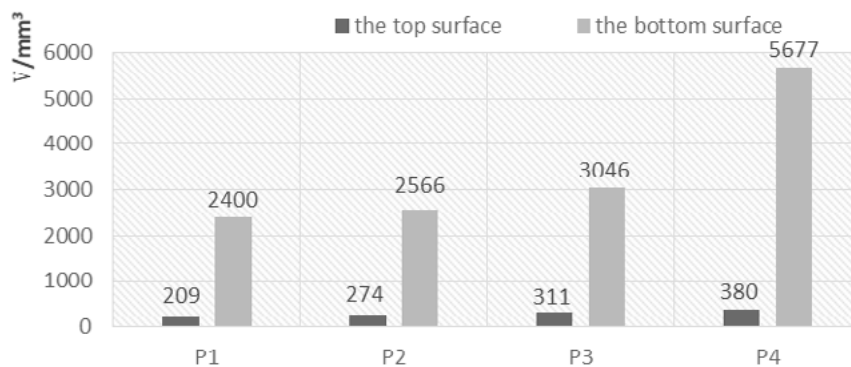


Figure 6: Explosion surface, back explosion surface funnel pit volume histogram

The obvious cracks (width \geq 0.1mm) are marked with red pen on the top and bottom surfaces. It can be seen that there are three types of cracks in the specimen subjected to the explosion shock: longitudinal crack, transverse cracks, and oblique cracks that radiates outward from the center of the explosion. The oblique cracks are concentrated around the fracture, and the transverse cracks and the longitudinal cracks are combined into a grid shape, which is more evenly distributed on the top and bottom sides of the specimens. The statistics of the three types of cracks are shown in Table 3.

Table 3: Number of cracks

Specimens number	The top surface crack			The bottom surface crack		
	Portrait	Landscape	Oblique	Portrait	Landscape	Oblique
P1	2	2	8	3	9	10
P2	2	5	13	2	7	15
P3	3	6	14	3	9	18
P4	3	10	13	3	9	16

With the increase of explosive mass, the number of oblique cracks and lateral cracks in the top surface increased, but the increase of longitudinal cracks was not obvious; the number of diagonal cracks on the bottom surface increased with the rise of explosives, while the number of transverse and longitudinal cracks remained almost unchanged. The spacing between two adjacent transverse cracks is about 13~15 cm, while the spacing between two adjacent longitudinal cracks is 10~13 cm, and the position of the transverse and longitudinal cracks is the location of the reinforcement. It should be pointed out that the amount of the oblique cracks is less than the amount of 300g explosive when the amount of explosive is 450g. This is because the energy is mostly concentrated in the falling concrete when the punching failure occurs, causing other parts to be affected.

The impact wave is less affected and the number of diagonal cracks is decreased. The RC slab forms a compression spalling crater on the top surface under the action of the blast loading. The concrete of the bottom surface spall to form a tensile spalling crater, the spallation penetrating and the punching failure will occur with the increase of the charge weight. For RC slabs of finite thickness under the contact explosion with a small amount of explosives, the main performance is the spallation damage. This is because the high temperature and high pressure generated in the early stage of the explosion acts on the RC one-way slab, which causes the top surface to form a crushed zone. At this time, the ultra-high pressure of the strong shock wave is mainly applied to the shock wave compression damage effect of the structure, and the crack appears to be “radial”. The crushed zone has a relatively small range, but consumes a large part of the energy, as a result the shock wave is attenuated into a compressive stress wave. At this point, there is a small spalling crater on the top surface of the slab, and the bottom surface has not yet exhibited visible macroscopic damage. As stress waves travel through the concrete, the impact compression wave caused by the explosion will be reflected at the bottom surface of the concrete, thus forming a tensile wave. Since the tensile strength of concrete is much lower than its compressive strength, when the tensile wave strength causes the concrete to reach a certain yield condition, tensile failure occurs and thereby forming a tensile spalling crater on the bottom surface.

The failure modes of the P1, P2 and P3 specimens used for the tests belong to this category. In this case, the specimens has two modes of overpressure failure and tensile failure. Increase the amount of explosives, which can cause the spalling crater on the top surface and the tensile spalling crater on the bottom surface to form spallation penetrating. Just then, the specimens present mainly overpressure failure and tensile failure. As the amount of explosives continues to increase, the concrete was completely punched out before

the material has not been crushed, generating an explosion punching phenomenon. The P4 specimen in the test showed such a phenomenon, in which case the concrete member was mainly shear fracture.

5. Conclusions

In this paper, the test of four RC one-way slabs which have the same material properties under contact explosion are conducted. The four RC one-way slabs named P1-P4 and are detonated under 150g, 225g, 300g and 450g emulsion explosives respectively. The failure modes and damage parameters are analyzed, and the failure mechanism is revealed. The results show that when the explosive mass is small, the specimens are tend to be tensile failure accompanied by transverse (longitudinal) cracks and radial cracks near the explosion point. With the increase of explosive mass, the failure modes of the RC one-way slabs transfer into punching failure, which is characterized by the concrete spalling near the explosion point and a large tensile spalling crater with a large number of transverse (longitudinal) cracks and radial cracks. The volume of the spalling crater increases accordingly; compared with P1, the top surfaces of P2, P3 and P4 increased by 31.1%, 48.8% and 81.8%. For the bottom surface, the volume of the spalling crater of P2, P3 and P4 increased by 6.92%, 26.91% and 136.54% in compared with P1, respectively.

6. Acknowledgment

The research reported in the paper is part of the Natural Science Foundation of Hunan Province, China (No. 2018JJ2470) and the Project supported by National Natural Science Foundation of China (No. 51308539). The financial support is highly appreciated.

7. References

- [1] Hao J W. Accident risk assessment and management of large bridges during operation period. 2015. (in Chinese)
- [2] Li L Y. Let the safety rules go from “on paper” to “on the road”. Safety and health, 2013(3):1-1. (in Chinese)
- [3] Low H Y , Hao H . Reliability analysis of RC slabs under explosive loading. Structural Safety, 2001, 23(2):157-178.
- [4] Low H Y , Hao H . Reliability analysis of direct shear and flexural failure modes of RC slabs under explosive loading. Engineering Structures, 2002, 24(2):189-198.
- [5] Xu K , Lu Y . Numerical simulation study of spallation in RC plates subjected to blast loading. Computers & Structures, 2006, 84(5-6):431-438.
- [6] Bibiana María Luccioni, Luege M . Concrete pavement slab under blast loads. International Journal of Impact Engineering, 2006, 32(8):1248-1266.
- [7] Ngo T ,Mendis P , Krauthammer T . Behavior of Ultrahigh-Strength Prestressed Concrete Panels Subjected to Blast Loading. Journal of Structural Engineering, 2007, 133(11):1582-1590.
- [8] Zhou X Q ,Kuznetsov V A , Hao H , et al. Numerical prediction of concrete slab response to blast loading. International Journal of Impact Engineering, 2008, 35(10):1186-1200.
- [9] András Schenker, Anteby I , Gal E , et al. Full-scale field tests of concrete slabs subjected to blast loads. International Journal of Impact Engineering, 2008, 35(3):184-198.
- [10] Wu C ,Nurwidayati R , Oehlers D J . Fragmentation from spallation of RC slabs due to airblast loads. International Journal of Impact Engineering, 2009, 36(12):1371-1376.

- [11] Silva P F , Lu B . Blast Resistance Capacity of RC Slabs. *Journal of Structural Engineering*, 2009, 135(6):708-716.
- [12] Pantelides C P , Garfield T T , Richins W D , et al. RC and fiber RC panels subjected to blast detonations and post-blast static tests. *Engineering Structures*, 2014, 76:24-33.
- [13] Thiagarajan. Experimental and finite element analysis of doubly RC slabs subjected to blast loads. *International Journal of Impact Engineering*, 2015, 75:162-173.
- [14] Assadilamouki A , Krauthammer T . Reevaluation of RC Slabs Subjected to Blast Effects// *Seismic Engineering*. ASCE, 2015.
- [15] J. S. KUANG, H. F. TSOI. Failure of Blast-Loaded RC Slabs.// *Proceedings of the Twelfth East Asia-Pacific Conference on Structural Engineering and Construction (EASEC12)*, Vol.4: Hong Kong, 26-28 January 2011. 2013:2658-2665.
- [16] Li J , Wu C , Hao H , et al. Experimental and numerical study on steel wire mesh RC slab under contact explosion. *Materials & Design*, 2017, 116:77-91.
- [17] Syed Z I , Raman S N , Ngo T , et al. The Failure Behaviour of RC Panels Under Far-field and Near-field Blast Effects. *Structures*, 2018:S2352012418300341.
- [18] Yan S, Zhang L, Wang D. Failure Mode Analysis of RC Slabs under Explosive Loading. *Journal of Shenyang Jianzhu University: Natural Science Edition*, 2005, 21(3): 177-180. (in Chinese)
- [19] Zhang XB, Yang XM, Chen YY, et al. The Collapse Effect of Explosive RC Slabs. *Journal of Tsinghua University (Science and Technology)*, 2006, 46(6): 765-768. (in Chinese)
- [20] Sun Wenbin. Experimental study on blast loading of RC slab. *Journal of Liaoning Technical University*, 2009, 28(2): 217-220. (in Chinese)
- [21] Failure Assessment Method of RC Slabs under Explosive Loading. *Journal of Building Structures*, 2009, 30(6): 60-66.
- [22] Wang W, Zhang D, Lu FY, et al. Near-field anti-explosion performance of square RC slab. *Explosion and Shock Wave*, 2012, 32(3): 251-258. (in Chinese)
- [23] Liu Y, Lu HB, Zhou BK, et al. Analysis of anti-contact explosion test of high strength RC plate. *Journal of the Chinese Ceramics*, 2012, 11(5):571-574. (in Chinese)
- [24] Chen WX, Lu HB, Hou XW, et al. Experimental study on anti-explosion performance of high strength steel RC slab. *JOURNAL OF VIBRATION AND SHOCK*, 2015, 34(10):135-141. (in Chinese)
- [25] Prepared by the Ministry of Construction of the People's Republic of China. Code for design of concrete structures. China Building Industry Press, 2002. (in Chinese)

Electrodiallytically treated MSWI fly ash use in clay bricks

L. Skevi^{1/2}, L. M. Ottosen², G. M. Kirkelund²

¹School of Physics, Faculty of Sciences, Aristotle University of Thessaloniki.

²Department of Civil Engineering, Technical University of Denmark

Abstract

Fly ash from municipal solid waste incineration (MSWI) is classified as hazardous waste, due to high heavy metal and salt content. Thus, beneficial use is restricted, and the fly ash hazardousness should be reduced before testing reuse options. Electrodialytic treatment can remove heavy metals and soluble salts and be used to decontaminate MSWI fly ash. In Greenland, MSWI fly ash is stored at uncontrolled disposal sites, and a more sustainable solution for handling fly ash is needed. At the same time, most construction materials are imported from Europe to Greenland, and increased use of local materials would greatly benefit the circular economy in the area. In this study, it was investigated if local Greenlandic resources could have potential in brickmaking. Two different clays; a Danish clay (used commercially in brick production) and one Greenlandic (not used commercially) and raw and electrodiallytically treated MSWI fly ash from Sisimiut, Greenland were used. Small clay discs with a 0, 10, 20 and 30 % substitution of clay by MSWI fly ash were fired at 1000°C for 24h. Substituting clay with fly ash generally resulted in lower technical properties of the clay discs. From this initial screening, the clay discs with electrodiallytically treated fly ash and Greenlandic clay showed the lowest porosity and water absorption, which could be beneficial for use as construction material in cold climates.

Keywords: heavy metals, circular economy, secondary resources, ceramics, Arctic.

1. Introduction

Incorporation of waste residues in building materials has been gained increased focus in the past years as a waste management practice on the one hand and a way to upgrade construction materials' properties on the other. Industrial wastes, like fly ash from coal combustion, silica fume and blast furnace slag are fine-grained materials with a high content in CaO, SiO₂, Al₂O₃ and other relative minerals, and this composition is compatible with cement-based and clay-based materials. Therefore, several studies investigate the application for partly replacement of cement and clay with these waste materials as secondary raw materials for the production of mortar, concrete and bricks [1, 2]. Ceramic materials made of clay, like bricks, are considered particularly attractive for the incorporation of wastes due to the heterogeneous composition of clay that can incorporate and stabilize various wastes in the matrix even if the wastes contain toxic substances. Also, there is a need for preservation of natural clay resources, and thus research on replacing part of clay for more sustainable brick production has been encouraged. It has, also, been demonstrated that the use of wastes as clay supplements in bricks do not affect significantly key properties of the final product [3], while in some cases they can even contribute to the enhancement of several of its properties.

Municipal solid wastes (MSW) account for about 10% of the total waste production, but due to their complex composition, their treatment presents certain difficulties. A common practice for avoiding the

landfill disposal of these solids wastes and thus for minimizing the environmental risk is incineration as it greatly reduces the mass and volume of the wastes. The miscellaneous composition of MSW depends on the sources of the wastes, which can vary for different countries according to waste management regulations and policies. Household and commercial wastes are the most common sources which may include different amounts of food waste, plastic and synthetic materials, even electrical devices and batteries when these are not recycled. As a result, MSW has a large content of organic and inorganic contaminants, such as heavy metals and alkaline salts. All these toxic compounds are finally highly concentrated in the residues of the incineration process. Handling of these residual materials, like fly ash, bottom ash and air pollution control residues (APC), can be very challenging. Disposal in landfills is a widely applied solution, but imposes a danger on the environment as a result of the leaching of the soluble elements which contaminate the soil and the water resources in the area. A more sustainable approach suggests the recycling and reusing of these materials. MSWI fly ash is an ultrafine material rich in calcium, silica and aluminium oxides and therefore it could be used as a cement and clay substitution for the production of sustainable building materials. However, because it also contains heavy metals, like Pb, Cd, Cr, Mo, Zn and alkali metal salts such as K and Na chlorides and sulphates it is classified as a hazardous waste. Thus, proper treatment for reducing the hazardousness of the material in acceptable limits is essential prior considering its possible beneficial uses.

Various techniques have been proposed for reducing the concentration of heavy metals and salts in MSWI fly ash [4]. Water washing is a simple method, often used as a pre-treatment before other techniques since it is more suitable for removing salts and very mobile fractions of heavy metals. Other techniques which stabilize heavy metals include carbonation, chemical stabilization and thermal and hydrothermal treatment. The electrodialytic treatment has been proposed as an alternative method for the removal of heavy metals and soluble salts and has been applied for the decontamination of MSWI fly ash [5,6]. The method relies on the application of an electric current to the waste material and the subsequent removal of heavy metal ions in the electric field [5]. Untreated and treated MSWI fly ashes have been tested in building materials in laboratory stage [7-10]. In [11] untreated Greenlandic MSWI fly and bottom ash were added in mortars as cement replacement, and it was concluded that up to 5% of ashes could be stabilized successfully in the mortar. In [3] it was tested if 20 % or 40% MSWI fly ash could replace clay for brick production and especially 40 % replacement resulted in deteriorating the properties of the final product and leaching of several heavy metals, especially an increase of Cr leaching was seen. There is a need to find the optimum replacement percentage of MSWI fly ash in brick products, for this application to be feasible. Removal of heavy metals and salts from the MSWI fly ash is also needed, to reduce the toxicity of the fly ash.

MSWI fly ash in Greenland is so far stored at uncontrolled disposal sites, before being shipped for end disposal abroad. Thus there is a need for a more sustainable and economically feasible solution. At the same time, most construction materials are imported from Europe to Greenland, while increased use of local materials would greatly benefit the circular economy in the area. Therefore, there is an option of using MSWI fly ash as a substitution of clay in bricks, which should stabilize the heavy metals and conserve primary resources. This study investigates the potential of brick production from Danish and Greenlandic clay that is partly substituted with MSWI fly ash, by screening the production on small clay discs. The effect of electrodialytic treatment of the fly ash in the final product is evaluated in comparison with that of the untreated waste.

2. Methodology

2.1 Experimental materials

Two different clays were used for the clay discs; commercially available Teglværksler (denoted T) from Wienerberger, Denmark and a clay sediment sampled from Sisimiut, Greenland (denoted S). MSWI fly ash was collected from the incineration plant in Sisimiut, Greenland and was used raw (denoted R) or

electrodiallytically treated in the clay discs. The electrodialytic treatment was performed in both a two- and a three-compartment cell (denoted E and D respectively), to remove heavy metals from the fly ash as a treatment method. More specific information and details about the electrodialytic treatment experiments can be found in [6]. Particle size distribution and mineralogy were determined on the separate electrodiallytically treated ashes, whereas heavy metal leaching and total content were measured on a mix of the two ashes (denoted ED). All notations of the experimental materials are shown in Table 1.

Table 1: Experimental materials

Clay	Symbol
Teglværksler (Danish clay)	T
Sisimiut ler (Greenlandic clay)	S
Fly ashes	
Treated fly ash (2 compartments)	E
Treated fly ash (3 compartments)	D
Mix E and D fly ashes	ED
Untreated (Raw) Sisimiut fly ash	R

2.2 Analytical methods

The Atterberg limits (liquid and plastic limits) were determined for the two clay samples to evaluate the plastic properties of the clays. The plastic limits (W_p) were determined by the rolling method (ISO/TS 17892-12), and liquid limits (W_L) were measured using the Casagrande method (DIN 18122-1). The particle size distribution was determined for all samples with a Malvern Mastersizer 2000 laser diffractometer on dry samples. Clay and ash mineralogy was studied by X-ray powder diffraction (XRD) for identification of major crystalline phases. The instrument was a PANalytical X'Pert Pro operating at 45 mA and 40 kV applying Cu K α radiation with a 2 Θ X'Celerator detector. The samples were scanned within 4–70 2 Θ for 2.5 h. The diffractograms were interpreted using the ICDD PDF-4 database for minerals. Total heavy metal concentrations were measured by Inductive Coupled Plasma – Optical Emission Spectrometry (ICP-OES) after pre-treatment according to DS 259. Heavy metal leaching was performed in a modified version of DS/EN 12457-1 (L/S 2), where 15 g ash was mixed with 30 mL distilled water (instead of 2 kg and 40 L as described in the standard) and suspended for 24 hours, before pH was measured in the suspension, filtration of the suspension and measurement of heavy metals in the eluate by ICP-OES.

2.3 Production of the discs

Twelve different clay mixtures with ash were made and compared to clay without fly ash (Table 2).

Table 2: Composition of the clay mixtures with the amount of fly ash given in wt%. The sample name follows the denotation in Table 1, and the numbers in the names of the samples refer to the percentage by weight of replaced fly ash.

Sample name	T	S	E	D	R
T0	100				
TED10	90		5	5	
TED20	80		10	10	
TED30	70		15	15	
TR10	90				10
TR20	80				20
TR30	70				30
S0		100			
SED10		90	5	5	
SED20		80	10	10	
SED30		70	15	15	
TR10		90			10
TR20		80			20
TR30		70			30

For the study, small brick specimens in the form of discs were constructed following the method that was applied in a previous study [3]. According to this method, the materials were mixed with a total weight of 2.3 g material, and distilled water was added to the material to obtain a paste-like texture. The mixture then absorbed the moisture for 24h. Next, the clay mixture was pressed into discs mechanically (Instron 6022), under a maximum load of 10 KN. The produced discs weighted approximately 2 g while their diameter and thickness (height) were around 20 mm and 3 mm respectively. Five discs of each mixture were produced, and their exact dimensions and weight was immediately measured with a micrometre scale gauge and a precision balance. The discs were then dried at 105°C for 24h and the dimensions and weight of the dried discs were again measured. Finally, the discs were fired at 1000°C for 24h and their dimension characteristics were again measured. The loss of mass (ML) and the linear shrinkage (LS) was determined between the wet, dry and fired condition, the total mass loss (TML) and total linear shrinkage (TLS) from wet to fired condition as described in the following equations. X is the diameter when referring to linear shrinkage and the mass when referring to the loss of mass.

$$DLS \text{ (or DML)} = \frac{x_{wet} - x_{dry}}{x_{wet}} \times 100 \% \quad (1)$$

$$FLS \text{ (or FML)} = \frac{x_{dry} - x_{fired}}{x_{dry}} \times 100 \% \quad (2)$$

$$TLS \text{ (or TML)} = \frac{x_{wet} - x_{fired}}{x_{wet}} \times 100 \% \quad (3)$$

Where:

DLS – dry linear shrinkage

FLS – fired linear shrinkage

DML – dry mass loss

FML – fired mass loss

TLS- total linear shrinkage

TML- total mass loss

The open porosity, dry density and water absorption were determined according to the procedure Ti-B-25 by the Danish Technical Institute. The discs were dried at 105°C, cooled to room temperature in a desiccator and weighed (m_{dry}). The discs were placed in a vacuum in the desiccator for 3 h, whereafter distilled water was added until the discs were submerged. The vacuum was again added for 1 h, whereafter the vacuum was released and the submerged discs were left at atmospheric pressure overnight. The water saturated discs were then weighed in water (m_{sw}) and air (m_{sa}) after being wiped for excess water. The open porosity, dry density and water absorption were then calculated as:

$$Open \text{ porosity} = \frac{m_{sa} - m_{dry}}{m_{sa} - m_{sw}} \cdot 100\% \quad (4)$$

$$Dry \text{ density} = \frac{m_{dry} \cdot \rho_w}{m_{sa} - m_{sw}} \cdot 100\% \quad (5)$$

$$Water \text{ absorption} = \frac{m_{sa} - m_{dry}}{m_{dry}} \cdot 100\% \quad (6)$$

Where ρ_w is the water density at room temperature.

Mineralogy (XRD) and heavy metal leaching were also performed on crushed clay discs.

3. Results and discussion

3.1 Characteristics of experimental materials

Geotechnical properties of the clays are shown in Table 3 and the particle size distribution of the raw materials, clays and treated fly ashes is shown in Figure 1. The plasticity index (I_p) can be used to evaluate the span between the plastic and liquid limits. Both clays used in this study present low plasticity, especially Sisimiut clay, which has a very low plastic index (<10). This agrees with results found by [3]) and indicate that their moulding range is very limited. Belmonte et al. [3] found higher plasticity index for mixtures of clay with fly ash than the clay itself, and the moulding of the clay discs with fly ash was not more difficult in practice than the clay itself. The two treated fly ashes, E and D, have similar particle size distribution as it is shown in the graph above. Also, their particles' size presents similar distribution with the one of the Sisimiut clay, although this the Sisimiut clay to have a slightly higher fraction of finer particles. Teglværks clay (T), on the other hand, has a larger volume percentage of coarse particles than the fly ashes and the Sisimiut clay. According to the Unified Soil Classification System (USCS) (ASTM D2487-17) both clays are classified as fine-grained soils (silt and clay) as more than 50% of their volume contains particles with fraction $d < 75 \mu\text{m}$. For both clays, the clay fraction ($< 2 \mu\text{m}$) was about 10% of their total volume, while approximately 45% of the volume of Teglværks and 65% of Sisimiut clay consisted of silt. The rest of their volume consisted of sand, 45% and 25% for Teglværks and Sisimiut clay, respectively. Finally, the raw untreated fly ash (R) consisted of finer particles than the treated fly ashes (E and D) and the two clays (T and S).

Taking into consideration the liquid limit (W_L) and plasticity index (I_p) of the clays as well as their particle size distribution according to the Casagrande plasticity chart [12], Teglværks clay is characterized as sandy lean clay, while Sisimiut clay as lean clay with sand.

Table 3: Geotechnical properties of the clays. Plasticity Index $I_p = W_L - W_p$.

Clays	Plastic Limit	Liquid Limit	Plasticity Index
	W_p (%)	W_L (%)	I_p (%)
T	15.2	28.5	13.3
S	14.2	22.5	8.3

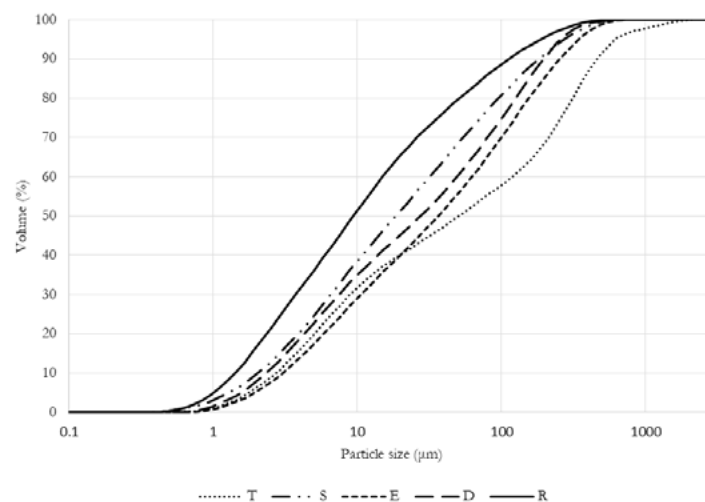


Figure 1: Particle Size Distribution of Teglværksler (T), Sisimiut clay (S), treated fly ashes (E&D) and raw fly ash (R)

The XRD diffractograms of clays and fly ashes are shown in Figure 2.

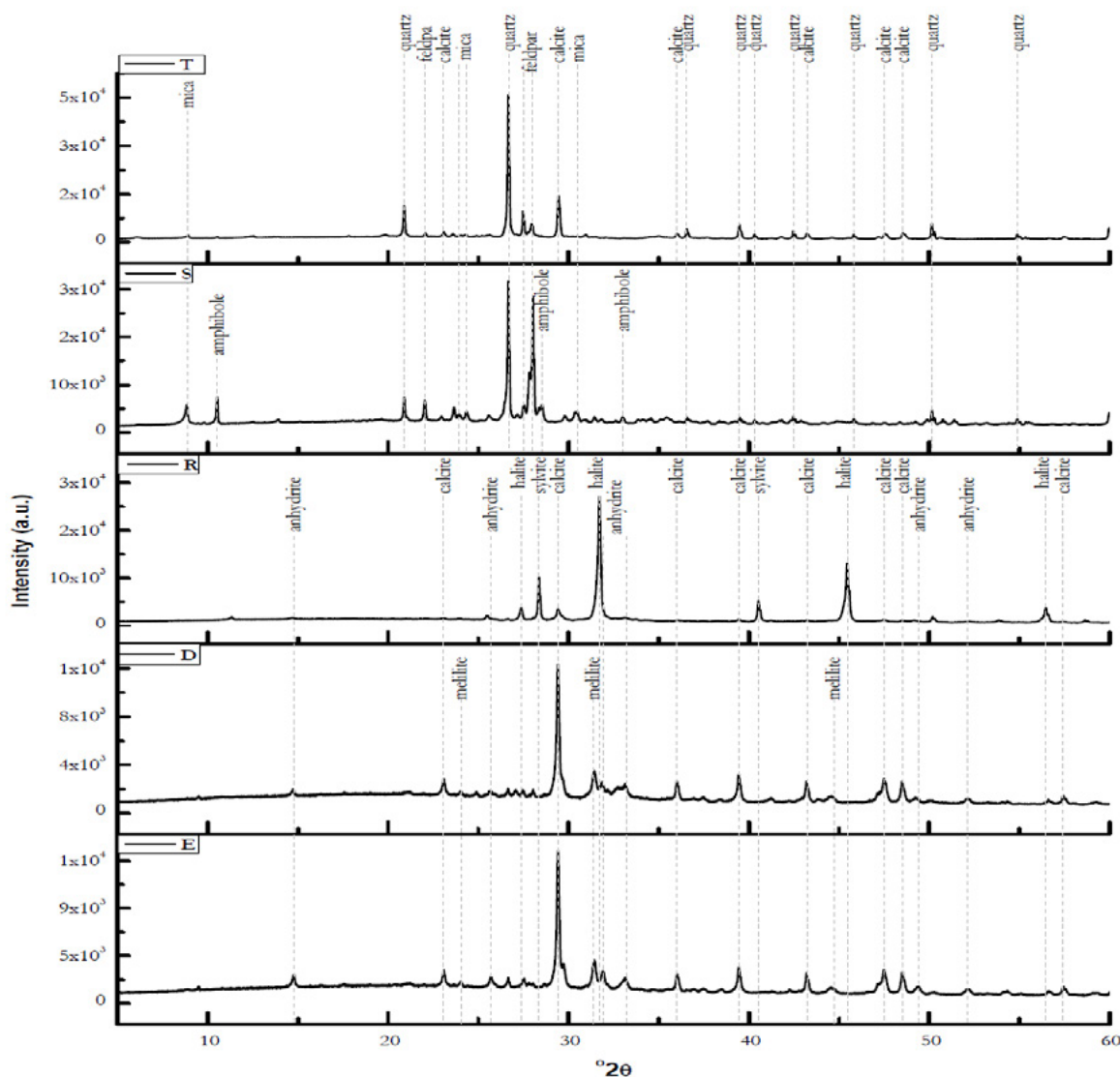


Figure 2: X-ray diffractograms of the experimental materials Teglvrærksler (T), Sisimiut clay (S), treated fly ashes (E&D) and raw fly ash (R)

As shown in the diffractogram, of Teglvrærks clay (T), this clay sample was dominated by quartz (SiO_2) and calcite (CaCO_3), and it also consisted of feldspars (albite ($\text{NaAlSi}_3\text{O}_8$) and microcline (KAlSi_3O_8) as well as micas (muscovite ($\text{KAl}_2(\text{AlSi}_3\text{O}_{10})$)). Sisimiut clay (S), on the other hand, mainly consisted of quartz and did not contain calcite. Instead, the second most dominant mineral phase in the Sisimiut clay was feldspars (albite, microcline and anorthite ($\text{CaAl}_2\text{Si}_2\text{O}_8$)), followed by amphibole (magnesianhornblende) and Fe – rich mica (phlogopite). This explains the light grey colour of Danish clay due to calcite, in comparison with the dark grey of the Greenlandic clay (photos of clays not shown). As for the fly ashes, the untreated raw fly ash (R) was dominated by salts: halite (NaCl) and sylvite (KCl). It also contained calcite and anhydrite (CaSO_4) as minor mineral phases. The two electrodialytically treated fly ashes (D and E) present identical mineralogy. As shown from their diffractograms they were calcareous but, unlike the untreated fly ash, they did not contain salts. Also, the phase of anhydrite (basanite) intensified in the electrodialytically treated ashes compared to the raw fly ash and traces of melilite mineral phases (gehlenite) were identified. It shows that the electrodialytic treatment is responsible for the removal of the salts in fly ashes D and E. Based on

the similar particle size distribution and mineralogy, it was determined to mix the two electrodiolytically treated ashes in for the further experiments.

Total heavy metal concentration and leaching of heavy metals, chloride and sulphate were measured for raw fly ash (R) and the mixture of the two treated fly ashes (ED). The results are shown in Table 4, in which the pH of the fly ashes is also given. The values are compared to the limits given by the Danish Ministry of Environment for use in geotechnical applications [13], as no limits exist for the use of waste in construction materials. The total metal concentrations show a significant reduction in the total content of heavy metals due to the electrodiolytic treatment, but the leaching of As, Cr, Ni and Zn increased, also to above the Category 3 limit. There was a significant reduction in the chloride and sulphate leaching, linked to the removal of chloride and sulphate containing mineral during the electrodiolytic treatment.

Table 4: Total heavy metal concentration and leaching of the fly ashes.

	Raw ash	ED ash	Category 3
Total concentration (mg/kg)	Average	Average	
As	277	29	>20
Cd	162	132	>0.5
Cr	109	71	>500
Cu	1,350	667	>500
Ni	32	73	>30
Pb	8,770	2,170	>40
Zn	21,600	8,680	>500
Leaching (µg/l)			
As	91	600	8-50
Cd	1560	2	2-40
Cr	550	1190	10-500
Cu	120	33	45-2000
Ni	46	125	10-70
Pb	397	35	10-100
Zn	109	340	100-1500
Cl	155·10 ⁶	1.7 ·10 ⁶	1.5·10 ⁶ - 3.0 ·10 ⁶
SO ₄	3.04·10 ⁶	0.75·10 ⁶	2.5 – 3.0 ·10 ⁶
pH	10.3	9.8	

3.2 Characteristics of the clay discs

The produced discs are shown in Figure 3, in the left the Teglværks clay discs and in the right the Sisimiut clay discs, both containing different amounts of substitution with fly ashes, treated (ED) and raw (R). It is seen in Figure 3 that as the amount of the fly ashes increases the colour of the discs gets lighter, both for the Danish (Teglværksler) and the Greenlandic (Sisimiut) clay mixtures. The stronger red colour of the Sisimiut S0 disc is probably linked to the Fe-minerals that were identified in this clay. There was a difference in the colour of the discs with raw fly ash and electrodiolytically treated fly ash. This was more dependent on the clay used than the ash since the disc with electrodiolytically treated fly ash in Teglværksler were darker than with raw fly ash, but the discs with Sisimiut clay were darkerst with raw fly ash.

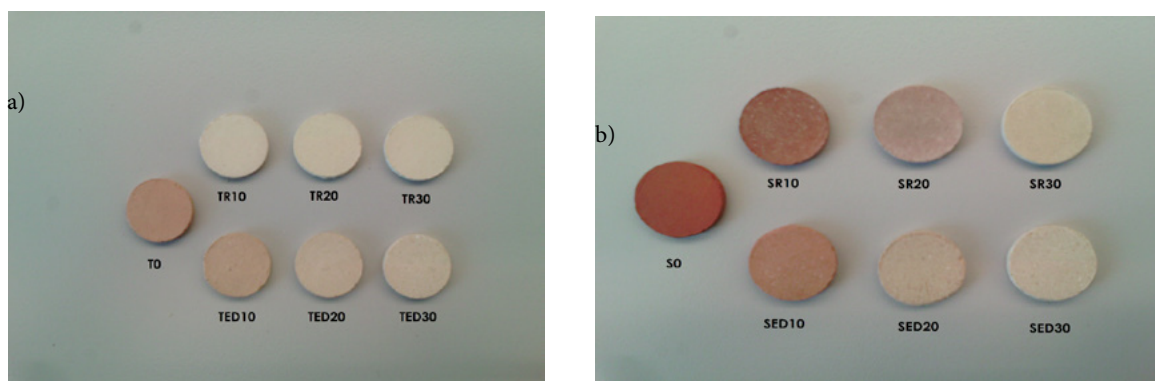


Figure 3: Colours of discs with substitution of clay with different amounts (0%, 10%, 20%, 30%) fly ash (R – raw, ED – treated. a) Teglværks (T) clay discs, b) Sisimiut (S) clay discs

The total loss of mass, total linear shrinkage, total volume change, porosity, dry density and water absorption of the produced discs are given in Figure 4. The total volume change of the discs containing raw fly ash (R) was negative for both types of clays, meaning that these discs expanded instead of shrinking as the other discs did, and their expansion was larger as the amount of fly ash increased. This can be attributed to a bloating effect due to gas from the decomposition of sulphates or carbonate [3]. On the contrary, the addition of more treated fly ash (ED) resulted in lower volume change for both clay discs, since sulphates are removed by electrodialytic treatment [5].

A lower mass loss but a higher linear shrinkage were seen for the Sisimiut clay discs compared to Teglværksler clay discs and increasing the amount of electrodialytically treated fly ash increased the volume change. This is clearly linked to the results of porosity, dry density and water absorption show in Figure 4. The porosity and water absorption increased by the addition of fly ash for both clay and fly ash types. Teglværks clay discs showed the highest porosity for substitution with raw fly ash, which is also linked to the higher mass loss for these clay discs compared to the Sisimiut clay discs. For the Sisimiut clays discs, the porosity was highest when treated fly ash was added, with corresponding lower densities of the discs and a higher water absorption, even if bloating occurred for the Sisimiut clay discs with raw ash.

The water absorption was lower for all Sisimiut clay discs than for the Teglværksler clay discs, also linked to the porosity. In bricks used in the building industry, typical ranges are: dry densities 1610-2120 kg/m³ [14, 15]; open porosities 18.8-39 % [15] and water absorption 22-37 % [16]. Only the water absorption is lower for some of the samples in this study, especially for the discs with Sisimiut clay and raw fly ash.

For the discs with electrodialytically treated fly ash, there was a difference when using Teglværksler or Sisimiut clay. The performance of the discs was lower with Teglværksler than the Sisimiut clay, which is also linked to the properties of the clays themselves. The low porosity, high density and low water absorption for the Sisimiut clay discs indicate good performance in cold climates. However, the pore size should be studied further to evaluate the possibility of resisting frost/thaw cycles.

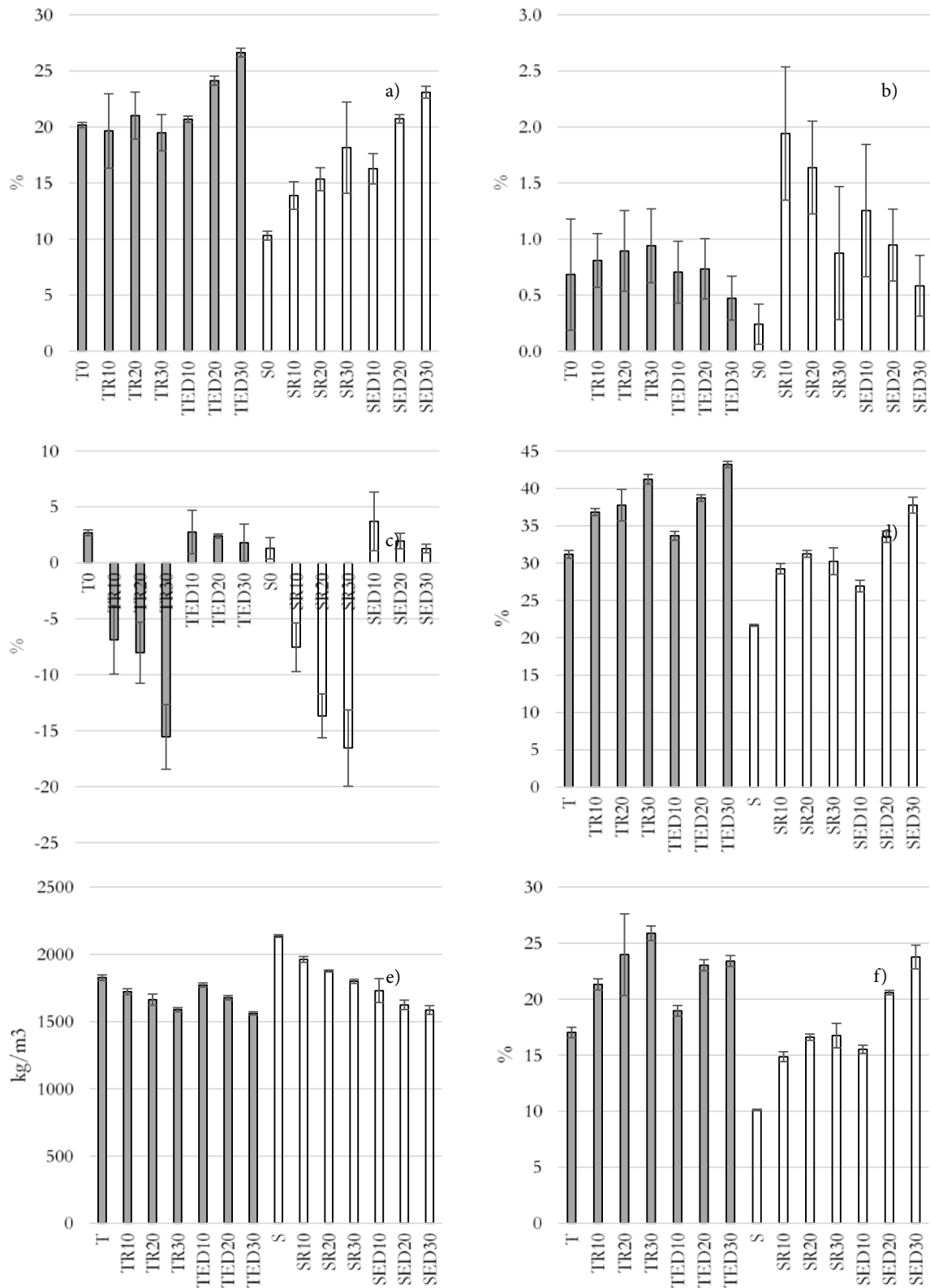


Figure 4: Physical properties of the clay discs: a) total mass loss, b) total linear shrinkage, c) total volume change, d) porosity, e) dry density, e) water absorption

The diffractograms of discs made of Teglværks (T) clay and treated fly ash (ED) in different proportions

is shown in Figure 5 and for discs made of Sisimiut clay in Figure 6.

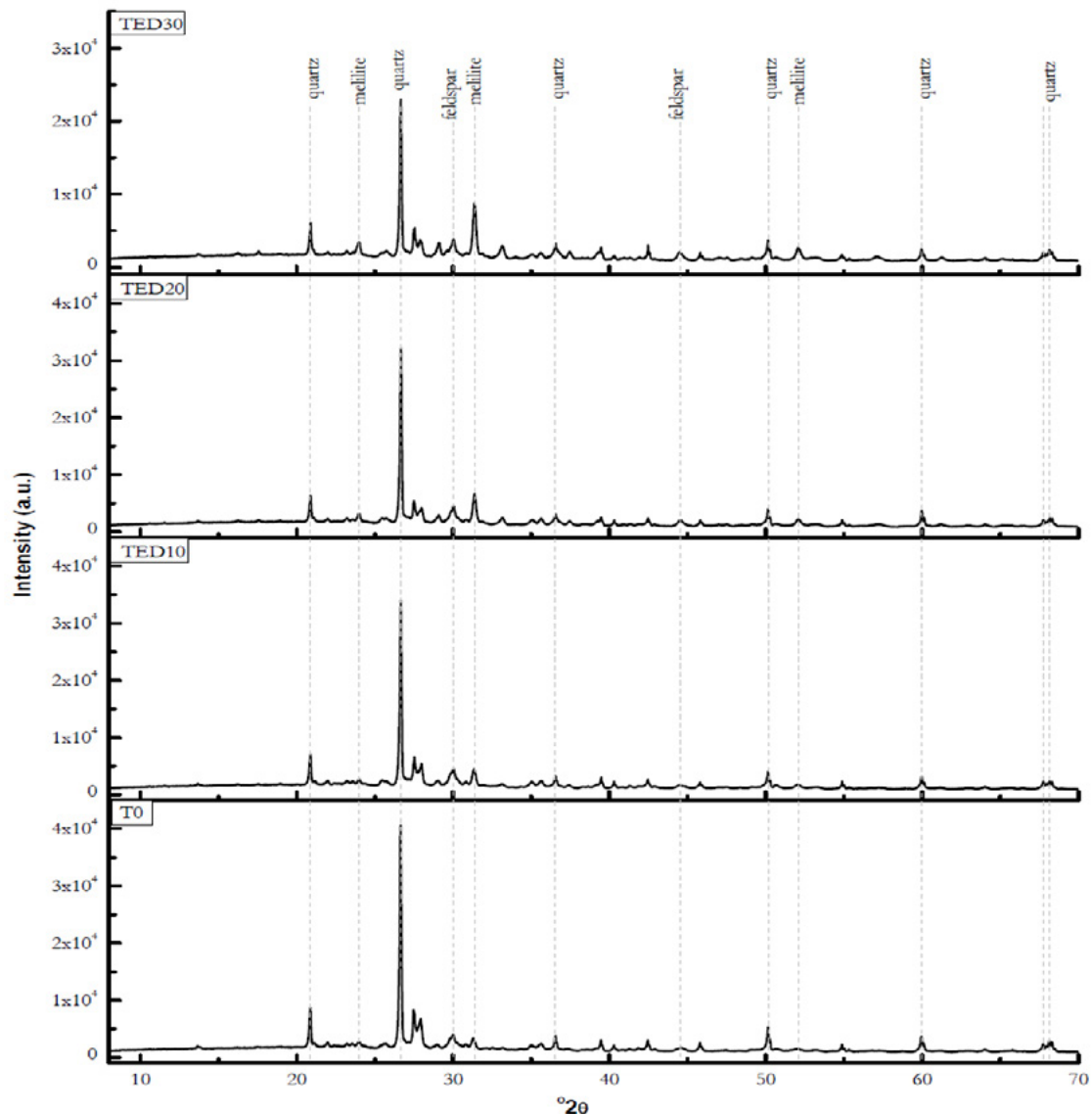


Figure 5: Diffractogram of Teglærks (T) clay discs with treated fly ash substitution of clay at 0%, 10%, 20% and 30%.

The reference discs with Teglærks clay, without the addition of fly ash, mainly contained quartz and feldspars (albite, microcline) as well as traces of melilite. As the amount of treated fly ash increases in the Teglærksler discs, the peak of quartz decreased significantly while that of melilite becomes more intense. In the discs with Sisimiut clay quartz was also the dominant mineral but feldspars (albite and microcline) were also abundant. Moreover, pyroxene was found in the control sample and increased by the addition of fly ash.

On the other hand, hematite that appeared in the control sample showed decreased peaks as the amount of fly ash increased. The occurrence of hematite in the Sisimiut discs, especially the control sample, justifies the red colour of the Sisimiut clay discs, unlike the yellowish colour of the Teglærks clay discs where there was no presence of an iron-based mineral.

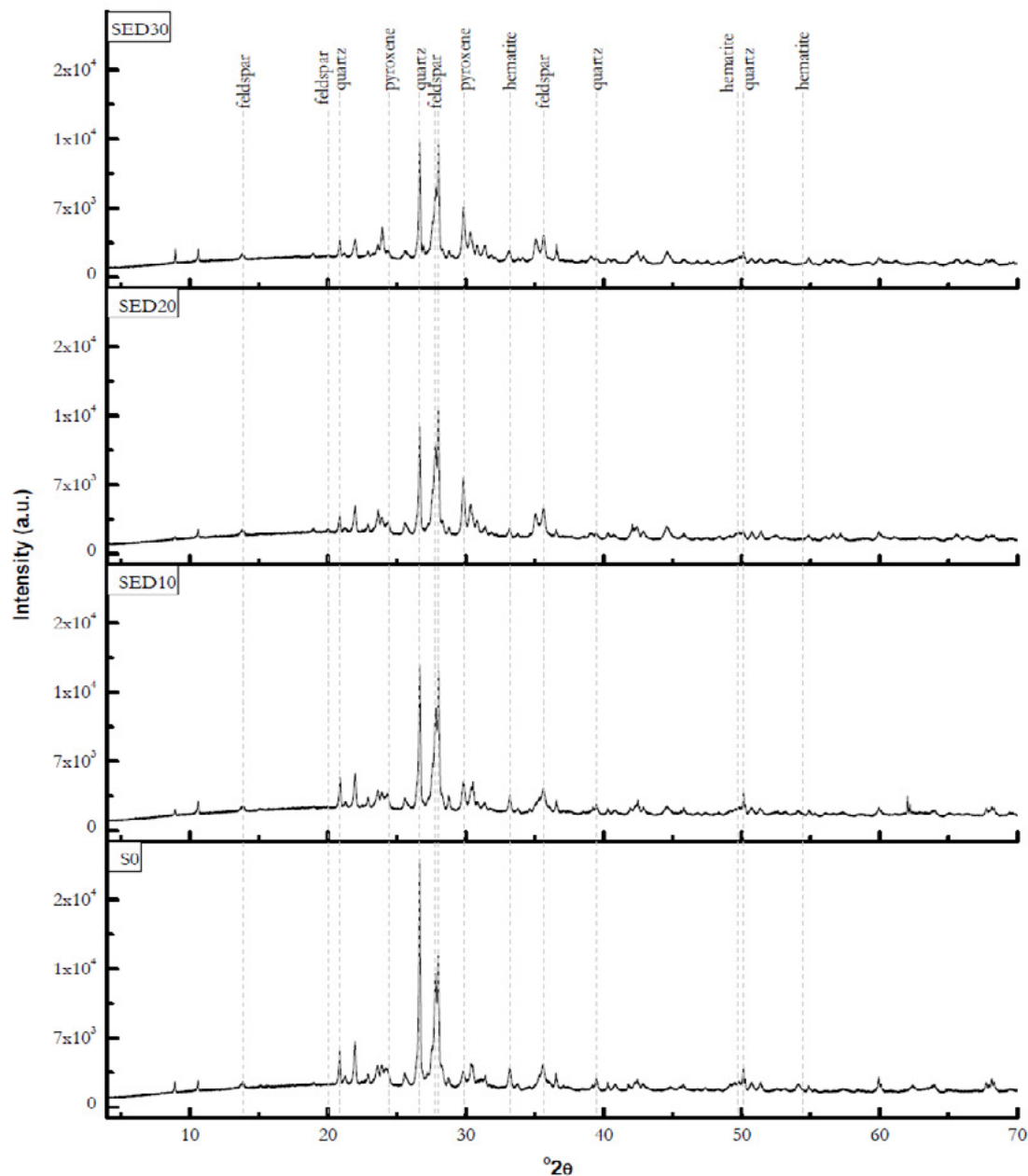


Figure 6: Diffractogram of Sisimiut (S) clay discs with treated fly ash substitution of clay at 0%, 10%, 20% and 30%.

Table 5 shows the leaching properties of the brick discs. There is no clear pattern in increased metal leaching with increasing addition of fly ash. However, these leaching results are from only one replicate, and there could be large uncertainties in the leaching values because of this. As leaching from most of the clay discs and Cr leaching from the TED10 sample was above the Category 3 guideline. The mobility of the metals was calculated, showing the extent of the immobilization of the metals when added in the bricks in comparison with the metals' leaching from the fly ashes. Belmonte et al. [3] observed increased mobility of As and Cr in clay discs containing 20 % and 40 % pre-treated MSWI fly ash by washing and electro-dialytic treatment. The contrary was observed in this study, were all samples showed immobilization in the clay matrix, except for the sample TED10, where Cr leaching increased compared to the initial leaching of the ED fly ash. Wan et al. [10] studied the incorporation of MSWI fly ash in 5×5×5 cm³ bricks and found that leaching of heavy metals both in batch leaching (determined by DS/EN 12457-1) and total leachability (determined by the Dutch leaching test at pH 4) was below the regulatory standards for these tests. This

could indicate that producing such a small number of the specimen as in this study should be used with care for conclusive studies of leaching properties and also that the leaching properties should be investigated further.

Table 5: Leaching of Teglværks and Sisimiut clay discs

Sample	pH	As (µg/l)	Cd (µg/l)	Cr (µg/l)	Cu (µg/l)	Ni (µg/l)	Pb (µg/l)	Zn (µg/l)
T0		115	<20	354	51	<20	<20	53
TR10	10.1	<20	<20	53	<20	<20	<20	<20
TR20	9.9	<20	<20	46	<20	<20	<20	<20
TR30	9.8	47	<20	74	<20	<20	<20	<20
TED10	11.2	50	<20	3240	33	<20	<20	31
TED20	10.7	75	<20	102	23	<20	<20	40
TED30	9.9	80	<20	<20	<20	<20	<20	80
S0		64	<20	<20	<20	<20	<20	39
SR10	10.1	<20	<20	<20	<20	<20	<20	<20
SR20	9.7	279	<20	<20	<20	<20	<20	<20
SR30	9.4	52	<20	<20	<20	<20	<20	<20
SED10	9.9	100	<20	<20	<20	<20	<20	33
SED20	9.7	64	<20	<20	<20	<20	<20	36
SED30	9.6	94	<20	<20	<20	<20	<20	38

4. Conclusions

The commercial clay consisted mainly of the minerals quartz, calcite, feldspars and mica, whereas the Sisimiut clay consisted of quartz, feldspars, amphibole and mica. The MSWI fly ashes consisted mainly of calcite and anhydrite and the raw fly ash also of halite and sylvite. The clay discs with Sisimiut clay presented a reddish colour compared to commercial clay, which gave white/greyish colour. Hematite was detected in the clay discs with Sisimiut clay, although increasing the fly ash proportion resulted in lighter colours. Leaching of Cr of untreated and treated fly ash exceeded the limits of Danish regulation for wastes in construction but was lower than for disposal at non-hazardous waste disposal sites. Apart from this, treated fly ash presented much lower heavy metal concentration than the untreated fly ash. Most heavy metals were incorporated into the clay disc matrix, and the mobility of metals decreased after firing. Expansion of the discs occurred for the samples containing raw fly ash, caused by bloating due to gas formation from the decomposition of minerals during firing. The expansion increased with the increased amount of fly ash in the clay discs. The porosity and water absorption increased with the addition of more fly ash while dry density decreased. The clay discs with Sisimiut clay showed the lowest porosity and water absorption, which will be beneficial for use in the cold climates. As the electrochemically treated MSWI fly ash showed better environmental performance than raw fly ash in the clay discs, there is a potential for using these Greenlandic raw materials in bricks, to support local production of construction materials.

5. Acknowledgement

Sabina June Hviid is thanked for help with the ICP and IC analysis and Erasmus + is acknowledged for providing a scholarship for Lorena Skevi.

6. References

- [1] Muñoz Velasco, P., Morales Ortíz, M.P., Mendivil Giró, M.A., and Muñoz Velasco, L. (2014). Fired clay bricks manufactured by adding wastes as sustainable construction material - A review. *Construction and Building Materials* 63, 97-107.
- [2] Raut, S.P., Ralegaonkar, R.V., and Mandavgane, S.A. (2011). Development of sustainable construction material using industrial and agricultural solid waste: A review of waste-create bricks. *Construction and Building Materials* 25, 4037-4042.
- [3] Belmonte, L.J., Ottosen, L.M., Kirkelund, G.M., Jensen, P.E., and Vestbø, A.P. (2018). Scree of heavy metal containing waste types for use as raw material in Arctic clay-based bricks. *Environmental Science and Pollution Research* 25, 32831-32843.
- [4] Quina, M.J., Bordado, J.C., and Quinta-Ferreira, R.M. (2008). Treatment and use of air pollution control residues from MSW incineration: An overview. *Waste Management* 28, 2097-2121.
- [5] Gunvor M. Kirkelund, C.M., Paula Guedes, Pernille E. Jensen, Alexandra B. Ribeiro, Lisbeth M. Ottosen (2015). Electrodialytic removal of heavy metals and chloride from municipal solid waste incineration suspension – test of a new two compartment experimental cell. In *Electrochimica Acta*, Volume 181. pp. 73–81.
- [6] Kirkelund, G.M., and Jensen, P.E. (2018). Electrodialytic treatment of Greenlandic municipal solid waste incineration fly ash. *Waste Management* 80, 241-251.
- [7] Quina, M.J., Bontempi, E., Bogush, A., Schlumberger, S., Weibel, G., Braga, R., Funari, V., Hyks, J., Rasmussen, E., and Lederer, J. (2018). Technologies for the management of MSW incineration ashes from gas cleaning: New perspectives on recovery of secondary raw materials and circular economy. *Science of the Total Environment* 635, 526-542.
- [8] Aubert, J.E., Husson, B., and Sarramone, N. (2006). Utilization of municipal solid waste incineration (MSWI) fly ash in blended cement Part 1: Processing and characterization of MSWI fly ash. *J Hazard Mater* 136, 624-631.
- [9] Huang, T.Y., and Chuieh, P.T. (2015). Life Cycle Assessment of Reusing Fly Ash from Municipal Solid Waste Incineration. *Procedia Engineering* 118, 984-991.
- [10] Chen, W., Klupsch, E., Kirkelund, G., Jensen, P., Ottosen, L., and Dias-Ferreira, C. (2017). Recycling of MSWI fly ash in clay bricks—effect of washing and electrodialytic treatment.
- [11] Kirkelund, G.M., Ottosen, L.M., Jensen, P.E., and Goltermann, P. (2016). Greenlandic waste incineration fly and bottom ash as secondary resource in mortar. *International Journal of Sustainable Development and Planning* 11, 719-728.
- [12] Casagrande, A (1948). Classification and identification of soils, *Transactions of the American Society of Civil Engineers*, 113, 103-112.
- [13] BEK nr 1672 15/12/2016. Bekendtgørelse om anvendelse af restprodukter, jord og sorteret bygge-og anlægsaffald. Ministry of Environment and Food in Denmark.
- [14] Dondi, M., Principi, P., Raimondo, M., Zanarini, G. (2000). The thermal conductivity of brick produced with Italian clays. *L'industria dei Laterizi*, 65, 309-320.

- [15] Dondi, M., Mazzanti, F., Principi, P., Raimondo, M., Zanarini, G. (2004). Thermal conductivity of clay bricks. *Journal of Materials in Civil Engineering*, *16*, 8-14.
- [16] Domone, P., Illson, J. (2010). *Construction materials: their nature and behaviour*. London and New York, Spon Press.

Experimental Studies on Fly Ash Gypsum Slurry

V.Revathi¹, S.Jayanthi²

¹K.S.R.College of Engineering, Tiruchengode, Tamilnadu

²Government College of Engineering, Bodinayakannur, Tamilnadu

E-mail: ¹revthiru2002@yahoo.com; hodcivil@ksrce.ac.in; ²gcebodi@gmail.com

Abstract

This study aimed to examine the performance of fly ash gypsum slurry in relation to the properties of its ingredients. Experiments were carried out to arrive at an optimum proportion of various ingredients for Fly ash-Gypsum slurry (F-G) mixtures having 150 mm, 300 mm, 375 mm, 425 mm and 500 mm flows. The designed mixtures were tested for flowability, density and compressive strength. The results show that even a small variation in water content drastically affected the flowability of F-G slurry. While flowability is mainly governed by water, observations indicated that flowability depends on the composition of the mixture ingredients and its properties. It is understood that the minimum volume of water required for the slurry having higher flows of more than 300 mm flow is 50%. Also, it is found that almost all FG mixtures show considerable compressive strength suitable for backfilling and structural filling applications.

Key words: Fly ash, Gypsum, flowability, Flowable Slurry, backfilling, structural filling

1. Introduction

Generally, soil backfilling is adopted to strengthen and support the foundation of a structure. Proper compaction is required more to ensure uniform and rigid filling than original soil. However, in many cases, the material is dumped into the trench, leading to poor compaction. This made the researchers use a low strength flowable material which does not require compaction. Flowable slurry or Controlled Low Strength Material (CLSM), an alternative to compacted soil fill, has been used increasingly in the construction industry as it has numerous advantages such as easy to place, strong, durable, free from settlement, free from compaction, excavatability and allows fast return to traffic. Flowable slurry is a self compacting cementitious material and it has a compressive strength of 8.3 MPa or less at the age of 28 days. Flowable slurry is mainly used in the areas of backfilling, structural filling, mining and underground construction, erosion control and pavement base. The chief benefit is that it makes use of industrial by-products [1]. *The properties of flowable slurry lie between soil and concrete.* The materials used, production and placing is similar to concrete. In service properties exhibits the characteristics of soil. Both fresh and hardened properties need to be considered to use flowable slurry for various applications.

In 1964, the U.S. Bureau of Reclamation documented the first known use of controlled low-strength material. It is perhaps the most novel material which found one of its earliest applications in the year 1964 as the bedding material for the 515 km long pipe line in the Canadian River Aqueduct project by the US Bureau of Reclamation. The use of CLSM reduced the project cost by 40% compared to that of conventional soil fill (Brewer 1994).

Flowability is the exclusive property of flowable slurry, which facilitates the materials to be self-leveling - to flow into and fill a void and be self-compacting without the need of compacting equipment. Flowability can be varied from stiff to fluid, depending upon the requirements. The flowable slurry is quantitatively described by its spread of flow. Similar to concrete/mortar, flowable slurry is a composite material. But it flows like a liquid. Flowability of flowable slurry mixtures is influenced by its ingredients, quantity, and the properties of the ingredients. When flowable slurry mixtures were developed with foundry sand and fly ash, proper amount of fly ash was required to obtain desired flowability [2-3]. Gandham indicated that flowability mainly depends on fly ash and water content in the mixture and phospho gypsum alone does not contribute to a satisfactory flowability [4]. Another study carried out by Nataraja et al showed that the mixture containing fly ash achieved the desired flowability with a lower w/c ratio, compared to mixture containing rice husk ash [5]. The mixture containing quarry dust achieved the desired flowability with lower w/c ratio compared to the mix containing sand. Use of cement kiln dust increased the water demand of flowable slurry to achieve a specific flowability [6-7].

Jason et al. carried out an experimental study using recycled crumb rubber and native silty sand to produce lightweight, soil-based, rubberized flowable slurry for a bridge approach repair. A Fluidizing agent was added to the mixtures to improve flowability and control bleeding. For the backfilling of a small bridge abutment, 200 mm flow was recommended, as it does not require to flow a significant distance [8]. Pierce et al pointed out that mixtures that flowed for more than 600 mm are considered unacceptable for flowable fill because the crumb rubber was segregated during the test. Rubberized flowable slurry is not flowable without the addition of sand. Fully rubberized CLSM provided poor workability [9].

FHWA (Federal Highway Administration) specifies that the density of high fly ash is in the range of 1460 kg/m³ to 1945 kg/m³ [10]. Charles et al reported that density of less than 800 kg/m³ can be obtained with the use of a foaming agent for flowable fly ash slurry [11]. It has been observed that the compressive strength depends on the quantity of the cement and its water content. A cement content of about 90 kg/m³ was required to produce a compressive strength greater than 0.345 N/mm² at the age of 28 days. As the water content increased compressive strength probably got reduced [11-15]. It could be said that flowability of flowable slurry, not only depends on the amount of water but also on the composition of ingredients.

Generally, 5% of OPC and 95% of fly ash is used as a binder in flowable slurry. Amitava Roy et al and Poon et al have mentioned that ordinary Portland cement can be completely replaced by alkalis and sulphates (industrial by-product/reagent grade) to obtain a binder with similar properties. The activated fly ash by industrial by-products as a binder in CLSM will boost the large-scale utilization of both fly ash and industrial wastes [16-17].

Phosphogypsum (PG) is a by-product obtained from the phosphoric acid process in fertilizer manufacturing. Only 15% of PG is being utilized by the cement and gypsum industries as a setting moderator for cement and for making gypsum plaster. The remaining 85% of PG creates an environmental problem. Around 6 million tons of phosphogypsum, available annually in India, can be used as a resource to activate fly ash so as to conserve natural resources, protect the environment and save energy([18-19].

In this context, the present work aims to develop flowable slurry using industrial waste by-products such as fly ash and gypsum. The study examined the performance of fly ash gypsum slurry in relation to the properties of ingredients which had not been addressed in the earlier work.

2. Methodology

2.1 Materials

2.1.1 Fly Ash

Fly ash obtained from Neyveli Lignite Corporation (NLC) was used in this study. The physical and chemical properties of the fly ash were carried out using the procedure prescribed by IS 1727-1967 (R2004) and the results are presented in Tables 1 and 2.

Table 1: Physical properties of fly ash

Sl. No.	Test Conducted	Observed Values	Required As Per IS 3812 - 2003
1	Specific Gravity	2.47	-
2	Initial Setting Time (min)	45	-
3	Final Setting Time (min)	280	-
4	Consistency (%)	35	-
5	Blain's Fineness (cm ² /gm)	3550	3200 min
6	Lime Reactivity (MPa)	7.1	4.5 min

Table 2: Chemical properties of fly ash

Sl. No.	Test Conducted	Observed Values (%)	Required As Per IS 3812 - 2003
1	Loss on Ignition LOI	3.74	5 % max
2	Silica as SiO ₂	35.87	25 % min
3	Iron as Fe ₂ O ₃	4.00	--
4	Alumina as Al ₂ O ₃ + SiO ₂	34.14	50 min
5	Calcium as CaO	14.25	--
6	Magnesium as MgO	3.64	5 % max
7	Sulphate as SO ₃	3.4	3 % max
8	Sodium as Na ₂ O	0.90	1.5 % max
9	Potassium as K ₂ O	0.06	--
10	Chloride	--	0.05 % max

2.1.2 Gypsum

The Phospho-gypsum used in this study was obtained from TANFAC (a fluoride industry), Cuddalore. Its specific gravity was found to be 2.70. The chemical properties of gypsum are shown in Table 3.

Table 3: Chemical properties of gypsum

Sl.No.	Chemical Composition	Observed Values (%)
1	Loss on Ignition	1.63
2	Insoluble Residue	0.5
3	Alumina as Al ₂ O ₃	0.75
4	Iron as Fe ₂ O ₃	0.82
5	Calcium as CaO	44.99
6	Magnesium as MgO	1.02
7	Sulphate as SO ₃	48.84
8	Purity	99.4

2.2 Mixture Proportion for Flowable F-G Slurry

For the experimental investigation, five different flow series of flowable slurry mixtures were considered. The mixtures were proportioned for the flow of 150 ± 50 mm, 300 ± 50 mm, 375 ± 25 mm, 425 ± 25mm and 500 ± 25 mm. All the mixtures were proportioned to obtain flowable slurry as defined by ACI Committee 229R (2005). The gypsum content in the binder was 10% by mass of fly ash. The water content

was arrived at by trial and error method in order to obtain the desired flowability. The details of mixtures are presented in Table 4. The F-G mixtures are designated as A, B, C, D and E.

Table 4: Mixture proportions of F-G slurry and fresh slurry properties

Sl. No	Flow Range (mm)	Mixture Designation	Mixture Ingredients				Flow/Spread (mm)
			Fly ash (kg/m ³)	Gypsum (kg/m ³)	Water (kg/m ³)	W/ (FA+ G)	
1	500 ± 25 flow	A	898.1	89.8	642.0	0.65	481.0
2	425 ± 25 flow	B	941.3	94.2	621.2	0.60	420.0
3	375 ± 25 flow	C	1053.4	105.3	579.4	0.50	391.0
4	300 ± 50 flow	D	1188.2	118.8	522.8	0.40	274.0
5	150 ± 50 flow	E	1366.6	136.7	451.0	0.30	185.0

2.3 Preparation and Testing

The calculated quantity of fly ash and gypsum were mixed in dry condition for about five minutes. The required quantity of water was slowly added and mixing was continued for another five minutes. Flow test as per ASTM D 6103 was carried out and fresh slurry density determined. The freshly prepared F-G slurry was tested for wet density. Cube specimen of 50 mm was used for determining the density of hardened F-G slurry. Cubes were de-moulded after 24 hours and humidity cured, until testing. Twelve specimens were prepared, cured and tested for each mixture. The test was carried out using 2000 kN compression testing machine. The load was applied on each specimen till its failure. The Ultimate load applied over a specimen that caused failure was noticed and recorded. The compressive strength was estimated using the equation

$$\text{Compressive strength} = P/A \quad (1)$$

where, P = Ultimate load in kN;

A = Cross sectional area of cube in mm²

3. Results and discussion

Fly ash gypsum slurry is characterized by its properties like flow, density and compressive strength. This part presents the results of the laboratory investigations and the observations made thereof.

3.1 Flow Test of F-G Slurry Mixtures

Flow of fly ash gypsum (F-G) slurry is an important property. Therefore, it is essential to understand the influence of F-G slurry ingredients on flow behaviour. Water is the predominant ingredient which influences the spread of the slurry. The quantity of water required to obtain a desired flow depends primarily on the quantity of fly ash, and gypsum in the mixture. The attempt made to understand the relationship between volume of solids and flowability is presented below.

F-G slurry consists of fly ash, gypsum and water. It is considered as a system consisting of only two prominent phases, namely, solids and liquid. Totally, five mixtures were made with flowability values of 150 mm, 300 mm, 375 mm, 425 mm and 500 mm. Experiments were carried out to arrive at the optimum proportions of ingredients for each mixture. The quantity of water required, relative ratios (RR) as well as successive relative ratio (SRR) of each flow are presented in Table 5. It is evident from the Table that the RR value of flow varies in the range of 1 to 1.42. However, the RR value of water varies from 1 to 1.42. It is evident that the RR value of F-G slurry with 500 mm flow increased three fold while the relative ratios

(RR) of water increased only 42%. This indicates that the flow of slurry is highly sensitive even to the little variations in water content. Also, it has been substantiated with computed successive relative ratios of flow and water. The SRR of flow varies in the range of 1.13 to 2.0, while corresponding values for water requirement varies in the range of 1.03 to 1.16. It is also observed that mixtures with higher flow are more sensitive to even marginal variation in water content than mixtures with low flow.

Also, for better understanding rheology of slurry, quantities of ingredients such as fly ash, gypsum and water are converted from mass to volume and presented in Table 6. It is inferred that the minimum volume of water required for the slurry having higher flows (more than 300 mm flow) is 50%. It is obvious that the water requirement increases with increase in flowability and thereby the content of solids gets reduced in the mixture.

Table 5: Water requirement of F-G slurry mixtures

Sl. No	Mixture Designation	Flow Range (mm) (x_i)	Flow Variation		lit / m ³ (y_i)	Water Requirements	
			Relative Ratio ($x_i/150$)	Successive Relative Ratio		Relative Ratio (RR)*	Successive Relative Ratio**
1	A	500	3.33		642	1.42	
2	B	425	2.83	1.17	621	1.37	1.03
3	C	375	2.5	1.13	579	1.28	1.07
4	D	300	2	1.25	523	1.16	1.1
5	E	150	1	2	451	1	1.16

* RR = y_1 / water requirements of corresponding filler having 150 mm flow

**SRR- 1.42/1.37=1.03 and so on..

Table 6: Phase system in F-G slurry mixtures

Sl.No	Mixture Designation	Flow Range (mm)	Volume of Fly Ash (%)	Volume of Gypsum (%)	Volume of Total Solids (%)	Volume of Water (%)
1	A	500	35	3.2	38.2	61.8
2	B	425	36.8	3.3	40.1	59.9
3	C	375	40.8	3.6	44.4	55.6
4	D	300	45.9	4.1	50	50
5	E	150	52.4	4.7	57.1	42.9

3.2 Density of F-G Slurry

The density of slurry depends on the type of ingredients present and their proportions. Generally, it will have a bearing on the yield, strength, durability and also shrinkage. Density of fresh slurry (wet density) and hardened slurry of all mixtures were determined and presented in Table 7. The wet density of F-G slurry is varying from 1620 kg/m³ to 1920 kg/m³, whereas, the dry density is in the range of 1600 kg/m³ to 1900 kg/m³. It is obvious that density increases both in fresh as well as hardened slurry with the increase in the volume of solids. A marginal reduction in density of wet slurry is noticed, on hardening. It is due to the evaporation of water from slurry during the hardening process. However, the loss of water has resulted in only a marginal reduction in yield of slurry. The yield of slurry is the hardened unit mass of the flowable slurry that could be obtained after the slurry settles and hardens at the ambient temperature. The results are in conformity with the reported density of slurry [10-14]. The reported density is in the range of 1460 kg/m³ to 1945 kg/m³.

Table 7: Density of fresh and hardened F-G slurry mixtures

Sl. No	Mixture Designation	Flow Range (mm)	Volume of Total Solids (%)	Wet Slurry Density (kg/m ³) (x)	Hardened Slurry Density (kg/m ³) (y)	Yield of the Slurry, (y/x) * 100
1	A	500	38.2	1620	1600	98.8
2	B	425	40.1	1730	1700	98.3
3	C	375	44.4	1850	1800	97.3
4	D	300	50	1900	1890	99.5
5	E	150	57.1	1920	1900	99

x - Wet Slurry Density (kg/m³); y - Hardened Slurry Density (kg/m³)

Also, an attempt has been made to compare the observed and the computed density of FG. The Density of the slurry in the hardened state is essential to compute the quantity of the materials required for a particular application. In order to compute optimum quantity of water required for the slurry for a specific application, an attempt has been made to arrive at an expression. Generally, dry density is computed using the following expression (1).

$$\text{Dry Density } (\gamma_d) = \frac{\gamma}{1 + w} \quad (2)$$

where γ_d – dry density in kg/m³

γ – wet density in kg/m³

w–water content (ratio of the weight of water to the weight of solids)

The above expression has been modified based on several laboratory trials to obtain the computed hardened density. The modified expression is presented below (2):

$$\text{Computer Hardened Density } (\gamma_{cd}) = \frac{\gamma}{1 + w / 100} \quad (3)$$

where γ_{cd} – dry density in kg/m³

γ – wet density in kg/m³

w–water binder ratio (ratio of the weight of water to the weight of binder)

The computed and observed densities are presented in Table 8. It is observed that the computed density of hardened slurry is in agreement with the measured densities. The maximum deviation of computed density from measured density is only 2%. The above expression can be used effectively to arrive at the optimum quantities of materials to obtain the required hardened density.

Table 8: Comparison between the observed and the computed hardened density of F-G slurry mixtures

Sl. No	Mixture Designation	Flow Range (mm)	Wet Slurry Density (kg/m ³)	Observed Hardened Slurry Density (kg/m ³) (x)	Water/ Binder Ratio W/(FA+ G)	Computed Hardened Density (y)	Computed / Observed Hardened Density (y/x)
1	A	500	1620	1600	0.65	1609.5	1.01
2	B	425	1730	1700	0.6	1719.7	1.01
3	C	375	1850	1800	0.5	1840.8	1.02
4	D	300	1900	1890	0.4	1892.4	1.00
5	E	150	1920	1900	0.3	1914.3	1.01

x - Wet Slurry Density (kg/m³); y - Hardened Slurry Density (kg/m³)

3.3 Compressive Strength of F-G Slurry

The cured specimens of various F-G slurry mixtures were tested for compressive strength at the age of

3, 7, 28 and 56 days. The test results are furnished in Table 9. The compressive strength mainly depends on the type of binder and the mixture proportion of ingredients used in slurry. ACI 229 R 2005 specified a compressive strength of maximum 8.3 MPa or less at the age of 28 days for controlled low strength material (CLSM). However, it has been reported in the literature that fly ash gypsum flowable slurry was made even with 10 MPa compressive strength (Gandham et al 1996). At the same time, fly ash slurry was also made with a compressive strength as low as 0.34 MPa (Naik et al 1990). The minimum compressive strength of 0.34 MPa can be used when later age excavability of the flowable slurry is predicted. It shows that fly ash slurry can be produced with a wide range of strengths depending on requirements.

The compressive strength of F-G slurry is varying from 1.7 MPa to 5.61 MPa at the age of 28 days. Hence, the F-G slurry produced in the present study can be considered as controlled low strength material. It is noticed that the compressive strength at all ages improved with an increase in the volume of solids. It is obvious that the increased volume of solids reduced the volume of water in slurry. This in turn improved the compressive strength of hardened slurry. The compressive strength gradually decreased with increase in the flow of slurry from 150 mm to 500 mm. Similar observations were made on flowable slurry by FHWA (1998), Krell.(1989), and Naik et al (1990, 2003). However, significant reduction in strength is noticed in the slurry having flowability greater than 375 mm. It must be due to the addition of much more water than the optimum quantity of water required for the hydration of the binder.

Table 9: Compressive strength of F-G slurry mixtures

Sl. No	Mixture Designation	Flow Range (mm)	Volume of Solids (%)	Compressive Strength at Various Ages (MPa)			
				3 days	7 days	28 days	56 days
1	A	500	38.2	1.43	2.01	2.36	2.72
2	B	425	40.1	0.36	1.41	1.70	3.10
3	C	375	44.4	2.62	3.72	5.00	5.70
4	D	300	50	2.96	4.19	5.41	5.90
5	E	150	57.1	3.20	5.60	5.61	6.50

4. Conclusions

This article presents a study carried out to evaluate the behaviour of F-G slurry. From the results and discussion the following conclusions are drawn:

The relative ratios and successive relative ratios of flow are significantly higher than the water requirement for F-G slurry. It shows that even a small variation in the water content drastically affects the flowability of slurry. Also, the mixtures with higher flow are much more sensitive to even marginal variation in the water content than the mixtures with low flowability. Further, it is noticed that a minimum of 50% volume of water is required for F-G slurry having flowability higher than 300 mm.

The wet and hardened density of FG slurry is in the range of 1620 to 1920 kg/m³ and 1600 to 1900 kg/m³, depending on the respective quantity of solids. The marginal reduction in the density of wet slurry is noticed, on hardening, in F-G slurry. It is due to the evaporation of water from slurry during hardening process. FG slurry mixes considered in the present study can be classified as regular flowable slurry, based on their density, as the density of all of the mixtures is more than 800 kg/m³.

The compressive strength at all ages improved with the increase in the volume of solids and reduction in flowability. Also, it is found that almost all FG slurry mixtures have shown compressive strength varies varying from 1.7 MPa to 5.61 MPa, at the age of 28 days, depending on the flow of mixtures. However, the considerable reduction in strength is noticed in the slurry having flowability greater than 375 mm. It must be due to the addition of much more water than the optimum quantity of water required for the hydration

of the binder.

The strength obtained for all the mixes are below 8.3 MPa, as specified by ACI 229 R. Therefore, it satisfies the strength requirement of flowable slurry. Also, all the mixes can be used as structural fills as the strengths of the mixes are between 0.69 to 8.3 MPa.

5. References

1. ACI Committee 229 R. (2005) 'Controlled Low Strength Materials (CLSM)' – ACI Concrete International Vol. 16, No.7, pp.55-64.
2. Bhat S.T. and. Lovell C.W. (1996) 'Design of Flowable Fill: Waste Foundry Sand as a Fine Aggregate' – Transportation Research Record No. 1546, pp 70-87.
3. Bhat S.T. and. Lovell C.W. (1997) 'Mix Design for Flowable Fill', Transportation Research Record, No. 1589, pp. 26-35.
4. Charles K.N., Frances McNeal and Dean Martin (1997) 'New Foaming Agent for CLSM Applications', Concrete International, Vol. 19, No. 4, pp. 44-47.
5. FHWA-RD-97-148 (1998) 'User Guidelines for Waste and By-Product Materials in Pavement Construction', U.S. Department of Transportation, Federal Highway Administration, Turner-Fairbank Highway Research Centre.
6. Gandham S. Seals R.K. and Foxworthy Paul.T. (1996) 'Phosphogypsum as a Component of Flowable Fill' – Transportation Research Record No.1546, pp.79-87.
7. Jason Y. Wu. and Mufan. Tsai. (2009) 'Feasibility Study of a Soil-Based Rubberized CLSM' –Waste Management Vol 29, No.2 pp. 636-642.
8. Krell William C. (1989a) 'Flowable Fly ash', Transportation Research Record No. 1234, pp. 8-12.
9. Lachemi M. Hossain K.M.A. Shehata M. and Thaha W. (2007) 'Characteristics of Controlled Low-Strength Materials Incorporating Cement Kiln Dust' – Canadian Journal of Civil Engineering, Vol. 34, No 4, pp.485-495.
10. Lachemi M. Hossain K.M.A. Shehata. M. and Thaha.W. (2008) 'Controlled Low Strength Materials Incorporating Cement Kiln Dust from Various Sources' – Cement and Concrete Composites, Vol. 30, No.5, pp.381-392.
11. Naik T.R., Ramme B.W. and Kolbeck H.J. (1990) 'Filling Abandoned Underground Facilities with CLSM Fly ash Slurry', Concrete International, Vol. 12, No. 7, pp. 19-25.
12. Naik T.R., Kraus R.N., Ramme B.W., Yoon-Moon Chun and Rakesh Kumar (2006) 'High-Carbon Fly Ash in Manufacturing Conductive CLSM and Concrete', Journal of Materials in Civil Engineering, Vol. 18, No. 6, pp.743-746.
13. Nataraja M.C. and Nalanda Y. (2008) 'Performance of Industrial By-Products in Controlled Low-Strength Materials (CLSM)', Waste Management, Vol. 28, No. 7, pp. 1168-1181.
14. Pierce C.E. and Blackwell M.C (2003) 'Potential of Scrap Tire Rubber as Lightweight Aggregate in Flowable Fill' – Waste Management Vol. 23 No.3, pp.197-208.
15. Ramme B.W., Naik T.R. and Kolbeck H.J. (1994) 'Use of Fly Ash Slurry for Underground Facility

Construction', Construction and Building Materials, Vol. 8, No. 1, pp. 63-67.

16. Amitava Roy, Paul Schilling, Eaton Harvill C. and Seals Roger K. (1992) 'Alkali Activation of Class C Fly Ash', Proceedings of Utilization of Waste Materials in Civil Engineering Constructions, ASCE National Convention, New York, Sept. 13-17, pp. 104-115.
17. Poon C.S., Kou S.C. Lam L. and Lin Z.S. (2001) 'Activation of Fly Ash/Cement Systems using Calcium Sulfate Anhydrite CaSO_4 ' – Cement and Concrete Research, Vol. 31, No. 6, pp. 873-881.
18. Mridul Garg Manjit Singh and Rakesh Kumar (1996) 'Some Aspects of the Durability of a Phosphogypsum-Lime-Fly Ash Binder' – Construction and Building Materials, Vol. 10, No. 4, pp. 273-279.
19. Manjit Singh (2007) 'Utilization of Waste Gypsum; An Indian Scenario' – Global Gypsum Magazine, pp. 22-28.
20. IS: 1727 – 1967 (R2004) Indian Standard Methods of Test for Pozzolanic Materials, The Bureau of Indian Standards, New Delhi.
21. IS 3812: Part 1: 2003 – Pulverized Fuel Ash - Specification - Part 1: For Use as Pozzolana in Cement, Cement Mortar and Concrete, The Bureau of Indian Standards, New Delhi.

Production of bioplastic from CO₂ with light energy by coupling *Cupriavidus necator* with inorganic photocatalysts

T. Zhang, P. Tremblay

State Key Laboratory of Silicate Materials for Architectures, Wuhan University of Technology, Wuhan 430070, PR China

School of Chemistry, Chemical Engineering and Life Science, Wuhan University of Technology, Wuhan 430070, PR China

International School of Materials Science and Engineering, Wuhan University of Technology, Wuhan 430070, P. R. China

Email of the corresponding author: tzhang@whut.edu.cn

Abstract

The cement industry is responsible for the release of 5% of worldwide anthropogenic emissions of the greenhouse gas carbon dioxide. One approach to reduce CO₂ emissions by cement plants is to feed CO₂ to biocatalysts for the production of valuable chemical products such as biofuels. Ideally, CO₂-based bioproduction should be powered by a ubiquitous energy source that is easy to access, free and renewable such as solar energy.

Massive research efforts have been deployed to develop productive and energy-efficient CO₂ bioprocesses relying on natural photosynthesis such as ethanol production by sugarcane or oil production by algae or cyanobacteria. Until now, one major hurdle with these processes is that natural photosynthesis has a low solar energy-to-specific product conversion efficiency, which limits productivity and increases space required for implementation. A possible response to this challenge is the development of hybrid photosynthesis systems where sunlight is harvested by more efficient inorganic devices, which then generate energy that can be used by microbial catalysts for the production of useful chemicals.

In this project, inorganic photocatalysts were used to drive the production of polyhydroxybutyrate (PHB) from CO₂ or organic carbon molecules by *Cupriavidus necator*. PHB is an industrially-relevant and biodegradable bioplastic generated by *C. necator* for energy and carbon storage purposes. Its synthesis required reducing power under the form of NADPH.

In our system, photocatalysts such as graphitic C₃N₄ and CdS harvest light energy to generate reducing equivalents that are used by *C. necator* for CO₂ reduction via the Calvin-Benson-Bassham pathway as well as in the conversion of the central metabolite acetyl-CoA into PHB. Our results indicate that solar energy-to-specific product conversion efficiencies obtained by coupling inorganic photocatalysts with *C. necator* could easily surpass the efficiency of natural photosynthesis-based bioproduction processes.

Keywords: Carbon dioxide emission, Solar energy, Inorganic photocatalyst, Microbial catalyst, Bioplastic

Study on the preparation of high quality autoclaved aerated concrete made from stone-sawing mud

H. Wan¹, Y. Hu², G. Liu^{1*}, J. Liu², Y. Qu²

¹ State Key Laboratory of Silicate Materials for Architectures, Wuhan University of Technology, Wuhan, China;

² School of materials science and engineering, Wuhan University of Technology, Wuhan, China.

Abstract

Stone-sawing mud is a by-product of the stone processing industry, which is difficult to be used. Testing results show that: in the stone-sawing mud, the SiO_2 content is more than 70%, particles sizes are small, specific surface area is about $375 \text{ m}^2/\text{kg}$ and the moisture content is about 22%. It implies that the stone-sawing mud could be directly used as siliceous raw material for preparation of the autoclaved aerated concrete (AAC) without drying-grinding, meanwhile alleviating the surrounding environmental pollution. This study mainly discusses the effect of the water materials ratio, mixing water temperature, aluminium powder content, cement content, stone-sawing mud and lime + gypsum content on the AAC properties. Experimental results show that with an increase of stone-sawing mud content and a decrease of lime content, the bulk density of AAC increases gradually, while its compressive strength firstly increases and then decreases. The maximum compressive strength of 3.60MPa and the bulk density of 606 kg/m^3 can be obtained when the water-binder ratio is 0.60, the mixing water temperature is 45°C , the aluminium powder content is 0.12%□ the stone-sawing mud content is 71% and the lime + gypsum content is 21% as well the mass ratio of them is about 4:1. The XRD and SEM results show that the crystallization of tobermorite crystals in the AAC with the stone-sawing mud grows into a leaf shape, and interleaves with each other to form a dense structure net, which makes the AAC with improved mechanical properties.

Keywords: stone-sawing mud; autoclaved aerated concrete; bulk density; strength.

1. Introduction

Stone-sawing mud is a by-product of the stone processing industry, which is difficult to be used. It can produce a lot of stone powder containing lots of water during the stone cutting processing. After precipitation, it forms the stone-sawing mud. It was reported that the processing of each ton of rock produced about 0.1 m^3 of sawing mud^[1]. In order to protect the saw blade, a small amount of cutting fluid was usually added to the cooling water during the process of cutting stone, which caused the stone-sawing mud paste to be weak acid and contain a small amount of phosphate and organic material, this could pollute the environment. Therefore, how to effectively utilize stone-sawing mud is an issue that relates to the protection of environment and groundwater.

The autoclaved aerated concrete (AAC) is an effective and scientific way to use the solid waste^[2]. It can not only greatly reduce the cost of manufacturing new wall materials, but also consume a lot of solid waste and has high utilization rate. AAC is a kind of lightweight, porous new building material with good performance

of light weight, good thermal insulation, machinability and non-combustion. It can be made into different specifications of the block, plate and insulation products widely used in industrial and enclosure filling structure of bearing or embosom filling structure, which makes it get much attention around the world and become the building materials vigorously promoted by many countries [3].

The AAC, whose main raw materials are the siliceous materials (river sand, fly ash and tailings containing silicon, etc.) and calcium materials (lime, cement), by adding gas agent [4] (aluminium powder) and adding water mixing, then a series of independent holes being formed by chemical reactions, is a porous silicate product prepared by the processes of pouring shape, cutting, autoclaved curing and so on [5]. Through many years of research, production and application, people have basically mastered the production process of using fly ash or river sand to prepare the AAC [6][7]. Matsushita F [8] studied the durability of AAC (degree of carbonation). Narayanan N [9], Alexanderson J [10] and others also thorough researched the structure and performance of AAC. Chen YL [11] used recycled desulfurization slag to produce AAC. Huang X [12] et al used low silicon copper tailings-cement clinker-wind-accretion sand-slag powder system to prepare no lime AAC. A large number of research results have accumulated rich experience in the scale production of AAC.

This research systematically studied the effects of preparation process parameters and material compositions on the performance of AAC based on raw materials of more than 70% of the stone-sawing mud and small amounts of lime and desulfurization gypsum and technology by adding stabilized foam agent to improve gas progress. The outcome of this study can be used to guide massively using the stone-sawing mud in the AAC production. It is meaningful to save the resources and protect the environment.

2. Experiment

2.1 Materials

2.1.1 Stone-sawing mud

The stone-sawing mud used in this study was from the stone processing factory in Hubei mountain area. Due to the geological reasons, the type of stone was mainly granite in this area, and its stone resources were extremely rich. As a result, the stone processing factory in this area had generated at least 6 million stone-sawing mud every year, which caused serious damage to the surrounding environment. The test showed that the powder of processing granite stone with higher SiO₂ content and small particle size, high water content. When used for preparing the raw materials of AAC, it doesn't need drying and grinding. The pH value of stone-sawing mud was 6.5, which was weak acidic. The moisture content of stone-sawing mud was about 22%, and sieving residue alone 80 microns was less than 15%, with an apparent density of 2.72g/cm³ and a surface area of 375m²/kg. The chemical compositions of stone-sawing mud were shown in Table 1, and its XRD analysis was shown in Figure1.

Table 1 Chemical composition of raw materials

Chemical composition (%)	SiO ₂	CaO	Al ₂ O ₃	Fe ₂ O ₃	MgO	SO ₃	K ₂ O	Na ₂ O	LOI
Stone-sawing mud	72.66	1.56	15.09	1.15	0.38	-	3.58	4.54	0.42
P.O42.5 cement	20.49	61.02	5.01	3.50	2.23	2.58	0.64	0.15	3.07
Desulfurization gypsum	2.61	30.5	0.66	-	0.92	43.40	-	-	20.12

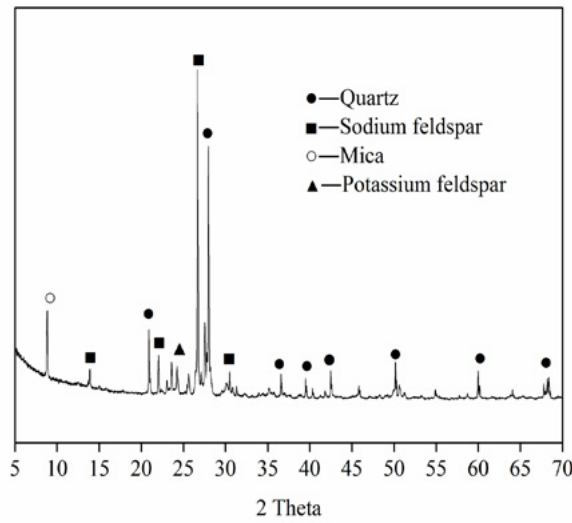


Figure 1. XRD analysis of stone-sawing mud.

2.1.2 Cement

The cement used in this study was P.O 42.5 ordinary Portland cement. Its physical properties and chemical compositions were shown in Table 1 and Table 2 respectively.

Table 2: Physical properties of Portland cement

Specific surface area (m ² /kg)	Setting time (min)		Flexural strength (MPa)		Compressive strength (MPa)		Cement stability
	Initial setting time	Final setting time	3d	28d	3d	28d	
348	165	220	7.8	8.6	26.3	49.9	qualified

2.1.3 Lime

The active CaO content in the lime used in this study was more than 80%, while the content of MgO was less than 5%. The digestion time was 14 min, with the sieve residue alone 80 microns less than 10%.

2.1.4 Desulfurization gypsum

Desulphurization gypsum used in this study was discharged from coal-fired power plants. Its chemical compositions were shown in Table 1.

2.1.5 Aluminium powder and foam stabilizer

Aluminium powder used in this study was mainly used for air-making.

2.2 Sample preparation and testing

According to Yingliang Chen's study ^[13], the mass ratio of lime to gypsum was about 4:1, in which case it can ensure the coagulation time of the slurry and the lime digestion speed more appropriate. Then, this ratio was adopted in this study, the materials composition and proportion of the base AAC were presented

in Table 3.

Table 3. Materials composition and proportion of the base AAC (wt %).

Cement	Sawing mud	Lime + gypsum	Aluminum powder	Stable foam agent
8	70	22	0.12	0.01

The whole processes to make the AAC sample were shown as follows: firstly, mix the slurry with the temperature during 40~45 °C; next, control the block-static stop time during 2~2.5h and the temperature during 55~60 °C. Then, make it under the conditions of the vacuum for 0.5h and increase pressure of 1.3MPa for 1.5h, and keep the pressure at 1.3MPa for 8h; finally, release pressure and cooling for 2h.

According to GB/T11969-2008 *Test method for the performance of autoclaved aerated concrete*, the 100mm x 100mm x 100mm standard specimen was prepared and then put it into the autoclave. The DRM-□ concrete thermal conductivity detector (Xiangtan Xiang Yi Instrument Co., Ltd.) was used to test the coefficient of thermal conductivity of AAC. X-ray diffraction (D/MACX-RB Japan RIGAKU) and scanning electron microscope (JSM-5610LV Japanese electronics co, LTD.) were employed to analyse the composition and microstructure of the samples.

3. Results and discussion

3.1 Effect of water-binder ratio on the slurry performance

The water-binder ratio was an important technological parameter in the preparation and production of AAC. Water-binder ratio directly impacted the coordination of water slurry thickening velocity and gas velocity of co-ordination, suitable water-binder ratio would keep the volume of slurry stability in the process of casting and made gas fully generate in the process of gassing, slurry expansion properly, which could ensure uniform of pore structure inside the AAC.

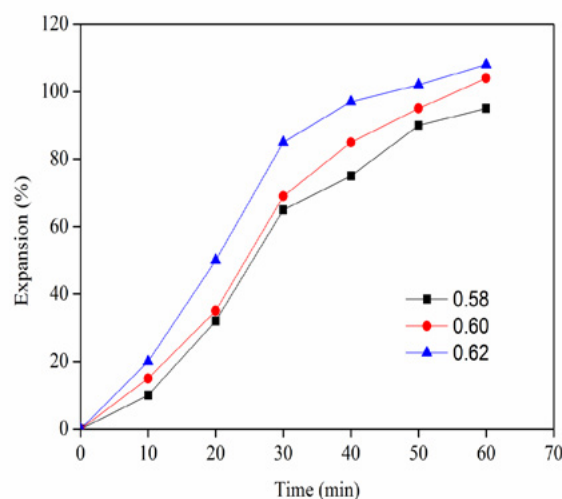


Figure 2. The relation curve of water-binder ratio with expansion height

Figure 2 was the result of the test of the water-binder ratio of 0.58, 0.60 and 0.62 respectively. The smaller the water materials ratio was, the greater the consistency of the slurry was, leading to the more difficulty

the gas phase became, and then, the smaller the swelling height was. When the water materials ratio was too large, the consistency of the slurry was low and the time of thickening would take longer. According to the Laplace equation:

$$p = p_0 + \frac{4\delta}{r} \quad (1)$$

Where: p —the pressure in the air bubble, Pa.

p_0 —the atmospheric pressure, Pa.

δ —slurry consistency, Pa •cm.

r —bubble radius, cm.

It could be seen from the Equation (1) that the pressure of the stomata was related to the bubble radius and viscosity of the slurry. With water-binder ratio increasing, the viscosity of the slurry dropped, it was easy to cause the stomata to accumulate and produce the large stomata, and the gas reaction was intense. The excessive accumulation of large stomata and the unstable gas state could easily lead to the collapse mode. When the water-binder ratio was too low, increasing speed of slurry viscosity and the block hardening time was quick and short respectively. When the block was hardened and gas process was still going on, it could cause the block to crack. Both of these conditions would lead to the decrease of the strength of the block.

On the premise of ensuring the fluidity and thickening of the slurry and the consistency of the gas velocity, the improvement of the water content could significantly improve the airflow effect of the slurry. The water materials ratio would change the flow degree of the slurry, and the appropriate flow degree could ensure that the bubbles were uniform and avoided the deviation of bulk density in the slurry tank. The experimental results showed that when the water materials ratio was 0.60, the flow of the slurry was good, and the embryonic body was full of gas, the volume stability was fine, and there was no collapse mode phenomenon.

3.2 Influence of temperature on the properties of slurry

The progress of the aluminium powder gas was closely related to the temperature of the materials. The slurry was higher in temperature, the raw materials were more active, and the solubility in the solution was more, the reaction speed was faster and the reaction degree was higher. On the contrary, when the slurry temperature was low, reaction speed dropped, the whole process of aluminium gas was extended, and it was not only causing the AAC bulk density big, but also leading the phenomenon of “holding gas”, which had a certain effect on the structure of pores.

But when the temperature of the slurry was too high, the early reaction speed would be too fast and the aluminium powder gas would violently react, which made it was easy to form irregular shape large pores and damaged to the porosity of pore wall around it, even produced crack when it was serious.

The temperature of different slurry had obvious influence on the process of slurry gas and thickening. The slurry temperature was affected by mixing water temperature and lime digestion temperature, while lime digestion temperature was restricted by raw materials, and it was usually controlled by changing the mixing water temperature to control the slurry temperature. As shown in Figure 3, when mixing water temperature was higher than 50°C, the amount of gas was large, but the slurry setting speed was quick and the fluidity loss was high, which had a certain influence on gas progress.

When the mixing water temperature was below 40°C, gas generation rate was slow and the inflation rate was low, which made its bulk density larger. Comprehensively considering the bulk density and compressive

strength, choosing the mixing water temperature of 45°C was more appropriate.

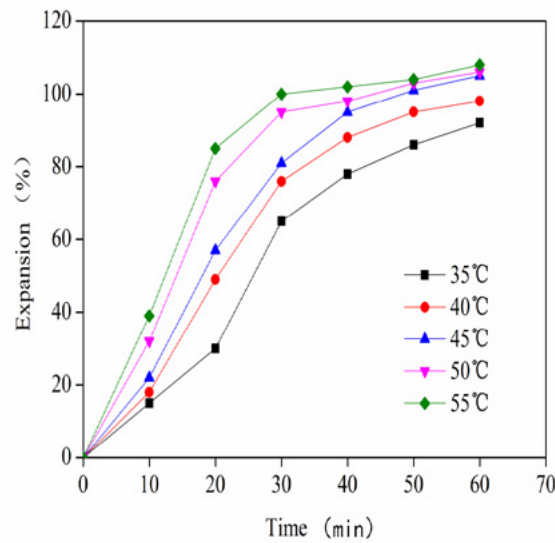


Figure 3. Mixing water temperatures and expansion height curve.

3.3 Influence of aluminium powder content on block performance

The aluminium powder was the gas agent which was most widely used. Its hair gas effect was good, and it was easy to control. The aluminium powder was made from the grinding particle produced by compressed air in a melting state. In order to prevent dust explosion and surface oxidation, the surface of aluminium powder usually had a layer of grease or a paste. Because of the slurry was highly alkaline, no degreasing was needed before using. But the aluminium powder particles were small and the surface was coated with grease, causing it was easy for particles reuniting.

So pre-distributed processing was required before using and then it could be mixed in the paste. In the slurry, the aluminium powder reacted with the $\text{Ca}(\text{OH})_2$ formed by lime digestion or the cement hydration, produced the hydrogen and the reaction equation was:



Figure 4 showed when the water materials ratio was 0.60, the curve of the aluminium powder content and the bulk density of the block. It could be seen from the Figure 4 that with the content of aluminium powder increasing, the bulk density of the block and the compressive strength of the block gradually reduced. Study^[14] had shown that increasing the content of aluminium powder in a certain range had little influence on the pore diameter of AAC, but as the aluminium content continued to increase, a big pore percentage of AAC would increase correspondingly and the block compressive strength would decrease obviously.

Considering that this test was the preparation of the AAC at the B06 level, which was the product of the bulk density of 600kg/m^3 , so it was more appropriate that the aluminium powder content was 0.12%.

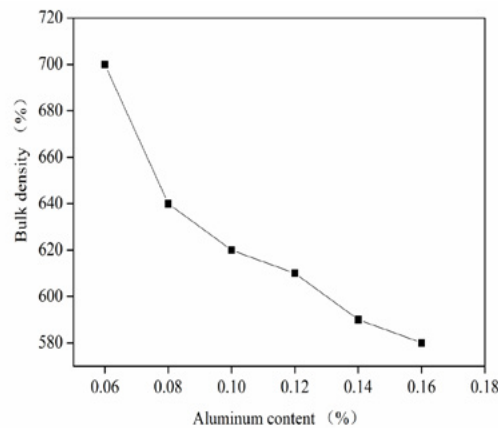


Figure 4. The relationship of aluminium powder content with masonry bulk density.

3.4 Effect of cement content on block performance

Cement in the AAC played a major role, which was to make the block had early compressive strength and easily to be cut. In the whole AAC reaction process, the cement only provided a small part of the calcium raw materials and made contribution to the strength due to the formation of hydrated calcium silicate gel. But in the AAC system, the main contribution of the strength was produced by the tobermorite crystals that were generated by the silica and calcium hydroxide in the autoclaved curing conditions. The later compressive strength of the block was not derived from the cement.

Table 4. Effect of cement content on AAC performance.

Number	Cement (wt%)	Sawing mud (wt%)	Lime + gypsum (wt%)	Aluminium powder (wt%)	Foam stabilizer (wt%)	Bulk density (kg/m ³)	Compressive strength (MPa)
A1	6	70	24	0.12	0.01	598	3.31
A2	7	70	23	0.12	0.01	601	3.38
A3	8	70	22	0.12	0.01	604	3.44
A4	9	70	21	0.12	0.01	617	3.26
A5	10	70	20	0.12	0.01	615	3.35

*The mass ratio of lime to gypsum was 4: 1; and the water-binder ratio was 0.60.

Table 4 was the impact of cement content on the bulk density and compressive strength of AAC. When the cement content increased, the compressive strength of AAC increased, when the cement content reached 8%, the strength reached the maximum. Then the compressive strength reduced with the increasing content of the cement. Besides making the body has early strength, cement mainly influenced on slurry thickening. The appropriate cement content could coordinate the slurry thickening speed and the gas making speed of aluminium powder to ensure a good stomatal structure, which was the key to improve the mechanical properties of products. In addition, the cement in the anti-carbonation and shrinkage performance were better than lime. However, the incorporation of excess cement would increase the cost of producing AAC, so the cement content of 8% was more appropriate.

3.5 Effect of siliceous and calcium raw materials contents on block performance

After determining appropriate water materials ratio, gas temperature, aluminium powder content and cement content, the test scheme of Table 5 was also designed in order to determine the best ratio of stone-

sawing mud, lime and gypsum, which made the performance of AAC better.

Stone-sawing mud and lime were the main siliceous materials and calcareous materials in AAC production process. The calcium hydroxide produced by lime and the SiO_2 in the stone-sawing mud were reacted under the conditions of autoclaved and generated the tobermorite and calcium silicate, which were the main source of the strength, while the gypsum was to inhibit the lime digestion and adjust the speed of the important role of slurry paste. The experimental results showed that when the mass ratio of lime to gypsum was about 4: 1, the mechanical properties of the block were better.

Table 5. Effect of stone-sawing mud, lime + gypsum on AAC performance.

Number	Cement (wt%)	Sawing mud (wt%)	Lime + gypsum (wt%)	Aluminium powder (wt%)	Foam stabilizer (wt%)	Bulk density (kg/m ³)	Compressive strength (MPa)
B1	8	69	23	0.12	0.01	602	3.13
B2	8	70	22	0.12	0.01	604	3.44
B3	8	71	21	0.12	0.01	606	3.60
B4	8	72	20	0.12	0.01	612	3.51
B5	8	73	19	0.12	0.01	619	3.34

*The mass ratio of lime to gypsum was 4: 1; and the water-binder ratio was 0.60.

It could be seen from Table 7, with the stone-sawing mud content gradually increasing and lime + gypsum content correspondingly reducing, the prepared block bulk density and compressive strength gradually increased. When the content of sawing mud was 71%, the content of lime + gypsum was 21% and the mass ratio of lime to gypsum was about 4: 1 (sample B3) and the bulk density of block was 606 kg/m³, the compressive strength reached the maximum of 3.60MPa. When the content of sawing mud continued increasing and the lime + gypsum content decreased, although the bulk density increased, the compressive strength of the block showed a downward trend, which was indicated that the system of stone-sawing mud (siliceous material) was surplus, Lime gypsum (calcium material) content was insufficient and the number of hydrated products in the hydrothermal synthesis reaction was not as good as that of sample B3. On the other hand, the more or less content of lime + gypsum in system would affect the thickening rate of slurry and gas velocity, thus affecting the size and distribution of the pores in the block and ultimately the compressive strength of the block would be affected.

3.6 Hydration products and microscopic analysis

The XRD analysis (Figure 5) showed that the main product of AAC was the calcium silicate hydrate (C-S-H) which mainly consisted of tobermorite ($5\text{CaO} \cdot 6\text{SiO}_2 \cdot 5\text{H}_2\text{O}$)^{[15][16]}. In addition, there was some quartz that partly participated in the reaction. The more the amount of tobermorite and C-S-H gel was produced, the higher the strength of AAC was. The quartz crystal in the sample was complete, had high crystallinity, played a skeleton role in the solid phase, and was also conducive to the strength of the structure.

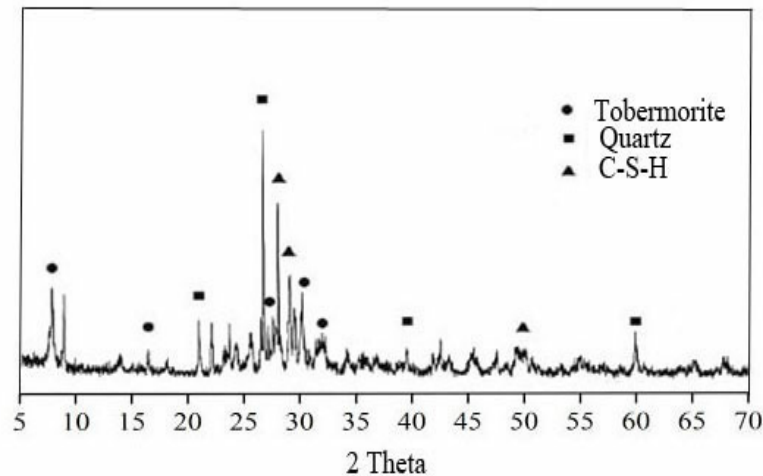
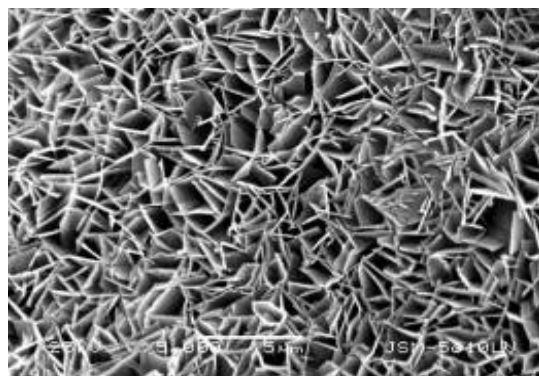
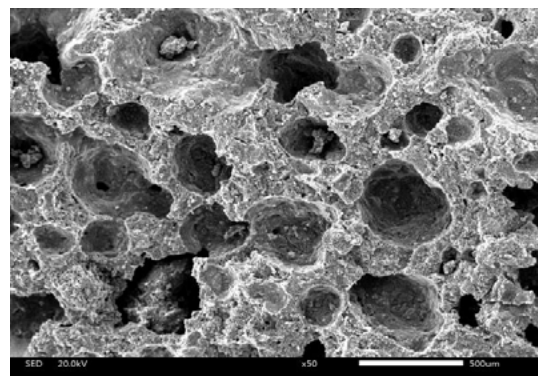


Figure 5. XRD analysis of AAC sample B3.



(a) X50



(b) X5000

Figure 6. SEM images of AAC sample B3.

The SEM images of the AAC sample B3 were shown in Figure 6. Besides to the macroscopic pores in the AAC, there were also many microspores at the pore wall (Figure 6a). The formation of pore had two main reasons: one was the water evaporation; the other was the chemical reaction. The macroscopic pores were uniformly distributed with a maximum size of around 10mm. In Figure 6 (b), there were also the tobermorite with a crystallized structure. The length of the blade was 2-3 μ m and the width around 1 μ m. The hydration products of the micro capillary in the AAC were the leaf shape tobermorite crystals with the double chain silicate structure and the tobermorite had good stability because they constituted net structure, which made AAC have good compressive strength.

3.7 The hydration reaction mechanism of AAC

At the initial reaction stage of AAC system, lime reacted with water in the slurry by digesting and forming calcium hydroxide to dissolve. The OH⁻ in calcium hydroxide provided enough alkalinity for the slurry, and the heat released from lime digestion improved the reaction speed. At the same time, the C₃S, C₃A and other minerals in the cement began to hydrate and formed hydrated calcium silicate, calcium hydroxide and calcium aluminate hydrate. Then, the system of liquid phase had certain alkalinity and SiO₂ began to dissolve in the liquid phase. The initial strength of the block was derived from the hydration products of C₃S, C₃A and other minerals in the cement^[17].

Under the conditions of alkali, environment, high temperature and high pressure for autoclaved curing, the system first produced a complete crystal of hydrogarnet ($C_3AS_nH_{6-2n}$)^{[18][19]}. With the increase of the autoclave time, the solubility of Si^{4+} and Al^{3+} in the liquid phase got improved, which changed the alkaline environment of hydrogarnet and can make it broken down. Then, hydrated calcium silicate was generated^{[20][21][22]}. Because the solubility of hydrated calcium silicate in the liquid phase is very low, when it reaches saturation will precipitate grain, the newly formed grain specific surface area is large, through the adsorption and water molecules connected to form a condensed state. During this period, more calcium-rich hydrated calcium silicate, such as C_2SH (A) and C_2SH_2 , was produced in the system. With the increase of the concentration of SiO_2 in the liquid phase, the calcium-rich C_2SH (A), C_2SH_2 cannot be stable, and gradually converted to CSH (B) type hydrated calcium silicate and tobermorite^[23]. Tobermorite crystals grow into leaves and flake, and interlace each other, forming the network skeleton structure of AAC gradually, which is beneficial to improve its mechanical properties. The stone-sawing mud contained not only quartz but also a small amount of soda feldspar ($Na_2O \cdot Al_2O_3 \cdot 6SiO_2$) and potassium feldspar ($K_2O \cdot Al_2O_3 \cdot 6SiO_2$), which may provide active Al_2O_3 and SiO_2 for the reaction. Further studies are needed on how the soda feldspar and potassium feldspar are involved in the hydration reaction of the AAC.

4. Conclusions

1. Stone-sawing mud has high SiO_2 content, small size and high water content. When used for preparing AAC, it doesn't need to be dried or ground, which are the good disposal pathways.
2. With an increase of the stone-sawing mud content and a decrease of the lime content, the bulk density of AAC increases gradually. The compressive strength of AAC firstly increases and then decreases and the maximum value 3.60 MPa can be obtained when the stone-sawing mud content is 71% and the lime content is 21%.
3. The hydration products of the micro capillary in the AAC based on stone-sawing mud are the leaf shape tobermorite crystals with the double chain silicate structure and the tobermorite have good stability because they constitute net structure, which makes the AAC with improved mechanical properties.

5. Reference

1. Torres R, Fernandes HR, Olhero S, et al. Incorporation of wastes from granite rock cutting and polishing industries to produce roof tiles. *J Eur Ceram Soc.* 2009;29(1):23-30.
2. Li XG, Liu ZL, Lv Y, et al. Utilization of municipal solid waste incineration bottom ash in autoclaved aerated concrete. *Constr Build Mater.* 2018;178:175-182.
3. Wakili KG, Hugi E, Karvonen L, et al. Thermal behaviour of autoclaved aerated concrete exposed to fire. *Cement Concrete Comp.* 2015;62:52-58.
4. Liu YQ, Leong BS, Hu ZT, et al. Autoclaved aerated concrete incorporating waste aluminum dust as foaming agent. *Constr Build Mater.* 2017;148:140-147.
5. Verian KP, Ashraf W, Cao Y. Properties of recycled concrete aggregate and their influence in new concrete production. *Resources Conservation Recycling.* 2018;133:30-49.
6. Uthaman S, Vishwakarma V, George RP, et al. Enhancement of strength and durability of fly ash concrete in seawater environments: Synergistic effect of nanoparticles. *Constr Build Mater.* 2018;187:448-459.
7. Shen WG, Liu Y, Wang ZW, et al. Influence of manufactured sand's characteristics on its concrete

- hr/>
- performance. *Constr Build Mater.* 2018;172:574-583.
8. Matsushita F, Aono Y, Shibata S. Carbonation degree of autoclaved aerated concrete. *Cement Concrete Res.* 2000;30(11):1741-1745.
 9. Narayanan N, Ramamurthy K. Structure and properties of aerated concrete: a review. *Cement Concrete Comp.* 2000;22(5):321-329.
 10. Alexanderson J. Relations between structure and mechanical properties of autoclaved aerated concrete. *Cement Concrete Res.* 1979;9(4):507-514.
 11. Chen YL, Ko MS, Chang JE, et al. Recycling of desulfurization slag for the production of autoclaved aerated concrete. *Constr Build Mater.* 2018;158:132-140.
 12. Huang XY, Ni W, Cui WH, et al. Preparation of autoclaved aerated concrete using copper tailings and blast furnace slag. *Constr Build Mater.* 2012, 27(1):1-5.
 13. Chen YL, Chang JE, Lai YC, et al. A comprehensive study on the production of autoclaved aerated concrete: Effects of silica-lime-cement composition and autoclaving conditions. *Constr Build Mater.* 2017;153:622-629.
 14. Font A, Borrachero MV, Soriano L, et al. Geopolymer eco-cellular concrete(GECC) based fluid catalytic cracking catalyst residue(FCC) with addition of recycled aluminium foil power. *J Clean Prod.* 2017;168:1120-1131.
 15. Tada S. Material design of aerated concrete—an optimum performance design. *Mater Struct.* 1986;19(109): 21-26.
 16. Isu N, Ishida H, Mitsuda T. Influence of quartz particle size on the chemical and mechanical properties of autoclaved aerated concrete (I) tobermorite formation. *Cement Concrete Res.* 1995;25(2):243-248.
 17. Hui-wen W, Yong H, Gang L, et al. Study on the structure and properties of autoclaved aerated concrete produced with the stone-sawing mud. *Constr Build Mater.* 2018, 184:20-26.
 18. Siauciunas R, Baltusnikas A. Influence of SiO₂ modification on hydrogarnets formation during hydrothermal synthesis[J]. *Cement Concrete Research.* 2003;33(11):1789-1793.
 19. Klimesch DS, Ray A. Hydrogarnet formation during autoclaving at 180°C in unstirred metakaolin-lime-quartz slurries. *Cement Concrete Res.* 1998;28(8):1109-1117.
 20. Klimesch DS, Ray A. DTA–TGA of unstirred autoclaved metakaolin–lime–quartz slurries. The formation of hydrogarnet. *Thermochimica Acta.* 1998;316(2):149-154.
 21. Klimesch DS, Ray A. Effects of quartz particle size on hydrogarnet formation during autoclaving at 180 degrees C in the CaO–Al₂O₃–SiO₂–H₂O system. *Cement Concrete Res.* 1998;28(9):1309-1316.
 22. Wan H, Yong H, Gang L, et al. Study on the structure and properties of autoclaved aerated concrete produced with the stone-sawing mud[J]. *Construction & Building Materials*, 2018, 184:20-26.
 23. Guo XL, Meng FJ, Shi HS. Microstructure and characterization of hydrothermal synthesis of Al-substituted tobermorite. *Constr Build Mater.* 2017;13

Mechanochemically activated clay as a sustainable cementitious binder

I. Tole, K. Habermehl-Cwirzen, A. Cwirzen

Building Materials, Department of Civil, Environmental and Natural Resources Engineering, Luleå
University of Technology, Lulea, Sweden

Abstract

High-temperature requirements, emission of hazardous substances from cement kilns and the significant CO₂ footprint in the calcination step are factors requiring special attention in the cement industry. Local and commonly occurring clays can be a sustainable alternative for producing cementitious binders. Structural disorder in natural clay minerals can be induced through mechanochemical activation (MCA), by which the material develops an enhanced reactivity. The treatment of a Swedish natural clay through intensive grinding is carried out in order to assess its potential as a sustainable cementitious binder. Several grinding parameters influence a MCA product. The filling ratio of the jar, the rotation speed, the time of grinding, as well as wet and dry environment, are varied to optimize the MCA process. The MCA process does not require high temperatures or added chemicals and shorter processing times can avoid high-energy requirements during fine grinding. The structural changes of the clay were analysed by X-Ray Diffraction (XRD). Analysis of the particle size distribution of the raw and processed clay suggested a correlation with the grinding duration. An increased ratio of grinding media versus the amount of ground material, while longer grinding duration increased the overall efficiency of the MCA process. The strength activity index (SAI) indicated an enhanced pozzolanic activity for the mechanochemically processed clay. Compressive strength tests have shown a strong correlation between an enhanced amorphization rate and increased compressive strength values.

Keywords: alternative cementitious binders, mechanochemical activation, sustainable building materials, mechanochemistry, clay.

1. Introduction

The building materials industry is facing several challenges for reducing the environmental impact coming from their production. The high amount of CO₂ emissions, the required high temperature, the volatile hazardous substances, the consumption of primary resources, etc., are some of the critical problems industries and researchers are tackling in order to increase the sustainability of building materials. Increasing the energy efficiency during clinker production, use of alternative fuels and alternative raw materials, and use of secondary cementitious materials (SCM) are some of the countermeasures to decrease the negative impact on the environment [1–3].

Different SCM, as blast furnace slag, silica fume, fly ash, calcined clays, etc., are largely used as partial replacement of cement. Use of calcined (highly kaolinitic) clays as a replacement of cement has shown very good pozzolanic reactivity, cost efficiency and good performance; moreover clay is a natural and widely available raw material [4]. Calcined highly kaolinitic clays are a dehydroxylated form of the 1:1 layer structure, called also metakaolinite [5]. Dehydroxylation of kaolin and other clay minerals can be achieved by mechanochemical activation (MCA) [6,7].

MCA is a process able to impose structural and chemical changes in the treated material through high-energy grinding, meanwhile avoiding the use of chemicals or high temperature requirements [8]. Amorphization of the clay minerals structure can be achieved in reasonable times with optimized process parameters. MCA can also amorphize and enhance the reactivity of such raw clay minerals as montmorillonite, illite and pyrophyllite [9–11].

The efficiency of MCA depends on several process parameters, as time of grinding, ball to processed material ratio, use of grinding aids, velocity, etc. Optimization of these parameters can give higher amorphization rates of the clay minerals structure in shorter time [12].

This study focused on the efficiency of the MCA in the amorphization of the structure and on the pozzolanic activity of a raw clay from Sweden. The process parameters as ball to powder ratio and time of grinding are varied in order to assess their influence on the processed material. Differently mechanochemically activated samples were investigated through indirect methods, as the so-called strength activity index (SAI), to evaluate their pozzolanic activity.

2. Methodology

2.1 Materials

The raw clay used in this study was collected in the Sollentuna municipality in Stockholm County in east central Sweden. Atterberg limits were used in order to characterize the geotechnical properties of the raw material, classifying it as clay. The chemical composition of the raw material is shown in Table 1:

Table 1: Chemical composition of the raw clay used in the study.

Component	Content
	wt. %
SiO ₂	52,6
Al ₂ O ₃	15,1
Fe ₂ O ₃	6,9
CaO	6,41
K ₂ O	3,78
MgO	2,51
Na ₂ O	1,68
TiO ₂	0,696

Dry grinding was carried out using a planetary ball mill, type Retsch PM 100, with a stainless steel jar of 500 mL volume. Twelve stainless steel balls with the same diameter of 20 mm were used. Two different regimes of ball to powder (B/P) and time of grinding were applied. The speed was set to 500 rotation per minute (rpm). Sample D0 was prepared by hand grinding for 1 minute.

Table 2: Process parameters of mechanochemically treated clay.

Sample	Ball/Powder	Time of grinding
	wt.ratio (g/g)	min
D0	-	-
D35	3	5
D320	3	20
D255	25	5
D2520	25	20

2.2 Methods

2.2.1 X-Ray diffraction

Changes of the crystallinity due to the MCA process were determined by X-ray diffractometer, (type Empyrean from PANalytical, using Cu-K α radiation with a wavelength of 1,54060 Å, generated at 45 kV and 40 mA. The step size was 0.0260 [°2 θ] and the scan step size 87.4650 seconds. The temperature during the measurement was kept at 25 °C. The samples for the XRD analysis were prepared in a backload holder.

2.2.2 Particle size distribution

The particle size distribution was measured by Dynamic Light Scattering (DLS). A Malvern Zetasizer equipped with a back-scattering detector was used for testing the processed clay. The samples were prepared as a suspension in distilled water and three measurements per sample were made.

2.2.3 Strength Activity Index (SAI)

The ASTM C125 standard defines pozzolan as “a siliceous and aluminous material which, in itself, possesses little or no cementitious value but which will, in finely divided form in the presence of moisture, react chemically with calcium hydroxide at ordinary temperature to form compounds possessing cementitious properties” [13]. Assessment of pozzolanic activity can be done by different direct and indirect methods. The strength activity index (SAI) is an indirect method to evaluate the pozzolanic reactivity through comparative compressive strength tests [14]. Mortar beams were produced using cement as a binder and replacing 20% of the cement with the processed clay. The mortar mixes were prepared in a Hobart mixer with a mixing time of 5 min. The mix design of the mortar beams is shown in the table below:

Table 3: Mix design of the mortar beams prepared for the SAI test

Sample	Cement	Sand	Processed clay	Processed clay	Water
	g	g	Sample ID	g	ml
M0	450	1350	-	-	225
MD35	360	1350	D35	90	225
MD320	360	1350	D320	90	225
MD255	360	1350	D255	90	225
MD2520	360	1350	D2520	90	225

After demoulding at 24 hours, the beams were stored in a water bath. Compressive strength tests after 7 and 28 days were done on all the samples. The SAI result is a percentage of the strength value of the control mortar beam to the strength value of the mortar beam prepared with 20% of cement replacement:

$$SAI = A/B \times 100 \% \quad (1)$$

where A is the compressive strength value for the beam with 20% of cement replacement and B is the compressive strength value of the control mortar sample. To assess pozzolanic activity of the tested sample, ASTM C618 requires a SAI greater than 0.75 after 7 and 28 days for FA and natural pozzolans at a cement replacement of 20% [14].

3. Results and discussion

Minerals as kaolinite (Kln), illite (Il), montmorillonite (Mnt), muscovite (Ms), quartz (Qz) and calcite (Ca) were identified from the XRD analysis of the untreated samples. The MCA process has induced amorphization of the structure of the processed clay. Higher ball-to-powder ratio and longer time of grinding has caused substantial structural changes. XRD graphs in figure 1 indicated decreased intensities of the main peaks. Peaks related to clay minerals, as kaolinite or muscovite, were altered easier than quartz,

which peaks are almost not changed. This phenomenon can be associated to the different hardness that the two substances have [15]. Analysis of the FWHM of the kaolinite peak [001] were done by using Lorentz fitting in order to better evaluate the changes on the structural order, figure 2. Increased values of the FWHM indexes were determined for samples D35, D320 and D255, implying gradual degradation of the kaolinite lattice for longer time of grinding and higher ball-to-powder ratio. Only the sample D2520 has indicated values of FWHM higher than 0.4, suggesting an amorphized structure [16,17].

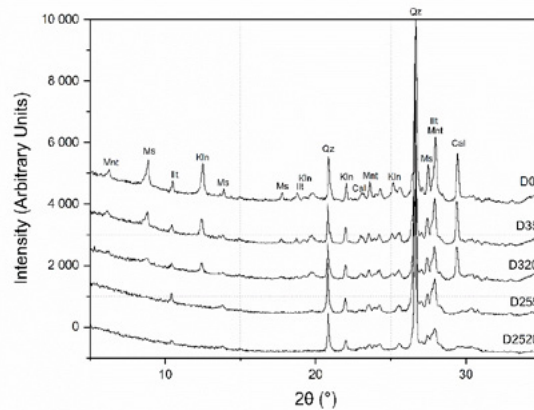


Figure 1: XRD diffraction patterns for different B/P ratio and grinding time of a Swedish raw clay.

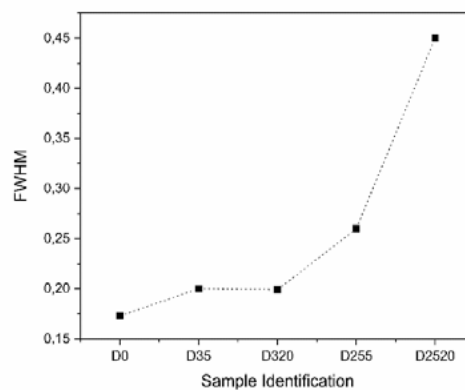


Figure 2: FWHM of the kaolinite peak [001] for the treated samples with different process parameters.

Particle size distribution has shown a direct correlation to the time of grinding and the ball-to-powder ratio values. Longer time of grinding and higher ball-to-powder ratio have led to an increased volume of smaller particles. The most amorphized sample, D2520, has also a higher volume of smaller particles as shown in figure 3.

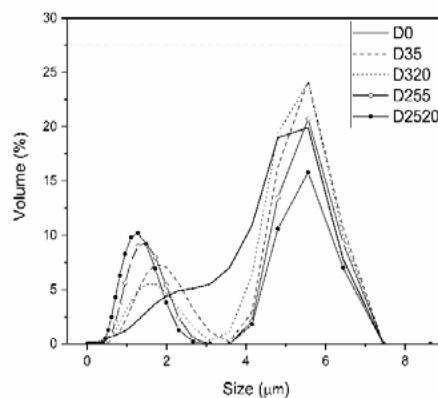


Figure 3: Particle size distribution of MCA clay with different process parameters.

Compressive strength tests results after 7 and 28 days are shown below in figure 4a) and 4b). The mechanical properties (after 7 days) of the mortar beams prepared with 20 % of replacement slightly decreased for the clay treated with lower ball-to-powder ratio (MD35, MD320) and with shorter time of grinding (MD35 and MD255). Sample MD2520 prepared with 20% of cement replaced by the processed clay, which has achieved higher amorphization of the structure through MCA, showed high compressive strength values after 7 days. After 28 days, the compressive strength of the samples prepared with 20% of cement replacement has reached higher values than the reference mortar sample prepared only with cement as a binder (M0). The replacement of cement by MCA clay indicated increased mechanical properties for all the analysed samples besides MD255. Sample MD255 has shown a slightly lower value of the compressive strength, while presenting a SAI index value (95%) higher than the minimum required (75%).

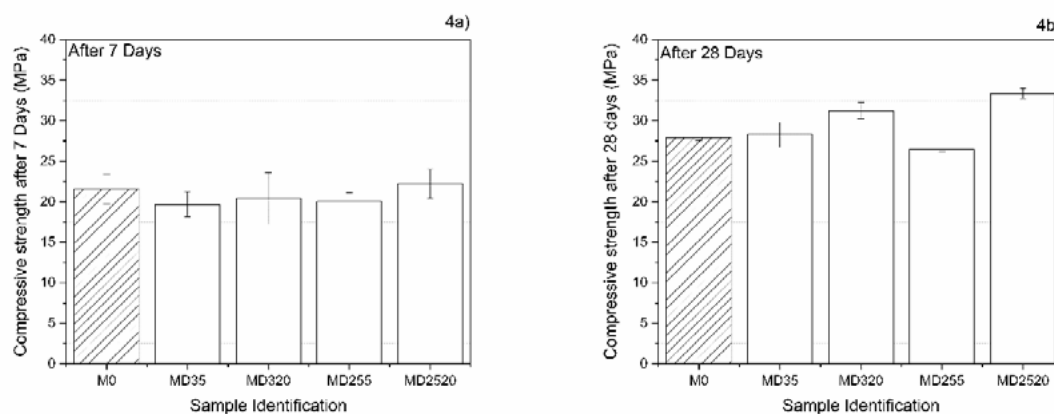


Figure 4: Compressive strength test results of reference mortar sample (M0) and mortar samples prepared with 20% of cement replaced by MCA clay, a) after 7 days, b) after 28 days

Calculation of the SAI index is done for the tested samples and the results are shown in figure 5. After 7 days the SAI indexes for all the samples prepared with 20% of cement replacement by the treated clay were higher than the required minimum of 75%. The maximum SAI index was registered for sample MD2520 with a value equal to 103%. Increased SAI index values were reported also for all the samples tested after 28 days. The minimum required value (75%) was exceeded for all samples. Sample MD2520 has reached a value of 120 % after 28 days, suggesting a direct relationship between the increased reactivity by MCA and the pozzolanic activity.

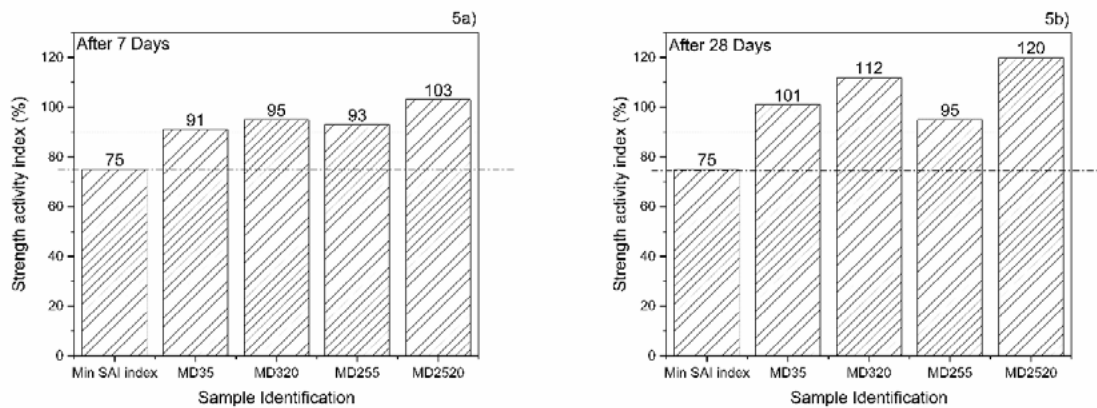


Figure 5: Strength activity index of mortar samples prepared with 20% of cement replaced by MCA clay, a) after 7 days, b) after 28 days

A more precise evaluation of the pozzolanic activity has to consider further direct tests on the studied samples. Frattini and Chapelle tests can give a clearer understanding of the increased pozzolanic activity of the ground clay. The filler effect, originated by the decreased particle size distribution, is another factor that can influence the mechanical properties of the material.

4. Conclusions

- MCA can be considered an environmentally friendly process able to increase the chemical reactivity of clay.
- Higher ball-to-powder ratios and longer time of grinding showed a better efficiency in the amorphization of the clay minerals structure.
- The particle size distribution is influenced by the process parameters of the mechanochemical activation. Higher amounts of smaller particles are achieved for longer time of grinding and for higher ball-to-powder ratios.
- MCA-treated clay showed good mechanochemical properties when used as a cement replacement. Compressive strength values measured after 7 and 28 days were increased for the mortar samples prepared with 20% of cement replacement by the MCA clay.
- SAI indexes, after 7 and 28 days, overpassed the minimum required value of 75%. Mortar prepared with the treated clay D2520 showed the best values of compressive strength and SAI indexes.
- Increased amorphization indicated an enhanced pozzolanic activity of the processed clay.

5. Acknowledgment

The authors would like to acknowledge the Swedish research council Formas for funding and supporting the “ClayCem” project.

6. References

- [1] M.C. Bignozzi, Sustainable cements for green buildings construction, *Procedia Eng.* 21 (2011) 915–921.
- [2] H. Justnes, How to Make Concrete More Sustainable, *J. Adv. Concr. Technol.* 13 (2015) 147–154. doi:10.3151/jact.13.147.

- [3] M. Schneider, M. Romer, M. Tschudin, H. Bolio, Sustainable cement production—present and future, *Cem. Concr. Res.* 41 (2011) 642–650.
- [4] K. Scrivener, F. Martirena, S. Bishnoi, S. Maity, Calcined clay limestone cements (LC3), *Cem. Concr. Res.* 114 (2018) 49–56.
- [5] F. Bergaya, G. Lagaly, *Handbook of clay science*, Newnes, 2013.
- [6] R. Hamzaoui, F. Muslim, S. Guessasma, A. Bennabi, J. Guillin, Structural and thermal behavior of proclay kaolinite using high energy ball milling process, *Powder Technol.* 271 (2015) 228–237.
- [7] S. Ding, L. Zhang, X. Ren, B. Xu, H. Zhang, F. Ma, The Characteristics of Mechanical Grinding on Kaolinite Structure and Thermal Behavior, *Energy Procedia.* 16 (2012) 1237–1240. doi:<https://doi.org/10.1016/j.egypro.2012.01.197>.
- [8] P. Baláž, M. Achimovičová, M. Baláž, P. Billik, Z. Cherkezova-Zheleva, J.M. Criado, F. Delogu, E. Dutková, E. Gaffet, F.J. Gotor, Hallmarks of mechanochemistry: from nanoparticles to technology, *Chem. Soc. Rev.* 42 (2013) 7571–7637.
- [9] H. Yang, W. Yang, Y. Hu, C. Du, A. Tang, Effect of mechanochemical processing on illite particles, *Part. Part. Syst. Charact.* 22 (2005) 207–211.
- [10] J.L. Pérez-Rodríguez, L.M.S. Del Villar, P.J. Sánchez-Soto, Effects of dry grinding on pyrophyllite, *Clay Miner.* 23 (1988) 399–410.
- [11] M. Xia, Y. Jiang, L. Zhao, F. Li, B. Xue, M. Sun, D. Liu, X. Zhang, Wet grinding of montmorillonite and its effect on the properties of mesoporous montmorillonite, *Colloids Surfaces A Physicochem. Eng. Asp.* 356 (2010) 1–9. doi:[10.1016/j.colsurfa.2009.12.014](https://doi.org/10.1016/j.colsurfa.2009.12.014).
- [12] I. Tole, K. Habermehl-Cwirzen, M. Rajczakowska, A. Cwirzen, Activation of a raw clay by mechanochemical process-effects of various parameters on the process efficiency and cementitious properties, *Materials (Basel).* 11 (2018). doi:[10.3390/ma11101860](https://doi.org/10.3390/ma11101860).
- [13] C. Astm, 125 Standard terminology relating to concrete and concrete aggregates, *Annu. B. ASTM Stand.* 4 (2003).
- [14] C. ASTM, Standard specification for coal fly ash and raw or calcined natural pozzolan for use in concrete, C618-12a. (2012).
- [15] É. Makó, R.L. Frost, J. Kristóf, E. Horváth, The effect of quartz content on the mechanochemical activation of kaolinite, *J. Colloid Interface Sci.* 244 (2001) 359–364. doi:[10.1006/jcis.2001.7953](https://doi.org/10.1006/jcis.2001.7953).
- [16] A. Tironi, M.A. Trezza, A.N. Scian, E.F. Irassar, Potential use of Argentine kaolinitic clays as pozzolanic material, *Appl. Clay Sci.* 101 (2014) 468–476. doi:<https://doi.org/10.1016/j.clay.2014.09.009>.
- [17] B. Ilić, V. Radonjanin, M. Malešev, M. Zdujić, A. Mitrović, Effects of mechanical and thermal activation on pozzolanic activity of kaolin containing mica, *Appl. Clay Sci.* 123 (2016) 173–181. doi:[10.1016/j.clay.2016.01.029](https://doi.org/10.1016/j.clay.2016.01.029)

Phase and dimensional stability of volcanic ash-based phosphate geopolymers at elevated temperatures

J.N. Yankwa Djobo^{1,2*}, A. Elimbi³ and D. Stephan²

¹Local Materials Promotion Authority/MIPROMALO/MINRESI, 2396, Nkolbikok, Yaoundé-Cameroon

²Building Materials and Construction Chemistry, Technische Universität Berlin, Gustav-Meyer-Allee 25, 13355, Berlin, Germany

³Department of Inorganic Chemistry, Faculty of Science, University of Yaoundé I, 812, Yaoundé, Cameroon

*Corresponding author: noeldjobo@gmail.com; noel.djobo@campus.tu-berlin.de

Abstract

Phosphate geopolymers are part of chemically bonded phosphate cements obtained from an aluminosilicate and phosphate solution. Their structure consisting of phosphate bonds make them suitable for use as refractory material. This study deals with the influence of phosphoric acid concentration (6, 8 and 10 mol/L) on the stability of volcanic ash-based phosphate geopolymers exposed to 100, 600 and 1000°C. The results reveal that the onset of crystallization is about 600°C with the formation of aluminium phosphate (V) and tridymite, then crystallisation of iron (III) phosphate (V) and hematite at 1000°C. The degree of crystallisation of these phases increases with phosphoric acid concentration. The geopolymers obtained with 8 mol/L of phosphoric acid showed the best thermal stability at 1000°C in term compressive strength change. The maximum thermal linear shrinkage recorded was 3%. The major phases of all geopolymers remain stable up to 1000°C, after which melting of phases happens.

Keywords. Volcanic ash; phosphate geopolymers; thermal stability.

1. Introduction

Geopolymers are known as 3D network inorganic polymer obtained by chemical reaction of a solid precursor (aluminosilicate) and a hardener in a liquid state. The latter may be potassium or sodium silicate solution, or phosphoric acid [1]. The geopolymer gained its popularity because of the potential low CO₂ emission and energy efficiency during its manufacturing compared to conventional cement. Moreover, the superior thermal stability of geopolymer compared to Portland cement has also increased the interest toward that material for high-temperature applications. However, this characteristic is closely related to the type of aluminosilicate used as well as the synthesis conditions [2–4]. For example, an addition of calcium sources to Metakaolin (MK) improves the thermal resistance of geopolymers in term of compressive strength compared to solely MK-based geopolymers when exposed at 1000°C [5]. It was reported a loss of 40% of initial strength after a cycle of heating-cooling of geopolymer from volcanic ash at 1000°C [6]. When prepared in alkaline medium, the phases of volcanic ash-based geopolymers are not stable beyond 1000°C as they start melting contrary to MK-based ones. It was also shown that volcanic ash based-geopolymers obtained with potassium silicate as alkaline solution develops superior stability at elevated temperatures

with thermal shrinkage less than 3% compared to the ones with sodium silicate [7]. In general, when exposed to elevated temperatures the physical properties of geopolymers obtained in alkaline solution are significantly deteriorated in the range of 750-900 °C [8,9]. The latter constitutes the highest temperature range of application of geopolymer obtained in alkaline medium in the field of heat resistance materials. This is due to cations present in the alkaline solution which lower the temperature of glass transition, hence induce sintering with decrease of the mechanical strength along with severe thermal shrinkage [4,7]. Up to now, few studies deal with the phase stability or physical properties of geopolymers obtained in an acidic medium after exposure at elevated temperatures.

The phases of MK-based geopolymers obtained with phosphoric acid were reported to be thermally stable, with linear shrinkage of 5.3% after exposure at 1450°C [10]. Also, phosphoric acid activation of synthetic Al_2O_3 - 2SiO_2 powders showed extremely high thermal stability of phases with no sign of melting up to 1550°C [11]. Recent work reported that the structural evolution of phases with temperature and their stability depend on the phosphate content of the matrix [12]. However, MK-based phosphate geopolymers have low thermal stability in term of compressive strength evolution. Bewa et al. reported a decrease of more than 75% of the compressive strength development only after exposure at 200°C [13]. While, Celerier et al. [14] showed the complete destruction and/or extensive cracks apparition with a significant decrease of the compressive strength of MK-based phosphate geopolymer after heating to 1000°C. These behaviours at elevated temperature were reported to depend on the Al/P ratio of the matrix, the reactivity of the MK used and its wettability. Moreover, the high-water content of the MK-based phosphate geopolymer was also responsible of the destruction of the binding phase because of the dehydroxylation that happens after heating. Since MK particles have a high specific surface area, thus high-water demand and high liquid to solid mass ratio are required for reaching good workability.

The investigation of geopolymers from volcanic ash and phosphoric acid has never been reported yet. Since the improved thermal stability of phases of MK-phosphate geopolymer was due to the high stability of the phosphate bond, the low thermal stability of phases of volcanic ash based geopolymer in alkaline solution could also be improved when synthesized in acidic medium. Moreover, volcanic ash has lower specific surface area compared to MK and generally low liquid to solid mass ratio is required for achieving good workability [15]. This work aims to investigate the influence of phosphoric acid concentration on thermal stability of volcanic ash-based phosphate geopolymers for high temperature application. These include the study of the transformation and transition of phases, the thermal shrinkage as well as porosity and compressive strength of geopolymers exposed to high temperatures. The thermal transformation and transition of phases were investigated by X-Ray diffractometry (XRD), Fourier transformed infrared spectroscopy (FTIR), Thermogravimetry analysis coupled with Differential Scanning Calorimetry (TGA-DSC) and Dilatometry analysis. The porosity was determined using mercury intrusion porosimeter (MIP).

2. Materials and methods

2.1 Materials

Volcanic ash (VA) was collected along “the Line of Cameroon” and ground in a ball mill to get a powder with particles size <200µm. The chemical analysis carried out by X-ray fluorescence is reported in Table 1. The particle size distribution carried out using laser particle size analyser (MASTERSIZER S, Malvern, UK) is depicted in Fig. 1. It shows a trimodal distribution with characteristic diameters as follows: $d_{10} = 0.26 \mu\text{m}$, $d_{50} = 3.7 \mu\text{m}$ and $d_{90} = 57 \mu\text{m}$. Orthophosphoric acid (H_3PO_4 , 85wt.-%) was used to prepare the hardeners. The latter were obtained by diluting the as received orthophosphoric acid with water to get concentrations of phosphoric acid solution 6, 8 and 10 mol /L.

Table 1: Chemical composition of volcanic ash from Cameroon

Oxides	SiO ₂	Al ₂ O ₃	Fe ₂ O ₃	CaO	MgO	Na ₂ O	TiO ₂	K ₂ O	MnO	P ₂ O ₅	LOI	Total
Wt. -%	40.41	15.90	13.46	8.87	8.45	1.75	3.08	0.91	0.21	0.88	4.25	98.17

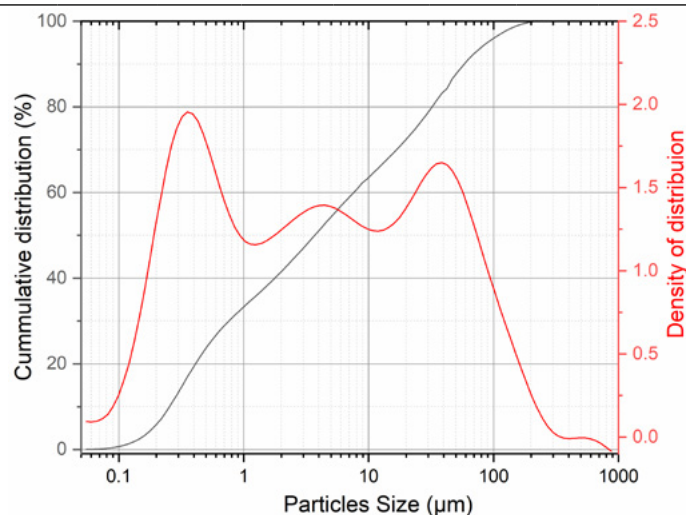


Fig. 1. Particles size distribution of milled volcanic ash

2.2 Experimental methods

The geopolymer pastes were prepared by mixing for 3 min volcanic ash and the hardeners according to liquid to solid mass ratios of 0.32, 0.36 and 0.4 respectively. These different ratios were chosen according to the workability of the pastes with each concentration of acid. The pastes obtained were poured in 40 mm cubic moulds, vibrated for 3 min and covered with a plastic foil to avoid cracks or pores due to rapid water evaporation. The specimens were kept at $27 \pm 3^\circ\text{C}$ for 24h before demolding, then stored in the same curing condition for 28d. Afterwards, the geopolymer specimens were heated to a temperature of 100, 600 and 1000°C at a heating rate of $5^\circ\text{C}/\text{min}$ in a programmable electrical furnace and kept at this temperature for 4h.

The analysis of the mineralogical composition of the geopolymers before and after exposure to elevated temperatures was carried out using X-ray diffractometry (Bruker X-ray diffractometer (D8 Discovery, US)). The changes on the chemical bonds of unheated and heated geopolymers were investigated by FTIR spectroscopy (Nicolet 5700 spectrometer using KBr method). The porosity and pore size distribution of unheated geopolymers were investigated by mercury intrusion porosimeter (Auto pore IV 9500 scanning mercury porosimeter with pore size range between 0.005 and $360 \mu\text{m}$).

The compressive strength of geopolymers before and after exposure to elevated temperatures was measured thanks to an Impact Test Equipment Limited. Thermal transformation and transition phases were monitored using Thermogravimetry analysis coupled with Differential Scanning Calorimetry (Linseis, Model STA PT1000). An optical dilatometer (ESS MISURA HSM ODHT Model 1600/80) was used to assess changes of length of specimens shaped $5 \times 5 \times 15 \text{ mm}^3$.

3. Results and discussion

3.1 Influence of phosphoric acid concentration on mineralogy at 27 and 1000°C

The phase compositions of raw volcanic ash and geopolymers before and after exposure to 1000°C are depicted in Figs 2 and 3 respectively. The main minerals identified in volcanic ash using X'Pert High Score Plus software are as follows: augite (PDF# 98-005-6926); albite high (PDF# 98-010-0499); jadeite-

diopside (PDF# 98-006-9709); forsterite, ferroan (PDF# 98-003-9795) and magnetite (PDF# 98-008-5807). In the unheated geopolymers, no new crystalline phases were identified (Fig. 2), but a significant decrease of peaks intensity of major minerals is visible. This behaviour is like what happens with volcanic ash-based geopolymers obtained in alkaline solution [16,17].

The intensities of the peaks of augite ($\text{Al}_{0.1}\text{Ca}_{0.83}\text{Fe}_{0.34}\text{Mg}_{0.77}\text{Na}_{0.02}\text{O}_6\text{Si}_{1.92}\text{Ti}_{0.02}$) at 29.80° (2.99\AA), 35.53° (2.52\AA) and 35.74° (2.51\AA) respectively decrease by 38, 27 and 28% respectively after reaction of volcanic ash with 6 mol/L acid solution. Also, intensities of the main peaks of albite ($\text{NaAlSi}_3\text{O}_8$) at $20=27.73^\circ$ (3.21\AA), 23.57° (3.77\AA) and 21.87° (4.05\AA) respectively are reduced by 26, 22 and 17% respectively. These data show that augite is more dissolved than albite.

This is likely due to the preferential dissolution of augite (Pyroxene group) in low pH (below 3-4) in comparison with albite (Feldspar group) [18,19]. However, the extent of dissolution of those minerals is not proportional to the acid concentration, though it remains low in volcanic ash. A tentative explanation to this behaviour might be the rapid dissolution of amorphous phase and fast setting as observed during mixing, which would have delayed the further dissolution of unreacted particles with time. Nevertheless, a deep investigation to understand the dissolution behaviour of volcanic ash in an acidic medium is required and this will be carried out in our upcoming studies.

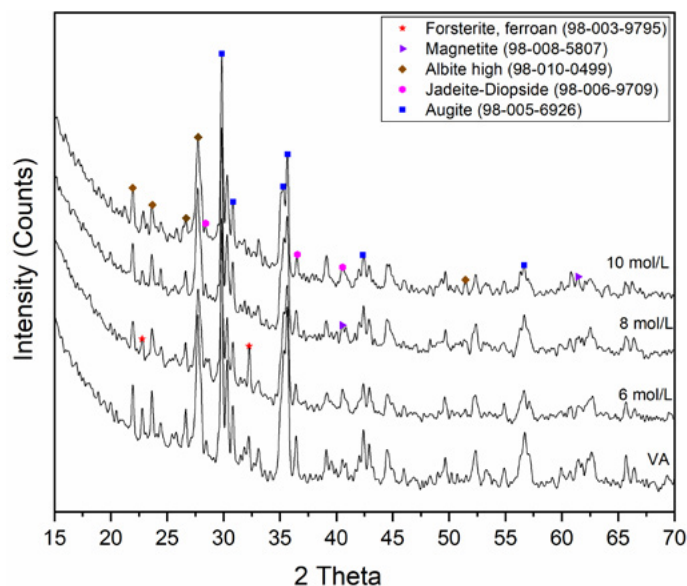


Fig. 2. X-ray patterns of volcanic ash and resulting geopolymers at 27 °C

The X-ray patterns of heated geopolymers at 1000°C (Fig. 3) show several changes in the phase compositions compared to unheated ones. The main diffraction peaks of minerals like Jadeite-Diopside (PDF# 98-006-9709); Forsterite, ferroan (PDF# 98-003-9795) and Magnetite (PDF# 98-008-5807) are no longer identifiable, which means that they were transformed into other phases. It can also be seen the significant decrease of intensities of peaks at $2\theta=29.80^\circ$ (2.99\AA) and 27.74° (3.21\AA) corresponding to the main peak of augite and albite respectively with acid concentration. This happens along with the change in the profile of the broad peak at $2\theta=35.74^\circ$ (2.51\AA) on the X-ray pattern of volcanic ash which becomes narrow.

The extent of the decrease of the main peak intensity of these major minerals shows that in addition to acid concentration, the stability of augite is more sensitive to temperature than albite. The new crystalline phases are aluminium phosphate (V) (PDF# 98-028-0307), tridymite (PDF# 98-009-4090), hematite (PDF# 98-008-8418) and iron (III) phosphate (V) (PDF# 98-009-8063). Their main peaks are as follows: $2\theta = 20.46^\circ$ (4.33\AA), 21.52° (4.12\AA) and 23.15° (3.84\AA) for aluminium phosphate (V); $2\theta = 20.32^\circ$ (4.36\AA), 21.62°

(4.10Å) and 23.08° (3.85Å) for tridymite; 2θ = 25.68° (3.46Å), 37.63° (2.38Å) and 20.33° (4.36Å) for iron(III) phosphate(V); 2θ = 33.25° (2.69Å), 35.72° (2.51Å) and 54.23° (1.70Å) for hematite. Iron phosphate minerals have the similar structure like the SiO₂-based minerals [20]. It can be noticed an increase of these main peak intensities with the increase of phosphoric acid concentration.

The formation of aluminium phosphate(V) and silica-based minerals such as tridymite are common in phosphate geopolymers treated at 1000°C [11,13,21–23]. The formation of these two minerals is due to the crystallization of amorphous AlPO₄-SiO₂ solid solution constituting the binding phase of the phosphoric acid-based geopolymer [23]. Thus, the increase of the amount of these minerals demonstrates the extent of dissolution of reactive phases that happens with the increase of phosphoric acid concentration. Moreover, the formation of hematite and iron phosphate is totally new in high-temperature heating of phosphate geopolymers. Their presence is a proof that in addition to AlPO₄-SiO₂ solid solution as binder in phosphate geopolymer there is also FePO₄ in the case of ferro-aluminosilicate materials like volcanic ash. Moreover, similarly to aluminium phosphate and tridymite, the presence hematite and iron phosphate come from the partly breakdown of the Fe-O-P bonds of the amorphous phase of the geopolymer binder.

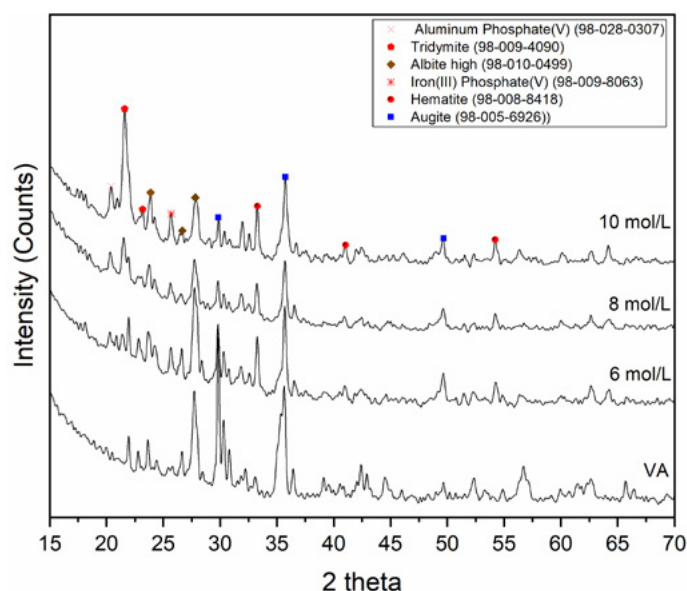


Fig. 3. X-ray patterns of geopolymer after heating at 1000°C

Structural bond changes in geopolymer with varying phosphoric acid concentration before and after exposure to elevated temperatures are highlighted in Figs 4 and 5 respectively.

The vibration band appearing at 1650 and 3420 cm⁻¹ in all IR spectra are respectively characteristic of bending and stretching vibrations of H-O-H and H-O bonds of water molecules. In Fig. 4, the band on VA at 1020 cm⁻¹ is characteristic of stretching vibrations of Si-O bonds of silicate chain. With 6 mol/L of phosphoric acid used as a hardener, that band has shifted by about 52 cm⁻¹ to a higher value after geopolymerization. It further shifted by 11cm⁻¹ when the acid concentration rises respectively to 8 and 10 mol/L. Such increase of wavenumber is also noticeable on the band at 750 cm⁻¹ of volcanic ash, which is characteristic of stretching vibration of Si-O bonds of the silicate network, that shifted to 792 cm⁻¹ on geopolymer. This observation indicates that there is formation of new stronger bonds as a result of reaction occurring [17,24]. Such a phenomenon can be attributed to the formation of new bonds among tetrahedra [AlO₄]⁵⁻, [FeO₄]⁵⁻ and [PO₄]⁵⁻.

The changes observed in that main vibration band also ascertain that increasing the concentration of phosphoric acid improves the extent of dissolution of reactive phases as stated by XRD patterns. The

bands appearing at 630, 578 and 541 cm^{-1} are respectively related to the various vibrating modes of the Si-O bonds in the silicate chains of volcanic ash [25]. Fig. 5. shows the IR spectra of geopolymer with varying acid concentration after heating at 1000°C.

After heating geopolymer, there is the significant decrease in the intensity of bands at 3420 and 1650 cm^{-1} which are characteristic of vibration modes of water molecules. Compared to the IR spectra of geopolymer cured at 27°C (Fig 4.) it can also be observed a shift of the wavenumber of the main band characteristic of Si-O vibration (1072-1083 cm^{-1}) to a higher value (1112 cm^{-1}) and the apparition of new bands at 1029 and 1064 cm^{-1} respectively.

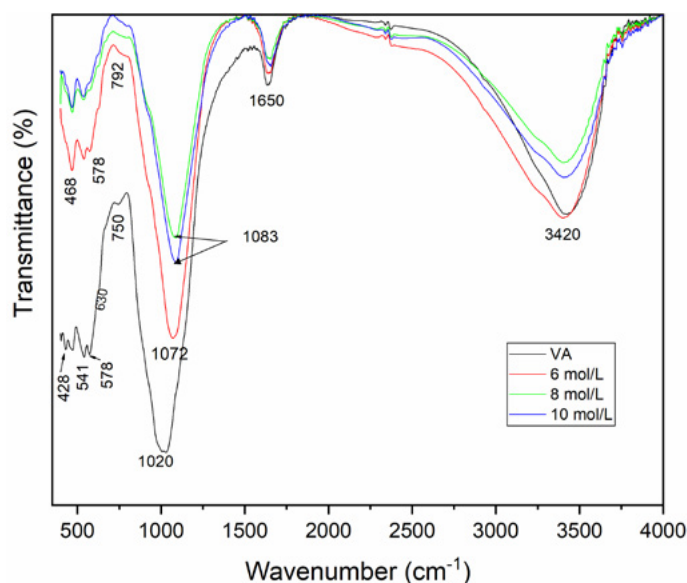


Fig. 4. IR spectra of volcanic ash and resulting geopolymers at 27 °C

Other changes are the disappearance of the vibration band at 541 cm^{-1} and the appearance of the band at 713 cm^{-1} after heating. Similar changes were observed in previous work [12,13]. In this study, these changes are attributed to the crystallization of tridymite and phosphate minerals as shown in XRD patterns of geopolymer after heating at 1000°C.

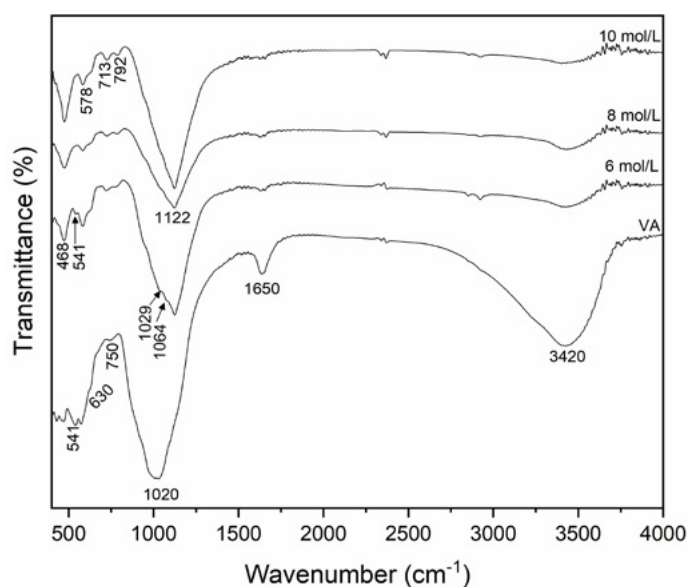


Fig. 5. IR spectra of geopolymer after heating at 1000°C

3.2 Influence of heating temperature on the mineralogy of phosphate geopolymer obtained with 10 mol/L acid concentration

Fig 6 shows the X-ray patterns of volcanic ash-based geopolymers obtained with 10 mol/L of phosphoric acid after exposure to various temperatures. As it can be seen, the crystalline phases initially present in unheated geopolymers remain stable up to 600°C, where the onset of crystallisation is observed. The latter phenomenon is however characterised by the formation of new minerals, aluminium phosphate (V) (PDF# 98-028-0307) and tridymite (PDF# 98-009-4090).

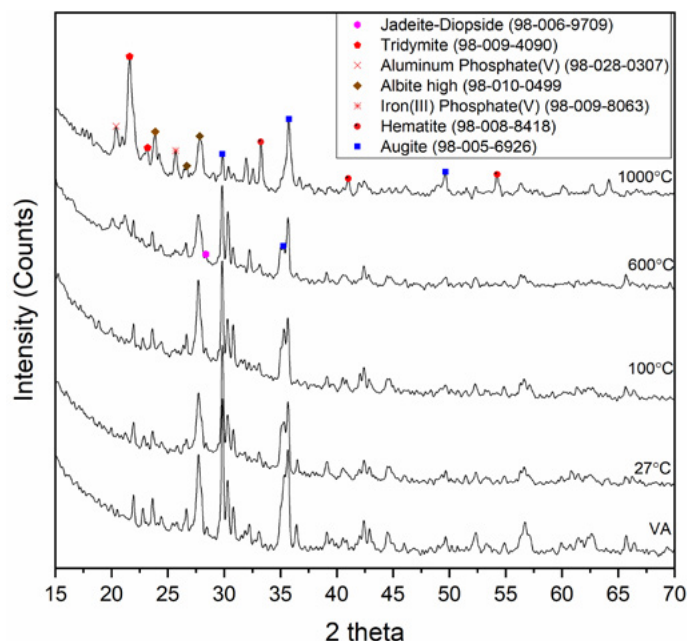


Fig. 6. X-ray patterns of geopolymer obtained with 10 mol/L acid concentration after heating at various temperatures

Although the initial minerals remain up to 600°C, their peak intensities somewhat diminish with increasing temperature. This is more prominent at 1000°C where other new minerals (hematite and iron (III) phosphate (V)) are formed along with the disappearance of some of the initial ones (jadeite-diopside; forsterite, ferroan and magnetite). There is also a significant increase of the peak intensities of aluminium phosphate (V) and tridymite at 1000°C.

It arises from these results that, the stability of minerals of the studied system are temperature sensitive and the onset of crystallization is at around 600 °C. The IR spectra of geopolymers obtained with 10 mol/L of phosphoric acid and heated at various temperatures are shown in (Fig. 7).

The effect of heating is highlighted by the main changes between 600 and 1000 °C. The latter include the shift of the main vibration band from 1093 to 1122 cm⁻¹, the disappearance of the bands at 541cm⁻¹ and the appearance of the bands at 713, 1029 and 1064 cm⁻¹. These results confirm the fact that the onset of crystallisation of phosphate geopolymers is around 600 °C and are in accordance with the XRD data (Fig. 6).

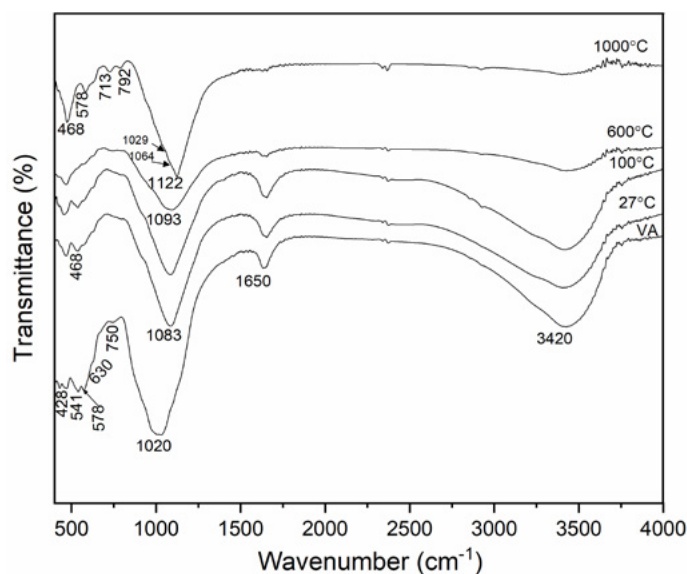


Fig. 7. IR spectra of geopolymer obtained with 10 mol/L acid concentration after heating at various temperatures.

3.3 Physical characteristics

3.3.1 Visual aspect

After maintaining geopolymers at various temperatures, changes in colour and the formation of cracks on the surfaces of some specimens were observed (Fig. 8). The specimens obtained with 6 mol/L of phosphoric acid show no sign of surface deterioration when exposed to 100°C, whilst other specimens show some cracks. The latter seem to be more prominent and larger on the specimen obtained with 10 mol/L of phosphoric acid than the one obtained with the concentration of 8 mol/L. The presence of these cracks can be due to the evaporation of free water present in the pores network or to the dehydroxylation of geopolymer binder. Thus, the extent of cracks demonstrates that the geopolymer obtained with 10 mol/L of phosphoric acid undergoes more damages at 100 °C compared to other specimens. At 600 °C, the geopolymer specimens obtained with 6 and 8 mol/L of phosphoric acid display minor microcracks and there are changes of initial colours from black to light and dark brown.

When heated to 1000°C all the specimens do not show any sign of external damage except the colour which is now light red and becomes dark with increasing phosphoric acid concentration. Based on a correlation between the change of colours and the mineral evolution with temperature, it can be concluded that the change of colour observed at 600 °C results from the crystallisation of aluminium phosphate(V) and tridymite, whereas those observed at 1000 °C corresponds to crystallisation of iron (III) phosphate and hematite.

3.3.2 Porosity

The total porosity and pore size distribution of unheated geopolymers are shown in Figs 9 and 10 respectively. Total porosity (Fig. 9) of geopolymers obtained with 6 or 8 mol/L of phosphoric acid are 22 and 21vol.-% respectively. The porosity significantly decreases to 10.7vol.-% when the acid concentration rises to 10 mol/L, which means that the latter has fewer pores compared to the formers. However, it is clearly shown in Fig.10a that the specimen obtained with 10 mol/L of phosphoric acid exhibits larger pore diameters than those obtained with 6 and 8 mol/L respectively. The pore size ranges (Fig.10b) are 0.01-5µm, 0.01-1µm and 0.027-5 µm for specimens with 6, 8 and 10 mol/L of phosphoric acid respectively. Within these pore diameter ranges, the geopolymers obtained with 6 and 10 mol/L of phosphoric acid have

a unimodal pore diameter distribution with maxima at 0.09 and 0.55 μm respectively. Whereas specimens obtained with 8 mol/L of phosphoric acid show a bimodal distribution with maxima at 0.04 and 0.06 μm respectively. This difference in pore size distribution indicates the heterogeneity of the microstructure, which is related to geopolymerization [23,26]. The effect of pore size distribution on the thermal stability of geopolymers will be well discussed in the next section.

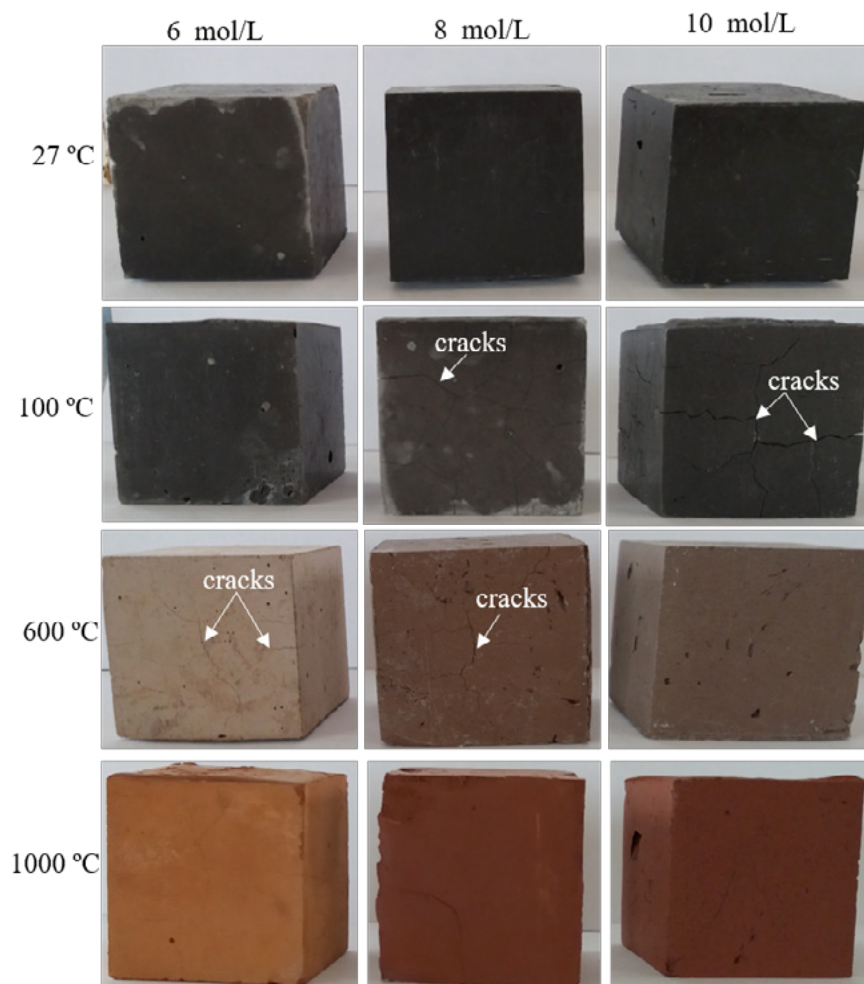


Fig. 8. Physical appearance of geopolymers before and after exposure to various temperatures

3.3.3 Compressive strength

Fig 11 depicts the 28d compressive strength evolution of geopolymer before and after heating at various temperatures for 4h. At room temperature, compressive strength increases with acid concentration. After heating at 100°C, the strength of geopolymer obtained with 6 mol/L of phosphoric acid increases by about 84% (49MPa) while that at the other temperatures decreases. For geopolymers obtained with 8 and 10 mol/L of phosphoric acid, the decrease of compressive strength is 14.7% (43MPa) and 17% (60MPa) respectively.

This trend correlates well with the observation made on (Fig 8) where major cracks were observed only on geopolymers obtained respectively with 8 and 10 mol/L of phosphoric acid. These observations allow to surmise that although high dissolution of reactive phase using hardener of 6 mol/L of phosphoric acid was observed in XRD patterns, the reaction of volcanic ash with 6 mol/L acid concentration remains low.

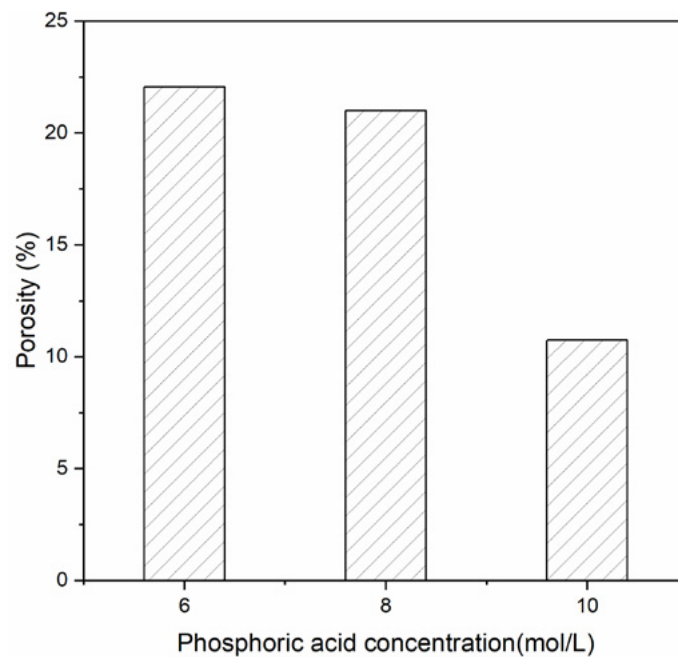


Fig. 9. Total porosity of geopolymers

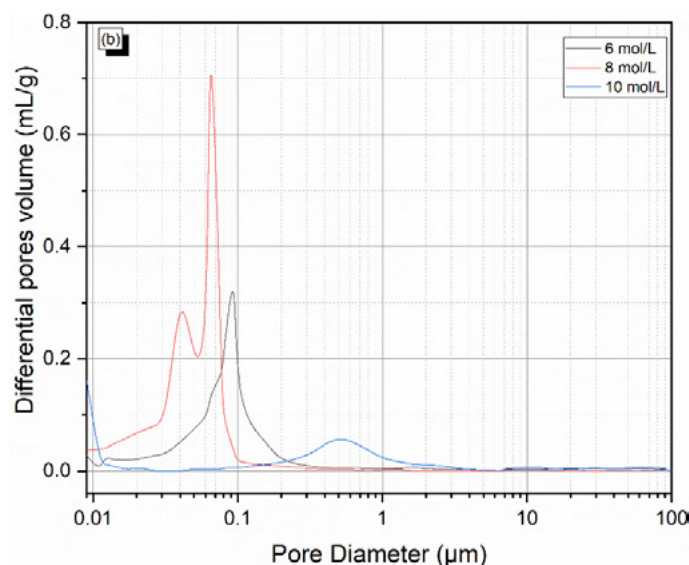


Fig. 10. Pores size distribution of geopolymers: (a) Cumulative pores volume, (b) Differential volume of intruded mercury.

Thus, when exposed at 100°C, the heat supplied rather improves the geopolymerization leading to a more condensed and stronger polymer chain. This seems to be the contrary for geopolymerization with 8 and 10 mol/L acid concentration. In these latter cases, the reactions that take place are faster and lead directly to the formation of strong geopolymer structures at room temperature. Thus, the heat supplied has rather triggered the dehydroxylation of the binding phase, leading to the formation of cracks, hence weakening of the structure.

The strength of geopolymer obtained with 10 mol/L of phosphoric acid continues to decrease till the temperature 1000°C (26.5MPa), whereas the strength of geopolymer obtained with 8 mol/L of phosphoric acid (56.5MPa) remains high compared to the one before heating. This difference of behaviour might be due to the pores size distribution of the geopolymers. In fact, the microstructure of the geopolymer obtained with 8 mol/L of phosphoric has high number of pores with various diameters, which allows

easy evaporation of water during the dehydroxylation stage of the binder with less impact on compressive strength.

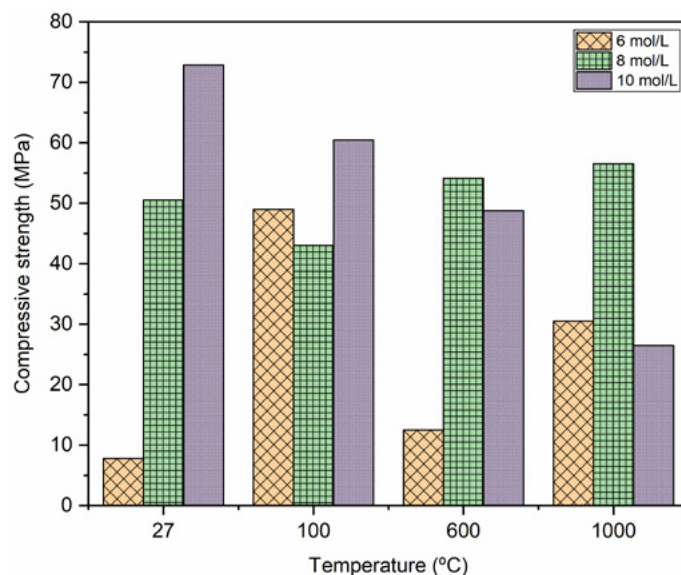


Fig. 11. Compressive strength evolution of geopolymers with temperature

3.4 Phases and dimensional stability

3.4.1 Mass loss and phase stability

The monitoring of the mass change, the phases transformation and transition of the geopolymer with temperature were carried out by TGA-DSC (Fig 12). The TGA curves are characterized by a single mass loss of 13-14wt% which starts nearly at room temperature and ends at around 600°C. That mass loss is accompanied by an endothermic peak at 86°C. These changes correspond to the removal of free water contained in the pores network and the dehydroxylation of polymer chains of the geopolymer binder [26,27]. Between 600 and 1000 °C, there is not any significant mass change.

The DSC curves show respectively a succession of three small exothermic peaks at 634-657 °C, 690 and 820°C, and an endothermic peak at 805 °C. The first one (634-657 °C) corresponds to the crystallization of ferrous/ferric phosphate minerals from the amorphous phase. In the crystallization process of iron phosphate glasses, that first peak is generally followed by a second exothermic peak at 820 °C related to the crystallization of ferric phosphate minerals (FePO_4) [28,29]. The latter obviously confirms the crystallization of iron (III) phosphate identified only in the XRD patterns of geopolymer maintained at 1000°C.

The endothermic peak at 805 °C corresponds to the decomposition of remaining amorphous iron phosphate FePO_4 to crystallized Fe_2O_3 [28]. This confirms the crystallization of hematite observed in XRD patterns. Noteworthy that during the phase transition of iron phosphate there is sometime a competition between decomposition FePO_4 into Fe_2O_3 and the crystallization of new form of FePO_4 [30]. The temperature of the apparition of the first exothermic peak (634-657 °C) shifts to lower value with increasing phosphoric acid concentration. This is due to the increase of the content of $\text{Fe}^{2+}/\text{Fe}^{3+}$ ions in the bulk composition [28]. The exothermic peak appearing at 690°C corresponds to the crystallization of aluminium phosphate and /or tridymite [23].

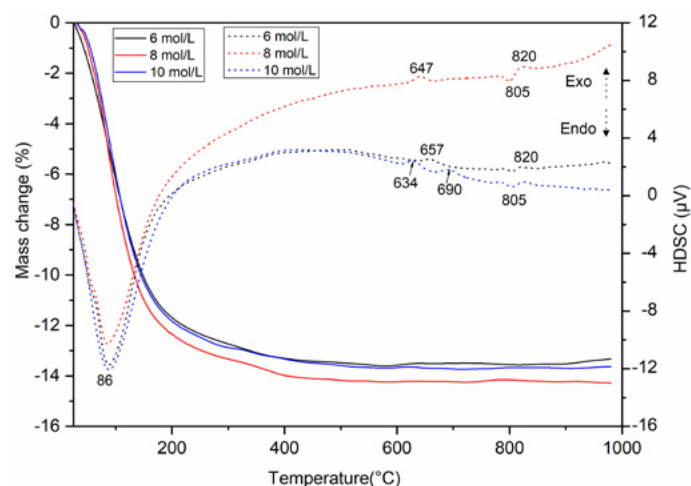


Fig. 12. TGA (solid lines) and DSC (dotted lines) curves of geopolymers with varying phosphoric acid concentrations

3.4.2 Dimensional stability

The dilatometry curves (Fig. 13a) show that up to 1000 °C, thermal linear shrinkage of geopolymers are 195, 2.9 and 3.1% respectively. These shrinkages are mainly observed in two temperature ranges (110-140 °C and 630-665 °C). It is worth pointing out that beyond 1000 °C the higher sintering of volcanic ash particles induces the beginning of melting of mineral phases [6,7]. This can explain the higher shrinkage beyond 1000°C. Hence, this shrinkage was not included in the total shrinkage calculation because the material melts and does not withstand.

The first shrinkage occurs between 25 to 600°C and reaches the maximum at 110-140 °C. This shrinkage is of about 1.6, 2.3 and 2.4% for geopolymer specimens obtained respectively with 6 8 and 10 mol/L of phosphoric acid. The increase of the first shrinkage with phosphoric acid concentration correlates with the extent of cracks as observed on the surface of specimens after exposure at 100 °C (Fig. 8). This shrinkage is linked to the mass loss recorded in TGA and which corresponds to evaporation of water.

The second shrinkage begins at around 600 °C and ends before 1000 °C, and is about 0.2, 0.6 and 0.7% for geopolymer specimens obtained respectively with 6, 8 and 10mol/L of phosphoric acid. This second shrinkage, which does not correspond to any mass loss, is due to the crystallization of ferrous / ferric phosphate minerals. The shift of the maximum temperature related to this second shrinkage (Fig. 13b) agrees with the similar phenomenon observed in the DSC curves (Fig.12), and which was ascribed to the increase of the amount of $\text{Fe}^{2+}/\text{Fe}^{3+}$ ions in the bulk composition.

The latter arising from the increased dissolution of the reactive phase of volcanic ash with the increase of phosphoric acid concentration. Most interesting in the differential curve of the percentage of expansion beyond 1000 °C is the delay of the temperature at which maximum shrinkage due to melting occurs (Fig. 13b). Such a behaviour means that the increase of dosage of phosphate bonds in the geopolymer binder prevent the early melting of phases.

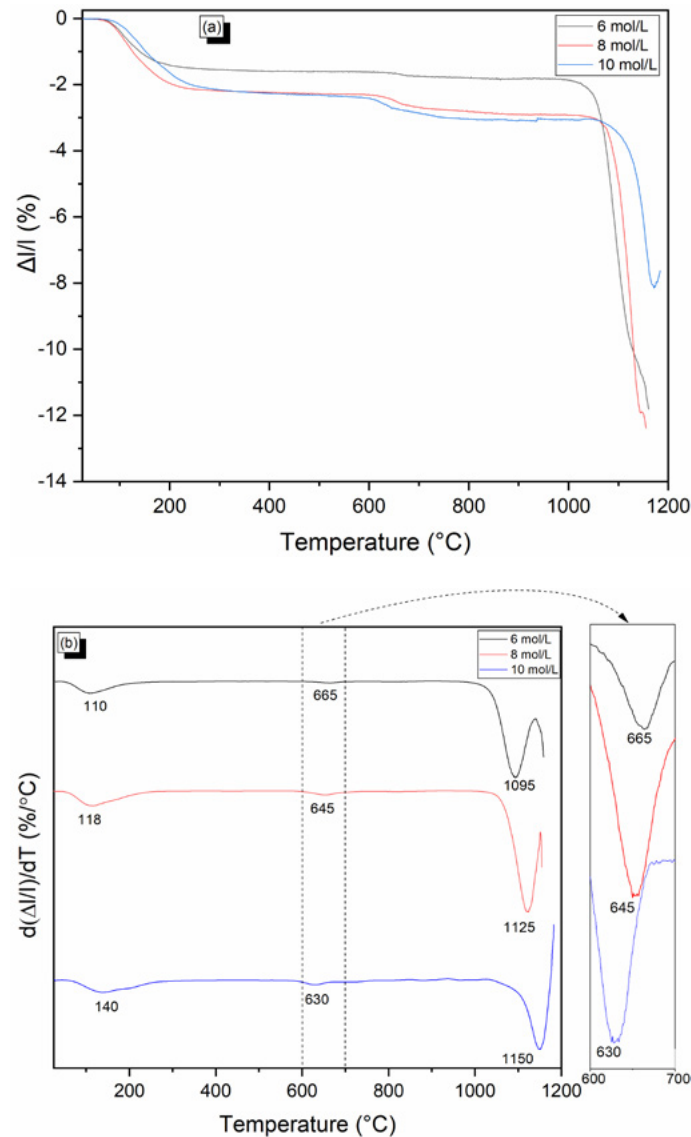


Fig. 13. Dimension change with temperature (a) % of expansion; (b) differential of the % of the expansion

4. Conclusion

The influence of phosphoric acid concentration on the thermal stability of volcanic ash-based phosphate geopolymers was reported. It appears that changes occurring in mineralogical phases are highly sensitive to temperature and phosphoric acid concentration. The major phases including geopolymer binder remain stable up to 1000 $^{\circ}\text{C}$ and beyond the latter temperature, the melting of geopolymers becomes predominant. The geopolymer binder is based on ferro-silico-aluminophosphate ($\text{AlPO}_4\text{-SiO}_2\text{-FePO}_4$) chains. The total porosity of unheated geopolymers decreases from 22 to 10% with increasing phosphoric acid concentration. The heterogeneity of pore diameter distribution enhances the thermal stability of geopolymers in term of strength loss and thermal shrinkage.

The maximum strength loss was 63 % and the highest thermal shrinkage 3% after heating geopolymers up to 1000 $^{\circ}\text{C}$. The geopolymers produced with phosphoric acid concentration of 8 mol/L demonstrated superior thermal stability. Thus, that phosphate geopolymer is suitable for high temperature application up to 1000 $^{\circ}\text{C}$.

5. Acknowledgements

Dr Jean Noël Yankwa Djobo is grateful to the Alexander von Humboldt foundation for supporting his postdoctoral research at the TU Berlin through the Georg Foster Postdoctoral research fellowship (CMR - 1201499 - GF-P). The authors are also thankful to Dr Elie Kamseu and Mr. Sylvain Tome for assistance in materials characterisation.

6. References

- [1] J. Davidovits, *Geopolymer Chemistry and Applications*, 4th ed, 2015.
- [2] M.M. Yadollahi, A. Benli, R. Demirboğa, Effects of elevated temperature on pumice based geopolymer composites, *Plast. Rubber Compos.* 44 (2015) 226–237. doi:10.1179/1743289815Y.0000000020.
- [3] H.K. Tchakouté, C.H. Rüschler, S. Kong, E. Kamseu, C. Leonelli, Thermal Behavior of Metakaolin-Based Geopolymer Cements Using Sodium Waterglass from Rice Husk Ash and Waste Glass as Alternative Activators, *Waste and Biomass Valorization*. (2016). doi:10.1007/s12649-016-9653-7.
- [4] A. Elimbi, H.K. Tchakoute, M. Kondoh, J.D. Manga, J. Dika Manga, Thermal behavior and characteristics of fired geopolymers produced from local Cameroonian metakaolin, *Ceram. Int.* 40 (2014) 4515–4520. doi:10.1016/j.ceramint.2013.08.126.
- [5] S.A. Bernal, E.D. Rodríguez, R. Mejía De Gutiérrez, M. Gordillo, J.L. Provis, Mechanical and thermal characterisation of geopolymers based on silicate-activated metakaolin/slag blends, *J. Mater. Sci.* 46 (2011) 5477–5486. doi:10.1007/s10853-011-5490-z.
- [6] P.N. Lemougna, K.J.D. MacKenzie, U.F.C. Melo, Synthesis and thermal properties of inorganic polymers (geopolymers) for structural and refractory applications from volcanic ash, *Ceram. Int.* 37 (2011) 3011–3018. doi:10.1016/j.ceramint.2011.05.002.
- [7] P.N. Lemougna, U.F. Chinje Melo, M.P. Delplancke, H. Rahier, Influence of the activating solution composition on the stability and thermo-mechanical properties of inorganic polymers (geopolymers) from volcanic ash, *Constr. Build. Mater.* 48 (2013) 278–286. doi:10.1016/j.conbuildmat.2013.06.089.
- [8] D.L.Y. Kong, J.G. Sanjayan, K. Sagoe-Crentsil, Comparative performance of geopolymers made with metakaolin and fly ash after exposure to elevated temperatures, *Cem. Concr. Res.* 37 (2007) 1583–1589. doi:10.1016/j.cemconres.2007.08.021.
- [9] D.L.Y. Kong, J.G. Sanjayan, Effect of elevated temperatures on geopolymer paste, mortar and concrete, *Cem. Concr. Res.* 40 (2010) 334–339. doi:10.1016/j.cemconres.2009.10.017.
- [10] L. Le-ping, C. Xue-min, Q. Shu-heng, Y. Jun-li, Z. Lin, Preparation of phosphoric acid-based porous geopolymers, *Appl. Clay Sci.* 50 (2010) 600–603. doi:10.1016/j.clay.2010.10.004.
- [11] L. Le-ping, C. Xue-min, H. Yan, L. Si-dong, G. Si-yu, The phase evolution of phosphoric acid-based geopolymers at elevated temperatures, *Mater. Lett.* 66 (2012) 10–12. doi:10.1016/j.matlet.2011.08.043.
- [12] M. Khabbouchi, K. Hosni, M. Mezni, C. Zanelli, M. Doggy, M. Dondi, E. Srasra, Interaction of metakaolin-phosphoric acid and their structural evolution at high temperature, *Appl. Clay Sci.* 146 (2017) 510–516. doi:10.1016/j.clay.2017.07.006.
- [13] C. Nobouassia Bewa, H.K. Tchakouté, D. Fotio, C.H. Rüschler, E. Kamseu, C. Leonelli, Water resistance and thermal behavior of metakaolin-phosphate-based geopolymer cements, *J. Asian Ceram. Soc.*

6 (2018) 271–283. doi:10.1080/21870764.2018.1507660.

[14] H. Celerier, J. Jouin, N. Tessier-Doyen, S. Rossignol, Influence of various metakaolin raw materials on the water and fire resistance of geopolymers prepared in phosphoric acid, *J. Non. Cryst. Solids*. 500 (2018) 493–501. doi:10.1016/j.jnoncrysol.2018.09.005.

[15] J.N.Y. Djobo, L.N. Tchadjié, H.K. Tchakoute, B.B.D. Kenne, A. Elimbi, D. Njopwouo, Synthesis of geopolymer composites from a mixture of volcanic scoria and metakaolin, *J. Asian Ceram. Soc.* 2 (2014) 387–398. doi:10.1016/j.jascer.2014.08.003.

[16] P.N. Lemougna, U.F. Chinje Melo, M.P. Delplancke, H. Rahier, Influence of the chemical and mineralogical composition on the reactivity of volcanic ashes during alkali activation, *Ceram. Int.* 40 (2014) 811–820. doi:10.1016/j.ceramint.2013.06.072.

[17] J.N.Y. Djobo, A. Elimbi, H.K. Tchakouté, S. Kumar, Reactivity of volcanic ash in alkaline medium, microstructural and strength characteristics of resulting geopolymers under different synthesis conditions, *J. Mater. Sci.* 51 (2016) 10301–10317. doi:10.1007/s10853-016-0257-1.

[18] Y. Chen, S.L. Brantley, Temperature- and pH-dependence of albite dissolution rate at acid pH, *Chem. Geol.* 135 (1997) 275–290. doi:10.1016/S0009-2541(96)00126-X.

[19] A.C. McAdam, M.Y. Zolotov, T.G. Sharp, L.A. Leshin, Preferential low-pH dissolution of pyroxene in plagioclase-pyroxene mixtures: Implications for martian surface materials, *Icarus*. 196 (2008) 90–96. doi:10.1016/j.icarus.2008.01.008.

[20] P. Reale, B. Scrosati, C. Delacourt, C. Wurm, M. Morcrette, C. Masquelier, Synthesis and Thermal Behavior of Crystalline Hydrated Iron(III) Phosphates of Interest as Positive Electrodes in Li Batteries, *Chem. Mater.* 15 (2003) 5051–5058. doi:10.1021/cm031107z.

[21] M. Irfan Khan, H.U. and Teoh. K. Min, Khairun Azizli, Suriati Sufian, M.I. Khan, T.K. Min, K. Azizli, S. Sufian, H. Ullah, Z. Man, Effective removal of methylene blue from water using phosphoric acid based geopolymers: Synthesis, characterizations and adsorption studies, *RSC Adv.* 5 (2015) 61410–61420. doi:10.1039/c5ra08255b.

[22] C.M. Guo, K.T. Wang, M.Y. Liu, X.H. Li, X.M. Cui, Preparation and characterization of acid-based geopolymer using metakaolin and disused polishing liquid, *Ceram. Int.* 42 (2016) 9287–9291. doi:10.1016/j.ceramint.2016.02.073.

[23] M. Lassinanti Gualtieri, M. Romagnoli, A.F. Gualtieri, Preparation of phosphoric acid-based geopolymer foams using limestone as pore forming agent - Thermal properties by in situ XRPD and Rietveld refinements, *J. Eur. Ceram. Soc.* 35 (2015) 3167–3178. doi:10.1016/j.jeurceramsoc.2015.04.030.

[24] J.N.Y. Djobo, A. Elimbi, H.K. Tchakouté, S. Kumar, Mechanical activation of volcanic ash for geopolymer synthesis: effect on reaction kinetics, gel characteristics, physical and mechanical properties, *RSC Adv.* 6 (2016) 39106–39117. doi:10.1039/c6ra03667h.

[25] I. Basile-Doelsch, R. Amundson, W.E.E. Stone, C.A. Masiello, J.Y. Bottero, F. Colin, F. Masin, D. Borschneck, J.D. Meunier, Mineralogical control of organic carbon dynamics in a volcanic ash soil on La Réunion, *Eur. J. Soil Sci.* 56 (2005) 689–703. doi:10.1111/j.1365-2389.2005.00703.x.

[26] M. Lassinanti Gualtieri, M. Romagnoli, S. Pollastri, A.F. Gualtieri, Inorganic polymers from laterite using activation with phosphoric acid and alkaline sodium silicate solution: Mechanical and microstructural properties, *Cem. Concr. Res.* 67 (2015) 259–270. doi:10.1016/j.cemconres.2014.08.010.

- [27] Y.S. Wang, J.L. Provis, J.G. Dai, Role of soluble aluminum species in the activating solution for synthesis of silico-aluminophosphate geopolymers, *Cem. Concr. Compos.* 93 (2018) 186–195. doi:10.1016/j.cemconcomp.2018.07.011.
- [28] C.S. Ray, X. Fang, M. Karabulut, G.K. Marasinghe, D.E. Day, Effect of melting temperature and time on iron valence and crystallization of iron phosphate glasses, *J. Non. Cryst. Solids.* 249 (1999) 1–16. doi:10.1016/S0022-3093(99)00304-X.
- [29] C.J.R.G. Oliver, F.C. Lovey, A. Caneiro, D.O. Russo, D.S. Rodríguez, F. Soldera, J.E. Fiscina, J.M. Rincón, Crystallization of iron phosphate glasses containing up to 19 wt.% UO₂, *J. Non. Cryst. Solids.* 356 (2010) 2986–2993. doi:10.1016/j.jnoncrysol.2010.06.034.
- [30] N. Aliouane, T. Badeche, Y. Gagou, E. Nigrelli, P. Saint-Gregoire, Synthesis and phase transitions of iron phosphate, *Ferroelectrics.* 241 (2000) 255–262. doi:10.1080/00150190008224999.

The Effect of NaOH Concentration on the Mechanical and Physical Properties of Alkali Activated Fly Ash-Based Artificial Lightweight Aggregate

P. Risdanareni ^{1,2}, K. Schollbach ^{3,4}, J. Wang ⁵, N. De Belie ¹

¹ Magnel Laboratory for Concrete Research, Ghent University, Tech Lane Ghent Science Park, Campus A, Technologiepark Zwijnaarde 60, B-9052 Ghent, Belgium.

² Department of Civil Engineering, Faculty of Engineering, State University of Malang, Semarang Street 5 Malang 65145, Indonesia

³ Tata Steel, R&D, Microstructure & Surface Characterization (MSC), P.O. Box 10.000, 1970 CA IJmuiden, the Netherlands

⁴ Department of the Built Environment, Eindhoven University of Technology, 5612AP Eindhoven, The Netherlands

⁵ Department of Civil Engineering, Xi'an Jiaotong University, Yanxiang road 99, 710029 Xi'an, China

Abstract

Aggregate is a non-renewable material that takes up a large portion of a concrete mixture. Replacing this material with artificial lightweight aggregate (LWA) that is generated from an industrial by-product such as fly ash, will significantly reduce the impact on the environment. Alkali-activation is a promising technique to generate LWA as it proved to provide better properties to the LWA in comparison to the use of a Portland cement – fly ash binder. However, only limited studies can be found on applying this technique to produce LWA. Furthermore, the concentration of alkali activators such as NaOH, is an important parameter that needs to be investigated in order to produce LWA with excellent properties. Thus, in this research the NaOH concentration was varied (4 M, 6 M or 8 M) in order to obtain the optimum for producing LWA. Later on, the produced LWA with a diameter of 2-4 mm was used to replace the fine aggregates in the mortar. The mechanical and physical properties of the produced LWA were investigated, such as water absorption, density, particle size distribution, crushing resistance, and mineralogy and the compressive strength of the resulting mortar. The results showed that a maximum compressive strength of 64 N/mm² at 28 days could be achieved by mortar containing LWA 8M. Increasing the concentration of NaOH up to 8M had no significant effect on the water absorption value, particle distribution, density and crushing resistance of LWA. The result from Quantitative X-Ray Diffraction (QXRD) revealed that there is also no significant difference in the quantity of amorphous phase formed in the LWA with increasing NaOH concentration. This finding suggests that alkali-activated fly ash LWA can in the future be synthesized with a lower concentration of NaOH starting from 4M.

Keywords: lightweight aggregate, fly ash, alkali-activated, NaOH concentration

1. Introduction

The global consumption of construction aggregate exceeded 48.3 billion tons per year in 2015 and is expected to increase by 5.2% annually [1]. On the other hand, by 2010 the global production of fly ash around the world was around 780 million metric ton and is expected to increase with 1.6% annually [2]. Based on the same report, around 53% of this ash is already used as supplementary material in cement production. Furthermore, as around 70% of the concrete mixture is the aggregate, reducing natural aggregate consumption by replacing it with artificial aggregate generated from waste material such fly ash will be an effective way to reduce the amount of non-renewable material consumption as the concrete mixture.

Several efforts on employing fly ash as raw material to produce pelletized lightweight aggregate (LWA) with cement, glass powder or clay as a binder have already been conducted by researchers [3–5]. Researchers also reported that several aspects such as hardening method, curing method, and pelletizing procedure affected the properties of pelletized LWA [4, 6, 7]. However, almost all the reports are focused on optimizing the properties of LWA which used clay or cement as a binder [3-7]. Only limited studies can be found on using alkali activation of fly ash in producing LWA, although this technique proved to improve the mechanical and physical properties of pelletized aggregate [8-9].

Based on the literature study, the alkali activator solution plays an important role in geopolymerization as silica and alumina dissolvent [10]. The type of alkali solution [10], the concentration of alkali activator [11], [12], the ratio between binder and solution [13], and the curing regime [11] significantly affect the geopolymerization. Based on the literature, NaOH with the concentration range of 8-12 Molars gives optimal mechanical properties in concrete and mortar application [11, 12, 14]. In the literature, Geetha et al found that the lower concentration of NaOH needed to synthesize geopolymer LWA is 8 molar [9]. Increasing the molarity of NaOH proofed to reduce water absorption and increase the strength of LWA. However, a higher concentration of NaOH caused workability issues of fresh concrete that lead to a decrease in the mechanical properties of concrete [12, 15]. On the other hand, Gorhan et al. found different behaviour of geopolymer paste in mortar application. They found that the optimum NaOH concentration for fly ash based geopolymer is 6 molar [14]. In artificial aggregate application, the ratio between liquid/solid needed is not as high as in mortar or in concrete, a high concentration of NaOH will significantly decrease the workability of wet LWA. Hence, the effect of different concentrations of NaOH for alkali-activated LWA production is studied, as lower concentrations will also decrease the LWA production cost.

Summarizing, the aim of this study is to find a suitable NaOH concentration that gives a positive effect on the properties of alkali-activated fly ash LWA. In order to avoid the workability issue from the high concentration of NaOH, a low concentration of NaOH in the range of 4 to 8 molars was chosen in this study. The properties of LWA such as water absorption, specific density, particle size distribution, crushing value and its mineralogy were investigated. Furthermore, the LWA with the fraction of 2-4 mm was applied into mortar as a natural fine aggregate replacement to investigate its effect on the mechanical properties of the resulted mortar.

2. Methodology

2.1 Materials

Fly ash (FA) from a thermal power plant in the Netherlands was used as a precursor to produce lightweight aggregate (LWA). The fly ash was sieved until passing the sieve of 125 micron. The chemical composition of FA is presented in Table 1. Based on the data in Table 1, it can be seen that the fly ash used in this research is rich in silica and alumina. Therefore, this material meets the requirement to become an alkali-

activated binder.

A liquid form of sodium silicate (Na_2SiO_3) which contains 26.3% silica, 7.9% sodium oxide, and 65.8% water and a powder form of sodium hydroxide (NaOH) with a purity of 97-98% was used as the alkali activator (AA). In order to obtain varied desired NaOH concentration, the NaOH was dissolved in the demineralized water until reaching the concentrations of 4, 6, and 8 Molar, respectively. Later on, sodium silicate and sodium hydroxide were mixed with a weight ratio of 1.5. Subsequently, the mixed alkali activator was left in room temperature conditions for at least 24 hours before use.

For mortar application, cement type I 52.5 N from Holcim was used as a binder while river sand with a fraction of 0/2 mm was used as the fine aggregate.

Table 1. Chemical Composition of fly ash

Compound	CaO	SiO ₂	Al ₂ O ₃	Fe ₂ O ₃	K ₂ O	MgO	CuO	ZnO	SO ₃	P ₂ O ₅	TiO ₂	LOI
% by Mass	3.790	57.400	26.167	5.987	1.877	1.433	0.015	0.023	0.982	0.881	1.127	0.319

2.2 Methods

2.2.1 Pelletizing Method

LWA was produced by agglomeration technique using a stainless steel pan granulator with a diameter of 500 mm and a depth of 95 mm. The pan granulator parameters that were chosen based on research by Baykal, *et al.* (2000), which are a speed of 60 rpm, a slope of 48° and pelletizing time of 20 minutes [7]. The weight ratio between fly ash and alkali activator of 0.25 was used based on previous research [8, 16, 17]. Firstly, fly ash was added into the pan, followed by adding alkali activator by means of spraying for about 10 minutes. During the pelletizing process, the powder form of fly ash turned into granules after being bonded with alkali activator liquid. Finally, due to gravity and the movement of the pan, the granules that had reached a stable form fell out from the pan. After that, wet granules were dried in curing room which have temperature of 28°C and relative humidity 95 ± 5 % for 24 hours. Dried LWA were sieved using sieve 2 mm in order to get LWA with particle size < 2 mm. Later on, the sieved LWA that have particle size < 2 mm were stored in sealed plastic bag in the curing room for 28 days before being used.

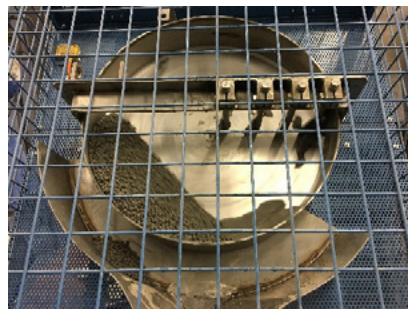


Fig 1. Pan granulator

2.2.2 Physical Properties Testing of LWA

- Mass Density and Water Absorption Test

Water absorption over 24 hours (WA_{24}) of all LWA was performed by following the guidelines of NBN EN 1097-6. The apparent particle density ρ_a (kg/m^3), the saturated surface dry (SSD) density ρ_{SSD} (kg/m^3) and the relative oven dried density ρ_{rd} (kg/m^3) were measured according to the same standard.

- Particle Size Distribution Test

Particle size distribution of all LWA was determined according to Belgian standard NBN EN 12620. The

standardized sieves column with the size of : 63, 45, 40, 31.5, 22.4, 20, 16, 14, 12.5, 10, 8, 6.3, 4, 2, 1, 0.5, 0.25, 0.125 and 0.063 mm were used. The data obtained from the cumulative percentage of material passing through each sieve were analyzed and plotted to a particle size distribution curve.

- **Crushing Resistance Value**

The strength of aggregates can be measured from its crushing resistance value. This test was performed by following Belgian standard NBN B11-205. Firstly, the dried aggregate sample was added into a metal cylinder mold with an inner diameter of 150 mm. After that, the no-friction plunger was put into the mold which was then loaded with 400 kN in 4 min and the load was maintained for 2 minutes before unloaded. Finally, the crushed aggregates were sieved with sieve number 2 mm in order to get data of aggregates that have a fraction < 2 mm. The crushing resistance value of aggregate was the mass ratio between the crushed aggregate that have a fraction <2 mm over the initial sample before loading.

- **Mineralogy of LWA**

X-ray diffraction (XRD) was used to determine the mineralogy of LWA while quantitative XRD (QXRD) was performed using Rietveld analysis. Firstly, around 10 wt% internal standard, in this case, ZnO was added into aggregate samples. Later on the mixed aggregate and ZnO were ground in a Mc Crone mill (Retsch) to a size of around 50 microns. The measurement was done with a D4 (Bruker) using a Co-Tube and equipped with a Lynx Eye detector. The settings were fixed divergence slits (0.5°), 0.04 rad Soller slits and a step size of 0.02.

2.2.3 Mortar Application

- **Mortar Mix Design and Production**

Mortar specimens were produced according to EN NBN 196 standard. The material needed for producing three mortar prisms with the size of 40x40x160 mm³ is presented in Table 2. In this research, LWA with the fraction of 2/4 was used as a natural fine aggregate replacement in producing mortar. 16 % of the total volume of fine aggregate was replaced with LWA, while water to cement ratio of 0.5 was used. This aggregate replacement percentage was chosen as river sand has the same fraction composition.

As LWA has high water absorption, LWA were treated to achieve SSD condition before use in order to limit the water absorption during mixing. Hence, the mass of LWA in oven dried condition (OD) and entrained water needed to achieve SSD condition of LWA are presented in Table 2.

Table 2. Mix design of prisms mortar sample

Type	LWA OD 2/4 (g)	Entrained Water (g)	Sand 2/4 (g)	Sand (g)	Cement (g)	Water (g)
Reference	0	0	220	1130	450	225
FA 4M	120	34	0	1196	450	225
FA 6M	122	32	0	1196	450	225
FA 8M	125	29	0	1196	450	225

- **Compressive Strength**

The fresh mortar samples were cured in curing room which has temperature of 28°C and relative humidity (RH) of 95 ±5% for 24 hours before being demolded. The compressive strength of the mortar prisms was determined according to EN NBN 196 standard. This test was conducted after 7, 14 and 28 days of the samples that were cured in the curing room which has temperature of 28°C and RH of 95±5%. The value of this test was determined by averaging the value of 3 replicated samples.

3. Results and discussion

3.1 Mass Density and Water Absorption

The mass, density and water absorption of all LWA are presented in Table 3. Based on Table 3, it can be seen that FA 8M has the highest apparent, oven dried and SSD density following by FA 6M and FA 4M. The apparent density of LWA was in the range of 2.2-2.3, oven dried density was in the range of 1.4 to 1.5 and SSD density of all specimens are 1.8. To be noted, artificial aggregate in the literature that uses cement as a binder has an apparent density in the range of 2.0-2.3, and 1.6-1.7 for sintered fly ash based geopolymer LWA [8, 17].

The relationship between apparent density and is oven dried density indicated the porosity of the material. The open porosity of all samples is in the range of 33-34 %; this result is similar with the research by Baykal *et al.* which reports open porosity in the range of 31-34 % for cold bonded fly ash LWA [7].

The water absorption of all samples is in the range of 22-23 %. This result is similar to previous literature that uses cement as a binder which has a water absorption in the range of 18.3-46.8 % [7, 18, 19]. However, the water absorption value obtained from this research is still quite high compared to geopolymer bottom ash LWA that has water absorption in the range of 10-12% [9]. This is due to a different size of LWA that have been tested, Geeta *et al.* only used aggregate with the size of 10-12.5 mm for water absorption tests [9]. The size of the aggregates is directly proportional to its strength and density [19]. In addition, LWA with a denser structure normally contains less pores which leads to lower water absorption [16].

Based on the results of the density and water absorption test of LWA, it can be concluded that increasing NaOH concentration proved to slightly reduce the water absorption and the open porosity of LWA and increase its density. The alkali solution acts as silica and alumina dissolvent of fly ash in geopolymer reaction, thus with a higher amount of OH⁻ in the highly concentrated NaOH, the more stable geopolymer formed [10].

Table 3. Mass Density and Water Absorption

Test	FA 4M	FA 6M	FA 8M
Apparent particle density ρ_a (kg/m ³)	2.2 ± 0.05	2.2 ± 0.01	2.3 ± 0.01
Oven Dried Density ρ_{rd} (kg/m ³)	1.4 ± 0.04	1.5 ± 0.01	1.5 ± 0.01
SSD particle density ρ_{ssd} (kg/m ³)	1.8 ± 0.01	1.8 ± 0.01	1.8 ± 0.07
$(\rho_a - \rho_{rd}) / \rho_a \times 100\%$	34.7 ± 2.1	34.1 ± 0.7	33.4 ± 0.2
Water absorption (%)	23.9 ± 1.8	23.2 ± 1.1	22.1 ± 0.3

3.2 Particle Size Distribution

Based on particle size distribution data that are displayed in Figure 2, FA 6M has more fine particles compared to the others. The FA 6M sample has approximately 9% pellets that have a diameter less than 2 mm, while FA 8M has 6% and FA 4M has 2%. For all samples, there is only less than 5% of pellets that have a particle size bigger than 10 mm. These big pellets usually have irregular shape due to not being perfectly compacted or sticking to each other during the pelletizing process. This result is quite similar with previous research by Tang *et al.* which has approximately 7% of pellets with a diameter less than 2 mm and 5% pellets with a diameter bigger than 10 mm for cold bonded bottom ash aggregate [16].

There is only a slight difference between the curve of FA 6M and 8M samples. However, according to NBN EN 12620 about the definition of minimum and maximum aggregate size, FA 8M and FA 4M meet the requirements of an aggregate 2/10, while FA 6M is classified as aggregate 2/8. Moreover, it can also

be noted that all of the LWA have less big particles compare to natural aggregate with the fraction of 2/8.

From the result above, it can be concluded that NaOH concentration has a slight effect on the pellets size according to the similarity of the particle size distribution of all LWA. This result has a good agreement with previous research by Shivaprasad *et al.* who found that the formation of geopolymer pellets depends more on liquid content rather than the Na₂O content [8].

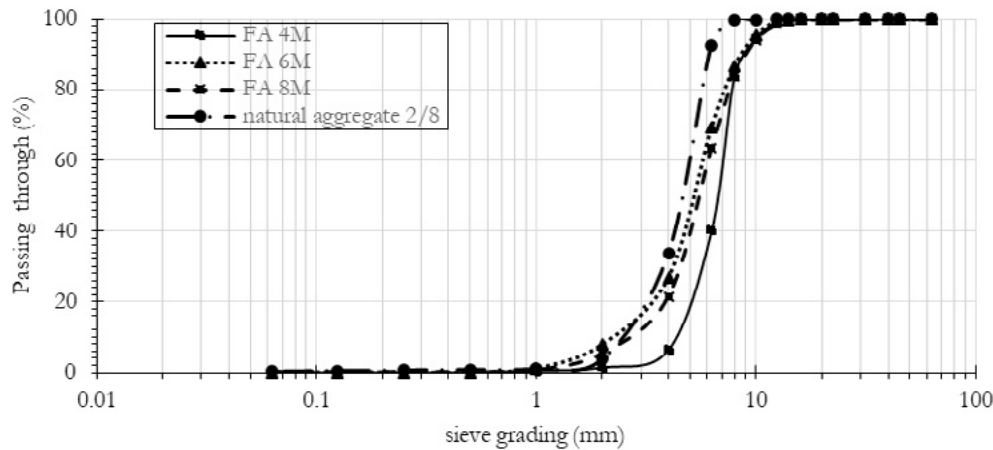


Fig.2 Particle size distribution of LWA

3.3 Crushing Resistance Value

Based on the result presented in Table 4, it can be concluded that increasing the molarity of NaOH up to 6 Molars brought a positive impact to aggregate strength. However, there is only a less than 5% difference in crushing resistance value among all samples. This result is entirely unexpected, as a higher concentration of NaOH was expected to give a higher crushing value. This slight difference was presumably due to a difference in the particle size of LWA. Furthermore, as some of the LWA were compacted after being tested, it is quite difficult to determine its crushed part.

Based on the literature, it can be noted that the crushing strength of LWA increases with the increase of particle size [19]. However, LWA in this research has quite a small fraction compared to LWA in the literature which mostly has a fraction of 4/16. Hence, it is quite difficult to find a suitable method to determine its crushing value [3, 4].

Compared to bottom ash and limestone aggregate, the crushing resistance value of this LWA is almost equal to limestone aggregate which has a particle size of 2/6 and a crushing strength of 63.8% [20]. Due to the different standard method that has been used to determine the strength of aggregates, it is quite difficult to compare the result obtained in this research with another LWA in the literature.

Table 4. Crushing Resistance (CR) value of LWA

Type	CR Value (%)
FA 4M	61.4 ±0.2
FA 6M	62.8 ±0.7
FA 8M	60.0 ±0.9

3.4 Mineralogy of LWA

Based on Quantitative X-Ray Diffraction (QXRD) analysis results displayed in Figure 4, the main phases in LWA are Amorphous (82-83%), Quartz (3.6-4%), Mullite (6.2-6.9%), Magnesioferrite (2.1-2.2%), Gaylussite (1-2.2%), and Hematite (1-1.2%). It can also be seen in Figure 4, that geopolymerization proved

to significantly dissolve Quartz and Mullite in fly ash into Amorphous gel. This phenomenon is indicated by the decreasing quantity of Quartz and Mullite and increasing quantity of amorphous phase in the resulting LWAs sample. However, the Rietveld method that has been used in this study cannot determine which part of the amorphous content is the aluminosilicate (N-A-S-H) gel or the unreacted glassy fly ash.

There is no significant difference in the quantities of amorphous and crystalline phases among all of the LWA samples. This result is not in accordance with the initial expectation that increasing the concentration of NaOH in the mixture will lead to increase the amorphous phase in LWA as there will be more OH⁻ to dissolve Quartz and Mullite in fly ash into alumina-silica gel [10]. However, a similar result was also obtained in the literature which investigated the microstructural properties of dry mixed geopolymer with low alkali activator concentration that obtained similar total amount of non-crystalline phase [21].

Based on previous research on QXRD of alkali activated low calcium fly ash, increasing the amount of amorphous product will lead to increase the strength of the geopolymer paste [22]. However, in this study, there is no trend occurring between the NaOH concentration and the strength of LWA, and there is no significant difference in amount of amorphous among all the samples. Therefore, it is quite difficult to draw conclusions in describing the correlation between the amorphous phase and the strength of LWA in this study.

As higher concentrations of NaOH probably only change the composition of the N-A-S-H gel, tests with lower concentration of NaOH (2M or less) will allow to obtain the best NaOH concentration to activate fly ash-based LWA.

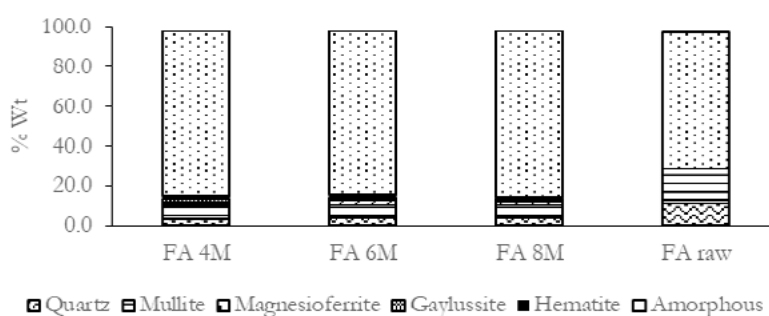


Fig. 4 QXRD analysis of LWA

3.5 Mortar Application

3.5.1 Compressive Strength

Based on mortar compressive strength data displayed in Figure 5, FA 8M provided the highest compressive strength at an age of 28 days followed by FA 6M and FA 4M. Until the age of 14 days, the FA 8M sample did not show high compressive strength.

Replacing 16% by volume of fine natural aggregate with fly ash LWA caused a reduction in compressive strength of the resulting mortar. The sample containing FA 8M LWA had the lowest compressive strength reduction. It has less than 5% reduction of strength with 16% replacement ratio. Compared to cold bonded and geopolymer LWA in the literature, this aggregate gives better mechanical properties. For example, cold bonded bottom ash aggregates have a reduction in the strength of 25% with a 50% replacement ratio [16]. Compared to geopolymer sintered aggregate with a NaOH concentration of 10 molar which caused a 16% strength reduction with 50% replacement rate, this LWA still had acceptable strength reduction [23].

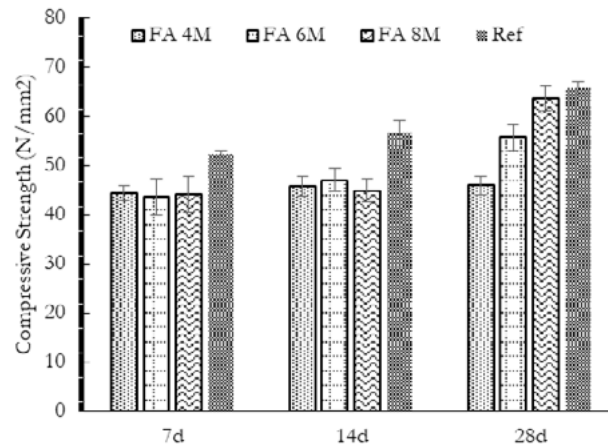


Fig. 5. Compressive Strength of mortar

4. Conclusions

This paper presents the effect of NaOH concentration on mechanical and physical properties of fly ash-based alkali activated LWA. From the results obtained in this study, the following conclusions can be drawn :

1. The mass density of LWA increased along with the increasing NaOH concentration while increasing NaOH concentration proved to slightly reduce the water absorption of LWA.
2. The concentration of NaOH has a slight effect on the particle size distribution of LWA.
3. There is some unexpected trend occurring in crushing resistance strength, FA 6M has a higher CR value than FA 8M. The difficulties to determine the real crushed part of LWA after CR test might cause this irregular trend.
4. Based on QXRD analysis, increasing the NaOH concentration have no significant effect on the quantity of the Amorphous phase formed.
5. The maximum compressive strength of 64 N/mm² and the strength reduction less than 5% could be achieved by mortar containing LWA 8M.

5. Acknowledgment

The authors would like to thank to Islamic Development Bank (IDB) and The Ministry of Research Technology and Higher Education of Indonesia (Kemristek DIKTI) for the financial support. A word of thanks also goes to the technicians of Magnel Laboratory for concrete research of Ghent University for their assistance during the experiments. The author would also like to thank TU Eindhoven for providing disk pelletizer and conducting XRD at their laboratory.

6. Reference

- [1] Freedonia, "World Construction Aggregates - Industry Study with Forecasts for 2015 & 2020," *Free. Gr.*, p. 6, 2012.
- [2] C. Heidrich, H. Feuerborn, and A. Weir, "Coal Combustion Products : a global perspective," *World Coal Ash Conf.*, p. 17, 2013.
- [3] M. Gesoğlu, T. Özturan, and E. Güneyisi, "Effects of fly ash properties on characteristics of cold-bonded fly ash lightweight aggregates," *Constr. Build. Mater.*, vol. 21, no. 9, pp. 1869–1878, 2007.
- [4] E. Güneyisi, M. Gesoğlu, Ö. Pürsünlü, and K. Mermerdaş, "Durability aspect of concretes composed of cold bonded and sintered fly ash lightweight aggregates," *Compos. Part B Eng.*, vol. 53, pp. 258–266, 2013.
- [5] I. Kourti and C. R. Cheeseman, "Properties and microstructure of lightweight aggregate produced from lignite coal fly ash and recycled glass," *Resour. Conserv. Recycl.*, vol. 54, no. 11, pp. 769–775, 2010.
- [6] R. Manikandan and K. Ramamurthy, "Effect of curing method on characteristics of cold bonded fly ash aggregates," *Cem. Concr. Compos.*, vol. 30, no. 9, pp. 848–853, 2008.
- [7] A. Gu, "Utilization of fly ash by pelletization process ; theory , application areas and research results," vol. 30, pp. 59–77, 2000.
- [8] K. N. Shivaprasad and B. B. Das, "Determination of optimized geopolymerization factors on the properties of pelletized fly ash aggregates," *Constr. Build. Mater.*, vol. 163, pp. 428–437, 2018.
- [9] S. Geetha and K. Ramamurthy, "Properties of geopolymerised low-calcium bottom ash aggregate cured at ambient temperature," *Cem. Concr. Compos.*, vol. 43, pp. 20–30, 2013.
- [10] H. Xu and J. S. J. Van Deventer, "The geopolymerisation of alumino-silicate minerals,," 2000.
- [11] D. Hardjito, "Studies on Fly Ash-Based Geopolymer Concrete," *Curtin Univ. Technol.*, no. November, p. 94, 2005.
- [12] R. M. Hamidi, Z. Man, and K. A. Azizli, "Concentration of NaOH and the Effect on the Properties of Fly Ash Based Geopolymer," *Procedia Eng.*, vol. 148, pp. 189–193, 2016.
- [13] C. Y. Heah *et al.*, "Study on solids-to-liquid and alkaline activator ratios on kaolin-based geopolymers," *Constr. Build. Mater.*, vol. 35, pp. 912–922, 2012.
- [14] G. Görhan and G. Kürklü, "The influence of the NaOH solution on the properties of the fly ash-based geopolymer mortar cured at different temperatures," *Compos. Part B Eng.*, vol. 58, pp. 371–377, 2014.
- [15] P. Risdanareni, J. J. Ekaputri, and Triwulan, *The influence of alkali activator concentration to mechanical properties of geopolymer concrete with trass as a filler*, vol. 803. 2015.
- [16] P. Tang, M. V. A. Florea, and H. J. H. Brouwers, "Employing cold bonded pelletization to produce lightweight aggregates from incineration fine bottom ash," *J. Clean. Prod.*, vol. 165, pp. 1371–1384, 2017.
- [17] N. U. Kockal and T. Ozturan, "Characteristics of lightweight fly ash aggregates produced with different binders and heat treatments," *Cem. Concr. Compos.*, vol. 33, no. 1, pp. 61–67, 2011.
- [18] P. Gomathi and A. Sivakumar, "Accelerated curing effects on the mechanical performance of cold bonded and sintered fly ash aggregate concrete," *Constr. Build. Mater.*, vol. 77, pp. 276–287, 2015.

-
- [19] M. Gesoğlu, E. Güneyisi, R. Alzebaree, and K. Mermerdaş, “Effect of silica fume and steel fiber on the mechanical properties of the concretes produced with cold bonded fly ash aggregates,” *Constr. Build. Mater.*, vol. 40, pp. 982–990, 2013.
- [20] P. Van den Heede *et al.*, “Sustainable high quality recycling of aggregates from waste-to-energy, treated in awet bottom ash processing installation, for use in concrete products,” *Materials (Basel)*, vol. 9, no. 1, pp. 1–24, 2016.
- [21] Z. Chen, J. S. Li, B. J. Zhan, U. Sharma, and C. S. Poon, “Compressive strength and microstructural properties of dry-mixed geopolymer pastes synthesized from GGBS and sewage sludge ash,” *Constr. Build. Mater.*, vol. 182, pp. 597–607, 2018.
- [22] G. V. P. Bhagath Singh and K. V. L. Subramaniam, “Quantitative XRD study of amorphous phase in alkali activated low calcium siliceous fly ash,” *Constr. Build. Mater.*, vol. 124, pp. 139–147, 2016.
- [23] P. Risdanareni, J. Jaya Ekaputri, I. Maulidiyawati, and P. Puspitasari, “Mechanical properties of concrete composed of sintered fly ash lightweight aggregate,” in *MATEC Web of Conferences*, 2018, vol. 195.

Performance evaluation of functional alkali activated lightweight composites produced with an eco-silica source based activator

X. Gao ¹, Q.L. Yu²

¹ School of Civil Engineering and Architecture, Wuhan University of Technology, Wuhan 430070, China

² Department of the Built Environment, Eindhoven University of Technology, P.O. Box 513, 5600 MB, Eindhoven, The Netherlands

Abstract

Alkali activated slag-fly ash lightweight composites with moderate densities between around 1200 and 1500 kg/m³ are prepared and characterized in this study. An eco-olivine nano-silica is applied to prepare sustainable silicate based activators to replace commercial sodium silicates. Na₂O contents of 2.0, 3.5 and 5.0 wt.% are investigated in order to reach a suitable balance between performance, costs and application. The results show the positive effect of density and Na₂O content on strength, while strength increment between Na₂O dosage of 3.5% and 5.0% are limited. The reduction of Na₂O content shows a dramatic delay of the reaction process up to around 3 d. The thermal conductivity and acoustical absorption properties of the lightweight products are characterized. A calculation on the carbon footprint shows an evident advantage of using alkali activated materials to replace Portland cement, also the utilization of olivine nano-silica further reduces the carbon emission of the activator by around 25%.

Keywords: alkali activation; eco-nano-silica; thermal properties; acoustic absorption; carbon emission.

1. Introduction

Lightweight concrete has been widely applied as both structural and non-structural components in a wide range of weights and strengths for various applications, due to its properties such as low density, good thermal insulation and fire resistance. In addition, Portland cement is commonly used as binding material for lightweight concrete, but its production is responsible for around 7% of the global carbon emissions and high energy costs. In order to reduce the negative environmental impacts, the development of sustainable alternatives such as alkali activated materials has been investigated because of the excellent mechanical properties, durability and thermal resistance together with low energy and carbon costs. Some efforts have also been spent on applying alkali activated materials in producing lightweight products; including for instance the study of design methodologies of ultra-lightweight geopolymers by applying the particle packing approach, the effect of key factors such as suitable ratios between binder, activator and aggregates [1]; the development of lightweight geopolymers with foaming agent especially for thermal insulating properties [2]; investigating the relations between density, mechanical properties and thermal conductivity of geopolymers with medium to low densities [3-5]; the utilization of different alkali binders and unconventional aggregates [6-8].

In alkali activated materials, the activator plays an important role on the activation process by providing necessary alkalinities for the decomposition of raw materials and formation of reaction products. The

commonly used activators are alkali hydroxides, silicates, carbonates, sulfates, aluminates or oxides; and it is widely accepted that silicate based ones usually result in ideal mechanical properties and relatively low porosity [9]. The silicate based activator exhibits advantages by providing the alkaline environment continuously and moderately, also the additionally provided silicates from the activator will participate into the reaction products and lead to a refined microstructure, and sufficient content of M_2O promotes the activation efficiency while exceeding dosage show limited further contribution. However, the primary drawback of silicate based activators is its negative environmental impact. The commercial process of sodium silicate production includes the melting of sodium carbonate and quartz sand around 1400 to 1500 °C with carbon release of above 400 kg/ton [10]. In order to achieve a more eco-friendly binder system, a green olivine nano-silica is applied as alternative silica source to prepare activator solutions in this study. The olivine nano-silica is produced by dissolving olivine stone in acid under temperatures lower than 95 °C, and this process shows advantages in carbon emission, energy consumption and total costs [11]. Therefore an alkali activated product with further reduced overall environmental impacts can be expected.

The objective of this study is to evaluate an eco-silicate source based alkali activator in designing lightweight composites, using blended alkali activated binder. The lightweight composites are designed with the aim to have moderate densities together with excellent mechanical, thermal and acoustic properties. The effect of activator dosages, addition of lightweight aggregates on early age reaction is investigated by using isothermal calorimeter. The mechanical properties, thermal conductivity and sound absorption properties are evaluated and the effect of the alkali content on these properties is investigated.

2. Methodology

2.1 Materials

The powder raw materials used in this work are blast furnace slag and Class F fly ash, their major chemical compositions are shown in Table 1. Commercial lightweight aggregates produced from natural expanded silicate with three particle sizes are applied: 0.5-1 mm, 1-2 mm and 2-4 mm, with particle densities of 600, 550 and 500 kg/m³, respectively. CEN standard sand is also used as fine aggregate. Analytical sodium hydroxide and laboratory prepared olivine nano-silica (19.04% SiO_2 and 80.96% H_2O by mass) were used to produce alkali activators. The olivine nano-silica was produced by dissolving olivine in acid at low temperatures, followed by a washing and filtering process [12,13]. Desired activator parameters were obtained by mixing calculated dosage of sodium hydroxide, olivine nano-silica and distilled water.

Table 1 Mix proportions of alkali-activated slag-fly ash composites (kg/m³)

Sample	Precursors			Activator		Sand	Lightweight aggregates		
	Slag	Fly ash	Nano-s	NaOH	H ₂ O		0-2	2-4	1-2
D15-5.0	384	96	170.8	30.9	77.7	370	200	150	30
D15-3.5	384	96	119.6	21.7	119.1	380	200	150	30
D15-2.0	384	96	68.3	12.4	170.7	390	200	150	30
D12-5.0	384	96	170.8	30.9	77.7	0	240	180	30
D12-3.5	384	96	119.6	21.7	119.1	10	240	180	30
D12-2.0	384	96	68.3	12.4	170.7	20	240	180	30
D14-3.5	384	96	119.6	21.7	119.1	260	230	140	30
D13-3.5	384	96	119.6	21.7	119.1	135	245	150	30

2.2 Sample preparation and testing methods

Three levels of equivalent Na_2O content were used in this study: 2.0%, 3.5% and 5.0% (by mass of the binder). A fixed activator modulus of 1.4 and a slag/fly ash mass ratio of 8/2 were used based on the previous experiences. Mixtures are designed to have oven dry densities between 1200 and 1500 kg/m^3 according to EN 206-1. The detailed mix proportions are presented in Table 2, for instance, sample with the label of D15-5.0 means it was designed to have a density level of 1500 kg/m^3 and a Na_2O content of 5.0%. Specimens were prepared and poured into molds of 40 x 40 x 160 mm^3 , then covered with a plastic film to prevent the moisture loss. All specimens were demolded after 24h of curing and cured at room temperature and a relative humidity of 95% until testing age.

The compressive strength was determined according to EN 196-1. Samples were tested at the ages of 7 and 28 d, respectively. The early age hydration heat release was investigated by an isothermal calorimeter with TAM Air, Thermometric. Measurements were carried out for 72 h under a constant temperature of 20 °C. The thermal conductivity (k) and the mass heat capacity (c) were measured by using a heat transfer analyser (ISOMET 2104). The acoustic absorption coefficient was measured according to EN 10534-2.

3. Results and discussion

3.1 Compressive strength

The 7 and 28 d compressive strength of samples with different density levels and a Na_2O content of 3.5% are shown in Figure 1. The relations between the oven dry density and strength are briefly depicted. It can be seen that as the density decreases, there is an obvious reduction in strength at both 7 and 28 d. The highest 28 d strength reaches 30.7 MPa in mixtures with a density of 1471 kg/m^3 , and it gradually reduces to 20.6 MPa in samples with a density of 1163 kg/m^3 . Considering the fact that those mixtures are having the same binder content, the reduced compressive strength is mainly attributed to the replacement of normal sand by lightweight aggregates, and a less overall capacity of the aggregates against compressive loading is resulted. The 7 d strengths share a similar tendency with the 28 d's. The 7 d compressive strengths shown in Figure 1 are all above 88% of the 28 d strength. This is because of the nature of the alkali activated binder system and the ceiling effect of the lightweight aggregates, which presents a relatively fast reaction process and exhibits large percent of the strength at early ages [14].

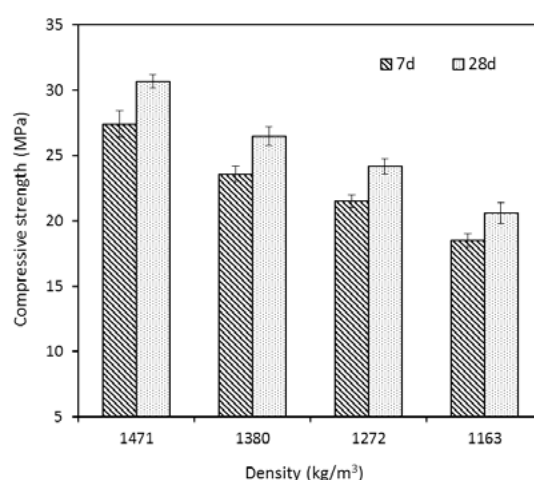


Fig. 1 Compressive strength of lightweight composites with different densities

Figure 2 depicts the effect of the equivalent Na_2O content on 28 d compressive strength of mixtures with two density levels: 1500 and 1200 kg/m^3 , represented with sample label of D-15 and D-12 in the figure. As can be seen in Figure 2 that there is an obvious increment of strength when increasing the Na_2O content

from 2.0% to 3.5%, and the increase of strength exhibits a limited scale when further increasing the Na₂O content to 5.0%.

This phenomenon reveals that both Na₂O content and density show an important influence on strength. On the one hand, increasing the alkalinity (Na₂O %) will promote the activation of the binder that consequently leads to a higher strength from the aspect of the binder matrix; while on the other hand, the usage of lightweight aggregate limits the strength development by the relatively low crushing strength of the aggregate.

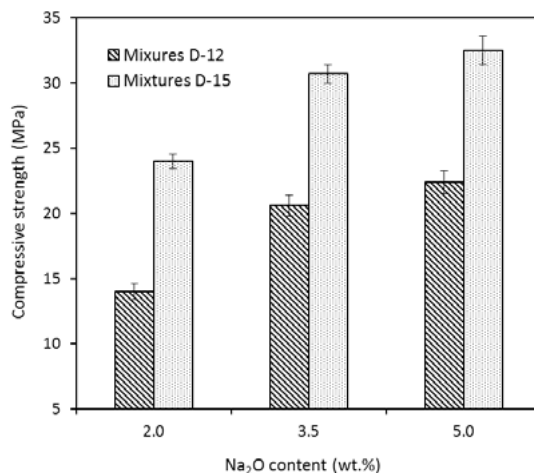


Fig. 2 Compressive strength of lightweight composites with different Na₂O contents

3.2 Reaction kinetics

The isothermal calorimeter test was performed on mixtures with the Na₂O content of 2.0%, 3.5% and 5.0%, respectively, and lightweight aggregates were added with an aggregate/binder ratio of 0.8, in order to evaluate their effect on the early age reaction. Figure 3 illustrates the normalized heat flows of samples with and without lightweight aggregates during the first 6 d; and shows that the mixtures with a Na₂O content of 5% exhibit a main reaction peak at around 16 h, with a peak intensity of 1.35 mW/g. The induction stage shows an induction period between around 6 and 10 h, followed by an evident increase of heat flow representing the intensive chemical reaction.

When reducing the Na₂O content to 3.5%, a significantly retarded reaction process can be observed. The induction period appears at around 9 to 22 h, the beginning of this stage is 3 h later than the one in sample with a Na₂O content of 5%, also the duration of this stage is more than 3 times longer. The location of the main reaction peak is also delayed to 37 h, which is 21 h later than the 5% Na₂O mixtures. Besides, the peak intensity is reduced to 0.63 mW/g and the deceleration period exhibits a more moderate reduction of heat release. A further lowered Na₂O dosage of 2.0% results in a dramatic delay of the reaction process.

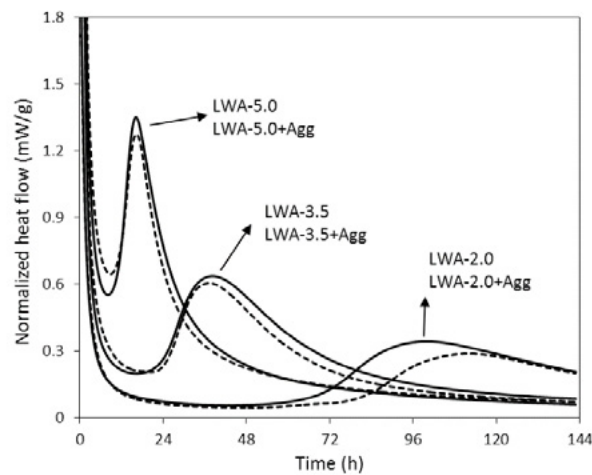


Fig. 3 Normalized heat releases of AA slag-fly ash lightweight composites

3.3 Thermal conductivity

In terms of the building materials, a low thermal conductivity contributes to an enhanced indoor thermal comfort, saving the energy cost and preventing the fire caused collapses; while lightweight concrete products based on alkali activated materials are capable of achieving those requirements with a further lowered environmental impact. Figure 4 shows the thermal conductivity of samples with a Na_2O content of 3.5% and different density levels used in this study, and a comparison with the available literature.

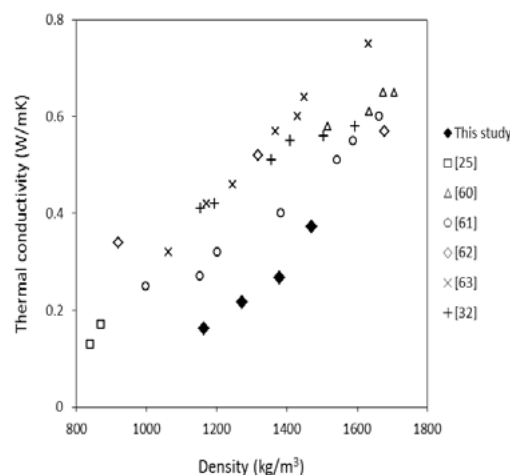


Fig. 4 Thermal conductivity of lightweight composites with different densities

A reduction of thermal conductivity with the decrease of the density can be observed in general. This is because that besides the density, the differences in matrix composition, type of binder and aggregates also show an influence on the property of thermal insulation [15-16]. The thermal conductivity reduces to 0.29 W/(m·k) in samples with a density level of 1400 kg/m³, with a reduction rate of 21.6%. The reduction of density from around 1500 to 1400 kg/m³ results in a decreased standard sand dosage of 31.6% by mass, indicating its negative influence on thermal insulation. Further reduction of the density to around 1300 and 1200 kg/m³ leads to further reduced thermal conductivities of 0.22 and 0.16 W/(m·k), respectively. It should be noticed that the thermal conductivity of 0.2 W/(m·k) can be classified to the T2 level of thermal insulation products based on the standard of EN 998-1. It can be seen from Figure 4 that the thermal conductivity values from this study are lower than that from the literature, which may indicate the advantage of using the alternative binder system together with the lightweight aggregate in this case.

3.4 Acoustical absorption

Owing to the massive addition of the porous lightweight aggregates, the resulting alkali activated lightweight concrete is expected to exhibit good sound absorption behaviours. Figure 5 exhibits the sound absorption coefficient as a function of frequency, four mixtures with a Na_2O content of 3.5% with different density levels were tested. For instance, the mixture with label of D-15 refers to the sample with a density around 1500 kg/m^3 . Generally speaking, the absorption coefficient is significantly increased with the decrease of density, in another word with the increase of lightweight aggregate content within the matrix; and all mixtures mainly show absorption of sound with medium frequencies between around 300 to 1700 Hz. Specifically, mixtures with a density of round 1500 kg/m^3 present a peak absorption coefficient of 0.2, between 800 and 1000 Hz. The peak absorption coefficient increases to around 0.35 and 0.52 in samples with a density about 1400 and 1300 kg/m^3 respectively, while the main absorption frequency range remains similar. A further reduction of density to around 1200 kg/m^3 results in an increased absorption coefficient to above 0.7, with shifted main absorption frequency to higher values. In terms of the low frequency and high frequency ranges, this lightweight product shows limited sound absorption effect. It should be mentioned that the medium frequency usually refers to the sound from humans and daily life.

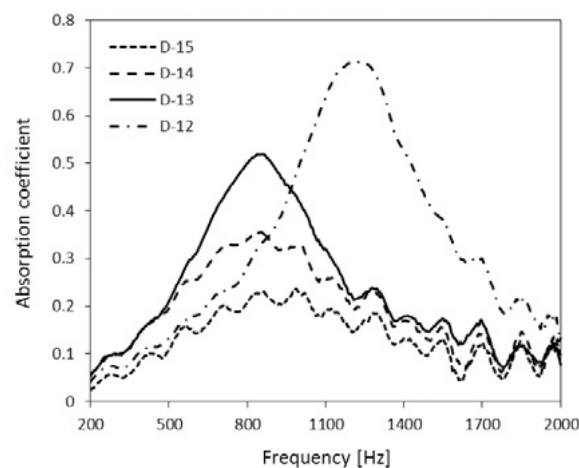


Fig. 5 Acoustic absorption of lightweight composites with different densities

3.5 Advantages in carbon footprint

Applying alkali activated materials shows an advantage in carbon emission towards Portland cement. While within the alkali binder systems, the Na_2O content is directly linked to the environmental issues. Moreover, the replacement of olivine nano-silica to commercial waterglass will further reduce the overall carbon emission. A calculation on the CO_2 footprint of the mixtures used in this study is shown in Table 2. The carbon footprint is usually calculated as the total CO_2 emissions in unit volume of concrete. The carbon footprint used in this calculation is $1.915 \text{ tCO}_2/\text{t}$ for NaOH , $1.514 \text{ tCO}_2/\text{t}$ for commercial waterglass, $0.82 \text{ tCO}_2/\text{t}$ for Portland cement, $0.143 \text{ tCO}_2/\text{t}$ for slag and $0.027 \text{ tCO}_2/\text{t}$ for fly ash. Concerning the olivine nano-silica, a CO_2 footprint of $0.461 \text{ tCO}_2/\text{t}$ is taken from the LCA analysis in VTT (EU F7th project, ProMine internal report), based on an average European industrial case scenario. The values shown above are based on the effective solids contents excluding water. It can be observed that the carbon emission of Portland cement is few times higher than alkali activated materials; the contribution of CO_2 is all from the cement clinkers. In terms of the alkali activated materials, the carbon emission from the binder accounts for around 37% to 69% of the overall emissions. When reducing the Na_2O contents from 5.0% to 2.0%, the carbon emission from the commercial sodium silicate based activator can be reduced by 60%, such a big reduction of carbon footprint may bring attentions on using suitable Na_2O dosages and reaching a balance between performances and environmental impact. Moreover, when olivine nano-silica is applied as

commercial waterglass replacement, the carbon emission in terms of activator can be further reduced by around 25%. In overall, those reduced carbon emissions from Na₂O content and alternative silica source provide great potentials for the future mix design and applications.

Table 2 Calculation on the carbon footprint (kg/m³)

Sample	Precursors	Activator (exclude H ₂ O)			CO ₂ emissions from activator	CO ₂ emis- sions from binder	Total CO ₂ emis- sions
		Oli- vine-na- no-s	Water glass	NaOH			
D15-5.0-NS		32.5	0	30.9	74.2		131.7
D15-5.0-WG		0	42.3	18.3	99.1		156.6
D15-3.5-NS	384 Slag +	22.7	0	21.7	52.0	57.5	109.5
D15-3.5-WG	96 Fly ash	0	29.6	12.8	69.3		126.8
D15-2.0-NS		13.0	0	12.4	29.7		87.2
D15-2.0-WG		0	16.9	7.3	39.6		97.1
Ref-OPC	480 OPC	0	0	0	0	393.6	393.6

4. Conclusions

This paper evaluates the mechanical properties, thermal property, acoustical absorption of eco-friendly alkali activated slag-fly ash lightweight composites (LWC) with different density classes. The effect of Na₂O contents and the utilization of alternative silica source on early age reaction and carbon footprints on the designed LWC are assessed. Mixtures with 28 d compressive strength up to 32.5 MPa and densities between 1200 and 1500 kg/m³ are resulted, and a direct correlation between strength and density is observed. The reduction of Na₂O content from 5% to 2% significantly prolongs the reaction process, but shows negligible effect on the silicate structure. Compared to the commercial waterglass, the utilization of olivine nano-silica reduces the carbon footprint from activator by around 25%. The lightweight concretes exhibit very low thermal conductivity between 0.16 and 0.37 W/(m·k), as well as good sound absorption coefficient up to 0.7 for medium frequencies. The application of alkali activated binders and applying this activator to lightweight concrete suggests an additional approach of preparing construction and building materials with multi-functional properties and greatly reduced environmental impacts.

5. Acknowledgment

China Scholarship Council is acknowledged for sponsoring the PhD research of X. Gao at Eindhoven University of Technology. In addition, thanks are given to J.T. van den Heuvel for helping with the experimental work and to Dr. M. Hornikx for the support with the sound absorption measurement.

6. Reference

- 1 Huiskes D, Keulen A, Yu Q, Brouwers H (2016) Design and performance evaluation of ultra-lightweight geopolymer concrete. Mater Des 89:516-526. doi: 10.1016/j.matdes.2015.09.167
2. Vaou V, Panias D (2010) Thermal insulating foamy geopolymers from perlite. Miner Eng 23(14):1146-1151. doi: 10.1016/j.mineng.2010.07.015
- 3 Posi P, Teerachanwit C, Tanutong C, Limkamoltip S, Lertnimoolchai S, Sata V, Chindaprasirt P (2013) Lightweight geopolymer concrete containing aggregate from recycle lightweight block. Mater Des (1980-2015) 52:580-586. doi: 10.1016/j.matdes.2013.06.001

-
- 4 Yang K-H, Lee K-H, Song J-K, Gong M-H (2014) Properties and sustainability of alkali-activated slag foamed concrete. *J Clean Prod* 68:226-233. doi: 10.1016/j.jclepro.2013.12.068
- 5 Aguilar RA, Díaz OB, García JE (2010) Lightweight concretes of activated metakaolin-fly ash binders, with blast furnace slag aggregates. *Constr Build Mater* 24(7):1166-1175. doi: 10.1016/j.conbuildmat.2009.12.024
- 6 Ibrahim WMW, Hussin K, Abdullah M, Kadir AA, Deraman LM, Sandu AV (2017) Influence of Foaming Agent/Water Ratio and Foam/Geopolymer Paste Ratio to the Properties of Fly Ash-based Lightweight Geopolymer for Brick Application. *Rev Chim* 68(9):1978-1982.
- 7 Al Bakri Abdullah MM, Yahya Z, Tahir M, Faheem M, Hussin K, Binhussain M, Sandhu AV (2015) Fly ash based lightweight geopolymer concrete using foaming agent technology *Rev Chim* 66(7):1001-3.
- 8 Al Bakri AMM, Kamarudin H, Nizar IK, Sandu AV, Binhussain M, Zarina Y, Rafiza AR (2013) Design, processing and characterization of fly ash-based geopolymers for lightweight concrete application. *Rev Chim* 64(4):382-387.
- 9 Brough A, Atkinson A (2002) Sodium silicate-based, alkali-activated slag mortars: Part I. Strength, hydration and microstructure. *Cem Concr Res* 32(6):865-879. doi: 10.1016/S0008-8846(02)00717-2
- 10 European Commission (2007) Reference document on best available techniques for the manufacture of large volume inorganic chemicals – solids and others industry.
- 11 Lazaro A, Brouwers H, Quercia G, Geus J (2012) The properties of amorphous nano-silica synthesized by the dissolution of olivine. *Chem Eng J* 211:112-121. doi: 10.1016/j.cej.2012.09.042
- 12 Lazaro A, Quercia G, Brouwers H, Geus J (2013) Synthesis of a green nano-silica material using beneficiated waste dunites and its application in concrete. *World J Nano Sci Eng* 3(3):41-51. doi: 10.4236/wjnse.2013.33006
- 13 Jonckbloedt RCL (1997) The dissolution of olivine in acid, a cost effective process for the elimination of waste acids. PhD Thesis, Utrecht University.
- 14 Gao X, Yu Q, Brouwers H (2015) Reaction kinetics, gel character and strength of ambient temperature cured alkali activated slag–fly ash blends. *Constr Build Mater* 80:105-115. doi: 10.1016/j.conbuildmat.2015.01.065
- 15 De Korte A, Brouwers H (2010) Calculation of thermal conductivity of gypsum plasterboards at ambient and elevated temperature. *Fire Mater* 34(2):55-75. doi: 10.1002/fam.1009
- 16 Zehner P, Schlunder EU (1970) Thermal conductivity of granular materials at moderate temperatures. *Chem Ing Tech* 42:933-41.

Effect of expansive agent on shrinkage and Long-term Performance of SCC

G. Ling ^{1,2}, Z. Shui ², T. Sun ^{2,*}, X. Gao ³, X. Li ^{1,2}, G. Wang ²

¹School of Materials Science and Engineering, Wuhan University of Technology, Wuhan 430070, China;

²State Key Laboratory of Silicate Materials for Architectures, Wuhan University of Technology, Wuhan 430070, China;

³School of Civil Engineering and Architecture, Wuhan University of Technology, Wuhan 430070, China;

*Correspondence: sunt@whut.edu.cn

Abstract

In this study, the effects of incorporating different expansive agent on the workability, mechanical properties and auto shrinkage behavior of self-compacting concretes (SCCs) have been investigated. UHA, MgO and Liquid expansive agent are added at 15%, 5% and 1% by cement weight. Academy of Construction Sciences (1986) and GL2000 model are utilized to calculate the shrinkage model of SCC with different expansive agent. Results show that at the compressive strength of SCCs at early ages is lower than those of the reference concrete, although while in the long term their strength increases as a result of pozzolanic reactivity by supplementary cementitious materials. Adding different expansive agents to mixtures impart a significant change in the measured autogenous shrinkage. Moreover, comparing the results calculated from the model and obtained from experiment, it is found that they were very similar. That is, the calculation model has fine accuracy and can predict the long-term performance of SCC.

Keywords: Self-compacting concrete, expansive agent, workability, autogenous shrinkage, long-term performance.

1. Introduction

Self-compacting concrete is characterized by excellent workability, which can be spread to a long distance without any vibration in complicated formwork, congested structure, and the areas which are hard to reach. The main benefit by using SCC in building structures is shortening the construction period, and it is widely applied in many construction industries due to its excellent workability. In order to obtain good performance, the amount of cementitious materials and water reducers in SCC is usually higher, which will have influence on the volume stability of SCC [1,2]. This is not to be neglected, especially for mass concrete engineering. Improving the volume stability of self-compacting concrete is becoming a subject of great concern [3-5].

Supplementary cementitious materials (SCMs) such as fly ash (FA), blast furnace slag (BFS) and silica fume (SF) are widely used in the preparation of SCC [6-8]. As proper amount of SCMs can improve the fluidity and stability of SCC, meanwhile, they can reduce the shrinkage of SCC and improve the volume stability. However, this effect of SCMs on shrinkage is limited [9]. A lot of research has been done to obtain more efficient methods to improve the volume stability of SCC [10,11]. The methods for mitigating shrinkage include adding mineral additives [12-14], chemical admixtures [15-20], fibers [21, 22], and by the control

of curing conditions such as internal curing [23]. The expanding agent were used for over four decades to minimize the effects of drying shrinkage. In that case, CaO-based expansive agent was utilized [24]. Compensation of the thermal shrinkage with delayed expansion of slow hydrating MgO is an effective and economic method for preventing the thermal cracking of concrete. The reason for the volume expansive is that the generation of ettringite (AFt), which was a hard rod-like crystal, processing the high certain strength. This method bring out good results by improving joint space and limit curing, but its practical application still requires special precautions. To overcome the limitations resulting from the use of individual products, and to minimize shrinkage, the effect of expansive agents has been tested. However, less research has been carried out on the combined use of different expansive agents on the shrinkage in SCC.

In this study, the effect of three different expansive agents (UHA, MgO and Liquid expansive agent) on the performance and shrinkage of SCC were investigated. Then, according to the Academy of Construction Sciences (1986) and GL2000 model, the shrinkage calculation model of SCCs with different expansive agents is calculated, and the long-term performance has been predicted.

2. Methodology

2.1 Materials

In the study, Fly ash (FA), blast furnace slag (BFS) and metakaolin (MK) were used as the replacement of cement, with up to 45% by weight of cement replaced. The type of Portland cement II•R was used in this study. FA and BFS utilized in this research as cementitious material obtained from power plant and steel mills, respectively. Metakaolin was obtained from Maoming Kaolinite Technology Co Ltd, which was produced by calcination of kaolin at 750 °C. The chemical compositions of the cementitious materials s are presented in Table 1.

Natural river sand with maximum size of 4.75 mm was utilized as fine aggregates. The values of specific gravity and water absorption are 2.66 and 0.55%, respectively. The limestone gravel with maximum size of 16 mm and with a specific gravity of 2670 kg/m³ was also used as coarse aggregates. Commercially available polycarboxylicether type superplasticizer (SP) possesses specific gravity of 1.07 is used in this research. Three different expansive agents are used in the paper, they are UHA, MgO and liquid expansive agent, the recommended dosage are 10-15%, 4-8% and 0-1%, respectively.

Table 1: Chemical composition of raw materials.

	SiO ₂	Al ₂ O ₃	CaO	MgO	Fe ₂ O ₃	K ₂ O	Na ₂ O	TiO ₂	SO ₃	LOI
	%	%	%	%	%	%	%	%	%	%
PII•R	18.93	4.67	62.49	0.77	3.98	0.72	0.13	0.27	4.43	3.26
FA	50.01	32.12	1.5	0.83	3.91	0.94	0.77	1.5	1.09	3.74
BFS	31.78	16.44	34.12	10.57	0.47	0.29	0.67	1.35	3.4	0.35
MK	57.37	38.63	0.03	0.07	0.77	0.49	0.39	0.4	0.15	1.04

2.2 Mixture proportions and specimen preparation

The water-to-binder (cement + FA+BFS+MK) mass ratio (w/b) of SCC was 0.33, and the replacement ratio of the supplementary cementitious materials was up to 45% by weight of the cement, as presented in Table 2 . All mixes were performed in accordance with ASTM C192 [24] in a power-driven revolving pan mixer. Cubes of 100×100×100 mm and 100×100×515mm were cast in steel moulds and compacted on a

vibrating table. The cube specimens were removed from moulds after casting for 24h, and then allowed to cure under standard conditions (20 ± 2 °C and relative humidity of 98%), for compressive strength test were carried out, respectively. The rectangular specimens of 100×100×515mm were test autogenous strains development.

Table 2: Mixture proportion of SCC (kg/m³).

NO.	W/B	SP	water	sands	gravels	cement	FA	GGBFS	MK	Expansive Agents		
										UHA	MgO	Liquid
		%	kg/m ³	kg/m ³	kg/m ³	kg/m ³	kg/m ³	kg/m ³	kg/m ³	kg/m ³	kg/m ³	kg/m ³
E ₀	0.33	5.0	165	859	761	275	165	40	20	0	0	0
E _U	0.33	5.5	165	859	761	275	132	7	20	75	0	0
E _M	0.33	4.5	165	859	761	275	153	28	20	0	25	0
E _L	0.33	5.0	165	859	761	275	165	40	20	0	0	5
E _{UM}	0.33	5.5	165	859	761	275	136	11	20	50	15	0
E _{ML}	0.33	4.5	165	859	761	275	158	33	20	0	15	3

2.3 Tests

The compressive strength was measured with hydraulic universal testing machine. Each proportion was measured as a set of 3 samples. Samples were tested for compressive strength after 3 days, 7 days and 28 days. Autogenous shrinkage measurement was conducted using non-contact sensors. This measurement technique accounted for the benefits of using the eddy-current displacement sensor (ECDS) for measuring autogenous shrinkage.

3. Results and discussion

3.1 Workability and mechanical properties of SCC

The slump flow and V-flow time tests have been carried out to evaluate the workability of SCCs which contain different amount of expansive agents, and the results are shown in Table 3. The slump flow of E_U and E₀ are approximate, but it should be noticed that the SP dosage of E_U is higher than E₀. This is because that a mass of fibers in UHA expansive agent will increase the viscosity and reduce the fluidity of SCC. Meanwhile, the homogeneity of SCC is improved, resulting in decrease of V-flow time for E_U. Compare E_M, E_L and E₀, it can be seen that mixing MgO and liquid expansive agent will increase the workability of SCC, and the influence of MgO expansive agent is more pronounced.

It is necessary to reduce the SP dosage when adding 5% MgO expansive agent to maintain the stability of SCC. Because the amount of UHA expansive agent is larger, the influence of UHA expansive agent on concrete performance is dominant. When composite using of UHA and MgO expansive agent (E_{UM}), the workability is similar to E_U, as the addition of UHA expansive agent is more, and its influence is dominant. Likewise, the workability of E_{ML} is similar to E_M. In general, the workability of each SCC mixture can meet the requirements of self-compacting.

Table 3: Workability and mechanical properties of SCC

NO.	Slump flow	V-flow time	3d Compressive strength	28d Compressive strength
	mm	s	MPa	MPa
E ₀	660	13	37.12	65.97
E _U	660	7.3	30.04	61.81
E _M	650	8.3	33.75	72.07
E _L	680	12	31.32	63.82
E _{UM}	665	9	30.20	65.48
E _{ML}	670	9	33.23	67.70

The compressive strength at 3 days and 28 days of SCCs which contain different expansive additive are evaluated and shown in Table 3. As shown in Table 3, the compressive strength of all SCC mixtures (E_U, E_M, E_L, E_{UM}, E_{ML}) are lower than the controlled E₀ at 3 days, but the compressive strengths of each mixtures at 28 days are similar to non-expansive mixtures (E₀). It is evident that, the strength of SCCs at 3 d decrease when adding 15% UHA (E_U) and 1% liquid expansive agent (E_L), and this reduction of the compressive strength was equal to from approximately 19.1% and 9.1% compared to E₀, respectively. Nevertheless, the compressive strength loss is 6.3% and 3.2% for E_U and E_L at 28 d, respectively. This may be due to the fact that UHA expansive agent contains a large amount of FA and has low pozzolanic activity, while liquid expansive agent will inhibit the hydration process of cement, which will lead to a decrease of strength of SCC at early age, but with the extension of curing time, these adverse effects are gradually weakened. The compressive strength of SCC increased by 9.2% when add 5% MgO expansive agent (E_M) at 28 d. This is because that the addition of MgO can improve the alkalinity of cement paste, promote the pozzolanic reaction of mineral admixtures, and thus improve the strength of concrete in the later curing age [25]. The compressive strength of SCC at 28 d does not change obviously when mixing 10% UHA and 3% MgO expansive agents (E_{UM}), and it increases slightly by adding 3% MgO and 0.6% liquid expansive agents.

3.2 Volume stability of SCC

Autogenous shrinkage of each SCC samples are continuously measured as a function of time up to 60 days and the results are shown in Fig. 1. By observing the autogenous shrinkage curve of each group of SCC samples, the autogenous shrinkage of concrete develops rapidly in 24 h after forming. Due to the hydration reaction of cement, the content of free water in concrete decreases fleetly during the first 24 h, and the volume of concrete changes obviously. The autogenous shrinkage rate of E₀ reached 150×10^{-6} at 1 d, and it is 211×10^{-6} at 7 d, increased 61×10^{-6} during 1 d to 7 d. The shrinkage rate of E_U was only 50×10^{-6} at 1 d and 66×10^{-6} at 7 d, it is equal to from approximately 33.3% and 31.3% of E₀. It can be assumed that the expansion effect of UHA is striking both during setting and later hydration. The shrinkage curve of E_M group is basically the same as E_U at first 24 h, and the shrinkage rate reaches 140×10^{-6} . But after that, the concrete begins to expand, and the shrinkage rate is only 59×10^{-6} at 7 d. During this process, the expansion amount is 81×10^{-6} . Therefore, it can be seen that the expansion effect of MgO expansive agent is mainly in the course of concrete curing. This is due to the formation of Mg(OH)₂ crystal by hydrolysis of MgO during concrete curing process, resulting in the volume expansion of SCC. During the condensation process of SCC that contains liquid expansive agents (E_L), the phenomenon of micro-expansion (expansion rate 50×10^{-6}) appeared in the early stages, with that rapid contraction occurred. The shrinkage rate is 230×10^{-6} at 1 d, 53.3% higher than E₀ at 1 d. and then the volume change slowed down. The shrinkage rate was 167×10^{-6} at 7 d, slightly lower than that of E₀.

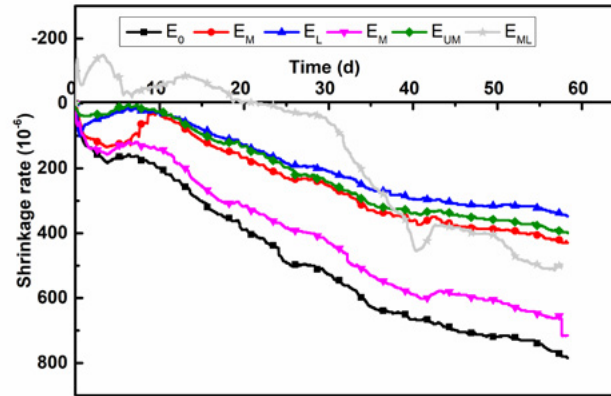


Fig. 1 The autogenous shrinkage curves of SCC with expansive agents at 60 days.

The shrinkage rate of concrete E_{UM} is 280×10^{-6} at 1 d, the total shrinkage rate 86.7% higher than E_0 . Subsequently, the shrinkage of E_{UM} slows down significantly and the expansion occurs. The shrinkage rate of E_{UM} was 149×10^{-6} at 7 d, 29.4% lower than that E_0 . The expansion is 91×10^{-6} during this process. It shows that the mixture of UHA and MgO expansive agent increases the shrinkage of concrete during the setting process, but has expansion effect in the curing process. The shrinkage rate of E_{ML} is -100×10^{-6} at 1 d, and -110×10^{-6} at 7 d. That is, the combined use of MgO and liquid expansive agent has a significant effect on reducing the shrinkage during condensation.

By analyzing the shrinkage curves of different SCC in 60 d, it can be seen that different expansive agents can reduce the shrinkage of SCC compared with SCC without expansive agents (E_0). The shrinkage rate of E_U , E_M , E_L , E_{UM} and E_{ML} at 60 d are 776×10^{-6} , 427×10^{-6} , 343×10^{-6} , 715×10^{-6} , 397×10^{-6} and 503×10^{-6} . UHA expansive agent can reduce the shrinkage of concrete in the early stage, then it has obvious expansive effect in 5-10 days, after that, there was a sustained reduction in shrinkage. MgO expansive agent has remarkable effect on reducing shrinkage. This effect initiates at first 12 h, and with the prolongation of curing time, it still has obvious effect. The shrinkage of SCC at 60 d is only inhibited for 8.7% by adding liquid expansive agent (E_L), the effect of reducing shrinkage is not obvious.

The effect of composite use of UHA and MgO expansive agent (E_{UM}) is between the two, and the shrinkage curve of E_{UM} at early age is similar to that of E_M , which indicates that MgO expansive agent plays a very important role in the early stage. However, due to the reduction of MgO, the expansion effect is weakened. MgO and liquid composite expansive agent are the most special group. From the Fig. 1, evident expansion could be found in the early stage, but the expansion effect is not adequate to resist shrinkage deformation after 15 d, as a result the component begin to retraction. Then, the shrinkage increased rapidly after 30 days, and outdid the other groups gradually.

3.3 Prediction of long-term performance of SCCs

The calculation methods for concrete shrinkage and creep mainly contains Academy of Construction Sciences (1986) model [26], CEB-FIP series model [27, 28], BS series model [29], GZ series model [31] and GL2000 model [32], and so on. The factors considered in these models are different, and the calculation accuracy is also different. The concrete self-shrinkage model selected in this modeling is the GL2000 model of the Academy of Construction Sciences (1986) and GL2000 model were employed in the course of this calculation. The basic equation for shrinkage development with time of concrete is as formula (1).

$$\varepsilon_s(t, t_c)_0 = \left(\frac{t - t_c}{t - t_c + 0.15(V/S)^2} \right)^{0.5} \times 10^{-3} \quad (1)$$

Where, t_c means the time when concrete begins to dry; t means the test time; $\varepsilon_s(t, t_c)$ means the concrete

shrinkage strain at age t ; V means the volume of specimens; S means the superficial area of specimens.

The influence function of environmental relative humidity on concrete shrinkage as formula (2).

$$f_s(RH) = 1.18 - 1.39 RH^4 \quad (2)$$

Where, $f_s(RH)$ means the influencing function of environmental relative humidity on Shrinkage of concrete; RH means the environmental relative humidity.

As for the effect of concrete compressive strength on shrinkage, according to GL2000 model, the function is as formula (3):

$$f_s(f_{cu,k}) = \left(\frac{30}{f_{cu,k}} \right)^{0.5} \quad (3)$$

Where, $f_s(f_{cu,k})$ means the influencing function of compressive strength grade on Shrinkage of concrete; $f_{cu,k}$ means the compressive strength grade of concrete.

In summary, the suggested formula for calculating concrete shrinkage is as formula (4):

$$\varepsilon_s(t, t_c) = \varepsilon_s(t, t_c)_0 \cdot f_s(RH) \cdot f_s(f_{cu,k}) \cdot f_s(T_{cement}) \quad (4)$$

Where, $\varepsilon_s(t, t_c)$ means the concrete shrinkage strain at age t ; $f_s(T_{cement})$ means influencing function of cement type on Shrinkage of concrete.

In the calculation, the starting drying time of concrete is 1d, the environment relative humidity is 55%, the compressive strength grade of concrete is C50, and the influence coefficient of cement is 0.7. The formula for calculating shrinkage of concrete is as formula (5):

$$\varepsilon_s(t) = 567 \times \left(\frac{t-1}{t+177} \right)^{0.5} \times 10^{-6} \quad (5)$$

The addition of expansive agent will affect the shrinkage of concrete, and the influence varies with the types and dosage of expansive agent. According to the experimental results of autogenous shrinkage, it can be seen that different expansive agents have different effects on the shrinkage of self-compacting concrete at the initial stage during concrete hardening, but in general, the trend of shrinkage curve for each SCC mixture is similarity. The difference is that after adding different expansive agents, the shrinkage of each SCC specimens varies in the first 10 days, and the final shrinkage value is also different. The equation for calculating the shrinkage of concrete considering the influence of expansive agent is as formula (6):

$$\varepsilon_{sn}(t) = f_{sh}(n) \times 567 \times \left(\frac{t-1}{t+177} \right)^{0.5} \times 10^{-6} \quad (6)$$

Since the volume stability of different SCC mixtures in the first 10 days are not regular, and its value has little influence on the long-term stability of SCC, the autogenous shrinkage test data after 10 days are choosed as the basis for analyzing the influence of expansive agents on autogenous shrinkage of SCC.

Comparing the autogenous shrinkage of SCC contains expansive agent to the controled SCC (without expansive agent). It is found that there is an obvious correlation between the proportion of their shrinkage value and time. On this basis, the fitting process and results of each group are obtained as shown in Fig. 2.

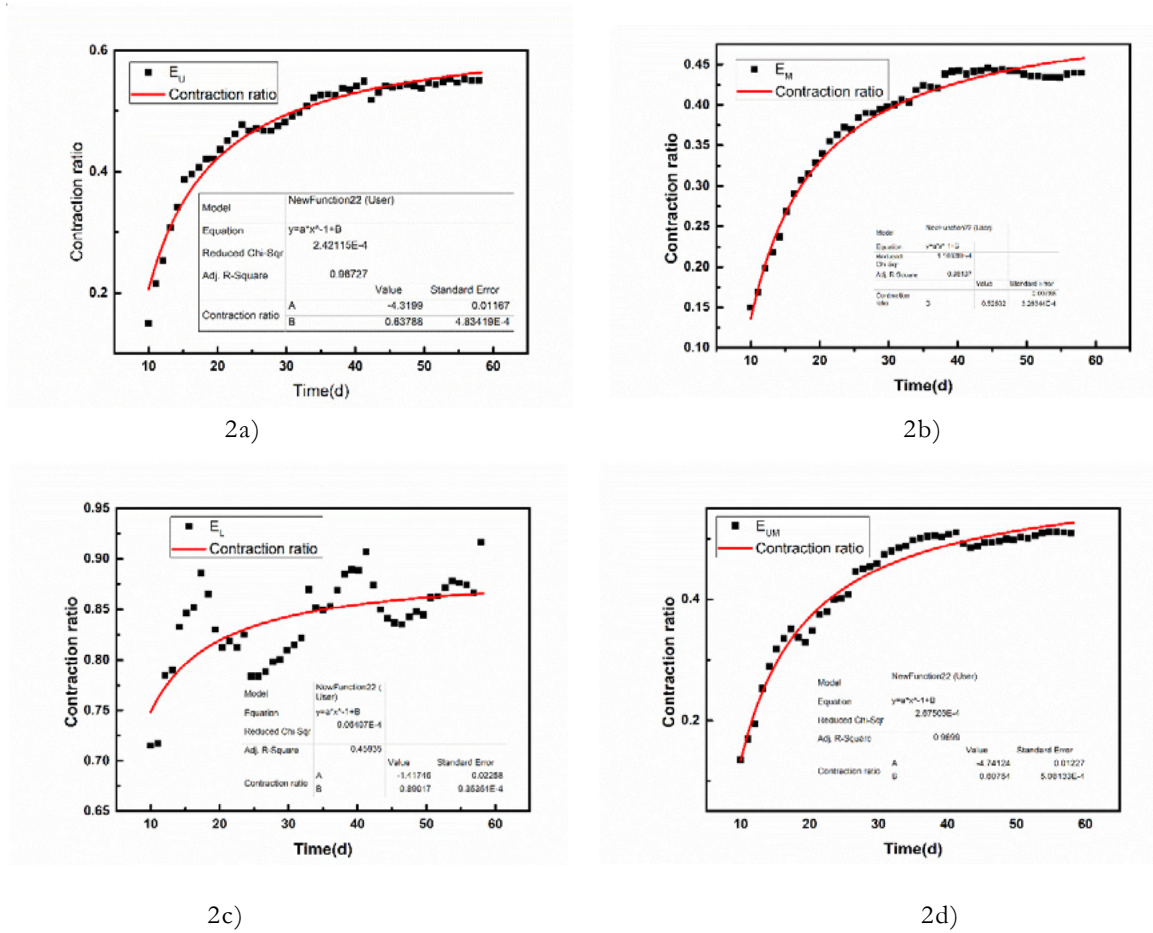


Fig. 2: Fitting of influencing parameters of different expansion agents.

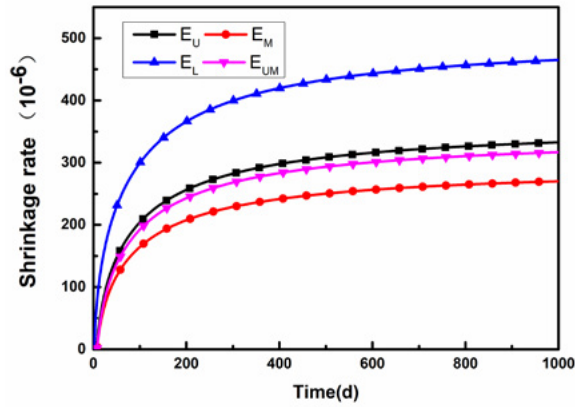


Fig. 3: Shrinkage curves of SCC contains expansion agents.

According to the data fitting process, the equation for calculating the shrinkage-time relationship of each

$$\varepsilon_{EU}(t) = \left(-\frac{4.320}{t} + 0.64\right) \times 567 \times \left(\frac{t-1}{t+172}\right)^{0.5} \times 10^{-6} \quad (7)$$

$$\varepsilon_{EM}(t) = \left(-\frac{3.894}{t} + 0.53\right) \times 567 \times \left(\frac{t-1}{t+172}\right)^{0.5} \times 10^{-6} \quad (8)$$

$$\varepsilon_{EL}(t) = \left(-\frac{1.417}{t} + 0.89\right) \times 567 \times \left(\frac{t-1}{t+172}\right)^{0.5} \times 10^{-6} \quad (9)$$

$$\varepsilon_{EUM}(t) = \left(-\frac{4.741}{t} + 0.61\right) \times 567 \times \left(\frac{t-1}{t+172}\right)^{0.5} \times 10^{-6} \quad (10)$$

The shrinkage curves of each group of specimens obtained from the formula with time are shown in Fig. 3. It can be seen that the shrinkage displacement curves are very close to the autogenous shrinkage test results. It shows that this prediction model has fine accuracy and has certain guiding significance for the prediction of long-term volume stability of concrete in practical engineering.

4. Conclusions

1. Utilizing UHA expansive agents has negatively effect on the workability of the fresh SCC, while MgO expansive agents has contrary effects. These effects can be compensated by adjusting the dosage of water reducing agent. Therefore, it can be concluded that the inclusion of the expansive additives in the studied dosages does not limit the workability properties of SCC.
2. Generally, the inclusion expansive in SCC induced a slight decrease of the compressive strength. This strength loss was more pronounced at an early-age than on the long-term.
3. In terms of autogenous shrinkage, the use of the different expansive agents can reduce the shrinkage of SCC compared with SCC without expansive agents, the effect of reducing shrinkage varies with expansive agents. In particular, the contemporaneous use of UHA and MgO proved to be very effective, and it caused strong initial expansion of SCC, which gradually decreased, but still remained positive after 60 days.
4. The shrinkage mode of SCCs with different expansive agents is obtained by utilizing Academy of Construction Sciences (1986) and GL2000 model, and the long-term performance has been predicted.

5. Acknowledgment

This work was financially supported by the National “Twelfth Five-Year” Plan for Science & Technology Support Development Program of China (No. 2014BAB15B01), YangFan Innovative & Entrepreneurial Research Team Project (No. 201312C12), the Hubei Key Laboratory of Roadway Bridge and Structure Engineering (Wuhan University of Technology) (No. DQJJ201510), the State Key Laboratory of Silicate Materials for Architectures (Wuhan University of Technology).

6. References

- [1] G. DS, 2005, The European guidelines for self-compacting concrete specification production and ues. Norfolk: The Self-Compacting Concrete European Project Group.
- [2] Rozière E, Granger S, 2007, Influence of paste volume on shrinkage cracking and fracture properties of self-compacting concrete, *Cem Concr Compos*, 29(8), 626-636, 10.1016/j.cemconcomp.2007.03.010.
- [3] M.S. Meddah AT-H, 2009, Durability performance and engineering properties of shale and volcanic ashes concretes, *ACI Mater J*, 106(4), 241-250, 10.1016/j.conbuildmat.2015.01.020
- [4] Behfarnia K, Farshadfar O, 2013, The effects of pozzolanic binders and polypropylene fibers on durability of SCC to magnesium sulfate attack, *Constr Build Mater*, 38, 64-71, 10.1016/j.conbuildmat.2012.08.035
- [5] Corinaldesi V, 2012, Combined effect of expansive, shrinkage reducing and hydrophobic admixtures for durable self-compacting concrete, *Constr Build Mater*, 36, 758-764, 10.1016/j.conbuildmat.2012.04.129.
- [6] Craeye B, De Schutter G, Desmet B, Vantomme J, 2010, Effect of mineral filler type on autogenous shrinkage of self-compacting concrete, *Cem Concr Res*, 40(6), 908-913, 10.1016/j.cemconres.2010.01.014.

- [7] José Oliveira M, Ribeiro AB, Branco FG, 2014, Combined effect of expansive and shrinkage reducing admixtures to control autogenous shrinkage in self-compacting concrete, *Constr Build Mater*, 52, 267-75, 10.1016/j.conbuildmat.2013.11.033.
- [8] Le HT, Müller M, Siewert K, Ludwig H-M, 2015, The mix design for self-compacting high performance concrete containing various mineral admixtures, *Mater Design*, 72, 51-62, 10.1016/j.matdes.2015.01.006.
- [9] Maltese C, Pistolesi C, Lolli A, Bravo A, Cerulli T, Salvioni D, 2005, Combined effect of expansive and shrinkage reducing admixtures to obtain stable and durable mortars, *Cem Con Res*, 35(12), 2244-2251, 10.1016/j.cemconres.2004.11.021.
- [10] Chatterji S, 1995, Mechanism of expansion of concrete due to the presence of dead-burnt CaO and MgO, *Cem Concr Res*, 25(1), 51-56, 10.1016/0008-8846(94)00111-B.
- [11] Collepardi M, Borsoi A, Collepardi S, Ogoumah Olagot JJ, Troli R, 2005, Effects of shrinkage reducing admixture in shrinkage compensating concrete under non-wet curing conditions, *Cem Concr Compos*, 27(6), 704-708, 10.1016/j.cemconcomp.2004.09.020.
- [12] Collepardi M, Troli R, Bressan M, Liberatore F, Sforza G, 2008, Crack-free concrete for outside industrial floors in the absence of wet curing and contraction joints, *Cem Concr Compos*, 30(10), 887-891, 10.1016/j.cemconcomp.2008.07.002.
- [13] Meddah MS, Suzuki M, Sato R, 2011, Influence of a combination of expansive and shrinkage-reducing admixture on autogenous deformation and self-stress of silica fume high-performance concrete, *Constr Build Mater*, 25(1), 239-250, 10.1016/j.conbuildmat.2010.06.033.
- [14] Z. Cao JX, 2003, *Construction Technology of Dam with MgO Concrete*. Beijing: China Electric Power Press.
- [15] Chen C LC, 2006, Study and application of MgO concrete, *Concrete*, 199(5), 45-53.
- [16] Polat R DR, Khushefati W H, 2015, Effects of nano and micro size of CaO and MgO, nano-clay and expanded perlite aggregate on the autogenous shrinkage of mortar, *Constr Build Mater*, 81, 268-275, 10.1016/j.conbuildmat.2015.02.032.
- [17] Güneyisi E GM, 2008, Properties of self-compacting mortars with binary and ternary cementitious blends of fly ash and metakaolin, *Mater Struct*, 41(9), 1519-1531, 10.1617/s11527-007-9345-7.
- [18] Güneyisi E GM, Özbay E, 2009, Evaluating and forecasting the initial and final setting times of self-compacting concretes containing mineral admixtures by neural network, *Mater Struct*, 42(4), 469-484, 10.1617/s11527-008-9395-5.
- [19] Laskar AI, Talukdar S, 2008, Rheological behavior of high performance concrete with mineral admixtures and their blending, *Constr Build Mater*, 22(12), 2345-2354, 10.1016/j.conbuildmat.2007.10.004.
- [20] Ponikiewski T, Go³aszewski J, 2014, The influence of high-calcium fly ash on the properties of fresh and hardened self-compacting concrete and high performance self-compacting concrete, *J Cleaner Prod*, 72, 212-221, 10.1016/j.jclepro.2014.02.058.
- [21] Vejmelková E, Keppert M, Grzeszczyk S, Skaliński B, Èerný R, 2011, Properties of self-compacting concrete mixtures containing metakaolin and blast furnace slag., *Constr Build Mater*, 25(3), 1325-1331, 10.1016/j.conbuildmat.2010.09.012.

- [22] Zhao H, Sun W, Wu X, Gao B, 2015, The properties of the self-compacting concrete with fly ash and ground granulated blast furnace slag mineral admixtures, *J Cleaner Prod*, 95, 66-74, 10.1016/j.jclepro.2015.02.050.
- [23] Güneyisi E, Gesoğlu M, Özbay E, 2010, Strength and drying shrinkage properties of self-compacting concretes incorporating multi-system blended mineral admixtures, *Constr Build Mater*, 24(10), 1878-1887, 10.1016/j.conbuildmat.2010.04.015.
- [24] ASTM. Standard Practice for Making and Curing Concrete Test Specimens in the Laboratory. USA1997.
- [25] D Shen MD, L Mo, 2012, Effect of restraint degree on the expansion and tensile splitting strength of concrete containing MgO-based expansive agent, *Concrete*, 10, 14-17.
- [26] CEB-FIP, 1978, Model Code for Concrete Structures.
- [27] ACI Committee 209, 1982, Prediction of Creep, Shrinkage and Temperature Effects in Concrete Structures [S].
- [28] ACI Committee 209, 1992, Prediction of creep, shrinkage and temperature effects in concrete structures[S], Manual of concrete practice, Part 1, American Concrete Institute, 209R 1-92.
- [29] BS 5400: Part4:1984. Code of Practice for Design of Concrete Bridges[S]. British standard Institute.
- [30] Z. P., Bazant, S. Baweja, 1995, Creep and shrinkage Prediction Model for Analysis and Design of Concrete Structures-Model B3, RILEM Recommendation, *Mater Struct*, 28, 357-365, 10.1007/BF02473152.
- [31] N. J. Gardner, J. W. Zhao, 1993, Creep and shrinkage Revisited, *ACI Mater J*, 90, 236-246, 10.1007/978-1-4612-5424-9.
- [32] N. J. Gardner and M.J, Lockman, 2001, Design provisions for Drying shrinkage and Creep of Normal-Strength Concrete, *ACI Mater J*, 98(2), 159-167.

Converter slag - ladle slag - gypsum ternary binder – effect of CaO slaking

E. D. Adesanya¹, K. M. Ohenoja¹, P. K. Kinnunen¹, M. H. Illikainen¹

Fibre and Particle Engineering Research Unit, University of Oulu, Finland¹:

Abstract

The present study reports on the utilization of steel slags as non-cement binders. Converter slag (also known as basic oxygen furnace slag, BOFS) and ladle slag (also known as ladle furnace slag or falling slag, LS), both generated as a by-product during steelmaking processes, were used. LS is highly calcareous and aluminous containing mayenite and calico-olivine as main phases. LS can react with water to produce cement-like hydration products, but optimal water/binder ratio is critical in order to prevent hydration product conversion and strength loss. Another option is to add an optimum amount of gypsum to produce ettringite and AH3 with good mechanical properties. CN slag utilization in concreting is affected by the volume instability caused by its high free lime content. Here, the free lime content is slaked through hydraulic weathering to form calcium hydroxide. The resulting slurry is then used as co-cementitious binder with ladle slag and gypsum in a ternary mix. This method was found to be successful and experimental results showed that free lime content in converter slag can be reduced ensuring volume stability through designed weathering. The new cementitious binder properties were structurally analysed through compressive strength, length change, and ultrasonic pulse velocity (UPV). The hydration products and hydration kinetics were determined through thermogravimetry analysis (TGA/DTA) and isothermal calorimetry.

Keywords: Steel slag, Free lime, Ettringite, Slaking, Portlandite.

* Standard cement chemistry notations were used, hence CaO represents C, Al_2O_3 as A and H_2O as H

1. Introduction

Steel slags are by-products from steelmaking process and in 2016 about 18.4 million tonnes of these slags were produced in Europe alone [1]. Only 4.4% of these produced slags are used in cement and concrete applications while approximately 23% are either landfilled or stored. These slags include Electric-arc furnace, ladle slag (LS, also known as refining slag) and basic-oxygen furnace (BOF) slag also known as converter slag (CN). Increasing global demand for cement, as well as governmental legislation and costs related to landfilling have prompted studies into utilising of these slags in cement and concrete as a sustainable alternative to OPC.

In contrast to the glassy granulated blast furnace slag (GGBFS) in which the calcium and magnesium oxides reacts to form non-expansive products and is widely used to supplement Portland cement, predominantly crystalline steel slags are composed of free lime (f-CaO) and free MgO (f-MgO). During hydration, these oxides form hydroxides which increases the volume of the matrix causing volumetric expansion and strength reduction in the mortar. This anomaly and steel slags (EAF and BOF) less cementitious activity has limited the use of steel slags as a cementitious binder. The volume instability of these slags have been previously reported [2,3], and mostly in cements and concretes they have been used as aggregates.

Various methods have been proffered to overcome the barriers of steel slags utilization in cements or as

a cementitious binder. Muhmood et al. [4] remelted and water quenched CN slag, and they reported an increase in the hydraulicity of the slag and also reduction in the f-CaO content. Jiao et al. [5] also remelted CN slag and reported significant reduction in f-CaO amount by adding 20% of silicon oxide (SiO₂) during remelting. Also, f-CaO and f-MgO in steel slags have been eliminated through accelerated carbonation to form carbonates [6–10]. Liang et al. [6] reported increase hydration activity and ettringite promotion when steel slag was carbonated before hydrating with Portland cement. Likewise after accelerated carbonation, Pang et al. [10] reported that the f-CaO content of BOF slag aggregate reduced from 7% to under 1%. Other previously studied methods to control f-CaO and f-MgO in steel slags include by natural weathering [3,11,12] and also through attrition scrubbing and chelation [13].

Here we aim to utilize steel slags in a synergistic-ternary mix of converter slag, ladle slag (LS) and gypsum and to determine the effect of slaking of f-CaO in CN on the hydrated properties of the ternary mix. Hydration kinetics through isothermal calorimetry, thermogravimetry analysis (DTA/TGA), compressive strength, volume shrinkage and expansion were determined.

2. Methodology

2.1 Materials

Ladle slag and converter slag used were supplied by SSAB Europe Oy (Raahe, Finland). Both slags were taken from the cooling pit where they have exposed to varying natural weather conditions. Both slags were sieved and the fractions below 2 mm then milled for 2 h. Gypsum used was purchased from VWR Finland (product no. 22451.360). Standard CEN Sand was used as aggregate in the mortars. The chemical compositions of the binders were analysed by X-ray fluorescence (XRF) (PANalytical Omnia Axiosmax) in oxides and presented in Table 1.

Table 1. Chemical compositions of the binders used in the study (%wt.).

Oxide	CaO	SiO ₂	Al ₂ O ₃	MgO	SO ₃	Fe ₂ O ₃	Others	f-CaO
LS	45.7	9.5	29.8	6.2	0.4	0.8	7.6	0.0
G	41.4	1.0	0.1	0.5	53.8	0.1	3.1	-
CN	49.7	12.6	1.6	2.0	0.3	24.8	8	7.0

The slags were milled using a laboratory sized 10L tumbling ball mill (Germatec) containing 200 steel balls with a diameter of 30mm. The f-CaO content in both slags was determined using the methodology described in SFS-EN 451-1:2004 [14]. The method quantifies dissolved amount of CaO in a specified mixture of butanoic acid, 3-oxo-ethyl ester, and butan-2-ol during 3h boiling time [15].

2.2 Preparation of samples

The samples were prepared according to the mix composition in Table 2. The converter slag was prepared a day before to slake the free lime prior to mixing with other binders. Equivalent amount of water and converter slag were mixed using a shear mixer for 4 mins and covered at ambient temperature for 24 h. After 24 h, Ladle slag-gypsum (LSG) blend was then added to the slaked converter slag (SCN) and mix using a Kenwood mixer. As a reference sample, non-slaked converter slag (CN) was also mixed with LSG. The resulting mortar mix was then jolted on a vibratory table and then cast in 50 x 50mm cubical molds for strength test and ultrasonic pulse velocity analysis, and 40 x 40 x 160mm molds for shrinkage and expansion measurements. Paste sample was prepared the same way without sand aggregates, for use in characterization analysis.

Table 2. Mix composition of the mortars used in the experiment.

Sample name	LS (g)	Gypsum (g)	CN (g)	Sand (g)	w/b
SCN-LSG	157.5	67.5	225	1000	0.5
CN-LSG	157.5	67.5	225	1000	0.5

2.3 Measurements

Compressive strength of the mortars at 7, 28 and 56 days was done using Zwick testing equipment with a load cell of 100kN and force speed of 2.4kN/s. The drying shrinkage and expansion were calculated using Eq. (1).

$$LC(\%) = \frac{L_i - L_x}{G} \quad (1)$$

where L_i is the difference between the comparator reading and the reference bar after 24 h, L_x is the length at each curing age (1, 3, 7, 14, 21, 28 and 56 days) of the mortar and G is the nominal length.

Ultrasonic pulse velocity was undertaken using a Matest ultrasonic pulse equipment (Matest, Italy) to check the quality of the mortars during curing period.

Thermogravimetric analysis (TGA) was carried out using a Netzsch STA 409PC/PG instrument. Approximately 25mg of milled paste samples was heated from 40 to 1000°C at a heating rate of 10°C/min in an aluminium crucible under a nitrogen protective atmosphere with a gas flow of 20mL/min. From the TGA data, quantification of calcium hydroxide (CH) was done according to Eq. (2)[16].

$$CH(\%) = \left(A \frac{74}{18} * B \frac{74}{44} \right) \quad (2)$$

where A and B are the area under DTA curve corresponding to the total mass lost due to the de-hydroxylation of CH and de-carbonation reaction respectively. The ratio 74/18 and 74/44 is the ratio of the molar mass of CH and H_2O and ratio of CH and CO_2 .

Calorimetry was undertaken on the paste samples using a TAM Air isothermal calorimeter. The paste samples were mixed ex-situ and approximately 8g of the paste was inserted into the ampoule and into the calorimeter. The measurement was performed for 5 days at 20°C. Dry binder mass was used to normalize the heat flow.

3. Results and discussion

3.1 Effect of slaking on hydration kinetics of the ternary binder

The calorimetry curves for the both binders are shown in Fig.1. The first peak corresponds to the heat released through initial dissolution and wetting of the solid particles in the binder [17,18]. Then an induction period which is influenced by the pre-treatment of CN slag in the binder. For SCN-LSG, the induction period was shorter with a difference of approximately 10 hrs to CN-LSG. This may be attributed to the possible reaction of the earlier formed calcium hydroxide (CH) with gypsum to form ettringite. Similar observation have been previously reported elsewhere [19]. The second significant peak is consistent with ettringite formations [20], the intensity of this peak was lower for CN-LSG compared with SCN-LSG. In cement systems, ettringite formation is limited by the formation of calcium hydroxide [21]. This favours ettringite formation in already slaked CN slag. Total heat released after 5 days of hydration was about 189 J/g and 174 J/g for SCN-LSG and CN-LSG respectively.

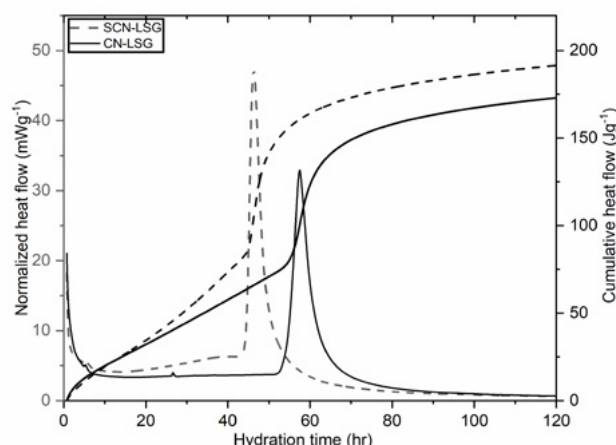


Figure 1: Heat flow and cumulative heat flow curves for SCN-LSG and CN-LSG during hydration.

3.2 Influence of slaking on $\text{Ca}(\text{OH})_2$ amount

The results from TGA/DTA (Fig.2) shows that slaking of converter slag influenced the amount of $\text{Ca}(\text{OH})_2$ produced during hydration. Four endothermic curves exist in the figure, the first endothermic curve between 50-250°C is attributed to the decomposition of ettringite [22]. The loss of water in gibbsite ($\text{Al}(\text{OH})_3$) is indicated by the second curve between 200-300°C [23]. The third curve (390-470°C) is attributed to dehydration of $\text{Ca}(\text{OH})_2$ /Portlandite (also see Eq. 4), and the endotherm between 650-770°C indicates carbonated phases most likely calcite [23]. Though the analysis was done in a nitrogen environment, carbonation of the sample during preparation is possible and its reaction path is shown in Eq. (5). The endotherm intensity of Portlandite curve of SCN-LSG is more than CN-LSG, which suggest that more f-CaO have been reacted during slaking. Calculated amount of 19% and 13% of CH were obtained for SCN-LSG and CN-LSG. Also, f-CaO amount determined according to SFS-EN 451-1:2004 [14], shows that the f-CaO content of the ternary mix paste was 0.23% and 0.61% for SCN-LSG and CN-LSG respectively after 28 days.

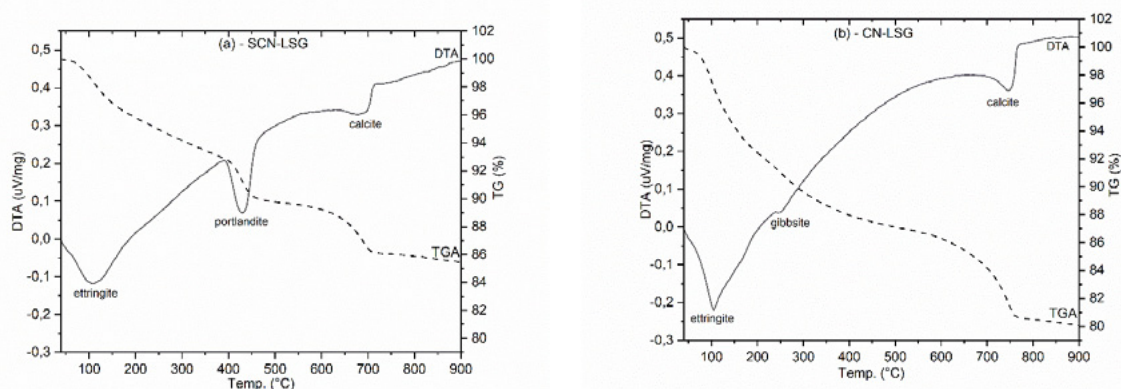


Figure 2: DTA/TGA curves of the ternary binders at 56 days (a) SCN-LSG and (b) CN-LSG.

The higher amount of Portlandite with slaked mortars is accrued to a faster reactivity of free lime during slaking than in un-slaked mortar. The fact that CaO reacts quickly during hydration can suggest that the large fraction of the f- CaO in steel slags will hydrate in a few days if it is exposed to water [24]. And also through fine grinding of the slag before slaking.



In ambient temperature (during slaking), the reaction in Eq. (4) proceeds to the left.



3.3 Volumetric shrinkage and expansion

The volumetric stability of both mortars was analysed through drying shrinkage and linear expansion test (Fig.3) and compared with mortars containing just ladle slag and gypsum (LSG) (see previous study [20]). The SCN-LSG and CN-LSG mortars shrunk for the first three days, with the former experiencing a higher shrinkage value. However, from 7 days both samples exhibited expansion with SCN-LSG showing a greater expansion value than CN-LSG. The increased expansion in this sample shows the existence of unstable phases in the binder and may be attributed to higher ettringite formation in the hardened mortar than in CN-LSG. In CN-LSG, the formation of ettringite is limited by portlandite formation.

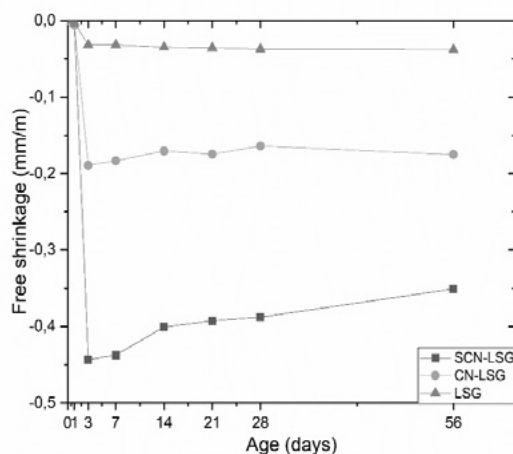


Figure 3: Length change of the mortars in comparison with a reference sample with no converter slag.

3.4 Ultrasonic pulse velocity of mortars

The mortars quality analysed through UPV in Fig. 4, shows SCN-LSG having a better microstructure than CN-LSG. The higher the rate of UPV the fewer the internal pores and cracks in the mortar anticipated. Overall, the mortars UPV continue to increase up to 56 days of analysis. The results here is consistent with the expected stability and quality of slaked slags forming calcium hydroxide before ternary mix than un-slaked slag in the ternary mix.

3.5 Compressive strength of mortars

The graph of the strength test obtained for the mortars containing slaked and un-slaked converter slag is shown in Fig. 5. Up to 28 days of curing, both mortar samples experienced similar strength, however after 56 days of curing CN-LSG experienced reduction in strength while SCN-LSG showed no strength gain after 28 days. The strength loss experienced with CN-LSG is attributed to the volume instability leading to cracks from the expansive reaction of f-CaO to CH. In addition, in Fig.6 is shown the physical appearance of both mortars, visible cracks can be seen with mortars with un-slaked converter slags after 7 days of the binder's hydration. The unchanged strength of SCN-LSG can be attributed to the dilution effect of CN slags.

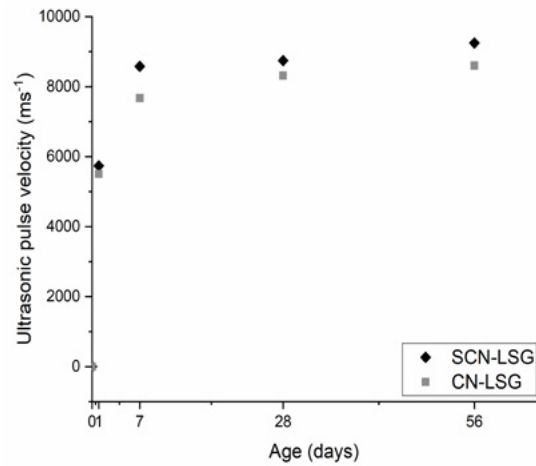


Figure 4: Ultrasonic pulse velocity for mortar samples.

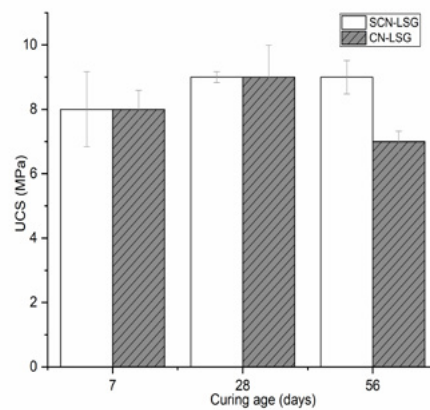


Figure 5: Compressive strength of the mortars at 7, 28 and 56 days after hydration.



Figure 6: Physical outlook appearance of both mortars after 56 days; Left: CN-LSG (NW) and Right: SCN-LSG (W).

The dilution effect occurs due to low-hydraulicity of CN slags in the ternary binder, which as a result may slow down the reaction kinetics of the co-binders. To further enhance the physical properties and applications of the ternary mortar mix, it is suggested a reduction to 30% of converter slag content in the mix.

4. Conclusions

The experimental findings in this study proffers a sustainable and economical method to free lime content reduction in steel slag and will contribute to utilization or reuse of steel slags in concrete materials. By slaking free lime in converter slag before mixing with other cementitious co-binders, the free lime content of the hardened binder was found to reduced from 7% to 0.23% after 28 days due to enhanced formation of portlandite verified through DTA/TGA. The calculated amount of portlandite from TGA at 56 days was 29% for slaked slag mortars and 13% for un-slaked slag mortars. After 56 days, 9 MPa compressive strength was achieved for the ternary mix mortars. However, the strength can be increased by reducing (30%) the amount of slaked converter content in the ternary mix.

5. Acknowledgment

This work was funded by Business Finland/ERAMIN2 and SSAB under the auspices of the FLOW project (24302797). Jani Österlund and Johannes Kaarre are acknowledged for their contribution to the laboratory work. The authors would also like to than SSAB for supplying the steel slags used in this study.

6. References

- [1] Euroslag, Statistics 2016, Euroslag. (n.d.). <https://www.euroslag.com/products/statistics/statistics-2016/> (accessed April 5, 2019).
- [2] Lizarazo-Marriaga Juan, Claisse Peter, Ganjian Eshmaiel, Effect of Steel Slag and Portland Cement in the Rate of Hydration and Strength of Blast Furnace Slag Pastes, *Journal of Materials in Civil Engineering*. 23 (2011) 153–160. doi:10.1061/(ASCE)MT.1943-5533.0000149.
- [3] N. Palankar, A.U. Ravi Shankar, B.M. Mithun, Durability studies on eco-friendly concrete mixes incorporating steel slag as coarse aggregates, *Journal of Cleaner Production*. 129 (2016) 437–448. doi:10.1016/j.jclepro.2016.04.033.
- [4] L. Muhmood, S. Vitta, D. Venkateswaran, Cementitious and pozzolanic behavior of electric arc furnace steel slags, *Cement and Concrete Research*. 39 (2009) 102–109. doi:10.1016/j.cemconres.2008.11.002.
- [5] J. Ma, Y. Zhang, T. Hu, S. Sun, Utilization of converter steel slag by remelting and reducing treatment, *IOP Conf. Ser.: Mater. Sci. Eng.* 382 (2018) 022088. doi:10.1088/1757-899X/382/2/022088.
- [6] X.-J. Liang, Z.-M. Ye, J. Chang, Study on hydration characteristics of carbonated steel slag and slag as Portland cement admixtures, *Gongneng Cailiao/Journal of Functional Materials*. 43 (2012) 1540–1544.
- [7] Monkman Sean, Shao Yixin, Shi Caijun, Carbonated Ladle Slag Fines for Carbon Uptake and Sand Substitute, *Journal of Materials in Civil Engineering*. 21 (2009) 657–665. doi:10.1061/(ASCE)0899-1561(2009)21:11(657).
- [8] S. Eloneva, E.-M. Puheloinen, J. Kanerva, A. Ekroos, R. Zevenhoven, C.-J. Fogelholm, Co-utilisation of CO₂ and steelmaking slags for production of pure CaCO₃ – legislative issues, *Journal of Cleaner Production*. 18 (2010) 1833–1839. doi:10.1016/j.jclepro.2010.07.026.
- [9] S. Eloneva, A. Said, C.-J. Fogelholm, R. Zevenhoven, Preliminary assessment of a method utilizing carbon dioxide and steelmaking slags to produce precipitated calcium carbonate, *Applied Energy*. 90 (2012) 329–334. doi:10.1016/j.apenergy.2011.05.045.
- [10] B. Pang, Z. Zhou, H. Xu, Utilization of carbonated and granulated steel slag aggregate in concrete, *Construction and Building Materials*. 84 (2015) 454–467. doi:10.1016/j.conbuildmat.2015.03.008.

- [11] G. Adegoloye, A.-L. Beaucour, S. Ortola, A. Noumowe, Mineralogical composition of EAF slag and stabilised AOD slag aggregates and dimensional stability of slag aggregate concretes, *Construction and Building Materials*. 115 (2016) 171–178. doi:10.1016/j.conbuildmat.2016.04.036.
- [12] C. Pellegrino, P. Cavagnis, F. Faleschini, K. Brunelli, Properties of concretes with Black/Oxidizing Electric Arc Furnace slag aggregate, *Cement and Concrete Composites*. 37 (2013) 232–240. doi:10.1016/j.cemconcomp.2012.09.001.
- [13] Y.-C. Ding, T.-W. Cheng, P.-C. Liu, W.-H. Lee, Study on the treatment of BOF slag to replace fine aggregate in concrete, *Construction and Building Materials*. 146 (2017) 644–651. doi:10.1016/j.conbuildmat.2017.04.164.
- [14] SFS-EN 451-1, Method of testing fly ash- Part 1: determination of free calcium oxide, 2004.
- [15] K. Ohenoja, P. Tanskanen, V. Wigren, P. Kinnunen, M. Körkkö, O. Peltosaari, J. Österbacka, M. Illikainen, Self-hardening of fly ashes from a bubbling fluidized bed combustion of peat, forest industry residuals, and wastes, *Fuel*. (2016). doi:10.1016/j.fuel.2015.10.093.
- [16] N. Shafiq, M.F. Nuruddin, Degree of hydration of OPC and OPC/Fly ash paste samples conditioned at different relative humidity, *International Journal of Sustainable Construction Engineering and Technology*. 1 (2011) 47–56.
- [17] E. Adesanya, K. Ohenoja, T. Luukkonen, P. Kinnunen, M. Illikainen, One-part geopolymer cement from slag and pretreated paper sludge, *Journal of Cleaner Production*. 185 (2018) 168–175.
- [18] C. Shi, R.L. Day, A calorimetric study of early hydration of alkali-slag cements, *Cement and Concrete Research*. 25 (1995) 1333–1346. doi:10.1016/0008-8846(95)00126-W.
- [19] M. Palou, E. Kuzielová, M. Žemlička, R. Novotný, J. Másilko, The effect of metakaolin upon the formation of ettringite in metakaolin–lime–gypsum ternary systems, *J Therm Anal Calorim*. 133 (2018) 77–86. doi:10.1007/s10973-017-6885-0.
- [20] H. Nguyen, E. Adesanya, K. Ohenoja, L. Kriskova, Y. Pontikes, P. Kinnunen, M. Illikainen, Byproduct-based ettringite binder – A synergy between ladle slag and gypsum, *Construction and Building Materials*. 197 (2019) 143–151. doi:10.1016/j.conbuildmat.2018.11.165.
- [21] B.A. Clark, P.W. Brown, Formation of Ettringite from Monosubstituted Calcium Sulfoaluminate Hydrate and Gypsum, *Journal of the American Ceramic Society*. 82 (1999) 2900–2905. doi:10.1111/j.1151-2916.1999.tb02174.x.
- [22] M. Fridrichová, K. Dvořák, D. Gazdič, J. Mokrá, K. Kulísek, Thermodynamic Stability of Ettringite Formed by Hydration of Ye'elimite Clinker, *Advances in Materials Science and Engineering*. (2016). doi:10.1155/2016/9280131.
- [23] N.C. Collier, TRANSITION AND DECOMPOSITION TEMPERATURES OF CEMENT PHASES - A COLLECTION OF THERMAL ANALYSIS DATA, *Ceramics - Silikaty*. (2016) 1–10. doi:10.13168/cs.2016.0050.
- [24] I.Z. Yildirim, M. Prezzi, Chemical, Mineralogical, and Morphological Properties of Steel Slag, *Advances in Civil Engineering*. 2011 (2011) e463638. doi:10.1155/2011/463638.

CSA as A Revisited Vernacular Technique for Earth Stabilization

B. Cicek¹, N. Pires Martins², C. Brumaud², G. Habert²

¹ Chair of Design and Structural Systems, Bauhaus-University Weimar, Weimar Germany,

² Chair of Sustainable Construction, ETH-Zürich, Zürich, Switzerland

Abstract

The Calcium Sulfoaluminate (CSA) is presently receiving a lot of interest in the building sector. It is being used to produce CSA-Cements, which generates less CO₂ than Ordinary Portland Cement (OPC), but still requires the production of clinker at high temperature. For the moment, its application is mainly limited to China. On the other hand, the considerable interest in modern earth-based building materials has led to the increase of new types of products such as precast earth, prefabricated earth panels and boards on the market. Their major drawbacks are the low water stability and moderate strength leading to cement stabilization, which as a consequence reduce their environmental advantage. This paper deals with the rediscovery of a vernacular technique of producing CSA for a new stabilized earth-mixture. The first laboratory analyses on this mix-design have proven a high water-resistance. Furthermore, the results show a remarkable increase in compressive strength. Finally, the characterization of the stabilization effect has been performed through X-ray powder diffraction patterns (XRD) and clearly identify the production of ettringite using very low CO₂ intensive raw materials. These results open a new avenue for earth stabilization and secure the implementation of this material in the conventional construction industry.

Keywords: Calcium Sulfoaluminate (CSA), stabilized earth, XRD, earth-based building materials

1. Introduction

Calcination is the release of CO₂ from carbonates during pyroprocessing of the raw mix. Calcination CO₂ is directly linked with the clinker production, used for the production of Portland cement. In addition, calcination of cement kiln dust is a relevant source of CO₂ in countries where such dust is discarded [1]. In fact, the kiln temperature required for the manufacture of CSA clinker is ~1250°C, which is 200°C lower than the temperature used for Portland cement clinker [2]. CSA cement, which is more expensive than a Portland cement (PC) can reduce only less than 14% of production temperature. Therefore, the production of cement types in general contributes significantly to global CO₂ emission. While we often talk about the environmental problems caused by very energy-intensive sectors, earthen architecture needs to be as stronger as it has been in the past. At present, there are a few countries, where environmentally friendly architecture is getting more and more popular. This popularity is due to a recently growing construction sector, which offers contemporary earthen products and completion methods to the planners and costumers [3]. However in contemporary earthen architecture, cement is being commonly used to stabilize the earth material. An environmental friendly strategy to substitute cement with other additives is needed. For this purpose, a variety of alternative materials with lower environmental impacts can be used. Their use is based on the importance of minimizing CO₂ emissions, as well as increasing interest

in the production of cementitious materials that develop good mechanical properties and good stability in corrosive environments[4]. This paper deals with an alternative solution, consisting in combining trass, gypsum and lime to replace the use of cement in a vernacular way.

1.1 CSA and Stabilization

CSA-cement forms predominantly ettringite (anhydrous calcium Sulfoaluminate), belite (dicalcium silicate) and gypsum (gypsum calcium sulphate). These reaction products are responsible for the stable strength of CSA concrete. In this study, it was aimed to produce similar water insoluble reaction products with the help of proposed additives to develop an earth-mix with a higher and durable strength. To overcome the common drawbacks of earth construction materials, utilizing the stabilization effect is a significant application. However, it was only in 1920 that a scientific approach could be developed [5]. Soil stabilization is known as the process that enables the control of dimensional changes that clays suffer when they come into contact with water [6]. While mechanical stabilization allows controlling the binder and water repellents, the chemical stabilization allows the dust control, water erosion-control and micro and macro structural stability [7]. Since ancient times, small proportions of lime [6], pozzolan and gypsum were used in combination with earth. Murthy *et al.* [7] classified the stabilizing agents as traditional and non-traditional. According to this classification gypsum, lime and pozzolans are traditional agents. Trass is rich in acid reactive components such as SiO_2 and Al_2O_3 , it shows a very high pozzolanicity in a highly alkaline environment. Lime alone has several effects on stabilization. It provides an environment with a high pH, which accelerates the pozzolanic reactivity. It extends the rapid hardening of gypsum and makes it possible to gain about extra 20 min of working time [17][18]. Also, lime reacts with the clay minerals of the soil, or with any other fine, pozzolanic components such as hydrous silica, to form a tough water-insoluble gel of calcium silicate, which cements the soil particles [19]. The interaction between clay particles and lime is, however, a long-term process. Diamond *et al.* [20] reports this stage as an accumulation of soil-lime reaction products, causing a slow development of strength. The addition of gypsum supplies mainly sulphate to the mixture which forms, together with the trass minerals, the ettringite.

Since the beginning of modern research on stabilization, several studies have tried to explain the effects of gypsum, lime and pozzolan stabilization. In 2007, Vroomen [8] researched the properties of cast gypsum-stabilized earth. According to this study, a great advantage of gypsum over cement is that it can be produced locally by small-scale enterprises and it demands a low amount of energy in production as it can be calcined at approx. 125°C instead of 1100°C. In 2011, Lopez *et al.* [9] studied the chemical reaction between soil, fly ash (15%), gypsum (10%), lime (2%). They stated, when fly ash and lime are mixed with water, there is no chemical reaction in the initial phase. However, with increasing curing time a pozzolanic reaction begins between the fly ash and the gypsum. In 2012, Pekmezci *et al.* [10] published a paper showing the performance of earth structure by using lime (2,5-5%) and gypsum (8-10%) addition. In this study, however, the fly ash, which is a by-product and classified as an artificial pozzolan, is being substituted with a natural pozzolan called trass. This is due to several drawbacks: its production is seasonally limited and its usage encourages the sectors producing by-products of burning processes and therefore, contributes to environmental impacts. Jackson *et al.* [11] reports, with the current decline in coal-fired energy, fly ash is now becoming technically and/or economically unfeasible for use in concrete. Furthermore, artificial pozzolans result from chemical and/or structural modifications of original material, which may have weak pozzolanic characteristics, or not. On the contrary, natural pozzolans do not require any treatment before their use [9].

2. Materials and procedures

2.1 Materials

The earth used for the preparation of stabilized earth specimens consists of 30% commercially available

mineral earth material for plastering (Stroba Naturbaustoffe Ag, Switzerland) and of 70% standard sand CEN EN 196-1. The X-ray powder diffraction technique revealed, thanks to Rietveld methods [32,33], that the main mineralogical components are muscovite/illite (24.8wt%), quartz (21.3wt%), kaolinite (21.3wt%) and smectite (16.6wt%). The complete mineralogical composition is given in Table 1.

Table 1: chemical composition of terrasol used for sample preparation

	Anastase	Calcite	Chlorite	Goethite	Kaolinite	Microcline	Muscovite/ Illite	Plagioclase- Albite	Pyrite	Quartz	Rutile	smectite
(%)	0.3	<0.2	1.1	9.1	21.3	2.3	24.8	1.2	0.4	21.3	1.6	16.6

Three different additives (trass, gypsum and lime) were used in combination to stabilize the earth material. The trass (Tubag, Germany) was used as pozzolanic additive. It is also known as “rheinischer Trass”. Its chemical composition, obtained through X-ray fluorescence spectrometry (XRF), is given in Table 2. Trass is a natural pozzolanic material, which can be found in various regions of the earth. The mineral composition of trass is mainly volcanic glass, zeolitized to a different extent (clinoptilolite), and secondary components from crystalloclasts of magnetite, zircon, apatite, biotite, quartz, sanidine, plagioclase [12]. XRD pattern of the trass is given in Figure 1. Commercially available hemihydrate gypsum ($\text{CaSO}_4 \cdot 1/2\text{H}_2\text{O}$) was used. Moreover, a hydrated lime ($\text{Ca}(\text{OH})_2$) was used as an additive.

Table 2: Chemical composition of the trass studied by X-ray fluorescence analysis. Values are given in mass % [13].

Component, (%)	SiO_2	Al_2O_3	TiO_2	Fe_2O_3	MgO	Mn_2O_3	P_2O_5	CaO	SO_3	K ₂ O	Na_2O
	56.90	18.50	1.10	6.30	2.20	0.2	0.2	5.20	0.20	5.70	3.50

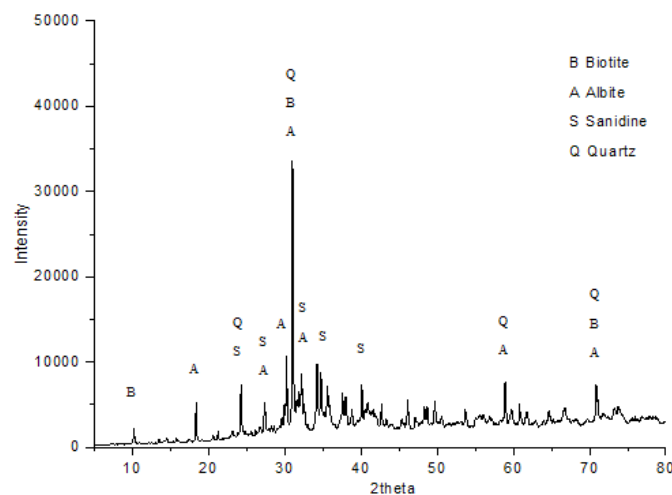


Figure 1: X-ray diffraction spectrum of the trass used in this study.

2.2 Sample preparation:

Three different stabilized earth samples were produced by using different proportion of trass, gypsum, and lime as additives to determine their efficiency on water resistance and on the strength of earth materials.

The mass of lime was kept constant at 2.5 wt% in all series: only the proportion of trass and gypsum was varied from one sample to the other. For all samples, the water to binder ratio was determined as 0.4 allowing to obtain a pourable material. The mix samples were poured into standard steel moulds (4cm x 4cm x 16cm). The mixture proportions and labelling of the stabilized earth samples are given in Table 3. After the addition of water, the mixing and the casting of specimens were no longer than 10 minutes. The mixing of the material was done manually. Samples were stored at 23°C and 50% relative humidity.

Moreover, to identify the pozzolanic reaction products, XRD analyses were performed on mix-designs mentioned in Table 3. The samples for the XRD analyses were prepared without earth. Therefore, the chemical interaction between additives and clay was not investigated in this study. XRD samples were cured for 7 days at 23°C and 50% relative humidity.

Table 3: The labelling and mixture proportions of the specimens

Labelling	PE	T10G8	T14G4	T16G2
Description	Plain earth with 30% terrasol and 70% standard sand	Earth with 10wt% trass, 8wt% of gypsum and 2.5wt% of lime	Earth with 14wt% trass, 4wt% of gypsum and 2.5wt% of lime	Earth with 16wt% trass, 2wt% of gypsum and 2.5wt% of lime

2.3 Procedures

The pozzolanic activity can be determined by physical, chemical or mechanical means. In this research, together with the water insertion test, the compressive strength (mechanical method) and XRD analysis (physical method) have been conducted to determine the pozzolanicity of the proposed mix-design. To determine the water resistance of stabilized and non-stabilized earth specimens, water insertion test was done. The water insertion was carried out according to the standard DIN 18945. The specimens were cured at 23°C and 50% relative humidity for 14 days. The loss of material was determined by filtering the residue in the dip tank. 7 and 28-day compressive strength tests were carried out on prismatic specimens with the dimensions of 40 x 40 x 160 mm. Mineralogy of the samples is determined on randomly oriented powder specimens with X-ray diffraction analysis [14]. X-ray diffraction measurements were made using a Bragg-Brentano X-ray diffractometer (D8 Advance, Bruker AXS, Germany) using CoK α radiation. The qualitative phase analysis was carried out with the software package DIFFRACplus (Bruker AXS) [15].

3. Results and discussions

3.1 Water Contact Tests

One of the main decaying factors in earth constructions is the presence of water. Once plain earth gets contact with water, it swells, and the dissolution and erosion are inevitable. To overcome this weakness, stabilization of earth can be a significant application. The loss of mass of the stabilized earth specimens and plain earth after the water insertion test is plotted in Figure 2. According to the water insertion test described in DIN 18945, the loss of mass has to be less than 5% of the total mass to be considered as acceptable. After 10 min. of water insertion, the loss of mass of the plain earth samples was determined as 38.406% of the total mass. However, as can be seen in Figure 2, all stabilized earth samples have shown similar behaviour and the loss of mass of all stabilized series is between 0.02-0.03 percent of total mass, which is significantly lower than the limit value. Moreover, no cracks were observed due to swelling: the proposed combination of additives significantly improved the water stability of the earth specimens. However, it can be observed that the change in trass/gypsum ratio does not influence the water resistance of the stabilized earth specimens.

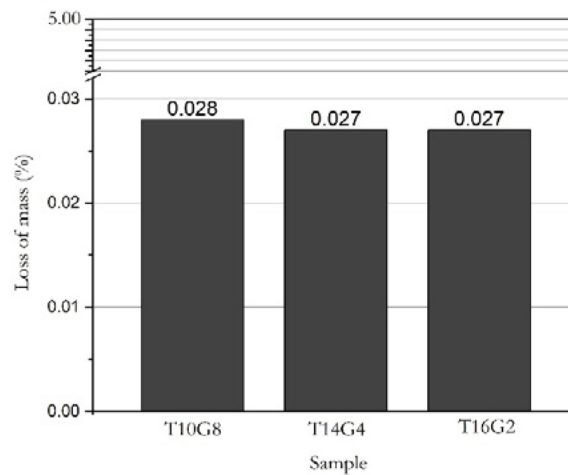


Figure 2: Loss of mass of stabilized earth samples after water insertion test.

3.2 Compressive strength

The 7 and 28-days results of compressive strength tests of stabilized earth specimens are shown in Figure 3. As can be seen in Figure 3, the maximum compressive strength is obtained for T16G2 samples containing 16wt% of trass and 2wt% of gypsum. While T10G8 containing the highest amount of gypsum does not show an increase in compressive strength from 7 to 28 days, the samples prepared with a higher amount of trass progressively gain strength from 7 to 28 days. Samples containing 14 and 16wt% of trass show a similar parallel behaviour of strength improvement from 7 to 28 days. Using higher content of trass allows improving the compressive strength of stabilized earth materials. These results show that the compressive strength of the earth material can be significantly improved with the proposed mix design of additives.

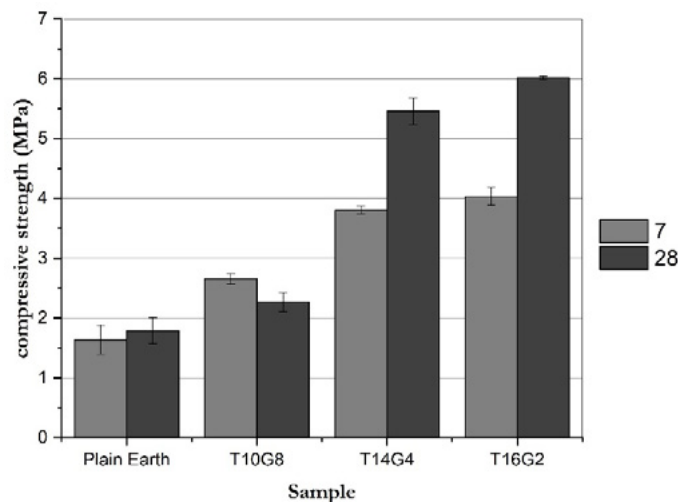


Figure 3: Compressive strength of the studied specimens.

3.3 XRD Analyses

The mechanism of stabilization is based on pozzolanic activity, which causes a durability effect in an environmentally friendly way. To better understand this mechanism and to identify the products of pozzolanic reactions, the mineralogical composition of the mix-designs were analysed with the help of X-ray diffraction (XRD). The XRD results of 7day cured mix-designs are given in Figure 4. As can be seen in the XRD pattern, the sample with 10 wt% of trass and 8 wt% of gypsum (T10G8) displays high amounts of gypsum. As expected, the intensity of gypsum peaks is being reduced by increasing the amount of trass. Very weak peaks of ettringite can be observed in T10G8. However, it can be noted that, with the

increasing amount of trass in samples, the intensity of the ettringite peak is getting higher. The reason for this behaviour is assumed to be the pozzolanic effect of trass. The chemical additives react with particles of trass to produce hydration products such as ettringite ($\text{Ca}_6\text{A}_{12}(\text{SO}_4)_3(\text{OH})_{12}\cdot 26\text{H}_2\text{O}$). A part of Aluminium is being consumed by the formation of ettringite. However, we found in all samples a notable amount of analcime ($\text{NaAlSi}_2\text{O}_6\cdot\text{H}_2\text{O}$), which also consumes a part of aluminium in trass. On the other hand, a great amount of calcite and muscovite was observed in all series.

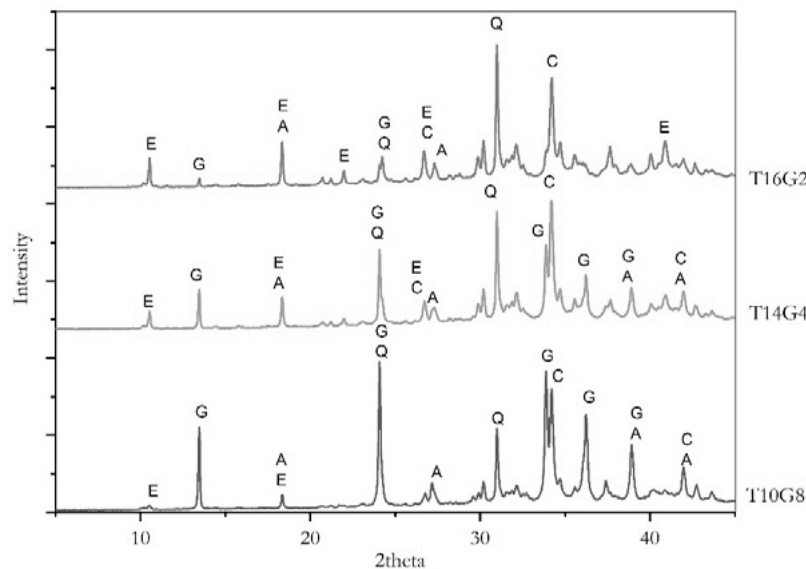


Figure 4: XRD pattern of the studied mixes of additives (without earth). (E; Ettringite, G; Gypsum, A; Analcime, Q; Quartz, C; Calcite)

4. Conclusions

This paper focuses on the stabilization effect of trass (pozzolan) + gypsum ($\text{CaSO}_4 \cdot \frac{1}{2}\text{H}_2\text{O}$) + lime ($\text{Ca}(\text{OH})_2$) system on the mechanical and physical properties of the unfired earth, as a vernacular solution to replace the use of cement in earth stabilization. The results drawn from this study can be summarized as follow:

1. The water-resistance and the compressive strength of the plain earth were improved by the presence of trass, gypsum and lime.
2. Ettringite, which is typical hydration product of Portland cement, could be produced with the proposed mix design.
3. With the increasing amount of trass, the precipitation of ettringite was increased. This provokes the progressively improvement of compressive strength of the stabilized earth.
4. Although samples containing the highest amount of gypsum showed in early age higher stability than plain earth samples, the strength improvement of these stabilized earth samples was mainly limited with the setting of gypsum alone.

5. Acknowledgment

Dr. Michael Plötze, Annette Röthlisberger and Marion Rothaupt from Institute for Geotechnical Engineering, ClayLab of ETH-Zürich supported us by XRD measurements. The authors are very thankful for their great contribution to this study.

6. References

- [1] Vanderborght, B.; Brodmann, U. Development, W. B. C. for S., 2001, *The Cement CO2 Protocol: CO2 Emissions Monitoring and Reporting Protocol for the Cement Industry*.
- [2] Chaunsali, P., and Mondal, P., 2015, "Influence of Calcium Sulfoaluminate (CSA) Cement Content on Expansion and Hydration Behavior of Various Ordinary Portland Cement-CSA Blends," *J. Am. Ceram. Soc.*, **98**(8), pp. 2617–2624.
- [3] Cicek, B., 2016, "A Methodolgy for an Active and Sustainable Earthen Construction Sector," *SBE16 Istanbul. Smart Metropoles, Integrated Solutions for Sustainable and Smart Building & Cities*, E. Erkal, A., Acuner, ed., Istanbul.
- [4] Gallardo H., M., Almanza R., J. M., Cortés H., D. A., and Escobedo B., J. C., 2016, "Mechanical and Chemical Behavior of Calcium Sulfoaluminate Cements Obtained from Industrial Waste," *J. Latin-American Assoc. Qual. Control. Pathol. Recover. Constr.*, **6**(1), pp. 15–27.
- [5] Houben, H., Guillaud, H., 1994, *Earth Construction – A Comprehensive Guide*, Intermediate Technology publications, London.
- [6] Mileto, C. Vegas, F., García Soriano, L., Cristini, V., ed., 2015, "Earthen Architecture: Past, Present and Future," *International Conference On Vernacular Heritage, Sustainability And Earthen Architecture*, CRC Press/Balkema, valencia, Spain, pp. 176–178.
- [7] Murthy, G., Kavya, S., Krishna, V., and Ganesh, B., 2016, "Chemical Stabilization of Sub-Grade Soil With Gypsum and NaCl," **9**(5), pp. 569–581.
- [8] Vroomen, R., 2007, "Gypsum Stabilised Earth," Eindhoven University of Technology, The Netherlands.
- [9] Marín López, C., Reyes Araiza, J. L., Manzano-Ramírez, A., Piñón, J. P., Hernández Landaverde, M. A., De Jesús, J., Bueno, P., and Marroquín De Jesús, Á., 2011, "Effect of Fly Ash and Hemihydrate Gypsum on the Properties of Unfired Compressed Clay Bricks," *Int. J. Phys. Sci.*, **6**(17), pp. 5766–5773.
- [10] Pekmezci, B. Y., Kafesçioğlu, R., and Agahzadeh, E., 2012, "Improved Performance of Earth Structures by Lime and Gypsum Addition," *Metu J. Fac. Archit.*, **29**(2), pp. 205–221.
- [11] Jackson, M. D., Oleson, J. P., Moon, J., Zhang, Y., Chen, H., and Gudmundsson, M. T., 2018, "Extreme Durability in Ancient Roman Concretes," *Am. Ceram. Soc. Bull.*, **97**(5), pp. 22–28.
- [12] Yoleva, A., Djambazov, S., and Chernev, G., 2011, "Influence of the Pozzolanic Additives Trass and Zeolite on Cement Properties," *J. Univ. Chem. Technol. Metall.*, **46**(3), pp. 261–266.
- [13] "Ein Werk Der Natur. TubagTrass" [Online]. Available: http://www.joostdevree.nl/bouwkunde2/jpgt/tras_1_tubag_trassbroschuere_24s_sept2010_www_tubag_de.pdf. [Accessed: 10-Apr-2019].
- [14] Bish, D.L., Plötze, M., 2011, "X-Ray Powder Diffraction with Emphasis on Qualitative and Quantitative Analysis in Industrial Mineralogy. In *Advances in the Characterization of Industrial Mineral*," G.E. Christidis, ed., EMU and Mineralogical Society, London, pp. 35–76.
- [15] Döbelin, N., Kleeberg, R., 2015, "Profex: A Graphical User Interface for the Rietveld Refinement Program BGMN," *J. Appl. Crystallogr.*, **48**, pp. 1573–1580.
- [16] Gava, G. P., and Prudêncio, L. R., 2007, "Pozzolanic Activity Tests as a Measure of Pozzolans'

Performance. Part 1,” *Mag. Concr. Res.*, **59**(10), pp. 729–734.

[17] Isik, B., and Tulbentci, T., 2008, “Sustainable Housing in Island Conditions Using Alker-Gypsum-Stabilized Earth: A Case Study from Northern Cyprus,” *Build. Environ.*, **43**(9), pp. 1426–1432.

[18] Kafescioglu, R., Toydemir, N., Özüekren, B., Gürdal, E., *Yapi Malzemesi Olarak Kerpici Alci Ile Stabilizasyonu*, Istanbul.

[19] Ingles, O.G., Metcalf, J. B., 1972, *Soil Stabilization. Principles and Practice*, Butterworths Pty. Limited, Sydney, Melbourne, Brisbane.

[20] Diamond, S., and Kinter, E. B., 1965, “Mechanisms of Soil-Lime Stabilization,” *Highw. Res. Rec.*, **92**, pp. 83–202.

Assessment of mine tailings as precursors for alkali-activated materials for on-site applications

R. Obenaus-Emler¹, M. Falah², M. Illikainen²

¹Montanuniversität Leoben, Leoben, Austria

²University of Oulu, Oulu, Finland

Abstract

Year after year the mining industry generates 5-7 billion metric tons of tailings worldwide. They are mostly disposed rather than valorised. The substantial amounts of tailings has led to growing concerns about their ecological and environmental impacts such as occupation of large areas of land, generation of windblown dust, and contamination of surface and underground water. Over the past years the mining industry has been subjected to increase environmental principles. As the consequence, besides waste rock and water management, tailings management becomes a progressively important factor for ecologic and economic reasons. Mine tailings from flotation processes are normally disposed in impoundments on the surface. This may cause environmental and safety problems including serious water pollution arising from contamination of surface water, groundwater, and soils due to the leaching of heavy metals, process reagents, and Sulphur compounds. Recently the process of alkali-activation and geopolymerisation has been explored as a potential method for tailings consolidation and heavy metal fixation. The tailings of many existing mining operations contain the aluminosilicate minerals needed for alkali-activation at least to some extent. From a sustainability point of view it makes sense to use alkali-activated products from tailings directly on the mine site as e.g. (1) backfill material applied to fill open cavities from the (underground) mining operation and (2) cover materials for surface deposits of tailings in order to store them ecologically safe and sealed off from the environment. Mine tailings from different mining operations around the world have been investigated regarding their potential use as precursors for alkali-activated materials. An assessment of the release of gel forming elements into alkaline solutions was performed by leaching experiments under various conditions (time, concentration of the solvent, and temperature). Compared to traditional alkali-activated precursor materials the release of aluminium and silicon is in general low for the mine tailings investigated. However, results indicate a favourable ratio of Si/Al for the formation of gels similar to other alkali-activated products. Additionally, the leached calcium can contribute to the strength of the resulting products by forming C-S-H gels when a considerable amount of Si is present in the pore solution either from the activator or dissolved from the material itself. The results of the leaching tests were used to facilitate the mix design for alkali-activated products. In order to increase the mechanical strength of the final product different approaches were considered: (1) addition of reactive materials (e.g. blast furnace slag), (2) increasing the reactivity of the tailings by grinding, and (3) increasing the reactivity by curing at elevated temperature. Depending on the tailings type, the mix design, and the curing conditions the final material shows a compressive strength in excess of 30 MPa even for curing at low temperatures. The investigated mine tailings can potentially be used for various applications on the mine site. With regard to specific target applications a further evaluation of long term properties of the resulting products (e.g. freeze-thaw resistance) has to be performed. Furthermore, results indicate that products with even higher

strength can be manufactured by further reducing the particle size of the tailings or by the addition of other reactive materials.

Keywords: Alkali-activated binders, mine tailings, alternative raw materials, environmental impact.

1. Introduction

Whenever a mine is developed, in general huge amounts of host rock have to be mined additionally and subsequently stored. The amount of (mostly valueless) waste rock varies much, depending on the ore body and whether the ore is mined from an open-pit or an underground mine. Due to intergrowth of minerals, even the mined ore itself contains valueless material. Furthermore, some ore might be left behind in the mine due to the chosen mining method, low grades, or other economic reasons. The dilution of the ore with waste rock can be substantial resulting in increased mineral processing costs and amount of tailings but no economic revenue. [1]

One of the major environmental issues of the mining industry is the waste streams that can reach over 90 % of the total mass for many ore types. When using a flotation process in mineral processing this waste stream (i.e. tailings), is a mixture of different minerals, process chemicals, and water in the form of a thick slurry. The tailings are mostly deposited in tailings storage facilities (TSFs) at the surface or sometimes used as paste backfill to fill underground cavities. Since the storage of tailings normally plays a minor role in the mining industry, little effort has been made regarding the valorisation of the tailings up to now.

Recently, more attention is paid to the deposition of tailings in TSFs at the surface by general public and especially legal authorities. Various problems are related to the storage of tailings at the surface [2]:

1. When tailings contain sulphide minerals, such as pyrite (FeS_2) or pyrrhotite (Fe_{1-x}S), oxidation in the presence of oxygen and water (either from rainfall, surface water streams or from mineral processing) results in the formation of sulphuric acid. If not being captured this may lead to severe ecological problems and the so called acidic mine drainage (AMD).
2. The huge amounts of tailings results in very large deposits on the surface, which the authorities do not permit any more or a suitable large space cannot be found or is strongly opposed by the communities close to the mine.
3. When dams are used for the deposit a dam failure can result in an ecological disaster.

As a consequence the disposal of mine tailings is a major environmental liability becoming increasingly important for current and future mining operations especially on ore bodies with low grades. In order to prevent the problems related to tailings storage, new approaches are needed and might even become critical for future mining operations. [1,2]

There are different ways and means to reduce the potential environmental hazards related to the storage of mine tailings and waste rock: (1) Isolation of waste materials from the nearby environment by capping, (2) chemical stabilization of especially mine tailings by adding chemicals or cementitious materials to immobilize heavy metals, and (3) a combination of these two methods. For the simultaneous use of isolation and stabilization techniques, the tailings surface can be treated by binders such as organic polymers, water glass or Ordinary Portland cement (OPC) to improve the resistance of the surface to erosion and reduce water infiltration, isolating the underlying tailings from the surrounding environment [3-5]. Although OPC has its benefits in the stabilization of certain mine tailings, it has several drawbacks such as low acid resistance, high cost as well as high energy consumption and CO_2 emissions related to the production of OPC.

Using the concept of alkali-activation, aluminosilicate raw materials can be turned into valuable cementitious-

like materials. Depending on their composition, the resulting alkali-activated materials or geopolymers have comparable properties to OPC, but may also show additional advantages such as rapid development of mechanical strength, high acid resistance, immobilization of toxic and hazardous materials, and a considerable reduction in greenhouse gas emissions [6-9]. Simplified, geopolymers can be formed by the reaction of aluminosilicate raw materials with highly alkaline solutions by leaching of Al and Si from the solid precursors with subsequent formation of a gel with a molar ratio of M:Al:Si roughly equal to 1:1:4, where M represents an alkali earth metal [6,10]. Initially metakaolin and fly ash were used as the main raw materials for geopolymers and have become model compounds for the comparison with other precursor materials. In recent years a number of other raw material sources (e.g. various other types of fly ash, natural minerals, metallurgical waste materials as well as their mixtures) have been studied to synthesize geopolymers [11].

The tailings of many existing mining operations contain the aluminosilicates needed for alkali activation at least to some extent and therefore offer an interesting alternative source material for alkali activated materials and geopolymers [11]. Even though natural rock can be thought of as a rather non-reactive material, the fine particle size distribution of the tailings might be advantageous right away or allowing for additional processes steps for substantially increasing the reactivity.

In a nutshell, this study addresses the valorisation of mine tailings as precursors to alkali-activated materials to be used for applications primarily at the mine site. The dissolution of relevant species is assessed by leaching in alkaline conditions and compared to other precursor materials. Furthermore, the compressive strength of alkali activated mixtures was determined in order to verify the suitability for the intended applications. The resulting alkali-activated materials can be used directly at the mine site as (1) a back fill material to fill underground cavities or (2) a covering layer for surface deposits of tailings. Depending on their properties the resulting materials could also be used for other applications (e.g. construction industry). The best-case scenario leads to a mining activity without any needs to deposit tailings on the surface or a minimized amount of tailings deposited on the surface using a covering layer for safely storing the tailings shielded from environmental conditions. Hence, in the near future mining operations can be more ecologically friendly and probably even more economically feasible compared to traditional mining operations.

2. Methodology

In order to assess the reactivity of solid precursor materials the leaching of relevant species in alkaline solutions was studied at a constant solid to liquid ratio with varying conditions for time, temperature and solvent concentration.

The results of the leaching experiments were taken into account for the mix design of alkali-activated materials and can also help to understand the possible reaction mechanisms during hardening. Enhancing the reactivity of the solid materials was investigated in order to increase the mechanical strength of the final products by the following approaches: (1) addition of other reactive materials, (2) increasing the specific surface area of the tailings, and (3) curing the products at elevated temperature. However, the main focus was put on using the tailings as delivered without further pre-treatment steps (like e.g. grinding or calcination) and thereby making it possible to apply solutions directly at the mine site without additional high investment into large infrastructures.

2.1 Materials

In this study the tailings from the following mining operations were investigated:

1. MT 1 – tailings from a copper/nickel mine (Northern Europe, low content of sulphides)
2. MT 2 – tailings from a copper/zinc mine (Southern Europe, high content of sulphides)
3. MT 3 – tailings from a platinum mine (Africa)
4. MT 4 – tailings from an iron ore mine (South America)

All tailings samples were supplied wet (mostly as slurries) and dried at 110 °C prior to any laboratory experiments. In order to prevent oxidation of samples containing a high amount of sulphides, only small portions were dried shortly before use.

Additionally to the tailings samples metakaolin (MK) and granulated blast furnace slag (GBFS) were used as solid additives. MK was delivered as a dry powder. GBFS was delivered moist with a particle size distribution smaller than 4 mm. The GBFS was dried at 110°C and comminuted using a ball mill to a final specific surface area of approximately 3300 cm²/g.

The chemical composition of solid materials was determined by XRF on fused beads of the original sample after determination of the loss on ignition (LOI). The qualitative mineralogical composition was determined by XRD on loose powder bed samples. Different particle size fractions of the samples were obtained by dry classification. The particle size distribution of the samples was determined by laser diffraction (dry dispersion).

Furthermore, a chemical grade concentrated sodium hydroxide solution (NaOH) and a sodium silicate solution (waterglass, Na₂SiO₃) were used. The concentrated NaOH solution was diluted to the desired concentration using deionized water. The waterglass solution used has a solids content of approximately 35,3 m% with a mass ratio Na₂O to SiO₂ of 3:10.

2.2 Leaching experiments

Leaching of solid precursor materials in alkaline conditions was performed using a similar procedure as described in literature (e.g. Xu and van Deventer [12,13]) using a solids to liquid ratio of 2 g per 100 ml of solvent. The standard conditions for the leaching experiments are a duration of 24 hours at a temperature of 40°C using a 5M NaOH solution, but additional parameter studies for relevant parameters have been performed for some materials. In order to prevent contamination of the leachates with Si from glass containers, plastic equipment was used for storage and during the experiments. The leaching was done by the following procedure:

1. Preheating of the solid precursor material in a sealable plastic container.
2. Addition of preheated solvent.
3. Mixing of solids and solvent using a bottle roller with 60 rpm for the desired reaction time.
4. Filtration of solids and leachate.
5. Dilution of the leachate 1:50 with deionized water.
6. Acidification to a pH between 2 and 3 using 4M HCl to prevent precipitation prior to analysis.
7. Determination of the concentration of leached species by ICP-MS.

The elemental concentrations of the leachates were corrected by the concentrations in the blank solvents treated by the same procedure.

In order to investigate the leaching residue after the experiment the filtration residue was washed with deionized water in order to eliminate excess NaOH of the leaching experiment. The residue was dried at 110°C and further investigated. However, the change of mass of the dried solid residue compared to the initial sample was below the detection limit for the chosen experimental setup (< 0,5 m%).

MT 3 was chosen for further leaching experiments with additional variation of the temperature. The experiments were carried out with 1M, 5M, and 10M NaOH solution for leaching durations of 24 and 72 hours.

2.3 Mix design and testing

The crucial property of resulting alkali-activated materials for this investigation was the uniaxial compressive strength. It was tested using small cylindrical samples with a diameter of 40 mm and a height of 30 mm.

With regard to a possible installation of the alkali-activated mixes by pumping the consistency is crucial for the mix design. In order to ensure a desired viscosity of the mix the liquid to solids ratio was kept constant for a given solid raw material. Since there is a high variation in the density of the activator solution depending on its composition (concentration) a certain volume of liquid activator solution was used for a given mass of solids. For the activator solution mix the NaOH solution and the waterglass solution were premixed and the volume adjusted to the desired amount by addition of deionized water. The activator solution was then mixed with the solids by hand in a small beaker with a rod until a homogeneous mix was obtained. The mix was poured into silicone moulds and compacted by vibration. The samples were then covered with a silicone mat and stored in locked boxes until testing at the chosen curing temperature. The compressive strength was determined by recording the maximum force using a universal testing machine.

For MT 1 an activator screening with mixtures of NaOH and waterglass solutions was performed initially with a constant amount of 27.5 ml of activator solution for 100 g of solid mine tailings. The samples were cured for 7 days at a temperature of 60°C prior to determination of the compressive strength. The results showed, that the highest strength was achieved when using waterglass solutions as an activator with only little to no further addition of NaOH. Therefore, further experiments were carried out using only waterglass solutions with concentrations between 10 to 30 m% of solid waterglass and testing after curing for 7, 14 and 28 days. Since the results were quite promising, further experiments were performed with the same recipes and curing at 40°C and room temperature (RT). The other mine tailings were studied less extensive.

In addition to the determination of the strength of the final products, selected samples with high strength have been further investigated by XRD and SEM.

3. Results and discussion

3.1 Material characterisation

Table 1 shows the characteristic parameters of the particle size distribution of the mine tailings as delivered. The fineness is governed by the specific ore characteristics and related to the intergrowth of the valuable minerals with the matrix minerals. In general the tailings show a high fineness which is favourable for alkali-activation. Table 2 summarizes of the chemical composition of the solid precursor materials. The metakaolin (MK) used in this study is a technical grade stoichiometric metakaolin with at least 95 m% of $\text{Al}_2\text{Si}_2\text{O}_5$ and a x_{50} of 1.5 μm . Table 3 gives an overview of the mineralogical composition (in alphabetical order) of the mine tailings samples. Due to the granulation process the GBFS has solidified in a glassy state and does not show any peaks in the XRD pattern.

Table 1: Characteristic parameters of the particle size distribution of mine tailings.

	MT 1	MT 2	MT 3	MT 4
	Cu/Ni tails	Cu/Zn tails	Pt tails	Fe tails
x_{90} [μm]	54	25	90	9.0
x_{50} [μm]	7.5	4.6	10	2.4
x_{10} [μm]	0.9	1.0	1.6	0.8

Table 2: Chemical composition of the solid precursor materials determined by XRF.

	MT 1	MT 2	MT 3	MT 4	GBFS
	Cu/Ni tails	Cu/Zn tails	Pt tails	Fe tails	
Na₂O	0.30	0.32	1.48	0.03	0.69
MgO	22.55	1.90	16.98	0.40	9.79
Al₂O₃	2.06	8.04	9.79	5.73	10.50
SiO₂	46.59	31.06	54.02	11.74	39.50
P₂O₅	0.02	0.06	0.02	0.29	
SO₃	1.24	0.24	0.16	0.09	1.37
K₂O	0.10	0.67	0.41	0.99	1.62
CaO	13.42	0.94	6.80	0.82	32.20
TiO₂	0.26	0.21	0.18	0.22	0.63
Cr₂O₃	0.31	<0.01	0.36	0.01	0.59
MnO	0.15	0.10	0.20	0.08	1.65
Fe₂O₃	11.92	35.50	9.34	77.30	
LOI	2.35	18.37	1.82	2.92	
Σ	101.27	97.41	101.56	100.62	98.54

Table 3: Mineralogical composition of the mine tailings determined by XRD.

	MT 1	MT 2	MT 3	MT 4
	Cu/Ni tails	Cu/Zn tails	Pt tails	Fe tails
Albite			X	
Antigorite	X		X	
Calcite	X		X	
Chlorite	X	X	X	
Diopside	X			
Enstatite			X	
Hematite			X	X
Lizardite	X			
Magnesiohornblende	X		X	
Muscovite	X	X	X	X
Pyrite		X	X	X
Quartz		X	X	
Siderite		X	X	X
Talc			X	

3.2 Leaching of solid precursor materials in alkaline solution

The sample of MT 1 has been chosen to study the influence of leaching time in more detail for 5M and 10M NaOH. The results of the leaching experiments at 40°C with test durations of 4, 8, 24 and 72 hours are summarized in Figures 1 and 2.

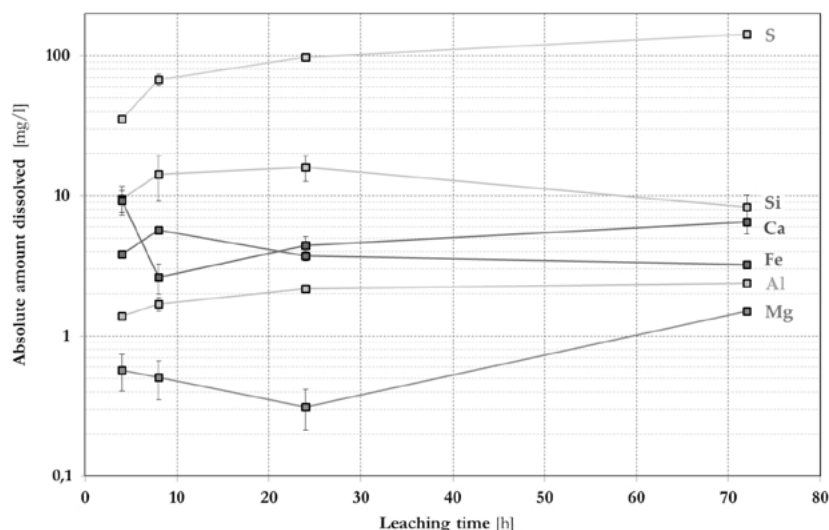


Figure 1: Results of the leaching experiments for MT 1 with 5M NaOH at 40°C.

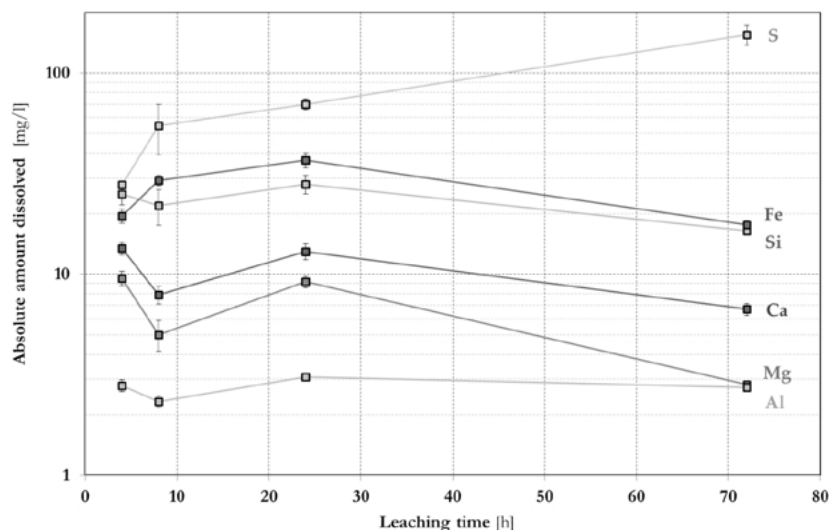


Figure 2: Results of the leaching experiments for MT 1 with 10M NaOH at 40°C.

The results show that the amount of dissolved species is increased for a higher concentrated NaOH solution (except for S and intermediate test durations). The maximum amount of dissolved species can be found after leaching durations of 24 hours especially for the experiments with 10M NaOH. This might be caused by subsequent formation of precipitates or gels from the solution reducing the amount of most of the species except Sulphur.

For leaching in 10M NaOH approximately 1.4 m% of the initial Al and 0.6 m% of the initial Si have been dissolved which adds up roughly to the detection limit for the mass balance. However, subsequent analysis of the leaching residue by XRF, XRD and SEM did not reveal whether precipitates have been formed or from which mineral phases the individual species have been dissolved.

For MT 3 the absolute amount of dissolved Si and Al in dependence of leaching duration and temperature are summarized in figures 3 and 4. Similar trends as for MT 1 can be observed from the leaching experiments of MT 3 although the maximum concentration of dissolved species is not reached after a leaching duration of 24 hours. The amount of dissolution is directly proportional to the concentration of the solvent but its dependence is not as strong as the influence of the leaching temperature. Increasing the temperature from 40°C to 80°C increases the amount of dissolved species roughly by a factor of 2. The results show that using a 1M NaOH solution at a temperature of 80°C the absolute amount of dissolved species is still

higher than using a 10M NaOH solution at 40°C even for shorter leaching duration. This means that a short thermal treatment at a higher temperature might be favourable for alkali activated materials in contrast to curing at moderate temperatures for a longer time.

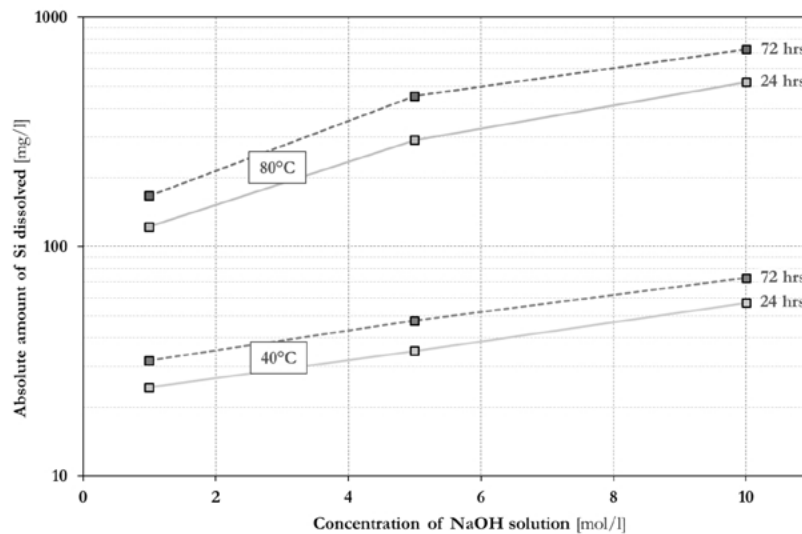


Figure 3: Absolute amount of dissolved Si from MT 3 for different leachate concentrations at various temperatures.

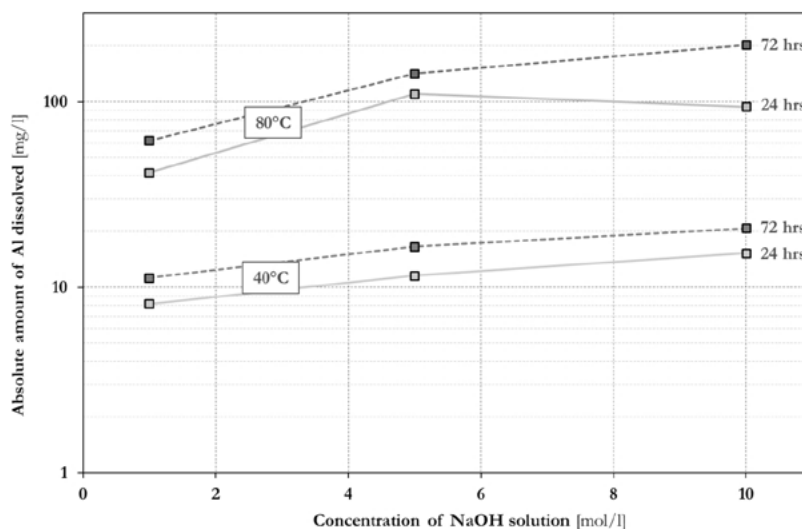


Figure 4: Absolute amount of dissolved Al from MT 3 for different leachate concentrations at various temperatures.

The experiments with MT 1 and MT 3 suggested to perform further tests with other materials with 5M and 10M NaOH solution for a test duration of 24 hours. A temperature of 40°C was chosen due to more simple and safe handling. The results are summarized in table 4. The mine tailings show little reactivity in alkaline solutions compared to granulated blast furnace slag and metakaolin.

For the mine tailings the amount of dissolved species corresponds to below 5 m% of the initial amount in the tailings sample whereas for GBFS roughly 60 m% and for MK roughly 80 m% are dissolved after a leaching duration of 24 hours.

Table 4: Summary of the absolute amount of species dissolved from MTs, GBFS, and MK in NaOH solutions at a temperature of 40°C and a leaching duration of 24 hours with a solids to liquid ratio of 2 g per 100 ml of solvent.

		MT 1	MT 2	MT 3	MT 4	GBFS	MK
		Cu/Ni tails	Cu/Zn tails	Pt tails	Fe tails		
Absolute amount dissolved [mg/l]	5M NaOH	Ca	4.4		7.4	28.0	
		Mg	0.3		0.5	1.8	
		Al	2.2	8.0	11.6	32.0	1977
		Si	16.0	14.0	35.2	80.2	2911
		Fe	3.7			1.3	
		S	97.2			9.5	
		Ca	13.0		4.1	23.3	21.8
	10M NaOH	Mg	9.2		0.6	3.6	2.3
		Al	3.1	14.5	15.3	70.2	603
		Si	28.0	58.0	57.0	134	2450
		Fe	37.0			2.5	1.9
		S	70.0			13.2	880

3.3 Mechanical properties of alkali-activated mixtures

The results of mixtures with MT 1 and waterglass are summarized in figure 5. In general a lower curing temperature resulted in lower strength especially for short curing times. The strength of MT 1 activated with waterglass solutions and cured for 28 days at RT ranges from 3.8 MPa up to 14.2 MPa depending on the concentration of solid waterglass in the activator solution. The early strength after curing for 7 days at room temperature was around 1 MPa only. In order to increase the early strength of the alkali-activated products two options have been tested:

1. Grinding of the original tailings with x_{50} of 7.5 μm to a product with x_{50} of roughly 6 μm increased the strength after curing at room temperature to 7.5 MPa for an activator solution with 15 m% of solid waterglass in the activator solution.
2. Replacing 10 m% of the original tailings with ground granulated blast furnace slag increased the strength in a similar way as (1).

The investigations with the other mine tailings have not been carried out as extensive as for MT 1. Hence, the results are not shown as detailed as for MT 1, but summarized in table 5. For MT 2, MT 3, and MT 4 mixtures of waterglass and NaOH have been used as activator solution using a similar screening process as for MT 1. Similarly, the amount of liquid activator has been adjusted in order to result in a mix with desired viscosity. In general a higher strength can be reached with a higher concentration of activator components in the solution. MT 2, MT 3, and MT 4 show lower strength compared to MT 1.

For MT 4 the addition of metakaolin was successfully tested to increase the strength of the final product. A strength up to around 30 MPa was achieved for curing at 60°C for 28 days. Due to the fine particle size of metakaolin the amount of liquid activator solution had to be adjusted.

Unfortunately XRD and SEM could not clearly identify the source related to the high strength of these materials. In contrast to geopolymers or alkali-activated materials the degree of reaction is rather low so that the microstructure of the alkali-activated materials from the mine tailings was found to be rather unchanged.

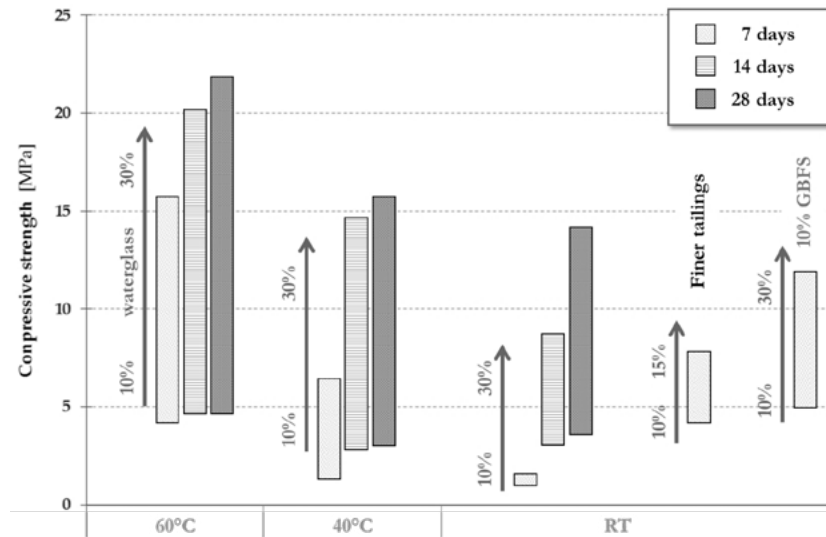


Figure 5: Compressive strength after 7, 14, and 28 days of samples made from MT 1 with waterglass solutions as an activator and curing at different temperatures. The lower end of the bars corresponds to recipes with the lowest concentration of waterglass in the activator solution (10 m%) and the upper end to the highest concentration tested in a given series. 'Fine tailings' corresponds to the same sample but ground to a x_{50} of roughly 6 µm. '10% GBFS' corresponds to a mixture where 10 m% of the mine tailings was replaced by granulated blast furnace slag.

Table 5: Overview of the strength of alkali-activated products from the mine tailing.

	Additives	Amount	Activator Composition	Curing		σ_c [MPa]
				T [°C]	t [days]	
MT 1	waterglass	27.5 ml / 100 g	waterglass	60	7	~ 5 to 15
					14	~ 5 to 20
					28	~ 5 to 22
	waterglass	27.5 ml / 100 g	waterglass	40	7	~ 1,5 to 6,5
					14	~ 3 to 15
					28	~ 3 to 16
	waterglass	27.5 ml / 100 g	waterglass	RT	7	~ 1.0 to 1.5
					14	~ 3 to 8
					28	~ 3.5 to 14
	Fine tails to reach $x_{50} \sim 6 \mu\text{m}$	27.5 ml / 100 g	waterglass	RT	7	~ 4 to 7,5
	GBFS (10 m%)	27.5 ml / 100 g	waterglass	RT	7	~ 5 to 12
MT 2		38.75 ml / 100 g	NaOH and waterglass	60	7	~ 1.0 to 3.5
MT 3		33.75 ml / 100 g	NaOH and waterglass	60	14	~ 1.5 to 5
					14	~ 1.0 to 2
		33.75 ml / 100 g	NaOH and waterglass	RT	28	~ 1.5 to 4
MT 4					7	~ 1.0 to 1.5
		37.5 ml / 100 g	NaOH and waterglass	60	14	~ 1.5 to 2
					28	~ 2 to 3
					7	~ 1.5 to 3
	Metakaolin (10 m%)	40 ml / 100 g	NaOH and waterglass	60	14	~ 3.5 to 6
					28	~ 5 to 30

4. Conclusions

The results of the leaching experiments showed, that in general the dissolution of significant species from

the mine tailings is little compared to reactive products like granulated blast furnace slag or metakaolin. However, alkali-activation can lead to final products with considerable strength depending on the curing conditions. Furthermore, finer ground tailings or reactive materials have a positive effect on the strength of the final products.

One possible on-site application of alkali-activated materials is mine backfill. Depending on the mining method and whether a primary or secondary stope is being filled, the ultimate strength of installed backfill ranges from 0.2 to 5 MPa. Secondary stopes, or areas where tailings are being placed for safe disposal only require sufficient strength to resist liquefaction, whereas primary stopes may need strength to stand vertical up to 50m high. Cut and fill operations – where quick access is crucial – often require rapid strength development (i.e. more than 2 MPa in approximately the first seven days after installation).

The results for alkali-activated products from the mine tailings indicate that an application as mine backfill seems possible. However, further material properties of the final products (e.g. water resistance) have to be determined additionally. Additionally, the setting behaviour of the backfill can be of importance, especially for long pumping distances.

For the covering layers of surface deposits of tailings a parameter set of physical and chemical properties can only be defined knowing the environmental conditions on the site of installation. Geochemical modelling can assess if such an application is possible with a specific alkali-activated product taking relevant physical and chemical properties into account.

Unfortunately a further assessment of high strength products did not reveal the source of the strength. The following reaction mechanisms are theoretically possible for the given chemical system when adding NaOH and waterglass as an activator:

1. **Waterglass bond:** Formation of a gel due to a reaction with polyvalent cations or due to a reaction with CO₂ leading to silification of dissolved Si according to: $\text{Na}_2\text{O} \cdot n\text{SiO}_2 \cdot x\text{H}_2\text{O} + \text{CO}_2 \rightarrow n\text{SiO}_2 \cdot x\text{H}_2\text{O} + \text{Na}_2\text{CO}_3$
2. **Formation of a C-S-H gel:** Formation of a gel due to the reaction of dissolved Ca from tailings with dissolved Si from the addition of waterglass and/or leached from the tailings.
3. **Formation of a N,C-A-S-H gel:** Formation of a gel as for the alkali-activation of granulated blast furnace slags or fly ash.
4. **Formation of a geopolymer gel.**

The first three reaction mechanisms seem likely depending on the concentration of relevant species in the pore solution of the mix. However, the formation of a geopolymer gel seems rather unlikely when using mine tailings only as the solid precursor material.

5. Outlook and further procedure

The results currently available don't allow for a direct link between the specific chemical and mineralogical composition of the tailings and their leaching behaviour or performance in alkali-activated materials. However, the data from the leaching experiments can be used for geochemical modelling to link dissolution to certain mineral phases. For that purpose a more detailed mineralogical assessment of the raw material as well as the leaching residues needs to be done by e.g. QEMSCAN. Additionally, modelling can help to assess the formation of gel phases taking place while hardening of the alkali-activated products.

6. Acknowledgment

The results presented in this paper are part of the research project ITERAMS – Integrated mineral technologies for more sustainable raw material supply. This project has received funding from the European Union's Horizon 2020 research and innovation programme under grant agreement No 730480.

7. References

- [1] Obenaus-Emler, R.; Illikainen, M.; Falah, M.; Kinnunen, P.; Heiskanen, K. (2019): Geopolymers from mining tailings for more sustainable raw material supply. MATEC Web of Conferences 274:05001, RICON17. doi: 10.1051/mateconf/201927405001.
- [2] Kossoff, D.; Dubbin, W.E.; Alfredsson, M.; Edwards, S.J.; Macklin, M.G.; Hudson-Edwards, K.A. (2014): Mine tailings dams: Characteristics, failure, environmental impacts and remediation. Applied Geochemistry 51, pp 229-245.
- [3] IAEA, The long term stabilization of uranium mill tailings (2004). doi:10.1016/j.jenvrad.2004.01.030.
- [4] Lange L.C.; Hills, C.D.; Poole, A.B. (1996): Preliminary Investigation into the Effects of Carbonation on Cement-Solidified Hazardous Wastes. Environmental Science and Technology 30, pp 25-30. doi:10.1021/es940702m.
- [5] Ahmari, S.; Zhang, L. (2013): Durability and leaching behavior of mine tailings-based geopolymer bricks. Construction and Building Materials 44, pp 743-750.
doi: 10.1016/J.CONBUILDMAT.2013.03.075.
- [6] Zhang, L.; Ahmari, S.; Zhang, J. (2011): Synthesis and characterization of fly ash modified mine tailings-based geopolymers. Construction and Building Materials 25, pp 3773-3781.
doi: 10.1016/J.CONBUILDMAT.2011.04.005.
- [7] Barnhisel, R.I.; Darmody, R.G.; Daniels, W.L.; Skousen, J.G.; Sexstone, A.; Ziemkiewicz, P.F. (2000): Acid Mine Drainage Control and Treatment. Reclamation of drastically disturbed lands, pp. 131-168. doi: 10.2134/agronmonogr41.c6.
- [8] Majidi, B. (2009): Geopolymer technology, from fundamentals to advanced applications: a review. Materials Technology 24, pp 79-87. doi: 10.1179/175355509X449355.
- [9] Drechsler, M.; Graham, A. (2007): Geopolymers – An Innovative Materials Technology Bringing Resource Sustainability to Construction and Mining Industries. Common Ground Proceedings 10th Australia new Zealand Conference on Geomechanics Brisbane. doi: 10.13140/2.1.1880.5762.
- [10] Van Deventer, J.S.J.; Provis, J.L.; Duxson, P.; Lukey, G.C. (2007): Reaction mechanisms in the geopolymeric conversion of inorganic waste to useful products. Journal of Hazardous Materials 139, pp 506-513. doi: 10.1016/J.JHAZMAT.2006.02.044.
- [11] Rao, F.; Liu, Q.: Geopolymerization and Its Potential Application in Mine Tailings Consolidation: A Review (2015). Mineral Processing and Extractive Metallurgy Review 36, pp 399-409.
doi: 10.1080/08827508.2015.1055625
- [12] Xu, H.; van Deventer, J.S.J.: The geopolymerisation of natural alumino-silicate minerals (1999). Geopolymer '99 Proceedings, pp 43-63.

- [13] Xu, H.; van Deventer, J.S.J: The geopolymerisation of natural alumino-silicate minerals (2000). International Journal of Mineral Processing 59, pp 247-266. doi: 10.1016/S0301-7516(99)00074-5.

Experimental development of alternative lightweight concretes

D. Zwicky

Professor, Dr. sc. techn., dipl. Bauing. ETH, Institute of Construction and Environmental Technologies iTEC, School of Engineering and Architecture Fribourg HEIA-FR, University of Applied Sciences and Arts Western Switzerland HES-SO, daia.zwicky@hefr.ch

Abstract - It is difficult to compete with normalweight concrete: it is pourable, usually self-compacting, hardening reasonably fast, cheap and locally available in large quantities. Its excellent fire protection and good acoustic insulation for airborne sound are further advantages in construction. But, regular concrete is very heavy, being disadvantageous for transportation and hoisting and results in the fact that a concrete structure predominantly supports its self-weight. Also, concrete qualities applied in building construction usually provide a far too high strength, as geometry is often dictated by constructability (minimum dimensions for concreting). Concrete further provides poor thermal insulation and unpleasant user experience (it “feels” cold), and is rather challenging to recycle. Last but not least, concrete manufacture is largely based on non-renewable resources and has a high environmental impact. Thus, alternative lightweight concretes should be further developed. Starting from earlier developments on “wood-based concrete” (or wood-cement compounds WCCs), essentially consisting of Portland cement (PC) and other mineral binders and of up to 60% of untreated sawdust, this study aimed at improving their mechanical properties by integrating an aggregate skeleton from organic aggregates (fruit pits, crushed nut shells) and lightweight aggregates from largely available or renewable resources (expanded clay and glass). 15 different recipes for “WooCon” (from wood-concrete) were designed and evaluated, in a first phase, for possible self-compaction as a basic fresh-state requirement for their targeted application in prefabrication. In a second phase, basic mechanical properties of 5 retained WooCon recipes were evaluated, by testing elastic modulus, compressive strength, and their development over 28 days as a further important prefabrication requirement. These results were also used to modify predictive expressions for correlating compressive strength and elastic modulus. In a third phase, estimates of economic and ecological performances were established, in order to assess the competitiveness of the newly developed WooCon recipes. The fourth evaluation phase of long-term properties (shrinkage and creep) of the 3 most promising WooCon recipes is currently ongoing. The study results show that adding an aggregate skeleton to WCCs, i.e. converting them into WooCon, can notably improve workability properties, up to self-compaction. Compressive strength can be doubled and elastic modulus can be tripled. Strength development can be predicted by generally accepted expressions and can even reach very rapid early hardening. Elastic modulus can be correlated quite accurately to compressive strength. In all evaluated mechanical properties, a marked influence of the applied percentage of organic aggregates could be observed. Economic impacts of WooCon majorly reside in costs for organic aggregates and cement, and result in unit prices up to 2.5 times higher than regular lightweight concrete (LC); however, if contextualised for mechanical elements, WooCon can perform better than regular LC. Lime filler and cement are the major contributors to ecological impact (global warming potential, GWP) but the overall result shows 75-80% reductions in comparison to regular LC.

Keywords: Alternative lightweight concrete, Lab tests, Fresh-state properties, Mechanical properties, Analytical predictions.

1. Introduction

This study aims at further developing wood-cement compounds (WCCs) as an alternative to regular lightweight concrete (LC), starting from the encouraging results from earlier developments. These WCCs essentially consist of Portland cement (PC) and other mineral binders and of up to 60% of untreated sawdust [1][2], one of the cheapest and most largely available renewable resource, usually having a maximum granular size of 2 mm with 95% smaller than 1 mm [1] (i.e. these WCCs are rather wood-based mortars).

They can be produced in standard manufacture processes, are pourable and (possibly) self-compacting [2], and material costs are approx. 30-35% lower than regular LC [3]. They show very low self-weight: 1'100--1'300 kg/m³ when saturated while oven-dry densities are between 450 kg/m³ and 870 kg/m³ [4]; at ambient humidity, material densities are around 650 kg/m³ to 1'100 kg/m³. They also provide excellent fire protection (min. 23'/cm [5]), have a thermal conductivity comparable to regular LC but show significantly higher thermal storage capacity [6], and considerably contribute to acoustic insulation [7]. End-of-life re-valorisation can be done by combustion, providing calorific values of 25-50% of wood chips but also 55-70% ash contents [8]. However, these ashes proved further effective as lightweight aggregates or can even be recalcinated, with reactivity ratios of up to 70% of virgin PC [9].

But, the main weaknesses of these structurally-targeted WCCs are slow strength development [2], very low stiffness (1-3 GPa) and compressive strength (2-5 MPa) and, above all, very high shrinkage (3-7‰ after 1 year) and creep coefficients (5.5-8.5 after 1 year) [1]. Adding sand to WCC and replacing an important part of PC by lime filler improves workability, strength and its development, stiffness, and shrinkage behaviour [10] but it also increases density and does not really subscribe to an ecological development (sand resources). Furthermore, application of these WCCs in structural slabs still results in some ecological challenges [11].

To further develop these WCCs, without being too far at the account of their advantageous performances, new recipe improvements were investigated [3]. Above all, the integration of an aggregate skeleton, made of organic components (e.g. fruit pits, nut shells) and lightweight aggregates from expanded clay and glass (i.e. largely available or renewable resources), targeting their transformation into real wood-based concretes, named "WooCon". Their manufacture procedures should keep to usual concrete processes, construction performances should be similar (i.e. pourable, self-compacting, reasonably fast hardening), and they should provide adequate mechanical performances. If material costs are somewhat higher, this can possibly be compensated through lower self-weight, appropriate fire protection, improved thermal properties, enhanced end-of-life re-valorisation (rather than down-cycling), and lower ecological impact.

2. Methodology

The study [3], forming the basis for this paper, was structured in several phases:

1. Preliminary survey research for locally available (lightweight) aggregates for possible application, considering availability, particle density, and particle size distribution PSD
2. Recipe design, with WCCs as a basis, and preliminary estimations of density and unit prize
3. Lab tests for evaluation of self-compaction properties and further workability performances, to identify the 5 most promising WooCon recipes
4. Lab tests for short-term stiffness, compressive strength and strength development, to identify the 3 most promising recipes for long-term testing
5. Estimative calculation and comparison of economic and ecological performances to regular LC

6. Launch of lab tests for long-term properties, i.e. shrinkage and creep, for the 3 retained WooCon recipes

The last phase is currently still ongoing, and is not further commented here. In phase 5, estimations are based on purchase prizes for the lab test quantities, not necessarily valid on an industrial upscaling. As the further development of WooCon may also involve spin-off activities, some degree of confidentiality is applied hereafter. Specific components and their overall percentages are given but detailed compositions incl. individual PSD as well as mixing process details are kept confidential.

2.1 Recipe design

For a good aggregate skeleton, PSD of different aggregate size classes should be combined appropriately. To do so, the development of recipes was based on the PSD limits proposed in [12], see Figure 1. Bearing further in mind the target of self-compaction, a limitation to aggregate sizes of 16 mm and a water/cement ratio (w/c) between 0.4 and 0.55 is considered [13]. In the first project phase, a limitation to 1'000 km of transportation, exclusion of edible sources, and available PSDs of aggregates were considered, resulting in the choice of the following basic ingredients as aggregate candidates (besides saw dust and lime filler):

- Mineral aggregates: lightweight expanded clay aggregates (LECA), expanded glass aggregates (e.g. “Misapor”, “Poraver”), sand, and gravel (besides lime filler and cement)
- Organic aggregates: crushed walnut shell, grape seeds, and cherry pits (besides sawdust)

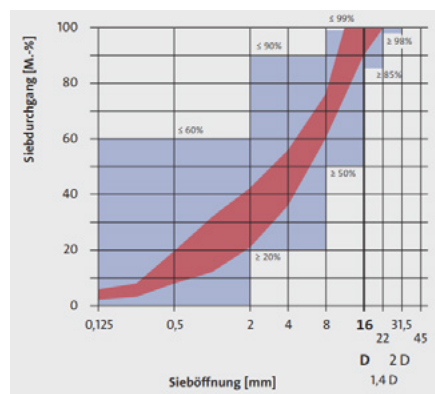


Figure 1: PSD limits for concrete aggregates [12].

2.2 Fresh-state properties

The first selection phase targeted at evaluating self-compaction and manufacturing performances. The latter considers mixing time, workability, necessary quantity of added water, and possible segregation effects while the former looks at slump flow classes, Table 1. For self-compacting concrete, SF2 is usually targeted in practice while the other two classes are only required or admitted, respectively, in special cases.

Table 1: Slump Flow (SF) requirements for self-compacting concrete [14].

Slump Flow class	Flow diameter
	mm
SF1	550-650
SF2	660-750
SF3	760-850

These different criteria are considered in a weighted multi-criterion ranking.

2.3 Mechanical properties

Density, elastic modulus and compressive strength were determined on cylinder specimens, with 150 mm diameter and 300 mm height, at 3, 7 and 28 days. Compressive strength was determined in an automatized test bench. For stiffness at 3 days, manual jack management was applied due to the expected low values, based on earlier experience. As results were considerably higher, the automatized test bench could also be used at 7 and 28 days. Test specimens were stripped 1 day after concreting and stocked in a climate chamber.

Strength development as a function of hardening time is assessed by [15]:

$$f_{cm}(t) = \beta_{cc}(t) \cdot f_{cm} = f_{cm} \cdot e^{s(1-\sqrt{28/t})} \quad (1)$$

where f_{cm} = average cylinder compressive strength, t = age in days, and s = strength development exponent. Specific exponents are derived from experimental results, and can be compared to values between 0.25 and 0.20 for normal and rapid cement hardening, respectively, in regular concrete. For lightweight concrete, high strength aggregates should provide $s = 0.05$ while $s = 0.25$ for low strength aggregates [15].

Correlations between average elastic modulus E_{cm} and f_{cm} are based on the expression from [16] for regular LC. It considers impacts of aggregate type and concrete density ρ

$$E_{cm} = k_E \cdot f_{cm}^{1/3} \cdot \eta_{lE} = k_E \cdot f_{cm}^{1/3} \cdot \left(\frac{\rho}{2200}\right)^2 \quad (2)$$

where k_E = aggregate type coefficient, and η_l = correction factor for LC stiffness. Experimental results are used to calibrate specific k_E values and are compared to standard values, varying between 8'000 and 12'000 for river bed gravel aggregates, between 8'000 and 10'000 for crushed lime aggregates, and between 6'000 and 8'000 for micaceous rock aggregates, respectively. Deviations from these values are possible, particularly for self-compacting concrete [16]. As this formulation contains 3 unknowns (aggregate factor, strength exponent, and density exponent) but only 2 independent test results are available, i.e. f_{cm} and ρ , more specific expressions cannot be calibrated from the test results.

2.4 Economic and ecological performances

Economic performances of the retained WooCon recipes were established, on the basis of lab test purchase prices (Table 2) to determine unit prices per m³. Organic aggregate prices are high because they are not sold (yet) in industrialised quantities.

Table 2: Approximate cost and GWP indicators of basic materials [3].

Component	Purchase price		GWP
	CHF/m ³	kg CO ₂ eq./m ³	
PC 52.5R	1'770	0.129	
Lime filler	330	0.155	
Sawdust	25	0.011	
Superplasticiser	8'300	0.030	
Sand / gravel	60	0.014	
Expanded clay	420	0.417	
Expanded glass	400	0.207	
Crushed walnut	3'800	0.001	
Grape seeds	4'500	0.001	
Cherry pits	3'300	0.001	
LC 12/13	500	0.417	
WCC with sand [2],[10]	230	0.114	

These cost estimations are further compared to a regular LC 12/13 [16] w.r.t. unit prices but also in a (simplified) construction context, considering material densities and strengths. Analogous evaluations are done for estimative ecological performance, for global warming potential (GWP) per m³ and in contextualized construction situations. Table 2 shows the admitted impact per WooCon component, partly based on [17]. Organic aggregates are principally waste and water is considered free.

3. Results and discussion

3.1 Recipe design

In all recipes, cement content was 300 kg/m³, with lime filler at 250 kg/m³, and sawdust at 60 kg/m³, with a constant ratio $w/c = 0.5$. As a function of the aggregate types incl. their individual PSD, the necessary proportions were determined with Figure 1.

Table 3 shows an overview of the WooCon recipes (respecting confidential information, see section 2), expected densities and unit prices. Mix designs with artificial mineral lightweight aggregates (expanded clay and glass) are interesting w.r.t. to unit price but generally result in greater density. Mix designs with organic aggregates result in lighter concrete mixes but also in considerably increased unit cost.

Table 3: General composition of WooCon aggregates and percentage of organic aggregates.

Recipe	LECA	MISAPOR	Sand/ gravel	Walnut shell	Grape seeds	Cherry pits	Organic aggregates	Density kg/m ³	Cost CHF/m ³
1	20%	68%	12%	–	–	–		890	350
2	45%	43%	12%	–	–	–		900	350
3	20%	25%	55%	–	–	–	0%	1'160	310
4	45%	–	55%	–	–	–		1'170	310
5	–	68%	32%	–	–	–		1'000	330
6	X	X	X	–	–	X	25%	910	540
7	X	X	–	X	–	X	37%	840	660
8-9	X	X	–	X	–	–	12%	820-830	470
10-11	X	X	–	–	X	–		820-830	490
12	–	X	–	X	X	X	57%	860	870
13	–	X	–	–	X	X		850	890
14	X	X	–	–	X	X	37%	840	680
15	–	X	X	–	X	X	45%	920	750
16	X	X	–	–	X	–	32%	840	700
17	–	X	–	–	X	–		830	700

3.2 Fresh-state properties

Mix designs 16 and 17 were not further considered due to their closeness to other recipes but at higher cost. The remaining 15 WooCon recipes were tested according to the multi-criteria approach, Table 4.

Purely mineral-based WooCon recipes perform relatively poor at the fresh state. This is partially due to long mixing time but, above all, due to the quantities of added water necessary to reach a satisfactory workability. This can essentially be explained by the very porous aggregates with very high water absorption. These voids must be filled before additional water is available for creation of the cement paste. Only recipe 3 attained the usually required slump flow class SF2.

Most recipes with organic aggregates perform considerably better at the fresh state; none reaches SF2 but all figure in class SF1. Recipes 11 and 15 showed the highest slump flows, close to the lower limit of SF2;

however, they also showed unacceptable segregation effects. Comparing to Table 3 shows no correlation between organic aggregate content and slump flow, nor to manufacture performance, in general.

Based on Table 4, recipes 6, 10, 12, 13 and 14 were retained for short-term hardened state testing. The necessary water to improve workability and slump flow can be explained by different reasons: mixer and handling equipment are moistened, binding some of the initial water; but, more important are the mix components: lime filler, sawdust, and porous aggregates absorb a lot of water and need to be saturated before water is available for the cement paste. Stripping of test specimens showed that the additional water leaches (“sweating” and evaporation). Nevertheless, w/c ratios are different from the target value, and result in 0.66, 0.69, 0.67, 0.64, and 0.74 for recipes 6, 10, 12, 13, and 14, respectively.

Table 4: Multi-criteria evaluation of fresh-state properties.

Criterion	SF diameter	Mixing time	Workability	Added water	Segregation	Slump Flow	Total
Weight		1	1	2	2	1	15
Maximum points	mm	2	2	3	1	3	
1	600	0	0	0	1	2	4
2	480	0	0	0	1	0	2
3	665	2	2	0	1	3	9
4	565	1	1	0	1	1	5
5	625	1	1	0	0	2	4
6	570	2	2	2	1	1	11
7	590	2	2	2	0	1	9
8	565	1	1	2	1	1	9
9	465	1	1	1	1	0	6
10	595	2	2	3	1	1	13
11	630	1	1	2	0	2	8
12	585	2	2	3	1	1	13
13	560	2	2	3	1	1	13
14	535	2	2	2	1	0	10
15	625	2	1	2	0	2	9

3.3 Mechanical properties

3.3.1 Density

Experimental density showed considerable difference to expected values (Table 3). Table 5 shows average values and coefficients of variation (COV). The latter confirm homogeneous mixing. As the experimental densities are approx. 1.8-1.9 higher than expected, further investigations were performed, besides the leaching identifies at stripping. Test samples prepared by wet-grinding, leading to sample saturation of the containing considerable amounts of porous and water-absorbing components (sawdust, expanded clay and expanded glass aggregates). Oven-drying at 120°C during 24h revealed approx. 25% humidity content.

A further reason was suspected in the possibility that material masses can partially occupy the same volume, i.e. the components settle when mixed, adding to the porosity. Rough experimental verification showed that dry-mixed components loose approx. 30 Vol.-% when wetted. Combining different components in groups of two showed that water is absorbed up to 90% by porous components, and that PC and lime filler are absorbed up to 30% in sawdust or expanded glass volumes. These effects needs to be considered when material densities and fabrication volumes are predicted.

Table 5: Experimental densities and comparison to expected values.

Recipe	Expected density kg/m ³	Experimental densities					
		At 3 days		At 7 days		At 28 days	
		kg/m ³	COV	kg/m ³	COV	kg/m ³	COV
6	910	1630	2%	1610	1%	1660	1%
10	830	1590	3%	1570	2%	1580	1%
12	860	1570	1%	1560	1%	1600	2%
13	850	1580	1%	1560	1%	1600	1%
14	840	1540	1%	1510	1%	1550	1%

3.3.2 Strength and development

Table 6 shows average values and COV of compressive strength at the different test days, also recalling the percentages of organic material in the aggregate skeleton.

Table 6: Compressive strength at different ages.

Recipe	Organic aggregates	Compressive strength							
		At 3 days			At 7 days			At 28 days	
		MPa	COV	s	MPa	COV	s	MPa	COV
6	25%	13.6	4.4%	0.138	14.9	0.9%	0.189	18.0	1.8%
10	12%	15.6	7.1%	0.093	17.2	3.9%	0.093	18.9	0.5%
12	57%	8.3	7.5%	0.243	11.2	3.6%	0.198	13.6	4.0%
13	57%	8.0	2.8%	0.233	10.6	3.7%	0.197	12.9	2.5%
14	37%	10.7	4.8%	0.128	11.8	3.5%	0.163	14.0	3.8%

Figure 2 (a) shows the correlation between content of organic aggregates in the skeleton and the reference strength at 28 days. A reduction trend in compressive strength as a function of organic aggregate content is visible, but only from a approx. 20% or $\eta_{fc} = (30/f_{ck})^{1/3} \leq 1$. In analogy to [16] where a reduction coefficient for high-strength concrete of is prescribed for determining design values, a correction factor $\eta_{fc,org}$ for organic aggregates is proposed, referring to a regular, purely mineral-based LC with $f_{cm,0} = 18.8$ MPa (i.e. value of recipe 10), shown as dashed line in Figure 2 (a):

$$\eta_{fc,org} = \left(\frac{0.2}{\rho_{org}} \right)^{1/3} \leq 1 \quad (3)$$

where ρ_{org} = percentage of organic aggregates in the skeleton.

The experimental results were also used to determine strength development exponents s , Eq. (1), Table 6. Such values cannot be determined for 28 days test results, see Eq. (1). Values are close to or below the value for PC 52.5R ($s = 0.20$), Figure 2 (b), except for 3 days test results of recipes 12 and 13. Overall, the WooCon recipes show a normal or rapid strength development for organic aggregates content up to approx. 40%. The higher is the organic content, the slower is the strength development. Referring to lightweight concrete, the strength development generally seems to be below or closer to low strength aggregates ($s = 0.25$) than to high strength aggregates ($s = 0.05$), except for recipe 10. This recipe has the lowest organic aggregate content, and it confirms that the mineral lightweight aggregates can be considered high strength.

Figure 2 (b) shows a clear influence of the percentage of organic aggregates: the higher it is, the slower is the strength development (recipe 6 is somewhat above this trend). Thus, organic aggregates seem to be low strength in the understanding of [15]. Except for recipes 12 and 13 with the highest organic aggregate contents, the strength development at 3 days is faster than at 7 days.

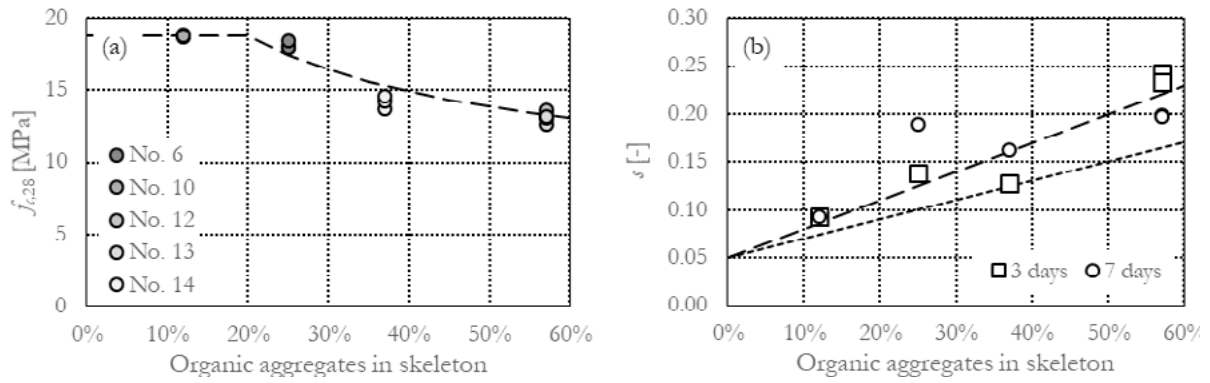


Figure 2: Correlation between organic aggregate content and (a) compressive strength at 28 days, and (b) strength development over 3 and 7 days.

The dotted line in Figure 2 (b) also shows a simple interpolation for high and low strength aggregate values from [15], admitting fast development ($s = 0.05$) for 100% mineral lightweight aggregates and normal development ($s = 0.25$) for 100% organic aggregates; as all experimental values are above this line (and thus, the mixes harden slower than predicted by this interpolation), there seems to be a limit of organic matter of approx. 70% where the upper limit of [15] is reached. Based on the few available results, a formulation for strength development of WooCon mixes s_{org} is proposed, shown as dashed line in Figure 2 (b):

$$s_{org} = 0.05 + 0.30 \cdot \rho_{org} \quad (4)$$

3.3.3 Correlation of elastic modulus and strength

Table 7 shows average values and COV at the different test days, also recalling the percentages of organic material in the aggregate skeleton. The values are given with two significant digits in view of practical relevance. Figure 3 (a) shows the correlation of experimental compressive strength and elastic modulus: not surprisingly, stiffness increases with increasing compressive strength which, in turn, depends on the organic content (Figure 2 (a)).

Table 7: Elastic modulus at different ages.

No.	Organic aggregates	Elastic modulus											
		At 3 days				At 7 days				At 28 days			
		MPa	COV	η_E	k_E	MPa	COV	η_E	k_E	MPa	COV	η_E	k_E
6	25%	6900	9%	0.55	5'300	7700	2%	0.54	5'800	9000	1%	0.57	6'100
10	12%	7700	6%	0.52	5'900	7700	6%	0.51	5'900	8500	1%	0.52	6'200
12	57%	4500	7%	0.51	4'400	5400	6%	0.50	4'800	6100	3%	0.53	4'800
13	57%	4600	3%	0.52	4'500	5400	3%	0.50	5'000	6500	4%	0.53	5'200
14	37%	5300	18%	0.49	4'900	5600	5%	0.47	5'200	6200	5%	0.50	5'200

Eq. (2) is used to determine individual k_E values, considering η_E from Table 7. For mineral aggregates only, k_E seems to be in the recommended order for micaceous rock aggregates (albeit, rather at the lower limit of $k_E = 6'000$), which seems principally plausible for the relatively soft lightweight mineral aggregates. Thus, the use of η_E alone is not sufficient for predicting the stiffness of LC containing organic aggregates and thus, the directives of [16] cannot be transposed to WooCon like that. There also seems to be a limit of approx. 20% of organic aggregate content below which no significant effect of using organic aggregates can be observed, as it is also the case for the compressive strength (Figure 2 (a)).

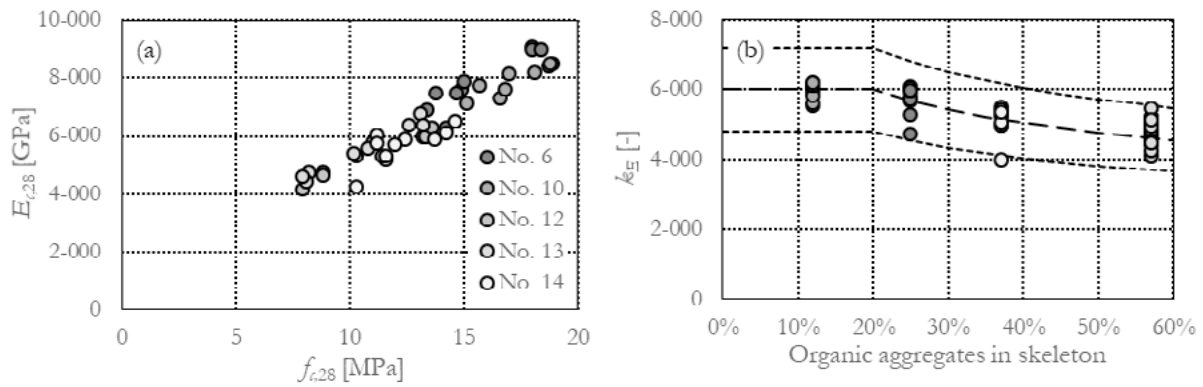


Figure 3: Correlation between (a) compressive strength and elastic modulus, and (b) organic aggregate content and average aggregate type coefficient [16].

Admitting that the expression for η_E and the exponent to f_{cm} in Eq. (2) remain unchanged, an additional correction factor $\eta_{E,org}$ for consideration of organic aggregates is proposed (based on the few available results), referring to a basic (and conservative) value of $k_{E,0} = 6,000$ for purely mineral-based LC (i.e. 0% organic aggregates), shown as dashed line in Figure 3 (b) together with a variation bandwidth of $\pm 20\%$:

$$\eta_{E,org} = \left(\frac{0.20}{\rho_{org}} \right)^{0.25} \leq 1 \quad (5)$$

Figure 3 (b) shows that, with this correction, there is a reasonable correlation to experimental results.

3.4 Economic and ecological performances

3.4.1 Economic performance

With the input from Table 2, the economic performance is determined per WooCon recipe and compared to a standard LC 12/13, having approximately the same average compressive strength, and to an earlier WCC containing sand [2],[10]. The elastic modulus of the LC is estimated from Eq. (2), admitting $k_E = 6,000$ and $\rho = 1,600 \text{ kg/m}^3$ (ca. average of WooCon recipes) while for the WooCon recipes and the earlier WCC the reported values are applied.

A first comparison addressed the cost per m^3 . Further comparisons, neglecting stability problems, relate to the cost of 1 m^2 of wall with 3 m height supporting 300 kN/m on top, failing in compression at the bottom and with self-weight being considered, and to the same wall limiting its shortening to 3 mm . These two cases require a certain thickness which, in turn, results in a cost per m^2 . All results are normalized to the performance of the regular LC, with Figure 4 showing the results.

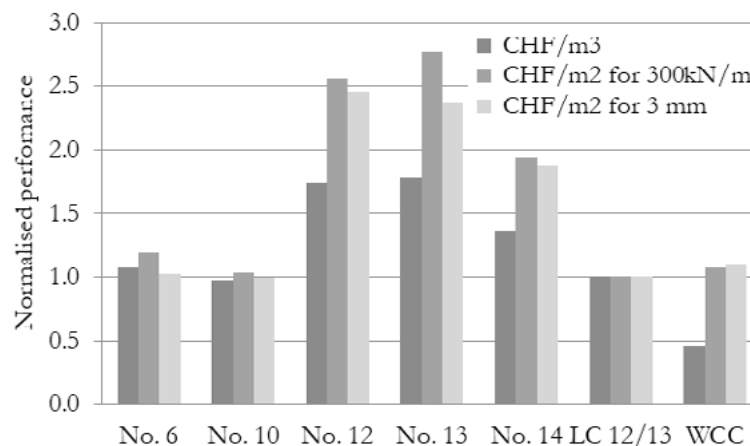


Figure 4: Comparison of economic performances.

Recipes 6 and 10 have cost per m³ comparable to a regular LC while recipes 12 and 13, with the highest contents of expensive organic aggregates, are up to approx. 75% more expensive. Recipe 14 costs approx. 35% more than a regular LC. All current recipes show considerably higher unit cost than the earlier WCC; this is not really a surprise, as further and more expensive components are added in the current mixes. 25-40% of cost are associated to the cement and lime filler, and 30-65% come from the organic aggregates.

In terms of cost per m² for strength of the evaluated wall, recipes 6 and 10 show an economic performance increase smaller than 20%. Recipes 12 and 13 cost up to 180% more. Recipe 14 almost reaches the double cost of a regular LC. Earlier WCC shows a comparable cost to the latter. Considering required stiffness in cost evaluation, recipes 6 and 10 perform as a regular LC while recipes 12 and 13 cost up to 150% more. Recipe 14 requires almost 90% of additional cost. Earlier WCC requires some 10% of additional cost in comparison to regular LC.

3.4.2 Ecological performance

Figure 5 shows comparative ecological performances, referring to the cases of economic performance.

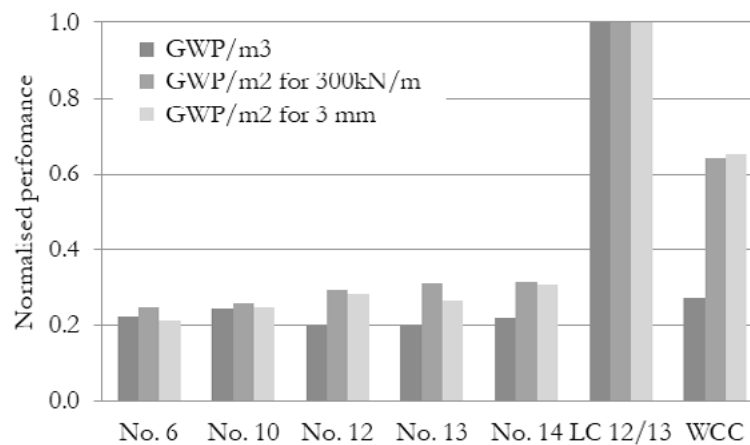


Figure 5: Comparison of ecological performances.

This comparison shows the greatest impact of using organic aggregates, resulting in a GWP reduction of approx. 80% in comparison to regular LC. All WooCon recipes also perform better than earlier WCC, with reductions of 20-30%. Considering GWP for strength of the evaluated wall, reductions of 70-75% are possible with WooCon in comparison to regular LC. Compared to earlier WCC, reductions of 50-60% are found. Considering stiffness requirements of the evaluated wall, GWP is reduced by 70-80% using WooCon instead of regular LC while reductions of 50-70% are found compared to earlier WCC.

3.4.3 Combined impacts

To compare ecological impact to economic consequences, reference is made to the cases of wall strength and wall stiffness, Figure 6. Recipes 6 and 10, with a moderate content of organic aggregates up to 25% are the most viable option. Comparing earlier WCC to regular LC, it becomes evident that this development was the good way to go, as cost remain approximately comparable but ecological impact is considerably reduced. However, their poor mechanical performance did require improvement, as explored here.

Adding an aggregate skeleton definitely did improve strength and stiffness, and can be achieved by very moderate cost increase if a wise selection of aggregate types is done. As replacing mineral lightweight aggregates with organic aggregates comes at increased price but also decreased mechanical performance, overall resulting in increased ecological impact, a compromise must be found. From the data collected in this study, it can be concluded that a maximum of approx. 25% of organic aggregate content should

be respected if material cost increases shall be limited to 20%. Going beyond this replacement ratio of mineral-based lightweight aggregates results in over-proportional cost increased for a small gain in ecological performance. The most important impact, however, would probably be achieved if organic aggregates would be available in industrial volumes.

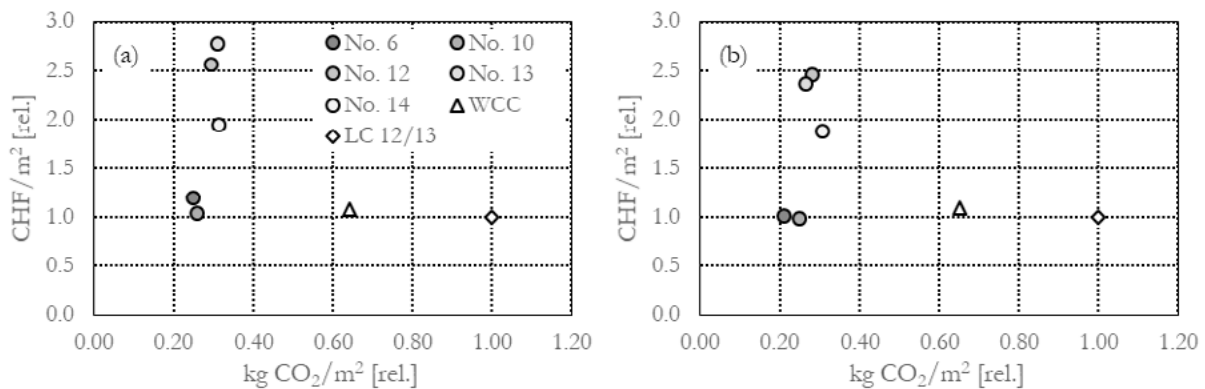


Figure 6: Comparison of ecological performances and economic consequences for (a) wall strength and (b) wall stiffness.

3.5 Outlook

Long-term properties evaluation, i.e. shrinkage and creep tests, is currently ongoing for recipes 6, 10, and 12, started at the beginning of February 2019 and extending over 1 year. Having three test benches available, two of the five recipes had to be discarded. Recipe 13 has been eliminated as it contained a fewer number of organic aggregates while recipe 14 was not further considered due to the poor slump flow performance.

Further advances of WooCon recipes target the replacement of lime filler and cement with more advanced cement types (e.g. CEM V or VI) as well as the development and the identification of new types of lightweight aggregates to be applied – obviously, with a limited ecological impact and at reduced cost.

4. Conclusions

The results of this study allow to draw the following conclusions:

- Integrating an aggregate skeleton in wood-cement compounds (WCC), transforming them into “real” lightweight wood-based concrete (WooCon) increases workability and allows attaining, for certain compositions, minimum slump flows required for self-compacting concrete. Mixes with organic aggregates generally perform better at fresh state than mixes with purely mineral-based aggregates.
- Density and production quantity predictions of hardened WooCon are challenging, due to the partial fusion of components into the same volumes (water into expanded aggregates, cement and lime filler into sawdust and expanded glass aggregates) and due to the water-absorbing behaviour (up to 25% of humidity in saturated samples). Overall, these effects may result in volume loss factors up to 1.9.
- Stiffness and strength of WooCon are considerably higher than those of WCC. Stiffness can go up to values comparable to timber while strength attains values comparable to regular low-strength lightweight concrete (LC), being principally suitable for structural applications. Both, stiffness and strength, depend on the content of organic matter in the aggregate skeleton, starting to decrease (in comparison to mineral-based LC) from approx. 20% organic content. Preliminary expressions for reduction factors as a function of organic aggregate content are proposed in the paper.
- Strength development of WooCon is comparable to regular LC and is principally acceptable for industrial fabrication. It also depends on the organic aggregates content: the more organic aggregates, the slower the strength development. A preliminary prediction expression is also given in the paper.

- Elastic modulus and compressive strength can be correlated according to code expressions. Predicting elastic modulus as a function of compressive strength also requires introducing a reduction coefficient for organic aggregate content higher than 20%, for which an expression is given in the paper.
- The economic performance of WooCon can be comparable to regular LC if organic aggregate content is limited to approx. 25%. Higher organic aggregate contents lead to more than proportional reductions of stiffness and strength, requiring larger material volumes. This conclusion strongly depends on the future development of potential availability of organic aggregates on industrial scale.
- The ecological performance of WooCon, compared to regular LC, is improved by up to 80%. An optimum organic aggregate content, for the input hypotheses, again seems to be at approx. 25%.
- Economic and ecological performance evaluations should always be contextualised, e.g. for same load-bearing capacity or stiffness of a structural element; comparing unit impacts alone may be misleading.

5. Acknowledgment

This paper is based on the results from a Master's semester project [3] by Mr. Adam Attila Meszes. His high personal investment and the practice-oriented approaches applied in the project are highly acknowledged.

6. References

1. Zwicky D. (2015). "Mechanical Properties of Wood-Cement Compounds". In: Proceedings of the 10th Conference on *Advanced Building Skins*, Berne, Switzerland, pp. 126-135.
2. Macchi N. & Zwicky D. (2016). "Pourable Wood-Cement Compounds – Properties, Potential and Challenges of a New Structural Material". In: Cruz P.J.S. (ed.), *Structures and Architecture: Beyond their Limits*, Proceedings of the 3rd *International Conference on Structures and Architecture* (ICSA), Guimarães, Portugal, Leiden: CRC Press/Balkema, pp. 145-152.
3. Meszes A.A. (2019). *Optimisation des recettes des bétons allégés par le bois*. Semester project report, Master course, Univ. of Applied Sciences and Arts of Western Switzerland HES-SO, School of Engineering and Architecture Fribourg HEIA-FR, Switzerland.
4. Ropp J. (2014). *Combustion and behaviour of a wood-cement composite (WCC) at high temperature*. Internal report AGP 38761, Systèmes Industriels de Bioénergies SIB, Institut de Génie Thermique IGT, Haute Ecole d'Ingénierie et de Gestion du Canton de Vaud HEIG-VD.
5. Ropp J. (2015). *Combustion of a timber-WCC slab*. Supplement to internal report AGP 38761, SIB, IGT, HEIG-VD, Switzerland.
6. Zwicky D. & Macchi N. (2016). "Wall Elements made of Timber and Wood-Cement Compounds – Building-Physical Properties and Structural Performance". In: Cruz P.J.S. (ed.), *Structures and Architecture: Beyond their Limits*, Proceedings of the 3rd *International Conference on Structures and Architecture* (ICSA), Guimarães, Portugal, Leiden: CRC Press/Balkema, pp. 75-83.
7. Maeder M. & Zwicky D. (2016). "Multi-functional Features of Pourable Wood-Cement Compounds – Mechanical, Building-physical, Economic and Ecological Performance"; In: Eberhardsteiner J., Winter W., Fadaei A. and Pöll M. (eds.), *Proceedings of the World Conference on Timber Engineering* (WCTE), Vienna, Austria, paper ID 1059.
8. Zwicky D. (2015). "Combustibility of Wood-Cement Compounds". In: Proceedings of the 10th Conference on *Advanced Building Skins*, Berne, Switzerland, pp. 164-172.

9. Ruch H. (2017). *Options de recyclage/ réutilisation des bétons allégés par le bois*. Semester project report, Bachelor course, HEIA-FR, Switzerland.
10. Macchi N. (2015). *Development of self-compacting wood-concrete compounds*. Semester project report, Master course, HES-SO, HEIA-FR, Switzerland.
11. Maeder M. and Zwicky D. (2016). “Ecological Performance of Timber / Wood-Cement Compound Composite Slabs”; In: Habert G. and Schlueter A. (eds.), *Expanding Boundaries: Systems Thinking in the Built Environment*, Proceedings of the *Sustainable Built Environment (SBE) regional conference*, Zurich, Switzerland, Zurich: vdf, pp. 702-706, DOI 10.3218/3774-6_113.
12. EN 12620 (2002). *Aggregates for concrete*.
13. Holcim (2015). *Guide pratique du béton – Concevoir et mettre en œuvre des bétons durables*. Holcim Edition, Switzerland, 6th edition.
14. EN 206-1 (2013). *Concrete – specification, performance, production and conformity*.
15. Model Code (2010). *Model Code: Final draft, Vol. 1*. Lausanne: fib, bulletin no. 65.
16. SIA 262 (2013). *Construction en béton*. Zurich: Swiss Society of Engineers and Architectes SIA.
17. KBOB (2016). *Ökobilanzdaten im Baubereich*, edition 2009/1, revision 2016.

Fire resistance of aerated alkali-activated cements

J. Rodriguez-Sanchez ^{1,2}, M. Fedorciuc-Onisa ², H. Kinoshita ¹, J.L. Provis ¹, S. MacLachlan ²

¹ Department of Material Science and Engineering, University of Sheffield, Sheffield S1 3JD, United Kingdom,

² Lucideon Limited, Stoke-on-Trent ST4 7LQ, United Kingdom.

Abstract

The present study investigates the effects of long-time exposure to moderate and high temperatures on the strength, mass, volume, and chemical composition of aerated alkali-activated cements. Pure metakaolin, pure ground granulated blast furnace slag and their blends with different weight ratios are studied to understand the roles of each solid precursor against fire attack. Different design compositions are also prepared with varied porosity to investigate the relationship between mechanical strength and porosity after fire exposure. Preliminary results show that the strength of foamed metakaolin-based specimens drops progressively when exposed at temperatures up to 750 °C, beyond which it starts to rise due to densification of the gels to form glass and ceramics. The results also suggest that all chemically and physically bound water within the samples is vaporized after 4 h exposure to 750 °C, while the volume shrinkage increases continuously from 11.8 % at 500 °C to 52.4 % at 1000 °C. The collapse of the pore structure and the loss of free water might be the main reasons for the large shrinkage rates and the strength loss of this composition type. The information obtained regarding the effects of composition and pore structures will allow a higher degree of control over the fire resistance properties of sustainable alkali-based concretes.

Keywords: Sustainability; Alkali-activated concrete; Porous concrete; Fire resistance.

1. Introduction

Its mechanical properties, abundance of raw materials, and relatively low-cost production have made Portland cement (PC)-based concrete the most commonly used construction material worldwide. However, when PC-based concrete is exposed to high temperatures, such as in a fire, physical and chemical transformations take place, resulting in deterioration of its mechanical properties. This deterioration varies according to the concrete mix proportions, constituents, and porous structure, and can be determined by complex physicochemical transformations occurring during heating [1].

The hydration of the silicate constituents of PC yields two main hydration products. Calcium-silicate-hydrate (C-S-H) is the most abundant whilst calcium hydroxide ($\text{Ca}(\text{OH})_2$), also known as portlandite, is the secondary phase and plays an important role in the chemical and microstructural composition of the cement paste and its behaviour against fire [2]. Its relatively low thermal decomposition temperature of about 400 °C determines the breakdown of PC pastes. Even if PC-based structures or construction materials are able to withstand a fire above that temperature, a complete evaluation of their remaining mechanical properties will still be necessary after cooling since the thermal decomposition of $\text{Ca}(\text{OH})_2$ is commonly followed by the expansive rehydration of lime (CaO) which can induce further damage in the long term, potentially with fatal consequences [3].

Another key parameter in determining fire resistance is the porosity of the concrete structure. During fire attack, gel water and pore solution are vaporized both out of the sample and towards the unheated face of the concrete body which is being attacked due to the lower pressures of these regions. However, if the permeability of the pore structure is not high enough, the steam can cause a moisture clog. As a result, the very dry zone which spans from the clog to the external surface of the concrete body will experience a continuous pressure build-up which may lead to its explosive spalling [4]. This phenomenon is common for PC-based concretes and especially for high strength PC concretes since they typically have a relatively small average pore size and low degree of pore connectivity, and both of these increase the risk of spalling [5,6].

Unlike PC, alkali-activated cements not only exhibit a much better behaviour against fire but also show excellent final mechanical properties, good chemical stability, and low attributed CO₂ emissions [7,8]. They are derived from the reaction of solid aluminosilicates sourced from metallurgical slags, coal fly ash and/or calcined clays, with an alkaline solution (typically hydroxide or silicate-based) that induces the formation of strong, insoluble binding phases including calcium-aluminium-silicate-hydrate, C-A-S-H, and/or sodium/potassium-aluminium-silicate-(hydrate), N/K-A-S-(H), gels [9], but not portlandite unless Portland cement or lime is added within the mixture design. The relatively high decomposition temperatures of these binding phases (which can be as high as 1000-1200 °C for N/K-A-S-(H) [10]), together with a larger average porosity and lack of chemical and mechanical structural damage caused by their dehydration, make alkali-activated concretes one of the most attractive substitutes for PC in applications which require outstanding fire resistance properties [7]. However, despite a large number of studies dealing with the fire resistance of alkali-activated cements [7,9–13], the effect of the alkali-activated cement composition and its pore structure on their fire resistance properties has not yet been studied systematically across the full range of compositions of potential commercial interest.

The present study investigates the effects of relatively long-time exposure (4 h) to moderate and high temperatures (500 – 1000 °C) on the strength (flexural and compressive), mass, chemical composition and shrinkage of alkali-activated cement samples with varying composition and porosity. The results will help in understanding the relationship between mechanical strength and porosity after fire exposure, which will allow a higher degree of control over the fire resistance properties of sustainable alkali-based concretes for multiple applications.

2. Methodology

2.1 Materials

2.1.1 Raw materials

The aluminosilicate sources used in this work are metakaolin (MK) Metafort, (Sibelco Ltd, Belgium), and ground granulated blast furnace slag (GGBS) from Hanson UK. Pure sodium hydroxide (NaOH) pellets and K120 potassium silicate solution (density 1.60 g/cm³) were supplied by Tennants Distribution Ltd. (Manchester, UK) to prepare the activator solutions. The foaming agent is supplied by Sika (Baar, Switzerland).

2.1.2 Specimen preparation

NaOH pellets were dissolved in water and subsequently mixed with K120 solutions using a mechanical mixer. Pure MK, pure GGBS or combinations of these powders were then added to the mixer batch and mixed with the activator solutions. The amounts of activator solution, GGBS and MK powders were adjusted to achieve target molar ratios of Na:K:Al:Si:H₂O, and activator/binder ratio. By the end of the mixing stage of the binder, foam was prepared and immediately mixed with the binder slurry at several binder/foam ratios (wt.). The foamed slurries were subsequently poured into three-gang moulds with 40

x 40 x 160 mm dimensions, and covered with polyethylene film. The specimens were then cured and subsequently demoulded afterwards for their characterization.

2.2 Methods

2.2.1 Pore structure

The pore structure of the specimens is assessed by mercury intrusion porosimetry (MIP). A geometrical model based on the Washburn equation, as shown in (1), is applied to determine the pore diameter.

$$D = -4 \gamma \cos \theta / P, \quad (1)$$

where D (m) is the calculated pore diameter, γ (N/m) is the surface tension, θ (°) is the contact angle between mercury and the pore wall, and P (Pa) is the applied pressure. The surface tension (γ) and contact angle (θ) selected in this study are 0.485 N/m and 140°, respectively [14]. The applied pressure (P) ranges from 0.007 to 207 MPa.

2.2.2 Fire resistance

Foamed geopolymer specimens with different compositions and binder/foam ratios were fired at 500 °C, 750 °C, and 1000 °C for 4 h. Then, the specimens were naturally cooled down inside the kiln before determining the volume changes, mass losses, chemical composition changes and strength changes. Volume changes were measured using a calliper, mass losses using a precision balance, and chemical changes by scanning the samples under X-ray fluorescence (XRF). Flexural strength changes were measured according to the EN 196-1 [15] standard three-point bending test on 40 x 40 x 160 mm prisms using an ELE international compressive stage, whereas compressive strength was measured by the EN 196-1 standard compression test on 40 x 40 x 40 mm cubes using the same instrument. At least three replicates for each mix design were tested, and all experiments are performed using the same batches of raw materials, activators and water.

3. Preliminary results

An important aspect of the selection of construction materials for residential and commercial applications is the ability to retain structural integrity during and after fire exposure. Figure 1 shows the effect of fire attack on the compressive and the flexural strength of pure MK samples with a final density, ρ , of 600 kg/m³.

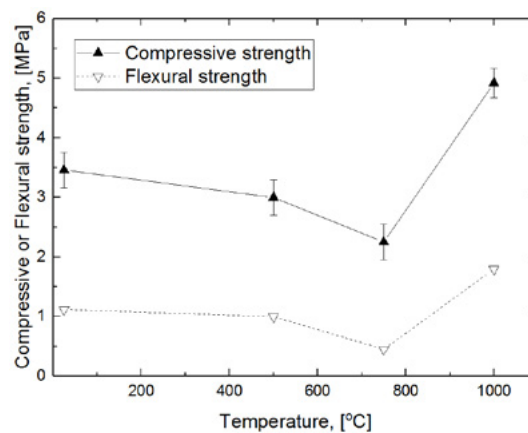


Figure 1: Compressive and flexural strength of MK-based samples ($\rho = 600 \text{ kg/m}^3$) after fire attack tests.

The compressive strength decreases from 3.46 ± 0.27 MPa at room temperature to 2.25 ± 0.34 MPa at 750

°C. Then, it rises up to 4.92 ± 0.22 after exposure to 1000 °C. A similar trend is observed for the flexural strength, but with lower values.

The mechanisms governing the strength variation are typically different for each kind of alkali-activated material. The strength of MK-based geopolymer binders usually tends to decrease gradually up to 800 °C, while it increases on exposure to 1000 °C [16], and the results in Figure 1 agree well with this trend. Duxson et al. [17] suggested that the transformation of reaction products from amorphous to crystalline (including anhydrous members of the zeolite family) at high temperatures can explain such behaviour. Amorphous aluminosilicate gels tends to lose free water below 200–300 °C with negligible change in the structural framework. After heating above this range, gels release chemically bound T–OH (T being either Si or Al) groups and condense to form T–O–T linkages, along with relocation of alkali cations, resulting in increased overall connectivity. The densified gels start to crystallise at a certain onset temperature, which is influenced greatly by the composition, in particular by the Si/Al ratio and alkali cation type [18]. For instance, Na-aluminosilicate geopolymer gel with Si/Al = 1.15 forms nepheline upon heating to 650 °C, and at 800 °C with Si/Al = 2.15 [17]. On the other hand, K-aluminosilicate geopolymer gels form tetragonal leucite at 1000 °C when starting from an initial composition of $\text{KAlSi}_2\text{O}_6 \cdot 4.78\text{D}_2\text{O} \cdot 0.72\text{H}_2\text{O}$ [13] or 1050 °C with a composition of $\text{KAlSi}_2\text{O}_6 \cdot 5.5\text{H}_2\text{O}$ [19].

The preliminary results included here are from samples which contain both Na and K cations and are characterized by Si/Al = 2.0. The chemical composition analysis is in progress to enable full description of the transformations taking place.

Figure 2 shows the relative change of volume and mass of MK-based samples ($\rho = 600 \text{ kg/m}^3$) after fire attack tests. In agreement with previous comments, it can be observed that the relative mass of the samples experiences very little changes when exposed to moderate temperatures (<5.0 % loss at 500 °C). It then drops considerably between 500 °C and 750 °C (up to ≈ 15.0 %) and then does not drop any further, even after exposure to 1000 °C (16.7 %), suggesting that all chemically and physically bound water within the samples has been vaporized. On the other hand, the relative volume of the specimens is less stable and it drops dramatically from 11.8 % at 500 °C to over a 52.0 % after firing at 1000 °C. The highest shrinkage increment appears between 750 °C and 1100 °C, and is probably related to a combined effect of gel sintering [20] and pore collapse.

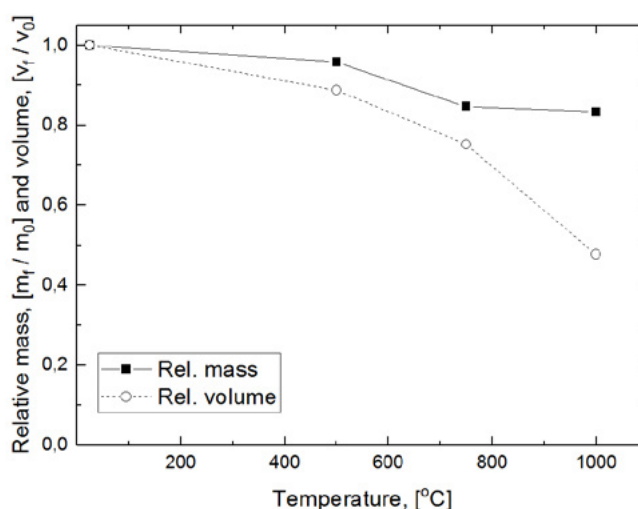


Figure 2: Relative changes of mass and volume of MK-based samples ($\rho = 600 \text{ kg/m}^3$) after fire attack tests.

Combining findings from strength and thermal shrinkage, our results agree well with previous studies [21] which have proposed that: (1) the large shrinkage along with the loss of free water are the main reason for the loss of strength below 800 °C; (2) the shrinkage due to the release of chemically bound –OH and gel densification at high temperature does not affect the strength to a major extent, and (3) the densification of the gels to form glass and ceramics above an onset temperature is the main reason for the post-cooling strength increase. Nevertheless, further studies and specially the characterization of the chemical changes will provide more information to explain the behaviour of the samples tested here.

4. Outlook

The present study is a work in progress. Further effort will complete the experimental programme and analyse and interpret the results.

To date, all tested samples had the same binder/foam ratio. The fire-resistance characteristics are expected to be better for those samples with a lower value, since a larger proportion of foam should yield more porous specimens and thus withstand heat transfer better. On the other hand, a larger porosity level will presumably result in poorer mechanical properties but the effect of fire attack still needs to be evaluated. Moreover, the role of the composition will be evaluated from the characterization of pure GGBS and MK/GGBS blends with different weight ratios. Based on previous results [11], samples with a higher initial amount of MK will be expected to exhibit better fire resistance properties since they will lead to the formation of N/K-A-S-(H) gels rather than C-A-S-H ones, which typically exhibit a lower thermal decomposition temperature. Furthermore, Duxson et al. [12] proposed that the resistance to dehydration shrinkage of alkali-activated MK samples is proportional to the Young's modulus of the samples. Binders with a higher Young's modulus should be able to withstand greater capillary strain forces developed during dehydration, and as such the onset temperature of the initial shrinkage will be higher. This future work will test these hypotheses and characterise the effect of the pore network structure and the Young's moduli.

5. Acknowledgment

The authors acknowledge the financial support of Innovate UK (Research and Innovation, United Kingdom) for the Knowledge Transfer Partnership grant (Grant no. 511331, KTP no. 11175).

6. References

- [1] G.A. Khoury, Effect of fire on concrete and concrete structures, *Progr Struct Eng Mater.* 2 (2000) 429–447.
- [2] S. Diamond, Calcium hydroxide in cement paste and concrete—microstructural appraisal. *Materials science of concrete special volume: calcium hydroxide in concrete*, Am. Ceram. Soc. (2001) 37–58.
- [3] G.A. Khoury, Compressive strength of concrete at high temperatures: a reassessment, *Mag. Concr. Res.* 44 (1992) 291–309. doi:10.1680/mac.1992.44.161.291.
- [4] M.Zeiml, D.Leithner, R.Lackner, H.A.Mang, How do polypropylene fibers improve the spalling behavior of in-situ concrete?, *Cem.Concr.Research.* 36 (2006) 929–942.
- [5] A. Behnood, M. Ghandehari, Comparison of compressive and splitting tensile strength of high-strength concrete with and without polypropylene fibers heated to high temperatures, *Fire Saf. J.* 44 (2009) 1015–1022. doi:10.1016/j.firesaf.2009.07.001.
- [6] K.D. Hertz, Concrete strength for fire safety design, *Mag. Concr. Res.* 57 (2005) 445–453. doi:10.1680/mac.2005.57.8.445.
- [7] F. Pacheco-Torgal, Z. Abdollahnejad, A.F. Camões, M. Jamshidi, Y. Ding, Durability of alkali-activated binders: A clear advantage over Portland cement or an unproven issue?, *Constr. Build. Mater.* 30 (2012) 400–405. doi:10.1016/j.conbuildmat.2011.12.017.
- [8] J.L. Provis, J.S.J. van Deventer, *Alkali Activated Materials*, Springer, 2014.
- [9] J.L. Provis, S.A. Bernal, Geopolymers and Related Alkali-Activated Materials, *Annu. Rev. Mater. Res.* 44 (2014) 299–327. doi:10.1146/annurev-matsci-070813-113515.
- [10] J.L. Provis, C.Z. Yong, P. Duxson, J.S.J. van Deventer, Correlating mechanical and thermal properties of sodium silicate-fly ash geopolymers, *Colloids Surfaces A Physicochem. Eng. Asp.* 336 (2009) 57–63. doi:10.1016/j.colsurfa.2008.11.019.
- [11] T.W. Cheng, J.P. Chiu, Fire-resistant geopolymer produce by granulated blast furnace slag, *Miner. Eng.* 16 (2003) 205–210. doi:10.1016/S0892-6875(03)00008-6.
- [12] P. Duxson, G.C. Lukey, J.S.J. Van Deventer, Physical evolution of Na-geopolymer derived from metakaolin up to 1000 °C, *J. Mater. Sci.* 42 (2007) 3044–3054. doi:10.1007/s10853-006-0535-4.
- [13] C.E. White, J.L. Provis, T. Proffen, J.S.J. Van Deventerz, The effects of temperature on the local structure of metakaolin-based geopolymer binder: A neutron pair distribution function investigation, *J. Am. Ceram. Soc.* 93 (2010) 3486–3492. doi:10.1111/j.1551-2916.2010.03906.x.
- [14] Y.S. Wang, J.L. Provis, J.G. Dai, Role of soluble aluminum species in the activating solution for synthesis of silico-aluminophosphate geopolymers, *Cem. Concr. Compos.* 93 (2018) 186–195. doi:10.1016/j.cemconcomp.2018.07.011.
- [15] BSI, BS EN 196-1:2016 Methods of testing cement. Determination of strength, (2016).
- [16] S.A. Bernal, E.D. Rodríguez, R. Mejía De Gutiérrez, M. Gordillo, J.L. Provis, Mechanical and thermal characterisation of geopolymers based on silicate-activated metakaolin/slag blends, *J. Mater. Sci.* 46 (2011) 5477–5486. doi:10.1007/s10853-011-5490-z.

-
- [17] P. Duxson, G.C. Lukey, J.S.J. Van Deventer, Evolution of gel structure during thermal processing of Na-geopolymer gels, *Langmuir*. 22 (2006) 8750–8757. doi:10.1021/la0604026.
- [18] D.L.Y. Kong, J.G. Sanjayan, K. Sagoe-Crentsil, Factors affecting the performance of metakaolin geopolymers exposed to elevated temperatures, *J. Mater. Sci.* 43 (2008) 824–831. doi:10.1007/s10853-007-2205-6.
- [19] P. Sarin, J.L. Provis, J.L. Bell, R.P. Haggerty, P.J. Chupas, J.S.J. van Deventer, P.E. Driemeyer, W.M. Kriven, Atomic Structure of a Cesium Aluminosilicate Geopolymer: A Pair Distribution Function Study, *Chem. Mater.* 20 (2008) 4768–4776. doi:10.1021/cm703369s.
- [20] P. Hlaváček, V. Šmilauer, F. Škvára, L. Kopecký, R. Šulc, Inorganic foams made from alkali-activated fly ash: Mechanical, chemical and physical properties, *J. Eur. Ceram. Soc.* 35 (2015) 703–709. doi:10.1016/j.jeurceramsoc.2014.08.024.
- [21] Z. Zhang, J.L. Provis, A. Reid, H. Wang, Geopolymer foam concrete: An emerging material for sustainable construction, *Constr. Build. Mater.* 56 (2014) 113–127. doi:10.1016/j.conbuildmat.2014.01.081.

Durability parameters of self-compacting concrete with binary and ternary combinations of Portland cement, limestone filler and metakaolin

L. R. M. Miranda¹, V. M. S. Capuzzo²

¹Magnel Laboratory for Concrete Research – Ghent University.

²Postgraduate Program in Structure and Civil Construction – University of Brasilia.

Abstract

The use of fine mineral additions in self-compacting concrete (SCC) is unavoidable to improve its self-sustaining characteristics and reduce consumption of Portland cement. The cement industry has been studying supplementary cementitious materials (SCM) that can fulfil world production demand, but it is important that this replacement is done rationally, ensuring that SCC performance is maintained for the setting conditions as well as the mechanical properties and durability. Corrosion of reinforcement is one of the main causes of concrete structures deterioration in urban environments rich in CO₂ been the carbonation of concrete one of the main mechanisms that lead to this corrosion. Carbonation is a phenomenon that occurs naturally in concrete structures, requiring the presence of a certain concentration of carbon dioxide and a certain moisture content in the atmosphere. Under natural exposure conditions (0.03 to 1% CO₂), the advance of the carbonation front takes several years to present analysable results. Therefore, many researches are developed using an accelerated test system. In this context, the aim of this work was to analyse the performance against accelerated carbonation of SCC with a 20% substitution of Portland cement by limestone filler and metakaolin, both isolated and in combination. The accelerated carbonation test followed the recommendations of ISO 1920-12: 2015. In addition, mechanical properties were measured and the mercury intrusion porosimetry (MIP) test was performed. The results of the mix containing only metakaolin were the best for all properties evaluated, indicating that the structure of its paste is the densest and most rigid of all concretes or that the use of metakaolin promoted an increase in the resistance of the paste transition zone with the aggregates. On the other hand, the mix with 20% of limestone filler had the worse mechanical performance and lower durability against carbonation. The filler effect was not able to compensate the Portland cement removal, probably due to the high w/c ratio adopted. The mix with the ternary combination, in general, presented a performance superior to the limestone one and inferior to metakaolin one, in all properties analysed.

Keywords: Carbonation, self-compacting concrete, supplementary cementitious materials.

1. Introduction

The use of fine mineral additions in SCC is inevitable to improve its self-compacting properties and reduce material consumption, especially Portland cement. This reduction decreases the heat of hydration generated by the high consumption of cement, besides bringing economic advantages. Several benefits can be seen in the use of mineral additions, and this use is already carried out in the production process or incorporated later as replacement or addition to the mass of cement used, so that the cement industry has been studying

supplementary cementitious materials that can fulfil world demand of production [1]. The use of mineral additions as a substitute for Portland cement is now a common practice in the construction industry, but it is important that this substitution be made in a rational way, ensuring that the performance of the SCC is maintained, both for the settings conditions and for mechanical properties and durability, resulting in the optimal design of a concrete with lower clinker amount. It is, therefore, necessary that the intrinsic requirements of any new system be evaluated [2].

This practice also comes with an environmental approach, as the construction sector is nowadays responsible for 40% energy consumption, 40% solid waste generation, 38% greenhouse gas emissions and 12% water depletion. One of the main environmental impacts of concrete itself comes from CO₂ emissions during Portland cement production, which accounts for more than 5% of the global anthropogenic release of CO₂. It is visible that reducing the clinker content of Portland cement will help to reduce the environmental impact of concrete [3-4]. Carbonation is one of the main causes of deterioration of concrete structures in urban environments rich in CO₂, being one of the principal mechanisms responsible for steel corrosion. The concentration gradient between the concrete and the environment leads to the diffusion of carbon dioxide, which reacts with the hydrated compounds of the cement, resulting in a reduction of the alkalinity of the system. Carbonation is a phenomenon that occurs naturally in concrete structures and it is directly related to the ease that carbon dioxide has to diffuse inside the concrete, the environmental conditions and the permeability properties of the concrete [5-7]. Works on carbonation in SCC fortify the vast incorporation of mineral additions and residues in the production of SCC, like [8] tungsten Mine Tailings, [9] waste glass powder, [10] municipal solid waste incineration (MSWI), [11] copper slag and [12] spent garnet.

Under natural exposure conditions (0.03 to 1% CO₂), the advance of the carbonation front takes several years to present analysable results. Therefore, many researches are developed using an accelerated test system, which submits the concrete to high levels of CO₂ and allows a rigid control of all exposure conditions, providing a rapid response of the behaviour of the material to carbonation. Due to no worldwide regulation analysis methods regarding accelerated carbonation test system, comparison of the results of researches conducted in several countries is difficult because of the great variability on test parameters. However, with the enactment of ISO 1920-12: 2015, which may be very relevant to future studies on accelerated carbonation, it is expected an improvement in this comparison possibility and a more solid database on the subject [7; 13-14].

In this context, the aim of this work was to analyse the performance under accelerated carbonation of self-compacting concretes with 20% replacement of Portland cement by limestone and metakaolin, isolated and combined, in order to verify the combined action of the additions. The fresh state parameters of the concretes were evaluated according to the definitions of Brazilian standard [16]. In addition, the mechanical properties were measured and the mercury intrusion porosimetry test was carried out to verify how the pore refinement influences the ingress of the deleterious agent.

2. Methodology

2.1 Materials

The following materials were used in the experimental program:

- Portland cement composite with filler (Brazilian CP II F - 40), with a minimum compressive strength of 40 MPa at 28 days;
- Limestone filler and metakaolin as mineral additions;
- Composition of two types of sands, a natural of quartz origin and a crushed of limestone origin, as small

aggregate;

- Two granulometric bands of large aggregate of limestone origin, one with a maximum characteristic size of 12,5 mm and the other with 19 mm;
- Third generation superplasticizer, with modified polycarboxylic ether chemistry.

The chemical composition of the fine materials used was obtained by the X-ray fluorescence spectrometry (EDX). From Table 1 is possible to notice the predominance of calcium oxide (75,2%) in the cement, since it is a composite cement with up to 10% of limestone, that is a high content of clinker and rich in calcium carbonate. The metakaolin, which is obtained from the calcination of kaolinite clays, is basically composed of silica (SiO_2) and alumina (Al_2O_3) in the amorphous phase. The limestone filler has 83.10% CaO by mass and the presence of SiO_2 (6.63%) in quartz and kaolinite is also observed.

Table 1: Chemical composition of the fine materials

Chemical compost	% by weight		
	Metakaolin	Limestone filler	Cement CP II F - 40
SiO_2	50,54	6.63	9.29
CaO	0.00	83.10	75.20
Al_2O_3	42.28	2.12	2.46
Fe_2O_3	3.23	2.16	4.41
TiO_2	1.63	0.26	0.53
K_2O	1.07	0.94	1.87
MgO	1.02	3.61	2.69
SO_3	0.09	0.23	2.76
SrO	0.00	0.96	0.47

2.2 Methods

2.2.1 Mix design

The experimental program carried out for the production and analysis of SCC was conceived considering a reference concrete (REF), with no substitution content and three scenarios of Portland cement substitution: 20% replacement of Portland cement by metakaolin (M20), 20% replacement of Portland cement by limestone (F20) and 20% Portland cement replacement by a composition of 15% metakaolin and 5% limestone (M15F5). The ternary mixture was performed because the synergy of the combination between calcined clays and limestone have presented favourable results as an alternative to clinker, as in the case of LC3 cement.

The SCC dosage was performed using the granular skeleton composition concept by the unit weight test. The granular skeleton of all mixtures was composed of 33.6% of gravel 19 mm, 14.4% of gravel 12.5 mm, 32% of crushed sand and 20% of natural sand. The limits determined by the ACI 237 R-07 of fixed binder consumption at 475 kg/m³ and fixed water/binder ratio (w/b) of 0.55 were used as criteria. The value of 0.55 was chosen because it comprises the aggressiveness class III of Brazilian standard NBR 6118 [26], one of the most vulnerable material scenarios. It was also determined that the slump-flow final value should be within the range of SF2 class (between 660 and 750 mm) delimited by Brazilian standard NBR 15823-1 [16] and the necessary adjustments were made by adding superplasticizer.

REF was the first concrete produced and from the determination of its unitary proportion the other mixtures were performed with the aforementioned Portland cement substitutions. This proportion was 1: 0: 0: 0.64: 1.03: 0.46: 1.08: 0.55 and is in the format Portland cement: limestone filler: metakaolin: natural sand: crushed sand: gravel 12.5 : gravel 19: w/b. The bulk consumption of the mixtures is shown in Table 2.

Table 2: Bulk consumption of the materials

	Mixture consumption (kg/m ³)								
	Cement	Limestone filler	Metakaolin	Natural sand	Crushed sand	Gravel 12,5	Gravel 19	Water	Superplasticizer
REF	475,00	0.00	0.00	306.11	489.77	220.40	514.26	261.25	1.66
F20	379.83	94.96	0.00	303.26	485.21	218.35	509.47	261.14	2.14
M20	380.00	0.00	95.00	299.98	479.96	215.98	503.96	261.25	7.12
M15F5	379.75	23.73	71.20	301.83	482.92	217.32	507.07	261.08	4.03

2.2.2 Fresh and hardened state test

In order to evaluate the SCC behaviour in the fresh state, slump-flow, t_{500} , V-funnel, L-box and visual stability index tests were performed according to self-compacting criteria established by Brazilian standard [16].

For the mechanical properties evaluation cylindrical specimens of 100 x 200 mm were cast, with top regularization by grinding. Each result presented consists of the average value obtained from three specimens. Axial compression strength test was performed according to [18] at the ages of 7, 14 and 28 days. The specimens stayed curing in a humid chamber until the determined ages. At 28 days, tensile strength by diametrical compression and static elastic modulus tests were also performed, following the recommendations of [19] and [20], respectively.

The accelerated carbonation test was performed in compliance with the recommendations of [15]. This standard sets the carbonation chamber conditions, with a temperature of 22 ± 2 ° C and relative humidity of $55 \pm 5\%$, but for hot climates, such as Brazil, the values change, passing to a temperature of 27 ± 2 ° C and relative humidity of $65 \pm 5\%$. CO₂ concentration shall be $3,0 \pm 0,5\%$ by volume for any climatic condition. Prismatic specimens of 400 x 100 x 100 mm were used. Before the test begins, the prismatic specimens were sealed with paraffin, leaving only two faces exposed to the test conditions for a direction in the CO₂ diffusion flow. They were then placed in the accelerated carbonation chamber for 70 days and carbonation front depth measurements were performed at 56, 63 and 70 days of exposure using a phenolphthalein pH indicator solution and a digital calliper with a resolution of 0,01 mm.

Mercury intrusion porosimetry was performed in pastes, in samples of approximately 1 cm³. The equipment used was AutoPore IV 9500 V1.05 from Micromeritics Instrument Corporation. During the test, mercury was intruded into the samples continuously at a 130° contact angle and a mercury surface tension of 4.85 x 10⁻¹ N/m with a pressure increase of 0.0007 to 414 MPa were considered.

3. Results and discussion

3.1 Fresh state

As a research premise the mixtures were fixed with variation only of the Portland cement substitution by SCM. In order to reach the defined slump-flow range, adjustments were made in the superplasticizer content. A higher superplasticizer content was required for the mixtures containing metakaolin, due to its high specific surface area influences the water demand and increases viscosity. The same was found by [21], who produced SCC with Portland cement substitutions by metakaolin at replacement levels of 5, 10, 15 and 20% and found that higher the content, higher the superplasticizer consumption. No evident exudation or segregation was observed in any of the concretes. According to the results shown in Table 3, it can be affirmed that they are all in agreement with [16] fluidity, passing ability and cohesion requirements.

Table 3: Results of fresh state characteristics

	REF	F20	M20	M15F5
t_{500} (s)	1.47	1.25	2.15	1.86
SLUMP-FLOW (mm)	683	685	675	690
V-FUNNEL (s)	2.95	2.69	3.16	2.26
L-BOX	0.82	0.9	0.9	0.87
SPECIFIC GRAVITY (kg/m ³)	2350	2310	2320	2300
SUPERPLASTICIZER (%)	0.35	0.45	1.1	0.85

3.2 Mechanical properties

According to the compressive strength, the concretes presented resistance gains with the advancing age and the mixtures containing metakaolin achieved higher performance than the reference concrete. The improvement in the resistance with metakaolin use in comparison to limestone filler is evident in the binary combinations, once M20 has achieved a resistance 50.9% higher than the REF and the F20 had a loss of 15.4%. Only F20 caused a decrease in compressive strength. The high reactivity mineral additions have a high surface area, responsible for potentiating lime fixation by pozzolanic activity, which promotes an increase in the compressive strength of the hydrated matrix [22]. In this context, it is expected that the mixes with metakaolin will increase resistance even with less clinker in the composition. The M15F5 increased by 29.4%.

Table 4 - Mechanical properties of self-compacting concretes at 28 days

	REF	F20	M20	M15F5
COMPRESSIVE STRENGTH (MPa)	41.0	34.7	61.8	53.0
TENSILE STRENGTH (MPa)	4.1	3.3	4.7	3.9
ELASTIC MODULUS (GPa)	31.9	29.7	36.5	33.7

This increase of resistance with the increase of the Portland cement substitution content by metakaolin was also obtained by [23], which produced SCC with substitutions of 7, 11, 14 and 20% metakaolin. [24], produced SCC with 10 and 20% replacement of Portland cement by metakaolin and 10, 20 and 30% substitution for blast furnace and fly ash granulated slag, and the mixtures with 20% metakaolin presented higher resistance. It is known that the use of inert materials in the concrete causes the filler effect, which promotes refinement of the pore system, since the fineness of particles serves as a nucleation point for the formation of hydrates. Because of this, it is common for concretes to increase strength, but the high water/binder ratio adopted for the mixtures in this work probably had greater influence.

In the tensile strength, the tendency of the concrete behaviour was similar to that observed in the compressive strength, but with lower percentages of gain or loss of resistance. M15F5 was the mixture with the highest behaviour change, since it presented a compressive strength gain of 29.4% in relation to the REF, and a decrease of 4.5% in tensile strength. The values found for elastic modulus in SCC, in general, are lower than those commonly observed in conventional concretes. According to [25], this is due to SCC higher paste content. Since the deformability of the paste is higher than that of the aggregates, a decrease in stiffness of the entire system occurs. In the mixtures containing metakaolin there was an increase in the elastic modulus values. M15F5 promoted a 5.7% increase in modulus of elasticity. On the other hand, the M20, as in the other properties, presented the highest result, with its elastic modulus being 14.5% higher than the reference concrete.

3.3 Accelerated carbonation

All values presented are the average of at least 6 readings taken along the surfaces of the specimens exposed to the CO₂ diffusion flow. There was an increase in the measured value with the advance of the time of SCC exposure to the accelerated carbonation environment, more accentuated in the limestone mixtures.

It can be seen (Figure 1) that at 56 days, the mixtures with limestone filler showed a carbonation depth lower than the REF, but with the advancement of the exposure time the value became higher. M15F5 presented values slightly higher than REF and M20 lower values, for all measurement times. It is noted that the carbonation values of M15F5 and M20 have a stabilizing tendency, while F20 showed a clear growth in time.

F20 had a bigger measured depth, with a value 24% higher than the REF at the end of the test. The increase caused by M15F5 was 4%, while the M20 promoted a decrease of 55%.

The limestone filler reacts more rapidly in the system with metakaolin than in the binary mixture of filler and Portland cement. These results point to synergistic effects on the combined substitution of additions. However, calcium hydroxide consumption may mean that high-level substitution mixtures may carbonate more quickly [1]. According to [3] the use of a larger amount of lime (>20%) requires reduction of the water/cement ratio to produce concrete with similar durability performance, which is not the case of the mixtures in this work.

In the limestone filler mixtures the advance of the carbonation front occurred in a uniform way, with the identification of a linear carbonation front. In the ones with metakaolin the advance of the carbonation front was very small, due to the improvement of paste quality. In the ternary mixture (M15F5) a weakening in the paste/aggregate transition zone was observed, which facilitated diffusion of the carbon dioxide. This tendency led to points with high carbonation depths and others with practically no advanced front, so that the average generated a slightly higher result than the REF, although visually its carbonated surface was smaller.

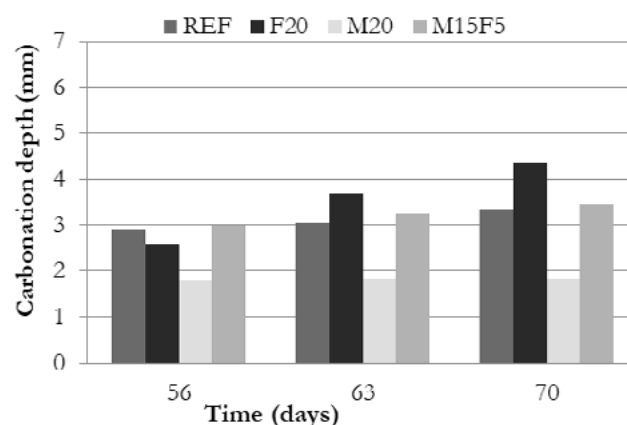


Figure 1: SCC carbonation depths

Using the equation that proposes that the carbonation depth is proportional to the square root of exposure time ($x=K \cdot \sqrt{t}$), the carbonation coefficients (K) of each mixture were determined using the depth readings of the specimens after 70 days of exposure. With this coefficient it is possible to estimate the time required to reach any desired carbonation depth value for the CO₂ concentration used in the accelerated test ($3.0 \pm 0.5\%$). The nominal cover recommended by [26], for concrete exposed to environmental aggression class III, is 40 mm. Thus, extrapolations were made to determine how much time it would take to carbonation front of each concrete in this study to reach that value.

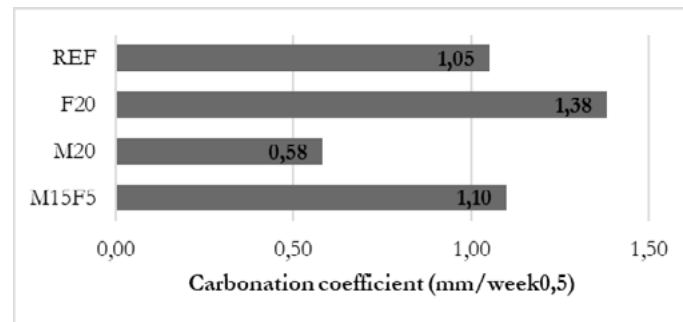


Figure 2: Specimens carbonation coefficient

In the REF, F20, M20 and M15F5 would be required approximately 27.83, 16.11, 91.22 and 25.36 years, respectively, for a carbonation depth of 40 mm.

It is known, however, that CO₂ concentration of the environment is around 0.04%, a value 75 times lower than the concentration used in the determination of the aforementioned carbonation coefficients. Thus, without considering other interactions of the structures with the environment and the deteriorations to which they can be subjected in situations of use, carbonation would take longer to reach the structures reinforced with the studied SCC mixtures than usual structures life expectancy. It can be seen that SCC is a good alternative for extending life of concrete structures, especially if carbonation is considered the main aggressive factor, even in mixtures with 20% less Portland cement in its composition.

3.4 Mercury intrusion porosimetry

The carbonation resistance of concrete is also influenced by its pore structure. The diffusivity of fluids/ions in the concrete is a function of the porosity and characteristics of the structure of the pore network (geometry, distribution, interconnectivity and tortuosity). The higher the porosity of the system, the greater the space available for the diffusion of carbon dioxide, therefore, the lower the resistance to carbonation of the system [27]. It is observed that the maximum value of intruded volume in the pores occurred in the mesopore range (0.002 to 0.05 μm), indicating a refined porous structure in the concretes. It is also possible to observe pores with dimensions above 50 μm which, according to [28], are spherical and correspond to the air voids incorporated. REF is the mixture with the lower amount of these macropores while F20 has the largest amount.

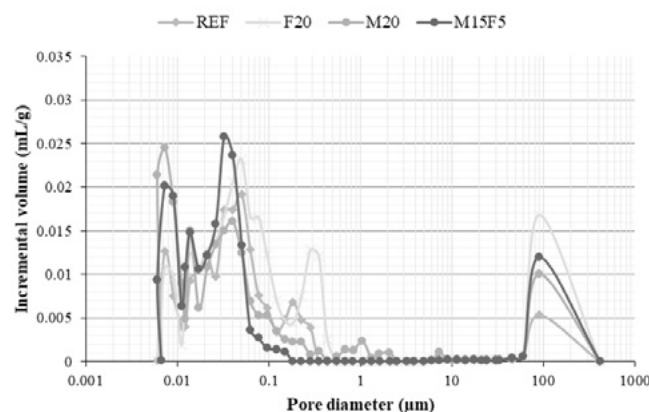


Figure 3: Relation between incremental volume and pore diameter in MIP test

In the region close to the diameter of 0.05 μm , the use of metakaolin caused an increase in pore volume, with the amount of M20 being higher, followed by M15F5, that is, a refinement characterized by an increase in volume of smaller pores. It is also noted that F20 showed a significant peak in the capillary pore range, in

addition to the greater amount of mesopores and greater amount of accumulated volume, which indicates higher susceptibility of this mixture to the entry of deleterious agents.

M20 presented largest volume of pores of small diameter. The amount of these pores increases with the formation of hydrates, which shows the pozzolanic action. In both mixtures containing metakaolin, a porous structure composed of a larger volume of mesopores is also observed, the action of the isolated addition (M20) being more pronounced than in combination with the limestone filler (M15F5). [29] studied the absorption characteristics of the concrete with the increased substitution of metakaolin and confirmed a reduction in the water absorption in the system due to the decrease of concrete porosity.

Both M20 and M15F5 showed the highest values of total pore area, probably due to the porosity refinement due to the formation of a higher amount of C-S-H by the pozzolanic action. F20 had the highest volume of intruded mercury. Regarding permeability, F20 once again had the highest observed value. In relation to tortuosity, M15F5 had the highest value among the mixtures, which in general presented close values.

4. Conclusions

- Through the analysis of the fresh state results it can be affirmed that the concretes complying the fluidity, passing ability and cohesion requirements defined by [16];
- As the granular skeleton was the same for all SCC, the variation in values is attributed to the stiffness of the pastes. Since M20 results were the best for all mechanical properties evaluated, it is understood that the structure of their paste is the densest and most rigid of all concretes or that the use of metakaolin increased the resistance of the transition zone between paste and aggregates;
- M15F5, in general, presented a performance superior to the mixture with limestone and inferior to the one with metakaolin, in all properties analysed;
- The mix with 20% of limestone filler (F20) had the worse mechanical performance and lower durability against carbonation. The filler effect was not able to compensate the Portland cement removal, probably due to the high w/c ratio adopted;
- At the same time as the pozzolanic reaction consumes the calcium hydroxide, and thus decreases the amount of the hydration product responsible for guaranteeing the alkalinity of the cementitious matrix, the formation of secondary C-S-H promotes a decrease in the pore diameter of the hydrated paste. Thus, even with the lowest amount of CH, the mix with metakaolin presented a better resistance to the advance of the carbonation front compared to the reference one, which shows that the pore refinement was effective in preventing the diffusion of CO₂, even in a less alkaline environment.

5. Acknowledgement

The authors would like to thank the Brazilian Coordination of Improvement of Higher Level Personnel (CAPES) for the Master's grant given during the time of this research.

6. References

- [1] M. Antoni, J. Rossen, F. Martirena, K. Scrivener, Cement substitution by a combination of metakaolin and limestone. *Cem. Concr. Res.* 42 (2012) 1579-1589, <http://dx.doi.org/10.1016/j.cemconres.2012.09.006>
- [2] Y. Dhandapani, T. Sakthivel, M. Santhanam, R. Gettu, R. G. Pillai, Mechanical properties and durability performance of concretes with Limestone Calcined Clay Cement (LC3). *Cem. Concr. Res.* 107 (2018) 136-151, <https://doi.org/10.1016/j.cemconres.2018.02.005>.

- [3] S.Palm, T. Proske, M. Rezvani, S. Hainer, C. Müller, C. Graubner, Cements with a high limestone content – Mechanical properties, durability and ecological characteristics of the concrete. *Constr. Build. Mater.* 119 (2016) 308-318, <https://doi.org/10.1016/j.conbuildmat.2016.05.009>.
- [4] G. De Schutter, K. Lesage, V. Mechtcherine, V. N. Nerella, G. Habert, I. Agusti-Juan, Vision of 3D printing with concrete — Technical, economic and environmental potentials. *Cem. Concr. Res.* 112 (2018) 25–36, <https://doi.org/10.1016/j.cemconres.2018.06.001>.
- [5] V. G. Papadakis, C. G. Vayenas, M. N. Fardis, Fundamental Modeling and Experimental Investigation of Concrete Carbonation. *ACI Mat. Jour.* 88 (1991) 363-373.
- [6] V. Shah, S. Bishnoi, Carbonation resistance of cements containing supplementary cementitious materials and its relation to various parameters of concrete. *Constr. Build. Mater.* 178 (2018) 219-232, <https://doi.org/10.1016/j.conbuildmat.2018.05.162>.
- [7] H. F. W TAYLOR, *Cement Chemistry*.(1997). 2 ed. Londres. Thomas Telford.
- [8] Y. J. Kim, Y. J. Kim, Y. W. Choi, An Experimental Research on Self-consolidating Concrete using Tungsten Mine Tailings. *KSCE Journal of Civil Engineering* 20(4) (2016) 1404-1410, <https://doi.org/10.1007/s12205-015-0196-4>.
- [9] M Matos, T. Ramos, S. Nunes, J. Sousa-Coutinho, Durability Enhancement of SCC With Waste Glass Powder. *Materials Research* 19 (2015) 67-74, <http://dx.doi.org/10.1590/1980-5373-MR-2015-0288>.
- [10] M. Carsana, M. Gastaldi, F. Lollini, E. Redaelli, L. Bertolini, Improving durability of reinforced concrete structures by recycling wet-ground MSWI bottom ash. *Materials and Corrosion* 67 (6) (2016) 573-582. <https://doi.org/10.1002/maco.201608881>.
- [11] R. Sharma, R. A. Khan, Durability assessment of self-compacting concrete incorporating copper slag as fine aggregates. *Constr. Build. Mater.* 155 (2017) 617-629, <https://doi.org/10.1016/j.conbuildmat.2017.08.074>.
- [12] H. L MUTTASHAR, M. A. M. ARIFFIN, M. N. HUSSEIN, M. W. HUSSIN, S. B. ISHAQ, Self-compacting geopolymer concrete with spend garnet as sand replacement. *Jour. Build. Eng.* 15 (2018) 85-94, <https://doi.org/10.1016/j.jobbe.2017.10.007>.
- [13] RICHARDSON, M. G. (1998). *Carbonation of reinforced concrete: Its causes and management*. New York: CITIS Ltd, Publishers
- [14] C. Pauletti, E. Possan, D. C. C. Dal Molin, Carbonatação acelerada: estado da arte das pesquisas no Brasil. *Ambiente Construído* 7 (2007) 7-20,
- [15] International Standard. ISO 1920-12:2015 – Testing of concrete – Part 12: Determination of the carbonation resistance of concrete – Accelerated carbonation method. Geneva, Switzerland.
- [16] Brazilian Association of Technical Standards. NBR 15823-1. Self-compacting concrete Classification, control and fresh state acceptance. ABNT, Rio de Janeiro, Brazil, 2017
- [17] American Concrete Institute. ACI 237R-07: Self-Consolidating Concrete. 2007.
- [18] Brazilian Association of Technical Standards. NBR 5739. Concrete – compressive strength of cylindrical samples. ABNT, Rio de Janeiro, Brazil; 2007
- [19] Brazilian Association of Technical Standards . NBR 7222. Concrete and mortar – Determination of

tensile strength by diametrical compression of cylindrical specimens. ABNT, Rio de Janeiro, Brazil; 2011

[20] Brazilian Association of Technical Standards . NBR 8522. Concrete – Determination of static elastic modulus to compression. ABNT, Rio de Janeiro, Brazil; 2008

[21] K. A. Melo, A. M. P. Carneiro, Effect of metakaolin's finesses and content in self-consolidating concrete. Constr. Build. Mater. 24 (2010) 1529-1535, <https://doi.org/10.1016/j.conbuildmat.2010.02.002>.

[22] J. HOPPE FILHO, A. GOBBI, E. PEREIRA, V. A. QUARCIONI, M. H. F. MEDEIROS, Pozzolanic activity of mineral additions to Portland cement (Part I): Pozzolanic activity index with lime (PAI), X-ray diffraction (XRD), thermogravimetry (TG/DTG) and modified Chapelle. Revista Matéria 22 (2017) <http://dx.doi.org/10.1590/s1517-707620170003.0206>.

[23] I.P. Sfikas, E.G. Badogiannis, K.G. Trezos, Rheology and mechanical characteristics of self-compacting concrete mixtures containing metakaolin. Constr. Build. Mater. 64 (2014) 121-129, <https://doi.org/10.1016/j.conbuildmat.2014.04.048>.

[24] S. Dadsetan, J. Bai, Mechanical and microstructural properties of self-compacting concrete blended with metakaolin, ground granulated blast furnace slag and fly ash. Constr. Build. Mater. 146 (2017) 658-667, <https://doi.org/10.1016/j.conbuildmat.2017.04.158>.

[25] European Federation For Specialist Construction Chemical And Concrete Systems – EFNARC. Specification and Guidelines for Self-Compacting Concrete. Specification, Production and Use. EFNARC, United Kingdom, 2005. 63p.

[26] Brazilian Association of Technical Standards . NBR 6118. Concrete Structural Projects – Procedure. ABNT, Rio de Janeiro, Brazil; 2017

[27] B. B. Das, B. Kondraivendhan, Implication of pore size distribution parameters on compressive strength, permeability and hydraulic diffusivity of concrete. Constr. Build. Mater. 28 (2012) 382-386, <https://doi.org/10.1016/j.conbuildmat.2011.08.055>.

[28] MEHTA. P.K.; MONTEIRO, P.J.M. Concreto: Microestrutura, propriedades e materiais. 3^a ed. São Paulo: Ed. IBRACON, 2014.

[29] J. M. Khatib, R. M. Clay, Absorption characteristics of metakaolin concrete. Cem. Concr. Res. 34 (2003) 19-29, [https://doi.org/10.1016/S0008-8846\(03\)00188-1](https://doi.org/10.1016/S0008-8846(03)00188-1).

Eco-synthesis of zeolite from coal fly ash

K.M. Klima, Q.L. Yu, H.J.H. Brouwers

Department of Built Environment, Eindhoven University of Technology, Eindhoven 5600 MB

Abstract

In this work, pure zeolite Na-P1 is successfully synthesized from Coal Combustion Fly Ash via the fusion process. The obtained phase can be applied as a reactive filler in geopolymer composite and can be assessed in terms of temperature stability. First, a known amount of Coal Combustion Fly Ash was subjected to calcination in a muffle furnace at 800°C in order to eliminate the unburnt carbon. After that, the sample was subjected to a hydrochloric acid treatment (4.5M) in a reflux condenser. It is intended to reduce the iron contained in the ash, but also to reduce other impurities like potassium, calcium or magnesium. Owing to the acid treatment it is possible to increase the efficiency of zeolite conversion.

This step allows synthesizing highly pure zeolite P1. The solid mixture of treated fly ash and NaOH with a mass ratio 1:1.25 undergoes the reaction, as a result of which the silicates and aluminates of sodium are obtained at 550°C in 1.5 hours in the muffle furnace. Further hydrothermal activation through grinding and mixing with deionized water in a mass ratio of 1:10 for 3 hours at room temperature was applied. The sample was kept in a drying oven at 85°C within 90 hours in a sealed container made of polypropylene. The identification of zeolite P was carried out using powder X-ray diffraction, scanning electron microscope and Fourier transform infrared spectroscopy. These methods allowed to identify the crystalline phase and confirm the effectiveness of the synthesis procedure.

The thermal properties and stability aspects of zeolite Na-P1 were determined by thermogravimetric-differential scanning calorimetry (TG-DSC). The study provides a protocol for synthesizing pure zeolite P1 from fly ash, in addition, it allows for the accomplishment of the first step toward fire resistant geopolymer synthesis by using coal combustion fly ash. Preliminary results show that the applied method of the synthesis successfully allows obtaining a pure product. The characterization of the material confirmed the presence of zeolite Na-P1 as well as the first test of thermal analysis was carried out. The heat resistance of synthetic zeolite P1 is up to 790°C, however, its performance in geopolymer matrix has to be investigated.

Keywords: Zeolite, fire-resistance, filler, geopolymer.

Influence of Particle Size Distribution and MSWI Bottom Ash Aggregate Replacement in Zero-Slump Concrete

P.M.F. van de Wouw, M.V.A. Floear, H.J.H. Brouwers

Department of the Built Environment, Eindhoven University of Technology, P.O. Box 513, 5600 MB Eindhoven, the Netherlands.

Abstract

In Europe, approximately 18 million tonnes of bottom ash (BA) is being produced annually through the incineration of municipal solid waste (MSWI). Currently, this is either stockpiled, limitedly applied as road base material, or, in the Netherlands, for some specifically treated BA fractions the application as aggregate in concrete is becoming more accepted. With the application of BA in concrete, stockpiling, the extraction of virgin materials, and the CO₂ production footprint can be reduced. Earth-moist or zero-slump concrete (ZSC) mass products are ideal for the incorporation of MSWI BA due to their absence of reinforcement, higher porosity, and primarily non-structural applications.

This study focusses on investigating how the mix design of ZSC is influenced by coarse and fine aggregate replacement with BA over a distribution modulus range. To this aim, a spherical central composite design approach is used to acquire a broad understanding on the interaction and influence of the 3 independent variables (sand replacement, gravel replacement, and distribution modulus (q)) on ZSC mix design.

It is found that for BA containing ZSC, pre-saturation of the BA reduces the required mixing water. Additionally, both the additions of fine and coarse pre-saturated BA increase the total amount of water in the system while an equal workability is maintained. In turn, this water can potentially contribute to internal curing at a later stage. Due to the porosity of the BA, the overall density of the concrete is found to decrease with an increase in both fine and coarse aggregate replacement. Furthermore, an increased q-value with an equal cement content and workability results in a lower powder content with a higher binder concentration in the powders, and therefore a lower water-binder ratio. Finally, for the particle packing optimisation with porous materials, the use of the envelope volume (including porosity and voids) of particles is proposed.

Keywords: Zero-Slump Concrete, MSWI Bottom Ash, Mix Design, Aggregate Replacement, Distribution Modulus.

1. Introduction

Through the incineration of municipal solid waste (MSWI) in a waste-to-energy plant, electric power and hot water are produced. Annually, this results in approximately 18 million tonnes of bottom ash (BA) being produced in Europe (1.7 million tonnes in the Netherlands) [1,2]. Currently, this is either stockpiled, limitedly applied as road base material, or, in the Netherlands, for some specifically treated BA fractions the application as aggregate in concrete is becoming more accepted [3].

Concrete, with a worldwide production of approximately 33 billion tonnes annually, accounts for the use of 27 billion tonnes of aggregates per year [4]. Hence, both the consumption of raw materials and the

lowering of the environmental impact of concrete have attracted attention in recent years [5,6]. To this end, the application of industrial by-products such as MSWI BA have been extensively studied as potential aggregate replacement for the production of concrete [7–13]. With the application of BA in concrete, stockpiling, the extraction of virgin materials, and the CO₂ production footprint can be reduced [14–17].

Concrete mass products such as paving blocks, kerbstones, masonry blocks, roofing tiles, sewage pipes, and concrete slabs, are produced with zero-slump concrete (ZSC), otherwise known as earth-moist concrete or no-slump concrete. Contrary to concrete with a plastic consistency, after filling and intense vibratory compaction under compression, the unhardened product is directly extractable and successively transferrable to a curing location with controlled conditions [18]. Most ZSC does not contain reinforcement which could be harmed by chlorides present in BA. In comparison with a regular vibrated concrete, alkali-silica reaction (ASR) is found to be less of a problem in ZSC due to a higher porosity and larger pores, enabling a bigger volume of ASR gel, resulting in less expansion and a lower amount of cracks [19]. Furthermore, since ZSC is scarcely used in a structural application, it is a safe application in the unforeseen circumstance that a deficiency should occur.

The packing of continuously graded particles was studied by Andreasen and Andersen (A&A) [20] who based their work on that of Fuller & Thomsen [21], resulting in a semi-empirical equation for the cumulative volume fraction $F(D)$. Funk & Dinger [22] further developed this work, introducing the modified version of the A&A equation:

$$F(D) = \frac{D^q - D_{min}^q}{D_{max}^q - D_{min}^q} \quad (1)$$

where

D = particle size;

D_{min} = minimum particle size;

D_{max} = maximum particle size;

q = distribution modulus.

Making use of the modified A&A equation, Brouwers and Radix [23] proposed a particle-packing based mix design method for self-consolidating concrete (SCC). This methodology is flexible regarding materials and applications by altering the physical constraints (real-world limits), logical constraints (boundary conditions reflecting requirements for the designed concrete), and policy constraints (boundary conditions set by standards and legislation). Therefore, it has been applied in applications such as: SCC [24–26], ultra-high performance concrete [27–29], ultra-lightweight concrete [30–32], and ZSC [33–36].

This study focusses on investigating how the mix design of ZSC is influenced by coarse and fine aggregate replacement by BA over a distribution modulus range.

2. Methodology

2.1 Materials

A mixture used for the carrier layer of ZSC products is used as a starting point. This mixture consists of five components: cement, fine and coarse aggregates, water, and a plasticising admixture. A blended Portland cement (CEM III/A 42.5N) was selected as binder because it works well in full scale production and has been proven to be beneficial for the implementation of BA [37,38]. To enable the optimisation of the particle size distribution (PSD) while maintaining an equal binder (cement) content (v/v %) throughout the different mixtures, a commercially available quartz powder is included in the mix design as inert virgin

filler. A quartz sand (125 μm -4.0 mm) extracted in the Netherlands is used in the original mix design and applied as fine virgin aggregate. To enable a continuous grading of particles in accordance with the modified A&A equation, a virgin quartz micro sand is used to fill the gap between the PSD of the cement and the fine aggregates. The coarse virgin aggregates consist of a broken limestone (1.0-11.2 mm) from Belgium. A lignosulfonate-based plasticising admixture is used to assist in the compaction of the ZSC mixtures. The plasticiser dosage is fixed at a plasticiser/binder ratio of 0.1% and, as the cement dosage is fixed, is therefore constant throughout all mixtures (v/v %).

The BA used in this study for the replacement of natural aggregates was obtained from a municipal solid waste-to-energy plant in the Netherlands. The investigated 63 μm -16 mm granulate fraction is the result of extensive prior treatment in the form of weathering, size reduction, dry and wet separation of organics, magnetic and para-magnetic extraction of metals, and washing. It has been sampled according to EN 932-1 [39]. Prior to further analysis, the material was dried at 105 °C to an oven-dry state where a constant mass was reached [40]. By doing so, the moisture content was determined (10.67%, $\pm 1.01\%$). After drying, a correct particle size distribution (PSD) can be obtained in accordance with EN 933-1 and EN 933-2 [41,42] (with additional sieve sizes: 22.4 mm, 11.2 mm, 5.6 mm, 2.8 mm, 1.4 mm, 710 μm , 355 μm , 180 μm , and 91 μm), and the effect of agglomeration during the sieve analysis is minimised. In order to investigate the influence of both fine and coarse aggregate replacement, the 63 μm -16 mm oven-dried BA is sieved into respectively a <2 mm and an >2 mm fraction which correlates best with the size fractions of the virgin aggregates replaced. By sieving a second set of BA samples at 2 mm prior to oven drying, the intrinsic moisture content of both the fine and coarse BA fraction generated was determined, being 13.70% ($\pm 0.03\%$) and 7.79% ($\pm 0.19\%$), respectively. Based on this, an overall pre-saturation level of 10.0% was chosen for the 63 μm -16 mm BA, resulting in a 12.5% and 7.1% pre-saturation for respectively the fine and the coarse BA fraction in order to minimise the loss of mechanical resistance, workability and durability. The corresponding pre-saturation water was added to the oven-dried BA fractions and left to equilibrate in an air tight container for a minimum of 1 week while being turned over daily.

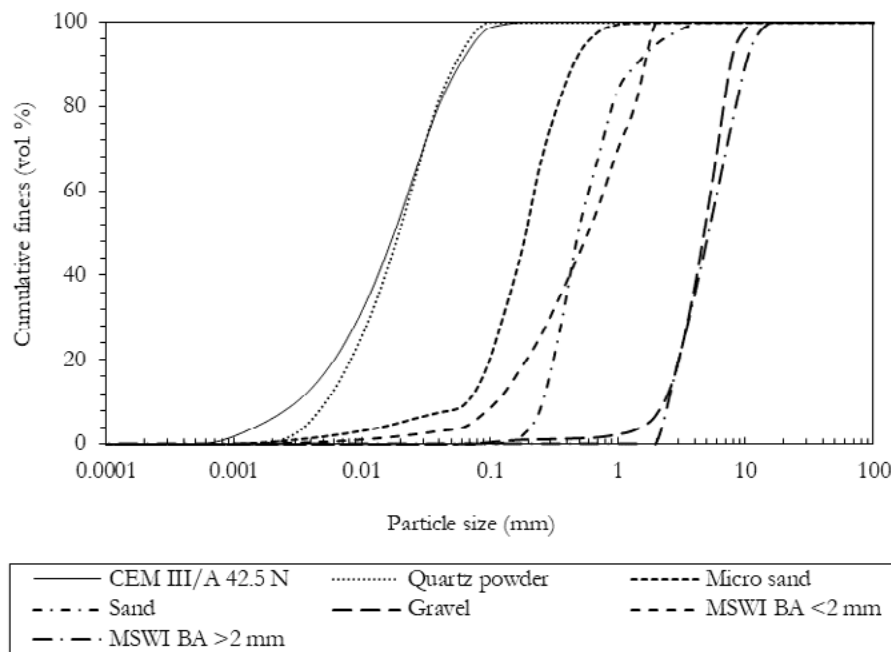


Figure 1 PSDs of all granular materials applied

With the addition of the quartz powder and micro sand to the standard mix design, a reference mix is created which allows an equal binder content, a continuous grading, and a compensation for differences

between the PSD of the virgin aggregates and the BA. Hence, including the pre-saturated coarse and fine BA fraction, a total of seven granular materials are used. Their PSDs are given in Figure 1.

2.2 Methods

2.2.1 Experiment design

This study employs a spherical central composite design approach [43] to acquire a broad understanding on the interaction and influence of the 3 independent variables (sand replacement, gravel replacement, and distribution modulus (q)) on ZSC mix design. Consequently, just 18 mix designs are needed out of a potential 125 (5^3) for 3 independent variables distributed over 5 levels in the ranges of 0-100% sand replacement, 0-100% gravel replacement, and a distribution modulus of 0.25-0.40 as suggested by Hüsken [34] (Figure 2), (Table 1), strongly reducing the necessary number of tests to quantify the above-mentioned correlations. To determine the reproducibility of the results, the design of centre point (15-18) is reproduced in quadruplicate.

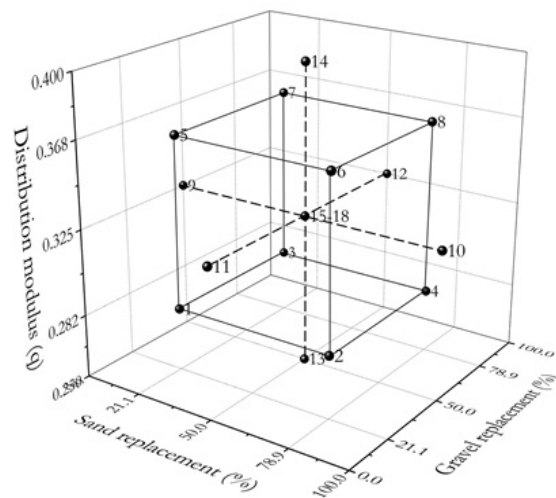


Figure 2 Geometric presentation of the inscribed central composite design for the 3 natural variables: (1) sand replacement (0-100%), (2) gravel replacement (0-100%), and (3) distribution modulus (q : 0.25-0.40).

Table 1 Mixture variable values

		Sand repl.	Gravel repl.	q
	Mix	(vol.-%)	(vol.-%)	
Factorial (cube points)	1	21.1	21.1	0.28
	2	78.9	21.1	0.28
	3	21.1	78.9	0.28
	4	78.9	78.9	0.28
	5	21.1	21.1	0.37
	6	78.9	21.1	0.37
	7	21.1	78.9	0.37
	8	78.9	78.9	0.37
Axial (star points)	9	0	50	0.33
	10	100	50	0.33
	11	50	0	0.33
	12	50	100	0.33
	13	50	50	0.25
	14	50	50	0.40
Centre (point)	15	50	50	0.33
	16	50	50	0.33
	17	50	50	0.33
	18	50	50	0.33

2.2.2 Mixture development methodology

The abovementioned 18 mix designs are defined by the values given in Table 1, the PSDs given in Figure 1, and the densities of the materials. Additional constraints are: BA <2 mm replaces both sand and micro sand, BA >2 mm replaces gravel, and the binder content is fixed (vol.-%). With the Brouwers and Radix'

mix design method [23], the ratios of all solid ingredients are calculated to compose the optimal particle gradation given by the modified A&A equation (Eq. 1). This is achieved by approaching unity for R^2 between composed mix PSD and the target PSD [44].

The algorithm in Brouwers and Radix' method [23] uses a volume-based expression of the particles based on the materials individual specific density (ρ^{spe}) as this is more suitable than using the retained mass of the sieve analysis when composing a mix with materials of different densities. However, in contrast to commonly used aggregates, BA contains a considerable porosity. ρ^{spe} solely takes into account the skeletal volume (solid material and closed pores) of the material, resulting in a larger effective volume at an equal ρ^{spe} for particles with an open porosity. Hence, ρ^{spe} is not applicable for porous materials. When the pores of the BA are assumed to be non-permeable to any of the present solid particles, the envelope volume (V_E) of particles, including porosity and voids, is most applicable.

Generally, the bulk density of both the original and the replacement material are used to exchange materials by volume. However, since the ZSC samples are compacted in the Intensive Compaction Tester (ICT, see 2.2.3), the compacted bulk density or ICT density (ρ^{ICT}) of the aggregates is determined under equal conditions. In this way, the PSD of the BA is adjusted to represent the PSD of replaced aggregates as closely as possible to achieve an equal void fraction (ϕ). Correlating the obtained ρ^{ICT} together with the ρ^{spe} of the considered virgin aggregate fraction, an average ρ^E is approximated for the equivalent BA fraction.

2.2.3 Sample preparation and testing

The solids for 3 specimens were dry mixed with a planetary mixer (Hobart, model A-200-FM) in a 10 litre bowl at 107 rpm for 1 minute prior to an additional 3 minutes after the addition of water and plasticizer. Sequentially, the mixing bowl was covered to prevent dehydration prior to further processing.

A gyratory ICT (Invelop Oy, model ICT-100R) is used for the compaction of the ZSC samples (Figure 3c.). The working principle of the ICT (Figure 3a.) relies on the application of a constant pressure (F_{ict}) on a sample placed in a cylindrical mould. The mould rotates at a maximum of 120 rpm for up to 512 work cycles (n) at a gyratory angle (α_{ict}) whereby the sample height (H_{ict}) is continuously measured. As a result of the gyratory inclination a shear movement develops, aiding the compaction (Figure 3b.). The settings applied, recommended by Hüsken [34] for ZSC samples produced with the ICT, are given in Table 2.

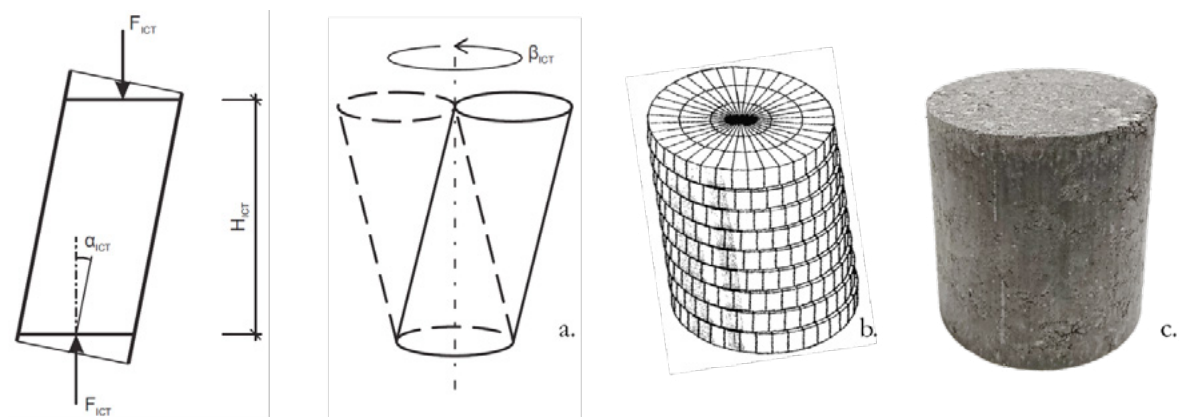


Figure 3 Intensive Compaction Tester: a. Working principle [34,45], b. Shear body of sample [46], c. ICT produced BA containing ZSC cylinder

Table 2 Gyrotory Intensive Compaction Tester settings

Parameter	Symbol	Units	Available range	Selected
Compaction pressure	F_{ict}	kPa	<330	250
Gyrotory angle	α_{ict}	mrad	<50	40
Cycle number	n	–	2–512	150
Velocity		rpm	30-120	60
Sample height	H_{ict}	mm	100-110	±105
Mould diameter	□	mm	100	100

The applied pressure can potentially affect the integrity of the particles due to crushing or grinding [47]. However, since the forces applied are (at least) comparable with ZSC production in practice, its occurrence is an acknowledged side effect of the process.

Multiple test samples of each mix were prepared with the ICT to determine the optimal moist state to achieve sufficient compaction (based on packing fraction), yet show no sign of excess water (the so-called “slurry point”) [35]. The 15 resulting recipes were used to create 6 concrete samples per mix for further analysis.

3. Results and discussion

As can be seen in Figure 4, the achieved R^2 is close to unity for all resulting values; however, sand replacement (R_s), gravel replacement (R_g), and distribution modulus (q) have a different influence. The R^2 value for R_s is rather stable with a slight increase at 50% replacement. This can be explained by the fact that the ratio between sand and micro sand is not fixed, resulting in less constraints to optimise the mixture. R_g shows a near unity value for 0% followed by a distinctly lower value at 20%, gradually increasing over the higher replacement levels. With a maximum particle size (D_{max}) of ±16.0 mm, the BA gravel is coarser than the replaced limestone gravel with a D_{max} of ±11.2 mm. In turn, at low replacement levels, with an equivalently low content of the largest size fraction, the adjustment of D_{max} from 11.2 mm to 16.0 mm cannot be compensated, resulting in a decreased R^2 . With an increase in q , R^2 decreases. This is caused by the reduced slope in the target curve for the smaller size fractions together with an increased slope for the larger size fractions, in turn resulting in a higher deviation.

The water content of the mixes is determined by the required workability and it depends on the 3 independent variables investigated (Figure 5). The total water content in the mix (W_t) is composed of the pre-saturation water in the BA (W_s) together with the water (including plasticiser) added during the mixing (W_m). For an increase in q , it can be seen that W_s remains rather stable, while W_t is reduced under the influence of W_m , which is related to a lower powder content (Figure 6). For an increase in q value, the binder content of the fines increases correspondingly, resulting in a lower W_t/B (Figure 7) which is in line with the findings of Hüsken [36].

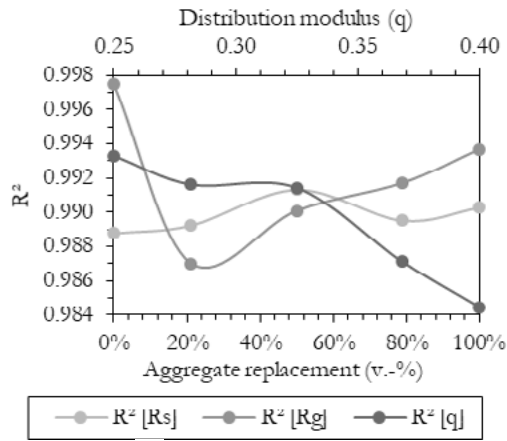


Figure 4 R_s , R_g , and q vs. R^2

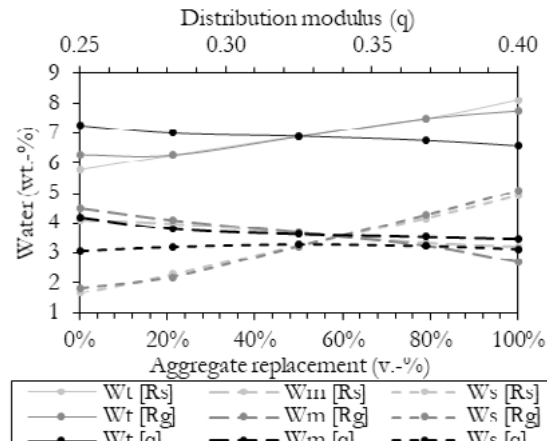


Figure 5 R_s , R_g , and q vs. W_t , W_m , and W_s

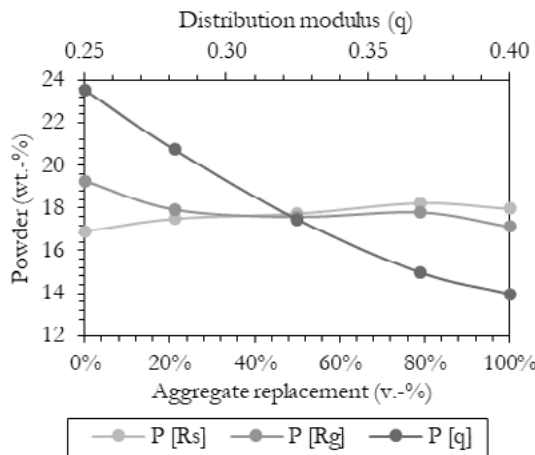


Figure 6 R_s , R_g , and q vs. powder content

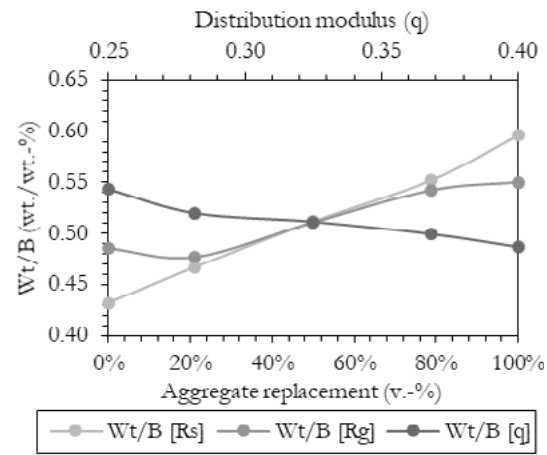


Figure 7 R_s , R_g , and q vs. W_t/B

As expected, Figure 6 shows a nearly constant powder content for R_s and R_g , and the small deviations can be linked to the deviations in material PSDs. In both W_t and W_s , an increase can be seen for R_s and R_g . W_m , however, decreases with an increase in replacement. This indicates that, during the mixing, per percent of fine and coarse BA replacement, sufficient water is released by the BA to reduce 0.23% and 0.39% of mixing water, respectively. Additionally, as the workability remains equal, it can be concluded that with the addition of both fine and coarse pre-saturated BA, the amount of water in the system is increased without a water increase in the paste (Figure 7). At a later stage, this additional water can contribute to hydration by supporting internal curing as suggested by Keulen et al. [38].

Based on the materials properties and the mix proportions, the theoretical maximum density of the mix can be calculated (Figure 8). For this purpose, ideal particle packing without any air content is assumed. For both R_s and R_g , as expected, the density decreases with increased replacement. The deviation from the trend at 0% replacement for R_g can be linked to the larger D_{max} of the BA >2 mm, inherently shifting the gradation curve and correlating properties.

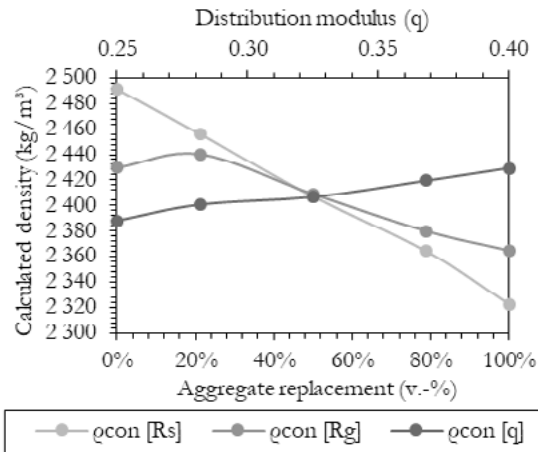


Figure 8 R_s , R_g , and q vs. calculated density

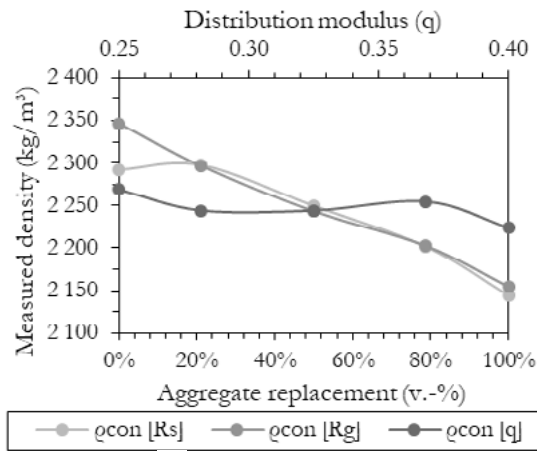


Figure 9 R_s , R_g , and q vs. measured density

The measured density of the compacted concrete samples is displayed in Figure 9. The deviation between the calculated and the measured density is a measure for the air content, shown in Figure 10.

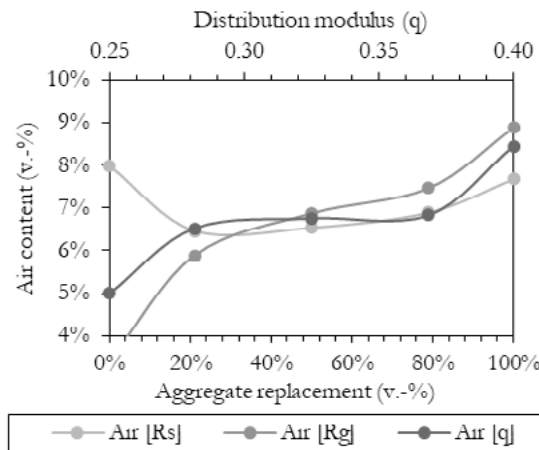


Figure 10 R_s , R_g , and q vs. calculated air content

Prior research and guidelines indicated an air content of 3-9% for ZSC [18,34,48,49]. Except for R_s at 0% and 100%, and q at 0.33, the values are in that range. In contrast to the presented ICT results, the compaction energy applied in practice is larger, in turn resulting in a lower air content closer to the 3-9% range.

4. Conclusions

Based on the presented results and discussion it can be concluded that for ZSC containing BA:

- pre-saturation of fine and coarse BA reduces the required mixing water correspondingly with 0.23% and 0.39% per percent of aggregate replacement by volume;
- at constant workability (and therefore a constant amount of water in the paste), the addition of both fine and coarse pre-saturated BA increases the total amount of water in the system. This additional water can potentially contribute to hydration by facilitating internal curing at a later stage;
- for constant cement content and workability, increasing the q -value leads to a reduced powder content and therefore a higher binder concentration in the powders, in turn, resulting in a lower water-binder ratio;

- the use of the envelope volume (including porosity and voids) of particles is proposed since the skeletal volume is an unsuitable characteristic for particle packing optimisation with porous materials. With this, the overall density of the concrete is found to decrease with an increase for both fine and coarse aggregate replacement with BA;
- the expected range for air content is only exceeded under specific conditions of the ICT compacted samples and is expected to improve in full scale operation.

Future work will extend the study into the influence of the investigated variables (sand and gravel replacement by MSWI BA and distribution modulus) on the hardened properties (e.g. technical quality, environmental impact, etc.) of the ZSC mixes.

5. Acknowledgment

The authors wish to express their gratitude to the NWO/TTW-foundation (project 13318, Development of eco-concretes by using industrial by-products), Mineralz, Attero, ENCI, v.d. Bosch Beton, Struyk Verwo, and CRH Europe Sustainable Concrete Centre for their provision of material, knowledge and financial support in this project, as well as to the Cement-Concrete-Immobilisates sponsor group at TU Eindhoven: Rijkswaterstaat Grote Projecten en Onderhoud, Graniet-Import Benelux, Kijlstra Betonmortel, Rijkswaterstaat Zee en Delta - District Noord, BTE, Selor, GMB, Icopal, BN International, Eltomation, Knauf Gips, Hess AAC Systems, Kronos, Joma, Cement&BetonCentrum, Heros, Inashco, Keim, Sirius International, Boskalis, NENERGY, Tata Steel, Millvision, Sappi, Studio Roex, Van Berlo Groep, PCS Innotec International, Nedvang, Baetsen, Noah (chronological order of joining).

6. References

- [1] CEWEP, Bottom Ash Factsheet, (2015). www.cewep.eu (accessed February 15, 2018).
- [2] CEWEP, Country Report 2012-2013 The Netherlands, 2014. www.cewep.eu.
- [3] CUR-voorschriftencommissie VC89, CUR Aanbeveling 116:2017 - AEC-granulaat als toeslagmateriaal voor beton, (2017) 126.
- [4] P.K. Mehta, P.J.M. Monteiro, Concrete: Microstructure, Properties, and Materials, Fourth, McGraw-Hill Education, New York, Chicago, San Francisco, Athens, London, Madrid, Mexico City, Milan, New Delhi, Singapore, Sydney, Toronto, 2014.
- [5] T. Xu, T. Galama, J. Sathaye, Reducing carbon footprint in cement material making: Characterizing costs of conserved energy and reduced carbon emissions, *Sustain. Cities Soc.* 9 (2013) 54–61. doi:10.1016/j.scs.2013.03.002.
- [6] E. Tkaczewska, R. Mróz, G. Łój, Coal-biomass fly ashes for cement production of CEM II/A-V 42.5R, *Constr. Build. Mater.* 28 (2012) 633–639. doi:10.1016/j.conbuildmat.2011.10.022.
- [7] R. Cioffi, F. Colangelo, F. Montagnaro, L. Santoro, Manufacture of artificial aggregate using MSWI bottom ash., *Waste Manag.* 31 (2011) 281–8. doi:10.1016/j.wasman.2010.05.020.
- [8] X.-G. Li, Y. Lv, B.-G. Ma, Q.-B. Chen, X.-B. Yin, S.-W. Jian, Utilization of municipal solid waste incineration bottom ash in blended cement, *J. Clean. Prod.* 32 (2012) 96–100. doi:10.1016/j.jclepro.2012.03.038.
- [9] U. Müller, K. Rübner, The microstructure of concrete made with municipal waste incinerator bottom ash as an aggregate component, *Cem. Concr. Res.* 36 (2006) 1434–1443. doi:10.1016/j.

cemconres.2006.03.023.

- [10] B. Quenee, G. Li, J.M. Siwak, V. Basuyau, Waste Materials in Construction Wascon 2000 - Proceedings of the International Conference on the Science and Engineering of Recycling for Environmental Protection, Harrogate, England 31 May, 1–2 June 2000, Elsevier, 2000. doi:10.1016/S0713-2743(00)80054-9.
- [11] R. Siddique, Use of municipal solid waste ash in concrete, *Resour. Conserv. Recycl.* 55 (2010) 83–91. doi:10.1016/j.resconrec.2010.10.003.
- [12] S. Sorlini, A. Abbà, C. Collivignarelli, Recovery of MSWI and soil washing residues as concrete aggregates, *Waste Manag.* 31 (2011) 289–297. doi:10.1016/j.wasman.2010.04.019.
- [13] B. Juric, L. Hanzic, R. Ilić, N. Samec, Utilization of municipal solid waste bottom ash and recycled aggregate in concrete., *Waste Manag.* 26 (2006) 1436–42. doi:10.1016/j.wasman.2005.10.016.
- [14] R. del Valle-Zermeño, J. Formosa, J.M. Chimenos, M. Martínez, A.I. Fernández, Aggregate material formulated with MSWI bottom ash and APC fly ash for use as secondary building material., *Waste Manag.* 33 (2013) 621–7. doi:10.1016/j.wasman.2012.09.015.
- [15] A.A. Al-Rawas, A. Wahid Hago, R. Taha, K. Al-Kharousi, Use of incinerator ash as a replacement for cement and sand in cement mortars, *Build. Environ.* 40 (2005) 1261–1266. doi:10.1016/j.buildenv.2004.10.009.
- [16] J.M. Chimenos, M. Segarra, M.A. Fernández, F. Espiell, Characterization of the bottom ash in municipal solid waste incinerator, *J. Hazard. Mater.* 64 (1999) 211–222. doi:10.1016/S0304-3894(98)00246-5.
- [17] C.C. Wiles, Municipal solid waste combustion ash: State-of-the-knowledge, *J. Hazard. Mater.* 47 (1996) 325–344. doi:10.1016/0304-3894(95)00120-4.
- [18] Stutech, Aardvochtig beton, Stutech report No. 22, 's Hertogenbosch, The Netherlands (in Dutch), 2005.
- [19] G. Lee, T.-C. Ling, Y.-L. Wong, C.-S. Poon, Effects of crushed glass cullet sizes, casting methods and pozzolanic materials on ASR of concrete blocks, *Constr. Build. Mater.* 25 (2011) 2611–2618. doi:10.1016/j.conbuildmat.2010.12.008.
- [20] A.H.M. Andreasen, Ueber die Beziehung zwischen Kornabstufung und Zwischenraum in Produkten aus losen Körnern (mit einigen Experimenten), *Kolloid-Zeitschrift.* 50 (1930) 217–228. doi:10.1007/BF01422986.
- [21] W.B. Fuller, S.E. Thomson, The Laws of Proportioning Concrete, *Trans. Am. Soc. Civ. Eng.* (1907).
- [22] J.E. Funk, D.R. Dinger, Predictive Process Control of Crowded Particulate Suspensions: Applied to Ceramic Manufacturing, Kluwer Academic Press, Boston, MA, 1994. doi:10.1007/978-1-4615-3118-0.
- [23] H.J.H. Brouwers, H.J. Radix, Self-Compacting Concrete: Theoretical and experimental study, *Cem. Concr. Res.* 35 (2005) 2116–2136. doi:10.1016/j.cemconres.2005.06.002.
- [24] X. Wang, K. Wang, P. Taylor, G. Morcou, Assessing particle packing based self-consolidating concrete mix design method, *Constr. Build. Mater.* 70 (2014) 439–452. doi:10.1016/J.CONBUILDMAT.2014.08.002.
- [25] M. Hunger, An integral design concept for ecological self-compacting concrete, 2010. doi:http://dx.doi.org/10.6100/IR674188.

- [26] M. Hunger, H.J.H. Brouwers, Natural Stone Waste Powders Applied to SCC Mix Design, *Restor. Build. Monum.* 14 (2008) 131–140. doi:10.1515/rbm-2008-6206.
- [27] R. Yu, P. Spiesz, H.J.H. Brouwers, Mix design and properties assessment of Ultra-High Performance Fibre Reinforced Concrete (UHPFRC), *Cem. Concr. Res.* 56 (2014) 29–39. doi:10.1016/j.cemconres.2013.11.002.
- [28] R. Yu, P. Spiesz, H.J.H. Brouwers, Development of an eco-friendly Ultra-High Performance Concrete (UHPC) with efficient cement and mineral admixtures uses, *Cem. Concr. Compos.* 55 (2015) 383–394. doi:10.1016/J.CEMCONCOMP.2014.09.024.
- [29] R. Yu, P. Spiesz, H.J.H. Brouwers, Development of Ultra-High Performance Fibre Reinforced Concrete (UHPFRC): Towards an efficient utilization of binders and fibres, *Constr. Build. Mater.* 79 (2015) 273–282. doi:10.1016/J.CONBUILDMAT.2015.01.050.
- [30] Q.L. Yu, P. Spiesz, H.J.H. Brouwers, Ultra-lightweight concrete: Conceptual design and performance evaluation, *Cem. Concr. Compos.* 61 (2015) 18–28. doi:10.1016/J.CEMCONCOMP.2015.04.012.
- [31] R. Yu, D.V. van Onna, P. Spiesz, Q.L. Yu, H.J.H. Brouwers, Development of Ultra-Lightweight Fibre Reinforced Concrete applying expanded waste glass, *J. Clean. Prod.* 112 (2016) 690–701. doi:10.1016/J.JCLEPRO.2015.07.082.
- [32] D.M.A. Huiskes, A. Keulen, Q.L. Yu, H.J.H. Brouwers, Design and performance evaluation of ultra-lightweight geopolymers concrete, *Mater. Des.* 89 (2016) 516–526. doi:10.1016/J.MATDES.2015.09.167.
- [33] G. Hüsken, H.J.H. Brouwers, Development of eco earth-moist concrete, 5950 (2009) 97–105.
- [34] G. Hüsken, A multifunctional design approach for sustainable concrete, 2010. doi:10.6100/IR693348.
- [35] G. Hüsken, H.J.H. Brouwers, On the early-age behavior of zero-slump concrete, *Cem. Concr. Res.* 42 (2012) 501–510. doi:10.1016/J.CEMCONRES.2011.11.007.
- [36] G. Hüsken, H.J.H. Brouwers, A new mix design concept for earth-moist concrete: A theoretical and experimental study, *Cem. Concr. Res.* 38 (2008) 1246–1259. doi:10.1016/J.CEMCONRES.2008.04.002.
- [37] B. Quenee, G. Li, J.M. Siwak, V. Basuyau, The use of MSWI (Municipal solid waste incineration) bottom ash as aggregates in hydraulic concrete, *Waste Manag. Ser.* 1 (2000) 422–437. doi:10.1016/S0713-2743(00)80054-9.
- [38] A. Keulen, A. van Zomeren, P. Harpe, W. Aarnink, H.A.E. Simons, H.J.H. Brouwers, High performance of treated and washed MSWI bottom ash granulates as natural aggregate replacement within earth-moist concrete., *Waste Manag.* (2016). doi:10.1016/j.wasman.2016.01.010.
- [39] EN 932-1, Tests for general properties of aggregates - Part 1: Methods for sampling, 1996.
- [40] S., Mindness, Young J F, Darwin D., *Concrete*, 2nd ed., Prentice Hall, Pearson Education, Inc. Upper Saddle River, NJ 07458, 2003.
- [41] EN 933-1, Tests for geometrical properties of aggregates - Part 1: Determination of particle size distribution - Sieving method, CEN, 2012.
- [42] EN 933-2, Tests for geometrical properties of aggregates - Part 2: Determination of particle size distribution - Test sieves, nominal sizes of apertures, CEN, 1995.

- [43] D.C. Montgomery, Design and Analysis of Experiments, 2012. doi:10.1198/tech.2006.s372.
- [44] R. Yu, Development of sustainable protective ultra-high performance fibre reinforced concrete (UHPFRC), 2014.
- [45] A. Käppi, E. Nordenswan, Workability of No-Slump Concrete, *Concr. Int.* 29 (2007) 37–41.
- [46] Invelop oy, Operating Instructions Intensive Compaction Tester model ICT-100R (c0251/C), 2005.
- [47] F. V. Mueller, O.H. Wallevik, Linking solid particle packing of Eco-SCC to material performance, *Cem. Concr. Compos.* 54 (2014) 117–125. doi:10.1016/J.CEMCONCOMP.2014.04.001.
- [48] D.A. Abrams, Proportioning Concrete Mixtures, in: *Proc. 18th Annu. Conv. Am. Concr. Inst.*, Detroit, Michigan, U.S., 1922: pp. 174–181.
- [49] R. Bornemann, Untersuchung zur modellierung des frisch- und festbetonverhaltens erdfeuchter betone., *Struct. Mater. Eng. Ser.* 4 (2005).

Influence of the Water- and Foaming Agent Dosage on Hardened Autoclaved Aerated Concrete

C. Straub^{a1,b}, M.V.A. Florea^b, G. Quercia^{a,b,c1}, H.J.H. Brouwers^b

^aMaterials innovation institute (M2i)

^bEindhoven University of Technology

^cTAKTL LLC

Abstract- The most important parameters for the production of Autoclaved Aerated Concrete (AAC) are water-to-powder ratio and foaming agent (Al powder) amount, yet their influence on the green- and final product properties are not sufficiently studied. Here, this influence is thoroughly investigated and quantified, and formulas for the interaction of these parameters are proposed. Moreover, various relations between final AAC properties (thermal conductivity, strength, etc.) and initial mix parameters are derived and explained. The results of this research demonstrate how an optimization of the initial ACC parameters can significantly improve the material behavior.

Keywords: autoclaved aerated concrete, AAC, green body, spread flow, compressive strength, density

1. Introduction

Autoclaved aerated concrete (AAC) has been known for a long time to be an insulating, lightweight and fire resistant building material [1]. Its advantages compared to other building materials are the possibility of creating monolithic wall structures and its eco-friendliness [2,3]. To further increase its eco-friendliness, new raw materials can be applied. It is a common approach to use alternative materials to extend or improve existing materials. In the case of AAC this idea is implemented already in the original patents [4–6]; for example, the use of fly ash instead of ground quartz is widely applied. There are basically two requirements for the application of new raw materials: a well-developed and optimized standard recipe and the complete characterization of this recipe (including technological parameters like mixing, slurry and green body behaviour, and detailed knowledge about the produced AAC itself).

In literature [1,2,7–22] different ranges for AAC recipes are given. However, details of the raw materials are not provided in most cases, or the formulated recipe is incomplete or not published due to confidentiality or intellectual properties protection issues [2,8,10,17,18,23–31].

For the process and product development of eco- and high performance autoclaved aerated concrete, accurate and complete information on raw materials and their related product performance are vital. The characterization of the produced AAC with substituted raw materials is limited to the final properties [8,10–13,17–22,24–26,32,33], and in these studies the material behaviour before hydrothermal hardening is not investigated. Also in industry, systematic studies are either not conducted, or the available know-how and experience are not published.

Two different AAC products can be compared only if their pore structures, respectively green bodies, are similar. For this hypothesis an adaptation of the recipe, especially of the water and foaming agent

amount, is necessary in case of the application of a replacement material. However, the data providing these important information is not properly documented, in some cases not even the water amount of the mix is provided [20,22,24,25,32], or the phrase “workable” mixtures or similar is used instead [16,19,26,32].

Another novel approach employed in this study is the scale of the moulds. In standards like [34] it is recommended to cut the specimens for the tests from the middle of the produced block, due to the influence of the surface on the texture and hence on the properties. A minimum distance from the mould wall to provide a undisturbed pore structure is 5 cm. Commonly the mould size for AAC castings in research papers [7,8,20,26,28,33,10,11,13,14,16–19] (e.g. 40x40x160 mm³) does not provide sample sizes unaffected by the wall effect.

Correlations between different material parameters were formulated [2,9,10,16,19,21,35], but to the best of the authors’ knowledge this is the first time that green parameters are incorporated. Similar research was already conducted on aerated (or surfactant based foamed) concrete [36–38], but aerated concrete and AAC are not comparable materials in the phase of the green body. Similarities occur as well with Al-foamed alkali activated materials [39], whereas the binding process and the intrinsic pH-value are significantly different.

Subsequently, the reference standard recipe needs to be fully characterized. In [1–3,15,40] it is described that a higher water content in the mix leads to a more liquid consistency, higher porosity and lower strength, but an expression of this relation is never given. A model for mix designs is provided on a linear basis in [1], as a guideline for the aimed properties. According to this model, at least 9 different castings are necessary for a rough overview in a small range. The current study investigates these interactions and proposes equations for a more detailed description. The aim is to provide a tool to minimize the number of trial castings. In order to mitigate all these issues, in this study a well-tested recipe developed in an industrial laboratory (provided by HESS AAC systems B.V.) was adopted as a reference standard recipe (Table 1 and Table 2).

In this study, the influence of initial and processing parameters on the final product properties are investigated. Apart from the common hardened properties like raw density and compressive strength, the main focus is on the parameters before autoclaving. This data is used to reveal correlations, which serves for the design of future recipes with other materials.

Another general approach followed for the whole investigation is the hypothesis that an adequate green body can lead to an optimized AAC, while an insufficient green body is unlikely to provide a suitable AAC.

2. Materials and Methods

2.1 Materials

All materials used for preparing the samples are technical grade and, if not indicated otherwise, match the recommended requirements for AAC production [1,2,15,41] or originated from AAC material suppliers (Table 1). All experiments follow a sand-based reference recipe (provided by HESS AAC Systems B.V., Table 2). Normally, in case of a design of an AAC recipe, the targeted (raw) density is mentioned. In this case the resulting density and its changes was one of the aims of the study. The target raw density range can be roughly given by $500 \pm 100 \text{ kg/m}^3$.

Table 1: Chemical and physical characteristics of the raw materials.

Parameter	Quartz	Anhydrite	Cement	Portlandite	Lime	
Chemical Analysis (XRF) [mass%]	Na ₂ O + K ₂ O	0.05	0.37	1.08	0.11	0.27
	MgO	-	1.20	0.96	0.33	0.58
	Al ₂ O ₃	0.85	0.65	4.88	0.13	0.40
	SiO ₂	98.6	1.55	15.7	0.30	0.67
	SO ₃	-	53.7	3.98	0.05	0.03
	CaO	0.01	38.9	66.5	70.1	95.9
	Fe ₂ O ₃	0.03	0.19	2.48	0.17	0.26
	LOI		3.08			
	DIN EN ISO 3262-1	0.26	(650 °C)	2.38	27.4	1.81
Phase content (XRD)	Quartz (low)	Anhydrite, gypsum / dolomite	Quartz, C ₃ S, C ₂ S, C ₄ (AF), C ₃ A	Portlandite, calcite*	Lime, portlandite**	
Specific density [g/cm³]	2.57	2.95	3.12	2.30	3.24	
Supplier	Quarzwerte GmbH	Knauf Gips KG	Cemex	Fels-Werke GmbH	Fels-Werke GmbH	
EN 459-1				CL 90-S	CL 90-Q (R5, P1)	
Product name	SIKRON SF 300	Anhydritstaub	CEM I 42.5 R	WKH 2/4 CL90	11/6	

* Calcite content ≈ 15 % (det. by LOI and density) / ** Portlandite content ≈ 10 % (det. by LOI and density), Slaking lime test (EN 459-2): $t_{60^\circ\text{C}} = 10$ min / $T_{\text{max}} = 75.8$ °C

To avoid confusion the naming of the materials was oriented, as far as possible, on their mineral names (IMA List of Minerals). For example the material that is called lime can as well be labelled as quicklime or burnt lime and regarding EN 459-1, the lime could be called CL90 Q, CAS-Number 1305-78-8. Similar synonyms are available for portlandite (hydrated lime, slaked lime, CL90 S, CAS: 1305-62-0). The aluminium powder was obtained from Benda-Lutz Skawina Sp. z o. o. / SunChemical with the specification/trade name Benda-Lutz® 5 6380.

Table 2 : AAC mix composition

Material	Proportion ω [mass%]
Quartz	66.7
Lime	8.3
Cement	20.0
Portlandite	2.5
Anhydrite	2.5
Aluminium	varied
Water	varied

2.2 Methodology

2.2.1 Characterization of raw materials

The analysis of the raw materials was performed as follows: the chemical analysis was performed using an X-Ray Fluorescence device (XRF, PANalytical Epsilon3) with pressed powder tablets; the Loss On Ignition (LOI) was performed in a muffle furnace according to EN ISO 3262-1 at 1000 °C if not indicated otherwise. The phase composition was measured using an X-Ray Diffractometer (XRD, PANalytical X'Pert PRO MPD with CuK _{α} radiation and an X'Celerator RTMS detector with back loading preparation). The Particle Size Distribution (PSD) was determined using a laser granulometer (Malvern Mastersizer 2000). The specific density of the powders was obtained by a helium pycnometer (Micromeritics AccuPyc II 1340).

2.2.2 Recipe design and mixing

The experiments were performed as follows: after preheating the specific water amount (dependent on the

water-to-powder-ratio, W/P ratio) to 45 °C, it was put in the mixer and stirred at slow speed. Separately, the aluminium powder was manually pre-dispersed with a small part (approximately 100-200 ml) of this water. Quartz and portlandite were successively added and mixed for minimum 60 seconds, in order to ensure homogeneity. The addition of lime, cement and anhydrite was performed within 30 s and then mixing continued for 90 s. Within the last 30 s of the mixing the aluminium powder suspension was added. Within 5 minutes from adding the lime and cement both casting and flow experiments were finished.

The investigated parameters (the influence of the mixing device, the water-to-powder ratio (W/P) and the amount of foaming agent) were varied as follows:

The rotation speed of the mixers were changed while adding the materials. It was tried to keep a constant vortex instead specific rpms.

Water-to-powder ratio: The mass ratio of water to total solids (W/P) was changed between 0.525 and 0.725 in steps of 0.1. Additionally, two extreme mixes with a W/P = 0.425 and 0.825 were made. While the mass of the solids remains unchanged, the water amount was varied. This was done due to the fact that the volume of a mix is more dependent on the foaming agent than on the volume of water or solids.

Foaming agent: The aluminium amount was varied between 0.067 % (mass percent in relation to total solids, ω_{Al}) and 0.1 % in 3 steps.

2.2.4 Hydrothermal treatment

The samples were demoulded the following day and placed directly in the autoclave (autoclave: Maschinenbau Scholz GmbH & Co. KG / steam generator: WIMA ED36). The autoclave was programed as follows: 20 min vacuum (-0.8 bar), heating up to 187 °C / 11 bar within 1.5 hours, holding a plateau of 187 °C / 11 bar for 5 hours, cooling down to 20 °C / 0 bar within 1.5 hours. This test program was chosen to be similar to industrial autoclave cycles [45]. After this treatment, at least 5 cm of each side of the sample were removed by band saw to obtain an undisturbed pore structure (no “wall-effect”).

2.2.5 Hardened state analysis

After autoclaving the material was cut for further analysis into 4 cubes (100*100*100 mm³) for raw density (or apparent density) and compressive strength measurements. The polished cubes were oven dried (60°C, forced ventilation) until constant weight. After cooling down to 20 °C the raw density ρ_{AAC} and the compressive strength σ (FORM+TEST Seidner+Co. GmbH, MEGA 110-200 D-S) were measured. The approach is comparable to the standards [34] and [46]. The thermal conductivity λ was measured using an ISOMET model 2104 heat transfer analyser (Applied Precision), by measuring multiple times on a polished surface.

3. Results & discussion

3.1 Characterization of raw materials

All materials fulfil the industrial guideline $d_{90} < 90 \mu m$ (Figure 1). The measured chemical composition, phase content and the suppliers of the materials are listed in Table 1. Normal tap water was used for all the mixes.

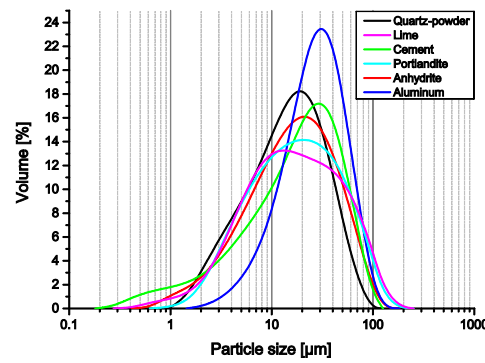


Figure 1: Particle size distribution of the raw materials used.

3.3 Hardened properties

During the autoclave hardening the material will undergo a complete change of its phases and microstructure while keeping the same outer dimensions and macroscopic visible structure.

For the characterization of the produced AAC the raw density ρ_{AAC} , the compressive strength σ and the thermal conductivity λ were measured.

While the sample with a water-to-powder ratio of 0.425 had already failed during green body preparation, the sample with 0.825 failed during autoclaving. It was necessary to repeat the experiment several times until enough suitable material was accumulated for further analysis. Therefore both mixes are not suitable from the production point of view.

After autoclaving the material showed the following behaviour: the raw density ρ_{AAC} (Figure 2) of the material is dependent on the water amount as well as on the amount of foaming agent. The range of the samples was within 390 and 570 kg/m³ (the maximum obtained value was 730 kg/m³, but the pore structure was not the typical bubble distribution as it is known for AAC, so this value was not taken into account). The raw density could be expressed as a function of the W/P ratio and the foaming agent amount ω_{Al} , for example:

$$\rho_{AAC} = G + f^{(W/P)*k} \quad (1)$$

where G represents the asymptote, being a function of the foaming agent amount (the specific formula is similar to this one). The fitting parameters are f (constant with mix design) and k , while the sum $G + k$ remains constant for each mix design (Figure 2).

For the plot in Figure 2 the initial input parameters as production parameters were chosen. From a scientific point of view it might be more suitable to use instead of the W/P the spread flow as expression of the viscosity. However, due to the higher error range of the spread flow a connection of spread flow and raw density are more difficult to obtain.

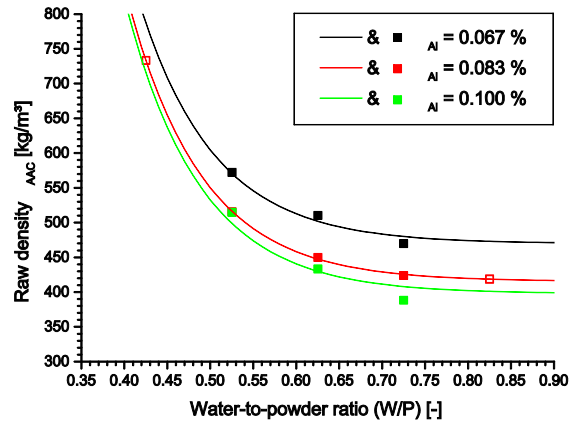


Figure 2: Comparison between the initial water-to-powder ratio (W/P), the foaming agent amount ω_{Al} and the raw density ρ_{AAC} of the final product. Two-dimensional visualization of the data, with fit according to Eq. (3) (lines).

This result seems to contradict the suggested relation from [1], that stated a linear correlation between the spread flow and the raw density. Due to the short range of investigated densities in [1], an approximation to linear behaviour is valid in practical approaches, especially considering the statistical variation of the values. However, for larger ranges the behaviour is better described in Figure 2.

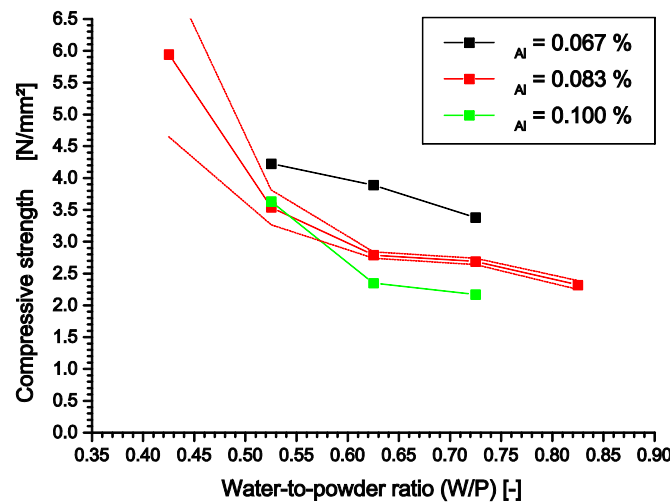


Figure 3: Comparison of the compressive strength σ as function of the water-to-powder ratio (W/P) and the foaming agent amount ω_{Al} . Two-dimensional visualization of the compressive strength. The dotted lines represent the standard deviation of the values for a foaming agent content of 0.083 %.

Together with the raw density, the most common value to describe an AAC is the compressive strength σ (Figure 3). The range of the obtained values is 2.3 - 4.2 N/mm². Due to the fact that the strength is dependent on the raw density, two normalization procedures are known in the industry, the A-Value [2]:

$$A\text{-Value} = \sigma / (\text{const.} * \rho_{AAC}^2) \quad (2)$$

where σ is the compressive strength [N/mm²], *const.* is 0.016 N/g² and ρ is the raw density [g/cm³]. This is the original formulation as published in [2], while a variation of it is given in [16]. The unit of the constant is theoretically [(N*cm⁶)/(g²*mm²)], if the A-Value should be dimensionless.

and the compensated compressive strength (CCS) [45]:

$$CCS = (\sigma / \rho_{AAC}) * \rho_{ref} \quad (3)$$

where ρ_{ref} [kg/m³] is the chosen reference raw density for which the value will be normalized.

While the A-Value approach (Eq. (2)) shows a constant behaviour (within the reported error range, according to literature this is 30 units, [2] respectively 50 units, [45]), the CCS-approach (Eq. (3)) shows a stronger dependency on the W/P ratio and especially the foaming agent amount.

4. Conclusions

The results presented above are part of a larger study which also takes into account all green properties of the AAC mixes and their relationship with the hardened properties. Additional properties such as thermal conductivity are also studied, together with various mixing parameters and slump flow measurement devices.

The following conclusions can be drawn from the findings presented in this study:

- It was proven that the investigated parameters, water-to-powder ratio and foaming agent amount, have a critical influence on the final AAC product.
- In the investigated parameters of the hardened AAC, the water-to-powder ratio is inversely correlated with the foaming agent amount and vice versa. This behaviour could also be observed for the raw density, the compressive strength and the thermal conductivity. It needs to be pointed out that the substitution level of the two ingredients (water and foaming agent) only applies in a quite narrow range within a given mix.
- If the water-to-powder ratio is too low (in this case lower than 0.525), the flowability of the slurry is affected and a uniform pore structure cannot be obtained. If the water-to-powder ratio is too high (in this case higher than 0.725), a suitable green body can be created, but then material failure occurs during hydrothermal hardening.
- The compressive strength of the AAC depends on its raw density, while the A-Value provides a more suitable independent value for the comparison of different mixes.

5. Acknowledgements

This research was carried out under Project Number M81.6.12478 in the framework of the Research Program of the Materials innovation institute M2i (www.m2i.nl), together with the industrial partner HESS AAC systems B.V. and the sponsors of the Building Materials research group at TU Eindhoven. Many thanks as well to Knauf Gips KG, Holcim (Deutschland) AG and Fels-Werke GmbH for supplying materials, as well as to the Fachgruppe Mineralogie/Geochemie from Martin-Luther Universität Halle-Wittenberg (Germany) for the use of their XRD.

Funding: This work was supported by the Materials innovation institute M2i (www.m2i.nl) [grant number M81.6.12478].

6. References

- [1] S. Reinsdorf, Leichtbeton Band II Porenbetone, VEB Verlag für Bauwesen, Berlin, Germany, 1963.
- [2] S.G. Zürn, Einfluss der Sandminerale auf die Bildung von Calciumsilikathydraten (CSH-Phasen), das Gefüge und die mechanischen Eigenschaften von Porenbetonprodukten Systematische Untersuchungen an synthetischen Sandmischungen mit Übertragung auf Produktionssande, Logos Verlag, Berlin, Germany, 1997.
- [3] S. Röbert, U.a., Silikatbeton Herstellung, Bewertung, Anwendung 2. stark bearbeitete Auflage,

VEB Verlag für Bauwesen, Berlin, Germany, 1987.

- [4] J.A. Eriksson, Verfahren zur Herstellung eines porösen Baustoffes aus Portlandzement, DE000000404677A, 1923.
- [5] J.A. Eriksson, Verfahren zur Herstellung von porösen Baustücken aus Beton, DE000000447194A, 1924.
- [6] J.A. Eriksson, Verfahren zur Herstellung poröser Kunststeine, DE000000454744A, 1924.
- [7] D. Lesueur, F. Mücke, H. Oeinck, U. Peter, C. Pust, F. Verhelst, Impact of quicklime reactivity and origin on autoclaved aerated concrete production, in: 5th Int. Conf. Autoclaved Aerated Concr., Bydgoszcz, Poland, 2011: pp. 101–110.
- [8] F. Matsushita, Y. Aono, S. Shibata, Particles size distribution of quartz sand for AAC production, in: 5th Int. Conf. Autoclaved Aerated Concr., Bydgoszcz, Poland, 2011: pp. 155–162.
- [9] I. Kadashevich, H.J. Schneider, D. Stoyan, Statistical modeling of the geometrical structure of the system of artificial air pores in autoclaved aerated concrete, *Cem. Concr. Res.* 35 (2005) 1495–1502. doi:10.1016/j.cemconres.2004.10.010.
- [10] A. Alhozaimy, G. Fares, A. Al-Negheimish, M.S. Jaafar, The autoclaved concrete industry: An easy-to-follow method for optimization and testing, *Constr. Build. Mater.* 49 (2013) 184–193. doi:10.1016/j.conbuildmat.2013.08.024.
- [11] A. Laukaitis, J. Kerien, M. Kligys, D. Mikulskis, L. Lekunait, Influence of mechanically treated carbon fibre additives on structure formation and properties of autoclaved aerated concrete, *Constr. Build. Mater.* 26 (2012) 362–371. doi:10.1016/j.conbuildmat.2011.06.035.
- [12] T. Mitsuda, K. Sasaki, H. Ishida, Phase Evolution during Autoclaving Process, *J. Am. Ceram. Soc.* 75 (1992) 1858–1863.
- [13] Y. Song, B. Li, E.-H. Yang, Y. Liu, T. Ding, Feasibility study on utilization of municipal solid waste incineration bottom ash as aerating agent for the production of autoclaved aerated concrete, *Cem. Concr. Compos.* 56 (2015) 51–58. doi:10.1016/j.cemconcomp.2014.11.006.
- [14] X.Y. Cong, S. Lu, Y. Yao, Z. Wang, Fabrication and characterization of self-ignition coal gangue autoclaved aerated concrete, *Mater. Des.* 97 (2016) 155–162. doi:10.1016/j.matdes.2016.02.068.
- [15] J.A.H. Oates, *Lime and Limestone Chemistry and Technology, Production and Uses*, Wiley-VCH Verlag GmbH, Weinheim, Germany, 1998.
- [16] A. Hauser, U. Eggenberger, T. Mumenthaler, Fly ash from cellulose industry as secondary raw material in autoclaved aerated concrete, *Cem. Concr. Res.* 29 (1999) 297–302. doi:10.1016/S0008-8846(98)00207-5.
- [17] W. Wongkeo, A. Chaipanich, Compressive strength, microstructure and thermal analysis of autoclaved and air cured structural lightweight concrete made with coal bottom ash and silica fume, *Mater. Sci. Eng. A.* 527 (2010) 3676–3684. doi:10.1016/j.msea.2010.01.089.
- [18] W. Wongkeo, P. Thongsanitgarn, K. Pimraksa, A. Chaipanich, Compressive strength, flexural strength and thermal conductivity of autoclaved concrete block made using bottom ash as cement replacement materials, *Mater. Des.* 35 (2012) 434–439. doi:10.1016/j.matdes.2011.08.046.

- [19] H. Kurama, I.B. Topçu, C. Karakurt, Properties of the autoclaved aerated concrete produced from coal bottom ash, *J. Mater. Process. Technol.* 209 (2009) 767–773. doi:10.1016/j.jmatprotec.2008.02.044.
- [20] X. Huang, W. Ni, W. Cui, Z. Wang, L. Zhu, Preparation of autoclaved aerated concrete using copper tailings and blast furnace slag, *Constr. Build. Mater.* 27 (2012) 1–5. doi:10.1016/j.conbuildmat.2011.08.034.
- [21] C. Karakurt, H. Kurama, I.B. Topçu, Utilization of natural zeolite in aerated concrete production, *Cem. Concr. Compos.* 32 (2010) 1–8. doi:10.1016/j.cemconcomp.2009.10.002.
- [22] T. Dietz, P. Daschner, Saving of energy and resources in the latest generation of AAC production plants, in: 5th Int. Conf. Autoclaved Aerated Concr., Bydgoszcz, Poland, 2011: pp. 57–62.
- [23] K. Matsui, J. Kikuma, M. Tsunashima, T. Ishikawa, S.Y. Matsuno, A. Ogawa, M. Sato, In situ time-resolved X-ray diffraction of tobermorite formation in autoclaved aerated concrete: Influence of silica source reactivity and Al addition, *Cem. Concr. Res.* 41 (2011) 510–519. doi:10.1016/j.cemconres.2011.01.022.
- [24] W. Pichór, Properties of autoclaved aerated concretes with cenospheres from coal ash, in: 5th Int. Conf. Autoclaved Aerated Concr., Bydgoszcz, Poland, 2011: pp. 163–170.
- [25] N. Narayanan, K. Ramamurthy, Microstructural investigations on aerated concrete, *Cem. Concr. Res.* 30 (2000) 457–464. doi:10.1016/S0008-8846(00)00199-X.
- [26] H. Connan, D. Klimesch, A. Ray, P. Thomas, Thermal characterisation of autoclaved cement made with alumina-silica rich industrial waste, *J. Therm. Anal. Calorim.* 84 (2006) 521–525. doi:10.1007/s10973-005-6674-z.
- [27] K. Matsui, A. Ogawa, J. Kikuma, M. Tsunashima, T. Ishikawa, S. Matsuno, Influence of addition of Al compound and gypsum on tobermorite formation in autoclaved aerated concrete studied by in situ X-ray diffraction, in: 5th Int. Conf. Autoclaved Aerated Concr., Bydgoszcz, Poland, 2011: pp. 147–154.
- [28] J. Kikuma, M. Tsunashima, T. Ishikawa, S. Matsuno, A. Ogawa, K. Matsui, Use of fine particle quartz sand for AAC production : model study by in situ x-ray diffraction and NMR, in: 5th Int. Conf. Autoclaved Aerated Concr., Bydgoszcz, Poland, 2011: pp. 71–77.
- [29] J. Kikuma, M. Tsunashima, T. Ishikawa, S. Matsuno, a. Ogawa, K. Matsui, Development of an in situ X-ray diffraction system for hydrothermal reactions and its application to autoclaved aerated concrete formation, *Powder Diffr.* 26 (2011) 126–128. doi:10.1154/1.3583565.
- [30] J. Kikuma, M. Tsunashima, T. Ishikawa, S. Matsuno, A. Ogawa, K. Matsui, M. Sato, Effects of quartz particle size and water-to-solid ratio on hydrothermal synthesis of tobermorite studied by in-situ time-resolved X-ray diffraction, *J. Solid State Chem.* 184 (2011) 2066–2074. doi:10.1016/j.jssc.2011.05.061.
- [31] J. Kikuma, M. Tsunashima, T. Ishikawa, S.Y. Matsuno, A. Ogawa, K. Matsui, M. Sato, In situ time-resolved X-ray diffraction of tobermorite formation process under autoclave condition, *J. Am. Ceram. Soc.* 93 (2010) 2667–2674. doi:10.1111/j.1551-2916.2010.03815.x.
- [32] K. Laskawiec, J. Malolepszy, G. Zapotoczna-Sytek, Influence of the amount and the kind fly ashes produced of coal combustion in fluidized bed boilers on properties autoclaved aerated concrete ., in: H.-M. Ludwig, H.-B. Fischer, K.A. Bode, C. Beuthan, S. Bähring (Eds.), *Proc. 18th Int. Conf. Build. Mater. (Ibausil)*, Weimar, Weimar, Germany, 2012.
- [33] N.Y. Mostafa, Influence of air-cooled slag on physicochemical properties of autoclaved aerated concrete, *Cem. Concr. Res.* 35 (2005) 1349–1357. doi:10.1016/j.cemconres.2004.10.011.

- [34] DIN EN 771-4, Berlin, Germany, 2003.
- [35] G. Rausch, J. Baumeister, D. Lehmhus, H. Stanzick, K. Stöbener, M. Wichmann, N. Zimmer, V. Zöllmer, FOAMINAL® Properties Overview and Design Guideline, Bremen, Germany, n.d.
- [36] M. Schauerte, R. Trettn, Neue Schaumbetone mit gesteigerten mechanischen und physikalischen Eigenschaften, in: H.-M. Ludwig, H.-B. Fischer, K.A. Bode, C. Beuthan, S. Bähring (Eds.), Proc. 18th Int. Conf. Build. Mater. (Ibausil), Weimar, Weimar, Germany, 2012.
- [37] J. Pinilla Melo, A. Sepulcre Aguilar, F. Hernández Olivares, Rheological properties of aerated cement pastes with fly ash, metakaolin and sepiolite additions, Constr. Build. Mater. 65 (2014) 566–573. doi:10.1016/j.conbuildmat.2014.05.034.
- [38] J. Jiang, Z. Lu, Y. Niu, J. Li, Y. Zhang, Study on the preparation and properties of high-porosity foamed concretes based on ordinary Portland cement, Mater. Des. 92 (2016) 949–959. doi:10.1016/j.matdes.2015.12.068.
- [39] A. Hajimohammadi, T. Ngo, P. Mendis, J. Sanjayan, Regulating the chemical foaming reaction to control the porosity of geopolymer foams, Mater. Des. 120 (2017) 255–265. doi:10.1016/j.matdes.2017.02.026.
- [40] H. Gundlach, Dampfgehärtete Baustoffe, Bauverlag GmbH, Wiesbaden, Germany / Berlin, Germany, 1973.
- [41] B. Walk-Laufer, Untersuchung des Einflusses von Sulfaten auf das System CaO-SiO₂-Al₂O₃-K₂O-H₂O mittels Wärmeflusskalorimetrie und in-situ Neutronenbeugung unter hydrothermalen Bedingungen, Universität Siegen, 2002.
- [42] DIN EN 1015-3, Berlin, Germany, 2004.
- [43] I. Mehdipour, A. Kumar, K.H. Khayat, Rheology, hydration, and strength evolution of interground limestone cement containing PCE dispersant and high volume supplementary cementitious materials, Mater. Des. 127 (2017) 54–66. doi:10.1016/j.matdes.2017.04.061.
- [44] DIN EN 196-3, Berlin, Germany, 1995.
- [45] L. Heinz, Private communication, (2015).

Effect of carbonation on chloride binding behaviors and hydration product formation of metakaolin-ground waste coral blended marine mortars

Y. Wang ^{1,2}, Z. Shui ¹, X. Gao ³, Y. Huang ², R. Yu ¹, Q. Song ^{1,2}

¹State Key Laboratory of Silicate Materials for Architectures, Wuhan University of Technology, Wuhan 430070, China

²School of Materials Science and Engineering, Wuhan University of Technology, Wuhan 430070, China

³School of Civil Engineering and Architecture, Wuhan University of Technology, Wuhan 430070, China.

Abstract

The construction of facilities on islands far from mainland is challenged by the lack of raw materials for concrete production. Nowadays, the locally available waste coral is used as concrete aggregate to relieve its dependency of raw materials from mainland, and acceptable hardened behaviors of coral aggregate concrete are achieved. However, waste coral recycled as aggregate can result in significant damage of workability because of porous structure of coral. To ease this adverse effect, the present work recycles waste coral as filler and coupled with metakaolin to prepare marine mortar. The waste coral filler (GWC) is ground from coral waste detritus, during which the pores in coral particles is damaged. Since GWC-metakaolin (MK) based mortars are exclusively used on islands, it can suffer from a heavy chloride attack. In this way, the chloride binding and diffusion behaviors of GWC-MK based mortar should be concerned more. Besides, the blended cementitious materials are normally easier to be carbonated. The resulting calcium hydroxide content reduction and calcium carbonate formation may have certain effects on the hydration production formation and chloride binding of GWC-MK based cementitious materials.

Concerning that, the present work utilized GWC and MK in marine mortar production. The GWC partially replaced cement at 10, 20 and 30 wt.%. MK was used to compensate the GWC addition induced adverse effects on hardened properties of mortar. The replacement ratio of cement with MK was 5 and 10 wt.%. The mortars were cast in 40mm*40mm*160mm steel moulds and cured in lime-saturated water at 20±1 °C. The carbonation-induced modification on chloride binding and hydrate assemblage of hardened mixtures were investigated. Based on the chloride binding capacity and porosity of GWC-MK based mortar, the variation in chloride diffusion of different mortar was explained. The results show that addition of GWC shows no obvious effect on the workability of fresh mixture, but obviously reduces the compressive strength and chloride resistance ability. GWC can involve in the formation of carboaluminate with the aluminum from either clinker or MK to improve the mechanical properties and chloride resistance. Carbonation can further promote carboaluminate formation and convert hemicarboaluminate to monocarboaluminate due to more carbonate available in the system. During chloride exposure, hemicarboaluminate and monocarboaluminate transform to Friedel's salt and meanwhile delayed ettringite formation is favored, but delayed ettringite formation is less remarkable for carbonated samples after chloride exposure. Due to the densification of matrix and improved chloride binding capacity, the chloride diffusion coefficient of GWC mortar is sharply

reduced with MK addition. The mortar with couple use of 20 wt.% GWC and 5 wt.% MK achieves half the chloride diffusion coefficient of plain mortar during a exposure duration of 6 months. And, the even higher amount of MK achieves even lower chloride diffusion coefficient.

Keywords: Carbonation, carboaluminate, Friedel's salt, chloride exposure, delayed ettringite.

1. Introduction

The shortage of raw materials for concrete production is a longstanding problem for the concrete production on islands far from mainland. This issue is drawing concerns more than ever due to the blooming exploitation of ocean. In tradition, the supply of raw materials for concrete production on the isolated islands is by cargo. However, this mode of transportation takes a long time and sometimes may be a risky option due to the unpredictable weather. Therefore, it is of great significance to find some local alternatives to relieve the dependence of facility construction there on the raw material supplied from mainland.

As commonly known, there is always an abundant deposit of coral reef around tropic islands. During some local engineering works, coral reefs are dug out inevitably and discard as waste nearby. The waste coral reef has the potential to be recycled as concrete ingredients because it is mainly composed of calcium carbonate in the forms of aragonite and calcite [1,2]. The properties of concretes with coral reef utilized as fine aggregate have been investigated and it is found that the properties of coral sand concrete demonstrates acceptable mechanical properties compared to normal river sand concrete [1,3]. As for the durability, recycling waste coral as fine aggregate is reported to improve the chloride resistance compared to river sand concrete [3,4], which was attributed to the denser microstructure of ITZ resulting from the internal curing of porous coral sand [5,6]. The internal curing was reported to obviously reduce the shrinkage of coral aggregate concrete, either [7,8].

Although it can conclude from previous researches that the proper use of waste coral as aggregate does not result in a noticeable degradation of hardened properties of concrete, the waste coral is very porous, the coral aggregate absorbs high amount of mixing water, leading to an obvious increase in superplasticizer dosage to maintain a suitable workability of fresh mixture [2,9,5]. In order to overcome this adverse effect, an alternative method of recycling waste coral as cement filler is proposed [10]. Since the pores in waste coral are seriously destroyed during grinding, the mixing water removed by adsorption of coral materials is prevented and therefore less effect is imposed on the workability of fresh concrete as reported [10]. Another beneficial effect to adopt ground waste coral (GWC) as filler is that less cement is used and the ecological properties of concrete is improved accordingly. However, due to the dilution effect of GWC addition, the mechanical properties of concrete may suffer an obvious declination. One effective manner to limit this drawback is to use alumina-rich pozzolan which benefits the performance of concrete through pozzolanic reaction and carboaluminate formation [11-13].

Metakaolin (MK) is a typical alumina-rich pozzolan, and its extraordinary ability to improve the mechanical properties and form carboaluminate with coral materials has been addressed, indicating that MK is a good candidate to improve the performance of GWC based cement mixtures [10]. However, as a material exclusively used in marine concrete, the chloride binding and diffusion of MK-GWC based marine concrete/mortar under chloride exposure deserves more concern. Besides, since the pozzolan blended cementitious materials generally suffer from a high risk of carbonation [14-16], the resulting pH dropping and calcium carbonate generation may show certain effects on the hydration production formation and chloride binding behaviors of GWC-MK based marine mortar. Therefore, more knowledge relating to these issues is needed.

The present work used ground waste coral (GWC) and metakaolin as partial substitution of cement to

prepare marine mortars. The effects of carbonation on hydration production formation and chloride binding capacity were investigated. Besides, the chloride diffusion profile under chloride exposure was also determined to measure chloride diffusion coefficient by fitting with Fick's 2nd law.

2. Methodology

2.1 Materials

Ordinary Portland cement of grade 42.5, commercial available metakaolin (MK), ground waste coral (GWC) and ISO sand were used to prepare cement mortar. The means particle sizes (by a granulometer) were 12.96 μm for cement, 3.45 μm for MK and 8.52 μm for GWC. GWC was produced by grinding waste coral detritus in a ball mill. The waste coral detritus was collected from a tropic island on a tropic island. The chemical composition of cementitious materials, X-ray diffraction (XRD) patterns of GWC and Scanning Electronic Scopic (SEM) image of coral detritus can be referred to Ref. [2]. It can be found that the aluminum oxide content in MK is more than 40 wt.% and the GWC mainly consists of aragonite and calcite rich in magnesium. Besides, the SEM image verifies the porous structure of coral materials as already addressed in other Ref. [4,5]. To adjust the workability of fresh mortar mixture, a polycarboxylate superplasticizer (PCE) was used.

2.2 Methods

2.2.1 Sample preparation

Six mortars with water to binder ratio of 0.5 and binder to sand ratio of 1/3 were designed as shown in Table 1. The mass of total binder (cement plus GWC plus MK) has been normalized to 1. The substitution of cement with GWC is 10, 20 and 30 wt.%, whereas that of cement with MK is 5 and 10 wt.% because the further higher amount of MK can result in significantly damage of workability. The fresh mixtures were placed in 40mm*40mm*160mm steel moulds and demoulded at 24 hours. Thereafter, specimens were cured in lime-saturated water at 20 \pm 1°C.

Table 1 Mix proportions of cement mortars

Mix	Cement	GWC	MK	Sand	w/b	PCE
REF	1.00	0	0	3	0.5	0
10C	0.90	0.10	0	3	0.5	0
20C	0.80	0.20	0	3	0.5	0
30C	0.70	0.30	0	3	0.5	0
5M20C	0.75	0.20	0.05	3	0.5	0.001
10M20C	0.70	0.20	0.10	3	0.5	0.002

2.2.2 Porosity and dried bulk density

At the curing age of 6 months, a saturation-drying method was employed to determine the porosity of mortar [17,18]. The mortar samples were firstly saturated with deionized water in a vacuum following the procedures to prepare samples for RCM test according to NT Build 492. Then, the initial weight (m_0 , g) and buoyant weight (m_w , g) of saturated samples were measured. Thereafter, water-saturated samples were dried in an oven at 105 °C for 2 weeks. In due time, the dried weight (m_d , g) of the samples were measured. In this way, the porosity (p , %) and dried bulk density (ρ_d , g/cm³) of hardened mortars can be calculated following Eqs. (1) and (2) respectively:

$$p = \frac{m_0 - m_d}{m_0 - m_w} \quad (1)$$

$$\rho_d = \frac{m_d \cdot \rho_H}{m_0 - m_w} \quad (2)$$

Here, ρ_H is the density of water, 1.00g/cm³.

1.1.1 Chloride diffusion profile determined from chloride exposure

At the curing age of 1 month, some mortar prisms were removed from the curing tank and a 40mm*40mm*60mm cuboid was cut off from each one. Thereafter, the five surfaces of remaining part of mortar prisms were coated with epoxy resin with the exception of the newly-cut surface. After the resin was completely dried, the coated samples were saturated with deionized water in a vacuum box, followed by immersing the coated samples in 0.5 M sodium chloride solution with the uncoated surface upward. The exposure solution was refreshed once a month. After 5 months of exposure, the specimens were removed and the resin was scraped down. Then, the specimens were ground layer by layer, perpendicular to the exposed surface (previously uncoated one). Each layer was 4 mm in thickness. The ground powder was dried in a vacuum at 50 °C for 24 hours. After that, the free chloride content was determined by measuring the water-soluble chloride content in the powder according to Ref. [19,20]. Exactly 4 gram of mortar powder and 40 ml of deionized water were added in a screw-capped vial and homogenized by vibration. After 24 hours of immersion, 5 ml of liquid was pipetted and neutralized with sulfuric acid. After that, it was titrated with 0.02 M silver nitrate with the indicator of potassium chromate to determine the chloride content. In this way, the free chloride in unit volume of mortar in certain layer can be calculated as Eq. (3) shown:

$$X = \frac{8 \cdot C_{Ag} \cdot V_{Ag} \cdot M_{Cl} \cdot \rho_d}{m} \quad (3)$$

Here:

X the free chloride content in mortar, mg/cm³ mortar;

C_{Ag} the concentration of silver nitrate, 0.01964 M;

V_{Ag} the consumed volume of silver nitrate, mL;

M_{Cl} the molar mass of chloride, 35.45 g/mol;

ρ_d the dry density of mortar, g/cm³;

m the mass of mortar powder, 4g;

Fick's 2nd law can be used to describe the non-steady diffusion of chloride in mortar. The equation of Fick's second law can be expressed as:

$$\begin{cases} \frac{\partial X}{\partial t} = D \cdot \frac{\partial^2 X}{\partial x^2}; t > 0, x > 0 \\ X(x, t)|_{x=0} = X_s \\ X(x, t)|_{t=0, x>0} = X_0 \end{cases} \quad (4)$$

The solution of Eq. (4) is Eq. (5):

$$X = (X_0 - X_s) \cdot \frac{2}{\sqrt{\pi}} \cdot \int_0^{\frac{x}{2\sqrt{Dt}}} e^{-\left(\frac{x}{2\sqrt{Dt}}\right)^2} d\frac{x}{2\sqrt{Dt}} + X_s = (X_0 - X_s) \cdot \operatorname{erf}\left(\frac{x}{2\sqrt{Dt}}\right) + X_s \quad (5)$$

Here:

- X_s the chloride content of surface layer, mg/cm³;
 X_0 the back ground content of chloride in mortar, mg/cm³;
 D the apparent chloride diffusion coefficient, cm²/month;
 x the depth from the exposed surface, mm;
 t the exposure time, month;

Based on Eq. (5), the apparent chloride diffusion coefficient can be determined by fitting the diffusion profile with this equation.

2.2.2 Chloride binding capacity of sound and carbonated mortars

After the mortars were cured in lime-saturated water for 3 weeks, slices with 10mm in thickness were cut from the middle of mortar prisms and then stored in a box to initiate the carbonation. The carbonation is carried out under the condition that 20±2 °C, 70±5 % in relative humidity and 20±3 vol.% in CO₂ concentration. One week later, the slices were removed from the carbonation box, followed by drying in a vacuum oven at 50 °C for 24 hours. Thereafter, the slices were ground to powder less than 74 μm in diameter. Then, exact 20g of mortar powder and 30 ml of 0.5 M lime-saturated sodium chloride solution were added in screw-capped vials. The vials were placed on an oscillator and shaken at the frequency of 200 times to avoid sediment. After the mortar powder was exposed for 1 month, 10 ml of exposure solution was pipetted out and diluted to 250 ml with deionized water. Then, 0.02 M silver solution was used to titrate the chloride in 5 ml of diluted exposure solution with the indicator of potassium chromate, as did in Section 2.3.2. In this way, the chloride bound by per gram of mortar powder can be calculated.

Meanwhile, the chloride binding capacity of samples free of carbonation (cured in lime-saturated water for 4 weeks) was also detected in the same way.

2.2.3 Formation of hydrates

Before and after the test of chloride binding capacity, the mortar powder was examined by Malvern Panalytical Empyrean diffractometer from 8°-28°, 0.01° per step and 2°/min to identify the assemblage of hydrates.

3. Results and discussion

3.1 Physical properties

Table 2 shows some important basic physical properties of mortars including spread diameter, compressive strength at 56 days, porosity at 6 months and dried bulk density at 6 months. The addition of GWC shows negligible impacts on the workability of fresh mixtures, despite that numerous literatures reported an obvious degradation of workability of coral aggregate concrete due to absorption of mixing water [2,9,5]. This means that the porous structure of coral is significantly destroyed and the mixing water absorption by coral materials is prevented. Meanwhile, a remarked reduction of compressive strength and increase of porosity are also observed. It is ascribed to the dilution effect induced by GWC addition, which results in loose structure of hardened mixture. GWC addition also leads to modest reduction of dried bulk density, probably due to less mixing water chemically bound in GWC blended mortars.

With the addition of MK, the compressive strength of GWC mortar is dramatically improved and porosity is significantly reduced, indicating that a densified microstructure is achieved. One well-known mechanism is that the pozzolanic reaction of MK to form cementitious products. However, another mechanism

exclusively existed in the system with carbonate materials is that the reaction of aluminum from pozzolans with calcium carbonate to form carboaluminate, which densifies the boundaries between carbonate materials and bulk paste [2]. The addition of MK also increases the dried bulk density of mortar. This may be related to the improved packing density and more water bound during hydration.

Table 2 Physical properties of mortars

Mix	Spread diameter	Compressive strength	Porosity	Dried bulk density
	mm	MPa	%	kg/m ³
REF	165	48.3	17.96	2115.1
10C	162	41.5	19.33	2114.8
20C	164	34.0	20.61	2085.4
30C	159	25.4	21.47	2064.3
5M20C	Not measured	46.0	19.54	2085.9
10M20C	Not measured	49.9	17.37	2094.6

3.2 Effect of carbonation on chloride binding capacity

Fig. 1 presents the chloride binding capacity of sound and carbonated samples. It is obvious that the chloride binding capacity of mortars can be reduced with GWC addition due to dilution effect, and improved with MK addition because of additional aluminum supplement. It is also observed that the blended mortars seem to experience a larger reduction in chloride binding capacity after carbonated. As already reported, the blended cement mixtures are easy to be carbonated compared to plain one because less calcium is available for CO₂ to react in blended ones [14-16]. Besides, it is also accepted that the formation of chloroaluminate and chloride adsorption on C-S-H gels can be benefited in the presence of sufficient calcium ions [21-24]. As in this study, the calcium ions in blended mortars can drop faster than plain one during carbonation due to the less calcium hydroxide available in blended samples. As a result, a more remarkable reduction of bound chloride is resulted for blended mortar. This means that for the concrete structures serve in chloride-rich environment, carbonation-induced steel corrosion may be the synergy of pore solution neutralization and bound chlorides reversing to free ones.

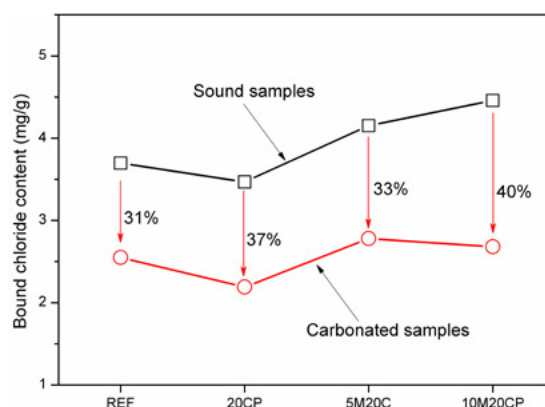


Fig. 1 Chloride binding capacity of sound and carbonated mortars

3.3 Effect of carbonation on phase assemblage

3.3.1 Hydration production before chloride exposure

Fig. 2 illustrates the XRD patterns of sound and carbonated samples before chloride exposure. The assemblage of hydrates is ettringite (Et, $C_6As_3H_{32}$), hemicarboaluminate (Hc, $C_4Ac_{0.5}H_{12}$), monocarboaluminate (Mc, C_4AcH_{11}), calcium hydroxide (CH) and calcite (Cc). It is evident that the addition of GWC improves the formation of Mc, which means GWC can perform the similar reactions to limestone and involve in the formation of carboaluminate [19,25]. After 5 wt.% MK included, the height of Mc diffraction peak almost maintains the same, but the width increases obviously, indicating more Mc formed. With the further addition of MK, a peak corresponding to Hc is generated, which is a type of carboaluminate formed when

reactive calcium carbonate is insufficient. As reported [25], only small fraction of limestone is reacted, probably the surface layer of limestone particles, because of the low solubility of calcite in pore solution. As in this study, although 20 wt.% of GWC can theoretically transform all aluminum in binder to Mc, actually only small fraction of carbonate in the surface layer of GWC particle can be considered as reactive. Thus, the use of 10 wt.% MK can result in formation of Hc.

Comparing to sound samples, the diffraction of CH is significantly reduced in carbonated ones, which is attributed to the reaction between CO₂ and CH to form calcite. Besides, it is also observed that the diffraction of Et and Mc of carbonated samples is stronger than that of sound ones. A large number of literatures have proved that calcite can stabilize Et at the expense of monosulfoaluminate (Ms, C_4AsH_{12}) as shown in Eq. (6) [26,27,11,28]. During carbonation, the formation of calcite is favored and the reaction shown in Eq. (6) is promoted. As a result, Et is further stabilized and stronger diffraction is observed after carbonation. Due to more calcite formed after hydration, more aluminum in MK can react with calcite to form monocarboaluminate, and also more calcite in system favors the transformation from Hc to Mc. The transformation of Hc to Mc is also observed elsewhere for the long-cured cement with alumina-rich pozzolans, which is attributed to the continuous dissolving calcite [11].

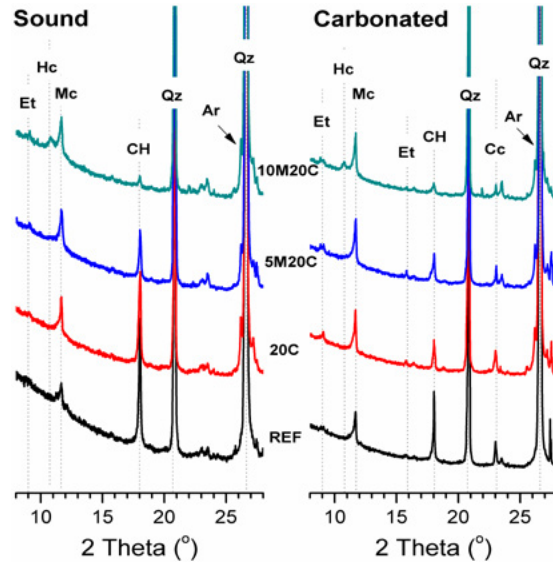
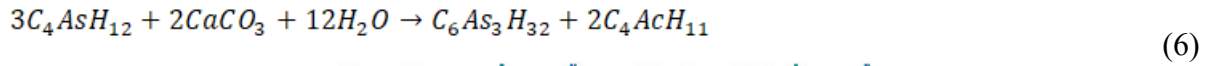
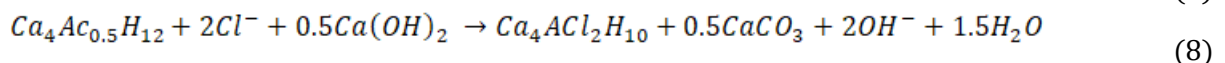
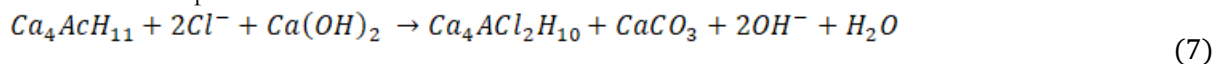
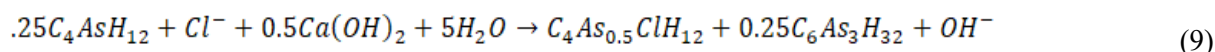


Fig. 2 XRD pattern of sound and carbonated mortars before chloride exposure (Et: ettringite; Hc: hemicarboaluminate; Mc: monocarboaluminate; CH: calcium hydroxide; Qz: quartz; Cc: calcite; Ar: aragonite)

3.3.2 Hydration production after exposure

Fig.3 illustrates the XRD patterns of sound and carbonated samples after chloride exposure. After exposed to chloride solution, Hc and Mc convert to Friedel's salt (Fs, $C_4ACl_2H_{10}$) for both sound and carbonated samples, as Eqs. (7) and (8) expressing [10,21]. During these reactions, the carbonates and hydroxyls previously bound in interlayers of Mc and Hc are replaced by chlorides at the expense of CH. However, the carbonated samples have higher ability to form Fs than sound ones. It is ascribed to the fact that less CH is available in carbonated samples for the formation of Fs [19]. The less Fs formed in carbonated samples after chloride exposure results in fewer bound chlorides.





Concomitantly, chloride exposure process increases the diffraction intensity of Et, indicating more Et formed. This phenomenon can be explained by two effects. The first one is that the sulfates in Ms and its solid solution is replaced by chloride, and the released sulfates react with Ms to form delayed Et in return [21]. The relevant reaction is depicted in Eq. (9). The second is that the sulfates previously adsorbed on the C-S-H gels are desorbed during chloride exposure [44-46]. Since chlorides can adsorb on C-S-H gels during exposure, the sulfates previously bound on C-S-H gels will reverse to free ones, and as a result promoting Et formation. It is also observed that after chloride exposure the diffraction of Et in sound mortars increase more remarkably than that in carbonated ones, indicating that sound samples have higher ability to form delayed Et during exposure. This phenomenon can be also attributed to the different amount of CH in sound and carbonated sample. The higher amount of CH can support a constant transformation of Ms to Et as depicted in Eq. 9. For the carbonated mortars, the CH available for the formation of Et is not as much as that in sound ones during chloride exposure. In this way, the reaction depicted in Eq. 9 may be restrained to some extent, and therefore less delayed Et is formed.

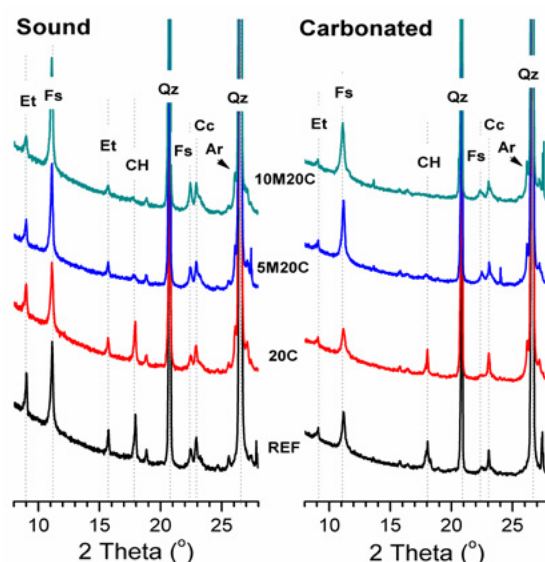


Fig. 3 XRD patterns of sound and carbonated mortars after chloride exposure (Fs: Friedel's salt)

3.4 Chloride diffusion profile and diffusion coefficient

Fig.4 illustrates the free chloride diffusion profiles of mortars after 5 months of chloride exposure. The use of GWC significantly promotes the chloride diffusion by increasing the chloride content and chloride ingress depths in mortar, because the loose structure is achieved with GWC addition as verified in Section 3.1. This means use of GWC in concrete structure is expected to result in higher risk of chloride-induced corrosion of embedded steel bars when serving in a chloride-rich environment.

After 5 wt.% MK is included, the microstructure of GWC blended mortar is densified as already proved in Section 3.1 and chloride diffusion is significantly restrained as a result. It is observed that 5 wt.% MK incorporation in GWC blended mortars achieves lower chloride penetration depth compared to REF sample. The higher amount of MK is found to further benefit the chloride resistance of GWC blended mortar.

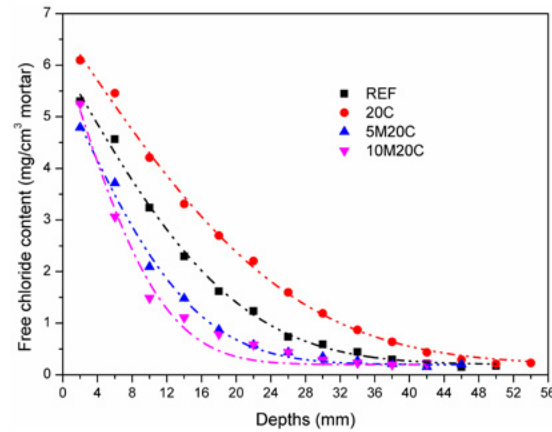


Fig.4 Free chloride profile of mortars after exposed in sodium chloride for 5 months

To further investigate the effect of GWC and MK on chloride diffusion of mortar, the apparent chloride diffusion coefficient is calculated by using Eq. (5) to fit the chloride diffusion profile. Since all the mortars show very similar background of chloride content as shown in Fig.1, the background of chlorides is fixed at 0.20 mg/cm³ mortar during fitting. The fitted apparent chloride diffusion and chloride concentration in surface layer are shown in Table 3. The chloride diffusion coefficient is almost doubled after 20 wt.% is incorporated. However, the chloride diffusion coefficient is dramatically reduced with MK addition. The chloride diffusion coefficient of GWC blended mortar declines to 1/2 of REF sample for 5 wt.% and 1/3 for 10 wt.% addition. It is accepted that the chloride diffusion in saturated concrete is governed by pore structure and chloride binding capacity [29]. The reduced porosity of GWC blended mortar with MK addition can inhibit chloride diffusion with no doubt. Since MK is an alumina-rich pozzolans, the chloride binding capacity of cement blend can be greatly modified with MK addition. Concerning that, the chloride binding capacity of the mixtures should be evaluated.

As for the free chloride content in surface layer (X_s in Table 3), GWC addition increases and MK addition reduces it. It is related to the porosity of mortars. Since GWC addition increase porosity, more chloride can intrude into the surface layer and improve chloride content. However, although porosity is further reduced with 10 wt.% addition, the chloride concentration of surface layer demonstrates a considerable increase. This phenomenon is probably linked to the carbonation of surface layer of mortar. As mentioned in Sections 3.2 and 3.3, chloride binding of hardened cement mixture is significantly determined from CH available. As a result, the sample with the highest amount of mineral admixtures (namely 10M20C) and therefore the lowest ability to resist carbonation can suffer a higher reduction of bound chloride content due to the excessive declination of CH during carbonation. This indicates that with the gradual carbonation during chloride exposure the large amount of chlorides previously bound in the surface layer of 10M20C can reverse to free ones and increase the free chloride content in surface layer.

Table 3 Chloride diffusion coefficient and chloride content in surface layer of mortar

Mix	D	X_s	R^2
	cm ² /month	mg/cm ³	
REF	25.16	6.02	0.996
20CP	43.19	6.70	0.997
5M20C	13.88	5.58	0.994
10M20C	8.04	6.17	0.982

4. Conclusions

This work prepares metakaolin (MK)-ground waste coral (GWC) based marine mortars exclusively serving on islands far from mainland. The chloride binding and hydration product formation of sound and carbonated mortar were investigated. The chloride binding capacity and porosity are combined to explain the variation in chloride diffusion behaviors observed in different mortars. Based on the results and discussion, the following conclusions can be drawn:

- GWC can involve in the formation of carboaluminate with the aluminum from either clinker or MK. Carbonation can further promote carboaluminate formation and convert hemicarboaluminate to monocarboaluminate due to more carbonate available in the system;
- During chloride exposure, hemicarboaluminate and monocarboaluminate transform to Friedel's salt and meanwhile delayed ettringite formation is favoured. These transformations are carried out at the expense of calcium hydroxide. Therefore, for the carbonated samples, the formation of Friedel's salt and delayed ettringite can be inhibited to some extent due to less calcium hydroxide available in a carbonated system;
- Addition of GWC imposes negligible influence on the workability of fresh mortar mixture, but harms the mechanical properties and microstructure of hardened mixture due to dilution effect. These degradations can be compensated by MK addition due to the synergy of secondary C-S-H gels and carboaluminate formation.
- Due to the densification of matrix and improved chloride binding capacity of GWC mortar, the chloride diffusion coefficient is sharply reduced with MK addition. The mortar with couple use of 20 wt.% GWC and 5 wt.% MK achieves half the chloride diffusion coefficient of plain mortar during a exposure duration of 6 months. And, the even higher amount of MK achieves even lower chloride diffusion coefficient.

5. Acknowledgment

The authors acknowledge the financial supports of “Nature Science Foundation Project of China (No.51679179)” and “Yang Fan Innovative & Entrepreneurial Research Team Project (No.201312C12)”.

6. Reference

1. Wang QK, Li P, Tian YP, Chen W, Su CY (2016) Mechanical Properties and Microstructure of Portland Cement Concrete Prepared with Coral Reef Sand. *J Wuhan Univ Technol* 31 (5):996-1001. doi:10.1007/s11595-016-1481-x
2. Wang Y, Shui Z, Gao X, Huang Y, Yu R, Li X, Yang R (2019) Utilizing coral waste and metakaolin to produce eco-friendly marine mortar: Hydration, mechanical properties and durability. *J Clean Prod* 219:763-774. doi:10.1016/j.jclepro.2019.02.147
3. Cheng SK, Shui ZH, Sun T, Yu R, Zhang GZ, Ding S (2017) Effects of fly ash, blast furnace slag and metakaolin on mechanical properties and durability of coral sand concrete. *Appl Clay Sci* 141:111-117. doi:10.1016/j.clay.2017.02.026
4. Wang XP, Yu R, Shui ZH, Song QL, Zhang ZH (2017) Mix design and characteristics evaluation of an eco-friendly Ultra-High Performance Concrete incorporating recycled coral based materials. *J Clean Prod* 165:70-80. doi:10.1016/j.jclepro.2017.07.096

5. Cheng S, Shui Z, Sun T, Yu R, Zhang G (2018) Durability and microstructure of coral sand concrete incorporating supplementary cementitious materials. *Constr Build Mater* 171:44-53. doi:10.1016/j.conbuildmat.2018.03.082
6. Hu S, Wang F, Ding Q (2005) Interface structure between lightweight aggregate and cement paste. *J Chin Ceram Soc* 33 (6):713-717. doi: 10.1016/0008-8846(90)90103-5
7. Liu JM, Ou ZW, Mo JC, Chen YZ, Guo T, Deng W (2017) Effectiveness of Saturated Coral Aggregate and Shrinkage Reducing Admixture on the Autogenous Shrinkage of Ultrahigh Performance Concrete. *Adv Mater Sci Eng*:11. doi:10.1155/2017/2703264
8. Chen F, Zhang G, Ding S, Qing M, Liu K (2016) Experimental study on the performance of coral sand concrete. *China Concrete and Cement Products* (7):16-21.
9. Wang A, Lyu B, Zhang Z, Liu K, Xu H, Sun D (2018) The development of coral concretes and their upgrading technologies: A critical review. *Constr Build Mater* 187:1004-1019. doi:10.1016/j.conbuildmat.2018.07.202
10. Wang Y, Shui Z, Huang Y, Sun T, Duan P (2018) Properties of coral waste-based mortar incorporating metakaolin: Part II. Chloride migration and binding behaviors. *Constr Build Mater* 174:433-442. doi:10.1016/j.conbuildmat.2018.04.076
11. De Weerd K, Kjellsen KO, Sellevold E, Justnes H (2011) Synergy between fly ash and limestone powder in ternary cements. *Cem Concr Compos* 33 (1):30-38. doi:10.1016/j.cemconcomp.2010.09.006
12. Nied D, Stabler C, Zajac M Assessing the Synergistic Effect of Limestone and Metakaolin. In, Dordrecht, 2015. *Calcined Clays for Sustainable Concrete*. Springer Netherlands, pp 245-251
13. Antoni M (2013) Investigation of cement substitution by blends of calcined clays and limestone. PhD, Ecole Polytechnique Fédérale de Lausanne,
14. Barbhuiya S, Chow P, Memon S (2015) Microstructure, hydration and nanomechanical properties of concrete containing metakaolin. *Constr Build Mater* 95:696-702. doi:10.1016/j.conbuildmat.2015.07.101
15. Kim HS, Lee SH, Moon HY (2007) Strength properties and durability aspects of high strength concrete using Korean metakaolin. *Constr Build Mater* 21 (6):1229-1237. doi:10.1016/j.conbuildmat.2006.05.007
16. Papadakis VG (2000) Effect of supplementary cementing materials on concrete resistance against carbonation and chloride ingress. *Cem Concr Res* 30 (2):291-299. doi:10.1016/S0008-8846(99)00249-5
17. Medjigbodo G, Rozière E, Charrier K, Izoret L, Loukili A (2018) Hydration, shrinkage, and durability of ternary binders containing Portland cement, limestone filler and metakaolin. *Constr Build Mater* 183:114-126. doi:10.1016/j.conbuildmat.2018.06.138
18. Kearsley EP, Wainwright PJ (2001) Porosity and permeability of coamed concrete. *Cem Concr Res* 31:805-812. doi:10.1016/S0008-8846(01)00490-2
19. Wang Y, Shui Z, Gao X, Yu R, Huang Y, Cheng S (2019) Understanding the chloride binding and diffusion behaviors of marine concrete based on Portland limestone cement-alumina enriched pozzolans. *Constr Build Mater* 198:207-217. doi:10.1016/j.conbuildmat.2018.11.270
20. Luo R, Cai YB, Wang CY, Huang XM (2003) Study of chloride binding and diffusion in GGBS concrete. *Cem Concr Res* 33 (1):1-7. doi:10.1016/S0008-8846(02)00712-3

-
21. Wang Y, Shui Z, Gao X, Huang Y, Yu R, Ling G (2019) Chloride binding behaviors of metakaolin-lime hydrated blends: Influence of gypsum and atmospheric carbonation. *Constr Build Mater* 201:380-390. doi:10.1016/j.conbuildmat.2018.12.162
 22. Shi ZG, Geiker MR, De Weerd K, Ostnor TA, Lothenbach B, Winnefeld F, Skibsted J (2017) Role of calcium on chloride binding in hydrated Portland cement-metakaolin-limestone blends. *Cem Concr Res* 95:205-216. doi:10.1016/j.cemconres.2017.02.003
 23. De Weerd K, Colombo A, Coppola L, Justnes H, Geiker MR (2015) Impact of the associated cation on chloride binding of Portland cement paste. *Cem Concr Res* 68:196-202. doi:10.1016/j.cemconres.2014.01.027
 24. Labbez C, Pochard I, Jonsson B, Nonat A (2011) C-S-H/solution interface: Experimental and Monte Carlo studies. *Cem Concr Res* 41 (2):161-168. doi:10.1016/j.cemconres.2010.10.002
 25. Zajac M, Rossberg A, Le Saout G, Lothenbach B (2014) Influence of limestone and anhydrite on the hydration of Portland cements. *Cem Concr Compos* 46:99-108. doi:10.1016/j.cemconcomp.2013.11.007
 26. Lothenbach B, Le Saout G, Gallucci E, Scrivener K (2008) Influence of limestone on the hydration of Portland cements. *Cem Concr Res* 38 (6):848-860. doi:10.1016/j.cemconres.2008.01.002
 27. Bizzozero J, Scrivener KL (2015) Limestone reaction in calcium aluminate cement–calcium sulfate systems. *Cem Concr Res* 76:159-169. doi:10.1016/j.cemconres.2015.05.019
 28. Matschei T, Lothenbach B, Glasser FP (2007) The role of calcium carbonate in cement hydration. *Cem Concr Res* 37 (4):551-558. doi:10.1016/j.cemconres.2006.10.013
 29. Martin-Perez B, Zibara H, Hooton RD, Thomas MDA (2000) A study of the effect of chloride binding on service life predictions. *Cem Concr Res* 30:1215-1223. doi:10.1016/S0008-8846(00)00339-2

Rejuvenators for High RAP Asphalt Mixes and New Preservation Techniques for Open-Graded Pavements

S.N. Nahar^{1,2}, F.B. Elzinga¹, B.J. Lommerts^{1,*}

¹Latexfalt bv, P.O. Box 6, 2396 ZG Koudekerk aan den Rijn, the Netherlands, www.latexfalt.com

²Department of Civil Engineering and Geosciences, Delft University of Technology, the Netherlands

* Author to whom communications should be addressed, bertjan.lommerts@latexfalt.com,

Abstract

The development of a full circular approach regarding road construction materials requires new and fundamental innovations. More in particular the recycling of RAP stemming from open-graded pavements is a challenge as oxidation has progressed significant during the more than a decade of service life of the surface layer, which results in a brittle, glassy material with poor flexibility and limited self-healing properties. Furthermore, these pavements are often produced using polymer modified bitumen and the re-compatibilization of aged binders requires deep insights into oxidation-induced phase behavior effects. In the present paper the option of rejuvenation of high RAP mixes will be reported using pre-blended bitumen with selected rejuvenators. These pre-blended materials are compared to regular soft bitumen, i.e. bitumen with a high maltene content, and other more softening materials. The interaction of rejuvenator blended bitumen with recovered binder obtained from oxidized RAP is studied by means of AFM and rheology. It is demonstrated that a full in-depth rejuvenation and re-compatibilization of the oxidized mastic can be accomplished, which is an important prerequisite for successful high RAP mix design. Dense and open-graded asphalt mixes consisting of at least 50% RAP can be designed without quality and durability implications. Furthermore, the re-compatibilization of aged bitumen is also successfully accomplished in-situ for open-graded or semi-open graded pavements, like porous asphalt and SMA. It has been demonstrated that the newly developed rejuvenating preservation technique for these pavements results in a significant reduction of stone loss and in an increase of the service life of the road of at least 50%. The latter has been determined for numerous pavements treated with the rejuvenator containing bituminous emulsion during a period of over five years, using LCMS monitoring techniques.

Keywords – asphalt recycling, rejuvenation, porous asphalt, road maintenance

1. Introduction

Durability of bitumen is a concern as bitumen undergoes oxidative ageing during production and service-life of asphalt pavement. Extent of oxidative ageing depends on the molecular make-up of bitumen that can vary depending on nature and source of the crude oil and refining process, environmental condition and mix design (Robertson et al., 1991).

Dutch highway road-network is mostly constructed using porous asphalt due to its numerous advantages; for instance driving comfort resulting from low noise level and less spraying of water during rain fall (The et al., 2016). On the contrary, the life-span of porous asphalt is rather limited. Due to its open structure and high porosity of porous asphalt, bitumen is exposed to ambient oxygen and temperature conditions.

Oxidative ageing causes an increase in molecular interaction within bitumen due to irreversible nature of the chemical reactions that take place during oxidation (Petersen et al, 1984). Oxidative ageing has more severe effect on two-layer porous asphalt, where the top layer is made of polymer modified bitumen.

An obvious change in physical property in oxidized bitumen is seen from its viscosity, stiffness increase and its limited adhesion property. As a result, loss of stones (i.e. raveling) and cracking are observed as main distress mechanisms in porous asphalt. Excessive raveling determines the critical pavement condition (Figure 1) and eventually the end of service life of porous asphalt (Kneepkens et al., 2004, The et al., 2016, Lommerts et al., 2016).

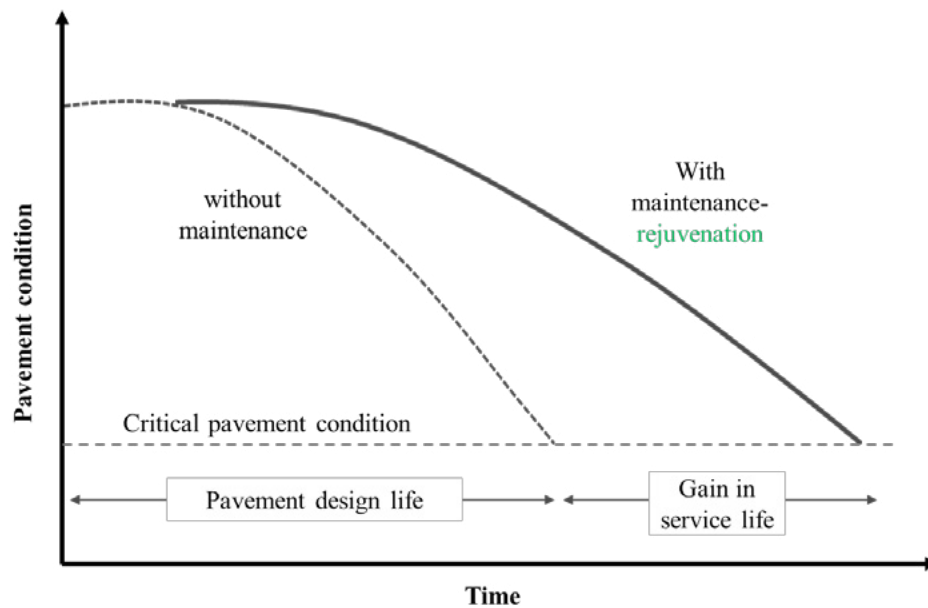


Figure 1: Improvement of pavement service life through rejuvenation.

As a solution to this undesirable effects of ageing of pavement materials, different strategies are implemented in practice. Among them preventive and reconstructive (i.e. recycling) treatments are popular where additive is used to replenish aged binder properties. These additives are commonly known as rejuvenator (Nahar et al., 2014, Lommerts et al., 2016).

At critical pavement condition, the wearing coarse is recycled to construct new asphalt pavement. Recycling of road materials is a common practice in the Netherlands since 1970 in the base asphalt layers with 50% to 70% allowable limit of recycled asphalt pavement (RAP) (Nahar et al., 2014). In current practices, the contractors are increasing the allowable limit of RAP and also adapting horizontal recycling; recycling of old wearing to new wearing course. Using a rejuvenator will be inevitable to revitalize highly aged, polymer modified bitumen containing wearing course.

Within the scope of this work, rejuvenator is developed with the purpose of restoring the mechanical and adhesive properties of bitumen during recycling and also during pavement maintenance in order to extend the service-life, Figure 1. This paper presents ageing susceptibility of bitumen and the effectiveness of rejuvenator in restoring the intrinsic properties of bitumen after being laboratory aged.

The first part of the paper presents the mechanical property restoration potential of rejuvenator. It is measured by comparing the penetration, softening point and other mechanical properties of neat, laboratory aged bitumen from pressure aged vessel (PAV), rejuvenated bitumen blends and the same system after being aged, as shown in Table-1.

Next part focuses on fundamental property of rejuvenated bitumen like mutual compatibility and phase behavior at the microstructural level. These properties are assessed for neat, aged, rejuvenated bitumens and aged rejuvenated system by using AFM and DSC.

This paper demonstrates methods that can clearly distinguish neat and aged bitumen and can evaluate rejuvenation potential of rejuvenator at fundamental level. The research also present a practical approach for in-situ rejuvenation of highly aged porous asphalt suitable for pavement preservation. This research is useful to predict durability of bitumen, compatibility of rejuvenator in base bitumen and long term performance of rejuvenated bitumen systems.

2. Materials & Methods

2.1 Material and sample preparation

Bitumen of penetration grade 70/100 from Total refinery is used for this research. The sample is aged in the laboratory using Pressure Ageing Vessel (PAV) for 65 hours at temperature 85°C and pressure 21 bar. Then rejuvenator is blended with aged bitumen to adjust the penetration to its neat value. Following that the rejuvenated binder system is aged again using the same PAV procedure for its investigation on susceptibility to ageing. Mechanical tests are performed with the focus on low and high temperature properties of all the samples. Finally, microstructural and thermal behavior of neat, aged and rejuvenated samples are measured using AFM and DSC technique.



Figure 2: Assessment scheme for evaluation of a rejuvenator.

For AFM study bitumen specimens are prepared by applying approximately 20 mg of sample on the 12-mm AFM sample substrate (i.e. steel disks of 0.5 mm thickness). The specimens are then heated for 30 seconds at 100°C on a heater plate to obtain a smooth bitumen film. Later, in order to have same thermal history for all the specimens, they are conditioned in an oven at 100 °C for 15 minutes. Prior to AFM imaging, the specimens were stored in closed petri dishes at the imaging temperature 21°C for 24 hours.

To perform thermal analysis using DSC, 10mg sample was taken in Tzero aluminium pans and was sealed with hermetic lids that are obtained from TA instruments.

Instrument and operational mode

Atomic Force Microscope (AFM)

Dimension Icon from Bruker AFM was used for this research, Figure 3(a). For AFM imaging, a cantilever with a tip of nominal end radius 8nm is scanned over the sample surface by a piezoelectric scanner. The changes in tip-sample interactions result in deflection of the cantilever which is measured by an optical-lever detection system.

In this research, Tapping-mode AFM was used to characterize the bitumen specimens. In this mode, the probe is driven near to its first resonant frequency. While the probe is scanned across the sample, amplitude is kept constant. In this way the tip maintains an intermittent contact over the sample surface by exerting moderate force that is suitable for bituminous materials.

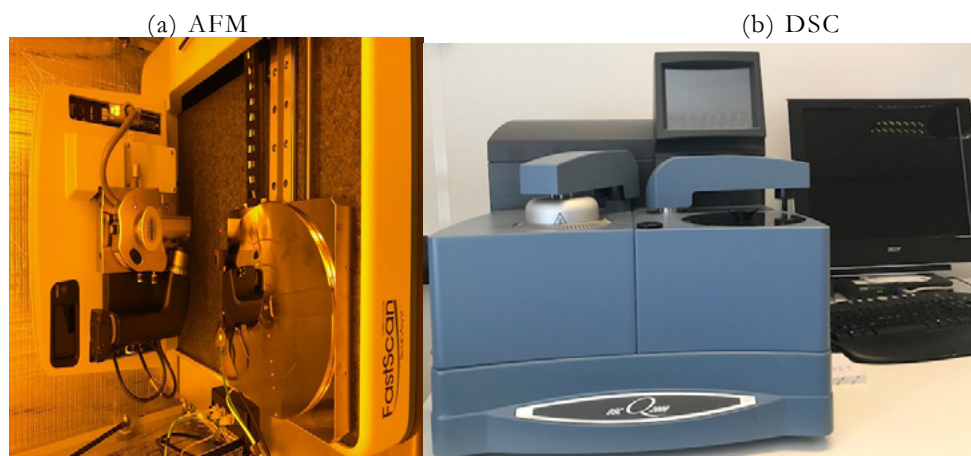


Figure 3: AFM instrumental set-up and operation principle: a) Dimension Icon-AFM set-up b) Differential scanning calorimetry (DSC) set-up from TA instruments.

The oscillating cantilever dissipates different amount of energy as it interacts with material heterogeneity on the sample surface, resulting two major sets of data simultaneously: topography and phase-contrast. Each image type provides specific information with respect to the sample surface. Topography images provide information of relative height of the various features of the material and phase contrast images present relative damping of oscillating cantilever which can again be related to cumulative measure of stiffness and adhesion forces between probe and the sample.

Probe and measuring environment

Cantilever RTESPA from Bruker which have nominal resonance frequency of 300 kHz and spring constant of 40 N/m is used for this research. Probe was scanned by 1 Hz (1 line/s) at ambient condition, 21 °C. Images are collected in 10×10 μm² scan size with pixel resolution of 512×512.

Differential Scanning Calorimeter (DSC):

DSC – Q2000 from TA instruments has been used to perform thermal analysis in bitumen (Figure 3b). While a conventional thermal analysis (DSC) is performed in bitumen, it provides a thermogram showing an overlap in endo- and exothermic events. Hence, Temperature modulated (M)-DSC is used to characterize bitumen that can distinguish overlapping thermal events.

In this method, a sinusoidal temperature fluctuation is superimposed over a linear heating or cooling rate. As a result, the sample temperature provides a sinusoidal response and there is a delay between the modulated heat flow and the response of the material. This results in a reversing (i.e. that responds to a change in heating rate) and non-reversing signal. Samples were measured with heating rate of 3 K/min between -90 and 150 °C. Analysis and deconvolution of the reversing and non-reversing signals were done using the TA software.

3. Results & Discussion

3.1 Mechanical properties

Mechanical tests are conducted in all samples to reveal the high and low temperature performance of materials. A small addition of 4.5% of rejuvenator to PAV aged bitumen could recover penetration and softening point and restore other properties as presented in Table 1.

All mechanical properties confirm recovery of functional properties of bitumen after addition of

rejuvenator. Penetration, softening point and low temperature properties data show that the rejuvenated system is more stable against oxidation compared to neat bitumen system. Low temperature flexibility is improved after adding rejuvenator and this rejuvenated system keeps its flexibility at low temperature after being aged in PAV.

Table 1: Mechanical properties of bituminous systems.

Material properties	Neat bitumen	PAV aged bitumen	Rejuvenated after PAV	Rejuvenated after PAV+additional PAV
Penetration (1/10mm)	79	29	80	46
ΔC_p (J/g°C)- DSC	0	0.17	0	0.05
Low temperature properties				
Glass transition temperature T_g (°C)- DSC	-17	-17	-24	-23
Frass breaking point(°C)	-15	-8	-18	-16
High temperature properties				
Softening point; R&B (°C)	45.4	55	47.8	53.6
G' ratio at 60°C (aged/neat bitumen)	1	9.8	3.4	10.7

3.2 Phase behavior of neat, aged and rejuvenated bitumen

Mutual compatibility of the rejuvenator and the base bitumen can be revealed by phase behavior of the system. An incompatibility may induce an additional phase to separate out, if there is a discontinuity in the molecular distribution. This phenomenon can occur in highly aged bitumen as well as in the presence of rejuvenator if it is not fully compatible with the base bitumen. Phase separation characteristics of bitumen in neat state, after oxidation and rejuvenation have been investigated using AFM. Topography and phase images obtained using this technique are presented in Figure 4. Mutual compatibility of the resulted molecular classes after oxidation or addition of rejuvenator can easily be evaluated using this technique.

AFM images in Figure 4 confirm existence of two phase system (i.e. elongated domains and matrix) for all bitumen samples. Two-phase microstructure is a characteristic feature of bituminous materials and has been reported in numerous literature (Nahar et al., 2014, Nahar et al., 2016).

Building blocks of this domains are assumed to be co-association of asphaltene and wax ($\geq C_{40}$) fraction of bitumen (Lesueur et al, 2009, Hofko et al., 2015, Nahar et al, 2016). Asphaltenes are known to self-associate to form an aggregate as inverted micelle of few molecular units and these aggregates mostly tend to flocculate to form a particle of asphaltenes of 2-30nm. These particles have a polar core and an apolar exterior (Yen, 1975). It is speculated that, the apolar exterior may act as an interaction sites for the apolar fraction, such as microcrystalline wax component of bitumen. Thus, these asphaltene particles first may act as a scaffold for the attachment of the wax molecules. While cooling from molten state of bitumen (i.e. a single phase system in terms of mechanical response properties) these domains phase separate following nucleation and growth mechanism (Nahar et al., 2016).

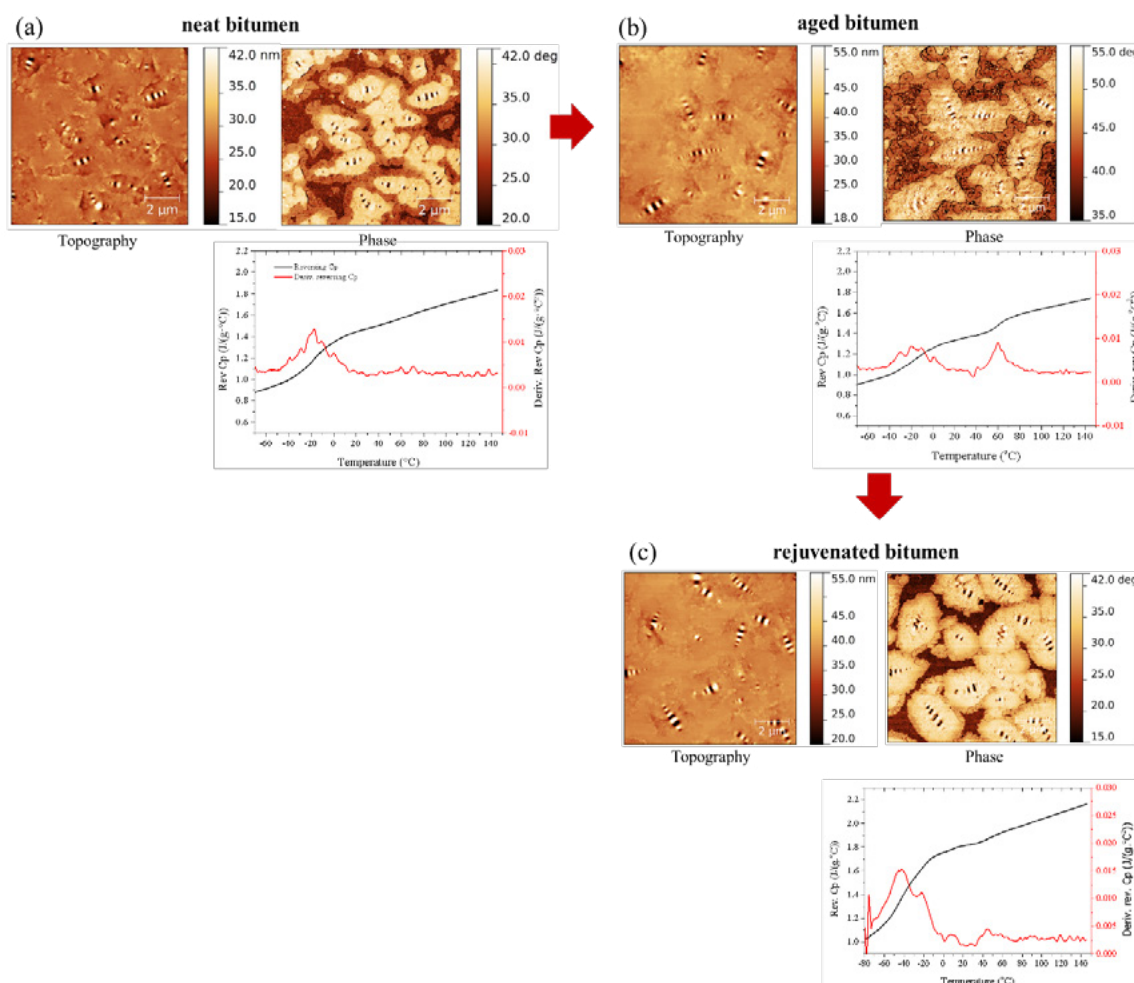


Figure 4: Phase and thermal behavior of (a) neat (b) aged and (c) rejuvenated bitumen.

After PAV ageing, an enhanced agglomeration is observed in the domain phase compared to neat bitumen, Figure 4a and 4b. From the phase image, a significant increase in phase shift is observed in the matrix phase of PAV aged bitumen. Phase images show the cumulative effect of the material property such as stiffness and adhesion of the probe to the material. From controlled nano-mechanical measurement it is known earlier that the phase showing higher phase shift corresponds to a stiffer and less adhesive phase and vice-versa (Nahar et al., 2016). Thus, the phase image also shows the proof of hardening of bitumen at microstructural level as expected after oxidation of bitumen.

During the process of oxidation, mostly polar functional groups, ketones and sulfoxides are formed in bitumen (Petersen, 1984). A characteristic shift from aromatics to resinous components are commonly known to occur in oxidized bitumen (Handle et al., 2017). This result in an increase in molecular interaction and as a consequence more asphaltene tend to agglomerate in oxidized bitumen. This change in physico-chemical property at molecular level translates to its change in mechanical properties showing increase in viscosity and modulus.

The added rejuvenator is compatible with the base bitumen as no foreign phase was observed in the blend. Re-dispersion of the domain phase is also observed through rejuvenation. Rejuvenated bitumen has shown property restoring performance from both the rheological data and microstructural properties of the binders. **Compatibility aspects and thermal behavior of neat, aged and rejuvenated bitumen**

Thermal events like change in specific heat capacity can be detected from the reversing curve from MDSC thermograms. An example of such a thermogram is shown in Figure 5(a) and the results of neat, aged and

rejuvenated bitumens are presented in Figure 4 a, b and c respectively coupled with AFM images.

The thermograms can provide insights on mutual compatibility of the phases in bitumen after oxidation and evaluates compatibility between the pre- blended rejuvenator and the base bitumen. Some useful parameters extracted from the data are glass transition temperature (T_g) of the maltene phase, heat capacity, ΔC_p measured at T_g . After oxidation the T_g shifts to a higher temperature and by rejuvenation again shifts back to neat bitumen state confirming the low temperature flexibility of the material.

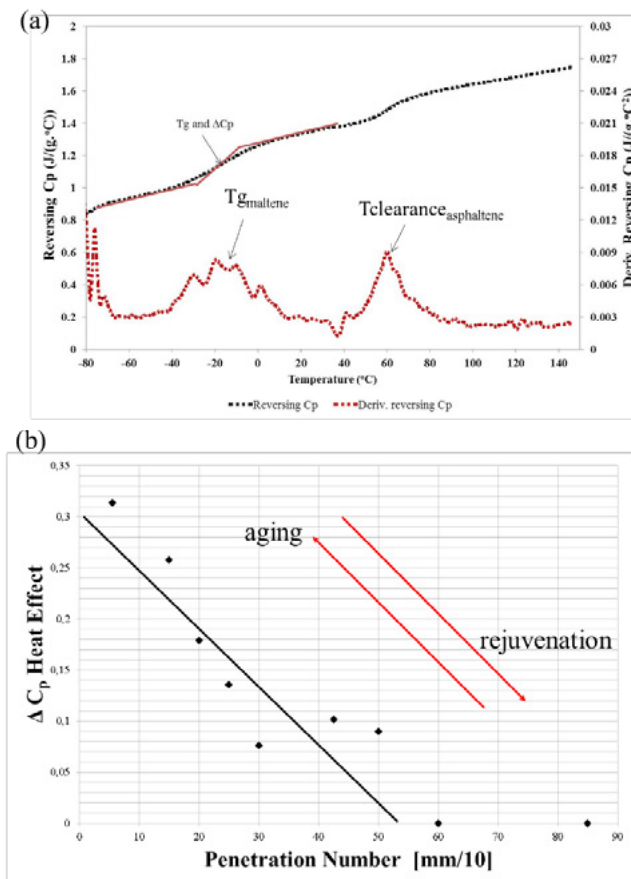


Figure 5: (a) Example of a thermogram showing glass transition and clearance temperature with corresponding ΔC_p . (b) Difference in specific heat capacity; ΔC_p at clearance temperature can be correlated to oxidation and rejuvenation characteristics of bitumen.

3.3 In-situ rejuvenation technology for preservation of porous asphalt

A novel multi-component emulsion Modimuls® ZV is introduced to the market to preserve open graded porous asphalt. Modimuls® ZV emulsion contains rejuvenating components with different breaking properties which can be sprayed onto the road surface using standard spraying technique. This rapid breaking emulsion is subsequently forced into the open structure by an high pressure jet air flow to facilitate impregnation of the components that can revitalize old oxidized bitumen in porous asphalt. Maintenance of porous asphalt and SMA using this technology has shown evidence to restore the functional properties of asphalt meeting the anti-skid requirements which has been concluded from extensive research on asphalt cores taken from trial sections (The et al., 2016, Lommerts et al., 2016). Some of the pavement surfaces were two-layer open graded asphalt, that were constructed using polymer modified bitumen. Modimuls® ZV technology has been validated by Dutch national roads agency Rijkswaterstaat (RWS) as in-situ rapid pavement maintenance technique to extend the service life of porous asphalt (The et al, 2016). Modimuls® ZV incorporates various functional properties such as good wetting of the internal structure of the open graded asphalt resulting good distribution of the binder. It promotes replenishment of asphalt to restore

viscoelastic and adhesive properties throughout the depth of asphalt. Abrasion tests such as Rotating Surface Abrasion Test (RSAT) are conducted on asphalt cores taken from Modimuls® ZV treated pavement sections of highways A6, A50, A73, A30, A1, A12. The results have shown a significant reduction in stone loss. Using Laser Crack Measurement System (LCMS) monitoring technique, degree of raveling in time has been determined from treated test sections. Treated pavement have been proven to be raveling resistant compared to untreated section. This simulates an increase in service life of more than 5 years (The et al., 2016).

4. Conclusions

Effectiveness of rejuvenator is evaluated through mechanical and fundamental assessment within the scope of work. From mechanical test results, it is apparent that addition of rejuvenator shows desired property recovery which is comparable to neat bitumen. Mutual compatibility and phase behavior of bitumen and rejuvenated systems have been successfully measured at microstructural level by using AFM and DSC.

The data provides useful information on miscibility of the rejuvenator to the base bitumen and mechanism of rejuvenation. Ageing susceptibility of bitumen and rejuvenated system are also evaluated and compared using the aforementioned techniques. AFM data sets provide insight on phase behavior and microstructure properties. While the durability aspects, low temperature properties of the bituminous systems are understood from ΔC_p and T_g value from DSC.

From the overall results, it is concluded that a good rejuvenator is compatible with base bitumen and is resistant to oxidation. The rejuvenation strategy in bitumen has been proposed in Figure 6.

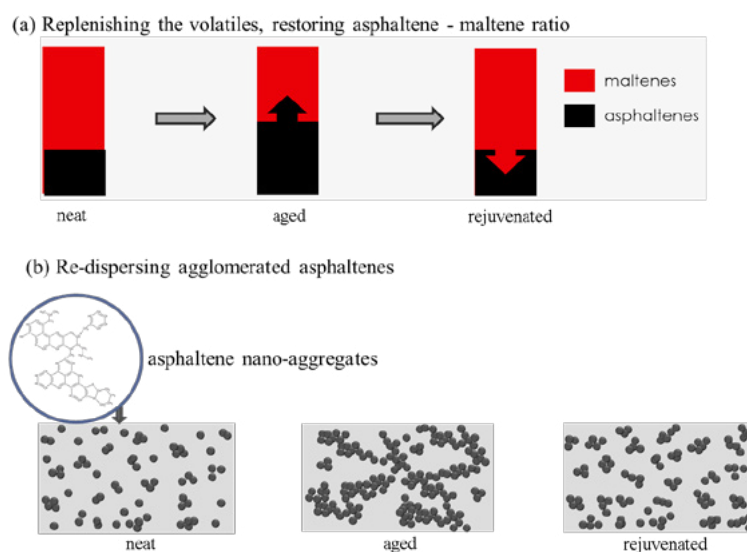


Figure 6: Influence of ageing and rejuvenation through replenishing volatiles and re-dispersion of asphaltene agglomerates.

During the process of ageing some volatiles (i.e. fraction of maltenes) are lost and some functional groups are oxidized in bitumen. This creates a shift in solubility parameter of the molecular fractions within the material and as a result more segregation of molecules occur (Figure 6b). Rejuvenator replenishes the lighter molecular fraction, maltenes and re-disperses the agglomerated molecules of aged bitumen.

Modimuls® ZV is proven as a fast applied, cost effective maintenance technique to extend the service life of porous asphalt. This maintenance technique is applicable to wide range of open graded asphalt, SMA and has the potential to replenish aged polymer modified bitumen. And service life of the open-graded asphalt pavement is demonstrated to extend more than 5 years. In this way the technology contributes to

low carbon foot print in the life-cycle cost of asphalt pavement.

5. References

1. Handle F., Harir M., Füssl J., Koyun A. N., Grossegger D., Hertkorn N., Eberhardsteiner L., Hofko B., Hospodka M., Blab R., Schmitt-Kopplin P. and Grothe H., "Tracking Ageing of Bitumen and Its Saturate, Aromatic, Resin, and Asphaltene Fractions Using High-Field Fourier Transform Ion Cyclotron Resonance Mass Spectrometry", *Energy Fuels*, (2017), 31 (5), pp 4771–4779.
2. Hofko B., Eberhardsteiner L., Füssl J., Grothe H., Handle F., Hospodka M., Grossegger D., Nahar S.N., Schmets A.J.M. and Scarpas A., "Impact of Maltene and Asphaltene Fraction on Mechanical Behavior and Microstructure of Bitumen", *Materials and Structures* (2015), pp. 1–13.
3. Kneepkens T., van Hoof Th., van Keulen W. and van Gent R.J., "Development of VIA-RAL for Porous Asphalt: more than just research, more pragmatism", *3rd Eurasphalt & Eurobitume Congress* (2004).
4. Lesueur D., "The colloidal structure of bitumen: Consequences on the rheology and on the mechanisms of bitumen modification", *Advances in Colloid and Interface Science* 145, 42 (2009).
5. Lommerts B. J., Struik J., Cotiugă I. and van Bochove G., "A New Preservation Technology for Porous Asphalt -a multi-modal, biopolymer stabilized, rejuvenating asphalt emulsion", *6th Eurasphalt & Eurobitume Congress* (2016), proceedings.
6. Nahar S.N., Schmets A., Schitter G., and Scarpas A. "Quantifying the Thermomechanical Response of Bitumen from Micro-Phase Properties". *Transportation Research Record*, Vol. 2574 (2016), pp. 101-110.
7. Nahar S.N., Qiu J., Schmets A.J.M., Schlangen E., Shirazi M., van de Ven M. F. C., Schitter G. and Scarpas A., "Turning Back Time: Rheological and Microstructural Assessment of Rejuvenated Bitumen". *Transportation Research Record* (2014), Vol. 2444, pp. 52-62.
8. Nahar S.N., "Phase separation characteristics of bitumen and their relation to damage-healing". *dissertation*, ISBN 978-94-6186-598-4, pp. 52-62.
9. Petersen J. C., "Chemical composition of asphalt as related to asphalt durability: state of the art", *Transportation Research Record* (1984).
10. Robertson R. E., Branthaver J., Plancher H., Duvall J., Ensley E., Harnsberger P., and Petersen J., "Chemical properties of asphalts and their relationship to pavement performance", *Technical Report Strategic Highway Research Program*, National Research Council, (1991).
11. The P., Voskuilen J., van de Ven M. F. C., "Life-prolonging preventive maintenance techniques for porous asphalt", *6th Eurasphalt & Eurobitume Congress* (2016), proceedings.
12. Yen T. F., "The role of trace metals in petroleum", *Ann Arbor Science Publishers Inc*, Ann Arbor , 01–30 (1975).



Organized by
**Eindhoven University
of Technology**

TU/e

In cooperation with
**Wuhan University
of Technology**

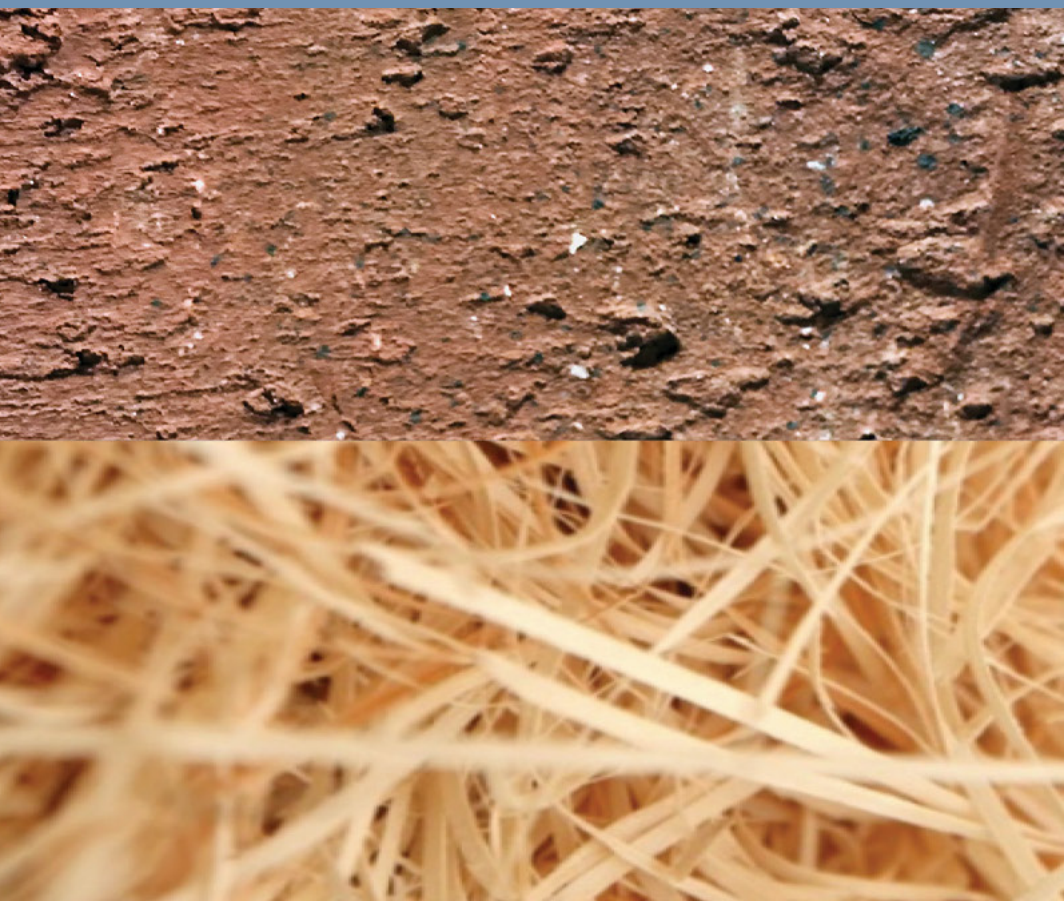


PROCEEDINGS ICSBM 2019

VOLUME 4 - Waste recovery, treatments and valorization

2nd International Conference on Sustainable Building Materials

August 12-15, 2019 - Eindhoven, The Netherlands
Editors: V. Caprai and H.J.H. Brouwers



and supported by



ICSBM 2019, Conference proceedings

A catalogue record is available from the Eindhoven University of Technology Library

ISBN of the volumes set: 978-90-386-4898-9

ISBN of Volume 4: 978-90-386-4913-9

Sponsored by: CRH, Eltomation - Wood cement board plant, Tata Steel Europe (Gold sponsors), VDZ, PCA (Bronze Sponsors).

Front page image: V. Caprai

Editors: V. Caprai and H.J.H. Brouwers

Organizing committee:

Conference Chairman: Prof. H.J.H. (Jos) Brouwers, Eindhoven

Conference Co-Chairman: Prof. Wen Chen, Wuhan

Conference Secretary: Mrs V. (Veronica) Caprai and Dr. M.V.A. (Miruna) Florea, Eindhoven

Dr. Qiu Li, Wuhan

Dr. Bo Yuan, Wuhan

Dr. Q. Yu, Eindhoven

Dr. F. Gauvin, Eindhoven

Dr. K. Schollbach, Eindhoven

Mr. Y. Chen, Eindhoven

Mrs. L.T.J. Harmsen, Eindhoven

Mrs. N.L. Rombley, Eindhoven

Table of Contents

Stress-strain behaviour of steel confined recycled aggregate concrete

M.J. Munir, S.M.S. Kazmi, Y.F. Wu, I. Patnaikuni..... 6

Influence of different recycled concrete aggregate treatment methods on the performance of concrete: a comparative assessment

S.M.S. Kazmi, M. J. Munir, Y.F. Wu, I. Patnaikuni..... 17

Effects of Recycled Aggregates on Concrete Compressive Strength

N. Siddiqui, M. Nasir, I. Nasir, D. Memon 30

Increasing the reactivity of modified ferro silicate slag by chemical adaptation of the production process

P.P. Sivakumar, L. Arnout, T. Lapauw, E. Gruyaert, N. De Belie, S. Matthys 36

Sustainable Recycling of Concrete Fine from Demolition

R. Meglin, S. Gilg, D. Wlodarczak, S. Stürwald, S. Kytzia 47

Water absorption methods for fine recycled concrete aggregates

L. Green Pedersen, L.M. Ottosen 62

Screening Untreated Municipal Solid Waste Incineration Fly Ash for Use in Cement-Based Materials – Chemical and Physical Properties

B.A.R. Ebert, B.M. Steenari, M. R. Geiker, G.M. Kirkelund 63

Qualification of Biomass Derived Ashes for Application as a Cement Replacement and Quantification of Biomass Streams in The Netherlands

N. Mühleisen, H. Jonkers, L. Tosti..... 75

Qualification of the residual reactivity of compacted recycled aggregates

Y. Hou, P. Mahieux, J. Lux, P. Turcry, A. Aitmokhtar 93

Production of Synthetic Wollastonite Mineral By Using Industrial Waste Materials

H.E. Yücel, H.Ö. Öz, O. Ersoy, M. Güneş, Y. Kaya..... 109

Sewage sludge ash as resource for phosphorous and material for clay brick manufacturing

L.M. Ottosen, I.M.G. Bertelsen, P.E. Jensen1 & G.M. Kirkelund1 119

Treatments to improve biomass fly ash quality

K. Ohenoja & M. Illikainen 132

Leaching behaviour of metals from mine tailings utilized as partial cement replacement in cement-based building materials

A.T. Simonsen, P. E. Jensen 133

Carbonation of recycled concrete aggregates: the effects of carbonation conditions on key aggregate properties	
A. Gholizadeh-Vayghan, A. Bellinkx, R. Snellings	135
Quantification of Remaining Unhydrated Cement in Concrete Waste	
D. Kulisch, A. Katz	146
Mechanism and kinetics of binding of meat and bone meal ash into the Portland cement clinker	
T. Staněk, P. Sulovský, M. Boháč.....	157
The impact of slag fineness on the reactivity of blended cements with high-volume non-ferrous metallurgy slag	
V. Hallet, N. De Belie, Y. Pontikes	170
Characteristics of mechanically activated converter steel slag	
Long term weathering of converter slag	
K. Schollbach, S. van der Laan	186
The leaching characteristics of chelatat- and water-based treated Municipal Solid Waste Incineration (MSWI) fly ash	
E. Loginova, M. Proskurnin, H.J.H. Brouwers	195
Synthesis optimization for hydrophobic surface modification of MSWI bottom ash fines	
Q. Alam, T. Dezaire, F. Gauvin, and H.J.H. Brouwers	210
Methods for determining and tracking the residual cement paste content of recycled concrete	
P.M.F. van de Wouw, M.V.A. Florea, H.J.H. Brouwers	218
The Optimized Application of Treated MSWI Bottom Ash in Concrete Mixtures	
M.V.A. Florea ¹ , A. Keulen, H.J.H. Brouwers.....	226
Characterization of air granulated converter slag and its leaching behaviour	
M. J. Ahmed, K. Schollbach, M.V.A. Florea, S.R. Van Der Laan, H.J.H Brouwers.....	239
Sodium hydroxide/carbonate activated GGBS-fly ash mortars incorporating recycled waste glass	
G. Liu, M. V. A. Florea, H. J. H. Brouwers	247
Circular Economy , key to sustainable construction	
B. (Bauke) Hoekstra Bonnema	254

Volume 4

Waste recovery, treatments and valorization

Stress-strain behaviour of steel confined recycled aggregate concrete

M.J. Munir¹, S.M. S. Kazmi¹, Y.F. Wu¹, I. Patnaikuni¹

¹School of Engineering, RMIT University, 376-392 Swanston St, Melbourne, Victoria-3001, Australia.

Abstract

Currently, utilization of recycled concrete aggregates is limited to non-structural applications owing to inferior properties. On the other hand, effect of confinement due to transverse reinforcement is ignored in the current design practice of concrete compression members. The focus of this study is to improve the performance of recycled aggregate concrete through confinement by pre-existing transverse reinforcement i.e., steel spirals in compression members leading towards sustainable construction. For this purpose, concrete cylinders were cast with 0%, 50% and 100% replacement ratios of recycled concrete aggregates and confined by steel spirals having pitches of 20 mm, 30 mm and 40 mm. Axial stress-strain behaviour of steel confined recycled aggregate concrete was examined in this study. Results showed that improved ductility and post peak behaviour were observed with the increase in confinement pressure. Increase in peak stress, peak strain and ultimate strain of concrete specimens was also observed with the increase in confinement pressure. Concrete specimens having 50% and 100% replacement ratio of recycled concrete aggregates and confined with 20 mm pitch of spiral reinforcement showed peak stresses higher than unconfined control specimens. Moreover, all the confined recycled aggregate concrete specimens showed peak strain, ultimate strain and toughness higher than unconfined control specimens. Currently, no such work is available in the extant literature to predict the axial stress-strain behaviour of steel confined recycled aggregate concrete. Based on the experimental results, a stress-strain model is proposed in this study. For this purpose, the effect of replacement ratios of recycled concrete aggregates is incorporated by modifying the parameters of stress-strain model for spirally confined normal aggregate concrete. The proposed model can effectively predict the stress-strain behaviour of both steel confined normal and recycled aggregate concrete.

Keywords: Spiral steel confinement, Recycled aggregate concrete, Axial stress-strain behaviour.

1. Introduction

A large amount of construction and demolition waste is produced every year around the globe. Approximately, 0.2 billion tons of concrete waste is produced annually in mainland of China [1]. Many attempts have been made by the researchers to use concrete waste as a raw material in the production of new concrete termed as recycled aggregate concrete (RAC). However, RAC shows inferior properties as compared to normal aggregate concrete (NAC). Utilization of recycled concrete aggregates (RCA) in the production of concrete resulted into 20% and 40% reduction of compressive strength and elastic modulus as compared to NAC, respectively [2, 3]. Due to inferior performance, practical applications of RAC are very limited.

Various techniques were adopted by the researchers to improve the performance of RAC [4-6]. For this purpose, either the adhered mortar is removed or strengthened. To remove the adhered mortar, techniques such as mechanical grinding, heat grinding, pre-soaking in water and pre-soaking in acid are used [7, 8]. Similarly, treatment of RCA through polymer emulsion, pozzolan slurry, calcium carbonate bio deposition,

sodium silicate solution and carbonation can strengthen the adhered mortar [7, 8]. However, most of these techniques are not energy efficient and cost-effective solutions to improve the properties of RAC. Concrete production cost can be increased to a great extent by adopting these techniques. Moreover, processing of a large amount of RCA is not a feasible solution for the construction industry. Therefore, there is still an utmost need to improve the properties of RAC by adopting an energy efficient and cost-effective solution.

Inferior performance of RAC can also be improved through different confinement techniques. Xiao et al. [9] and Zhao et al. [10] explored the use of fibre reinforced polymer (FRP) as the confining material for RAC. Improved strength was observed for RAC confined with FRP as compared to conventional concrete. Spiral steel can also be used to confine RAC. This article focuses on the behaviour of RAC cylinders confined with steel spirals. For this purpose, twenty-seven concrete cylinders confined by spiral reinforcement with varying confinement pressures and replacement ratios of RCA were tested under axial compression. Currently, no model is available in the extant literature to predict the axial stress-strain behaviour of steel confined RAC. Based on the experimental results, a stress-strain model is also proposed in this study. For this purpose, the effect of replacement ratios of RCA is incorporated by modifying the parameters of stress-strain model for spirally confined NAC. The proposed model can effectively predict the stress-strain behaviour of both steel confined NAC and RAC.

2. Methodology

2.1 Materials

In this study, normal concrete aggregates (NCA) and RCA were used with maximum size of 14 mm. Table 1 shows the physical properties of these aggregates. Particle size distribution of NCA and RCA is shown in Figure 1.

Mix designs of concrete used during the study are presented in Table 2. The steel spirals were made of 3 mm diameter wire and had the yield strength of 688 MPa. The cross-sectional area of the spiral is 7.55 mm².

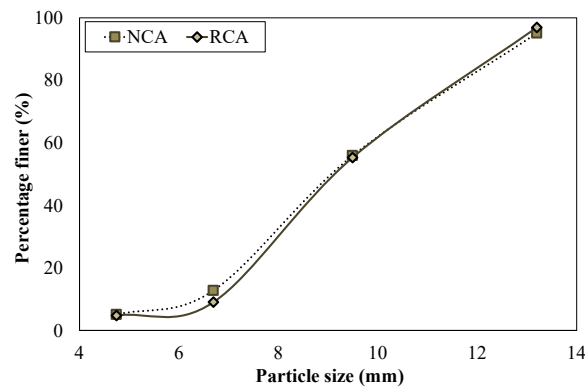


Figure 1: Particle size distribution of coarse aggregates.

Table 1: Physical characteristics of coarse aggregates.

Physical characteristic	NCA	RCA
Bulk density (kg/m ³)	1512	1413
Specific gravity	2.53	2.32
Water absorption (%)	2.06	7.61

Table 2: Details of mix designs.

RCA replacement ratio	Cement	Sand	NCA	RCA	Water
%	kg/m ³	kg/m ³	kg/m ³	kg/m ³	kg/m ³
0	451.5	708.7	822.5	-	202.1
50	451.5	708.7	411.3	411.3	224.9
100	451.5	708.7	-	822.5	247.5

2.2 Methods

Twenty-seven (27) concrete cylinders (150 x 300 mm) confined by spiral reinforcement (with no longitudinal reinforcement and concrete cover) having 20 mm, 30 mm and 40 mm pitches of spirals and 0%, 50% and 100% replacement ratios of RCA were prepared and tested under axial compression. Table 3 shows the details of test specimens.

Table 3: Details of test specimens.

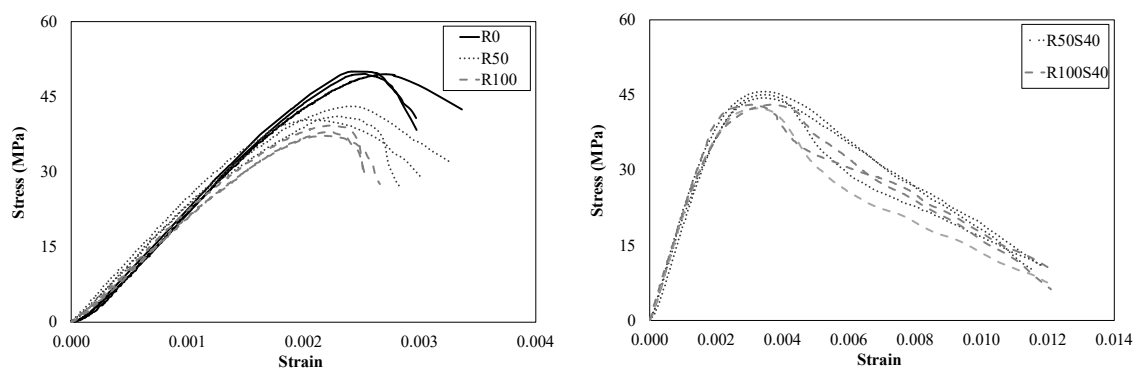
Specimen label	Pitch of spiral	Replacement ratio of RCA
	mm	%
R0	-	0
R50	-	50
R50S20	20	50
R50S30	30	50
R50S40	40	50
R100	-	100
R100S20	20	100
R100S30	30	100
R100S40	40	100

All the specimens were tested using an MTS machine and axial displacement of the specimens was measured through two linear variable displacement transducers.

3. Results and discussion

3.1 Effect of RCA replacement ratios

Stress-strain behavior of concrete specimens is presented in Figure 2. A higher initial slope and peak were observed in case of R0 specimens as compared to R50 and R100 specimens. For R0 specimens, descending part of the curve was also observed higher in comparison with R50 and R100 specimens.



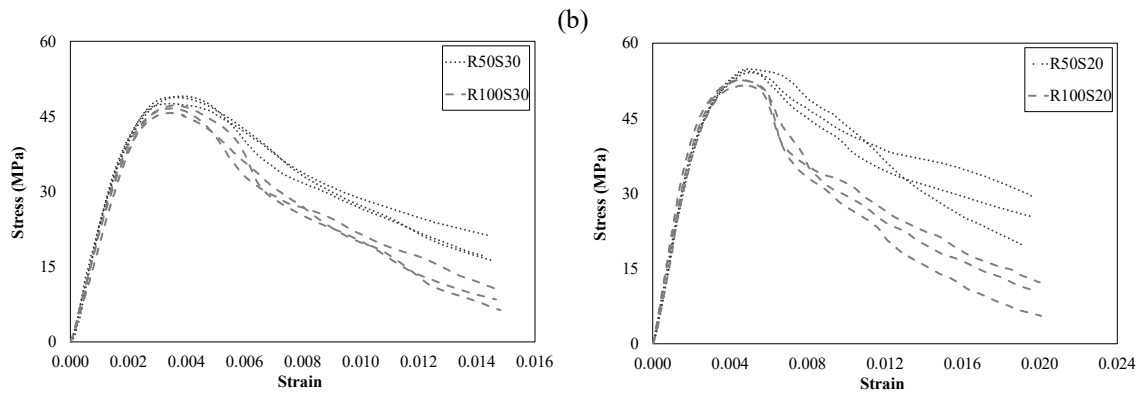


Figure 2: Effect of replacement ratios of RCA on stress-strain curves of concrete specimens.

This may be attributed to the sudden collapse i.e., more brittle failure of R50 and R100 specimens after the peak load as compared to R0 specimens. In previous study, Xiao et al. [11] also observed steeper descending branches of stress-strain curves of RAC as compared to NAC. The curves of R50S20, R50S30 and R50S40 were also observed higher than R100S20, R100S30 and R100S40, respectively. However, confinement effect was observed more prominent in case of confined R100 (R100S20, R100S30 and R100S40) specimens than confined R50 (R50S20, R50S30 and R50S40) specimens. In previous study, Wang et al. [12] also reported increase in strength and ductility enhancement of confined concrete with the reduction in concrete strength. Therefore, steel confinement is an effective way to improve the performance of RAC.

3.2 Effect of confinement pressures

Stress-strain behavior of RAC with respect to different confinement pressures is presented in Figure 3. All the stress-strain curves showed a linear relationship in the ascending branch however, ductility and post peak behavior were observed different with the increase in confinement pressure. Higher stress-strain curves of RAC were observed for high confinement pressures as compared to low confinement pressures and unconfined concrete specimens. Figure 3 shows the movement of peak strain towards the right side of the curve with the increase in confinement pressure. Specimens with high confinement pressure also showed high energy dissipation capacity through increase in area under the curve as compared to specimens with low confinement pressure or unconfined specimens. All the unconfined specimens showed brittle behavior whereas, ductility enhancement was observed in case of confined specimens with the increase in confinement pressure. This may be related to the increase in effective area of confined concrete core with the decrease in pitch of spiral reinforcement [12]. It can be seen that increase in confinement pressure significantly affected the compressive strength, stiffness and energy absorption capacity of RAC.

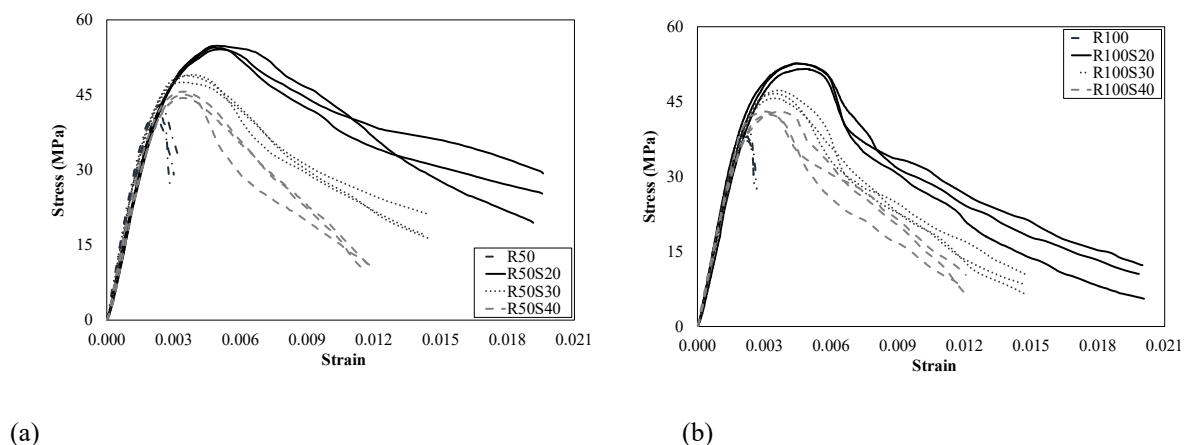


Figure 3: Effect of confinement pressures on stress-strain curves of concrete specimens.

3.3 Stress-strain relationship

Table 4 shows the results of peak stress, peak strain, ultimate strain, modulus of elasticity and toughness of concrete specimens obtained through stress-strain curves. With the increase in replacement ratio of RCA, reduction in peak stress, peak strain, ultimate strain, elastic modulus and toughness was observed. However, increasing confinement pressure improved the peak stress, peak strain, ultimate strain and toughness of specimens. Still, all the confined specimens showed further reduction in elastic modulus of concrete, which may be attributed to the shrinkage of concrete around spiral reinforcement. According to the theory of the multiaxial stress state, peak stress of concrete can be greatly enhanced through lateral confinement pressure [12]. Various researchers also reported the improvement in performance of concrete through lateral confinement [12, 13].

Concrete specimens having 50% and 100% replacement ratio of RCA and confined with 20 mm pitch of spiral reinforcement showed peak stresses higher than unconfined control specimens. Moreover, all the confined RAC specimens showed peak strain, ultimate strain and toughness higher than unconfined control specimens. Therefore, inferior performance of RAC can be improved by providing the confinement through spiral reinforcement.

Table 4: Test results of concrete specimens.

Specimen label	Peak stress	Peak strain	Ultimate strain	Elastic modulus	Toughness
	MPa			MPa	MPa
R0	49.7	0.0025	0.0031*	24300	0.07
R50	41.5	0.0023	0.003*	24300	0.06
R50S20	54.5	0.0049	0.0194 ⁺	20500	0.18
R50S30	48.5	0.0036	0.0144 ⁺	21400	0.12
R50S40	45.1	0.0035	0.0118 ⁺	21500	0.10
R100	38.2	0.0022	0.0026*	22000	0.05
R100S20	52.3	0.0046	0.02 ⁺	21000	0.17
R100S30	46.5	0.0035	0.0148 ⁺	21300	0.11
R100S40	42.8	0.0033	0.012 ⁺	21500	0.10

* with respect to sudden drop of load

+ with respect to first fracture of spiral

3.4 Analytical modelling

3.4.1 Database and existing models

Table 5 shows the summary of experimental database used in this study. As most of the experimental studies involve the role of longitudinal reinforcement, limited test results are available in the literature regarding the effect of spiral steel confinement on concrete. Moreover, no data is available in the present literature regarding stress-strain behaviour of spiral steel confined RAC. Table 6 presents the summary of existing stress-strain models for peak stress and peak strain of spiral steel confined NAC.

In the models, f_{cc} and f_c are the peak stresses of confined and unconfined concrete specimens, respectively; ϵ_{cc} and ϵ_{co} are the peak strains (i.e., strain corresponding to peak stress) of confined and unconfined concrete specimens, respectively; f_1 is the confinement pressure; f_y and d_{sp} are the yield strength and diameter of spiral steel reinforcement, respectively; A_s and A_l are the cross-sectional areas of spiral and longitudinal steel reinforcement, respectively; s is the centre to centre spacing of spiral steel reinforcement and D is the diameter of confined concrete specimens.

Table 5: Summary of experimental database.

Researchers	Diameter	Number	Concrete strength f_c	Confining pressure f_1	Type of concrete
Richart et al. [14]	mm		MPa	MPa	
	254	18	14.7	1.0-10.4	NAC
Mander et al. [15]	500	15	24.0-32.0	1.0-4.3	NAC
Sheikh and Toklucu [16]	203-356	27	29.7-30.5	1.7-6.8	NAC
Assa et al. [17]	145	24	25.0-85.0	2.5-28.3	NAC
Li et al. [18]	240	14	52.0-82.5	1.8-20.2	NAC
Wei and Wu [19]	150	12	36.4	3.2-12.9	NAC
Present study	150	18	37.2-43.0	1.8-3.5	RAC

3.4.2 Stress-strain behaviour

In this study, Mander et al. [22] model (for spiral steel confined NAC) is used to predict the stress-strain behaviour of spiral steel confined RAC. The model is expressed as follows:

$$\frac{f_{cn}}{f_{cc}} = \frac{x \cdot r}{r - 1 + x^r} \quad (1)$$

where

$$x = \frac{\epsilon_c}{\epsilon_{cc}} \quad (2)$$

$$r = \frac{E_c \epsilon_{cc}}{E_c \epsilon_{cc} - f_{cc}} \quad (3)$$

$$E_c = 5000 \sqrt{f_c} \quad (4)$$

Where, E_c is the elastic modulus of concrete specimens. Parameters such as f_{cc} and ϵ_{cc} are considered critical in the above-mentioned model to determine the behaviour of spiral steel confined concrete specimens. In this study, these parameters are predicted for steel confined NAC through different existing models using the experimental database. Then, the best performing model is selected and further modified to incorporate the effect of RCA replacement ratios.

Table 7 presents the comparison between different existing models in predicting the peak stress and peak strain of spiral steel confined NAC. The performance of existing models is evaluated using the following error index [19]:

$$Error\ index = \sum \frac{|Exp. - Ana. |}{|Exp. |} / n \quad (5)$$

where n is total number of confined concrete specimens and Exp. & Ana. are experimental and analytical results of specimens, respectively. Based on the error index, Wei and Wu [19] model can be considered as the best performing model to predict the peak stress and peak strain of steel confined NAC. In this study, Wei and Wu [27] model is further modified to incorporate the effect of RCA replacement ratios. For this purpose, regression analysis of the experimental database is performed and following model is proposed.

$$\frac{f_{cc}}{f_c} = 1 + k_1 \frac{f_1}{f_c} \quad (6)$$

$$\frac{\epsilon_{cc}}{\epsilon_{co}} = 1 + (20.6 - 14.67R^{1.06}) \frac{f_1}{f_c} \quad (7)$$

where

$$k_1 = 5.35f_1^{-0.14} + (20.22R^2 - 34.61R)f_1^{-1} \quad (8)$$

$$f_1 = \frac{2f_s A_s}{Ds} \quad (9)$$

Where, R is the RCA replacement ratio ranging from 0 (i.e., 0% RCA replacement ratio) to 1 (i.e., 100% RCA replacement ratio).

Table 6: Existing models for spiral steel confined NAC.

Model	Peak stress	Peak strain	Parameters
Richart et al. [20]	$\frac{f_{cc}}{f_c} = 1 + 4.1 \frac{f_1}{f_c}$	$\frac{\varepsilon_{cc}}{\varepsilon_{co}} = 1 + 5 \left(\frac{f_{cc}}{f_c} - 1 \right)$	$f_1 = \frac{2f_y A_s}{Ds}$
Shah et al. [21]	$\frac{f_{cc}}{f_c} = 1 + \left(1.15 + \frac{21}{f_c} \right) \frac{f_1}{f_c}$	$\varepsilon_{cc} = 1.491(10^{-5})f_c + 0.0296 \frac{f_1}{f_c} + 0.00195$	$f_1 = \frac{2f_y A_s}{Ds}$ $f_{1e} = 0.5k_e \rho_s f_y$
Mander et al. [22]	$\frac{f_{cc}}{f_c} = 2.254 \sqrt{1 + 7.94 \frac{f_{1e}}{f_c} - 2 \frac{f_{1e}}{f_c} - 1.254 \frac{\varepsilon_{cc}}{\varepsilon_{co}}}$	$\frac{\varepsilon_{cc}}{\varepsilon_{co}} = 1 + 5 \left(\frac{f_{cc}}{f_c} - 1 \right)$	$\rho_s = \frac{4A_s}{Ds}; k_e = \frac{1 - \frac{s'}{2D}}{1 - \rho_{cc}}$ $s' = s - d_{sp}; \rho_{cc} = \frac{4A_l}{\pi D^2}$ $f_1' = \frac{\rho_s f_y}{2} \left(1 - \sqrt{\frac{s}{1.25D}} \right)$ $k_1 = 5.1 \left(\frac{f_c}{f_y} \right)^{0.5} \left(\frac{d_{sp}}{\rho_s} \right)^{0.25}$ $k_2 = \frac{66}{s f_c^{1.7}}; \rho_s = \frac{4A_s}{Ds}$
El-Dash and Ahmad [23]	$\frac{f_{cc}}{f_c} = 1 + k_1 \frac{f_1'}{f_c}$	$\frac{\varepsilon_{cc}}{\varepsilon_{co}} = 1 + k_2 \frac{f_1'}{\varepsilon_{co} f_c}$	$\rho_s = \frac{4A_s}{Ds}$
Hoshikuma et al. [24]	$\frac{f_{cc}}{f_c} = 1 + 3.83 \frac{\rho_s f_y}{f_c}$ $\frac{f_{cc}}{f_c} = 1 + 0.73 \frac{\rho_s f_y}{f_c}$	$\varepsilon_{cc} = 0.00218 + 0.0332 \frac{\rho_s f_y}{f_c}$ $\varepsilon_{cc} = 0.00245 + 0.0122 \frac{\rho_s f_y}{f_c}$	$\rho_s = \frac{4A_s}{Ds}$
Razvi and Saatcioglu [25]	$\frac{f_{cc}}{f_c} = 1 + k_{1e} \frac{f_1}{f_c}$	$\varepsilon_{cc} = \varepsilon_{co1}(1 + 5k_3 K)$	$f_1 = \frac{2f_s A_s}{Ds}; k_{1e} = 6.7f_1^{-0.17}$ $K = \frac{k_{1e} f_1}{f_c}; k_3 = \max. \left(\frac{40}{f_c}, 1.0 \right)$ $\varepsilon_{co1} = 0.0028 - 0.0008k_3$
Assa et al. [17]	$\frac{f_{cc}}{f_c} = 1 + 3.36 \frac{f_{rp}}{f_c}$	$\frac{\varepsilon_{cc}}{\varepsilon_{co}} = 1 + 21.5 \frac{f_{rp}}{f_c}$	$f_{rp} = \max. \left(\frac{16f_y A_s}{Ds f_c^{0.34} e^{\frac{6s}{D}}}, \frac{2f_y A_s}{Ds} \right)$ $f_{1e} = 0.5k_e \rho_s f_y; \rho_s = \frac{4A_s}{Ds}$ $k_e = \frac{1 - \frac{s'}{2D}}{1 - \rho_{cc}}; s' = s - d_{sp}$ $\rho_{cc} = \frac{4A_l}{\pi D^2}$
Li et al. [19]	$\frac{f_{cc}}{f_c} = 2.254 \sqrt{1 + 7.94 \alpha_s \frac{f_{1e}}{f_c} - 2 \alpha_s \frac{f_{1e}}{f_c} - 1.254 \frac{\varepsilon_{cc}}{\varepsilon_{co}}}$	$\frac{\varepsilon_{cc}}{\varepsilon_{co}} = 1 + 384 \left(\frac{f_{1e}}{f_c} \right)^2$	$\alpha_s = 3.1 \frac{f_{1e}}{f_c} \text{ for } f_c > 52 \text{ MPa}$ $\alpha_s = (21.2 - 0.35f_c) \frac{f_{1e}}{f_c} \text{ for } f_c \leq 52 \text{ MPa}$
Wei and Wu [19]	$\frac{f_{cc}}{f_c} = 1 + k_1' \frac{f_1}{f_c}$	$\frac{\varepsilon_{cc}}{\varepsilon_{co}} = 1 + 20.6 \frac{f_1}{f_c}$	$f_1 = \frac{2f_s A_s}{Ds}; k_1' = 5.35f_1^{-0.14}$

Table 8 shows the performance of proposed model to predict the peak stress and peak strain of both steel confined NAC and RAC. It is observed that the proposed model can be effectively used to predict the peak stress and peak strain of both steel confined NAC and RAC with an average error index of 5% and 14%, respectively. Equation 4 for elastic modulus of concrete specimens is also further modified to incorporate the effect of RCA replacement ratios as follows:

$$E_c = (5000 - 2739R^2 + 4416R)\sqrt{f_c} \quad (10)$$

Table 7: Prediction of peak stress and peak strain for steel-confined NAC.

Model	f_{cc}/f_c				$\square_{cc}/\square_{co}$			
	$f_{cc, ana.} / f_{cc, Exp.}$	SD	COV	Error index	$\square_{cc, ana.} / \square_{cc, Exp.}$	SD	COV	Error index
			%	%			%	%
Richart et al. [20]	1.02	0.13	13.08	11.86	1.06	0.23	24.25	19.74
Shah et al. [21]	0.79	0.17	13.21	19.62	0.87	0.34	29.72	26.17
Mander et al. [22]	1.05	0.12	12.85	12.10	1.15	0.24	27.65	21.91
El-Dash and Ahmad [23]	0.88	0.22	19.41	12.35	0.48	0.86	41.13	111.75
Hoshikuma et al. [24]	1.34	0.14	19.16	39.67	1.46	0.18	26.97	32.33
Razvi and Saatcioglu [25]	1.09	0.11	11.86	13.63	0.91	0.33	30.43	25.91
Assa et al. [17]	0.84	0.11	9.27	15.15	0.80	0.35	28.06	31.55
Li et al. [18]	1.01	0.41	41.24	22.07	1.94	0.35	66.94	53.14
Wei and Wu [19]	1.02	0.11	11.59	10.26	1.07	0.23	24.26	19.78
Proposed	1.02	0.11	11.59	10.26	1.07	0.23	24.26	19.78

SD = Standard deviation & COV = Coefficient of variation

Ultimate strain (i.e., strain corresponding to first fracture of spiral steel reinforcement) of spiral steel confined NAC and RAC can also be calculated by equation 11, which is modified form of ultimate strain model proposed by Wei and Wu [19].

$$\frac{\epsilon_{cu}}{\epsilon_{co}} = 1.75 + 0.83R + 900\epsilon_{su} \left[\frac{f_1}{f_c} \right] \quad (11)$$

Where, ϵ_{cu} is the ultimate strain of steel confined specimens and ϵ_{su} is the fracture strain of spiral steel reinforcement.

Table 8: Prediction of peak stress and peak strain for steel-confined NAC and RAC.

Model	f_{cc}/f_c				$\square_{cc}/\square_{co}$			
	$f_{cc, ana.} / f_{cc, Exp.}$	SD	COV	Error index	$\square_{cc, ana.} / \square_{cc, Exp.}$	SD	COV	Error index
			%	%			%	%
Proposed	1.01	0.05	5.36	4.77	1.01	0.14	13.57	14.37

3.4.3 Performance of model

Figure 4 presents the comparison between the experimental and analytical stress-strain curves of spiral steel confined RAC. The analytical stress-strain curves are observed close to the experimental results. Based on the results, proposed model can be effectively used to predict the stress-strain curves of spiral steel confined NAC and RAC. However, the proposed model is based on a limited test database and detailed experimental study is required to further improve the model.

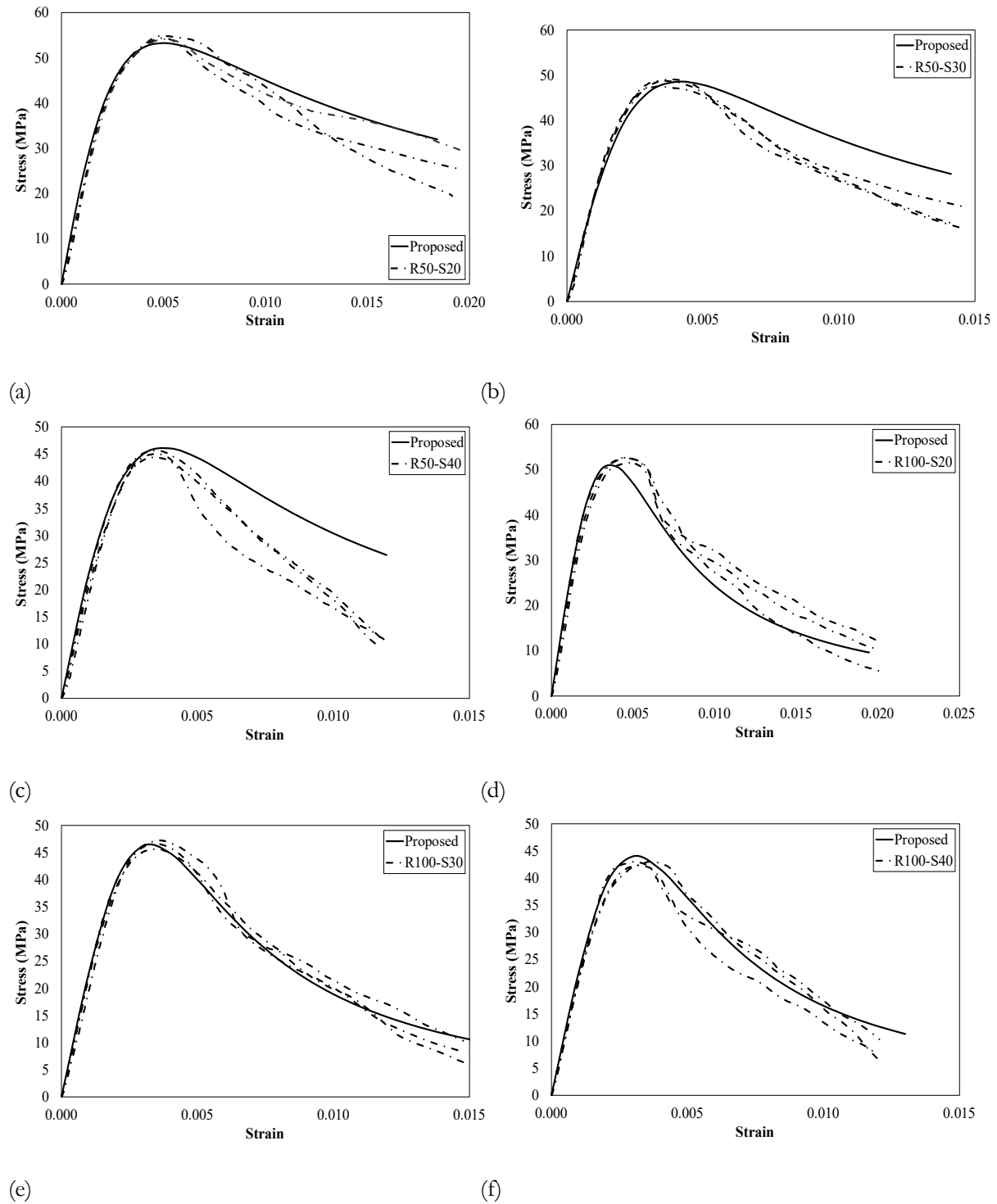


Figure 4: Comparison of proposed stress-strain model with experimental results of steel confined RAC.

4. Conclusions

This article focuses on the behavior of RAC cylinders confined with steel spirals. For this purpose, twenty-seven concrete cylinders confined by spiral reinforcement with varying confinement pressures and replacement ratios of RCA were tested under axial compression. Based on the study, following conclusions are drawn:

- Improved ductility and post peak behaviour of confined recycled aggregate concrete specimens were observed with the increase in confinement pressure.
- Increase in peak stress, peak strain and ultimate strain of concrete specimens was also observed with the increase in confinement pressure.
- Concrete specimens having 50% and 100% replacement ratio of recycled concrete aggregates and confined with 20 mm pitch of spiral reinforcement showed peak stresses higher than unconfined control specimens.
- All the confined recycled aggregate concrete specimens showed peak strain, ultimate strain and toughness higher than unconfined control specimens.
- Increase in confinement pressure improves the stress-strain behaviour of specimens. Therefore, inferior performance of RAC can be improved by providing the confinement through spiral reinforcement.
- Based on the experimental results, a stress-strain model is proposed in this study. For this purpose, the effect of replacement ratios of recycled concrete aggregates is incorporated by modifying the parameters of best performing stress-strain model for spirally confined NAC.
- The proposed model can effectively predict the stress-strain behavior of both spiral steel confined NAC and RAC.

5. Acknowledgment

Scholarships provided by RMIT to the student authors are highly acknowledged.

6. References

- [1] J. Xiao, W. Li, C. Poon, Recent studies on mechanical properties of recycled aggregate concrete in China—A review, *Science China Technological Sciences* 55(6) (2012) 1463-1480.
- [2] J. Xiao, W. Li, Y. Fan, X. Huang, An overview of study on recycled aggregate concrete in China (1996–2011), *Construction and Building Materials* 31 (2012) 364-383.
- [3] S.C. Kou, C.S. Poon, D. Chan, Influence of fly ash as cement replacement on the properties of recycled aggregate concrete, *Journal of Materials in Civil Engineering* 19(9) (2007) 709-717.
- [4] S.M.S. Kazmi, M.J. Munir, Y.-F. Wu, I. Patnaikuni, Effect of macro-synthetic fibers on the fracture energy and mechanical behavior of recycled aggregate concrete, *Construction and Building Materials* 189 (2018) 857-868.
- [5] Y. Kim, A. Hanif, S.M.S. Kazmi, M.J. Munir, C. Park, Properties enhancement of recycled aggregate concrete through pretreatment of coarse aggregates – Comparative assessment of assorted techniques, *Journal of Cleaner Production* 191 (2018) 339-349.
- [6] S.M.S. Kazmi, M.J. Munir, Y.-F. Wu, I. Patnaikuni, Y. Zhou, F. Xing, Axial stress-strain behavior of macro-synthetic fiber reinforced recycled aggregate concrete, *Cement and Concrete Composites* 97 (2019)

-
- [7] M. Behera, S.K. Bhattacharyya, A.K. Minocha, R. Deoliya, S. Maiti, Recycled aggregate from C&D waste & its use in concrete – A breakthrough towards sustainability in construction sector: A review, *Construction and Building Materials* 68 (2014) 501-516.
- [8] C. Shi, Y. Li, J. Zhang, W. Li, L. Chong, Z. Xie, Performance enhancement of recycled concrete aggregate – A review, *Journal of Cleaner Production* 112 (2016) 466-472.
- [9] J. Xiao, Y. Huang, J. Yang, C. Zhang, Mechanical properties of confined recycled aggregate concrete under axial compression, *Construction and Building Materials* 26(1) (2012) 591-603.
- [10] J.L. Zhao, T. Yu, J.G. Teng, Stress-strain behavior of FRP-confined recycled aggregate concrete, *Journal of Composites for Construction* 19(3) (2015) 10.1061/(ASCE)CC.1943-5614.0000513.
- [11] J. Xiao, K. Zhang, A. Akbarnezhad, Variability of stress-strain relationship for recycled aggregate concrete under uniaxial compression loading, *Journal of Cleaner Production* 181 (2018) 753-771.
- [12] W. Wang, M. Zhang, Y. Tang, X. Zhang, X. Ding, Behaviour of high-strength concrete columns confined by spiral reinforcement under uniaxial compression, *Construction and Building Materials* 154 (2017) 496-503.
- [13] J.G. Teng, J.L. Zhao, T. Yu, L.J. Li, Y.C. Guo, Behavior of FRP-confined compound concrete containing recycled concrete lumps, *Journal of Composites for Construction* 20(1) (2016) 04015038.
- [14] F. Richart, A. Brandtzaeg, R. Brown, The failure of plain and spirally reinforced concrete in compression, Engineering Experiment Station, Bulletin no. 190, University of Illinois, Urbana, USA, 1929.
- [15] J.B. Mander, M.J.N. Priestley, R. Park, Observed stress-strain behavior of confined concrete, *Journal of Structural Engineering* 114(8) (1988) 1827-1849.
- [16] A.S. Shamim, T.T. Murat, Reinforced concrete columns confined by circular spirals and hoops, *ACI Structural Journal* 90(5) (1993) 542-553.
- [17] B. Assa, M. Nishiyama, F. Watanabe, New approach for modeling confined concrete. I: Circular columns, *Journal of Structural Engineering* 127(7) (2001) 743-750.
- [18] B. Li, R. Park, H. Tanaka, Stress-strain behavior of high-strength concrete confined by ultra-high- and normal-strength transverse reinforcements, *ACI Structural Journal* 98(3) (2001) 395-406.
- [19] Y. Wei, Y.-F. Wu, Compression behavior of concrete columns confined by high strength steel wire, *Construction and Building Materials* 54 (2014) 443-453.
- [20] F. Richart, A. Brandtzaeg, R. Brown, A study of the failure of concrete under combined compressive stresses, Engineering Experiment Station, Bulletin no. 185, University of Illinois, Urbana, USA, 1928.
- [21] S.P. Shah, A. Fafitis, R. Arnold, Cyclic loading of spirally reinforced concrete, *Journal of Structural Engineering* 109(7) (1983) 1695-1710.
- [22] J.B. Mander, M.J.N. Priestley, R. Park, Theoretical stress-strain model for confined concrete, *Journal of Structural Engineering* 114(8) (1988) 1804-1826.
- [23] K.M. El-Dash, S.H. Ahmad, A model for stress-strain relationship of spirally confined normal and high-strength concrete columns, *Magazine of Concrete Research* 47(171) (1995) 177-184.
- [24] J. Hoshikuma, K. Kawashima, K. Nagaya, A.W. Taylor, Stress-strain model for confined reinforced concrete in bridge piers, *Journal of Structural Engineering* 123(5) (1997) 624-633.

Influence of different recycled concrete aggregate treatment methods on the performance of concrete: a comparative assessment

S.M. S. Kazmi¹, M.J. Munir¹, Y.F. Wu¹, I. Patnaikuni¹

¹School of Engineering, RMIT University, 376-392 Swanston St, Melbourne, Victoria-3001, Australia.

Abstract

Rapid urbanization and infrastructure development around the globe is causing surge in the construction and demolition (C&D) waste generation resulting into exhaustion of natural resources and waste disposal problems. Recycling of C&D waste in the concrete is considered a sustainable way. However, recycled concrete aggregates (RCA) with inferior properties are produced as compared to virgin natural aggregates. This study aims to improve the RCA performance utilizing different treatment methods and to evaluate the properties of the resulting recycled aggregate concrete (RAC). For this reason, modified carbonation treatment along with four other treatment methods (i.e. carbonation, acetic acid immersion, acetic acid immersion with rubbing and acetic acid immersion with carbonation) were adopted to improve the quality of RCA. Variety of physical properties of RCA were evaluated to understand the effect of treatment methods. Compressive, split tensile and flexural strength tests were performed on all the concrete mixes incorporating treated RCA. Moreover, stress-strain behavior of RAC with treated and un-treated RCA was also studied. 20% and 17% drop in the water absorption was observed for the RCA treated by the modified carbonation and carbonation techniques, respectively. Decrease in the crushing value was also observed for the all the treated RCA. Mechanical properties of RAC incorporating treated RCA were also enhanced, with the maximum improvement observed for mixes having RCA treated by the modified carbonation and acid immersion with rubbing methods. For instance, 24% and 28% rise in compressive strength was noticed in the modified carbonation and acid immersion with rubbing treated RCA mixes, respectively. Scanning electron microscopy of RAC incorporating treated RCA also showed a dense microstructure as compared to un-treated RCA mix. Therefore, RCA treated by modified carbonation and acid immersion with rubbing techniques can be used in the production of sustainable concrete having enhanced mechanical performance leading towards eco-friendly and clean construction.

Keywords: Recycled aggregate concrete, accelerated carbonation treatment, acid treatment, mechanical performance, stress strain behaviour.

1. Introduction

Swift development, population growth and industrialization around the globe are generating huge amount of construction and demolition (C&D) waste. On the other hand, natural resources are being depleted and shortage of landfill sites is also becoming a major problem nowadays. For instance, China produces around 200 million tons [1], while Japan, USA and European countries generate about 900 million tons of C&D waste each year [2]. Similarly, Australia produces around 7.5 million tons of C&D waste annually [3]. Therefore, recycling of C&D waste in new construction projects in the form of recycled concrete aggregates (RCA)

is considered as the best possible way to protect environment and preserve natural resources. Utilization of RCA in the new construction projects has already been promoted by many countries worldwide [4]. However, inferior properties of RCA as compared to natural coarse aggregates (NCA) result into lower quality concrete in terms of mechanical and durability performance [4, 5]. This reduction of mechanical and durability performance of recycled aggregate concrete (RAC) may be attributed to the old adhered mortar with RCA and higher amount of interfacial transition zone (ITZ) in the RAC as compared to natural aggregate concrete (NAC) [6, 7]. Replacement of RCA with NCA results into the reduction of the compressive strength and elastic modulus of concrete [4, 8-10]. 20-40% loss in split tensile strength was also reported by previous researchers [11, 12]. Flexural strength and modulus of elasticity of RAC was also dropped in the past studies [12-15]. Due to inferior performance of RAC as compared to NAC, application of RCA is restricted to low level non-structural applications such as road subbase material [4]. Enhancement of the inferior properties of RCA has been studied by many researchers in the past [16]. Different techniques were adopted to improve the performance of RAC including improvement of concrete mixing method, coating of RCA, addition of supplementary cementitious materials (SCM) in RAC, removal of adhered mortar from RCA surface [4, 16]. Altering the concrete mixing method by using two stage mixing and triple stage mixing with SCM can surge the compressive strength of RAC [17-19]. RCA surface coating is another positive method for the enhancement of inferior performance of RCA's. For example, higher density resulting in to improved compressive strength was detected by surface coating of RCA with silica fume and fly-ash [20]. Similarly, Katz also observed 15% rise in compressive strength of RAC by incorporating silica fume treated RCA [21]. Moreover, shear and compressive strengths of RAC can be improved up to 30% and 15% respectively by treating RCA with paste having inorganic admixtures [22]. SCM incorporation in the RAC can enhance the ITZ and cement matrix ensuing the improved durability and mechanical performance. About 9% surge in the 10 years compressive strength of RAC was also observed after using the fly ash [23]. The mortar adhered on the surface of RCA has adverse effects on the mechanical and durability performance of RAC [16, 24]. Therefore, exclusion of old adhered mortar from the surface of RCA is a helpful method to improve the performance of RCA in the resulting RAC. Old adhered mortar can be removed using different methods i.e. mechanical and heat grinding of RCA [25-27] and pre-soaking of RCA in water and acidic solutions [28, 29]. There are certain disadvantages of these adhered mortar removal techniques i.e. increased consumption of energy as well as higher CO₂ emission, higher amount of waste fine material production causing environmental burden and increase of chloride and sulphate contents in RCA resulting into inferior durability performance of concrete [4, 16]. Calcium carbonate deposition on the surface of RCA through bio deposition and carbonation methods can enhance the performance of RCA. Bio deposition of calcium carbonate using the bacteria can decrease the water absorption of RCA and improves the quality of resulting concrete [30]. However, most of the techniques cannot be applied at a large-scale due to higher cost, difficult execution, time consumption and other environmental issues [4, 16].

To avoid the short comings of the acid treatment of RCA, low concentration of acetic acid has been used in the past study [31]. Acetic acid reacts with calcium hydrate (C-H), calcium silicate hydrate (C-S-H) and calcium carbonate in the old adhered mortar of RCA. The adhered mortar loses the strength due to the reaction and can be removed from RCA surface by mechanical rubbing. Acetic acid treatment of RCA is cheaper, safer and cleaner as compared to other acid treatments [31]. Moreover, value added products can be obtained after RCA treatment with acetic acid and waste acetic acid solution after treatment can be used as an admixture in concrete [31, 32]. Accelerated pre-carbonation of RCA has been recognized as the most feasible method to improve the mechanical and durability performance of RAC [4, 7, 16]. During the accelerated pre-carbonation, calcium carbonate is produced on the surface of RCA as a reaction product resulting into dense pore structure [1, 4]. Therefore, the enhanced microstructure of pre-carbonated RCA

results into much improved performance in terms of water absorption, density and crushing strength leading towards RAC with improved properties.

Although various investigators have studied different treatment methods of RCA to enhance the inferior performance of RAC as compared to NAC. Limited work is available regarding the comparative assessment of different treatment methods of RCA with respect to the performance of RAC for the similar source of RCA. This study aims to investigate the effect of different RCA treatment techniques on the compressive strength, split tensile strength, flexural strength, elastic modulus and stress-strain behaviour of RAC. For this purpose, five different treatment techniques of RCA, i.e. carbonation, acetic acid immersion, acetic acid immersion with rubbing, acetic acid immersion with carbonation and modified carbonation were adopted during the study. Treatment techniques like carbonation and acetic acid immersion are considered most effective and environment-friendly techniques in improving the properties of RAC [4, 31]. These techniques were further improved in this study to achieve enhanced RAC performance. For this purpose, acetic acid immersion with rubbing, acetic acid immersion with carbonation and modified carbonation techniques were performed on RCA to explore the effect of improved treatment techniques on the performance of RAC. Moreover, this study also explores the effect of different treatment methods on the stress-strain behaviour of concrete with treated RCA.

2. Methodology

2.1 Materials

RCA having maximum aggregate size of 20 mm and less than 5% impurities were used in this study. Crushed granite fragments were used as NCA. Figure 1 depicts the grading of NCA and RCA. Table 1 shows the physical properties of NCA and RCA used in this study. RCA possesses approximately five times higher water absorption than NCA, which may be attributed to the adhered mortar on the surface of RCA. Portland cement of type P.II52.5R and river sand having apparent density of 2600 kg/m³ were used. Tap water was used for all the concrete mixes prepared in this study. All the fine and coarse aggregates were dried in oven for 24 hours at 105°C before the production of concrete. Due to high water absorption, RCA absorb a large amount of water needed for hydration of cement in the first few minutes of concrete mixing [33]. Therefore, additional water was added with respect to the water absorption of fine and coarse aggregates in all the concrete mixes for better control of the water content. Similar method has been adopted in the past studies [14, 15].

2.2 Treatment of RCA

Accelerated carbonation treatment method was used to obtain carbonated recycled concrete aggregates (C-RCA) [4]. RCA were pre-conditioned at 25°C and relative humidity of 50% to provide RCA with essential moisture content for accelerated carbonation i.e. 40-70%. Afterwards, RCA were placed in air tight steel chamber with a capacity of about 100 litres and vacuumed to -1.0 bar. CO₂ was then inserted in the chamber and 100% CO₂ concentration with +0.8 bar pressure was maintained for 24 hours in the chamber.

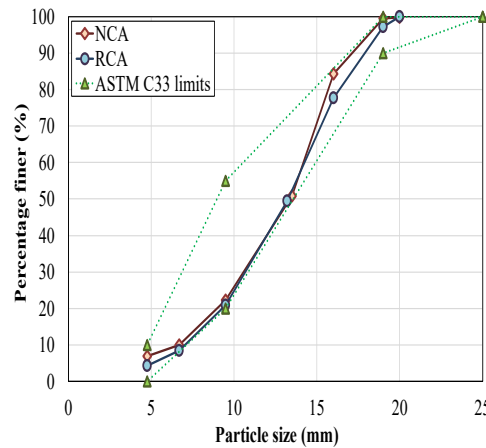


Figure 1: Grading of NCA and RCA.

Table 1: Physical properties of the aggregates used in the study.

Type of aggregates	Water absorption	Oven dried specific gravity	Bulk density	Crushing value	Adhered mortar
	%		kg/m ³	%	%
NCA	1.3	2.51	1513	27.0	-
RCA	6.85	2.17	1414	31.0	34.5
C-RCA	5.65	2.23	1438	30.46	33.5
A-RCA	6.44	2.24	1367	30.17	31
AR-RCA	6.35	2.22	1415	29.25	28
AC-RCA	6.76	2.24	1394	29.64	32
MC-RCA	5.47	2.25	1442	30.74	34

During the accelerated carbonation process, reactive components in the old adhered mortar of RCA are very essential for the performance enhancement of RCA [34]. Therefore, the accelerated carbonation treatment was modified by first submerging RCA in lime saturated water for 24 hours and then allowing them to dry at 25°C and relative humidity of 50% for three days to introduce some additional calcium into the pores of old adhered mortar artificially. Afterwards, RCA were carbonated using the same accelerated carbonation technique discussed above to obtain modified carbonated recycled concrete aggregates (MC-RCA).

RCA were washed and dried after immersion in the 3% acetic acid solution for 24 hours to remove the old adhered mortar and to obtain acetic acid treated recycled concrete aggregates (A-RCA), similar to previous study [31]. Moreover, mechanical rubbing for 5 minutes was also performed on A-RCA using an empty concrete mixer to obtain acetic acid treated and rubbed recycled concrete aggregates (AR-RCA). Furthermore, A-RCA were carbonated in the accelerated carbonation chamber to produce acetic acid treated and carbonated recycled concrete aggregates (AC-RCA).

2.3 Methods

ASTM C127 [35] and BS 812-110 [36] were followed to calculate the water absorption, specific gravity, crushing value and bulk densities of all the treated and un-treated aggregates. The old adhered mortar content of the treated and untreated RCA was evaluated using method developed by Abbas et al. [37]. Table 2 shows the mix details of all the concrete mixes prepared in this study. All the concrete mixes were prepared according to ASTM C192 / C192M - 16a [38] using a double shaft concrete mixer. Workability of all the concrete mixes was observed between 100-200 mm and no segregation or bleeding was noticed in any of the mix proportions. For each mix twelve (12) concrete cylinders having diameter 150 mm and height 300 mm were prepared and cured for 28 and 90 days in moist curing chamber with temperature 20°C and relative humidity 95%. Moreover, three concrete prisms (75 mm x 75 mm x 275 mm) were also

prepared and cured for 28 days.

After the curing of 28 and 90 days, split tensile and compressive strength tests were performed on the concrete cylinders according to ASTM C496 / C496M-17 [39] and ASTM C39 / C39M-18 [40], respectively. To examine the stress-strain behaviour, applied load and deformation of specimens were measured during the test. MTS machine having capacity of 3000 KN was used for the compression and tensile tests. Load was recorded using a data acquisition system and the axial deformation was recorded using four linear variable displacement transducers (LVDTs) mounted at 90° relative to each other. All the concrete specimens were tested under displacement control at the rate of 0.3 mm/min. Modulus of elasticity of all the specimens was also determined using Equation 1.

$$E \text{ (GPa)} = \frac{\sigma_2 - \sigma_1}{\epsilon_2 - \epsilon_1} \quad (1)$$

Where, E is the modulus of elasticity of concrete, ϵ_1 is the strain value of 0.00005, σ_1 and σ_2 are the stresses corresponding to ϵ_1 and 0.4xpeak stress, respectively and ϵ_2 is the strains corresponding to σ_1 . Flexural strength of the concrete prisms (75 mm x 75 mm x 275 mm) was calculated at the age of 28 days in accordance with ASTM C293 / C293M-16 [41]. In addition to the mechanical performance, microstructure of treated and un treated RAC was also observed using Quanta FEG 250 scanning electron microscope.

Table 2: Mix proportions of concrete with treated and untreated RCA.

Constituents	Concrete ID						
	NAC	RAC	C-RAC	A-RAC	AR-RAC	AC-RAC	MC-RAC
Cement (kg/m ³)	288.06	288.06	288.06	288.06	288.06	288.06	288.06
Sand (kg/m ³)	528.82	528.82	528.82	528.82	528.82	528.82	528.82
NCA (kg/m ³)	710.18	-	-	-	-	-	-
RCA* (kg/m ³)	-	663.71	674.98	641.85	664.57	654.12	639.94
Water (kg/m ³)	138.27	138.27	138.27	138.27	138.27	138.27	138.27
Extra water (kg/m ³)	9.23	45.46	42.93	41.34	42.20	41.60	35.00

*Concrete ID's C-RAC, A-RAC, AR-RAC, AC-RAC and MC-RAC, RCA shows the amount of respective treated aggregates.

3. Results and discussion

Table 1 depicts the physical properties (i.e. water absorption, specific gravity, bulk density, crushing value, and old adhered mortar content) of all types of coarse aggregates used in this study. It was observed that all the treated RCA showed improved performance in terms of physical properties, similar to previous studies [7, 16].

Table 3: Effect of RCA treatment on the mechanical performance of RAC.

Concrete ID	Compressive strength		Split tensile strength		Flexural strength	Modulus of elasticity
	28 days	90 days	28 days	90 days		
	MPa		MPa		MPa	GPa
NAC	27.81	31.09	3.40	4.3	7.06	28.55
RAC	18.91	22.96	2.58	3.3	4.15	18.49
C-RAC	21.60	27.75	2.82	3.79	5.06	20.02
A-RAC	21.03	25.79	2.62	3.2	4.52	21.44
AR-RAC	23.60	30.48	3.17	3.42	6.65	23.82
AC-RAC	21.17	24.07	2.76	3.25	4.74	20.73
MC-RAC	24.27	29.00	3.07	3.75	5.28	23.52

Table 3 depicts the average compressive strength of tested specimens after 28 and 90 days of curing. The

average compressive strength values of NAC specimens were observed as 27.8 and 31.1 MPa for 28 and 90 days, respectively, which reduced to 18.9 and 23.0 MPa, respectively for the 100% replacement ratio of RCA. Moreover, increase in compressive strength with the curing age was observed for all the specimens. Drop in compressive strength of RAC may be attributed to the presence of porous adhered mortar and weak ITZ in the RCA [12]. Similar reduction in compressive strength due to 100% replacement ratio of RCA was also reported by many researchers [12, 42]. Increase in compressive strength was observed for the mixes incorporating treated RCA. Accelerated carbonation treated RCA mixes (C-RAC, AC-RAC and MC-RAC), depicted rise in compressive strength as compared to RAC as shown in Table 3. For instance, 14.2 and 28.3% increase in 28-day compressive strength was observed for the C-RAC and MC-RAC specimens as compared to RAC specimens, respectively. This increase in the compressive strength may be attributed to filling of pores in the old adhered mortar by the CaCO_3 after the accelerated carbonation reaction, similar to previous studies [16, 34]. Table 3 also shows higher compressive strength values for the acetic acid treated RCA mixes (A-RAC, AR-RAC and AC-RAC) as compared to RAC mix. For example, 24.8% increase in the compressive strength was noted for the AR-RCA specimens as compared to RAC specimens. Removal of old adhered mortar due to acetic acid with rubbing treatment densifies the pore structure of AR-RAC resulting into increased compressive strength akin to previous study [31]. For the accelerated carbonation treated RCA incorporated concrete specimens, maximum and minimum 28-day compressive strength was observed for the MC-RAC and AC-RAC specimens respectively. Similarly, for the acid treated RCA incorporated specimens, maximum and minimum 28-day compressive strength was observed for the AR-RAC and AC-RAC specimens respectively. Moreover, Table 3 also shows that 85% and 87% compressive strength of NAC can be achieved by using acetic acid with rubbing and modified carbonation treatment techniques, respectively. Therefore, the adverse effects of RCA can be offset by above mentioned treatments making RAC suitable for structural use resulting into sustainable and eco-friendly construction.

Table 3 displays the average modulus of elasticity values of all the tested specimens after 28 days of curing. Drop in elastic modulus values was observed for RAC specimens as compared to NAC specimens. For instance, the average modulus of elasticity value of NAC specimens was observed as 28.55 GPa, which reduced to 18.49 GPa for the 100% replacement ratio of RCA. Similar reduction in modulus of elasticity was also observed by Xiao et al. [43] for the concrete specimens with 100% replacement ratio of RCA. The drop in the elastic modulus of RAC may be attributed to the inferior modulus of elasticity of RCA due to the presence of porous old adhered mortar [43]. Rise in the modulus of elasticity values was observed for the mixes incorporating treated RCA as compared to RAC mix. Approximately, 29% and 27% increase in the modulus of elasticity values was observed for AR-RAC and MC-RAC specimens, respectively as compared to RAC specimens. The increase of modulus of elasticity after RCA treatment may be related to the removal of porous old adhered mortar by acetic acid with rubbing treatment [31] and densification of adhered mortar through CaCO_3 precipitation by modified carbonation treatment of RCA [34]. For the accelerated carbonation treated RCA incorporated concrete specimens, maximum and minimum modulus of elasticity was observed for the MC-RAC and C-RAC specimens respectively. Similarly, for the acid treated RCA incorporated specimens, maximum and minimum modulus of elasticity was observed for the AR-RAC and AC-RAC specimens respectively. Table 3 also shows that around 83% of modulus of elasticity of NAC can be attained by using acetic acid with rubbing and modified carbonation treatments.

Table 3 depicts the split tensile strength of the concrete specimens made with treated and untreated RCA at two different ages (i.e. 28 and 90 days). Drop in split tensile strength was observed for the mix containing RCA as compared to NAC. However, the mixes having treated RCA showed improved split tensile strength as compared to untreated RCA mix. For instance, 24% reduction in the split tensile strength was observed

for RAC as compared to NAC, similar to previous study [12] . Moreover, 22.8% and 18.8% rise in the split tensile strength was noted for AR-RAC and MC-RAC, respectively as compared to RAC. This may be due to removal of loose mortar after acetic acid with rubbing treatment [31] and pore filling by CaCO_3 after the lime carbonation treatment [34]. It was also observed that the split tensile strength of all the treated and untreated aggregate mixes increased with the age of concrete.

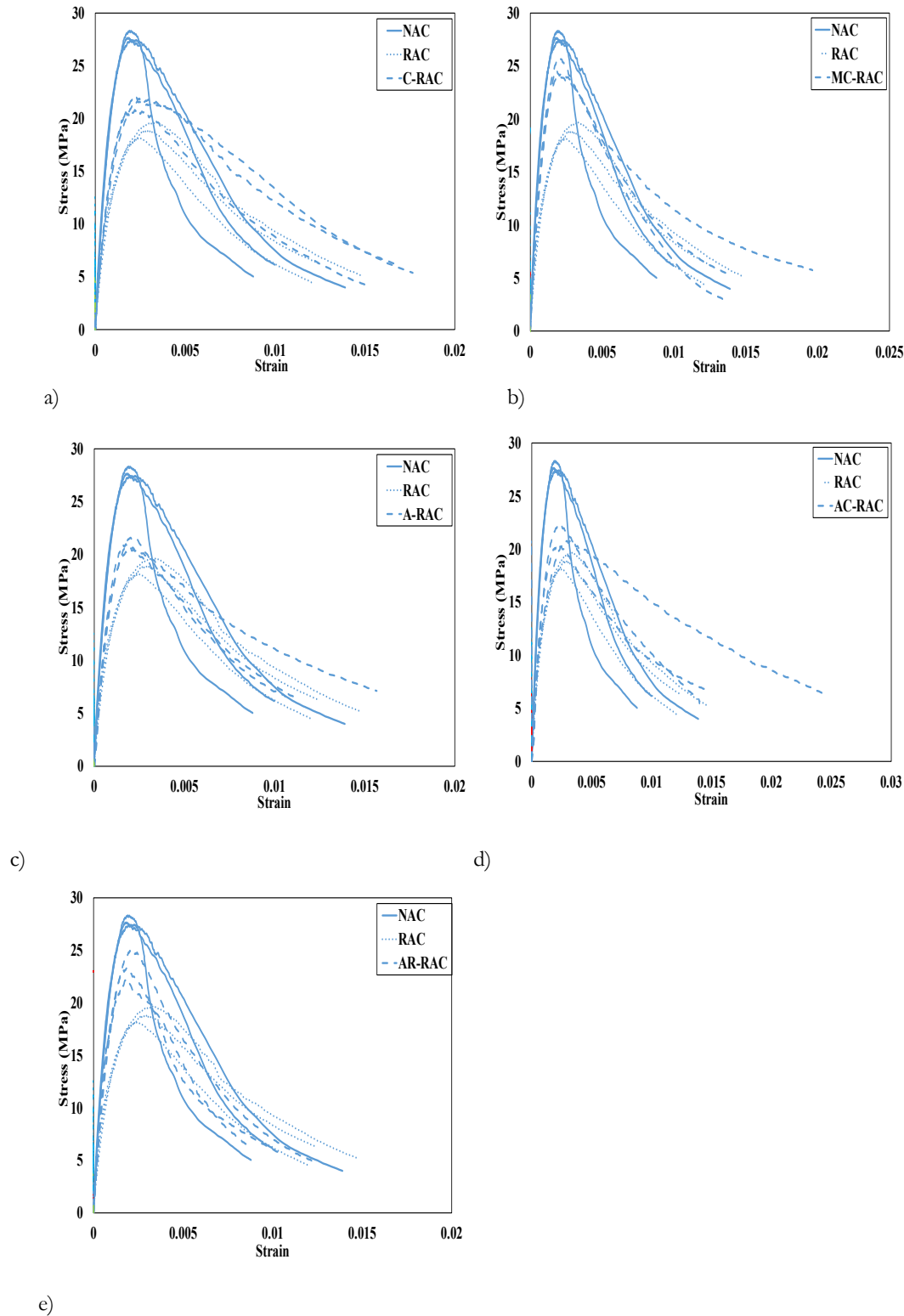


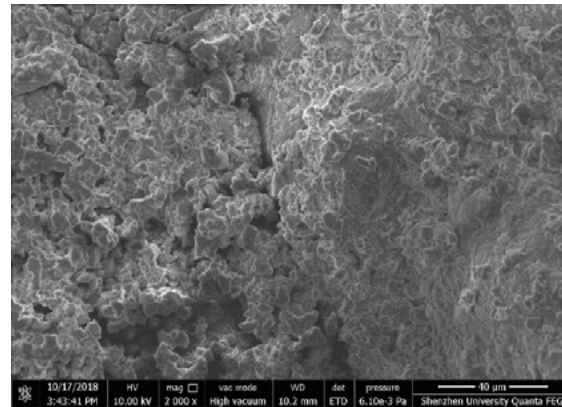
Figure 2: Effect of RCA treatment on the stress-strain behaviour of a) C-RAC specimens b) MC-RAC specimens c) AC-RAC specimens d) A-RAC specimens, and e) AR-RAC specimens.

For the accelerated carbonation treated RCA incorporated concrete specimens, maximum and minimum 28-day split tensile strength was observed for the MC-RAC and AC-RAC specimens respectively. Similarly, for the acid treated RCA incorporated specimens, maximum and minimum 28-day split tensile strength was observed for the AR-RAC and A-RAC specimens respectively. AR-RAC and MC-RAC gained approximately 93% and 90% of split tensile strength of NAC. Therefore, acetic acid with rubbing and modified carbonation treatment may be considered helpful techniques to improve the quality of RAC resulting in eco-friendly and sustainable construction.

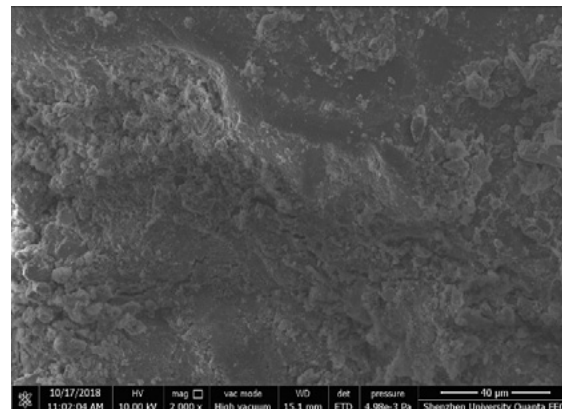
Table 3 shows the 28 days flexural strength of all the tested concrete specimens. Reduction in the flexural strength was observed for all the RCA incorporated concrete specimens as compared to NAC. This may be attributed to the poor bond between old and new cement pastes in RAC. Similar observations were reported in previous studies [12, 44]. However, increase in flexural strength was noted for the RAC incorporating treated RCA as compared to RAC. For instance, 22% and 27% rise in the flexural strength was observed for the C-RAC and MC-RAC specimens, respectively as compared to RAC specimens. This may be attributed to the densification of concrete pore structure by CaCO_3 deposition resulting into improved ITZ and better bond between old and new cement pastes [34]. Moreover, about 60% increase in the flexural strength was observed for the AR-RAC specimens as compared to RAC specimens. This increase in flexural strength may be due to the removal of weaker adhered mortar by the acetic acid and rubbing treatment of RCA [31]. Similar increase in the flexural strength due to RCA treatment was also reported in previous studies [4, 34]. For the accelerated carbonation treated RCA incorporated concrete specimens, maximum and minimum flexural strength was observed for the MC-RAC and AC-RAC specimens respectively. Similarly, for the acid treated RCA incorporated specimens, maximum and minimum flexural strength was observed for the AR-RAC and A-RAC specimens respectively. Therefore, acetic acid treatment with rubbing and modified carbonation methods can be adopted to improve the mechanical performance of RAC.

Figure 2 shows the effect of different types of RCA treatments on the axial stress strain curves of all the concrete specimens. Change in the shape of the stress strain curves was observed for RAC specimens as compared to NAC specimens. For example, RAC specimens showed more flatter stress strain curves as compared to their counterpart i.e. NAC. Moreover, smaller initial slope (modulus of elasticity), lower peak value (compressive strength) and steeper descending branches of stress strain curves were observed for RAC specimens, which may be attributed to more brittle nature of RAC. Similar observations were reported by past researchers [45]. Smaller area under stress strain curves of the RAC specimens as compared to NAC specimens also shows reduced energy absorption capacity of the RAC specimens. In the case of accelerated carbonation treated RCA mixes (C-RAC, AC-RAC and MC-RAC), improved stress strain curves were observed as compared to RAC as depicted in Figure 2. Similar improvement was also reported in the past research [46]. The effect of RCA treatment in relation to strength improvement was observed maximum for MC-RAC specimens and minimum for AC-RAC specimens. Moreover, Figure 2 also shows higher stress strain curves for the acetic acid treated RCA mixes (A-RAC, AR-RAC and AC-RAC) as compared to RAC mix. Maximum improvement in stress strain behaviour was observed for the AR-RAC specimens, reflecting the positive impact of acetic acid immersion with rubbing treatment in increasing energy dissipation capacity of RAC.

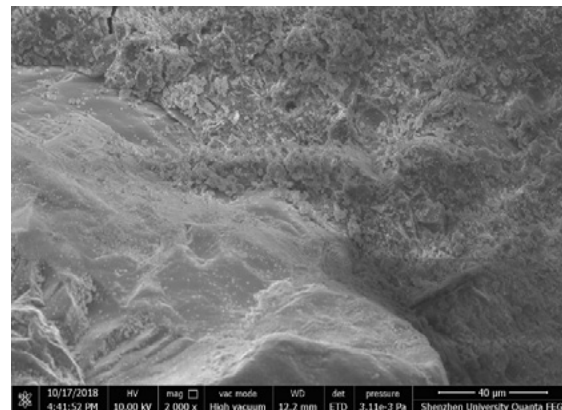
Figure 3 shows the microstructure of RAC, AR-RAC and MC-RAC after the compression test. In case of RAC, porous microstructure with weak bond between mortar paste and RCA was observed. Large cracks were also observed in RAC, mainly on the interface of mortar paste and RCA. In case of AR-RAC and MC-RAC, dense microstructure was observed. Bond between mortar paste and treated RCA was also observed better than untreated RAC.



3a)



3b)



3c)

Figure 3: Microstructure of a) RAC specimens b) AR-RAC specimens, and c) MC-RAC specimens.

4. Conclusions

Following conclusions can be drawn from this study

1. Physical properties of treated RCA (i.e., water absorption, crushing strength and bulk density) were improved as compared to untreated RCA.
2. Rise in split tensile strength of RAC was observed for treated RCA as compared to untreated ones. However, 28 days split tensile strengths of AR-RAC and MC-RAC were observed 93% and 90% of split tensile strength of NAC, respectively.

3. Flexural strength was also improved due to RCA treatment. Flexural strengths of AR-RAC and MC-RAC were observed 94% and 75% of flexural strength of NAC, respectively.
4. Improved stress-strain behaviour i.e., increase in compressive strength, elastic modulus and energy dissipation capacity was observed for RAC with treated RCA as compared to RAC with untreated RCA. The stress-strain behaviour of AR-RAC and MC-RAC was observed very close to the stress-strain curves of NAC reflecting the positive impact of RCA treatment techniques such as acetic acid immersion with mechanical rubbing and modified carbonation on the performance of RAC.
5. Although increase in compressive strength and modulus of elasticity of RAC was observed for treated RCA as compared to untreated RCA. Compressive strength and modulus of elasticity of RAC with treated RCA were observed lower than NAC. However, compressive strengths of AR-RAC and MC-RAC were observed 85% and 87% of compressive strengths of NAC, respectively. Similarly, values of elastic modulus of AR-RAC and MC-RAC were observed 83% and 82% of elastic modulus of NAC, respectively. Therefore, treatment techniques such as, acetic acid immersion with mechanical rubbing and modified carbonation may be considered helpful to improve the properties of RAC resulting into eco-friendly and sustainable construction.

5. Acknowledgment

Scholarships provided by RMIT to the student authors are highly acknowledged. Moreover, authors are also thankful to the College of Civil Engineering, Shenzhen University for the financial and technical support throughout the experimental program.

6. References

- [1] J. Xiao, W. Li, C. Poon, Recent studies on mechanical properties of recycled aggregate concrete in China—A review, *Science China Technological Sciences* 55(6) (2012) 1463-1480.
- [2] N.D. Oikonomou, Recycled concrete aggregates, *Cement and Concrete Composites* 27(2) (2005) 315-318.
- [3] Productivity Commission, Waste management: productivity commission draft report., Australian Government, Canberra, Australia, 2006.
- [4] D. Xuan, B. Zhan, C.S. Poon, Assessment of mechanical properties of concrete incorporating carbonated recycled concrete aggregates, *Cement and Concrete Composites* 65 (2016) 67-74.
- [5] M.J. Munir, Y.-F. Wu, S.M.S. Kazmi, I. Patnaikuni, Y. Zhou, F. Xing, Stress-strain behavior of spirally confined recycled aggregate concrete: An approach towards sustainable design, *Resources, Conservation and Recycling* 146 (2019) 127-139.
- [6] I.F. Sáez del Bosque, W. Zhu, T. Howind, A. Matías, M.I. Sánchez de Rojas, C. Medina, Properties of interfacial transition zones (ITZs) in concrete containing recycled mixed aggregate, *Cement and Concrete Composites* 81 (2017) 25-34.
- [7] J. Zhang, C. Shi, Y. Li, X. Pan, C.-S. Poon, Z. Xie, Performance Enhancement of Recycled Concrete Aggregates through Carbonation, *Journal of Materials in Civil Engineering* 27(11) (2015) 04015029.
- [8] J. Xiao, W. Li, Y. Fan, X. Huang, An overview of study on recycled aggregate concrete in China (1996–2011), *Construction and Building Materials* 31 (2012) 364-383.

-
- [9] S.C. Kou, C.S. Poon, D. Chan, Influence of Fly Ash as Cement Replacement on the Properties of Recycled Aggregate Concrete, *Journal of Materials in Civil Engineering* 19(9) (2007) 709-717.
- [10] Y. Kim, A. Hanif, S.M.S. Kazmi, M.J. Munir, C. Park, Properties enhancement of recycled aggregate concrete through pretreatment of coarse aggregates – Comparative assessment of assorted techniques, *Journal of Cleaner Production* 191 (2018) 339-349.
- [11] R.S. Ravindrarajah, C.T. Tam, Properties of concrete made with crushed concrete as coarse aggregate, *Magazine of Concrete Research* 37(130) (1985) 29-38.
- [12] N. Kisku, H. Joshi, M. Ansari, S.K. Panda, S. Nayak, S.C. Dutta, A critical review and assessment for usage of recycled aggregate as sustainable construction material, *Construction and Building Materials* 131(Supplement C) (2017) 721-740.
- [13] S.-C. Kou, C.-S. Poon, Long-term mechanical and durability properties of recycled aggregate concrete prepared with the incorporation of fly ash, *Cement and Concrete Composites* 37(Supplement C) (2013) 12-19.
- [14] S.M.S. Kazmi, M.J. Munir, Y.-F. Wu, I. Patnaikuni, Effect of macro-synthetic fibers on the fracture energy and mechanical behavior of recycled aggregate concrete, *Construction and Building Materials* 189 (2018) 857-868.
- [15] S.M.S. Kazmi, M.J. Munir, Y.-F. Wu, I. Patnaikuni, Y. Zhou, F. Xing, Axial stress-strain behavior of macro-synthetic fiber reinforced recycled aggregate concrete, *Cement and Concrete Composites* 97 (2019) 341-356.
- [16] D. Xuan, B. Zhan, C.S. Poon, Durability of recycled aggregate concrete prepared with carbonated recycled concrete aggregates, *Cement and Concrete Composites* 84 (2017) 214-221.
- [17] V.W.Y. Tam, C.M. Tam, Diversifying two-stage mixing approach (TSMA) for recycled aggregate concrete: TSMA_s and TSMA_{sc}, *Construction and Building Materials* 22(10) (2008) 2068-2077.
- [18] V.W.Y. Tam, C.M. Tam, Y. Wang, Optimization on proportion for recycled aggregate in concrete using two-stage mixing approach, *Construction and Building Materials* 21(10) (2007) 1928-1939.
- [19] V.W.-Y. Tam, X.-F. Gao, C.M. Tam, Comparing performance of modified two-stage mixing approach for producing recycled aggregate concrete, *Magazine of Concrete Research* 58(7) (2006) 477-484.
- [20] J. Li, H. Xiao, Y. Zhou, Influence of coating recycled aggregate surface with pozzolanic powder on properties of recycled aggregate concrete, *Construction and Building Materials* 23(3) (2009) 1287-1291.
- [21] A. Katz, Properties of concrete made with recycled aggregate from partially hydrated old concrete, *Cement and Concrete Research* 33(5) (2003) 703-711.
- [22] H. Choi, H. Choi, M. Lim, M. Inoue, R. Kitagaki, T. Noguchi, Evaluation on the Mechanical Performance of Low-Quality Recycled Aggregate Through Interface Enhancement Between Cement Matrix and Coarse Aggregate by Surface Modification Technology, *International Journal of Concrete Structures and Materials* 10(1) (2016) 87-97.
- [23] S.-C. Kou, C.-S. Poon, M. Etxeberria, Influence of recycled aggregates on long term mechanical properties and pore size distribution of concrete, *Cement and Concrete Composites* 33(2) (2011) 286-291.
- [24] B.B. Mukharjee, S.V. Barai, Influence of Nano-Silica on the properties of recycled aggregate concrete, *Construction and Building Materials* 55(Supplement C) (2014) 29-37.

-
- [25] O. Gjorv, Sakai, K., Concrete Technology for a Sustainable Development in the 21st Century, CRC Press, London, 2000.
- [26] K. Bru, S. Touzé, F. Bourgeois, N. Lippiatt, Y. Ménard, Assessment of a microwave-assisted recycling process for the recovery of high-quality aggregates from concrete waste, *International Journal of Mineral Processing* 126 (2014) 90-98.
- [27] H. Tateyashiki, Properties of concrete with high quality recycled aggregate by heat and rubbing method, *Journal of Critical Incidents* 23(2) 61.
- [28] V.W.Y. Tam, C.M. Tam, K.N. Le, Removal of cement mortar remains from recycled aggregate using pre-soaking approaches, *Resources, Conservation and Recycling* 50(1) (2007) 82-101.
- [29] A. Katz, Treatments for the Improvement of Recycled Aggregate, *Journal of Materials in Civil Engineering* 16(6) (2004) 597-603.
- [30] A.M. Grabiec, J. Klama, D. Zawal, D. Krupa, Modification of recycled concrete aggregate by calcium carbonate biodeposition, *Construction and Building Materials* 34 (2012) 145-150.
- [31] L. Wang, J. Wang, X. Qian, P. Chen, Y. Xu, J. Guo, An environmentally friendly method to improve the quality of recycled concrete aggregates, *Construction and Building Materials* 144 (2017) 432-441.
- [32] P. Chen, J. Wang, L. Wang, Y. Xu, X. Qian, H. Ma, Producing vaterite by CO₂ sequestration in the waste solution of chemical treatment of recycled concrete aggregates, *Journal of Cleaner Production* 149 (2017) 735-742.
- [33] M.C.S. Nepomuceno, R.A.S. Isidoro, J.P.G. Catarino, Mechanical performance evaluation of concrete made with recycled ceramic coarse aggregates from industrial brick waste, *Construction and Building Materials* 165 (2018) 284-294.
- [34] B.J. Zhan, D.X. Xuan, C.S. Poon, Enhancement of recycled aggregate properties by accelerated CO₂ curing coupled with limewater soaking process, *Cement and Concrete Composites* 89 (2018) 230-237.
- [35] ASTM C127, Standard test method for relative density (specific gravity) and absorption of coarse aggregate, American Society for Testing and Materials, West Conshohocken, PA,, 2015.
- [36] BS 812-110, Testing aggregates. Methods for determination of aggregate crushing value (ACV), British Standards Institution, London, UK,, 2014.
- [37] A. Abbas, G. Fathifazl, O. Burkan Isgor, A. Razaqpur, B. Fournier, S. Foo, Proposed Method for Determining the Residual Mortar Content of Recycled Concrete Aggregates, *Journal of ASTM International* 5(1) (2008) 1-12.
- [38] ASTM C192 / C192M - 16a, Standard Practice for Making and Curing Concrete Test Specimens in the Laboratory, American Society of Testing and Materials, West Conshohocken, PA, 2016.
- [39] ASTM C496 / C496M-17, Standard Test Method for Splitting Tensile Strength of Cylindrical Concrete Specimens, American Society for Testing and Materials, West Conshohocken, PA,, 2017.
- [40] ASTM C39 / C39M-18, Standard Test Method for Compressive Strength of Cylindrical Concrete Specimens, American Society for Testing and Materials, West Conshohocken, PA,, 2018.
- [41] ASTM C293 / C293M-16, Standard Test Method for Flexural Strength of Concrete (Using Simple Beam With Center-Point Loading), American Society for Testing and Materials, West Conshohocken, PA,,

2016.

[42] M. Behera, S.K. Bhattacharyya, A.K. Minocha, R. Deoliya, S. Maiti, Recycled aggregate from C&D waste & its use in concrete – A breakthrough towards sustainability in construction sector: A review, *Construction and Building Materials* 68 (2014) 501-516.

[43] J. Xiao, J. Li, C. Zhang, Mechanical properties of recycled aggregate concrete under uniaxial loading, *Cement and Concrete Research* 35(6) (2005) 1187-1194.

[44] M.B. de Oliveira, E. Vazquez, The influence of retained moisture in aggregates from recycling on the properties of new hardened concrete, *Waste Management* 16(1) (1996) 113-117.

[45] J. Xiao, K. Zhang, A. Akbarnezhad, Variability of stress-strain relationship for recycled aggregate concrete under uniaxial compression loading, *Journal of Cleaner Production* 181 (2018) 753-771.

[46] S. Luo, S. Ye, J. Xiao, J. Zheng, Y. Zhu, Carbonated recycled coarse aggregate and uniaxial compressive stress-strain relation of recycled aggregate concrete, *Construction and Building Materials* 188 (2018) 956-965.

Effects of Recycled Aggregates on Concrete Compressive Strength

N. Siddiqui¹, M. Nasir¹, I. Nasir¹, D. Memon²

¹ Department of Civil Engineering, Sir Syed University of Engineering and Technology, Karachi.

²Magnel Laboratory for Concrete Research, Department of Structural Engineering, Faculty of Engineering, Ghent University, Belgium

Abstract

Sustainable construction is the major concern for environment and different techniques are being adapted to foster the goal of sustainability. This study aims to investigate the performance of crushed tested concrete samples obtained from the concrete research institutions. The concrete samples are crushed to achieve the aggregates that are used to prepare new samples and tested to examine compressive strength. The compressive strength of samples prepared with normal aggregates concrete (NAC) are compared to compressive strength of recycle aggregates (RAC) to create a conclusion. It was examined from the experimental results that recycle aggregates have the potential to replace the normal aggregates.

Keywords: recycle aggregates, tested aggregates, compressive strength.

1. Introduction

Globally, the demand of aggregates has increased up to 26.8 billion tons per year [1]. The rapid use of natural aggregates is a universal matter of concern; thus intense pressure is coming on the construction industry to propose a sustainable solution without compromising the performance of concrete. A large quantity of construction waste is generated by demolishing the structures or the damage caused to material while manufacturing. This waste mostly ends up being discarded in landfills. The use of waste concrete as recycled aggregates in new concrete is beneficial from the view point of sustainability and resources reservation. In this regard, the study for the utilization of various recycled building materials is promoted.

A large number of experimental studies have been carried out in recent times to explore the procedures, uses and properties of recycling of construction waste and recycled material. In past many researchers have investigated the effect of recycled coarse aggregate on concrete compressive strength.

Wang et. al. (2011) carried out an experimental study to investigate the effect of recycled coarse aggregate on concrete compressive strength. The experiment was carried out with 30 concrete mix proportions to achieve the compressive strength in the range of 20 to 60 MPa. The cubes were casted from natural coarse aggregate concrete as well as recycled coarse aggregate concrete. The 28-days results show that the concrete strength is affected by the strength of different types of recycled aggregates used. The effect of type of aggregate was more obvious for high strength concrete as compared to normal weight concrete [2]. Another experimental study undertaken by Khan et. al. (2018) used a concrete mix of 1:2:4 using water-cement ratio of 0.4 and 0.5 and varying percentages of recycled coarse aggregate [3]. Azzawi (2016) tested recycle aggregate concrete made from crushed tile and concluded that the tensile strength, compressive strength and elastic modulus are affected with the use of recycled aggregate replacing more than 25% of natural coarse aggregate [4].

2. Experimental setup

2.1 Preliminary tests for aggregates

This study targets the comparison of compressive strength of concrete made with natural coarse aggregate and recycled coarse aggregate with varying water-cement ratio of 0.50, 0.60 and 0.70 at different mix proportions i.e. 1:2:4 and 1:4:8. To examine the behaviour of recycle aggregate concrete (RAC), following tests were conducted to observe the characteristics of aggregates, both natural and recycled, before using it in concrete:

- (a) Water-absorption test
- (b) Apparent specific gravity
- (c) SSD specific gravity
- (d) Bulk specific gravity

The detailed results of preliminary tests are shown below in Fig. 1. ASTM 127-93 prescribes the procedure to measure and calculate the water absorption, apparent specific gravity and bulk density. As summarized in the standard, the procedure is followed as a sample of aggregate is washed, drained and placed in a wire basket and immersed in water for 24 hours. The sample is weighed while submerged in water. The aggregate is then removed from water after 24 hours and transferred to an absorbent cloth to surface dry. This surface dried sample is then weighed. After that, the sample is placed in oven to dry and then weighed after 24 hours. With the relationships of mass and weight the specific gravity and absorption are calculated [5].

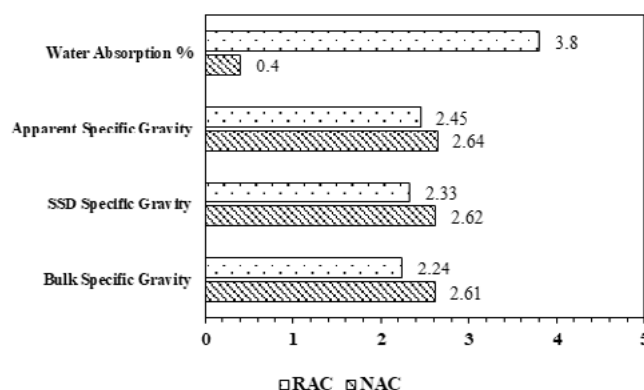


Figure 1: Different test results for NCA and RCA

The specific gravity for natural aggregates ranges from 2.5 to 3.0 and for recycled aggregates it ranges from 2.3 to 2.6. The water absorption capacity for natural aggregates is 0.1% to 2.0% and for recycled aggregates it is 3% to 12%. It was noted that recycled aggregate showed higher water absorption capacity as compared to natural aggregate but it lies within the range specified for recycled aggregate. The apparent specific gravity, SSD specific gravity and bulk specific gravity tend to decrease for the recycled aggregate as compared to the natural aggregate.

2.2 Concrete mix

The concrete mix design is the critical parameter in the success of the recycle aggregate concrete. The calculation of the mix design consists of ordinary Portland cement, coarse aggregate, fine aggregate and water. The Ordinary Portland cement (Type I) used in this study conforms to BS-EN 197-1:2000 and its chemical composition and physical properties are shown below in Table 1. Two kinds of concrete mixes were used i.e. 1:2:4 at water-cement ratio 50%, 60% and 70% whereas the concrete mix of ratio 1:4:8

with the water-cement ratio 70% was used. Trial concrete mixes were carried out at 50% and 60% at 1:4:8 concrete ratio but were not suitable as concrete started to crumble and adequate mixing was not possible.

Table 1: Chemical composition and physical properties of OPC used (Manufacturer's specifications, only MgO and SO₃ specification available)

Chemical Composition of OPC		Physical Properties	
MgO	1.50	Fineness (cm ² /gm)	2800
SO ₃	2.50	Initial setting time(min)	120
Insoluble residue I.R.	0.30	Final setting time (hrs)	3.25
Loss on ignition L.O.I.	1.65	Soundness (mm)	0.50
Lime Saturation Factor L.S.F.	0.91	Compressive strength 28-d (N/mm ²)	45.0

The ratio of concrete mix remained same for both natural coarse aggregate (NCA) and recycled coarse aggregate (RCA). The fine aggregate passed through #4 sieve and the fineness modulus of 2.8 was calculated. Whereas, natural coarse aggregate was used with maximum size of 10 mm. The recycled aggregates were fetched from the debris located at the reinforced concrete lab at Sir Syed University of Engineering and Technology, Karachi. The left-over aggregates are around one to two years old. Before using the recycled aggregate, the aggregates were crushed into approximate 15 mm size and were allowed to sieve through 19 mm and retained at 9.5 mm. The detail of the concrete mixes is shown in Table 2 and Table 3:

Table 2: Mix proportion at 1:2:4

Type of aggregate (concrete ratio)	Mix Proportions (kg)			Water/ cement ratio
	Cement	Fine aggregate	Coarse aggregate	
NAC (1:2:4)	1.34	2.68	5.36	0.50
	1.34	2.68	5.36	0.60
	1.34	2.68	5.36	0.70
RAC (1:2:4)	1.34	2.68	5.36	0.50
	1.34	2.68	5.36	0.60
	1.34	2.68	5.36	0.70

Table 3: Mix proportion at 1:4:8 ratio

Type of aggregate (concrete ratio)	Mix Proportions (kg)			Water/ cement ratio
	Cement	Fine aggregate	Coarse aggregate	
NAC (1:4:8)	0.725	2.90	5.80	0.70
RAC (1:4:8)	0.725	2.90	5.80	0.70

2.3 Workability test

The workability of the freshly made concrete of all the mixes was also tested according to ASTM C143-90a. The slump test was used in order to test the consistency and adequacy of w/c ratio of the concrete mixes. The results indicated low workability for all the concrete mixes which was suitable for road construction. The test results are shown below in Figure 2. There was no slump observed at w/c ratio of 0.50 for 1:2:4 concrete mix, both using natural coarse aggregate and recycled coarse aggregate.

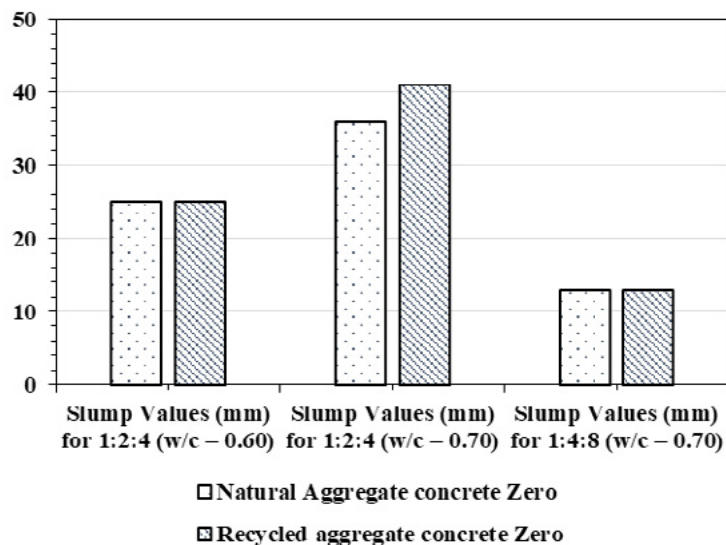


Figure 2: Slump test results for concrete mixes (1:2:4 and 1:4:8) at varying w/c ratios

3. Experimental program

With the calculated mix, 32 cubes of size 150 mm x 150 mm x 150 mm were casted according to BS 1881: PART 108: 1983. The concrete cubes were casted in total in which 24 cubes were prepared at mix design ratio (1:2:4 at w/c of 0.50, 0.60 and 0.70) and 8 cubes were prepared at mix design ratio (1:4:8 at 0.70 w/c). Similarly, total 32 samples of reinforced concrete beams of size 500 mm x 100 mm x 100 mm were casted, out of which 24 beams of concrete ratio 1:2:4 at w/c of 0.50, 0.60 and 0.70 and 8 beams were of concrete ratio 1:4:8 at w/c of 0.70. The beams were provided with four rebar of #4 size (12.7mm nominal diameter). The specimens were un-moulded after 24 hours and kept for curing under standard conditions as prescribed by ASTM C192-90a, for 28 days. The cubes were tested under compression on 28 days using Compression Testing Machine (CTM) as per the procedure described in ASTM C36-86.

There are two loading methods used for testing the flexural strength of a specimen, which are third-point loading and centre point loading. In this study the beams were tested under centre-point loading as shown in Figure 3. The specimen was tested on Universal Testing Machine (UTM) and loaded continuously with a constant load rate until failure.



Figure 3: Flexural testing of RCA beam specimens on UTM

4. Results

Due to limited testing facilities, this study is only examined for the compressive strength of concrete cubes and flexural strength of reinforced concrete beams.

4.1 Compressive strength of concrete cubes

Table 4 shows the results for the cube specimens tested under compression. The results indicate that the test cube achieved substantial strength at w/c ratio of 0.70 when used with the concrete mix proportion of 1:2:4 and it tends to increase for the mix proportion of 1:4:8. The lower w/c ratio makes proper mixing harder. Also, the recycled aggregate was not wet enough and it absorbed more water than required thus leaving less water for the hydration process to be completed and gain strength. The compressive strength of recycled aggregate concrete cubes decreases by 35% at w/c ratio of 0.6 for M15 concrete and it increases by 27% for M7.5 concrete.

Table 4: Average compressive strength of control cubes (NAC) and test cubes (RAC) at 28 days

Concrete Mix	W/C Ratio	Average Compressive Strength MPa (Ksi)	
		Control Cubes (NAC)	Test Cube (RAC)
1:2:4	0.50	24 (3.47)	2.34 (0.34)
1:2:4	0.60	19.30 (2.80)	12.82 (1.86)
1:2:4	0.70	14.50 (2.10)	13.20 (1.91)
1:4:8	0.70	0.41 (0.06)	0.55 (0.08)

4.2 Flexural strength of reinforced concrete beams

Table 5 shows the results for the beam specimens' flexural strength. The results show that at higher w/c ratio the flexural strength of beams casted with NCA and RCA shows good agreement and very less difference can be seen, however, at lower w/c ratios the flexural strength of NCA beam specimen was at least 50% higher as compared to RCA beam specimens.

Table 5: Flexural strength of control beams (NAC) and test beams (RAC) at 28 days

Concrete Mix	W/C Ratio	Flexural Strength MPa (Ksi)	
		Control Beams (NAC)	Test Beams (RAC)
1:2:4	0.50	26.33 (3.82)	10.06 (1.46)
1:2:4	0.60	29.78 (4.32)	19.37 (2.81)
1:2:4	0.70	25.78 (3.74)	23.16 (3.36)
1:4:8	0.70	8.75 (1.27)	8.06 (1.17)

5. Conclusions

The experiments carried out in this study conclude the following:

- For recycled aggregate concrete, the 28-days compressive strength can be obtained close to that of natural aggregate concrete at water-cement ratio of 0.7 (both 1:2:4 and 1:4:8), whereas their strength was noted to decrease than the control concrete for the same mix proportions at water-cement ratio of 0.50 and 0.60.
- It is suggested that the recycled aggregates must be used in wet condition to yield better result for compressive strength.
- The cracking of the recycled concrete beams was comparable to the typical concrete beams, with a

linear elastic behaviour before the first flexure cracks occurred, and then the main steel yielded, and eventually the concrete crushed.

- The beams without shear reinforcement fails at a much lower value of cracking load. This happened due to the fact that the weakest link in recycled concrete is the mortar adhered to the recycled aggregate and it fails more rapidly as compared to natural aggregate concrete.
- Aggregate interlock and bond between concrete and the reinforcement are mechanisms that seem to work correctly in reinforced concrete beams made with recycled coarse aggregate.

Further experiments are advised to understand more about the behaviour of concrete prepared with recycle aggregates.

6. Acknowledgments

The authors would like to thank Sir Syed University of Engineering and Technology, Karachi for providing resources and Higher Education Commission, Pakistan for the financial support. The authors are also highly grateful to undergraduate students Muhammad Ahsan Siddiqui, Hassan Raza, Muhammad Ismail and Fahad Ali of Civil Engineering department, Sir Syed University of Engineering & Technology for their contribution in this research.

7. References

- [1] Ashraf M. Wagih, H. Z. E.-K., Magda Ebid, Samir H. Okba (2013), Recycled construction and demolition waste as aggregate for structural concrete.” HBRC Journal: 193-200.
- [2] Wang Z., W. L., Cui Z., Zhou M. (2011), “Effect of recycled coarse aggregate on concrete compressive strength.” Trans. Tianjin University **17**: 229-234.
- [3] Khan A. R., F. S., Ayub T. (2018), Mechanical properties of concrete made up from recycled coarse aggregates. 14th ASEC Conference in Jordan. Jordan University of Science & Technology.
- [4] Al-Azzawi, A. A. (2016), “Mechanical properties of recycled aggregate concrete.” ARP Journal of Engineering and Applied Sciences **11**(19): 1-6.
- [5] ASTM, A. (2004 & 1993), Standard Method of Test for Specific Gravity and Absorption of Coarse Aggregate.

Increasing the reactivity of modified ferro silicate slag by chemical adaptation of the production process

P.P. Sivakumar^{1,3}, L. Arnout⁴, T. Lapauw⁴, E. Gruyaert², N. De Belie¹, S. Matthys¹

¹ Magnel Laboratory for concrete Research, Department of Structural Engineering, Ghent University, Tech Lane Ghent Science Park, Campus A, Technologiepark Zwijnaarde 60, B-9052 Ghent, Belgium.

² Technology Cluster Construction, Structural Mechanics and Building Materials, Department of Civil Engineering, KU Leuven, Gebroeders De Smetstraat 1, B-9000 Ghent, Belgium.

³ SIM vzw, Technologiepark 48, Zwijnaarde B-9052 Ghent, Belgium.

⁴ Resourcefull BVBA, Dekenstraat 10, B-3000 Leuven, Belgium.

Abstract

Modified Ferro Silicate (MFS) slag can be used as an alternative Supplementary Cementitious Material (SCM) to make concrete sustainable and to enhance the circular economy. Given their pozzolanic characteristics, these MFS slags can be used as SCM. However, due to the low CaO content of the MFS slag, they have slower reaction and dissolution rate than Ca rich by-products such as Ground Granulated Blast Furnace slags (GGBFS). Increasing latent hydraulic properties of the slag could potentially also increase the overall reactivity of the slag. In this respect, the objective was set to increase the CaO content of the MFS slag, by addition of CaCO₃ during its fuming process. In order to investigate the feasibility, at first, lab scale tests were performed and reported in this paper. Currently available MFS slag was remelted and chemically adapted at 1220 ± 10 °C. Two mixes were synthesized in which respectively 10 and 20 wt.% of CaCO₃ was added to the MFS slag. After melting the slag in a reducing atmosphere, it was water quenched in order to obtain an altered slag with a high glassy phase comparable to the current MFS slag. Chemical composition and mineralogy of CaCO₃ altered MFS slag was determined and its reactivity was assessed by the novel R³ reactivity assessment technique proposed by RILEM TC 267-TRM. Finally, altered MFS slag was compared with the unaltered MFS slag to study the influence of CaO content on the slag reactivity and dissolution. R³ Calorimetric analysis and CH consumption showed an enhanced dissolution rate for altered slag suggesting that incorporation of CaO in the system tends to improve the reactivity. Moreover, XRD and in-situ XRD analysis of the R³hydrated paste provided sufficient information that increasing the Ca content in the glassy phase tends to improve the dissolution of Fe which contributes to formation of Fe-AFt and stable Fe-Mc after 24 h.

Keywords: modified ferro silicate slag, thermal and chemical alteration, supplementary cementitious materials, reactivity assessment, compressive strength.

1. Introduction

In Europe, annual production of Copper (Cu) slag has reached approximately 5.56 million tons [1–3] and in Belgium, about 132,240 tons of secondary Cu slags are produced by Belgian recycling plants [4]. Management of the Cu slag is a huge burden to industries due to the increasing need for Cu metal on

the world market [5]. Cu slags can be usually categorized as 1) Cu slag generated from pyro metallurgical refining of Cu ore, 2) Secondary Cu slag synthesized from pyro metallurgical refining of metal scraps or recyclable materials. Depending on the production process of the Cu metal, the chemical composition and mineralogy of the obtained Cu slag may vary. In general, Cu slag is a siliceous rich glassy material due to the quick solidification by water quenching.

Beside management of Cu slag, more general problems for which an urgent solution is needed are global warming and resource shortage. One of the main contributors to global warming and resource shortage is the cement industry. To decrease the adverse effect on the environment, supplementary cementitious materials (SCM) based on Cu slag can be used for concrete. SCM based on Cu slags represent a viable alternative to widely used pozzolanic sources such as fly ash, silica fume, metakaolin etc., due to their silica rich glassy phase which potentially contributes to pozzolanic reaction [6]. By incorporating these Cu slags without any further modification as SCM in concrete, sustainability and circular economy can be easily achieved.

Different scientific publications have laid a foundation and showed Cu slags can be used as an SCM in combination with Ordinary portland cement (OPC) to make concrete [5–9]. In the work of Moura et al. [10], Cu slag was used as a pozzolanic SCM to make concrete with 20 wt.% replacement level (relative to the cement weight). Investigations such as compressive strength, splitting tensile strength, absorption rate by capillary suction and carbonation rate were carried out on the Cu slag replaced concrete. The authors finally concluded that addition of Cu slag to the concrete increased the concrete axial compressive and splitting tensile strength (after 28 days), decreased the absorption rate by capillary suction and the carbonation depth, thus improving the mechanical properties and durability. In addition, in the work of Al-Jabri et al. [11], concrete incorporating 13.5 wt.% of Cu slag and 1.5 wt.% of cement by-pass dust (CBPD) was tested for compressive strength, tensile strength, flexural strength and stress-strain behaviour at three water to binder ratios of 0.5, 0.6, 0.7. Findings of the authors showed an adverse effect on the early age mechanical properties due to the low CaO content (6 wt.%) in Cu slag compared with 63 wt.% in OPC.

In addition, Zain et al. [12] evaluated the influence of Cu slag on the hydration mechanism for OPC mortars with a replacement level of 0 wt.%, 2.5 wt.%, 5 wt.%, 7.5 wt.% and 10 wt.% (through thermogravimetric analysis and compressive strength). It was reported that addition of Cu slag induced no significant change in the hydration mechanism of OPC, however increased initial and final setting time were observed. Early age strength of the Cu slag mortar was generally lower than the reference mortar and the ideal replacement level for the optimum strength at (1, 3, 28, 90, 180 and 365 days) was 5 wt.% replacement level. In the work of Tixier et al. [8], effect and hydration of Cu slag in the presence of lime or cement were investigated. Three types of paste such as 1) 95 wt.% Cu slag + 5 wt.% hydrated lime (water/solid = 0.23) 2) 85 wt.% Cu slag + 10 wt.% micro silica + 5 wt.% hydrated lime (W/S = 0.23) 3) 85 wt.% OPC + 15 wt.% Cu slag (W/S = 0.23) were subjected to semi quantitative XRD and TGA/DTA. The authors stated that paste containing Cu slag and hydrated lime showed reduction in CH content after 28 days indicating the pozzolanic properties of the Cu slag.

Several authors provided information that incorporation of Cu slag as SCM showed induced dissolution rate of the system (clinker + Cu slag) leading to a slower reactive behaviour and strength contribution. This behaviour is usually observed due to the low content of CaO and increased SiO₂ content in the glassy phase of the granulated Cu slag making it to exhibit pozzolanic properties. When CaO content would be increased in the glass phase, Cu slag could be used as a SCM with improved reactivity. So, in this paper, the CaO content is increased in a proprietary Modified Ferro Silicate (MFS) slag (secondary Cu slag) by remelting the slag in the lab at 1220 ± 10 °C with addition of CaCO₃ and followed by water quenching to

obtain a CaO rich glassy slag. Reactivity of the altered MFS slag was examined by novel reactivity tests for supplementary cementitious materials, as proposed by RILEM TC 267-TRM [13]. Reactivity assessment is termed as R³ and R³ stands for rapid, reproducible and relevant. The assessment uses chemicals such as KOH, K₂SO₄, CaCO₃ and CH to activate the SCM by mimicking the alkaline pore solution created by OPC. Reactivity of the SCM can be calculated by investigating the CH consumption and heat release of the paste.

2. Methodology

2.1 Materials

Patented MFS slag from Metallo Belgium was used as the starting material for thermal processing. Two mixes were created including 90 wt.% MFS slag + 10 wt.% CaCO₃ (termed as “MFS-C1”) and 80 wt.% MFS slag + 20 wt.% CaCO₃ (termed as “MFS-C2”). Lab grade KOH, K₂SO₄, CaCO₃ and CH (less than 5 wt.% CaCO₃) were used to synthesise R³ model paste. Concentrated H₂SO₄, HF, H₃BO₃, Ce(SO₄)₂ were used as a reagent to determine the Fe²⁺ ions content in the MFS slag by titration method.

2.2 Methods

2.2.1 Synthesis, characterisation of MFS and altered MFS slag powder and mortar

Chemical composition of the MFS and altered MFS slags was determined by wavelength-dispersive X-ray fluorescence spectrometer. Mineralogy of the MFS slag and altered MFS slag were determined using X-ray diffraction. 10 wt.% internal standard (crystalline ZnO) was used for XRD preparation to quantify the diffractogram pattern using Rietveld analysis (3 iteration). Two samples containing 90 wt.% MFS slag + 10 wt.% CaCO₃ and 80 wt.% MFS slag + 20 wt.% CaCO₃ were fired separately for 1 h at a maximum temperature of 1220 ± 10 °C in a closed Fe crucible, using an induction furnace (Type TF 4000, Indutherm GmbH, Germany). The thermally remelted MFS slag was water quenched by tilting, to obtain a glassy phase content around 90 wt.%. The quenched raw material was milled in an attritor mill (Wiener 1S). Specific surface area and particle size distribution of the milled slag were assessed by the Blaine method (EN 196-6) and laser diffraction analysis respectively. The obtained particle size distribution and specific surface area of the slag powder is given in Table 1.

Table 1: Particle size distribution and specific surface area of the MFS and altered MFS slags

Component	Particle Size			Specific Surface Area (cm ² /g)
	d ₁₀ (μm)	d ₅₀ (μm)	d ₁₀₀ (μm)	
MFS	2.9	12.0	45.5	3800 ± 190
MFS-C1	3.5	15.4	49.4	3750 ± 190
MFS-C2	3.1	13.4	47.3	3800 ± 190

2.2.2 Fe²⁺ / Fe³⁺ measurement in the MFS slag

The titration method used to determine the quantitative presence of Fe²⁺ ions in the MFS slag was adopted from [14]. The setup includes a magnetic stirring plate, teflon beaker, argon atmosphere and reagents such as H₂SO₄, HF, H₃BO₃, Ferroine indicator, Ce(SO₄)₂ and H₂O. First, 0.1 g of MFS slag was added to 20 ml of demineralised H₂O in a teflon beaker closed by a lid. Next, 4 ml of 40 wt.% H₂SO₄ and 2 ml of 50 wt.% HF were also added to the suspension containing MFS slag and H₂O. In order to completely dissolve the MFS slag and to neutralise the HF, the mixing was carried out for 2 h using a magnetic stirrer. After 2 h, 2.5 g of H₂BO₃, 5 ml of 40 wt.% H₂SO₄, and 1 ml of 0.0001 M ferroine indicator were added to the solution containing MFS slag. Then the prepared solution was titrated against 0.01 M Ce(SO₄)₂ until the end point (orange red to colourless). From the titrated volume, FeO content of the MFS sample can be calculated

using equation (1) whereas M.W is the molecular weight (g/mol), vol is the volume (ml) and conc is the concentration (M). A scaling factor of 10 was used in the denominator to convert ml (volume of CeSO₄) and mass (g) into wt.%. Fe²⁺ ions content in the MFS slag was finally obtained from the ratio of FeO content obtained from titration and FeO content obtained from XRF (equation 2). Three iterations were carried out and the average value was mentioned as the final Fe²⁺ content.

$$\text{FeO content}_{\text{titration}} (\text{wt. \%}) = \frac{\text{M.W of FeO} \times \text{vol of CeSO}_4 \text{ titrated} \times \text{conc of CeSO}_4}{\text{mass of MFS slag} \times 10} \quad (1)$$

$$\frac{\text{Fe}^{2+}}{\Sigma \text{Fe}} (\text{wt. \%}) = \frac{\text{FeO content}_{\text{titration}}}{\text{FeO content}_{\text{XRF}}} \quad (2)$$

2.2.3 Reactivity assessment of MFS and altered MFS slag by R³

The mix design used to synthesise R³ modelled paste as published in [13] is given in Table 2. All components used in the preparation of paste were stored at 40°C for 24 h. After 24 h, the R³ model paste was synthesised using the mix design mentioned in Table 2 and cured at 40°C for 7 days. Hydration of the R³ paste is stopped through solvent exchange by placing it in isopropanol for 15 minutes. The hydration stopped sample was later stored in an oven at 40 °C till the experiments were carried out. CH consumption through TGA analysis was investigated in the hydration stopped 7 days old R³ paste as explained in [13]. Isothermal calorimetry at 40°C was used to measure the heat release during the hydration of the R³ paste over a period of 7 days [13]. An X-ray diffraction scan with a step size 0.020° and counting time of 2.5 s per step in a 2θ range from 5° to 15° was recorded on the hydration stopped 7 days old R³ samples to investigate the presence of crystalline binder phases. In-situ XRD measurement was carried out during the first 24 h on the R³ modelled paste with a step size 0.020° and counting time of 1.5 s per step in the 2θ range from 7° to 20°. In the experiment described, a total of 88 scans were recorded in the period of 24 h with an acceleration voltage and current of 40 kV and 40 mA respectively. The in-situ measurement was carried out at 40°C and during the measurement all samples were covered with kapton film (7.5 μm thickness) to prevent carbonation and dehydration of the sample.

Table 2: Mix design for R³ model paste

Component	SCM	CH	H ₂ O	KOH	K ₂ SO ₄	CaCO ₃
Mass (g)	11.11	33.33	60	0.24	1.2	5.56

3. Results and discussion

3.1 Characterisation of the MFS slags

The chemical composition in Table 3 shows that FeO and SiO₂ make up more than 80 wt.% of the MFS slag 3. On the contrary only ~ 4 wt.% of CaO is present in its initial content. MFS-C1 and MFS-C2 slags showed presence of nearly 10 wt.% and 15 wt.% CaO respectively (Table 3). Mineralogy of the MFS slag quantified through the Rietveld analysis shows that MFS slag possesses slightly higher content of glassy phase than MFS-C1 and MFS-C2 (Table 4). This is due to the fact that MFS slag was synthesised and quenched at the industrial scale whereas the MFS-C1 and MFS-C2 were remelted slags quenched at lab scale. The titration method used to determine the Fe²⁺ ions content showed presence of 90 wt.% Fe²⁺ ions (Table 5), suggesting the contribution of Fe in the hydration mechanism can also be due to Fe²⁺ as explained in section 3.2.3. Fe²⁺ content was determined only for MFS slag and not for altered MFS slag. However, Fe²⁺ content for altered MFS slag can also be reported as 90 wt.% assuming no change of oxidation state could occur during the thermal processing of (MFS slag) in a Fe crucible since MFS slag stays in equilibrium with the Fe crucible.

Table 3: Chemical composition of the MFS slags and altered MFS slags in wt.%

Component	FeO	SiO ₂	Al ₂ O ₃	CaO	Others
MFS	42.7	38.2	9.0	3.8	6.3
MFS-C1	40.9	36.7	8.5	9.4	4.5
MFS-C2	38.9	34.8	8.1	14.2	4

Table 4: Mineralogy of the MFS slag and altered MFS slags in wt.%

Phase	Glass	Spinel	Others
MFS	92.7 ± 0.8	6.7 ± 0.5	0.7 ± 0.2
MFS-C1	88.4 ± 1.2	9.2 ± 0.9	2.1 ± 0.8
MFS-C2	87.6 ± 1.6	9.9 ± 0.4	2.5 ± 0.5

Table 5: Fe²⁺ and Fe³⁺ content in the MFS slag in wt.%

Fe ²⁺ / ΣFe	Fe ³⁺ / ΣFe	Fe ²⁺ / Fe ³⁺	Fe ³⁺ / Fe ²⁺
90	10	9	0.11

3.2 Reactivity screening of MFS slags by R³ assessment

3.2.1 Calorimetric analysis

The evolution of heat during the hydration reaction of SCM is considered vital because it can give an idea on the reactivity of the SCMs. The isothermal calorimetry was used to assess the evolution of heat as per the RILEM TC 267-TRM protocol (Figure 1). From Figure 1a, three main exothermic peaks were observed (after discarding the initial 1 h) upon the activation of MFS slags with alkalis. From Figs. 1a and 1b, the following is observed:

1. Initial heat release (Fig. 1a) within the region of 1 to 2 h is possibly due to the rapid dissolution of the reactive ions such as SO₄²⁻, CO₃²⁻ present in the R³ modelled paste. As seen in Fig 1a), the heat release in this region for the MFS slag is subjected to a retardation effect possibly due to the presence of Zn ions in higher amount compared to MFS-C1 and MFS-C2.

In addition, heat release between 4 to 6 h is generally dissolution of ZnO and residual elements present in MFS slag. For instance [15] studied the hydration of OPC in the presence of Zn ions and stated that Zn²⁺ ions in presence of alkaline medium tend to form species such as Zn(OH)₃⁻, Zn(OH)₄²⁻ and/or Ca(Zn(OH)₃)₂·2H₂O resulting in an exothermic reaction and retarding effect. Moreover, altered MFS slags showed lower heat production rate in this region and retardation effect compared to the MFS, due to the presence of less ZnO (loss of ZnO during thermal processing). For instance [16-17] proposed a model and optimum process for continuous fuming of Zn bearing residues. It is stated in their findings that liquidus temperature of ZnO in the system of CaO-FeO-Fe₂O₃-PbO-SiO₂-ZnO ranges from 1100 to 1200 °C. With their findings, it can be assumed that ZnO can be lost during re-melting of the MFS slag at 1220 °C for 1 h.

Gradual increase in the heat release can be found in the region from 20 to 60 h (Fig. 1b). This peak possibly indicates the participation of Ca ions from slags to form binder phase such as C-S-(A)-H, AFt or AFm phases since this peak is more pronounced for “Ca” modified MFS slags. Moreover with increase in CaO content in the glass phase as for MFS-C2, an enhanced heat profile can be observed.

Although, the MFS-C1 and MFS-C2 showed enhanced heat release in the duration between 20 to 60 h, cumulative heat production (Figure 1c) for the MFS-C1 & MFS-C2 slag was only slightly higher than for

the MFS slag due to the increased heat profile of MFS slag between 4 to 8 h.

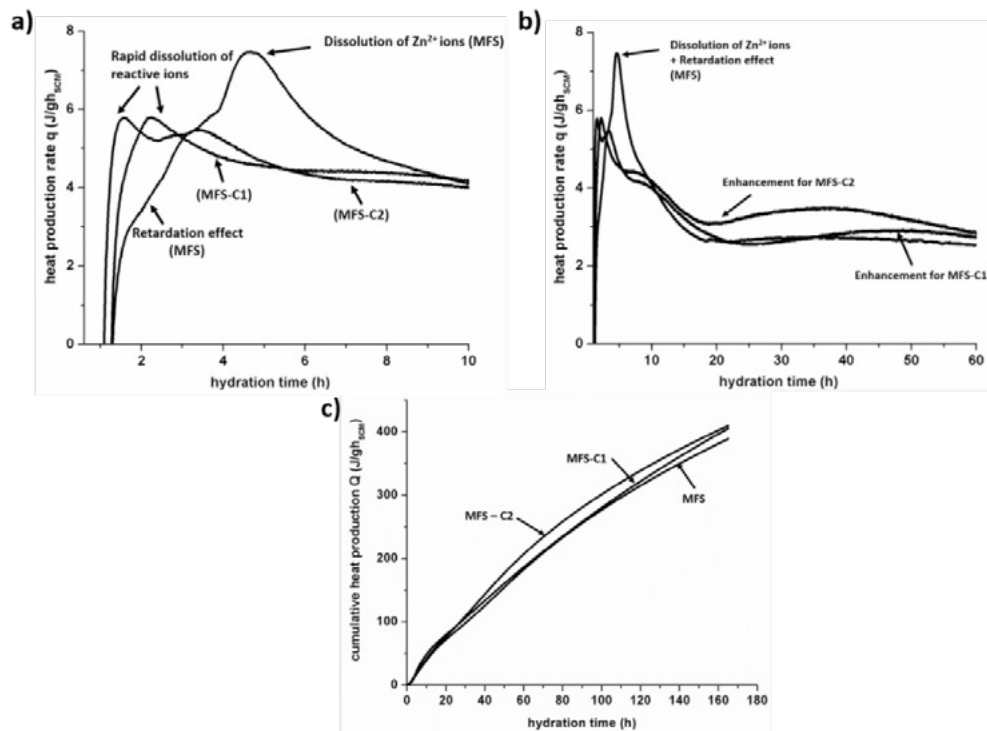


Figure 1 Analysis of the R³ model paste: a) calorimetric profile till 10 h - heat production rate (J/h.g_{SCM}) vs hydration time (h); b) calorimetric profile till 60 h - heat production rate (J/h.g_{SCM}) vs hydration time; c) calorimetric profile - cumulative heat production (J/h.g_{SCM}) vs hydration time

3.2.2 CH consumption

CH consumption calculated for the MFS slag along with MFS-C1 and MFS-C2 as per the RILEM TC 267-TRM protocol is shown in Fig. 2a. From this figure, it can be seen that Ca altered MFS slags have consumed higher amount of CH compared to the MFS slag, possibly due to pozzolanic reaction. This seems contrary to the initial expectation that presence of Ca in the system tends to improve the latent hydraulic properties by self-reacting with H₂O to produce C-S-H along with CH [18-19] which would imply decreased CH consumption for Ca rich MFS slags. However, the actual results can most likely be attributed to the enhanced slag dissolution rate which increases with the increasing CaO content in the system. Due to this reason, more CH is consumed by the Si²⁺ ions as a result of pozzolanic activity than for the MFS slag. For instance, [20] studied the early hydration mechanism of the alkalis with slag (GGBFS) with different sodium activators. The author finally concluded that early hydration of the slag in the presence of alkalis is more dominated by the Ca²⁺ dissolved from the slag than by the initial pH of the activators. Due to this fact, presence of Ca²⁺ ions in the glassy phase of MFS-C2 improves the dissolution rate and reactivity. In addition, [13] also published the results of a Round Robin Test (RRT) conducted on wide range of SCM as per R³ model. From their results, it is noted that calcium rich fly ash (Ca/Si = 0.3) showed comparable result in CH consumption as MFS-C2 (Ca/Si = 0.4). However, silica rich fly ash (Ca/Si = 0.01) showed decreased CH consumption compared to the MFS-C2. Thus supporting the hypothesis that increased Ca²⁺ could also enhance the pozzolanic reaction, thus consuming more CH.

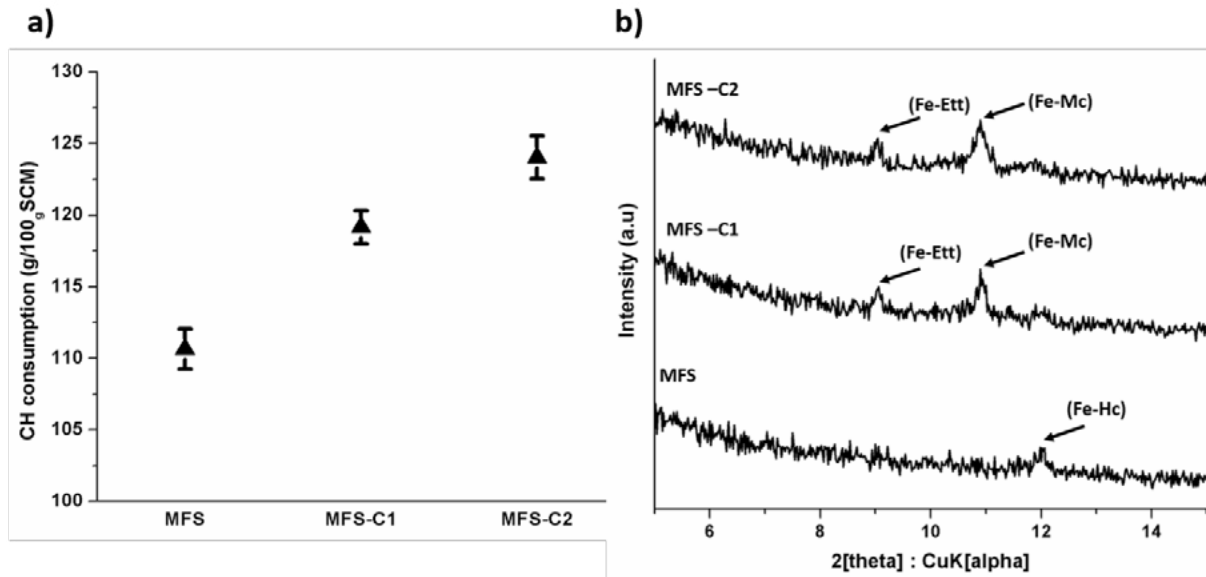


Figure 2 Analysis of the R³ modelled paste: a) CH consumption from TGA analysis; b) XRD analysis of the R³ modelled paste

3.2.3 XRD analysis

XRD analysis of the R³ hydrated paste at 7 days shows the possible formation of crystalline binder phases with the MFS slags (Fig 2b). The main hydration products as a result of pozzolanic reaction or latent hydraulic behaviour are usually C-(A)S-H, AFt and AFm. However, these reaction products strongly depend on the chemistry of the SCMs. Upon activation of the SCM, the glassy phase of SCM slowly dissolves and releases continuously Ca²⁺, Si²⁺, Al³⁺, and OH⁻ ions (depending on its mineralogy) into the solution, which precipitate as calcium silicate hydrates C-S-H, ettringite (AFt) and/or AFm phases. Commonly occurring AFm phases are Al-hemi carbonate (Al-Hc) and Al-mono carbonate (Al-Mc). Moreover, [21], [22] proposed that hemi carbonate is usually unstable with respect to mono carbonate in presence of CO₃²⁻.

MFS slag and Ca altered MFS slags contain about 40 wt.% FeO (Fe²⁺ = 90 wt.%, Fe³⁺ = 10 wt.%) in their glassy phase. Upon activation of the MFS slags, preferably Fe²⁺ ions can dissolve and form Fe containing AFm and/or AFt [23]. From XRD analysis, three distinct peaks in the range around the 2θ = 9–9.2°, 11–11.3° and 12–12.3° can be observed. It can be speculated that due to the presence of low Al content in the MFS slag these peaks around 2θ = 9.1°, 11° and 12.1° correspond to the Fe incorporating AFt phase, Fe-Mc and Fe-Hc respectively. For instance, [23–26] proposed that a main peak at 2θ = 9.13° corresponds to Fe-AFt, 2θ = 11° corresponds to Fe-Mc and 2θ = 12.1° corresponds to Fe-Hc. As also seen in Fig 2, the presence of the Fe-AFt and Fe-Mc are only noticed for the Ca altered slag, possibly proposing that increasing Ca content in the glassy phase tends to improve the dissolution of Fe which contributes in formation of Fe-AFt and stable Fe-Mc. In addition [27] proposed that Al³⁺ in the AFt phase can be substituted by Fe³⁺ as well as by Cr³⁺. Moreover, it is quite important to distinguish between the AFt/AFm phase incorporating Al and/or Fe due to the possible formation of solid solution series between Al-ettringite and Fe-ettringite [28]. Solid solution is a solid mixture containing minor component (in this case: Al³⁺) within the crystal lattice replacing the major component (in this case: Fe²⁺) [29–31]. For instance, due to the presence of Al³⁺ ions in the MFS slag and Ca rich MFS slag, Fe-AFt and Fe-Mc/Hc found from XRD analysis can also incorporate Al³⁺ ions. Further investigations through synchrotron X-ray absorption spectroscopy or Mössbauer spectroscopy are needed to verify the contribution of Fe in hydration and incorporation of Al³⁺ ions in the system.

3.2.4 In-situ XRD measurement of the R³ hydrated MFS slags

Investigation of the evolution and devolution of the crystalline phases for the first 24 h in the R³ modelled paste was carried out by in-situ XRD. In-situ XRD analysis of the R³ modelled paste did not show formation of a crystalline phase in the first 24 h (Figure 3). As discussed in the XRD analysis results, MFS slag and Ca altered MFS slag showed presence of AFt ($2\theta = 9.1^\circ$) and AFm ($2\theta = 11^\circ$ and 12.1°) phases after 7 days. However, no phase evolution can be seen from in-situ XRD stating that phases such as AFt and AFm tend to form only after 24 h in R³ modelled paste for MFS slag and Ca adapted MFS slags. With respect to the CH, no clear change in intensity can be observed around $2\theta = 18^\circ$ for all samples suggesting that CH could be consumed only after 24 h.

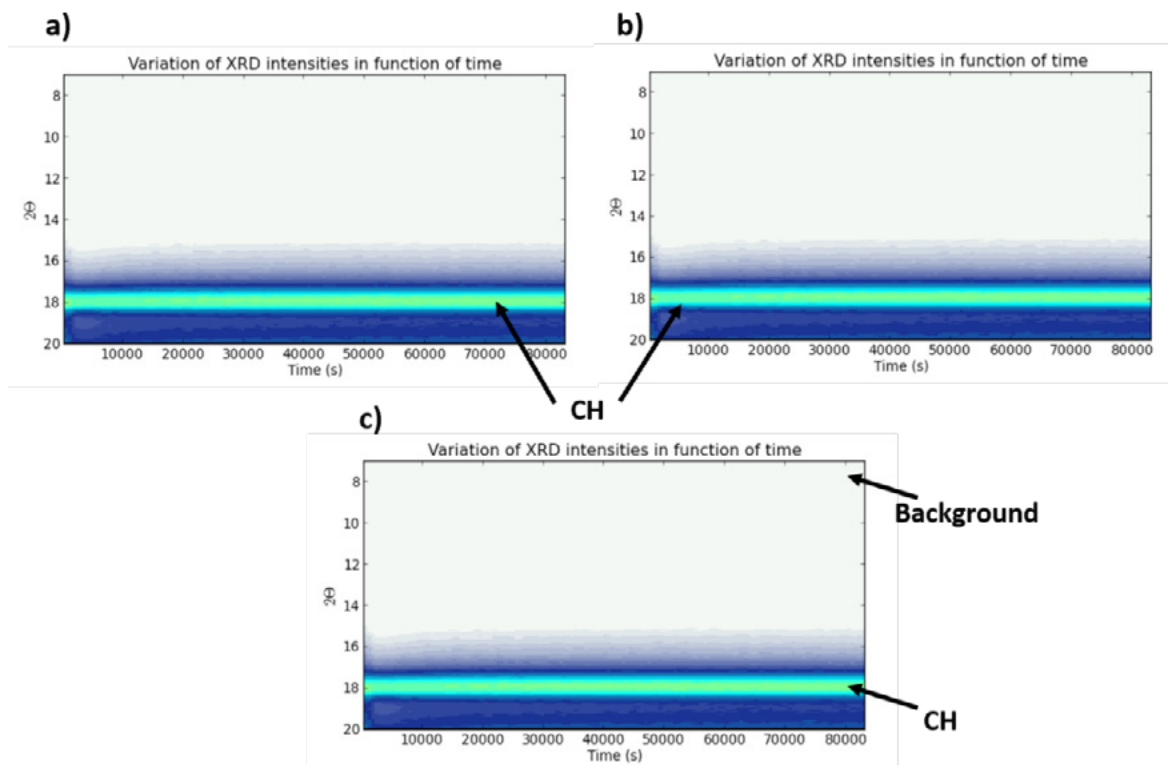


Figure 3 In-situ XRD analysis of the R³ modelled paste: a) MFS; b) MFS-C1; c) MFS-C2

4. Conclusions

In this work, the reactivity of proprietary MFS slag was improved by thermal and chemical alteration at $1220 \pm 10^\circ\text{C}$ for 1 h with CaCO_3 at lab scale. Reactivity assessment through RILEM TC 267-TRM showed that Ca rich MFS slag showed improved reactivity in both calorimetric analysis and CH consumption. The following can be stated as the main findings of this work:

1. As the heat release is attributed to the dissolution and formation of the phases, it was observed that MFS-C2 showed slightly increased heat production rate compared to MFS and MFS-C1 indicating that the presence of “Ca” in the system tends to increase the reactivity.
2. Enhanced slag dissolution was observed with increasing CaO in the MFS-C1 and MFS-C2. Thus, more CH was consumed by the Si^{2+} in the system as a result of pozzolanic activity compared to MFS slag.
3. Zn^{2+} ions from MFS slag in presence of alkaline medium tend to form species such as $\text{Zn}(\text{OH})_3^-$, $\text{Zn}(\text{OH})_4^{2-}$ and/or $\text{Ca}(\text{Zn}(\text{OH})_3)_2 \cdot 2\text{H}_2\text{O}$ resulting in a retardation effect and strong heat release. However, further investigation through pore solution analysis is needed to verify the dissolution and participation of Zn^{2+} ions from the MFS slag.

4. XRD analysis after 7 days showed that increasing the Ca content in the glassy phase tends to improve the dissolution of Fe which contributes to the formation of Fe-AFt and stable Fe-Mc. However, in-situ XRD used to investigate the reaction mechanism did not show formation of binder for the first 24 h and suggested that the Fe-AFt and stable Fe-Mc likely formed after 24 h.

To increase the reactivity of the current industrial MFS slag, a promising solution is addition of CaCO_3 to the production process. However, industrial implementation of this process may raise questions regarding the sustainability since addition of CaCO_3 to the production process also emits CO_2 which contributes to the global warming. So, as a next step, an industrial by-product with glassy phase containing mainly CaO in its chemical composition will be used as an additive for the thermal processing of the MFS slag. By using this by-product as a raw material for thermal processing, increased circular economy will be achieved.

5. Acknowledgment

The work has been performed in the Magnel Laboratory for Concrete Research, Department of Structural Engineering, Ghent University and financed by the SIM MARES program. The authors would like to thank the industrial partner Metallo Belgium for helping with the XRF analysis. The authors would also like to thank SCRiPTS research group, Department of Chemistry, Ghent University for helping with the TGA measurement. In addition, the authors wish to thank COCOON research group, Department of Solid State Sciences, Ghent University for helping with the XRD and in-situ XRD measurement.

6. Reference

- [1] B. Gorai and R. K. Jana, "Characteristics and utilisation of copper slag—a review," *Resour. Conserv. Recycl.*, 2003.
- [2] S. H. Chew and S. K. Bharati, "Use of Recycled Copper Slag in Cement-Treated Singapore Marine Clay," in *Advances in Environmental Geotechnics*, 2011.
- [3] S. K. Bharati and S. H. Chew, "Geotechnical Behavior of Recycled Copper Slag-Cement-Treated Singapore Marine Clay," *Geotech. Geol. Eng.*, 2016.
- [4] C. Hagelüken, "Recycling of Electronic Scrap At Umicore's Integrated Metals Smelter and Refinery," *World Metall. - Erzmetall*, 2005.
- [5] K. Murari, R. Siddique, and K. K. Jain, "Use of waste copper slag, a sustainable material," *Journal of Material Cycles and Waste Management*. 2014.
- [6] W. A. Moura, J. P. Gonçalves, and M. B. L. Lima, "Copper slag waste as a supplementary cementing material to concrete," *J. Mater. Sci.*, 2007.
- [7] K. S. Al-Jabri, R. A. Taha, A. Al-Hashmi, and A. S. Al-Harthy, "Effect of copper slag and cement by-pass dust addition on mechanical properties of concrete," *Constr. Build. Mater.*, 2006.
- [8] R. Tixier, R. Devaguptapu, and B. Mobasher, "The effect of copper slag on the hydration and mechanical properties of cementitious mixtures," *Cem. Concr. Res.*, 1997.
- [9] R. A. Taha, A. S. Alnuaimi, K. S. Al-Jabri, and A. S. Al-Harthy, "Evaluation of controlled low strength materials containing industrial by-products," *Build. Environ.*, vol. 42, no. 9, pp. 3366–3372, 2007.
- [10] W. A. Moura, J. P. Gonçalves, and M. B. L. Lima, "Copper slag waste as a supplementary cementing material to concrete," *J. Mater. Sci.*, vol. 42, no. 7, pp. 2226–2230, 2007.

- [11] K. S. Al-Jabri, R. A. Taha, A. Al-Hashmi, and A. S. Al-Harthy, "Effect of copper slag and cement by-pass dust addition on mechanical properties of concrete," *Constr. Build. Mater.*, vol. 20, no. 5, pp. 322–331, 2006.
- [12] M. F. M. Zain, M. N. Islam, S. S. Radin, and S. G. Yap, "Cement-based solidification for the safe disposal of blasted copper slag," *Cem. Concr. Compos.*, 2004.
- [13] X. Li *et al.*, "Reactivity tests for supplementary cementitious materials: RILEM TC 267-TRM phase 1," *Mater. Struct. Constr.*, 2018.
- [14] P. CLOSE, H. M. SHEPHERD, and C. H. DRUMMOND, "Determination of Several Valences of Iron, Arsenic and Antimony, and Selenium in Glass," *J. Am. Ceram. Soc.*, 1958.
- [15] M. A. Trezza, "Hydration study of ordinary portland cement in the presence of zinc ions," *Mater. Res.*, 2008.
- [16] K. Verscheure, M. Van Camp, B. Blanpain, P. Wollants, P. Hayes, and E. Jak, "Continuous fuming of zinc-bearing residues: Part I. Model development," *Metall. Mater. Trans. B Process Metall. Mater. Process. Sci.*, 2007.
- [17] K. Verscheure, M. Van Camp, B. Blanpain, P. Wollants, P. Hayes, and E. Jak, "Continuous fuming of zinc-bearing residues: Part II. The submerged-plasma zinc-fuming process," *Metall. Mater. Trans. B Process Metall. Mater. Process. Sci.*, 2007.
- [18] E. Özbay, M. Erdemir, and H. I. Durmuş, "Utilization and efficiency of ground granulated blast furnace slag on concrete properties - A review," *Construction and Building Materials*. 2016.
- [19] B. Pacewska, M. Nowacka, M. Aleknevičius, and V. Antonovič, "Early hydration of calcium aluminate cement blended with spent FCC catalyst at two temperatures," in *Procedia Engineering*, 2013.
- [20] C. Shi and R. L. Day, "A calorimetric study of early hydration of alkali-slag cements," *Cem. Concr. Res.*, 1995.
- [21] B. Lothenbach, G. Le Saout, E. Gallucci, and K. Scrivener, "Influence of limestone on the hydration of Portland cements," *Cem. Concr. Res.*, 2008.
- [22] H. J. Kuzel and H. Pöllmann, "Hydration of C3A in the presence of $\text{Ca}(\text{OH})_2$, $\text{CaSO}_4 \cdot 2\text{H}_2\text{O}$ and CaCO_3 ," *Cem. Concr. Res.*, 1991.
- [23] T. Matschei, B. Lothenbach, and F. P. Glasser, "The AFm phase in Portland cement," *Cem. Concr. Res.*, 2007.
- [24] B. Z. Dilnesa, E. Wieland, B. Lothenbach, R. Dähn, and K. L. Scrivener, "Fe-containing phases in hydrated cements," *Cem. Concr. Res.*, 2014.
- [25] B. Z. Dilnesa *et al.*, "Iron in carbonate containing AFm phases," *Cem. Concr. Res.*, 2011.
- [26] G. Möschner, B. Lothenbach, J. Rose, A. Ulrich, R. Figi, and R. Kretzschmar, "Solubility of Fe-ettringite ($\text{Ca}_6[\text{Fe}(\text{OH})_6]_2(\text{SO}_4)_3 \cdot 26\text{H}_2\text{O}$)," *Geochim. Cosmochim. Acta*, 2008.
- [27] V. Albino, R. Cioffi, M. Marroccoli, and L. Santoro, "Potential application of ettringite generating systems for hazardous waste stabilization," *J. Hazard. Mater.*, 1996.
- [28] G. Möschner, B. Lothenbach, F. Winnefeld, A. Ulrich, R. Figi, and R. Kretzschmar, "Solid solution

between Al-ettringite and Fe-ettringite ($\text{Ca}_6[\text{Al}_{1-x}\text{Fe}_x(\text{OH})_6]_2(\text{SO}_4)_3 \cdot 26\text{H}_2\text{O}$),” *Cem. Concr. Res.*, 2009.

[29] N. H. Perry *et al.*, “ Co_3O_4 – Co_2ZnO_4 spinels: The case for a solid solution,” *J. Solid State Chem.*, 2012.

[30] W. Schirmer, “Physical Chemistry of Surfaces,” *Zeitschrift für Phys. Chemie*, 2011.

[31] B. D. Hosterman, “Raman Spectroscopic Study of Solid Solution Spinel Oxides,” *UNLV Theses/Dissertations/Professional Pap. Pap. 1087*, 2011.

Sustainable Recycling of Concrete Fine from Demolition

R. Meglin¹, S. Gilg¹, D. Wlodarczak², S. Stürwald¹, S. Kytzia¹

¹ HSR University of applied sciences Rapperswil, Switzerland

² JURA Management AG, Switzerland

Abstract

In Switzerland, concrete fines from construction and demolition waste (C&DW) are usually down-cycled for low quality purposes. Therefore, companies have few incentives to improve the demolition process separating the coarse aggregates, sand and the hardened cement matrix. The use of concrete fines from demolition waste, however, could increase value added for companies if properly used in the cement and concrete production. These could be used either to replace part of the raw materials in clinker production or as supplementary cementitious materials (SCM's) reducing the clinker content in cement. Furthermore, they can also be used to replace virgin sand in the concrete production. All these alternative uses of concrete fines will effect CO₂-emissions in the Life-Cycle of concrete as well as resource consumption and production costs.

In the ongoing research project "CLOSE", we investigate alternative uses of fines from construction and demolition waste and evaluate their benefits from an environmental and an economic perspective. We also assess possible effects on the quality of concrete produced with these secondary materials, also considering the carbonation of the concrete fines. We work in close collaboration with cement producer JURA Materials, as industry partners, using simulation methods as well as comprehensive material testing according the Swiss standards for cement and concrete.material testing. For the evaluation of environmental and economic impacts, we use Life-Cycle-Assessment focussing on GWP (including the effect of carbon uptake by carbonisation of crushed concrete) as well as cost calculation methods. It is a feasibility study to identify the most promising use of recycled concrete fines and show requirements for appropriate demolition processes and preparation process as well.

In this early-stage paper, we focus on using crushed concrete fine as a raw material substitute in cement production and discuss the chemical composition of construction and demolition waste (C&DW), the carbon uptake and Life-Cycle-Assessment (LCA). First preliminary results are presented and discussed.

Keywords: concrete, cement, recycling, construction and demolition waste, LCA

1. Introduction

In Switzerland, around 15 million tons of construction & demolition waste (C&DW) were produced in 2014 [1], of which approximately 7 million tons are concrete and mixed demolition waste (e.g. masonry). According recent studies [2], [3] the amount of construction waste from building construction will increase significantly due to a higher demolition and renovation ratio. It is assumed, that the amount of C&DW in the building construction will increase to 9 million tons in 2025. In Figure 1 it can be seen, that the biggest increase is to be expected in concrete waste, as the amount of mixed construction waste will remain stable. This is due to the fact, that there is an increasing demolition ration of buildings from 1961 and younger,

which are mainly made of concrete. Today, the highest demolition rate is still at buildings aged around 60 to 70 years (build 1947 until 1960), where the share of masonry is higher than concrete [2].

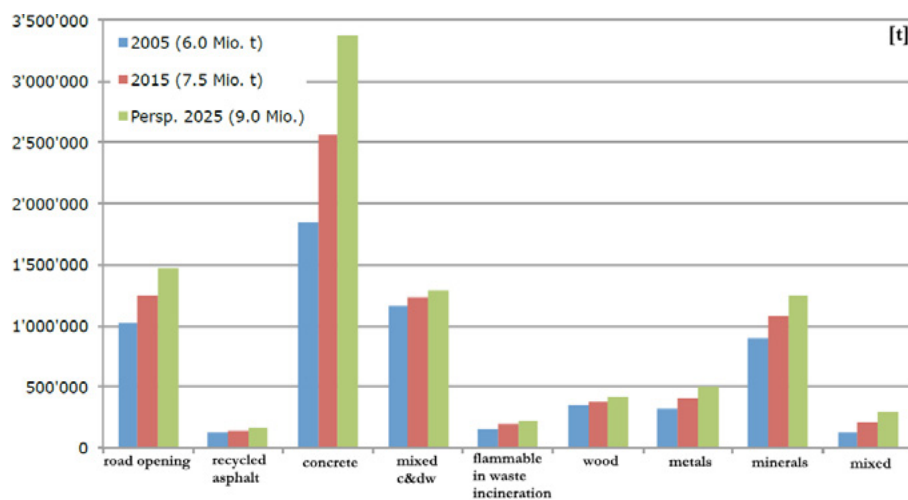


Figure 1: Development 2005-2025 of construction waste by material group in the building construction [2]

As result of the increasing amount of waste, the Federal Office for the Environment of Switzerland(FOEN) declared in 2016, that all waste such as municipal waste or construction and demolition waste “must be recycled or recovered for energy” [4]. The condition is, that the recovery “does less harm to the environment than (a) any other form of disposal; and (b) the manufacture of new products or the acquisition of other heating fuels”. In addition, the “Recovery must be carried out according to the state of the art”. Around 70-80 % of the overall C&DW, as of today, is recycled for building materials, while the rest is deposited or burned in waste incineration plants [1], [5]. However, most of the processed C&DW is “down-cycled” into materials with subordinate technical requirements such as lean concrete or as road subbase material [6]. One reason for the Downcycling is the crushed concrete sand with grain sizes smaller than 4 mm. The European Cement Research Academy [7] states, that the re-use of crushed concrete is a challenge due to the less favourable properties of the crushed concrete fines.

By considering the above-mentioned amount of concrete waste in the building construction sector in Switzerland, it becomes clear, that there is a high potential in the optimisation of the use of the crushed concrete sand. In 2015, approximately 2.5 million tons of concrete waste have accrued. When crushing this concrete waste to aggregate of a typical grading curve (for example Fuller 0/32 mm), we can estimate, that there is a share of around 35 % (0.875 million tons) of crushed concrete fines 0/4 mm. As stated before, this sand is usually used for low-quality purposes, which means, that the special properties of the sand, for example the possible reactivity of the cement paste, remains unused.

The Swiss cement and concrete industry makes a major contribution to the recycling of waste. As shown in Figure 2, secondary materials are used in various processes along the value chain as alternative fuels and raw materials (AFR) in cement kilns, as supplementary cementitious materials (SCMs) in the cement mill or concrete production or as aggregates in concrete production. This common practice reduces the burden on the environment in three ways: by saving natural resources (lime, marl, gravel, sand, coal and oil), by reducing waste and by reducing greenhouse gas emissions [6]. The latter effect in particular is decisive, as the contribution of the cement and concrete industry to the greenhouse effect is considerable, accounting for around 8% of total carbon dioxide emissions worldwide [8]. For years, the industry has been using conventional technologies to reduce CO₂ emissions: increasing energy efficiency, clinker substitution and the use of alternative fuels. However, their potential has now largely been exhausted. As a result, little

progress is being made in reducing CO₂ emissions [9], [10].

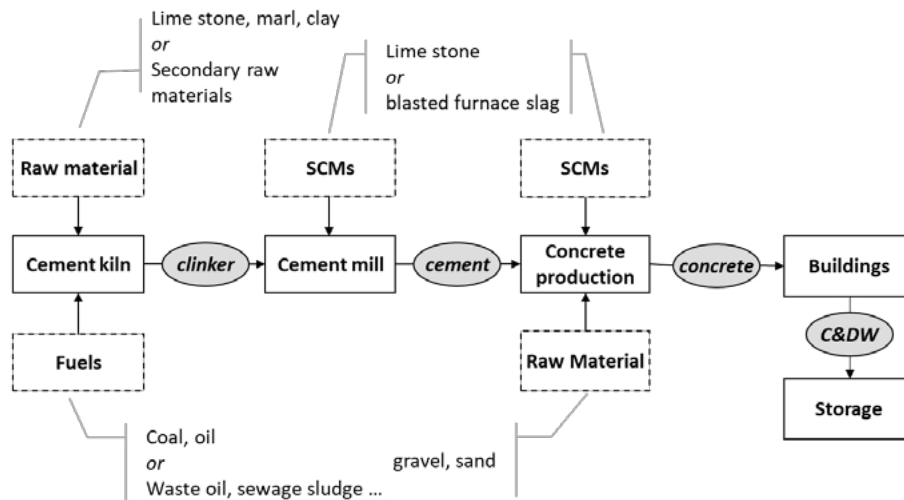


Figure 2: value chain of cement and concrete

[11] suggest that recycling of concrete fine from demolition could further reduce CO₂ emissions in the concrete product system. Yet, quality of crushed sand has a significant influence on the possibilities of returning the crushed sand to cement and concrete production. On the one hand it depends on the methods of concrete demolition treatment [12]–[14] and on the other hand it is also influenced by whether the storage of concrete demolition increases the uptake of CO₂ in the cement paste. This storage is currently being discussed in the cement industry in order to make an additional contribution to climate protection [15]–[17].

This is where the here presented research project CLOSE comes in. Its aim is to optimize the usage of concrete demolition waste, especially the crushed concrete fines as a by-product. The economic efficiency of concrete recycling will be significantly improved if this crushed sand can be used profitably in cement and concrete production. In the CLOSE project, three technically viable applications of this crushed sand are to be evaluated according to sustainability criteria with a focus on climate protection, resource conservation and waste avoidance.

In order to develop concrete specifications for the further development of concrete demolition processing methods, it must be known which crushed sand quality is to be aimed for. This requirement depends on how the crushed sand is returned to the cement and concrete production. Possible applications (see Figure 2) would be: (i) as a raw meal substitute, (ii) as additives in cement mills or concrete production or (iii) as aggregates in concrete production.

Looking at the year 2015, 4.2 million tons of cement were produced in Switzerland [9] which corresponds to a consumption of raw materials of approx. 5 million tons. Considering the above calculated amount of available crushed concrete fines (0.875 million tons), the possible substitution of raw material in the clinker production is calculated to 17 %. In the same period, 39.8 million tons of concrete were produced [18]. Assuming, that around 70 % of the concrete is aggregate and 35 % of that is the fine fraction of sand 0/4 mm, the amount of virgin sand used for the concrete production is approx. 9.75 million tons. That leads to a maximum substitution ratio of concrete fines of 9 %, assuming that all of the available crushed concrete fines are usable.

Based on these interrelationships, an evaluation of the possible application sites of crushed sand represents an essential prerequisite for the development of suitable processing methods.

In the project, the following research questions are to be answered:

1. To what extent can CO₂ emissions be reduced in cement production (taking carbonation into account)?
2. To what extent can the consumption of natural resources (lime, marl, gravel, coal and oil) in cement production be reduced by recycling crushed concrete sand?
3. What are the risks for cement and concrete quality?
4. What are the requirements for the quality and quantity of the cement paste present in the crushed sand?

In this paper, we focus on using crushed concrete fine as a raw material substitute in cement production. By investigating the chemical composition, calculating the carbon uptake and investigating the life cycle of concrete regarding the carbon uptake, we try to answer the first and second above-mentioned questions.

2. State of research

2.1 Concrete fines as raw material for the clinker production

In recent years, several studies have dealt with the quality of construction and demolition waste and their use in the cement and concrete production. On the one hand, the focus was placed on the treatment processes of C&DW, on the other hand several studies investigated the quality of the aggregates for the use as a raw material in the cement industry and came to the conclusion, that the fine aggregate can be used as a raw material [6], [7], [14], [19], [20].

2.1.1 Chemical composition of the crushed concrete fines

Raw materials containing calcium (Ca), silicon (Si), aluminium (Al) and iron (Fe) as main components are used for the production of cement clinker [21]. These are usually limestone, clay and marl. Therefore, the chemical composition of the crushed concrete determines the possibilities for the usage of the concrete fines [22].

One study stated [14], that “if the recycled material consists mainly of concrete, it can serve as a CaO-containing component in cement production, if the proportion of bricks predominates, it can be used as an Al₂O₃ carrier.”. Several studies investigated the chemical composition of recycled concrete fines [14], [19], [20], [23]. As recycled crushed concrete sand mainly contains CaO and SiO₂ it is particularly suitable as a clay substitute in clinker production due to its chemical composition [22]. However, depending on the used virgin aggregate (silicate or calcite), the content of CaO and SiO₂ may vary significantly (see Table 1), which makes it essential to determine the chemical compositions of the material which is to be utilized.

Table 1: chemical composition of crushed concrete materials [22]

	[M-%]	SiO ₂	Al ₂ O ₃	Fe ₂ O ₃	CaO	MgO	K ₂ O	Na ₂ O	SO ₃
Crushed concrete materials n = 65	Ø	64.8	6.1	2.5	12.3	1.2	1.7	0.8	0.6
	Min	16.0	2.1	0.9	5.0	0.4	0.3	0.1	0.3
	Max	77.9	9.2	4.2	37.5	6.5	4.9	1.7	1.3

2.1.2 Burnability

One aim of the project is to investigate the possibility to minimize the environmental impact by using crushed concrete fines. As the burning process of the clinker production represents the highest energy demand in the value chain, it is essential, that the usage of crushed concrete fines as a substitute for raw material does not lead to a higher energy demand or higher CO₂-emissions. According to [6], a reduction of the firing temperature when using crushed concrete fines as substitution is possible, which would reduce

the energy demand of the clinker production. However, it must be noted, that the synthesis of C_3S does not take place completely during the firing process, which leads to a low early strength [20], [23]. The higher the substitution rate, the lower is the C_3S content, which, in the end, leads to a loss of compressive strength.

2.2 Carbon uptake

Concrete is able to capture CO_2 in its service life through carbonation, leading to a significant decrease of the total CO_2 emissions in the value chain of concrete [24], [25]. In this process, the CO_2 from the air is bound by the calcium hydroxide $Ca(OH)_2$ in concrete forming calcium carbonate $CaCO_3$. As this process depends on several boundary conditions like accessible surface, cement composition, concrete quality or exposure conditions [26], there is no consensus in research as to how much CO_2 can be rebound. The values in recent studies vary between 10 and 40 % [16], [25], [27].

2.2.1 Surface area

Even if the values of the possible uptake fluctuate in current research and are subject to uncertainties, all studies clearly show that the CO_2 absorption in the recycling phase is significantly higher than during the lifetime (see Figure 3), as the crushing of the concrete significantly increases its specific surface area and exposes areas that have not yet been carbonated. It is stated that crushed construction and demolition waste (C&DW) can bind more CO_2 than the concrete in the actual construction and, therefore, contributes to further reduce CO_2 emissions if prepared and stored in a favorable way [26], [28].

2.2.2 Water-Cement-Ratio

A higher water/cement ratio (w/c-ratio) causes a higher porosity leading to a higher surface area exposed to CO_2 . According a recent study [29], the carbonation rate is highest at a w/c-ratio of 0.6. Another study [30] also concluded that mortar and concrete with a higher w/c-ratio can bind more CO_2 as another study set an optimum w/c-ratio at 0.45 [31].

2.2.3 Humidity

According to [33], the maximum speed of carbonation can be achieved at a relative humidity of 60 to 80%. Humidity plays an important role for two reasons. Firstly, the presence of water is a prerequisite for starting the chemical reaction. On the other hand, too much moisture inhibits the reaction, as the CO_2 can penetrate less quickly. Therefore, a relative humidity of 50 to 70% is assumed to be optimal for carbonation [26].

2.2.4 Targeted carbonation

Due to the carbonation process the density of the cement paste increases, while the porosity decreases. This is due to the fact that the end product of the chemical reaction, $CaCO_3$ has a higher density than the starting product $Ca(OH)_2$. For this reason, there are already several studies dealing with targeted carbonation. The aim is not only to reclaim CO_2 , but also to improve the properties of the crushed sand. According to [15], [31], [33], the treatment of aggregates with CO_2 leads to an increase in bulk density and thus to a reduction in porosity. In particular, capillary porosity is reduced, which has a positive effect on compressive strength compared to a reference concrete with the same aggregate.

In the case of using the crushed concrete fines as substitute of raw material in the clinker production, as described in this paper, a low carbonation ratio is desired, as otherwise the bound CO_2 must be released again in the combustion process in the clinker production.

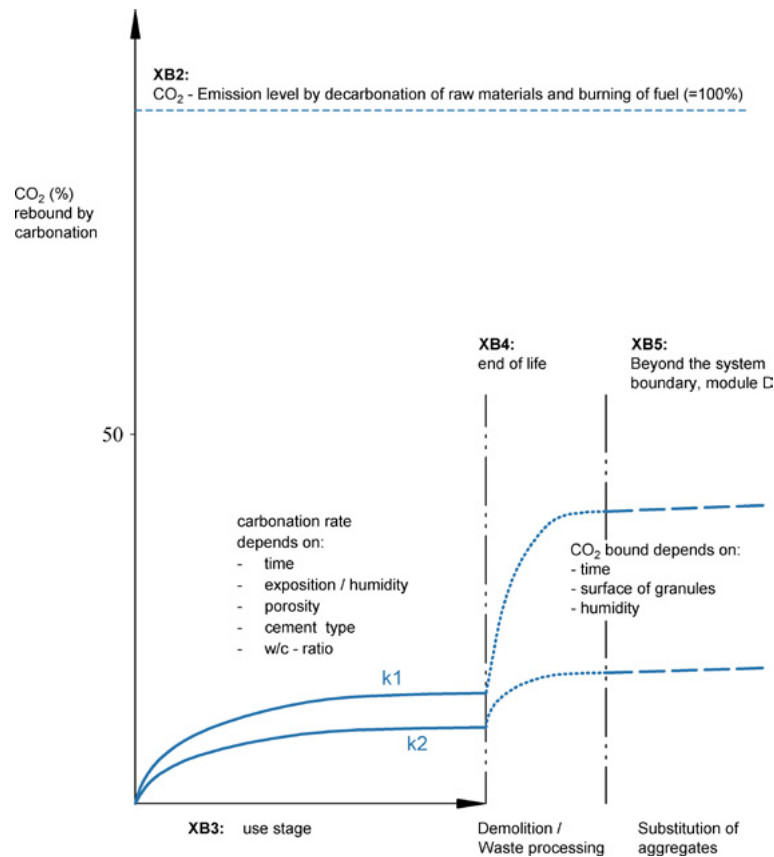


Figure 3: Rebinding of CO₂ by carbonation of concrete [32]

2.3 Life-Cycle-Assessment of concrete

Life cycle assessment (LCA) is a methodological framework used to assess environmental impacts of a product or service from a life cycle perspective, including resource extraction, production, use and end-of-life activities (e.g. waste treatment). Its development started in the 1960s focusing on the comparison of environmental impact of consumer goods and first studies in the construction sector appear in the 1980s [34]. A common methodological framework wasn't developed until the late 1990s when the International Organization for Standardization (ISO) published its 14040 series [35], [36]

Since then, the interest in LCA rapidly increased. It encouraged the development of a specific methodological framework for LCA of building materials and products with a set of environmental data defined by pre-set categories of parameters based on the ISO14040 series. It results in Environmental Product Declarations (EPDs) and was standardized on a general level by ISO (ISO Technical committee (TC) 59 'Building Construction') [37] as well as by the European Committee for Standardization (CEN) in its Technical Committee (TC) 350 'Sustainability of construction works'. This led to the emergence of EPD programs (mostly in Europe, Canada and the US) that started developing and publishing specific methodological frameworks for product categories, called PCRs (Product Category Rules). In 2015, [38] state that more than 28 EPD programs exist worldwide referring to ISO 14025" (...), providing more than 2256 PCR documents and more than 3600 EPDs. Yet, the growing number of LCA studies for construction materials also revealed the need to further develop the method [34], [39]–[42].

Looking at different LCA studies for concrete there is a surprisingly wide range in the results for different environmental impacts such as Global Warming Potential (GWP) or Cumulative Energy Demand (CED). Some of this variation can be explained by the use of different data sources or methodological choices [38], [43], [44]. Yet, even within an identical methodological framework using the same data sources, results

can vary up to 100% for the same type of concrete [45]. For LCA experts, this reveals the need to further develop the method [34], [39]–[42].

Along the value chain of cement and concrete production several strategies have been identified to reduce environmental impacts [11], [46]–[48]. The most significant strategies are:

- improving the energy efficiency of cement plants and substituting fossil fuels in the cement kiln
- reducing the clinker content in cement (clinker to cement ratio)
- reducing the cement content in concrete
- optimizing the use of concrete in construction

By implementing all strategies in parallel by different stakeholders, it is claimed, that CO₂-emissions of concrete production worldwide could be reduced by about 80 % until 2050 [47].

Considering carbonation, it is assumed, that recycling demolished concrete could further reduce CO₂ emissions from the cement and concrete industry. At the same time, the consumption of mineral raw materials can be reduced [19]. Two effects are decisive for this:

Through the targeted processing and storage of concrete demolition, the rebinding of CO₂ in the cement paste can be significantly increased. Individual studies estimate that 10-15% of the amount of carbon dioxide produced in the cement kiln during clinker production can be bound during a few years [26], [49]. Carbonation causes limestone to form and compact in the cement stone. This limestone can be used as a secondary raw material in cement production.

The production of concrete granulate also results in a fine fraction (crushed sand) consisting of sand, hard cement stone and fine foreign particles (such as wood and plastic particles). Due to insufficient quality, crushed sand is not yet used in a targeted manner. The CO₂-intensive cement stone is lost unused. However, this material could be reused in cement and concrete production and thus contribute to reducing environmental pollution.

The described project will evaluate to what extent the environmental impacts of the cement and concrete industry can be reduced by further developing processes for recycling concrete demolition. The focus is on the use of crushed sand - a residue from the recycling process - in various processes along the value chain (Figure 2).

2.4 Standards

In Europe, the chemical composition of cement is defined in EN 197-1:2011 [50]. This standard limits the main and secondary constituents as well as their respective contents. The development of low CO₂-cement with high substitution rates of the constituents would not be possible within the framework of this standard. As the Swiss cement industry aims to reduce the CO₂ emissions caused by the cement production, the guideline 2049 [51] was published to expand the possible usage of inorganic components and to support the usage of sustainable cement. In this guideline, new technical requirements and limits of the main and secondary constituents are set which make it possible to develop new cement compositions. This guideline also regulates the requirements and tests for the durability of concrete produced with the new cement.

However, these standards would only be relevant in the case of the use of crushed sand as a supplementary cementitious material in the cement mill. When using the crushed concrete sand as a substitute of raw material in the clinker production, the requirements for the clinker in accordance with the standards is given

by calculating the setting parameters to produce the respective reference clinker (see 3.2).

3. Methodology and Data

To determine the properties of the crushed concrete fines and estimate the potential for their use as alternative raw material, several testing methods and calculations are used. These are described in the following subsections.

3.1 Polarized light microscopy

As a first indicator to validate the possible usage of the crushed concrete fines, the ratio of aggregate to hardened cement paste is assessed. For this purpose, a sample of the crushed concrete fine 0/4 mm is poured into a fluorescent plastic compound and processed into a thin section. This thin section is then examined under the petrographic microscope and the ratio of aggregate to hardened cement paste estimated.

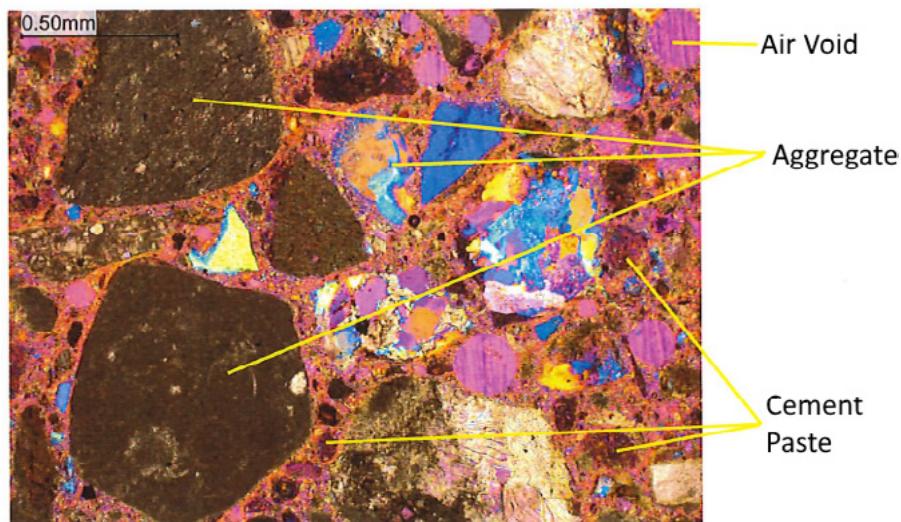


Figure 4: microscopic image in polarized light

In Figure 4 a picture of crushed concrete fines collected within this project can be seen. First preliminary result of this first sample have shown that the content of hardened cement paste is approximately around 15 %. Further microscopic investigation will lead to results that are more robust.

3.2 XRF

To determine the chemical composition of the crushed concrete fines, an X-ray fluorescence spectroscopy (XRF) with wavelength dispersive spectrometers is carried out. The specific elements of the sample are identified by measuring the energy of the emitted radiation, while the amount of the elements are measured by the intensity of the emitted radiation. With the elements Calcium oxide (CaO), Silicon dioxide (SiO₂), Aluminium oxide (Al₂O₃) and ferric oxide (Fe₂O₃) the setting parameters lime saturation factor (LSF), silicate modulus (SM) and alumina modulus (AM) can be calculated as follows:

$$\text{lime saturation factor (LSF)} = \frac{100 \text{ CaO}}{2.8 \text{ SiO}_2 + 1.18 \text{ Al}_2\text{O}_3 + 0.7 \text{ Fe}_2\text{O}_3} \quad (1)$$

$$\text{silicate modulus (SM)} = \frac{\text{SiO}_2}{\text{Al}_2\text{O}_3 + \text{Fe}_2\text{O}_3} \quad (2)$$

$$\text{alumina modulus (AM)} = \frac{Al_2O_3}{Fe_2O_3} \quad (3)$$

These parameters are then used to calculate the needed amounts of raw materials to produce a pre-defined reference clinker with corresponding properties. With the results, we can estimate how much raw material can be replaced by the crushed concrete fines.

First preliminary results of XRD-analysis in this study can be seen in Table 2. These samples of processed C&DW were collected in two different recycling centres in Switzerland. It can be seen, that the contents of the relevant elements (CaO, SiO₂, Al₂O₃ and Fe₂O₃) can differ significantly. Especially the difference of around 13 % in the content of CaO must be noted, as it has a crucial impact on the usage of the crushed concrete fines. This difference results in different lime saturation factors (LSF), which are used to determine the maximum substitution rate in cement production. [21] states, that the LSF for ordinary portland cement should be between 92 and 102. Since the LSF of the investigated samples is between 21 and 28 (see Table 2), the assumption can be expressed that these samples are only partly suitable to be used as substitution in the cement production. Therefore, further investigations are needed before a definitive statement can be provided.

Table 2: preliminary XRF results of two samples of crushed concrete fines

		sample 1	sample 2
particle size	mm	0-4	0-4
ignition loss	%	23.50	20.88
SiO ₂	%	47.66	41.12
Al ₂ O ₃	%	5.22	4.87
Fe ₂ O ₃	%	2.31	2.20
CaO	%	39.16	25.96
MgO	%	2.32	2.09
SO ₃	%	0.57	0.40
K ₂ O	%	0.98	0.85
Na ₂ O	%	0.80	0.63
TiO ₂	%	0.24	0.22
P ₂ O ₅	%	0.09	0.09
Mn ₂ O ₃	%	0.08	0.07
SrO	%	0.07	0.06
Cr ₂ O ₃	%	0.01	0.01
ZnO	%	0.01	0.01
Na ₂ O-Eq	%	1.10	1.18
LSF		27.78	21.23
SM		6.37	5.82
AM		2.25	2.22

3.3 LCAs of concrete

In previous own studies [52] we used an LCA to evaluate how environmental impacts of concrete product systems are affected by

1. variations of technical parameters, such as cement content, clinker cement ratio, origin of aggregate or fuel mix, and
2. alternative methodological choices in LCA, such as allocation regarding carbon uptake.

As stated before, the project CLOSE aims to reduce the environmental impacts in the cement- and concrete production. In context with the use of the crushed concrete sand as a raw material substitute, the consideration of CO₂ uptake is particularly important (see 2.2). Therefore, the results of LCAs without allocation (see 3.3.2) will be extended with a calculated carbon uptake according [32] (see 3.3.3).

3.3.1 System under investigation

The investigated concrete product system also corresponds to the here described value chain shown in Figure 2: We analysed the system with two alternative system boundaries.

System boundary A “cradle to gate” includes

- Cement production with kiln and mill with all corresponding up-stream processes needed to supply raw materials (lime stone, clay etc.), fuels (coal, oil etc.) and electricity. The supply of alternative fuels is also included, but the allocation of the associated environmental impacts
- Concrete production with all corresponding upstream processes needed to supply raw materials (gravel, limestone etc.) and electricity.
- Transport processes between cement and concrete production are explicitly included. All other transport processes are modelled as part of the upstream processes of supplied materials and energy.

System boundary B “Cradle to grave” includes the system defined as “cradle to gate” as well as the use of concrete during the service life of a structure and storage of crushed concrete at a recycling plant or landfill. We model these processes to analyse carbon uptake (see following section). No environmental impacts are analysed for these processes.

We compared environmental impacts of one cubic meter of concrete (functional unit) of an ordinary construction concrete in Switzerland focussing on the Global warming potential (GWP) according IPCC 2011 (100 years in kg CO₂eq).

The life cycle inventory was set up in SimaPro 8.5. The data basis for the LCI is ecoinvent Version 3.4 from November 2017. As basis, the process “Concrete, sole plate and foundation {CH} | concrete production, for civil engineering, with cement CEM II/A | Cut-off, U” in its version 3.0.2.0 was used and modified in order to enable varying the concrete mix design. The electricity represents the Swiss electricity production mix in 2014. The mix designs of the respective concrete can be seen in Table 3:

Table 3: mix design of the concretes for LCA [52]

		280 CEM I round	300 CEM I round	320 CEM I round	350 CEM I round	280 CEM I crushed	280 CEM II / A round	280 CEM II / B round	280 CEM III / A round	280 CEM III / B round	280 CEM III / C round
		1	2	3	4	5	6	7	8	9	10
cement-content	kg/m ³	280	300	320	350	280	280	280	280	280	280
clinker-ratio	%	95	95	95	95	95	80	65	35	20	5
blast furnace slag	%						15	30	60	75	90
gypsum	%	5	5	5	5	5	5	5	5	5	5
sand	kg/m ³	668	678	678	657	668	668	668	668	668	668
gravel	kg/m ³	1221	1241	1212	1201	1221	1221	1221	1221	1221	1221
water	kg/m ³	190	190	190	190	190	190	190	190	190	190
Fuel mix						Swiss mix 2014					

3.3.2 Results without allocation

Different scenarios were defined to analyse how environmental impacts are affected by variations of technical parameters in LCA. We focus on the technical parameters with a significant influence on environmental impacts of the product system [47]: cement content level, clinker-cement-ratio and geometric shape of the aggregates (round vs. crushed). Carbon uptake is not considered as technical parameter because no technologies have been implemented up to now to increase CO₂ binding during service life and recycling. An ordinary construction concrete with 280 kg/m³ and round aggregates was chosen as reference.

Table 4: results of LCAs without allocation

	1	2	3	4	5	6	7	8	9	10
IPCC 2011 GWP 100a [kg CO ₂ eq]	231.25	246.94	262.34	285.48	234.13	208.79	186.33	141.42	118.96	96.50

The results of the LCAs are shown in Table 4. It can be seen, that the environmental impact, calculated as GWP, increases as the cement content increases in the mix designs 1 – 4. The increasing usage of ground granulated blast furnace slag in the mixes 6 – 10 results in decreasing CO₂-emissions. The usage of crushed aggregate (mix 5) instead of round aggregates leads to a slight increase of the GWP of 3 kg CO₂ eq.

3.3.3 Results considering carbon uptake

In DIN EN 16757 [32] an allocation method for the carbon uptake is presented. There, several calculations are made to estimate the carbon uptake in total, during service life of concrete structures and through its usage stage and in its end-of-life phase. The formula for calculating the maximum carbon uptake is as follows:

$$CO_2 - \text{uptake} = \left(\frac{\% \text{ reactive CaO}}{100} \right) \times \text{binder content} \times \frac{\text{molar weight of CO}_2}{\text{molar weight of CaO}} \quad (4)$$

Where the amount of reactive CaO is about 65 %, the molar weight of CO₂ is 44 g/mol and for CaO 56 g/mol, respectively [32]. If we apply the calculation to the mix designs investigated in [52] (see Table 3), the following maximum carbon uptake are as follows:

Table 5: results considering CO₂ uptake according [32], [52]

	1	2	3	4	5	6	7	8	9	10
max. carbon uptake [kg CO ₂]	136	146	155	170	136	114	93	50	29	7
75 % carbon uptake [kg CO ₂]	102	109	116	127	102	86	70	38	21	5

In Table 5 it can be seen, that a maximum carbonation would lead to a significant uptake of carbon dioxide from the air, which in turn would lead to a significant lower environmental impact regarding CO₂. However, it must be noted that the carbonation of concrete depends on several conditions (see 2.2). Assuming, that around 75 % of the carbonation can be reached during service life and end-of-life phase [32], up to 127 kg CO₂ can be bound back in the mix 4 with 350 kg cement. Due to its chemical composition, blast furnace slag is not able to capture CO₂ like ordinary Portland cement, which can also be seen in Table 5 (mix 6 – 10).

3.3.4 Carbon uptake of crushed concrete in the cement production

This carbon uptake is highly relevant for the usage of the crushed concrete sand as substitute for raw material, as a high carbonation would lead to a high amount of CO₂, which must be expelled again during the burning process. However, exactly this amount of bound CO₂ would be used as a credit for environmental

product declarations (EPD) as it is not counted as geogenic CO₂. In that case, double counting has to be considered and avoided.

A low carbonation, and therefore a low CO₂ amount in the substitute would lead to a lower energy demand in the burning process as the burning temperatures or burning time can be optimized. This would lower on the one side the overall environmental impacts of the clinker production, but also the economic impacts as the production process can be optimized.

4. Discussion and conclusions

Efforts to optimise the recycling of mineral construction waste today focus on mixed demolition, as there are currently too few recycling possibilities for this secondary building material. The demolition of concrete is not yet considered a problem and the potential of its recycling is not yet sufficiently recognised.

This will change in the coming years or decades, because:

- The amount of concrete demolition will increase once the concrete structures from the second half of the last century have reached the end of their useful life. Since 1960, the proportion of concrete structures/components in the building stock has increased continuously. Therefore, the proportion of mixed demolition in mineral construction waste will decrease in the future and the proportion of concrete demolition will increase accordingly.
- The possible uses of RC concretes in structural engineering will increase and with it the demands on the building material. Today, qualitative deficiencies in the concrete granulate are compensated by adjustments in the concrete mix design (more cement, more admixtures). This leads to higher costs and environmental pollution. In the future, attempts will be made to improve the quality of concrete demolition.
- The pressure on the cement industry to make its contribution to climate protection is increasing (e.g. through higher CO₂ fees and measures taken by public clients). Many representatives of this industry see a promising approach to solving this problem by rebinding CO₂ in concrete. For this, the greatest potential lies in the rebinding capacity in the crushed sand of the concrete demolition.

For these reasons, efforts to develop new processes for the separation and processing of C&DW will increase significantly in the coming years and further investigations for the usage of C&DW will be necessary. The here described research project improves the decision-making basis for the development of new technologies and possibilities to use a material which, until now, is down-cycled.

As this project is still in an early stage, further investigations has to be carried out in order to present robust results and discuss these results regarding the alternative uses of fines from construction and demolition waste and their benefits from an environmental and an economic perspective.

5. Acknowledgment

Supported by the Federal Office for the Environment FOEN (UTF 591.03.19) and the Gebert Rüf Foundation (GRS-049/18).

6. References

- [1] D. Hiltbrunner, "Das Bauwerk als Rohstofflager," vol. 22, pp. 65–69, 2017.
- [2] F. Guerra and B. Kast, "Bauabfälle in der Schweiz - Hochbau Studie 2015 [Construction waste in Switzerland - Building Construction Study 2015]," Bern, 2015.

- [3] S. Schubert and C. Hoffmann, “Grundlagen für die Verwendung von Recyclingbeton mit Mischgranulat,” EMPA, Abteilung Ingenieur-Strukturen, 2011.
- [4] Swiss Waste Ordinance, *Ordinance on the Avoidance and the Disposal of Waste*. 2015, pp. 1–46.
- [5] J. Almeida and C. Wälti, “Ent-Sorgen? Abfall in der Schweiz illustriert,” Bern, Nr. 1615, 2016.
- [6] C.-T. Galbenis and S. Tsimas, “Use of construction and demolition wastes as raw materials in cement clinker production,” *China Particuology*, vol. 4, no. 2, pp. 83–85, 2007.
- [7] C. Müller, J. Reiners, and S. Palm, “Closing the loop: What type of concrete re-use is the most sustainable option?,” 2015.
- [8] F. Preston and J. Lehne, “Making Concrete Change,” Chatham House, the Royal Institute of International Affairs, 2018.
- [9] CemSuisse, “Annual Report 2018 key figures,” Association of the Swiss Cement Industry, Bern, 2018.
- [10] WBCSD, “Global Cement Database on CO₂ and Energy Information, Getting the Numbers Right,” 2013. [Online]. Available: <http://www.wbcscement.org/index.php/key-issues/climate-protection/gnr-database>.
- [11] CEMBUREAU, “The Role of Cement in the 2050 Low Carbon Economy,” Brussels, 2013.
- [12] K. Weimann and C. Adam, “RECDemo - Vollständige Verwertung der Sandfraktion aus dem Bauschuttrecycling,” pp. 1–4, 2017.
- [13] C. Müller and B. Dora, *Verwertung von Brechsand aus Bauschutt*, vol. 506. Berlin: Beuth, 2000.
- [14] A. Muller, K. Rubner, and A. Schnell, “Potential of Construction and Demolition Waste as Raw Material,” *Chemie Ing. Tech.*, vol. 82, no. 11, pp. 1861–1870, 2010.
- [15] M. Seidemann and H.-M. Ludwig, “Einfluss von carbonatisierten sekundären Gesteinskörnungen auf die Eigenschaften von Recyclingbeton,” in *Mineralische Nebenprodukte und Abfälle. Aschen, Schlacken, Stäube und Baurestmassen*, K. J. Thomé-Kozmiensky, Ed. TK-Vlg, 2015, pp. 639–651.
- [16] A. Leemann and F. Hunkeler, “Carbonation of concrete: assessing the CO₂ uptake,” 2016.
- [17] A. Leemann and F. Moro, “Carbonation of concrete: the role of CO₂ concentration, relative humidity and CO₂ buffer capacity,” *Mater. Struct. Constr.*, vol. 50, no. 1, pp. 1–14, 2017.
- [18] M. Gauch, C. Matasci, I. Hincapié, R. Hörler, and H. Böni, “Material- und Energieressourcen sowie Umweltauswirkungen der baulichen Infrastruktur der Schweiz,” BAFU Bundesamt für Umwelt, 2016.
- [19] J. Schoon, K. De Buysser, I. Van Driessche, and N. De Belie, “Fines extracted from recycled concrete as alternative raw material for Portland cement clinker production,” *Cem. Concr. Compos.*, vol. 58, pp. 70–80, Apr. 2015.
- [20] E. Kwon, J. Ahn, B. Cho, and D. Park, “A study on development of recycled cement made from waste cementitious powder,” *Constr. Build. Mater.*, vol. 83, pp. 174–180, 2015.
- [21] J. Stark and B. Wicht, *Zement und Kalk*. Basel: Birkhäuser Basel, 2011.
- [22] A. Müller, *Baustoffrecycling*, vol. 63, no. 11–12. Wiesbaden: Springer Fachmedien Wiesbaden, 2011.

- [23] C. Diliberto, A. Lecomte, J. M. Mechling, L. Izoret, and A. Smith, "Valorisation of recycled concrete sands in cement raw meal for cement production," *Mater. Struct. Constr.*, vol. 50, no. 2, p. 333, 2017.
- [24] S. Butera, T. H. Christensen, and T. F. Astrup, "Life cycle assessment of construction and demolition waste management," *Waste Manag.*, vol. 44, pp. 196–205, Oct. 2015.
- [25] A. L. Empa, A. Beton, and H. Widmer, "Berechnung der CO₂ - Aufnahme während der Nutzungsdauer zementgebundener Baustoffe," 2018.
- [26] S. Baetzner and R. Pierked, "Release and uptake of carbon dioxide in the life cycle of cement," 2007.
- [27] F. Collins, "Inclusion of carbonation during the life cycle of built and recycled concrete: Influence on their carbon footprint," *Int. J. Life Cycle Assess.*, vol. 15, no. 6, pp. 549–556, Jul. 2010.
- [28] E. Possan, E. F. Felix, and W. A. Thomaz, "CO₂ uptake by carbonation of concrete during life cycle of building structures," *J. Build. Patbol. Rehabil.*, vol. 1, no. 1, p. 43, 2016.
- [29] A. B. Bauchemie, "Kohlendioxidaufnahme von Stahlbetonbauten durch Karbonatisierung," 2012.
- [30] T. Kikuchi and Y. Kuroda, "Carbon Dioxide Uptake in Demolished and Crushed Concrete," *J. Adv. Concr. Technol.*, vol. 9, no. 1, pp. 115–124, 2011.
- [31] M. Thiery, P. Dangla, P. Belin, G. Habert, and N. Roussel, "Carbonation kinetics of a bed of recycled concrete aggregates: A laboratory study on model materials," *Cem. Concr. Res.*, vol. 46, pp. 50–65, Apr. 2013.
- [32] EN 16757, *Sustainability of construction works - Environmental product declarations - Product Category Rules for concrete and concrete elements*. Berlin: Beuth Verlag GmbH, 2017.
- [33] B. Lagerblad, *Carbon dioxide uptake during concrete life cycle – State of the art*, vol. CBI 2005:2, no. February. Stockholm: Cement- och betonginstitutet TS - Sweden National Library Libris T4 - State of the art M4 - Citavi, 2005.
- [34] M. Buyle, J. Braet, and A. Audenaert, "Life cycle assessment in the construction sector: A review," *Renew. Sustain. Energy Rev.*, vol. 26, pp. 379–388, Oct. 2013.
- [35] SN EN ISO 14040:2006 *Umweltmanagement - Ökobilanz - Grundsätze und Rahmenbedingungen*. SNV Schweizerische Normen-Vereinigung, 2006.
- [36] D. G. I. for S. DIN Deutsches Institut für Normung e. V., *DIN EN ISO 14044:2006 Umweltmanagement-Ökobilanz - Anforderungen und Anleitungen*. SNV Schweizerische Normen-Vereinigung, 2006.
- [37] ISO/DIS 21930, "Sustainability in buildings and civil engineering works - Environmental declaration of building products (Draft version)." 2016.
- [38] A. Passer *et al.*, "Environmental product declarations entering the building sector: critical reflections based on 5 to 10 years experience in different European countries," *Int. J. Life Cycle Assess.*, vol. 20, no. 9, pp. 1199–1212, Sep. 2015.
- [39] A. F. Abd Rashid and S. Yusoff, "A review of life cycle assessment method for building industry," *Renew. Sustain. Energy Rev.*, vol. 45, pp. 244–248, May 2015.
- [40] V. Augiseau and S. Barles, "Studying construction materials flows and stock: A review," *Resour.*

Constr. Recycl., vol. 123, pp. 153–164, 2017.

- [41] A. Petek Gursel, E. Masanet, A. Horvath, and A. Stadel, “Life-cycle inventory analysis of concrete production: A critical review,” *Cem. Concr. Compos.*, vol. 51, pp. 38–48, Aug. 2014.
- [42] P. Van Den Heede and N. De Belie, “Environmental impact and life cycle assessment (LCA) of traditional and ‘green’ concretes: Literature review and theoretical calculations,” *Cem. Concr. Compos.*, vol. 34, no. 4, pp. 431–442, Apr. 2012.
- [43] C. Dossche, V. Boel, and W. De Corte, “Use of Life Cycle Assessments in the Construction Sector: Critical Review,” *Procedia Eng.*, vol. 171, pp. 302–311, 2017.
- [44] A. Ehrenberg, “Methoden zur Bewertung des ökologischen Einflusses von Eisenhüttenschlacken,” *Strasse und Autobahn*, no. 10, pp. 836–843, 2018.
- [45] NSF, “NRMCA Member Industry-Wide EPD for Ready Mixed Concrete,” 2016.
- [46] “TECHNOLOGY ROADMAP,” in *Encyclopedia of Production and Manufacturing Management*, Springer US, 2006, pp. 781–782.
- [47] A. D. et al. Favier, “a Sustainable Future for the European Cement and Concrete Industry,” 2018.
- [48] A. J. Boero, A. D. Ramirez, D. A. Salas, J. Duque-Rivera, D. M. Petroche, and C. R. Rodríguez, “Environmental impacts, life cycle assessment and potential improvement measures for cement production: a literature review,” *J. Clean. Prod.*, vol. 113, pp. 114–122, 2015.
- [49] F. Xi *et al.*, “Substantial global carbon uptake by cement carbonation,” *Nat. Geosci.*, vol. 9, no. 12, pp. 880–883, Dec. 2016.
- [50] BS-EN197-1:, *Cement Part 1: Composition, Specifications and Conformity Criteria for Common Cements*, no. November. SIA swiss society of engineers and architects, Zurich, 2011, p. 50.
- [51] SIA MB 2049, *Data Sheet 2049 Requirements for new cements*. SIA swiss society of engineers and architects, Zurich, 2014.
- [52] R. Meglin and S. Kytzia, “Environmental Assessment in the Building Materials Industry: How Are the Results of Life-cycle-assessment (LCA) for Concrete Influenced by Technology and Regulations? (unpublished),” in *Fifth International Conference on Sustainable Construction Materials and Technologies (SCMT5)*, 2019.

Water absorption methods for fine recycled concrete aggregates

L.G. Pedersen¹, L. M. Ottosen¹

¹Department of Civil Engineering, Technical University of Denmark

²Department of Structural Engineering, Norwegian University of Science and Technology

Email of the corresponding author: logrep@byg.dtu.dk

Abstract

When recycling concrete as aggregates, an important part to investigate is to use the fraction of fine recycled concrete aggregates (FRCA) as it constitutes 40-60% of the crushed concrete. If the FRCA is to be recycled in concrete and mortar, it is necessary to know the properties of the FRCA to guarantee a sufficient performance of the new concrete, and especially the morphology and water absorption are of major importance. This study investigates (FRCA) and methods for measuring water absorption.

FRCA has a significantly higher water absorption than fine natural aggregates and the attached mortar in the FRCA often add binding properties, this makes the standard test difficult to implement. The standard testing procedure of water absorption measurement for FRCA can, therefore, have low reproducibility and reliability, due to the assessment of the saturated-surface-dry state indicates a reliance on the test operator and the different properties of the recycled and natural aggregates.

In order to investigate methods for measuring water absorption, the FRCA's properties were characterised, and the standard test method, EN 1097-6, was analysed and compared with two proposed methods as an alternative. The proposed methods are evaporative methods, where the drying kinetics is measured of an initially water-saturated powder layer, by two different test set up and a conductivity method with the decreasing conductivity as a function of the water content. The FRCAs were obtained from demolition sites in the area around Copenhagen. The morphology of the FRCA was studied in a microscope. The comparison of the methods for measurement of water absorption indicates that measurements by the two alternative methods give more cohesion and reliable results for FRCA than the standard method.

Keywords: Concrete, Recycled concrete aggregates, Fine aggregates, Water absorption

Screening Untreated Municipal Solid Waste Incineration Fly Ash for Use in Cement-Based Materials – Chemical and Physical Properties

B.A. R. Ebert¹, B. Steenari², M.R. Geiker³, G.M. Kirkelund¹

¹Department of Civil Engineering, Technical University of Denmark, Denmark

²Chemistry and Chemical Engineering, Chalmers University of Technology, Sweden

³Department of Structural Engineering, Norwegian University of Science and Technology, Norway

Abstract

Concrete manufacturing impacts the environment and construction industry sustainability. The impact is reducible by either using less cement or replacing it with secondary cementitious materials (SCMs). Limited potential for further reduction has been identified, due to low SCM availability. Fly ash from municipal solid waste incineration (MSWI) is an unused material, that could be used as an SCM to further reduce the environmental impact. Before implementing MSWI fly ash for use in cement-based materials, its chemical and physical properties should be evaluated. The present study aims to evaluate the potential of using untreated MSWI fly ash in cement-based materials and its quality, by comparing the chemical properties of MSWI fly ash samples with the chemical requirements of coal fly ash specified in EN 450-1 2012, as well as analysing their potential as filler materials. The screened ash in the present study was sourced from different types of combustion units, in different locations, and from the same location at varying times. MSWI fly ash samples were acquired from three different combustion units, located in Denmark, Sweden and Greenland respectively. Two fly ash samples were acquired from both the units in Denmark and Greenland, sourced several months apart and one from the unit in Sweden. The screening showed that the five fly ash samples, based on their chemical properties, were unsuited for use in cement-based materials. The samples potential as filler materials were found to be limited for all but one sample that had a slightly finer particle size distribution than CEM I cement.

Keywords: Screening, Characterization, MSWI Fly Ash, Cement

1. Introduction

Construction of new buildings and infrastructure consume large quantities of manmade goods and raw materials, greatly impacting the environment and sustainability of the construction industry. In 2016, the production of cement contributed to 8% of the global anthropogenic CO₂ emissions [1]. The environmental impact is not caused by production emissions alone, also the large amount of cement consumed during construction [2].

The environmental impact can be reduced by making concrete with less cement, replacing part the cement with SCMs [3]. Cement has already been partially replaced with SCMs to great effect, retaining or improving the quality of the concrete, through latent hydraulic or pozzolanic reactions [3]. Limited potential for further CO₂ reduction has been identified, due to a low availability of certain SCMs, and can be solved by introducing new sources of SCMs [4].

In the past decades, several countries have introduced changes to their disposal of municipal solid waste, recycling or incinerating the waste instead of landfilling it. Municipal solid waste incineration results in several by-products, such as fly ash that are unused and landfilled, due to its toxic heavy metal content [5]. It has been proposed that MSWI fly ash could be used for cement production or in concrete as an SCM [6] where the heavy metals can be sequestered, reducing heavy metal leaching [7].

Before untreated MSWI fly ash can be utilized in cement-based materials, and the heavy metals sequestered, it must first be screened based on its quality. This is accomplished by first characterizing MSWI fly ash samples, and evaluate their chemical and physical properties. The chemical properties were evaluated by comparing them with the chemical requirements specified in the European standard EN 450-1 2012 [8], concerning the content of chloride, sulphate, free and reactive calcium, silicon dioxide, aluminium oxide, iron oxide magnesium oxide, as well as phosphate content and total content of alkalis. The standard specifies a maximum for loss on ignition (LOI) as well. Additionally, the chemical properties are also assessed based on a Thermogravimetric analysis and x-ray diffraction analysis and the ashes water solubility, pH and conductivity.

The physical properties were evaluated based on the samples potential as filler materials, by analysing the particle size distribution and comparing it with the requirements of filler materials discussed by Mooseberg-Bustnes et al. [9] and Scrivener et al. [10]. According to Moosberg-Bustnes et al. [9], particles, less than 125 µm in diameter can have a physical effect, filling intergranular voids and improving the packing density, and a surface chemical effect by enhancing hydration as nucleation sites. According to Scrivener et al. [10] the hydration is only enhanced if the particle size distribution of the filler materials is finer than the cement used. Furthermore, filler materials may increase the degree of hydration through dilution. Untreated MSWI fly ash has been evaluated before. Previous research has partly focused on fly ash samples sourced once from a single type of combustion unit in a single location.

The present study evaluates untreated MSWI fly ash, based on ash sourced from different types of combustion units, in different locations, as well as samples sourced from the same units several months apart. Samples were acquired from three different combustion units located in Denmark, Sweden and Greenland respectively. Two samples were taken from both the combustion unit in Denmark and Greenland, several months apart, and one sample from Sweden.

2. Methodology

2.1 Materials

The five fly ash samples evaluated in the present study were obtained from commercial MSW combustion units, incinerating waste for heat and power. Two of the ashes, designated Arc-Fa1 and Arc-Fa2, were obtained from Amager Bakke, Denmark, in early 2018 and late 2018 respectively. An additional two ashes were obtained from the incinerator in Nuuk, Greenland, designated Nuuk-Fa1 and Nuuk-Fa2, in 2017 and 2018 respectively.

The final ash sample was obtained from Ryaverket in Borås, Sweden, designated Rya-Fa, in mid-2018. The five fly ash samples were sampled on-site by the operators. Relevant data about the three combustion units are included in Table 1. Included data represents the average operating conditions during the periods of sampling.

Table 1: Average operating conditions of combustion units during sampling periods.

	Amager Bakke	Nuuk Incineration	Ryaverket
Furnace	Grate Fired	Grate Fired	Fluidized Bed
Incineration Temp. [°C]	1025	1064	900
Waste type	Household/Industrial	Household/Construction	Household/Industrial
Boiler Ash separation	Gravitation	Gravitation/Cyclone	Gravitation/Cyclone
Flue gas filter type	Electrostatic	Electrostatic	Textile
Incineration Capacity $\left[\frac{\text{ton}}{\text{Day}}\right]$	1680	40	300
Fly Ash $\left[\frac{\text{ton}}{\text{Day}}\right]$	14.8	0.3	8.9
Bottom Ash $\left[\frac{\text{ton}}{\text{Day}}\right]$	237	4.7	17.8

2.2 Analytical Methods

The evaluated samples were dried at 50°C. Each experiment was made in triplicate, with the exception of the XRF and XRD analysis.

2.2.1 Particle size distribution

The particle size distribution of the five ash samples was measured with a Malvern Mastersizer 2000 particle size analyser. The particle size distribution was measured in a dry state. CEM I 52.5 N (MS/LA/≤2) cement with a bulk and absolute density of 1.1 and 3.2 g/cm³ was used for comparison between cement and the five fly ash samples. A Malvern Mastersizer 2000 determines the particle size distribution based on light scattering from spherical particles, although MSWI fly ash does not necessarily contain spherical particles.

Chemical Properties

2.2.2 Loss on Ignition

Loss on ignition (LOI) was measured at 950°C using a muffle furnace. 5.000 g ash was ignited, in uncovered crucibles for 24 hours, and subsequently cooled in a desiccator, ensuring constant mass had been achieved.

2.2.3 pH and Conductivity

The pH and conductivity of the ashes were measured on samples suspended in demineralized water, at L/S 2.5. Plastic bottles containing 5.00 g ash and 12.5 ml demineralized water was shaken for an hour at 195 rpm. The pH and conductivity were afterwards measured with a radiometer analytical electrode and conductivity meter respectively.

2.2.4 Water Soluble Fraction

The weight percentage of the water-soluble fraction was measured at L/S 5 with three consecutive washings. 100.00 g of ash was mixed with 500 ml demineralized water in an Erlenmeyer flask and shaken manually. The liquid phase was decanted through a filter, repeating this step for each wash. After the third washing, the entire sample was filtered and dried at 50°C until a constant mass had been achieved, and the mass loss weighed.

2.2.5 Water Soluble anion Content

The content of water-soluble anions was measured with Ion Chromatography (IC) at L/S 2.5. Samples of 10.00 g ash were mixed with 25 ml demineralized water in 50 ml bottles and shaken for 12 hours at 195

rpm. The liquid phase was extracted with a 0.45 μm filter syringe, and the content of Cl^- , SO_4^{2-} , and NO_3^- measured.

2.2.6 Carbonate Content

The carbonate content of the ashes was determined as an equivalent weight percentage of CaCO_3 , henceforth referred to as $\text{CaCO}_{3\text{eq}}$, from the volume by reaction with hydrochloric acid. The carbonate content in the ashes was determined based on a standard curve made from CaCO_3 . Samples of 2.5000 g ash were mixed with 20 ml 10 % HCl in a tightly closed bottle, connected to a Schiebler apparatus for volume readings.

2.2.7 Element content analysis

The elemental content of the five fly ash samples was determined using XRF analysis. Elements analysed were Si, Al, Fe, Ca, Mg, Na, K, S, Cl and P. The analysis was performed by an external laboratory using a SPECTRO GmbH X-LAB 2000 with a Pd-tube on ash samples ground to a particle size below 200 μm . Based on the element content, the equivalent content of oxides was calculated for comparison with En 450-1 2012 [8].

2.2.8 X-Ray Diffraction

X-Ray-Diffraction was performed using a PanAlytical X'pert PRO Θ - Θ System, with a target metal anode, made from Cu and 5 mm beam masks. Intensities were measured from 0 to 90 degrees. Samples were crushed with a mortar in order to increase the fineness, and backloaded into samples holders. Peak identification was performed using simple phase identification. The detection limit of the XRD analysis is $> 2 \text{ wt. } \%$.

2.2.9 Thermogravimetric analysis

Thermogravimetric analysis was performed using a NETZSCH STA 449 F3 Jupiter, fitted with a silicon carbide furnace and top loading. Aluminium oxide forms were filled with approximately 35 mg ash and initially heated to 29°C for 10 minutes. After 10 minutes, the temperature was raised to 900°C, at 10°C/min. Nitrogen was used as a purge gas, at a constant flow of 50 ml/min. The results are included as the first derivative of the temperature dependent mass loss.

3. Results and discussion

3.1 Physical properties

The particle size distributions of the five ash samples are depicted in Figure 1. Rya-Fa and Nuuk-Fa1 had the most similar size distributions, with average $d_{10,50,90}$ values of 8 μm , 19 μm , 41 μm , and 8 μm , 22 μm , 53 μm respectively. Arc-Fa1 deviated significantly from Nuuk-Fa1 and Rya-Fa. Arc-Fa1 consisted of finer particles than both Rya-Fa and Nuuk-Fa1, with a d_{10} value of 3 μm , similar to CEM I cement. Furthermore, approximately 28 % of Arc-Fa1 had a particle size below 10 μm . Arc-Fa1 was found to contain significantly coarser particles than Rya-Fa and Nuuk-Fa1, with d_{50} and d_{90} values of 50 μm and 248 μm .

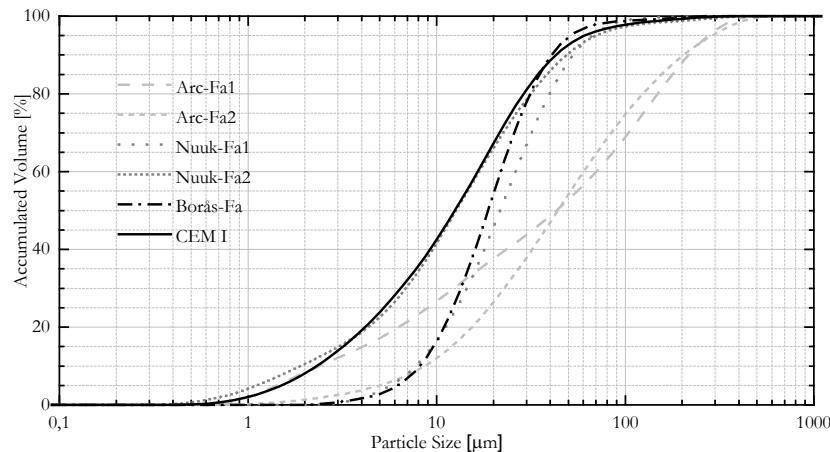


Figure 1: Particle size distribution of the five fly ash samples and CEM I cement.

Date of sampling was found to greatly affect the particle size distribution. Arc-Fa2 contained finer particles than Arc-Fa1 with a d_{10} value of 9 μm and approximately 13% of Arc-Fa2 had a particle size below 10 μm , with d_{50} and d_{90} values of 44 μm and 204 μm respectively. Significant differences could be observed between Nuuk-Fa2 and Nuuk-Fa1 as well. Nuuk-Fa2 contained both smaller particles than Nuuk-Fa1, with $d_{10,50,90}$ values of 2, 13 and 49 μm , and in slightly larger amounts, resembling CEM I cement in particle size distribution.

Remond et al. [11] and De Boom and Degrez [12] studied the particle size distribution of MSWI fly ash. Remond et al. [11] determined that MSWI fly ash had a size distribution between class C1 cement and the standard sand specified in NF/EN 196-1, with particle sizes between 1 μm and 600 μm , and a d_{50} of approximately 180 μm . They determined that MSWI fly ash had a larger spread in particle size than class C1 cement and standard sand. De Boom and Degrez [12] investigated electrostatic precipitator fly ash, with particles sizes between 0.1 μm and 1000 μm , and an approximate d_{50} of 55 μm . De Boom and Degrez [12] pre sieved their ashes using a 1000 μm sieve. The evaluated fly ash samples of the present study, deviate from Remond et al. [11] and De Boom and Degrez [12], with the exception of the samples from Amager Bakke. Arc-Fa1 and Arc-Fa2 had similar d_{50} values as the findings of De Boom and Degrez [12], and a similar large spread as reported by Remond et al. [11].

The potential filler effect of the five fly ash samples in the present study appears limited. According to Moosberg-Bustnes et al. [9], the addition of fine particles, with a maximum size of 125 μm can affect cement-based materials in two ways. It can have a physical effect, filling intergranular voids, improving the Packing density, and a surface chemical effect by enhancing hydration as nucleation sites. According to Scrivener et al. [10] the hydration enhancement is relatively minor for materials with a particle size distribution similar to cement and is only improved if the materials has a finer distribution than the cement. Furthermore, filler materials may increase the degree of hydration through dilution, Scrivener et al. [10]. Samples from Amager Bakke had particles larger than 125 μm and are not expected to contribute to the packing density or act as nucleation sites. Nuuk-Fa1 and Rya-Fa consisted of particles below 125 μm , and could potentially improve the packing density of cement-based materials. Both are coarser than CEM I and are therefore not expected to enhance the hydration as nucleation sites, only through dilution. Nuuk-Fa2 consisted of finer particles than CEM I, and could potentially act as nucleation sites to some extent, in addition to improving the packing density, and the degree of hydration through dilution. Based on its potential as a filler material, Nuuk-Fa2 would be the ash best suited for use in cement-based materials.

The obtained results in both the present study and by Remond et al. [11] and De Boom and Degrez [12]

suggests that the particle size distribution of MSWI fly ash can vary greatly, both depending on the location, combustion unit type and the time of sampling. The results indicate that the quality of MSWI fly ash as a filler material varies, between having a filler effect to some extent and potentially no effect at all.

3.2 Chemical properties

The calculated content of oxides is given in Table 2, together with the chloride concentrations and LOI. Included in Table 2 are the requirements specified in EN 450-1 2012 [8], and concentration ranges determined in other studies [8,13-24]. The measured pH, conductivity and equivalent CaCO_3 are included in Table 3. The measured water solubility and water soluble Cl^- , SO_4^{2-} and NO_3^- anions are included in Table 4. The DTG curves of the thermogravimetric analysis are shown in Figure 2. The diffractograms from the XRD analysis are included in Figure 3.

The five fly ash samples of the present study were characterized as having a low calculated content of both SiO_2 and Fe_2O_3 , varying between 4.5 and 6.0 respectively. The calculated content of Al_2O_3 was found to vary between the ash samples. The ashes from Nuuk and Ryaverket had 4.0 and 4.5 wt. % Al_2O_3 respectively, while Arc-Fa1 and Arc-Fa2 had a calculated content of 2.3 and 1.5 wt. % respectively. The evaluated samples all contained less reactive SiO_2 than specified in En 450-1 2012 [8], and had a combined content of SiO_2 , Fe_2O_3 and Al_2O_3 approximately equal to one-seventh the specified limit in EN 450-1 2012 [8]. Based on published literature [8,13-24] the potential SiO_2 content in MSWI fly ash varies between 0.1-38.0 wt. %, and the combined content of SiO_2 , Fe_2O_3 and Al_2O_3 between 2.1 and 56.1 wt. %. Municipal solid waste incineration fly ash could potentially have more than the required 25 wt. % reactive SiO_2 but does not contain enough SiO_2 , Fe_2O_3 and Al_2O_3 for the combined requirement.

Table 2: Calculated content of oxides [wt. %] as well as Cl and LOI [wt. %].

Included are DS/EN 450-1-2012 limit values and composition range given by published articles [8,13-25].

	Arc-Fa1	Arc-Fa2	Nuuk-Fa1	Nuuk-Fa2	Rya-Fa	En 450-1	Lit. Range
SiO_2	4.9	4.5	4.7	5.6	6.0	≥ 25	0.1 – 38.0
Al_2O_3	2.3	1.5	4.0	4.3	4.5	-	0.1 – 17.2
Fe_2O_3	1.1	1.0	0.7	0.8	1.7	-	0.5 – 6.8
$\Sigma (\text{SiO}_2, \text{Al}_2\text{O}_3, \text{Fe}_2\text{O}_3)$	8.3	7.0	9.4	10.7	12.2	≥ 70	2.1 – 56.1
CaO	21.0	13.4	33.6	40.6	40.6	$\leq 1.5/10^*$	7.4 – 42.2
MgO	0.8	0.7	0.9	1.3	1.7	≤ 4.0	0.5 – 7.2
Cl	8.9	3.0	20.0	22.0	12.0	≤ 0.1	2.9 – 31.7
SO_3	22.5	35.0	7.7	8.2	8.7	≤ 3.0	2.2 – 26.2
K_2O	13.3	14.5	10.7	11.3	2.4	-	0.5 – 15.7
Na_2O	17.5	9.17	21.6	21.6	6.2	-	2.0 – 17.0
$\text{Na}_2\text{O}_{\text{eq}}$	26.3	18.7	28.6	29.0	7.8	≤ 5.0	2.3 – 26.9
P_2O_5	1.4	3.0	1.3	1.8	1.7	≤ 5.0	0.3 – 1.7
LOI	3.8 ± 0.3	10.7 ± 7.5	31.2 ± 6.1	9.2 ± 0.2	21.4 ± 1.4	$\leq 9.0^{**}$	ND

*Free calcium oxide limit / Reactive calcium oxide limit.

**Category C

The five fly ash samples had calculated contents of CaO between 13.4 and 40.6 wt. %, MgO between 0.8 and 1.7, and P_2O_5 between 1.3 and 3.0 respectively. The five fly ash samples contained less MgO and P_2O_5 than the specified EN 450-1 2012 [8] limit and significantly higher CaO than the specified. The Ca in the five fly ash samples are likely not present in the ashes as free or reactive CaO. The XRD analysis, Figure 3, indicated that the Ca could be present as either CaSO_4 or CaCO_3 in the ashes, confirmed by among other Remond et al. [11] and Weibel et al. [15] as well, and the thermogravimetric analysis that showed mass loss corresponding to CaCO_3 . Compared to published articles [8,13-24] the calculated content of CaO, MgO

and P_2O_5 of the present study exhibited similar variations as the published literature, except Arc-Fa2 that had a higher content of P_2O_5 .

The measured content of Cl and the calculated content of SO_3 , varied greatly between the five fly ash samples of the present study, 3.0-22.0 wt. % and 7.7-35.0 wt. % respectively. Arc-Fa1 and Arc-Fa2 both had low amounts of Cl and high amounts of SO_3 , while Nuuk-Fa1 and Nuuk-Fa2 contained high amounts of Cl and low amounts of SO_3 , with Rya-Fa having similar amounts of Cl and SO_3 . A similar relationship could be observed in the studied articles [8,13-24], where the ashes either had a low Cl and high SO_3 content, or a low SO_3 and high Cl content. All five fly ash samples exceed the EN 450-1 2012 [8] limits for both Cl and SO_3 . The published articles studied [8,13-24], show similar results.

The five fly ash samples of the present study have varying degrees of calculated Na_2O_{eq} content, that for all samples exceed the 5.0 wt. % limit specified in EN 450-1 2012 [8]. With the exception of Rya-Fa, the five fly ash samples of the present study had a higher calculated content of Na_2O_{eq} , than reported in the published articles [8,13-24]. Although the five fly ash samples of the present study exceed the Na_2O_{eq} criteria, published articles indicate that the MSWI fly ash can contain less Na_2O_{eq} than specified in EN 450-1 2012 [8].

Large variations in LOI was observed between the five fly ash samples, varying between 3.8 wt. % and 31.2 wt. %. Variations between samples sourced from the same combustion unit could be observed as well, with the LOI increasing by 6.9 wt. % between Arc-Fa1 and Arc-Fa2, and decreasing 22 wt. % between Nuuk-Fa1 and Nuuk-Fa2. EN 450-1 2012 [8] specifies LOI limit values of 5.0, 7.0, and 9.0 wt. %. These limits are imposed, to inhibit the effect of unburned carbon on air-entraining admixtures. All of the fly ash samples exceed these limit values, making them unsuited for cement-based materials, with the exception of Arc-Fa1. Although, the measured LOI could be caused by other compounds, such as CO_2 release from $CaCO_3$ heating

The four fly ash samples with an LOI greater than 9 wt. % all had $CaCO_{3eq}$ contents between approximately 10 and 13 wt. %, while Arc-Fa1 contained 4.3 wt. % and a LOI of 3.8 wt. %. X-ray diffraction analysis indicated peaks for $CaCO_3$ in Nuuk-Fa1, Nuuk-Fa2 and Rya-Fa. $CaCO_3$ peaks were not observed in Arc-Fa1 and Arc-Fa2, suggesting that a different carbonate phase could be present in Arc-Fa1 and Arc-Fa2 or that the HCl used during the $CaCO_{3eq}$ measurement reacted with other phases than carbonates.

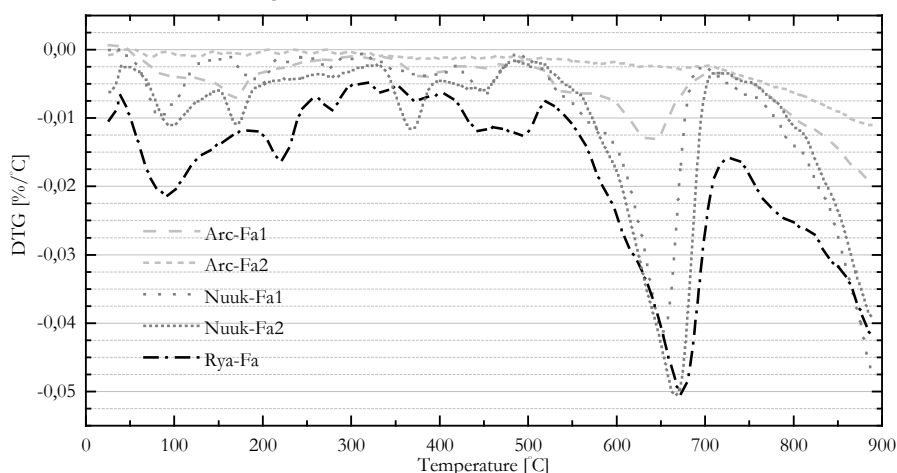


Figure 2: DTG analysis of the five fly ash samples.

The DTG curves indicated that the majority of the mass loss occurred after 500°C and 700°C. Additionally, several small dips occurred between 0 and 500°C, at varying temperatures, potentially indicating mass loss

from several different phases.

According to Galan et al [27], calcium carbonate decomposes between 700 and 1000°C in an N₂ atmosphere, corresponding to the mass loss after 700°C observed in the present study, indicating that Ca is partially present as CaCO₃. The observed mass loss between 500 and 700°C could indicate the presence of an unknown carbonate. Arc-Fa2 was found to have the largest fraction of CaCO_{3eq}, without showing any significant mass loss between 500 and 1000°C, suggesting that the HCl used during the CaCO_{3eq} measurement reacted with other phases than carbonates. Several of the discrepancies discussed here, regarding the CaCO_{3eq} and TGA measurements cannot be explained and should be investigated further.

Four of the five fly ash samples were alkaline, with a pH between 11 and 12, and electrical conductivities between 90 and 150 mS/cm². Pedersen et al. [19] measured the pH of two MSWI fly ash samples from different combustion units and determined their pH to be 10.8 and 12.2 respectively.

The pH of Arc-Fa2 differs from these results with a pH of 6.47, indicating that ash with a neutral pH can be produced as well as alkaline ash. The lower pH of Arc-Fa2 could be caused by its high ratio of sulphur to other elements. X-ray diffraction analysis indicated the presence of several different sulphur compounds in Arc-Fa2, not observed in the other ash samples.

Table 3: Measured pH, conductivity, equivalent CaCO₃ and water solubility of the five fly ash samples.

	Arc-Fa1	Arc-Fa2	Nuuk-Fa1	Nuuk-Fa2	Rya-Fa
pH [-]	12.0 ± 0.1	6.5 ± 0.0	11.6 ± 0.0	11.9 ± 0.0	11.5 ± 0.0
Conductivity [mS/cm]	113.7 ± 3.5	94.7 ± 1.3	149.6 ± 21.1	146.8 ± 4.5	93.5 ± 1.2
CaCO _{3eq} Content [wt.%]	4.3 ± 0.2	13.0 ± 0.1	11.8 ± 0.8	10.4 ± 0.1	9.9 ± 0.1

High solubility in water was observed in the five fly ash samples, varying between approximately 27.7 wt. % and 55.7 wt. %. The element content analysis indicated that the majority of the ash samples contained K, Na, Cl and S. The measured K, Na, Cl and S could be present in a soluble form. X-ray diffraction indicated that the five fly ash samples either contained NaCl, KCl or both. NaCl or KCl were confirmed as potential phases by other studies as well, Remond et al. [11] and Weibel et al. [15]. Of the five fly ash samples, Rya-Fa contained the smallest amount of potassium, sodium, chlorine and sulphur and was also the least soluble ash. Nuuk-Fa1 and Nuuk-Fa2 both contained similar amounts of K, Na, Cl and S, although Nuuk-Fa1. Arc-Fa1 and Arc-Fa2 had varying solubility's; at 39.4 and 55.7 wt. % respectively. Both had a significantly lower content of Cl than the other fly ash samples, containing higher amounts of soluble sulphur instead.

Sulphate was not present as water-soluble anions in as high amounts in Nuuk-Fa1, Nuuk-Fa2 and Rya-Fa, indicating that the sulphate where bound in non-soluble form. Arc-Fa1 and Arc-Fa2 also contained non-soluble sulphate, as the wt. % removed did not match the measured wt. %. Chlorine was removed from the ash samples, in amounts matching the wt. % measured with XRF analysis, indicating that the majority of the chlorine in the ashes was water soluble after three washing at L/S 5. The Removed amount of Cl in Rya-Fa, were 5% higher than found with XRF, indicating that the amount of Cl in Rya-Fa is higher than measured with XRF.

Table 4: Measured wt. % water solubility and content of water-soluble Cl^- , SO_4^{2-} and NO_3^- anions.

		Arc-Fa1	Arc-Fa2	Nuuk-Fa1	Nuuk-Fa2	Rya-Fa
Water Solubility	[wt.%]	39.4 ± 0.5	55.7 ± 2.3	42.4 ± 1.3	38.0 ± 0.6	27.7 ± 0.9
Cl^-	[wt.%]	8.1 ± 0.1	2.3 ± 0.2	19.1 ± 0.9	22.2 ± 0.4	17.6 ± 0.5
SO_4^{2-}	[wt.%]	7.5 ± 0.0	21.1 ± 0.6	0.8 ± 0.0	0.6 ± 0.0	0.0 ± 0.0
NO_3^-	[ppm]	194 ± 3	503 ± 17	84 ± 2	270 ± 10	2396 ± 87

Regardless of the type of combustion unit, furnace, incineration temperature and flue gas filter type, or the country it is located in evaluated in the present study, they all produced fly ash of insufficient quality for use in cement-based materials, when compared to the specified limits in EN 450-1 2012 [8]. The five fly ash samples studied did not contain enough reactive SiO_2 , or Fe_2O_3 and Al_2O_3 as specified, and could therefore have limited benefits when mixed with cement-based materials. Instead, the ashes exceeded the limits for free and reactive CaO , Cl , SO_3 , $\text{Na}_2\text{O}_{\text{eq}}$ and LOI , potentially having negative consequences if mixed with cement-based materials. Additional analyses indicated that the ashes did not contain free or reactive CaO or that the LOI was exceed due to unburned carbon. Any potentially negative consequences would therefore be limited to Cl , SO_3 and the total content of alkalis $\text{Na}_2\text{O}_{\text{eq}}$. The only limits in EN 450-1 2012 [8] not exceeded was the MgO and P_2O_5 limits. Sampling MSWI fly ash from the same combustion unit months apart showed both significant and less significant changes to the chemical properties. Arc-Fa2 contained significantly more SO_3 and Cl Compared to Arc-Fa1. The differences between the two samples could also be observed with the pH, $\text{CaCO}_{3\text{eq}}$ and solubility. Arc-Fa2 was more soluble in water and had a neutral pH, instead of an alkaline pH. The two samples had different peaks occurring in their diffractograms as well. The two samples could, therefore, have different results when mixed with cement. Nuuk-Fa1 and Nuuk-Fa2 had a very similar chemical composition with the exception of a varying LOI , with almost identical diffractograms, and could have similar results when mixed with cement. Municipal solid waste incinerators are therefore capable of having both a steady and non-steady output. Regardless of when the samples was sourced, fly ash of insufficient quality for use in cement-based materials were produced.

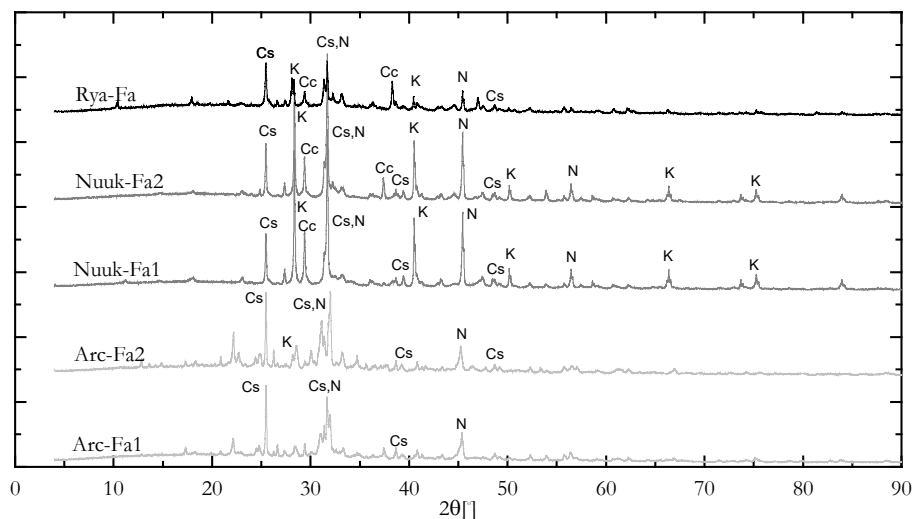


Figure 3: Diffraction graphs of the five fly ash samples. Cs = CaSO_4 , Cc = CaCO_3 , K = KCl and N = NaCl . Other potential phases include CaClOH , K_2ZnCl_4 , KNaSO_4 and $\text{Mg}_2\text{NaOH}(\text{SO}_3)_2 \cdot \text{H}_2\text{O}$.

When compared to published literature [8,13-24], MSWI fly ash appears to have an average chemical composition of insufficient quality to be used in cement-based materials. Hamernik and Frantz [18] studied fly ashes of above average quality and analysed the pozzolanic activity index, replacing 35%

cement with MSWI fly ash containing a combined content SiO_2 , Fe_2O_3 and Al_2O_3 above 50 wt. %. They concluded that their MSWI fly ashes had cement pozzolanic indexes comparable to coal fly ash, but showed no cementitious properties. Pozzolanic reactions in cement occur between $\text{Ca}(\text{OH})_2$ and amorphous SiO_2 forming C-S-H or with amorphous aluminosilicate forming calcium aluminate hydrate phases or calcium aluminate silicate hydrate phases as described by Justness [3]. Any occurrence of pozzolanic reactions are therefore limited when the five fly ash samples of the present study are mixed with cement and water, due to the low content of SiO_2 , Fe_2O_3 and Al_2O_3 and would not have a similar effect as described by Hamernik and Frantz [18].

4. Conclusions

The presented study aimed at assessing the quality of untreated MSWI fly ashes with regard to their use in cement-based materials. The assessment was based on the chemical requirements specified in the European standard EN 450-1 2012 [8] and potential use as filler materials based on their particle size distribution. To assess the filler potential, the requirements for improving the packing density, enhancing hydration and dilution effect was used, as discussed by Mooseberg-Bustnes et al. [9] and Scrivener et al. [10]. The following can be concluded based on the results.

A total of five fly ash samples was acquired from three combustion units for the evaluation, Arc-Fa1, Arc-Fa2, Nuuk-Fa1, Nuuk-Fa2 and Rya-Fa. Arc-Fa2 and Nuuk-Fa2 were sampled several months after Arc-Fa1 and Nuuk-Fa1. Sampling from the same combustion unit several months apart indicated that the incinerator in Nuuk produced fly ashes with similar chemical properties, while Amager Bakke (Arc-Fa) produced fly ash with varying chemical properties. Regardless of the time of sampling, the combustion unit type or the units' location, all the investigated MSWI fly ash samples did not fulfil the chemical property requirements specified in EN 450-1 2012 [8]. The samples did not contain enough reactive SiO_2 or have a high enough combined content of SiO_2 , Fe_2O_3 and Al_2O_3 , indicating limited pozzolanic activity. The five fly ash samples exceeded the limits for free and reactive CaO, Cl, SO_3 as well as equivalent content of alkalis $\text{Na}_2\text{O}_{\text{eq}}$ and LOI, potentially having several negative consequences if mixed with cement-based materials. Additional tests indicated that the CaO in the could be present as CaCO_3 instead of free or reactive CaO. The limits for MgO and P_2O_5 content were not exceeded.

Contrary to the observed chemical properties, Nuuk-Fa1 and Nuuk-Fa2 was not physically similar and had different particle size distributions. Furthermore, it was found that all five fly ash samples had different particle size distributions with different potential as filler material when compared to the requirements discussed by Mooseberg-Bustnes et al. [9] and Scrivener et al. [10]. Arc-Fa1 and Arc-Fa2 contained particles larger than 125 μm and would only improve the packing density and enhance hydration with limited effect. The two samples could still potentially improve hydration through dilution. Nuuk-Fa1 and Rya-Fa had a particle size distribution less than 125 μm and could potentially improve the packing density. Their particle size distribution was coarser than cement and would potentially only enhance hydration through dilution. Nuuk-Fa2 had a finer particle size distribution slightly finer than cement and could potentially both improve packing density and enhance the hydration of cement-based materials.

5. Acknowledgement

Amager Resource Center is acknowledged for their cooperation in obtaining ash from their facility. Furthermore, Kommuneqarfik Sermersooq and Borås Energy och Miljö, are acknowledged for sampling and sending the fly ash samples from the Nuuk incinerator in Greenland and Ryaverket in Sweden. Finally, the lab technicians Ebba Schnell, Malene Møller, Anna Schroeder and Natasja Dueholm are recognized for their assistance in measuring the many properties of the fly ashes.

6. References

- [1] Jos G.J. Olivier; Greet Janssens-Maenhout; Marilena Muntean; Jeroen A.H.W. Peters, Trends in global co 2 emissions 2016, (2016) 86.
- [2] H. Justnes, How to Make Concrete More Sustainable, *J. Adv. Concr. Technol.* 13 (2015) 147–154. doi:10.3151/jact.13.147.
- [3] H. Justnes, Influence of SCMs on hydration and durability of blended cements - Chemical and Physical Principles, *J. Chinese Ceram. Soc.* 13 (2554) 1359–1371.
- [4] K.L. Scrivener, V.M. John, E.M. Gartner, Eco-efficient cements: Potential, economically viable solutions for a low-CO₂, cementbased materials industry, (2016).
- [5] H. Zhang, Y. Zhao, Toxicity Analysis of Municipal Solid Waste Incineration (MSWI) Fly Ash, 2009 3rd Int. Conf. Bioinforma. Biomed. Eng. (2009) 1–4. doi:10.1109/ICBBE.2009.5163694.
- [6] C. Ferreira, A. Ribeiro, L. Ottosen, Possible applications for municipal solid waste fly ash, *J. Hazard. Mater.* 96 (2003) 201–216.
- [7] L. Kozakova, T. Bakalar, M. Zelenak, M. Prascakova, Solidification of MSWI fly-ash with regard to hazardous metals leaching, *Acta Montan. Slovaca.* 18 (2013) 129–139.
- [8] D.S. En, Dansk standard Flyveaske til beton – Del 1: Definition , specifikationer og overensstemmelses- kriterier, (2012).
- [9] H. Moosberg-Bustnes, B. Lagerblad, E. Forssberg, The function of fillers in concrete, *Mater. Struct. Constr.* 37 (2004) 74–81. doi:10.1617/13694.
- [10] K.L. Scrivener, B. Lothenbach, N. De Belie, E. Gruyaert, R. Snellings, A. Vollpracht, TC 238-SCM : hydration and microstructure of concrete with SCMs State of the art on methods to determine degree of reaction of SCMs, (2015) 835–862. doi:10.1617/s11527-015-0527-4.
- [11] S. Remond, P. Pimienta, D.P. Bentz, Effects of the incorporation of Municipal Solid Waste Incineration fly ash in cement pastes and mortars I. Experimental study, *Cem. Concr. Res.* 32 (2002) 303–311. doi:10.3130/jaabe.3.1.
- [12] A. De Boom, M. Degrez, Belgian MSWI fly ashes and APC residues: A characterisation study, *Waste Manag.* 32 (2012) 1163–1170. doi:10.1016/j.wasman.2011.12.017.
- [13] T.C. Lee, M.K. Rao, Recycling municipal incinerator fly- and scrubber-ash into fused slag for the substantial replacement of cement in cement-mortars, *Waste Manag.* 29 (2009) 1952–1959. doi:10.1016/j.wasman.2009.01.002.
- [14] K.L. Lin, K.S. Wang, B.Y. Tzeng, C.Y. Lin, The reuse of municipal solid waste incinerator fly ash slag as a cement substitute, *Resour. Conserv. Recycl.* 39 (2003) 315–324. doi:10.1016/S0921-3449(02)00172-6.
- [15] G. Weibel, U. Eggenberger, S. Schlumberger, U.K. Mäder, Chemical associations and mobilization of heavy metals in fly ash from municipal solid waste incineration, *Waste Manag.* 62 (2017) 147–159. doi:10.1016/j.wasman.2016.12.004.
- [16] G.J. Song, K.H. Kim, Y.C. Seo, S.C. Kim, Characteristics of ashes from different locations at the MSW incinerator equipped with various air pollution control devices, *Waste Manag.* 24 (2004) 99–106. doi:10.1016/S0956-053X(03)00073-4.
- [17] C.H. Lu, J.C. Chen, K.H. Chuang, M.Y. Wey, The different properties of lightweight aggregates with the fly ashes of fluidized-bed and mechanical incinerators, *Constr. Build. Mater.* 101 (2015) 380–388. doi:10.1016/j.conbuildmat.2015.10.068.

-
- [18] J. Hamernik, G. Frantz, Physical and Chemical Properties of Municipal Solid Waste Fly Ash.pdf, *ACI Mater. J.* (1991).
 - [19] A.J. Pedersen, L.M. Ottosen, A. Villumsen, Electrodialytic removal of heavy metals from different fly ashes: Influence of heavy metal speciation in the ashes, *J. Hazard. Mater.* 100 (2003) 65–78. doi:10.1016/S0304-3894(03)00064-5.
 - [20] A.P. Bayuseno, W.W. Schmahl, Characterization of MSWI fly ash through mineralogy and water extraction, *Resour. Conserv. Recycl.* 55 (2011) 524–534. doi:10.1016/j.resconrec.2011.01.002.
 - [21] Y. Liu, L. Zheng, X. Li, S. Xie, SEM/EDS and XRD characterization of raw and washed MSWI fly ash sintered at different temperatures, *J. Hazard. Mater.* 162 (2009) 161–173. doi:10.1016/j.jhazmat.2008.05.029.
 - [22] K.S. Wang, K.L. Lin, Z.Q. Huang, Hydraulic activity of municipal solid waste incinerator fly-ash-slag-blended eco-cement, *Cem. Concr. Res.* 31 (2001) 97–103. doi:10.1016/S0008-8846(00)00423-3.
 - [23] V. Funari, R. Braga, S.N.H. Bokhari, E. Dinelli, T. Meisel, Solid residues from Italian municipal solid waste incinerators: A source for “critical” raw materials, *Waste Manag.* 45 (2015) 206–216. doi:10.1016/j.wasman.2014.11.005.
 - [24] F.Y. Chang, M.Y. Wey, Comparison of the characteristics of bottom and fly ashes generated from various incineration processes, *J. Hazard. Mater.* 138 (2006) 594–603. doi:10.1016/j.jhazmat.2006.05.099.
 - [25] K.S. Wang, K.L. Lin, T.Y. Lee, B.Y. Tzeng, The hydration characteristics when C2S is present in MSWI fly ash slag, *Cem. Concr. Compos.* 26 (2004) 323–330. doi:10.1016/S0958-9465(02)00144-0.
 - [26] A. Polettoni, R. Pomi, P. Sirini, F. Testa, Properties of Portland cement - Stabilised MSWI fly ashes, *J. Hazard. Mater.* 88 (2001) 123–138. doi:10.1016/S0304-3894(01)00292-8.
 - [27] I. Galan, F.P. Glasser, C. Andrade, Calcium carbonate decomposition, *J. Therm. Anal. Calorim.* 111 (2013) 1197–1202. doi:10.1007/s10973-012-2290-x.

Qualification of Biomass Derived Ashes for Application as a Cement Replacement and Quantification of Biomass Streams in The Netherlands

N. Mühleisen^{1,2}, H. Jonkers¹, L. Tosti^{3,4}

[1] Delft University of Technology, Faculty of Civil Engineering & Geosciences, Section of Materials & Environment – Microlab, Stevinweg 1, 2628 CN Delft, The Netherlands

[2] SGS INTRON B.V., Doctor Nolenslaan 126, 6136 GV Sittard, The Netherlands

[3] Wageningen University and Research, Department of Soil Quality, P.O. Box 47, 6700 AA, Wageningen, The Netherlands

[4] ECN part of TNO, P.O. Box 15, 1755 ZG, Petten, The Netherlands

Abstract

Biomass combustion has long served as a source of energy. Due to environmental concerns, its use is on the rise. Global estimates project that biomass derived ash will reach 476 million tonnes per year. Currently limited applications for these biomass-derived ashes exist. A better understanding of the ash properties is needed to find suitable applications. New applications will keep these minerals in the circular economy.

This work identifies biomass derived ashes with a composition necessary for hydraulic properties. Either the ash already contains hydraulic minerals, or it can be processed to yield hydraulic minerals. The investigation used information from the Phyllis 2 database and the ALLASKA database. Ash suitability was determined by the chemical and mineralogical composition. This was evaluated based on the original biomass source and the conversion technology. The first aim of this study was to identify calcium and silicon rich biomass ashes. These ashes can contain hydraulic minerals or have the chemical composition necessary to form them. The amount of cement produced can be reduced if biomass derived ash is used as a cement replacement. The amount of CO₂ associated with cement production can be reduced if biomass derived ash is used to replace cement raw materials. The second aim of this study was to estimate the potential cement and CO₂ reduction in the Netherlands. Applicable biomass waste streams available in The Netherlands were quantified. Wood and woody biomass (WWB) and herbaceous and agricultural biomass (HAB) contained an average of 12.3 and 40.2 M.-% SiO₂. WWB contained CaO with a concentration up to 65.0 M.-%. Ashes derived from the Organic residues and contaminated biomass (OR-CB) category paper sludge showed the potential to provide both CaO and SiO₂. These minerals were present in the necessary quantities to either contain clinker minerals or form them. The type of combustion technique used impacts the ash quality. Fluidized beds were shown to produce ashes that have higher contents of CaO and SiO₂. The authors identified biomass waste streams were in The Netherlands, with the potential to serve as a source of energy. Verge grass, forestry thinnings, agricultural wastes and industrial wastes can produce valuable ash. These streams result in an estimated 2.0 Mtonnes of ash.

Keywords: Biomass derived ash; Clinker minerals; Alternative cements

1. Introduction

Biomass' stake in the production of energy has increased in recent decades. Currently biomass provides about 8% of the world's energy for heat, electricity and transportation fuels. According to predictions biomass use could grow to 33-50% by 2050. Of the total biomass derived energy, 95-98% stems from direct combustion [1] which produces biomass derived ash. If biomass derived energy grows to the predicted range, we will produce 476 million tons of biomass ash annually (assuming 7 billion tons of biomass combusted with a 6.8% ash yield).

Producing energy with biomass instead of coal has positive environmental impacts [2] but negative impacts for the concrete industry. Coal-derived fly ash has partially replaced ordinary Portland cement (OPC) in concrete applications for decades. European standard EN-450 only tolerates fly-ash derived from coal combustion or co-combustion of coal and biomass. For co-combustion, the biomass must be clean wood and comprise only 50 M.-% or less. At these percentages, coal properties dominate the fly ash properties and composition. European standards do not allow pure biomass derived ashes in blended cements. Currently this is a minor problem given the small quantities of biomass ash produced. But with the combustion of more biomass and less coal, this problem will grow in the future.

The composition of biomass derived ash differs from coal-derived ash. Biomass ash often has higher alkali metal and chloride contents. These elements can create durability problems in concrete, making biomass ash less attractive for concrete applications. To determine if biomass derived ash is a suitable replacement for coal derived ash, researchers have investigated their ability to partially replace cement in concrete applications.

Some biomass ashes are valuable as a partial cement replacement. One such ash is rice husk ash (RHA). Due to its high contents of amorphous silica, RHA can improve the strength and durability of concrete [3]–[9]. When replacing 10 M.-% of OPC with RHA with a particle size of 6-10 μm , the concrete has a stronger interfacial transition zone and lower permeability[3], [10]. Farmers in south east Asia produce RHA when the agricultural waste is burnt in open fields. This method of combustion gives little control over efficiency and produces variable ashes. A similar agricultural waste is sugar cane bagasse ash (SCBA). Farmers produce SCBA in South America. They combust sugar cane bagasse waste to provide heat and power to processing the sugar cane [11]–[14]. Due to more controlled combustion conditions, the ash has a higher level of consistency. Replacing 20% of OPC with SCBA improves the early strength and increases the density of the concrete microstructure. The higher density reduces water permeability and chloride penetration [15], [16]. Combining different biomass sources before combustion can also produce a functional ash. Thailand produces large quantities of both sugar and rice. These crops result in the annual production of roughly 66 million tonnes of sugarcane bagasse and 10 million tons of rice husk. Combustion of 82.5% bagasse, 15% rice husk, and 2.5% chop wood in small power plants produces electricity for the sugar mills [17]. Using this ash to replace 20% of cement results in a higher compressive strength and a 65% reduction in the chloride diffusion coefficient [18].

Researchers have also investigated the application of woody biomass derived ash (WBA) as a cement replacement. Using WBA as a partial cement replacement reduces the compressive, flexural, and tensile strength of concrete. But when the SiO_2 content is high enough, the strength increases with longer hydration times [19]. Unlike RHA and SCBA, WBA contains less SiO_2 and does not function as a pozzolanic admixture. The chemical and physical properties of WBA vary greatly and are difficult to predicted [20]. But given the predominance of CaO in woody biomass and the conversion temperatures, reactive calcium silicates can be present.

Most research into cement replacement with biomass is locally based. Investigations focuses on the use of a single regional biomass derived ash. There is limited research on the general trends which would make application more widespread. Additionally, when biomass derived ash is used as a cement replacement, typically lower replacement rates (10-20%) are evaluated. To have a larger reduction in the CO₂ emissions associated with cement production higher replacement rates are necessary. One possible method to produce a more equivalent cement replacement is to use the biomass derived ash as a clinker raw material replacement. Currently the research into the use of biomass derived ash as a cement raw material replacement is limited to a few types of biomass. Most studies focus on the performance of municipal sewage sludge [21], [22] and waste from the paper industry [23]–[25] as raw materials for the production of cement

The presence of hydraulic minerals in biomass derived ash could allow for higher replacement rates. This work seeks to ultimately increase the amount of cement (or cement raw materials) which are replaced by biomass derived ash. Higher replacement rates will lower the CO₂ emissions associated with cement production by reducing the amount of clinker produced or reducing the amount of limestone that is decarbonated in the production of clinker. Additionally, identification of the biomass sources and conversion technology which enables the formation of hydraulic minerals could enable the intentional production of hydraulic biomass derived ash as a by-product in future energy production.

The aim of this study is the identification of calcium and silicon rich biomass ashes. These ashes can contain hydraulic minerals or have the chemical composition necessary to form them. The investigation covered the ash production chain from biomass selection through combustion technology. Information was obtained from the Phyllis 2 database and the ALLASKA database. The authors assessed the ashes on their chemical composition, mineralogy and physical properties. The compositions were assessed on parameters like the input biomass and conversion technology. Those parameters which were beneficial to the biomass ash composition were identified. The extent to which they can be manipulated to get an ash with high potential for application to (partial) replace cement will be assessed. In the context of the Netherlands, the volume of the identified biomass waste streams available were quantified. The amount of cement produced can be reduced if biomass derived ash is used as a cement replacement. The amount of CO₂ associated with cement production can be reduced if biomass derived ash is used to replace cement raw materials. The second aim of this study was to estimate the potential cement and CO₂ reduction in the Netherlands based on the calculated volumes.

2. Materials and Methods

2.1 Biomass and Biomass Derived Ash Data

2.1.1 *Phyllis 2 database*

Developed within the PHYDADES European project, the Phyllis2 database provides reliable information on biomass fuels and biomass ashes. The database contains almost 3000 records of individual biomass or waste materials. The ECN Phyllis scheme groups biomass batches into 16 different classes based on practicality and plant physiology. The authors grouped the classes relevant to this study in three distinct categories: wood and woody biomass (WWB), herbaceous and agricultural biomass (HAB) and organic residues and contaminated biomass (OR-CB). Segregation of the data into these categories allowed for easier interpretation and drawing conclusions on ash composition based on biomass type.

The authors limited WWB to the class untreated wood. Untreated wood encompasses all fresh wood including park wood waste and wood from saw mills. This category includes both hardwoods and softwoods. These two divisions cover many individual tree species (such as beech, birch, oak, pine, poplar and willow). This category also includes different tree parts, including bark, cork, leaves and needles.

The HAB group includes plants, grass, straw and some organic residues. The plant group comprises fruits, vegetables and flowers or garden plants and residues from agriculture and horticulture. Grass encompasses subgroups like hemp, jute and kenaf as well as verge grass. Verge grass is a mixture of different (unidentified) grass species. Straw and grass are physiologically similar but here straw refers to the dry stalks of cereal plants after removal of the grain and chaff. This includes wheat, barley, rice and maize. Husk shells and pits are an organic residue included in this group.

The OR-CB includes all organic residue that are not a direct result of agriculture and horticulture. This encompasses waste paper, residues from the food industry, the organic fraction from domestic waste, municipal solid waste (MSW) and refuse derived fuel (RDF). Furthermore, OR-CB includes the sludge. This covers sludge from sewage water treatment, the paper industry, waste water treatment, and food processing. Lastly OR-CB includes treated wood. Treated wood encompasses composted wood, demolition wood, preserved wood and particle board.

2.1.2 The Allaska Database

The ALLASKA database was built under the ash program at Värmeforsk (Thermal Engineering Research Association) with the intention of promoting the environmentally responsible utilization of ashes. The database is a collection of quantitative information on the properties of residues from combustion processes in Swedish power plants. The ALLASKA database contains information on geotechnical data, leaching properties, chemical composition, particle size and organic contents of ash residues coming from the combustion of biomass and waste materials in different types of boilers.

In this study, the ALLASKA database analysis was limited to biomass-based fuels. Biomass derived ashes were evaluate based on the reactor in which they were generated, i.e. in a pulverised fuel reactor (PF), grate stoker furnace (GSF), circulating fluidized bed (CFB) or a bubbling fluidized bed (BFB).

2.2 Methods of Analyses

The data from the two different databases was statistically analysed based on their chemical compositions. Attention was given to the clinker mineral forming elements (Ca, Si, Al and Fe) and notice was taken of those which can have adverse effects on clinker production and cement hydration (alkalis and phosphorous). The main objective was to find biomass-derived ashes that

1. Feature hydraulic properties and can act directly as a cement replacement or
2. Have the necessary composition to act as a clinker raw material replacement.

Therefore, the focus of this specific study was on calcium and silicon rich biomass ashes that could potentially contain calcium silicate based hydraulic minerals such as alite (C_3S) and belite (C_2S) or form them when subjected to a secondary thermal treatment. Ashes were sought with CaO concentrations of 61-69M.-% and SiO_2 concentrations of 15-20M.-%.

3. Results

3.1 Phyllis Database

3.1.1 Clinker Forming Oxides

To determine a relationship between ash composition (express as % of oxides of the ash residue) and the biomass source, data from the Phyllis database was first grouped into three distinct categories. Subsequently the concentrations of the 4-main clinker mineral forming oxides were examined per category. Figure 1 depicts the SiO_2 fractions for the averaged WWB, HAB and ORCB categorized samples relative to one another.

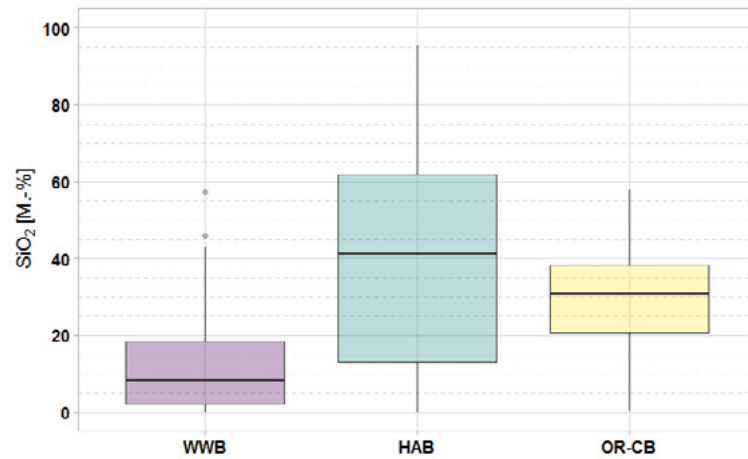


Figure 1: SiO_2 contents of biomass ash samples from the Phyllis database for the categories wood and woody biomass (WWB), herbaceous and agricultural biomass (HAB) and organic residues and contaminated biomass (OR-CB). Target SiO_2 concentration is 15-20 M%.

In view of a composition that could either contain or produce clinker minerals, the SiO_2 fraction of the raw feed should be around 15-20M.-%. Parts of the interquartile range of WWB and HAB cover the target concentration. WWB shows a range of 0 to 57.2 M.-% with an average of 12.3 M.-%. The median is 8.3 M.-% and the third quartile group (Q3) covers the desired range. HAB shows a range of 0 to 95.6 M.-% with an average of 40.2 M.-%. The median is 41.3 and the second quartile group (Q2) covers the desired range. Despite having a median between the other two groups (30.8 M.-%), the interquartile range of OR-CB falls above the theoretically favoured range.

To draw conclusion on the potential applicability of WWB and HAB ash regarding SiO_2 content, the sub-categories must be examined independently. As can be seen in Figure 2, the sub-category of husk shell & pits covers the desired SiO_2 range in its Q2. The median of husk shell & pits is 20.5 M.-%. The sub-categories of WWB are shown in Figure 3. Softwood has a preferable SiO_2 concentration to hardwood with medians of 15.6 M.-% and 2.4 M.-% respectively.



Figure 2: SiO_2 concentration within the herbaceous and agricultural biomass (HAB) sub-categories: grass, reed, husk & pit, barley, corn, wheat straw, rice straw, straw, and agricultural residues from the Phyllis database. Target SiO_2 concentration is 15-20 M%.

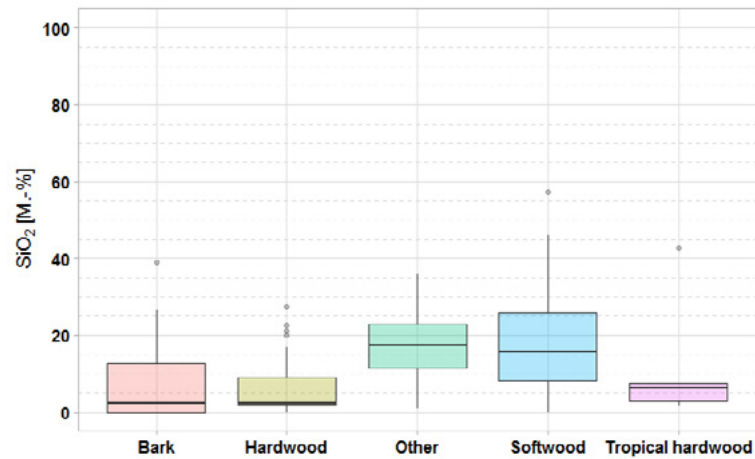


Figure 3: SiO₂ concentration within the wood and woody biomass (WWB) sub-categories: bark, hardwood, other, softwood and tropical hardwood from the Phyllis database. Target SiO₂ concentration is 15-20 M%.

With respect to CaO content, theoretical optimal contents of biomass derived ashes fall in the range of 61-69M.-%. On average the WWB CaO contents are the highest with a median concentration of 33.3 M.-% (Figure 4). While the Q3 is below the desired range the fourth quartile group (Q4) included part of the range. Both HAB and OR-CB fall significantly below the desired amounts of CaO but they have a few outliers with notable CaO. In the category HAB, one specific sample derived from rape straw contained 66.0 M.-% CaO. The next highest value (50.3 M.-% CaO) also originated from rape straw. In the category OR-CB, the two highest CaO contents came from paper residue with 60.4 and 57.4 M.-% (Figure 6).

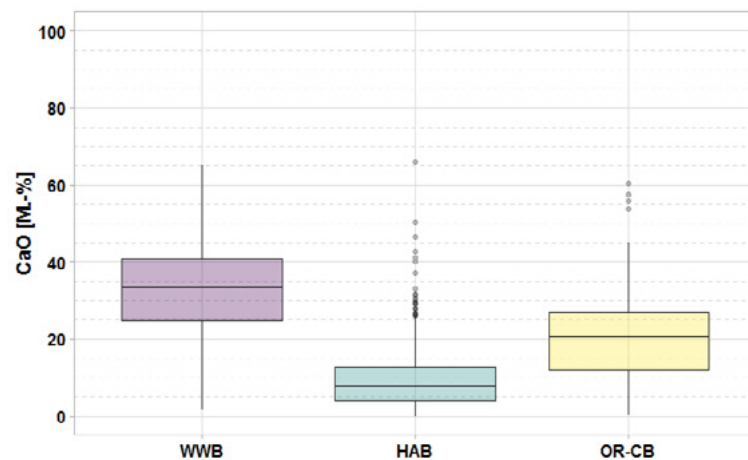


Figure 4: CaO concentration of biomass ash samples from the Phyllis database for the categories wood and woody biomass (WWB), herbaceous and agricultural biomass (HAB) and organic residues and contaminated biomass (OR-CB). Target CaO concentration is 61-69 M%.

In Figure 5 both bark and hardwoods feature the highest median CaO content, 39.2 and 36.9 M.-% respectively. The Q4 of hardwood begins to cover the desired range of CaO. All the other WWB sub-categories fall below what is necessary. Considering the CaO content of the hardwoods, no clear trends could be identified. While samples of oak, poplar willow and birch ashes were all found amongst the 25% with the highest CaO content, they also amounted to the 25% with the lowest. There is no information as to which part of the trees the samples originated from and as a result, different tree sections could provide the explanation for the high distribution. Since tropical hardwood and softwood derived ashes have lower CaO contents, they are less suitable for clinker production.

While rape straw can potentially provide enough CaO, the remaining biomass sources in the HAB category cannot. OR-CB ashes also exhibit a lower average CaO content. But the variability in CaO content of OR-CB ashes appeared large, as reflected by a range of 0.2 to 60.4M% and a standard deviation of 13.3. Looking deeper at the individual sub-categories, OR-CB derived ashes show trends (Figure 6). Two waste paper ashes and two treated wood ashes are outliers and contain substantial CaO. On average, paper sludge has the highest CaO contents, but does not have any individual sample that fall into the desired range.

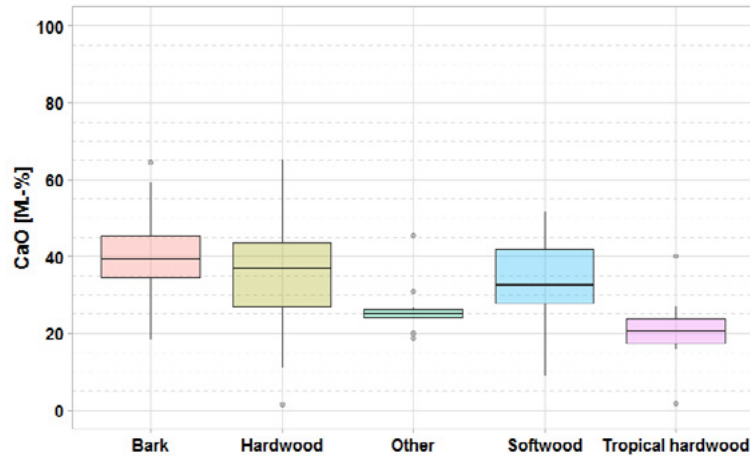


Figure 5: CaO content for individual wood and woody biomass (WWB) derived sub-categories: Bark, hardwood, softwood, tropical, other and treated wood from the Phyllis database. Target CaO concentration is 61-69 M%.

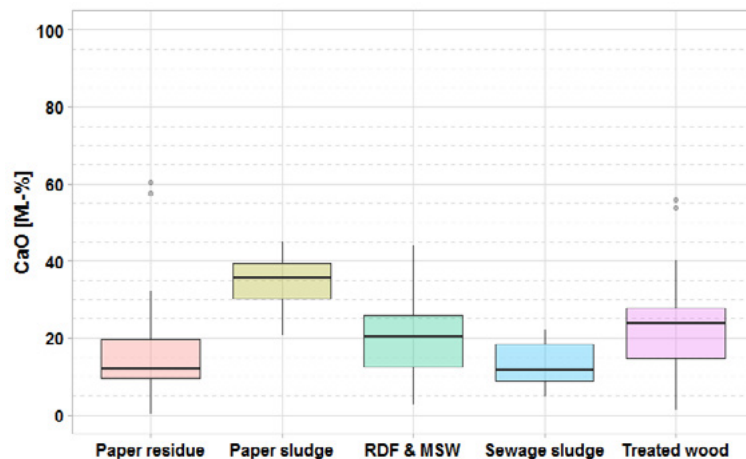


Figure 6: CaO concentration in OR-BD broken down into sub-categories: RDF & MSW, sewage sludge, paper sludge, paper residue from the Phyllis database. Target CaO concentration is 61-69 M%.

In addition to CaO and SiO₂, both Al₂O₃ and Fe₂O₃ should be present in the biomass derived ash if it is to be used as a clinker replacement or raw feed for clinker production. Theoretically the ash should therefore contain between 3 and 5 M.-% of each. Concerning the 3 biomass stream categories investigated, most of the samples fell in the desired range, however some subcategories were prone to elevated contents of one or both oxides. Paper, RDF & MSW derived ashes, for example, tended to have higher contents of Al₂O₃, often in the range exceeding 15M.%. Also, sewage sludge ash was generally too high in both Al₂O₃ and Fe₂O₃. Similar elevated contents of Al₂O₃ and Fe₂O₃ were found in ashes of treated woods.

3.1.2 Ternary Diagrams

The identification of the individual oxides is useful; however, the biomass source needs to provide a balance

of multiple oxides to be used as single raw material for clinker production or replacement of cement. Therefore it is useful to view the composition of the different biomass derived ashes in a ternary diagram like the one shown Figure 7. Each point in the plot represents the composition of a single sample. With the main clinker forming oxides normalized to 100% and the samples of the three biomass categories distinguished by colour, trends can be identified and those samples which fall in the desired region can be selected. While all three categories are represented within the semi-circle that encompasses the desired composition, HAB appears to be the most recurrent. The OR-CB samples appear to be the most disordered while both WWB and HAB showing strong tendency to contain more SiO_2 . Alongside the higher SiO_2 concentration WWB also shows a preference for higher CaO concentrations. Conversely HAB showed lower concentrations of CaO .

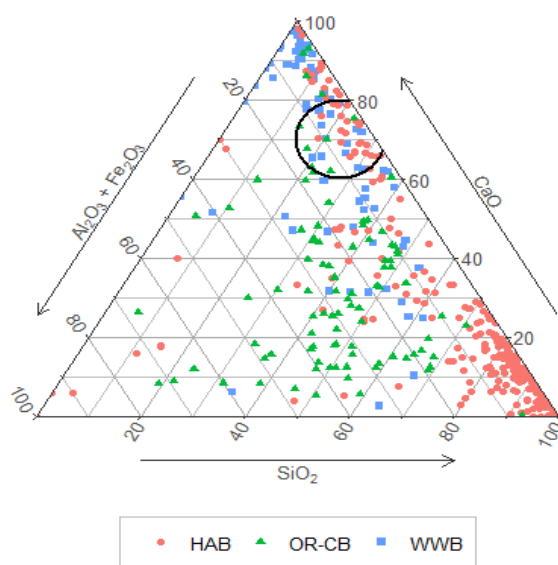


Figure 7: Ternary diagram with the main clinker forming oxides normalized to 100% with the three biomass categories (WWB, HAB and OR_CB) distinguished by colour. The semi-circle represents the area of desired composition and HAB appears to be the most recurrent biomass type in this range.

While Figure 7 shows the ternary diagram that includes the oxides necessary for clinker production, in the case of biomass derived ash it is more informative to expand the oxides depicted because the alkali oxides can be critical to clinker mineral formation. Therefore, for better visualization of the oxide proportions present, the ash compositions are plotted in a ternary diagram composed of the three glass science categories in Figure 8. Most of the samples do not fall into the desired range apart from a few. Only two HAB samples are found in this section since most of them were richer in $\text{SiO}_2 + \text{Fe}_2\text{O}_3 + \text{Al}_2\text{O}_3$ and had low levels of $\text{CaO} + \text{MgO}$. A few more OR-CB samples were detected in these composition ranges, however, in general they also tended to be richer in $\text{SiO}_2 + \text{Fe}_2\text{O}_3 + \text{Al}_2\text{O}_3$. WWB has the most biomass samples falling in the desired range. Woody biomass tends to be richer in CaO and since larger quantities of CaO are necessary for clinker this appears a more promising biomass source.

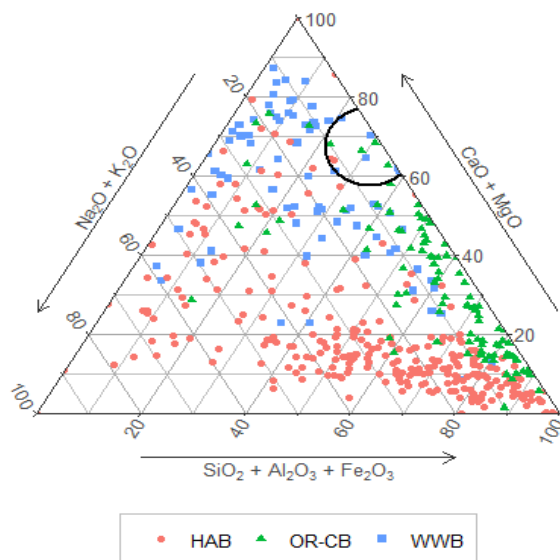


Figure 8: Ternary diagram with the most abundant oxides grouped based on function in clinkering and normalized to 100% for the three biomass categories (WWB, HAB and OR_CB) as distinguished by colour. The semi-circle represents the area of desired composition and WWB appears to be the most recurrent biomass type in this range.

3.1.3 Physical Properties (Ash content)

In addition to the chemical composition of the ash, another important characteristic dependent on the biomass source is the ash content. To make use of the biomass ash after biomass combustion there must be a significant amount of material available. The Phyllis 2 database provides the ash content from most of the material entries. As depicted in Figure 9, the mean ash content of samples grouped in the WWB, HAB and OR-CB categories are 2.2% 5.2% and 7.1 M.-% respectively. Although OR-CB showed the highest average ash content it also showed the largest standard deviation.

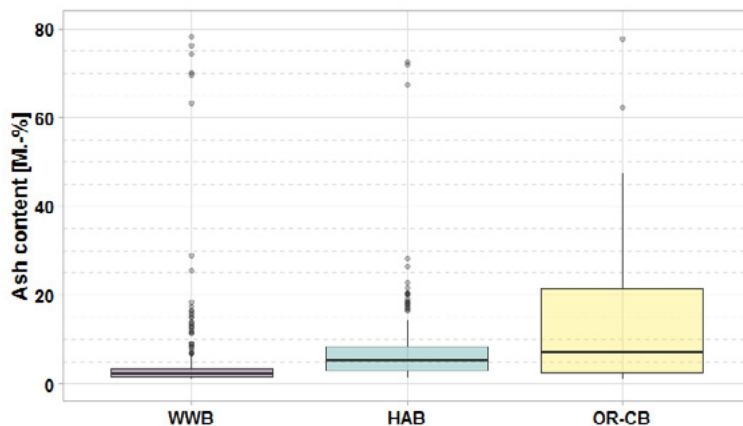


Figure 9: Ash content as a mass percentage of the total biomass mass for the categories wood and woody biomass (WWB), herbaceous and agricultural biomass (HAB) and organic residues and contaminated biomass (OR-CB). OR-CB results in the most ash and WWB the least.

3.2 Effect of Conversion Technology on Ash Composition (ALLASKA Database)

In addition to the biomass source, the conversion technology also affects the composition of the resulting ash. Conversion technology can be grouped together by reactor types, however there can still be differences based on operational parameters (i.e. changes in firing temperature). For any given reactor type, the general process is consistent. In this section, the average composition of biomass derived ashes which have been

produced in a pulverised fuel reactor (PF), grate stoker furnace (GSF), circulating fluidized bed (CFB) and bubbling fluidized bed (BFB) will be evaluated. The biomass selection was limited to wood and woody biomass since (as seen in the previous section) this category showed the smallest most accurate range in the contents of the major oxides with the median CaO content being 33.3 M.-% and the median SiO₂ content being 8.3 M.-%.

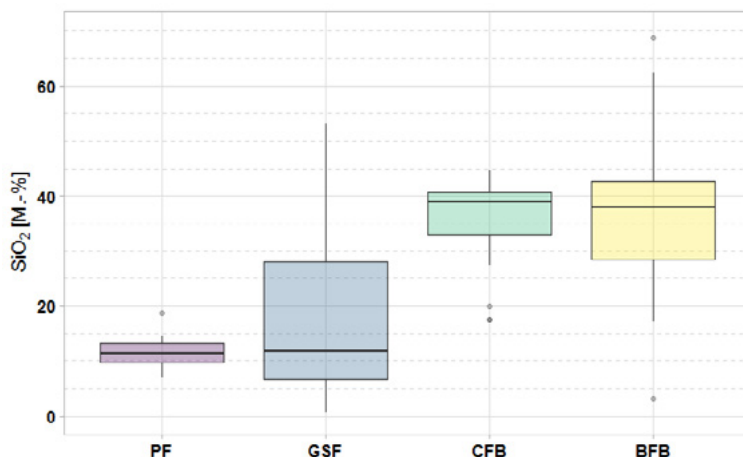


Figure 10: SiO₂ content in woody biomass ash after thermal conversion in 4 different boilers; pulverised fuel reactor (PF), grate stoker furnace (GSF), circulating fluidized bed (CFB) and bubbling fluidized bed (BFB). Target SiO₂ concentration is 15-20 M.-%.

Statistical representations of the SiO₂ and CaO contents for ashes produced in a PF, GSF, CFB and BFB can be seen in Figure 10 and Figure 11 respectively. After conversion in a pulverised fuel boiler, significantly lower quantities of SiO₂ are present relative to the other boilers. Half of the samples had contents between 10.2 and 14.5 M.

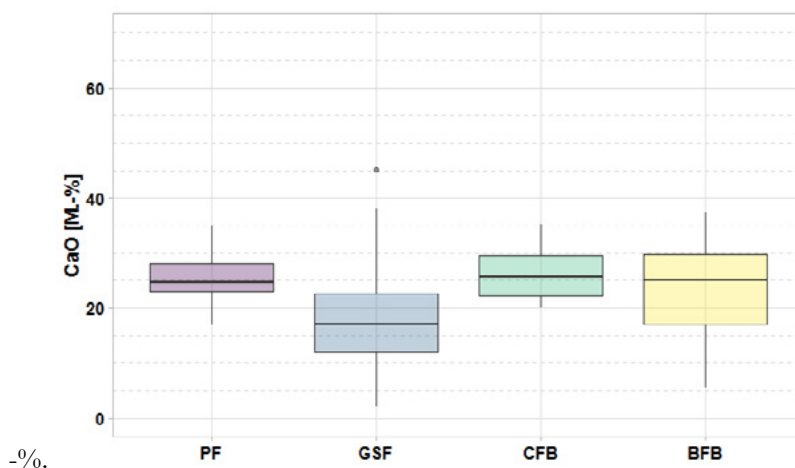


Figure 11: CaO content in woody biomass ash after thermal conversion in 4 different boilers; pulverised fuel reactor (PF), grate stoker furnace (GSF), circulating fluidized bed (CFB) and bubbling fluidized bed (BFB). Target CaO concentration is 61-69 M.-%.

While lower, this is not far below the 15-20 M% range which is theoretically required in raw feed to produce OPC. The CaO content in the ash produced in a PF is on par with the other technologies, in fact the second highest amount. It is interesting to note that the PF ash had a significantly smaller content range for both CaO and SiO₂, suggesting more consistency in the composition of the resulting ash. Conversely, GSF derived ashes showed a very wide range for both SiO₂ and CaO contents. While the average SiO₂ content falls directly in the theoretically required range, the distribution appeared too large and the average CaO content falls far below what is theoretically required. Based on these characteristics GSF technology

appears less suitable for producing ash useful as raw material for production of OPC. The CFB and BFB derived ashes had remarkably similar SiO₂ and CaO contents with the average SiO₂ concentration for BFB falling slightly above that of CFB and the average CaO content for BFB falling slightly below that of CFB. However, the whole distribution was remarkably similar, as was the range and standard deviation. The relatively small differences observed are likely due to the similarities in the combustion technologies between these two methods. In terms of SiO₂ and CaO content, these data suggest that both BFB and CFB techniques result in an ash with high SiO₂ and low CaO relative to the desired ranges. In terms of producing an ash for clinker raw material replacement or cement replacement, PF is most suitable. Concerning the oxides of elements that are present in smaller quantities, less distinct trends can be observed based on the combustion system involved. In Figure 12, the average concentration of oxides (Al, Fe, Mg and K) in the range of 2-10 M.-% can be seen and in Figure 13, the minor oxides, i.e. those accounting for less than 2 M.-% on average (Na, Mo, P and Ti) can be seen for each of the 4 conversion systems. Concerning the minor oxides, there are very few differences and it can be concluded that the conversion system has little to no effect on the presence of minor oxides in the resulting ash. Some variation in the oxides present in slightly larger quantities can be observed. The ash resulting from both BFB and CFB had higher average contents of Al₂O₃ in comparison to GSF and PF. GSF and PF resulted in ashes that contained higher amounts of K₂O than either BFB or CFB (5.7 and 10.5 vs 4.1 and 3.4 M.-%).

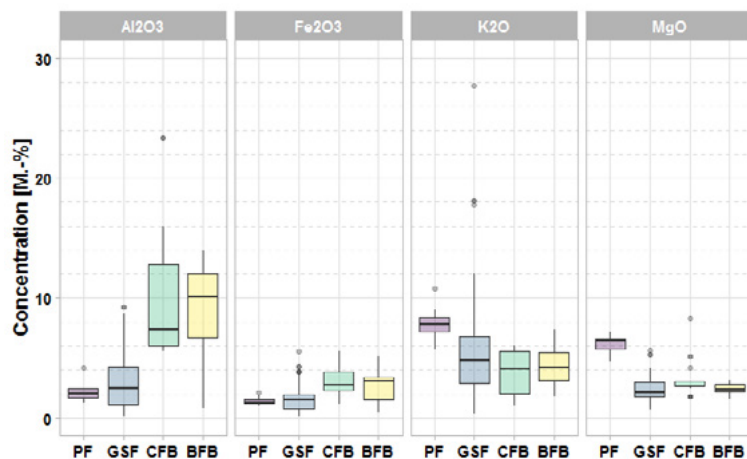


Figure 12: Distribution of oxides in woody biomass ash after thermal conversion in 4 different boilers (BFB and CFB had higher average contents of Al₂O₃).

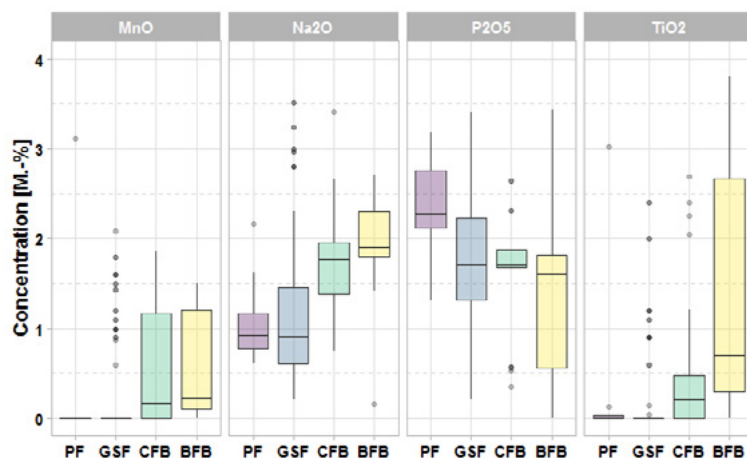


Figure 13: Distribution of minor oxides (i.e. < 2 M.-%) in woody biomass ash after thermal conversion in 4 different boilers (the conversion system has little to no effect on the presence of these minor oxides).

4. Biomass Waste Available in The Netherlands

Using biomass waste streams for energy production can provide an environmentally friendly and economically attractive alternative. Energy crops are not a viable option for biomass energy sources since they take land away from agricultural purposes (leading to less sustainable farming practices) and introduce monocultures [27]. However, biomass can still be an environmentally attractive energy source, particularly if it stems from waste streams or by-products. Many human activities lead to the production of supplemental biomass. Most supplementary biomass is produced in forestry and agricultural practices as well as in the maintenance of nature areas and public parks [27], [28]. Other supplementary biomass streams include organic domestic waste, sludges and industry wastes. Specifically, in The Netherlands, wood thinnings, straw, verge grass, crop residues and greenhouse waste represent primary types of biomass waste [28], [29]. Since these are the waste streams that above were shown to provide CaO and SiO₂, their volumes should be further explored and compared to that of cement consumption in the Netherlands.

To understand how much cement could be replaced with a biomass derived alternative, the current amount of biomass available for combustion and the amount of thereby derived ash must be quantified. Most supplementary biomass is produced in agricultural and forestry practices as well as in the maintenance of nature areas and public parks [27]. Additionally, in The Netherlands industrial practices produce relevant amounts of biomass waste. To simplify the calculation of available biomass, sources have been broken down into three different categories; maintenance, agriculture and industry.

4.1 Maintenance waste

Maintenance biomass is the waste produced in the maintenance of different types of land areas and is typically verge grass or woody biomass. Table 1 gives a breakdown on the different land uses in The Netherlands, their area and the amount of biomass they produce annually [28], [30].

Table 1: Maintenance biomass produced in The Netherlands based on surface area and dry matter yield.

	Surface Area	Biomass dry matter yield	Available biomass dry matter
	[10 ³ ha]	[tonnes DM/ha/year]	ktonnes/year
Transportation	116	3	348
Built up area	356	1	356
Semi built area	51	2	102
Recreation	103	3	309
Forest and nature	490	3.5	1715
Inland waterway	368	1	368
Total	1484		3198

Table 2: Calculation of maintenance biomass ash quantity.

	Available biomass dry matter	Ash fraction	Available ash
	[ktonnes/year]	[%]	[ktonnes]
Transportation	348	13.9	48.4
Built up area	356	13.9	49.5
Semi built area	102	13.9	14.2
Recreation	309	13.9	43.0
Forest and nature	1715	8.2	140.6
Inland waterway	368	13.9	51.2
Total	3198		346.9

Assuming that verge grass has an average ash content of 13.9% and woody biomass from park maintenance has an average ash content of 8.2% [31] the derived ash can be calculated (see Table 2). The total amount of maintenance biomass derived ash which could theoretically replace cement is over 295 ktonnes.

4.2 Agricultural waste

The amount of biomass waste stemming from agricultural practices can be similarly calculated (Table 3). In 2012 there was 2251000 ha of farm land from which about 12 tonnes of dry matter can be extracted per ha per year. This results in 27012 ktonnes of biomass. However not all this biomass is waste; using an average harvest index for the main crops cultivated in The Netherlands (0.45) the amount of biomass waste can be calculated to be 14857 ktonnes. Based on an average ash fraction of 9.35 this results in 1389 ktonnes of ash after combustion (see Table 4) [31].

Table 3: Calculation of biomass waste based on agricultural land surface area, dry matter (DM) yield and harvest index.

Surface Area	Biomass DM yield	Available biomass DM	Harvest index	available waste
[10 ³ ha]	[tonnes DM/ha/year]	[ktonnes/year]		[ktonnes]
2251	12	27012	0.45	14857

Table 4: Calculation of agricultural waste biomass derived ash.

Available biomass waste	Ash fraction	Available biomass ash
[ktonnes]		[ktonnes]
14856.6	9.35	1389

4.3 Industrial waste

Industrial wastes can also provide streams of biomass waste and this work has particularly identified paper waste as a potential cement raw material replacement. Paper waste is typically recycled and reused in the production of new paper. This process can only be repeated so many times before the fibres degrade too much and the quality of the paper is too low. At this point the paper is still suitable for combustion and since the original material was biomass, it is still considered biomass combustion. It was reported that in 2012 of the total recyclable waste produced in The Netherlands 24.3% was paper waste which is about 4.0 Mtonnes [30]. Assuming an average ash content of 8.6% roughly 344 ktonnes of ash result [31].

Table 5: Total amount of biomass derived ash from the three identified categories which is available for cement replacement based on the 2012 estimates [tonnes].

	Biomass derived ash
Maintenance	347 000
Agricultural	1 389 000
Industrial	344 000
Total	2 080 000

5. Discussion

5.1 Phyllis Database

Based on the analysis of the biomass sources and the ash composition of samples within the Phyllis 2 database, it can be concluded that particular biomass waste streams appear more suitable than others as either a cement replacement or as an alternative raw feed for clinker production. While some streams showed abundant concentrations of either SiO₂ or CaO, a few sources had the potential to provide all the

necessary elements in roughly the theoretically appropriate quantities (i.e. 61-69 M.-% of CaO and 15-20 M.-% of SiO₂).

It was apparent that within the WWB category both bark and hardwood had the potential to provide the most relevant contents of CaO. While some samples within these two subgroups fell below the required amounts, the majority provided ample CaO required for the formation of hydraulic clinker minerals. In addition, from the OR-CB category, paper sludge was found to contain CaO in amounts that are on the lower limit of what is required and therefore show potential as source of CaO for formation of hydraulic clinker minerals. Regarding HAB, Rape straw from the sub-category straw has potential to provide sufficient CaO.

Potential sources of SiO₂ were more abundant, however, the content of most sources exceeded the theoretically required SiO₂ threshold (20 M.-%). From the WWB category, softwood showed potential as did husk shell & pits from the HAB category. From the category OR-CB, waste paper, treated wood and, to some extent, paper sludge provided potentially sufficient SiO₂ without being in excess (22.5 to 39.7 M.-%). RDF + Plastic derived ashes appeared also as an optional SiO₂ source, but these are considered less desirable because they are not biomass based and the combustion of plastic (even as a waste treatment solution) should be avoided.

Generalizations are difficult to make for the SiO₂ and CaO composition of sewage sludge ash because there appeared to be high variability [32]. Considered to be a semi-biomass, the element composition can be more variable than natural biomass due to processing and the origin of materials [1]. In a survey of 42 different studies Cry et. al found that the mean content was 36.1 M.-% for SiO₂, 14.8 M.-% for CaO, 14.2 M.-% for Al₂O₃, 9.2 M.-% for Fe₂O₃, 11.6 M.-% for P₂O₅ and 2.8 M.-% for SO₃. Therefore, due to the high variability of its composition and high concentration of P₂O₅, sewage sludge ash appears not to be a favourable source for clinker replacement or as an alternative raw feed for clinker production.

Regarding the elevated concentrations of Al₂O₃ and/or Fe₂O₃ detected in the subcategories paper, RDF & MSW, sewage sludge and treated wood ash, all these biomass streams had undergone additional processing prior to combustion and this could have been most likely the source of Al₂O₃ and Fe₂O₃. Rarely does a pure biomass stream show an excess of either of these two oxides, indicating that their presence stems more from the processing and human intervention than the actual biomass.

OR-CB, and in particular paper residue, appears to be the best biomass derived ash source for potential cement replacement since it provides both Ca and Si while also having the highest ash content. Wood ash also has potential given that some samples were on the higher side of CaO content while still containing SiO₂. Furthermore, WWB showed the lowest deviations in element contents, reflecting more consistency in the composition of the waste stream.

In addition to the chemical composition of the ash, another important characteristic dependent on the biomass source is the ash content. The ash content is a critical parameter since it dictates the volume of material derived from the different types of biomass. WWB had the lowest ash content (2.2 M.-%) while OR-CB had the highest (7.1 M.-%) and the largest range. The OR-CB group includes all organic residue that is not a direct residue from agriculture and horticulture (waste paper, residues from the food industry, domestic waste municipal solid waste and refuse derived fuel). The higher ash content and broader range are most likely the result of the diversity of the category. Furthermore, OR-CB includes treated organic residues like sewage water sludge, paper industry sludge, food industry sludge, composted wood, demolition wood, preserved wood and particle board. The processes of these materials prior to combustion introduces external compounds which adds to the ash fraction. When these external compounds are inorganic they

can have a significant impact on the ash fraction, which is not always ideal.

5.2 ALLASKA Database

Based on the analysis of the conversion technology and ash composition extracted from the data within the ALLASKA database, it can be concluded that some conversion technologies are more beneficial than others as the resulting ash can potentially act as either a cement replacement or as raw feed in the production of clinker. It was observed that both CFB and BFB produce ashes that, on average, have higher contents of the desired oxides CaO and SiO₂. Also, these two types of conversion systems showed higher consistency in ash composition as variability in range was small. These two types of fluidized beds also provided ash with more desirable values with respect to minor element oxides. The samples produced in these reactors had more Al₂O₃ and less K₂O on average.

In terms of the data extracted from the ALLASKA database, both a BFB and CFB are best for converting woody biomass into energy while producing an ash with the potentially right elemental make up for clinker. GSF has less value for producing an ash that can be suitable for OPC production as can be concluded based on the large variability of SiO₂ and CaO concentrations and the undesirable CaO contents of the produced ash. PF showed more consistency in ash composition and acceptable concentrations of SiO₂ and CaO. However, the excessive amounts of K₂O reported in the PF produced ash make it inapplicable as a clinker raw material substitute. It can be concluded that way of processing of the biomass and the thermal conversion parameters involved can be influential with respect to the final composition of the derived ash. In the case of pelletized fuel, increases in the Ca content were detected in the fly ash. Additionally, the bed material in fluidized beds can greatly affect the composition of the bottom ash. These parameters can therefore be used to alter the content of elemental oxides to benefit most of what is present in the biomass.

5.3 Possible cement replacement

From the three identified biomass categories, combustion of the ash would result in more than 2.0 Mtonnes of biomass ash for cement application. In 2013, no clinker was produced in The Netherlands per Eurostat, however, ENCI Maastricht has reported the production of less than 600 tonnes of clinker [33], [34]. The Netherlands has a limited supply of raw materials for clinker production, namely limestone, consequently all cement manufactured in the country is produced by blending imported clinker with domestically produced waste streams such as slag. Per the United Nations Department of Economic and Social Affairs Statistics Division, The Netherlands imported a net 0.63 Mtonnes of cement clinker in 2013 (0.63 Mtonnes imported and 0.002 Mtonnes exported) [35]. All the imported cement clinker could potentially be replaced by domestically produced biomass derived ash. Additionally, The Netherlands imported a net 2.7 Mtonnes of Portland cement and hydraulic binders, for a total of 3.3 Mtonnes Portland cement, hydraulic binders and cement clinker. This statistic fits with the reported usage of 4.2 Mtonnes of hydraulic binders consumed in The Netherlands in 2013 [36] given that the imported clinker was blended with industrial wastes to produce cements like CEM II-S and CEM III. If 100% of these biomass waste streams were combusted and applied as a cement replacement (negating the difference in chemical composition), theoretically 100% of clinker imports could be avoided. The amount of hydraulic binder imports could also be reduced by 52% (or more given the potential to blend with industrial wastes). This oversimplification serves as an indication of potential impact, however more investigations into the functional properties of biomass derived cements is necessary for specific values to be calculated. While these estimates do make many assumptions, they also negate the growing stake of biomass in energy production and the vested interest in a circular economy. Given the current potential and the environmentally minded changes being made in society [37] the use of biomass derived ash as a cement replacement holds potential and deserves further research.

6. Conclusions

6.1 Conclusions on composition

A potentially ideal ash for cement replacement or clinker production can be achieved based on the ashes of particular biomass streams. SiO₂ can be obtained from WWB (wood and woody biomass), HBA (herbaceous and agricultural biomass) or OR-CB (organic residues and contaminated biomass). Higher concentrations of CaO are necessary for cement replacement or clinker raw material replacement but they are more difficult to find in biomass. Most notable CaO can be obtained from bark and hardwood in the WWB category, rape straw in the HAB category or paper residue in the OR-CB category. Ashes derived from the OR-CB category paper sludge showed the potential to provide both CaO and SiO₂ however the extent of their reactivity remains to be investigated.

Based on this investigation, the oxides present in the different biomass streams indicate that replacement of clinker raw materials has more potential than direct cement replacement. While there are plenty of biomass sources with an abundance of SiO₂ which could function pozzolanically, to reach higher cement replacement rates hydraulic minerals are necessary. Individual biomass streams have CaO and SiO₂ present in quantities more likely to produce belite than alite. Furthermore, given the conversion temperatures below 1000 °C it is unlikely that alite would be formed during energy production. To be an equivalent cement replacement, both alite and belite are necessary. However, blending different biomass ash streams and subjecting them to a secondary thermal treatment could produce but alite and belite. Therefore, the use of biomass derived ashes as a clinker raw feed replacement is a progression worth more investigation.

6.2 Conclusions on conversion system

Circulating fluidized beds (CFB) and bubbling fluidized beds (BFB) produce ashes that on average have higher contents of the desired oxides CaO and SiO₂ with a smaller deviation range and are also more desirable concerning minor elemental oxides since they had more Al₂O₃ and less K₂O (compared to pulverized fuel reactors and grate stoker furnaces).

6.3 Conclusions on potential replacement in The Netherlands

This study estimates that more than 2.0 Mtonnes of biomass ash are produced annually in The Netherlands. In 2013, The Netherlands imported a total of 3.3 Mtonnes Portland cement, hydraulic binders and cement clinker. That same year roughly 4.2 Mtonnes of hydraulic binders consumed. If 100% of these biomass waste streams were combusted and applied as a cement replacement theoretically 100% of clinker imports could be avoided. The amount of hydraulic binder imports could also be cut in half.

7. References

- [1] S. V. Vassilev, D. Baxter, L. K. Andersen, and C. G. Vassileva, "An overview of the composition and application of biomass ash. Part 1. Phase–mineral and chemical composition and classification," *Fuel*, vol. 105, pp. 40–76, Mar. 2013.
- [2] A. Demirbas, "Combustion characteristics of different biomass fuels," *Prog. energy Combust. Sci.*, vol. 30, no. 2, pp. 219–230, 2004.
- [3] M. F. M. Zain, M. N. Islam, F. Mahmud, and M. Jamil, "Production of rice husk ash for use in concrete as a supplementary cementitious material," *Constr. Build. Mater.*, vol. 25, no. 2, pp. 798–805, 2011.
- [4] P. K. Mehta, "Properties of blended cements made from rice husk ash," in *Journal Proceedings*, 1977, vol. 74, no. 9, pp. 440–442.

- [5] D. J. Cook, R. P. Pama, and B. K. Paul, "Rice husk ash-lime-cement mixes for use in masonry units," *Build. Environ.*, vol. 12, no. 4, pp. 281–288, 1977.
- [6] V. M. H. Govindarao, "Utilization of rice husk-a preliminary-analysis," *J. Sci. Ind. Res.*, vol. 39, no. 9, pp. 495–515, 1980.
- [7] M. N. Al-Khalaf and H. A. Yousif, "Use of rice husk ash in concrete," *Int. J. Cem. Compos. Light. Concr.*, vol. 6, no. 4, pp. 241–248, 1984.
- [8] A. Dass, "Pozzolanic behaviour of rice husk-ash," 1984.
- [9] H. Chao-Lung, B. Le Anh-Tuan, and C. Chun-Tsun, "Effect of rice husk ash on the strength and durability characteristics of concrete," *Constr. Build. Mater.*, vol. 25, no. 9, pp. 3768–3772, 2011.
- [10] V. P. Della, I. Kühn, and D. Hotza, "Rice husk ash as an alternate source for active silica production," *Mater. Lett.*, vol. 57, no. 4, pp. 818–821, 2002.
- [11] N. Amin, "Use of bagasse ash in concrete and its impact on the strength and chloride resistivity," *J. Mater. Civ. Eng.*, vol. 23, no. 5, pp. 717–720, 2010.
- [12] V. S. Batra, S. Urbonaitė, and G. Svensson, "Characterization of unburned carbon in bagasse fly ash," *Fuel*, vol. 87, no. 13–14, pp. 2972–2976, 2008.
- [13] N. Chusilp, C. Jaturapitakkul, and K. Kiattikomol, "Utilization of bagasse ash as a pozzolanic material in concrete," *Constr. Build. Mater.*, vol. 23, no. 11, pp. 3352–3358, 2009.
- [14] M. Frías, E. Villar, and H. Savastano, "Brazilian sugar cane bagasse ashes from the cogeneration industry as active pozzolans for cement manufacture," *Cem. Concr. Compos.*, vol. 33, no. 4, pp. 490–496, 2011.
- [15] D. D. Bui, J. Hu, and P. Stroeve, "Particle size effect on the strength of rice husk ash blended gap-graded Portland cement concrete," *Cem. Concr. Compos.*, vol. 27, no. 3, pp. 357–366, Mar. 2005.
- [16] G. C. Cordeiro, R. D. Toledo Filho, L. M. Tavares, E. de M. R. Fairbairn, and S. Hempel, "Influence of particle size and specific surface area on the pozzolanic activity of residual rice husk ash," *Cem. Concr. Compos.*, vol. 33, no. 5, pp. 529–534, 2011.
- [17] P. K. Mehta, P. J. M. Monteiro, J. M. Monteiro, and P. J. Monteiro, *Concrete: microstructure, properties and materials*. McGraw-Hill Publishing, 2013.
- [18] V. Horsakulthai, S. Phiuvanna, and W. Kaenbud, "Investigation on the corrosion resistance of bagasse-rice husk-wood ash blended cement concrete by impressed voltage," *Constr. Build. Mater.*, vol. 25, no. 1, pp. 54–60, Jan. 2011.
- [19] R. Siddique and M. I. Khan, *Supplementary cementing materials*. Springer Science & Business Media, 2011.
- [20] R. Rajamma, R. J. Ball, L. A. C. Tarelho, G. C. Allen, J. A. Labrincha, and V. M. Ferreira, "Characterisation and use of biomass fly ash in cement-based materials," *J. Hazard. Mater.*, vol. 172, no. 2–3, pp. 1049–1060, 2009.
- [21] J. Hong and X. Li, "Environmental assessment of sewage sludge as secondary raw material in cement production – A case study in China," *Waste Manag.*, vol. 31, no. 6, pp. 1364–1371, Jun. 2011.
- [22] Y. Lin, S. Zhou, F. Li, and Y. Lin, "Utilization of municipal sewage sludge as additives for the

production of eco-cement,” *J. Hazard. Mater.*, vol. 213–214, pp. 457–465, Apr. 2012.

- [23] L. H. Buruberri, M. P. Seabra, and J. A. Labrincha, “Preparation of clinker from paper pulp industry wastes,” *J. Hazard. Mater.*, vol. 286, pp. 252–260, Apr. 2015.
- [24] L. Simão *et al.*, “Waste-containing clinkers: Valorization of alternative mineral sources from pulp and paper mills,” *Process Saf. Environ. Prot.*, vol. 109, pp. 106–116, Jul. 2017.
- [25] A. R. G. Azevedo *et al.*, “Development of Methodology for the Characterization and Incorporation of Waste from the Paper Industry in Cementitious Materials,” Springer, Cham, 2019, pp. 583–590.
- [26] A. A. Usón, A. M. López-Sabirón, G. Ferreira, and E. Llera Sastresa, “Uses of alternative fuels and raw materials in the cement industry as sustainable waste management options,” *Renew. Sustain. Energy Rev.*, vol. 23, pp. 242–260, Jul. 2013.
- [27] A. Faaij, I. Steetskamp, A. van Wijk, and W. Turkenburg, “Exploration of the land potential for the production of biomass for energy in the Netherlands,” *Biomass and Bioenergy*, vol. 14, no. 5–6, pp. 439–456, May 1998.
- [28] L. P. L. M. Rabou, E. P. Deurwaarder, H. W. Elbersen, and E. L. Scott, “Biomass in the Dutch energy infrastructure in 2030.” 2006.
- [29] I. H. E. M. Stassen, “Biogas and biomass technology: Energy generation from biomass and waste in the Netherlands,” *Renew. Energy*, vol. 5, no. 5–8, pp. 819–823, Aug. 1994.
- [30] Centraal Bureau voor Statistics, “StatLine,” 2013. [Online]. Available: <https://opendata.cbs.nl/statline/#/CBS/nl/>.
- [31] Energy Research Centre of the Netherlands, “Phyllis2 Database for biomass and waste,” 2012. [Online]. Available: <https://phyllis.nl/>.
- [32] M. Cyr, M. Coutand, and P. Clastres, “Technological and environmental behavior of sewage sludge ash (SSA) in cement-based materials,” *Cem. Concr. Res.*, vol. 37, no. 8, pp. 1278–1289, Aug. 2007.
- [33] ENCI, “Milieu- en veiligheidsverslag Maastricht 2013-2014,” 2014.
- [34] European Commission, “Eurostat. Total production by PRODCOM list (NACE Rev. 2) - annual data,” 2013. [Online]. Available: <https://ec.europa.eu/eurostat/data/database>.
- [35] UN Data, “Commodity Trade Statistics Database,” 2018. [Online]. Available: <http://data.un.org/>.
- [36] CEMBUREAU, “World Statistical Review 2004-2014,” 2017.
- [37] European Commission, “A Roadmap for moving to a competitive low carbon economy in 2050,” 2011.

Qualification of the residual reactivity of compacted recycled aggregates

Y. Hou¹, P. Mahieux¹, J. Lux¹, P. Turcry¹, A. Ait-Mokhtar¹

¹: Laboratoire des Sciences de l'Ingénieur pour l'Environnement (LaSIE), UMR CNRS 7356, Université de La Rochelle, Avenue Michel Crépeau, 17000 La Rochelle, France.

Abstract

Recycled Aggregates (RA) are a very complex mineral construction material, containing mainly cementitious materials, natural aggregates and to a lesser extent, fired clay brick and bituminous materials. Due to this specificity, RA has a potential residual reactivity that we propose to study in this research paper. By scale reducing of a previous research program on the in-situ experimental platform, mixed fine RA and water were compacted according to the European Standard NF EN 13286-53 to form cylindrical specimens of 5 cm in diameter and 5 cm in height. They were placed under four enclosures with controlled relative humidity, including an accelerated carbonation condition (RH 53±5%, RH 95±5%, RH 65±5% and RH 65±5% with 3% CO₂). Their physical, chemical and mechanical properties have been subsequently measured over time for one year. The results show that under natural conditions, the carbonation coefficient is lower for larger values of RH. The dynamic modulus and the compressive strength of all samples significantly increased during the first month. In view of our experimental results, we assume that this increase of inter-granular cohesion is due to drying and by cementing, induced by residual carbonation of RA particles containing cementitious materials. The effect of accelerated carbonation does not seem to improve the mechanical characteristics by comparison with the other conditions (i.e. natural carbonation), even if we still observe a significant mass gain.

Keywords: Recycled Aggregates, residual hydraulic reactivity, carbonation, road construction.

1. Introduction

Construction and Demolition Waste (CDW) is a major waste source in the world, with approximately 3 billion tons generated per year [1, 2]. EUROSTAT has recently published data showing that EU member states generate 850 million tons of CDW each year. In France, the construction industry produces about 230 million tons of the CDW every year, while at the same time, consuming almost 400 million tons of natural aggregates (NA) [3]. To address this issue, the Waste Framework Directive (WFD) has encouraged EU member states to recycle at least 70% of non-hazardous and inert CDW by 2020. To reduce the storage of CDW and the consumption of natural aggregate resources, the construction industry and public or private laboratories have been collaborating on multiple French national projects (e.g. Recybéton, FASTCARB) optimise the use of recycled aggregates, giving them a high added value.

Recycled aggregates (RA) have been used in road engineering in many French regions since the 2000s and technical and environmental guides have emerged to frame their uses. However, we note that these materials are still characterised as natural aggregates (NA), without taking into account their specificities and their potentialities. The results of a previous research project, titled RECYMENT (2014–2016) and

conducted in our lab, LaSIE, showed that RA, derived from a conventional demolition waste recycling platform, were certainly very complex but also reactive and efficient in the long term, indeed, even better than NA [4]. The current issue is that the public owners are still reluctant to use RA in the construction of roads. However, older researches [5] have demonstrated that fears about potential chemical or physical incompatibility between RA and NA have no real basis. In 2011, Hornych made an inventory of recycling practices in several European countries [6]. Among the countries studied, the case of Sweden is particularly interesting because RA was being used there for pavement structures, depending on the strength of the concrete with which the original materials were manufactured. A module of 450 MPa was assigned to them for sizing. In the Netherlands, studies on test sites have been carried out indicating that the modulus is between 600 and 800 MPa in the short term (depending on the proportion of concrete in the RA) but can reach more than 1000 MPa in the long term. Arm [7] investigated the long-term behaviour of compacted RA using triaxial tests (containing at least 95% of concrete). The author found an increase over time of the stiffness modulus, whereas, in the case of natural aggregates, the modulus remained constant. More recently, other authors have observed these same trends. Vegas et al. [8] have performed CBR tests and have shown a gain in the medium-term puncture resistance, which they attributed to the residual hydraulicity of cementitious materials contained in RA. However, there has been little deep discussion about the reasons for the gain in resistance of compacted RA, which is used in pavement structures.

Some researchers [9, 10] have demonstrated that the unhydrated residual materials in RA can rehydrate. Shui et al. [11] proposed the preheating of the fine recycled concrete aggregates to facilitate the rehydration reactivity. The result revealed that the C-S-H gel, ettringite, and calcium hydroxide reappeared in the initial crystalline hydrated products of fine recycled concrete aggregates but with the changed microstructure of the rehydration products, which was looser than that of the ordinary cement paste. Poon et al. [12] studied the self-cementing properties of the sub-based materials prepared with recycled concrete aggregates and reported that the fine recycled concrete aggregates could be affected by the age, grade, and amount of cementitious materials used in the original concrete, determining the self-cementing properties. So far, research characterising the residual reactivity of RA in the concrete, no many studies exist which the residual reactivity of RA in the construction of roads.

All studies show that the recycled aggregates can substitute for natural aggregates in road construction; however, discussing the causes of compacted RA reactivity is necessary. To address this gap in the research, this study investigates the role of the constituents contained in RA, which originated from the recycling platform. We mixed fine RA and water with the packing density of specimens $C=0.68$ to made Compacted Recycled Sand (CRS) of 5 cm in diameter and 5 cm in height. To characterise the physical and mechanical properties and the capacity for uptake of CO_2 of CRS, we determined the mass loss, dynamic modulus, compressive strength, and carbonation depths as a function of time, respectively. Taking into account the impact of the real environment (dry and wet), the CRS were placed under four enclosures with controlled relative humidity, including an accelerated carbonation condition.

2. Materials and specimens

2.1 Origin of RA

The RA with 0/6 mm particle size fraction (RA 0/6) used in this study was provided by a recycling platform located in La Rochelle (France). On-site, the CDW was subjected to primary crushing and screening before testing in the laboratory. At first, the hand sorting on particles of 4/6 mm size fraction was realised in accordance with the European Standard NF EN 933-11 [13] in view to characterise and quantify the constituents of the RA. The nature and the mass proportions of each constituent are presented in Table 1.

Table 1: Constituent of 4/6 RA with NF EN 933-11[13].

Description of constituents	Mass proportion
	%wt.
Rc (concrete, concrete products, mortar, concrete masonry units)	82.9
Ru (unbound aggregate, natural stone, hydraulically bound aggregate)	16.3
Ra (bituminous materials)	-
Rb (clay masonry units, calcium silicate masonry units, aerated non-floating concrete)	0.1
Rg (glass)	0.6
X (other: cohesive, metals, non-floating wood, plastic, gypsum plaster,..)	0.1

The Rc and Ru constituents are the major materials contained in the 4/6 mm fraction of the tested RA, accounting for 99.2%. This preliminary result is satisfactory and in accordance with the European Standard and the French application guides in road technology [13, 14]. This distribution is tributary of the high technicality used on recycling platform and, of course, the incoming materials.

2.2 Mixing and compaction

The water content ($w=10\%$) and the packing density of specimens ($C=0.68$) were fixed to obtain an initial compressive strength of 1 MPa, which corresponds to the aimed compressive strength for authorising the road traffic in the construction phase in accordance with the French standard NF P 94-102-1 [15]. Considering that the confection of one specimen lasts about 10 minutes, about 3% of the water incorporated in the blend was absorbed by the cementitious materials. This value was determined from the curve of water absorption as a function of time, which is not presented in this paper. Therefore, the corrected intergranular water content is equal to 7% (Figure 1) that is close to the maximal relative humidity measured by isothermal absorption and sorption test (also not presented in this paper). Dried RA 0/6 and water were mixed with a mechanical blender to made cylindrical specimens of compacted sand (CRS) with 50 mm in diameter and 50 mm in height in accordance with the European Standard NF EN 13286-53 [16]. Each specimen was demoulded immediately after casting (Figure 2).

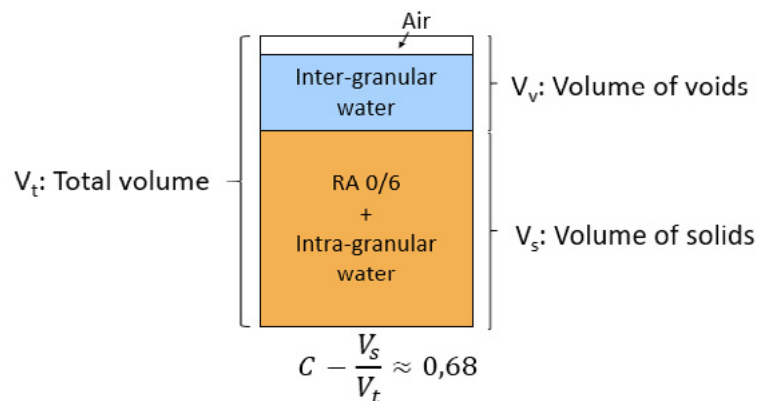


Figure 1: A schematic of the composition of specimens, $V_t = 98.2 \text{ cm}^3$; $V_v = 31.4 \text{ cm}^3$; $V_s = 66.8 \text{ cm}^3$.

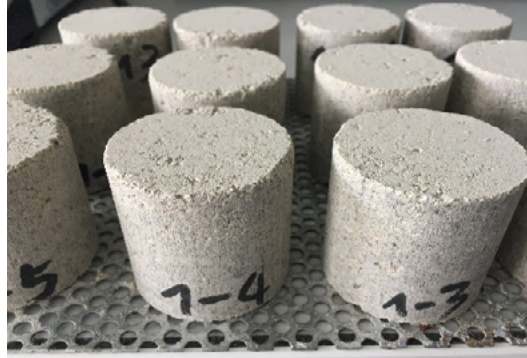


Figure 2: Specimens CRS deposited in controlled RH condition enclosure.

2.3 Curing conditions

The specimens were stored at $20 \pm 2^\circ\text{C}$ in four enclosures with different relative humidities (Figure 3). The enclosures contained wet air, at $53 \pm 5\%$, $65 \pm 5\%$ and $95 \pm 5\%$ RH, respectively. These enclosures were used to simulate three significantly different environments in accordance with the water vapour sorption isotherm. The RHs were controlled by saturated salt solutions (Magnesium nitrate for RH 53.5%, Ammonium nitrate for RH 65%, and demineralised water for RH 95%). Table 2 shows the specimens treated using natural and accelerated carbonation. Under the natural condition, the CO_2 concentration in the enclosures was the ambient concentration (0.05%), and under the accelerated carbonation condition, the enclosure was filled with a mix of air and CO_2 with a concentration of 3% at $65 \pm 5\%$ RH (Figure 3 (c)). The CO_2 concentration was increased from 0.05% to 3% then stabilised, after the masses of specimens were stabilised in the enclosure RH 65%. In this enclosure, there is ventilation to homogenize the CO_2 concentration in the whole volume.

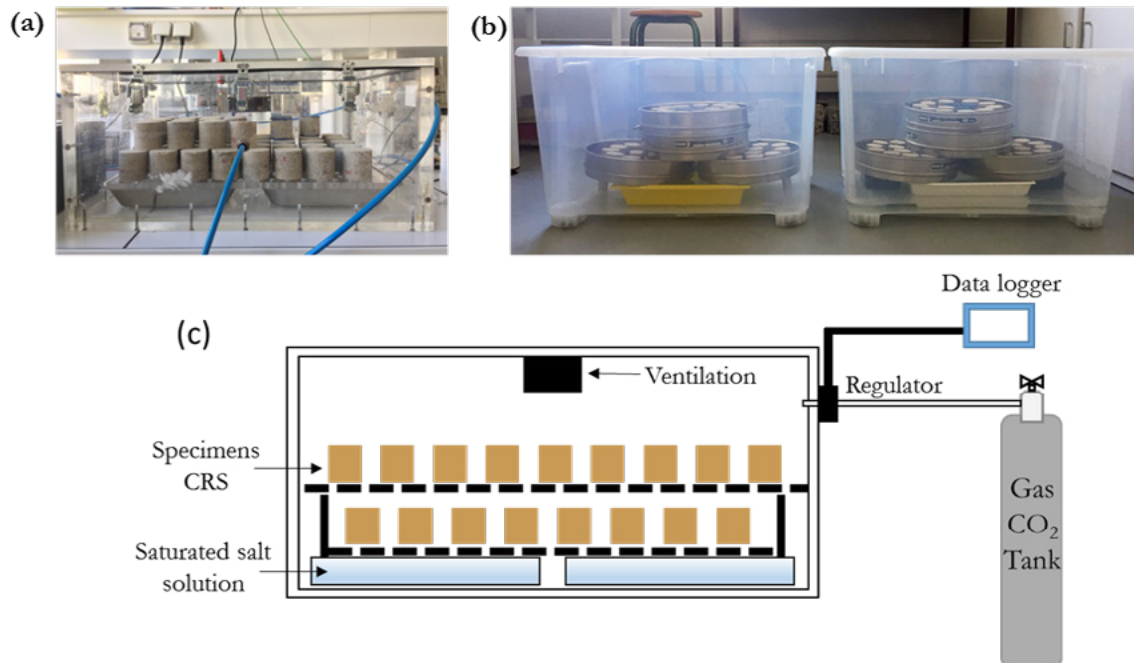


Figure 3: (a) Enclosure at RH=65% and $\text{CO}_2=3\%$ (b) Enclosures at RH 53.5% and 65% $\text{CO}_2 \approx 0.05\%$ (c) Experimental setup of $\text{CO}_2=3\%$ curing at RH=65%.

Table 2: Curing conditions of specimens.

Curing conditions	Specimen	RH	After casting	After hydric stabilisation
		%		
Natural carbonation (CO ₂ ≈0.05%)	RH 53% Nat.	53.5	Enclosure (T= 20±2 °C, CO ₂ ≈0.05%)	Enclosure (T= 20±2 °C, CO ₂ ≈0.05%)
	RH 65% Nat.	65		
	RH 95% Nat.	95		
Accelerated carbonation (CO ₂ =3%)	RH 65% Acc.	65	Enclosure	Enclosure
			(T= 20±2 °C, CO ₂ ≈0.05%)	(T= 20±2 °C, CO ₂ =3% add ventilation)

3. Methods

3.1 Thermogravimetric analysis (TGA)

TGA was performed with a Setaram Setsys Evolution 16/18 apparatus on three RA samples, namely: Ru and Rc from 4/6 RA (RA 4/6_Ru and RA 4/6_Rc) and RA 0/6. Around 150-190 mg of sampled materials were heated from 20 °C to 1000 °C at a 10 °C/min heating rate, under neutral argon atmosphere.

3.2 Mass variations of specimens

As explained before, the water content used to prepare the CRS is close to the water content at saturation. Due to this reason, the specimens should dry over time in all exposures conditions. The specimens were periodically weighed to follow the hydric variation until their mass stabilisation (error <0,1%). The mass loss was calculated using the following equation:

$$\varepsilon = \frac{M_i - M_t}{V_{app}} \times 100\% \quad (1)$$

where V_{app} is the apparent volume of the specimen (98.2 cm³), M_i is the initial mass of the specimen, and M_t is the mass of the specimen at time t.

3.3 Mechanical properties

Mechanical properties had been studied using two methods. The first one was destructive and consisted in axial compressive tests, and the second one was a non-destructive method using ultrasonic waves propagation. As for the mass loss, the mechanical properties were measured periodically at the beginning to 270 days. Three specimens per date were tested for each curing conditions.

The compressive strength of the specimen was determined by a Zwick/Roell Z100 brand 10 kN press with a constant loading speed of 20 N/s according to the European standard NF EN 13286-41 [17].

The ultrasonic waves propagation characterises the specimen structures and can be used to determine the dynamic Young's modulus by measuring wave velocities. Figure 4 (a) shows a schematic diagram of the experimental setup. A Proceq Pundit apparatus with a pair of piezoelectric transducers pulser-receiver (a frequency of 500 kHz) transmitted longitudinal and transverse ultrasonic waves into a specimen. To assume a good transmission of the waves under specimen, a coupling gel was put at the interfaces. At each age, the weight of specimens was measured to calculate the wet bulk density (ρ). On a signal curve presented in Figure 4 (b), the first echo was a weak longitudinal wave, which arrives at short time T_L , while the first strongest shear wave echo appears in the signal at long time T_T . According to T_L and T_T , it is possible to calculate the longitudinal wave velocity V_L and shear wave velocity V_T . The dynamic Young's modulus was determined by the equations in Figure 4 (c).

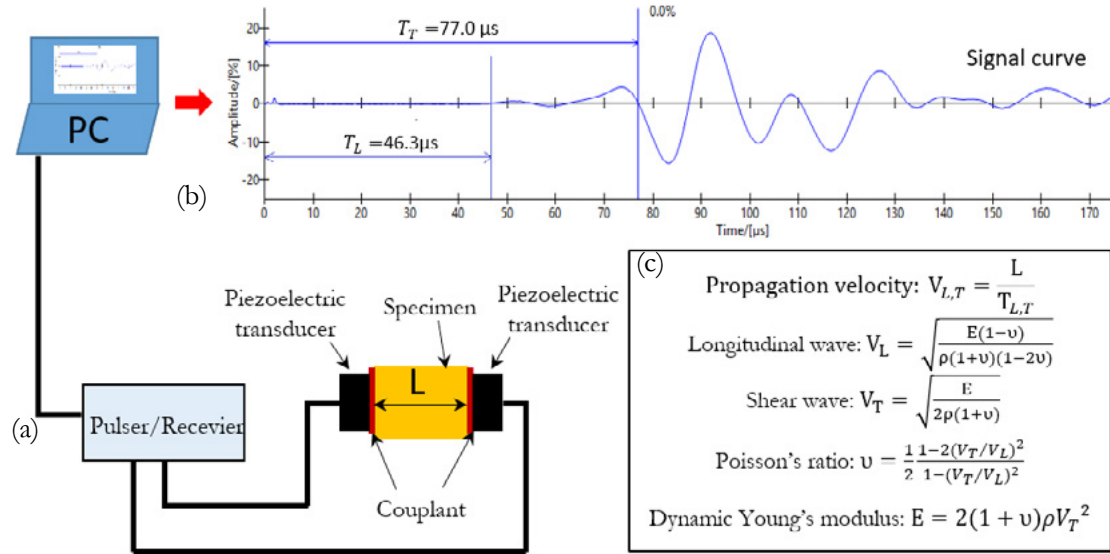


Figure 4: (a) A schematic diagram of the experimental setup for the shear wave measurements, (b) an example of a signal curve, (c) the equations for calculating dynamic Young's modulus.

3.4 Carbonation depths

After splitting of a specimen, carbonation depths were measured after spraying a phenolphthalein alcoholic solution on the cross sections. This indicator presents an uncolored area where the pH is less than 9, that is a carbonated area.

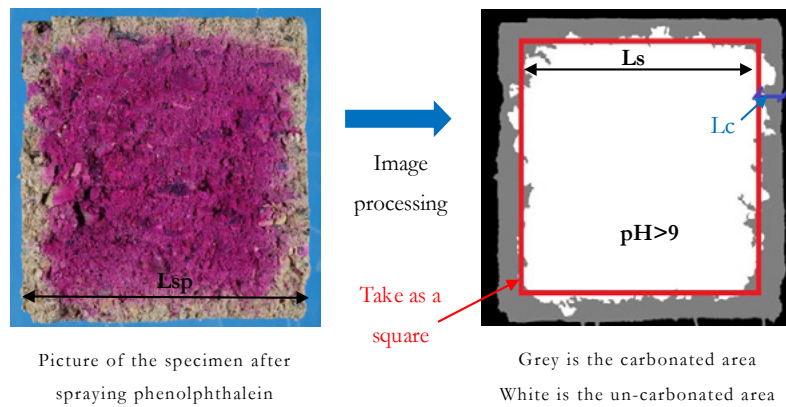


Figure 5: The step of analysing the carbonated area.

As shown in Figure 5, pictures of the specimen were taken with a camera Fujifilm X-T20 then binarized by an image processing IMAGEJ. The values of uncarbonated area (S) were converted from the pixel into square millimetre (about 1 pixel equals 245-275 mm²). This area looked roughly like a square. The length of the uncarbonated area (Ls) can be calculated by:

$$L_s = \sqrt{S} \quad (2)$$

finally, the carbonation depth Lc in mm can be determined by the following equation:

$$L_c = \frac{L_{sp} - L_s}{2} \quad (3)$$

where L_{sp} is the length of the specimen.

4. Results and discussion

4.1 Preliminary characterisation of RA

The particle density and water absorption were determined according to the European Standard NF EN 1097-6 [18] and summarised in Table 3.

Table 3: Physical properties of RA.

Materials	Size	Particle density	Water absorption
	mm	g/cm^3	%wt.
RA	0-6	2.52	4.27

The particle density of RA is between the densities of concrete and natural aggregates ($2.4 - 2.9 \text{ g/cm}^3$) and could be considered as a current aggregate for concrete (between 2 and 3 g/cm^3) but, the water absorption is high with 4.27%wt. unlike natural aggregates (below 3%wt.) currently used for construction. The high water absorption is likely due to the cementitious matrix contained in Rc particles. It is for this major reason that it is difficult to incorporate recycled sand as a fine aggregate for concrete. For greater perspective, the particle density and water absorption were compared to results from the literature (Figure 6).

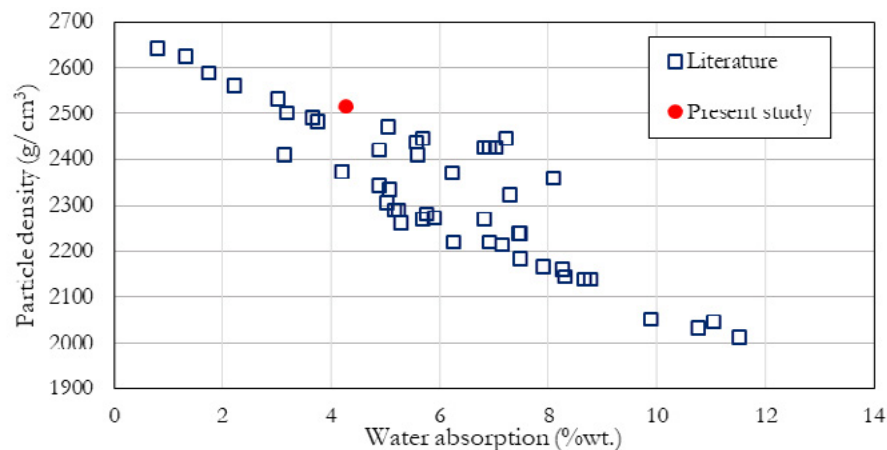


Figure 6: Relationship between density and water absorption [19].

Juan and Gutiérrez had highlighted a linear relationship between these two physical properties [19]: the lower the particle density, the higher is the water absorption. As shown in Figure 6, our results are in good accordance with this linear relationship. Moreover, the water absorption of RA could indirectly give the amount of cementitious matrix present.

Mineralogical analysis of RA is not obvious given the large diversity of mineral phases from the constituents and requires many analyses to be exhaustive. However, two tracers could be easily qualified and quantified by thermogravimetric analysis (TGA) to determine the amount of cementitious matrix and evaluate its carbonation. Portlandite $\text{Ca}(\text{OH})_2$, which is one of a major phase of hydrated cement, and calcium carbonate CaCO_3 , can be distinguished from natural aggregates and carbonation as a function of their decomposition temperature. To get more accurate results, data were analyzed from the TGA curves and the differential thermogravimetric curves (DTG) that are presented in Figure 7.

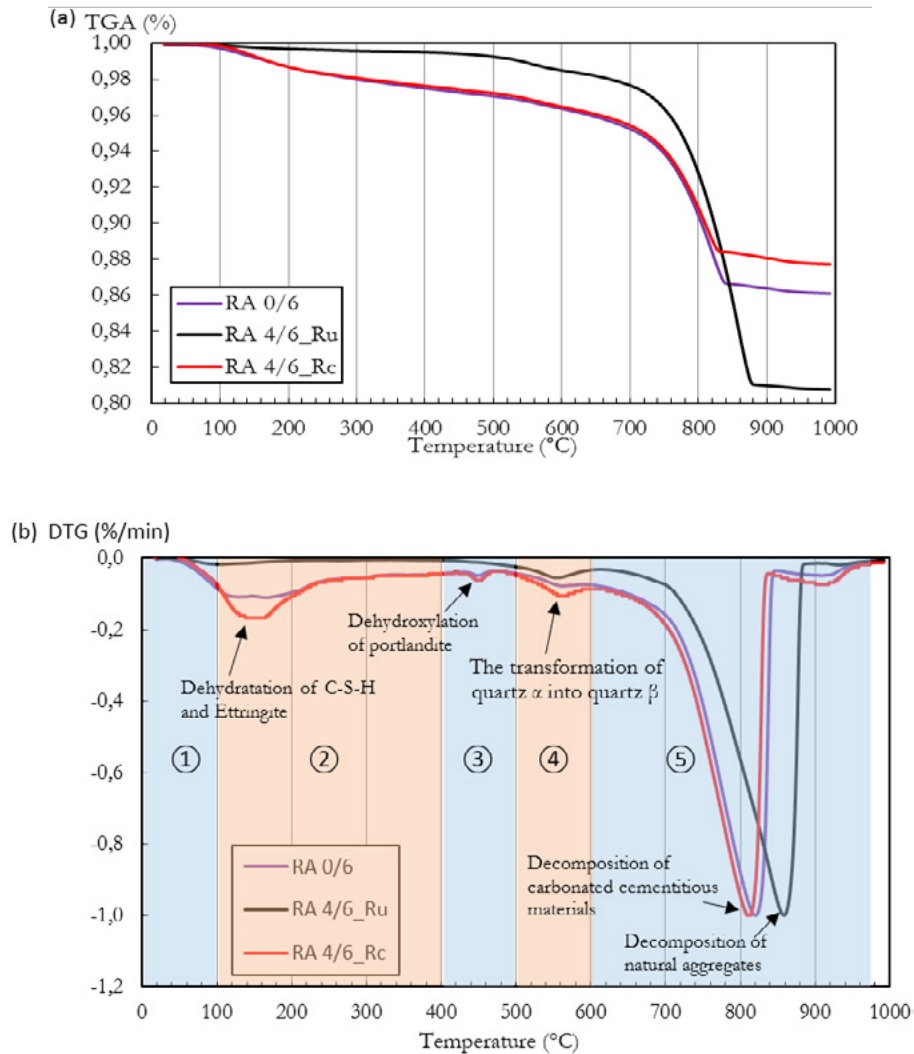


Figure 7: TGA curves (a) and DTG curves (b) of the RA 0/6, RA 4/6_Ru, RA 4/6_Rc.

The TGA curves (Figure 7 (a)) highlight the temperature ranges corresponding to the decarbonation of carbonated cementitious materials and of natural aggregates. Moreover, on the DTG curves (Figure 7 (b)) four peaks can be clearly distinguished and explained as follows in accordance with the decomposition temperature ranges:

1. From ambient temperature to around 100°C: even if the sample has been dried in an oven at 105°C before TGA, an amount of free water remains in each material. The weight loss is more important for RA 0/6 and RA4/6_Rc, which means that the hydrated cement paste begins to decompose;
2. From 100°C to 400°C: Except for the RA 4/6_Ru, the weight loss is attributed to the dehydration of the cement hydrates (especially C-S-H and Ettringite) [20], that is more important for RA0/6_Rc due to the nature of this material.
3. From 400°C to 500°C: the weight loss observed in this temperature range is currently attributed to the deshydroxylation of the Portlandite [21]. As the previous temperature range, the weight loss is more important for RA 4/6_Rc. Note that this material is not totally carbonated and could store more CO₂ to form carbonate in specific conditions (i.e. 2.3 Curing conditions).
4. From 500°C to 600°C: the peak in this temperature range corresponds to the allotropic transformation

of quartz α into quartz β [22]. This allotropic transformation is significant for all three materials and comes from siliceous natural aggregates.

5. From 600 to 975°C: this weight loss corresponds to the decarbonation of calcium carbonate CaCO_3 . There is a clear difference between RA 0/6 and RA 4/6_Rc by comparison with the RA 4/6_Ru. According to Sauman, calcium carbonates, formed by carbonation of cement hydrates, can be poorly crystallised and have unstable forms. They decompose between 500 and 800 °C [23], i.e. in a lower temperature range than natural limestone mineral phase.

Table 4 presents the mass proportions of the Portlandite and the calcium carbonates determined by TGA (Figure 7).

Table 4: Mass proportions of Ca(OH)_2 and CaCO_3 in RA 4/6_Ru, RA 4/6_Rc, and RA 0/6.

	RA 4/6_Ru	RA 4/6_Rc	RA 0/6
Ca(OH)_2 (%wt.)	0.98	1.64	1.54
CaCO_3 (%wt.)	41.3±0.8	21.1±0.6	26.0±0.6

The mass proportion of CaCO_3 in RA 4/6_Ru is more than twice higher than the global material RA 0/6 and the RA 4/6_Rc. Limestone constitutes a large part of natural materials Ru. Conversely, the mass proportion of Portlandite in RA 4/6_Ru is negligible but not more significant for the RA 0/6 and RA 4/6_Rc.

The mass proportion of CaCO_3 comes from both the natural limestone aggregates and the carbonates formed by carbonation during the service life of the concrete and/or just after crushing on the recycling platform. It is impossible to distinguish them quantitatively with TGA. Another analysis by XRD could allow this by quantifying the different carbonates forms, i.e. Vaterite, Aragonite, and Calcite separately.

Considering the hand sorting results for RA 4/6_Rc and RA 4/6_Ru (Table 1), the mass proportion of CaCO_3 in the RA 4/6 size fraction can be considered equal to 24%wt. ($82.9 \times 21.1 + 16.3 \times 41.3$). By comparison with the RA 0/6 ($\approx 26\%$ wt.), it can be assumed that the 0/4 size fraction is not significantly different.

4.2 Carbonation depth

Figure 8 shows the average of the carbonation depths under the natural and accelerated conditions. The carbonation depths are the averages of three specimens at the age of 7, 15, 30, 50, 180 and 270 days after casting. The four images on the right are the cross section of the specimens after spraying the phenolphthalein alcoholic solution at 180 days. As shown in Figure 8, the specimens under RH 65% Acc. are entirely carbonated within 8 hours according to pH drop. Under natural conditions, carbonation depths are lower for high values of RH. This could be explained by a slower diffusion of CO_2 for these more water-saturated specimens [24]. Note the presence of an offset from the origin for the RH 65% Nat. and RH 95% Nat. conditions, and that this one is more important in the second case. This is because the specimens are almost totally water-saturated, preventing the diffusion of CO_2 in porous media. Said diffusion is delayed because of the higher water content in the RH 65% Nat. and RH 95% Nat. conditions, which have lower kinetics of weight loss, unlike RH 65% Acc. and RH 53% Nat., as shown in Figure 9.

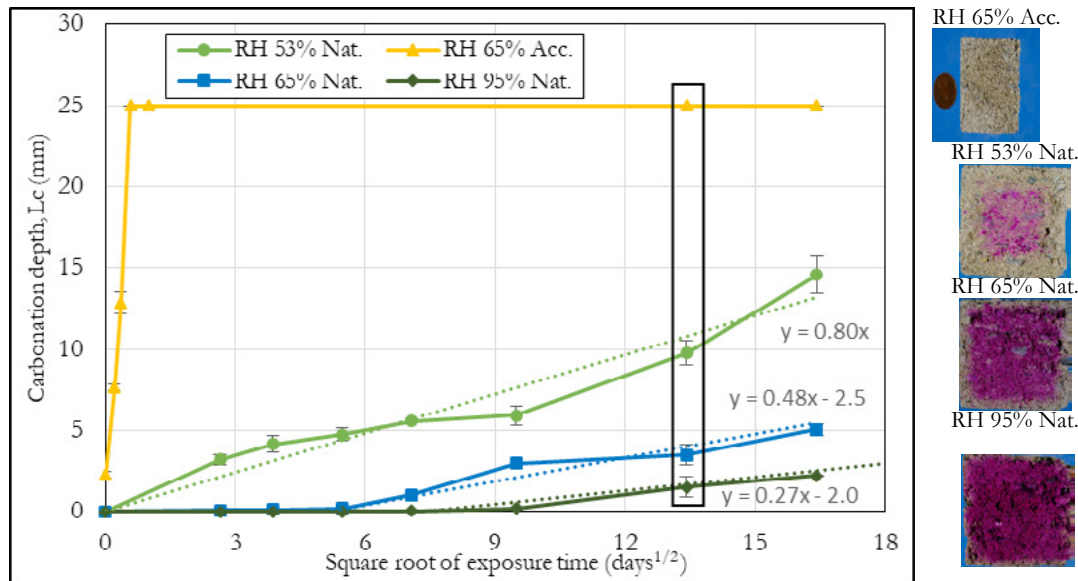


Figure 8: Relationships between the carbonation depths (L_c) and the square root of exposure time of specimens under different conditions.

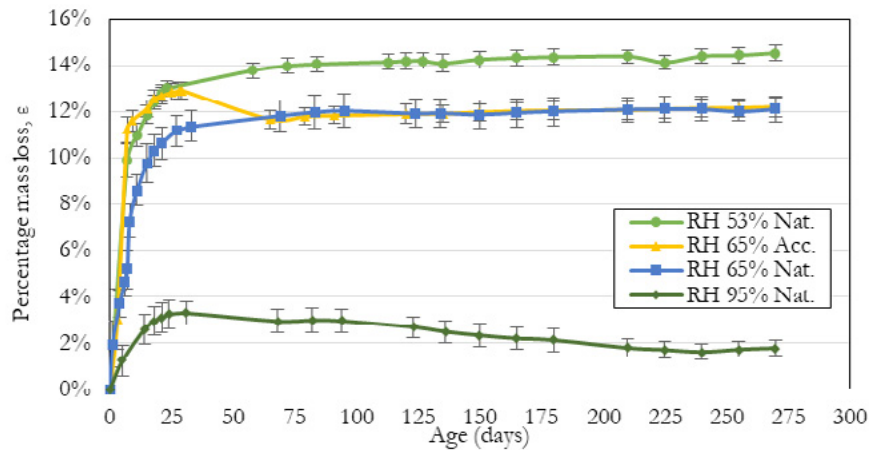


Figure 9: Percentage mass loss of specimens under different conditions in 270 days.

For a reinforced concrete element, the carbonation phenomenon gradually progresses from the external surface in contact with its environment to the inner. The European Standard NF EN 16757 [25] proposes a model to predict the evolution of carbonation depth $X_c(t)$ in mm as a function of the square root of time (t expressed in years). A carbonation coefficient k_t , expressed in $\text{mm}/\text{year}^{1/2}$, allows us to take into account the properties of concrete, the properties of the reinforced concrete element and the environment in which it is exposed (equation 4).

$$X_c(t) = k_t \cdot \sqrt{t} \quad (4)$$

For the CRS, the evolution of the phenomenon seems to be similar. Three carbonation coefficients were estimated for RH 53% Nat., RH 65% Nat., RH 95% Nat. with respectively 0.8, 0.5 and 0.27 $\text{mm}/\text{day}^{1/2}$. According to the European Standard NF EN 16757, the carbonation coefficients of concrete with a strength class lower than 15 MPa are as follows:

- 16.5 $\text{mm}/\text{year}^{1/2}$ (about 0.86 $\text{mm}/\text{day}^{1/2}$) for the indoor in dry climate;
- 11.6 $\text{mm}/\text{year}^{1/2}$ (about 0.6 $\text{mm}/\text{day}^{1/2}$) for the indoor with cover;
- 5.5 $\text{mm}/\text{year}^{1/2}$ (about 0.29 $\text{mm}/\text{day}^{1/2}$) for exposed to rain.

It is interesting to note that the natural carbonation rates of the studied CRS are close to the rate of low-strength concrete (in indoor conditions). In our case, the carbonation rate depends on the proportion of Rc particles contained in RA and on the connectivity and water saturation of the compacted sand. However, it is impossible in the current state of knowledge to determine the effect of intra-granular porous media of Rc particles.

The proportion of CaCO_3 in the carbonated area can help to determine the carbonation degree under different RHs. The mass proportion of CaCO_3 in the carbonated area at the age of 180 days was determined by TGA and shown in Table 5.

Table 5: Calculated amounts of CaCO_3 in the carbonation area of specimens under different conditions at the age of 180 days.

	RH 53% Nat.	RH 65% Acc.	RH 65% Nat.	RH 95% Nat.
CaCO_3 (%wt.)	31.5 ± 1.16	33.2 ± 0.16	30.7 ± 0.05	29.1 ± 0.04

Compared with the proportion of CaCO_3 in RA 0/6 (26.0%wt., in table 4) at 0 days, we found that the CaCO_3 in the carbonated areas increases between 3.1%wt. and 7.2%wt. The proportion is higher in accelerated conditions as a result of the high concentration of CO_2 in this enclosure. Conversely, the proportion of CaCO_3 in RH 95% is the lowest value but higher than the initial proportion. All these results prove that RA can uptake CO_2 by carbonation in each exposure condition, which confirms the trends observed with the carbonation depths determined by phenolphthalein spraying. Another interesting finding is that at the age of 270 days, for RH 65% Acc., the proportion of CaCO_3 is higher with $34.5 \pm 0.64\%$ wt. Over time, the materials continue to uptake CO_2 by carbonation, proving that the carbonation depths distinguished by pH cannot define the carbonation degree.

4.3 Mechanical properties

The ultrasonic wave propagation can display the development of dynamic modulus under different conditions. Figure 10 shows the development of dynamic modulus E as a function of time, normalised by the initial values E_{ini} . The results are the average of three specimens for each condition.

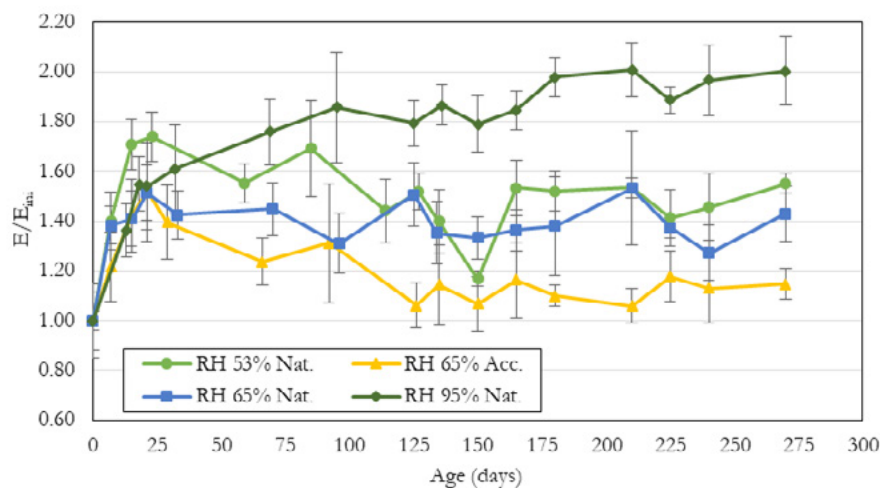


Figure 10: Time-evolution of the dynamic modulus related to the initial dynamic modulus under different conditions.

The evolution of dynamic modulus shows two distinct phases. The first is from 0 to 21 days: E/E_{ini} of all specimens linearly increases. This increase can be associated with the decrease of water content because

the mass of specimens reduces linearly during this period (Figure 9). Take note that the E/E_{ini} under RH 53% Nat. is higher than the others, coinciding with the trends obtained by carbonation depths. We can propose that before 21 days, except for an influence of water content, the dynamic modulus is improved by an increased carbonation depth.

The second phase is after 21 days: The effect of the exposure condition on E/E_{ini} could be identified more easily. Under RH 95% Nat., E/E_{ini} continues to increase. During this period, the specimens at 95% RH gain mass (Figure 9). In explaining the increase of E/E_{ini} , we suppose that the water reacts with the residual cementitious materials and forms new crystalline products, which could fill the porous media in the specimens. In contrast, under RH 53% Nat. and RH 65% Nat., E/E_{ini} tends to decrease and then to stabilise. Notably, the high CO_2 concentration, added into the enclosure RH 65% Acc., could not improve the dynamic modulus. This is in contrast to the conclusion of Nakarai and Yoshida [26]. In the present study, accelerated carbonation has a negative effect on the mechanical properties of the CRS. Other experimental investigations, such as XRD and micro tomography, should allow a better understanding of the evolution of the microstructure.

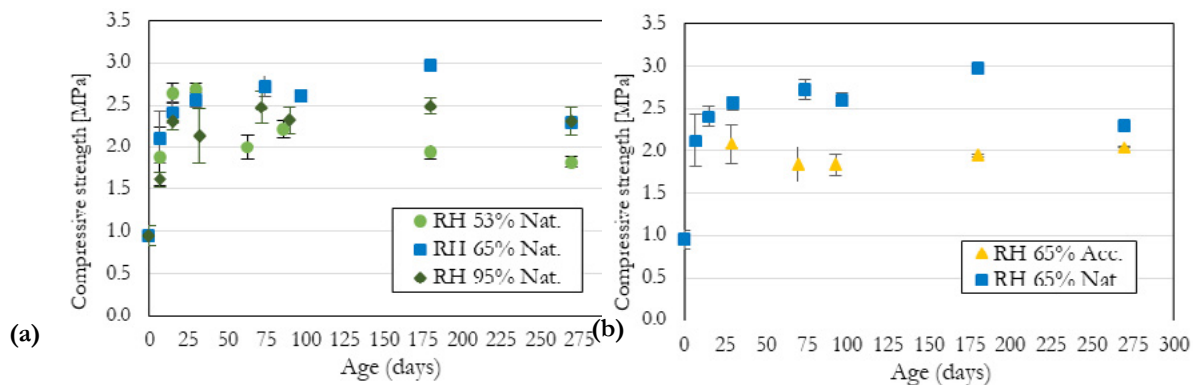


Figure 11: Development of compressive strength of specimens under different conditions. (a) Under natural conditions and different RH. (b) Under RH=65%, natural carbonation condition VS accelerated carbonation condition.

Apart from the dynamic modulus, we can also synthesize the results of compressive strength to analyse the development of mechanical properties (Figure 11). In order to clarify the possible reasons for the time-evolution of compressive strength, the results have been divided into two Figures.

As seen in Figure 11, two distinct phases are also found in the evolution of compressive strength. During the first 30 days, the compressive strength increases to a value 2.1–2.7 times higher than the initial value. After 30 days, the compressive strength can be considered almost constant. From Figure 11a, it is also observed that no difference exists in compressive strength for each condition. Thus the strength is not affected by the residual cementitious material hydration and natural carbonation. Moreover, carbonation does not improve the compressive strength because the results for RH 65% Acc. are notably lower than for RH 65% Nat (Figure 11b), as opposed to some other findings [27, 28], which were focused on the carbonation of concrete and recycled concrete aggregates. We suppose that the RA used in the specimens had been carbonated by the carbonation of $Ca(OH)_2$ during the crushing at the recycling platform and transport. Therefore, under a high CO_2 gas concentration (RH 65% Acc.), the $CaCO_3$ is mostly generated from the carbonation of C-S-H gel, which would have caused the weak strength as found in previous studies [26, 29].

Figure 12 shows the relationships between the compressive strength and the water content of specimens under different conditions.

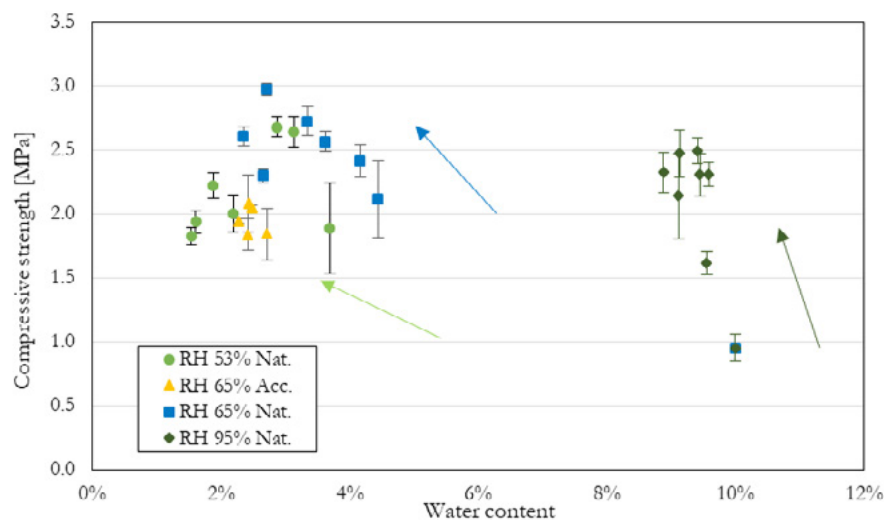


Figure 12: Relationships between the compressive strength and the water content of specimens under different conditions.

This graph completes the analysis of Figure 12, from which the reader can clearly observe that the mechanical properties increase as a function of time, regardless of the amount of water contained in the material. Two parameters appear to control this evolution: on the one hand, the residual hydration of the cement and / or the hydration of the clay bricks by pozzolanic reaction for a high relative humidity; and on the other hand, the water content which, in weak proportion, ensures the bonding of the particles by the capillary bridges. In all cases, an important point is that whatever the amount of water contained in the material, the mechanical properties remain stable in the long term. For applicability in road engineering, this stability offers a better examination and guarantee of durability in the long term.

5. Conclusions

This work investigated the potential residual reactivity of RA under four conditions of RH: 53±5%, 95±5%, 65±5% and 65±5% with 3% CO₂. Based on the results of carbonation depths and mechanical properties, the following conclusion can be made:

1. Under natural conditions, the carbonation coefficient is lower for larger values of RH and is of the same order of magnitude of the carbonation coefficient of Ordinary Portland Concrete. The reason can be that water fills the pores in specimens, which can prevent CO₂ diffusion. Besides, RA can uptake CO₂ by carbonation in each exposure condition what is confirmed by the trends observed with the carbonation depths. These prove that RH can not only limit the carbonation rate but also control the carbonation degree.
2. The dynamic modulus increases with the decrease of water content until the age of 21 days and dynamic modulus under RH 53% Nat. is the highest. We suppose that except for an influence of water content, the dynamic modulus is improved by carbonation before 21 days. In the long term, E/E_{ini} continues to increase under RH 95% Nat. We suppose that the increase of dynamic modulus is due to the hydrated residual cementitious materials that could fill the pores in the specimen. While the carbonation rate is more important under the accelerated condition, we observe that the dynamic modulus is not improved. It is opposite to the finding of Nakarai and Yoshida [26].
3. The compressive strength increases under all conditions in the first month and then is almost stable. The absorbed water into aggregates that form links between aggregates can explain this increase. The compressive strength under RH 65% Nat. is higher than that under RH 65% Acc., the reason could be

the carbonation of C-S-H gel.

4. The relationship between the compressive strength and the water content point out that the water content affects the strength. Compressive strength increases with the decrease of water content in the same way as the dynamic modulus.

So far, we studied the performance CRS used RA, and the results propose that RA has reactivity under different environments. The following step is to study the microstructure of CRS. The research can be extended to the analysis of the pozzolanic reaction that could improve the strength of pavement structures in the long term.

6. Acknowledgement

The authors are grateful to the ADEME agency and the Region of Nouvelle Aquitaine in France, which funded this project. They wish to thank Jean David Lau Hiu Hoong for the technical contribution, and other professors and the laboratory of La Rochelle University (LaSIE).

7. References

- [1] Akhtar, A., Sarmah, A.K., n.d. Construction and demolition waste generation and properties of recycled aggregate concrete: A global perspective. Journal of Cleaner Production. <https://doi.org/10.1016/j.jclepro.2018.03.085>
- [2] Rao, A., Jha, K.N., Misra, S., 2007. Use of aggregates from recycled construction and demolition waste in concrete. Resources, Conservation and Recycling 50, 71–81. <https://doi.org/10.1016/j.resconrec.2006.05.010>
- [3] Le recyclage des déchets produits par l'activité de BTP en 2014 | Données et études statistiques [WWW Document], n.d. URL <https://www.statistiques.developpement-durable.gouv.fr/le-recyclage-des-dechets-produits-par-lactivite-de-btp-en-2014> (accessed 3.17.19).
- [4] Mahieux, P.-Y., Turcry, P., Lux, J., Audo, M., Hamdoun, H., Nelfia, L.O., Aït-Mokhtar, A., 2016. Déchets inertes du BTP : Vers de nouvelles voies de recyclage.
- [5] Denot Agathe, and Jérôme Crosnier. 2009. «Compatibilité physico-chimique de graves de recyclage avec les autres matériaux utilisés en voirie: Un réel enjeu » Bulletin des Laboratoires des Ponts et Chaussées, no 275 (avril): pp 85-96.
- [6] «Matériaux non traités, Synthèse des pratiques documentées.» Journées Techniques Routes. Nantes, 2011.
- [7] Arm, M. «Self-cementing properties of crushed demolished concrete in unbound layers: results from triaxial tests and fields test.» Waste Management 21, 2001: 235-239.
- [8] Vegas, I., J. A. Ibanez, A. Lisbona, A. Saez de Cortaraz, et M. Frias. «Pre-normative research on the use of mixed recycled aggregates in unbound road sections.» Construction and Building Materials 25, 2011: 2674-2682.
- [9] Chai, L., Monismith, C.L., Harvey, J., n.d. Re-cementation of Crushed Material in Pavement Bases 28.
- [10] Paige-Green, P., n.d. A PRELIMINARY EVALUATION OF THE REUSE OF CEMENTITIOUS MATERIALS 10.
- [11] Shui, Z., Xuan, D., Wan, H., Cao, B., 2008. Rehydration reactivity of recycled mortar from concrete

waste experienced to thermal treatment. Construction and Building Materials 22, 1723–1729. <https://doi.org/10.1016/j.conbuildmat.2007.05.012>

[12] Poon, C.-S., Qiao, X.C., Chan, D., 2006. The cause and influence of self-cementing properties of fine recycled concrete aggregates on the properties of unbound sub-base. Waste Management 26, 1166–1172. <https://doi.org/10.1016/j.wasman.2005.12.013>

[13] NF EN 933-11. Tests for geometrical properties of aggregates - Part 11: classification test for the constituents of coarse recycled aggregate

[14] Cerema, Guide d'application, Acceptabilité environnementale de matériaux alternatifs en technique routière, les matériaux de déconstruction issus du BTP, 2016.

[15] NF P 94-102-1. Soils: investigation and testing - Soil treated with hydraulic binder, possibly combined with lime, for use as a selected fill - Part 1: definition - Composition – Classification.

[16] NF EN 13286-53. Unbound and hydraulically bound mixtures - Part 53: methods for the manufacture of test specimens of hydraulically bound mixtures using axial compression.

[17] NF EN 13286-41. Unbound and hydraulically bound mixtures - Part 41: test method for the determination of the compressive strength of hydraulically bound mixtures.

[18] NF EN 1097-6. Tests for mechanical and physical properties of aggregates - Part 6: Determination of particle density and water absorption

[19] de Juan, M.S., Gutiérrez, P.A., 2009. Study on the influence of attached mortar content on the properties of recycled concrete aggregate. Construction and Building Materials 23, 872–877. <https://doi.org/10.1016/j.conbuildmat.2008.04.012>

[20] G. Mounajed and W. Obeid. Modélisation du comportement thermo-hygro-mécanique des bétons à hautes températures. Rapport intermédiaire pour le livre BHP 2000, document MOCAD, 2001.

[21] Villain, G., Thiery, M., Platret, G., 2007. Measurement methods of carbonation profiles in concrete: Thermogravimetry, chemical analysis and gammadensimetry. Cement and Concrete Research 37, 1182–1192. <https://doi.org/10.1016/j.cemconres.2007.04.015>

[22] Grattan-Bellew, P.E., 1996. Microstructural investigation of deteriorated Portland cement concretes. Construction and Building Materials 10, 3–16. [https://doi.org/10.1016/0950-0618\(95\)00066-6](https://doi.org/10.1016/0950-0618(95)00066-6)

[23] Z. Sauman, Carbonation of porous concrete and its main binding components, Cem. Concr. Res. 1 (1971) 645–662.

[24] Namouniara, D.K., 2015. Etude expérimentale de la diffusion du CO₂ et des cinétiques de carbonatation de matériaux cimentaires à faible dosage en clinker (phdthesis). Université de La Rochelle.

[25] NF EN 16757. Sustainability of construction works - Environmental product declarations - Product category rules for concrete and concrete elements.

[26] Nakarai, K., Yoshida, T., 2015. Effect of carbonation on strength development of cement-treated Toyoura silica sand. Soils and Foundations 55, 857–865. <https://doi.org/10.1016/j.sandf.2015.06.016>

[27] Shi, C., Liu, M., He, P., Ou, Z., 2012. Factors affecting kinetics of CO₂ curing of concrete. Journal of Sustainable Cement-Based Materials 1, 24–33. <https://doi.org/10.1080/21650373.2012.727321>

[28] Zhang, J., Shi, C., Li, Y., Pan, X., Poon, C.-S., Xie, Z., 2015. Performance Enhancement of Recycled Concrete Aggregates through Carbonation. *Journal of Materials in Civil Engineering* 27, 04015029. [https://doi.org/10.1061/\(ASCE\)MT.1943-5533.0001296](https://doi.org/10.1061/(ASCE)MT.1943-5533.0001296)

[29] Ho, L.S., Nakarai, K., Ogawa, Y., Sasaki, T., Morioka, M., 2017. Strength development of cement-treated soils: Effects of water content, carbonation, and pozzolanic reaction under drying curing condition. *Construction and Building Materials* 134, 703–712. <https://doi.org/10.1016/j.conbuildmat.2016.12.065>

Production of Synthetic Wollastonite Mineral By Using Industrial Waste Materials

H.E. Yücel¹, H. Ö. Öz¹, O. Ersoy², M. Güneş¹, Y. Kaya¹

¹Nigde Omer Halisdemir University, Department of Civil Engineering, 51240, Nigde, Turkey.

²Hacettepe University, Department of Geological Engineering, 06800, Ankara, Turkey.

Abstract

Wollastonite is a mineral that is used as industrial raw material in several kind of areas. One of these areas is construction industry in which it is used as an admixture to produce cementitious materials. Wollastonite mineral positively effects mechanical and durability properties of cementitious materials due to its acicular particle structure, which is the most important property for the product manufactured with wollastonite. Wollastonite mineral can be produced synthetically by using various waste materials to ensure environmental waste management and to produce sustainable construction materials. Theoretical composition of wollastonite with acicular particle structure is approximately 48% CaO and 52% SiO₂. Therefore, minerals having high CaO and SiO₂ content can be used to produce this mineral. Especially, industrial waste materials such as silica fume (SF), granulated blast furnace slag (GBFS) and marble powder (MP) can be the key minerals for the production of wollastonite. In this study, four different synthetic wollastonite (SW) productions were performed by using SF, GBFS, MP, sintered marble powder (SMP) and quicklime (QL). SF was used as source of SiO₂ in all productions. QL, GBFS, MP and SMP were used as source of CaO. The production of SWs were performed by using a new technique. This new technique consists mainly of mechanochemical process, hydrothermal process and sintering process. SEM, XRF and XRD analysis were applied to the manufactured mixtures. Results of the analysis indicated that all mixtures produced synthetically were wollastonite. However, SWs produced with SF-QL (SQ), SF-GBFS (SG) and SF-MP (SM) mixtures did not have an acicular particle structure. Moreover, the acicular particle formation of SWs was obtained from SF-SMP (SS) mixture.

Keywords: Synthetic wollastonite mineral, industrial waste materials, silica fume, granulated blast furnace slag, marble powder.

1. Introduction

Wollastonite mineral is a shape of naturally occurring acicular, white colour (usually) calcium silicate (CaSiO₃) with high modulus of elasticity [1, 2]. Wollastonite is a relatively hard material with a hardness of 4.5 to 5.5 on the Mohs scale with a specific gravity of 2.9 [3, 4]. This mineral containing approximately 90% of CaO and SiO₂ minerals may include a low amount of elements such as iron, aluminium, manganese, magnesium, sodium and potassium. Manganese and iron elements affect its colour [3, 5-9]. Wollastonite that found as α -wollastonite and β -wollastonite in nature has many beneficial physical and chemical properties such as low thermal expansion, low oil and water adsorption and chemical inertness [3, 8]. Nowadays, wollastonite mineral has been extensively known worldwide for its major industrial importance thanks to these properties [1]. Wollastonite mineral with acicular particle structure is used primarily in ceramics, plastics, paints, paint fillers, rubbers, coatings, adhesives and refractories [1, 3, 5]. Natural wollastonite generally consists only in small amounts and is frequently existed with other minerals such as calcite, diopside and garnet etc. [3, 10].

Therefore, an interest has been aroused in research to improve pure synthetic wollastonite (SW), especially wollastonite powder with high aspect ratios for all of the applications mentioned above [3, 5]. Moreover, the aspect ratio and the size of natural wollastonite mineral are limited by the condition of the deposits. If the wollastonite can be synthesized artificially and its aspect ratio and size can be checked, new applications such as fillers for engineering plastics and for bioactive materials with superior toughness will become possible [11].

There are three methods to produce wollastonite mineral at the present time. These three methods are wet method, liquid phase reaction method and solid state reaction method. Wet method is generally applied at low temperatures (less than 200°C) with high pressure. This method can be further separated to hydrothermal reaction, sol-gel processing and colloid emulsion technique. In liquid phase reaction method, starting mixtures are melted inside of appropriate crucibles at a compound close to wollastonite together with other oxides such as boron oxide (B_2O_3) or sodium oxide (NaOH) to lower the melting temperature. The liquid is solidified, occasionally cast into thin layers, followed by different heat treatments [3]. Solid state reaction method is based upon the reaction of silica (SiO_2) with calcium carbonate ($CaCO_3$) or calcium oxide (CaO) at high temperatures (above 800°C). These methods have some advantages and disadvantages. The highest-aspect-ratio wollastonite can be produced with the wet method among three methods. In liquid phase reaction method, high-aspect-ratio wollastonite powder can be produced. However, the working temperature is generally higher than 1400°C. In this case, the liquid phase is a mixture of basic CaO and acidic SiO_2 of 1:1 molar ratio, with some metal oxides added for various purposes. In solid state reaction method can be utilized different cheap raw materials such as calcite, silica fume (SF), natural siliceous carbonates, marble waste and tailing materials. However, these raw materials fail to produce acicular particles. For the solid state reaction method, formation of wollastonite in the products is observed with XRD analysis. However, the wollastonite produced with this method does not show acicular shapes. When the aspect ratio of produced wollastonite is not important, the solid state reaction method is most effective.

SF, calcite, granulated blast furnace slag (GBFS) and marble powder (MP) are some of the above mentioned waste materials. CaO, is one of the most basic materials for the production of wollastonite, is a mineral obtained by sintering of $CaCO_3$ (calcite). It is possible to find calcite formation in almost every region of Anatolia. Especially, in the Nigde region in Turkey, there are calcite quarries that have a very rapid production increase in the last 10 years and these quarries have a reserve of 10 million tons. SF is a by-product obtained from the industry that produces silicon metal or ferrosilicon [12]. SF has a consumption amount of 1 million tons in the world and this mineral is widely used as an additive material in cement and concrete [13]. Slags are wastes obtained as a result of metallurgical processes such as the production of metals or purification of pure metals [14]. In United States, the iron and steel industry produces about 18 million m³ of slag each year [15, 16]. In Turkey, blast furnace slag can be obtained from only Eregli Iron and Steel Company about 550000 tonnes/year, and thousands tonnes of slag waste for each year are stored in iron steel factories [16]. MP is production waste of marble factories [17]. An average of 30% of the marbles processed in the marble factories occurs as production waste. It is known that marble blocks processed each year in Turkey are approximately 2200000 tonnes. Therefore, it can be said that 660000 tons marble dust is discarded without the assessment [17].

Waste materials mentioned above need to be evaluated especially in industries such as construction and building. In addition, these waste materials can be evaluated in the production of wollastonites which can be used as cement substituting material in concrete/mortar in construction industry. Kalla et al. [9] highlighted that compressive strength and flexural strength of concrete incorporating 10% wollastonite instead of cement increased with respect to control mixture. In addition, wollastonite intensifies the microstructure of mortars/concretes due to its filling effect and reduces the water absorption of the material [18, 19].

In this study, wollastonite mineral known beneficial effects on concrete/mortar were produced by using waste materials. In the production of SW; QL, SF, GBFS, MP and sintered marble powder (SMP) were used as raw materials. SEM, XRF and XRD analysis were performed to determine particle texture, chemical composition and patterns of the produced SWs, respectively. According to results of analysis, in addition to providing environmental benefit by using waste materials in the production of SW, wollastonite can be produced and it can be contributed to the construction industry.

2. Methodology

In this study, four different SW were produced by using SF, QL, GBFS, MP and SMP. SW production was performed by using autoclave and sintering methods. This production method consists of three stages. These stages can be classified as mechanochemical process, hydrothermal process and sintering process. SF was used as SiO_2 source for all mixtures in the production of SW, while QL, GBFS, MP and SMP were used as CaO source for SQ, SG, SM and SS mixtures, respectively. The mixtures were named using the initials of their abbreviations. For example, the SQ mixture consisting of SF and QL minerals was named using S from the SF mineral used as SiO_2 source and the Q from QL mineral used as CaO source. The grain size distributions and XRF analysis of these materials are shown in Figure 1 and Table 1, respectively. The CaO and SiO_2 contents of the mixtures were calculated as 1:1 mol with the aid of XRF analysis. The waste material contents of the four mixtures are listed in Table 2. The pure water contents used for all mixtures were determined with respect to the consistency of the mixtures. The pure water contents and pure water/total solids contents of the mixtures are also presented in Table 2. The SMP used as CaO source in the IV mixture was obtained as a result of sintering of the MP in the ash furnace, which was set at 40 °C per minute and waiting for 1 hour at 1000 °C.

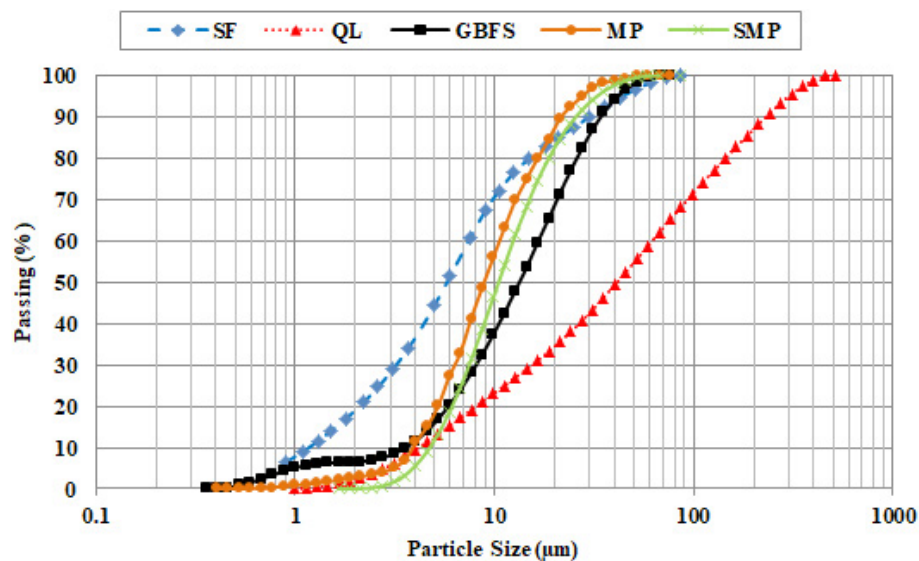


Figure 1: Grain size distributions of SF, QL, GBFS, MP and SMP minerals.

The mixtures prepared by using the mixing proportions given in Table 2 are shown in Figure 2. The mixtures were placed into the ball agate and the agate was placed in the ball mill. The ball mill was stirred for 30 minutes at a speed of 250 RPM and mechanochemical process began. The obtained mixture was placed in autoclave by placing in teflon and waited for 48 hours at 200 °C. Hydrothermal autoclave technique, which provides the formation of better crystal structure with moisture, pressure and temperature, forms the hydrothermal process part of the production stage.

Table 1: XRF analysis of waste materials.

Chemical Analysis (%)	SF	QL	GBFS	MP	SMP
CaO	0.547	91.259	38.834	46.151	78.601
SiO ₂	93.534	0.309	36.824	0.621	1.535
Al ₂ O ₃	0.778	0.071	13.314	0.204	0.414
Fe ₂ O ₃	0.881	0.104	0.727	0.148	0.245
MgO	0.794	1.725	5.648	7.636	17.919
SO ₃	0.113	0.434	0.562	0.116	0.152
K ₂ O	0.995	0.007	0.777	0.020	0.050
Na ₂ O	0.404	0.013	-	0.049	0.007
ZnO	0.012	-	0.001	-	-
Mn ₃ O ₄	0.060	-	1.170	-	0.009
Cr ₂ O ₃	0.003	-	0.005	-	-
V ₂ O ₅	0.002	-	0.016	-	-
P ₂ O ₅	0.088	-	0.009	-	0.014
SrO	-	0.047	0.058	0.027	-
BaO	-	0.020	0.157	-	-
CuO	-	0.011	-	-	-
HfO ₂	-	-	0.005	-	-
ZrO ₂	-	-	0.018	-	-
TiO ₂	-	-	0.761	0.024	0.116
Loss of Ignition	1.930	5.500	1.920	45.000	0.900

Table 2: Mixing proportions.

Code	Pure water (gr)	SF (gr)	QL (gr)	GBFS (gr)	MP (gr)	SMP (gr)	pw/s*
SQ	215.931	77.080	66.874	-	-	-	1.5
SG	182.147	8.856	-	173.291	-	-	1.0
SM	52.700	19.250	-	-	36.450	-	1.0
SS	46.480	11.010	-	-	-	12.230	2.0

*pure water/total solid content of mixture

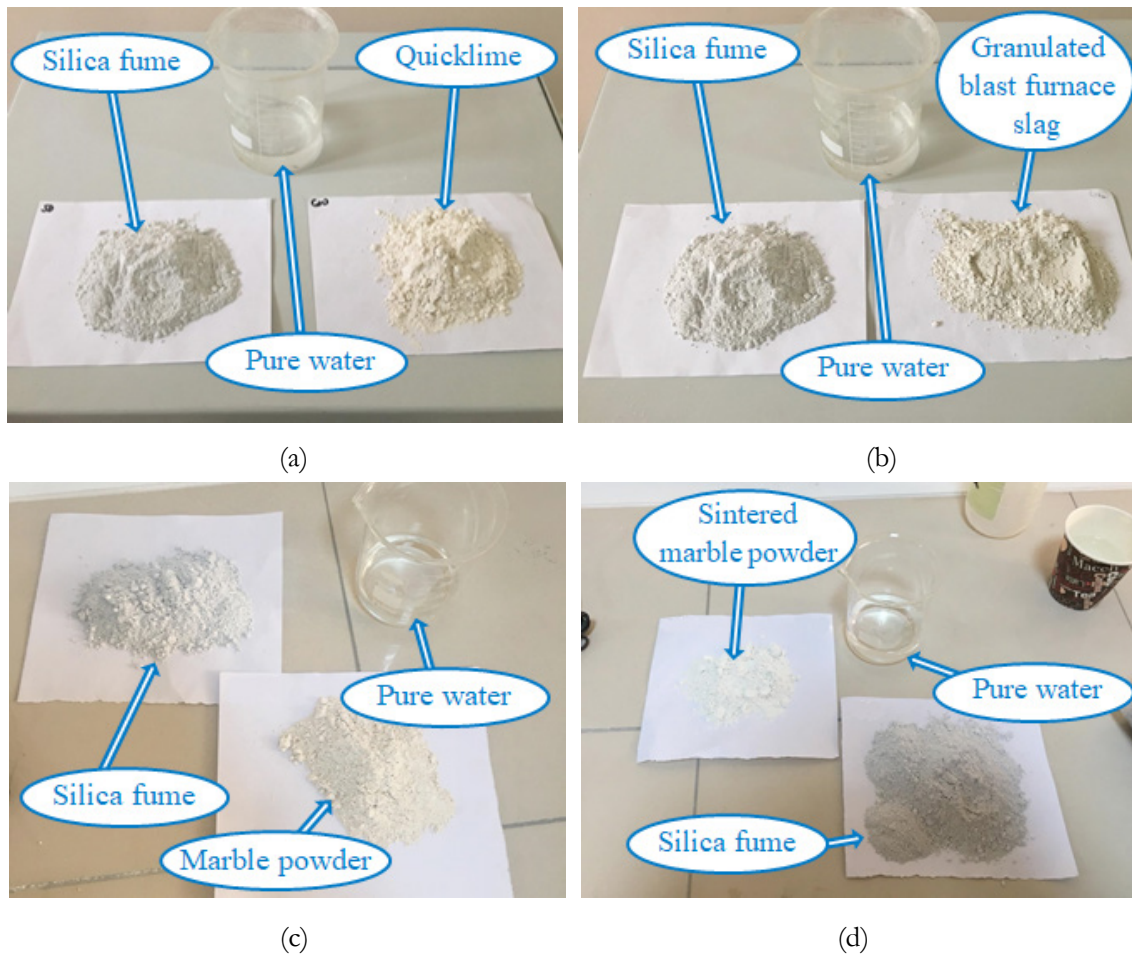
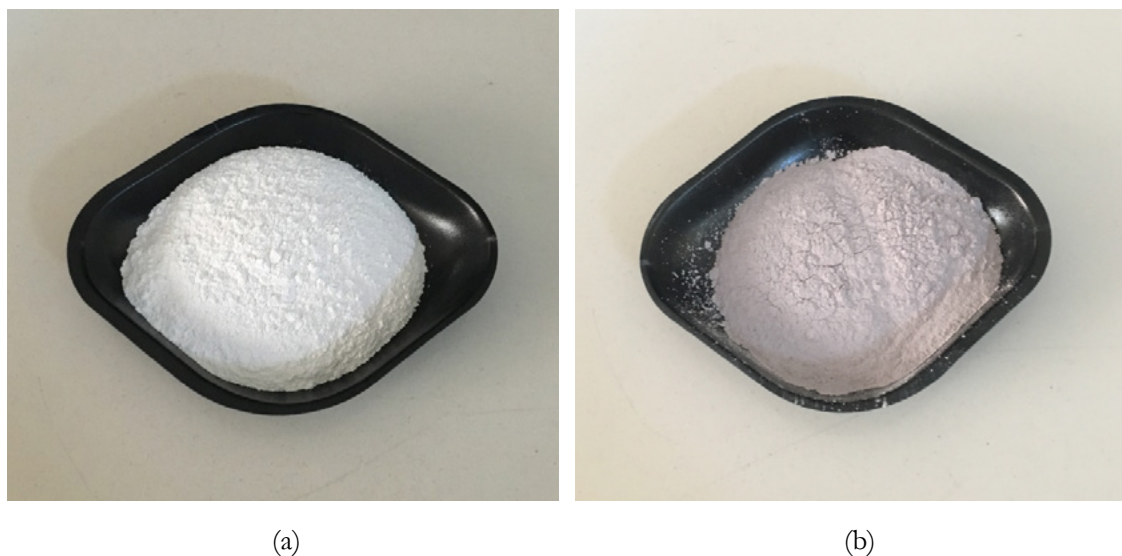


Figure 2: Materials used in (a) SQ, (b) SG, (c) SM and (d) SS mixtures.

Autoclave was removed from the oven at the end of 24 hours and left to room temperature. When the autoclave was opened, tobermorite (calcium silicate hydrate mineral) was obtained. The tobermorite was ground and made ready for sintering. Approximately 250 grams of ground tobermorite was placed in crucibles. The ash furnace was set to wait for 1 hour at 1000 °C, increasing by 40 °C/min. The sintering process forms the solid state reaction process of SW production. The sintering process was completed in this way and SW presented in Figure 3 was stored in a sample bag in an environment away from moisture.



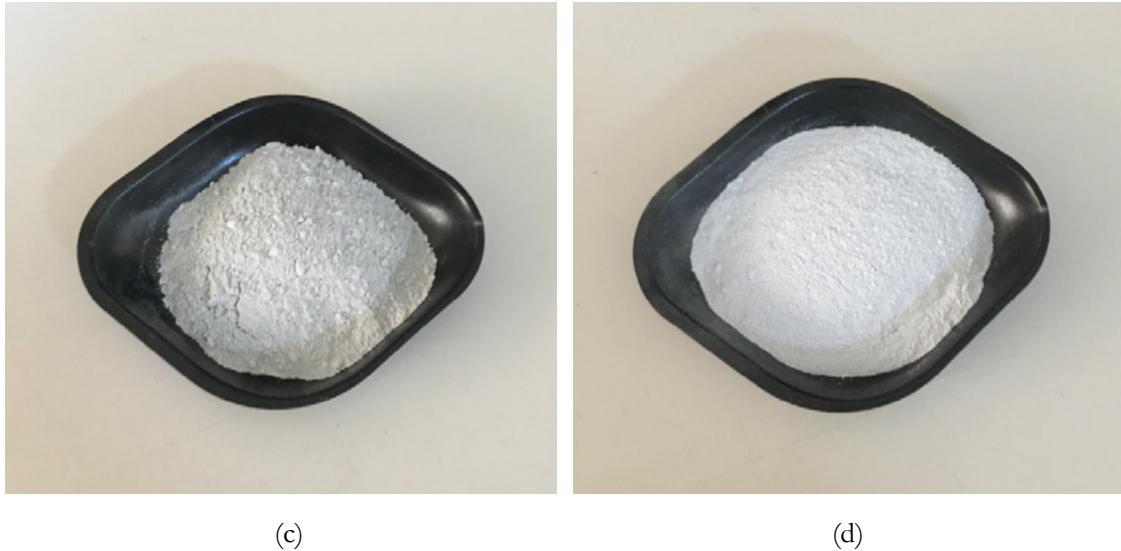
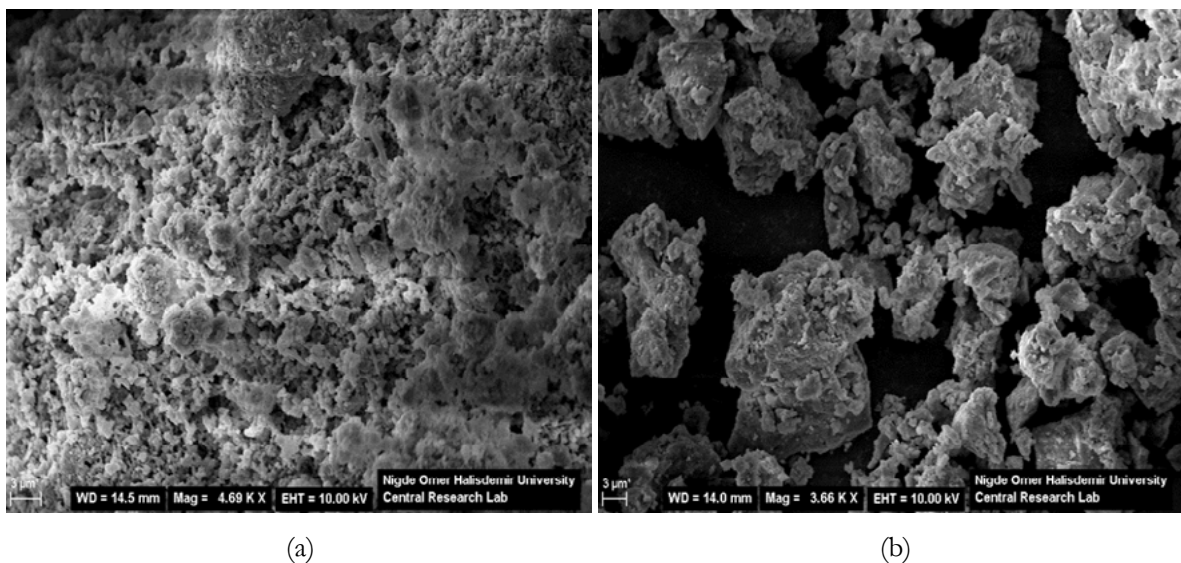


Figure 3: SW produced with (a) SQ, (b) SG, (c) SM and (d) SS mixtures

3. Results and discussion

3.1 SEM

The SEM images of SWs obtained from SQ, SG, SM and SS mixtures are presented in Figure 4. When the SEM analysis of SWs was examined, no acicular structure was observed in SWs obtained from SQ, SG and SM mixtures. In the SW produced with SS mixture, a very limited number of acicular particle structures were observed. In addition, the formation of agglomerated particles was generally observed for all produced SWs. The differences of chemical compositions of SWs produced by using waste materials can be seen in Table 1. Although CaO and SiO₂ were kept constant for all SW mixtures, the other elements in raw materials such as MgO and Al₂O₃ have been disrupted the purity of CaO and SiO₂. Therefore, it was seen that there is no directly acicular particle structure of SWs. In addition, it was observed that the SiO₂ content in SF used as a source of SiO₂ in the production of SWs is about 93% levels and not enough for the formation of the acicular particle structure [20].



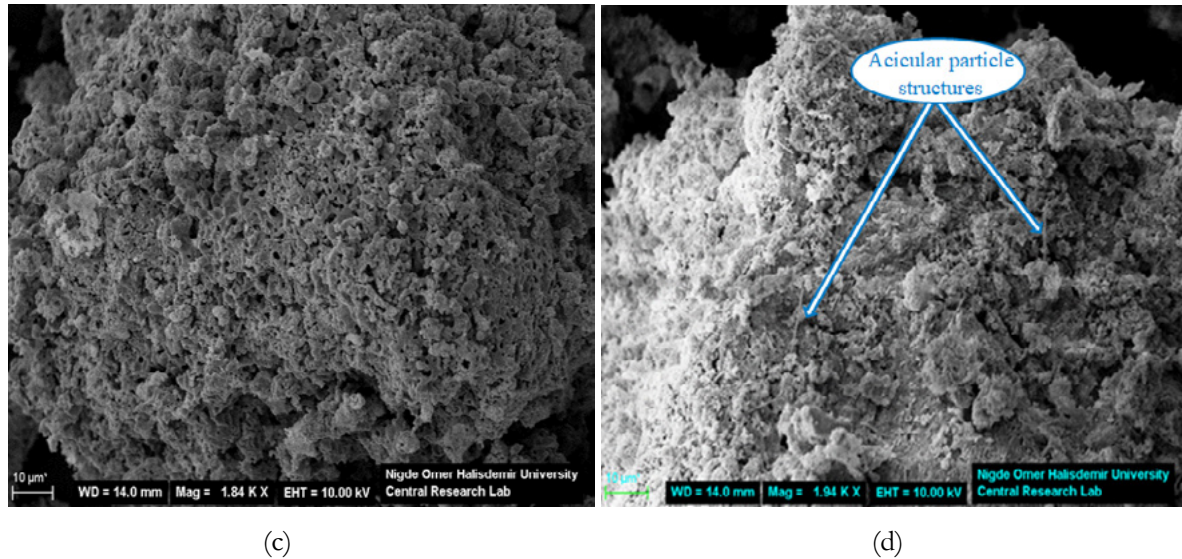


Figure 4: SEM images obtained from (a) SQ, (b) SG, (c) SM and (d) SS mixtures

3.2 XRF

The chemical composition results obtained from XRF analysis of SW are listed in Table 3. According to the results, SWs produced with SQ, SG, SM and SS mixtures mainly includes CaO in the ratios of 53.883%, 47.984%, 48.839% and 47.590% and SiO₂ in the ratios of 42.857%, 34.514%, 40.786% and 43.406%, respectively. These ratios obtained from the mixtures are similar to chemical composition of wollastonite found in various countries given in Table 4. In addition, because of the different quantity of other elements found in raw materials, the content of some elements of the SWs were higher than that of natural wollastonite. Therefore, as seen in SEM pictures, SWs obtained from waste materials could not show generally acicular particle structure.

Table 3: XRF analysis of SWs obtained from wastes.

Chemical Analysis (%)	SQ	SG	SM	SS
CaO	53.883	47.984	48.839	47.590
SiO ₂	42.857	34.514	40.786	43.406
Al ₂ O ₃	0.324	9.376	0.400	0.382
Fe ₂ O ₃	0.666	1.119	0.710	0.687
MgO	0.970	-	7.076	5.914
SO ₃	0.343	1.147	0.261	0.210
K ₂ O	0.667	0.949	0.645	0.523
Na ₂ O	0.149	0.202	0.176	0.139
P ₂ O ₅	0.074	0.026	0.060	0.065
TiO ₂	-	1.233	-	-
MnO	0.067	1.451	0.047	0.044
Loss of Ignition	0.800	1.000	0.880	0.500

Table 4: Chemical composition (%) of wollastonite from several countries [9].

Chemical Analysis (%)	Finland	USA	India	Kenya	Mexico	China
CaO	45	47	48	42	47	43-50
SiO ₂	52	51	49	55	52	46-53
Al ₂ O ₃	0.4	0.3	0.7	0.1	0.5	0.3-0.4
Fe ₂ O ₃	0.2	0.6	0.4	0.07	0.2	0.1-0.2
MgO	0.6	0.1	0.06	0.8	0.08	0.2
K ₂ O	0.01	NR	0.1	0.04	0.04	NR
Na ₂ O	0.1	NR	0.02	0.04	0.02	NR
TiO ₂	max. 0.05	0.05	Traces	0.01	0.06	NR
MnO	max. 0.01	0.1	0.1	0.01	0.4	NR

max: maximum; NR: not reported.

3.3 XRD

XRD patterns of natural wollastonite and SWs obtained from SQ, SG, SM and SS mixtures are presented in Figure 5.

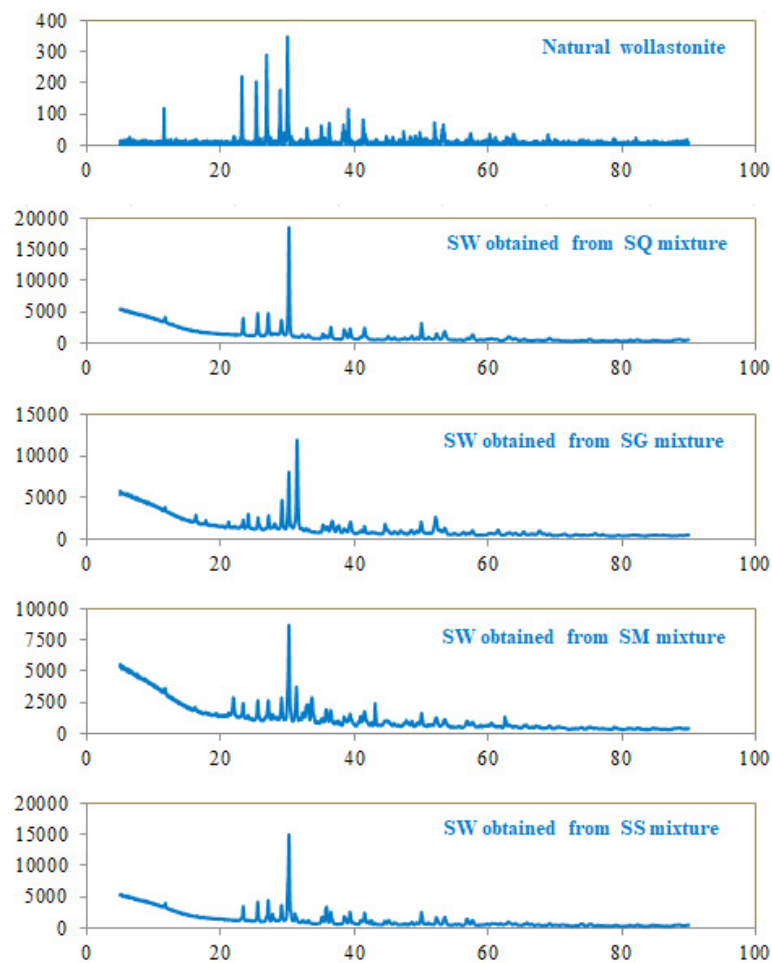


Figure 5: XRD patterns of natural wollastonite and SQ, SG, SM and SS mixtures.

Large-sized peaks show alpha wollastonite and small-sized peaks show beta wollastonites in wollastonite graph as seen in Figure 5. When the patterns obtained from the XRD were examined, similar peaks with natural wollastonite were obtained from the SWs produced with SQ, SG, SM and SS mixtures. The similarity obtained from these results indicated that all the SWs produced in the laboratory are wollastonite. However, changes in small-scale peaks were observed due to chemical differences of materials. In addition, these changes are due to the contents of α -wollastonite and β -wollastonite between natural wollastonite and produced SWs [21].

4. Conclusions

In this study, wollastonite mineral has been produced synthetically with industrial waste materials. Results of SEM analysis demonstrated that SWs produced with only SS mixtures had acicular particle structure with very small amount. However, the other three SWs produced with industrial wastes did not show the acicular particles. Based on the XRD analysis results, all of the SWs produced by using four different mixtures are wollastonite. In addition, XRF analysis of SWs obtained from SQ, SG, SM and SS mixtures indicated that CaO and SiO₂ ratios of all SWs are similar to wollastonites in different countries of the world.

5. Acknowledgment

The authors gratefully acknowledge the financial assistance of the Scientific and Technical Research Council of Turkey (TUBITAK) provided under Project: MAG-217M182.

6. References

- [1] M.A. Wahab, I.A. Latif, M. Kohail, A. Almasry, 2017, The use of Wollastonite to enhance the mechanical properties of mortar mixes, *Construction and Building Materials*, 152, 304–309.
- [2] A.S. Luyt, M.D. Dramicanin, Z. Antic, V. Djokovic, 2009, Morphology, mechanical and thermal properties of composites of polypropylene and nanostructured wollastonite filler, *Polymer Testing*, 28, 348–356.
- [3] L. Zhu, H.Y. Sohn, 2012, Growth of 2M-Wollastonite polycrystals by a partial melting and recrystallization process for the preparation of high-aspect-ratio particles, *Journal of Ceramic Science and Technology*, 03(04), 169-180.
- [4] J.R. Copeland, 1987, *Handbook of reinforcements for plastics*, Van Nostrand, New York, (Chapter 8).
- [5] R.L. Virta, 2011, Wollastonite – a versatile industrial mineral, *U.S.Geol. Surv. Fact Sheet FS- 002 – 01*.
- [6] Z.X. Ma, H. Li, G.S. Gai, X.F. Hu, 2000, The present situation and conception of milling technology for preparation of needle-like wollastonite powder, *Bulletin of the Chinese Ceramic Society*, 6, 42-45.
- [7] G.C. Hawley, 2010, Wollastonite, *Minerals Engineering*, 62(6), 84-87.
- [8] R.L. Virta, 1999, Wollastonite. *U.S. Geol. Surv., Annual Publications* 83.1 – 83.2.
- [9] P. Kalla, A. Rana, Y.B. Chad, A. Misra, L. Csetenyi, 2015, Durability studies on concrete containing wollastonite, *Journal of Cleaner Production*, 87, 726-734.
- [10] I. Kotsis, A. Balogh, 1989, Synthesis of wollastonite, *Ceramics International*, 15(2), 79-85.
- [11] S. Hayashi, M. Sugai, Z. Nakagawa, T. Takei, K. Kawasaki, T. Katsuyama, A. Yasumori, K. Okada, 2000, Preparation of CaSiO₃ whiskers from alkali halide fluxes, *Journal of the European Ceramic Society*

20, 1099-1103.

[12] J. Liu, D. Wang, 2017, Influence of steel slag-silica fume composite mineral admixture on the properties of concrete, *Powder Technology*, 320, 230-238.

[13] A. Yeğınobalı, 2001, Silis dumanı ve çimento kullanımı, TÇMB AR-GE Y 01 01. İstanbul.

[14] Ö. Erdoğan, 2007, Effects of mineral admixtures on the fresh and hardened properties of self compacting concretes: binary, ternary and quaternary systems, PhD Thesis, Gaziantep University Graduate School of Natural & Applied Sciences, Gaziantep, Turkey.

[15] G.A. Khater, 2002, The use of saudi slag for the production of glass-ceramic material, *Ceramics International*, 28, 59-67.

[16] G. Kaya, S. Turan, Yüksek fırın curufunun seramik sektöründe katma değeri yüksek ürünlerin eldesinde değerlendirilmesi, *Mühendis ve Makina*, 45(536), 48-60.

[17] M.O. Saf, 2015, Sentetik C-S-H bileşiklerinin kendiliğinden yerleşen betonların taze ve sertleşmiş özelliklerine etkisi, İstanbul Teknik Üniversitesi, Fen Bilimleri Enstitüsü, Yüksek Lisans Tezi, İstanbul, Turkey.

[18] R. Mathur, A.K. Misra, P. Goel, 2007, Influence of wollastonite on mechanical properties of concrete, *Journal of Scientific and Industrial Research*, 66, 1029-1034.

[19] G.D. Ransinchung, B. Kumar, V. Kumar, 2009, Assessment of water absorption and chloride ion penetration of pavement quality concrete admixed with wollastonite and microsilica, *Construction and Building Materials*, 23, 1168-1177.

[20] Ohnemuller, Walter, Solf, Alexander, U.S. Patent 3861935, 1975.

[21] L. Zhu, H.Y. Sohn, 2012, Growth of 2M-wollastonite polycrystals by a partial melting and recrystallization process for the preparation of high-aspect-ratio particles, *Journal of Ceramic Science and Technology*, 3(4), 169-180.

Sewage sludge ash as resource for phosphorous and material for clay brick manufacturing

L.M. Ottosen¹, I.M.G. Bertelsen¹, P.E. Jensen¹ & G.M. Kirkelund¹

¹Department of Civil Engineering, Brovej, Building 118, Technical University of Denmark, 2800 Lyngby, Denmark

Abstract

Sewage sludge ash (SSA) contains the critical raw material phosphorous. Internationally, research is carried out on utilization of SSA as secondary resource in concrete, bricks or lightweight aggregates; however, the high phosphorous content calls on recovery prior to such use. In the present investigation, phosphorous was recovered from SSA by electrodialytic separation (EDS) and the treated ash (SSA-EDS) was tested as clay substitute in brick manufacturing. For comparison, similar tests were conducted with SSA. The SSA had a reddish colour from a high iron oxide content. The SSA was milled to $d_{50} = 37 \mu\text{m}$ prior to use as clay substitute (0-50%). During EDS, 85-91% phosphorous was recovered, the alkaline pH of the SSA (10.2) was reduced to acidic (3.7), and the content of iron oxides increased. The reference brick material was yellow. The colour turned increasingly reddish with increasing percentage of SSA and especially SSA-EDS, and the reddish colour is seen as an advance. The clay contained about 17% carbonates, a major cause for firing mass shrinkage. As the carbonate content decreased with increasing clay substitution, the shrinkage mass did decrease accordingly. When fired at 1000 °C, all brick materials had apparent densities and open porosities within the range of bricks used in the building industry. SEM micrographs showed that mixes with SSA-EDS fired at 1050 °C contained a glassy phase with isolated spherical pores, which may be related to the high hematite content of SSA-EDS. The open porosity decreased with increasing substitution with SSA-EDS when fired at 1050 °C, the reversed order compared to firing at 1000 °C.

Keywords: Brick manufacturing, sewage sludge ash, secondary resources, clay substitute, phosphorous

1. Introduction

Sewage sludge incineration is extensively practiced in European countries such as the Netherlands, Switzerland, and Germany. Sewage sludge ash (SSA) is unavoidably formed and research is carried out internationally in order to valorise this waste product. One research line is to utilize SSA in construction materials. Most research has been conducted on the use as partly cement replacement in concrete [1-3], as partly clay replacement in clay bricks [4-5], or by itself, where it is utilized that SSA itself can sinter and form new ceramic materials [7]. It is though important to recognise that SSA can be an important future secondary resource for phosphorous (P), and that the P is lost for recovery if incorporated into construction materials. Recovery of P from secondary resources is important, since P is a finite, essential resource, underlined by P being in the list of critical raw materials for the EU [8]. The P concentration is generally high in SSA and can even be within the range of economical grade phosphate rock [9].

Different techniques are under development for P recovery from SSA. A group of techniques is based on wet extraction (mainly acid extraction). A major challenge with wet extraction is the simultaneous extraction

of heavy metals and P, which requires a second step after the extraction, where P and heavy metals are separated. We have developed and patented a technology, electrodialytic separation (EDS), which is a one-step process where P extraction and heavy metal separation occur simultaneously [10]. Recovery of 80-90% P from SSA and simultaneous separation of heavy metals has been obtained at laboratory scale. The produced P product has a low content of heavy metals corresponding to the very low end of commercial P fertilizers [9]. An SSA after EDS for P recovery (SSA-EDS) was previously seen to have potential as cement replacement in mortar [11]. At 20% replacement, the compressive strength decreased with 8% (out of 60 MPa), and the mortar got an intense red colour, however, the workability was decreased and work needs to be done to improve this property. In the present paper, SSA-EDS is investigated used as partly replacement for clay in clay bricks. Clay, which after firing, result in the traditional red coloured bricks is becoming scarce in Denmark, as deeper in the quarrels, the Ca/Fe ratio determines the bricks to become yellow. In this investigation, it is suggested to use SSA both as replacement for the natural raw material (clay) with a secondary resource in brick manufacturing and as a colouring agent, which gives sought after red bricks. The aim is to investigate the properties of brick material with different replacement percentages of clay with SSA-ED (0-50%) and investigate the colour potential. The work consists of two parts: (I) comparison of SSA and SSA-EDS as clay replacement material and (II) influence of firing temperature on the material properties when replacing clay with different percentages of SSA-EDS.

2. Methodology

2.1 Materials

SSA was collected at the wastewater treatment plant Avedøre Spildevandscenter BIOFOS in Copenhagen, Denmark (February 2015). The sewage sludge was incinerated in a fluidized bed combustor at about 850 °C. The plant treats wastewater from 255.000 person equivalents (PE). Phosphorous is removed from the wastewater through chemical precipitation with Fe, and due to the subsequent high content of iron-oxides, the SSA has the characteristic red colour. The SSA was sampled as a mix of electrofilter ash and bag filter ash (2%). The SSA was collected directly from the process line and stored in sealed plastic containers at room temperature. As SSA and SSA-EDS are quite coarse-grained compared to clay [11], the SSA was milled in a vibrating cup mill (FRITSCH – pulverisette 9) for 10 sec prior to being mixed into the clay in this investigation (Part I) or prior to EDS (Part II).

The clay used was from the brick manufacturer Wienerberger in Helsingør, Denmark. The clay was ready for use in the manufacturing of yellow clay bricks when sampled for this investigation.

2.2 Characterization of SSA and clay

Particle size distribution was measured using a Malvern Mastersizer 2000 with a dry SSA sample. The carbonate content of the clay was determined volumetrically by the Scheibler-method and calculated assuming that all carbonate present is calcium carbonate. The pH was measured in a suspension of 1:2 ash:distilled water after 1 hour of agitation. Loss on Ignition (LoI) was found after 30 minutes at 550°C. Solubility in water was evaluated: 50.0 g ash suspended in 500 ml distilled water and agitated for 1 min. After settling, the water was decanted. New 500 ml distilled water added. This was repeated so the ash was washed three times. Finally, the suspension was filtered and the ash dried at 105°C and weighed. The water solubility was measured in two replicates. The elemental concentrations of Cd, Cr, Cu, Zn, P, S and K in SSA and SSA-DES were measured by ICP-OES after pre-treatment according to Danish standard (DS 259 2003), where 1.0 g of dry sample and 20.0 mL 7.3 M HNO₃ were heated at 200 kPa (120 °C) for 30 min. The liquid was separated from the solid particles by vacuum through a 0.45 µm filter and diluted to 100 ml.

2.3 EDS of SSA for P recovery

The EDS for P recovery from SSA was conducted in a two compartment cell as described in [9] (figure 1). The SSA was suspended in distilled water in the anode compartment, and an electric current was applied to recover P and simultaneously remove heavy metals to have a clean P product. At the end of the treatment, the recovered P is in the filtrate of the anolyte and the solubilized heavy metals in the catholyte. Filtration separates SSA-EDS and the filtrate with the recovered P.

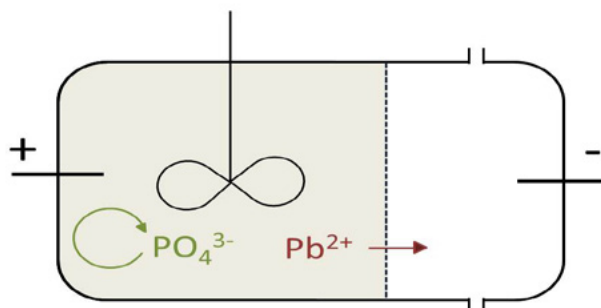


Figure 1: ED cell. The ash is suspended in water in the anode compartment and a cation exchange membrane (marked as dotted line) separates the two compartments.

The experiments were conducted in a cylindrical cell. The length of the anode compartment with SSA suspension was 10 cm and the length of the cathode compartment 5 cm. The internal diameter of both compartments was 8 cm. The cation exchange membrane was from Ionics. The platinum coated titanium wire electrodes (diameter 3 mm) were obtained from Permascand® and the length of the electrodes inside the cell was approximately 4 cm. A power supply (Hewlett Packard E3612A) was used to maintain a constant current of 50 mA. The specific parameters for the EDS process were chosen from the best results obtained in [9]: 25 g SSA (milled for 10 sec.) was suspended in 350 ml distilled water and 50 mA was applied for 6 days. The SSA was kept suspended by an overhead stirrer (RW11 basic from IKA). In the cathode compartment 500 mL 0.01 M NaNO₃ adjusted to pH 2 with HNO₃ was circulated. During experiments, pH was adjusted manually in the cathode compartment to between 1 and 2 daily with 1 M HNO₃. At the end of the EDS experiments, the suspension was filtered at atmospheric pressure and the SSA-EDS was dried at 105°C. The pH and contents of Cd, Cr, Cu, Zn, P, S and K were measured in the SSA-EDS.

To have sufficient SSA-EDS for production of brick discs, eight EDS experiments were conducted: 5 experiments for part (I) and 3 experiments for part (II). It was previously shown [9] that repeatability of EDS results with the same SSA is high, and thus SSA-EDS from all the experiments within each part of the investigation were mixed before analysing the chemical content of selected elements. The brick discs were produced with EDS-SSA from the mixed samples.

2.4 Production and properties of brick discs

Torres et al. (2009) [12] demonstrated that initial tests conducted on small-scale brick discs were a useful screening tool for selecting the best mixtures composition when incorporating wastes (from natural rock cutting and polishing) in clay to produce roof tiles. In this paper, a similar approach was adapted, using the same disc size as described by Torres et al. (2009) [12], however, it is SSA or SSA-EDS, treated SSA, which is mixed into the clay.

When mixing the clay material, 15 g dry blended clay and SSA/SSA-EDS was mixed with distilled water

by hand until a uniform mass with a good workability was obtained. The mass of distilled water needed to obtain this state increased with increasing replacements. The liquid to solid (L/S) ratio in the reference mix was 0.25, which was the lowest, and L/S was highest for the mixtures with 50% replacement with SSA and SSA-EDS (about 0.50). The mixes were stored overnight in sealed plastic beakers. Discs were produced from about 2.5 g of the mixes by uniaxial compression in a purpose built stainless steel die [13] placed in an Instron-6022. A load of 10 kN (equivalent to the forming pressure of 31.8 MPa) was applied. During the compression, water was pressed out of the mixture. The green discs had a diameter of 2.0 cm and a height of 3.5 - 4 mm. The weight of the unfired discs after compression (m_0) were measured. The discs were dried at 105 °C for 24 h before the weights ($m_{105^\circ\text{C}}$) were measured again. From these measurements, the water content of the unfired discs after the compression were calculated as $(m_0 - m_{105^\circ\text{C}})/m_0$. The discs were fired at 950, 1000 or 1050 °C for 2 h in a Nerbertherm laboratory furnace, using an average heating and cooling rate of 6.0°C/min.

Brick discs were prepared from different mixtures, see Table 1.

Table 1: Overview of the clay replacement percentage and firing temperature for the produced clay brick discs

	Replacement (wt%)	950°C	1000°C	1050°C
Ref	0	X	X	X
	10		X	
SSA	30		X	
	50		X	
SSA-EDS	10	X	X	X
	30	X	X	X
	50	X	X	X

After cooling, the diameters were measured. Weights were measured as well, and the firing mass loss found:

$$\text{Firing mass loss: } ((m_{105^\circ\text{C}} - m_{1000^\circ\text{C}}) / m_{105^\circ\text{C}}) * 100\% \quad (1)$$

The open porosity and density were determined. The discs were placed in a desiccator under vacuum for approximately 3 h. After 3 h, distilled water at room temperature was led into the desiccator, so that the discs were completely submerged. Vacuum was maintained for 1 h and hereafter, air was let into the desiccator and the submerged discs were left at atmospheric pressure overnight. The water-saturated discs were weighed in water (m_{sw}) and in air after wiping excess water of the surface (m_{sa}). The different properties were calculated as:

$$\text{Volume} = V = (m_{sa} - m_{sw}) / \rho_w \quad (2)$$

$$\text{Volume open pores} = V_{op} = (m_{sa} - m_{1000^\circ\text{C}}) / \rho_w \quad (3)$$

$$\text{Dry mass density} = m_{1000^\circ\text{C}} / (V - V_{op}) \quad (4)$$

$$\text{Open porosity} = ((m_{sa} - m_{1000^\circ\text{C}}) / (m_{sa} - m_{sw})) * 100\% \quad (5)$$

$$\text{Apparent density} = ((m_{1000^\circ\text{C}} * \rho_w) / (m_{sa} - m_{sw})) \quad (6)$$

Where ρ_w (970 kg/m³) is the density of water at room temperature

The firing mass loss was measured in 7 replicates. Dry mass density, open porosity and apparent density in

3 replicates.

3. Results and discussion

3.1 Characterization of SSA (as received) and SSA-ED

The carbonate content of the clay was $17.9 \pm 0.4\%$. The grain size d_{50} for the SSA as received was $120 \mu\text{m}$, and after milling, the d_{50} was decreased to $37 \mu\text{m}$. The LoI of the SSA was very low ($0.3 \pm 0.005\%$) revealing a good incineration and following low mass loss from organic matter during firing of the brick discs. The water solubility was 1.4% , representing soluble salts. Soluble salts in brickmaking raw materials is of concern for manufacturers as they can cause a production fault known as “drier scum” [14], however the problematic range and type of salts was not stated, and it is here considered that the content of soluble salts in the SSA is in an acceptable level.

The initial 25 g were reduced to 14-15 g during EDS, i.e. a mass reduction of 40%. The dissolution was due to acidification of the SSA suspension from electrolysis at the anode. The pH of SSA was 10.2, and the pH of SSA-EDS was 3.7. Thus, the SSA was originally alkaline, while the ash became acidic after EDS. Table 2 shows the concentrations of selected heavy metals and macro elements in the SSA before and after EDS in the two parts of the experimental work. The heavy metal concentrations in SSA depend on the corresponding concentrations in the wastewater treated in the facility and do subsequently vary, however, the order in concentration reported (in mg/kg) is generally the same as here $\text{Cd} < \text{Cr} < \text{Cu} < \text{Zn}$ [3], [13], [14].

The concentrations of heavy metals and macro elements changed during EDS as seen in table 2. The removed percentage of all these elements was thus slightly higher in the EDS experiments in part (II) than in part (I), which corresponds well to the mass reduction of SSA, which was also slightly less in the part (I) experiments.

Table 2: pH and concentrations of selected elements in SSA and SSA-EDS in the two batches in part (I) and (II)

	Concentration (mg/kg)				Concentration (g/kg)		
	Cr	Cu	Cd	Zn	K	S	P
SSA	40 ± 0.1	541 ± 14	2.2 ± 0.03	1986 ± 56	5.8 ± 0.2	6.1 ± 0.1	94.6 ± 3.1
SSA-EDS (I)	55 ± 0.5	395 ± 7.9	1.5 ± 0.09	1600 ± 37	3.7 ± 0.08	1.0 ± 0.01	25.4 ± 0.7
SSA-EDS (II)	45 ± 0.9	440 ± 15	0.8 ± 0.1	1890 ± 60	3.6 ± 0.2	0.6 ± 0.02	15.7 ± 0.6

The Cr concentration increased during EDS, showing that Cr was bound mainly in the least soluble fraction of the SSA. The concentration of all other chemical elements in table 2 decreased. When taking into account the total mass reduction of 40% (part I) and 45% (part II), the percentages of these chemical elements remaining in the SSA-EDS were:

Part (I): $\text{S} (10\%) < \text{P} (16\%) < \text{K} (38\%) < \text{Cd} (41\%) < \text{Cu} (44\%) < \text{Zn} (48\%) < \text{Cr} (83\%)$

Part (II): $\text{S} (6\%) < \text{P} (9\%) < \text{Cd} (19\%) < \text{K} (34\%) < \text{Cu} (44\%) < \text{Zn} (52\%) < \text{Cr} (62\%)$

The P concentration in this batch of SSA is the same order (but in the lower end) of concentrations reported for SSA from other batches from the same plant: 90 g/kg [3], 110 g/kg [9] and [15] 123 g/kg . The economic grade of phosphate rock varies from 25% to 37% P_2O_5 [16] corresponding to $110\text{--}160 \text{ g P/kg}$ phosphate rock. Thus, the concentration in the SSA batch 94.6 g P/kg SSA was only slightly less than the mined natural ores. In the EDS experiments of the present investigation 91% and 84% P was recovered in the experiments of part (I) and (II), respectively, which is in the same range as reported in [9], [17] in similar

EDS experiments. Kappel et al (2018) [11] reported concentrations as oxides measured by XRF in SSA and SSA-EDS from the same incineration plant: the contents of SiO_2 and Fe_2O_3 about doubled during EDS (from 18.6% to 39.4% SiO_2 and 15.75 to 27.3% Fe_2O_3), while the content of Al_2O_3 was reduced slightly from 8.3 to 6.6 %. Similar concentration ranges are expected in the SSA and SSA-EDS of the present investigation.

On the basis of the XRD analysis, Kappel et al (2018) [11] identified of the minerals quartz, feldspar and hematite in SSA and SSA-EDS. Cheeseman et al (2003) [7] reported quartz, whitlockite (calcium magnesium phosphate mineral) and some hematite in an SSA from UK, and Anderson (2002) [18] quartz, calcite, hematite, anhydride, feldspar and glassy phase ~70% in another SSA from UK. Thus, quartz and hematite were identified in all three ashes. The high concentration of hematite is due to the use of iron salts to precipitate P in the wastewater treatment facility. Other facilities use mainly Al salts and this strongly influences the chemical properties of the SSA [10], [19]. Thus, caution must be taken when generalizing results on utilization SSA in brick production, as the characteristics in the SSA varies, which must be expected to influence the brick quality. Significant changes in specifications carries a potential risk for production problems during brick manufacturing [14]. Thus, attention must be given to the characteristics of the specific SSA, when evaluating how and if it is best utilized in brick manufacturing.

3.2 Properties of brick discs

3.2.1 Colour of brick discs

The original yellow colour of the reference discs changed towards more red colours with increasing replacement of clay with SSA and SSA-ED, see figure 2. The red colour was more intense for the brick discs with SSA-EDS than for the corresponding discs with SSA, most clearly seen for 30% replacement. It is the higher content of iron oxides in SSA-EDS, which give this difference. The discs fired at 1050 °C and at replacements of 30% and 50% clay with SSA-EDS were significantly darker than the discs with same replacement but lower firing temperature. The red colour obtained at 30% replacement and 1000 °C was similar to traditional Danish red bricks.

3.2.2 Water content of discs after pressing

The water content of the green discs after pressing and before firing is shown in table 3. There is no significant difference in water content between the discs with SSA and SSA-EDS within each substitution percentage when considering the standard deviations. The water content increased with increasing substitution with SSA or SSA-EDS. The SSA particles are porous [10], [14] and thus they can absorb water, which will increase the overall water content.

Table 3: Water content of unfired discs after pressing

	Ref	10%	30%	50%
SSA	9.4 ± 0.6	10.2 ± 0.5	14.6 ± 3.1	15.2 ± 0.7
SSA-EDS (I)		10.3 ± 0.6	12.6 ± 1.2	16.2 ± 1.7
SSA-EDS (II)	9.8 ± 0.9	10.6 ± 0.6	13.6 ± 0.5	16.8 ± 0.8

3.2.3 Comparison of brick discs with SSA and SSA-EDS

The firing mass loss decreases with increasing percentages of SSA and SSA-EDS mixed into the clay (figure 3). The decreasing firing mass loss with increasing clay replacement with SSA is in consistency with what was reported by [4]. Firing mass loss can be due to removal of chemically bound water and volatilization of compounds within the brick [4]. The decomposition of CaCO_3 in the clay is a major contributor to the

shrinkage mass decrease. At increasing clay substitutions with SSA and SSA-EDS, the CaCO_3 content in the mix decreases, and following the shrinkage mass.

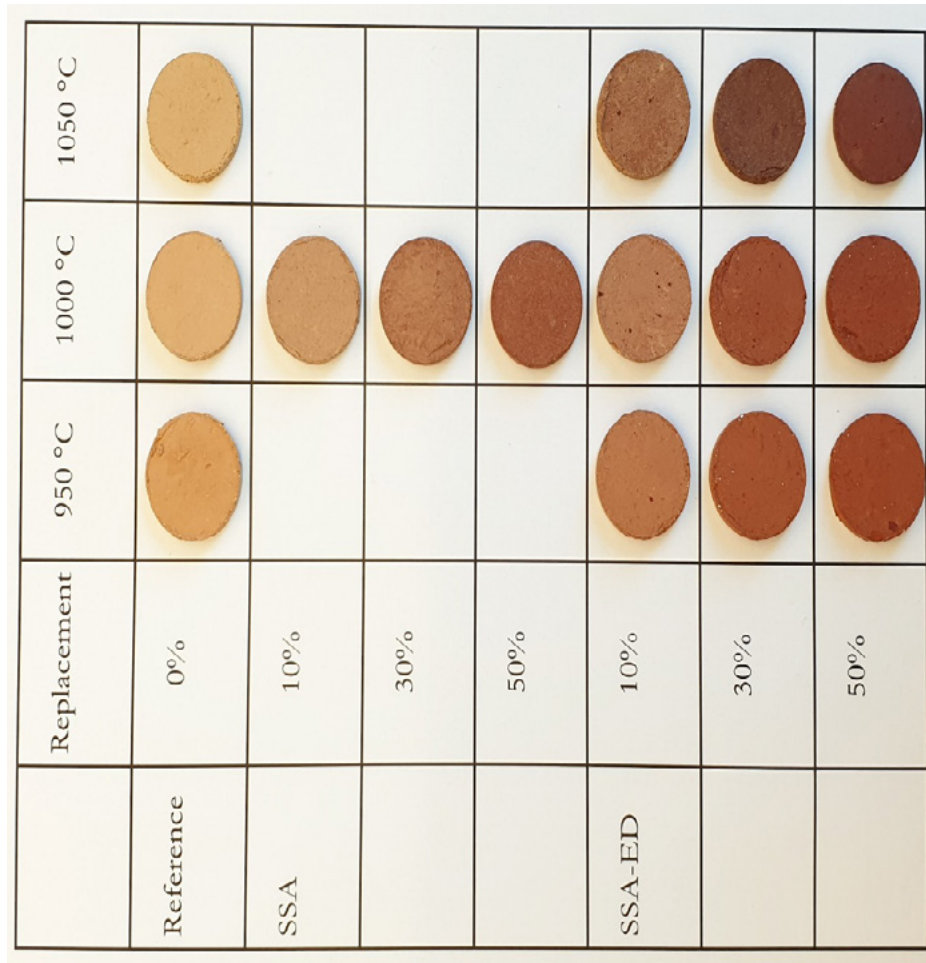


Figure 2: Colours of the brick discs in the investigation

The shrinkage mass decreases linearly with the clay substitution from 0-50% with SSA ($R^2 = 0,9995$) and from 10-50% replacement with SSA-EDX ($R^2 = 0,9996$), (figure 4). The linear relation between shrinkage mass and percentage of clay substitution with SSA-EDS does not include the reference. This is likely due to the acidic nature of SSA-EDX, which dissolves a small fraction of the carbonates in the clay when mixing. Thus, the carbonate content in the reference discs is higher than the background of carbonates in the discs with SSA-EDS. In addition, the carbonate content decreases relatively more with increasing percentage of SSA-EDX and thus the gradient differs from the one for SSA. The firing mass loss is smaller for the discs with SSA than for those with SSA-EDS even though the carbonate content is considered slightly higher in the discs with SSA. This indicates that there are phases contributing to the firing mass loss, which concentrate in the ash during EDS. Hematite can dissociate and form gas at temperatures as low as 1000 °C [20], and the higher hematite concentration in SSA-EDS than in SSA can be contributing to the higher firing mass loss for discs with SSA-EDS.

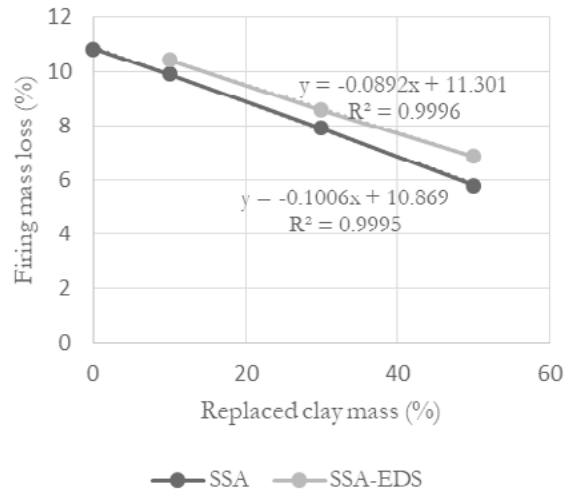


Figure 3: Firing mass loss as function of replacement percentage

Figure 4 shows the apparent density, density of the solid mass and open porosity the discs in Part (I), all fired at 1000 °C. The apparent density decreases, whereas the density of the solid mass and the porosity increases with increasing replacement of clay with SSA and SSA-EDS.

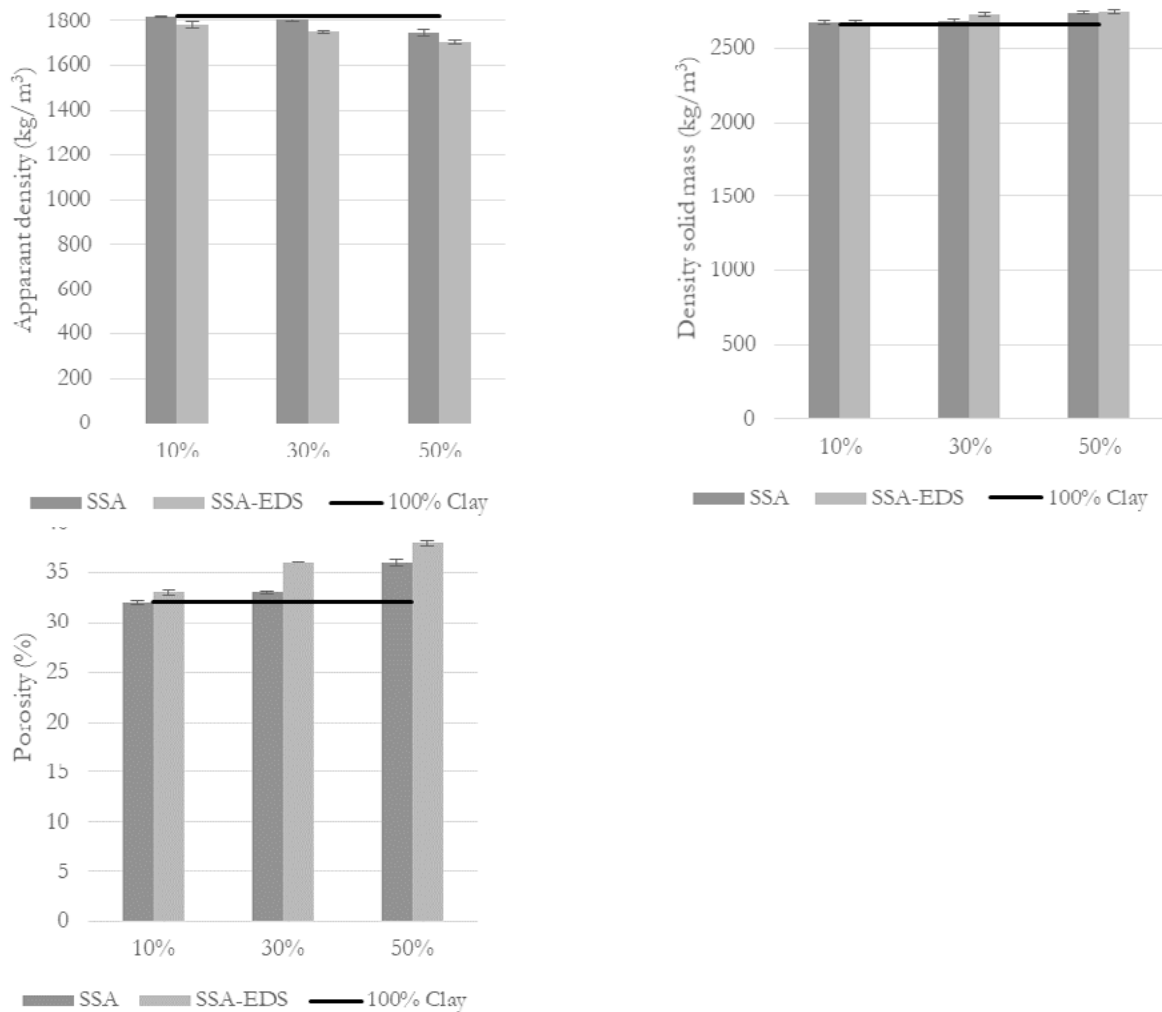


Figure 4: Properties of brick discs fired at 1000 °C with SSA or SSA-ED: (a) apparent density, (b) density of the solid mass, and (c) open porosity.

The discs with SSA had higher apparent density and lower porosity than the discs with SSA-EDR. The decrease in apparent density is in consistency of what was reported by [4]. Apparent densities of clay bricks, which are used in the building industry, are in the range of 1610–2120 kg/m³ [21] and open porosities in the range of 19–39 vol% [21]. Both apparent density and porosity of all the brick discs in figure 4 are within these ranges, though the parameters are close to the upper and lower limit, respectively, in regards to the discs with 50% SSA-EDS. This is encouraging; however, it must be taken into consideration that this result cannot be transferred directly to the manufacturing of bricks for the building industry, as the manufacturing of the small brick discs differs from the procedures at brickworks.

Summing up, the properties of the brick discs are different when SSA-EDS is used as clay substitute instead of SSA. The firing shrinkage mass decreases, whereas the open porosity apparent density and dry mass density increases. Of major importance to the differences are probably the acidic nature of SSA-EDS and the increased hematite content. In accordance to the properties included in this investigation, all the brick discs have properties as brick used in the building industry.

3.2.4 Properties of brick discs with SSA-ESD fired at different temperatures

Figure 5 shows the firing shrinkage at 950 °C, 1000 °C and 1050 °C for the different clay/SSA-EDS mixes in part (II) of the investigation. The differences in firing shrinkage between the three temperatures within each substitution percentages are very small. On the contrary, the firing shrinkage is highly dependent on the replacement percentage. The more SSA-EDS, the lower firing shrinkage, which is likely due to the decreasing content of CaCO₃ as discussed in paragraph 3.2.3.

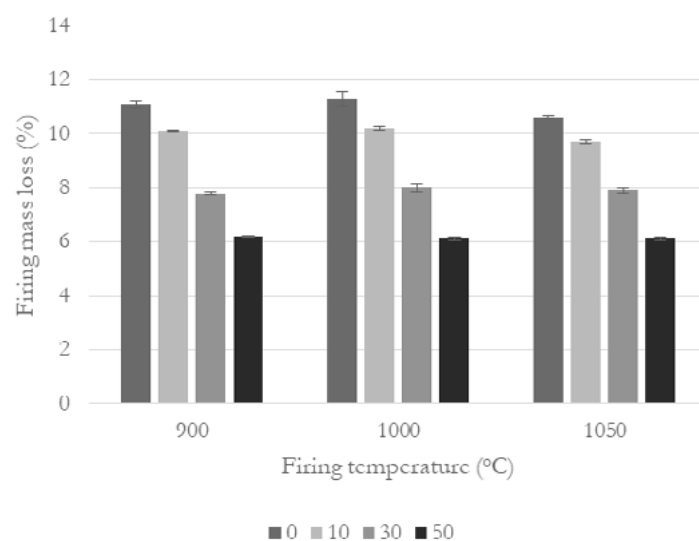


Figure 5: Firing shrinkage for brick discs with different replacements of clay with SSA-EDS and different temperatures.

The open porosity of the discs with SSA-EDS is seen in figure 6. It is evident that the porosity is highly influenced by the firing temperature between 1000 and 1050 °C. Until 1000 °C the porosity slightly increases with increasing clay replacement and at 1050 °C the order is reversed causing a significant decrease in open porosity. A similar finding was reported by [4], who reported that the cold water absorption for bricks with clay/SSA mixes had increasing water absorption with SSA content when fired at 1040 °C and the order was reversed at 1120 °C. The shift was thus found to be between 1000 °C and 1050 °C in the present investigation and between 1040 °C and 1120 °C for another SSA by [4], i.e. the general temperature for the shift may be in the range of 1040 °C and 1050 °C. The open porosity for the discs with 30 and 50% clay

substitution with SSA-EDS (12.5% and 23.6%) is lower than the range of 19–39 vol% stated for bricks used in the building industry by [21]. The firing temperature of 1050 °C must be considered too high for firing clay bricks with 30-50 % replacements with SSA-EDS.

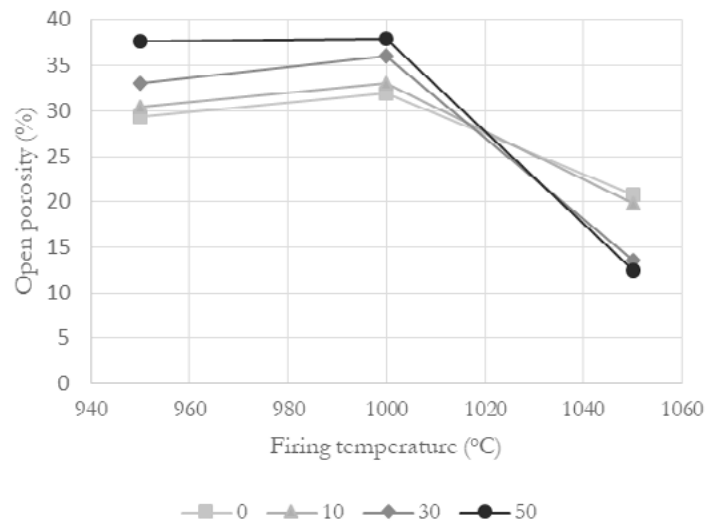


Figure 6: Open porosity of brick discs with different replacement percentages of clay with SSA-EDS and different temperatures.

Figure 7 shows SEM micrographs of a fracture surface of a reference disc and a disc with 50% clay replaced with SSA-EDS, both fired at 1050 °C. The disc with SSA-EDS had a glassy-like phase, which was not seen in the reference disc (figure 7a and 7b). This is in accordance to Anderson (2002) [18], who also saw a glassy phase when firing clay and SSA at 1050 °C.

This indicates that EDS did not remove the compounds present in SSA involved in this vitrification. The glassy-like phase in the disc with SSA-EDS had isolated pores of about 5-15 µm with an almost spherical shape (figures 7b and 7d). The same pattern with a sintered phase and isolated pores was not seen in the reference disc. Cheeseman et al. (2003) [7] studied sintering of 100% SSA and found that at 1040 °C, a relatively low-density material, which appeared to be hard and well sintered with a glassy surface. A SEM micrograph of the fracture surface showed that the matrix contained a significant volume of isolated, approximately spherical pores, typically 20-30 µm [7].

This finding is similar to the one in the present investigation. The isolated, spherical pores are likely formed by bloating, which is the phenomenon utilized in the production of lightweight aggregates. Two conditions necessary for bloating, which have long been recognized are (1) that a material must produce a high temperature glassy phase with a viscosity high enough to trap a gas and (2) that some substance must be present that will liberate a gas at a temperature at which a glassy phase has formed [20]. Riley (1951) [20] found that pyrite, hematite and dolomite provide the constituents necessary to cause gas evolution at a temperature high enough (>1000 °C) for the bloating to take place. As hematite is a major mineral in SSA-EDS [11], it is likely that hematite took part in the bloating of the sintered phase seen in figure 7b and 7d.

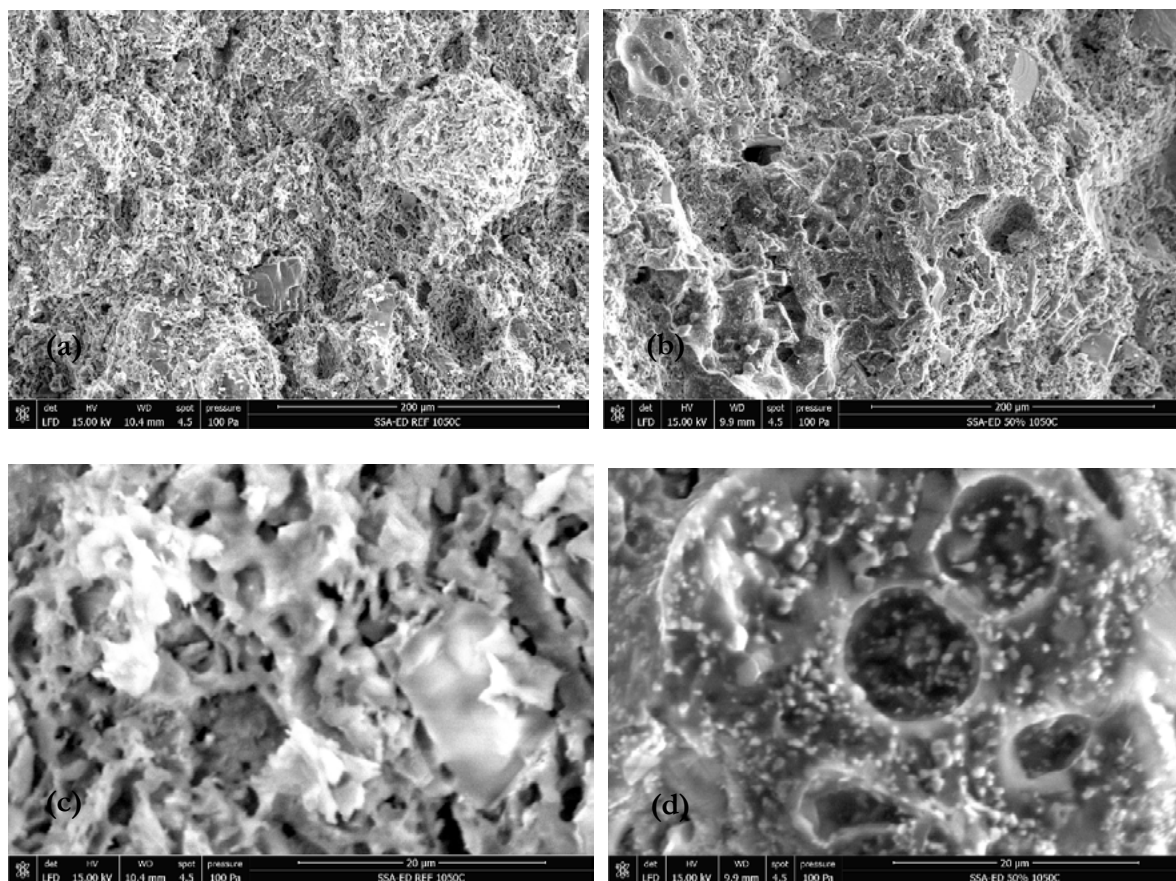


Figure 7: Fracture-face of morphology of discs fired at 1050 °C (a) reference disc and (b) disc with 50% SSA substituting clay (Same magnification), and high magnification (c) reference disc and (d) disc with 50% clay substitution with SSA (see scale at the lower bars the SEM micrographs).

Anderson (2002) [18] also reported formation of a glass phase when firing a clay/SSA mixture (5% SSA) at 1050-1070 °C and a decrease in porosity (measured as water absorption). As the glassy phase develops, it draws the particles closer together, thereby reducing the internal packing voids thus making the product less porous [18]. This explanation may be underlined in the present investigation by the decreased diameter for the discs with 30% and 50% SSA-EDS fired at 1050 °C, which were about 0.4 and 0.8 mm (out of the 20 mm), respectively. All other discs kept the initial diameter (± 0.2 mm) after firing.

Very small particles ($< 2 \mu\text{m}$) were caught in the sintered phase (figure 3d). Whether these particles are crystalline or amorphous was not determined. They might be crystalline since Cheeseman et al. (2003) [7] reported that sintering of 100% SSA indicated that no significant crystalline transformations occurred during sintering and that the original crystalline phases quartz, calcium magnesium phosphate and some hematite was identified by XRD both before and after firing at 1040 °C.

4. Conclusions

Electrodialytic separation (EDS) for recovery of phosphorous from sewage sludge ash (SSA) changes the overall composition of the ash. When used as clay substitution in brick making, major important changes in SSA characteristics were seen from EDS. Of major importance is considered, that the hematite concentration increases during EDS reaching levels of about 25 wt%. The hematite content gave a reddish coloured brick material (the reference material from firing clay was yellow), and the colour change was most intense for SSA-EDS. The hematite also caused formation of a glassy-like phase with closed, spherical

pores when discs were fired at 1050 °C. This glassy-like phase strongly influenced the open porosity of the material. When fired at 1000 °C, the open porosity slightly increased with increasing clay substitution with SSA-EDS, whereas at 1050 °C, the order was reversed, and the open porosity decreased significantly with increasing SSA-EDS content. The overall open porosity of the brick material decreased to 12.5 and 13.6 %, when 30 and 50% clay was replaced with SSA-EDS and the mix was fired at 1050 °C. These porosities are low and outside the levels of generally used bricks. When fired at 1000 °C, the same mixes gave open porosities within the general range. From this investigation, it can be concluded that SSA-EDS can potentially be used in brick manufacturing similarly to SSA, however, attention must be given to the firing temperature at higher substitutions due to the increased content of hematite, which here strongly influences the brick properties.

5. References

- [1] Donatello, S.; Cheeseman, C.R. (2013) Recycling and recovery routes for incinerated sewage sludge ash (ISSA): a review, *Waste Management* 33(11), 2328–2340
- [2] Lynn, C.J.; Dhir, R.K.; Ghataora, G.S.; West, R.P. (2015) Sewage sludge ash characteristics and potential for use in concrete, *Construction & Building Materials* 98, 767–779
- [3] Kappel, A.; Ottosen, L.M.; Kirkelund, G.M. (2017) Colour, compressive strength and workability of mortars with an iron rich sewage sludge ash. *Construction & Building Materials*, 157, 1199–1205
- [4] Trauner, E.J. (1993) Sludge ash bricks fired to above and below ash-vitrification temperature. *J. Environ. Eng.* 119(3), 506-519
- [5] Lin, DF; Weng, CH (2001) Use of sewage sludge ash as brick material. *Journal of Environmental Engineering* 127(10), 922-927
- [6] Suzuki, S.; Tanaka, M.; Kaneko, T. (1997) Glass-ceramic from sewage sludge ash. *Journal of Materials Science* 32(7), 1775-1779
- [7] Cheeseman, C.R.; Sollars, C.J.; McEntee, S. (2003) Properties, microstructure and leaching of sintered sewage sludge ash. *Resources, Conservation and Recycling* 40, 13–25
- [8] COM (2017) 490 On the 2017 list of Critical Raw Materials for the EU
- [9] Ottosen, L. M.; Jensen, P.E.; Kirkelund, G.M (2016) Phosphorous recovery from sewage sludge ash suspended in water in a two-compartment electrodialytic cell. *Waste Management* 51, 142-148
- [10] Ottosen, L.M.; Kirkelund, G.M.; Jensen, P.E. (2013) Extracting phosphorous from incinerated sewage sludge ash rich in iron or aluminum. *Chemosphere*, 91(7), 963-969
- [11] Kappel, A.; Viader, R.P.; Kowalski, K.P.; Kirkelund, G.M.; Ottosen, L.M. (2018) Utilization of electrodialytically treated sewage sludge ash in mortar. *Waste and Biomass Valorization*, 9(12), 2503-2515
- [12] Torres P., Fernandes H.R., Olhero S., Ferreira J.M.F. (2009) Incorporation of wastes from granite rock cutting and polishing industries to produce roof tiles. *J Eur Ceram Soc* 29, 23–30
- [13] Chen, W.; Ottosen, L.M.; Jensen, P.E.; Kirkelund, G.M.; Schmidt, J.W. (2014) A comparative study on electrodialytically treated bio-ash and MSWI APC-residue for use in bricks. *Proceedings of the 5th International Conference on Engineering for Waste and Biomass Valorization (WasteEng2014) Rio de Janeiro* (ISBN: 979-10-91526-03-6), 648-662
- [14] Anderson, M.; Skerratt, R.G. (2003) Variability study of incinerated sewage sludge ash in relation to

future use in ceramic brick manufacture. *British Ceramic Transactions*, 102(3) 109-203

[15] Ebbbers, B.; Ottosen, L.M.; Jensen, P.E. (2015) Comparison of two different electrodialytic cells for separation of phosphorus and heavy metals from sewage sludge ash. *Chemosphere*, 125, 122-129

[16] Gupta, D.K., Chatterjee, S., Datta, S., Veer, V., Walther, C., 2014. Review. Role of phosphate fertilizers in heavy metal uptake and detoxification of toxic metals. *Chemosphere* 108, 134–144

[17] Guedes, P.; Couto, N.; Ottosen, L.,M.; Kirkelund, G.M.; Mateus, E.; Ribeiro, A.B. (2016) Valorisation of ferric sewage sludge ashes: Potential as a phosphorus source. *Waste Management* 52, 193-201

[18] Anderson, M. (2002) Encouraging prospects for recycling incinerated sewage sludge ash (ISSA) into clay-based building products. *Journal of Chemical Technology and Biotechnology*, 77, 352-260

[19] Wiebusch, B.; Seyfried, C.F. (1997) Utilization of sewage sludge ashes in the brick and tile industry. *Wat. Sci. Tech.* 36(11), 251-258

[20] Riley, C.M. (1951) Relation of chemical properties to bloating of clays. *American Ceramic Society* 34(4), 121-128

[21] Dondi M, Mazzanti F, Principi P, Raimondo M, Zanarini G (2004) Thermal conductivity of clay bricks. *J Mater Civ Eng* 16:287–287.

Treatments to improve biomass fly ash quality

K. Ohenoja & M. Illikainen

University of Oulu, Fibre and particle engineering research unit, Po Box 4300, 90570 Oulu, Finland

Email of the corresponding author: katja.ohenoja@oulu.fi

Abstract

Fluidized bed combustion (FBC) is an efficient, environment-friendly, and commonly used combustion method. Unlike the traditionally used pulverized coal combustion (PCC) technology, FBC has less SO_x and NO_x emissions because of its lower burning temperature (800–900 °C vs. 1300–1700 °C) and in situ capturing of SO₂ via direct reaction with Ca-based sorbents during the firing process. In addition to this, FBC technology can utilize mixture of low-grade fuels that have fluctuating quality, composition, and moisture content, which however causes challenges to utilize produced fly ash. On the other hand, cement industry has pressures to decrease CO₂ emissions and therefore different cement substitutional industrial side streams has been studied intensively. PCC fly ash as a cement replacement material is already widely studied and adopted by the concrete industry to partially replace cement produced from traditional raw materials. However, since energy industry is all the time increasing the usage of renewable energy sources (biomass and wastes), it is reasonable to study fly ashes originating from the combustion of these fuels. The use of FBC fly ash as cement replacement material is one promising way to utilize these fly ashes: They have pozzolanic and self-cementitious property, which means that they react with cement and water. FBC fly ashes react also alone with water to produce cement-like reaction products. Also alkali-activation is promising method to utilize FBC fly ashes as a light-weight aggregates, for instance. Nevertheless, there is a lack of standardization for the use of FBC fly ash in construction. Current US (ASTM C 618) and European (EN 450-1) standards governing the use of fly ash as a mineral admixture in concrete do not contain the utilization of FBC ashes. However, it can be expected that in the future standards will cover also FBC and/or biomass fly ashes fulfilling the standard requirements. Fly ashes originating from biomass and waste combustion do not often meet the standard requirements because they may contain excessive amount of sulphate, chloride and lime, for instance. This study presents different treatments to improve fly ash quality to fulfil the standards and to improve their mechanical strength. These treatments can be mechanical or chemical: grinding, sieving, classification and chemical additives.

Keywords: classification, fluidized bed combustion, grinding, sustainable binder utilization, waste.

Leaching behaviour of metals from mine tailings utilized as partial cement replacement in cement-based building materials

A.M.T. Simonsen¹, P.E. Jensen¹

¹Arctic Technology Centre, Department of Civil Engineering, Technical University of Denmark

Email of the corresponding author: ansim@byg.dtu.dk

Abstract

Future depletion of supplementary cementitious materials, such as coal fly ash, causes a need to investigate alternative materials for the production of blended cements. Utilizing mine tailings has previously proved suitable as a potential chemical and physical contributor in cement-based building materials. The novel utilization of mine tailings must however not compromise on the environmental impacts caused by the use of metal enriched waste materials. This study investigates the toxic risk of mine tailings utilized as partial cement replacement in cement-based building materials according to leaching of metals.

The study tested 8 different mine tailings samples used as 5% by weight of the cement content in mortar specimens along with a reference mortar sample. The leaching potential (total digestion) was compared to the leaching behaviour (leach batch tests) of crushed mortar specimens with 5% cement replacement for metals prone to pose a health risk (Cd, Ni and Pb). Total digestions and leach batch tests on crushed mortar specimens were carried out 1 month (2017) and 1 year (2018) after curing to determine metal stabilization/solidification as a function of time.

The results from the leaching potential (total digestion) showed 2 out of 8 mine tailings samples used as partial cement replacement to exceed the Danish metal levels recognized to pose a potential environmental risk when incorporated in construction materials for Cd and Pb. Except for MT6 for Pb, leaching behaviour (leach batch tests) was lower than the leaching potential for all metals and mine tailing samples. Except for Pb in MT6 and MT8, high leaching potential did not correspond to high leaching behaviour since all samples showed similar leaching behaviour. For all metals and mine tailings samples, leaching behaviour decreased markedly over time from 1 month to 1 year of curing. The reference sample showed lower or similar leaching potential and behaviour as the mortar samples with mine tailings.

The results of the study support previous findings of metal fixation as the alkaline cementitious environment in cement-based building materials showed to stabilize metals in the cement matrix according to time. It was shown, that metal enriched mine tailings samples do not differ markedly from the reference samples in leaching potential or leaching behaviour. The study also showed that except for Pb, the metal leach behaviour was not determined by the leaching potential of the tailings.

This could indicate that other physicochemical characteristics of mine tailings affect the release of metals. This study thereby provides useful preliminary information to a better understanding of binding and leaching processes of waste materials as a component in cement-based materials.

Keywords: Mine tailings, cement replacement, metal leaching test, stabilization/solidification

Carbonation of recycled concrete aggregates: the effects of carbonation conditions on key aggregate properties

A. Gholizadeh-Vayghan^{1,2}, A. Bellinkx^{1,3}, R. Snellings¹

¹Sustainable Materials Management, VITO; 200 Boeretang, Mol, Belgium

²K. N. Toosi University of Technology; 1346 Valiasr St, Tehran, Iran

³Faculty of Engineering Technology, University of Hasselt; 42 Martelarenlaan, Hasselt, Belgium

Abstract

Concrete is the most frequently used material in the construction sector, which generates massive amounts of residues each year due to demolition. A major challenge with the reuse of recycled concrete aggregates (RCA) in making new concrete is the presence of hydrated cement residues on RCA surface and bulk, which leads to high water absorption and an inferior transition zone. Carbonation is known to have positive effects on the surface properties of RCA as it converts the portlandite present to calcium carbonate resulting in a lower porosity and better surface characteristics. In this research, the effects of carbonation conditions (namely CO₂ pressure: 1-5 bars, temperature: 20-60 °C, time: 1-4 hours, and relative humidity of the carbonation atmosphere: with and without buffering to saturation) on the apparent particle density, water absorption, and wear resistance of RCA is investigated. RCA samples are produced by crushing hardened concrete with known composition after curing for four weeks. Two moisture conditions are generated in RCA prior to carbonation: 1- “Wet”: where the RCA is soaked in water for a prolonged duration of time, and 2- “Seasoned”: where the RCA is stored at 95% relative humidity for 48 hours prior to testing.

The results suggest that regardless of the carbonation settings, carbonation under “Wet” conditions leads to no meaningful drop in water absorption or wear resistance, which is concluded to be due to lack of CO₂ uptake in the presence of moisture. The “Seasoned” RCA also showed no potential for carbonation when the chamber humidity level was boosted to water vapor saturation. However, “Seasoned” RCA showed significant potential for carbonation and thus drop in water absorption if the humidity of the carbonating environment is not boosted. CO₂ pressure showed positive effects on the carbonation outcome of “Seasoned” RCA. While the water absorption of such RCA carbonated at 1 bar was found to be approximately 4.4±0.8% less than that of untreated RCA, 18.0±1.8% drop in the same parameter was observed when the CO₂ pressure was raised to 5 bars.

Keywords: Recycled concrete aggregates, Carbonation, Preconditioning, Water absorption, Wear resistance

1. Introduction

The construction and demolition industries are accountable for the largest portion of anthropogenic residues in the European Union (25-30% of the total wastes generated) [1] with rapidly growing figures as existing infrastructure approaches the end of their service lives. While nearly 450 million tons of such waste is produced each year in the European Union [2], it remains to be the least recycled waste (25-30%

recycle rate) in this region [3]. Of particular importance is concrete, which is by far the most frequently used construction material with immense amounts of residues generated every year due to demolition of buildings and infrastructure. Due to its limited life cycle, all of the produced concrete eventually has to be demolished. The common practice of concrete recycling involves crushing steps to convert the concrete rubbles to smaller granules [4] (referred to as recycled concrete aggregates: RCA's). RCA is commonly used as road base material or partial replacement for the coarse aggregates in new concrete mixtures. Only 30% of the demolished concrete is reused in such applications within the European Union [3] while the rest is landfilled. Aside from the very low recycling rate (compared to countries such as U.S. and Japan: 82% and 80% recycling rate, respectively), it is used in lower-grade applications, which do not portray a sustainable development model at the long term. With the growing environmental concerns and scarcity of landfill spaces, it is imperative to advance the state of knowledge and practice to enable closed-loop recycling of demolished concrete.

RCA is generally known for its inferior physical and mechanical properties. In their review paper, Shafiuddin et al. [5] concluded that in comparison with normal concrete aggregates, RCA has significantly higher water absorption (3-12%), lower abrasion and impact resistance (reportedly up to 45% and 25%, respectively), and results in lower RCA concrete slump, greater slump loss over time (up to 50% more), and up to 50% and 60% more drying shrinkage and creep, respectively. Part of the reason for the sub-par performance of RCA is the presence of hydrated cement paste in the grains. The high porosity of the adhering cement paste is the driving force for high water absorption and high shrinkage when used in new concrete [6]. The drawbacks of conventionally produced RCA are not limited to fresh properties of concrete. The compressive strength of concrete incorporating RCA can be up to 25% less than that of normal aggregate concrete depending on the quality of RCA [5]. The inferior mechanical properties are attributed to the formation of a weak ITZ between the old and new cement paste [6]. As such, lowering the porosity or water absorption capacity of the adhering cement and strengthening its surface hardness can result in considerable enhancement in the performance of RCA in concrete.

With the knowledge that has been developed on portland cement, researchers have proposed different methods to improve the surface properties of RCA. Surface coating of RCA with a pozzolanic slurry [7, 8, 9], poly-vinyl alcohol polymer [10], and water glass [8] have been explored in the past with satisfactory results. Shi et al. [6] reviewed different RCA treatment techniques reported in the literature and concluded that carbonation is an efficient and environmentally friendly method for enhancing the properties of RCA.

Indeed, carbonation is gaining more attention among researchers due to its positive influences on the physical and mechanical properties of the hardened cement matrix, ease of application, and environmental implications. The presence of portlandite and C-S-H in the hardened cement paste makes it prone to carbonation, which is followed by some 10% increase in volume of portlandite. This is because the resultant of carbonation (CaCO_3) has a molar volume of $36.9 \text{ cm}^3/\text{mol}$ while that of the reactant (Ca(OH)_2) is $33.5 \text{ cm}^3/\text{mol}$. Carbonation also leads to an increase in the mechanical strength of the old cement matrix [6, 11]. Numerous publications on the subject of carbonation of RCA can be found in the literature with the aim of improving the water absorption and mechanical properties of this material. Zhao et al. reported an average of about 30% drop in water absorption of RCA after storing in an accelerated carbonation room [12]. Zhan et al [13] reported a 16.7% drop in water absorption of RCA after exposure to accelerated carbonation settings (low relative humidity (RH), 10 kPa CO_2 pressure, and an ambient temperature of 23 °C). Zhang et al. [14] reported 23-28% drop in such parameter after carbonating aggregates at 20 °C, 60% RH and 20% CO_2 concentration (results varied depending on aggregate type). Considerable improvements in the mechanical properties of RCA (e.g., aggregate crushing value, impact value and Los-Angeles abrasion value) as a result of carbonation has also been reported [5, 11, 12].

A number of factors seem to have an effect on the above properties of RCA. The CO₂ pressure, ambient temperature and relative humidity, carbonation time, and aggregate moisture condition appear to be the governing carbonation factors. Most of the existing literature lends itself to the investigation of carbonation under ambient or close to ambient atmospheric pressure while a research by Shi et al. [6] suggests that if CO₂ pressure exceeds 0.5 MPa, the strength development will be insignificant. The authors suggested that this is probably because the strength obtained through carbonation of portlandite is counteracted by the deterioration of the C-S-H structure. Junior et al. [15] reported a decrease of as much as 51% in strength of concrete after prolonged exposure to 20% CO₂ environment. As such, it appears that the CO₂ pressure and carbonation time should be chosen carefully to only carbonate the portlandite. A full in-depth carbonation of both portlandite and C-S-H might result in excessive increase in volume and loss of structural integrity. As such, it might be beneficial to limit the carbonation to the outer surface of RCA in order to limit the volumetric expansion and avoid any damage to the cement matrix in recycled aggregates. If the aggregates are fully wet during carbonation, the carbonation depth will probably be limited to the outer crust. The resulting increase in the volume of precipitate on the surface may significantly lower the permeability of RCA causing a considerable drop in water absorption.

Unfortunately, no systematic research quantifying the effects and interactions of such factors on the physical and mechanical properties of RCA can be found in the literature. The notion of crust carbonation is not dealt with in the past and there seems to be a need for further research with a focus on this topic. The present paper investigates the effects and interactions of aggregate preconditioning (moisture condition), ambient relative humidity, CO₂ pressure, ambient temperature, and carbonation time (referred to as variables) on the apparent particle density, water absorption and resistance to wear (referred to as response parameters) of laboratory-made RCA. The objective of this research is to first quantify and evaluate the statistical significance of the above variables on each response parameter and then find the ideal carbonation settings.

2. Methodology

A base concrete mixture is first produced, cast and moist cured for production of RCA. After four weeks, the concrete is crushed using a jaw crusher in different steps to generate aggregates with gradation similar to that of starting granules. The >3 mm fraction is tested for its water absorption and wear resistance and then subjected to 10 different carbonation conditions for the above five variables each tested in two levels in an adaptive factorial design of experiments. The carbonated RCA specimens are then tested for the same properties and the results of each experiment is used in deciding on the next carbonation settings. The ideal combination of variable levels for maximum drop in water absorption is finally determined.

2.1 Materials

CEM I 52,5 N is used as the source of portland cement in making the base concrete. 0/3 G_F85 siliceous river sand, 2/7 G_C90/15 and 7/14 G_C85/20 limestones are also used as the sources of fine aggregates, small and large coarse aggregates, respectively. Table 1 shows the mixture proportions of the base concrete. A high effective water-to-cement ratio of 0.57 is chosen to promote high water absorption by RCA and to ensure the applicability of the research findings to extreme situations where extra water is added to concrete to help mixing and compaction.

Table 1: Mixture proportions of the base concrete

Cement	Water	0/3 sand	2/7 limestone	7/14 limestone
kg/m ³	kg/m ³	kg/m ³	kg/m ³	kg/m ³
360	205	535	535	710

Figure 1 shows the sieve analysis results of the fresh aggregates. The physical properties of aggregates are also listed in Table 2. It is observed that the water absorption of 2/7 and 7/14 aggregates are below 1.0% while that of the 0/3 river sand is no more than 0.37%. The surface wear resistance of 7/14 limestone is also tested in accordance with EN 1097-2 (micro-Deval resistance to wear), which was found to be $16.0 \pm 0.52\%$. The reported value, often referred to as the micro-Deval factor, shows the mass percentage of the aggregates worn out during the test, indicated by the passing of the 1.6 mm sieve. Note that the reported error margins all pertain to 90% confidence interval (i.e., $4.46 \times$ standard deviation) throughout the paper.

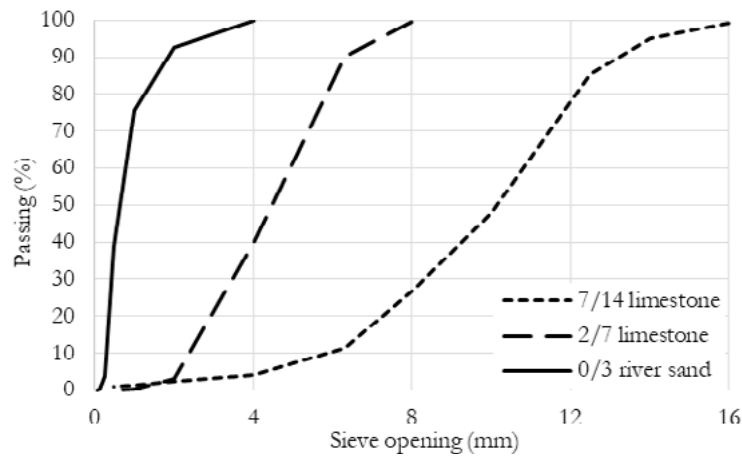


Figure 1: Sieve analysis results of fresh aggregates

Table 2. Physical and mechanical properties of fresh aggregates

Aggregate	Saturated surface dry density	Water absorption	Micro-Deval factor
	kg/m ³	(%)	(%)
7/14	2686	0.64	16.0 ± 0.52
2/7	2665	0.82	NA
0/3	2642	0.37	NA

2.2 Methods

The base concrete mixture is sealed cured for 4 weeks and tested for its compressive strength. The mixture showed a slump of 18 cm and a 28-day compressive strength of 57.6 MPa (three 15cm×15cm×15cm cubic specimens) when tested per EN 12350-2 and EN 12390-3, respectively. The remaining moulded concrete is crushed by first crushing to <9 mm rubbles using a hand-driven point-press hydraulic jack, and further crushing to aggregates using a laboratory jaw crusher. The crusher opening is first set at 10 mm opening and all rubbles are passed through. Next, the resulting grains are crushed once more at 8.5 mm opening. This was found to yield aggregates with satisfactorily low flaky/needle-shaped grains and a particle size distribution similar to those of the starting aggregates.

The obtained RCA is screened for the passing of 3 mm as the fines often show excessively high cement content and water absorption capacity. The literature is consistent in reporting the poor performance of fine RCA especially in high dosages [6,¹⁶,¹⁷]. As such, the experimental program is geared towards studying the effect of carbonation on the properties of the >3 mm fraction. The test fractions are then washed, dried and stored for carbonation procedures.

A 2-level adaptive factorial design of experiments (DoE) is deployed for studying the effects of aggregate Moisture condition (“Wet” or “Seasoned”), Relative humidity of the carbonation atmosphere (with or

without boosting to saturation; referred to as “Boosted” or “Not boosted”), CO₂ pressure (“1 bar” or “5 bars”), Temperature (“20 °C” or “60 °C”), and carbonation Time (“1 hour” or “4 hours”). Table 3 shows how the two levels of each variable are realized.

Table 3: Detailed description of carbonation parameters

Variable	Acronym (unit)	Level	Description
Moisture condition	MC (-)	“Wet”	The aggregates were soaked in water for one week before carbonation. Drained on sieve 1 mm for 10 minutes before carbonation.
		“Seasoned”	The aggregates were first dried at 80 °C for 1 day and then placed inside a climate chamber set at 95% relative humidity for 48 hours.
Relative humidity	RH (%)	“Boosted”	500 ml of water was placed inside the chamber 2 hours before carbonation.
		“Not-boosted”	The above step was not taken.
CO ₂ pressure	P _{CO2} (bar)	“1 bar”	Rapid increase from ambient CO ₂ pressure (~0 bars) to the test level in the carbonation chamber
		“5 bars”	
Temperature	T (°C)	“20 °C”	Tests were run at 20±3 °C ambient temperature.
		“60 °C”	Aggregates and CO ₂ chamber were preheated to 60 °C before carbonation.
Time	t (hours)	“1 hour”	Pressure maintained at the maximum specified value for the specified duration.
		“4 hours”	

The list of variables in Table 3 is considered to include all potentially influencing variables on RCA carbonation. Each recipe of carbonation is initiated by first soaking or seasoning representative RCA samples as described in Table 3. Next, the aggregates and the carbonation chamber are brought to the test temperature two hours before the test. A nylon tray containing 500 ml of water is placed inside the chamber in the case of “Boosted” experiments two hours in advance. The aggregates are then placed inside the chamber and the carbonation is initiated by quickly injecting CO₂ into the chamber to achieve the designated CO₂ pressure. The pressure is preserved at that level for the specified time and finally the chamber is flushed with nitrogen for 2 minutes. Upon completion of carbonation, the aggregates are taken out and dried at 80 °C for 24 hours to remove all the water trapped or generated during carbonation. Next, they are soaked in water for 24 hours and tested for their apparent particle density and water absorption in duplicates per EN 1097-6. Then, the 10-14 mm fraction is sieved and extracted for micro-Deval test for resistance to wear in accordance with EN 1097-2 (two samples tested). The passing of sieve 1.6 mm after 12,000 revolutions is sieved, washed, dried, and weighed. The mass ratio of such portion to the initial mass is reported as the micro-Deval factor of the carbonated RCA.

The test conditions are initially chosen as follows (which were thought to be the best carbonation conditions to start with): “Wet” aggregates under “Boosted” RH, carbonated at “1 bar” CO₂ pressure for “1 hour” at “20 °C” temperature. The said conditions are referred to as Exp. 1 in Table 4. In the next experiment, the pressure is raised to 5 bars to see the effect of CO₂ pressure (Exp. 2). These two experiments are then repeated at 60 °C to explore the effect of temperature (Exp. 3 and Exp. 4). As later discussed in the

results section, the unsatisfactory results led the authors to dial back the temperature to 20 °C and instead investigate the outcome of carbonation under “Not boosted” conditions for longer durations of time at both 1 and 5 bars (Exp. 5 and Exp. 6). As such, Exp. 1 and Exp. 2 were repeated under “Not boosted” conditions for 4 hours. The micro-Deval tests were temporarily dropped from the experiments in order to focus on water absorption and find carbonation settings that indeed improve this parameter. After obtaining unsatisfying results from carbonation of “Wet” RCA (regardless of CO₂ pressure, temperature, relative humidity and time), the aggregate moisture condition was switched to “Seasoned” while the relative humidity was studied in both “Boosted” and “Not boosted” conditions (tested at 1 and 5 bars for 1 hour: Exp. 7 to Exp. 10).

Table 4: The experimental units representing the studied carbonation settings

Exp. no.	MC	RH	T (°C)	P _{CO₂} (bars)	Time
1	Wet	Boosted	20	1	1
2	Wet	Boosted	20	5	1
3	Wet	Boosted	60	1	1
4	Wet	Boosted	60	5	1
5	Wet	Not boosted	20	1	4
6	Wet	Not boosted	20	5	4
7	Seasoned	Boosted	20	1	1
8	Seasoned	Boosted	20	5	1
9	Seasoned	Not-boosted	20	1	1
10	Seasoned	Not boosted	20	5	1

3. Results and discussion

The chosen sequence of crushing steps was found to result in RCA with a particle size distribution close to those of starting 0/3 siliceous sand and 7/14 limestone. Figure 2 shows the sieve analysis results of the >3 mm and <3 mm fractions of RCA in comparison with the 0/3 and 7/14 aggregates.

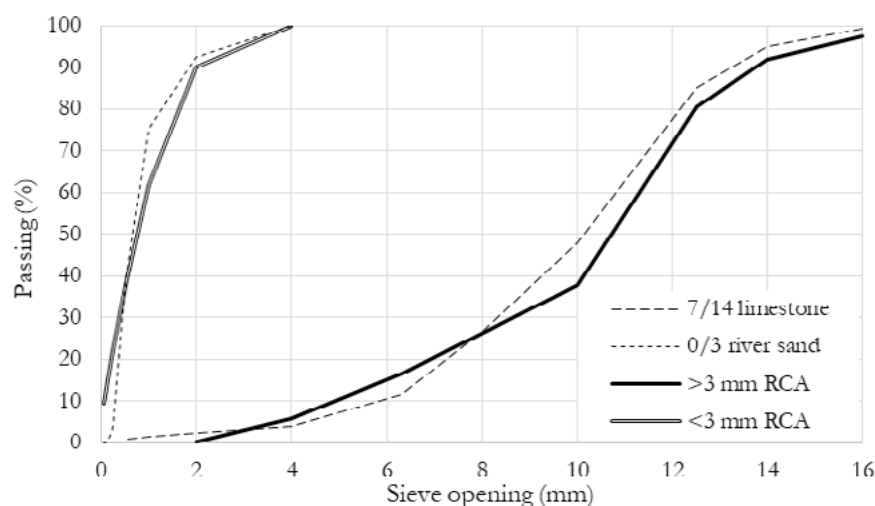


Figure 2: Sieve analysis results of RCA in comparison with the fresh aggregates

It is observed that the coarse RCA has a particle size distribution close to that of 7/14 limestone. Maintaining similar particle size is important for having a comparable basis for the water absorption of RCA. This is

because it eliminates the particle size effect and helps determine 1- how much change in water absorption and micro-Deval resistance to wear will take place due to the presence of hydrated cement paste on RCA, and 2- how much change in the said parameters a given carbonation procedure can result in.

While the water absorption of 7/14 limestone was 0.64%, the untreated (i.e., not carbonated) RCA was found to be capable of absorbing $5.26 \pm 0.12\%$ water when tested per EN 1097-6 which is mainly due to the presence of hydrated cement paste in the grains. The starting limestone aggregate showed no more than $16.0 \pm 0.52\%$ wear-out in the micro-Deval test while that of the untreated RCA was found to be $26.3 \pm 2.62\%$. As such, the presence of hydrated cement paste has resulted in some $722 \pm 19\%$ increase in water absorption and $64 \pm 21\%$ increase in micro-Deval factor.

The results of RCA carbonation in “Wet” conditions are shown in Figure 3 and Figure 4, all demonstrating the adverse effect of excessive humidity on carbonation outcome. Figure 3 suggests that regardless of carbonation temperature and pressure, carbonation in “Wet” conditions does not reduce water absorption. Note that despite that the average values of water absorption have mostly increased compared to the control (i.e., the “Not carbonated” RCA), the differences are not statistically significant (p -value >0.05 in all cases). Nonetheless, if one is to judge merely by average values, one may conclude that in three out of four carbonation conditions, the average water absorption has even increased. This could be attributed to the fact that soaking RCA in water causes (visible) leaching of portlandite from the adhered cement paste, which in turn results in an increase in RCA porosity and thus water absorption. During the carbonation process itself, some extra water is produced due to the conversion of portlandite to calcium carbonate and water. When excessive free water is already available on the RCA surface (due to soaking), carbonation was found to cause further portlandite leaching. This was visually confirmed by the occasional formation of milky water ponds at the bottom of the carbonation chamber. The micro-Deval factor results (Figure 3) are in line with the findings on water absorption. The effect of carbonation on this parameter is barely significant (p -value $=0.057$). Dunnett comparison of the four experimented carbonation conditions at 90% confidence level suggests that despite the slight drop in average micro-Deval factor due to carbonation, the differences from the control (i.e., “Not carbonated” RCA) are not significant.

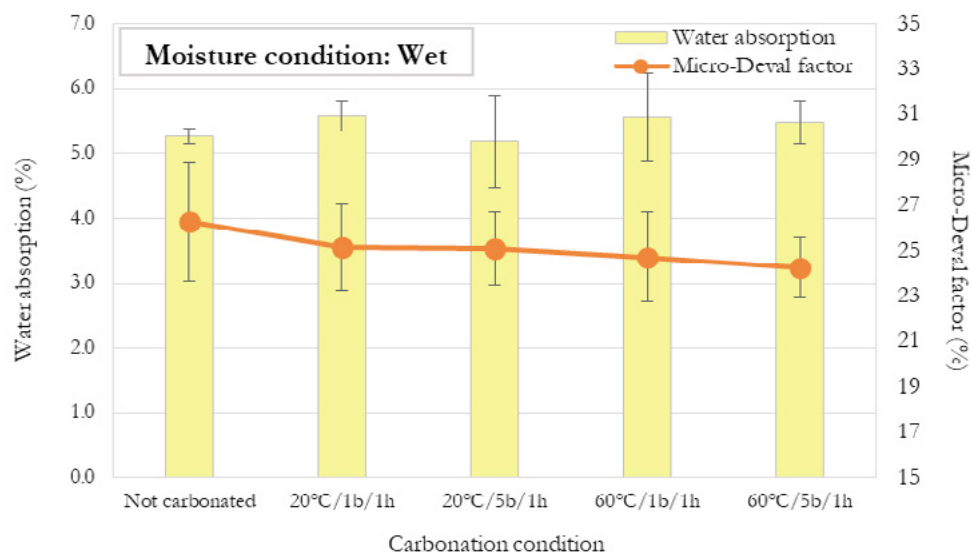


Figure 3: Water absorption and micro-Deval factor of “Wet” RCA carbonated at different temperature and CO₂ pressure levels in comparison with “Not carbonated” RCA

It was originally expected to observe meaningful changes (i.e., increase) in the RCA apparent particle density

after carbonation (due to CO₂ uptake). Figure 4 suggests that all carbonated samples have an apparent particle density numerically larger than that of the control (i.e., not carbonated). However, the differences are not statistically significant (for the “Wet conditions”). Both t-test and Dunnett comparison test results suggest that the variations are not conclusive. The above discussed leaching of portlandite or calcium carbonate from RCA in each carbonation run is thought to be counteracting the effect of carbonation on density.

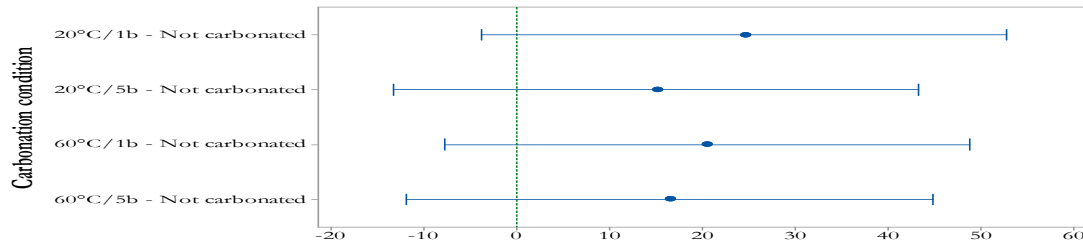


Figure 4: Dunnett Simultaneous 90% confidence intervals of the differences between the mean apparent density of RCA before and after carbonation each carbonation condition for “Wet” RCA carbonated under “Boosted” humidity conditions for 1 hour (if an interval does not contain zero, the corresponding mean is significantly different from the control mean)

In fact, the initial perception was to observe an inverse correlation between apparent particle density and water absorption (i.e., denser grains were thought to have less water absorption capacity), and similar correlation between apparent particle density and micro-Deval factor. However, no correlation was observed between the micro-Deval factor and the other two parameters. To the authors’ surprise, however, the correlation between the water absorption and apparent density was found to be direct and rather significant ($r = 0.607$; $p\text{-value} = 0.063$). The correlation matrix of apparent density, water absorption and micro-Deval factor are shown in Table 5.

Table 5: The correlation matrix for water absorption, apparent density and micro-Deval factor of “Wet” RCA

Parameter	Micro-Deval factor (%)	Water absorption (%)
Water absorption (%)	$\begin{bmatrix} -0.37 \text{ (0.327)}^* \\ -0.543 \text{ (0.131)} \end{bmatrix}$	-
Apparent density (kg/m ³)		+0.607 (0.063)

*Figures in parentheses are the p-values of correlation coefficient. A p-value greater than 0.05 indicates an insignificant correlation.

The above observations propelled the authors to further investigate the possibility of excessive humidity being the underlying cause for the unexpected results. As such, in the first step the chamber relative humidity was switched from “Boosted” to “Not-boosted” to see if any improvement will occur in the results if the carbonation time is also extended to 4 hours. Yet, little success was achieved. The “Wet” RCA carbonated at 1 bar, 20 °C for 4 hours showed a water absorption capacity of $5.70 \pm 0.63\%$, while that of same RCA carbonated under similar settings except at 5 bars was found to be $5.45 \pm 0.45\%$. Therefore, it can be concluded that “Wet” RCA does not show any improvement in the 24-hour water absorption capacity after carbonation at 1 to 5 bars, 20 to 60 °C, under “Boosted” or “Not-boosted” conditions for 1 to 4 hours.

The obtained results led the authors to further eliminate the availability of moisture during carbonation. To this end, similar carbonation experiments (but only at 20 °C) were carried out on RCA “Seasoned” at 95% RH. Since such RCA was first dried in the oven prior to exposure to 95% RH, they appeared dry on the outer surface (i.e., same appearance as oven-dried RCA). The carbonation was carried out at both

“Boosted” and “Not boosted” chamber humidity (please refer to Table 3 for the definition of these terms) at 1 and 5 bars.

The results clearly confirm that similar to the case of “Wet” RCA, carbonation of “Seasoned” RCA under “Boosted” RH at 1 to 5 bars for 1 hour results in no reduction in water absorption. $5.34 \pm 0.20\%$ and $5.41 \pm 0.40\%$ were recorded for the mean water absorption of “Seasoned” RCA carbonated at 1 and 5 bars, respectively. However, carbonation of the same RCA under “Not boosted” conditions led to a meaningful improvement and a breakthrough for the cases of 1 and 5 bar CO_2 pressure, respectively. The water absorption of the “Seasoned” RCA carbonated at 1 bar was found to be $5.03 \pm 0.16\%$ while that of RCA carbonated at 5 bars was measured as low as $4.32 \pm 0.50\%$. This means $4.4 \pm 0.8\%$ and $18.0 \pm 1.8\%$ relative drop in water absorption, respectively. These results are visually presented in Figure 5.

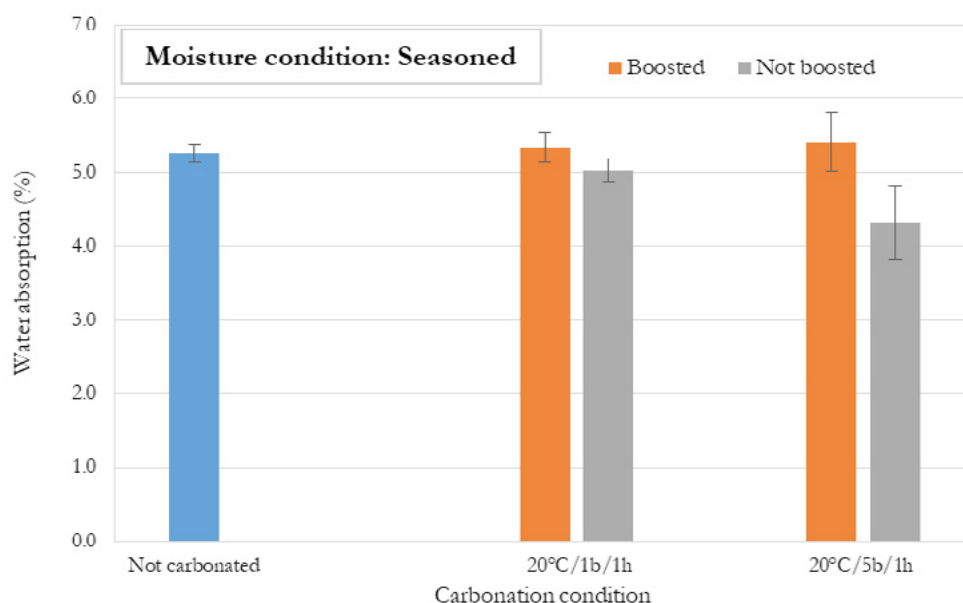


Figure 5: Water absorption “Seasoned” RCA carbonated at different relative humidity and CO_2 pressure levels in comparison with “Not carbonated” RCA

The apparent particle density readings of such carbonated RCA specimens were also found to be as those of “Wet” RCA but with less variations in readings (due to the lack of uncontrolled leaching of calcium carbonate from the specimens, unlike the case of “Wet” RCA). The results are also shown in Figure 6. In three out of four cases, a significant increase in apparent particle density was observed. Interestingly enough, the least particle density was recorded for the RCA with the least water absorption (i.e., Not-boosted/5b/1h). No clear correlation between the apparent particle density and water absorption could however be established ($r = 0.25$; $p\text{-value} = 0.487$).

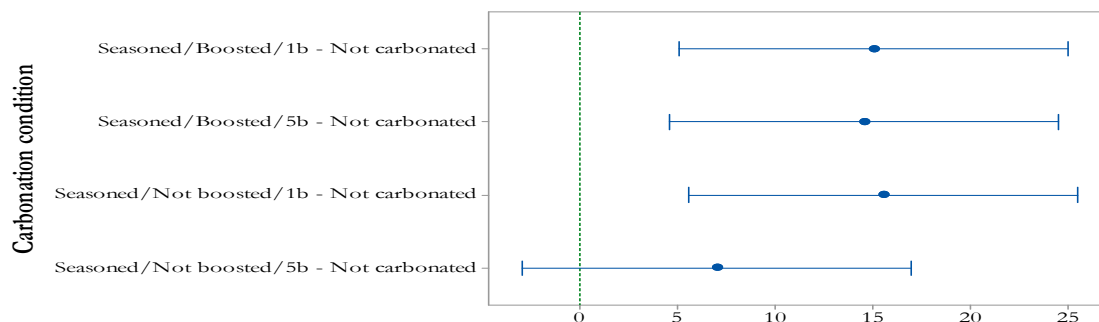


Figure 4: Dunnett Simultaneous 90% confidence intervals of the differences between the mean

apparent density of RCA before and after carbonation each carbonation condition for “Seasoned” RCA carbonated at 20 °C for 1 hour (if an interval does not contain zero, the corresponding mean is significantly different from the control mean).

Given the apparent particle density is oven-dried mass/oven-dried volume, it seems that as carbonation takes place (leading to a drop in water absorption), both the numerator and the denominator increase in such a way that the increase in the fraction is not in line with decrease in water absorption. As such, the apparent density values cannot be used as a source of judgement for water absorption capacity of RCA.

Nonetheless, comparing the 17.9% drop in water absorption for the case of “Seasoned” RCA carbonated at 5 bars with the insignificant variations in such parameter for the outputs of other carbonation settings suggests that RCA should be carbonated at high pressures under very limited access to moisture. Moreover, it can be concluded that carbonation does not take place for aggregates with excessive moisture contents.

4. Conclusions

The undertaken experimental program led to the following findings:

- Carbonation of recycled concrete aggregates under wet conditions does not lead to any improvements in water absorption and surface wear resistance, regardless of CO₂ pressure, temperature, time and availability of moisture in the carbonating atmosphere.
- No correlation was found between the apparent density and water absorption of recycled concrete aggregates carbonated under wet conditions.
- Such correlation was strongly significant in the case of recycled concrete aggregates preconditioned at 95% relative humidity prior to carbonation.
- Carbonation of recycled concrete aggregates preconditioned at 95% relative humidity in the presence of water vapor has excessively low efficiency.
- Carbonation of recycled concrete aggregates preconditioned at 95% relative humidity in the absence of water vapor at 1 bar CO₂ pressure leads to some 4% drop in water absorption. This is while increasing such pressure to 5 bars leads to an extra 14% drop in water absorption capacity.
- High pressure carbonation (i.e., 5 bars CO₂ pressure) under limited humidity conditions is recommended for the best results.

5. Acknowledgment

The authors gratefully acknowledge VITO SBR funding for the provision of time and resources.

6. References

- 1 European Commission, 2018, Construction and Demolition Waste (CDW), Available at: http://ec.europa.eu/environment/waste/construction_demolition.htm
- 2 Osmani, M., 2011, Construction waste, In *Waste*, Academic Press, 207-218.
- 3 World Business Council for Sustainable Development, 2009, Concrete Recycling: The cement sustainability initiative, Available at: <http://www.wbcsdcement.org/pdf/CSIRecyclingConcrete-FullReport.pdf>.
- 4 Bru, K., Touzé, S., Bourgeois, F., Lippiatt, N. and Ménard, Y., 2014, Assessment of a microwave-assisted recycling process for the recovery of high-quality aggregates from concrete waste, *International Journal of Mineral Processing*, 126, 90-98.

- 5 Safiuddin, M., Alengaram, U. J., Rahman, M. M., Salam, M. A., & Jumaat, M. Z., 2013, Use of recycled concrete aggregate in concrete: a review, *Journal of Civil Engineering and Management*, 19(6), 796-810.
- 6 Shi, C., Li, Y., Zhang, J., Li, W., Chong, L., & Xie, Z., 2016, Performance enhancement of recycled concrete aggregate—a review, *Journal of Cleaner Production*, 112, 466-472.
- 7 Katz, A., 2004, Treatments for the improvement of recycled aggregate, *Journal of materials in civil engineering*, 16(6), 597-603.
- 8 Li, J., Xiao, H., & Zhou, Y., 2009, Influence of coating recycled aggregate surface with pozzolanic powder on properties of recycled aggregate concrete, *Construction and Building Materials*, 23(3), 1287-1291.
- 9 Kong, D., Lei, T., Zheng, J., Ma, C., Jiang, J., & Jiang, J., 2010, Effect and mechanism of surface-coating pozzalanics materials around aggregate on properties and IT'Z microstructure of recycled aggregate concrete, *Construction and Building Materials*, 24(5), 701-708.
- 10 Kou, S. C., & Poon, C. S., 2010, Properties of concrete prepared with PVA-impregnated recycled concrete aggregates, *Cement and Concrete Composites*, 32(8), 649-654.
- 11 Xuan, D., Zhan, B., & Poon, C. S., 2016, Assessment of mechanical properties of concrete incorporating carbonated recycled concrete aggregates, *Cement and Concrete Composites*, 65, 67-74.
- 12 Zhao, Z., Remond, S., Damidot, D., Courard, L., & Michel, F., 2016, Improving properties of recycled concrete aggregates by accelerated carbonation, *Proceedings of the 4th International Conference on Sustainability Construction Materials and Technologies*.
- 13 Zhan, B., Poon, C. S., Liu, Q., Kou, S., & Shi, C., 2014, Experimental study on CO₂ curing for enhancement of recycled aggregate properties, *Construction and building materials*, 67, 3-7.
- 14 Zhang, J., Shi, C., Li, Y., Pan, X., Poon, C. S., & Xie, Z., 2015, Influence of carbonated recycled concrete aggregate on properties of cement mortar, *Construction and building materials*, 98, 1-7.
- 15 Junior, A. N., Toledo Filho, R. D., Fairbairn, E. D. M. R., & Dweck, J., 2014, A study of the carbonation profile of cement pastes by thermogravimetry and its effect on the compressive strength, *Journal of Thermal Analysis and Calorimetry*, 116(1), 69-76.
- 16 Hu, J., Wang, Z., & Kim, Y., 2013, Feasibility study of using fine recycled concrete aggregate in producing self-consolidation concrete, *Journal of Sustainable Cement-Based Materials*, 2(1), 20-34.
- 17 RILEM 121-DRG, 1994, Specification for concrete with recycled aggregates, *Materials and Structures*, 27, 53-70.

Quantification of Remaining Unhydrated Cement in Concrete Waste

D. Kulisch¹, A. Katz¹

¹Faculty of Civil and Environmental Engineering, National Building Research Institute, Technion – Israel Institute of Technology, Haifa, Israel

Abstract – In concrete recycling processes, the reuse of concrete waste as aggregate in new concrete usually requires a beneficiation process, which separates the natural aggregate from the attached cement paste/mortar. The old cement paste is considered harmful for the recycled aggregates quality; thus, its removal is recommended and only the clean natural aggregate is used as recycled aggregate. As a result, the majority of concrete recycling studies focus on the aggregate. This work focuses on the old cement paste itself, which presents remaining unhydrated cement and therefore, presents a recovery potential for further use in new cement paste/concrete not only as aggregate (inert) but also as active addition with cementing properties. This work presents the results of the quantification phase. In concrete structures, complete hydration is not achieved and unhydrated cement remains, which may be due to several factors: particle size of the cement, water/cement (w/c) ratio of the paste, curing duration and conditions, lack of water or space for hydration, etc. Since nowadays concrete with lower w/c ratios is often in use, there is an increasing amount of unhydrated cement, which represents a pronounced potential for recovery and reuse. Old concrete structures are usually made with higher w/c that allows better hydration but with larger cement grains that do not allow complete hydration. This work includes both low and high w/c representing old and new concrete structures. The parent cement pastes used in this work were prepared in laboratory using different w/c ratios and curing durations, referring to normal and high strength concrete. After crushing and grinding, different methods for quantifying the degree of hydration and the remaining unhydrated cement were used including x-ray diffraction (XRD) and thermal analysis (TGA/DTA). In addition, the hydration process was simulated by NIST model. Results from different methods show that hydration was not complete and all cements has not undergone full hydration, which indicates the presence of unhydrated cement in significant amounts. The degree of hydration is indeed lower than one (0.59-0.90 depending on the factors cited above), and there is a significant amount of remaining cement that did not undergo hydration (up to 25%). XRD results also provide information that most of the remaining cement is in the form of belite. These results indicate that the material has a recovery potential and it could be further used in new cement paste/concrete as active addition with active cementing properties.

Keywords: Unhydrated cement, degree of hydration, concrete waste.

1. Introduction

The construction sector is responsible for a significant global environmental impact, due to the consumption of natural resources and energy, the generation of waste and the emission of carbon dioxide (CO₂). Since concrete is the most used material in construction industry, by reducing its negative environmental impact it is possible to improve sustainability of the construction sector [1]. One of the main possible paths is through cement production.

In recent years, global cement production have reached around 4 billion tons per year (4.05 billion ton in 2017, 4.1 billion ton in 2018 [2]), with a projection to achieve around 5.2 billion tons by 2019 [3], which represents an enormous prospect of economic and environmental impact.

In addition, major portions of construction and demolition waste (C&DW) in many countries consists of concrete waste [4]. In concrete recycling processes, the technology for producing recycled aggregate from C&DW is available and relatively inexpensive [5]. The uses of recycled aggregate include both base/sub-base infrastructure and structural applications. Each application requires a different quality and therefore, a different treatment. The use of recycled aggregate in new concrete requires a beneficiation process, which usually separates the natural aggregate from the attached cement paste/mortar.

The old cement paste/mortar is considered harmful for the recycled aggregates quality; thus, its removal is recommended. When concrete waste is crushed, a certain amount of paste/mortar from the original cement mortar remains attached to the aggregate particles, which forms a weak, porous and cracky layer [6] – as illustrated in Fig. 1. As a result, recycled aggregates present less density, high porosity and high water absorption capacity [7].

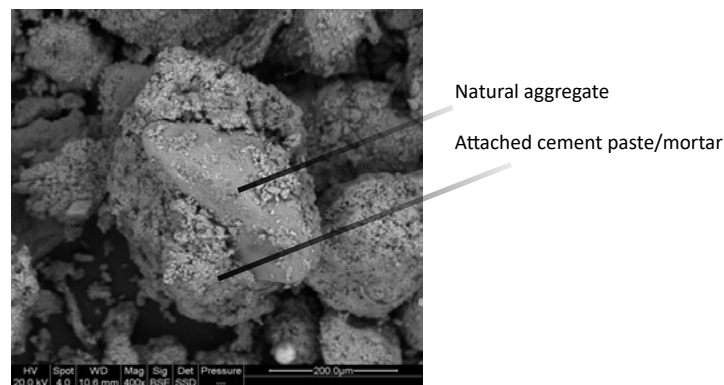


Figure 1: SEM-BSE image of crushed C&DW [8].

There are several techniques for removing the attached cement paste/mortar: thermal treatment (heating method) [9], [10]; mechanical treatment (the eccentric-shaft rotor method/mechanical grinding method) [11]; thermal-mechanical treatment (heating and rubbing method) [9], [11]; chemical-mechanical treatment (freeze-thaw method) [12]; microwave-assisted treatment [11]; ultrasonic cleaning [13]; acid treatment [11], [12], [6]; silica fume impregnation [13]; polymer treatment [14]; etc. In all the cited techniques, the clean natural aggregate is used as recycled aggregate, while the attached cement paste/mortar is of no use. As a result, the majority of concrete recycling studies focus on the recycled aggregate only, clean from the attached cement paste/mortar. This work focuses on the old cement paste/mortar itself, which presents remaining unhydrated cement and therefore, presents a recovery potential for further use in new cement paste/concrete not only as aggregate (inert) but also as active addition with cementing properties.

This work is based on two important hypotheses: the first is that part of the cement remains unhydrated in old concrete; and the second is that it is possible to recover this residual cement in order to use it in new concrete.

The cement hydration progress can be described in terms of degree of hydration: for a complete hydration, the degree of hydration is one and for any other hydration, the degree of hydration is lower than one. For these last cases, an amount of unhydrated/unreacted cement remains in the hydrated cement paste, even after long hydration time [15]–[17]. This may be due to several parameters as follows.

Cement particle size: large grains of cement may never achieve complete hydration. In grains with a diameter greater than 20-25 µm, there is always a core of cement that does not undergo hydration [18]. Greater values are described in [15]: cement particles larger than 45 µm are difficult to hydrate and those larger than 75 µm may never hydrate completely.

Water amount necessary for complete hydration: the complete hydration of cement requires a minimum amount of water in order to combine chemically with all the cement grains, which means that cement pastes with low w/c ratios may never achieve complete hydration. A few examples of the use of low w/c ratios in concrete production are high strength concrete (HSC) and high performance concrete (HPC).

Lack of space for hydration: the topics lack of water and lack of space for hydration are strongly connected. If the cement paste presents a significantly low value of w/c ratio, there will not be sufficient water to completely hydrate all the cement grains. In addition, hydration products occupy a larger volume than the original cement grain - around 2-2.2 times larger [15], [18], [19].

The critical value of w/c as 0.38 is determined experimentally in [20], which provides enough space for all the cement to react with no capillary porosity left, which means that with zero porosity, the maximum degree of hydration is achieved. For values of w/c lower than 0.38, complete hydration cannot be achieved. The same value is found in [21] and similar values are found in [17]. With lower value of w/c ratio, the capillary porosity is reduced and there will not be sufficient available space for hydration products. As a result, the hydration will stop even if there is still unreacted cement and available water. Lack of water and lack of space as two of the most important factors of controlling hydration [22].

Curing duration and conditions: hydration can end prematurely if the curing conditions (duration, relative humidity and temperature) are not appropriate, regardless of the w/c ratio. Curing conditions ensure that sufficient water is available to the cement grains in order to sustain the rate and degree of hydration necessary to achieve the desired concrete properties at the required time [23]. An example of material that do not receive appropriate conditions of curing is residual material from concrete plants.

Cement components present low solubility and therefore, the hydration process takes place mainly on the surface of the grains [18]. As a result, residual unhydrated cement grains are covered with a layer of hydration products (hydration shell of calcium silicate hydrate C-S-H), whose thickness increases as the process of hydration advances. With the increasing of this layer thickness, the hydration rate is reduced as the process depends on the penetration of the water through that layer [18]. The evolution of hydration is controlled by water diffusion through the layer of hydrated cement surrounding the anhydrous remnants of cement grains [24]. The cement hydration proceeds by dissolution of its components (alite as the main component) and precipitation of C-S-H [24] – see Fig. 2.

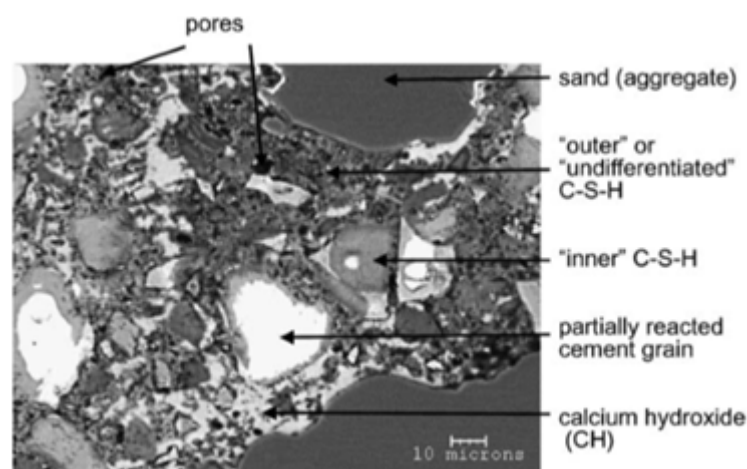


Figure 2: Typical SEM-BSE image of a Portland cement mortar [25].

The unhydrated core of cement grains constitute strength in reserve [26]. The amount of remaining

cement after hydration was estimated by different methods and it is noticeable that this amount can achieve significant values (up to 23% in volume), which represents a pronounced potential for recovery and reuse. As seen above, due to the enormous amount of cement produced worldwide, substantial economic and environmental impact could be done.

2. Methodology

The overall work program consists of two phases: (I) an estimation of quantities of residual unhydrated cement in old cement paste; (II) a study of the effect of the residual unhydrated cement on the properties of new concrete (recovery). This study presents the results of phase I. Recycled cement paste fines are produced in order to verify the amount of unhydrated core of cement grain, its exposure and its potential use in new cement paste. The production is performed by controlled parameters: w/c ratio and hydration period (curing duration).

2.1 Materials

2.1.1 Parent cement paste

The parent cement paste is prepared with different w/c ratios and curing durations. Part of the material refers to normal strength concrete, with w/c ratio between 0.4 and 0.6; and part to high performance concrete (HPC), with lower w/c ratios (0.3-0.2).

The material used to produce the parent material is cement CEM I 52.5 N, tap water and superplasticizer admixture (SP), when needed. The chemical composition of the cement is obtained by inductively coupled plasma (ICP), in addition to physical properties (Table 1). The SP used in this study is Glenium 27, a liquid high range water reducing/ superplasticizing admixture based on chains of modified polycarboxylic ether, with specific gravity of 1.044 and active/solid content of 20% (by mass). Preliminary tests are performed and the workability of the cement pastes is adjusted by the addition of SP. Cement paste specimens are produced as shown in Table 2. The specimens are prepared in 50 mm cube moulds.

Table 1: Chemical analysis of CEM I 52.5 N (values in % unless specified otherwise).

CaO	SiO ₂	Al ₂ O ₃	Fe ₂ O ₃	MgO	TiO ₂	K ₂ O	Na ₂ O	P ₂ O ₅	Mn ₂ O ₃	SO ₃
62.16	19.02	5.42	3.82	1.31	0.53	0.37	0.22	0.4	0.05	2.48
Cl (ppm)		IR	FL	LOI ₂₅₀	LOI ₉₅₀	LOI _{tot}	Specific area		Specific density	
375		0.76	2.8	0.41	2.52	2.93	4679 cm ² /g		3.125 g/cm ³	

Table 2: Composition of cement paste produced in laboratory for later crushing and grinding.

	CP0.60	CP0.40	CP0.30	CP0.25	CP0.20
Cement (kg/m ³)	1056.3	1363.8	1572.9	1697.6	1779.6
Total water (kg/m³)*	633.8	545.5	471.9	424.4	355.9
SP dosage (%)**	-	0.2%	0.4%	1%	2.5%
w/c ratio	0.60	0.40	0.30	0.25	0.20

* total water amount includes the water contained in the liquid SP and the water added to the mixture.

** SP dosage as a percentage of the active/solid content (by mass) in relation to the mass of cement.

Curing is started one day after casting, when the specimens are removed from the moulds and placed in water at (20±1)°C for 1, 3 and 28 days (for normal strength CP0.60 and CP 0.40); and for 7 and 28 days (for high performance CP0.30, CP0.25 and CP0.20). Different curing durations are studied in order to establish

a connection between age and hydration rate achieved at each age.

2.1.2 Recycled cement paste fines/residual anhydrous cement

After curing, the specimens are dried in oven at 105°C until reaching constant mass and after, they are transferred to a vacuum desiccator in order to maintain dried samples in dry conditions. These dry conditions are maintained in order to avoid the absorption of air humidity and possible changes in hydration rate. Subsequently, the specimens are tested for compressive strength, followed by crushing in a jaw crusher and grinding in a vibratory ball mill in order to achieve the fine size. The milling was performed for 30 minutes with a material/grinding aid ratio of 1/20 (stainless steel cylpebs used as grinding aid).

2.2 Methods

The hydration process is simulated by NIST cement hydration model [27]. Two different situations are studied: comparing different w/c ratios with the same cement particle size; and comparing different cement particle sizes with the same w/c ratio. For both cases, the parameters are specific gravity of cement (3.125); maximum degree of hydration (1); number of cycles (200); maximum steps per cycle (5000); maximum probability for CH nucleation (0.01); scale factor for CH nucleation (10000).

The experimental program consists of compressive strength according to [28], [29]; followed by particle size distribution (PSD), thermal analysis and X-ray diffraction (XRD). The measurements of PSD were performed using Malvern Mastersizer 2000, with water and isopropyl alcohol as dispersion liquids. Thermogravimetric analysis (TGA) and differential thermal analysis (DTA) are performed from 105°C to 950°C at a heating rate of 10°C/min. XRD is analysis using Rietveld refinement.

3. Results and discussion

3.1 Cement hydration model

The analysis of constant cement particle size (21 µm) is presented in Figure 3 and Table 3, while the analysis of constant water/cement ratio (0.4) is presented in Figure 4 and Table 4.

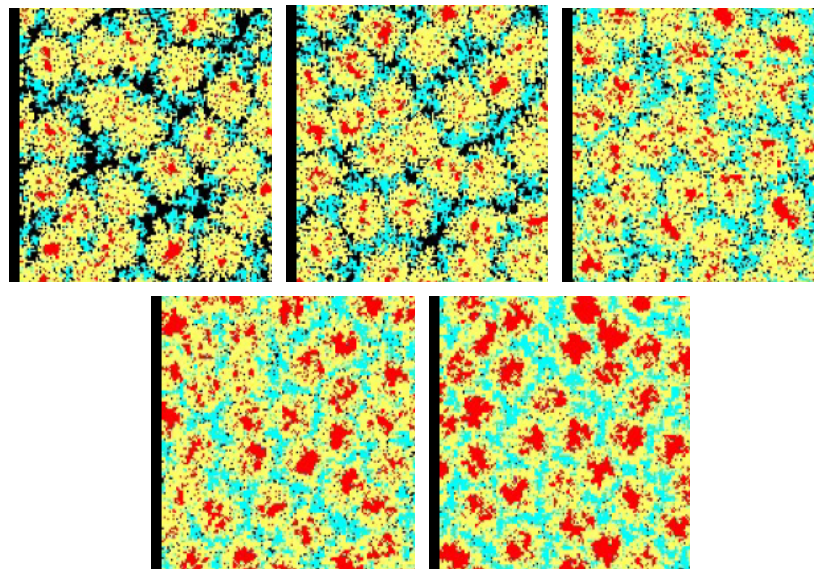


Figure 3: NIST model after maximum hydration (w/c = 0.6, 0.5, 0.4 from left to right in the upper row; w/c = 0.3, 0.25 from left to right in the lower row). Color code: porosity (black), cement (red), C-S-H (yellow), CH (cyan)

Table 3: NIST hydration model percentages - diameter of C_3S circles: 21 μm .

w/c	Maximum hydration (%)	Remaining porosity (%)	Remaining cement (%)	C-S-H (%)	CH (%)
0.60	85	25.9	4.9	50.9	18.3
0.50	83	19.5	6.2	54.7	19.6
0.40	79	9.2	9.2	60	21.5
0.30	67	2.7	16.5	59.4	21.3
0.25*	59	1	22.9	56.1	20.1

*minimum value allowed

It is interesting to notice that the amounts of C-S-H and C-H are not in constant increase with the decrease of w/c ratio: somewhere between 0.3-0.4, the maximum values are achieved, followed by a decrease. It is in accordance to the minimum w/c ratio required for complete hydration described in the literature.

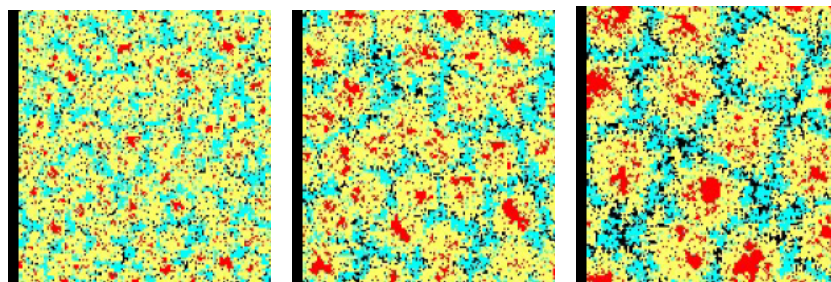


Figure 4: NIST model after maximum hydration (diameter of C_3S circle = 11, 21, 31 μm from left to right). Color code: porosity (black), cement (red), C-S-H (yellow), CH (cyan)

Table 4: NIST hydration model percentages – w/c = 0.4.

Diameter of C_3S circles (μm)	Maximum hydration (%)	Remaining porosity (%)	Remaining cement (%)	C-S-H (%)	CH (%)
11	84	6.8	6.7	63.7	22.9
21	79	9.2	9.2	60	21.5
31	73	12	12.1	55.9	20

From Fig. 4 and Table 4 is possible to notice that even a very fine-graded cement does not achieve complete hydration and some of the cement remain unhydrated.

Both factors present a clear influence on degree of hydration and amount of remaining cement: lower w/c ratio and larger particles present lower degree of hydration and higher amount of remaining cement. Significant values of remaining cement can be achieved (up to 23% in volume), which represents a pronounced potential for recovery and reuse.

3.2 Compressive strength

Compressive strength results are presented in Table 5.

Expected results show that lower w/c ratio presents higher strength in all ages. In addition, early ages specimens present partial hydration.

Table 5: Compressive strength results (MPa).

	w/c	1 day	3 days	7 days	28 days
Normal strength concrete	0.60	12.09	15.89	-	25.92
	0.40	35.98	45.63	-	56.78
	0.30	-	-	64.14	78.83
High-strength concrete	0.25	-	-	83.75	80.48
	0.20	-	-	91.59	117.7

3.3 Particle size distribution (PSD)

The samples measured in this stage, in addition to cement, were CP0.6-28days, CP0.3-7days and CP0.2-7days (Fig. 5).

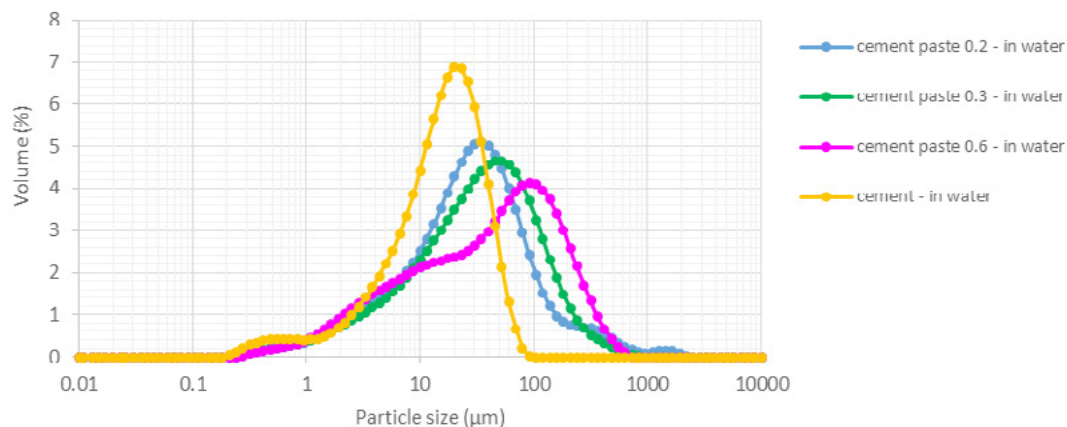


Figure 5: PSD measurements.

There is no significant difference between water and isopropyl alcohol as liquid dispersion for all samples. When working with cementing materials, there is a tendency of using an inert liquid (not water) to avoid hydration. However, the equipment manual presents an indicator called “residual”, which implies how well the calculated data was fitted to the measurement data. Residual under 1% indicates a good fit, and residual over 1% may imply use of incorrect refractive index and absorption values for the sample and dispersant. Regarding this indicator, samples in water dispersion presented lower values (lower than 1%), while samples in isopropyl alcohol dispersion presented values up to 5.6%, concluding that water dispersion is a better fit. In addition, since the test period of time is very short, hydration may not be considered.

PSD results show that stronger cement pastes (with lower w/c ratio) present similar PSD to cement PSD. In addition, the value of mass median diameter is compared (MMD or d(0.5) represents the size at which 50% of the sample is smaller and 50% is larger). All d(0.5) values of cement pastes are higher than the cement value (14.97 μm). The d(0.5) value increases with the increase of w/c ratio: 26.16, 31.42 and 41.38 μm, respectively for CP0.2-7days, CP0.3-7days and CP0.6-28days. These results are contrary to the expected, since weaker pastes should break more easily and therefore, smaller d(0.5) values would be expected for high w/c ratio. Further analysis is needed.

3.4 Thermal analysis

Results are shown in Fig. 6. All samples present 3 visible weight losses: around 115°C, referent to gypsum dehydration; around 475°C, referent to portlandite (calcium hydroxide) dehydroxylation; around 715°C, referent to calcite (calcium carbonate) decarbonation. This third weight loss is higher at the sample CP0.2-7days, which may indicate the occurrence of carbonation. From the results, the amount of portlandite

(calcium hydroxide) was calculated. Since carbonation has occurred, the amount of calcite (calcium carbonate) should be calculated and taken into consideration.

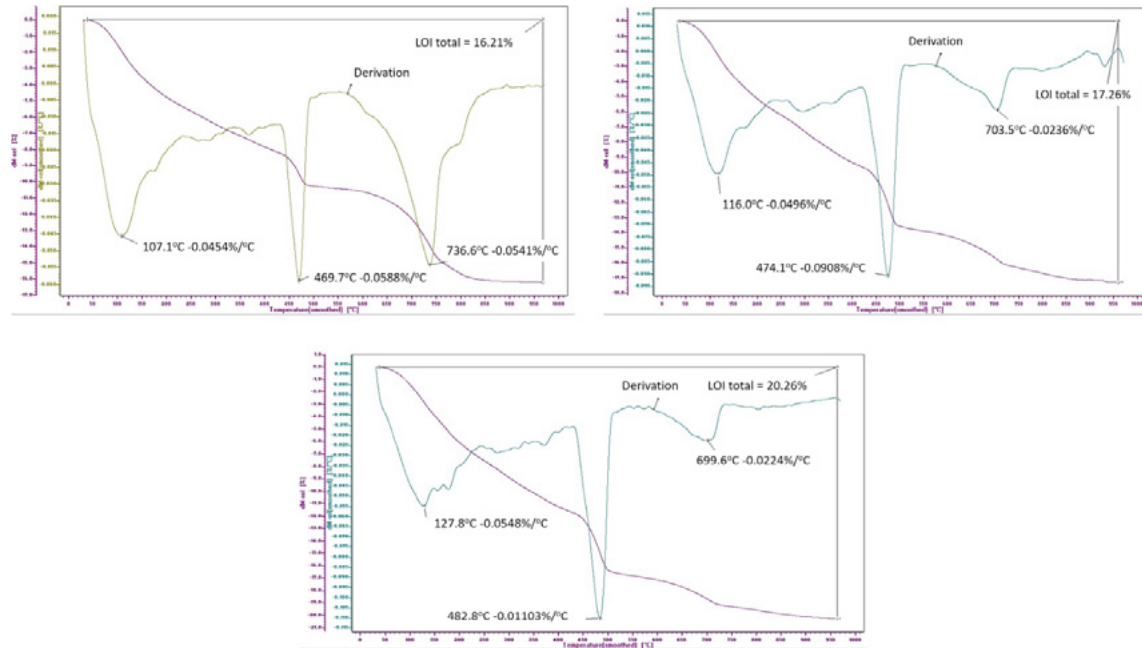


Figure 6: DTA results for CP0.2-7days (upper left), CP0.3-7days (upper right) and CP0.6-28days (lower).

The degree of hydration cannot be directly extracted from the results; however, an indirect calculation can be performed based on the non-evaporable water content (W_n), by dividing W_n by 0.23. The number 0.23 comes from [17], where the non-evaporable water represents about 23% of the mass of the anhydrous cement (1g of anhydrous cement requires 0.23g of W_n for full hydration). W_n is calculated by the difference between the weight at initial temperature (105°C) and the weight at final temperature (950°C), corrected by the loss of ignition (LOI) of the cement.

3.5 X-ray diffraction (XRD)

XRD is performed and the results are present in Table 6:

Table 6: Quantitative evaluation (%wt.).

Phase	Anhydrous cement	CP0.2-7days	CP0.3-7days	CP0.6-28days
C_3S	60.93	8.3	3.5	1.6
C_2S	12.93	11.6	12.9	10.8
C_4AF	12.4	4.2	2.9	0.1
C_3A	5.85	1.6	1.0	0.6
Portlandite	-	10.1	13.0	18.6
Calcite	-	1.7	1.5	1.3
Amorphous content	-	62.6	65.3	67
Portlandite corrected for carbonation	-	11.4	14.1	20

The amount of portlandite is corrected for possible carbonation. The amount of silicates (alite and belite) indicates the presence of unhydrated cement: around 20% for CP0.2-7days, 16% for CP0.3-7days and 12% for CP0.6-28days. In addition, the low amount of remaining alite indicates that most of the remaining cement is in the form of belite.

The degree of hydration can be calculated by 1 minus the division of the weight fraction of the anhydrous cement phases after hydration (corrected by the diluted effect) by the initial weight fraction of the anhydrous cement phases (obtained from XRD of anhydrous cement). Table 7 summarizes the testing results for degree of hydration and amount of remaining cement by different methods.

Table 7: Results comparison.

Degree of hydration (%)					
w/c	NIST	TGA	DTA	XRD	Average (Std. Deviation)
0.2	59	59	64	66.5	62.1 (3.8)
0.3	67	64	71	71.3	68.3 (3.5)
0.6	85	83	90	77.3	83.8 (5.3)
Remaining cement (%)					
w/c	NIST	TGA	DTA	XRD	Average (Std. Deviation)
0.2	22.9	25	22	25.7	23.9 (1.7)
0.3	16.5	19	15	20.3	17.7 (2.4)
0.6	4.9	6	3	13.1	6.8 (4.4)

4. Conclusions

Results indicate that for low w/c ratios, there is a good agreement between the all methods, for both degree of hydration and amount of remaining cement.

Regarding the degree of hydration, TGA and NIST model present lower values (59% for w/c of 0.2; 65% for w/c of 0.3), while XRD and DTA present higher values (65% for w/c of 0.2; 71% for w/c of 0.3). For higher w/c ratios, there is a large discrepancy between the methods.

Regarding the amount of remaining cement, w/c of 0.2 presents on average 23.9% and w/c of 0.3 presents on average 17.7%. Once again, for higher w/c ratios, there is a large discrepancy between the methods.

For both degree of hydration and amount of remaining cement, TGA appears to be more fitted.

XRD results also provide information that most of the remaining cement is in the form of belite.

It should be considered that the particle size used in NIST model was 21 μm , which is different from the particle size of the real cement used in the testing procedures.

All results indicate, as expected, that hydration was not complete and not all cement has undergone hydration, which indicates the presence of unhydrated cement in significant amounts. The specific methods for exposing the unhydrated core and further recovery have not been decided yet.

5. Acknowledgment

The support of the Ministry for Construction and Housing and the Rothschild Foundation is gratefully appreciated.

6. References

- [1] N. Kisku, H. Joshi, M. Ansari, S. K. Panda, S. Nayak, and S. C. Dutta, "A critical review and assessment for usage of recycled aggregate as sustainable construction material," *Constr. Build. Mater.*, vol. 131, pp. 721–740, 2017.
- [2] H. G. van Oss, "Cement," *U.S. Geological Survey, Mineral Commodity Summaries*, 2019. [Online]. Available: <https://minerals.usgs.gov/minerals/pubs/commodity/cement/mcs-2019-cemen.pdf>.

- [3] J. Green, "Global demand for cement to reach 5.2 billion t," *World Cement*, 2015. [Online]. Available: <https://www.worldcement.com/europe-cis/27082015/global-demand-cement-billion-tons-449/>. [Accessed: 12-Sep-2017].
- [4] A. Akhtar and A. K. Sarmah, "Construction and demolition waste generation and properties of recycled aggregate concrete: A global perspective," *J. Clean. Prod.*, vol. 186, pp. 262–281, 2018.
- [5] V. W. Y. Tam, M. Soomro, and A. C. J. Evangelista, "A review of recycled aggregate in concrete applications (2000–2017)," *Constr. Build. Mater.*, vol. 172, pp. 272–292, 2018.
- [6] V. W. Y. Tam, C. M. Tam, and K. N. Le, "Removal of cement mortar remains from recycled aggregate using pre-soaking approaches," *Resour. Conserv. Recycl.*, vol. 50, no. 1, pp. 82–101, 2007.
- [7] M. Behera, S. K. Bhattacharyya, A. K. Minocha, R. Deoliya, and S. Maiti, "Recycled aggregate from C&D waste & its use in concrete - A breakthrough towards sustainability in construction," *Constr. Build. Mater.*, vol. 68, pp. 501–516, 2014.
- [8] D. Kulisch, "Recycled aggregate as a replacement for fine aggregate in concrete production," Technion – Israel Institute of Technology, 2015.
- [9] H. Shima, H. Tateyashiki, R. Matsushashi, and Y. Yoshida, "An Advanced Concrete Recycling Technology and its Applicability Assessment through Input-Output Analysis," *J. Adv. Concr. Technol.*, vol. 3, no. 1, pp. 53–67, 2005.
- [10] M. S. de Juan and P. A. Gutiérrez, "Study on the influence of attached mortar content on the properties of recycled concrete aggregate," *Constr. Build. Mater.*, vol. 23, no. 2, pp. 872–877, 2009.
- [11] A. Akbarnezhad, K. C. G. Ong, M. H. Zhang, C. T. Tam, and T. W. J. Foo, "Microwave-assisted beneficiation of recycled concrete aggregates," *Constr. Build. Mater.*, vol. 25, no. 8, pp. 3469–3479, 2011.
- [12] L. Butler, J. S. West, and S. L. Tighe, "The effect of recycled concrete aggregate properties on the bond strength between RCA concrete and steel reinforcement," *Cem. Concr. Res.*, vol. 41, no. 10, pp. 1037–1049, 2011.
- [13] A. Katz, "Treatments for the Improvement of Recycled Aggregate," *J. Mater. Civ. Eng.*, vol. 16, no. 6, pp. 597–603, 2004.
- [14] V. Spaeth and A. Djerbi Tegguer, "Improvement of recycled concrete aggregate properties by polymer treatments," *Int. J. Sustain. Built Environ.*, vol. 2, no. 2, pp. 143–152, 2013.
- [15] P. K. Mehta, *Concrete: Structure, Properties, and Materials*. New Jersey, 1986.
- [16] R. H. Mills, "Factors influencing cessation of hydration in water-cured cement pastes," *Highm. Res. Board Spec. Rep. - Highm. Res. Board*, no. 90, pp. 406–424, 1966.
- [17] A. M. Neville, *Properties of Concrete*, 4th ed. Harlow, Essex, England, 1995.
- [18] I. Soroka, *Building Materials – Properties and Uses. Part One: Cementitious Materials, Mortars and Concrete*. 1989.
- [19] H. S. Wong and N. R. Buenfeld, "Determining the water-cement ratio, cement content, water content and degree of hydration of hardened cement paste: Method development and validation on paste samples," *Cem. Concr. Res.*, vol. 39, no. 10, pp. 957–965, 2009.

-
- [20] T. C. Powers, "Physical Properties of Cement Paste," *Res. Dev. Lab. Portl. Cem. Assoc.*, vol. II, no. Bulletin 154, pp. 577–609, 1960.
 - [21] H. F. W. Taylor, *Cement Chemistry*, Second. London: Thomas Telford, 1997.
 - [22] J. W. Bullard *et al.*, "Mechanisms of cement hydration," *Cem. Concr. Res.*, vol. 41, no. 12, pp. 1208–1223, 2011.
 - [23] ACI Committee 308, "Guide to external curing of concrete," pp. 1–36, 2016.
 - [24] S. Garrault, T. Behr, and A. Nonat, "Formation of the C - S - H Layer during Early Hydration of Tricalcium Silicate Grains with Different Sizes," *J. Phys. Chem. B*, vol. 110, pp. 270–275, 2006.
 - [25] K. L. Scrivener, "Backscattered electron imaging of cementitious microstructures: Understanding and quantification," *Cem. Concr. Compos.*, vol. 26, no. 8, pp. 935–945, 2004.
 - [26] M. L. Gambhir, *Concrete Technology: Theory and Practice*, 5th ed. New Delhi, 2013.
 - [27] D. P. Bentz, "Cement hydration modelling software," *Cement hydration and percolation processes modelling programs*. NIST National Institute of Standards and Technology, 2000.
 - [28] SI26-4.1, *Testing concrete: Strength of hardened concrete - Compressive strength*. 2010.
 - [29] EN12390-3, *Testing hardened concrete: Compressive strength of test specimens*. 2009.

Mechanism and kinetics of binding of meat and bone meal ash into the Portland cement clinker

T. Staněk¹, P. Sulovský², M. Boháč¹

¹Research Institute for Building Materials, Hněvkovského 65, 617 00 Brno, Czech Republic

²Department of Geology, Faculty of Science, Palacký University, tř. 17. listopadu 12, 771 49 Olomouc, Czech Republic

Abstract

Meat and bone meal (MBM) is one of the alternative fuels with good calorific value used in cement production. The main problem with MBM combustion in a cement kiln is the high content of P_2O_5 , which incorporates in clinker phases, influencing phase composition of clinker and hence the quality of the cement. In cement industry, only limited amount of MBM is burned to prevent adverse effect on the clinker properties, i.e. within a safe maximum amount of around 0.5% P_2O_5 in clinker and only exceptionally more. P_2O_5 has a significantly negative effect on the nucleation of alite as a main clinker phase and it stabilizes belite by means of entering its structure. At 4.5 wt. % P_2O_5 in the clinker, the alite formation is completely blocked. Research on kinetics of reactions between clinker and MBM proved reduction of negative reactions and minimization of migration of P_2O_5 into the clinker minerals using undispersed P_2O_5 carrier. The carrier in lump form eliminates the negative effect of P_2O_5 on the formation of the main clinker phase alite. The research was conducted by means of XRD and optical and electron microscopy. Optical microscopy revealed that a thin belite layer of about 100 μm was formed at the ash and clinker interface and electron microanalysis showed that P_2O_5 migrated inside the clinker to a distance of less than 250 μm from the interface. It is not possible to influence clinker outside this area. By analyzing the ash residues in the clinker, it was found that an alkaline calcium phosphate with a structure close to nagelschmidite, which does not have a negative impact on the hydration of cement, is formed. It is possible to prepare high quality cement from the clinker containing ash residues from MBM in an amount corresponding to up to 10 wt. % P_2O_5 in clinker. The work was completed with preparation of cement with 7 wt. % of P_2O_5 in the clinker, which exhibited good technological properties. In addition, cements with increased P_2O_5 content have significantly reduced the leachability of toxic elements.

Keywords: Portland cement clinker, meat and bone meal, phosphorous pentoxide, cement.

1. Introduction

Meat and bone meal (MBM) is one of the alternative fuels used in cement production. It has good calorific value (16 - 20 GJ / t) and at the same time, a biodegradation occurs there as well as possible disposal of harmful substances at high temperatures in the cement kiln. In particular, the destruction of dead animals infected with various diseases, including the highly dangerous BSE (bovine spongiform encephalopathy), appears to be useful and effective [1,2].

MBM is dosed in the cement kiln dispersed in a flow of air or fuel and its particles spontaneously burn. The combustion residues, consisting of calcium phosphate (mainly hydroxylapatite - $Ca_5(PO_4)_3(OH)$) then react

with clinker in its whole volume. P_2O_5 influences clinker melt properties [3], enters into the structure of clinker phases [4] and influences the phase composition of clinker [5-8] and thus the quality of the cement [7,9].

In practice, the cement works combust only such amounts of MBM that negatively influence the clinker properties only to a small extent, i.e. only up to a safe maximum amount of 0.5, rarely up to 1 wt. % P_2O_5 in clinker.

It was experimentally proven that P_2O_5 has negative effect on the nucleation of alite crystals, stabilizing C_2S . $\alpha-C_2S$ forms a continuous solid solution with C_3P above 1,450 °C [10] with a miscibility gap at 1,500 °C [11]. Negative effect of increased belite and free lime content at the expense of alite was observed from 0.7 wt. % of P_2O_5 . With the increasing content of P_2O_5 , CaO does not completely react with belite to form alite even after 4 hours burning at 1450 °C, which can be considered as equilibrium burning. Alite formation is completely blocked at 4.5 wt. % of P_2O_5 in the clinker [8].

This paper explains the reaction kinetics of phenomenon at the clinker/MBM ash interface and suggests the possibility of multiply increase of the amount of co-incinerated MBM compared to the normal state. During that, clinker with residues of MBM ash are formed without a significant direct negative effect of P_2O_5 on the formation of the main clinker phase alite and from it prepared cement shows high-quality technological parameters.

2. Methodology

2.1 Materials

Raw meal from common cement raw materials was prepared for experimental work. The composition of the raw meal, its chemical composition and result of sieve analysis are shown in Tables 1 and 2. The phase composition of the equilibrium burned clinker from this raw meal (until CaO has completely reacted) determined by microscopy point-counting method (see Chap. 2.2) is shown in Table 3.

Table 1: Composition and basic chemical parameters of experimental raw meal.

Sign	Content of component in wt. %				Basic chemical parameters		
RM-99	Limestone	Sand	Clay shale	Fe correction	LSF	SR	AR
	75.46	3.51	20.06	0.97	99	2.5	1.6

$$LSF = \frac{100 \times CaO}{2.8 \times SiO_2 + 1.18 \times Al_2O_3 + 0.65 \times Fe_2O_3} \quad (1)$$

$$SR = \frac{SiO_2}{Al_2O_3 + Fe_2O_3} \quad (2)$$

$$AR = \frac{Al_2O_3}{Fe_2O_3} \quad (3)$$

Where:

LSF - Lime saturation factor

SR - Silica ratio

AR - Alumina ratio

Table 2: Granulometric analysis of raw meal RM-99.

Sign	Rest in wt. % on sieves with openings in mm				
RM-99	0.045	0.063	0.090	0.125	0.200
	27.2	18.1	8.4	2.9	0.3

Table 3: Phase composition of equilibrium burned clinker from raw meal RM-99 in wt. %.

Sign	C ₃ S	C ₂ S	C ₃ A	C ₄ AF
C-99	71.0	13.7	10.0	5.7

MBM ash was prepared by burning at 750 °C for 4 hours. Chemical composition of this ash is shown in Table 4.

Table 4: Chemical composition of MBM ash.

Component	Content in wt. %
SiO ₂	1.77
TiO ₂	<0.01
Al ₂ O ₃	0.48
Fe ₂ O ₃	0.67
P ₂ O ₃	37.02
MnO	0.022
MgO	1.49
CaO	47.11
Na ₂ O	4.18
K ₂ O	2.63
SO ₃	0.56
Cl ⁻	2.60
LOI	7.11
Ash content	21.25

2.2 Methods

Reactions of ash particles in cement raw meal were simulated by two ways:

1. **Sandwiches** – compressed tablets 40 mm in diameter consisted of the layer of finished clinker or raw meal for clinker burning and the layer of MBM ash.
2. **Tablets** – tablets of different diameters pressed from MBM ash were homogenized with raw meal and larger tablets 40 mm in diameter were pressed from this mixture.

In the first part of the experiment, sandwiches with layer of ground clinker and layer of ground ash from MBM were prepared. Phase composition of ground clinker is shown in Table 3 and chemical composition of MBM ash is shown in Table 4. Sandwiches were burned at 1,450 °C, they were incoherenced and the layers were separated after burning.

Therefore, in the next part of the experiment, the tablets consisted of MBM ash with diameter of 20 mm were pressed and homogenized with ground clinker C-99 and then pressed to the form of larger tablet 40 mm in diameter. Burning were done at programmable super kanthal furnace at 1,450 °C for 1, 2 and 4 hours. Other samples were prepared by the same way – tablet of MBM ash in tablet from raw meal RM-99. Burning were done at 1,450 °C for 0, 30, 60 and 90 min. Incoherence of the tablet was noticable after burning and pulling of the samples from the furnace and the inner tablet, which was initially formed from MBM ash fell out from the finally clinker tablet.

After that, pellets from MBM ash, 5 mm in diameter were prepared on pelletizing plate. These pellets were mixed with the raw meal RM-99 and tablets of 40 mm in diameter were pressed from this mixture. Estimated content of P_2O_5 in clinker was 5 wt. % (91 wt. % RM + 9 wt. % MBM ash). The burning of large amount of clinker for cement preparation was carried out at 1,450 °C with an isothermal dwell for 2 hours. Sample identification - C-5P-T.

Subsequently, experimental burnings with raw MBM were performed. Firstly, solid pellets from MBM in the small pelletizing machine MGL 200 were made (see Figure 1). These pellets were mixed with the raw meal RM-99 and the mixture was burned to clinker. The ratio between RM and MBM contents was chosen, that the total content of P_2O_5 was similar to the previous case. The burning of larger amount of clinker for cement preparation was carried out in the same way at 1450 °C with isothermal dwell for 2 hours. Sample identification – C-5P-MBM.



Figure 1: Preparation of pellets from MBM in the granulator line MGL 200

Phase composition of experimental clinker samples was analyzed by optical microscopy and X-ray diffraction.

Burned clinkers were crushed below 1 mm. Polished sections were prepared from the 0.045–1 mm size fraction. Quantitative phase composition of prepared clinkers was determined by point-counting method in polished sections [12]. For perfect differentiation of individual phases, the surface of polished section was etched in vapor of acetic acid [13]. Quantitative phase composition is expressed in vol. % and for calculation of wt.% the following densities of clinker minerals were used: C_3S – 3.15; C_2S – 3.28; C_3A – 3.03; C_4AF – 3.77; free CaO – 3.35 and C_3P alkalic – $3.07 \text{ g} \cdot \text{cm}^{-3}$.

Qualitative determination of phases in clinker was analysed by powder X-ray diffraction of the clinkers with a Bruker D8 Advance diffractometer with variable slits and a position sensitive detector. The diffractometer was operated at 40 kV and 30 mA, using Ni-filtered $\text{CuK}\alpha$ of $\lambda = 1,541,718 \text{ \AA}$, recording 6–80° in $0.02^\circ 2\theta$ increments with 188 s counting time per step and total scan time of 1 h 5 m 59 s.

Electron microprobe CAMECA SX100 was used for the analysis of clinker phases and concentration changes of selected elements on the clinker – MBM ash interface. The analytical conditions were: accelerating

voltage 15 kV, beam current 20 nA and spot size 2 μm . The standards used for internal calibration were natural standards - wollastonite (Ca, Si), barite (S), orthoclase (K, Al), andradite (Fe), jadeite (Na), rhodonite (Mn), pyrope (Mg), hydroxylapatite (P), and synthetic TiO (Ti); all elements were analyzed on their $K\alpha$ lines. The lower limits of detection varied between ~ 0.01 wt. % (e.g. for P, S, Si, Al, Ca) and ~ 0.02 wt. % (e.g. Ca, K, Mn, Fe). The acquired counts, corrected for background, were recalculated to oxides using the PAP correction procedure included in the CAMECA PeakSight automation program. The EMPA results in wt.% oxides were recast into composition formulae in atoms per formula unit (apfu).

Specific weight of cements was determined by the pycnometer method and specific surface by the Lee-Nurse permeability method according to the British standard B. S. 12:1958. Clinkers with the addition of gypsum were ground to approximately same surface area in a laboratory ball mill.

According to the standard EN 196-1, mortar prisms were prepared from the cements and the development of compressive strength was tested after 2, 7, 28 and 90 days of hydration. Normal consistency, soundness, start and time of the setting were determined according to EN 196-3. Hydration heat of cements after 7 days of hydration was determined according to EN 196-8.

Fly ash containing elevated levels of toxic elements was used to monitoring the immobilization of toxic elements. Fly ash was mixed in 1 : 1 ratio with cement C-5P-MBM and as well as the reference cement CEM I 52.5N. The test prisms prepared from these mortars were after demolding placed in humid environment (temperature 20 $^{\circ}\text{C}$, relative humidity 90%). After 28 days of hydration the test bodies were ground to 1 – 10 mm and this material was leached according to EN 12457-4. The decanted leachates were filtered through a 0.45 μm pore filter. The leachates were analyzed by ICP-MS (Agilent).

3. Results and discussion

3.1 Sandwich experiments

Sandwich experiments revealed, that most of the MBM ash layer is separated from the clinker layer. A thin reaction rim composed of belite grains is formed in place, where the two layers remain connected (see Figure 2). The width of the reaction rim and the belite grains increase with the burning time (see Table 5).

Table 5: Approximate width of reaction belitic rim and average size of belitic grains in rim.

Burning time [hours]	1	2	4
Width of layer [μm]	75	110	140
Size of belite grains [μm]	20	40	50

Sandwich interfaces were studied by electron microanalysis. The results showed that diffusion in the solid state occurred only in the immediate vicinity of its own interface, more precisely to a distance of about 500 μm from it. Diffusion occurred in both directions, as evidenced, for example, by increased concentrations of Al_2O_3 and alkalis, typical for the phosphate zone in the clinker zone at the interface. In substance, only Si is diffused from the clinker layer into the layer formed by the melting and recrystallization of the MBM ash.

The joint occurrence of some oxides (Al_2O_3 , K_2O , Na_2O) is evidenced by the very similar concentration curves of these oxides. The depth of the zone, where the main phases of the two parts of the sandwich were influenced is 300 - 500 μm . Point analysis in the immediate vicinity of the interface are analysis of the solid solution C_2S - C_3P , at a distance of > 200 μm from the interface, the second phase fraction already decreases below 5%. The concentration profiles at the clinker-MBM ash interface are shown in Figures 3 and 4.

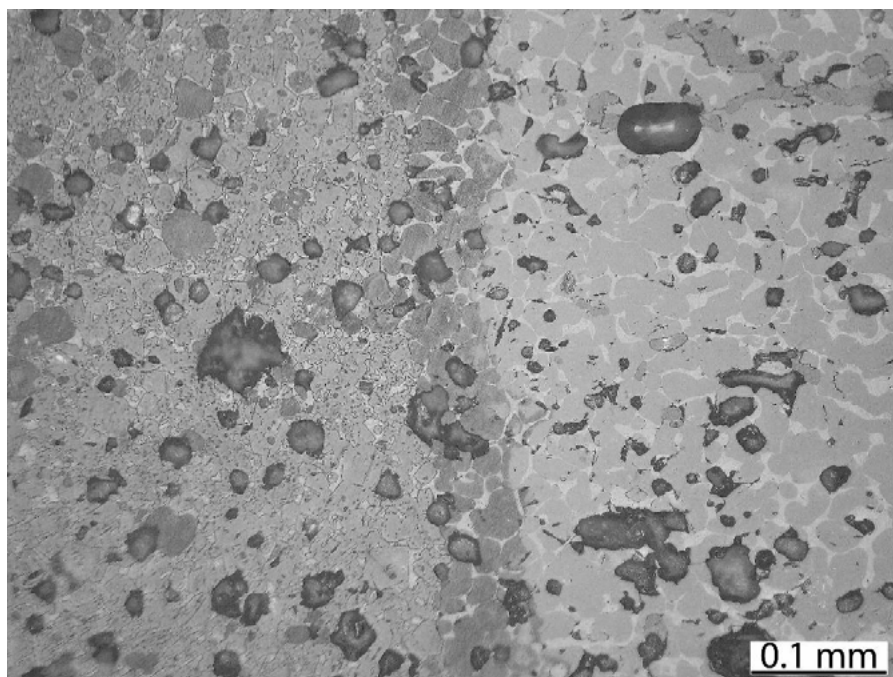


Figure 2: Microstructure of the sandwich cross section (1,450 °C, 2 hours), from left to right – layer of clinker formed by light gray crystals of alite and dark gray grains of belite, dark gray grains of belitic reaction rim (in the middle), lighter right part is formed by burned MBM ash (reflected light, etched by acetic acid vapor).

As follows from the concentration profiles of Si and P (Figure 3), the diffusion of Si towards the ash layer from the MBM is much more significant than the diffusion of P towards the clinker, where the concentration decreases to zero already at a distance of less than 250 μm . The diffusion of Si into the MBM ash layer is most significant to a depth of about 350 μm , gradually decreasing from this distance, while at a distance of 1.25 mm, about 10% of the atoms of P are replaced by atoms of Si.

Correlation coefficients were calculated from the values of individual cations from C_2S - C_3P analysis. It follows that there is a very strong correlation between phosphorus and sodium ($r = 0.983$), the positive correlation between K and P is also significant ($r = 0.763$), beside between P and C is significantly negative correlation ($r = -0.988$, and -0.827 , respectively).

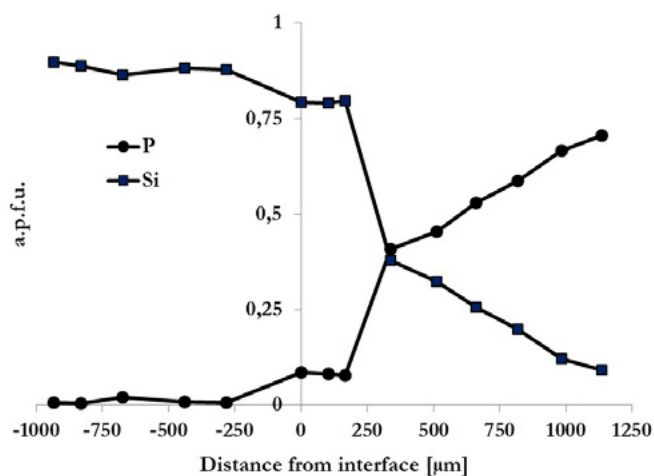


Figure 3: Concentration profiles of Si and P through clinker (left) / MBM ash (right) interface, burning at 1,450 °C, 2 hours (a.p.f.u. - atoms per formula unit).

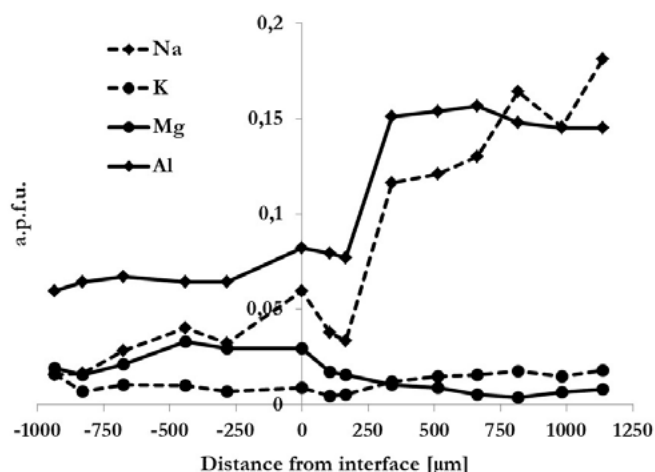


Figure 4: Concentration profiles of Al, K, Na and Mg through clinker (left) / MBM ash (right) interface, burning at 1,450 °C, 2 hours (a.p.f.u. – atoms per formula unit).

3.2 Experiments with tablets

The newly formed clinker with residues after MBM ash tablets was analyzed by X-ray diffraction and electron microprobe to determinates qualitative phase composition. It was found that the residues are not formed by apatite, but by alkaline calcium phosphate, which with its diffraction spectrum is closest to mineral nagelschmidtite ($\text{Ca}_3(\text{PO}_4)_2 \cdot 2(\alpha\text{-Ca}_2\text{SiO}_4)$). Apatite is represented here only in a small amount and belite in the orthorhombic modification α' doped with P_2O_5 occurs here.

Microstructure of the newly formed clinker with tablets of burned MBM ash interface in shown in Figure 5. There is not a clearly visible reaction rim as in the case of a sandwich prepared from a clinker (see Figure 2).

The electron microanalysis of phosphate residues revealed that they are formed by the oval grains of $\text{Ca} \pm \text{Na, K}$ phosphate with a small proportion of Si, which are bounded by a boundary material, which has a composition corresponding to ferrite, rarely aluminate. It has been found that the composition of the predominant phase of these residues is very variable, both in the cationic and in the anionic part. K_2O (1.7 - 12.6%), Na_2O (1.1 - 6.0%), CaO (39 - 60%), P_2O_5 (10.6 - 32.0%) and SiO_2 (1.3 - 16.4%) have the largest variance. Statistical analysis of ratios $(\text{Na} + \text{K}) : \text{Ca}$ and $\text{P} : \text{Si}$ showed that there is a relatively strong positive correlation between them ($r = 0.73$). It means, alkali is bound to the phosphate component in silicophosphates, not to the silicate. According to X-ray diffraction analysis, these phases correspond by the structure closest to nagelschmidtite $\text{Ca}_3(\text{PO}_4)_2 \cdot 2(\alpha\text{-Ca}_2\text{SiO}_4)$, which is a mineral formed in nature by high temperature (contact) metamorphosis of phosphorus-rich sediments and has also been described from slags. The amount of alkali, especially potassium, is too high to be neglected by comparing to the theoretical composition of nagelschmidtite, and the fact that the stoichiometric ratio of $\text{P} : \text{Si}$ is 1 : 1 in the theoretical formula of nagelschmidtite found in only 4 of 27 analysis. Thus, it will be rather one of the phosphates described in [14], in which, at position A of compounds of the A_2XO_4 type, Ca and Na occur. For example, $\text{Ca}_5\text{Na}_2(\text{PO}_4)_4$ with a structure close to nagelschmidtite was synthesized by these authors, but they also mention the existence of a much wider range of $\text{Ca} : \text{Na}$ - from $\text{Ca}_{4.8}\text{Na}_{2.4}(\text{PO}_4)_4$ to $\text{Ca}_{5.2}\text{Na}_{1.6}(\text{PO}_4)_4$. Due to the approximation of the ionic radii of sodium and potassium, the existence of phases in which potassium, together with calcium, would also emerge is certainly not excluded.

The analyses show that the Na_2O content varies between 3.0 and 10.4% in the phases that are darker in the backscattered electrons, the K_2O content varies between 1.5 and 4.3%. After conversion to atomic

quotients, $(Na + K) / Ca$ ratio ranges from 0.1 to 0.5, most often about 0.17, which would correspond to the empirical formula $Ca_6(Na, K)[(PO_4)_{3.5}]$. In the lighter phases, the alkali contents are low and correspond to carbonate hydroxyapatite. Si content is low in both phase types, silicophosphate is rarely found with them.

Analyses of alite and belite in clinkers with residues of MBM ashes show very low average contents of P_2O_5 (about 0.1% in alite, 0.3 - 0.6% in belite) in contrast with belite in clinkers with finely dispersed P_2O_5 carrier, where content of P_2O_5 is normally higher than 6.0% with a total content of 4.5 wt. % P_2O_5 in clinker [8].

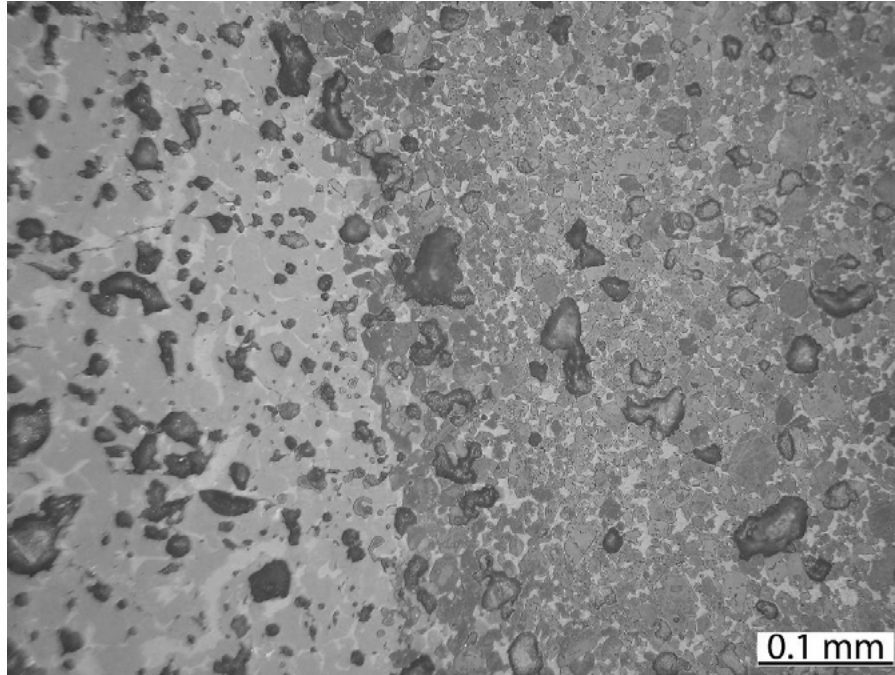


Figure 5: Microstructure on the MBM ash / clinker interface in clinker C-5P-T (1,450 °C, 2 hours), dark gray drops near interface in burned MBM ash are grains of C_{free} (reflected light, etched by acetic acid vapor).

3.3 Cement preparation and their parameters

Quantitative phase composition of clinker burned using MBM ash pellets and raw MBM determined by microscopy is shown in Tables 6 and 7. Chemical composition of both clinkers is presented in Table 8.

Table 6: Quantitative phase composition of clinker C-5P-T in wt. %.

Phase	C-5P-T	C-5P-T*	C-99 ^s
C_3S	53.2	64.1	71.6
C_2S	13.3	15.9	10.8
C_3A	5.8	6.9	12.4
C_4AF	10.3	12.4	4.4
C_{free}	0.5	0.7	0.8
$C_{free} II$	0.2	-	-
$M_{free} II$	0.1	-	-
$C_3P alk$	16.6	-	-

Where: $C_{free} II$ – free CaO from MBM ash

$M_{free} II$ – free periclase from MBM ash

*phase composition of clinker without phases from MBM ash

C-99^s – clinker burned at the same conditions from reference meal RM-99

Table 7: Quantitative phase composition of clinker C-5P-MBM in wt. % (explanations see Table 6).

Phase	C-5P-MBM	C-5P-MBM*	C-99 ^s
C ₃ S	55.0	67.1	71.6
C ₂ S	10.7	13.1	10.8
C ₃ A	7.9	9.7	12.4
C ₄ AF	6.8	8.2	4.4
C _{free}	1.6	1.9	0.8
C _{free} II	0.4	-	-
M _{free} II	0.2	-	-
C ₃ P alk	17.4	-	-

Table 8: Chemical composition of clinkers C-5P-T and C-5P-MBM in wt. %.

Phase	C-5P-T	C-5P-MBM
SiO ₂	19.45	18.13
TiO ₂	0.24	0.26
Al ₂ O ₃	4.22	4.40
Fe ₂ O ₃	3.06	2.93
P ₂ O ₅	6.45	7.09
MnO	0.064	0.076
MgO	1.05	1.28
CaO	63.42	63.38
Na ₂ O	0.75	0.90
K ₂ O	0.79	0.59
SO ₃	0.08	0.35
LOI	0.34	0.41
Total	99.91	99.80

The results in Tables 6 and 7 showed that P₂O₅, which is released from ash inclusions, partially affects the phase composition of the surrounding clinker (see difference in columns 2 and 3 in the tables). However, with a content of about 6.5 (resp. 7) wt. % P₂O₅ in clinker its influence is acceptable.

The basic characteristics of cements prepared from clinkers whose phase composition is shown in Tables 6 and 7 are shown in Table 9. Cements prepared from clinkers with residues of MBM ash with the same content of solidification regulator and with approximately the same specific surface have high-quality technological properties. The results are compared with the reference cement (CEM-99) and shown in Tables 10 - 12. The results show that the clinker parameters with MBM ash residues are of high quality and comparable to the reference cement.

Table 9: Specific weight [kg/m³] and specific surface [m²/kg] of prepared cements.

Parameter	CEM-5P-T	CEM-5P-MBM	CEM-99
Specific weight	3,122	3,127	3,132
Specific surface	358	354	366

Table 10: Compressive strength [MPa] of prepared cements according to EN 196-1.

Cement	2 days	7 days	28 days	90 days
CEM-5P-T	18.4	39.0	57.9	63.3
CEM-5P-MBM	21.7	37.6	60.5	65.0
CEM-99	20.0	50.4	67.4	69.3

Table 11: Determination of setting development, normal consistency and soundness according to EN 196-1.

Cement	Normal consistency [%]	Start of setting [hours : mins]	Setting time [hours : mins]	Soundness [mm]
CEM-5P-T	25.3	2:20	3:30	0.7
CEM-5P-MBM	27.0	5:20	6:10	1.7
CEM-99	26.0	5:00	5:50	0.3

Table 12: Hydration heat of cement after 7 days of hydration according to EN 196-8.

Cement	Hydration heat [kJ/kg]
CEM-5P-T	292
CEM-5P-MBM	337
CEM-99	368

During the research of hydration and durability of P-enriched cements was found a very important property of these cements. It is their ability to increase the immobilization of toxic elements. This phenomenon was observed both with cements containing MBM ash residues, and with cements with phosphorus incorporated in clinker silicates. The leachability of hazardous elements added to the mortars from these cements has substantially decreased both in elements forming cations and in anions-forming hazardous elements [15].

Table 13 demonstrates an example of the immobilization ability of the cement C-5P-MBM from clinker containing 7 wt. % P_2O_5 in form of residues from MBM ash.

Analogues of apatite, in which a part of calcium or phosphate ions has been replaced by other ions are over the range of pH these phases can encounter in materials based on Portland cement or in their immediate vicinity in outdoor applications (pH 6 – 12), are insoluble. It was evidenced that in aqueous environment (e.g. in soil solution) occurs in the presence of apatite ion exchange, by which cations of metals like Pb, Zn, Co or Cd substitute Ca^{2+} ions in the structure of apatite [16,17]. Similar exchange is known to happen with the phosphate anion, which can be replaced by arsenate, selenate, chromate or vanadate ions [18-20].

Table 13: Comparison of leachabilities of hazardous elements.

Element	Element content in eluate [µg/l]		Leachability of mortar from cement with 7% P_2O_5 compared to the leachability of mortar made of CEM I 52.5N [%]
	CEM I 52.5N	CEM-5P-MBM	
As	7.59	0.97	13
Cr	262.8	97.2	37
Cu	1.27	0.37	29
Pb	3400	350	10
Zn	650	210	32
Mn	261.5	9.1	3
Sb	1.30	0.28	22
V	1.50	0.51	34

4. Conclusions

From the results it is clear that the reaction between the ash particles from the MBM and the surrounding clinker (or raw meal for clinker burning) is slow and does not have a significant impact on the phase composition as in the case of the scattered P_2O_5 carrier.

- During the reaction, narrow belitic rim is formed at the interface of clinker-ash on the clinker side. In this rim, belitic grains increase due to recrystallization. When we used raw meal, this belitic line is not so clearly formed and also alite crystals occur there. A higher concentration of CaO close to the interface of both components is noticeable.
- Also, electron microanalysis showed a slight reaction and migration of elements at the interface of MBM ash and clinker. It was found that the Si diffusion into the layer of MBM ash is much more significant than the phosphorus diffusion into the clinker, where its content is almost zero already at a distance of less than 250 μm .
- By analyzing the ash residues in the clinker, it was found that the mineral produced by burning is radiographically the closest to nagelschmidtite ($Ca_3(PO_4)_2 \cdot 2(\alpha-Ca_2SiO_4)$). However, electron microanalysis has shown that the mineral has a variable composition, especially a low SiO_2 and a high alkali content. It is therefore rather an alkaline calcium phosphate with a structure close to nagelschmidtite.
- Because the migration of P_2O_5 to clinker is negligible, its entry into clinker silicates is also negligible. Thus, there is only a slight manifestation of the negative effect of P_2O_5 on clinker formation, i.e. decreasing the alite content and the increase of belite content. With total analytically determined content of 6.5 - 7 wt. % P_2O_5 in the clinker decreased the alite content by only 6 - 10 wt. %. In the case of using the scattered P_2O_5 carrier in the clinker already at 4.5 wt. % P_2O_5 completely blocks alite formation and produces a purely belitic clinker with a high free CaO content that does not enter into reaction.

These conclusions revealed the possibility of a significant multiple increase of the co-incinerated MBM in the cement rotary kiln compared to the current state. In practice, the MBM must be firstly modified by compacting, for example, by the pelletizing method or by pelletizing or granulating presses or biomass fuel production machines. So produced compacted pellets can be dosed either directly into the raw meal, or into any part of the rotary kiln, possibly also into the main burner. MBM pellets will gradually burn out, utilizing their energy potential for clinker burning, and the resulting ash residues remain in the form of inert alkaline calcium phosphate residues in clinker granules. Cements prepared from clinkers with MBM ash residues showed good technological parameters. In addition, the apatite structure contained in these cements causes immobilization of a variety of toxic elements.

5. Acknowledgement

This paper was elaborated with the Institutional support for long-term conceptual development of research organizations by the Ministry of Industry and Trade of the Czech Republic.

6. References

- [1] Scheuer A., 2003, Verwertung von Sekundärstoffen in der Zementindustrie, Cement International 1, 48–66.
- [2] Conesa J. A., Fullana A., Font R., 2003, Thermal decomposition of meat and bone meal, J. Anal. Appl. Pyrolysis 70, 619-630.

- [3] Timašev V. V., Osokin A. P., 1982, Physico-chemical bases of the structure formation and properties of clinker (in Russian), Cement 9, 4-6.
- [4] Ifka T., Palou M., Baráček J., Šoukal F., Boháč M., 2014, Evaluation of P_2O_5 distribution inside the main clinker minerals by the application of EMPA method, Cem. Concr. Res. 59, 147-154.
- [5] Goetz-Neunhoeffler F., Neubauer J., 1998, Effects of raw meal substitution by sewage sludge on OPC clinker studies by Rietveld analysis, Proc. 20th Inter. Conf. Cem. Microscopy, Guadalajara, Mexico, 130-138.
- [6] Pech M., Douillet G., 2002, Operational experience in co-incineration of animal meal in cement kilns, Proc. 5th International VDZ-Congress, Düsseldorf, 352-356.
- [7] Puntke S., 2004, Auswirkungen des Phosphateintrages in Drehofenanlagen der Zementindustrie auf Klinkermineralogie und Zementeigenschaften, Thesis (PhD), Clausthal University of Technology.
- [8] Staněk T., Sulovský P., 2009, The influence of phosphorous pentoxide on the phase composition and formation of Portland clinker, Materials Characterisation, 60, 749-755.
- [9] Lieber W., 1974, The influence of phosphates on the hydration of Portland cement, Proc. 6th ICCG, Moscow, 110, 3-13 Sept. 1974, Supplementary Paper, Section 2-6.
- [10] Nurse R.W., Welch J.H., Gutt W., 1959, High-temperature phase equilibria in the system dicalcium silicate-tricalcium phosphate, J. Chem. Soc. 34, 1077-1083.
- [11] Gutt W., 1963, High-temperature phase equilibria in the system $2CaO.SiO_2 - 3CaO.P_2O_5 - CaO$, Nature 197, 142-143.
- [12] Chromý S., 1978, Accuracy and precision of microscopic qualitative phase analysis of Portland clinker (in Czech), Silikáty 22, 215-226.
- [13] Chromý S., 1974, Anfärben des freiem CaO und Silikate in anschliffen von Portlandklinker, Zement-Kalk-Gips 27, 79-84.
- [14] Celotti G., Landi E., 2003, A misunderstood member of the nagelschmidtite family unveiled: structure of $Ca_5Na_2(PO_4)_4$ from X-ray powder diffraction data, J. Europ. Ceram. Soc. 23, 851-858.
- [15] Staněk T., Sulovský P., 2015, Mechanism of Immobilization of Toxic Elements in Special Binders, Advanced Materials Research 1124, 3-9.
- [16] Ioannidis T.A., Zouboulis A.I., 2006, Detoxification of a highly toxic lead-loaded industrial solid waste by stabilization using apatites, J. Hazard. Mat. 97, 173-191.
- [17] Gómez del Río J., Sanchez P., Morando P.J., Cicerone D.S., 2006, Retention of Cd, Zn and Co on hydroxyapatite filters, Chemosphere 64, 1015-1020.
- [18] Vega, E. D.; Pedregosa, J. C.; Narda, G. E., 1999, Interaction of oxovanadium(IV) with crystalline calcium hydroxyapatite: surface mechanism with no structural modification, J. Phys. Chem. Solids, 60, 759-766.
- [19] Duc M., Lefevre G., Fedoroff M., Jeanjean J., Rouchaud J.C., Monteil-Rivera F., Dumonceau J., Milonjic S., 2003, Sorption of selenium anionic species on apatites and iron oxides from aqueous solutions, J. Environment. Radioact. 70, 61-72.
- [20] Vega, E. D.; Pedregosa, J. C.; Narda, G. E., 2009, Adsorption of oxovanadium (IV) from aqueous

solutions by nanoparticulated hydroxyapatite, Thermodynamic and kinetic study, J. Argent. Chem. Soc. 97, 1-12.

The impact of slag fineness on the reactivity of blended cements with high-volume non-ferrous metallurgy slag

V. Hallet^{1,2}, N. De Belie², Y. Pontikes¹

¹ KU Leuven, Department of Materials Engineering, Kasteelpark Arenberg 44, 3001 Leuven, Belgium

² Magnel Laboratory for Concrete Research, Department of structural engineering, Ghent University, Tech Lane Ghent Science Park, Campus A, Technologiepark Zwijnaarde 60, B-9052 Ghent, Belgium

Abstract

Non-ferrous metallurgy slags, when highly amorphous, have shown to behave as supplementary cementitious materials, albeit typically with low reactivity. Due to this feature, high-volume replacement of ordinary Portland cement (OPC) with non-ferrous metallurgy slag is not encouraged. A classical method of increasing slag reactivity is by increasing the fineness of the slag, and this was investigated in the present work. To do so, a non-ferrous metallurgy slag was milled to specific surface areas of 4500 cm²/g and 6500 cm²/g, as determined by the Blaine permeability method. The influence of the fineness on the slag reactivity was investigated using the RILEM R3 isothermal calorimetry procedure. Results demonstrated that the reactivity of these slags is similar to that observed for siliceous fly ashes and increases with slag fineness. Moreover, isothermal calorimetry on blends of OPC with 30, 50 and 70 wt% slag of both finenesses was conducted to investigate the reaction kinetics, and a retarding effect of the slag on the Portland clinker hydration was observed. Finally, compressive strength was tested at 2, 7 and 28 days and compared with the calorimetric results and with thermogravimetric analysis at 28 days. At late ages, the increased reactivity for higher slag fineness led to more hydration products and consequently higher compressive strengths. However, at early ages, the strength remained low and increased slag fineness did not yield significant compressive strength enhancement; early strength enhancement likely requires different activation methods.

Keywords: non-ferrous metallurgy slag, fineness, reactivity, supplementary cementitious material

1. Introduction

Non-ferrous metallurgy (NFM) slags may be suitable supplementary cementitious materials (SCMs) from a strength-perspective, as they have been shown to contribute to the compressive strength of blended cements when highly amorphous [1]. However, in contrast to the generally used blast furnace slags of ferrous metallurgy, these non-ferrous metallurgy slags have higher iron contents and lower calcium contents [2] thereby decreasing the reactivity and dissolution rate [3]. Consequently, the NFM slag volumes that can be incorporated in blended cements are usually limited [4].

A typical method of increasing the reactivity of a SCM is by fine grinding in order to increase the specific surface area. For example Kiattikomol et al. [5] investigated the influence of the fineness on the reactivity of a range of fly ashes and reported increased strengths both at early (3 days) and late (90 days) ages for increased fineness. Studies on iron-rich NFM slags have been less extensive, but for example Benkendorff

[6] reported that compressive strengths may also increase by increasing the fineness of a lead/zinc slag, similar in composition to the slag used in this work.

As it is known that the specific surface area of SCMs can have a major impact on the reaction kinetics [7, 8], the reaction kinetics of OPC blended with NFM slags were investigated using isothermal calorimetry. Afterwards a reactivity test was used in order to determine the increase of the reactivity of the slag with increasing fineness. Recently a wide variety of reactivity tests was compared by the RILEM TC 267-TRM [9], and the R³ (rapid, relevant and reliable) isothermal calorimetry test [10] was determined to most closely correlate to the mortar compressive strength. Additionally, the technical committee reported values obtained by this test for classical SCMs such as fly ashes and blast furnace slags of ferrous metallurgy. Furthermore, Snellings et al. have recently also reported values for other non-ferrous metallurgical residues [11]. This allows to rank the NFM slag used in this work with respect to other classical or possibly future SCMs. Consequently, this R³ isothermal calorimetry test was used as a reactivity test to investigate the influence of the NFM slag fineness on its reactivity. Finally, compressive mortar strengths were obtained and compared with the isothermal calorimetry results as well as correlated with the amount of bound water and Ca(OH)₂ in order to explain the observed behaviour.

2. Methodology

2.1 Materials

NFM slag was obtained from a pilot installation after high-temperature treatment and granulation, yielding a highly amorphous slag with a composition and phase assemblage as shown in table 1, obtained from X-ray fluorescence spectroscopy (XRF; S8 TIGER, Bruker) and X-ray powder diffraction (D2 Phaser, Bruker) respectively. Additionally, a synthetic slag was used, the composition of which as determined by XRF is shown in table 2. The OPC used in this work was a CEM I 52.5N type with a specific surface area of 3478 (±18) cm²/g, as determined by the Blaine permeability method (EN196-6 [12]). All the chemicals used to prepare the R³ mixtures, i.e. KOH, K₂SO₄, Ca(OH)₂ and CaCO₃, were analytical grade chemicals.

Table 1: Chemical composition and phase assemblage, both in wt% of the NFM slag.

Elements	Composition	Phases	Chemical formula	Phase content
FeO	35-45	Wüstite	FeO	8
SiO ₂	25-30	Spinel	(Mg, Fe)(Al, Fe) ₂ O ₄	11
CaO	15-20	Quartz	SiO ₂	<1
Al ₂ O ₃	3-6	Undetected/ Amorphous	/	80
MgO	1-2			
Other	7-12			

Table 2: Chemical composition of the synthetic clean slag.

Elements	Composition (wt%)
FeO	49.9
SiO ₂	25.4
CaO	19.3
Al ₂ O ₃	4.8
Other	0.6

2.2 Methods

The slag was milled to specific surface areas of 4533 (±28) cm²/g and 6491 (±49) cm²/g, as determined by the Blaine permeability method (EN 196-6 [12]), using high-intensity milling in an stirred ball mill. The slags are thus coded as “Bl 4500” and “Bl 6500” for the least and most fine slag, respectively. The resulting

particle size distribution (Fig. 1) of the raw materials was also measured using laser diffraction (LS 13 320, Beckman Coulter) on dry powders, using $n = 1.73$ and $k = 0.1$ as optical parameters for both the cement and the slag. This yields a d_{50} of $11.79 \mu\text{m}$, $9.17 \mu\text{m}$ and $4.70 \mu\text{m}$ for OPC, BI 4500 and BI 6500, respectively.

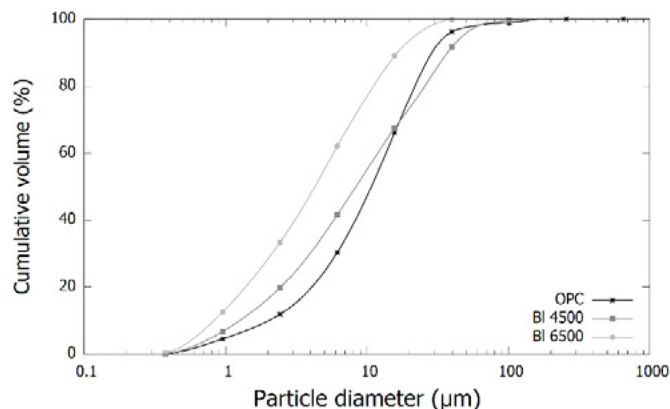


Figure 1: Cumulative particle size distribution of the raw materials.

In addition to a reference pure cement paste, blended cement pastes were prepared by replacing OPC with 30, 50 and 70 wt% of slag with both finenesses and mixing with water to obtain a liquid/solid (L/S) mass ratio of 0.4. These pastes were investigated using isothermal calorimetry (TAM Air, TA instruments) at 20°C for 7 days in order to record the reaction heat during hydration. The heat flow and cumulative heat of hydration of the blends is reported from 1 hour after mixing to avoid taking into account the influence of introduction of the ampoules to the channels. It should be noted that this also means that the initial heat due to wetting and dissolution is not taken into account and not discussed in the results. Isothermal calorimetry was also used in the R^3 isothermal calorimetry reactivity test, which was conducted on model mixes as described in [9]. In this reactivity test, a solid mix is prepared as 22.22 wt% slag (as SCM), 66.66 wt% $\text{Ca}(\text{OH})_2$ and 11.12 wt% CaCO_3 . This solid is mixed in a L/S mass ratio of 1.23 with a simulated pore solution composed of 97.66 wt% H_2O , 0.39 wt% KOH and 1.95 wt% K_2SO_4 . The materials were kept at 40°C prior mixing, and 15 g of the paste was subsequently used for isothermal calorimetry measurements at the same temperature (40°C).

Furthermore, blended cement pastes were hydrated for 28 days and then investigated using thermogravimetric analysis (TGA; TGA/SDTA851, Mettler Toledo) on samples where the hydration was stopped by solvent exchange on crushed pastes. This solvent exchange was done by immersion (30 sec stirred, 5 min unstirred) in isopropanol (2x) and diethyl ether (1x) followed by drying for 8 min in at 40°C . The latter was conducted from 30°C to 980°C in inert atmosphere (100 ml/min N_2) with a heating rate of $10^\circ\text{C}/\text{min}$. The amount of bound water is calculated from the weight loss between the initial weight and the weight at 550°C , which assumes all isopropanol or diethylether was removed in the drying step of the solvent exchange. The $\text{Ca}(\text{OH})_2$ content in the paste was determined using the tangential method.

Finally, mortars with 30, 50 and 70 wt% slag of either fineness in the solid binder were prepared and tested in compressive strength as described in EN196-1 [13], although with a L/S mass ratio of 0.4.

3. Results and discussion

The effect of the slag content on the heat flow during early hydration (Fig. 2a) shows a clear decrease of the main hydration peak with increasing slag content. Considering that this peak is typically attributed to the dissolution of C_3S and the formation of C-S-H, this decrease can be explained in part by the decreased OPC content. At later ages (20-25h) there is a shoulder which can be attributed to the renewed dissolution of C_3A [14]. With increasing slag content, there appears to be enhancement of this shoulder. Presently the

exact cause for this enhancement is not fully clear. A closer investigation on quartz blended systems by Berodier [8] reported enhancement even though the quartz is considered to behave as an inert filler and related the enhancement to rapid C_3A dissolution as a consequence of lower sulphate presence in the pore solution, which would inhibit that dissolution. As in the blended system in this work no additional sulphate source was added, this may be a possible cause as well. Moreover, Quennoz and Scrivener [15] proposed that the acceleration rate of the peak of C_3A reaction is related to the available C_3A surface for dissolution. Hence the lower amount of reaction products formed at these early ages with decreasing OPC content may lead to higher availability of the C_3A surface for dissolution and thus increase the dissolution rate as well. At even later times ($>40h$) there is another broad shoulder, more clearly seen after normalizing the heat flow to the OPC content (Fig. 3a), which is likely related to AFm formation [16].

Finally, after several days the slag starts reacting, yielding increased heat flows for 30 and 50 wt% replacement of OPC with respect to pure OPC hydration, shown in Fig. 2a at the end of the measurement (150-168h). While the replacement of OPC by 70 wt% slag does not lead to a heat flow increase per gram solid at these ages, the heat flow normalized to the OPC content is higher, showing also slag reaction in this mix. Despite the extra heat flow from the slag reaction, the cumulative heat after 7 days (Fig. 2b) clearly decreases with increasing slag content, as the slag reaction does not make up for the decreased OPC content at early ages.

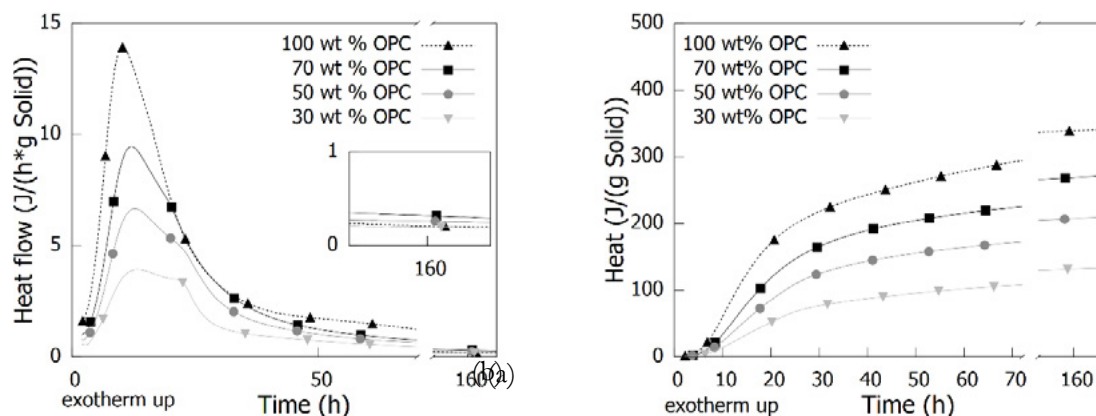


Figure 2: Heat flow (a) and cumulative heat release (b) per gram solid during hydration of OPC blended with non-ferrous metallurgy slag (low fineness, Bl 4500). The insert in (a) shows a zoomed in view of the heat flow at later times.

The comparison of the heat flow normalized to the OPC content is presented in Fig. 3a for the blended cements with the highest amount of slag (70 wt% slag, 30 wt% OPC) as the differences are most pronounced there and similar to the effects seen at other replacement levels. The replacement of OPC by NFM slag leads to a delay in the onset of the reaction from 3.75 h for OPC to 4.12 h for a 30-70 OPC-slag (low fineness) blend. Moreover, with increased fineness, the onset of reaction increases further to 4.62 h. The onset of reaction is defined here similarly to Schöler et al. [7] as the intersection of the horizontal line through the minimum of the induction period and the best fit through the inflection point of acceleration of the main hydration peak. In addition to the retardation of the onset of hydration, the acceleration rate and the maximum heat release of the main hydration peak decreases with increasing slag content and fineness.

The NFM slag used in this work contains 7-12 wt% of various residual elements, among which are several elements which are known to retard cement hydration, even in small quantities, such as Zn [17]. If these elements would leach out of the slag in the early hydration period they might cause the retarding effect of the slag. Therefore a clean slag, i.e. without any residual metals (“clean”), and with similar composition than the original slag (Table 2) was blended with OPC in a 30-70 wt% OPC-slag ratio and the heat flow during hydration was measured (Fig. 4). The clean slag shows a similar behaviour to the original slag (Bl 4500) and

it can be concluded that the residual elements in the original slag are most likely not the (main) cause of the retarding effect of the slag. It should be noted that the clean slag had a slightly lower specific surface area ($\pm 4000 \text{ cm}^2/\text{g}$) which likely accounts for the slightly decreased retardation when using this slag, though a small part may still be caused by the lack of residual elements. Considering this result, other effects are most likely causing the retardation. In fly ashes a similar retarding effect is sometimes observed [7, 18] and authors have explained this by different effects. Fajun et al. [18] reported decreased Ca^{2+} contents in the pore solution and suggested that the fly ash surface acts as a Ca^{2+} sink by chemisorption. In addition, Schöler et al. [7] recently found increased aluminium levels in the pore solution of fly ash-containing blended cements and attributed the retardation to the hindering effect of aluminium on C_3S dissolution [19] and C-S-H nucleation. Considering the similarity in behaviour of these NFM slags with that in the aforementioned literature for fly ashes, it is likely that the cause is similar in these blends.

The increase in fineness also appears to decrease the enhancement of the shoulder due to renewed C_3A dissolution in the 20-25 h region, discussed before. Since the slag contains around 0.5 wt% SO_3 , this decreased enhancement may be explained by higher release of sulphates from the slag due to the higher surface area, thereby slightly increasing inhibition of C_3A dissolution.

Finally, the heat release normalized to the OPC content increases by addition of the slag as well as by increasing the fineness of the slag. The former shows the reactivity of the slag, while the latter indicates the expected reactivity enhancement due to the fineness increase.

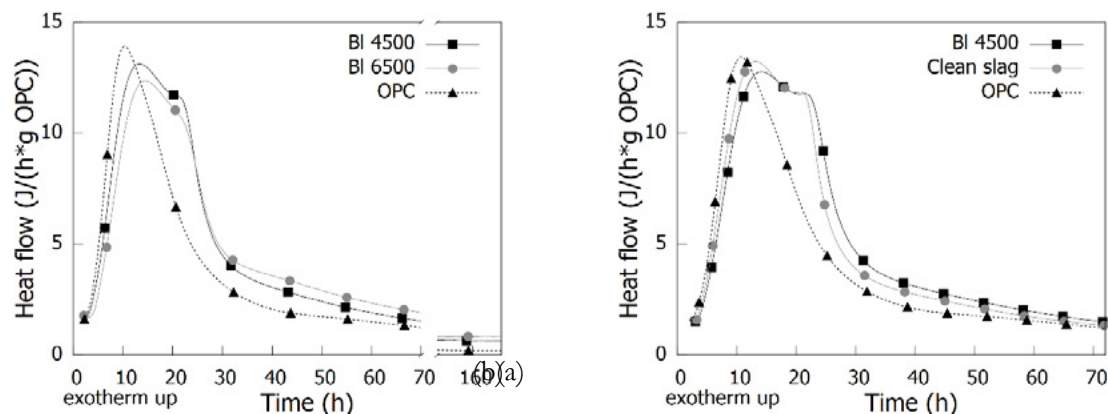


Figure 3: Heat flow per gram OPC comparison of blends with 30 wt% OPC and 70 wt% slag with (a) different fineness or (b) with and without (“clean”) trace elements.

Due to the increase of the retarding effect of the slag with increasing slag fineness, the cumulative heat released (Fig. 4a) by OPC replacement with fine slag is lower until the paste has hydrated for 3 days. However, afterwards, the inherent slag reactivity increase with higher fineness leads to higher cumulative heat release, increasing so with higher slag content.

At the lowest slag content (30 wt%), the cumulative heat is statistically the same for both finenesses though the difference is expected to grow at later ages. The inherent slag reactivity was confirmed by the R^3 calorimetry test (fig 4b), where the finer slag (BI 6500) showed higher cumulative heat release, both after 3 and 7 days as the effect of the slag on C_3S and C_3A hydration is neglected in this model system which does not contain OPC. Comparison of the values obtained in the R^3 reactivity test (table 3) with literature values for classical SCMs [9] shows that the values most closely resemble those obtained for siliceous fly ashes.

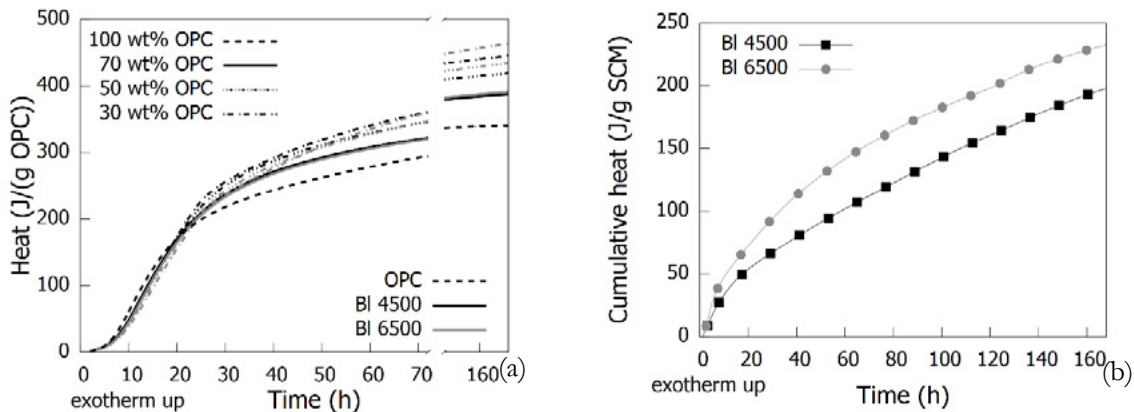


Figure 4: Cumulative heat released in the first 7 days (a) per gram OPC in the blended cement pastes and (b) per gram SCM from the R³ pastes.

Table 3: Cumulative heat of the R³ model systems comprising slag of different fineness and comparison with literature data of fly ashes.

SCM	SCM fineness (cm ² /g)	Cumulative heat after 3 days (J/g SCM)	Cumulative heat after 7 days (J/g SCM)
NFM Slag	4500	114	197
	6500	156	232
Fly Ash 1 ([9], "SFA I")	4420	81.6	162.5
Fly Ash 2 ([9] "SFA E")	6910	119.6	214.1

Compressive strengths and strength activity indices (SAI)¹ of mortars are presented in Figure 5. It is clear that the strength increases with time and OPC content. After 28 days compressive strengths of the blended cements with medium to low slag content (50 wt% or less) reach SAIs higher than the OPC content, indicating contribution of the slag to the strength, as expected from the calorimetry results and R³ reactivity tests.

Moreover, there is a clear effect of the fineness at later ages (> 7 days), which is more distinct for a slag content of 50 wt%. In fact, by increasing the slag fineness from 4500 to 6500 cm²/g allows an increase of the slag content from 30 wt% to 50 wt% while keeping the strength approximately equal, making the slag fineness a suitable tool to tailor the late age strength.

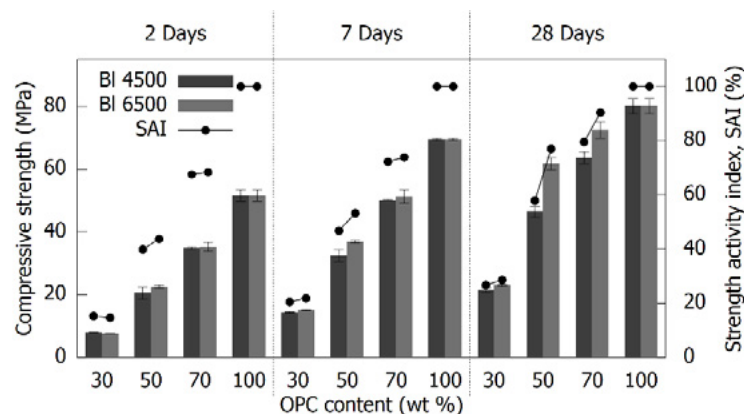


Figure 5: Compressive strength and strength activity indices (SAI) of mortars. Error bars indicate the standard deviation.

1 Strength activity index, SAI = $\frac{Str_{blended\ cement}}{Str_{reference\ OPC}}$ at each hydration time.

However, at early ages (2 days) there is no significant strength increase due to increased slag fineness. At high slag content, the strength may even decrease slightly. This can be linked to the calorimetry results, where the cumulative heat for this blend is lower for a finer slag until after 3 days of hydration. In general, the lack of strength increase at early age is most likely related to the lack of reaction of the slag at these ages in combination with the retarding effect of the slag on the hydration of the cement phases.

Using TGA the amount of $\text{Ca}(\text{OH})_2$ and bound water after 28 days can be determined, where the former is important for the pozzolanic reaction while the latter gives an indication of the amount of hydrated phases that are present in the binder. After normalization of the $\text{Ca}(\text{OH})_2$ and bound water content to the OPC content (fig 6a), the effect of the slag can be more closely investigated. With increasing slag content, the amount of bound water normalized to OPC increases, as reported before [1], showing the contribution of the slag to the hydration products. Moreover, increasing the fineness also increases the amount of bound water, indicating enhanced formation of hydration products which explains the increased strengths after 28 days. However, for high slag contents (70 wt% slag) the increase in bound water content is similar to the blends with 50 wt% slag, while the strength increase is much lower.

Hence for these blended cements with high slag content there may be some phases forming that don't contribute as much to space-filling and strength while still taking up water. The $\text{Ca}(\text{OH})_2$ content normalized to OPC stays relatively constant, with a slight decrease for blends with high contents of fine (BI 6500) slag, most likely due to the higher slag reactivity which consumes more $\text{Ca}(\text{OH})_2$ in the pozzolanic reactions.

Correlating the bound water content and $\text{Ca}(\text{OH})_2$ content with the compressive strength (fig 6b) reveals that the former correlates well while the correlation with the latter is much worse, due to consumption of $\text{Ca}(\text{OH})_2$ in the (strength-enhancing) pozzolanic reactions. Since the $\text{Ca}(\text{OH})_2$ is not expected to give significant contribution to strength and is being consumed in the pozzolanic reactions, the correlation of the bound water with the strength improves further by subtracting the water bound in $\text{Ca}(\text{OH})_2$ in the cement paste.

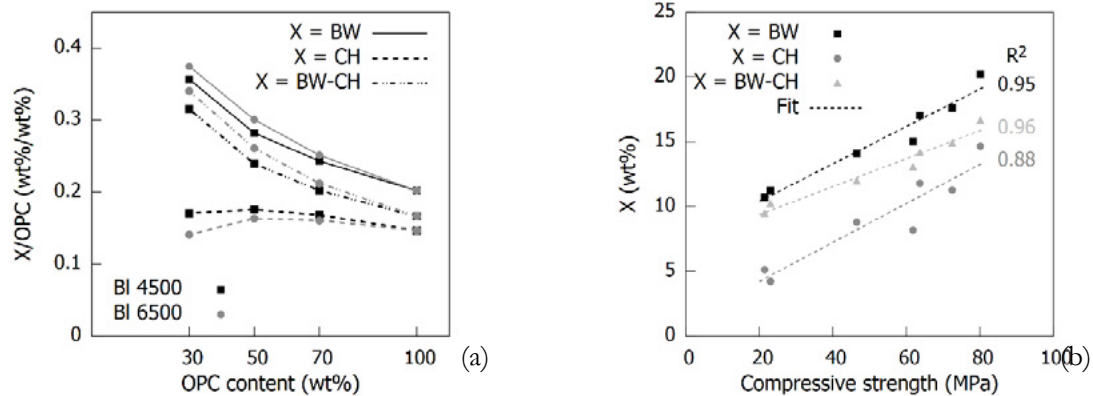


Figure 6: (a) Bound water and $\text{Ca}(\text{OH})_2$ content at 28 d, normalized to the OPC content. The estimated relative error is 10% . (b) Correlation of the bound water content or $\text{Ca}(\text{OH})_2$ content with the compressive strength. Error bars are not shown for clarity. In both figures: BW = bound water content, CH = $\text{Ca}(\text{OH})_2$ content and BW-CH = bound water content excluding water from $\text{Ca}(\text{OH})_2$.

4. Conclusions

The heat of hydration of OPC blended with non-ferrous metallurgy slag and the influence of the specific surface area of the slag on the reactivity in these systems was investigated. Heat release of blended cement pastes at early ages revealed decreasing reaction heat with increasing slag content. Additionally a retarding effect of the slag on the hydration of the cement phases was observed which could not be explained by the trace elements in the slag.

The R³ isothermal calorimetry reactivity test showed that the slag was similar in reactivity to siliceous fly ashes and that increasing the fineness yields a more reactive slag. However due to the retarding effect of the slag and limited slag reaction at early age, the early strength did not significantly improve by increasing the slag fineness. In contrast, at later ages compressive strength did increase with slag fineness due to increased formation of hydration products.

Therefore enhancement of the early age strength should be an important aim in further research. Additionally, further clarification of the cement retarding effect of the slag might be obtained by investigating the pore solution of the blended cements at early ages.

5. Acknowledgment

V. Hallet would like to thank Flanders Innovation & Entrepreneurship (VLAIO) for the doctoral fellowship funding. The authors would also like to thank J.J. Van De Sande and R. Murillo Alarcón for the production of the synthetic clean slag used in this work.

6. References

- [1] V. Hallet, T. Hertel, N. De Belie, Y. Pontikes, (2019) “High-volume OPC replacement by iron-rich non-ferrous metallurgy slag”, in: Proceedings of the 6th international Slag Valorisation Symposium, Edited by A. Malfiet, A. Peys, A. Di Maria. 101-104.
- [2] N.A. Piatak, M.B. Parsons, R.R. Seal II, (2015) “Characteristics and environmental aspects of slag: A review”, *Applied Geochemistry*, 57, 236-266, doi: j.apgeochem.2014.04.009 .
- [3] A. Paul, A. Youssefi, (1978) “Alkaline durability of some silicate glasses containing CaO, FeO and MnO”, *Journal of Materials Science*, 13, 97-107, doi: 10.1007/BF00739279 .
- [4] M.A. Rahman, P.K. Sarker, F.U.A. Shaikh, A.K. Saha, (2017) “Soundness and compressive strength of Portland cement blended with ground granulated ferronickel slag”, *Construction and Building Materials*, 140, 194-202, doi: j.conbuildmat.2017.02.023 .
- [5] K. Kiattikomol, C. Jatarapitakkul, S. Songpiriyakij, S. Chutubtim, (2001) “A study of ground coarse fly ashes with different finenesses from various sources as pozzolanic materials”, *Cement and Concrete Composites*, 23, 335-343, doi: 10.1016/S0958-9465(01)00016-6 .
- [6] P.N. Benkendorff, (2006) “Potential of lead/zinc slag for use in cemented mine backfill”, *Mineral Processing and Extractive Metallurgy*, 115, 171-173, doi: 10.1179/174328506X109149 .
- [7] A. Schöler, B. Lothenbach, F. Winnefeld, M. Ben Haha, M. Zajac, H. Ludwig, (2017) “Early hydration of SCM-blended Portland cements: A pore solution and isothermal calorimetry study”, *Cement and Concrete Research*, 93, 71-82, doi: 10.1016/j.cemconres.2016.11.013 .
- [8] E.M.J. Berodier, (2015) “Impact of the Supplementary Cementitious Materials on the kinetics and microstructural development of cement hydration” (Doctoral Dissertation)
- [9] X. Li, R. Snellings, M. Antoni, N. Mariel Alderete, M. Ben Haha, S. Bishnoi, Ö. Cizer, M. Cyr, K. De Weerd, Y. Dhandapani, J. Duchesne, J. Haufe, D. Hooton, M. Juenger, S. Kamali-Bernard, S. Kramar, M. Marroccoli, A. Mary Joseph, A. Parashar, C. Patapy, J. L. Provis, S. Sabio, M. Santhanam, L. Steger, T. Sui, A. Telesca, A. Vollpracht, F. Vargas, B. Walkley, F. Winnefeld, G. Ye, M. Zajac, S. Zhang, K. L. Scrivener (2018), “Reactivity tests for supplementary cementitious materials: RILEM TC 267-TRM phase 1”, *Materials and Structures*, 51, 151, doi: <https://doi.org/10.1617/s11527-018-1269-x> .
- [10] F. Avet, R. Snellings, A.A. Diaz, M. Ben Haha, K. Scrivener, (2016) “Development of a new rapid, relevant and reliable (R³) test method to evaluate the pozzolanic reactivity of calcined kaolinitic clays”, *Cement and Concrete Research*, 85, 1-11, doi: 10.1016/j.cemconres.2016.02.015 .
- [11] R. Snellings, H. Kamyab, (2019) “Reactivity of non-ferrous metallurgical slags and sludges measured by the RILEM R3 test”, in: Proceedings of the 6th international Slag Valorisation Symposium, Edited by A. Malfiet, A. Peys, A. Di Maria. 357-360.
- [12] “Methods of testing cement - Part 6: Determination of fineness,” European Committee for Standardisation (CEN), Brussels, Belgium, EN 196-6:2018 (2018).
- [13] “Methods of testing cement - Part 1: Determination of strength,” European Committee for Standardisation (CEN), Brussels, Belgium, EN 196-1:2005 (2005).
- [14] C. Hesse, F. Goetz-Neunhoeffler, J. Neubauer, (2011) “A new approach in quantitative in-situ XRD of cement pastes: Correlation of heat flow curves with early hydration reactions”, *Cement and Concrete*

Research, 41, 123-128, doi:10.1016/j.cemconres.2010.09.014 .

[15] A. Quennoz and K.L. Scrivener, (2012) “Hydration of C3A-gypsum systems”, Cement and Concrete Research, 42, 1032-1041, doi:10.1016/j.cemconres.2012.04.005 .

[16] A. Quennoz and K.L. Scrivener, (2013) “Interactions between alite and C3A-gypsum hydrations in model cements”, Cement and Concrete Research, 44, 46-54, doi: 10.1016/j.cemconres.2012.10.018 .

[17] M. Gawlicki, D. Czamarska, (1992) “Effect of ZnO on the hydration of Portland cement”, Journal of Thermal Analysis, 38, 2157-2161, doi: 10.1007/BF01979629 .

[18] W. Fajun, M.W. Grutzbeck, D.M. Roy, (1985) “The retarding effects of fly ash upon the hydration of cement pastes: The first 24 hours”, Cement and Concrete Research, 15, 174-184, doi: 10.1016/0008-8846(85)90024-9 .

[19] L. Nicoleau, E. Schreiner, A. Nonat, (2014) “Ion-specific effects influencing the dissolution of tricalcium silicate”, Cement and Concrete Research, 59, 118-138, doi: 10.1016/j.cemconres.2014.02.006

Characteristics of mechanically activated converter steel slag

Winnie Franco Santos¹, Katrin Schollbach², Qingliang Yu¹, Sieger van der Laan^{1,2}, H.J.H.Brouwers¹

¹Department of the Built Environment, Eindhoven University of Technology, P.O. Box 513, 5600 MB Eindhoven, the Netherlands

²Tata Steel, R&D, Microstructure & Surface Characterization (MSC), P.O. Box 10.000, 1970 CA IJmuiden, the Netherlands.

Abstract

Converter steel slag is a by-product of the steelmaking. It presents latent hydraulic properties due to the presence of cement phases such as C_2S . Literature has reported that converter steel slag has no or negligible reactivity with a heat release of around 20 J/g with the calorimeter in the first days. This work aims to assess the effect of mechanical activation to decrease particle size and introduce lattice defects, on the cementitious property of converter steel slag. The results show that hydration occurs even without a chemical activator and that it can be increased further through progressive grinding. The converter steel slag was ground in four different series. Prolonged milling resulted in a decrease of particle size and increase of the amorphous content. The calorimetric analysis of slags mixed with water indicated the occurrence of exothermic reactions and the maximum released heat was 75 J/g for the slag with an average particle size (d_{50}) of 21 μm .

Keywords: converter steel slag; mechanical activation, reactivity, mineralogy.

1. Introduction

The growing demand for materials by the building industry leads to intense exploitation of natural resources and a high consumption of energy. Therefore, the need to develop potential alternative materials and innovative techniques is required. By-products from other industrial manufacturing processes, like ground granulated blast-furnace slags and fly ash, are already used as sustainable alternatives to Portland cement. Another by-product is converter steel slag, also referred to as basic oxygen furnace (BOF) slag, of steel production (ca. 100 kg/ton of steel) [1,2]. It is generated during the purification of pig iron when burned lime and dolomite are added in the process to react with the impurities. From this reaction, a silicate melt is resulted, containing CaO , SiO_2 , Fe_2O_3 , FeO , MgO , Al_2O_3 , MnO . Some other minor components such as P_2O_5 , TiO_2 , and V_2O_5 can also be present [3][7]. Despite the high variability of the chemical composition of steel slag the mineral composition is very constant and consists of potentially hydraulic phases such as polymorphs of dicalcium silicate Ca_2SiO_4 (C_2S) and other major phases as Wuestite, Mg Wuestite (FeO) and Srebrodolskite ($CaFeO$) [5].

Although steel slag has been used as coarse or fine aggregate in concrete and backfill materials, these applications can cause expansion problems related to the volume instability when a high amount of free lime ($f-CaO$) is present in the steel slag [3,6]. Nevertheless, posttreatment of the steel slag can contribute to controlling the volume stability and potentially valorising it as a hydraulic binder.

Steel slag presents latent hydraulic properties and low hydration rate when compared to conventional Portland cement, nevertheless this can be enhanced by increasing the specific surface area (SSA) of slag through mechanical activation (MA) [7–10]. The reactivity of slags has been found to depend on the source

of slag, the type of raw materials used, method and the rate of cooling [11].

The reactivity of the slag also depends on the comminution process[6] to mechanically activate the slag. The portion of small particles is expected to increase as the grinding time increases. The long grinding time experienced by some researchers for steel slag in comparison to cement clinkers can be explained by a high metallic iron content [8].

Wang et al.[12] observed that the hydration rate of steel slag increases as the (SSA) increases and the hydrating degree of steel slag becomes similar for all particle sizes at the curing age of 180 days. The early hydration reaction can become faster and can produce more hydration products. Kriskova et al. [13] also reported that the amount of heat released increased with milling time, but indicated that surface area is not the only factor influencing reactivity. There can be structural changes in the crystal lattice as well that also promote hydration. However, mechanical activation of converter steel slag is still poorly understood, because many studies pay little attention to the mineralogy of the slag. For that reason, it is important to consider and continue the investigation of the mechanical activation of steel slag through mineralogical characterization.

The present study provides an evaluation of the influence of the mechanical activation (MA) on converter steel slag using physical and chemical characterization with X-ray fluorescence analysis (XRF) and X-ray diffraction (XRD) and addresses the reactivity and influence of amorphization on phases of converter steel slag. With the MA of the slag particles, we aim to enhance the properties so it can work in applications as an alternative binder.

2. Methodology

2.1 Materials

The employed converter steel slag (CSS) used was provided by Tata Steel (IJmuiden, The Netherlands). A representative fraction of 1-2mm granulate was provided for our experiments. In this study improvement by mechanical activation (MA) was attempted for the material and different particle sizes were compared. The analysis of the reactivity was performed on the MA slag.

2.2 Methods

Mechanical activation was performed using a Retsch RS 300 XL disc mill at a constant speed of 912 min⁻¹. To determine the effect of milling time on powder fineness six treatment periods were selected (5, 9, 13 and 15 min) for every single batch of 1kg for a grinding jar volume of 2,000ml. For this procedure, there were no pauses during the milling. The particle size distribution was obtained by laser diffraction technique using a Mastersizer 2000 from Malvern with the sample dispersed in isopropanol. The elemental composition of converter slag was determined by X-ray fluorescence analysis (XRF) expressed as a percentage of oxides. The analysis was performed applying a XRF spectrometer from PANalytical (Epsilon 3 range, standardless OMNIAN method), on fused beads. The loss of ignition was evaluated by heating the sample to 1100°C for 1 hour and measuring the mass change. The morphology of the particles was determined by Scanning Electron Microscopy (SEM) measurements using a JEOL JSM-7001F SEM equipped with two 30mm² SDD detectors (Thermo Fisher Scientific) and NORAN – System7 hardware with NSS.3.3 software. The SEM accelerating voltage was 15kV, the beam current 6.2nA and the step size of the measurement used for Spectral Imaging was 1 µm. The sample was prepared by mounting it in epoxy (Struers EpoFix) and polished to a flat surface without the use of water. It was then coated with about 10 nm of carbon. In order to investigate the mineralogy before and after milling the crystalline phases were identified using a Bruker D2 X-ray diffractometer (XRD), Co radiation, step size 0.02, fixed divergence slits. The patterns were identified with the Bruker software Plus-EVA and quantified with Bruker software Topas by the Rietveld

method. For this purpose 10wt.% of crystalline Si was added to the samples and homogenized with the XRD mill McCrone Retsch grinding for 1 minute on speed level 1. The determination of the influence of the different particle sizes on CSS hydration was investigated by monitoring the reactivity by a Tam Air isothermal calorimeter (TA Instruments) at 20°C for 48h, as after this period the heat flow measurements show constant values. This period was chosen due to the rapid reaction of the steel slag. Water to binder ratio (w/b) of 0.4 was used for the milled material in the calorimeter tests.

3. Results and discussion

3.1 Chemical composition and physical characteristics of the materials

The chemical composition of the converter steel slag is given in Table 1. As expected, it is mainly composed of CaO, Fe₂O₃, SiO₂, and MgO, while TiO₂, V₂O₅, Cr₂O₃, ZrO₂ are also present as minor constituents. The contents of Fe₂O₃ and MgO are significantly higher than those in Portland cement, while the content of CaO is lower. When converter steel slag is heated in air to 950°C for loss of ignition determination a mass gain is induced due to the oxidation of metallic or divalent iron, or manganese.

Table 1- Chemical composition of converter steel slag investigated measured by X-ray Fluorescence.

Converter Slag	MgO	Al ₂ O ₃	SiO ₂	P ₂ O ₅	CaO	TiO ₂	V ₂ O ₅	Cr ₂ O ₃	MnO	Fe ₂ O ₃	ZrO ₂	LOI
wt. %	8.1	3.3	12.2	1.4	37.8	1.4	1.1	0.3	4.3	28.5	0.1	-1.6

Powder X-ray diffraction (XRD) shows that the crystalline phases present in the converter steel slag are Brownmillerite, C₂S-α, and C₂S-β, Mg, Fe-wuestite and Magnetite, as shown in Figure 1.

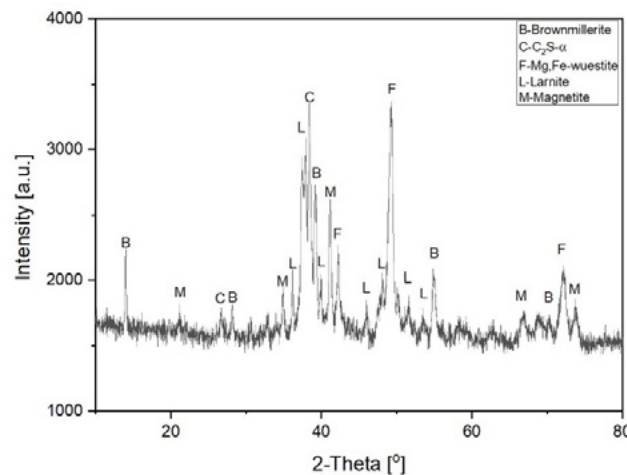


Figure 1 XRD Pattern of CSS.

3.2 Particle size distribution (PSD)

In order to choose an optimum particle size that would result in the highest heat flow of hydration, and to investigate if milling the material would affect the mineral phases, tests were carried out by changing the milling time. Figure 2 shows the variation of particle size distribution.

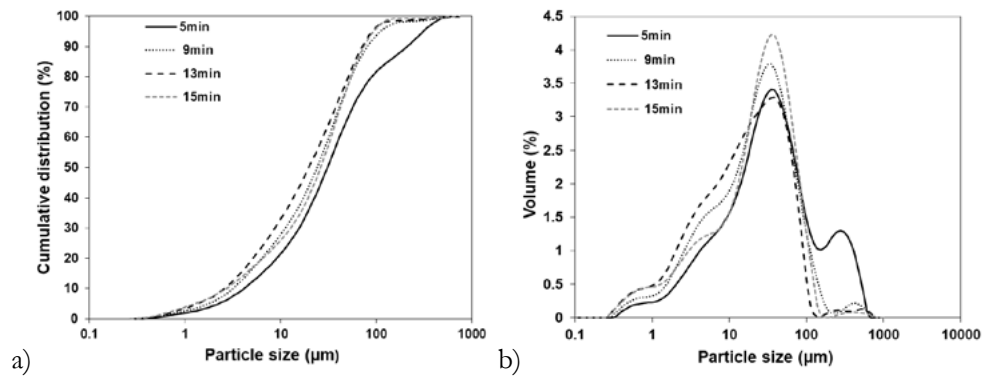


Figure 2- a) cumulative particle size distribution and b) particle size distribution of Converter Steel Slag milled in different stages with the DM.

Figure 2 shows the reduction of the particle size is related to the milling time. In Figure 2-a large shift can be seen from stage 5 min to stage 9 min. After that stage, the shift between the other stages is moderate. From Figure 2-b one can notice that starting from 5 min, there is a prominent shoulder between 5 and 9 min indicating the reduction of the present coarser particles considerably (100-1000μm) in the second stage (9min). Table 2 presents the median particle sizes of the material after each milling stage. From 9 minutes until 15 minutes there is a continuous increase in fines. At 15min, the diameter increases (21μm) because fines begin to form agglomerates bonding to larger particles by weak van der Waals forces. This effect was also observed by Caprai et al. and Chauruka et al. [14,15] when using different materials in a ball mill. Further milling was not carried out as the compaction of the agglomerates can decrease the effectiveness of the mill.

3.3 Particle Morphology of Milled CSS

The SEM images in Figure 2 show the morphological features of the CSS after 5 minutes and 15 minutes milling. The particles retained their angular shape and sharp edges after 5 minutes but after 15 minutes in the disc mill, the agglomeration of fines bonded with larger particles can be observed. As perceived in the particle size distribution (Figure 2), an optimum milling stage was reached.

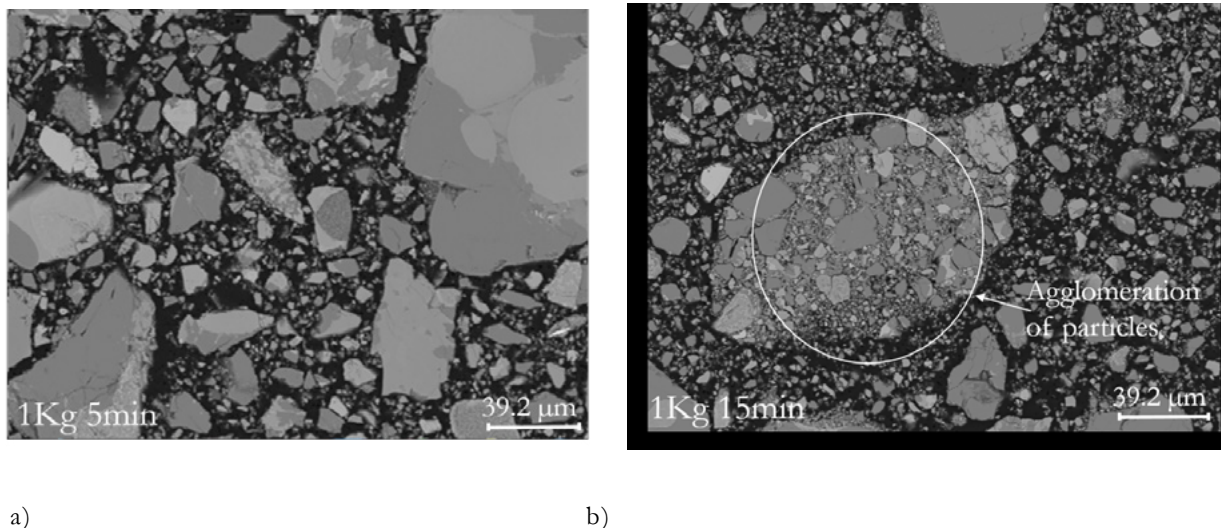


Figure 3: Particles morphology of converter steel slag milled in a disk mill (DM) after a) 5 minutes and b) 15 minutes

3.3 The influence of the mechanical activation on properties of converter steel slag

3.3.1 Amorphization of the particles

To quantify the mineralogical composition of the CSS as received, the material was reduced to a diameter of 48 μ m to compare with the stage 15 min. Before the XRD measurement, both samples were milled in a McCrone Micronizer mill to ensure equal particle size obtained by gentle milling to not influence the XRD results. The Rietveld quantification is presented in Table 3. Based on the quantitative data, the amount of C₂S- α , C₂S- β , and Mg, Fe-wuestite decreases, while the amorphous content increases after milling 15 min with the disk mill.

Table 3 Mineral composition of CSS before and after MA treatment (15min) based on Rietveld analysis, in wt. %.

Mineralogical Composition	Chemical Compound	CSS 48 μ m	St. Dev.	15 min	St. Dev.
Brownmillerite	Ca ₂ (Al,Fe) ₂ O ₅	15.5	0.6	16.4	0.5
C ₂ S- α	Ca ₂ SiO ₄	11.2	0.6	8.1	0.5
Mg,Fe-wuestite	(Mg, Fe)O	19.8	3.2	15.5	3.3
Larnite C ₂ S- β	Ca ₂ SiO ₄	17.2	0.6	12.4	0.5
Magnetite	Fe ₃ O ₄ (FeO, Fe ₂ O ₃)	7.2	0.3	7.0	0.3
Amorphous	-	29.2	4.9	40.7	4.8

3.3.2 Converter steel slag reactivity with water

The heat release of the milled converter slag mixed with water was determined to assess the reactivity of converter slag (water/slag = 0.4). The respective heat release of each slag at different milling times is shown in Figure 4.

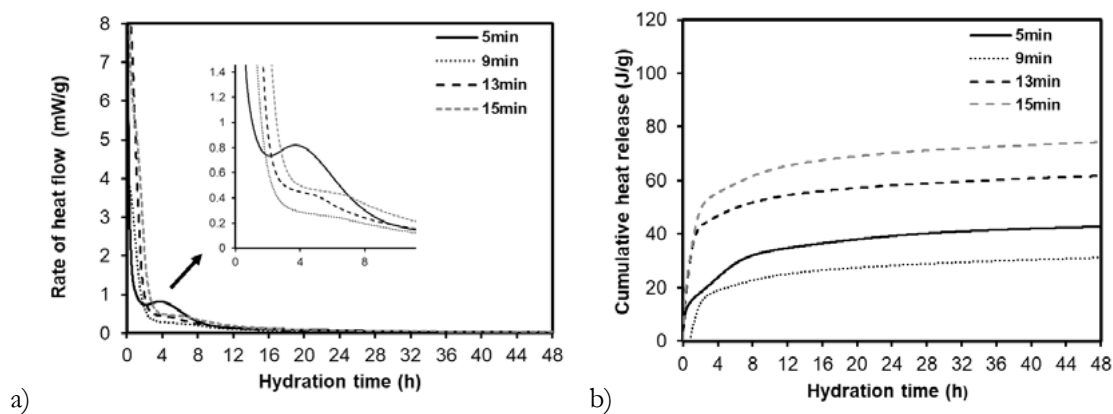


Figure 4: a) Rate of heat flow and b) cumulative heat release of Converter Steel Slag milled with different times.

The rate of heat flow was negligible during the 48h of measurement. (Figure 4). Nevertheless, Figure 4-b presenting the cumulative heat release shows that the reactivity of the material increases following the reduction of the particle size. The cumulative heat released within the first 48h is 74.78J/g for 15 min milling and just 20J/g for 5 minutes milling. For comparison, the heat release of a Portland cement CEM I 42.5N is around 240J/g. The results show that increasing the fineness of the slag can enhance hydraulic reactivity.

4. Conclusions

- The MA treatment has a beneficial effect to enhance the converter steel slag hydraulic properties

without a chemical activator, by reducing the particle size of converter steel slag, showing that it can potentially be used as a binder.

- After 15 min of milling the particles agglomerated, nevertheless, it didn't influence the cumulative heat release.
- Disc milling results in amorphization of the samples. The amorphous content increased and α -C₂S, β -C₂S, and Fe, Mg-wuestite decreased. Both C₂S- α and C₂S- β show a higher degree of amorphization compared to Mg, Fe-wuestite.

Based on the results obtained further analysis needs to be done to characterize and investigate the nature of the hydration reaction and the behaviour of slag during milling.

5. Acknowledgment

The authors would like to acknowledge the financial support by NWO (The Netherlands Organisation for Scientific Research) for funding this research (project no.10023338) and M2i (Materials Innovation Institute) for managing this project. Furthermore, the authors wish to express their gratitude to the following sponsors of this research: Tata Steel; Enci; Hess AAC Systems; Kijlstra Betonmortel; V.d. Bosch Beton; Inashco.

References

- [1] J. Zhao, P. Yan, D. Wang, Research on mineral characteristics of converter steel slag and its comprehensive utilization of internal and external recycle, *J. Clean. Prod.* 156 (2017) 50–61. doi:10.1016/j.jclepro.2017.04.029.
- [2] H. Yi, G. Xu, H. Cheng, J. Wang, Y. Wan, H. Chen, An overview of utilization of steel slag, *16* (2012) 791–801. doi:10.1016/j.proenv.2012.10.108.
- [3] J. Malolepszy, J. Deja, W. Brylicki, Durability of mortars and concrete containing ground converted slag, *IV CANMET/ACI Int. Conf. Durab. Concr. c* (1997) 189–206.
- [4] The European Slag Association, Position paper on the Status of Ferrous Slag complying with the Waste Framework Directive and the REACH Regulation, 2012.
- [5] C. van Hoek, J. Small, S. van der Laan, Large-Area Phase Mapping Using PhAse Recognition and Characterization (PARC) Software, *Micros. Today.* 24 (2016) 12–21. doi:10.1017/S1551929516000572.
- [6] H.M. Ludwig, W. Wulfert, W. Ruhkamp, B. Moser, Mobilization of the hydraulically active phases in LD slags by producing ultrafine material, *Cem. Int.* 15 (2017) 76–86.
- [7] W. Qiang, S. Mengxiao, Y. Jun, Influence of classified steel slag with particle sizes smaller than 20 μ m on the properties of cement and concrete, *Constr. Build. Mater.* 123 (2016) 601–610. doi:10.1016/J.CONBUILDMAT.2016.07.042.
- [8] E. Belhadj, C. Diliberto, A. Lecomte, Characterization and activation of Basic Oxygen Furnace slag, *Cem. Concr. Compos.* 34 (2012) 34–40. doi:10.1016/j.cemconcomp.2011.08.012.
- [9] Q. Wang, P. Yan, Hydration properties of basic oxygen furnace steel slag, *Constr. Build. Mater.* 24 (2010) 1134–1140. doi:10.1016/j.conbuildmat.2009.12.028.
- [10] Q. Wang, J. Yang, P. Yan, Cementitious properties of super-fine steel slag, *Powder Technol.* 245 (2013) 35–39. doi:10.1016/j.powtec.2013.04.016.
- [11] S.C. Pal, A. Mukherjee, S.R. Pathak, Investigation of hydraulic activity of ground granulated blast

Long term weathering of converter slag

K. Schollbach¹, S. van der Laan¹

¹Tata Steel, R&D, Microstructure & Surface Characterization (MSC), P.O. Box 10.000, 1970 CA IJmuiden, the Netherlands

Abstract

Converter slag, also known as basic oxygen furnace (BOF) slag, is produced during steel making and contains mainly C_2S , C_2F , and RO phases ($CaO-FeO-MnO-MgO$ solid solutions) among which varying levels of free lime can be present. Its high density makes it useful as armour stone, for stabilizing embankments of waterways. Due to its high strength and abrasion resistance it has been applied as asphalt aggregate. However, it is avoided for applications in concrete because of the expansion problems associated with hydration of free lime. It is commonly believed that weathering of slag is effective to mitigate the free-lime expansion. Four batches of single BOF heats were investigated which had been stored outside for 19 years, exposed to all weather conditions, in drained boxes. Three batches still contained large solid blocks of around 5 to 20cm with some lichen growth. One sample however had broken into many smaller fragments of around 1 to 2cm, presumably due to a high initial content of C_3S that was reduced from 15 to 5wt% during weathering. All samples still contained unreacted free lime showing that the reactions are ongoing and that weathering of slag may not be entirely effective in avoiding expansion related durability problems, especially long term. In addition to free lime and C_3S , the RO phase $(Fe,Mg)O$ showed some reactivity during long term weathering.

Keywords: converter slag, weathering, supplementary cementitious materials, XRD

1. Introduction

Iron- and steel making produces a variety of slags at different stages of the process. The best known one in the building materials industry is blast furnace slag, which is generated in the furnace where iron ore is smelted to produce pig iron. On average about 0.25 to 0.3t of this slag are produced per t of iron in the EU[1]. Due to excellent pozzolanic properties after granulation it is the main component of CEM III [2] and often used in geopolymers [3]. In contrast converter slag is produced during the conversion of iron into steel and rarely used as a building material, although it is also available in large quantities. About 0.15t of converter slag is produced per t of steel[1] with the worldwide steel production estimated to be 1,8 Bt in 2018 [4]. It is also referred to as BOF (Basic Oxygen Furnace) or BOS (Basic Oxygen Steelmaking) slag, LD (Linz-Donawitz) slag, steel furnace slag or simply steel slag. The last two should be avoided however, because they are also used for electric-arc-furnace (EAF) slag, which has different properties.

The reason for the low utilization of converter slag is two-fold: low reactivity makes it undesirable as a supplementary cementitious material and volume instability can interfere with its use as a concrete aggregate.

The composition of converter slag is variable (Table 1 and 2) and depends on the steel making process as well as the quality of the raw materials, but the most common phases are C_2S which occurs in both the monoclinic β and the orthorhombic a'_H form, as well as $C_2(A,F)$ and RO phases ($CaO-FeO-MnO-MgO$

solid solutions). $C_2(A,F)$ and β - C_2S are also part of Portland cement clinker and as such some hydraulic reactivity could be expected in converter slag. However several studies have found that the reactivity is low and that the addition of converter slag to cement or concrete has very little positive or even negative effects on strength development [5-7].

Table 1: Mineralogical composition of converter slag [8-9]. Magnesiowuestite, free lime and periclase are RO-phases.

Formula	Name	Amount (wt%)
β - C_2S	Larnite/Alite	} 30-50
α'_H - C_2S	Bredigite	
$C_2(A,F)$	Srebrodolskite	15-25
$(Fe,Mg)O_{1-x}$	Magnesiowuestite	20-30
Fe_3O_4	Magnetite	0-10
CaO	Free lime	0-10
C_3S	Hatruite/Belite	0-5
MgO	Periclase	0-2

Table 2: Chemical composition of converter slag [7, 10, 11]

Oxide	CaO	FeO/Fe ₂ O ₃	SiO ₂	MgO	MnO	Al ₂ O ₃	P ₂ O ₅	TiO ₂
wt%	35-50	15-25	10-20	5-10	2-7	1-5	0.5-2	0-2

Converter slag as an aggregate in concrete can lower the durability due to the presence of free lime or MgO. The free-lime and MgO can react with water to form hydroxides which is accompanied by volume expansion [12], and can lead to cracks and subsequent low durability. Free lime can form either directly out of the melt near liquidus as primary phase or be present as undissolved lime. It can also form near the solidus when the slag becomes saturated with CaO or even subsolidus from the exsolution of C_3S into C_2S and CaO during the slow cooling of the slag [13]. MgO fragments in the slag can be derived from refractory wear, and MgO-rich RO (magnesiowuestite) forms as liquidus phase in converter slag. To some extent the cooling rate of slag can be influenced, which effects the mineralogy, however, it is difficult to avoid free-lime and MgO-phase in the slag because CaO is needed as a fluxing agent and MgO is added to protect the refractories of the furnace. For this reason, converter slag is often restricted to applications that are less sensitive to volume expansion such as unbound aggregate for stabilizing waterway embankments or creating road base. However, if it contains no free-lime, it can also be applied as asphalt aggregate because of its high strength and abrasion resistance.

One approach to mitigate the free lime problem is weathering of up to 1 year by storing the slag outside [10, 14]. In addition, converter slag can be monitored by measuring the free lime content either chemically or via XRD or by measuring the expansion following a 1-7 day steam test (EN 1744-1). However, there is very little information available on the influence of weathering, especially long-term on the mineralogy of converter slag. It is unclear how much of the free lime or MgO present in fresh converter slag reacts over time and if other phases could cause expansion too. All these parameters could have implications for the long-term durability of building materials containing converter slag aggregate.

This paper analyses 4 different batches of converter slag that were produced at Tata Steel Ijmuiden in 2000/2001 and then placed outside for weathering. Scanning Electron Microscopy (SEM) with Energy-dispersive X-ray spectroscopy (EDX), quantitative X-Ray diffraction (XRD) and X-Ray fluorescence (XRF) were used to investigate the changes in free lime content and in the other mineral phases during that time.

2. Methodology and materials

The initial XRD measurements of the unweathered slag were done using a D5000 (Bruker) with Cu radiation. For the measurements of the weathered slag a D8 (Bruker) with a Cu tube, energy filtering and a Lynx Eye detector was used. Before measuring, the weathered samples were milled using a McCrone XRD mill (Retsch) adding 10wt% Si as an internal standard. All diffraction patterns were quantified using Topas 5 (Bruker). For SEM/EDX analysis, the samples were embedded in resin, cut, polished without the use of water and then carbon coated. The measurement was done using a JEOL JSM-7001F SEM equipped with 2 Solid State EDS Detectors (ThermoScientific NS7) with an accelerating voltage of 15 kV and beam current of 6.2nA. The converter slag samples were stored outside in Ijmuiden in uncovered plastic boxes with holes in the bottom to allow rain water drainage (Figure 1). The original size of the pieces was in the range of around 10 to 20cm. The unweathered slag is referred to by the batch numbers A, B, C and D, while the corresponding weathered slag samples are named A_w, B_w, C_w and D_w.

3. Results

3.1 Sample description

Figure 1 shows photos of the original converter slag taken in 2000/2001 as well as its appearance today. The 4 samples were chosen based on differences in appearance out of around 30 batches stored for long term weathering. Batch A and B were chosen due to their original appearance. Batch A had a bright white colour, while A represents the more typical dark converter slag. Batch C and D were chosen based on their current appearance. Batch C_w contained large pores, similar to scoria, while sample D_w was the only batch that had visibly reduced in size from around 20cm to 1-5cm.

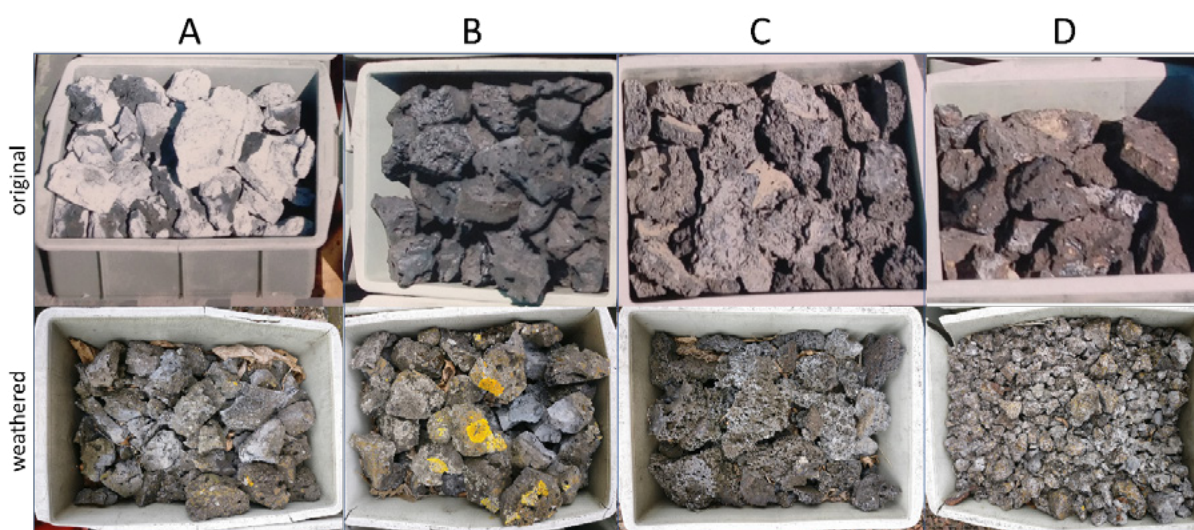


Figure 1: Photos of the converter slag batches investigated. Some weathered slags are overgrown with lichen (yellow)

3.2 Original Converter slag

The chemical composition of the samples measured before weathering is given in Table 3. All slags were rapidly cooled, which means that the slags were tipped from a 30t slag pot onto a cold steel slab, quenching from end-of-converter-process temperature to ambient. The thickness of the slag layer determined the rate of heat loss. XRD measurements of the original slag show that Batch A, B and C contain C₂S, srebrodolskite, and RO phase (Mg,Fe)O, as well as some free lime (Figure 2). The (Mg,Fe)O peaks are very wide due to the presence of (Mg,Fe)O with varying compositions and lattice parameter, which leads to

overlapping peaks. Batch D however is very rich in free lime and C_3S with very little srebrodolskite (Table 3). The srebrodolskite content is low due to the low Al^{3+} and probably Fe^{3+} content. This also means less Ca can be bound in this phase, leaving it available to form C_3S and free lime.

The measurements were quantified (Table 4) although the quality suffers from the poorer resolution available at the time, but it still gives an indication of the mineralogical composition.

Table 3: Original chemical composition of the investigated converter slag batches. All results in wt%.

Batch	Al_2O_3	MgO	P_2O_5	CaO	SiO_2	TiO_2	MnO	FeO
A	0.5	8	1.6	45.7	11.8	1.9	4	26.6
B	2.9	12	1.3	38.3	10.6	1.7	4.6	28.5
C	2.5	13	1.3	41.6	12.6	2.2	4.8	22
D	0.7	9.5	1.2	44.7	12.7	1.8	3.9	25.4

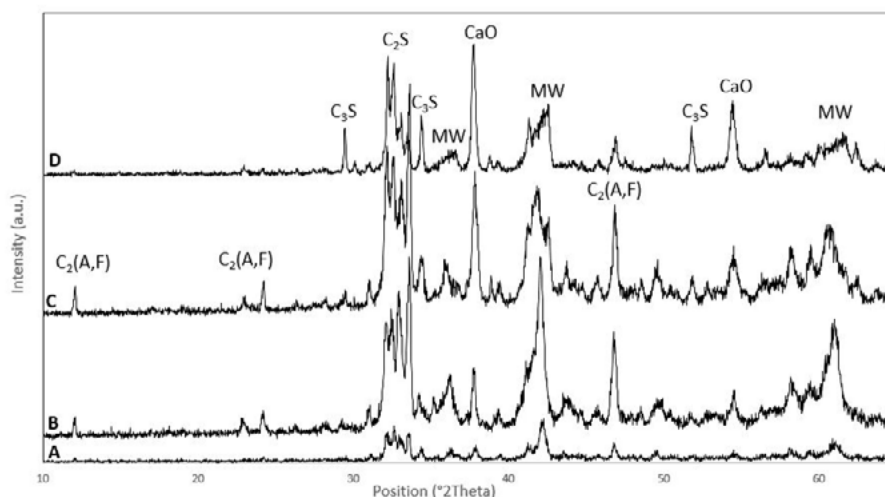


Figure 2: Original XRD measurements of converter slag before weathering. Differences in intensities are due to different measuring times.

Table 4: Mineralogical composition of original converter slag before weathering (left) and after (right). Amorphous content of the original slag could not be determined, because no internal standard was added at the time. Lime is a RO-phase but listed separately due to its importance for volume stability. All results are in wt%.

Batch	A	B	C	D	Batch	A _w	B _w	C _w	D _w
Lime	5.4	4	9.1	18.2	Lime	3.8	2.5	6.5	9.7
RO phase	37.4	40.8	35.4	36.9	RO Phase	27	26.2	18.1	22
Srebrodolskite	19.1	28.2	25.1	8.4	Srebrodolskite	20	24.4	24.6	3.2
$C_2S (\alpha'_H + \beta)$	38	25.8	28.6	21.3	$C_2S (\alpha'_H + \beta)$	45.5	31.5	31.7	18.7
C_3S			1.7	15.2	C_3S			3.5	5.1
Magnetite		1.2			Portlandite				7.1
					Quartz	0.1	0.1	1.6	0.1
					Calcite	2.2	1.1	0.3	2.3
					Pseudobrookite	0.5	0.4	0.3	0.3
					Iron				1.5
					Green rust			0.7	
					Amorphous	0.9	13.9	12.4	29.9

3.3 Weathered converter slag

3.3.1 Composition

After almost 20 years of exposure to the elements, samples were taken from the converter slag and analysed with XRD (Table 5)(Figure 3). Regarding the phases that are important for weathering, all samples still contained noticeable amounts of free lime, while their calcite contents were low. Sample C_w and D_w also contained unreacted C_3S . No portlandite was found except for sample D_w . The $Ca(OH)_2$ in D_w could be suspect and may have formed during milling out of free lime because the sample was insufficiently dried. Small amounts of green rust were present in C_w , which is an iron containing Layered Double Hydroxide (LDH) that is likely a weathering product. Weathered samples, except for A, contain amorphous phase.

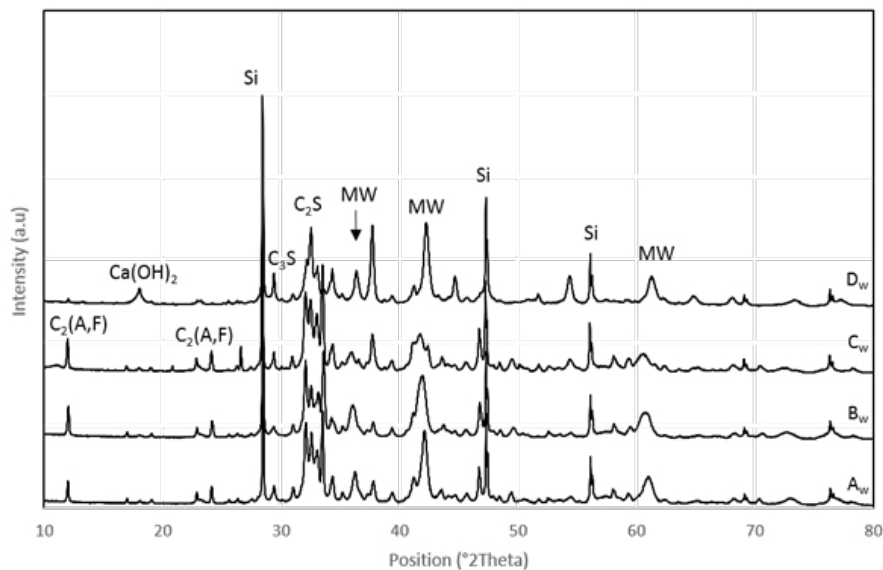


Figure 3: XRD measurements of converter slag after weathering.

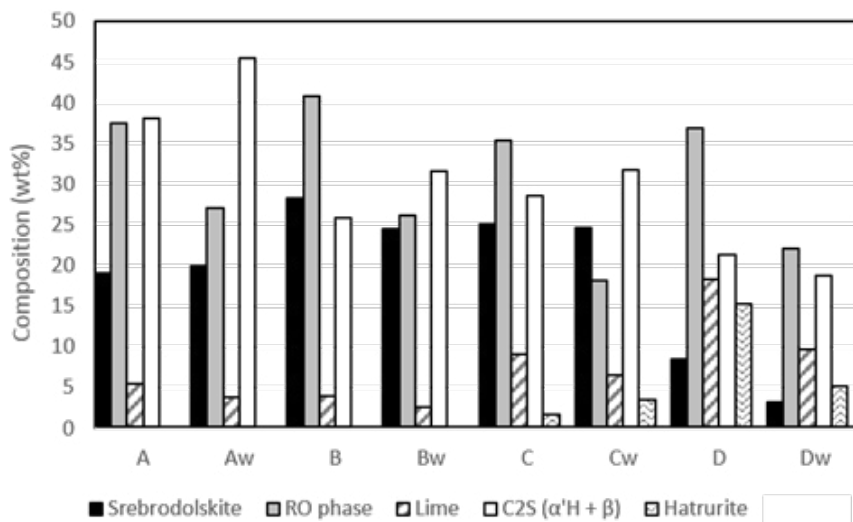


Figure 4: Differences in converter slag before and after long term (w denotes the weathered samples).

Comparison of the two datasets is complicated because of the difference in quality between the old and recent XRD-patterns (energy filtering), and the lack of information on the amorphous content of the original samples. However, in the case of A_w at least the amorphous content is very low, and it can be assumed that this was also the case in the unweathered slag A. We therefore assumed that the other original

slag samples B, C and D, also contained very little amorphous phase. This makes a direct comparison possible and shows that long term weathering reduced free lime and the other RO phases by around 30% (Figure 4), while the srebrodolskite content remained stable at around 20wt%. In contrast C_2S appears to become enriched. Samples B/B_w and C/C_w show trends similar to A/A_w , the only difference is that C_w contains small amounts of C_3S . The C_3S content seems to be enriched after weathering, just like the C_2S , however the difference is not very large and considered to be well within the error of the quantification for Batch C. It is however clear that some unreacted C_3S remains. The enrichment of C_2S in these samples may be due to an overall mass loss that occurs when weathering products are washed out. If that is the case reactive phases will decrease while stable phases appear to increase. These results also show that the outer appearance of the first three batches before or after weathering does not correlate with significant differences in mineralogical composition.

In Sample D_w a clear reduction of free lime and C_3S can be seen after long term weathering, C_2S appears to be stable while the srebrodolskite content was reduced by around 60%. The C_3S content in Batch D is also the main reason for the extreme volume instability, more so than the high lime content. It forms C-S-H gel in contact with water, a reaction that is also associated with volume expansion and could explain the high amorphous content in D_w (30wt%).

Based on these results the reactivity of converter slag phases during long term weathering can be ranked from most reactive to least reactive as follows: $C_3S/CaO > RO \text{ phase} > \text{Srebrodolskite} > C_2S$. C_3S and CaO are highly reactive phases, which is why the XRDs show a clear reduction in their content after weathering. The same reduction is visible for the other RO-phases, indicating reactivity even if they have a lower solubility than CaO and no hydraulic reactivity like C_3S . Srebrodolskite also seems to be reactive to some extent, even if it dissolves at a lower rate than the RO-phase, It would explain why it appears to be stable in samples A_w , B_w and C_w but shows a clear reduction in D_w . C_2S is either enriched or shows a very small reduction in all cases, making it very stable during long term weathering.

3.3.2 Microstructure

Because it showed the largest weathering effects Sample D_w was analysed further using SEM. Figure 5 shows calcite formation inside a pore next to a phenocryst of C_3S . The C_3S appears to be partially hydrated (lower part) and contains (Fe,Mg)O inclusions that formed first in the melt, followed by C_3S . This phenocryst of C_3S is embedded in a matrix of primarily C_2S and (Fe,Mg)O.

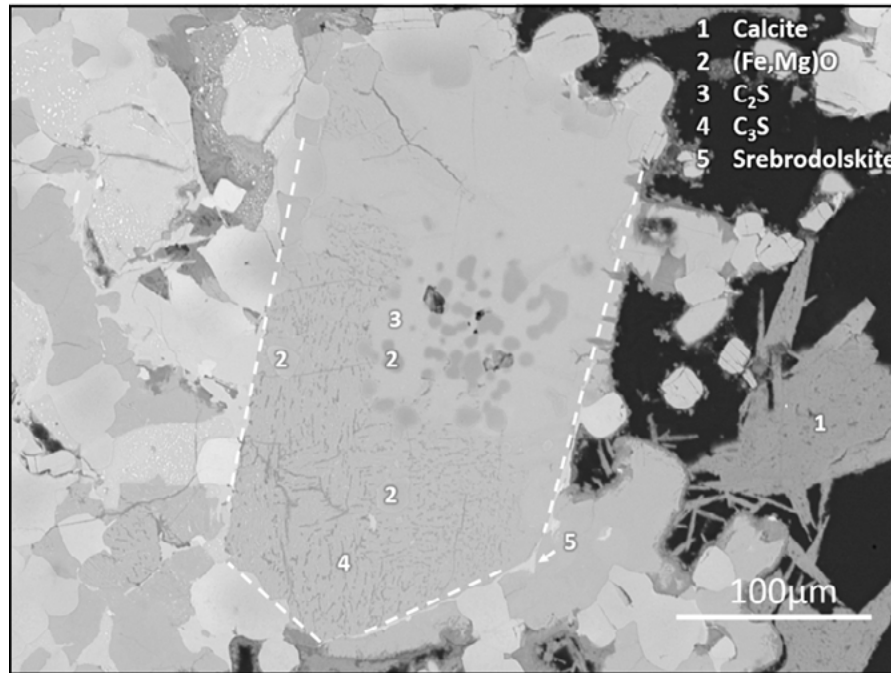


Figure 5: SEM-Image of Sample D_w. A large C₃S phenocryst with (Fe,Mg)O inclusions is embedded in a matrix of C₂S and (Fe,Mg)O. Calcite formed as a weathering product inside a pore.

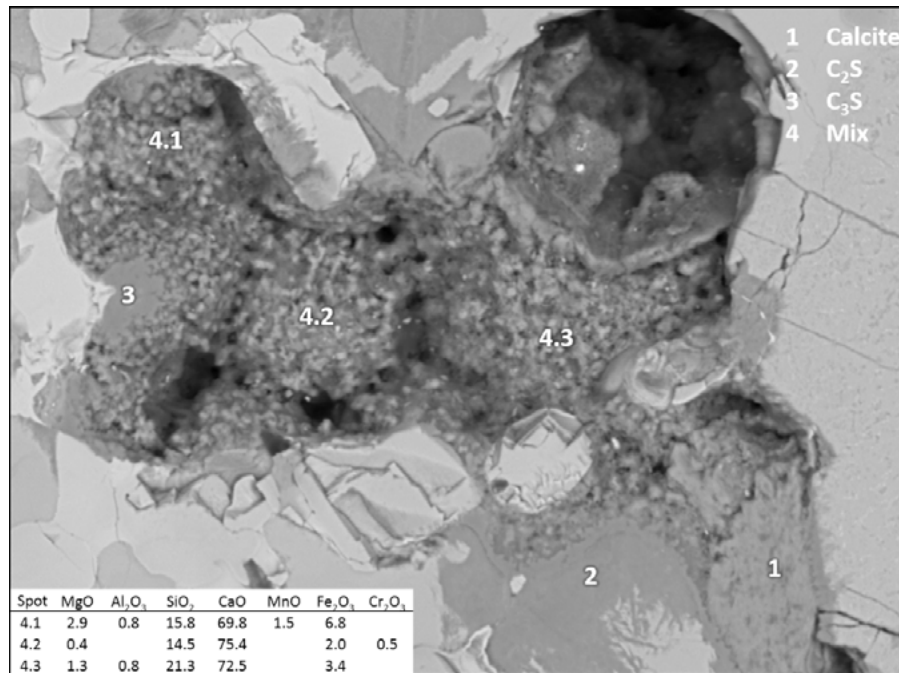


Figure 6: SEM-Image of Sample D_w. A pore filled with hydration/weathering product (Mix) surrounded by partially reacted C₂S, calcite and C₃S. The inset in the lower left corner gives the EDX composition of spots 4.1 to 4.3.

Weathering products also formed inside pores (Figure 6). It is most likely amorphous C-S-H or C-F-S-H (marked 4 in Fig. 5) with a variable composition, because the only crystalline weathering product that could be detected via XRD was calcite. The pore is surrounded by partially reacted C₂S (marked 2 in Fig. 5) and C₃S (marked 3 in Fig. 5).

4. Conclusion

- Four different batches of converter slag produced at Tata Steel Ijmuiden in 2000/2001 were placed outside for long-term weathering experiments and analysed in 2019. Batches A, B and C had a similar chemical and mineralogical starting composition with C_2S , srebrodolskite, magnesioferrite (Fe,Mg)O and free lime ($\sim 4-9wt\%$) present. Batch D contained very high amounts of free lime ($\sim 18wt\%$), C_3S ($\sim 15wt\%$) and lower amounts of srebrodolskite and C_2S .
- After weathering only 20 to 30% of the free lime had reacted in all samples. The presence of C_3S and free lime in Batch D caused a dramatic reduction in grain size from around 15-20 μm to 1-5 μm . This process is expected to continue and possibly accelerate, because only about 50% of the C_3S had reacted and the surface area of the grains is still increasing due to volume expansion and cracking.
- The reactivity of the converter slag phases from most to least reactive under long term weathering conditions can be ranked as follows: $C_3S/CaO > RO \text{ phase} > Srebrodolskite > C_2S$.

5. Acknowledgement

The authors would like to thank Arthur Horn and James Small for the help with sample preparation and measurements.

6. References

- [1] H. Van Oss, "Slag - Iron and Steel," in *U.S. Geological Survey Minerals Yearbook—2002*, 2002.
- [2] E. Özbay, M. Erdemir, and H. İ. Durmuş, "Utilization and efficiency of ground granulated blast furnace slag on concrete properties – A review," *Constr. Build. Mater.*, vol. 105, pp. 423–434, Feb. 2016.
- [3] A. Mehta and R. Siddique, "An overview of geopolymers derived from industrial by-products," *Constr. Build. Mater.*, vol. 127, pp. 183–198, Nov. 2016.
- [4] world steel association, "Global crude steel output increases by 4.6% in 2018." [Online]. Available: worldsteel.org. [Accessed: 20-Sep-2019].
- [5] Q. Wang, P. Yan, J. Yang, and B. Zhang, "Influence of steel slag on mechanical properties and durability of concrete," *Constr. Build. Mater.*, vol. 47, pp. 1414–1420, Oct. 2013.
- [6] S. Kourounis, S. Tsivilis, P. E. Tsakiridis, G. D. Papadimitriou, and Z. Tsibouki, "Properties and hydration of blended cements with steelmaking slag," *Cem. Concr. Res.*, vol. 37, no. 6, pp. 815–822, Jun. 2007.
- [7] J. N. Murphy, T. R. Meadowcroft, and P. V. Barr, "Enhancement of the Cementitious Properties of Steelmaking Slag," *Can. Metall. Q.*, vol. 36, no. 5, pp. 315–331, 2014.
- [8] C. J. G. van Hoek, J. Small, and S. R. van der Laan, "Large area phase mapping using PhAse Recognition and Characterization (PARC) software," *Micros. Today*, vol. 24, no. 03, 2016.
- [9] J. Waligora, D. Bulteel, P. Degruilliers, D. Damidot, J. L. Potdevin, and M. Measson, "Chemical and mineralogical characterizations of LD converter steel slags: A multi-analytical techniques approach," *Mater. Charact.*, vol. 61, no. 1, pp. 39–48, 2010.
- [10] J. Guo, Y. Bao, and M. Wang, "Steel slag in China: Treatment, recycling, and management," *Waste Manag.*, vol. 78, pp. 318–330, Aug. 2018.
- [11] J. Waligora, D. Bulteel, P. Degruilliers, D. Damidot, J. L. Potdevin, and M. Measson, "Chemical

and mineralogical characterizations of LD converter steel slags: A multi-analytical techniques approach,” *Mater. Charact.*, vol. 61, no. 1, pp. 39–48, Jan. 2010.

[12] G. Wang, Y. Wang, and Z. Gao, “Use of steel slag as a granular material: Volume expansion prediction and usability criteria,” *J. Hazard. Mater.*, vol. 184, no. 1–3, pp. 555–560, Dec. 2010.

[13] M. Allibert *et al.*, “Slag atlas,” in *Slag Atlas*, 1995.

[14] P.-Y. Mahieux, J.-E. Aubert, and G. Escadeillas, “Utilization of weathered basic oxygen furnace slag in the production of hydraulic road binders,” *Constr. Build. Mater.*, vol. 23, no. 2, pp. 742–747, Feb. 2009.

The leaching characteristics of chelatant- and water-based treated Municipal Solid Waste Incineration (MSWI) fly ash

E. Loginova,^{1*} M. Proskurnin,² H.J.H. Brouwers¹

1. Department of the Built Environment, Unit Building Physics and Services, Eindhoven University of Technology, P.O. Box 513, 5600 MB Eindhoven, The Netherlands

2. Chemistry Department, Lomonosov Moscow State University, Leninskie Gory 1-3, GSP-1 119991 Moscow, Russia

Phone: +31 40 247 27 60; Fax: +31 40 243 85 95; E-mail: Proskurnin@gmail.com

(*) To whom correspondence should be addressed

Abstract

The challenge of sustainable use of MSWI residues such as fly ash is particularly acute. One of the possible uses of these residues is making secondary building materials. However, MSWI fly ash is highly contaminated with hazardous elements such as Pb, Zn, Cd, Cu, etc. Its treatment to reduce the environmental impact is required before reuse or disposal. Here, the efficiency of a new three-step combined treatment with two complexing agents (ethylenediaminetetraacetate and gluconate) to increase the toxic-element elution from fly ash in contrast to conventional water-only treatments is shown. The compositions of raw and differently treated (reagent-combined and water-only treatments) MSWI fly ash were compared by the standard leaching test. For Cd, Cu, and Zn, the combined treatment is 10–1000-fold more efficient than the water-only one. It was shown that the same WFA, which seems non-hazardous according to the leaching test after being washed with water, proves to be extremely hazardous when more properties are taken into account. Thus, it is relevant not only to study the leaching of WFA components and the factors affecting it, but also to pay detailed attention to amounts of elements remaining in the material after treatments.

Keywords: MSWI fly ash; Potentially Toxic Element; Residue Treatment; Environmental impact; Leaching

Table of Nomenclature

AAS

Atomic Absorption Spectrometry

COMBY

Combined chelatant treatment

EDTA

Disodium ethylenediaminetetraacetate

IC

Ion Chromatography

ICP-AES

Inductively Coupled Plasma – Atomic Emission Spectroscopy

LL

Legislation Limit

LOI

Lost On Ignition

L/S

Liquid to Solid

Na-GI

Sodium Gluconate

1. Introduction

The utilization of waste residues challenge has been dealt with for over 25 years [1]. During the incineration process of municipal solid waste, ash residues are approximately 80% (w/w) bottom ash and 20% (w/w) fly ash [2]. High concentrations of chloride, sulfate, lead, zinc, copper, etc. turn waste fly ash (**WFA**) into a “hazardous waste” [3–5]. Due to the landfill space reduction along with environmental regulations concerning potential leaching of various pollutants into ground waters [6], these residues should be treated. To convert WFA into a safe material suitable for landfilling or reuse, it is necessary to reduce the leaching of potentially toxic elements (**PTEs**).

Main ways to achieve this goal have been: water washing in combination with solidification [7–9], stabilization using various chemicals [10,11], adding silica fume to hydrated WFA pastes [12], carbonation [13,14], and thermal treatments [15,16]. However, recently, metal extraction from WFA [17,18] to retrieve valuable metals has become comparably attractive [19,20]. As metal concentrations in WFA are considerable, research has been focused on making this extraction as efficient as possible [21,22]. However, currently these methods are not being aimed to reduce the WFA contamination level.

Among other applications, the WFA is considered as a promising cement substituent in the production of concrete [7,23–25] or lightweight artificial aggregates [26]. WFA is conventionally water-treated [27], and the subsequent leaching test estimates its suitability for reuse. However, the washing procedure is not very economically feasible, reported liquid-to-solid ratios (**L/S**) are high (above 10) [28] or the procedure is not optimized, and the leaching test is not performed on the final product (containing WFA) to test the treatment efficiency [23]. Moreover, unlike coal-combustion fly ash (**CCFA**) mostly consisting of spherical particles [29], WFA particles are not studied well. They presumably consist of an inert glassy core surrounded by a porous, partially dissolvable mineral matrix layer (Al, Si, and Ca are the main components) covered with easily soluble alkali-metal chlorides [30]. Thus, washing WFA may decompose the matrix, which would lead to a PTE release. Hence, if the potentially soluble part of WFA does not dissolve entirely, WFA can be hazardous if washed again or incorporated in cement.

Thus, water-only treatments proved to be effective for readily soluble salts but not all PTEs. Several assisting agents (separately) for heavy-metal recovery (Zn, Pb, Cu, Mn, and Cd) from WFA were studied due to their high complexation constants [31], and it was reported that disodium ethylenediaminetetraacetate (**EDTA**) and sodium gluconate are especially efficient for Zn and Pb [8]. However, a detailed study on the effectiveness of these complexing agents and their combined use for WFA purification was not performed.

Therefore, the goal is to study the effectiveness of the combined use of chelatants (EDTA and gluconate) to improve PTE extraction from WFA while using lower water volumes. Apart from complexation constants, the agents were selected due to their ability to simulate the matrix decomposition of WFA particles, a process that might have occurred outdoors with assistance of environmental agents. The study involved the comparison of untreated and treated WFA by the standard leaching test and the analysis of individual hazardous elements in the leachates and remaining WFA material.

2. Materials and Methods

WFA was supplied by the municipal solid waste-to-energy incinerator plant of AVR-Van Gansewinkel (Duiven, the Netherlands).

2.1 Samples and reagents

Deionized water (a Milli-Q Academic system, Millipore) was used for the preparation of all the solutions and washing. Nitric acid (69%, for analysis, ISO-grade, AppliChem Panreac) was used for all the operations with ICP–AES. All standard solutions were from High Purity Standards. A mixture of ICP-AM-6 (100 mg/L of Al, Sb, B, Ba, Be, Cd, Ca, Co, Cr, Cu, Fe, Li, Mg, Mn, Mo, Ni, K, Na, Si, Pb, Tl, Sr, V, Zn) and ICP-MS-68B (100 mg/L of Sb, Ge, Hf, Mo, Nb, Si, Ag, Ta, Te, Sn, Ti, W, Zr) standard solutions was used for the calibration in the range 0.01–10 mg/L. A mixture of an ICP-AM-15 standard solution (10000 mg/L of Na, K, Ca, and Mg), P (10000 mg/L), and S (10000 mg/L) was used for the calibration in the range 1–100 mg/L. An internal standard solution of Sc (20 mg/L) was prepared from a standard solution (Inorganic Ventures, 1000 mg/L).

2.2 Equipment

2.2.1 Inductively coupled plasma atomic emission spectrometry

Inductively coupled plasma atomic emission spectrometry (ICP–AES) provides rapid and highly sensitive multielemental quantification of MSWI fly ash with high accuracy and precision [32,33]. An ICP–OES 5100 SVDV spectrometer (Agilent Technologies) was operated in the axial mode (the auxiliary gas flow, 1.2 L/min; coolant gas flow, 14 L/min; nebulizer gas flow, 0.8 L/min). All emission lines were measured simultaneously.

2.2.2 Flameless atomic-absorption spectrometry coupled with pyrolysis

An RA-915+ Mercury Analyzer (Ohio Lumex Co.), a portable multifunctional atomic absorption spectrometry (AAS) instrument with Zeeman high-frequency modulation of polarization for background correction, with a RP-91C pyrolysis attachment (Lumex) was used for mercury determination.

2.2.3 Ion chromatography

Ion chromatography (IC) was selected as a standard method for chloride and sulfate in leachates [34]. A Thermo Scientific Dionex ion chromatograph 1100, 2×250 mm AS9-HS ion-exchange columns, the isocratic flow (0.25 mL/min) was used. Ion detection was accomplished by measuring a suppressed conductivity making use of an electrolytically regenerated suppressor (Thermo Scientific Dionex AERS 500 2 mm). As eluent, a 9 mM solution of sodium carbonate was used.

2.2.4 Auxiliary Equipment

An XP 504 analytical balance (Mettler Toledo), 15-D0438 riffle boxes (sample splitters, CONTROLS Group), an SM-30 shaking table (Edmund Bühler GmbH), a UF 260 drying oven (Memmert), and a Multiwave 3000 (Anton Paar) microwave oven for digestion with a 60-bar rotor were used throughout. Automatic Eppendorf Research pipettes (Eppendorf International) were used for the preparation of calibration solutions. A-class polypropylene volumetric flasks (Vitalab) with volume (50.00 ± 0.12) mL and (100.00 ± 0.20) mL and polypropylene test tubes (Axygen) were used for the preparation of calibration and test solutions.

2.3 Procedures

2.3.1 Sample preparation

Fresh WFA samples were used for analyses and treatments. The material was oven-dried at 105°C to a constant mass. Next, the WFA fraction above 500 μm was sieved out (3.8% w/w), because it contained significant amounts of unburned carbon. LOI at 550°C of the fraction above 500 μm is 16.84. Next, the material was used for the standard leaching test. Subsequently, treated samples were collected and subjected to the standard leaching test again to assess the treatment efficiency.

2.3.2 Standard leaching test

The standard leaching test [35] was performed on untreated WFA and the fraction below 500 μm (5 replicates of 40 g each) to evaluate the level of PTEs, chloride, and sulfate. This test was also used to evaluate the combined (**COMBY**) and water-only (**WATER-3**) treatments (Section 3.3.2 below). After the standard leaching test (24 h shaking, L/S 10, 200 rpm), the samples were filtered through 17-30 and 0.2- μm filters to prepare leachates for ion chromatography and ICP–AES/AAS.

2.3.3 COMBY and WATER-3 treatment procedures

To test the efficiency of complexing agents, individual solutions of EDTA and sodium gluconate (**Na-Gl**) were used. A WFA sample (40 g) was added to 200 mL of 0.05M EDTA and shaken for 20 min (200 rpm). The mixture was filtered (17-30 and 0.2- μm filters), and the washing water was collected for further analysis. The same procedure was repeated for another WFA portion, but Na-Gl instead of EDTA was used.

Figure 1 illustrates the scheme for both treatments consisting of three steps. WATER-3 serves as a reference, it follows all steps from COMBY, but instead of the additive solutions deionized water was used. Due to the dissolution of soluble components, in all cases L/S was taken with respect to the initial sample mass.

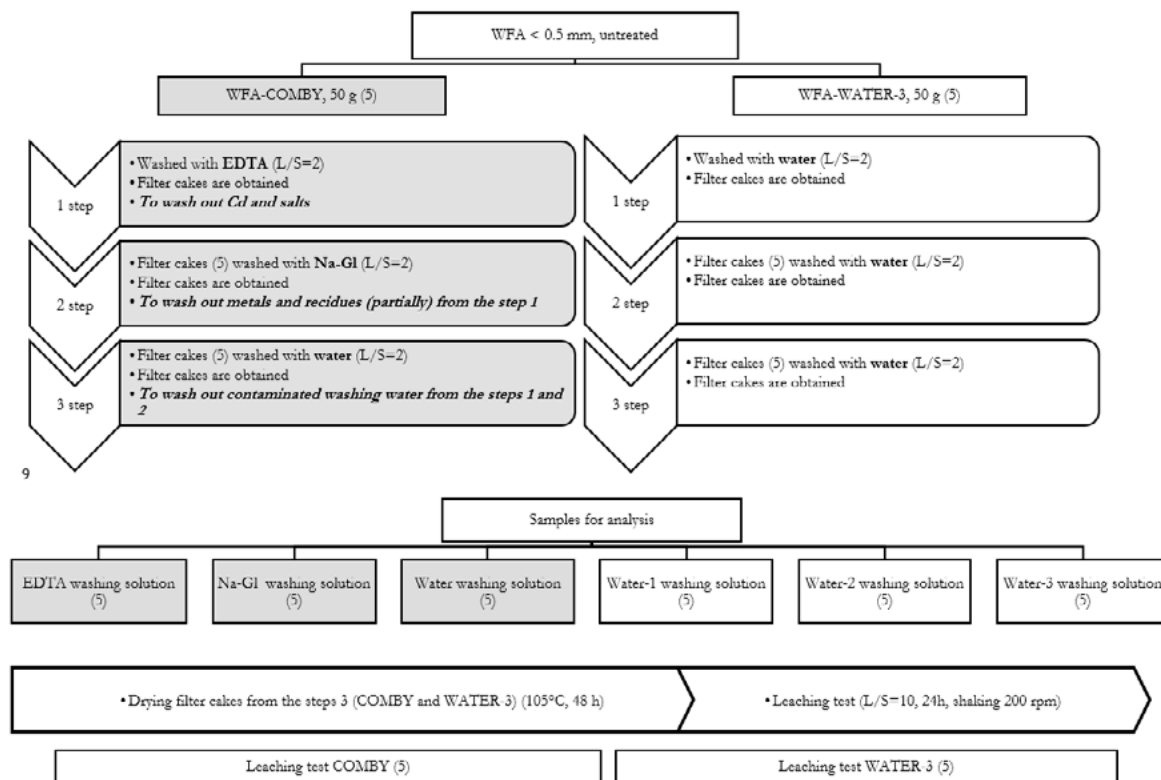


Figure 1: Scheme of WATER-3 and COMBY treatments and analysis (figures in parentheses denote the number of replicates for each stage) [36].

3. Results and discussion

3.1 Untreated WFA properties

3.1.1 Comparison of leaching vs. bulk element composition

The standard leaching test results (L/S 10) (**Table 1**) on the untreated WFA show that Cr, Pb, Cd, Mo, and Zn concentrations exceed the legislation limits (**LL**) significantly (leachate pH 13) [36].

Table 1: PTEs in the WFA: their total content, leaching, and legislation limits (LL) [36].

Element	Leaching	LL [37]	Times over LL (for leaching)
	mg/kg	mg/kg	
Sb	< 0.02	0.32	–
As	< 0.1	0.9	–
Ba	2.9 ± 0.3	22	–
Cd	0.10 ± 0.01	0.04	2.5
Co	< 0.1	0.54	–
Cr	1.9 ± 0.2	0.63	3
Cu	0.10 ± 0.01	0.9	–
Hg	< 0.001	0.02	–
Mo	6.7 ± 0.7	1	6.7
Ni	< 0.01	0.44	–
Pb	26 ± 3	2.3	11.3
Se	< 0.02	0.15	–
Sn	< 0.02	0.4	–
V	< 0.05	1.8	–
Zn	21 ± 2	4.5	4.7

In addition to high metal concentrations, WFA leachates after the standard leaching test contain large amounts of chloride (110 ± 10 g/kg) and sulfate (50 ± 1 g/kg). It is similar to the previous findings, where the effectiveness of a water treatment is shown [9,38–40].

3.2 Selection of complexing agents

Na-Gl and EDTA were selected because they are less aggressive than strong acids or bases, change the pH within 1.5 points only, which is important if being compared with water, and show their effectiveness in the extraction of Zn and Pb from WFA [8,38]. Thus, besides eliminating chloride and sulfate, these treatments elute PTEs. To test their effectivity, three independent treatments were performed (L/S 5; 20 min): water only, EDTA (0.05M), and Na-Gl (0.05M).

The results (Figure 2) show that, firstly, each of them efficiently elutes different metals, and secondly, they different affect the standard leaching test results for the treated material. Na-Gl is more effective in most cases (except for Ba, Sr, Mo, and Cd). It is vital to acknowledge its ability to elute major WFA matrix elements, calcium, aluminum, and iron. This may lead to matrix decomposition releasing an additional portion of PTEs, which could not be released during the standard leaching test or treatment with water. PTEs, which showed the excess over the LL according to the standard leaching test, were Cr, Cd, Mo, Pb, and Zn. However, significant amounts of Cu (by Na-Gl) and Cd (by EDTA) can also be liberated from WFA due to high stability constants ($\log\beta_{1,Cu-EDTA} = 18$; $\log\beta_{1,Cu-Gl} = 36$; $\log\beta_{1,Cd-EDTA} = 17$; and $\log\beta_{1,Cd-Gl} = 10$) [41–43]. Being complementary, both agents were used sequentially in one treatment (COMBY) to elute the maximum number of PTEs [36].

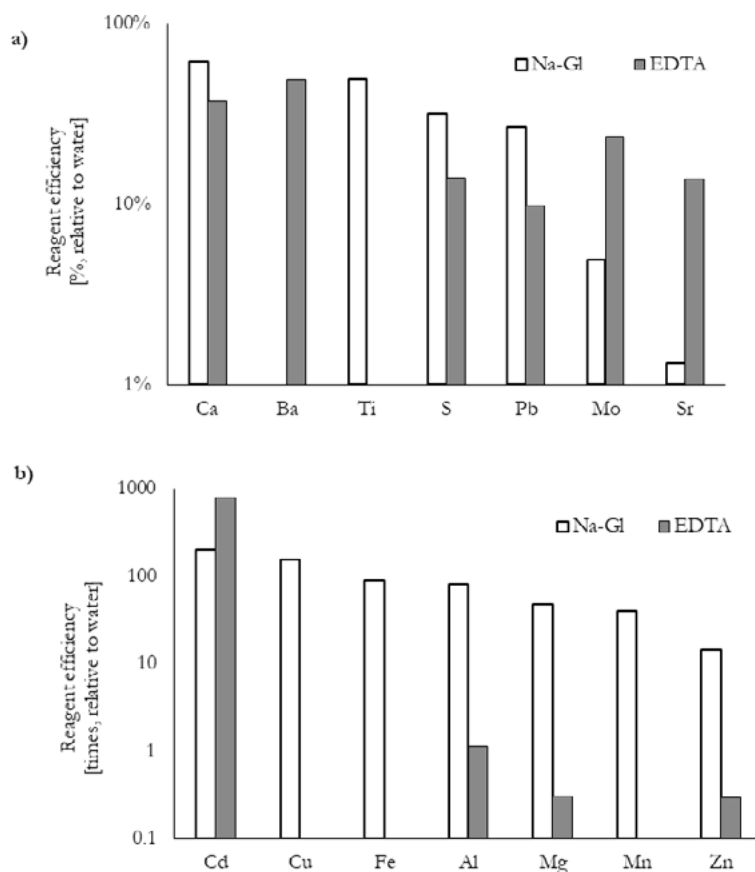


Figure 2: Reagent efficiency relative to water: a) for elements, it is comparable to water) b) for elements, it is much higher than for water [36].

3.3 Two-reagent and water-only treatment comparison

Treatment parameters are the time of contact, L/S, and the number of steps. The priority task was to make a treatment which ensures the efficient chloride elution because its concentration is 100-fold higher than the LL. For a decrease in the chloride level by 98-99%, 15-30 min of washing is enough [7,28,38,39]. In several studies, several-steps washing with L/S 1-3 proved to be more efficient than single-step ones with larger L/S [7,39,44,45]. In most papers on this topic, the number of washing steps is limited to 2-3 [28,39]. Given that the studied WFA is severely polluted (Table 1) and retains a large water amount (about 30% after being in contact with water for about 20 min), we used a three-step washing procedure to remove the contaminated water. To minimize its amount, L/S 2 (relative to the initial sample mass) was used at each step. This ratio was selected empirically by obtaining a WFA–water paste with a viscosity low enough for its rapid mixing. EDTA was used at the first step as it elutes large amounts of Cd (*ca.* 1000-fold higher than the LL), and this also provided more iterations of rinsing out the contaminated water after this step. During the second step, Na-Gl was applied, and during the third, distilled water. All three steps together (¹EDTA/²Na-Gl/³water) comprise COMBY. For the sake of comparison, a WATER-3 treatment was applied. The procedure is the same as COMBY but instead of additives, only distilled water was used at all steps [36].

3.3.1 Treatment results (elution)

Figure 3 shows the step-by-step elution for certain elements during both treatments. Taking into consideration that, for almost all metals, each step provides a significant PTE liberation, the number of steps cannot be less than three. The elution character for these two treatments differs for all metals (Figure

3). For WATER-3, the concentrations of almost all the metals decrease in each step. This could be attributed to a change in pH at each step, however during COMBY pH drops are similar (see Figure 3 insets). For COMBY, the pH after the first step decreases more than with WATER-3. This probably occurs due to the removal of alkaline compounds (mainly Ca) with EDTA. A pH change after the second step is the same, so the elution of such metals as Pb and Zn would have to be even less than in the first step [46], but it is the opposite. Thus, it is worthwhile to look for another reason for such an elution character [36].

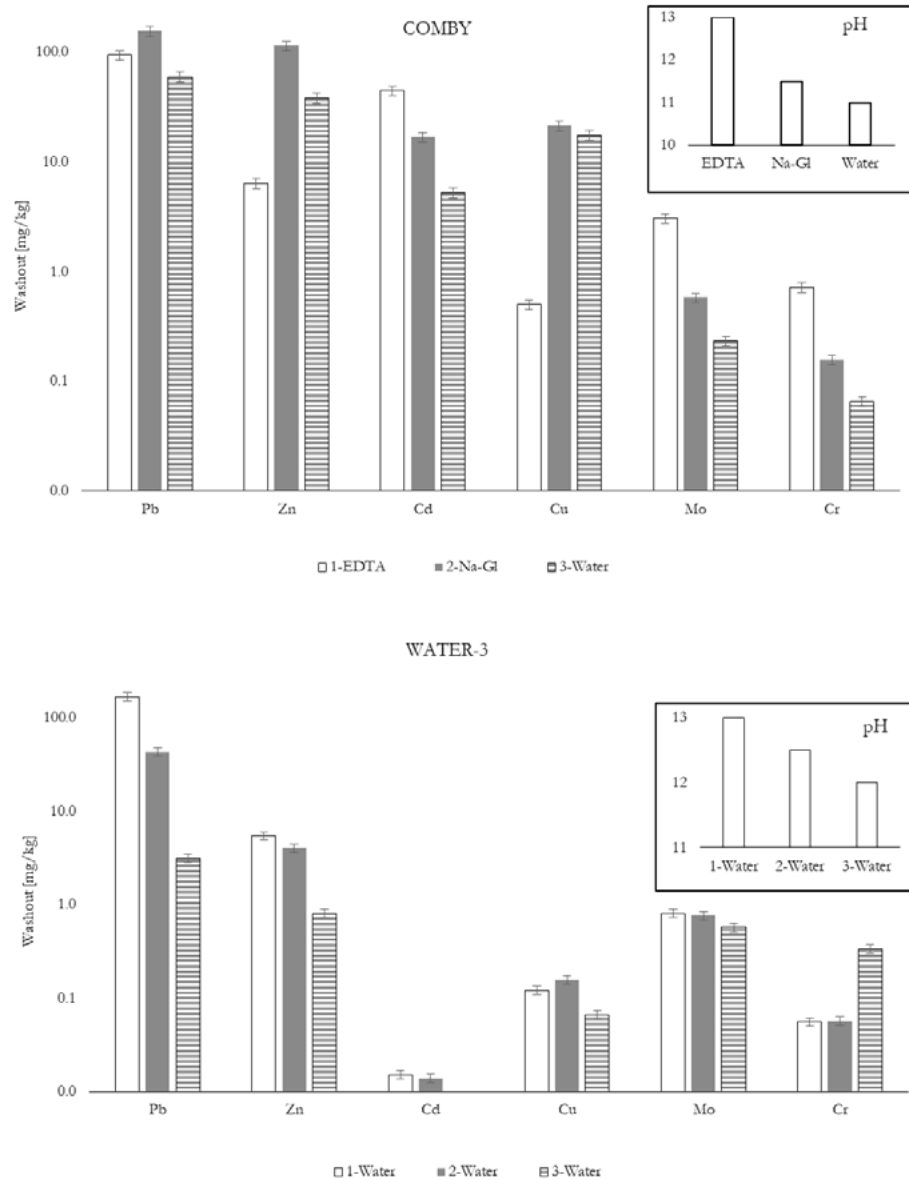


Figure 3: Elution of metals during WATER-3 and COMBY treatments for each step; insets: pH of the washing waters during each step [36].

3.3.2 Standard leaching test results on treated WFA

Table 2 presents the standard leaching test results (L/S 10) for both treatments. Only elements with concentrations above the LL are shown. It is worthwhile to give a small remark regarding the LLs for chloride and sulfate. In this study, the environmental legislation for CCFA (LL (sulfate), 30,000 mg/kg; LL (chloride), 1000 mg/kg) could have been applied [47] because WFA is closer in some properties to CCFA rather than to MSWI bottom ash. However, because hereby no evidence of complete WFA similarity to CCFA was presented, the legislation criteria for non-shaped building materials were used instead, see Table

2 [37]. It is rather negligible in the context of this study because the goal was not to demonstrate the WFA leaching results after a treatment, but to show what changes the WFA undergoes. The treatment selection or other decision regarding the further utilization of WFA can be made using these criteria though. Therefore, the LL values are taken for clarity, so that the challenge level can be estimated.

Table 2: Standard leaching test results for untreated WFA and after treatments (for metals which concentrations exceed the legislation limit (LL)); underlined, more than the LL; bold, became worse after the treatment; italicized, became better after the treatment [36].

Element	Leaching test		Leaching test results (after treatments)	
	WFA untr.	LL	COMBY	WATER-3
			mg/kg	
Cd	0.10 ± 0.01	0.04	10 ± 1	< 0.02
Cr	2.0 ± 0.2	0.63	0.50 ± 0.05	4.4 ± 0.4
Cu	0.10 ± 0.01	0.9	3.6 ± 0.4	< 0.02
Pb	21 ± 2	2.3	85 ± 9	< 0.05
Mo	6.7 ± 0.7	1	1.4 ± 0.2	<u>3.3 ± 0.3</u>
Zn	21 ± 2	4.5	38 ± 4	0.40 ± 0.04
			g/kg	
Cl ⁻	110 ± 10	0.62	1.6 ± 0.2	<u>1.9 ± 0.2</u>
SO ₄ ²⁻	50 ± 5	2.4	19 ± 2	<u>16 ± 2</u>

Table 2 shows that COMBY causes a strong increase in the PTE leaching except for Cr and Mo. In general, COMBY, which elutes matrix elements such as Ca, Fe, Al, Mg, and Zn, promotes the liberation of PTEs enclosed in the matrix (Figure 2). At the same time, WATER-3 elutes orders of magnitude less amounts of these matrix elements, keeping PTEs inside. Therefore, after WATER-3, the concentrations of a considerable number of PTEs (except for Cr and Mo) are below the LL. Both treatments were not targeted to completely elute anions. Table 2 shows that both treatments were similarly effective in eluting chloride (COMBY, 99%; WATER-3, 98%), and close to each other for sulfate elution (COMBY, 62%; WATER-3, 68%).

Table 2 shows that Cd leaching from the untreated WFA (using the standard leaching test) is only twofold higher than the LL (0.10 mg/kg). However, COMBY increased Cd leaching by about 100 times (10 mg/kg), while during WATER-3 it has decreased by more than fivefold (< 0.02 mg/kg). At the first two steps of WATER-3, a very small amount of Cd was liberated (0.03 mg/kg, Figure 3), while during COMBY it was much larger at all the three steps (67.0 mg/kg). As at three steps of COMBY, the eluted Cd amount is decreasing (45, 17, and 5 mg/kg, respectively), while the matrix component elution at the 1st step for water and EDTA is similar, it might be concluded that EDTA transformed all available Cd to soluble species on the surface layers. If some additional Cd sources would have been uncovered by dissolving the matrix, an increase in its concentration at each subsequent step would have been observed. The ability of Na-Gl to elute Cd is also significant (0.10 mg/kg), although less than of EDTA due to a lower complexation constant (Section 3.2), and despite its use in the second step of COMBY, an increase in concentration also did not occur. As WATER-3 is reagent-free, only a small amount of soluble Cd got into the washing water (0.04 mg/kg), and the standard leaching test indicates WFA-WATER-3 as apparently non-hazardous. However, a very significant increase in the cadmium leaching using chelating agents shows that such a “clean” WFA may have a hazard under the action of environmental substances [48].

Figure 3 shows that a significant amount of Cr (0.7 mg/kg) is liberated at the 1st step of COMBY, less at the second step (0.2 mg/kg), and at the third step a negligible amount (0.1 mg/kg) is eluted, and according to the standard leaching test results its level satisfies the regulations. At the same time, for WATER-3, a small amount (0.1 mg/kg) of Cr is liberated at the first two steps, and at the third step its amount increases

threefold. Eventually, WFA-COMBY leaches twofold Cr (4.4 mg/kg) as the untreated WFA (2.0 mg/kg). The solution pH decreases during the treatment; however, at pH 8-13, Cr leaching does not vary this much [46]. On the other hand, Figure 4 illustrating a comparison of Mg, Al, and Fe leaching at all steps, reveals that it is 2-3-fold larger at the first step of COMBY (and Mg is not released at all at the first step of WATER-3), and at the 2nd and 3rd steps for COMBY, the elution of these components is 1-2 orders of magnitude higher than that of WATER-3. It might be suggested that Cr is encapsulated in the matrix. Thus, as for Cd, the standard leaching test with L/S 10 does not show how much Cr will potentially leach out later, during the use of WFA-based materials.

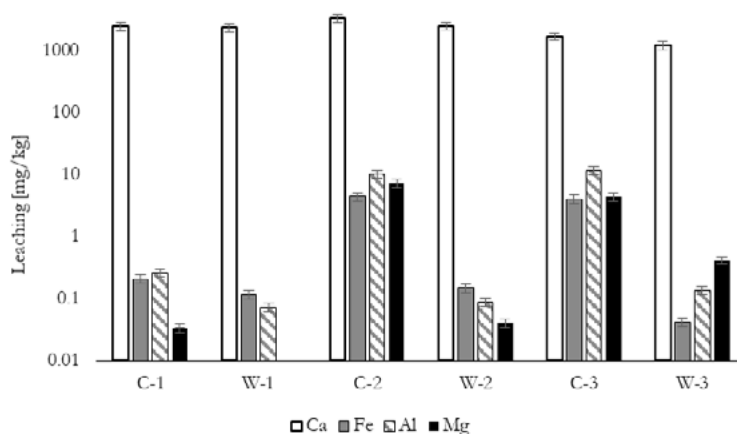


Figure 4: Matrix components elution during COMBY (marked C) and WATER-3 (marked W) treatments [36].

Considering the standard leaching test results (Table 2), for untreated WFA Cu leaching was below the LL, but after COMBY it has increased significantly. The character of Cu elution differs from cadmium (for which the standard leaching test results after treatments were similar, Figure 3 and Table 2). Apart from very high complexation constants, the reason for such an elution character is also the matrix decomposition, elements are liberated 10-fold less effectively at the first step of COMBY, as if blocking Cu leaching. For WATER-3, these components are liberated only slightly, so approximately the same Cu elution is observed at all three steps.

After WATER-3, the concentration of Pb in leachates is less than the LL; however, after COMBY, the WFA looks extremely hazardous (Table 2). In addition, even in the case of WATER-3, much more Pb is liberated at the first (168.8 mg/kg) and subsequent (43.5 and 3.2 mg/kg) stages than during the standard leaching test on the untreated WFA (Figure 3, contact times are 20 min at every washing step and 24 h for the standard leaching test). This can be explained by the fact that during the standard leaching test, calcium salts can re-precipitate (e.g. CaSO_4), with which Pb salts tend to co-precipitate [49]. Thus, in a short time of COMBY this does not happen, and all available Pb transfers to the solution. This phenomenon is not observed for other metals because their chlorides and sulfates have rather high solubilities.

Mo concentration in leachates have decreased after both treatments, and for COMBY it was close to the LL (Table 2). The elution character in both cases as well indicates a link to the elution of matrix components: in WATER-3 it is slow, so at all steps a similar amount of metal is liberated (0.8, 0.8, and 0.6 mg/kg, respectively); for COMBY, a much larger amount is eluted immediately (3.1 mg/kg), presumably, because of a high complexation constant ($\log \beta_{\text{L,Mo-EDTA}} = 20$) [31], and at the following steps it decreases (0.6 and 0.2 mg/kg). The standard leaching test for the untreated WFA showed 6.7 ± 0.7 mg/kg of Mo, and the mass balance for treatments and liberated/left amounts for COMBY was $3.9 \pm 0.4 / 1.4 \pm 0.1 = 5.3 \pm 0.5$ mg/kg, and for WATER-3 was $2.2 \pm 0.2 / 3.3 \pm 0.3 = 5.5 \pm 0.5$ mg/kg, indicating that, probably, the rest of Mo (Table 1) is encapsulated in the silicate matrix and is unlikely to pose further threat.

For WATER-3, Zn level has decreased to an environmentally acceptable level (Table 2). However, for COMBY, it has become twofold worse than before the treatment. During WATER-3, it is very probable that only readily soluble Zn species are eluted, and at every step the elution decreases (5.5, 4.0, and 0.8 mg/kg). For COMBY, there is no significant Zn leaching at the first step (6.4 mg/kg), but at the second one, 18-fold higher amounts of the metal eluted (115.4 mg/kg). This can result from the matrix elements beginning to be effectively liberated at the Na-GI step of COMBY, entailing enhanced Zn leaching [36].

4. Conclusions

Thus, the leaching properties of untreated and treated WFA are studied. As a whole, the efficiency of a three-step combined treatment with two complexing agents (ethylenediaminetetraacetate and gluconate) to increase the toxic-element elution from fly ash in contrast to conventional water-only treatments is shown.

- The main metal impurities in the WFA are Cd, Cr, Mo, Pb, and Zn. Their leaching exceeds the legislation limits by 3-11 times. The leaching of anions exceeds the corresponding limits by 25-1000 times. Leaching of chloride is 110 g/kg, and sulfate is 50 g/kg.
- The ability of gluconate to elute metals from the WFA is especially efficient (10-200-fold higher than of water) for Cd, Cu, and Zn; and EDTA is the most efficient for Cd (800-fold higher than of water).
- The ability of combined treatment to elute metals in comparison with water-only is 40% higher for Pb, 15 times higher for Zn, 1800 times higher for Cd, 115-fold higher for Cu, and 2 times higher for Mo and Cr.
- As a result of combined treatment, the WFA has become even more hazardous than before the treatment. In the case of water-only treatment, the WFA appears to be much cleaner than before the treatment.

It is necessary to highlight that the same WFA, which, according to the leaching test results, looks non-hazardous from almost all points after being washed with water, proves to be extremely hazardous (it matches the criteria for even more hazardous category than the untreated one). The aim underneath this research is to draw attention to the issue of WFA processing once again. If the extraction of metals turns out to be economically feasible for a certain country, it would be rather insubstantial to incorporate the material in concrete. We believe that these findings will help in issues related to treating, processing, and utilizing WFA. For further research, it is expedient to study the mechanisms of mutual elution of matrix components and PTEs in detail, as well as to investigate the structure of WFA and how, if used as secondary building materials, it affects the target material properties. The full data on this completed study can be found here [36].

5. Acknowledgements

The authors express their gratitude to Katrin Schollbach (TU/e Eindhoven) for her advice in preparing the manuscript text. The authors express their gratitude to the NWO/TTW-foundation (project 13318, Development of eco-concretes by using industrial by-products), Van Gansewinkel Minerals, Attero, ENCI, v.d. Bosch Beton, Struyk Verwo, and CRH Europe Sustainable Concrete Centre for their provision of material, knowledge and financial support in this project, as well as to the Cement-Concrete-Immobilisates sponsor group at TU Eindhoven: Rijkswaterstaat Grote Projecten en Onderhoud, Graniet-Import Benelux, Kijlstra Betonmortel, Rijkswaterstaat Zee en Delta - District Noord, BTE, Selor, GMB, Geochem Research, Icopal, BN International, Eltomation, Knauf Gips, Hess AAC Systems, Kronos, Joma, Cement&BetonCentrum, Heros, Inashco.

6. References

- [1] J.J.J.M. Goumans, H.A. van der Sloot, T.G. Aalbers, Waste materials in construction, in: Proc. Int. Conf. Environ. Implic. Constr. with Waste Mater., Elsevier, Maastricht, the Netherlands, 10-14 November 1991, 1991: p. 672.
- [2] C.C. Wiles, Municipal solid waste combustion ash : State of the knowledge, J. Hazard. Mater. 3894 (1995) 20. doi:10.1016/0304-3894(95)00120-4.
- [3] M. Kamon, T. Katsumi, Y. Sano, MSW fly ash stabilized with coal ash for geotechnical application, J. Hazard. Mater. 76 (2000) 265–283. doi:10.1016/S0304-3894(00)00203-X.
- [4] B. Nowak, P. Aschenbrenner, F. Winter, Heavy metal removal from sewage sludge ash and municipal solid waste fly ash — A comparison, Fuel Process. Technol. 105 (2013) 195–201. doi:10.1016/j.fuproc.2011.06.027.
- [5] B. van der Bruggen, G. Vogels, P. van Herck, C. Vandecasteele, Simulation of acid washing of municipal solid waste incineration fly ashes in order to remove heavy metals, J. Hazard. Mater. 57 (1998) 127–144. doi:10.1016/S0304-3894(97)00078-2.
- [6] C.W. Lovell, T.C. Ke, W.H. Huang, J.E. Lovel, Bottom ash as highway material, in: 70th Annu. Meet. Transp. Res. Board, Transportation Research Board, Washington, DC, 1991: pp. 106–116. <http://onlinepubs.trb.org/Onlinepubs/trr/1991/1310/1310-014.pdf>.
- [7] T. Mangialardi, Effects of a washing pre-treatment of municipal solid waste incineration fly ash on the hydration behaviour and properties of ash—Portland cement mixtures, Adv. Cem. Res. 16 (2004) 45–54. doi:10.1680/adcr.2004.16.2.45.
- [8] C. Ferreira, A.B. Ribeiro, L.M. Ottosen, Study of different assisting agents for the removal of heavy metals from MSW fly ashes, in: D. Almorza, C.A. Brebbia, D. Sales, V. Popov (Eds.), Waste Manag. Environ., WIT Press, Southampton, 2002: pp. 171–179. <https://www.witpress.com/Secure/elibrary/papers/WM02/WM02018FU.pdf>.
- [9] T. Mangialardi, Disposal of MSWI fly ash through a combined washing-immobilisation process, J. Hazard. Mater. 98 (2003) 225–240. doi:10.1016/S0304-3894(02)00359-X.
- [10] T.T. Eighmy, B.S. Crannell, L.G. Butler, F.K. Cartledge, E.F. Emery, D. Oblas, J.E. Krzanowski, J.D. Eusden, E.L. Shaw, C.A. Francis, Heavy metal stabilization in municipal solid waste combustion dry scrubber residue using soluble phosphate, Environ. Sci. Technol. 31 (1998) 3330–3338. doi:10.1021/es970407c.
- [11] M.J. Quina, J.C.M. Bordado, R.M. Quinta-Ferreira, Chemical stabilization of air pollution control residues from municipal solid waste incineration., J. Hazard. Mater. 179 (2010) 382–92. doi:10.1016/j.jhazmat.2010.03.016.
- [12] X. Li, Q. Chen, Y. Zhou, M. Tyrer, Y. Yu, Stabilization of heavy metals in MSWI fly ash using silica fume, Waste Manag. 34 (2014) 2494–2504. doi:10.1016/J.WASMAN.2014.08.027.
- [13] H. Ecke, Sequestration of metals in carbonated municipal solid waste incineration (MSWI) fly ash, Waste Manag. 23 (2003) 631–640. doi:10.1016/S0956-053X(03)00095-3.
- [14] A. De Boom, J.-E. Aubert, M. Degrez, Carbonation of municipal solid waste incineration electrostatic precipitator fly ashes in solution, Waste Manag. Res. 32 (2014) 406–413. doi:10.1177/0734242X14527637.

- [15] M.-Y. Wey, K.-Y. Liu, T.-H. Tsai, J.-T. Chou, Thermal treatment of the fly ash from municipal solid waste incinerator with rotary kiln, *J. Hazard. Mater.* 137 (2006) 981–989. doi:10.1016/j.jhazmat.2006.03.024.
- [16] F. Huber, D. Blasenbauer, O. Mallow, J. Lederer, F. Winter, J. Fellner, Thermal co-treatment of combustible hazardous waste and waste incineration fly ash in a rotary kiln, *Waste Manag.* 58 (2016) 181–190. doi:10.1016/j.wasman.2016.09.013.
- [17] A.J. Pedersen, Evaluation of assisting agents for electrodialytic removal of Cd, Pb, Zn, Cu and Cr from MSWI fly ash, *J. Hazard. Mater.* 95 (2002) 185–198. doi:10.1016/S0304-3894(02)00138-3.
- [18] C. Kersch, G.F. Woerlee, G.J. Witkamp, Supercritical Fluid Extraction of Heavy Metals from Fly Ash, *Ind. Eng. Chem. Res.* 43(1) (2003) 190–196. doi:10.1021/ie030114u.
- [19] K. Karlfeldt Fedje, C. Ekberg, G. Skarnemark, E. Pires, B.-M. Steenari, Initial studies of the recovery of Cu from MSWI fly ash leachates using solvent extraction, *Waste Manag. Res.* 30 (2012) 1072–1080. doi:10.1177/0734242X12441385.
- [20] J. Tang, B.M. Steenari, Solvent extraction separation of copper and zinc from MSWI fly ash leachates, *Waste Manag.* 44 (2015). doi:10.1016/j.wasman.2015.07.028.
- [21] G. Weibel, U. Eggenberger, S. Schlumberger, U.K. Mäder, Chemical associations and mobilization of heavy metals in fly ash from municipal solid waste incineration, *Waste Manag.* 62 (2017) 147–159. doi:10.1016/j.wasman.2016.12.004.
- [22] J. Tang, M. Petranikova, C. Ekberg, B.-M. Steenari, Mixer-settler system for the recovery of copper and zinc from MSWI fly ash leachates: An evaluation of a hydrometallurgical process, *J. Clean. Prod.* 148 (2017) 595–605. doi:10.1016/J.JCLEPRO.2017.02.015.
- [23] L. Bertolini, M. Carsana, D. Cassago, A.Q. Curzio, M. Collepardi, MSWI ashes as mineral additions in concrete, *Cem. Concr. Res.* 34 (2004) 1899–1906. doi:10.1016/j.cemconres.2004.02.001.
- [24] O. Ginés, J.M. Chimenos, A. Vizcarro, J. Formosa, J.R. Rosell, Combined use of MSWI bottom ash and fly ash as aggregate in concrete formulation: Environmental and mechanical considerations, *J. Hazard. Mater.* 169 (2009) 643–650. doi:10.1016/j.jhazmat.2009.03.141.
- [25] N. Saikia, S. Kato, T. Kojima, Production of cement clinkers from municipal solid waste incineration (MSWI) fly ash, *Waste Manag.* 27 (2007) 1178–1189. doi:10.1016/J.WASMAN.2006.06.004.
- [26] F. Colangelo, F. Messina, R. Cioffi, Recycling of MSWI fly ash by means of cementitious double step cold bonding pelletization: Technological assessment for the production of lightweight artificial aggregates, *J. Hazard. Mater.* 299 (2015) 181–191. doi:10.1016/j.jhazmat.2015.06.018.
- [27] J.E. Aubert, B. Husson, N. Sarramone, Utilization of municipal solid waste incineration (MSWI) fly ash in blended cement. Part 1: Processing and characterization of MSWI fly ash, *J. Hazard. Mater.* 136 (2006) 624–631. doi:10.1016/j.jhazmat.2005.12.041.
- [28] C. Hoi, K. Lam, J. Patrick, B. Bullet, G. McKay, Utilization of municipal solid waste incineration ash in Portland cement clinker, *Clean Technol. Environ. Policy.* 13 (2011) 607–615. doi:10.1007/s10098-011-0367-z.
- [29] D.P. Mishra, S.K. Das, A study of physico-chemical and mineralogical properties of Talcher coal fly ash for stowing in underground coal mines, *Mater. Charact.* 61 (2010) 1252–1259. doi:10.1016/J.MATCHAR.2010.08.008.

- [30] H. Kitamura, T. Sawada, T. Shimaoka, F. Takahashi, Geochemically structural characteristics of municipal solid waste incineration fly ash particles and mineralogical surface conversions by chelate treatment, *Environ. Sci. Pollut. Res.* 23 (2016) 734–743. doi:10.1007/s11356-015-5229-5.
- [31] A.E. Martell, L.G. Sillén, *Stability Constants of Metal-ion Complexes: Inorganic ligands*, Chemical Society, London, 1971. <https://books.google.ru/books?id=wU1amQEACAAJ>.
- [32] N. Alba, S. Gassó, T. Lacorte, J.M. Baldasano, Characterization of Municipal Solid Waste Incineration Residues From Facilities with Different Air Pollution Control Systems, *J. Air Waste Manage. Assoc.* 47 (1997) 1170–1179. doi:10.1080/10473289.1997.10464059.
- [33] N. Saqib, M. Bäckström, Chemical association and mobility of trace elements in 13 different fuel incineration bottom ashes, *Fuel*. 172 (2016). doi:10.1016/j.fuel.2016.01.010.
- [34] R. Ito, G. Dodbiba, T. Fujita, J.W. Ahn, Removal of insoluble chloride from bottom ash for recycling, *Waste Manag.* 28 (2008) 1317–1323. doi:10.1016/j.wasman.2007.05.015.
- [35] EN 12457-4, *Characterisation of waste - Leaching - Compliance test for leaching of granular waste materials and sludges*, CEN, 2002.
- [36] E. Loginova, M. Proskurnin, H.J.H. Brouwers, Municipal solid waste incineration (MSWI) fly ash composition analysis: A case study of combined chelant-based washing treatment efficiency, *J. Environ. Manage.* 235 (2019) 480–488. doi:10.1016/J.JENVMAN.2019.01.096.
- [37] Dutch Soil Quality Decree, Regulation of the State Secretary for Housing, Planning and the Environment and the State Secretary for Transport, Public Works and Water Management, The Netherlands, *Staatscourant* nr. 469, 3 December 2007, 2007. <https://zoek.officielebekendmakingen.nl/stb-2007-469.html>.
- [38] F. Colangelo, R. Cioffi, F. Montagnaro, L. Santoro, Soluble salt removal from MSWI fly ash and its stabilization for safer disposal and recovery as road basement material, *Waste Manag.* 32 (2012) 1179–1185. doi:10.1016/j.wasman.2011.12.013.
- [39] A. De Boom, M. Degrez, Combining sieving and washing, a way to treat MSWI boiler fly ash, *Waste Manag.* 39 (2015). doi:10.1016/j.wasman.2015.01.040.
- [40] E. Mulder, Pre-Treatment of MSWI fly ash for useful application, *Waste Manag.* 16 (1996) 181–184. doi:10.1016/S0956-053X(96)00040-2.
- [41] D.T. Sawyer, Metal-Gluconate Complexes, *Chem. Rev.* 64 (1964) 633–643. doi:10.1021/cr60232a003.
- [42] P. Warwick, N. Evans, S. Vines, Studies on metal gluconic acid complexes, 29th Int. Symp. Sci. Basis Nucl. Waste Manag. 932 (2005) 959–966.
- [43] Dojindo, Metal Chelates, *Anal. Biol. Prod.* (2017) 252–253. https://www.dojindo.com/Images/Product Photo/Chelate_Table_of_Stability_Constants.pdf.
- [44] D.H. Vu, K.-S. Wang, J.-H. Chen, B.X. Nam, B.H. Bac, Glass–ceramic from mixtures of bottom ash and fly ash, *Waste Manag.* 32 (2012) 2306–2314. doi:10.1016/j.wasman.2012.05.040.
- [45] C. Ferone, F. Colangelo, F. Messina, L. Santoro, R. Cioffi, Recycling of Pre-Washed Municipal Solid Waste Incinerator Fly Ash in the Manufacturing of Low Temperature Setting Geopolymer Materials, *Materials (Basel)*. 6 (2013) 3420–3437. doi:10.3390/ma6083420.

- [46] M.J. Quina, J.C.M. Bordado, R.M. Quinta-Ferreira, The influence of pH on the leaching behaviour of inorganic components from municipal solid waste APC residues, *Waste Manag.* 29 (2009) 2483–2493. doi:10.1016/j.wasman.2009.05.012.
- [47] G.C.H. Doudart de la Grée, M.V.A. Florea, A. Keulen, H.J.H. Brouwers, Contaminated biomass fly ashes - Characterization and treatment optimization for reuse as building materials, *Waste Manag.* 49 (2015) 96–109. doi:10.1016/j.wasman.2015.12.023.
- [48] J. Buffle, F.L. Greter, W. Haerdi, Measurement of complexation properties of humic and fulvic acids in natural waters with lead and copper ion-selective electrodes, *Anal. Chem.* 49 (1977) 216–222. doi:10.1021/ac50010a012.
- [49] H. Lu, W. Zhang, Y. Yang, X. Huang, S. Wang, R. Qiu, Relative distribution of Pb²⁺ sorption mechanisms by sludge-derived biochar, *Water Res.* 46 (2012) 854–862. doi:10.1016/j.watres.2011.11.058.

Synthesis optimization for hydrophobic surface modification of MSWI bottom ash fines

Q. Alam, T. Dezaire, F. Gauvin, and H.J.H. Brouwers

Department of the Built Environment, Eindhoven University of Technology, P. O. Box 513, 5600 MB, Eindhoven, the Netherlands..

Abstract

In this study, hydrophobic functionalization of the ≤ 0.125 mm fraction of municipal solid waste incineration (MSWI) bottom ash by creating a hydrophobic surface layer was investigated, focusing on the optimization of the surface modification protocol. Moreover, the influence of surface modification on the leaching behavior of bottom ash was studied. The original and hydrophobic bottom ash (BA) was analyzed with X-ray photoelectron spectroscopy (XPS). Hydrophobicity was assessed with static contact angle measurements with the sessile drop technique. The hydrophobic layer was grafted with a wet-chemistry method, in which 1H, 1H, 2H, 2H-perfluorooctyl triethoxysilane (fluorosilane) were tested. First, the reaction conditions were optimized and the influence of weight percentage (wt.%) of the functionalizing agent, the solvent, pH, and reaction temperature on the static water contact angle (CA) were investigated. The surface characterization involved investigating the nature of adsorption, especially differentiation between physically and chemically adsorbed functionalizing agents. Subsequently, one-batch leaching test was performed to determine the influence of hydrophobic functionalization on the leachability of heavy metals, chloride and sulphates.

Keywords: Hydrophobic, Surface functionalization, MSWI, Bottom ash, Leaching

1. Introduction

In recent years, municipal solid waste incineration (MSWI) has attracted increased interest as a waste-to-energy conversion technique due to the rapid worldwide increase in solid waste generation. Landfilling, as a widely used but least favorable waste disposal technique, is facing increased challenges related to growing environmental concerns and land space restrictions [1]. MSWI accomplishes a volume reduction of 70-90%, and energy recovery 20-30% for electricity or up to 80% if used for heating. After incineration, a small amount of approximately 30 wt.% inert incineration ash remains [2]. These incineration ashes comprise large quantities of inert by-products [3]. Bottom ash (BA) is the most abundant by-product, accounting for more than 80% concerning generated volumes [4]. Due to the recent Dutch initiative “Green Deal B-76” in 2020, 100% of BA produced in the Netherlands must be upgraded to primary building material level [5].

Earlier studies have shown that BA can be used as an aggregate in concrete [1]. However, MSWI BA is often contained heavy metals, chlorides, and sulfates [6,7], making it unsuitable for application in building materials without a proper pre-treatment. Currently, the BA undergoes a treatment, which involves separation of unburnt materials, removal of metals, followed by sieving and washing. After this treatment, only the BA fraction with sizes between 4 and 32 mm is used in building materials. However, the fraction with particle sizes below 4 mm, which is rich in contaminants has limited applications [8,9]. Recently, a combination of washing and sieving has been successfully applied to this <4 mm fraction [10], bringing

the leaching of contaminants under the Dutch legal limit. However, the clean fraction of BA was obtained by removing the finest particles, sized below 0.125 mm, from the bottom ash fraction before and during washing. This fraction contains the most contaminants and contributes the most to the leaching of heavy metals, chlorides, and sulfates. To meet the goals set by the Green Deal initiative, proper treatment of these fine particles is required.

This study will investigate a treatment method for the ≤ 0.125 mm fraction. Since removing the contaminants from these particles appeared to be challenging, modification of the particles will be studied to prevent leaching of contaminants. Because these contaminants are leached by water, it is presumed that hydrophobic functionalization of the fine particles could decrease the leachability [11,12]. Still, even when hydrophobic functionalization does not help to decrease the leaching of contaminants, making the particles hydrophobic will add a new useful property to the material. Consequently, the research question of this project is the following: what is a suitable treatment for the hydrophobic functionalization of the ≤ 0.125 mm MSWI BA fraction, preventing leaching of heavy metals, chlorides, and sulfates? A wet-chemistry method will be investigated to modify the particle properties. Hydrophobicity of the acquired samples will be assessed, and the method will be optimized accordingly. After the wet-chemistry treatment, the bottom ash surface will be characterized to investigate the nature of adsorption, after which the influence of the treatment on the leaching behavior will be examined. The objective of this research is the development of a wet-chemistry treatment for the MSWI BA particles sized below 0.125 mm, making it hydrophobic, the characterization of the functionalized surface, and the subsequent investigation of the influence of the hydrophobic functionalization on the leachability of heavy metals, chlorides, and sulfates.

2. Methodology

2.1 Materials

BA ≤ 4 mm used in this study was provided by Heros Sluiskil, the Netherlands. The received BA ≤ 4 mm fraction was then separated into three different fractions, ≤ 0.125 mm (BA-S), 0.125 – 1 mm (BA-M), and 1–4 mm (BA-L), using a vibratory sieve shaker (Retsch AS 450 Basic) according to DIN EN 933-1. The BA-S fraction was used in this study. 1H, 1H, 2H, 2H-perfluorooctyl triethoxysilane (98%) was purchased from Sigma-Aldrich. NaOH tablets ($\geq 97.0\%$) and 32% HCl were purchased from VWR Chemicals.

2.2 Methods

2.2.1 Functionalization protocol

5 g of BA was refluxed for 5 hours in a conventional reflux set-up in a round bottom flask of 250 ml, in a mixture with 150 ml ethanol, 50 ml water and a specific amount of fluorosilane. Before adding the bottom ash, first, the silane was hydrolyzed at pH 3–4 (fluorosilane) for 1 h. After the reaction, the bottom ash was separated from the reaction mixture by vacuum filtration, and dried overnight at 60 °C. The influence of the following parameters were investigated: mass ratio silane – bottom ash, pH of the mixture (adjusted with droplets of 0.1 M NaOH or 0.1 M HCl solution to a pre-determined pH-value), and reaction temperature.

2.2.2 Hydrophobicity assessment

Static water contact angles (CA) were measured using the sessile drop technique (Dataphysics CA Systems OCA, TBU 90E) to assess the degree of hydrophobicity. The samples were prepared by pressing approximately 5 g of BA together at 40 kN for 1 minute in a 40 mm diameter press tablet set. Water droplets of 2.000 μ L were disposed on the surfaces of these tablets. Reported CA values to correspond with the average measured CA of five separate measurements, and the margin of error was defined as the 95% confidence interval of these five measurements.

2.2.3 Material characterization

TGA measurements were performed using a Perkin Elmer Pyris 6 TGA 400 System, in the temperature range 45 - 600 °C at a heating rate of 1 °C/min, under a nitrogen flow of 40 ml/min. The surface elemental composition was analysed with X-ray photoelectron spectroscopy (XPS) using a Thermo Scientific K-alpha spectrometer equipped with a monochromatic Al K α X-ray source.

2.2.4 Leaching tests

Leaching tests were performed with the most hydrophobic sample for each compound. Leaching liquids were obtained by shaking a mixture of approximately 4 g BA and 40 g distilled water (L/S ratio 10), for 24 h in a horizontally placed, sealed PE bottle on a linear reciprocating shaking device (Stuart SSL2) at a constant rate of 250 rpm with the amplitude of 20 mm. After the extraction, leachates were filtered. The liquid was diluted 5 times in a 25 ml volumetric flask. The liquid was acidified with 50 μ l 6.5 wt.% ultrapure HNO₃ solution to prevent precipitation and subsequently filtered again. The contents of the leaching liquids were determined by inductively coupled plasma-optical emission spectroscopy (ICP-OES; Varian 730-ES). Furthermore, the concentrations of sulfates and chlorides in the leachates were determined by ion chromatography (IC) (Dionex 1100) equipped with an ion exchange column AS9-HS (2 \times 250 mm). A 9 mM solution of Na₂CO₃ was used as an eluent with an isocratic flow of 0.25 ml/min. The detection of ions was done by measuring suppressed conductivity using an electrolytically regenerated suppressor (Dionex AERS 500, 2 mm).

3. Results and discussion

3.1 Surface modification

The influence of the wt.% of fluorosilane relative to the BA mass, pH of the solvent, and reaction temperature on the CA values were investigated. The result of the wt.% variation on the contact angle of modified sample is shown in Figure 1. and the results of the pH and reaction temperature variation are shown in Figure 2.

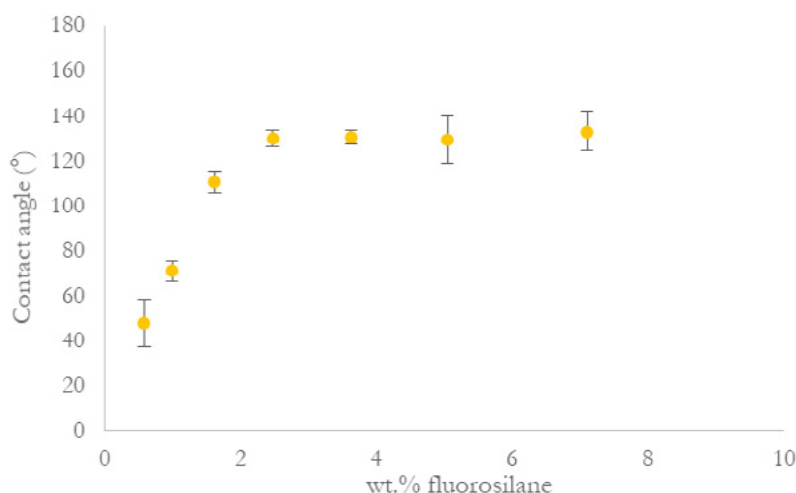


Figure 1. The contact angle values of the modified bottom ash with the addition of fluorosilane (wt.%).

Figure 1 shows the expected relation between the wt.% functionalizing agent and the contact angle values. The plateau value was reached around at 2.5 wt.%. Further addition of the functionalization agent did not result in the increase of contact angle. Moreover, no significant influence of the solvent pH and reaction temperature was observed as shown in Figure 2. An optimum temperature was expected in the temperature

variation graph, because of the difference between the expected optimum temperature of hydrolysis and condensation equilibria, however, the result did not correspond with the expectations. This could mean that the equilibria do not change in this process when the temperature is changed, likely because the utilized functionalizing agent is already completely hydrolyzed during the activation before the condensation reaction starts. Aside from the influences of reaction temperature, pH and wt.% fluorosilane, Figure 1 shows that the fluorosilane yielded very hydrophobic samples. The best samples were obtained with a wt.% above 2.5 wt.%, at a pH of 13, and with a reaction temperature of 70 °C. The most hydrophobic sample had an average CA of $142^\circ \pm 3.5$. One of the measurements of this sample is shown in Figure 3.

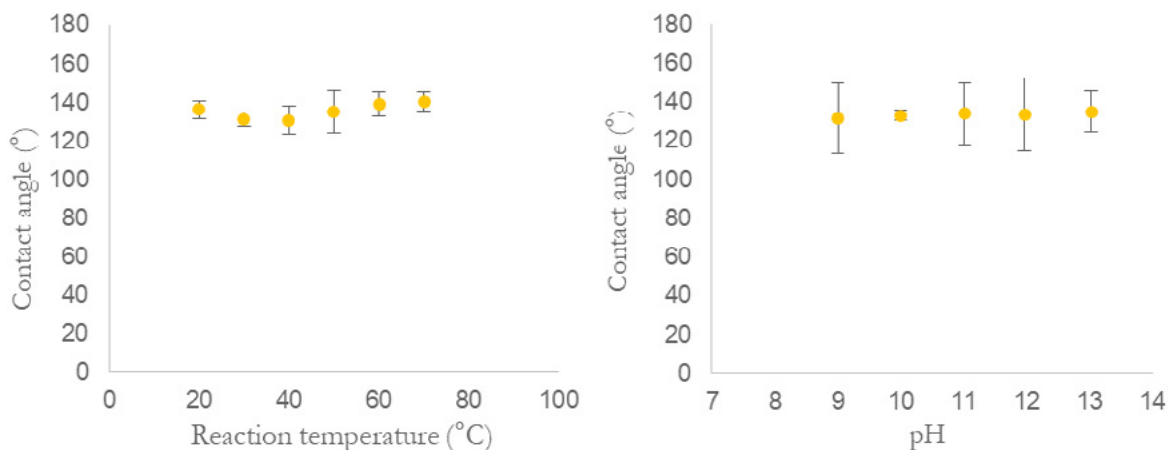


Figure 2. The effect of synthesis temperature (left side) and pH (right side) on the contact angle of hydrophobic bottom ash.

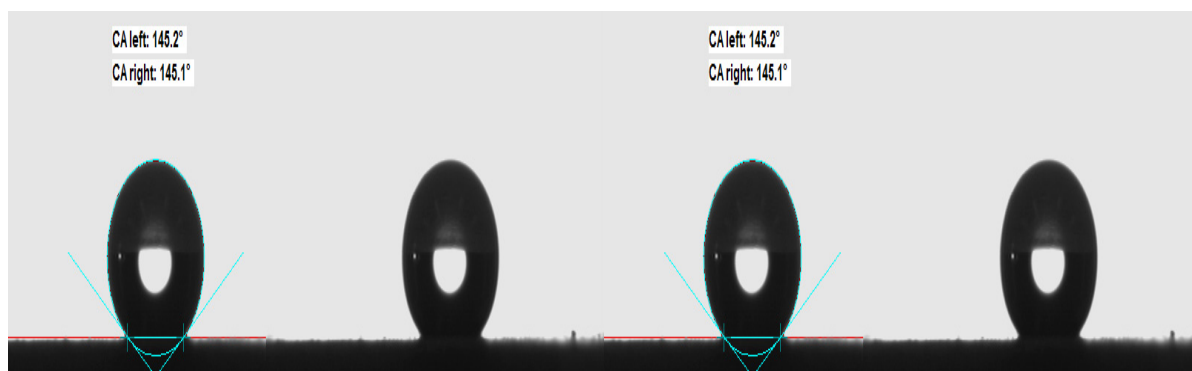


Figure 3. The contact angle of the hydrophobic bottom ash modified with 5.14% of fluorosilane, measured via sessile drop technique.

It is interesting to notice that the contact angle values of samples with high fraction of fluorosilane show a large margin of error. The part of the large error margin can be explained by the measurement technique itself since CAs are measured with static contact measurements, which have in general a relatively high margin of error. Especially with hydrophilic surfaces (in case of original bottom ash fraction), the margin of error was big with static contact angle measurements, because water droplets tend to collapse gradually within a few seconds. Because of the time delay between surface contact and the actual contact angle measurement, static contact angle measurements gave less unambiguous results, especially with hydrophilic surfaces. Another factor was the preparation of the sample. To get representative results for the sample as a whole, a homogeneous distribution of the different minerals in BA is necessary. The functionalizing agent could react better or worse with different minerals. During the investigation, however, it was observed that some samples had a more homogeneous distribution of different phases than others as shown in Figure 4.

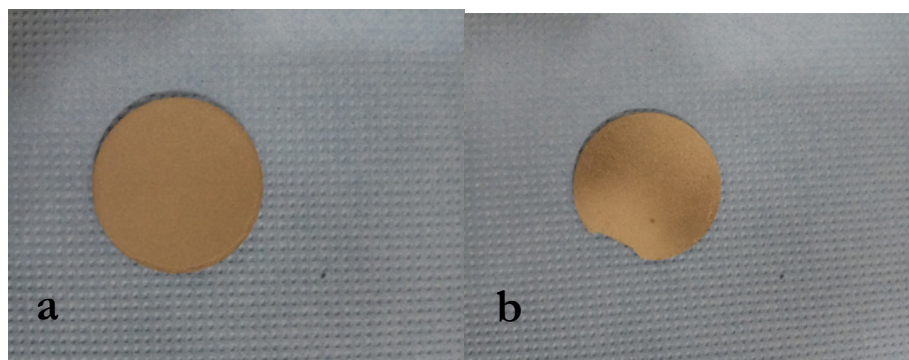


Figure 4. (a): pressed tablet of homogeneously distributed BA, visible as a uniform color of the tablet. And (b): pressed tablet of heterogeneously distributed BA, visible as darker and lighter areas in the tablet.

3.2 Surface characterization

The elemental composition of the surface was determined with XPS. The measurements were carried out on the silane reference sample and on the most hydrophobic sample of BA modified with fluorosilane. The results are shown in Table 1.

Table 1. Atomic percentage of elements on the surfaces of untreated BA, the most hydrophobic BA sample after treatment with fluorosilane and the atomic percentages in the original compounds.

Sample	O _{1s} (%)	Ca _{2p} (%)	C _{1s} (%)	Al _{2s} (%)	Na _{1s} (%)	F _{1s} (%)
0% silane reference	63.6	9.6	17.4	7.4	1.9	-
BA + fluorosilane	40.5	6.7	23.7	7.4	-	21.7
Pure fluorosilane	12	-	32	-	-	52

Table 1 shows that all samples have a surface composition that consists of oxygen atoms and some smaller amounts of Ca, C, Al, and a little Na in the case of the 0% silane reference sample. These atomic concentrations suggested that the surface of the BA particles mainly consists of carbonates and aluminates. This analysis also showed that some Na was present at the surface. According to earlier studies, Na indeed accumulates at the surface in the form of NaCl [10]. Analysis of the functionalized samples showed that the amount of Na atoms on the surface decreased below the detection limit when a layer of the functionalizing agent was applied on the surface, probably due to the dissolving of NaCl during the functionalization process.

3.3 Thermogravimetric Analysis

Figure 5 shows the TGA of BA functionalized with 5.14 wt.% fluorosilane, compared to a reference sample that was treated similarly to the fluorosilane sample, except that no fluorosilane was added to the reaction mixture. The figure shows that two steps could be distinguished, where the derivate of the weight plots diverged. The first weight loss step took place between 45 and 165 °C, whereas the second weight loss step took place between 225 and 472 °C.

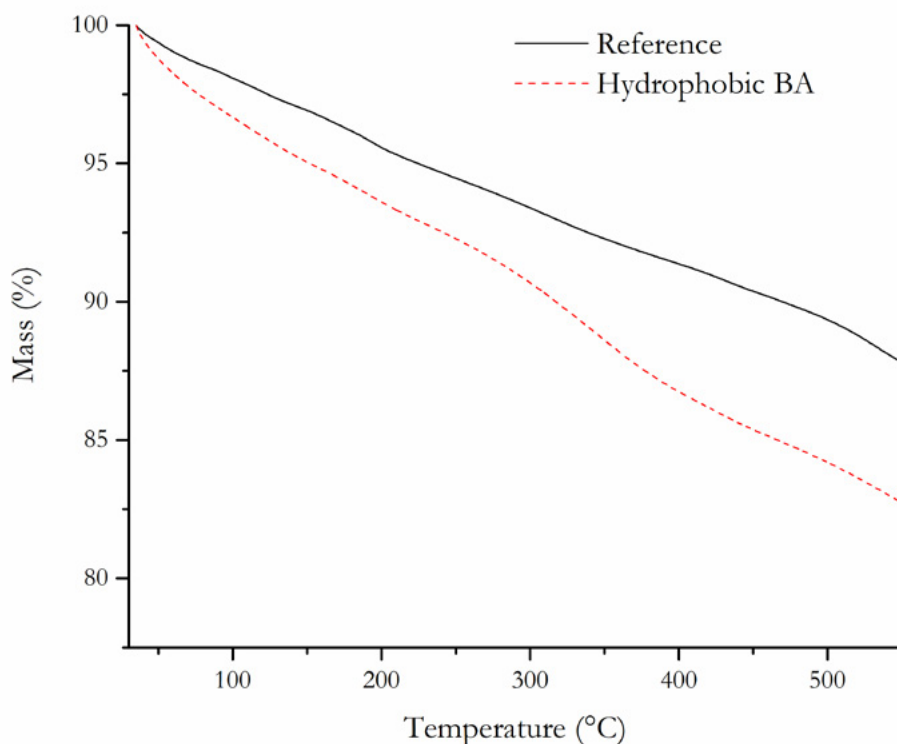


Figure 5. Thermogravimetric analysis of BA-S functionalized with 5.14 % (m/m) of FS, and reference (BA-S underwent same modification protocol in the absence of FS).

The weight losses in the first step, was approximately 2 percent point higher than the weight loss of the reference sample. This weight loss could be attributed to the desorption of physisorbed fluorosilane, but also different water contents of the functionalized sample and the reference sample. In the second step, the weight loss was approximately 3% higher for the functionalized sample, which presumably corresponded to the loss of chemically bonded fluorosilane. The weight decreases was more significant in the temperature range of approximately 330 - 360 °C.

When the TGA curve of the reference sample was subtracted from the TGA curve of hydrophobic sample, the weight loss due to the functionalizing agent can be tracked. The weight loss can be divided into two different stages. The first weight loss correspond to 2% and the loss is attributed to the physisorbed silane that it is linked with surface, just due to the physical adsorption. The second step of the weight loss is accounts for 3.2%, and happens in the higher temperature ranges. Here the energy required to remove the silane from the sample indicates the presence of chemisorption. In the chemisorption, the silane are attached with the surface via silanol bonds and the breakdown of these bonds requires higher energy, which happens at the high temperature range of 330 °C onwards. The two-steps pattern of weight loss did not correspond with the predicted three-step weight loss pattern. However, it could be possible that the predicted second and third step, corresponding with respectively the desorption of physisorbed polycondensate fluorosilane and the desorption of chemisorbed fluorosilane, overlapped in this measurement. This would also be a good explanation for the big temperature range in which the observed second step takes place, compared to the much shorter weight loss step for stearic acid.

3.4 Leaching analysis

To investigate the influence of hydrophobic functionalization on the leachability, leaching test was performed, and subsequently, the leachates were analyzed with ICP-OES and IC. The results are shown in Table 12. The results of the silane samples indicated that hydrophobic functionalization with silanes slightly

decreased the leaching level compared with the untreated BA. Summarizing, hydrophobic functionalization with silanes yielded a significant reduction in contaminant leaching. Although hydrophobic samples achieved large reductions in the leaching levels, the levels of Cu, Sb, Se and SO_4^{2-} remained above the legal limits.

Table 2. Determined concentrations of contaminants after leaching tests of original and functionalized samples, and their allowed emission limits regulated by the soil quality decree. [13]

Parameters	Non-shaped materials (mg/kg d.m.)	BA ≤ 0.125 mm (mg/kg d.m.)	Hydrophobic BA (mg/kg d.m.)
Ba	22.00	0.51	0.47
Cr	0.63	1.14	0.87
Cu	0.90	6.53	2.59
Mo	1.00	1.20	0.98
Sb	0.32	0.91	0.76
As	0.90	0.16	0.17
Cd	0.04	<L.D.	<L.D.
Co	0.54	0.05	0.05
Pb	2.30	<L.D.	0.03
Ni	0.44	0.07	0.06
Se	0.15	0.45	0.39
Sn	0.40	<L.D.	<L.D.
V	1.80	0.12	0.13
Zn	4.50	0.52	1.07
Cl ⁻	616	11,367	537
SO_4^{2-}	1,730	20,979	19,483

4. Conclusions

The hydrophobicity of the BA ≤ 0.125 mm fraction was successfully modified from hydrophilic to hydrophobic. As expected, the highest contact angles values (CA) were obtained with high fraction of fluorosilane ($> 2.5\%$), with values reaching the superhydrophobic range (145°). The amount of added functionalizing agent appeared to be the only influential factor on the hydrophobicity: Indeed, the pH, reaction time, and temperature did not have a significant influence on the hydrophobicity as seen with CA measurements. The threshold of weight fraction of fluorosilane that can react with the BA-S was characterized to be around $2.5 - 3 \%$ (m/m). Adding more fluorosilane did not increase the hydrophobicity of the BA-S because as characterized by TGA and GC-MS, the excess of silane cannot be chemically bonded to the active sites and therefore forms additional silane layer that is physisorbed to the BA. Moreover, leaching of potentially toxic elements Cr, Cu, Mo and Sb from the functionalized bottom ash reduced by 28, 61, 13 and 22 %, respectively. The decrease in the leaching is attributed to the functionalized protocol in which these contaminants were washed away and after the modification due to the hydrophobic nature of particles.

5. Acknowledgment

The authors would like to acknowledge the financial support provided by NWO (Nederlandse Organisatie voor Wetenschappelijk Onderzoek), the Netherlands, under the project number 10019729: “Environmental concrete based on the treated MSWI bottom ashes”. Special thanks to Prof. dr. A. Caballero Martinez from the department of chemical engineering for providing us with XPS.

6. References

- [1] A. Abbà, M.C. Collivignarelli, S. Sorlini, M. Bruggi, On the reliability of reusing bottom ash from municipal solid waste incineration as aggregate in concrete, *Compos. Part B Eng.* 58 (2014) 502–509. doi:10.1016/j.compositesb.2013.11.008.
- [2] R. del Valle-Zermeño, J.M. Chimenos, J. Giró-Paloma, J. Formosa, Use of weathered and fresh bottom ash mix layers as a subbase in road constructions: Environmental behavior enhancement by means of a retaining barrier, *Chemosphere*. 117 (2014) 402–409. doi:10.1016/J.CHEMOSPHERE.2014.07.095.
- [3] X. Dou, F. Ren, M.Q. Nguyen, A. Ahamed, K. Yin, W.P. Chan, V.W.-C. Chang, Review of MSWI bottom ash utilization from perspectives of collective characterization, treatment and existing application, *Renew. Sustain. Energy Rev.* 79 (2017) 24–38. doi:10.1016/j.rser.2017.05.044.
- [4] C.C. Wiles, Municipal solid waste combustion ash: State-of-the-knowledge, *J. Hazard. Mater.* 47 (1996) 325–344. doi:10.1016/0304-3894(95)00120-4.
- [5] V.G. Groep, B. V Twence, B-76 Green Deal : More sustainable practical use of EfW plant clinker, n.d.
- [6] Q. Alam, K. Schollbach, C. van Hoek, S. van der Laan, T. de Wolf, H.J.H. Brouwers, In-depth mineralogical quantification of MSWI bottom ash phases and their association with potentially toxic elements, *Waste Manag.* 87 (2019) 1–12. doi:10.1016/J.WASMAN.2019.01.031.
- [7] Q. Alam, K. Schollbach, M.V.A. Florea, H.J.H. Brouwers, Investigating washing treatment to minimize leaching of chlorides and heavy metals from MSWI bottom ash, in: 4th Int. Conf. Sustain. Solid Waste Manag., Limassol, Cyprus, 2016. <http://uest.ntua.gr/cyprus2016/proceedings/proceedings.html>.
- [8] J.M. Chimenos, A.I. Fernández, A. Cervantes, L. Miralles, M.A. Fernández, F. Espiell, Optimizing the APC residue washing process to minimize the release of chloride and heavy metals, *Waste Manag.* 25 (2005) 686–693. doi:10.1016/j.wasman.2004.12.014.
- [9] J. Chimenos, A. Fernández, R. Nadal, F. Espiell, Short-term natural weathering of MSWI bottom ash, *J. Hazard. Mater.* 79 (2000) 287–299. doi:10.1016/S0304-3894(00)00270-3.
- [10] Q. Alam, M.V.A. Florea, K. Schollbach, H.J.H. Brouwers, A two-stage treatment for Municipal Solid Waste Incineration (MSWI) bottom ash to remove agglomerated fine particles and leachable contaminants, *Waste Manag.* 67 (2017) 181–192. doi:10.1016/J.WASMAN.2017.05.029.
- [11] Y. Liu, Y. Li, X. Li, Y. Jiang, Leaching behavior of heavy metals and PAHs from MSWI bottom ash in a long-term static immersing experiment., *Waste Manag.* 28 (2008) 1126–36. doi:10.1016/j.wasman.2007.05.014.
- [12] N. Saqib, M. Bäckström, Chemical association and mobility of trace elements in 13 different fuel incineration bottom ashes, *Fuel*. 172 (2016) 105–117. doi:10.1016/j.fuel.2016.01.010.

Methods for determining and tracking the residual cement paste content of recycled concrete

P.M.F. van de Wouw¹, M.V.A. Florea¹, H.J.H. Brouwers¹

¹Department of the Built Environment, Eindhoven University of Technology, P.O. Box 513, 5600 MB Eindhoven, the Netherlands.

Abstract

The attached cement paste on recycled concrete aggregates (RCA) is the main factor causing impaired quality of the new concrete. Since attached mortar is not as hard or strong as natural aggregates, its presence weakens the overall performance of the RCA. Additionally, the attached mortar is known to cause a higher water absorption, an increased water cement ratio, and therefore a more porous and weaker concrete. Due to the negative influence of the attached mortar on the RCA properties, ideally all mortar should be removed from the original natural aggregates, returning the recycled concrete into its original aggregates and hardened cement paste (HCP). In order to study the efficiency of treatments designed to achieve this purpose, methods for estimating the amount of HCP attached to the original aggregates need to be used. Such methods, which include e.g. composition tests (XRF, XRD), thermogravimetric analysis or chemical methods are generally time-consuming and complex. In this study, a more straightforward method based on oxide composition is proposed and corroborated with the results from other test results.

Keywords: Recycled concrete, oxide composition, hardened cement paste, cement content, aggregates.

1. Introduction

Generally, it can be assumed that recycled concrete aggregate (RCA) is better applicable when its properties resemble that of natural aggregate (NA). According to Mindess et al., “aggregates should be hard and strong, free of undesirable impurities and chemically stable” [1]. The attached (residual) mortar or cement paste is the main concern in using recycled concrete aggregates in new concrete; it accounts for the main difference between NA and RCA. The attached paste on incorporated recycled concrete aggregates is the main factor causing impaired quality of the new concrete. Since attached mortar is not as hard or strong as NA, its presence weakens the overall performance of the RCA. Additionally, the attached mortar causes a higher water absorption, an increased water cement ratio, and therefore a more porous and weaker concrete [2]. Due to the negative influence of the attached mortar on the RCA properties, ideally all mortar should be removed from the original natural aggregates (ONA), returning the recycled concrete (RC) into its original aggregates and hardened cement paste (HCP). Because of depletion of geologically exploitable gravel sources in the Netherlands, a degree of reliance on imports seems unavoidable for coarse virgin aggregates [3], hereby a demand is created for the production of high quality RCA.

In order to study the efficiency of treatments designed to better separate the attached HCP from the ONA in recycled concrete fractions, methods for estimating the amount of HCP attached to the original aggregates need to be used. Such methods include e.g. oxide and mineralogical composition tests, thermogravimetric analysis for the quantification of portlandite, carbonates and free and bound water [4,5], or chemical

methods are generally time-consuming and complex [6–12]. In this study, a more straightforward method based on oxide composition is proposed and corroborated with the results from other test results.

2. Methodology

2.1 Materials

The concrete demolition waste used as initial material in this study was generated during the renovation and evacuation process of the cyclotron building at the Eindhoven University of Technology (TU/e). After the decommissioning phase, 119 concrete elements with a combined volume of 127 m³ became available for recycling. Prior to receiving the material, the steel reinforcement was removed by crushing the elements with a concrete pulveriser. Due to the fact that the concrete was predestined to be applied as road base material, the material was then crushed to RCA using an excavator operated jaw crusher with unknown settings. At this point, the material was piled up before being transferred into 1 m³ flexible intermediate bulk containers (FIBC).

2.2 Methods

2.2.1 Sample preparation

The RC fractions investigated are produced in an optimised crushing process from a course RCA fraction (>10 mm) which was obtained by screening the initial recycled concrete (RC) on a Mogensen 5 deck sizer (model: 0554), fitted with an effective screen mesh of 10.0 mm under a 15° angle, running with an 8 mm amplitude of linear vibration at a 45° angle. Consecutively, the course RCA was crushed with a jaw crusher-based crusher explicitly designed for concrete recycling with the aim of producing RCA with a high degree of HCP removal. The sampling of the processed material was done in accordance with EN 932-1 [13] from the output conveyor of the crusher. Prior to further testing, the material was oven-dried at 105 °C to a constant mass. In accordance with EN 933-1 and EN 933-2 [14,15], the materials was dry sieved, determining its particle size distribution (PSD). Additional to the mesh sizes described in EN 933-2 [15], intermediate sieves following the same logarithmic distribution were added: 91 µm, 180 µm, 355 µm, 710 µm, 1.4 mm, 2.8 mm, 5.6 mm, 11.2 mm, and 22.4 mm.

2.2.2 Composition tests

The elements in the materials (computed as oxides) were determined by energy-dispersive X-ray fluorescence (EDXRF) using a PANalytical Epsilon 3 instrument (a 9 W / 50 kV rhodium X-ray tube, a silicon drift detector) equipped with Omnian software 1.0.E (PANalytical). The samples for EDXRF were 40-mm fused beads prepared from pre-dried powdered samples, 0.95 g, with a 67.00% Li₂B₄O₇ – 33.00% LiBO₂ flux, 9.50 g; and 0.32 ml of a 4 M LiBr solution as a non-wetting agent using a LeNeo fluxer (Claisse) at 1065 °C with Pt-Au crucibles.

The loss on ignition (LOI) of the materials was determined according to EN 196-2:2005 [16], yet measuring the mass loss of samples at 1000 °C instead of 950 °C to a constant mass in accordance with [17]. The additional thermal analysis using a Netzsch STA 449 F1 Jupiter was performed by thermogravimetric analysis (TGA) to determine the mass loss for specific temperature intervals and by differential scanning calorimetry (DSC) to determine the quartz content of the various size fractions. At about 573 °C, the endothermal crystalline phase changes from α -quartz to β -quartz without loss of mass [18]. The thermal analysis was performed in Pt crucibles in inert atmosphere (N₂) up to a maximum temperature of 1000°C. The peak area on the DSC curve of both the heating and the cooling step of 20 °C / minute was analysed and correlated to measurements of samples containing a known amount of α -quartz, quantifying the quartz

content of the measured samples. In contrast to prior studies, pure quartz is used for the calibration since the quartz content of the original aggregates used is unknown [4,19–21].

3. Results and discussion

Figure 1 shows the particle size distribution and of the recycled concrete used in this study. Further on, the complete 0-45 mm particle size range will be used and the individual narrow size fractions will be quantified in terms of their composition and HCP and aggregate content.

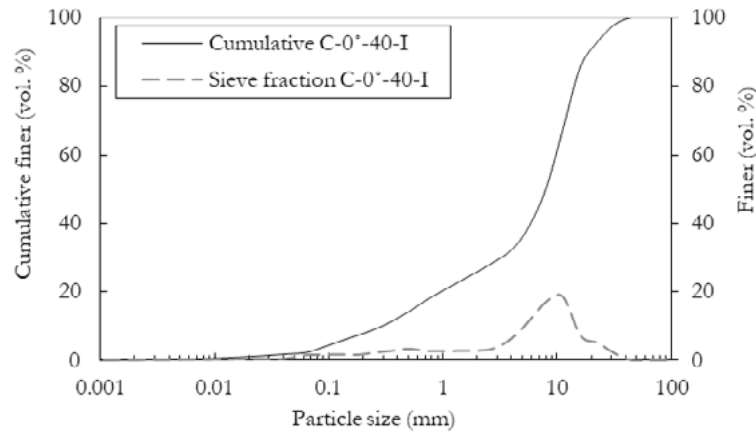


Figure 1 PSDs of the recycled concrete used

Since ENCI, currently a subsidiary of the Heidelberg Cement Group, was founded in 1926 and is the longstanding leader on the Dutch cement market, it is highly likely that ENCI cement was used for the production of the concrete. The earliest chemical composition which could be retrieved was from 1982 (Table 1). According to ENCI, this chemistry is similar to the cement which was produced in 1967. Both the clinker used in 1967 and 1982 was produced in the same wet clinker ovens 5, 6 and 7.

Figures 2 and 3 show respectively the oxide compositions determined by XRF of the recycled concrete samples for the main (Al_2O_3 , SiO_2 , CaO , and Fe_2O_3) and minor oxides (MgO , SO_3 , K_2O , TiO_2 , and MnO) for the oxides in common with the cement oxide composition (Table 1). Corresponding LOI is given in Figure 5.

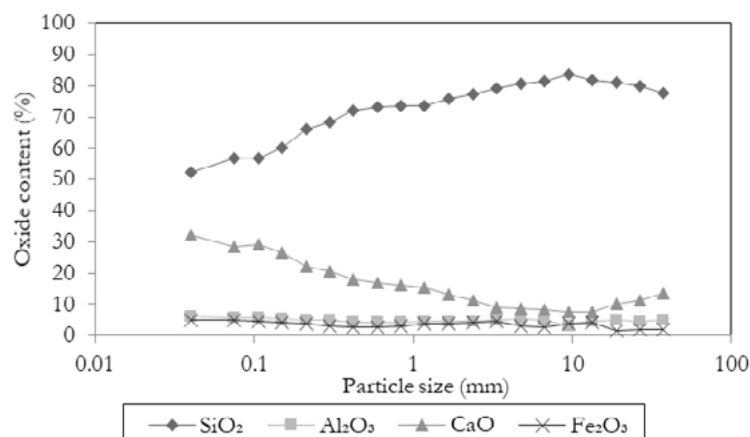


Figure 2 Al_2O_3 , SiO_2 , CaO , and Fe_2O_3 content of all RC fractions vs. particle size

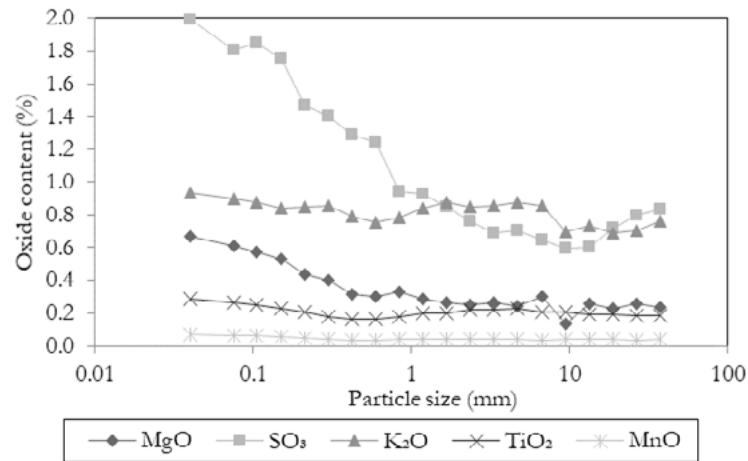


Figure 3 MgO, SO₃, K₂O, TiO₂, and MnO content of all RC fractions vs. particle size

Table 1 Cement composition, ENCI CEM I 1982

MgO	Al ₂ O ₃	SiO ₂	SO ₃	K ₂ O	CaO	TiO ₂	Cr ₂ O ₃	MnO	Fe ₂ O ₃	LOI
1.71	5.64	21.54	3.02	0.81	63.01	0.30	0.00	0.05	3.02	0.90

CaO shows a relatively constant decrease in content with an increase in particle size until it reaches a near stable value in particles larger than 5.6 mm, while SiO₂ shows an opposite trend. In the Netherlands, siliceous river aggregates are commonly used, therefore, these trends can indicate relatively clean aggregates and a concentration of cement stone in the fines. Even though visual inspection of the aggregates supports this theory, the absence of non-siliceous aggregates or siliceous fillers cannot be assured, making the quantification of the quality of liberation based on SiO₂ or CaO content uncertain. Other oxides might also not be used as cement specific tracer since Al₂O₃ and MgO can occur in natural aggregates, Fe₂O₃ content can be altered by contamination from either rebar or processing, and the deviations between the different samples for K₂O, TiO₂, and MnO can be within the measurement error of the equipment used. SO₃, however, can be used as a cement specific tracer oxide since the initial RCA is clean (from e.g. gypsum) and it is an element unlikely to be found in natural aggregates in the Netherlands. Through the oxide composition of the unhydrated cement and the SO₃ content of the RCA sample, the initial cement content is calculated (Figure 4).

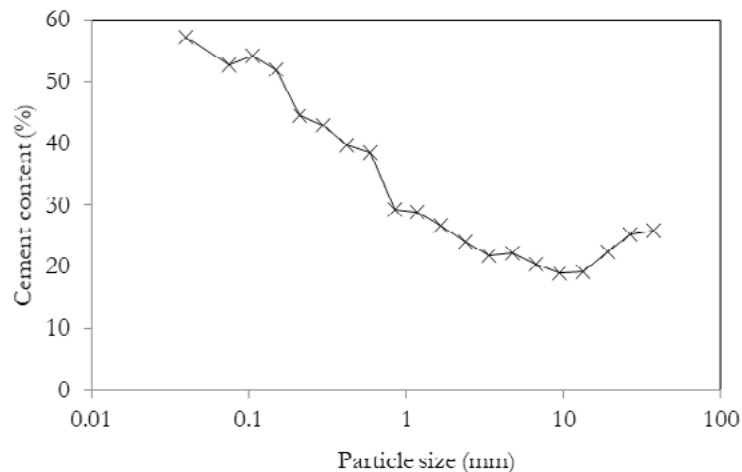


Figure 4 Calculated content of cement of all RC fractions vs. particle size

The thermogravimetric analysis of all fractions gave information about the mass losses at various temperatures, which can be correlated to the content of portlandite, calcite, and chemically bound water in the hardened cement paste for each sample [5,22]. Figure 5 shows the associated mass losses. It can be observed that the trend obtained for the cement content in Figure 5 correlates to the one of the total LOI at 1000 °C. The contents of portlandite and calcite can also be used to estimate the total hardened paste content of each fraction, but large uncertainties can be introduced by the presence of limestone aggregates or fillers, and through the carbonation of the HCP. Since the values for the portlandite content were lower than expected for uncarbonated pastes, it was decided to recalculate the carbonate content as portlandite, in order to account for the degree of carbonation of the samples.

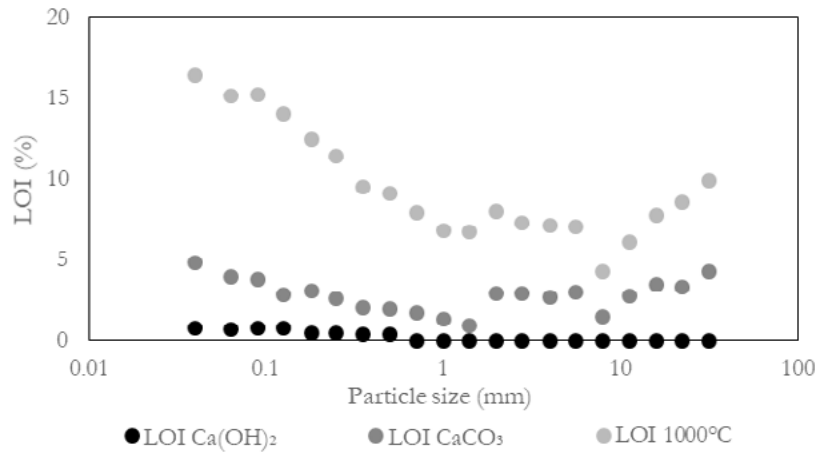


Figure 5 LOI for Ca(OH)₂, CaCO₃, and total LOI (1000°C) of all RC fractions vs. particle size

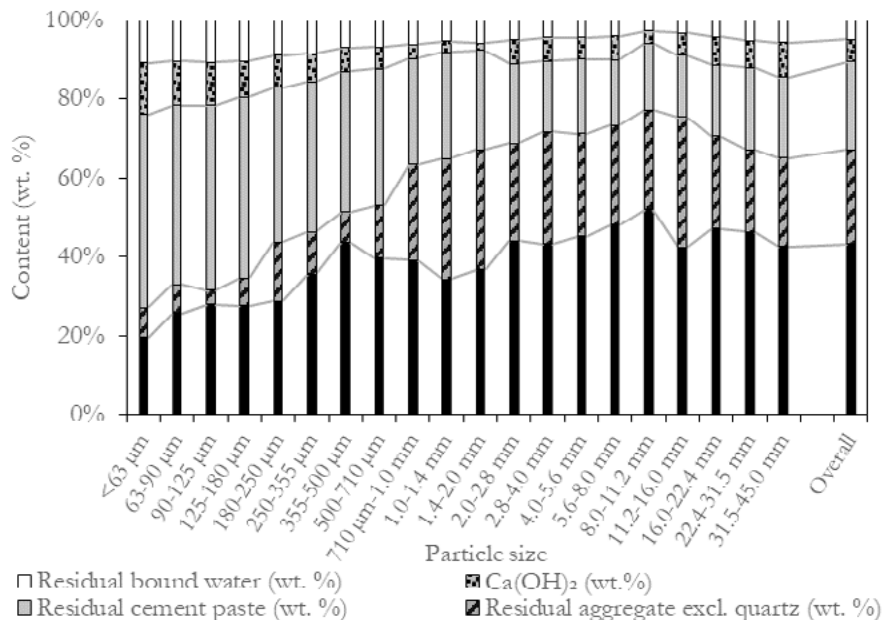


Figure 6 Estimated composition of all RC size fractions considered. HCP comprises: Ca(OH)₂, residual cement paste, and residual bound water. Aggregates include: quartz and residual aggregate contents

From the DSC measurements, the quartz content of the samples can also be accurately determined [22]. This will also be presented separately, and together with the so-termed residual aggregates, make up the complete aggregate fraction for each sample.

Collecting all the data presented above, Figure 6 shows the estimated composition of all considered recycled concrete size fractions. Here, a trend can be observed for the contents of HCP and aggregates of the samples with particle size. The content of HCP is highest for the finest particles, and then diminishes up to a particle size of 11.2-16.0 mm. For larger particles, a slight ascending trend can be observed for the HCP content. An opposite trend can be observed for the aggregate content of all samples. These findings are in line with the ones in [22], and the shift in trends >16.0 mm can be explained by the maximum aggregate size of the initial concrete. Once the size of the RC fraction produced exceeds this maximum size, the material contains more HCP, approaching the composition of the overall initial concrete for the largest fractions.

4. Conclusions

Based on the presented results and discussion it can be concluded that the proposed method is able to estimate the amount of hardened cement paste (HCP) attached to the original aggregates, solely based on its oxide composition. By using an oxide tracer in the cement, in contrast to other methods, this method is independent of the composition of both aggregates and fillers, making it suitable for a wide range of applications, given that the recycled concrete (RC) is clean.

Furthermore, the presented data shows that, out of RC, the optimised crushing method used is able to produce gravel and sand fractions which are cleared from HCP, a fine fraction enriched in HCP, and an oversized fraction (<15 wt. %) suitable for refeeding to the crushing process.

The data presented here is part of a larger study, which includes correlations between the bound water and various hydrated products, as well as a mineralogical study of the aggregates. The proposed method of using the sulphate content as a tracker for the initial cement percentage of an RC sample is then tested and validated on other recycled concrete compositions and sized, and the results compared to a complete panel of chemical and physical characterization.

5. Acknowledgment

The authors wish to express their gratitude to the NWO/TTW-foundation (project 13318, Development of eco-concretes by using industrial by-products), Mineralz, Attero, ENCI, v.d. Bosch Beton, Struyk Verwo, and CRH Europe Sustainable Concrete Centre for their provision of material, knowledge and financial support in this project, as well as to the Cement-Concrete-Immobilisates sponsor group at TU Eindhoven: Rijkswaterstaat Grote Projecten en Onderhoud, Graniet-Import Benelux, Kijlstra Betonmortel, Rijkswaterstaat Zee en Delta - District Noord, BTE, Selor, GMB, Icopal, BN International, Eltomation, Knauf Gips, Hess AAC Systems, Kronos, Joma, Cement&BetonCentrum, Heros, Inashco, Keim, Sirius International, Boskalis, NENERGY, Tata Steel, Millvision, Sappi, Studio Roex, Van Berlo Groep, PCS Innotec International, Nedvang, Baetsen, Noah (chronological order of joining).

6. References

- [1] S., Mindness, Young J F, Darwin D., Concrete, 2nd ed., Prentice Hall, Pearson Education, Inc. Upper Saddle River, NJ 07458, 2003.
- [2] R. Kumutha, K. Vijai, Strength of Concrete Incorporating Aggregates Recycled from Demolition Waste, Asian Res. Publ. Netw. 5 (2010) 64–71.
- [3] M.J. Van Der Meulen, S.F. Van Gessel, J.G. Veldkamp, Aggregate resources in the Netherlands, (2005) 379–387.
- [4] M.V.A. Florea, H.J.H. Brouwers, Properties of various size fractions of crushed concrete related to process conditions and re-use, Cem. Concr. Res. 52 (2013) 11–21. doi:10.1016/j.cemconres.2013.05.005.

- [5] Y.A. Villagrán-Zaccardi, H. Egüez-Alava, K. De Buysser, E. Gruyaert, N. De Belie, Calibrated quantitative thermogravimetric analysis for the determination of portlandite and calcite content in hydrated cementitious systems, *Mater. Struct.* 50 (2017) 179. doi:10.1617/s11527-017-1046-2.
- [6] a. Akbarnezhad, K.C.G. Ong, M.H. Zhang, C.T. Tam, Acid Treatment Technique for Determining the Mortar Content of Recycled Concrete Aggregates, *J. Test. Eval.* 41 (2013) 20120026. doi:10.1520/JTE20120026.
- [7] G. Nichols, *Sedimentology and stratigraphy*, 2009. doi:10.1017/CBO9781107415324.004.
- [8] V.W.Y. Tam, C.M. Tam, K.N. Le, Removal of cement mortar remains from recycled aggregate using pre-soaking approaches, *Resour. Conserv. Recycl.* 50 (2007) 82–101. doi:10.1016/j.resconrec.2006.05.012.
- [9] J. Walter Lee Sheppard, *Corrosion and Chemical Resistant Masonry Materials Handbook*, Noyes Publications, Park Ridge, 1986.
- [10] W.H. Kessler, D. W., Insley, H., and Sligh, *Physical Mineralogical and Durability Studies on Building and Monumental Granites of the United States*, (1940).
- [11] ICSC: International Programme on Chemical Safety and the European Commission, Calcium Chloride (Anhydrous), (2012). <http://www.inchem.org/documents/icsc/icsc/eics1184.htm> (accessed September 25, 2016).
- [12] S. Gangolli, *The Dictionary of Substances and Their Effects*: C. Royal Society of Chemistry, 1999.
- [13] EN 932-1, Tests for general properties of aggregates - Part 1: Methods for sampling, 1996.
- [14] EN 933-1, Tests for geometrical properties of aggregates - Part 1: Determination of particle size distribution - Sieving method, CEN, 2012.
- [15] EN 933-2, Tests for geometrical properties of aggregates - Part 2: Determination of particle size distribution - Test sieves, nominal sizes of apertures, CEN, 1995.
- [16] EN 196-2, Method of testing cement - Part 2: Chemical analysis of cement, CEN, 2013.
- [17] P.J. Lechler, M.O. Desilets, A review of the use of loss on ignition as a measurement of total volatiles in whole-rock analysis, *Chem. Geol.* 63 (1987) 341–344. doi:10.1016/0009-2541(87)90171-9.
- [18] Z. Shui, D. Xuan, H. Wan, B. Cao, Rehydration reactivity of recycled mortar from concrete waste experienced to thermal treatment, *Constr. Build. Mater.* 22 (2008) 1723–1729. doi:10.1016/j.conbuildmat.2007.05.012.
- [19] M.V.A. Florea, Z. Ning, H.J.H. Brouwers, Activation of liberated concrete fines and their application in mortars, *Constr. Build. Mater.* 50 (2014) 1–12. doi:10.1016/j.conbuildmat.2013.09.012.
- [20] M.V.A. Florea, H.J.H. Brouwers, Recycled concrete fines and aggregates: the composition of various size fractions related to crushing history, in: *Proc. 18th Int. Conf. Build. Mater. (IBAUSIL 2012)*, Weimar, Germany, 12-15 September 2012, 2012: pp. 1034–1041.
- [21] M.V.A. Florea, H.J.H. Brouwers, The influence of crushing method on recycled concrete properties, in: *H.C. Uzoegbo, W. Schmidt (Eds.), Proc. Int. Conf. Adv. Cem. Concr. Technol. Africa*, BAM Federal Institute for Materials Research and Testing, Berlin, Johannesburg, South Africa, 28-30 January 2013, 2013: pp. 1041–1050.

- [22] M.V.A. Florea, H.J.H. Brouwers, Properties of various size fractions of crushed concrete related to process conditions and re-use, *Cem. Concr. Res.* 52 (2013) 11–21. doi:10.1016/j.cemconres.2013.05.005.

The Optimized Application of Treated MSWI Bottom Ash in Concrete Mixtures

M.V.A. Florea¹, A. Keulen², H.J.H. Brouwers¹

¹Department of Built Environment, Eindhoven University of Technology, Eindhoven, the Netherlands

²Innovation Centre for Sustainable Construction, CRH, Amsterdam, the Netherlands

Abstract

This study investigates the suitability of municipal solid waste incineration bottom ash granulates as natural aggregate replacement in concrete mixes. Bottom ash is a heterogeneous material, consisting of glass particles, synthetic ceramics fragments, minerals (quartz, calcite, lime, feldspars), paramagnetic and diamagnetic metals and unburnt organic matter. The proportion of these constituents can vary with the particle size and will affect the properties of the final concrete mix. The separation and washing techniques also influence both the particle size and constituent proportions of the MSWI bottom ash. Therefore, different size fractions of bottom ash granulates were studied, with various dimension ranging between 0 and 20 mm. These were further separated into smaller particle ranges, and their chemical and mineralogical composition studied. Leaching tests were performed on different size fractions, along with quantifying the aluminium content. The water content and density of all materials was measured. Based on this information, new mortar and concrete recipes were designed and tested for mechanical and environmental properties. The results show that this type of material can be used successfully as aggregate in concrete recipes.

Keywords: MSWI, bottom ash, treatment, concrete, leaching

1. Introduction

Municipal solid waste incineration (MSWI) plants generate several types of solid residual materials. Typical residues of MSWI by grate combustion are bottom ash, boiler ash, fly ash and air pollution control (APC) residues, among others. Boiler ash represents the coarse fraction of the particles carried over by the flue gases from the combustion chamber, while fly ashes are made up of the fine particles in the flue gases downstream of the heat recovery units. APC residues include the fine material captured prior to effluent gas discharge into the atmosphere.

Bottom ash contains elevated concentrations of Br, Cu, Mo, Sb, Cl⁻ and SO₄²⁻, among others. Certain waste particles contain large concentrations of contaminants, which can lead to higher emissions. Experimental research has shown that the largest part of the contaminants (heavy metals) is absorbed by the smaller size bottom ash particles (sludge). Chimenos [1] quantified the metal content of bottom ash by particle size, concluding that the concentrations of Pb, Zn, Cu, Mn, Sn, Cr, Ni and Cd all peak in the 0-2 mm fraction and continue to decrease steeply in bottom ash particles in the 2-6 mm fraction; larger particles have much lower metal concentrations. Mueller et al. [2] also studied the distribution of certain contaminants in the bottom ash. Acid and water soluble chlorides and sulphates, as well as aluminium were found to decrease in concentration with the increase of particle size. The leaching of chlorides and sulphates, as well as of ionic species of Cu and Sb are evaluated in [3].

Upgrading MSWI bottom ash to a new building material is a sustainable approach which leads to lower

landfilled quantities of the material as well as reducing the demand for natural aggregates in concrete. In order to obtain a suitable building material from the bottom ash, a complex sequence of treatment steps is necessary. These treatment steps include fractionation, metal recovery (both ferrous and non-ferrous), screening and wet cleaning of the bottom ash into a clean granulate fraction. The use of bottom ash particles as aggregates in mortars and concretes have been studied in literature. Al-Rawas et al. [4] used bottom ash as sand replacement in mortars, up to 40% of natural sand; all samples achieved a higher compressive strength than the reference after 28 days. However, the slump of the samples decreased significantly with the increase of bottom ash use.

The use of bottom ash as concrete aggregate is also investigated by Müller and Rübner [2]. Two mechanisms are identified as the cause of durability issues in concrete containing bottom ash- the reaction of metallic aluminium in bottom ash with the alkali environment, and the possibility of ASR. Pera et al. [5] used 4-20 mm bottom ash as aggregate in concrete. The study found that bottom ash has a lower density, a higher water demand and lower strength than natural gravel. Moreover, the main detrimental factor was the content of metallic aluminium. It is concluded that, if the bottom ash is alkali-treated to remove the metallic aluminium, it can be used as 50% replacement of aggregates in concrete without affecting the durability. The review in [6] concluded that concrete incorporating bottom ash as 50% replacement of aggregates can achieve a 28 days compressive strength of 25 MPa. Courard et al. [7] proposed the use of bottom ash as aggregate in concrete pavement tiles; the conclusion is that a sufficiently aged bottom ash (minimum six weeks) that has undergone post-incineration treatment (removal of ferrous parts and sieving) can be successfully used for this purpose. Moreover, sufficient compaction was deemed necessary, to compensate the higher water demand of the bottom ash.

2. Treatment methods of MSWI bottom ash granulates

Sabbas et al. [8] summarize the possible treatments for bottom ash. The main classes of such operations are physical and chemical separation, stabilization/solidification techniques and thermal treatment. The first category comprises a larger number of possible treatment steps, which are commonly used in combination to treat bottom ashes: size separation, magnetic separation, eddy current separation, washing, chemical extraction/precipitation etc. The second category comprises weathering (aging) of the bottom ash, as well as the use of binders for immobilizing contaminants. Santos et al. [9] concluded from a literature review that a weathering step reduces the leaching of Pb, Mo and Zn from bottom ash, but it is not useful in the case of Cr, Cu and Sb. Mangialardi [10] found that a washing step is capable of removing the contaminants (Al, Cd, Pb, Zn) through two different mechanisms: precipitation of aluminium hydroxide and adsorption of cadmium, lead and zinc ions onto floc particles of $Al(OH)_3$.

Three treatment sequences were used to generate the materials investigated in this study. All final treated bottom ash fractions are termed FCG, and referred to by their particle sizes. A first material, termed FCG 0-8, was selected from bottom ash treated following a 3-steps process. An improved line of treatment was used to generate a 2-20 mm fraction, referred to as FCG 2-20. The differences between the treatment stages and the obtained granulates will be described in detail in the following section.

2.1 Phase 1 of bottom ash treatment

The first cleaning treatment of bottom ash comprised five steps, which include both physical and chemical separation steps, as classified in [8]:

Step 1. Weathering fresh MSWI bottom ash

The fresh material is weathered for around 6 months. Weathering reduces the quantitative leaching of heavy

metals (e.g. copper) and further reduces the reactivity of the material.

Step 2. Dry separation MSWI bottom ash

Bottom ash from the depot is first treated by extracting the large fraction of ferrous metals < 400 mm (overhead magnet). The generated bottom ash fraction is crushed to obtain a 0-40 mm fraction.

Step 3. Dry separation and metals recovery

The fraction 0-40 mm is treated with overhead magnets and separated in many smaller fractions. The fractions are treated with overhead magnets and with 3 eddy current magnet systems for optimal recovery of non-ferrous metals. Organics and plastics are largely recovered. All mineral fractions are mixed together generating one mineral granulate fraction 0-40 mm. A 0-8 fraction of the bottom ash is separated after this stage, which will be investigated further under the name of “FCG 0-8” in order to show the relevance of the washing step on the whole treatment phase.

Step 4. Wet separation and washing treatment

The mineral bottom ash fraction 0-40 mm is treated in a mobile washing plant. The input fraction is firstly separated from ferrous parts with overhead magnet and then split into four fractions: an organic floating fraction, a 0-63 µm sludge, a fine granulate 63 µm-2 mm fraction and a coarse granulate fraction 2-40 mm. The organic fraction is reused in the incineration process. The sludge fraction contains the largest amount of heavy metals and salts. The wet cleaning technique is based on concentrating the potential contaminants from the input fraction into the sludge fraction. The fine granulate fraction is more or less a sandy fraction and the coarse fraction is a stony/glassy granulate fraction. The washing water from the washing plant is treated and filtered and reused within the process. No process water discharge is needed. The washed granulate fraction 2-40 mm is further treated with the mobile ferrous and non-ferrous unit.

Step 5. Final treatment of the bottom ash granulate

The total washed fraction 2-40 mm is treated with overhead magnet reducing the total of small ferrous particles. In addition, extra non-ferrous metals are recovered with an eddy current system.

This final material is then separated in three fractions: a 0-8 mm, an 8-16 mm and a 16-40 mm.

2.2 Phase 2 of bottom ash treatment

Freshly produced MSWI bottom was also treated on site to produce a new building material. The initial fresh bottom ash consists of 80% mineral material (sintered ash, stone, glass and ceramics), 5-13% ferrous metals, 2-5% non-ferrous metals (Cu, Al, Zn, Pb) and 1-3% unburnt organic material (paper, textiles, plastic). The final fraction is a 2-20 mm heterogeneous aggregate, which is called FCG. The treatment process is a combination of dry and wet separation techniques [11-13], which can be divided into five separate steps. Since these five steps present multiple differences from the two treatment lines presented above, they will be described again in detail.

Step 1. Weathering of fresh MSWI bottom ash

Freshly produced bottom ash (a batch of 1000 t) is transported from the MSWI incineration towards a depot. The fresh material is weathered for around 3 months. Longer weathering can strongly influence the further oxidation of ferrous and non-ferrous metals.

Step 2. Dry separation MSWI bottom ash

The weathered bottom ash is first treated by extracting the large fraction of ferrous metals < 400 mm using an overhead magnet. The generated bottom ash fraction is separated with a drum sieve (60 mm mesh) in two fractions, particles under 31.5 mm and above 31.5 mm. Both fractions are again treated by extracting the large fraction of ferrous metals using 2 overhead magnets. The fraction 0-31.5 mm is the input material for the 3rd step and is further treated, extracting large non-ferrous metals, large minerals e.g. stones and slag and the large unburnt organic fraction.

Step 3. Wet separation and washing treatment

The mineral bottom ash fraction 0-31.5 mm is treated with a mobile wet separation-washing plant; this step is similar to Step 4 presented in the case of FCG 0-8, with the difference that in this process the maximum particle size is 31.5 mm instead of 40 mm.

Step 4. Dry separation and metals recovery washed granulate

The washed granulate fraction 2-31.5 mm is treated with an overhead magnet for the separation of ferrous metals and separated in two fractions: 2-16 mm and 16-31.5 mm. Both fractions are treated with an overhead magnet and additionally with a cascade double sequenced eddy current magnet system for optimal recovery of non-ferrous metals. A separation into two divided partial fractions is needed, creating more favourable particle size fractions and particle densities, which is needed for an optimal non-ferrous recovery. The fraction 16-31.5 mm is additionally treated (handpicked) for the recovery of stainless steel. Both fractions are mixed together generating one mineral granulate fraction. Step 4 is the final treatment step for introducing the granulate (non-shaped) building material as base material for the road and construction industries. However, an additional step is necessary for generating a material which is usable as concrete constituent.

Step 5. Final treatment of the bottom ash granulate (for application in concrete)

The final fraction of Step 4 can be additionally treated for application in concrete. The total fraction is treated with a drum magnet, reducing the amount of small ferrous particles, which would interact with the cementitious matrix when applied in concrete and thus lead to a change in colour of the product. In addition, extra non-ferrous metals are recovered with a double sequenced eddy current system. The total fraction is finally sieved (mesh 22 mm) into a final granulate fraction 2-20 mm. The final FCG fraction contains 55-60% SiO₂, ~ 10% CaO and ~ 6% Al₂O₃, which is close to other secondary building materials used in concrete. This fraction will be investigated further in this study, and referred to as FCG 2-20.

2.3 Leaching behaviour of the MSWI bottom ash granulates

An important analysis for secondary building materials which needs to be performed in order to establish their possibility of use as building materials is the leaching of contaminants. In the Netherlands, the legislative document that regulates the use of building materials is the Soil Quality Decree [14].

The leaching results, determined following the requirements of the NEN 7375 standard [15] for the two considered fractions, FCG 0-8 and FCG 2-20 mm are shown in Table 1. The aim of the treatment of the bottom ash was to achieve either the acceptable emissions of non-shaped building materials for FCG, or the requirements of shaped materials for prefabricated concrete containing FCG.

The FCG 0-8 was expected to be the most contaminated step, due to its least sophisticated treatment method, as well as to its smallest particle size. Its leaching of contaminants is within the norm [14], except for antimony, chlorides and sulphates (5 times higher than the accepted limit).

Table 1 Leaching data of the FCG 0-8 and 2-20 fractions, which can be compared to the maximum levels for non-shaped materials, as demanded by the Soil Quality Decree [14].

Contaminant	FCG 0-8 (mg/kg)	FCG 2-20 (mg/kg)	Non-shaped materials (mg/kg)
Antimony (Sb)	0.34	0.41	0.32
Arsenic (As)	< 0.050	0.1	0.9
Barium (Ba)	< 0.60	0.28	22
Cadmium (Cd)	< 0.0010	0.01	0.04
Chromium (Cr)	0.052	0.1	0.63
Cobalt (Co)	< 0.030	0.1	0.54
Copper (Cu)	0.2	0.13	0.9
Mercury (Hg)	0.0005	0.005	0.02
Nickel (Ni)	< 0.050	0.1	0.44
Molybdenum (Mo)	0.61	0.36	1
Lead (Pb)	< 0.10	0.1	2.3
Selenium (Se)	0.029	0.039	0.15
Tin (Sn)	< 0.030	0.1	0.4
Vanadium (V)	< 0.20	0.1	1.8
Zinc (Zn)	< 0.30	0.2	4.5
Bromide (Br)	< 0.50	4.1	20
Chloride (Cl)	3000	690	616
Fluoride (F ⁻)	5.5	72	55
Sulphate (SO ₄ ²⁻)	6400	2300	1730

The elements that had leaching values close to the limit (mainly Cu and Br) have shown a clear decrease after both Step 3 and Step 5 of the treatment. Chlorides and sulphates, as well as Sb, have decreased by a considerable percentage, but are still above the legal limit. The leaching of these elements makes the use of FCG 2-20 only possible as concrete aggregates when used in prefab concrete elements, because the contaminants will be bound by the cementitious matrix and the “shaped materials” limits will apply.

3. Materials used in concrete mixtures

3.1 Powders

The particle size distributions (PSDs) of the employed powders were analysed using a Mastersizer 2000 laser granulometer. The obtained PSDs, were used in the mix design process, as detailed in Section 5.1. CEM III/B 42.5N was used in testing the FCG 0-8. CEM II/A-LL 42.5 was used for the FCG 2-20 mix. These PSDs can be found in Figures 1 and 4.

3.2 Aggregates

All aggregates were used as-received in the test program, in wet conditions as this is the case in practice. However, the water content was determined for each aggregate fraction, by drying at $105 \pm 5^\circ\text{C}$ for 24 hours. These values were taken into account when designing the mixes for the test program. The water/cement ratio of the mix was adjusted to take into account the water content of each aggregate type. Table 2 summarizes the water content of each of the considered aggregates.

Table 2. Physical properties of all aggregates used (*estimated value).

Material	Water content (% initial mass)	Water content (% d. m.)	D _{min} (μm)	D _{max} (μm)	Density (g/cm ³)
Sand N1	0.05	0.05	128	125	2.65
Gravel G1	0.10	0.10	275	5600	2.65
Gravel G2	0.10	0.10	710	8000	2.65
FCG 0-8	12.65	14.48	60.3	8000	2.45*
FCG 2-20	1.69	1.72	63	22400	2.41
Sand S1	3.40	3.52	125	8000	2.64
Gravel G3	3.38	3.50	125	16000	2.57
Gravel G4	0.89	0.91	2000	22400	2.57

Commercially available natural aggregates were used as reference for the test program. A 0-2 sand (Sand N1), a 2-8 gravel (Gravel G1) and an 8-16 gravel (Gravel G2) were selected. The PSD of these aggregates were determined through dry sieving (Figure 1), and the results used in the mix design algorithm. In a further step, certain percentages of these aggregates were replaced by FCG with the same PSD range. A second test program is centred on the use of FCG 2-20 as prefabricated concrete constituent; the recipe designed using this material is compared with a reference one, which contains three types of aggregates: a natural sand termed N3 and two gravel types termed G3 and G4. The properties of these aggregates are also included in Table 2.

4. FCG 0-8 results

The FCG fraction 0-8 generated through the treatment phase 1a was used in the first part of the test program on laboratory scale. Figure 1 presents the cumulative particle size distributions of all materials used in the first part of the tests, together with the computed target PSD and the actual mix PSD. These last two curves were obtained using an optimization algorithm [16]. Using this algorithm, the deviation between the optimal distribution and the actual one can be calculated. The ideal case would be reached when the value of the deviation equals zero. The purpose of the optimization is to lower the value of the deviation as much as possible. The R² value, which is another measure of how well the composed mix matches the target line, is included for each composed mix in its description (Table 3).

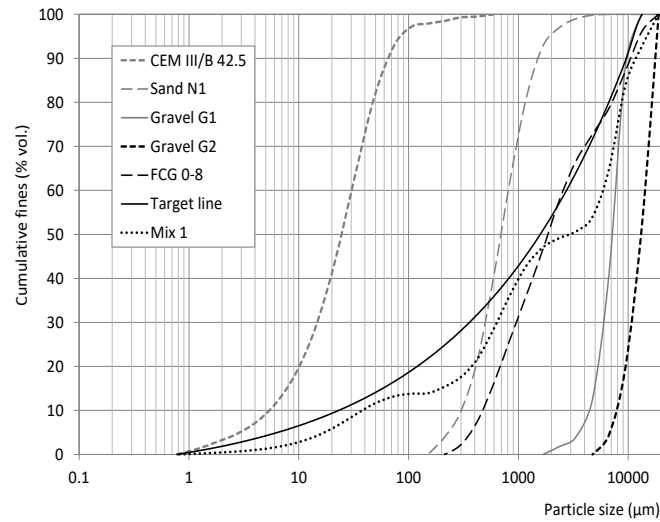
4.1 Composition of the designed mixtures

In order to assess the suitability of FCG as aggregates replacement, 9 different concrete mixes were prepared, which follow two optimized recipes. For each mix, four batches were prepared, each batch for 3 test specimens.

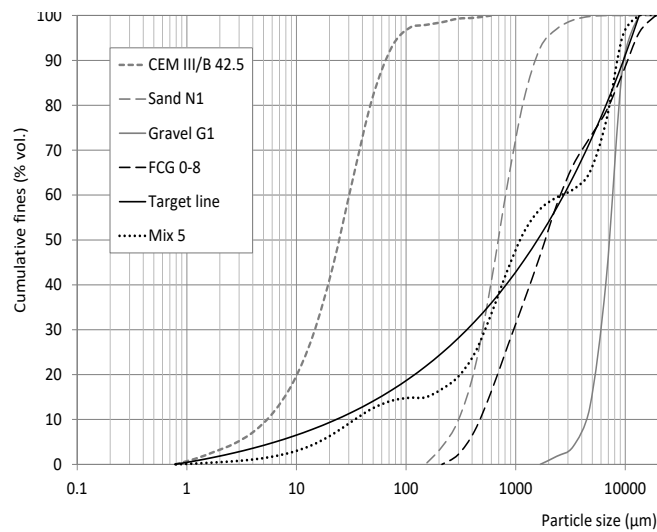
Table 3. Proportion of the FCG 0-8 as aggregate replacement for the 9 mixes, and the deviation of each mix from the target PSD.

	% FCG 0-8	Deviation	R ²
Recipe 1			
Mix 1	0	1658.5	0.908
Mix 2	10	1500.4	0.933
Mix 3	15	1438.2	0.935
Mix 4	25	1428.6	0.935
Recipe 2			
Mix 5	0	968.7	0.946
Mix 6	10	917.1	0.959
Mix 7	15	892.4	0.960
Mix 8	25	859.4	0.961
Mix 9	35	825.8	0.962

Table 3 presents the composition of all these mixes, with regard to the replacement levels of FCG 0-8. The replacement levels used were 0, 10, 15 and 25% FCG 0-8 on Recipe 1 (with Mix 1 as reference) and 0, 10, 15, 25 and 35% FCG 0-8 on Recipe 2 (with Mix 8 as reference). FCG 0-8 has a PSD between the ones of the Sand N1 and the Gravel G1. Because of this, the replacement using FCG 0-8 will be done by replacing 65% of the sand and 35% of the gravel, as FCG 0-8 has 65% of its particles under 2 mm.



a.



b.

Figure 1. Example of target line determined using the optimization algorithm, for the reference mixes of a. Recipe 1 and b. Recipe 2.

The two columns “Deviation” (integrated area between the target line and the actual PSD curve of the chosen mix) and “R²” (the coefficient of determination) included in Table 3 are methods of measuring the fit between the target line computed using the optimization algorithm and the actual recipe grading curve. The lower the deviation or the higher R² is, the better the packing of the mix. Because the difference between the qualities of the mixes is easier to compare on the deviation value, rather than on R² which can have very similar values (see Table 3), the deviation will be used from now on as a measure of the particle packing quality. Figure 1 shows an example of the output of the optimization algorithm, in which the difference between the two designed mixes (Recipe 1-Mix 1 and Recipe 2-Mix 5) can be observed.

According to the deviation values of the mixes, the replacement of natural aggregates by FCG 0-8 should be beneficial for the mix, as the packing density improves. Therefore, mixes 2-4 and 6-9 are expected to perform slightly better than the initial mixes (1 and 5). However, the packing density is not the only influencing factor for the final strength of the samples, as the properties of the FCG also can play an important role.

It was observed during the preparation of the samples that the mixes became increasingly stiffer as the proportion of FCG 0-8 was increased. The standard compaction method did not produce optimum results, as in the case of the reference recipes. The water addition should be therefore adjusted to the higher water demand of the FCG aggregates. In the current test, the same water to cement ratio was used for all samples, in order to ease the comparison between the results. The distribution modulus q was chosen to be 0.3.

Table 4 summarizes the amount of each component for a batch of concrete for Recipes 1 and 2. The amount of water is already corrected for the water content of the aggregates. All samples were mixed, mould and cured according to the EN 196-1 standard [17].

4.2 Mechanical strength results

In this section, graphs comparing the compressive and flexural strength of all composed mixes (Table 3) will be shown and discussed. Figures 2 and 3 correlate the compressive and flexural strengths of Mixes 1-4 and Mixes 5-9 respectively with the level of FCG 0-8 replacement in the mix.

Table 4. Proportion of each component in kg/m³ of concrete for Recipe 1 and Recipe 2 reference mixtures.

	CEM III/B 42.5	Sand N1	Gravel G1	Gravel G2	Water
Recipe 1	263	668	669	283	131
Recipe 2	281	842	749	-	170

In the case of the compressive strength (Figure 2a), an addition of 10% FCG is beneficial, the results being slightly better than for the reference mix at all 3 test dates: 3, 7 and 28 days. For a replacement of 15% FCG 0-8, a decrease of approximately 10% in compressive strength can be observed. This is still encouraging since the strength decrease is slightly lower than the aggregate replacement level. For the 25% FCG 0-8 however, the decrease in compressive strength is more significant.

Similar results can be seen from Figure 2b, which depicts the average flexural strength of Mixes 1-4 for the test dates of 3, 7 and 28 days. The increase in strength for the 10% FCG 0-8 replacement is even more pronounced than in the case of compressive strength, but also the decreases at 15% and 25% FCG 0-8 are higher. These results indicate that a 10% replacement of natural aggregates with FCG 0-8 is beneficial for the mix, and a 15% replacement can still be accepted. However, a higher replacement level (in this case 25%) is detrimental to the mechanical properties of the concrete mix.

Figure 3 shows the strength development of the mixes based on Recipe 2 (Table 3), which is optimized for the replacement of FCG 0-8. It needs to be mentioned that, as it can be seen in Table 4, Recipe 2 has a 6.8% higher cement content, and also a higher water/cement ratio than Recipe 1. These factors influence the final mechanical properties, but the following comparison between the latter will highlight differences which are much higher than what can be expected through just the increased cement content and therefore must also be due to the type of aggregates employed.

In the case of compressive strength (Figure 3a), the replacement of up to 25% of the natural aggregates did not affect the results obtained after 3 days of curing. For the 7 and 28 days tests, a decrease is observed for the 10 and 15% FCG 0-8, but the strength stays the same for the mixes with 25% and 35% FCG 0-8. For the mix with 35% FCG 0-8 the results for 3 and 7 days are slightly below the ones obtained from Mixes 2-4 (Figure 2a), but the strength attained after 28 days is with approximately 70% higher in the case of Mix 8 (Recipe 2, 25% FCG 0-8), as can be seen in Figure 3a.

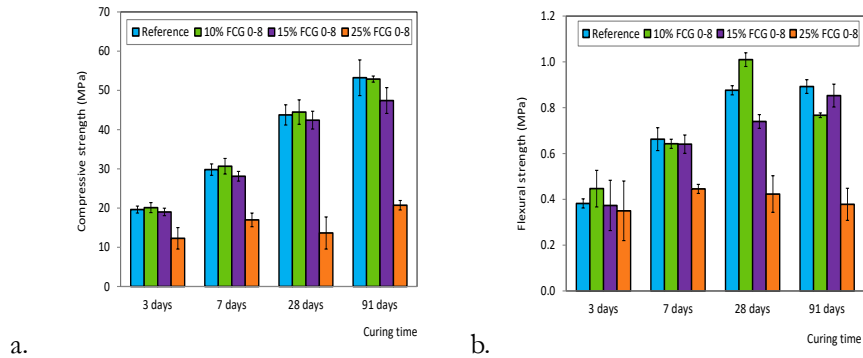


Figure 2. a. Compressive and b. flexural strength for 0-25% FCG 0-8 replacement by mass in Recipe 1 (Table 3).

The compressive strength of Mix 4 (Recipe 1, 25% FCG 0-8) is similar to the one of Mix 9 (Recipe 2, 35% FCG 0-8) after 28 days. This shows that Recipe 2 is better suited for the replacement of FCG 0-8 aggregates, and also that this can be further improved. In Figure 3b, a comparable trend can be observed in the case of flexural strength for the 3 days tests- a replacement of up to 25% FCG 0-8 does not influence the results significantly. The decrease after 7 and 28 days is more visible, but still it is not greater than 10%. Again, for the mix with 35% FCG 0-8 there is a sudden decrease in strength. When comparing to the results obtained for Mixes 2-4 (Recipe 1, Table 4), the same trend as in the case of compressive strength can be observed. Also here, the 35% replacing of natural aggregates with FCG 0-8 gives the same strength as Mix 4 (25% FCG 0-8, Recipe 1) after 28 days, and much higher values for the replacement level of 25%.

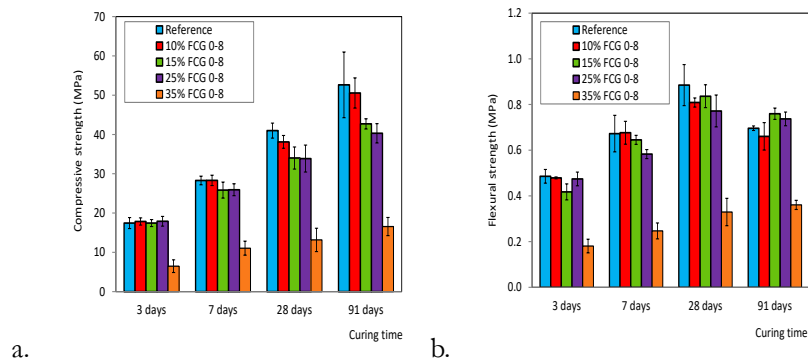


Figure 3. a. Compressive and b. flexural strength for 0-35% FCG 0-8 replacement by mass in Recipe 2 (Table 3).

The decrease of strength that can be observed can be in a large part explained by the higher water demand of the FCG, as drier mixes are harder to compact, and a lower degree of compaction will lead to decreased compressive strength. Adjusting the water to cement ratio with the replacement level of natural aggregates by FCG can solve this issue.

5. FCG 2-20 results

5.1 Concrete design

The bottom ash granulates FCG 2-20 obtained at the end of the treatment were used in a concrete mix designed for kerb stones to replace 20% of the aggregates.

The initial reference mix was composed of 13% cement (a CEM II/A-LL 42.5) and three types of aggregates: a 0-4 mm natural sand (termed N3) and two gravel types, a 2-8 mm (termed G3) and an 8-16 mm (termed G4), shown in Figure 4. The ratio of the aggregates N3:G3:G4 by mass in the reference sample is 1:2:3. Out of the total volume of the aggregates, 20% was replaced by FCG 2-20, and the recipe adjusted to keep the same cement/aggregates and water/cement ratios.

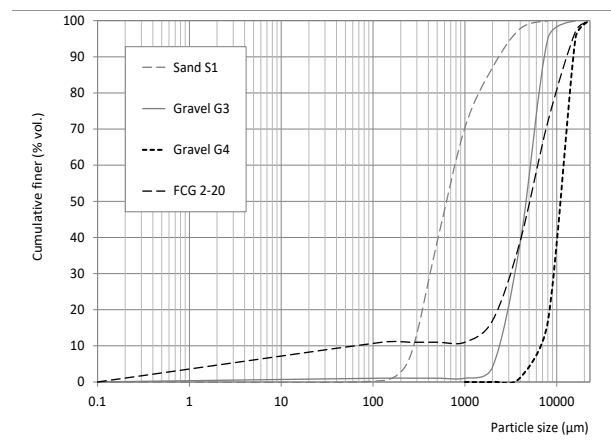


Figure 4. Particle size distributions of all used aggregates.

5.2 Mechanical strength results

The kerb stones produced had the dimensions of 1000 x 200 x 100 mm. The total production of this pilot test was of 5.5 m³ of concrete- about 275 kerb stones. From these elements, cylinders of 100x100 mm were drilled and tested for compressive strength. The flexural strength was tested according to EN 1340 [18], except for the curing requirements.

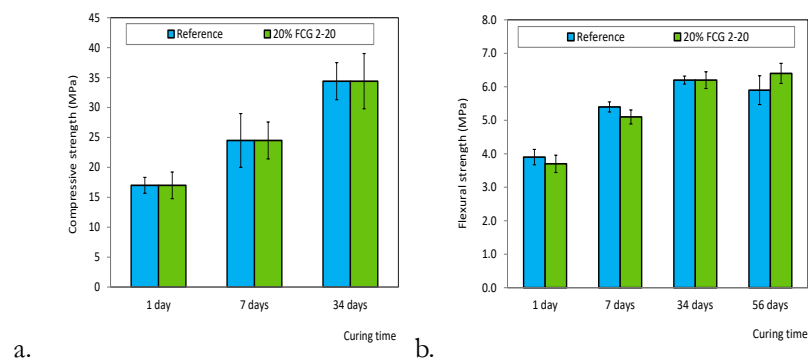


Figure 5. a. Compressive and b. flexural strength of the hardened samples.

The stones were kept in storage under usual factory conditions (15-18°C, 47-67% relative humidity) until the test date. Figure 5 shows the strength development of the reference sample (termed “reference”) and the FCG-containing stones (termed “sample”). At early ages (1 and 7 days), the compressive strength loss of the sample containing 20% vol. FCG was 17-18% of the reference concrete. However, after 35 days,

this difference was of only 11%. The flexural strength, which is the most important parameter in the case of kerb stones, had an even more promising behaviour. At early ages, the loss of flexural strength was of only 5.1-5.5%, and after 35 days the FCG-containing kerbs reached the same flexural strength values as the reference concrete. After 56 days, the FCG-sample reached a flexural strength higher with ~ 10% than the reference sample.

5.3 Leaching results

The two designed earth moist kerb stone recipes were tested for leaching after 64 days, as required by [14]. Table 5 presents the obtained values on both the shaped kerb stones (in mg contaminant/m² sample) and the crushed blocks (in mg contaminant/kg sample). The maximum values required by the Soil Quality Regulation [14] for non-shaped materials can be found in Table 1.

Table 5. Leaching data of the kerb stones (reference mix and 20% FCG 2-20 mix).

Contaminant	Crushed reference (mg/kg d.m.)	Crushed sample (mg/kg d.m.)	Shaped reference (mg/m ²)	Shaped sample (mg/m ²)	Shaped materials [14] (mg/m ²)
Antimony (Sb)	0.017	0.01	0.4	0.4	8.7
Arsenic (As)	< 0.05	< 0.05	4.0	4.0	260
Barium (Ba)	4.5	6.6	19	20	1500
Cadmium (Cd)	< 0.001	< 0.001	0.1	0.1	3.8
Chromium (Cr)	0.1	0.08	4.0	4.0	120
Cobalt (Co)	0.04	0.04	2.4	2.4	60
Copper (Cu)	< 0.05	0.33	4.0	4.0	98
Mercury (Hg)	< 0.0004	< 0.0004	0.0	0.0	1.5
Nickel (Ni)	< 0.05	< 0.05	4.0	4.0	81
Molybdenum (Mo)	0.012	0.021	0.8	0.8	144
Lead (Pb)	< 0.1	0.82	8.0	8.0	400
Selenium (Se)	< 0.007	< 0.007	0.6	0.6	4.8
Tin (Sn)	< 0.02	< 0.02	1.6	1.6	50
Vanadium (V)	< 0.1	< 0.099	8.0	8.0	320
Zinc (Zn)	< 0.2	< 0.2	16	16	800
Bromide (Br)	< 0.5	< 0.5	2	2	670
Chloride (Cl ⁻)	18	41	88	80	110000
Fluoride (F ⁻)	3	3.2	128	96	2500
Sulphate (SO ₄ ²⁻)	30	26	960	960	165000

The fact that the leaching of all contaminants was under the required legal limit, for both the shaped and the crushed samples confirms the fact that the combination of cleaning treatments and incorporation of the FCG 2-20 in a concrete matrix renders the bottom ash granulates as appropriate aggregate for such products.

6. Conclusion and discussion

Bottom ashes from Dutch incinerators were investigated in this study, with the scope of determining their suitability for use in concrete recipes. In the first part of the study, a cleaned bottom ash fraction termed FCG 0-8 mm was applied as sand replacement in concrete recipes. It was shown that, using an optimized particle packing, the FCG 0-8 can be used to replace up to 25% of the sand and gravel in the concrete mix without significant loss of mechanical strength. In the second part of this study, the FCG has been treated in order to obtain a suitable building material for concrete mixes or prefab elements. Five separate treatment steps were used in order to achieve this, consisting, among others, of particle size separations, washing procedures and the removal of ferrous and non-ferrous metals. The resulting fraction is termed

FCG 2-20 and contains less than 0.3% non-ferrous metals and less than 0.1% metallic iron. Almost all the contaminant leaching values were under the legal limits after the whole treatment process. However, because chlorides and sulphates still had a slightly raised leaching value, the material was used in the production of shaped building blocks. Kerb stones were produced using a 20% by volume replacement of the aggregates with FCG 2-20. The final aspect of the kerb units did not differ from the reference samples. The compressive strength was slightly lower than expected, which can be explained by the non-standard curing conditions. The low relative humidity during curing has affected the strength of the samples, since at low w/c ratios as employed in this study, the porous samples can easily dry out. Also, the cement used has a slow hydration rate, which will further delay the development of strength. The strength results were extremely positive, with a flexural strength after 35 days of the same level as the reference recipe. After 56 days the flexural strength of the FCG-containing sample reached a flexural strength 10% higher than the reference. This is an indication that the cement content of the recipe can be lowered when using FCG instead of natural aggregates, while keeping the flexural strength of the sample to the same level. The 20% replacement of aggregates is a sustainable option, by reducing the amount of natural sand and gravel and by decreasing the need for cement (and therefore the CO₂ footprint). All in all, the FCG produced from upgraded and treated municipal solid waste incineration bottom ash have proven to be suitable for the use in prefabricated concrete such as kerb units.

6. References

- [1] Chimenos, J. M., Segarra, M., Fernandez, M. A. & Espiell, F. Characterization of the bottom ash in municipal solid waste incinerator. *J. Hazard. Mater.* 64, 211–222 (1999).
- [2] Müller, U. & Rübner, K. The microstructure of concrete made with municipal waste incinerator bottom ash as an aggregate component. *Cem. Concr. Res.* 36, 1434–1443 (2006).
- [3] Tang, P., Florea, M. V. A. & Brouwers, H. J. H. The characterization of MSWI bottom ash. *18th Int. Conf. Build. Mater. (IBAUUSIL), Weimar* 2–1192–2–1199 (2012).
- [4] Al-Rawas, A. A., Wahid Hago, A., Taha, R. & Al-Kharousi, K. Use of incinerator ash as a replacement for cement and sand in cement mortars. *Build. Environ.* 40, 1261–1266 (2005).
- [5] Pera, J., Coutaz, L., Ambroise, J. & Chababbet, M. Use of incinerator bottom ash in concrete. *Cem. Concr. Res.* 27, 1–5 (1997).
- [6] Siddique, R. Use of municipal solid waste ash in concrete. *Resour. Conserv. Recycl.* 55, 83–91 (2010).
- [7] Courard, L., Degeimbre, R., Laval, A.-L., Dupont, L. & Bertrand, L. Utilisation des mâchefers d'incinérateur d'ordures ménagères dans la fabrication de pavés en béton. *Mater. Struct.* 35, 365–372 (2002).
- [8] Sabbas, T., Poletini, A., Pomi, R., Klein, R. & Lechner, P. Management of municipal solid waste incineration residues. *Waste Manag.* 23, 61–88 (2003).
- [9] Santos, R. M., Mertens, G., Salman, M., Cizer, Ö. & Van Gerven, T. Comparative study of ageing, heat treatment and accelerated carbonation for stabilization of municipal solid waste incineration bottom ash in view of reducing regulated heavy metal/metalloid leaching. *J. Environ. Manage.* 128, 807–821 (2013).
- [10] Mangialardi, T. Disposal of MSWI fly ash through a combined washing-immobilisation process. *J. Hazard. Mater.* 98, 225–240 (2003).
- [11] Stekette, J. J., Duzijn, R. F. & Born, J. G. P. Quality improvement of MSWI bottom ash by enhanced aging, washing and combination processes. *Stud. Environ. Sci.* 71, 12–23 (1997).

- [12] Cioffi, R., Colangelo, F., Montagnaro, F. & Santaro, L. Manufacture of artificial aggregate using MSWI bottom ash. *Waste Manag.* 31, 281–288 (2011).
- [13] Cossu, R., Lai, T. & Pivnenko, K. Waste washing pre-treatment of municipal and special waste. *J. Hazard. Mater.* 207, 65–72 (2012).
- [14] Soil Quality Regulation - Regeling bodemkwaliteit, VROM, Den Haag: Ruimte en Milieu. Ministerie van Volkshuisvesting, Ruimtelijke Ordening en Milieubeheer. (2013).
- [15] EN 7375 Uitloogkarakteristieken-Bepaling van de uitloging van anorganische componenten uit vormgegeven en monolitische materialen met een diffusieproef. (2004).
- [16] Hüsken, G. & Brouwers, H. J. H. Earth-moist concrete: application of a new mix design concept. *Cem. Concr. Res.* 38, 1246–1259 (2009).
- [17] EN 196-1 Methods of testing cement. Determination of strength. (2005).
- [18] EN 1340 Concrete kerb units — Requirements and test methods. (2003).

Characterization of air granulated converter slag and its leaching behaviour

M. J. Ahmed¹, K. Schollbach², M.V.A. Florea¹, S.R. Van Der Laan², H.J.H Brouwers¹

¹Department of Built Environment, Eindhoven University of Technology, Eindhoven, the Netherlands

² Tata Steel, R&D, Microstructure & Surface Characterization (MSC), P.O. Box 10.000, 1970 CA IJmuiden, the Netherlands

Abstract

In the current study, an air granulated converter slag has been characterized. It was granulated by pouring liquid slag in front of a strong fan and the obtained granules were sieved into five different fractions of 2mm, 1mm, 0,5mm, 0,25mm and <0,25mm in order to determine the influence of the cooling speed, because small granules are cooled faster. Detailed bulk chemical and mineralogical composition of every fraction was established by XRF (X-ray fluorescence) spectroscopy and powder-XRD (X-ray diffraction) with Rietveld refinement. One batch leaching tests according to EN 12457-2 were carried out and the supernatant analyzed by ICP-OES (Inductively coupled plasma-optical emission spectroscopy). The mineral phases present in the slag were divided into three main categories 1) common mineral phases of slag 2) weathering products 3) contaminants. All fractions except <0,25mm exhibited high leaching values for chromium and vanadium. The smallest fraction <0,25mm showed low value of chromium such as 0,11 and 0,12 mg/kg while in case of vanadium, it found to be less than detection limit of the instrument.

Keywords: air granulated slag, cooling rate, dicalcium silicate, vanadium, chromium

1. Introduction

Steel slag is the main byproduct of steel making. Steel slag is generated from lime and dolomite added in the basic oxygen furnace and forms when oxygen is blown onto the pig iron from the blast furnace to remove S (sulfur), P (phosphorus), C (carbon) and other constituents to produce crude steel. The so-called converter steel slag differs from the slag produced in the blast furnace process [1-2]. It is estimated that the global annual production of steel currently is more than 1.6 billion metric tons. The annual amount of steel making slag lies in the range of 315Mt to 420Mt globally [3]. The modern integrated LD (Lindz-Donawitz)/converter steel plants mass produce around 90-100kg of steel slag per tonne of steel production. The cooling method and mineralogy determines the bulk properties of slag such as major and minor elements, leachability, volume expansion, crushing strengths, abrasion resistance, all relevant for the recycling potential [4-5].

Steel slag is utilized in the cement industry as aggregate for cement based products, raw material for iron correction of clinker as well as admixture for cement base materials. The presence of dicalcium silicate (C_2S), tricalcium Silicate (C_3S), tetracalcium-aluminoferriite (C_4AF) and other mineral makes it a potential building material [6-7]. But the low cementitious characteristics form a barrier for civil application of steel slag in cement. The overall utilization of steel slag is still less than 30% after more than 50years of research and many avenues have been investigated from cooling methods to post-processing of slag [8-9].

The research has corroborated that there are low amounts of C_3S present in the slag, in most converter slags only dicalcium silicate exists. Thus steel slag can be considered less hydraulic than Portland cement clinker being dominated by dicalcium silicate (40 to 60wt.%) instead of C_3S [10]. In addition the C_4AF phase consists predominantly of the ferric endmember, which is also less reactive than its aluminous counterpart [11]. When applying converter slag as SCM (supplementary cementitious materials), the main problem that restricts the utilization of high amounts of steel slag is low early age strength. To deal with this problem, various approaches have been reported such as mechanical activation, alkali activation and varying cooling condition (water quenching, dry granulation and air granulation of slag) [11-12]. As a rule, the hydraulic activity of a slag, structure and phase composition depends on the chemical composition and thermal history [13-14].

Prior to the effective utilization of steel slag, the leaching behaviour needs to be investigated. Steel slag usually contain minor amounts of heavy metals, in particular chromium and vanadium. The leaching behaviour of slag is highly dependent upon the mode of cooling (water quenching, air cooling and air granulation) and mineralogical composition. There have been studies showing that quenching of electric arc furnace steel slag in water leads to less leaching of toxic metals due to high amorphous content. In addition the glassy amorphous structure exhibits better chemical resistance toward decomposition by acid than the crystalline structure [15].

In the current studies, an air granulated converter steel slag has been taken from Tata Steel, the Netherlands. The converter slag was sieved into different fractions: 2mm, 1mm, 0,5mm, 0,25mm, <0,25mm to study the influence of the cooling speed. Every fraction is characterized by XRF, powder XRD, Rietveld refinement. And detailed leaching behaviour has been observed with the one batch leaching test and ICP-OES.

2. Methodology

2.1 Materials

Air granulated slag was provided by TATA steel, the Netherlands. A sample was sieved into fractions: 2mm, 1mm, 0,5mm, 0,25mm, <0,25mm for characterization as shown in Fig. 1. The bigger particle size is associated with a somewhat slower cooling rate while small particle cooled more rapidly.



Figure 1: Morphology of air granulated slag sieved into different fractions. The smaller fractions c) 0,5mm d) 0,25mm and e) <0,25mm have contamination that can be observed with the naked eye.

A representative sample has been taken from every fraction of granulated converter slag. For his purpose, a static sample splitter has been used. Prior to analysis, every sample was dried in oven at 100°C.

2.2 Methods

2.2.1 XRF (X-ray fluorescence):

The chemical composition of every fraction of granulated slag was determined with X-ray fluorescence (XRF; PANalytical Epsilon 3, standardless) using fused beads as shown in Table 2. Gain on ignition (GOI) was measured at 1000 °C until a constant mass was reached. For the preparation of fused beads, the residue from the GOI was mixed with borate flux by keeping the sample to flux ratio (1:12) respectively, a mixture

of 67 % Li_2BO_7 and 33 % LiBO_2 (Claisse). Moreover, 150 μL of 4 M LiBr was added to the mix as a non-wetting agent. The mixture was placed in a borate fluxer oven (classisse leNeo) for 24 mins at 1065 °C.

2.2.2 Powder-XRD (X-ray diffraction)

XRD diffractograms were measured with a Bruker D4 (Source: Co K α_1 1,7901 Å and K α_2 1,7929 Å, Detector: LynxEye, with variable slits) to understand the mineralogical composition of air granulated slag of every fraction. For phase recognition, X'Pert Highscore Plus with the ICDD PDF-2 database was employed. For quantitative analysis, an internal standard (Si: 10wt.% of the total sample) was mixed homogenously with the sample. TOPAS 4,2 Bruker software was utilized for quantification.

2.2.3 ICP-OES (Inductively Coupled Plasma-Optical Emission Spectroscopy):

The ICP-OES has been used to analyze the leaching behaviour of heavy metals quantitatively. An ICP-OES spectrometer (Spectroblue FMX36, Autosampler series: 121705A280, auxiliary gas flow) has been used for quantitative analysis of leachate. Prior to measurement with ICP-OES, every leachate was subjected to acidification with nitric acid (65% suprapure) to ensure a pH value ≤ 2 at $21 \pm 3^\circ\text{C}$.

2.2.4 Sample Washing

To eliminate the potential foreign contamination of slag sample during collection of granulated slag, the surface dust of the granules was removed with anhydrous isopropanol followed by diethyl ether. Only those contamination were removed by washing that had particle size smaller than the slag fraction. That's why, the mass loss due to washing have fluctuating values as shown in Table 1. The anhydrous isopropanol is used to avoid any kind of dissolution of granulated slag. While diethyl ether is used to quick removal of isopropanol. To eliminate all organic solvent, the sample is dried in oven at 40°C under vacuum. The sample is marked as washed (W) and not-washed (NW). For this purpose, the mass loss due to washing has been calculated as shown in following Table 1.

Table 1: Mass loss during organic washing of air granulated converter slag.

Slag fraction	Mass Loss (weight %)
2mm	1,6%
1mm	0,6%
0,5mm	17,7%
0,25mm	2,2%
<0,25mm	14,3%

2.2.5 Leaching Analysis

All fractions of granulated slag have been contacted with deionized water with L/S=10 (10g in 100ml of the deionized water). All the reactors were agitated horizontally at 300 rpm for 24h at $21 \pm 2^\circ\text{C}$. After the experiment, the sample was filtered and stored at 5°C . For ICP-OES analysis, the supernatants was filtrated to $0,2\mu\text{m}$ (Polyethersulfone membrane). Additionally the pH of each sample was measured. Prior to measure pH, the pH meter has been calibrated with buffer solution of known pH at 20°C .

3. Result and Discussion

The bulk composition of every fraction of granulated slag is shown in Table 2. The major oxides are CaO , Fe_2O_3 , SiO_2 , MgO and Al_2O_3 . From the above analyses, it appears that droplet size correlates with a higher calcium and silica contents, while the smaller granules appear to be more iron rich.

Table 2: Oxide composition of granulated slag.

^a S _F (mm)	MgO	Al ₂ O ₃	SiO ₂	P ₂ O ₅	SO ₃	CaO	TiO ₂	V ₂ O ₅	Cr ₂ O ₃	MnO	Fe ₂ O ₃	Total
2	8,2	4,1	13,6	1,2	0,8	44,9	1,4	0,6	0,2	4,2	20,8	100
1	8,3	3,4	13,4	1,2	1,4	44,9	1,4	0,7	0,2	4,2	21,0	100
0,5	8,0	6,0	13,2	1,2	0,5	43,3	1,4	0,6	0,2	4,1	21,6	100
0,25	6,1	8,5	17,5	0,8	0,7	32,8	1,2	0,5	0,2	3,1	28,4	100
<0,25	6,0	9,6	20,4	0,6	1,2	26,4	1,1	0,42	0,2	3,1	31,0	100

a=Slag Fraction

3.1 Mineralogical Composition of granulated slag

The mineralogical composition of the slag size fractions is shown in Table 3. While Fig. 2 shows an example of an XRD diffractogram of the air granulated slag.

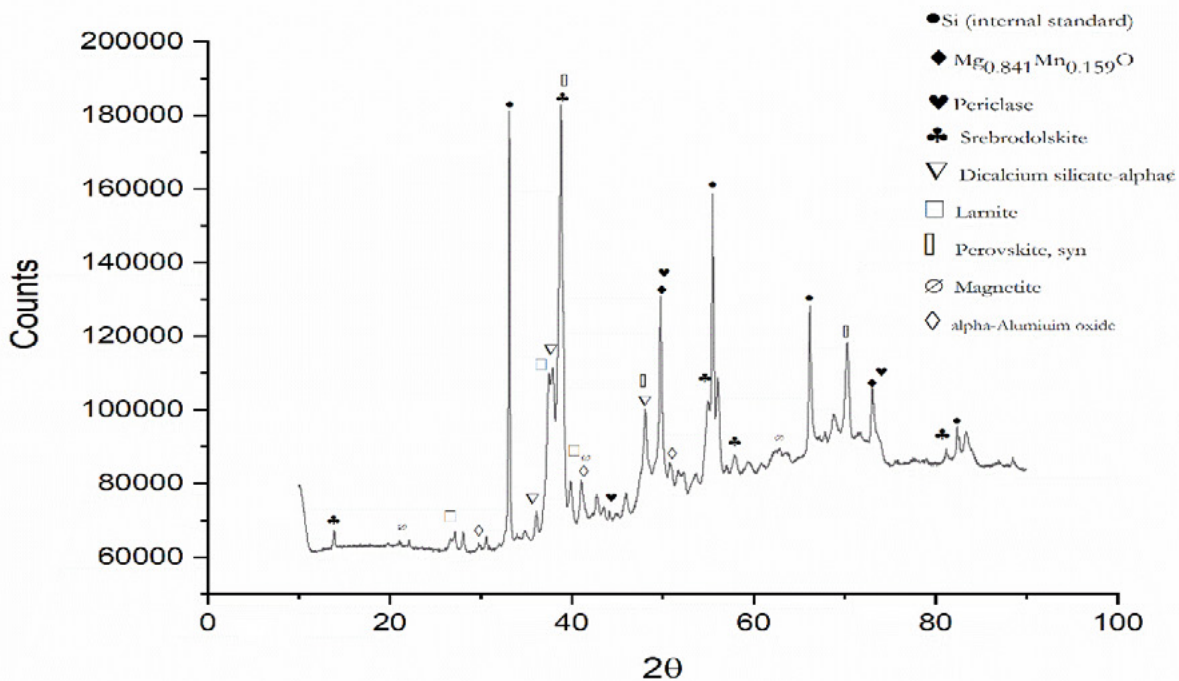


Figure 2: Powder-XRD of the 0,5mm fraction of granulated slag with Si as an internal standard.

Converter slag exhibits relatively constant mineralogical composition, but the mineral phase proportions vary. The most abundant converter slag minerals are larnite, dicalcium silicate-alpha H', calcium ferrite, lime and magnesio-wuestite as shown in Table 3. The mineral phases like pseudobrookite, perovskite, protoenstatite and nauqite are not usually observed in converter slag but are likely formed in the slag due to the quick cooling. Calcite and lepidocrocite are weathering products, while the other minerals such as quartz and corundum are contaminants. The amount of quartz and calcite is very pronounced (around 21-24%) in the smaller fractions. It is not clear if the high amorphous content in the fine fractions is due to amorphous phase generated during air granulation or if it is a result of amorphous contaminants. This means that the bulk chemical composition measured with XRF is not representative of the actual composition of the granulated converter slag. But it can be corrected by removing the known amount of hematite, calcite, quartz and corundum from the bulk composition as shown in Table 4. It is quite clear from the table that the major oxide composition is more aligned to their mineralogical composition.

Table 3: Rietveld refinement of different fractions of air granulated converter slag.

Mineral Phases	Formula	2mm	1mm	0,5mm	0,25mm	<0,25mm
Larnite, β -C ₂ S	Ca ₂ SiO ₄	21,0	18,9	13,9	6,2	2,7
α H'-C ₂ S	Ca ₂ SiO ₄	20,9	21,4	26,4	19,0	
Fe-wuestite	(Fe,Mg)O	4,6	4,3	4,0	3,5	5,9
Mg-Wuestite	(Mg,Fe)O	8,1	4,1	2,7		
Mn - Wuestite	(Fe,Mn)O		1,0	0,3		
Periclase	MgO	2,1	5,6	7,8	6,7	
Magnetite	Fe ₃ O ₄	2,5	2,0	2,8	6,6	10,3
Srebrodolskite	Ca ₂ Fe ₂ O ₅	24,1	21,4	20,8	12,6	10,3
Pseudobrookite	Fe ₂ TiO ₅	0,3	0,3	0,3	0,1	0,5
Lime	CaO	0,1		0,1		
Quartz	SiO ₂				8,9	13,3
Calcite	CaCO ₃			0,3	4,0	17,9
Perovskite	CaTiO ₃	7,6	10,0	12,5	8,4	1,7
Protoenstatite	Mg ₂ Si ₂ O ₆	1,2	0,7			
Graphite	C	0,3	0,2			
Naquite	FeSi	0,7	0,5	0,6	0,3	
Vaterite	CaCO ₃	1,1	0,8	1,0	0,7	
Rutile	TiO ₂	0,4	0,4	0,5		0,2
Corundum	Al ₂ O ₃	2,9	1,7	3,0	5,6	0,8
Hematite	Fe ₂ O ₃				2,1	1,9
Albite	NaAlSi ₃ O ₈					1,1
Titanite	CaTiSiO ₅				0,5	
Lepidocrocite	γ -FeO(OH)				2,8	
Clinoenstatite	MgSiO ₃					2,1
Moissanite 2H	SiC					0,3
Amorphous		2,0	6,8	3,0	12,1	31,0
Total		100	100	100	100	100

It was expected that all granulated slag size fractions have the same bulk composition, but the large converter slag granules appear to contain more C₂S than the smaller ones. The most plausible reason is that solid phenocrysts of periclase and C₂S are present in the liquid converter slag before cooling. It appears that the C₂S is incorporated preferentially in the large size fractions, while the MgO phenocrysts are preferentially incorporated into the smaller granules. Therefore, they tend to be enriched in CaO and SiO₂, with a lower MgO and Fe₂O₃ content.

Based on the variation in bulk composition it seems the addition of C₂S and MgO controls the small

differences in chemical bulk composition of the granulated slag sizes. It can be observed that the large granules seem to be indeed richer in C₂S phenocrysts compared to the small granules, while the smaller size fractions contain more MgO.

Table 4: Corrected oxide composition of air granulated converter slag. The fraction <0,25mm was not included because of the strong contamination.

Slag Fractions	MgO	Al ₂ O ₃	SiO ₂	P ₂ O ₅	CaO	TiO ₂	V ₂ O ₅	Cr ₂ O ₃	MnO	Fe ₂ O ₃
2mm	8,5	1,2	14,1	1,2	46,6	1,5	0,6	0,2	4,4	21,6
1mm	8,6	1,8	13,8	1,2	46,3	1,4	0,7	0,2	4,3	21,6
0,5mm	8,5	3,2	14	1,3	45,7	1,5	0,6	0,2	4,3	20,7
0,25mm	7,4	3,3	12,2	1,0	37,9	1,5	0,6	0,2	3,7	32

3.2 Leaching Analysis

The leaching values of heavy metals in granulated slag are presented in Table 5.

Table 5: Leaching values of granulated slag of 1mm, 2mm, 0,5mm, 0,25mm and <0,25mm respectively.

Slag fractions	Permissible Emission value	1mm_ ^a W	2mm_W	0,5mm_aW	0,25mm_W	<0,25mm_W
	(mg / kg)	(mg / kg)	(mg / kg)	(mg / kg)	(mg / kg)	(mg / kg)
Contact time (hours)	24	24	24	24	24	24
pH (20°C)		10,84	11,0	10,89	9,62	11,11
Antimony (Sb)	0,32	0,19	0,19	0,17	0,18	L.D.
Arsenic (As)	0,9	0,22	0,21	0,15	0,15	L.D.
Barium (Ba)	22	0,02	0,11	0,02	0,11	0,04
Chromium (Cr)	0,63	1,83	1,70	1,91	2,42	0,11
Molybdenum (Mo)	1	0,14	0,14	0,002	0,011	0,022
Vanadium (V)	1,8	10,84	11,49	11,43	8,84	L.D.
Zinc (Zn)	4,5	0,06	0,06	0,07	0,08	0,28

^a=Washed, Cd, Cu, Hg, Co, Pb, Ni, Se, Sn=below detection limit, c=Lower than Detection limit

In most fractions of granulated slag, heavy metals are below the permissible emission limits in building

materials [17], except for vanadium and chromium. The smallest fraction exhibits leaching values of vanadium below the detection limit and chromium lies below the permissible limit but this is likely due to the high amount of inert contaminants such as calcite and quartz. In general the leaching of vanadium and chromium is much higher than reported for standard cooled converter slag.

4. Conclusion

In the present studies, the air granulated converter slag has been characterized by XRF spectroscopy and powder- XRD as well as leaching behaviour. The following conclusions can be made on the basis of this study.

- The chemical bulk composition of granulated slag varies in the different size fraction of the slag, although they were all produced from the same slag batch. Large fractions exhibit a somewhat higher amount of calcium and silicon, while the smaller fractions are richer in magnesium and iron. This seems to be the result of an unequal distribution of dicalcium silicate and (Mg, Fe)O.
- The air granulated slag contains the same phases as standard cooled slag: C_2S , Mg-Wuestite, srebrodolskite and magnetite. Additionally, perovskite is formed due to quick cooling.
- 2mm, 1mm, 0,5mm and 0,25mm fractions of air granulated slag show leaching value above the legal limit for chromium and vanadium, which seems to be a result of increased reactivity compared to standard slag due to air granulation.

As a next step calorimetric measurements will be performed to determine the hydraulic reactivity of the granulated slag. SEM/EDX measurements will be carried out to understand the microstructure and locate the source of chromium and vanadium.

5. Acknowledgment

The authors would like to acknowledge the financial support by NWO (The Netherlands Organisation for Scientific Research) for funding this research (project no.10023338) and M2i (Materials Innovation Institute) for managing this project. Furthermore, the authors wish to express their gratitude to the following sponsors of this research: Tata Steel; Enci; V.d. Bosch Beton; Beton Mortel; Inashco; Hess.

6. Reference

1. Wulfert, H., Ludwig, H. M. & Wimmer, G. A new process for production of cement clinker from steelmaking slags. *Cem. Int.* (2017).
2. Horii, K., Tsutsumi, N., Kitano, Y. & Kato, T. Processing and reusing technologies for steelmaking slag. *Nippon Steel Tech. Rep.* (2013).
3. Eloneva, S., Teir, S., Salminen, J., Fogelholm, C. J. & Zevenhoven, R. Steel converter slag as a raw material for precipitation of pure calcium carbonate. *Ind. Eng. Chem. Res.* (2008). doi:10.1021/ie8004034
4. van Zomeren, A., van der Laan, S. R., Kobesen, H. B. A., Huijgen, W. J. J. & Comans, R. N. J. Changes in mineralogical and leaching properties of converter steel slag resulting from accelerated carbonation at low CO₂ pressure. *Waste Manag.* (2011). doi:10.1016/j.wasman.2011.05.022
5. Guo, J., Bao, Y. & Wang, M. Steel slag in China: Treatment, recycling, and management. *Waste Management* (2018). doi:10.1016/j.wasman.2018.04.045
6. Eloneva, S. Reduction of CO₂ emissions by mineral carbonation: steelmaking slags and raw material with a pure calcium carbonate end product. *TKK Dissertations* (2010).

7. Dhoble, Y. N. & Ahmed, S. Review on the innovative uses of steel slag for waste minimization. *Journal of Material Cycles and Waste Management* (2018). doi:10.1007/s10163-018-0711-z
8. Cao, L. *et al.* Process to utilize crushed steel slag in cement industry directly: Multi-phased clinker sintering technology. *J. Clean. Prod.* (2019). doi:10.1016/j.jclepro.2019.01.260
9. Murphy, J. N., Meadowcroft, T. R. & Barr, P. V. Enhancement of the Cementitious Properties of Steelmaking Slag. *Can. Metall. Q.* (2014). doi:10.1179/cm.1997.36.5.315
10. Li, Y. & Dai, W. Bin. Modifying hot slag and converting it into value-added materials: A review. *Journal of Cleaner Production* (2018). doi:10.1016/j.jclepro.2017.11.171
11. Kriskova, L. *et al.* Effect of mechanical activation on the hydraulic properties of stainless steel slags. *Cem. Concr. Res.* (2012). doi:10.1016/j.cemconres.2012.02.016
12. Sajedi, F. Mechanical activation of cement-slag mortars. *Constr. Build. Mater.* (2012). doi:10.1016/j.conbuildmat.2011.05.001
13. Yu, P., Wang, S., Li, Y. & Xu, G. A Review of Granulation Process for Blast Furnace Slag. *MATEC Web Conf.* (2016). doi:10.1051/mateconf/20166806007
14. Mostafa, N. Y., El-Hemaly, S. A. S., Al-Wakeel, E. I., El-Korashy, S. A. & Brown, P. W. Characterization and evaluation of the hydraulic activity of water-cooled slag and air-cooled slag. *Cem. Concr. Res.* (2001). doi:10.1016/S0008-8846(01)00497-5
15. Loncnar, M., Zupančič, M., Bukovec, P. & Jaklič, A. The Effect of Water Cooling on the Leaching Behaviour of EAF Slag From Stainless Steel Production. *Mater. Tehnol.* (2009).
16. Haha, M. Ben, Lothenbach, B., Saout, G. Le & Winnefeld, F. Cement and Concrete Research Influence of slag chemistry on the hydration of alkali-activated blast-furnace slag — Part I : Effect of MgO. *Cem. Concr. Res.* (2011). doi:10.1016/j.cemconres.2011.05.002
17. wetten.nl - Regeling - Regeling bodemkwaliteit - BWBR0023085. Available at: <https://wetten.overheid.nl/BWBR0023085/2018-11-30#BijlageA/2019>. (Accessed: 5th June 2019)

Sodium hydroxide/carbonate activated GGBS-fly ash mortars incorporating recycled waste glass

G. Liu, M. V. A. Florea, H. J. H. Brouwers

Department of the Built Environment, Eindhoven University of Technology, P. O. Box 513, 5600MB, Eindhoven, The Netherlands, Email: G.Liu@tue.nl

Abstract:

Due to its pozzolanic reactivity, waste glass has been widely studied as Supplementary Cementitious Materials (SCM) in conventional concrete production in recent years. Waste glass is an amorphous, SiO_2 rich material, which can be used as the Si source in alkali activated materials, for example, alkali activated ground granulated blast furnace slag GGBS or fly ash (FA) based geopolymers. This paper investigates the application of waste glass powder as part of the binder in slag-fly ash systems activated by blended ($\text{NaOH}/\text{Na}_2\text{CO}_3$) activators. To investigate the reaction kinetics, mechanical performance and durability properties of waste glass blended alkali activated GGBS-FA binders, calorimetry, XRD, setting time, strength and resistance to carbonation tests were conducted. The results show that glass powder has a higher reactivity compared to fly ash but still lower than GGBS. The mechanical performance of different samples is mostly controlled by the Ca/Si of dry mixtures and the activator type. After the slag-fly ash binder system was modified by the waste glass, a significant enhancement of resistance to carbonation was identified for $\text{NaOH}/\text{Na}_2\text{CO}_3$ activated mortars, which shows an increase of 300% on the carbonation resistance ability compared to the reference sample.

Keywords: alkali activation, slag-fly ash binder, waste glass, reaction kinetics, carbonation

1 Introduction

With the increasing consumption of glass products, a high amount of waste glass is being produced all over the world. On account of being un-biodegradable, waste glass causes a high pressure on landfills. In consideration of environmental protection, it is an efficient method to apply waste glass in new building materials. In previous studies, waste glass (WG) exhibited a potential as ingredient in concrete; for example, waste glass fractions can not only be used as aggregates [1][2], but also supplementary cementitious materials as ground granulated blastfurnace slag (GGBS) or coal fly ash [3]–[6]. In recent years, recycled waste glass has attracted more attention for sustainable application in building materials. Since waste glass (WG) contains a high amorphous content of silica, a potential of pozzolanic reaction has been identified [7]. A microstructure improvement was observed after waste glass addition in concrete [8]. In the latest studies, WG was also used combined with GGBS or fly ash (FA) for alkali activated concrete. The high content of amorphous silica can be used to produce the precursor of alkali activate materials to replace water glass [9]–[12]. In a previous study, the blended activators, which combine sodium hydroxide, water glass or sodium carbonate, show an overage performance compared to single activator [12]. There are some reports that waste glass can play a role similar to sodium silicate (water glass) on microstructure modification [11]. Waste glass is prone to be attacked by the alkali solution, and a higher dissolution rate of waste glass in $\text{NaOH}/\text{Na}_2\text{CO}_3$ solution than in NaOH solution at the same sodium concentration has been observed

[13]. As well known, the selection of the binder's composition and activator of alkali activated concrete can have large influences on concrete durability performance. It has been reported that the higher silicate modulus of the activator provides a higher resistance for carbonation of alkali activated slag [14]. However, the influence of waste glass as binder in alkali activated slag-fly ash system on mechanical and durability performance by using different activators is still not clear. Therefore, the application of waste glass in slag-fly ash alkali activated systems still needs more focus. The activator types, reaction mechanism, mechanical and durability performance need further study.

The present study evaluates the application of waste glass in slag-fly ash alkali activated binder systems. The waste glass was used to replace slag, fly ash or total binder by 20%, respectively, to study the influences of waste glass on the performance of slag-fly ash binder systems. The sodium hydroxide-sodium carbonate blended solution was selected as the activator.

2 Materials and methods

2.1 Materials characterization

The recycled waste glass fractions (mixed colour) were supplied by a glass recycling plant. Then, a ball mill was used to ground it into a fine powder. Ground granulated blast furnace slag (GGBS) was supplied by ENCI, IJmuiden, Netherlands. Class F fly ash was supplied by Vliegasunie B.V., the Netherlands. Table 1 shows the chemical composition of waste glass, GGBS and fly ash.

Table 1 Chemical composition of recycled glass, GGBS and fly ash

Oxide	Waste glass (% mass)	GGBS (% mass)	Fly ash (% mass)
Na ₂ O	14.651	/	/
MgO	1.298	8.57	1.141
Al ₂ O ₃	1.93	13.214	26.98
SiO ₂	68.328	29.407	51.442
SO ₃	0.086	2.639	1.121
K ₂ O	0.702	0.424	1.84
CaO	11.904	42.665	5.83
TiO ₂	0.062	1.487	1.78
Cr ₂ O ₃	0.117	0.001	0.034
MnO	0.022	0.398	0.057
Fe ₂ O ₃	0.364	0.366	8.271
ZnO	0.009	/	0.022
BaO	0.061	0.081	/
PbO	0.05	/	0.009
P ₂ O ₅	/	/	0.849

2.2 Test methods

2.2.1 Activator preparation

The activator was prepared from solid sodium hydroxide pellets, sodium carbonate and distilled water. The equivalent Na₂O% to binder ratio is 10%.

2.2.2 Experiments

The calorimetry test was performed using an isothermal calorimeter (TAM Air, Thermometric). All measurements were conducted for 150 h under a constant temperature of 20 °C. The setting time was measured according to the Vicat needle method as described in EN 196-3 [15]. The strength tests were carried out according to EN 196-1 [16]. Carbonation curing was conducted by a carbonation chamber. The related parameters are RH 65%, 25 °C, 20% of CO₂ dosage and atmosphere pressure.

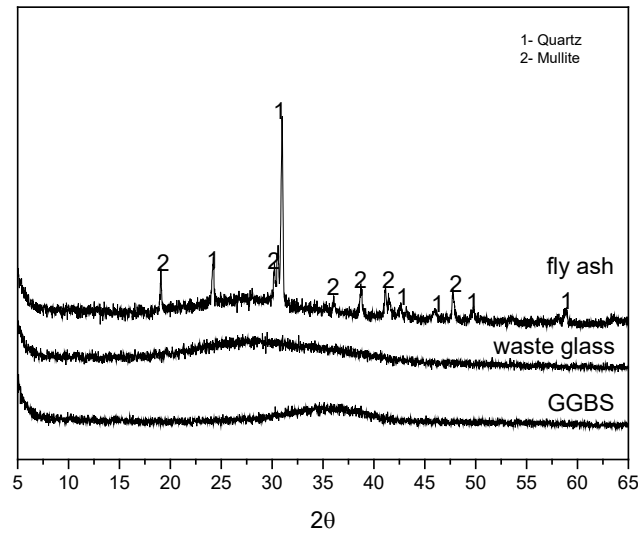


Fig. 1 XRD patterns of all materials employed as binder

The XRD of raw materials is shown in Fig. 1. The particle size distribution of recycled waste glass powder, GGBS, fly ash, and sand are shown in Fig. 2.

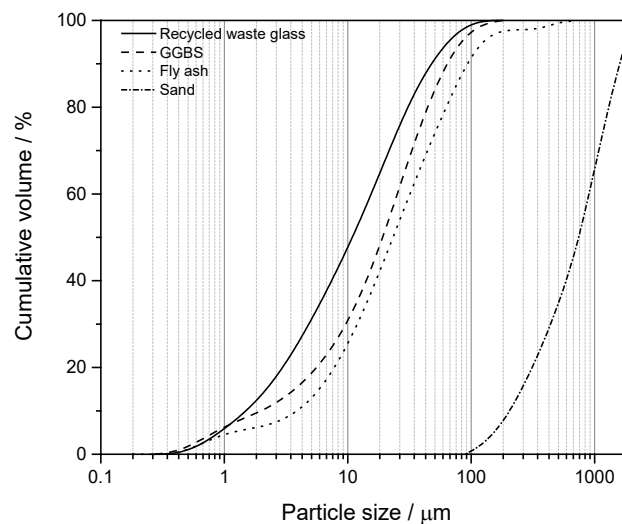


Fig. 2 Particle size distribution of materials employed as binder

Table 2 Mix design for 1 m³

Sample ID	GGBS / kg	Fly ash / kg	Recycled glass / kg	Sand / kg	Activator /	w/b
NC1	251.5	251.5	0	1509.0	274.6	0.4
NC2	252.4	151.4	100.9	1514.3	275.5	0.4
NC3	150.0	250.0	100.0	1500.1	272.9	0.4
NC4	200.9	200.9	100.5	1507.2	274.3	0.4

3. Results and discussion

3.1 Reaction kinetics and products characterization

As shown in Fig. 3, the sodium carbonate-sodium hydroxide activated blends show the initial dissolution, induction, acceleration to deceleration and stable periods [17]–[19]. The variation of peaks intensity can be observed according to the difference of binder systems.

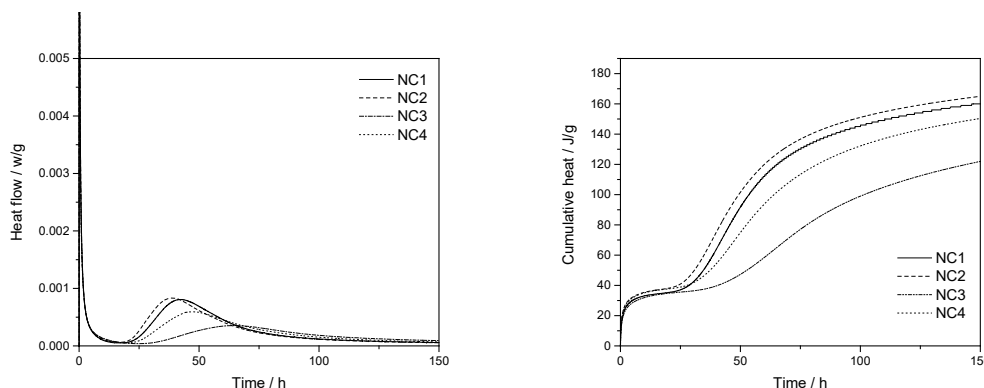


Fig. 3 Calorimeter results of mixtures (a) heat flow and (b) cumulative heat

For NaOH/Na₂CO₃ series samples, the highest reaction intensity and reaction rate is observed for the NC2 sample. NC3 shows a relative low reactivity, while NC2 shows the highest cumulative heat during the reaction. In slag-fly ash binder systems, the higher slag proportion usually induces high reaction intensity and cumulative reaction heat [28]. These results indicate that the waste glass powder may show a medium reactivity compared to GGBS and FA.

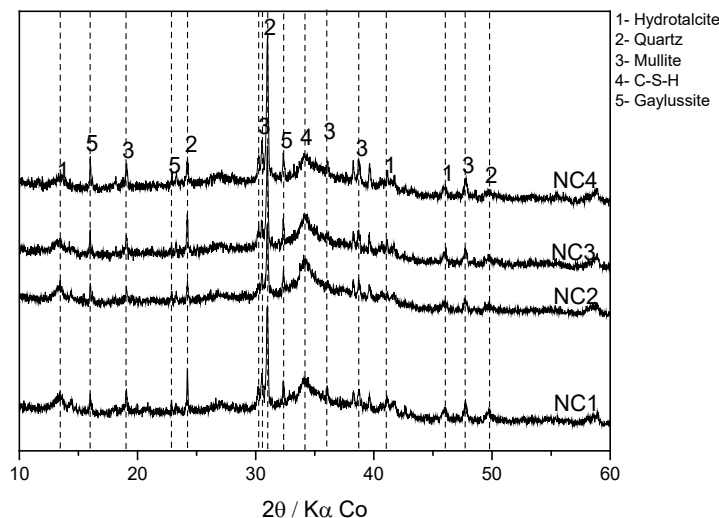


Fig. 4 XRD of different mixtures

The XRD patterns of paste samples are shown in Fig. 4. As can be seen, some minerals exist in all mixtures, regardless of the activator types (for example, quartz and mullite, which are the residual minerals in fly ash). In comparison to the XRD data of raw GGBS and FA, many new peaks were formed after 28 days reaction. Gaylussite was formed after 28 days curing. The addition of waste glass in binders shows no significant effect on the variation of reaction products.

3.2 Setting and mechanical behaviours

The setting behaviour and mechanical performance are shown in Table 3. NC2 and NC4 exhibit almost the same duration to the setting, which is shorter than the reference NC1. The longest setting time is shown by NC3. This observation is in accordance with the results of the calorimetry test in Section 3.1.1. The addition of waste glass powder seems to reduce the setting time, except for NC3.

Table 3 Setting and mechanical performance of mortars

Sample ID	Initial setting (min)	Final setting (min)	Flexural strength (MPa)		Compressive strength (MPa)	
			7 days	28 days	7 days	28 days
NC1	320	410	5.20	6.29	16.38	25.68
NC2	306	380	4.84	5.30	16.09	23.89
NC3	370	470	3.23	5.12	12.38	17.99
NC4	307	379	4.18	5.13	14.00	21.62

The reference sample (NC1) achieves a compressive strength of 25.7 MPa, while 23.9 MPa, 18.0 MPa and 21.6 MPa are achieved by waste glass containing samples NC2, NC3 and NC4, respectively. The difference in mechanical performance is possibly induced by the chemical composition of binders. The slag component is a critical parameter of strength behaviour for alkali activated slag based materials [20]. As can be seen from Table 2, NC3 has the lowest GGBS content, and also shows the lowest compressive strength after 28 days curing. When waste glass was used to replace 20% of fly ash or total binder, the setting time was reduced, however, the reduction of strength also can be observed.

3.3 Resistance to carbonation

Fig. 5 clearly exhibits the different carbonation depth of mortars. After the waste glass was blended in the GGBS-FA system, the resistance to CO₂ penetration was improved. The reference sample NC1, without glass addition, shows a carbonation depth around 14 mm. When the waste glass replaced 20% fly ash, the carbonation depth decreased to less than 6 mm (NC2).

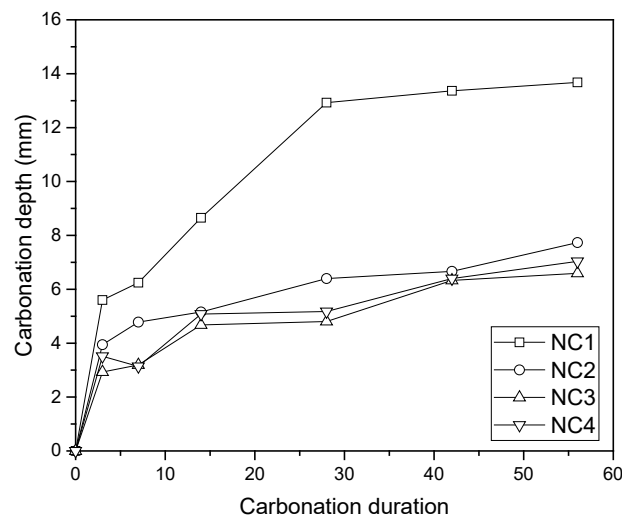


Fig. 5 CO₂ penetration depth of mortars with different carbonation ages

The sample containing waste glass replacing 20% GGBS also accounts for a carbonation depth around 7.5 mm. From the above results, it can be seen that all waste glass blended mortars show a lower compressive strength than the reference. However, a significant higher resistance to CO₂ was observed after the waste glass addition. This may be due to the modifying effect of pore size distribution after the addition

of waste glass. In a previous study, the high Si available through the pozzolanic reaction usually induces a small pore size of reaction products [21].

4. Conclusions

Waste glass was used as part of the binder, replacing GGBS, FA or total replacement in mortars activated by a blended activator. The reaction kinetics and products were characterized. The setting and mechanical performance were tested, and the resistance to carbonation was evaluated. The following conclusions can be drawn:

1. The incorporation of waste glass as part of the binder in alkali-activated GGBS-FA systems exhibits no significant effect on the reaction products. The calorimetry results show that when 20% of fly ash was replaced by waste glass, the reaction intensity and cumulative heat were enhanced.
2. The reduction of the initial and final setting time was observed after 20% fly ash or 20% total binder were replaced by waste glass powder. However, the addition of waste glass induced a strength reduction.
3. The incorporation of waste glass in GGBS-FA binder contributed to a significant enhancement (of up to 300%) of resistance to accelerated carbonation penetration.

5. Acknowledgements

This research was carried out under the funding of China Scholarship Council and Eindhoven University of Technology. Furthermore, the authors wish to express their gratitude to the following sponsors of the Building Materials research group at TU Eindhoven: Rijkswaterstaat Grote Projecten en Onderhoud; Graniet-Import Benelux; Kijlstra Betonmortel; Struyk Verwo; Attero; Enci; Rijkswaterstaat Zee en Delta-District Noord; Van Gansewinkel Minerals; BTE; V.d. Bosch Beton; Selor; GMB; Icopal; BN International; Eltomation, Knuaf Gips; Hess AAC Systems; Kronos; Joma; CRH Europe Sustainable Concrete Centre; Cement & Beton Centrum; Heros; Inashco; Keim; Sirius International; Boskalis; NENERGY; Millvision; Sappi and Studio Roex (in chronological order of joining).

6. References

- [1] A. Shayan and A. Xu, "Value-added utilisation of waste glass in concrete," *Cem. Concr. Res.*, vol. 34, no. 1, pp. 81–89, 2004.
- [2] A. Shayan and A. Xu, "Performance of glass powder as a pozzolanic material in concrete: A field trial on concrete slabs," *Cem. Concr. Res.*, vol. 36, no. 3, pp. 457–468, 2006.
- [3] K. Li, Q. Zeng, M. Luo, and X. Pang, "Effect of self-desiccation on the pore structure of paste and mortar incorporating 70% GGBS," *Constr. Build. Mater.*, vol. 51, pp. 329–337, Jan. 2014.
- [4] C. Hu, "Microstructure and mechanical properties of fly ash blended cement pastes," *Constr. Build. Mater.*, vol. 73, pp. 618–625, Dec. 2014.
- [5] S. Wang, E. Llamazos, L. Baxter, and F. Fonseca, "Durability of biomass fly ash concrete: Freezing and thawing and rapid chloride permeability tests," *Fuel*, vol. 87, no. 3, pp. 359–364, Mar. 2008.
- [6] M. Wu, C. Li, and W. Yao, "Gel/space ratio evolution in ternary composite system consisting of portland cement, silica fume, and fly ash," *Materials (Basel)*, vol. 10, no. 1, 2017.
- [7] A. Shayan and A. Xu, "Performance of glass powder as a pozzolanic material in concrete: A field trial on concrete slabs," *Cem. Concr. Res.*, vol. 36, no. 3, pp. 457–468, Mar. 2006.

-
- [8] G. Liu, M. V. A. Florea, and H. J. H. Brouwers, "Performance evaluation of sustainable high strength mortars incorporating high volume waste glass as binder," *Constr. Build. Mater.*, vol. 202, pp. 574–588, Mar. 2019.
 - [9] M. Torres-Carrasco and F. Puertas, "Waste glass as a precursor in alkaline activation: Chemical process and hydration products," *Constr. Build. Mater.*, vol. 139, pp. 342–354, May 2017.
 - [10] M. Vafaei and A. Allahverdi, "High strength geopolymer binder based on waste-glass powder," *Adv. Powder Technol.*, vol. 28, no. 1, pp. 215–222, Jan. 2017.
 - [11] F. Puertas and M. Torres-Carrasco, "Use of glass waste as an activator in the preparation of alkali-activated slag. Mechanical strength and paste characterisation," *Cem. Concr. Res.*, vol. 57, pp. 95–104, Mar. 2014.
 - [12] R. Martinez-Lopez and J. Ivan Escalante-Garcia, "Alkali activated composite binders of waste silica soda lime glass and blast furnace slag: Strength as a function of the composition," *Constr. Build. Mater.*, vol. 119, pp. 119–129, Aug. 2016.
 - [13] M. Torres-Carrasco and F. Puertas, "Waste glass as a precursor in alkaline activation: Chemical process and hydration products," *Constr. Build. Mater.*, vol. 139, pp. 342–354, 2017.
 - [14] Z. Shi, C. Shi, S. Wan, N. Li, and Z. Zhang, "Effect of alkali dosage and silicate modulus on carbonation of alkali-activated slag mortars," *Cem. Concr. Res.*, vol. 113, pp. 55–64, Nov. 2018.
 - [15] D. EN, "Methods of testing cement – Part 3: Determination of setting times and soundness," 2009.
 - [16] BS EN, "Methods of testing cement —Part 1: Determination of strength," vol. 3, 2005.
 - [17] X. Gao, Q. L. Yu, and H. J. H. Brouwers, "Reaction kinetics, gel character and strength of ambient temperature cured alkali activated slag–fly ash blends," *Constr. Build. Mater.*, vol. 80, pp. 105–115, Apr. 2015.
 - [18] F. Puertas *et al.*, "Alkali-activated slag concrete: Fresh and hardened behaviour," *Cem. Concr. Compos.*, vol. 85, pp. 22–31, Jan. 2018.
 - [19] G. Fang, H. Bahrami, and M. Zhang, "Mechanisms of autogenous shrinkage of alkali-activated fly ash-slag pastes cured at ambient temperature within 24 h," *Constr. Build. Mater.*, vol. 171, pp. 377–387, May 2018.
 - [20] N. Marjanović, M. Komljenović, Z. Bašćarević, V. Nikolić, and R. Petrović, "Physical–mechanical and microstructural properties of alkali-activated fly ash–blast furnace slag blends," *Ceram. Int.*, vol. 41, no. 1, pp. 1421–1435, Jan. 2015.
 - [21] H. Ye, C. Cartwright, F. Rajabipour, and A. Radlińska, "Understanding the drying shrinkage performance of alkali-activated slag mortars," *Cem. Concr. Compos.*, vol. 76, pp. 13–24, Feb. 2017.

Circular Economy , key to sustainable construction

B. (Bauke) Hoekstra Bonnema

Tata Steel , Marketing Construction , PO Box 10.000, 1970 CA IJmuiden Netherlands.

Email of the corresponding author: bauke.hoekstrabonnema@tatasteel.com

Abstract

Global increase in population and increase in wealth/consumption provides a challenge for raw materials and resources. The construction industry is with 40% of global material use and 20% of water use by far the largest consumer of raw materials. Moreover emissions in this sector amount to 50% of global CO₂ emission and 35% of global waste.

The development of low carbon buildings and structures and associated reduction in energy/material consumption is one of the biggest challenges currently facing the construction industry. Circular economy principles provides solutions for material and energy reduction.

Europe is a continent with a low amount of raw materials , hence the focus of the EU on recycling / re use of materials : in december 2015 the EC launched its Circular Economy package with clear targets for recycling and reducing waste.

Steel plays a vital role in the Circular Economy, since steel is light weight, providing large transport and foundation saving. Steel structures are constructed/built using demountable fixings (screws/bolts) , providing an option for flexible/adaptable buildings. The flexibility ensures that buildings can be modified to ensure a long functional life of building, reducing waste streams. Moreover the demountability provides options for re-use of building components and materials in a new application . Already a large share of steel beams are being re-used at the end of life of a building in new applications. The re-use of building components provides a significant energy saving since steel does not need to be re-melted and no new raw materials are needed

Tata Steel provides solutions for design for re-use , developing BIM (Building Information Modelling) solutions for tagging and tracing building materials and working with providers of so-called material passports of buildings to ensure/enable re-use.. Moreover new coating systems like HPS 200 and Prisma by Tata Steel provides up to 40 years maintenance free protection against corrosion , ensuring durable steel structures.

Contrary to other materials, steel has a well developed recycling infra structure , since the value of scrap is considerable , scrap will be returned to the steel industry in order to be remelted into a new steel applications. In fact steel is the most recycled material in the world.

By rapid cooling and quenching , low grade steel can even be up-cycled into a higher value application. Almost all other building materials are being downcycled and eventually turn to waste at the end of life of a building or are being landfilled or incinerated. Due to this characteristics is steel is the only permanent material in society , endless re-used/recycled providing a solution to the global resource shortage .

Keywords: Circular Economy, recycling, low carbon buildings, re-use.



Organized by
**Eindhoven University
of Technology**

TU/e

In cooperation with
**Wuhan University
of Technology**

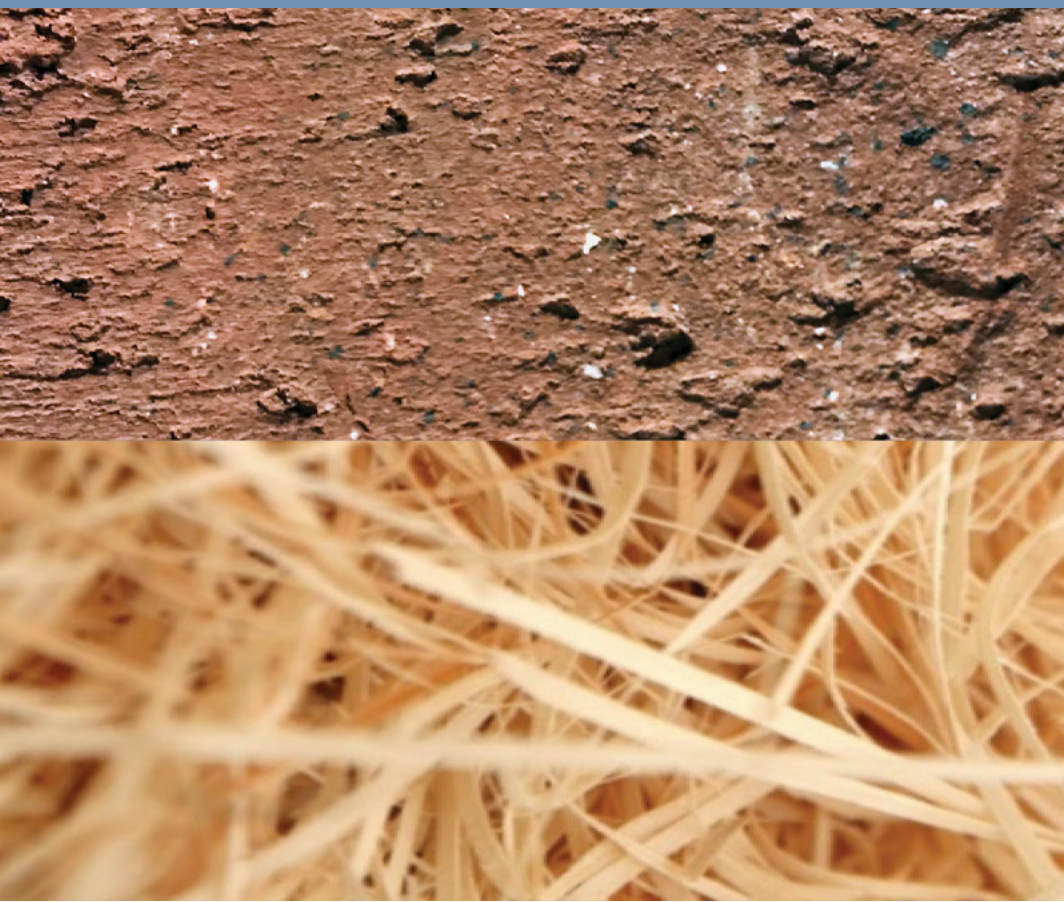


PROCEEDINGS ICSBM 2019

VOLUME 5 - Biogenic and functionalized materials

2nd International Conference on Sustainable Building Materials

August 12-15, 2019 - Eindhoven, The Netherlands
Editors: V. Caprai and H.J.H. Brouwers



and supported by



ICSBM 2019, Conference proceedings

A catalogue record is available from the Eindhoven University of Technology Library

ISBN of the volumes set: 978-90-386-4898-9

ISBN of Volume 5: 978-90-386-4914-6

Sponsored by: CRH, Eltomation - Wood cement board plant, Tata Steel Europe (Gold sponsors), VDZ, PCA (Bronze Sponsors).

Front page image: V. Caprai

Editors: V. Caprai and H.J.H. Brouwers

Organizing committee:

Conference Chairman: Prof. H.J.H. (Jos) Brouwers, Eindhoven

Conference Co-Chairman: Prof. Wen Chen, Wuhan

Conference Secretary: Mrs V. (Veronica) Caprai and Dr. M.V.A. (Miruna) Florea, Eindhoven

Dr. Qiu Li, Wuhan

Dr. Bo Yuan, Wuhan

Dr. Q. Yu, Eindhoven

Dr. F. Gauvin, Eindhoven

Dr. K. Schollbach, Eindhoven

Mr. Y. Chen, Eindhoven

Mrs. L.T.J. Harmsen, Eindhoven

Mrs. N.L. Rombley, Eindhoven

Table of Contents

Bio-based admixtures

W. Schmidt	6
------------------	---

Functionalization of fibres for cement-based materials – selected test methods

J. von Werder, A. Gardei, B. Meng.....	16
----------------------------------------	----

Reduced graphene oxide-coated copper foam composite cathode for the microbial electrosynthesis of acetate from carbon dioxide

P. Tremblay, T. Zhang.....	26
----------------------------	----

Prewashed wood ash for utilization in cement-based materials

N.M. Sigvardsen, J. Pedersen and L.M. Ottosen.....	28
----------------------------------------------------	----

Investigating the efficiency of “in-house” produced hydrogels as internal curing agents in cement pastes

J.R. Tenório Filho, E. Mannekens, D. Snoeck, N. De Belie	29
----------------------------------------------------------------	----

The course of water absorption and desorption from superabsorbent polymers (SAP) in cementitious environment

M. Kalinowski, P. Woyciechowski.....	36
--------------------------------------	----

Study on Self-healing Cementitious Materials with Hydrogels Encapsulating Phosphate

X. Liu, Y. Tang, Z. Liu, W.Chen, Q. Li, W. Chen.....	46
------------------------------------------------------	----

Biosorption of heavy metal ions of lead and zinc by *Trichoderma reesei* based on response surface method

Y. Sun, R. Yu, Z. Shui, D. Qian, B. Rao, J. Huang	55
---------------------------------------------------------	----

Use of peach shell as lightweight aggregate in pervious concrete

F. Wu, C. Liu, L.Zhang, Y. Lu, Q.L. Yu.....	64
---------------------------------------------	----

A concrete composite from biologically based binders and mineral aggregates for constructional 3D-printing

J. Christ, H. Koss, L.M. Ottosen	75
----------------------------------------	----

A silica aerogel synthesized from olivine and its application as a photocatalytic support

Y.X. Chen, Y. Hendrix, K. Schollbach, H.J.H Brouwers	88
------------------------------------------------------------	----

The influence of cellulose-based micro and nanomaterials on early-age properties of cement grouts

H. Karimi, Q.L. Yu, H.J.H. Brouwers.....	96
------------------------------------------	----

The recycling potential of waste wood into wood-wool/cement composite

F. Berger, F. Gauvin, and H.J.H. Brouwers.....	103
------------------------------------------------	-----

Mechanical properties and shrinkages of coir fibers reinforced light-weight aggregate concrete

X.X. Zhang, F. Gauvin, H.J.H. Brouwers 115

Super-hydrophobic magnesium oxychloride cement (MOC): from structural control to self-cleaning property evaluation

Z.Y. Qu, F.Z. Wang, Q.L. Yu, H.J.H. Brouwers 127

Durability of photocatalytic mortars

A.M. Kaja, H.J.H. Brouwers, Q.L. Yu..... 135

Self-cleaning and air purification performance of Portland cement paste with low dosage of nanodispersed TiO₂ coatings

Z. Wang, F. Gauvin, P. Feng, H.J.H. Brouwers, Q.L. Yu 136

Innovative production technologies and applications in the field of Wood Cement Products

E.J.B. van Elten 146

Volume 5

Biogenic and functionalized materials

Bio-based admixtures

W. Schmidt

Bundesanstalt für Materialforschung und -prüfung, Division: Technology of Construction Materials.

Abstract

Due to the high carbon emissions linked to concrete production and a rapidly increasing demand for cementitious materials, particularly in the global South, it is inevitable to use cement in concrete more efficiently. This can be achieved best by minimising the Portland cement content in the binder and by developing concrete mixtures with low water to cement ratios. For both approaches, chemical admixtures are required to cope with the negative rheological influences of supplementary cementitious materials that are often observed, and the higher solid volume fraction, respectively.

However, particularly in the growing economies of the Southern hemisphere, where a massive part of the future construction activities will take place, the supply chains are often poor with regard to performance enhancing chemical admixtures, and local production facilities are lacking today.

This paper presents case studies of polysaccharide based alternative admixtures such as acacia gum, cassava starch and the gum of the bark of *Triumfetta pendrata* A. Rich, which can be used effectively as superplasticizer, robustness enhancer, and thixotropy incorporating agent, respectively. Their modes of operation are discussed based on their zeta potentials and hydrodynamic diameters in the presence of calcium ions. Eventually, local value chains are discussed for bio-based by products on the example of cassava peels wastes.

Keywords: admixtures, concrete, cassava, acacia gum, *Triumfetta pendrata* A. Rich.

1. Introduction

Cement production consumes a high amount of raw materials, required high energy and involved chemical processing. Thus, it contributes significantly to global CO₂ emission. Global cement production is estimated at 4.6 Gt/a [1] in 2015 and will rise to values between 6 and 13.5 Gt/a in 2050 [2, 3]. However, since cement is urgently required to build structures and infrastructures with concrete, and concrete is the only material in the world that can meet the global demand for construction materials, the situation is aggravated as the world's population increases from today 7.3 to 9.7 billion in 2050 [4]. The production of cement creates high carbon emissions from fuelling, but even more from decarbonation of calcium carbonate from the limestone to convert it to calcium oxide, resulting in assumedly more than 8% of all the greenhouse gases released by human activity and carbon emission estimates for concrete in the order of magnitude of 10% of all global carbon emissions [5]. Yet, other materials have even higher carbon footprints and energy demands [6, 7], which makes concrete inevitable as mass construction material.

Consequently, the only way to make the construction industry more environmentally friendly means making concrete technology greener and using cement in concrete more efficiently. This means that the water cement ratios in concrete have to be reduced by using chemical admixtures that help to control the rheology despite the lower water content [23]. In Africa, the efficient usage of cement is even more important, since the cement prices are significantly higher than in other parts of the world, when expressed in local

purchasing power (Fig. 1). The efficient use of chemical admixtures for higher performance materials, thus, can have a tremendous leverage towards a better global climate.

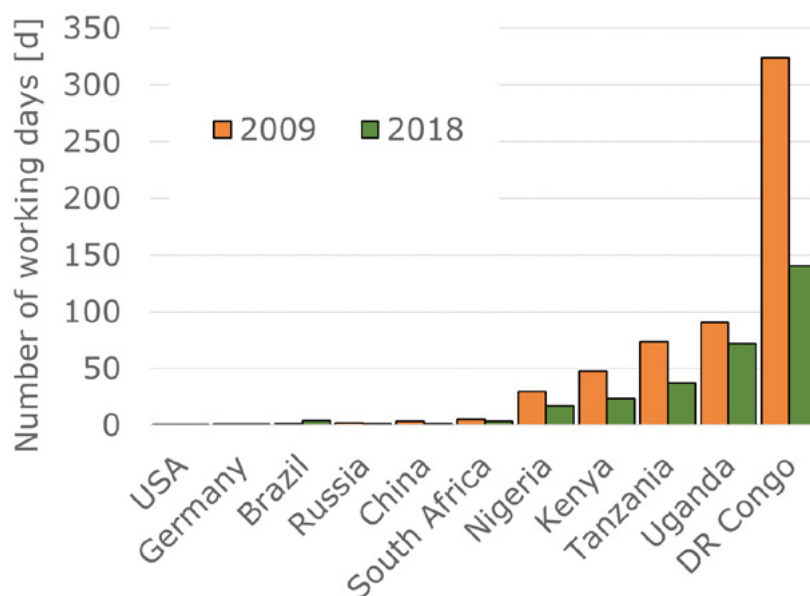


Figure 1: cement price differences in different countries in the world expressed in number of working days for an average income earner to purchase a ton of cement for the years 2009 and 2018. Price information obtained from local inhabitants.

Furthermore, this inevitably calls for blending cement with more sustainable supplementary cementitious materials [8]. In most developing countries in sub-Saharan Africa, the established materials such as ground granulated blast furnace slag or fly ash are hardly available, but agricultural wastes are available in large quantities with a growing potential for the agricultural industry on the continent [9, 10]. Thus, using bio materials as pozzolanic materials is getting more important in research, globally, but particularly in Africa. Some notable studies that demonstrate the use of ashes of rice husk, sugar cane straw and groundnut husk as pozzolanic components in concrete are presented in [11-20]. They have shown that mechanical and durability properties can be enhanced, depending upon the amorphous silica content. Africa provides 60% of the global unused arable land [21]. Thus, the continent has a tremendous potential for further development of the agricultural harvest. Hence, vegetable ashes are a real potential for many African countries to make concrete technology greener and more economically viable by creating local value chains.

Nevertheless, the use of agricultural by-products as cementitious materials often comes along with new challenges for the workability, since the rough and fissured surfaces absorb more water than cement, which demands for chemical admixtures again to control the rheology.

Hence, chemical admixtures help to use cement in concrete more efficiently by reducing the required water and helping to cope with the challenges arising from the use of supplementary cementitious materials used to reduce the amount of Portland cement clinker in the binder. However, many regions in the world, particularly in the Southern hemisphere lack supply of chemical admixtures, that often have to be imported from Europe, North America or Asia. As a result, they are available only in limited variability and at high costs [22]. This limits the applicability of sustainable and high performance applications in regions of the Southern hemisphere, particularly on the African continent, which is a real obstacle for Africa's enormous innovation potential and rapid economic upswing [9].

Feasible alternatives to traditional synthetic polymers are innovative and efficient admixtures based on locally available plant-based bio-materials. It has already been shown that high performance concrete can be

developed [23], and complex rheological properties can be achieved [24-26] with bio-based polysaccharides. In addition, new markets can be created [27].

This paper shows a review of some potentially viable bio-polymers that can be used for high performance applications in concrete technology.

2. Case studies

2.1 Acacia gum as superplasticizer

Acacia gum can be found in various modifications all over the African continent. The most important global exporters are Senegal and Sudan, while there is hardly a real market in other countries. Acacia gum has shown to be an excellent superplasticizer, though, its effect depends strongly on the solid volume fraction. Fig. 2 shows the torque change of cement pastes with different polymer dosages of two qualities of acacia gum from Sudan and South Africa in comparison to two polycarboxylates (PCE) and a lignosulfonate.

At low dosage, the acacia gum acts as a stabilising agent, which can be seen from the increasing torque. However, upon addition of higher amount the torque decreases indicating a reduced viscosity. Both acacia gums show this liquefying effect. The gum from Sudan shows even higher efficiency than the pre-cast PCE, while the South African gums has similar effect to the ready-mix PCE and the lignosulfonate.

The effect of acacia gums depends strongly on the solid volume fraction. A liquefying effect can only be observed, when the w/c is moderately low. At extremely low w/c no liquefying effect can be observed.

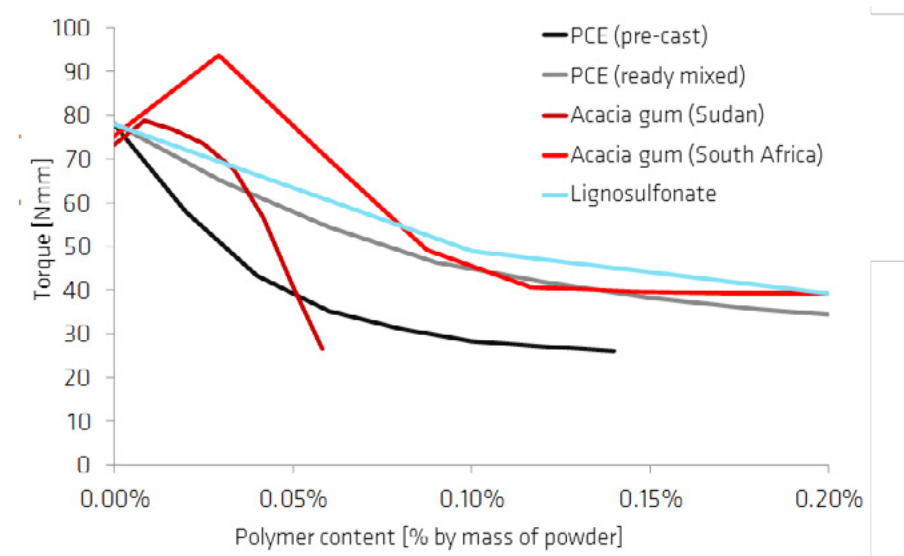


Figure 2: effect of different polymer dosages on the torque at rotational speed of 240 rpm in cement pastes with a solid volume fraction of 0.40.

2.2 Cassava starch as stabilising and plasticizing admixture

Cassava is the third most important source of starch in the world after rice and maize. It feeds about half a billion people in the Southern hemisphere. Major cassava producers can be found in East Asia, Africa, and South America (Fig. 3), the most important of which is Nigeria where about 20% of the global cassava is being produced.

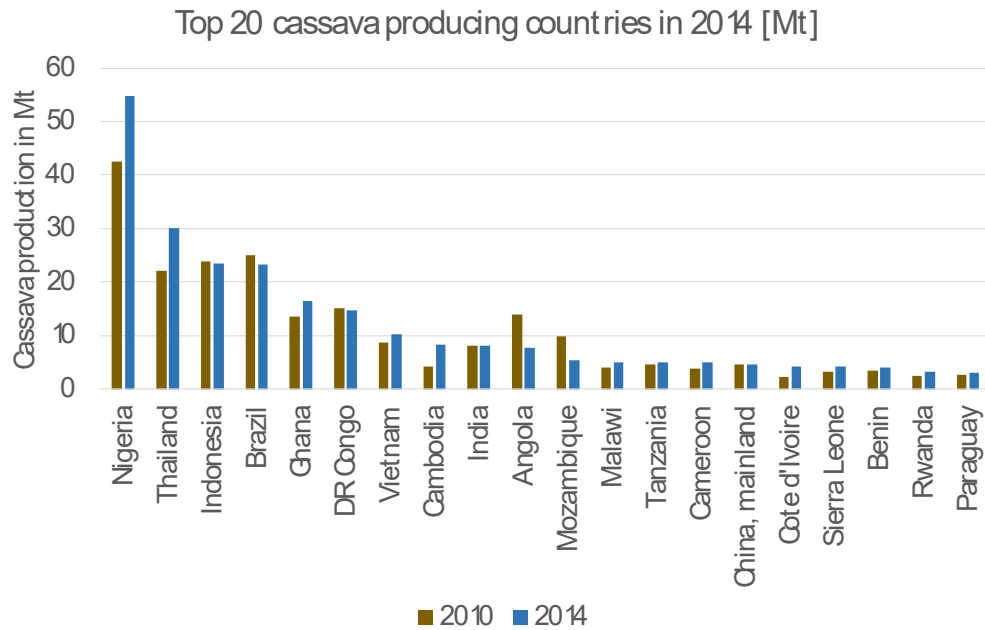


Figure 3: top 20 cassava producing countries in 2010 and 2014.

Cassava tubers are rich in starch, and like potato starch it contains around 80% amylopectin and 20% amylose. Nevertheless, potato starch is typically used to increase the stability of cementitious systems by increasing the viscosity, while cassava starch can incorporate plasticizing effects as well (Fig. 3). Depending on dosage and solid volume fraction, cassava can thus help to generate a softer consistency, while, due to the viscosity enhancing properties of the starch, the coherence of the cementitious system is increased, which creates higher robustness.

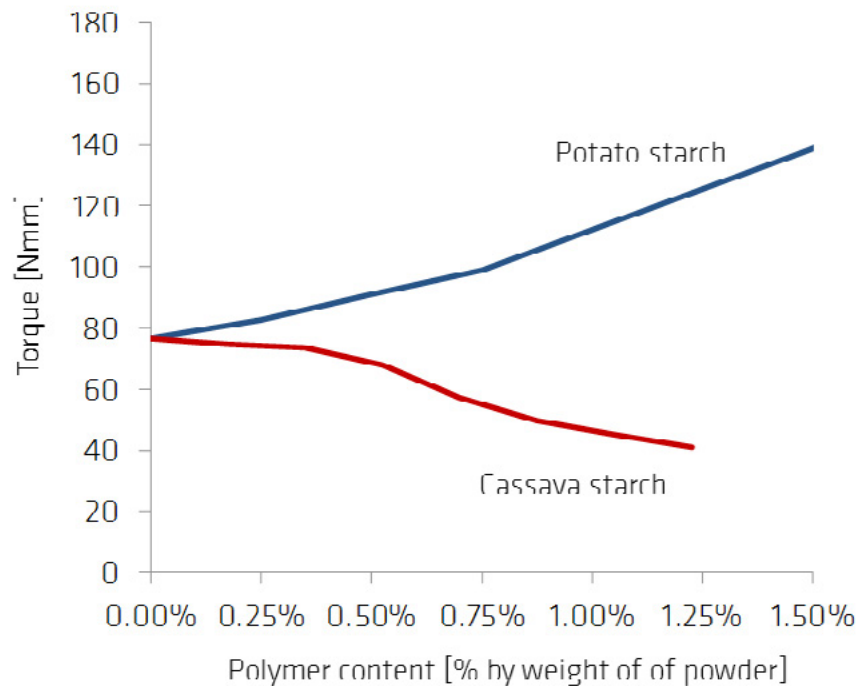


Figure 4: Torque change in cement pastes at a solid volume fraction of 0.4 and a rotational speed of 240 rpm due to the addition of potato starch and cassava starch.

2.3 *Triumfetta pendrata* A. Rich to enhance thixotropy

The gum of the malvaceous plant *Triumfetta pendrata* A. Rich is typically used as food consistency regulating agent for a typical Cameroonian dish called 'nkui'. The easily water-soluble polymers incorporate a very cohesive consistency to the soup. Mixed with concrete, the polymers have little effect in cement pastes only, but in the presence of superplasticizers they bear the capacity to totally reverse the liquefying effect by dramatically increasing the yield stress without significantly affecting the plastic viscosity. Flowable systems, thus, build up a thixotropic structure within short period of time.

The effect is shown in Fig. 5. The red curves show the flow values on the Haegermann table without strokes. The blue curves show the results of the respective samples after 15 strokes. The strokes significantly increase the flow values for both systems, with and without the addition of nkui gum.

The effect of the gum becomes most obvious at a w/c of 0.4. While the system without gum spreads wide without strokes, the system with gum nearly shows no flow, but after 15 strokes, the flowability with and without gum are nearly identical. The strong thixotropic effect of the gum can be used beneficially, e.g. in all kinds of additive processing such as 3D-printing.

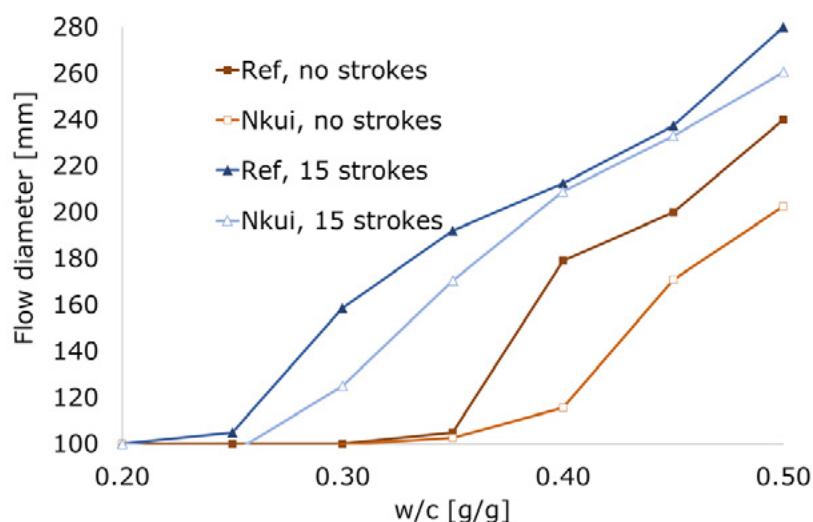


Figure 5: flow values (Haegermann cone) of cement pastes with 0.35% PCE (bwoc) in the presence of 0.08% Nkui gum (bwoc) and without the gum. Blue curves show results after 15 strokes, red curves show results without strokes.

3. Discussion of results

The results of some rheological experiments in the presence of different bio-gums were presented. In the case of the present polymers the following conclusions can be made:

- Acacia gum can be used as superplasticizer. However, at low dosages they act as stiffening agents.
- Cassava starch can be used as slight plasticizer and consistency regulator.
- The gum of the bark of *Triumfetta pendrata* A. Rich incorporates strong thixotropy.

Zeta potential measurements and measurements of the hydrodynamic radii provide some indicators for the different behaviours of the gums. Although their zeta potentials vary greatly in water, in the presence of calcium ions, their zeta potentials are all negative in the same order of magnitude between -7.4 and -13.2 mV. Thus, all polymers can be assumed to adsorb on cementitious particles, which alone cannot explain their effect. Their major difference lies in their polymer sizes and agglomeration tendency.

The acacia gum polymers tend to agglomerate to form a large variety of polymer sizes. The range goes from 20 nm to 1 μ m. Thus, it can be assumed that polymers are packed densely in the liquid phase, which explains, why at low dosages they have a stiffening tendency. Only, when the water between the particles is sufficiently high, the polymers become more mobile, and thus may create a kind of a ball bearing effect in the liquid phase, while the adsorbed polymers sterically keep the cement particles in distance, thus, causing the excellent flow properties.

The cassava starch also adsorbs on particles in the cementitious system. The present cassava starch polymers are significantly smaller in size (\sim 150 nm) than what is reported in literature for potato starch (amylopectin $>$ 500 nm) [28], which explains the different effects shown in Fig. 4. While potato starch polymers are particle sized and, thus, hinder particles from movements [25], the investigated cassava starch polymers are much smaller, so that the particle stabilising effect becomes much smaller, and steric effects become more prominent.

The *Triumfetta pendrata* A. Rich polymers seem to significantly form huge agglomerates in the presence of calcium ions. The agglomerates being formed show sizes up to 5 μ m, which is particle size. This agglomeration explains the strong thixotropic structural build up. Since the calcium linking is not stable, the structure easily breaks down under shear forces, giving the material good flow under forces.

The present figures and the table show the clear difference between the use of synthetic polymers and biopolymers. While synthetic polymers can be modified according to the requirements, bio-gums have to be taken as they are. This means, the polymers' effects have to be understood at first, and then their best use can be determined. However, despite their different effects all polymers can be applied in different high-performance applications. Thus, they provide enormous potentials for greener concrete admixtures.

Table 1: Zeta potentials and hydrodynamic radii of the present polymers in different ionic media, measured with dynamic light scatter.

	Acacia gum		Cassava starch		Bark gum of <i>Triumfetta pendrata</i> A. Rich	
	Water	Saturated limewater	Water	Saturated limewater	Water	Saturated limewater
Zeta potential [mV]	-16.3	-7.7	0.6	-7.4	-25.3	-13.2
D_{hyd} [nm]	Distinct peaks at \sim 10 nm and \sim 100 nm	Broad range between \sim 20 nm and \sim 1 μ m	Distinct peak at \sim 150 nm	Distinct peak at \sim 120 nm	Distinct peak at \sim 250 nm	Distinct peaks at \sim 700 nm and 5 μ m

4. Local value chain potentials

Considering the scarcity of chemical admixtures in many countries of the Southern hemisphere, bio-based solutions can become a viable option, particularly since plants containing promising polysaccharides grow all over the African and South American continents. This easy availability creates potentials for local value chains that support the local markets as well.

Cassava is one most promising example. The peels of cassava have limited use in livestock feeding as they cannot be digested by most animals. Thus, the peels are typically dumped away. They require large spaces, where the waste rots away, creates malodour and attracts insects. Sometimes the wastes are burnt to save the space for dumping, but the ashes are not further used any more.

However, instead of dumping, the organic starch content that is still adhered to the peels can easily be

obtained to become a precursor for a concrete chemical admixture to enhance the performance and save cement in concrete. After obtaining the starch, the residual peels can still be burnt, thus, create energy for example for brick production. After burning, the ashes were shown to have pozzolanic properties, thus, help reducing the Portland cement content in the binder for concrete. The concept is shown in Fig. 6.

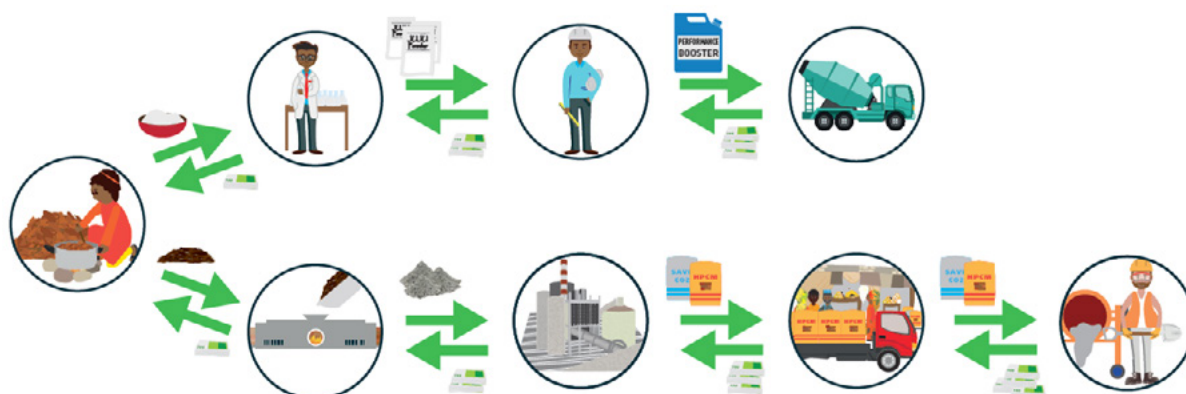


Figure 6: possible new value chains based on today simply dumped cassava peels. An organic and an inorganic value chain can be created from the same residues in parallel. Both value chains help making concrete more sustainable, by enhancing the concrete properties and reducing the Portland cement content in the binder, respectively.

5. Conclusions

The present results and interpretation have shown some remarkable properties of bio-gums obtained from acacia gum, cassava starch and the gum of the bark of *Triumfetta pendrata* A. Rich. The mode of operation of the different gums in the cementitious system is complex and requires further understanding. Much of the effects can be explained by the polymer sizes and size distributions as well as their interactions with particle surfaces and calcium ions in the aqueous phase of cement paste.

6. Acknowledgment

Some of the present result were obtained within the framework of the German African Innovation Incentive Award provided by the Federal Ministry of Education and Research. The author gratefully acknowledges the financial support for this research

7. References

- [1] K. Carstensen and O. Rapf, "A blueprint for a climate friendly cement industry," WWF, Nürnberg, Germany 2008.
- [2] CEMBUREAU, "Cement & concrete: key facts & figures," t. E. c. association, Ed., ed, 2015.
- [3] P. Edwards. (2016). *The Rise and Potential Peak of Cement Demand in the Urbanized World*. Available: <http://cornerstonemag.net/the-rise-and-potential-peak-of-cement-demand-in-the-urbanized-world/>
- [4] UN. (2015). *World Population Prospects: The 2015 Revision*. Available: <http://www.un.org/en/development/desa/news/population/2015-report.html>
- [5] "Concrete CO2 Fact Sheet," 2008, Available: <http://www.nrmca.org/greenconcrete/concrete%20co2%20fact%20sheet%20june%202008.pdf>.
- [6] K. Scrivener, V. M. John, and E. M. Gartner, "Eco-efficient cements: Potential, economically viable solutions for a low-CO₂, cement-based materials industry," United Nations Environment Programme 2016.

-
- [7] L. Barcelo, J. Kline, G. Walenta, and E. Gartner, "Cement and carbon emissions," *Materials and Structures*, journal article vol. 47, no. 6, pp. 1055-1065, 2014.
- [8] J. W. Wilson and Y. C. Ding, "A Comprehensive Report on Pozzolanic Admixtures, the Cement Industry, Market and Economic Trends and Major Companies Operating in the Far East, with Reference to Pagan Island," 2007.
- [9] W. Schmidt, "Potentials for sustainable cement and concrete technologies – comparison between Africa and Europe," presented at the Proceedings of the 1st International Conference on Construction Materials for a Sustainable Future, Zadar, Croatia, 19 - 21 April 2017, 2017.
- [10] W. Schmidt, "Why Africa can spearhead innovative and sustainable cement and concrete technologies globally," in *KEYS Knowledge Exchange for Young Scientists: Valorisation of Industrial By-products for Sustainable Cement and Concrete Construction – Improvement of Solid Waste Management*, N. S. Msinjili and W. Schmidt, Eds. Accra, Ghana: BAM, 2016, pp. 7-19.
- [11] K. Olonade, A. M. Olajumoke, A. O. Omotosho, and F. A. Oyekunle, "Effects of sulphuric acid on the compressive strength of blended cement-cassava peel ash concrete," (in English), *Construction Materials and Structures*, pp. 764-771, 2014.
- [12] M. A. Salau and K. A. Olonade, "Pozzolanic Potentials of Cassava Peel Ash," *Journal of Engineering Research*, vol. 16, no. 1, pp. 10-21, 2011.
- [13] W. Schmidt, N. S. Msinjili, S. Pirskawetz, and H. C. Kühne, "Efficiency of high performance concrete types incorporating bio-materials like rice husk ashes, cassava starch, lignosulfonate, and sisal fibres," in *First International Conference on Bio-based Building Materials*, Clermont-Ferrand, France, 2015, vol. 208-2014: RILEM.
- [14] N. van Tuan, Y. Guang, and B. D. Dai, "Study the Hydration Process of Cement Blended with Rice Husk Ash by Means of Isothermal Calorimetry," in *13th International Congress on the Chemistry of Cement*, Madrid, Spain, 2011.
- [15] B. Chatveera and P. Lertwattanakurk, "Evaluation of sulfate resistance of cement mortars containing black rice husk ash," *Journal of Environmental Management*, vol. 90, no. 3, pp. 1435-1441, Mar 2009.
- [16] T. S. Ketkukah and E. E. Ndububa, "Groundnut Husk Ash (GHA) as a Pozzolana Material in Mortar," *International Journal of Science and Technological Research*, vol. 3, no. 2, pp. 209-214, 2006.
- [17] I. C. Mayowa, "Making Durable Concrete Through Inhibition of Chloride Ion Penetration by Pozzolanic Reaction," in *1st Symposium on Knowledge Exchange for Young Scientists (KEYS) - Sub-Saharan African Standards for Cement and Concrete Research and Raw Materials, Quality Control and Maintenance of Cementitious Products*, Dar es Salaam, Tanzania, 2015, pp. 145-150: BAM.
- [18] N. S. Msinjili, W. Schmidt, A. Rogge, and H. C. Kühne, "Optimising available resources for production of good concrete properties," in *Advances in Cement and Concrete Technology in Africa*, Dar es Salaam, Tanzania, 2016, pp. 323-332: BAM.
- [19] M. Frias, E. Villar Cocina, and E. Valencia-Morales, "Characterisation of sugar cane straw waste as pozzolanic material for construction: Calcining temperature and kinetic parameters," *Journal of Waste Management*, vol. 27, pp. 533-538, 2007.
- [20] O. Cizer, K. Van Balen, J. Elsen, and D. Van Gemert, "Carbonation and hydration of calcium hydroxide and Calcium silicate binders with Rice Husk Ash," in *2nd International Symposium on Advances in*

Concrete through Science and Engineering, Quebec City, Canada, 2006.

- [21] A. Perry, *The Rift: A New Africa Breaks Free*. Little, Brown and Company 2015.
- [22] W. Schmidt, N. S. Msinjili, and H.-C. Kühne, “Materials and technology solutions to tackle the challenges in daily concrete construction for housing and infrastructure in sub-Saharan Africa,” *African Journal of Science, Technology, Innovation and Development*, pp. 1-15, 2018.
- [23] W. Schmidt, N. S. Msinjili, H. C. Uzoegbo, and J. K. Makunza, “Admixture Concepts for the Sub-Saharan African Environment with Indigenous Raw Materials,” in *SP-302 Eleventh International Conference on Superplasticizers and Other Chemical Admixtures in Concrete*, V. M. Malhotra, Ed., 2015, pp. 491-505.
- [24] W. Schmidt, I. L. Tchegnina Ngassam, R. Mbugua, and K. A. Olonade, *Natural rheology modifying admixtures for concrete* (Rheologische Messungen an Baustoffen). tredition GmbH, 2017.
- [25] W. Schmidt, H. J. H. Brouwers, H.-C. Kühne, and B. Meng, “Interactions of polysaccharide stabilising agents with early cement hydration without and in the presence of superplasticizers,” *Construction and Building Materials*, vol. 139, pp. 584-593, 2017.
- [26] W. Schmidt, I. Tchegnina Ngassam, K. Olonade, Mbugua, R, and H.-C. Kühne, “Plant based chemical admixtures – potentials and effects on the performance of cementitious materials,” *RILEM Technical Letters*, vol. 3, pp. 124-128, 2019.
- [27] W. Schmidt and M. J. Barucker-Sturzenbecher, “Bio-based concrete (<https://vimeo.com/310549146>),” ed. Berlin, 2019, p. 7:51.
- [28] W. Schmidt, H. J. H. Brouwers, H.-C. Kühne, and B. Meng, “The working mechanism of starch and diutan gum in cementitious and limestone dispersions in presence of polycarboxylate ether superplasticizers,” *Applied Rheology*, vol. 23, no. 5, p. 12, 2013.

Parallel session contributions

Functionalization of fibres for cement-based materials – selected test methods

J. von Werder¹, A. Gardei¹, B. Meng¹

¹*Bundesanstalt für Materialforschung und -prüfung, Unter den Eichen 87, 12205 Berlin, Germany, julia.von-werder@bam.de*

Abstract

The low tensile strength of cement-based materials can be improved by the addition of fibres. In a joint research project, an industrial partner designed special coatings for polymer and carbon fibres by integrating surfactants and hydrophilic compounds. Aim of the developed functionalization was to ensure an even coverage of the fibre surfaces and to anchor them chemically in the cement-based matrix. Task of the BAM was to quantify the effect of the improved bond. In a first step a workable mortar adjusted to the strength of the tested fibres was developed and the fibre distribution assessed by light microscopy and computed tomography. To test the new coating for its efficiency to prevent cracking during hardening and to improve the loadbearing behaviour new test setups were developed or existing methods were adjusted. The experiments showed that the functionalization leads to a reduction of the crack area measured after the exposure of the wet mortar to strong drying conditions in the wind channel. Regarding the efficiency to mitigate shrinkage cracks the functionalisation turned out to be more efficient for fibres made from polyacrylonitrile (PAN) than for carbon fibres. An improvement of the tensile strength after cracking of the cementitious matrix could only be documented for the coated carbon fibres. It could be quantified, however, only in the three-point bending tests because the fibres turned out to be too brittle for the applied single fibre pull-through test.

Keywords: fibres, functionalization, mortar, computed tomography, shrinkage

1. Introduction

Cement based materials play a decisive role in the building materials sector because of their economic and technical benefits. To further improve their applicability and durability regarding special applications, they are more and more frequently equipped with fibres made from different types of material like for example steel, carbon or polymers. Due to their superior mechanical performance, even carbon nano tubes are used [1]. Fibres are added because of different reasons. Within renders as part of external thermal insulation composite systems (ETICS) for example their purpose is to permanently absorb the tensile and flexural stress resulting from thermal and hygric loads [2]. In other cases, their primary aim is to reduce shrinkage cracking during the hardening process [3,5] or to prevent explosive spalling in case of fire [6].

The effectiveness of fibres is based on the dissipation of the fracture energy due to the adhesive friction between the fibres which are in most cases hydrophobic and the hydrophilic hardened cement paste. This pure physical interaction between fibres and matrix requires a certain amount and length of fibres [2] for a specific load case which can lead to technical restrictions in terms of workability especially for slender components with high requirements regarding mechanical strength (ultra-high-performance concrete).

Aim of a joint research project with an industrial partner was therefore, to improve the fibre performance

by the integration of surfactants and hydrophilic compounds into a new polymeric coating. The functionalization was designed to allow an even coating and to make the surface of the fibres hydrophilic so that a chemical bond between the fibres and the hardened cement paste is established [7,9]. The preparation process of the fibres was developed and continuously refined by the project industrial partner. Task of the BAM was to quantify the improved chemical bond between the fibres and the cementitious matrix due to the new functionalization. To evaluate the effect on the mechanical performance and the shrinkage cracking in comparison to uncoated reference fibres existing tests had to be adjusted and new test set-ups had to be developed

2. Methodology

2.1 Materials

To analyse the performance of the functionalization a mortar with a good workability allowing a homogeneous distribution of the fibres had to be designed. Furthermore, the strength of the mortar had to be carefully adjusted so that a differentiation between the performance of the standard untreated fibres (reference) and the chemically functionalized fibres was feasible. To achieve a significant number of evaluable cracks in the wind tunnel test, the formulation was impoverished by adding a substantial proportion of limestone powder (Table 1).

Table 1: Formulation of the cement mortar to evaluate the effectiveness of the functionalization

Component	Weight
	g
CEM I 32,5 R	270
limestone powder	1145
standard sand	1350
water	550

Fibres for test were selected from different material types: polyacrylonitrile (PAN), polypropylene (PP) and carbon (Table 2). The carbon fibres were covered by an epoxy-coating. In the course of the research project two different batches of the same carbon fibres were ordered.

For mixing the fibres into the mortar two different modes were tested: in the first case they were added in a wet state immediately after the treatment with the agent and in the other case they were put in after the treatment agent had dried on their surface.



1a)



1b)



1c)

Figure 1: PAN fibres (1a), PP fibres (1b) and carbon fibres (1c).

Table 2: Physical properties of the fibres used in the study.

Sample	Length	Diameter	Young's Modulus	Tensile strength	Raw density	Fibre surface (dry)
	mm	µm	kN/mm ²	N/mm ²	g/cm ³	cm ² /g
PAN	4;6;8;12	15	15-20	330-530	1,18	2250
PP	4,6; 6	15,4	4-18	320-560	0,9	
Carbon	6	7	240	4.000		

2.2 Methods

The workability of the mortar, depending on the amount of fibres added, was quantified by the flow spread according to DIN EN 1015-3 [10].

Because of their fluorescent properties, the distribution of the PAN-fibres within the cementitious matrix was analysed in a first step two dimensionally by optical microscopy employing ultraviolet light. For this microscopic analysis polished cross sections of standard prisms (40 x 40 x 160 mm³) were used. The three-dimensional analysis of the fibre distribution was performed by x-ray computer tomography (3D-CT) using small cores with a maximum diameter of 10 mm and a minimum length of 20 mm. These samples were drilled out of solidified standard mortar prisms, which were impregnated with epoxy resin for stabilization. The measuring principle of the 3D-CT is based on the radiography of a sample from different angles during the stepwise rotation around 360°. By specific reconstruction algorithms the spatial distribution of the X-ray absorptivity coefficient α is calculated from the individual images and visualized three-dimensionally by the allocation of greyscales (Figure 2).

The distribution of the carbon fibres could only be examined under the light microscope. Due to the small difference in x-ray absorptivity to the mortar matrix a three-dimensional analysis by CT was not possible.

The flexural strength after the incipient crack was quantified by calculating the energy of deformation from the area under the load-deflection-curve resulting from a three-point bending tests of mortar prisms (mean value of a set of three mortar prisms 40 x 40 x 160 mm³).

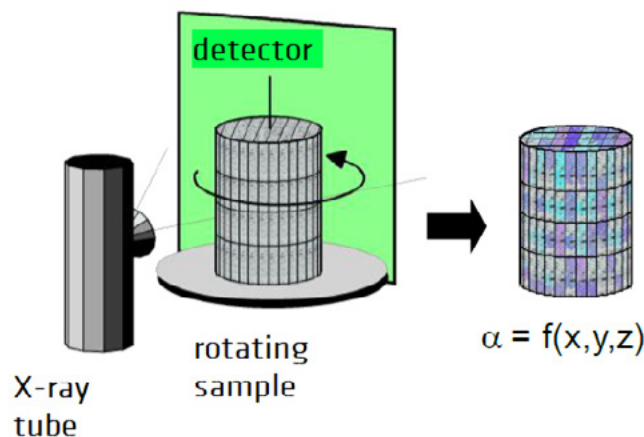
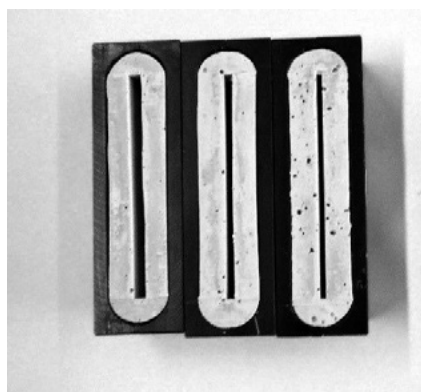
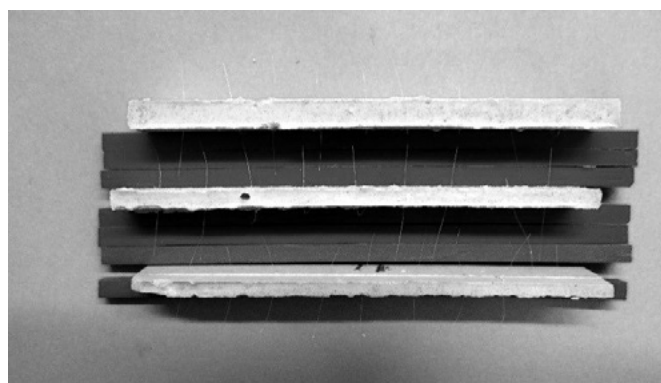


Figure 2: Measuring principle of the 3D-CT.

To exclude effects due to the distribution and orientation of the fibres, the improvement of the bond between the fibres and the matrix was additionally quantified by a fibre pull-through test. For the test set-up individual fibres with a larger diameter (PAN: 80 µm and PP: 72 µm) and a length of 2 cm were embedded into the fresh mortar of small specimens with a thickness of 2, 3 and 4 mm (Figure 3).



3a)



3b)

Figure 3a: Form work of the samples made for the individual fibre pull-through test

Figure 3b: Specimens in the thickness of 2,3 and 4 mm with embedded fibres

The shrinkage behaviour was evaluated according to the test procedure of the German Institute for Building Technology (DIBt) for the entrance examination for the approval of polymer fibres to be used in concrete [11,13]. To provoke shrinkage cracks, paving slabs of the size 30 x 30 cm² were plastered with the different fibre-mortar mixes and afterwards rapidly dried in a wind channel at 30 °C and 50 % relative humidity at a wind speed of 5 m/s (Figure 4).

For the analysing procedure after rapid drying three areas (16 x 16 cm²) were selected, and digitized (with a resolution of 50 µm/pixel). From these images the length and the width of all cracks above 100 µm were measured and the crack opening area was calculated.



Figure 4: Wind channel with four previously plastered paving slabs (30 x 30 cm) in a climate chamber operated at 30° C and 50 % relative humidity

3. Results and discussion

As expected, the addition of fibres had a significant impact on the properties of the freshly mixed mortar. Figure 5 shows the correlation between increasing fibre content and increasing stiffness of the mortar, which is reflected by a decreasing flow spread and confirms the observations by [14]. The decreasing flow spread with increasing volume content of fibres is most prominent for the carbon fibres (Figure 5) and least pronounced for the PP fibres. The mode of addition of the functionalized fibres (in the wet or dry state) as well as the length of the fibres seems to have no or rather a minor impact on the flow spread in such tests.

The analysis of the two-dimensional fibre distribution revealed that an increasing fibre content favours

the agglomeration of fibres (Figure 6). The three-dimensional analysis further illustrates that the spatial distribution is not homogeneous in terms of amount and preferred orientation (Figure 7). The smaller amount of untreated PP fibres in the reference sample (Figure 7a) indicates that the functionalization improves their even distribution (Figure 7b). As already confirmed for the mortar with 0,5 Vol.-% of PAN fibres by optical microscopy (Figure 6a) the 3D-CT images show that also the mortar with 0,5 Vol.-% of PP fibres does not agglomerate. It could be demonstrated that the orientation distribution function derived from the 3D-CT results can be used for calculation of the effective elastic properties of polymer fibre reinforced concrete [15, 16].

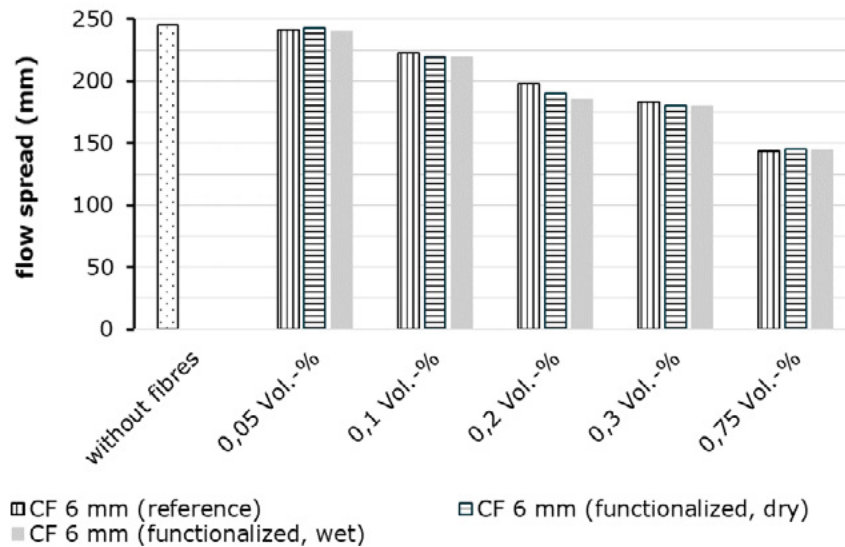
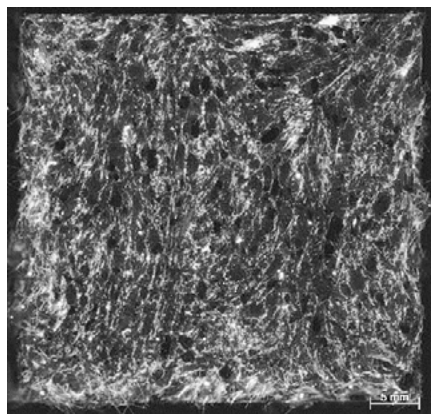
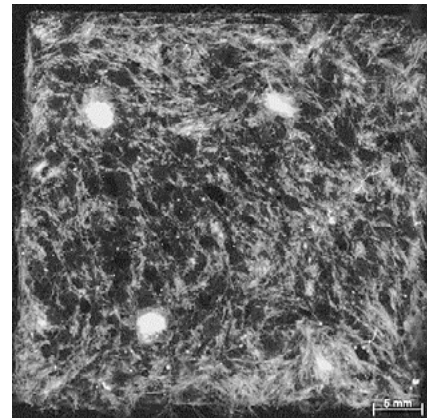


Figure 5: Flow spread fibres according to the fibre content and the mode of addition (mean of two measurements with a maximum standard deviation of 6 mm)



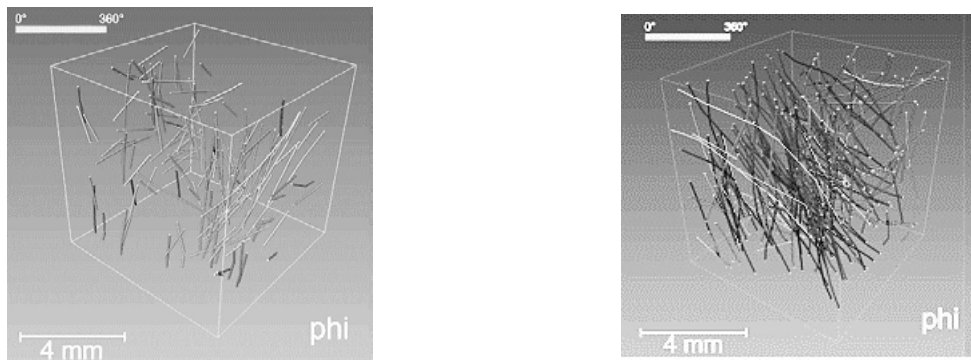
6a)



6b)

Figure 6: Sections of mortar prisms with PAN fibres (length = 4 mm) under UV-light

6a) 0,5 Vol.-% 6b) 1,0 Vol.-%



7a)

7b)

Figure 7: Three-dimensional distribution of PP in the cement mortar (fibre-content: 0.5 Vol.-%, fibre length: 4,6 mm) analysed by CT with colour code attributed to the fibre orientation

7a) reference 7b) functionalized, wet

The load deflection curves from the three-point bending test, shown in Figure 8, illustrate if maximum load has been reached the matrix breaks and the load is transferred to the fibres. The higher the load related to the deformation, the more efficient is the transfer of loads due to adhesion and friction. To compare the mechanical performance of the mortars the energy of deformation is calculated which is represented by the area below the load-deflection curve. For the addition of 0.05 Vol.-% of carbon fibres the energy of deformation increases up to 50 %, when the functionalized carbon fibres are compared to the hydrophobic reference (Figure 9). To provide reliable statistics, however, numerous retries were performed in which it turned out that the magnitude of improvement also depends on the batch of fibres. Whereas one batch of carbon fibres exhibited a comparable low energy of deformation in the not treated reference state, the next order was characterized by a high level already for the reference so that the potential for improvement decreased. Using scanning electron microscopy, no differences could be distinguished regarding the surface structure of the fibres, so that chemical differences of the epoxy coating might be an explanation.

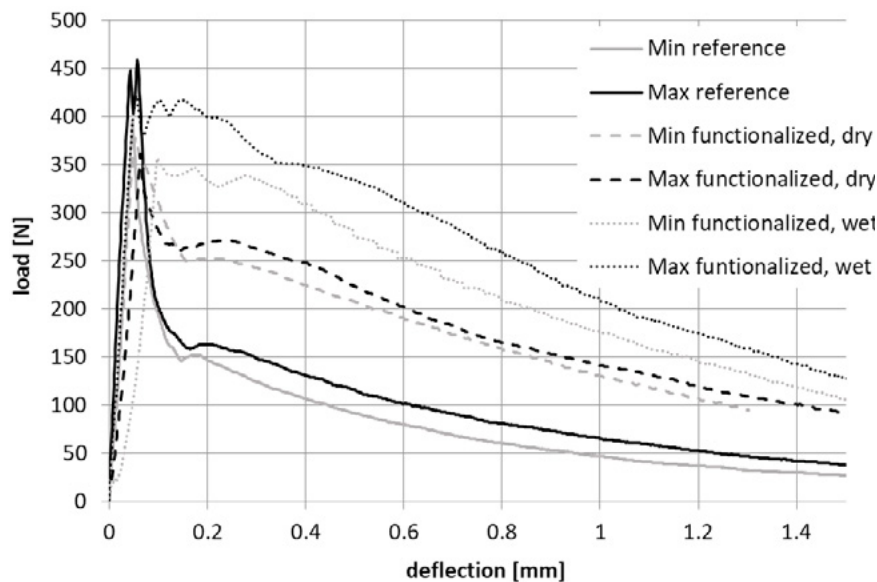


Figure 8: Envelope curves of the minimum and maximum values for load and deflection of three mortar prisms with 0,05 Vol.-% carbon fibres, not treated versus functionalized, added in the wet and in the dry state

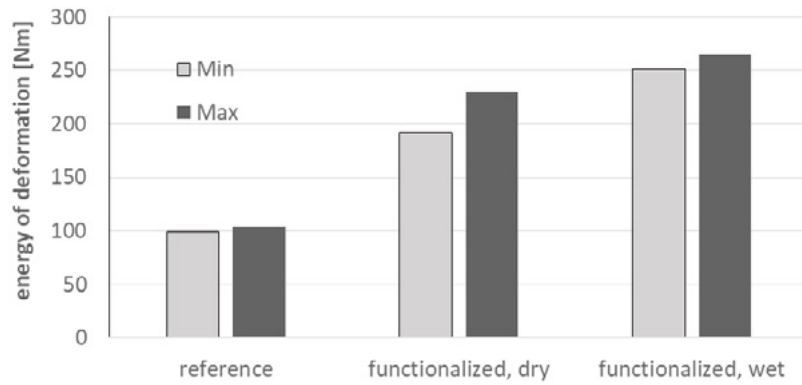


Figure 9: Energy of deformation calculated from the area under the envelope curves from Figure 8 until a deflection of 1 mm

As expected, optimum fibre contents can be defined regarding the optimization of the post-cracking behaviour. While for mortars containing the not treated fibres (reference) the energy of deformation increases up to a fibre content of 0.3 Vol.-% (Figure 10), the maximum is already reached at 0.1 Vol.-% for the functionalized fibres.

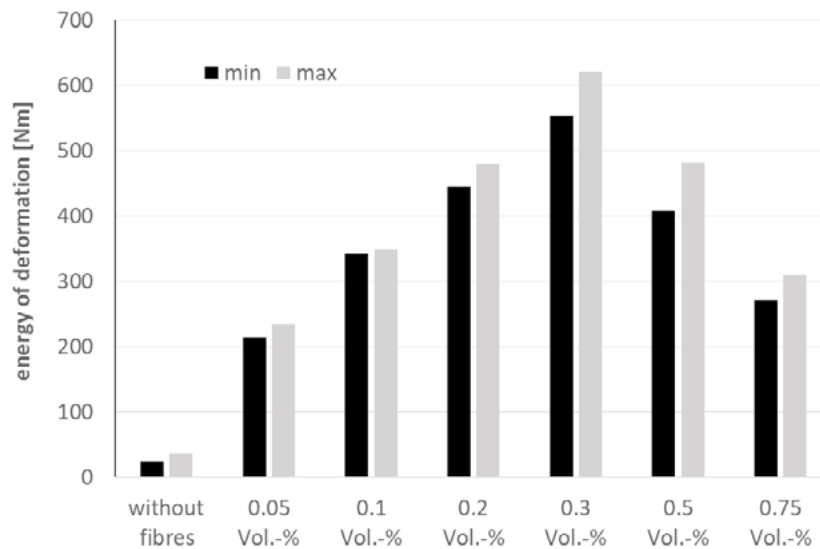
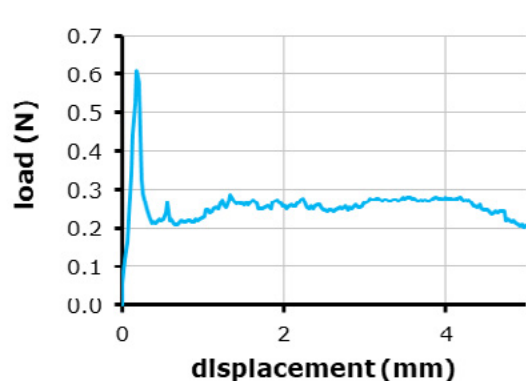


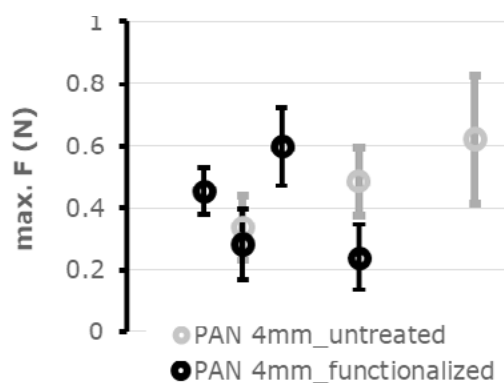
Figure 10: Minimum and maximum values (3 prisms) of the energy of deformation of mortars with increasing contents of not treated carbon fibres (reference)

Whereas the addition of fibres increases the energy of deformation for all types of materials, only for the much stiffer carbon fibres a further improvement by the functionalization of the fibres could be measured. The reason for the inefficiency of the functionalization applied to the elastic PAN and PP fibres could be the lateral contraction under load, which might lead to a delamination of the chemical bond between the hydrophilic fibre surface and the cementitious matrix. The results gained for the elastic fibres in the three-point bending test are confirmed by the individual fibre pull-through test. The load-displacement curve illustrates that after reaching the maximum load the bond between the fibre and the cementitious matrix breaks abrupt and subsequently the fibre is pulled out through the sample (Figure 11a). The PAN fibres exhibited in general higher maximum pull-out loads as the PP fibres. Both types of fibres however show no increase in the maximum load for the functionalized fibres compared to the reference, as shown in Figure 11b for the PAN fibres. The improvement of the mechanical performance by the functionalization of the carbon fibres quantified by the energy of deformation could unfortunately not be verified by the pull-through test. The brittle fibres broke while imbedding them into the mortar specimens so that the actual

test could not be performed.



11a)



11b)

Figure 11a): load displacement curve of an untreated PAN fibre with an embedment depth of 4 mm

Figure 11b): Median values of the maximum loads (n=9) for the reference fibres and the functionalized PAN fibres with an embedment depth of 4 mm

The analysis of the crack formation due to shrinkage promoted by the wind tunnel test turned out to be very sensitive to slightest changes in the test conditions. The simultaneous test of several specimens positioned one after another (Figure 4) or in different heights did not generate consistent results. Also, specimens which were positioned in the wind channel with a delay of 10 minutes were not comparable to specimens moved immediately after manufacture. A further challenge was to define the content of untreated reference fibres. The volume had to be adjusted to allow enough crack formation so that a reduction due to the functionalization could be measured. After many preliminary tests and retries it could be proved that a fibre amount of 0,05 Vol.-% is suitable to evaluate the functionalization of the PAN fibres and for the carbon fibres an even smaller amount of 0,025 Vol.-% is enough. For the PAN-fibres the addition of untreated fibres did not decrease the formation of shrinkage cracks whereas the addition of functionalized fibres reduced the average crack opening area by about 50 %. The samples containing standard carbon fibres exhibited a reduction of about 10 % compared to the samples without fibres and the functionalization of the fibres further reduced the average crack opening area further by about 30 % (Figure 12).

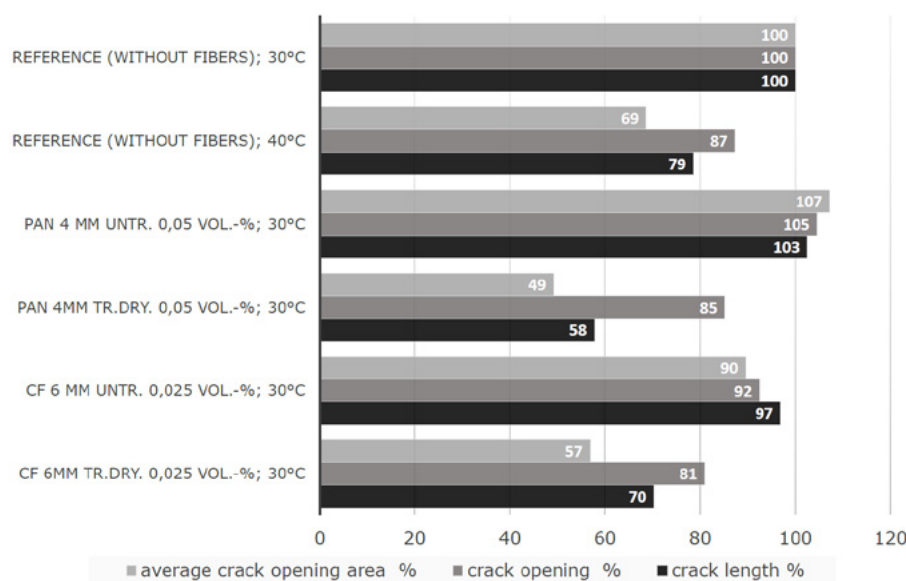


Figure 12: Geometrical parameters of the shrinkage cracks analysed after the wind tunnel test

normalized to 100 % of the specimen without fibres

4. Conclusions

- The tests performed confirm that the special functionalization developed by the project partner is efficient in improving the bond behaviour between the fibres and the cementitious matrix.
- To assess the efficiency of the functionalization in reducing shrinkage cracking a very lean mortar had to be formulated. Only after diluting the mortar with a high amount of limestone powder and strongly reducing the amount of fibres enough cracks were formed in the wind tunnel test.
- The test set-up to evaluate the crack formation during accelerated shrinkage in the wind tunnel proved to be very sensitive to slightest changes in the test conditions and therefore requires adequate statistics.
- For the mortar selected it could be demonstrated that the functionalization effectively reduced the average crack opening area for the elastic PAN fibres as well as for the brittle carbon fibres. Due to their worse performance in the individual pull-through test the analysis of the PP fibres regarding shrinkage cracking was deferred.
- The potential increase in ductility of the functionalization was evaluated by calculation of the energy of deformation derived from three-point bending tests. An improved mechanical behaviour could only be measured for the functionalized carbon fibres. The degree of improvement further proofed to depend on the batch of fibres. The maximum amount of functionalized fibres for achieving effectiveness was specified as 0,1 Vol.-%
- The results derived from the individual pull-through test confirmed that the functionalization of the polymer fibres does not affect the load transfer after incipient crack and are therefore in accordance with the results from the bending test. Because of their brittleness the pull-through test could not be performed with the carbon fibres.
- The analysis of the three-dimensional fibre distribution by CT revealed that the polymer fibres added in small amounts do not agglomerate but are not homogeneously distributed and oriented. The calculation of the effective elastic properties based on the derived orientation distribution function requires therefore adequate statistics.

5. Acknowledgment

This work was supported by the Bundesministerium für Bildung und Forschung (BMBF) grant 13N13306. The authors wish to express their gratitude to Natalia Rachmatulin for her comprehensive contribution to the achievements.

6. References

- [1] A. Sobolkina, V. Mechtcherine, C. Bellmann, A. Leonhardt, 2013, Investigation of the surface properties of carbon nanotubes, 1st International Conference on the Chemistry of Construction Materials, Berlin, 157-160
- [2] T. Schrepfer: Faserbewehrte Putze auf hochdämmenden Untergründen. Bauphysik 30 (2008), Heft 2, S. 117-122.
- [3] P. Balaguru: Contribution of Fibers to Crack Reduction of Cement Composites During the Initial and Final Setting Period, ACI Materials Journal 91 (3) (1994), 280-288.
- [4] N. Banthia, R. Gupta, Influence of polypropylene fiber geometry on plastic shrinkage cracking in concrete, Cement and Concrete Research 36 (2006), 1263-1267.

-
- [5] C. Qi, J. Weiss, J. Olek: Characterization of plastic shrinkage cracking in fiber reinforced concrete slabs using image analysis and a modified Weibull function, *Materials and Structures* 36 (2003), 386-395.
- [6] K. Pistol, F. Weise, B. Meng, U. Diederichs: Polypropylene fibres and micro cracking in fire exposed concrete. *Advanced materials research* 897 (2014), 284-289; *Trans Tech Publ.*
- [7] Patent DE 4316 667 C1 (13.5.1993) "Hydrophile synthetische Armierungs- und Prozessfasern mit silikataffinen Eigenschaften"
- [8] Patent WO 94/26969 (24.11.1994) "Variable liquid surface finishing medium"
- [9] J. Peschel, H. Seibt, D. Ballschuh, R. Ohme: Sulfobetaine, Teil 5: Anwendung von Sulfobetainen als neue Zusatzstoffe für Chemiefaserpräparationen. *Tenside Surf. Det.* 30 (1993) 321
- [10] DIN EN 1015-3: Methods of test for mortar for masonry - Part 3: Determination of consistence of fresh mortar (by flow table); German version EN 1015-3:1999+A1:2004+A2:2006
- [11] Prüfplan für die Zulassungsprüfung von Polymerfasern zur Verwendung in Beton nach DIN EN 206-1 in Verbindung mit DIN 1045-2 mit nachgewiesener Wirksamkeit. Deutsches Institut für Bautechnik, Mai 2012.
- [12] DIN EN 206-1: Beton – Teil 1: Festlegung, Eigenschaften, Herstellung und Konformität. Beuth Verlag GmbH, Berlin Juli 2001.
- [13] DIN 1045-2: Tragwerke aus Beton, Stahlbeton und Spannbeton – Teil 2: Beton – Festlegung, Eigenschaften. Herstellung und Konformität. Beuth Verlag GmbH, Berlin August 2008.
- [14] H. Hähne: Eigenschaften von mit Polyacrylnitril-Fasern verstärktem Beton. *Beton und Stahlbetonbau* 88 (1993), H. 1, S. 5-9
- [15] T. Mishurova, N. Rachmatulin, P. Fontana, T. Oesch, G. Bruno, E. Radi und Igor Sevostianov: Evaluation of the probability density of inhomogeneous fiber orientations by computed tomography and its application to the calculation of the effective properties of a fiber-reinforced composite in *International Journal of Engineering Science* 122 (2018) pp 14-29, Elsevier, 2018
- [16] T. Mishurova, F. Léonard, T. Oesch, D. Meinel, G. Bruno, N. Rachmatulin, P. Fontana und Igor Sevostianov: Evaluation of fiber orientation in a composite and its effect on material behavior, 7th Conference on Industrial Computed Tomography, Leuven, Belgium (iCT 2017) lecture and contribution in the conference proceedings

Reduced graphene oxide-coated copper foam composite cathode for the microbial electrosynthesis of acetate from carbon dioxide

P. Tremblay^{1,2,3}, T. Zhang^{1,2,3}

¹State Key Laboratory of Silicate Materials for Architectures, Wuhan University of Technology, Wuhan 430070, PR China

²School of Chemistry, Chemical Engineering and Life Science, Wuhan University of Technology, Wuhan 430070, PR China

³International School of Materials Science and Engineering, Wuhan University of Technology, Wuhan 430070, P. R. China

Abstract

5% of all man-made emissions of the greenhouse gas carbon dioxide in the world is generated by the cement industry. The bioconversion of CO₂ into multicarbon products of interest such as biofuels is a particularly efficient and versatile strategy to create value from greenhouse gas and to reduce their footprint on the environment. Chemical or biological CO₂ reduction requires an energy source, which ideally should be renewable and inexpensive. One promising and novel technology for biological CO₂ reduction is microbial electrosynthesis (MES) where a biocatalyst uses electrons from the cathode of an electrochemical system to reduce inorganic carbon into useful organic carbon molecules.

In essence, MES makes it possible to plug biocatalysts into the power grid and tap energy for biological CO₂ conversion. Electrochemical systems for MES are usually powered by renewable sources of electricity such as wind or solar. Additionally, MES reactions can also be partly driven by useful biological oxidation reaction at the anode such as organic carbon removal from municipal, commercial or industrial wastewater. Here, we describe the development of a novel high-performance cathode for MES made of a copper foam core and coated with reduced graphene oxide (rGO). Copper is a highly conductive and inexpensive cathode material widely employed in electrochemical apparatuses. However, the antimicrobial properties of copper limit its usage in bioelectrochemical systems.

Thus, we coated biocompatible and conductive rGO on copper foam and tested the resulting electrode in a MES system where the acetogenic bacterium *Sporomusa ovata* was catalyzing the conversion of electricity and CO₂ into acetate. The novel composite cathode combines the outstanding physicochemical and electrical properties of copper with the biocompatibility of rGO to enable the fast MES of acetate at a rate of 1697.6 mmol m⁻² d⁻¹. A current density of -21.6 A m⁻² and a Coulombic efficiency of 70.2 % were also observed. Acetate production rate by MES with the rGO-coated copper foam cathode was 21.3 times and 7.6 times faster than uncoated copper foam and pure rGO foam cathodes, respectively.

The results demonstrated the potential of copper in bioelectrosynthesis systems and led to the conclusion that rGO-copper foam composite is a promising cathode material for the scaling up of MES and the reduction of CO₂ emitted by industries such as cement.

Keywords: Carbon dioxide emission, Bioproduction, Microbial electrosynthesis, Bioelectrochemistry, Acetate

Prewashed wood ash for utilization in cement-based materials

N.M. Sigvardsen¹, J. Pedersen¹ and L.M. Ottosen¹

¹Department of Civil Engineering, Technical University of Denmark, Kgs. Lyngby, Denmark

Email of the corresponding author: nimasi@byg.dtu.dk

Abstract

In the transition towards a more sustainable energy system, renewable energy sources, e.g. wood, are of significant importance in the withdrawal of the coal-fired power plants. This leads to a decrease in the availability of the by-product coal fly ash, which is traditionally used in the concrete production, and to an increase in the residual waste, wood ash. The performance of wood ash in cementitious materials varies markedly throughout the literature depending on the physicochemical characteristics, determined by, e.g. the wood product, temperature, combustion method, and on pretreatment of the wood ash before utilization. This aim of this study was to determine the influence from the physicochemical characteristics of wood ash from grate combustion of wood pellets and the properties of cementitious materials. The work includes both with partial cement replacements with the untreated (marked WA) and prewashed WA (marked WA-W).

The WA was divided into two portions. One portion was subjected to a washing treatment as follows: WA and distilled water were mixed to an L/S (liquid-to-solid) ratio 5 and shaken for 1 min. After settling, the water was decanted. This procedure was repeated three times and the suspension was vacuum-filtered. The morphology of the particles for cement, WA and WA-W was evaluated with SEM. Cementitious materials with 10 wt% cement replacement with WA and WA-W, respectively, were investigated. The w/b-ratio for all mixes was kept at 0.55. The workability was determined according to EN 196-3, the setting time according to EN 196-3 and the compressive strength at 7, 14, 28, 60 and 90 days according to EN 196-1. Development of phases were measured on cement paste with 10 wt% cement replacement with WA and WA-W, respectively, by XRD and TGA at 7, 14, 28, 60 and 90 days. Reference tests were conducted for all test with 100 wt% cement.

Use of WA and WA-W in the mortar mix resulted in a decrease in the workability due to the water absorption of the WA and WA-W and a delay in the setting time compared to reference mixtures. A more distinctive decrease in the compressive strength was seen for WA compared to WA-W. The delayed setting time and the decrease in compressive strength can both be attributed to the clinker dilution effect for both ashes. The rounded particles (filler effect) determined by SEM and the increase in portlandite content determined by TGA for WA-W can explain the higher compressive strength when WA-W is utilized compared to WA. The phase development showed a decrease for portlandite and the ettringite content for pastes containing WA and WA-W, more profound for WA. Thus, the washing treatment of wood ash from grate combustion of wood pellets facilitates a wood ash more suitable for utilization in cement-based materials.

Utilization of wood ash in cementitious materials presents new challenges. However, due to the possibility for hydraulic activity and the particles to function as a filler, the potential for wood ash as a partial cement replacement should be taken into consideration for new and sustainable cementitious materials.

Keywords: wood ash, prewashing, cementitious materials

Investigating the efficiency of “in-house” produced hydrogels as internal curing agents in cement pastes

J.R. Tenório Filho^{1,2}, E. Mannekens³, D. Snoeck¹, N. De Belie¹

¹Magnel Laboratory for Concrete Research, Department of Structural Engineering, Faculty of Engineering and Architecture, Ghent University, Tech Lane Ghent Science Park, Campus Ardoyen, Technologiemarkt Zwijnaarde 60, B-9052 Gent, Belgium.

²SIM vzw, Technologiemarkt 48, Zwijnaarde B-9052 Ghent, Belgium.

³Chemstream bvba, Drie Eikenstraat 661, 2650 Edegem, Belgium.

Abstract

Appropriate curing is of utmost importance to guarantee that a concrete structure (or any cementitious material) achieves proper hydration and can provide the user with the best of its desired properties. For most of conventional concrete compositions external curing has proven to be effective, but the advent of the (ultra) high performance showed a different reality. Given its finer microstructure, the water from external curing methods cannot always penetrate the whole depth of the structure. External curing thus is not efficient in preventing problems such as cracking due to autogenous shrinkage, but a solution could be to include an internal curing system. Alternative inclusions such as lightweight aggregates and shrinkage-reducing admixture (SRA) have been studied and used as internal curing agents. Recently, researchers have been investigating the use of hydrogels or superabsorbent polymers for internal curing purposes and the results are promising. In this paper three different “in-house” produced polymers are studied as internal curing agents in cement pastes. The polymers differ in chemical composition leading to different properties. Initially they were tested for the water uptake in artificial cement pore solution by means of a filtration test and further tested in cement pastes with a range of w/c ratios from 0.30 to 0.40. Their efficiency as internal curing agents was assessed by means of autogenous shrinkage measurements with corrugated tubes for a period of seven days. All three polymers showed promising results in the mitigation of the autogenous shrinkage but two of them with the pitfall of requiring a higher amount of additional water. To summarize, the hydrogels are indeed interesting as internal curing agents but attention should be given to their chemical composition and physical aspects since for each application different properties are required.

Keywords: hydrogels, autogenous shrinkage, cement, superabsorbent polymers.

1. Introduction

Most of the deteriorating mechanisms acting on concrete structures are related to the ingress of aggressive agents inside structures. Even before reaching its hardened state, a cement-based material is subjected to crack formation especially due to the effects of shrinkage during the early age. The formed porosity of the material can become the perfect path for the ingress of those aggressive agents. After the formation the water intrusion causes a drop in pH of the concrete that can lead to steel corrosion; the ingress of

chlorides causes the de-passivation of the protective film, the intrusion of CO_2 can cause carbonation and both processes can accelerate the corrosion.

The shrinkage phenomena, especially when referring to autogenous and plastic shrinkage, are inherent to the hydration process of the cementitious material and (among other factors) are a function of the water-to-cement ratio and curing conditions (temperature and humidity). The autogenous shrinkage is related to the self-desiccation initiated in the pores of the material due to the hydration process [1].

Appropriate curing is of utmost importance to guarantee that a concrete structure (or any cementitious material) achieves proper hydration and can provide the user with the best of its desired properties. For most of conventional concrete compositions external curing has proven to be quite effective, but the advent of the (ultra) high performance showed a different reality. Given its finer microstructure, the water from external curing methods cannot always penetrate the whole depth of the structure. External curing thus is not efficient in preventing problems such as cracking due to autogenous shrinkage, but a solution could be to include an internal curing system. Alternative inclusions such as lightweight aggregates and shrinkage-reducing admixture (SRA) have been studied and used as internal curing agents. Recently, researchers have been investigating the use of hydrogels or superabsorbent polymers (SAPs) for internal curing purposes and the results are promising [2-4].

Superabsorbent polymers (or hydrogels) are a natural or synthetic water-insoluble 3D network of polymeric chains cross-linked by chemical or physical bonding. They possess the ability to take up a significant amount of fluids from the environment (in amounts up to 500 times their own weight). The swelling and posterior water release are of great interest in the study of smart self-healing materials but can also be explored to promote self-sealing [2-5]. In this paper, three different in-house produced SAPs are presented as alternative for promoting internal curing in cement pastes.

All SAPs are produced with different co-monomers (Figure 1), each of them being designed to have different swelling capacities. The required properties of the SAPs were based on the properties found in literature for commercially available SAPs aiming at a proper internal curing of cementitious materials.

The internal curing efficiency of the SAPs was evaluated by means of an autogenous shrinkage test. A filtration test and slump flow test were also performed to assess the water uptake by the SAPs and their influence in the workability of the mixtures.

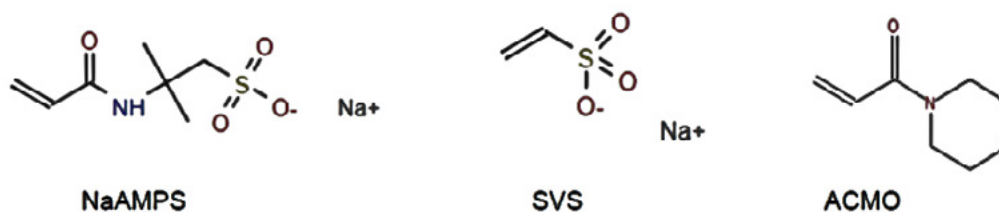


Figure 1: Co-monomers that were used in the SAPs from ChemStream.

2. Methodology

2.1 Materials

All tests were performed on cement pastes produced with cement type CEM III-B 42.5N – LH/SR; a polycarboxylate superplasticizer (at a constant dosage of 0.3 m% in relation to the cement mass; Glenium 51, 35% conc.); an effective water to cement ratio of 0.3; three different hydrogels (all in-house produced) with a dosage in the range of 0.023 m% to 0.4 m%. The composition of the studied mixtures can be found

in Table 1.

Table 1: Composition of the mixtures studied.

Mixture	Cement [kg/m ³]	Mixing water [kg/m ³]	Superplasticizer [kg/m ³]	SAP [kg/m ³] (m%)	Additional water [kg/m ³]	w/c	
						Effective	Total
REF1	1620	486	4.86	0	0	0.3	0.3
REF2	1490	447	4.47	0	0	0.354	0.354
SAP1.1	1490	447	4.47	0.34 (0.023%)	80.46	0.3	0.354
SAP1.2	1198	359.4	3.59	1.31 (0.11%)	259.96	0.3	0.517
SAP2.1	1490	447	4.47	2.01 (0.135%)	80.46	0.3	0.354
SAP2.2	1393	417.9	4.17	2.78 (0.2%)	139.3	0.3	0.4
SAP3	1490	447	4.47	5.96 (0.4%)	80.46	0.3	0.354

All SAPs were produced by ChemStream and have been tested specifically for use in cementitious materials.

SAP type 1 is a SAP composed of 2 co-monomers NaAMPS (2-acrylamido-2-methyl-1-propanesulfonic acid sodium salt) and SVS (sodium vinyl sulfonate) that are lightly cross-linked. Both co-monomers contain the sodium salt form of a sulphonic acid group, which leads to a very densely charged hydrogel with great osmotic power for absorbing water. This type of SAP-composition is based on ChemStream's prior art EP2835385.

SAP type 2 is a SAP that is similar to SAP type 1, since it mainly consists of co-monomer NaAMPS, but it is 'diluted' with a non-charged or neutral monomer ACOMO (acryloyl morpholino acrylate) (20% mol).

SAP type 3 is also very similar to SAP type 1, because it is solely composed of monomer NaAMPS but with a lower absorption capacity.

More information on the properties of the SAPs can be found in Table 2.

Table 2: Properties of the SAPs.

SAP	Mean particle size D ₅₀ [μm]	Absorption capacity* [g/g]	Soluble materials [%]
SAP1	100	275	36
SAP2	100	261	9
SAP3	100	54	8

* For absorption in demineralized water after 24 hours

2.2 Methods

The absorption capacity of the SAPs was evaluated by means of a filtration test using cement filtrate (1 kg of cement CEM III-B 42.5N – LH/SR and 5 l of demineralized water) at 10 min and 24h after the first contact of the dry hydrogels with water.

Afterwards the absorption capacity in real cement pore fluid was assessed by means of slump flow test with the cement pastes mentioned in Table 1. The principle of this test is to add a certain amount of SAPs to a cement paste with w/c of 0.354 (theoretical value for a complete hydration of the system according to [6, 7]) until the slump flow measured equals the value of the reference cement paste REF1. By doing so, it is assumed that the difference in water content of both reference mixtures (w/c of 0.054) is totally absorbed

by the SAPs. The average slump of the reference mixture REF1 was 300 ± 15 mm. The measurements were performed after 10 min counted from the moment the water was added to the mixture.

The internal curing effect of the SAPs was evaluated by means of a shrinkage test, performed with corrugated tubes, in compliance with ASTM C1698-09. The measurements of deformation were performed automatically with linear variable differential transducers (LVDT) with a range of 5 mm (Figure 2). From the total deformation curve, the autogenous shrinkage strain was calculated zeroing the deformations at the knee-points of the original curves [8] (Figure 3).



Figure 2: Set up for the autogenous shrinkage measurement.

In some cases, the amount of SAP determined to absorb the additional amount of water corresponding to the additional 0.054 in the w/c ratio was not enough to completely mitigate the autogenous shrinkage of the mixture. For those cases, the amount of SAP was increased and the additional water inserted in the system was corrected to achieve a fully mitigation of the autogenous shrinkage. This justifies the existence of mixtures SAP1.2 and SAP2.2 (shown in Table 1) for which results will be presented in the following section.

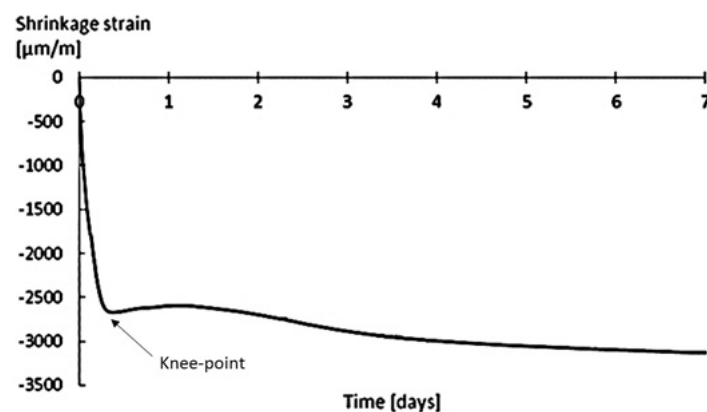


Figure 3: Illustration of the knee-point in the shrinkage strain curve over time for a cement paste.

3. Results and discussion

The absorption capacity of the SAPs in the different media shows different trends in behavior for the studied hydrogels (Figure 4).

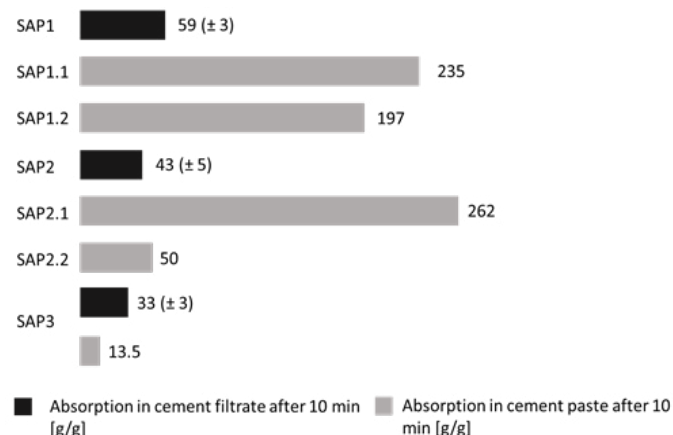


Figure 4: SAP1 and SAP2 present a higher absorption capacity in cement paste in comparison with cement filtrate. SAP3 shows the opposite.

SAP1 and SAP2 both present a higher absorption capacity in the cement paste in comparison to the cement filtrate solution. The opposite was noticed with SAP3, which is in accordance to the behavior of commercially available hydrogels reported in other studies [9]. By increasing the amount of SAPs in the system (mixtures SAP 1.2, and SAP 2.2) the increase in the required additional water did not show a linear behavior. This is also mentioned by [10] and can be explained by the change in the concentration of ions in the system that occurs when more water is added and its influence on the sorption/desorption kinetics of SAPs.

In terms of chemical composition, SAP1 is more densely charged in comparison to SAP2 and SAP3 which theoretically would lead to a higher absorption capacity. The fact that this absorption is higher in the cement paste in comparison to the cement filtrate shows evidence that more variables are influencing the kinetics of the SAPs once they are in contact with the paste (the presence of superplasticizer, for example).

The results for autogenous shrinkage of the mixtures are shown in Figure 5.

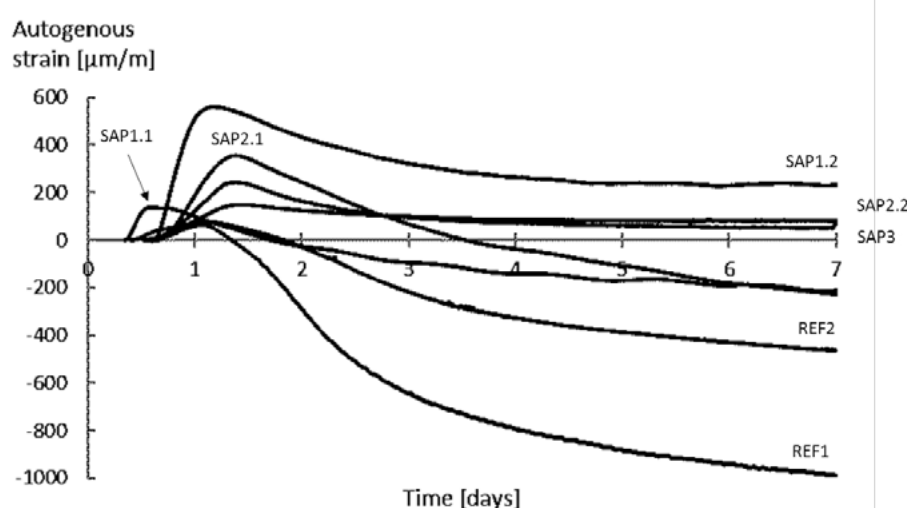


Figure 5: All SAPs promote a reduction in the autogenous strain of the cement paste in comparison to the references without SAPs. SAP3 shows the most promising result in terms of additional water and effective internal curing.

All SAPs promote a reduction in the autogenous strain in comparison to the both references. Considering only the mixtures SAP1.1, SAP2.1 and SAP3 in comparison with the REF2 (all of them with the same total

w/c ratio) only SAP3 is able to completely mitigate the autogenous shrinkage. Still, both mixtures SAP1.1 and SAP2.1 show a shrinkage strain lower than the reference.

In both mixtures SAP1.2 and SAP2.2 there is complete mitigation of the autogenous shrinkage during the complete period of testing (seven days). However, the total w/c ratio of both mixtures is higher in comparison to the references (0.517 and 0.4). In that case, in order to verify the real efficiency of the SAPs in those mixtures, new references should be mixed with the same w/c ratios (0.517 and 0.4) to assess till what extent the mitigation of shrinkage is due to the controlled released of water promoted by the SAPs or due to the higher amount of free water in the system. Also for clarification of that matter, the water release of the SAPs in the mixtures should be investigated, especially for SAP1 and SAP2. This should reveal why SAP3 showed a completely mitigation of the autogenous shrinkage with the same w/c ratio as REF2 while the other SAPs needed to be added in a dosage higher than initially defined.

4. Conclusions

Despite the differences in chemical composition and properties, all SAPs showed promising results. In the range of 0.2-0.4 m% a complete mitigation of autogenous shrinkage was obtained with a very small increase in the total w/c of the mixtures and an amount of 0.1% led to a reduction of around 80% in the shrinkage strain.

SAP1 and SAP2 showed a different behavior depending on the amount of SAP and water in the system, in comparison with SAP3. Further study is needed to investigate the kinetics of water release by the SAPs in the different situations presented in this paper.

The addition of SAPs and water in the system might also have effects (not only positive) on other aspects of the cementitious materials such as mechanical strength, setting time, microstructure and so on. All these influences should be taken into account when deciding to use a specific type of SAP and a balance should be made between its positive and negative influences in order to choose the SAP that best suits a certain application.

5. Acknowledgment

The work has been financed by SIM program SHE (Engineered Self-Healing Materials) within the ICON project iSAP (Innovative SuperAbsorbent Polymers for crack mitigation and increased service life of concrete structures).

6. References

- [1] Sahinagic-Isovic, M., Markovski, G., Cecez, Marko. Shrinkage strain of concrete – causes and types. Journal of the Croatian Association of Civil Engineers, GRADEVINAR 64 9, 727-734. 2012.
- [2] Snoeck, D. Self-Healing and Microstructure of Cementitious Materials with Microfibres and Superabsorbent Polymers. Doctorate thesis – Faculty of Architecture and Engineering/Ghent University. Belgium, 2015.
- [3] Mechtcherine, V., Dudziak, L., & Hempel, S. Mitigating early age shrinkage of Ultra-High-Performance Concrete by using Super Absorbent Polymers (SAP). Paper presented at the Creep, Shrinkage and Durability Mechanics of Concrete and Concrete Structures, Ise-Shima, Taylor & Francis, 847-853. 2009.
- [4] Jensen, O.M. Use of superabsorbent polymers in construction materials. Paper presented at the International Conference on Microstructure Related Durability of Cementitious Composites, Nanjing, RILEM Publications S.A.R.L., 757-764. 2008.

-
- [5] Mignon, A., Snoeck, D., Dubruel, P., Van Vlierberghe, S., De Belie, N. Crack mitigation in concrete : superabsorbent polymers as key to success? *Materials*, 10(3), 237. 2017.
- [6] Powers, T.C., & Brownyard, T.L. Studies of the physical properties of hardened Portland cement paste (Vol. 22). Cornell: Portland Cement Association, Research Laboratories, pp. 892. 1948.
- [7] Jensen, O.M., & Hansen, P.F. Water-entrained cement-based materials I. Principles and theoretical background. *Cement and Concrete Research*, 31(4), 647-654. 2001.
- [8] Lyu, Y. Autogenous Shrinkage of Cement-Based Materials: From the Fundamental Role of Self-Desiccation to Mitigation Strategies Based on Alternative Materials. Doctorate thesis – Faculty of Architecture and Engineering/Ghent University. Belgium, 2017.
- [9] Tenório Filho, José Roberto; Snoeck, D. ; Belie, N. . The effect of superabsorbent polymers on the cracking behavior due to autogenous shrinkage of cement-based materials. In: 60 Congresso Brasileiro do Concreto, 2018, Foz do Iguaçu. *Anais do 60 Congresso Brasileiro do Concreto*, 2018.
- [10] Ma, X., Yuan, Q., Liu, J., Shi, C. Effect of water absorption of SAP on the rheological properties of cement-based materials with ultra-low w/b ratio. *Construction and Building Materials*, 195, 66-74. 2019.

The course of water absorption and desorption from superabsorbent polymers (SAP) in cementitious environment

M. Kalinowski¹, P. Woyciechowski¹

¹Warsaw University of Technology, Department of Civil Engineering.

Abstract

Superabsorbent polymers (SAP) are compounds that are able to absorb water increasing their mass and volume, resulting in mass exceeding the starting value by hundreds times or more. Their absorption capacity depends on the water absorption environment – the higher alkali content, the worse is the capacity. In terms of concrete technology, the laboratory tests results indicate that the SAP absorption capacity in tap water is about ten times higher than in the environment of liquid solution of alkali content which is to simulate the cement paste environment. Taking into consideration the potential function of SAP in hardening process of cement binder as an. internal curing agent, the course of desorption of water from SAP particles should be taken into consideration while designing composites. The paper investigates the course of SAP water absorption/desorption in the environment of cement pastes of water/cement ratio ranging from 50 to 0.5, by means of a teabag tests. In regards to absorption tests results it was found that the absorption capacity of SAP decreases along with the decrease of the water/cement ratio. To evaluate the dynamics of course of water absorption of SAP, the time of reaching the 95% of the maximal absorption was analysed. Depending on the water/cement ratio of the absorption environment, it occurred within 2-40 minutes from the preparation of cement paste. The methodology of tests of water desorption from SAP included obtaining full saturation of SAP in the tap water and placing it in the cement paste solutions of water/cement ratios varying from 50 to 0.5. and determining the course of SAP mass change in time. It was found that in cementitious environment the process of water desorption from SAP was much slower than in case of water absorption. Desorption tests lasted approx. 24 h depending on the water/cement ratio. Obtained results show strong impact of paste characteristics on the course of SAP water absorption and desorption in various cementitious composites.

Keywords: superabsorbent polymers, absorption, desorption, water migration, cement composites.

1. Introduction

Superabsorbent polymers (SAP) could be described as a group of cross-linked polyelectrolyte polymers capable of absorbing high amounts of water while maintaining a three-dimensional structure [1-2]. Due to high osmotic pressure caused by accumulation of ions in SAPs structure, when exposed to water environment superabsorbent polymers swell, i.e. absorb water, in order to reduce aforementioned pressure [3]. With such a model of SAPs interaction with water solutions in mind, its absorption capacity depend not only on the chemical composition of any given SAP but is also influenced by external pressures resulting from SAPs change in volume in the process of absorbing water [4]. Additionally, the alkalinity of the environment in which the absorption takes place has an influence on the overall absorption capacity [5].

In concrete technology SAP is used as an internal curing agent – if the balance between osmotic pressure

within SAP saturated with water and the internal stresses in cementitious composite is lost, SAP is able to reduce its volume, i.e. desorb water [6]. By using this effect, the kinetics of water migration within the capillary network can be altered and wide range of composite properties can be affected as a result, including modification of the degree of hydration [7], autogenous shrinkage [8], compressive strength [9] or changes in pore network distribution itself [10]. With such an impact on properties of cementitious composites, in order to fully predict and control the influence of SAP only on the properties that one wants to alter, as much information on properties of SAP in cementitious environment as possible should be gathered, including SAPs granulation and its properties concerning course of water absorption and desorption in the cement paste environment. Those properties would be crucial to predict SAPs capabilities to modify the capillary network and alter the water migration within the cementitious composite.

In order to evaluate water absorption properties of SAP, several testing methods have been developed, including teabag method test and others [11]. Usually, these tests are performed in liquid solutions that are to simulate the pH and alkali content of cement paste. However, those variables are not the only ones that have the influence on SAP properties in a cement paste. Another property of cement pastes that cannot be taken into account in an absorption tests performed in a liquid environment is that cement paste environment could be described as a porous fluid consisting of several phases. Those contribute to changes in the kinetics of water migration compared to tests performed in liquid water solutions, i.e. by taking into account the impact of solid particles of cement in the absorption/desorption environment on the SAP properties and the capillary pressures resulting from presence of several phases in the cement paste. By studying and experimenting with SAP behaviour in the environment most similar to the one of cementitious composite, ambiguous SAP influence may be easier to quantify.

The aim of the study was to investigate the course of water absorption and desorption from SAP in cementitious environment and identify variables that have the biggest impact on SAP properties. By modifying the content of cement particles in tested solutions, i.e. by performing water absorption/desorption tests in cement pastes of different water-cement ratios, an environment most close to the actual SAP activation environment in concrete technology was created. SAP is most usually used in concrete technology as an internal curing agent. It would suggest that the desorption mechanics of those polymers should have the biggest significance when designing cement composites modified with that kind of modifier. The role of internal curing agents in composite is to maintain the internal humidity within the pore/capillary network at as high level for as long as possible. Without understanding SAPs properties concerning course of water desorption and focusing only on the water absorption properties, full potential of SAP may be yet not fully achieved in concrete technology. By focusing only on SAP absorption properties, a misinterpretation of its properties is indicated by assumption that the course of water desorption from SAP is directed in the same way as course of water absorption but with negative coefficients.

The information about SAP absorption potential in activation environments characterized by different water-cement ratios may also ensure an useful approximation of the change in SAP properties dependent on water-cement ratio and help to improve its effectiveness in concrete technology. Others articles on the subject of SAP absorption characteristics in different environments suggest that absorption potential in liquid environments with high alkali content is of a level of magnitude lower than in the environment of water. By confirming this hypothesis, simplification of SAP properties could be formed and the design process of cement composites incorporating SAP could be developed.

2. Methodology

2.1 Materials

Cement CEM I 42,5 N was used as a binder in all of the tested cement pastes. Its properties were in accordance with EN 196 standard. In order to obtain cement pastes with various water-binder ratios, water with properties in accordance with EN 1008 standard was used. Prepared cement pastes that served as water absorption/desorption environment for SAP were characterized by different water-binder ratios (Tab. 1). The water-cement ratios of the tested cement pastes were designed between 0.5 and 500. While it's unreasonable to think that water-cement ratios above 0.5 have any use in concrete technology, especially concerning UHPC or other high performance cement composites, the range of properties of tested cement pastes was designed in order to track the change in SAP properties dependant on the change from liquid environment of absorption to the one of porous liquid. As the properties of porous liquid in cement pastes start to present themselves in a solution of water-cement ratio approx. 1-2, those values had to be included in the research program. Furthermore, this experiment was conducted in order to track the properties of SAP that could be used in concrete, not in order to design new types of cement pastes with extremely high water-cement ratios. The cement paste with water-cement ratio of 500 was to simulate water activation environment with pH level of 12.3.

Table 1: Water-binder ratios of cement pastes which served as water absorption/desorption environment.

Cement paste ID	Water-cement ratio [g/g]
CP05	0,5
CP1	1,0
CP2	2,0
CP5	5,0
CP50	50,0
CP500	500,0

Superabsorbent polymer which properties were tested during experiments was characterized by granulation measured using HORIBA Compact Laser Diffraction Particle Size Analyzer (Fig. 1) ranging from 175 to 595 [μm] and was of properties presented in Tab. 2.

Table 2: Material characterization of the superabsorbent polymer used in research program.

Characteristic	SAP S
Chemical characterization	Potassium acrylate and acrylic acid polymer
Solubility in water	Insoluble
Polymerization process	Invert suspension polymerisation

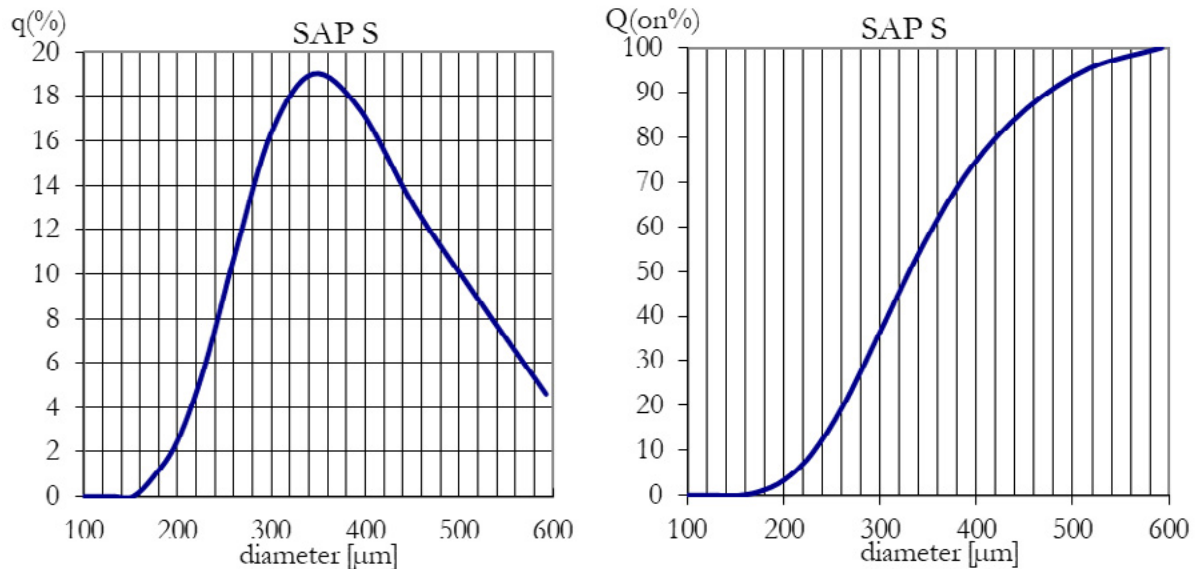


Figure 1: SAP S granulation measured by means of Laser Diffraction.

2.2 Methods

In order to estimate the influence of water-binder ratio of the cement paste on the absorption properties of SAP, a regular teabag method test was conducted. It included sealing a known mass of SAP in a teabag of a known mass and measuring the increase in mass dependent on a time spend in the absorption environment. In order to mitigate the influence of cement paste mass gathering on the outer side of the teabag, a reference sample with no sealed SAP was prepared and put into cement paste of the same water-binder ratio. The increase of mass on the reference sample was then subtracted from the sample with sealed SAP at every measurement point. The test lasted for 60 minutes as it proved sufficient to reach maximal water absorption capacity of SAP in each of the tested cement pastes.

A slightly modified methodology was adopted in a case of desorption tests in order to determine SAPs water desorption parameters. It involved preparing fully saturated SAP teabag sample in tap water environment which was then inserted into cement paste of a given water-binder ratio. Unlike the absorption test, desorption tests lasted approx. 24 hours. The reduction in mass of the teabag sample was then considered as the amount of water that was released from SAP into the cement paste. As in the absorption tests, a reference sample was prepared for each of the tests in order to mitigate the effect of mass increase on the outer side of the teabag exposed to cement paste environment which would have significant impact on the results if left unchecked.

3. Results and discussion

The absorption tests results (Fig. 2) suggest a decrease in SAP water absorption capacity along with a decrease of water-binder ratio of the cement paste which served as an absorption environment. Obtained results were in accordance with other experiments on the subject [12], however the change from liquid absorption environment to gel cement paste could suggest an additional explanation for the reduced absorption capacity in cement pastes with lower water-cement ratios. The SAP water absorption capacity in any given absorption environment was defined as an asymptote value of the hyperbolic trend line that estimated the course of SAP water absorption (Tab 3). The time of SAP activation was defined as the time required for tested SAP to reach the level of 95% of the asymptote value (Tab 3). The influence of alkali content of the solution on the properties of SAP is undeniable – however additional effect reducing the SAP water absorption capacity in certain environments, in form of solid particles in the absorption

environment is present in cement pastes. The aforementioned influence presents itself in form of different times required by SAP to achieve its maximal saturation in any of the tested absorption environments (Tab. 3).

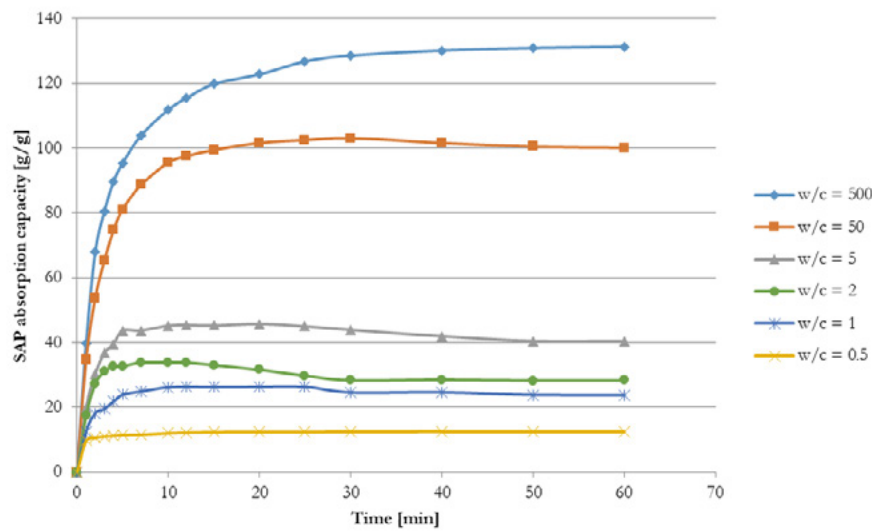


Figure 2: SAP water absorption capacity vs time for cement pastes of different water-binder ratios serving as water absorption environments.

Table 3: Asymptote values for hyperbolic trend lines that estimated the course of SAP water absorption and the time required for SAP to reach 95% of its maximal water absorption capacity.

Cement paste ID	Asymptote value [g/g]	95% of the asymptote value [g/g]	Time required by SAP to reach 95% of water absorption capacity [min]
CP500	135,3	128,5	40,1
CP50	105,8	100,5	24,1
CP5	44,1	41,9	5,4
CP2	31,2	29,6	2,5
CP1	25,5	24,2	6,4
CP05	12,2	11,6	3,4

This phenomena could be explained by shortage of water in the close distance from the teabag containing SAP. As the water is removed from between cement particles, an increasing in strength capillary pressure reduces the water migration within the capillary network towards the area of SAP absorption. Also, as the cement grains have high surface areas, there's a limited volume of water that can overcome combined effect of the surface tension of the cement grains, the capillary forces of the porous liquid and the influence of the ions present in the cement paste. The influence of all those variables was combined and resulted in a decrease in SAP water absorption capacity as the water-cement ratio of the cement paste that served as water absorption environment.

The course of SAP water absorption capacity in a function of water-binder ratio of tested cement pastes (Fig. 4) shows a logarithmic dependence between absorption capacity achieved at any time by SAP and the water-binder ratio of the cement paste which served as an absorption environment.

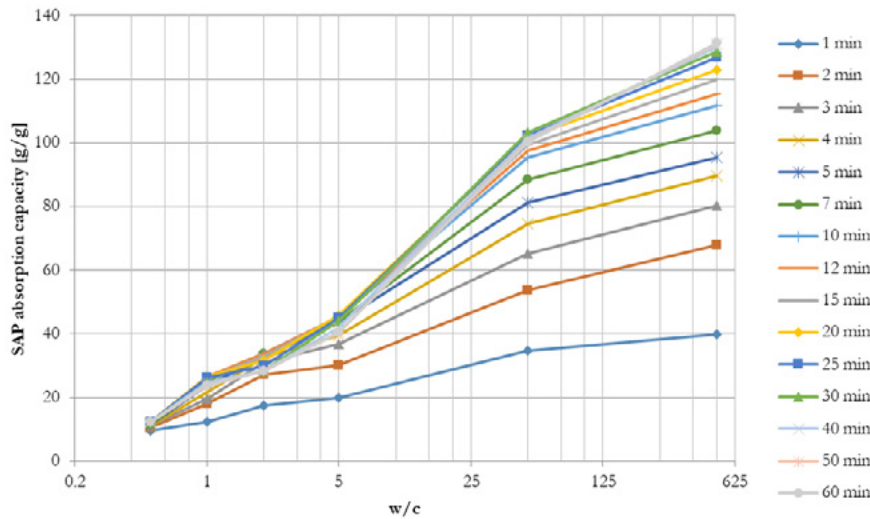


Figure 4: SAP water absorption capacity vs w/c ratio, for different measurement points.

With small differences in the coefficients of the logarithmic trend lines between different time of measurements, one can observe that the hypothetical water-binder ratio of the cement paste environment in which the SAP water absorption capacity would be zero, presented itself between 0.2-0.3, the amount of water that is usually used in full for hydration purposes [13]. Unfortunately, water absorption tests in cement pastes characterized by such low water-binder ratios would be extremely inaccurate, hence this hypothesis would be difficult, if not impossible, to confirm experimentally.

Between tested cement paste a severe difference in SAP water absorption capacities were observed. The cement paste with water-binder ratio at 500 illustrates the maximal SAP water absorption capacity. The absorption in cement paste characterized by water-binder ratio of 0.5 was approx. 10 times lower than the SAP maximal water absorption capacity. It's reasonable to assume that in absorption environments characterized by even lower water-cement ratios, SAPs water absorption capacity would be further limited, although this motion would need to be verified experimentally. However, the assumption that SAP water absorption potential in cement pastes of water-cement ratio of 0.5 is approx. 10 times lower than the one of SAP activated in water presents itself as an reasonable starting point for designing cement composites modified with SAP. As the water desorption from SAP tests were performed in cementitious environments, the duration of those test was dependant on the properties of cement pastes and the course of hydration – the last measurement was performed after 24 hours from placing the teabag containing SAP in the test solution. The desorption tests results (Tab 4 and Fig 6) suggest even stronger influence of an additional variable except the ion content in the water desorption environment on the course of water migration from SAP.

Table 4: Initial and final results of SAP absorption capacities in different desorption environments.

Cement paste that served as SAP water desorption environment	Initial SAP water absorption capacity [g/g]	Final SAP water absorption capacity after 24 h [g/g]	105 % of SAP water absorption capacity in cement paste that served as water desorption environment [g/g]
CP50	132.1	110.5	111.1
CP5	132.1	36.8	46.3
CP2	130.3	11.4	32.8
CP1	131.9	14.4	26.8
CP05	130.4	30.3	12.8

As cement paste with low water-cement ratio cannot be treated as a fluid, presence of alkali in cement pastes allows to explain the logarithmic dependant desorption in a function of water-binder of the cement paste which served as a desorption environment only to a certain w/c, below which the properties of a porous liquid start to control the course of water desorption from SAP. Below that w/c ratio, other phenomena block the movement of water from SAP to cement paste, mostly the change in the parameters of a capillary network. When exposed to high capillary pressure resulting for local presence of additional water (desorbed from SAP under the influence of alkali originating from cement paste), the network loses its homogeneity, preventing continuous rapid desorption from SAP. That was the case with unusual course of water desorption from SAP in cement paste of a 0.5 water-cement ratio.

Results of the SAP water desorption test in this environment suggest, that in order for SAP to reduce its water absorption capacity to the level achieved in SAP water absorption tests, much more time would be required, i.e. that the water desorption process in cementitious environments characterized by low water-cement ratios lasts longer than 24 hours. The process of hydration and the properties of porous fluid such as cement paste limit the intensivity of the water desorption process from SAP. It indicates that much more time would be required for SAP to desorb its water to the water absorption level SAP achieved in absorption tests in a cement paste of a water-cement ratio of 0.5.

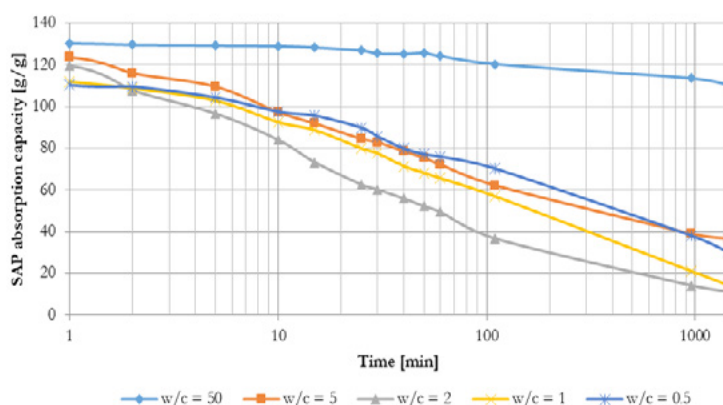


Figure 6: SAP water absorption capacity over time in cement pastes of different water-binder ratios serving as water desorption environments.

Several variables have the influence on water migration from SAP. In water desorption environments that could be described as fluids (characterized by water-cement ratio higher than 2), the ion content of the desorption environment is probable to have the biggest impact on SAP desorption (Fig 7). SAP water desorption process in all of the tested cement pastes that served as a SAP water desorption environment was characterized by logarithmic dependence. With time, in cement pastes with water-cement ratios lower than 2, the influence of other variables started to impact the course of water desorption from SAP, i.e. slowing the water desorption process. It is possibly prone to change in the properties of the desorption environment with a reduction of water-cement ratio.

Water migration in cement pastes does not occur in the entire volume of the desorption environment but is limited to migration through capillary/pore network. By adding additional restrictions on the water movement throughout the desorption environment, an increase in internal pressures further limit the rate of water desorption from SAP. It leads to conclusion, that the course of water desorption from SAP depends not only on the chemical properties of the SAP or the desorption environment, but also on the physical properties of the desorption environment.

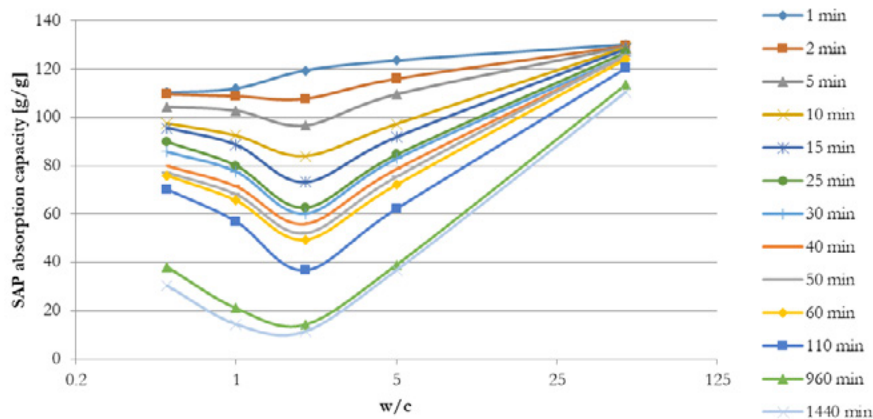


Figure 7: SAP water absorption capacity over specific measurement times in cement pastes characterized by different water-binder ratios serving as water desorption environments.

Research on the topic of SAP influence on the internal humidity in cementitious composites suggest that SAP contributes to the maintenance of internal humidity within concrete volume at the high level for a longer time than in reference mixes [14]. Most of experiments carried out suggest a certain SAP dosing method to the rest of the mix components – by introducing it as a non-saturated powder [15]. After its introduction into the mix, SAP is to absorb water from the mix and then, under the influence of internal pressures (hydrostatic, capillary etc.) is to desorb water and by doing so, maintain the internal humidity at a high level [16].

Research presented in this article suggest different approach to the phenomenon of water desorption from SAP. By adding SAP as a gel saturated with water to the rest of the components of the cement mix, the water migration is to occur only in a form of water desorption from SAP. As presented in the article, the rate of water desorption from SAP to an environment of a low water-cement ratio is much slower than in the case of SAP water absorption. This property of SAP introduces an additional period of intense water desorption from SAP into a cement composite. It occurs within first days after the preparation of the mix – in the time when intensive hydration occurs. The influence of this change in the properties in water migration within composites structure and its influence on the properties of concrete should be investigated further but it is safe to assume that this change would have an effect on the pore network distribution and consecutively, on other properties of the composite.

4. Conclusions

On the basis of conducted research following conclusions were made:

- SAP absorption capacity in environments characterized by low water-cement ratios could be approximated as one tenth of SAP absorption capacity in water environment.
- The rate of SAP water absorption process increases along with a decrease of water-cement ratio of the absorption environment.
- The influence of porous liquid properties on the course of SAP water desorption is observed in paste with low water-cement ratios.
- The time required for SAP saturated with water to reduce its water content due to the desorption in paste to the level of absorption capacity in paste prolongs as the water-cement ratio of the environment decreases.
- The process of water desorption from SAP has a slower rate than the process of SAP water absorption

in the same environment.

5. References

1. Mignon, A.; Snoeck, D.; Dubruel, P.; Van Vlierberghe, S.; De Belie, N., 2017, Crack Mitigation in Concrete: Superabsorbent Polymers as Key to Success? *Materials*, 10, 237, DOI: [10.3390/ma10030237](https://doi.org/10.3390/ma10030237).
2. Ghobashy M.,M. Superabsorbent, Hydrogels, S. Haider and A. Haider, IntechOpen **2018**, DOI: 10.5772/intechopen.74698.
3. Snoeck, L.F.; Velasco, P.; Mignon, A.; Van Vlierberghe, S.; Dubruel, P.; Lodewyckx, P.; De Belie, N., 2015, The effect of superabsorbent polymers on the microstructure of cementitious materials studied by sorption experiments. *Cem. Concr. Res.*, 77, 26-35, DOI: 10.1016/j.cemconres.2015.06.013.
4. Yu, Y.; Liu, L.; Kong, Y.; Zhang, E.; Liu, Y., 2011, Synthesis and properties of N-maleyl chitosan-cross-linked poly (acrylic acid-co-acrylamide) superabsorbents. *J. Polym. Environ.*, 19, 926–934, DOI: 10.1007/s10924-011-0340-2.
5. Lee, H.X.D.; Wong, H.S.; Buenfeld, N.R., 2018, Effect of alkalinity and calcium concentration of pore solution on the swelling and ionic exchange of superabsorbent polymers in cement paste. *Cem. Concr. Compos.*, 88, 158–164, DOI: [10.1016/j.cemconcomp.2018.02.005](https://doi.org/10.1016/j.cemconcomp.2018.02.005).
6. Farzarian, K.; Ghahremaninezhad, A., 2018, Desorption of superabsorbent hydrogels with varied chemical compositions in cementitious materials. *Mat. Struct.*, 51, 3, DOI: 10.1617/s11527-017-1128-11.
7. Hasholt, M.T.; Jensen, O.M.; Kovler, K.; Zhutovsky, S., 2012, Can superabsorbent polymers mitigate autogenous shrinkage of internally cured concrete without compromising the strength? *Constr. Build. Mater.*, 31, 226–230, DOI: [10.1016/j.conbuildmat.2011.12.062](https://doi.org/10.1016/j.conbuildmat.2011.12.062).
8. Schrofl, C.; Mechtcherine, V.; Gorges, M., 2012, Relation between the molecular structure and the efficiency of superabsorbent polymers (SAP) as concrete admixture to mitigate autogenous shrinkage. *Cem. Concr. Res.*, 42, 865–873, DOI: [10.1016/j.cemconres.2012.03.011](https://doi.org/10.1016/j.cemconres.2012.03.011)
9. Pourjavadi, A.; Fakoorpoor, S.M.; Hosseini, P.; Khaloo, A., 2013, Interactions between superabsorbent polymers and cement-based composites incorporating colloidal silica nanoparticles. *Cem. Concr. Compos.*, 37, 196–204, DOI: [10.1016/j.cemconcomp.2012.10.005](https://doi.org/10.1016/j.cemconcomp.2012.10.005)
10. Snoeck, D.; Schaubroeck, D.; Dubruel, P.; De Belie, N., 2014, Effect of high amounts of superabsorbent polymer and additional water on the workability, microstructure and strength of mortars with water-to-cement ration of 0.50. *Constr. Build. Mater.*, 72, 148–157, DOI: [10.1016/j.conbuildmat.2014.09.012](https://doi.org/10.1016/j.conbuildmat.2014.09.012)
11. Mechtcherine V., Reinhardt, H.-W., 2012 Application of Superabsorbent Polymers (SAP) in Concrete Construction, State-of-the-Art Report Prepared by Technical Committee 225-SAP; Springer Science & Business Media: Berlin, Germany.
12. Lee, H.X.D.; Wong, H.S.; Buenfeld, N.R., 2018, Effect of alkalinity and calcium concentration of pore solution on the swelling and ionic exchange of superabsorbent polymers in cement paste. *Cem. Concr. Compos.*, 88, 158–164, DOI: [10.1016/j.cemconcomp.2018.02.005](https://doi.org/10.1016/j.cemconcomp.2018.02.005)
13. Powers, T.C.; Brownyard, T.L., 1946, Studies of the physical properties of hardened Portland cement paste. *J. Am. Concrete Inst.*, 43, 101–132.
14. Chiwon Song, Young Cheol Choi, Seongcheol Choi, 2016, Effect of internal curing by

superabsorbent polymers – Internal relative humidity and autogenous shrinkage of alkali-activated slag mortars, *Constr and Build Mat*, 123, 198-206, DOI: [10.1016/j.conbuildmat.2016.07.007](https://doi.org/10.1016/j.conbuildmat.2016.07.007)

15. Justs, J.; Wyrzykowski, M.; Bajare, D.; Lura, P., 2015, Internal curing by superabsorbent polymers in ultra-high performance concrete. *Cem. Concr. Res.*, 76, 82–90, DOI: doi.org/10.1016/j.cemconres.2015.05.005

16. Woyciechowski, P.; Kalinowski, M., 2018, The Influence of Dosing Method and Material Characteristics of Superabsorbent Polymers (SAP) on the Effectiveness of the Concrete Internal Curing, *Materials*, 11(9), 1600, DOI: [10.3390/ma11091600](https://doi.org/10.3390/ma11091600)

Study on Self-healing Cementitious Materials with Hydrogels Encapsulating Phosphate

X. Liu², Y. Tang², Z. Liu², W.Chen¹, Q. Li¹, W. Chen^{1*}

¹State Key Laboratory of Silicate Materials for Architectures, Wuhan University of Technology, 430070 Wuhan, Hubei, PR China

²School of Materials Science and Engineering, Wuhan University of Technology, 430070 Wuhan, Hubei, PR China

Abstract

At present, commonly-used self-healing methods include capsule encapsulation healing agents, hollow fiber encapsulation healing agents, or direct addition of microbial bacteria. Some methods heal cracks by producing minerals such as calcium carbonate. In this study, a novel self-healing cementitious material is developed by using a hydrogel impregnated with phosphate as the healing agent. Hydrogel has a sensitive response mechanism to changes in the external environment compared to other healing agent. The aim is to form a hydroxyapatite-type mineral as healing products in the crack during the self-healing process by controlling the release of phosphate. Hydrogels were used as a carrier to encapsulate phosphate and added to cement paste to manufacture self-healing cementitious materials. The self-healing mechanism of this material is mainly when the crack is induced in the cementitious material, and the phosphate in the hydrogel is released into the pore solution in the crack due to the change of the osmotic pressure. Water and carbon dioxide penetrate into the fracture and form bicarbonate ion (HCO_3^-), and the Ca^{2+} and OH^- ions released from the cement matrix react with the phosphate ions and HCO_3^- to form hydroxyapatite-type mineral which can heal the crack. The self-healing efficiency was evaluated by the water permeability test. The results show that the hydrogels successfully preserved the phosphate in the paste and the self-healing agent produced dense hydroxyapatite on the sample in the simulated pore solution. The self-healing efficiencies is more than 60% on the water permeability. The self-healing products were carbonated and calcium deficient hydroxyapatite (CCDHA) according to XRD and FTIR analysis.

Keywords: Self-healing cementitious materials, Hydrogel, Hydroxyapatite, Self-healing efficiency

1. Introduction

The self-healing technology has been widely used in concrete because it can fill external cracks and internal cracks in time when the concrete structure is destroyed, which greatly reduces the maintenance cost and prolongs the service life of the concrete structure [1-3]. Self-healing in concrete is mainly divided into the following two types: autogenous healing and autonomous healing. Autogenous healing is the natural process of crack repair occurring in concrete in the presence of moisture, the healing mechanism is based on the continued hydration of unhydrated cement particles and the formation of calcium carbonate at the crack edge. Its maximum healing width can reach $300\mu\text{m}$ [4]; Self-healing is a self-healing ability of an artificially designed cementitious material. At present, commonly-used self-healing methods include capsule encapsulation healing agents [1], hollow fiber encapsulation healing agents [5], or direct addition of microbial bacteria [6]. Its maximum healing width can reach $970\mu\text{m}$ [7, 8]. Most of the healing products

are C-S-H, ettringite, CaCO_3 , polymer binder [9, 10], etc., and there are few self-healing materials using hydroxyapatite as a healing product.

Varieties of self-healing materials are generally encapsulated by a polymer or glass to release the healing component of the cementitious material when cracks occur. Some studies have used hydrogels as carriers to carry and protect bacteria to healing cracks and achieve excellent healing results [6, 11]. Hydrogels have a hydrophilic three-dimensional network structure that is chemically cross-linked or physically cross-linked, and is often used as a drug delivery vehicle due to its adjustable physical properties, controlled degradability, and ability to protect unstable drugs from degradation. The release rate of the drug in the hydrogel is significantly related to the difference between the internal and external ion osmotic pressure and the pore size of the hydrogel surface. The smaller the ion osmotic pressure difference inside and outside, the slower the rate of release [12]. As an important component of bone tissue, hydroxyapatite (HA) plays an important role in the self-healing phenomenon of bone tissue, the solubility of hydroxyapatite is much less than the solubility of calcium carbonate, so hydroxyapatite-type minerals were formed and healed the cracks through the reaction between phosphate released from hydrogels and Ca^{2+} from the paste. According to the encapsulated and sustained release characteristics of hydrogels, it is proposed to use hydrogel encapsulated phosphate as a cementitious material healing component. After the hydrogel encapsulates the phosphate, most of the water in the gel is bound by the hydrophilic hydrogel, leaving only a small amount of free water and phosphate, and the internal osmotic pressure of the hydrogel is larger. Then, the internal healing agent has a lower outward permeation rate with the same ions concentration in the cement slurry, which can effectively protect the healing agent.

In this study, a novel self-healing cementitious materials is developed by using a hydrogel impregnated with phosphate as the healing agent. The self-healing mechanism of this materials is mainly when the crack is induced in the cementitious material, and the phosphate in the hydrogel is released into the pore solution in the crack due to the change of the osmotic pressure. Water and carbon dioxide penetrate into the fracture and form HCO_3^- , and the Ca^{2+} and OH^- ions released from the cement matrix react with the phosphate ions and HCO_3^- to form hydroxyapatite-type mineral which can heal the crack. A variety of analytical testing methods were used to analyse and evaluate the phosphate release process, the characteristics of healing products in the crack and the healing effect.

2. Methodology

2.1 Materials

An ordinary Portland cement complying with the Chinese standard GB 175-2016 classified as P.O. 42.5 (Huaxin Cement Co, Ltd). The oxide compositions of cement are listed in Table 1.

Table 1: Chemical composition of cement (wt%)

Oxide	Al_2O_3	SiO_2	Fe_2O_3	CaO	K_2O	SO_3	Na_2O	MgO	LOI
OPC	5.86	21.50	2.85	59.81	0.67	2.06	0.20	2.23	3.70

LOI: Loss on ignition at 1000°C

Disodium hydrogen phosphate (Na_2HPO_4), sodium dihydrogen phosphate (NaH_2PO_4), acrylic acid (AA), N,N-methylene BIS acrylamide (BIS), sodium hydroxide (NaOH), sodium dodecyl sulfate (SDS) \square N_2 gas with purity of 99.99% and sodium carbonate (Na_2CO_3) are used. All chemicals are AR grade.

The mix design of self-healing cementitious materials in this experiment is shown in Table 2. The hydrogel used in the experiment is divided into two types. Where H is a blank hydrogel without phosphate, HP is a self-healing hydrogel containing phosphate, and the hydrogel is added in 3% by mass of cement.

Table 2: the mix design of self-healing cementitious materials (kg/m³)

Type	Cement	Water	Hydrogel
HP	1875	656.25	Hydrogels encapsulated phosphate 56.25
H	1875	656.25	Blank Hydrogels 56.25

2.2 Methods

The method of synthesizing hydrogel is as follows: 2 grams of Na₂HPO₄ and 2 grams of NaH₂PO₄ are simultaneously dissolved in 10 grams water and stirred until the PH value of the buffer solution is 7. 2 grams of AA and 0.1 grams of BIS are added into the solution, bubbled with N₂ gas for 10 min. then 0.1 grams of APS is added into solution followed by consistently stirred after which a clear solution is obtained. The solution was sealed and placed at 60 °C for 4 h to form a PAA hydrogel with acrylic acid as a monomer, N,N-methylene BIS acrylamide as a crosslinking agent and sodium dodecyl sulfate as an initiator [13]. If no phosphate is added to the solution, the hydrogel H can be synthesized. The obtained gel is dried under Vacuum freeze dryer and grinded with a ball mill, the particle size of the HP is about 300µm.

The hydrogel swelling performance and the test of phosphate release performance are as follows□ prepare 200ml deionized water and 0.01mol/L NaOH solution as simulated pore solution respectively. The simulated pore solution was prepared by adding 200 grams of water to 20 grams of cement, filtering after half an hour, adding 0.3 g of Na₂CO₃ to remove Ca²⁺ in the solution, and filtering to obtain a clear simulated pore solution. Since the release of the hydrogel in the cement slurry is mainly in the initial stage of the cement hydration reaction, this method is used in order to simulate the pore solution in the initial stage of the hydration reaction. In order to avoid affecting the kinetics of phosphate release in the hydrogel caused by the reaction of PO₄³⁻ in the hydrogel and the Ca²⁺ reaction in the simulated pore solution, the same concentration of sodium carbonate was used to remove the Ca²⁺ but the total ion concentration in the solution remained unchanged.

2 g of hydrogel powder was placed in a dialysis bag (RC membrane, 6.16 ml/cm, protein molecular weight cutoff 3500) suspended in deionized water, 0.01 mol/L calcium hydroxide solution and simulated pore solution, 5ml of supernatant was taken from the solution at different time to test the phosphorus concentration, and the quality of the hydrogel in the dialysis bag was measured. The mass of hydrogel powder is referred to as m₀, the mass of hydrogel absorbed solution at different time periods is referred as m_t. Calculating the degree of swelling (Q) according to the following equation:

$$Q_t = (m_t - m_0)/m_0 \quad (1)$$

The preparation method of the hydrogel immersed in the simulated pore solution contain the hardened cement slurry to produce the healing product is as follows: 2 grams of hydrogel powder encapsulated phosphate is added into 200 grams of deionized water, placing a cement paste block curing 28 days with a fresh section after cutting in deionized water and sealed with plastic wrap. After placing for three days, a white substance will form on the surface of the fresh section of the cement. The white substance on the surface was separated from the cement by an ultrasonic disperser, dried by a vacuum freeze dryer, and then the phase and microscopic morphology of the white substance were tested by XRD and SEM.

The research method of the release of hydrogel phosphate in the cement matrix is as follows: Plain cement paste without HP is casted into the cubic mould with a layer thickness of 20 mm. 1 gram of HP powder are then dispersed on top of the fresh paste layer followed by slightly tapping the mould. The cubic mould is then filled with plain cement paste without HP again. The specimens are splitted along the HP powder layer after being cured for 1, 7, 14 and 28 days and use a fine brush to collect the hydrogel from the middle of the interlayer faces. The collected hydrogel was placed in a muffle furnace and calcined at 700 °C for two hours.

The weighing was taken out, and the weight of the ashes after the burning of the hydrogel was compared with that of the original hydrogel. The mass percentage of phosphate out of hydrogel was calculated by comparing the hydrogel masses of each curing age.

Each set of self-healing cementitious materials is made into a cylindrical specimen of $\Phi 50\text{mm} \times 50\text{mm}$, and all specimens were demoulded after 1 day of curing and transferred to the curing chamber at 20°C and 95%RH for 28 days. After the cylindrical sample is fixed with five layers of scotch tape along the side, place the side of the sample on the compressive testing machine and the ramp speed was adjusted into 0.1 KN/S. When the sample cracks, stop the compressive testing machine and record the width of the crack by using the crack width observation instrument. After cracking, all specimens were return in the curing chamber

The water permeability is performed on three vacuum saturated specimens in each batch according to Chinese standard GB/T 25993-2010. The specimens are loading with a compressive testing machine to generate crack after curing 28 days and record the width of the crack, then the total weight of the permeated water of the crack was tested for 5 minutes to calculate the amount of water permeating the sample and the water permeability. The water permeability is calculated as the average of three specimens, according to the following equation

$$E = \frac{G_s}{G_b} \quad (2)$$

In the equation, E is the self-healing efficiency of properties, G_s is the water permeability after curing, G_b is the water permeability after cracking.

3. Results and discussion

3.1 The morphology of hydrogel

The morphology of synthetic hydrogels H and HP is shown in Figure 1. Figure 1(a) is an SEM image of a hydrogel that is not encapsulated with phosphate, it can be seen from the figure that the hydrogel exhibits a fibrous network formed by cross-linking between monomers. The SEM image of hydrogel encapsulated phosphate is shown in Figure 1(b), unlike hydrogels that not encapsulated phosphate, the hydrogels encapsulated phosphate have no obvious fibrous network structure. The addition of phosphate causes wrinkles in the network inside the hydrogels. There are small pore structures on the surface of both hydrogels.

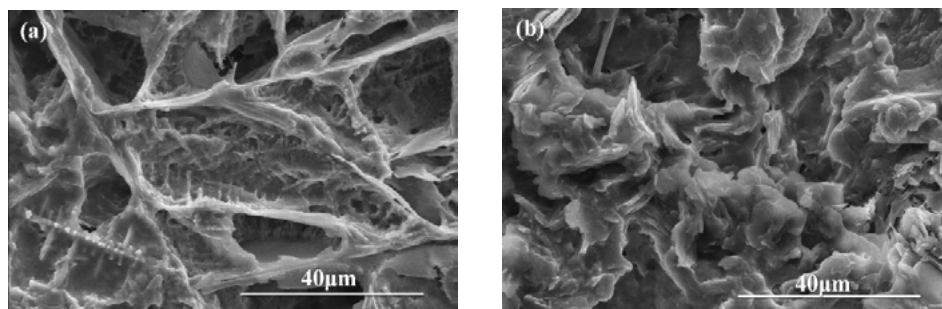


Figure 1: The SEM pattern of the hydrogels, (a) blank hydrogels, (b) hydrogel encapsulated phosphate

3.2 The hydrogel swelling performance and the diffusion of phosphate

The diffusion of phosphate in hydrogel encapsulated phosphate into various solutions are shown in Figure 2(a). It can be seen from the figure that the phosphate in hydrogel diffuse rapidly into deionized water and sodium hydroxide solution in the first 7 hours, but the diffuse rate is significantly reduced in the simulated pore solution. The highest diffusion rate is found in the deionized water, followed by NaOH solution and

pore solution. The release of phosphate ions from hydrogels in different solutions can be resulted from the difference in the osmotic pressure due to the different ions strength of different solutions [14]. The great the internal and external osmotic pressure difference, the faster the exchange speed. The ion concentration in the hydrogel is similar to that in the simulated pore solution, and the internal ion concentration of the hydrogel is larger than that in the simulated pore solution, and the diffusion rate is slower in the cement slurry solution. The hydrogel swelling performance in various solutions are shown in Figure 2(b). The swelling rate of the hydrogel in various solutions is the same as the tendency of the phosphate diffusion curve, the consistent tendency in deionized water and NaOH solution. A obvious different between deionized water and pore solution could be resulted from the difference in the osmotic pressure due to the different ions strength of different solutions.

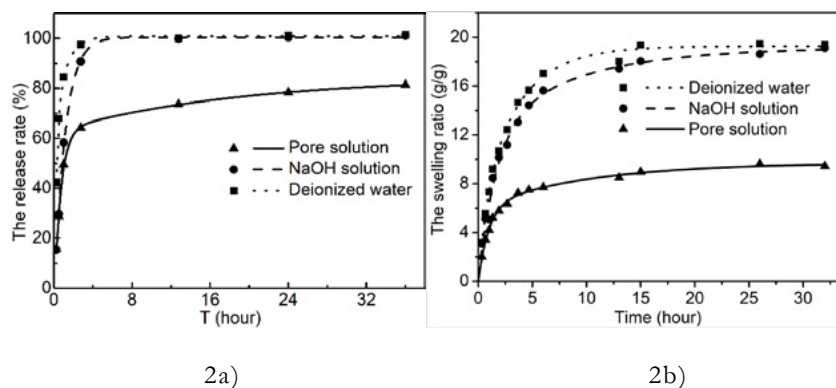


Figure 2: 2a) Diffusion curves of phosphate ion and 2b) the swelling properties of hydrogel immersing in different solutions

3.3 Diffusion of phosphate out of hydrogel in cement paste

A major feature of self-healing cementitious materials is the ability of materials to respond the formation cracks spontaneously. It means the self-healing cementitious materials can release the healing agent to form the healing product, and should not release the healing agent when the matrix not broken. The diffusion of phosphate out of hydrogel in cement paste is shown in Figure 3.

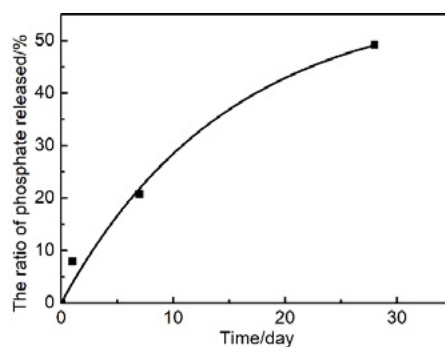


Figure 3: The release ratio of phosphate from hydrogels

It can be seen from the figure that the diffusion of phosphate out of hydrogel in cement paste is rapidly decrease after curing 7 days, but the diffuse rate is slowly reduced after curing 28 days, the phosphate in the hydrogel released a total of about 50% in the cement paste during curing 28 days. The main reason for this phenomenon is that the ion concentration of the cement pore solution is low in the initial stage of cement hydration, resulting in rapid exchange of ions in the cement slurry and hydrogel. The ions concentration of the pore solution increases with the hydration time in the later stage of cement hydration, then the ions exchange between the cement matrix and hydrogel decreases, which reduces the diffusion rate of phosphate. These results indicated that the hydrogel can prevent the unfavourable release of phosphate

without crack formation in the cement paste and is suitable for the self-healing cementitious materials.

3.4 The healing product in pore solution

The XRD pattern and SEM image of healing product created by putting the hydrogel into the simulated pore solution contain the hardened cement slurry are shown in Figure 4. Calcium deficient hydroxyapatite (CDHA, PDF-09-0432) is identified in the precipitated products, the formation of CDHA is due to the lack of calcium ions on the surface of the cement paste. It can be seen from the Figure 4(a) (b) that a large number of spherical substance appear around the cement hydration product, A large amount of needle-shaped substances are scattered around the surface of the spherical substance. The broad peak width of XRD pattern indicated the low crystallinity nature of healing products, this is also consistent with the CDHA morphology in the SEM. This is mainly due to the fact that hydroxyapatite will priority generated as amorphous calcium phosphate during crystallization, and then amorphous calcium phosphate is gradually converted to hydroxyapatite. The low crystallinity nature of CDHA is generated due to the difference in the ratio of calcium to phosphorus, The CDHA form a relatively stable packing structure, indicating good bonding between the hydroxyapatite and the cement matrix.

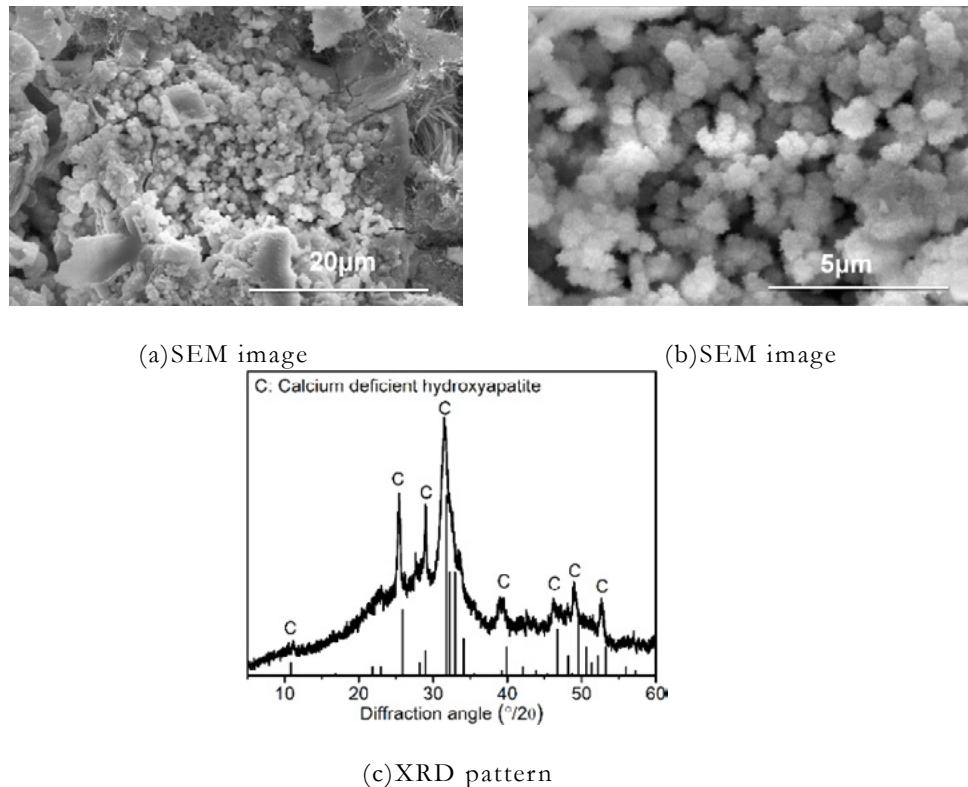


Figure 4: the XRD pattern and SEM image of simulated products

3.5 Self-healing efficiency of HP

The crack healing area of the specimens after self-healing at different ages are shown in Figure 5(a). It can be seen from the figure that the hydrogels encapsulated phosphate is more than hydrogels not encapsulated phosphate for the crack healing area. The healing area ratio can reach 90% for the addition of HP after healing 28 days, and the healing area ratio of H is merely about 40% after healing 28 days. It indicated that the phosphate of hydrogels can fill the crack by producing the healing products. The water permeability of specimens after self-healing at different ages are shown in Figure 5(b). The water permeability is gradually decreased with the increase of time of self-healing. The water permeability of HP is dramatically by 60% after self-healing for 28 days by standard condition, but the water permeability of H is merely 40% after self-healing for 28 days. The results suggest that the phosphate of hydrogels is essential for the crack

healing, the self-healing cementitious materials with hydrogels encapsulated phosphate has an efficiency in the properties restoration in 28 days of self-healing.

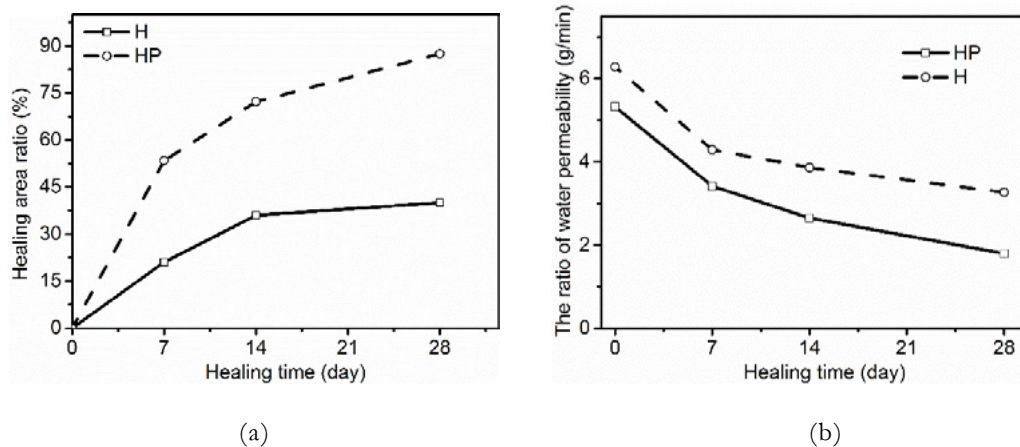
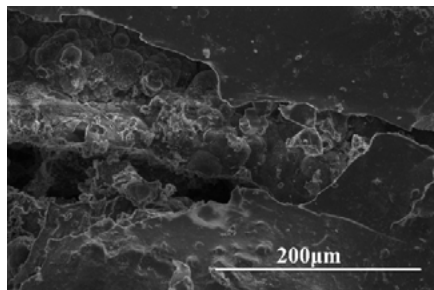


Figure 5: the self-healing efficiency (a) Healing area after self-healing for different ages (b) Water permeability of specimens after self-healing for different ages

3.6 Self-healing products in cement paste after cracking

The morphology of self-healing products in the crack of cement paste after healing 14 days is shown in Figure 6. The edge of the crack is filled with a pleated spherical morphology of hydroxyapatite, and the particle size is approximately 40 μ m, which is very similar to the healing product in the simulated solutions. Figure 6(a) shows that the close accumulation of healing product particles indicates that the mechanical properties are better. Figure 6(b) the crack section is filled with cubic calcium carbonate and spherical hydroxyapatite.



6a)

6b)

Figure 6: 6a) CDHA grew from both sides to the center of a crack 6b) a close look of morphology of CDHA and calcite

The particle size is about 40 μ m, which is also a wrinkled sphere. It can be seen from the figure that there are more hydroxyapatite and less calcium carbonate, which is because the solubility product of hydroxyapatite is much lower than that of calcite, which leads to its superiority in calcium ion competition [15].

The XRD pattern and FT-IR spectra of products of healing products formed in the cracks are shown in Figure 7. According to the XRD pattern of the healing products, the products consisted of hydroxyapatite and calcite, the XRD spectrum of hydroxyapatite is extremely different from calcium-deficient hydroxyapatite [16]. In the FT-IR spectra of products of healing products formed in the crack, the peaks at 3431 and 1648 cm^{-1} , which are represented to the adsorbed water in hydroxyapatite, the peaks at 1038, 960, 557, 607 cm^{-1} , which are assigned to PO_4^{3-} ; The peak at 1460 cm^{-1} arises from the CO_3^{2-} , This also corresponds to the phenomenon of coexistence of hydroxyapatite and calcite in SEM image and indicates the healing products

is CCDHA.

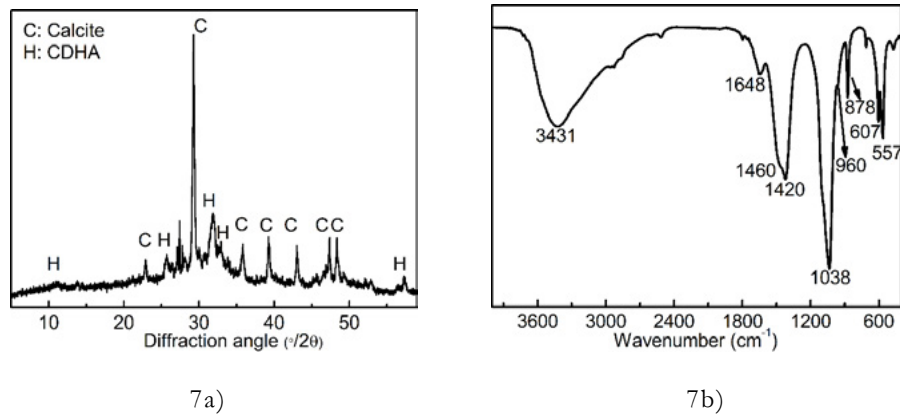


Figure 7: (a) The XRD pattern and (b) The FT-IR spectra of healing products formed in the crack

4. Conclusions

In this study, a novel self-healing cementitious materials is developed by using a hydrogel impregnated with phosphate as the healing agent. According to the results obtained, the following conclusions can be drawn.

- (1) The self-healing cementitious materials were prepared by encapsulating phosphate with hydrogels and adding it to cement paste. The hydrogels is an excellent self-healing carrier by effectively encapsulated phosphate and not release the phosphate into the cement paste during the mixing or curing.
- (2) Calcium deficient hydroxyapatite (CDHA) is identified on the surface of harden cement slurry with presence of simulated pore solution and hydrogels encapsulated phosphate.
- (3) The crack healing area ratio of the specimens with the addition of HP after self-healing at 28 days can reach 90%, the water permeability of the specimens with the addition of HP is dramatically by 60% after self-healing for 28 days by standard condition
- (3) The phosphate in the hydrogel can form the carbonated calcium deficient hydroxyapatite and healing the cracks by mixing the calcium ions in the cement matrix when the crack is generated, and the healing products are mainly carbonated calcium deficient hydroxyapatite and calcite.

5. Acknowledgment

This research has been financially supported by the National Natural Science Foundation of China (grant numbers 51672199); the Fundamental Research Funds for the Central Universities (grant number WUT: 2017-YB-008□ 2019III018GX); and the 111 Project (No. B18038)

6. Reference

- [1] Kanellopoulos A, Qureshi T, Al-Tabbaa A. Glass encapsulated minerals for self-healing in cement based composites [J]. Construction and Building Materials, 2015, 98:780–791.
- [2] Wu M, Johannesson B, Geiker M. A review: Self-healing in cementitious materials and engineered cementitious composite as a self-healing material [J]. Construction and Building Materials, 2012, 28(1): 571-583.
- [3] Ramm W, Biscopig M. Autogenous healing and reinforcement corrosion of water-penetrated separation cracks in reinforced concrete [J]. Nuclear Engineering and Design, 1998, 179(2):191-200.
- [4] Aldea C M, Song W J, Popovics J S, Shah S P. Extent of healing of cracked normal strength concrete [J].

Journal of materials in civil engineering, 2000, 12(1): 92-96.

[5] Di Shengkui L H. Self-Monitoring and Repairing Based on Crack of Concrete Beam Embedded with SMA [J]. Journal of Building Materials, 2009, 12(1): 27-31.

[6] Wang J, Mignon A, Snoeck D, et al. Application of modified-alginate encapsulated carbonate producing bacteria in concrete: a promising strategy for crack self-healing [J]. Frontiers in microbiology, 2015, 6: 1088.

[7] Tang W, Kardani O, Cui H. Robust evaluation of self-healing efficiency in cementitious materials – A review [J]. Construction and Building Materials, 2015, 81:233-247.

[8] Wang J Y, Soens H, Verstraete W. Self-healing concrete by use of microencapsulated bacterial spores[J]. Cement & Concrete Research, 2014, 56(2):139-152.

[9] B. Yuan, Y. Yang, Y. Wang, and K. Zhang, Self-healing efficiency of EVA-modified cement for hydraulic fracturing wells [J]. Constr. Build. Mater, 2017. 146:563–570.

[10] Sisomphon K, Copuroglu O, Koenders E A B. Self-healing of surface cracks in mortars with expansive additive and crystalline additive [J]. Cement and Concrete Composites, 2012, 34(4):566-574.

[11] Wang J Y, Snoeck D, Vlierberghe S V, et al. Application of hydrogel encapsulated carbonate precipitating bacteria for approaching a realistic self-healing in concrete [J]. Construction & Building Materials, 2014, 68(68):110-119.

[12] Li J, Mooney D J. Designing hydrogels for controlled drug delivery [J]. Nature Reviews Materials, 2016, 1(12): 16071.

[13] Chen Q, Liu C, Jiang G, Liu X, Yang M, Liu F. Studies on swelling behavior of poly (acrylic acid-co-octadecyl methacrylate) hydrophobic association hydrogels with high mechanical properties [J]. Acta Polymerica Sinica, 2010, 6: 797.

[14] Mignon A, Graulus G J, Snoeck D, et al. pH-sensitive superabsorbent polymers: a potential candidate material for self-healing concrete [J]. Journal of materials science, 2015, 50(2): 970-979.

[15] Mostafa N Y. Characterization, thermal stability and sintering of hydroxyapatite powders prepared by different routes [J]. Materials Chemistry and Physics, 2005, 94(2-3):333-341.

[16] A. Siddharthan, S.K. Seshadri, T.S. Sampath Kumar, Microwave accelerated synthesis of nanosized calcium deficient hydroxyapatite [J]. J.Mater. Sci. Mater. Med. 15 (2004) 1279–1284.

Biosorption of heavy metal ions of lead and zinc by *Trichoderma reesei* based on response surface method

Y. Sun^{1,2}, R. Yu^{1*}, Z. Shui¹, D. Qian^{1,2}, B. Rao², J. Huang²

¹ State Key Laboratory of Silicate Materials for Architectures, Wuhan University of Technology, Wuhan 430070, China

² School of Materials Science and Engineering, Wuhan University of Technology, Wuhan 430070, China

Abstract

Biosorption is a method of heavy metal removal. In the study, Response Surface Method (RSM) is utilized to get the optimal concentration of lead and zinc solution, and the inoculation amount of *Trichoderma reesei* (CCTCC AF 2015005 QM6a). Accordingly, the obtained results showed that the optimum condition is 0.8mg/L, 0.83mg/L of lead and zinc solution respectively and the inoculation amount of fungi is 300 uL. In this condition, Pb and Zn are best removed from the liquid media of *Trichoderma reesei* (CCTCC AF 2015005 QM6a) fungi, with an average of 27% and 56%, respectively. Value of correlation coefficient ($R^2=0.9977$ and 0.9734 , respectively) and significant value for model $p < 0.0001$ indicated validity of model fitness and adequate for optimization.

Keywords: Biosorption, Response Surface Method, *Trichoderma reesei*, lead, zinc

1. Introduction

The presence of heavy metal ions in the environment causes serious threat to human, animals and the environment. Heavy metal ions in the environment usually come from many sources, i.e. mining, electroplating, metal processing, automobile manufacturing, dyeing, textile, fertilizer and petroleum industries, which is harmful for the environment.[1,2] To solve the problem and reduce harm of heavy metal accumulation on human body, some of physical or chemical treatment ways such as chemical oxidation and reduction, precipitation, adsorption, solidification, electrolytic recovery and ion exchange are used for heavy metal removal in some study.[3,4] However, application of such processes is sometimes restricted due to economical or technical constraints and secondary pollution because of the addition of chemical reagents. Therefore, there is a need for an innovative method with low cost and advanced security that metal ions can be removed economically and safely. Microorganisms, i.e. bacteria, fungi and yeasts, as the most usually used organisms in biotechnology, are frequently studied over many years. And biosorption technology is considered to be one of the most effective and environmentally friendly technologies of heavy metal removal from waste water.[5-10] Especially, using fungi to remove heavy metal ions from waste water has drawn more and more attention in recent years as well as a very broad application prospect, among which, *Trichoderma reesei* is one of the most popular commercial cellulases. And the adsorption of *Trichoderma reesei* on heavy metal Cr(VI) has been studied.[11] However, the adsorption of *Trichoderma reesei* on other heavy metals such as lead and zinc have drawn few researchers' attention. Thus, it is necessary to study the biosorption of *Trichoderma reesei* on lead and zinc. Plenty of studies in heavy metal absorption by using fungi have shown good results in heavy metal removal, but almost all have used shake flask cultures

along with Sabouraud Dextrose Broth[12,13], which is more expensive compared to PDB thus increasing the cost of experiments. PDB can easily be made in the laboratory and cheap and accessible. By using PDB as nutrients can easily reduce the experimental cost.

In this study, response surface methodology (RSM) has been developed as an effective tool for optimization of reaction conditions, i.e. concentration of lead and zinc and inoculation amount for fully utilization of biosorption of *Trichoderma reesei* (CCTCC AF 2015005 QM6a).

2. Materials and methods

2.1 Microorganism

In the study, *Trichoderma reesei* (CCTCC AF 2015005 QM6a) from China Center for Type Culture Collection (CCTCC) is used as adsorbent material. A spore suspension was obtained by growing on potato dextrose agar (PDA) for two days and then cultured in the potato dextrose broth (PDB) for 72 hours in the condition of 20 °C, illuminating and 150 r/min in the table concentrator. The strains used in this experiment are kept in the refrigerator (4°C), and the remaining strains are kept in the refrigerator (-80°C).

2.2 Preparation of heavy metal solution

Before operating the experiments, the media and deionized water useful for the next step were sterilized in autoclave for 121 °C, 30 min in the autoclave. The preparation of heavy metal ion solution is obtained by fully mixed dissolution of deionized water and Pb(NO₃)₂ and Zn(NO₃)₂. The ranges of concentrations varied according to the design of part 2.4. After weighing the chemicals, place them in deionized water and use a magnetic mixer to fully promote dissolution.

2.3 Inoculation of *Trichoderma reesei*

The inoculation amount of *Trichoderma reesei* is determined by the design of response surface method. Before inoculation, firstly, the mycelium of the strain is evenly dispersed to make it distributed in the culture medium uniformly, so as to ensure that the amount of the strain in each culture medium is approximately the same. The liquid volume of the inoculated fungi solution was calculated into the volume of the heavy metal solution.

2.4 Measurement of heavy metal ion concentration

The concentration of heavy metal ion solutions with the fungal medium was determined by using full spectrum direct reading plasma emission spectrometer (Inductively Coupled Plasma-Optical Emission Spectr, Prodigy 7/Prodigy 7, USA). Select 5 ml of the uniform solution after the reaction (avoiding the fungi), and compare with the concentration of the solution before reaction. The removal rate of the strain is calculated by the following equation:

$$\text{Removal rate (R\%)} = \frac{[\text{Concentration before reaction (counting strain volume)} - \text{Concentration after reaction}]}{\text{Concentration before reaction (counting strain volume)}} \times 100\% \quad (1)$$

2.5 Response surface methodology

The central composite design (CCD) of response surface methodology (RSM) is utilized to determine the optimum operational conditions for the biosorption process. Every numeric factor is varied over 5 levels: plus and minus alpha, plus and minus 1 (factorial points) and the center point.[14]. Three factors, i.e., concentration of lead, concentration of zinc and inoculation amount of *Trichoderma reesei*, and varies from 0.5 mg/L~2mg/L, 0.5mg/L~1.5mg/L, 300 uL~1000uL, respectively. And the range of variation is shown in Table 1.

Table 1: Range of variation

Factors	Variables	Low actual	High actual	Low Coded	High coded
X1	Concentration of lead (mg/L)	0.8	1.7	-1.000	1.000
X2	Concentration of zinc (mg/L)	0.7	1.3	-1.000	1.000
X3	Inoculation amount (uL)	300	1000	-1.000	1.000

Table 2: Central composite design and experimental responses.

Run	X1	X2	X3	Response 1	Response 2
1	1.25	1	61.37	0.860658	0.413809
2	0.5	1	650	0.369979	0.44457
3	1.25	1	1238.63	0.901682	0.508715
4	0.8	0.7	300	0.595091	0.311385
5	0.8	1.3	1000	0.632161	0.566632
6	1.7	0.7	300	1.28242	0.321636
7	0.8	1.3	300	0.616915	0.547159
8	1.25	1.5	650	1.00219	0.725871
9	1.25	0.5	650	1.02338	0.271081
10	0.8	0.7	1000	0.675207	0.308048
11	1.25	1	650	0.955306	0.473142
12	1.7	1.3	300	1.30144	0.597697
13	1.7	0.7	1000	1.36635	0.351149
14	1.7	1.3	1000	1.34437	0.596442
15	2	1	650	1.52814	0.477513
16	1.25	1	650	0.939204	0.465596

Total 16 experimental groups were designed by the central composite design (CCD) model and performed as shown in Table 2. As shown in Table 1, the X1, X2 and X3 represents concentration of lead , zinc, and inoculation amount of fungi, respectively. And response 1, 2 are the concentration of lead and zinc after

reaction, respectively.

3. Results and discussions

3.1 Effect of variables on the removal of lead

As shown in Table 3, the variance of the removal of lead is analyzed. The present model is not only the define optimum conditions for lead removal but also showed combined effect of variables i.e. concentration of lead and zinc and inoculation amount of fungi. The Model F-value of 295.29 implies the model is significant. There is only a 0.01% chance that a “Model F-Value” this large could occur due to noise. The “Lack of Fit F-value” of 5.58 implies the Lack of Fit is not significant relative to the pure error. There is a 31.04% chance that a “Lack of Fit F-value” this large could occur due to noise. Non-significant lack of fit is good.

The concentration of Pb after biosorption of *Trichoderma reesei* is shown in equation 2.

Concentration of Pb after biosorption of fungi (mg/L)

$$=0.94+0.35*A-4.380E-003*B+0.021*C+2.283E-003*A*B+3.936E-003*A*C-0.013*B*C+7.404E-003*A^2+0.030*B^2-0.017*C^2 \quad (2)$$

Table 3: Analysis of variance (ANOVA) for response surface quadratic model

Sources	Sum of squares	DF	Mean square	F value	Prob>F	
Model	1.66	9	0.18	295.29	0.0001	Significant
A-Concentration of Pb	1.63	1	1.63	2615.80	0.0001	
B-Concentration of Zn	2.620E-004	1	2.620E-004	0.42	0.5411	
C-Inoculation amount	6.210E-003	1	6.210E-003	9.94	0.0197	
Residual	3.747E-003	6	6.244E-004			
Lack of Fit	3.617E-003	5	7.234E-004	5.58	0.3104	Not significant
Pure error	1.296E-004	1	1.296E-004			
Cor total	1.66	15				

DF: degree of freedom.

Table 4 showed the analysis of variance table of the model. The “Pred R-Squared” of 0.9832 is in reasonable agreement with the “Adj R-Squared” of 0.9944.

Table 4: Analysis of variance of the model

Response1	R2	Adj-R2	Pred-R2	Mean	Std. Dev.
Concentration of lead after biosorption	0.9977	0.9944	0.9832	0.96	0.025

Figure 1 illustrates the current lambda=1, and the best lambda=1.04, low C.I. =0.33 and high C.I.=2.88. The data do not require a transformation, as current value of confidence interval it contains is very close to the optimum value. After reviewing all the statistical outputs for design evaluation and three-dimensional plots, the minimum value of standard error relatively low, which indicates the design points and polynomial fitness of the model, as shown in figure 2. And the relationship between the concentration of lead after biosorption is showed in figure 3.

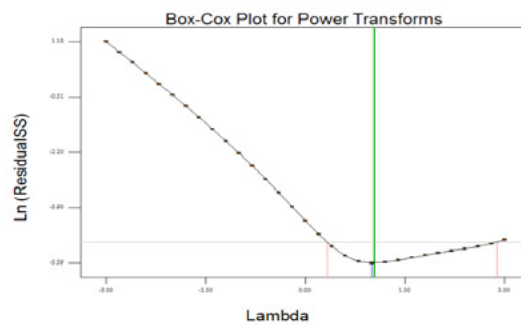


Figure 1: Box-Cox plot for power transforms

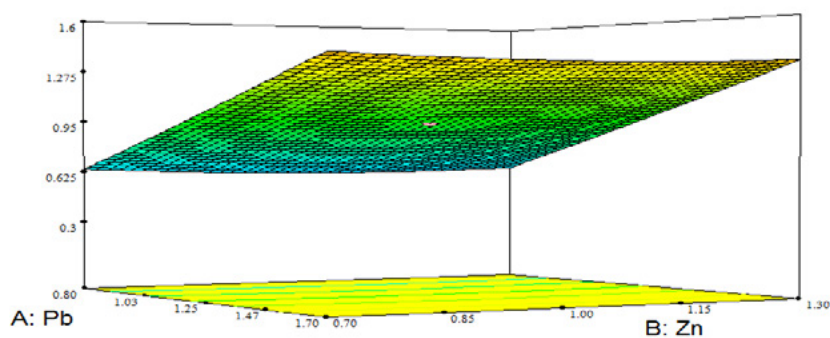


Figure 2: Three-dimensional graph of results

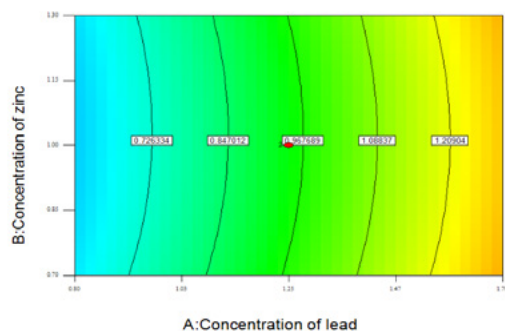


Figure 3: Two-dimensional graph of results

3.2 Effect of variables on the removal of zinc

As shown in Table 5, the variance of the removal of zinc is analyzed. The quadratic regression showed that the model was significant because the value of F-test is less than 0.05 and model F value 146.27 which indicated the significance of the model terms. And Table 6 showed the R square.

The “Pred R-Squared” of 0.9499 is consistent with the “Adj R-Squared” of 0.9667. Figure 4 illustrates the variance of the biosorption of fungi on Zn by model. And the experimental results of the removal of zinc are shown in figure 5. As can be seen, the results showed an approximate linear relationship between X2 and response 2.

Table 5: Analysis of variance (ANOVA) for response surface quadratic model

Sources	Sum of squares	DF	Mean square	F value	Prob>F	
Model	0.24	3	0.079	146.27	□ 0.0001	Significant
A-Concentration of Pb	2.618E-003	1	2.618E-003	2615.80	0.0483	
B-Concentration of Zn	0.23	1	0.23	0.42	□ 0.0001	
C-Inoculation amount	3.047E-003	1	3.047E-003	9.94	0.0375	
Residual	6.504E-003	12	5.420E-004			
Lack of Fit	6.475E-003	11	5.877E-004	5.58	0.1700	Not significant
Pure error	2.847E-004	1	2.847E-005			
Cor total	0.24	15				

Table 6: Analysis of variance of the model

Response1	R ²	Adj-R ²	Pred-R ²	Mean	Std. Dev.
Concentration of zinc after biosorption	0.9734	0.9667	0.9499	0.46	0.023

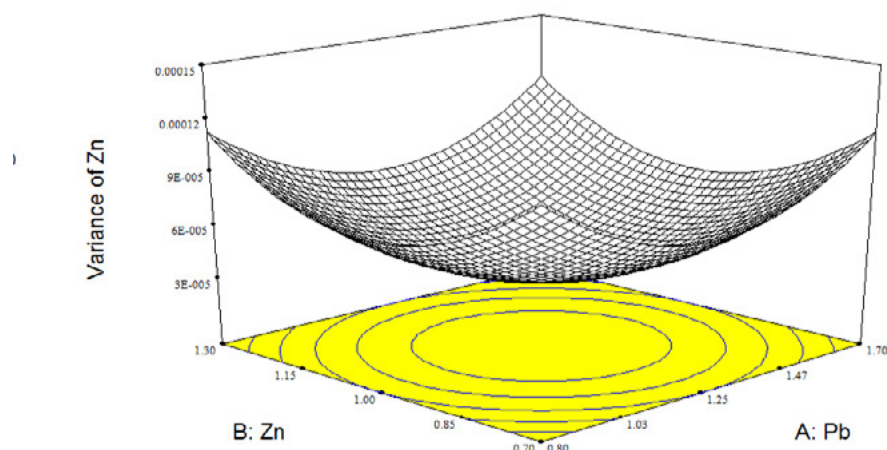


Figure 4: Three-dimensional graph of variance of Zn by model

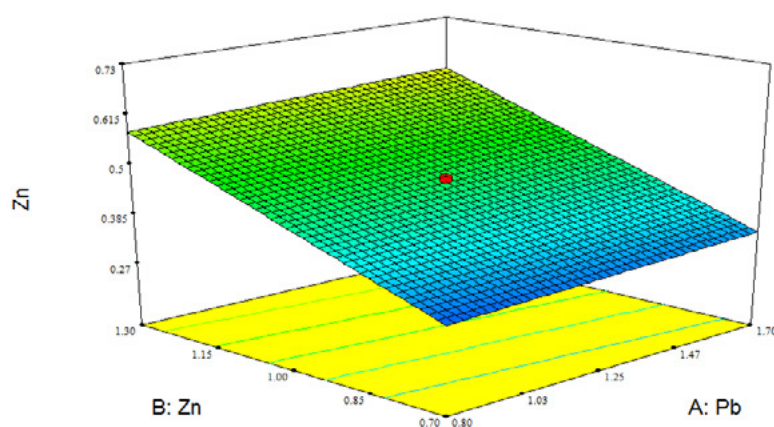


Figure 5: Three-dimensional graph of results

4 Conclusions

This study demonstrates that *Trichoderma reesei* (CCTCC AF 2015005 QM6a) offers a new method of biosorption of the heavy metals i.e. lead and zinc. Response surface method was utilized to establish the model between the heavy metal removal and the concentration of lead and zinc and the fungi that taking effect. Response surface methodology (RSM) is a powerful tool not only can be used for optimization of the process control in biosorption of heavy metal but also for the additional knowledge supplied about the optimization processes in any part of experimental domain. The optimum response 1 (concentration of lead) is 0.8 mg/L, and as for response 2 (concentration of zinc), the optimum concentration is 0.83mg/L,

in the condition of the inoculation amount of fungi is 300 uL. The characteristic of mycelium of *Trichoderma reesei* offers nucleation sites for the biosorption of heavy metal ions.

5 Acknowledgements

The authors acknowledge the financial supports of National Nature Science Foundation Project of China (No. 51608409), National Science and Technology Support Program of China (2014BAC01B02), the National Key Research and Development Program of China in 13th Five-Year (2016YFC0305101), Yang Fan plan of Guangdong Province (201312C12), Major science and technology project in Zhongshan city, Guangdong province (2017A1021).

6 References

1. Rapoport, A.I., Muter, O.A., Bisorption of hexavalent chromium by yeast. *Process Biochemistry*. 30(1995), 145–149.
2. Caravelli, A.H., Giannuzzi, L., Zaritzky, N.E., Reduction of hexavalent chromium by *Sphaerotilus natans* a filamentous micro-organism present in activated sludges. *Journal of Hazardous Materials*. 156(2008), 214–222.
3. Eccles, H., Treatment of metal contaminated waste: why select a biological process? *TIBTECH*. 17(1999), 462–465
4. Li, H., Li, Z., Liu, T., Xiao, X., Peng, Z., Deng, L., A novel technology for biosorption and recovery hexavalent chromium in wastewater by biofunctional magnetic beads. *Bioresource Technology*. 99(2008), 6271–6279.
5. Crisafulli, R., Milhome, M.A., Cavalcante, R.M., Silveira, E.R., De Keukeleire, D., Nascimento, R.F., Removal of some polycyclic aromatic hydrocarbons from petrochemical wastewater using low-cost adsorbents of natural origin. *Bioresource Technology*. 99(2008), 4515 – 4519.
6. Elangovan, R., Philip, L., Chandraraj, K., . Biosorption of chromium species by aquatic weeds: kinetics and mechanism studies. *Journal of Hazardous Materials*. 152(2008), 100–112.
7. Febrianto, J., Kosasih, A.N., Sunarso, J., Ju, Y.H., Indraswati, N., Ismadji, S., Equilibrium and kinetic studies in adsorption of heavy metals using biosorbent: a summary of recent studies. *Journal of Hazardous Materials*. 162(2009), 616–645
8. Mohan, D., Rajput, S., Singh, V.K., Steele, P.H., Pittman Jr., C.U., Modeling and evaluation of chromium remediation from water using low cost bio-char, a green adsorbent. *Journal of Hazardous Materials*. 188(2010), 319–333.
9. Ng, I.S., Tsai, S.W., Ju, Y.M., Yu, S.M., Ho, T.H., Dynamic synergistic effect on *Trichoderma reesei* cellulases by novel beta-glucosidases from Taiwanese fungi. *Bioresource Technology*. 102(2011), 6073–6081.
10. Park, D., Yun, Y.S., Ahh, C.K., Park, J.M., Advanced kinetic model of the Cr(VI) removal by biomaterials at various pHs and temperatures. *Bioresource Technology*. 99(2008), 1141–1147.
11. Ng I S, Wu X, Yang X, et al., Synergistic effect of *Trichoderma reesei* cellulases on agricultural tea waste for adsorption of heavy metal Cr(VI)[J]. *Bioresource Technology*. 145(4)(2013):297-301.
12. Dacera, D., Babel, S., Removal of heavy metals from contaminated sewage sludge using *Aspergillus Niger* fermented raw liquid from pineapple wastes. *Bioresour. Technol.* 99(2008), 1682-1689.

13. Hu, L., Wan, J., Zeng, G.M., Chen, A.W., Chen, G.Q., Huang, Z., He, K., Cheng, M., Zhou, C., Xiong, W., Lai, C., Xu, P., Comprehensive evaluation of the cytotoxicity of CdSe/ZnS quantum dots in *Phanerochaete chrysosporium* by cellular uptake and oxidative stress. *Environ. Sci. (2017) Nano*. <https://doi.org/10.1039/c7en00517b>.
14. Design-Expert® Software, Version 6 User's Guide, 2001.

Use of peach shell as lightweight aggregate in pervious concrete

F. Wu^{1,2}, C. Liu^{1,3,4}, L. Zhang^{3,4}, Y. Lu^{3,4}, Q.L. Yu²

¹ Institute of Disaster Management and Reconstruction, Sichuan University-The Hong Kong Polytechnic University, No.1Huanghe Road, Chengdu 610065, China.

² Department of the Built Environment, Eindhoven University of Technology, P.O. Box 513, 5600 MB Eindhoven, The Netherlands.

³ College of Water Resource and Hydropower, Sichuan University, No.24 South Section 1, Yihuan Road, Chengdu 610065, China.

⁴ State Key Laboratory of Hydraulics and Mountain River Engineering, Sichuan University, No.24 South Section 1, Yihuan Road, Chengdu 610065, China.

Abstract

Peach shell (PS) is considered as an agricultural waste, which can be used as a lightweight aggregate in concrete due to its porous and lightweight properties. However, few literatures investigated the PS used as an aggregate in pervious concrete (PC). In order to expand the application of the PS in concrete, this study presents the use of PS used as an alternative aggregate in PC. A series of PC mixes were prepared with 0%, 25%, 50%, 75% and 100% replacement of normal weight aggregate (NWA) by PS, while the other parameters were set as constant. The results showed that the replacement of NWA with PS significantly reduced density, compressive strength and splitting tensile strength of PC, while increased the total void ratio and water permeability coefficient. Clogging test results showed that sand and dredged silt had a significant impact on the water permeability coefficient of PC, and the use of the large-grained aggregates in PC had better clogging resistance than the small-grained aggregates. When the PS is used as a coarse aggregate in PC, it cannot be used to fully replace the coarse aggregate. Based on the results of this study, the NWA was replaced by 25% PS, the compressive strength, splitting tensile strength and water permeability coefficient of PC were 7.9MPa, 0.91MPa and 9mm/s, respectively.

Keywords: Pervious concrete, Peach shell, Lightweight aggregate, Permeability, Clogging.

1. Introduction

Demand for concrete has been steadily increasing due to the economic development and increasing population [1]. The exploitation of natural aggregates has led to the scarcity of raw materials, which not only increases the cost of concrete but also destroys the surface landscape. Therefore, in order to achieve the sustainable development of the concrete industry, the utilization of various industrial by-product wastes and agricultural wastes as alternative raw materials for concrete has become one of the research hot issues all over the world [2]. Previous research has shown that some industrial and agricultural wastes can be successfully incorporated into concrete, including rubber, apricot shell, oil palm shell, seashell, plastics, wood and coconut shell, etc. [3-5].

Pervious concrete (PC) is a special type of concrete consisting of cement, a single grade of coarse aggregate,

little or no sand and a small amount of water [6]. Typically, the workability and strength of PC is much lower than that of normal weight concrete due to the lack or only small amount of sand in PC [7], and the permeability coefficient of ordinary PC is between 1.4 mm/s and 12.2 mm/s, the porosity varies from 14% to 35%, and the 28-day compressive strength is usually between 2.8 MPa and 28.0 MPa [8]. Although low-strength PC is not suitable for load-bearing purposes, they can be used in parking lots, drainage pavements and sidewalks, etc. [9].

The main function of the PC is to realize the spontaneous circulation of rainwater for sponge city by penetrating rainwater from the road surface to the underground soil [10]. The studies about previous concrete focused on the permeability coefficient, porosity and clogging performance of PC rather than its strength characteristics [10]. At present, the production of PC usually uses normal weight aggregate (NWA) as a single-grain aggregate, such as crushed granite, limestone and dolomite, etc. Recently, with the rise of the trend towards the use of various types of wastes as aggregates in concrete, some wastes such as recycled aggregate, rubber, seashell and palm oil clinker have also been used in the manufacture of PC [11-13]. Normally, the performance of the PC depends on the replacement ratio and the amount of the wastes. Although the wastes used as a substitute for NWA reduce the strength of PC, they are recycling wastes and reducing the consumption of NWA, which is conducive to the sustainable development of PC. The low-strength PC made of various wastes is adequate for low-strength structures such as sidewalks, parking lots and road shoulders, etc..

Peach is one of the main fruits in China, most of them are used for the products of peach drinks, candied fruit and canned food. The planting area and output of peach in 2016 in China were 742.1 k hm² and 13.1 million tons, respectively [14]. Peach shell (PS) is considered as agricultural waste and has no industrial application value. Due to crushed PS is renewable, which has lightweight and porous properties, it can be considered as an alternative aggregate for the manufacture and production of lightweight aggregate concrete (LWAC) [15]. However, there are few limited literatures on the use of such agricultural waste as an alternative aggregate in PC.

In this study, the peach shell (PS) was used to replace the normal weight aggregate (NWA) for producing pervious concrete (PC). NWA of different volume ratios was replaced by PS, while the other parameters were kept constant. The properties investigated included basic physical properties (density, total void ratio and water permeability coefficient), mechanical properties (compressive and splitting tensile strength) and clogging properties.

2. Methodology

2.1 Materials

2.1.1 Cement

Type I 42.5 grade ordinary Portland cement was used as the binder. The Blaine specific surface area and the specific density of the cement are 3532 cm²/g and 3.14 g/cm³, respectively. All mixtures were prepared with a cement content of 360 kg/m³.

2.1.2 Aggregate

In this study, a single-sized normal weight aggregate (NWA) with a 4.75-9.6mm was used and obtained from crushed pebbles. Single-sized peach shell (PS) with 4.75-9.6mm diameter was used as an alternative aggregate, and they were collected from a local orchard. The aggregates used in this study are presented in Figure 1, and the physical properties of aggregates are shown in Table 1. The specific gravity of the NWA was 2.66 g/cm³ and the bulk density was 1449 kg/m³. However, the specific gravity and density of the PS

were only 1.33 g/cm³ and 538 kg/m³, respectively. The density of PS was significantly lower than that of the NWA due to the presence of the round microscopic pores on the surface and interior of PS. However, the microscopic pore structure also increases the water absorption of PS, resulting in its much higher water absorption than that of the NWA.

Table 1: Physical properties of aggregates.

Physical property	Coarse aggregate	
	NWA	PS
Aggregate size (mm)	4.75-9.6	4.75-9.6
Specific gravity (g/cm ³)	2.66	1.26
Fineness modulus	4.9	5
Bulk density (kg/m ³)	1449	538
Water absorption (24h) (%)	0.5	16.7



Figure 1: a) Normal weight aggregate, b) Crushed peach shell and (c) SEM image of peach shell.

2.1.3 Mix proportions, mixing and casting

The mix proportions of all concrete are summarized in Table 2. For all mixes, cement and water were kept constant. In these pervious concretes, the NWA in the control mix was replaced with crushed PS by mass. The ratio of the PS substitute for the NWA was 25%, 50%, 75% and 100%, respectively. A concrete without PS was also prepared and used for a control purpose.

Table 2: Mix proportion of concretes (kg/m³).

Mix	Cement	Water	W/C	Coarse aggregate		
				NWA	PS	PS/total Coarse aggregate ratio
Control	360	108	0.3	1550	0	0
PS-25	360	108	0.3	1162.5	135	25%
PS-50	360	108	0.3	775	270	50%
PS-75	360	108	0.3	387.5	405	75%
PS-100	360	108	0.3	0	540	100%

The mixing of all the mixtures was done in the laboratory with an ambient temperature of 23±2°C. Firstly, the NWA, PS and cement were mixed in a circular drum mixer for 2 min. Then 70% of water was added and mixed for 2 min, and the remaining 30% of water was then added and mixed for 3 min.

After that, all mixtures were cast in different sized oiled moulds. 100mm×100mm×100mm cube specimens were used for compressive strength test, splitting tensile strength test and porosity test. The cylindrical specimens with a diameter of 100mm and a height of 200 mm were used for the clogging test and

permeability test. All the mixtures were compacted by a vibrating table. Immediately, after compaction, all specimens along with the mould were covered by the plastic sheathing for preventing moisture evaporation. After 24 h, all specimens were removed from the molds and stored in water until the test age.



Figure 2: The apparatus for permeability test.

2.2.3 Clogging test

Generally, the sediment containing both coarse and fine particles is most significant for reducing the permeability coefficient of pervious concrete [18]. The clogging test was performed in this study to evaluate the clogging performance of peach shell pervious concrete (PSPC). The clogging material used in this study was based on the blended material proposed by Dang et al. [12]. That is, the clogging material was made of 75% dredged silt (0-80 μ m) and 25% sand (0-4mm), which could be used to simulate field conditions. Before the clogging material was used, they were added to the water and mixed well until a uniform suspension was obtained at a concentration of 1% (Figure 3).

The same device was used for the clogging test and permeability test. The clogging test applied a cyclic test method, and a detailed test process is as follows: Firstly, the initial permeability coefficient was measured by the method of falling head test; Secondly, a suspension of clogging material was prepared at a concentration of 1%; Thirdly, the suspension was poured from the upper surface of the specimen and it slowly permeated the specimen through the pore structures inside the specimen; Fourthly, after the suspension was completely drained, the permeability coefficient of the specimen was determined by falling head test method when the clogging material still presented on the surface of the specimen; Finally, these above steps were repeated for at least four times.



Figure 3: a) Clogging material mixed by sand and dredged silt, b) The suspension of clogging material has a concentration of 1%.

3. Results and discussion

3.1 Density, total void ratio and water permeability coefficient

The density, total void ratio and water permeability coefficient of concretes are shown in Table 3. The results showed that with the content of PS increased, the density of PC significantly decreased while the total void ratio and water permeability coefficient increased. Generally, the typical density of PC varies from 1500 kg/m³ to 2000 kg/m³, and the porosity between 15 % and 35 %, and the water permeability coefficient ranges from 1.4 mm/s to 12.2 mm/s [8]. In this study, the density of concrete containing PS varied from 825 kg/m³ to 1568 kg/m³, which was lower than the control concrete without any PS due to the density of the PS lower than that of the NWA.

Table 3: Physical properties of concretes.

Mix	Density (kg/m ³)	Total void ratio (%)	Water permeability coefficient (mm/s)
Control	1693	26.6	7.9
PS-25	1568	28.4	9.0
PS-50	1424	31.7	9.5
PS-75	1069	35.1	10.3
PS-100	825	37.2	11.2

ACI 522 [19] recommended that the porosity of PCs was usually between 15 % and 35 %. The total void ratio of all PCs varied from 26.6% to 37.2%, and except for PS-75 and PS-100, other mixtures were within the specified range reported by ACI 522. The total void ratio of PC significantly increased with the increasing PS content. When the NWA in the PC was replaced by 100% PS, the PS-100 mix had the highest total void ratio of 37.2%, which was 39.8% higher than that of the control mix. In addition, with the increase of total void ratio, the density decreased. A good linear relationship with a good correlation coefficient ($R^2=0.96$) between total void ratio and density was presented in Figure 4.

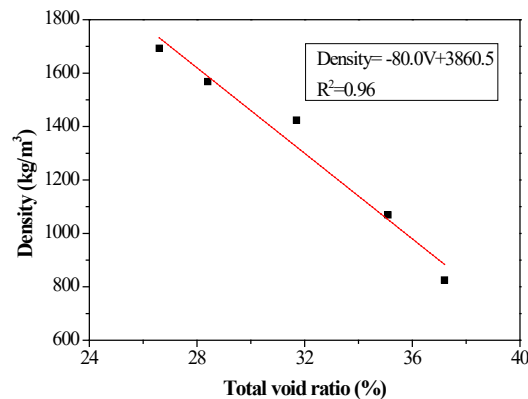


Figure 4: Relationship between total void ratio and density.

Generally, the permeability of PC depends on the connectivity of the internal pores and pore diameter [8]. The water permeability coefficient of PCs varied from 7.9 mm/s to 11.2 mm/s. The water permeability coefficient was lowest without any PS. However, when the NWA was replaced by 100% PS, the water permeability coefficient was increased by 41.8%, compared to the control concrete. The relationship between total void ratio and water permeability coefficient was shown in Figure 5. As expected, the water permeability coefficient of PCs increased as the void ratio increased.

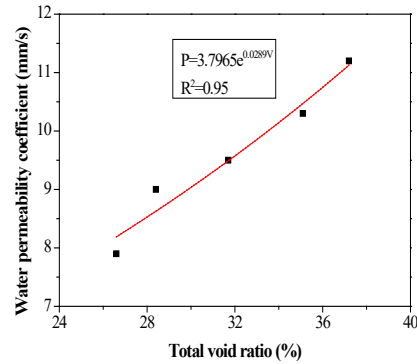


Figure 5: Relationship between total void ratio and water permeability coefficient.

3.2 Compressive and splitting tensile strength

The 28-day compressive strength of all PCs varied from 1.9 MPa to 9.2 MPa, as shown in Table 4. With the PS content increased, the compressive strength significantly decreased. When the NWA was replaced by 100 % PS, the compressive strength reduced by 79.0% compared to the control mix. Güneyisi et al. [8] reported that the strength of PC mainly depends on the bond strength between the aggregate and cement paste. The failure pattern of PC containing PS is presented in Figure 8. The cracks of PC containing PS not only propagated through the interfacial transition zone (ITZ) but also passed through the PS aggregate. The reason for the incorporation of PS to significantly reduce the strength of PCs can be attributed to the following: Firstly, PS is an organic matter, which results in the weak bond in the ITZ [4]. Secondly, the shrinkage of PS also is an important influence on the aggregate-paste binding ability [14]. Thirdly, the strength of PS is much lower than that of the NWA [15], which also contributed to the low compressive strength of PC.

Table 4: Mechanical properties of concretes.

Mix	Compressive strength (MPa)			28-day splitting tensile strength (MPa)
	7-day	14-day	28-day	
Control	5.6	7.8	9.2	1.08
PS-25	4.9	6.7	7.9	0.91
PS-50	2.6	3.8	5.1	0.73
PS-75	1.4	2.5	3.2	0.56
PS-100	1	1.3	1.9	0.28



Figure 6: Failure pattern of PC containing PS.

The relationship between total void ratio and water permeability coefficient and compressive strength are presented in Figure 7 and Figure 8, respectively. It was clear that the compressive strength decreased as the total void ratio and water permeability coefficient increased.

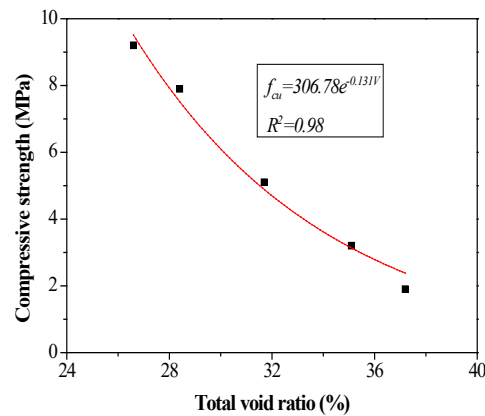


Figure 7: Relationship between total void ratio and compressive strength.

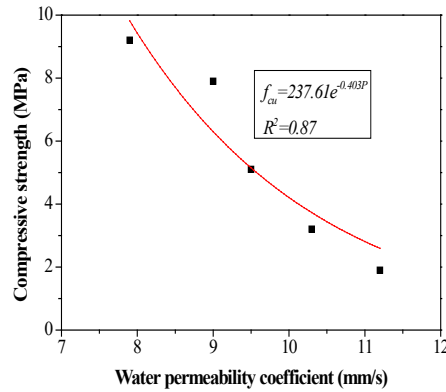


Figure 8: Relationship between water permeability coefficient and compressive strength.

The splitting tensile strength results are also presented in Table 4. The splitting tensile strength decreased as the increase in PS content. The splitting tensile strength of all PCs ranged from 0.28 MPa to 1.08 MPa. Wu et al. [15] reported that PS can be used to produce lightweight aggregate concrete by replacing 100 % NWA. However, the use of 100 % PS instead of NWA for the manufacture of PC is not feasible. When PS is used in PC, the content of PS should not exceed 25%. The relationship between compressive strength and splitting tensile strength is shown in Figure 9. The results showed that the splitting tensile strength increased as the increase of compressive strength.

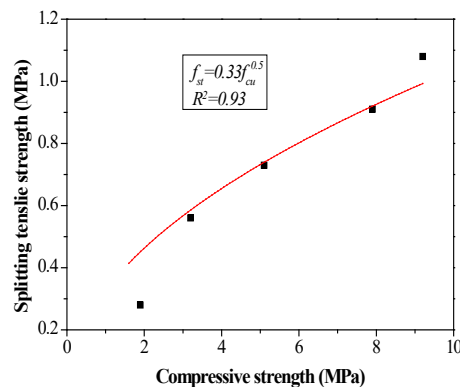


Figure 9: Relationship between compressive strength and splitting tensile strength.

3.3 Clogging test results

The relationship between clogging cycles and water permeability coefficient is shown in Figure 10. The results showed that the water permeability coefficient of PC decreased gradually after each clogging cycle due to the suspension containing clogging material was poured into the upper surface of the PC, which could penetrate into the PC and deposited on the pore wall [12]. After the fourth clogging cycle, the water permeability coefficient of the Control, PS-25, PS-50, PS-75 and PS-100 were 0.2 mm/s, 0.4 mm/s, 0.6 mm/s, 0.9 mm/s and 1.3 mm/s, respectively, which decreased by 97.5%, 95.6%, 93.7%, 91.3% and 88.4%, respectively, compared to the initial value. The results also indicated that dredged silt and sand had a significant impact on the permeability of PC, and the PC with higher porosity had better clogging resistance.

The detailed blocking process may be as follows: firstly, the sand grains entered the large pore structure inside the PC, and then the dredged silt grains filled the remaining voids and increased the blockage of the permeable pores, resulting in the water permeability coefficient decreased rapidly. Dang et al. [12] found that after the first plug cycle, the water permeability coefficient of PC containing 2-4 mm was reduced by 95% of the initial value. In this study, after the first cycle, the water permeability coefficient of the Control, PS-25, PS-50, PS-75 and PS-100 mixes decreased by 50.6 %, 46.7 %, 38.9 %, 28.2 % and 28.6 %, respectively, compared to the initial values.

This may be contributed to the PS and the NWA used in this study have a particle size of 4.75-9.6 mm, which are larger than the particle size of seashell of 2-4 mm, and consequently resulting in a higher porosity of PC. Therefore, the large-grained aggregates are more advantageous than the small-grained aggregates in resisting clogging.

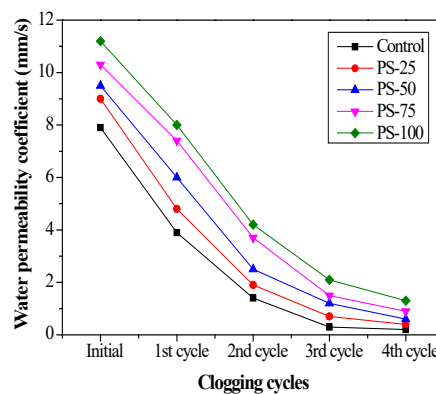


Figure 10: Relationship between clogging cycles and water permeability coefficient.

Changes in the top surface of the PS-50 mix during the clogging test are shown in Figure 11. It is clear that after the second clogging cycle, most of the suspensions containing the clogging material could not penetrate the PS-50 mix and only remained on the upper surface, resulting in the lower water permeability coefficient.

After the fourth clogging cycle, the clogging material was almost fully deposited on the surface of the PS-50 mix, and water could hardly penetrate through the PS-50 mix.

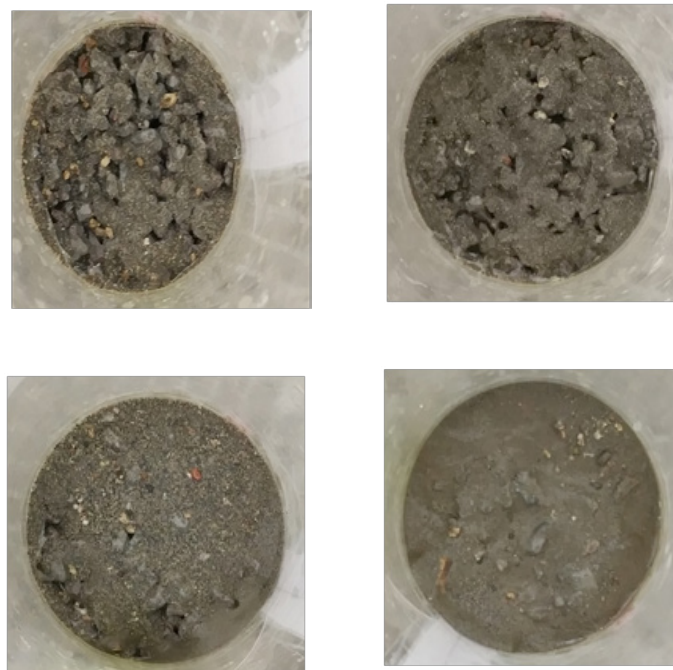


Figure 11: Changes in the top surface of the PS-50 mix during clogging test a) First cycle, b) Second cycle, c) Third cycle and d) Fourth cycle.

4. Conclusions

In this study, the peach shell (PS) was used as a substitute for the normal weight aggregate (NWA) to produce pervious concrete (PC). The physical properties (density, total void ratio and water permeability coefficient), mechanical properties (compressive and splitting tensile strength) and clogging properties of PC were investigated. The following conclusions can be drawn based on the present study:

- The replacement of the NWA with the PS reduces density, compressive strength and splitting tensile strength of PC while increasing the total void ratio and water permeability coefficient. When the NWA is replaced by 100 % PS, the density, compressive strength and splitting tensile strength decrease by 51.3 %, 79.0 % and 74.1 %, respectively. However, the total void ratio and water permeability increases by 39.8 % and 41.8 %, respectively, compared to the control mix.
- The low strength of the PS aggregate results in low mechanical properties of the PC. However, the compressive strength, splitting tensile strength and water permeability coefficient of PS-25 mix are 7.9 MPa, 0.91 MPa and 9 mm/s, respectively. Therefore, it is feasible that the use of PS to produce the PC with suitable mechanical properties by adding less than 25 % PS.
- Clogging materials made of sand and dredged silt have a significant impact on the water permeability coefficient of PC. The large-grained aggregates are more advantageous than the small-grained aggregates in resisting clogging. The water permeability coefficient of PC decreases gradually after each clogging cycle, after the fourth clogging cycle, the water permeability coefficient of the Control, PS-25, PS-50, PS-75 and PS-100 decreased by 97.5 %, 95.6 %, 93.7 %, 91.3 % and 88.4 %, respectively, compared to the initial values.

5. Acknowledgment

This work was funded by the Graduate Student's Research and Innovation Fund of Sichuan University

(Grant No. 2018YJSY091), and the Key Laboratory of Geological Hazards Mitigation for Mountainous Highway and Waterway, Chongqing Municipal Education Commission Chongqing Jiaotong University (Grant No. kfxm2018-01), the China Scholarship Council (CSC) Fund (Grant No. 201806240037) and Eindhoven University of Technology.

6. References

- [1] Huiskes, D.M.A., Keulen, A., Yu, Q.L., Brouwers, H.J.H., 2016, Design and performance evaluation of ultra-lightweight geopolymer concrete, *Materials & Design*. 89, 516-526, DOI: 10.1016/j.matdes.2015.09.167.
- [2] Sata, V., Wongsu, A., Chindaprasirt, P., 2013, Properties of pervious geopolymer concrete using recycled aggregates, *Constr. Build. Mater.* 42, 33-39, DOI: 10.1016/j.conbuildmat.2012.12.046.
- [3] Mo, K.H., Alengaram, U.J., Jumaat, M.Z., Yap, S.P., Lee, S.C., 2016, Green concrete partially comprised of farming waste residues: a review, *Journal of Cleaner Production*. 117, 122-138, DOI: 10.1016/j.jclepro.2016.01.022.
- [4] Wu, F., Liu, C.W., Zhang, L.W., Lu, Y.H., Ma, Y.J., 2018, Comparative study of carbonized peach shell and carbonized apricot shell to improve the performance of lightweight concrete, *Construction and Building Materials*. 188, 758-771, DOI: 10.1016/j.conbuildmat.2018.08.094.
- [5] Wu, F., Liu, C.W., Sun, W., Zhang, L.W., 2018, Mechanical Properties of Bio-based concrete containing blended peach shell and apricot shell waste, *Materiali in Tehnologije*. 52(5), 645-651, DOI: 10.17222/mit.2018.065.
- [6] Chindaprasirt, Prinya., Peem, Nuaklong., Yuwadee, Zaetang., Purimpat, Sujumnongtokul., and Vanchai Sata, 2015, Mechanical and thermal properties of recycling lightweight pervious concrete, *Arabian Journal for Science and Engineering*, 40(2), 443-450, DOI: 10.1007/s13369-014-1563-z.
- [7] Dang, Hanh Nguyenab., Nassim, Sebaibia., Mohamed, Boutouila., Lydia, Leleyterb., Fabienne, Baraudb, 2014, A modified method for the design of pervious concrete mix, *Constr. Build. Mater.* 73, 271-282, DOI: 10.1016/j.conbuildmat.2014.09.088.
- [8] Erhan, Güneyisi., Mehmet, Gesoğlu., Qays, Kareem., Süleyman, İpek., 2016, Effect of different substitution of natural aggregate by recycled aggregate on performance characteristics of pervious concrete, *Materials and Structures*, 49, 521-536, DOI: 10.1617/s11527-014-0517-y.
- [9] Bhutta, M.A.R., Tsuruta, K., Mirza, J., 2012, Evaluation of high-performance porous concrete properties, *Constr. Build. Mater.* 31, 67-73, DOI: 10.1016/j.conbuildmat.2011.12.024.
- [10] Shu, Xiang., Huang, Baoshan., Wu, Hao., Dong, Qiao., Burdette, Edwin G., 2011, Performance comparison of laboratory and field produced pervious concrete mixtures, *Construction and Building Materials*, 25, 3187-3192, DOI: 10.1016/j.conbuildmat.2011.03.002.
- [11] Gesoğlu, M., Güneyisi, E., Khoshnaw, G., İpek S., 2014, Investigating properties of pervious concretes containing waste tire rubbers, *Constr. Build. Mater.* 63, 206-213, DOI: 10.1016/j.conbuildmat.2014.04.046.
- [12] Dang, Hanh Nguyen., Mohamed, Boutouil., Nassim, Sebaibi., Fabienne, Baraud., Lydia, Leleyter., 2017, Durability of pervious concrete using crushed seashells, *Construction and Building Materials*, 135, 137-150, DOI: 10.1016/j.conbuildmat.2016.12.219.
- [13] Hussein, Adebayo Ibrahim., Hashim, Abdul Razak., 2016, Effect of palm oil clinker incorporation on properties of pervious concrete, *Construction and Building Materials*, 115, 70-77, DOI: 10.1016/j.

conbuildmat.2016.03.181.

[14] Wu, F., Liu, C., Sun, W., Ma, Y., & Zhang, L., 2019, Effect of peach shell as lightweight aggregate on mechanics and creep properties of concrete, *European Journal of Environmental and Civil Engineering*, 1-19, DOI: 10.1080/19648189.2018.1515667.

[15] Wu, F., Liu, C., Diao, Z., Feng, B., Sun, W., Li, X., & Zhao, S., 2018, Improvement of mechanical properties in polypropylene-and glass-fibre-reinforced peach shell lightweight concrete, *Advances in Materials Science and Engineering*, 2018, DOI: 10.1155/2018/6250941.

[16] Montes, F., Valavala, S., Haselbach, L., 2005, A new test method for porosity measurements of Portland cement pervious concrete, *Journal of ASTM International*, 2(1):13, DOI: 10.1520/JAI12931.

[17] Narayanan, N., Jason, W., Jan, O., 2006, Characterizing enhanced porosity concrete using electrical impedance to predict acoustic and hydraulic performance, *Cem Concr Res*, 36:2074-2085, DOI: 10.1016/j.cemconres.2006.09.001.

[18] Schaefer, V.R. Kevern, J.T., 2011, An Integrated Study of Pervious Concrete Mixture Design for Wearing Course Applications, National Concrete Pavement Technology Center, Iowa State University, Iowa, p. 158.

[19] A. Committee, 2010, Report on pervious concrete (ACI 522R-10), American Concrete Institute.

A concrete composite from biologically based binders and mineral aggregates for constructional 3D-printing

J. Christ¹, H. Koss¹, L.M. Ottosen¹

¹Department of Civil Engineering, Technical University of Denmark, Brovej 118, 2400 Kgs. Lyngby

Abstract

The paper presents an alternative binder for structural 3D-printing with composite materials. The binder eases the control of setting times after extrusion through thermoplastic hardening properties. The material could therefore enable the production of thin-walled geometries in large-scale 3D-printing with higher degrees of freedom in respect to overhanging geometries without supporting structures. The proposed composite material is made from mineral aggregates and biological gels, resourced from animal tissue and bone. The used mineral aggregates are not deviating significantly from conventional concrete or mortar.

So far, the research determined a maximum flexural- and compressive strength of 8 MPa and 21 MPa. Furthermore, first material compositions are introduced and respective material properties tested. As a conclusion, the paper presents limitations and potentials of the concrete for the use as structural building material and the use within large-scale 3D-printing.

Keywords: Bio-based concrete, constructional 3D-printing, biopolymers, concrete composite, mineral aggregates

1. Introduction

Additive manufacturing and 3D-printing in the construction sector is a rapidly growing field of interest in research and industry [1], [2]. Possible material savings and a higher degree of freedom in shape forming increase both, sustainability in construction and architectural expression [3]. Some of the materials used for constructional three dimensional extrusion processes are steel ([4], [5]), carbon fibre[6], or polymers ([7], [8], [9]). The main focus however lays on the printing with concrete ([1], [3], [10]), due to proven beneficial properties of cementitious materials, such as durability, inexpensiveness, fire resistance, structural strength and its plasticity during extrusion.

The current focus on cementitious concrete has its drawback regarding its sustainability account. This is due to the high amount of energy used under production, the CO₂-emissions of the chemical process during calcination of limestone and the high transport efforts due to dependency on centralised large-scale production sites. In many cases, the extruded material comprises substantially higher cementitious shares than conventionally casted concretes [11]–[13]. Additionally, extensive admixtures are being used to adapt the composite's performance as intended, enabling rapid viscosity change from liquid to solid during the printing process by thixotropic or chemical procedures. The combination of large limitations in reinforcement integration [3] and low early-age strength of concrete causes buckling and moment failures during printing, and restrain degree-of-freedom to an almost vertical build up.

The here presented research proposes an alternative concrete composite, based on biologically (bio-) based binding materials, for constructional 3D-printing. This concrete is in the following referred to as Biopolymer Concrete (BPC). The novelty of the material is the compound of biopolymers, resourced from animal tissue, bones, fish, shellfish, or algae as binding material in concrete, purposed for additive manufacturing processes. The intention is to completely replace any cementitious share in the composite with the biopolymer- and water- based binders. Sought after properties of the BPC with regards to constructional 3D-printing are rapid viscosity change due to its thermoplastic hardening. Possibly, higher material savings in comparison to cementitious concrete could be reached by enabling higher resolution prints, i.e. thin-walled and overhanging geometries, through the rapid solidification.

Different sources for the binding material are considered. As a first prove of construction-worthiness of the novel material, the research presented here is conducted with BPC samples made of bone glue, a biologically resourced gel from animal tissue and bones (meat industrial waste products). The samples were tested for compressive- and flexural strength with different binder contents in the composite material. Other properties relating to the construction process, i.e. printability of the concrete, such as hardening and drying time as well as shrinkage, density and thermoplasticity have been tested explicitly or will be discussed based on available information.

2. Methodology

2.1 Materials

The tested BPC composite material was manufactured using bone glue as bio-based binding material, and mineral aggregates. In the following, the individual components, are described and characterized.

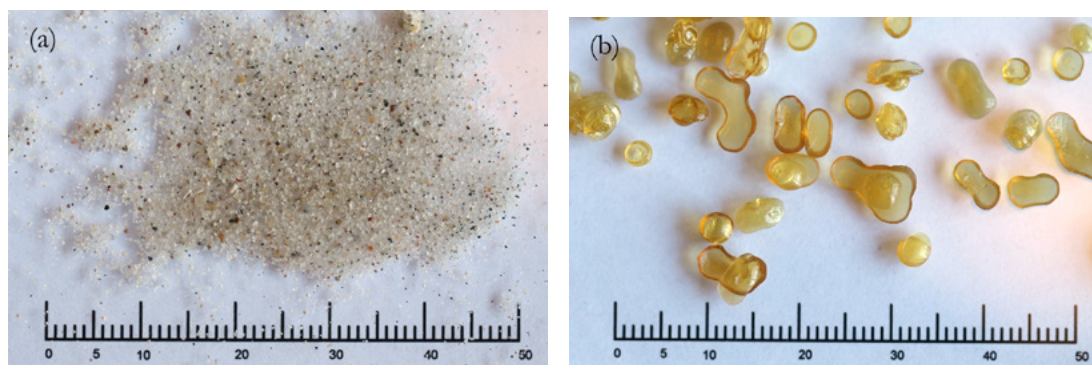


Figure 1: Raw materials used for BPC – (a) Mineral aggregates: Sand with a grain size distribution between 0-2mm, (b) biologically based binder granulate: bone glue – in [mm]

2.1.1 Mineral Aggregates

The used mineral aggregates are limited to sand with a grain size composition of 0-2mm (Figure 1 - a). The used sand is taken from the Great Belt strait in Denmark, part of the Baltic Sea. Due to the maritime origin,

The small grain size was chosen to:

reach a sufficient homogeneity of the composite material for small sample sizes

assure applicability for constructional 3D printing, for which rather small grained aggregates are used (as in [12], [13]) to enable thin extrusion processes and high resolution.

the rounded shape adds to good workability of the fresh concrete mix

2.1.2 Bio-based binding material

Bone glue is used as a biologically based binder to produce test specimen in this paper. The material is commercially available and extracted from industrial waste in food production (animal tissue and bones). It is traditionally used as adhesive for carpentry, woodwork, as well as for restoration and instrument making. Under soaking of water and the influence of heat, covalent bonds of long chained bio-polymers dissolve and a biological gel is separated from the raw biological material by Gelatinization. The adhesive is dried and sold in form of granulate (see Figure 1 – b).

The bone glue was purchased from DICTUM [14], a supplier for woodworking tools and materials. The delivered glue granulate has a grain size of 2-7mm (Figure 1 – b). Covered with water, the granulate dissolves and the gel liquefies. This process is intensified when adding heat to the solution. Both, water content and temperature in particular affect the viscosity of the gel significantly (thermoplasticity) and are hence pivotal to the workability of the composite material. The viscosity ^{decreases} significantly when increasing the binder's temperature to 70°C. The raw granulates density is $1.3 \frac{g}{cm^3}$ ¹.

2.1.3 Nomenclature

To specify the composition of the tested BPC materials, a coding indicating the different constituents by letters and numbers of mass percent is used. In this study, specific constituents are water (**W**), bone glue (**BG**) and Great Belt sea sand 0-2mm (**Z1**). Symbols for less specified groups or more general terms would be glue granulate (**GG**) or binder (**b**). This system allows to write unspecific (1) and specified (2) balanced equations describing BPC materials:

$$b1 = 44GG + 56W \quad (1)$$

$$BPC1 = 10(44BG56W)90Z1 \quad (2)$$

Equation (2) omits arithmetic operators (+) as used in equation (1). The unspecified glue granulate in equation (1) is in equation (2) replaced with the specific reference to bone glue. In this way, the notation allows defining parent types and sub groups of binders and composites. Finally, a specific sample of any BPC material is identified by a unique number at the end of the material code separated by a dot. The fifth sample made of BPC1 would bear the code:

$$BPC1.5 = 10(44BG56W)90Z1.5 \quad (3)$$

All numeric values and ratios refer to the material's weight and to compositions under mixing. The specified material proportions do not account for hardened samples, since water content decreases during drying.

2.1.4 Mixture

The tested compositions consist of bone glue, water and mineral aggregates. The specifications of the different BPC materials are listed in Table 1. In all cases, a W/GG-ratio of 1.25 has been chosen due to benefits in the workability of the heated mass. This was found during preliminary experiments. Material coding is according to Section 2.1.3.

2.2 Methods

The used methods for mixing, moulding and testing are largely inspired by the standardised procedures for cementitious mortar and concrete as described in EN 196-1 [15]. However, due to thermoplastic properties of the binding material, some adaptations were made. The steps in sample production, testing and property

¹ Characterised by weight and volumetric analysis with water bath. A weight scale with an accuracy of 0.01g was used, as well as a single graduated 100ml cylinder to measure the volumetric increase of 50ml of water by adding 20g of binder granulate.

characterisation are in the following described in more detail.

2.2.1 Composite production

The production of the concrete composite, including the process for moulding and drying is compiled in Table 2, with approximate durations of the individual steps.

Table 1: Overview of the used material compositions.

#	Sample	Binder-content	Glue granulate-content	Water-content	Aggregate-content
[-]	[-]	[wt.%]	[wt.%]	[wt.%]	[wt.%]
BPC1	10(44BG56W)90Z	10	4.44	5.56	90
BPC2	15(44BG56W)85Z	15	6.67	8.33	85
BPC3	20(44BG56W)80Z	20	8.89	11.11	80
BPC4	25(44BG56W)75Z	25	11.11	13.89	75

Table 2: In-sum process specifications for the production of bio-based concrete composite samples.

Process #	Process specification	Duration	Notes
1	Soaking of GG in W	>1h	Soaking of glue granulate in water
2	Heating	~1h	Heating of Z and b in oven to 70°C
3	Mixing	2min	Mixing in mortar blender, standardised in EN196-1 [15]
4	Moulding	3min	Moulded on vibration table until solidity is reached
5	Thermoplastic hardening	1 day	1 day left in mould - actual thermoplastic hardening time substantially lower - dependant on geometry, ambient temperature, etc.
6	Demoulding		Demoulding 1day after casting
7	Dry-hardening A	1 day	Dry hardening under room temperature
8	Dry-hardening B	4-48 days	Dry hardening in well ventilated oven at 50°C

1. Soaking of GG in W: Soaking the glue granulate in water for >1 hour, until a homogenous concentration of gel in the GG-W mix could be reached. The granulate increases its volume in reaction with water. The viscosity in this step depends on both, amount of added water and soaking time, and can range from solid to liquid. Frequently, the mix has been stirred with a glass spatula.
2. Heating of constituents: The viscosity of the GG-W mix can be decreased by heating (thermoplasticity). The water addition can be thereby decreased due to temperature control. To avoid sudden cooling and undesired hardening during the mixing process of the binder, aggregates are heated as well. Both materials are heated to 70°C to ensure the plasticity of the mix. Higher temperatures were avoided to prevent damage of the molecular structure.

Mixing of constituents: The heated constituents are mixed with a mortar blender for conventional cementitious material (Mixer specification: Seger – Tonindurtie), standardised in EN196-1 [15]. The mixing vessel is prior tempered to 70°C to prevent premature cooling of the mass. A homogenous material mix could be assumed after 2 minutes of mixing. The mixing and moulding was conducted at room temperature, giving a time limitation for the mixing. Due to cooling, the mass becomes unworkable after a short time (about 5-10min).

Moulding: The composite material is poured into moulds. This is done in a rather rapid fashion to prevent the material from premature stiffening. The moulds were filled on a vibration table to prevent large cavities and larger inhomogeneity inside the sample. The vibration was conducted with 60-80Hz until the material

increased in viscosity (approx. 3min). Prism moulds with dimensions of 40x40x160mm (width/height/length) after EN 196-1 [15], as well as cylinders with a measurement of 50x100mm (diameter/height) were used. Metal surfaces of the moulds needed to be covered with a thin PE-foil to prevent the corrosion caused by the acidic nature of the bio-binder.

1. Thermoplastic hardening: Thermoplastic hardening occurs directly after the binding material is removed from a heat source and placed in a cooler ambient temperature. The material's viscosity increases noticeably throughout mixing and moulding process.
2. Demoulding of the samples was conducted one day after moulding, to support the integrity of the sample by reaching additional strength through the outset of the dry hardening process.
3. Dry hardening: Even if the material shows stiffness after the thermoplastic hardening process, the material still contains water which prevents the biopolymers to form stronger bonds. After all water is evaporated, the material is considered as hardened. The duration of this process is dependent on water content, dimension of the sample, aggregate content and porosity. To accelerate the process for testing, samples were, after one day drying under room temperature, placed in a well ventilated oven (Oven specification: Memmert UF 160) at 50°C. For most samples, an oven drying time of 21 days was chosen.

2.2.2 Structural testing of cylindrical samples

A total of 12 cylindrical samples, 50mm diameter and 100mm height, were casted to determine compressive strengths. For loading tests, an 'Instron-6025' with a capacity of 100kN was used to load the samples, as well as for recording of force and displacement. Circular platens with a diameter of 50mm were used to slender the apparatus' loading surface down to the geometry of the material cylinders. Force was applied with a loading rate of 2400 N/s.

The moulding and drying of the samples left the top and bottom surfaces of the cylinders uneven. The samples were cut with a circular saw to a length of ~90mm before testing and after drying. The sawing was conducted slowly and without any water-cooling of the blade to prevent the material from weakening by water soaking.

2.2.3 Structural testing of prism samples

Prism samples with the size of 40x40x160mm were tested for flexural- and compressive strength according to EN196-1 [15].

For flexural strength, the prism samples were tested in a three-point bending test as standardized with a distance of the supporting rollers of 100mm and a loading rate of 50N/s on an 'Instron-6022' with a loading capacity of 10kN. The specimen was mounted with the from the moulding created even surfaces in contact with the flexure device.

The compressive strength was measured for each of the two fragments obtained from the segmentation when measuring the flexural strength. Above and below, the specimen was loaded on a surface of 40x40mm. The orientation of the samples for compressive strength was in accordance to the flexural tests, described above. Loading was applied at a rate of 2400N/s with an 'Instron-6025' testing machine with a loading capacity of 100kN.

2.2.4 Density-measurements of the composite

Calculated as ratio of individually measured mass (accuracy 0.01g) and volume (accuracy 0.01mm).

2.2.5 Shrinkage

Shrinkages of prism samples were determined by evaluating the differences in length before and after dry hardening, i.e. immediately after demoulding and before testing. Therefore, shrinkage information relates only to the dry-hardening process during this time and not to thermoplastic-hardening.

2.2.6 Dry-hardening times

The binding material develops strength over the thermoplastic- and the dry-hardening period. The duration of the thermoplastic hardening was short and easy controllable by temperature. The duration of the dry-hardening depends on geometry, porosity, ambient temperature and binder or water contents. A total of 12 cylindrical samples of BPC3 have been tested in compression (see Section 2.2.1 and 2.2.2) to evaluate the rapidity of the drying process. The sample production was conducted as indicated in Table 2. The duration of step 8 was varied. Three samples have been tested, respectively after 4, 12, 22 and 48 days of oven drying at 50°C. To keep samples comparable, the W/GG and b-content has not been varied and kept on 1.25 and 20%.

3. Results and discussion

3.1 Results

Examples of BPC are seen in Figure 2.

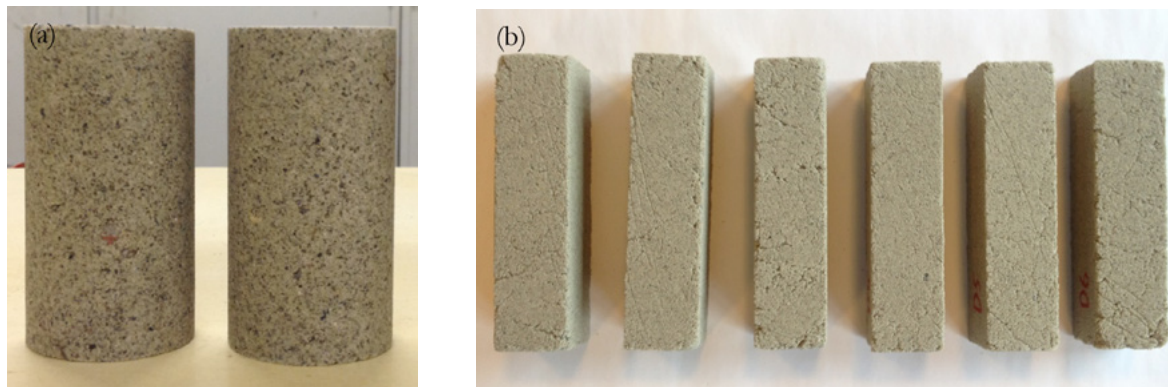


Figure 2: Biopolymer Concrete (BPC) Samples: (a) circular cylinders 100mm high and 50mm in diameter, (b) square prism samples with a length of 160mm and a cross-section of 40x40mm.

3.1.1 Property variations under hardening

The two hardening characteristics, thermoplastic- and dry-hardening, are key-influencer on the materials strength and viscosity. The thermoplastic hardening time already occurs after several minutes after discontinuity of heat exposure, the material's viscosity increases and the composite gains integrity. Due to the obvious relation of the material's temperature to its fluidity, the rapidity of the process is thought to be connected with the composite's geometry, heat capacity, water content, initial- and ambient temperature. The observations of this process proposes therefore, its simple controllability. The subsequent dry hardening can be described as the water loss through evaporation and extends, dependant on the water content, over a longer period of time.

Figure 3 shows the dependency of the compressive strengths on this dry-hardening duration. Illustrated results display that the material strength is increasing for an increase of dry-hardening time, suggesting that the strength of the material is strongly dependant on its water content. Hence, a high water content implies low strength and an advanced drying process a higher strength. The four data points were tested with a respective sample quantity of three, namely samples BPC3.1-12 (Figure 2 – a). The mean of each tested

point in time has been connected by a smoothened line. A substantial increase of compressive strength was observed (until 22 days), where after the graph flattens. The flattening starts between 12 days and 22 days, an exact point in time, however, could not be determined. For the values around the flattening, the graph shows larger variabilities. Contrary, minor variations were observed for short and extensive dry-hardening durations. A bend in the smoothened curve of Figure 3 denotes a characteristic change of drying rapidity.

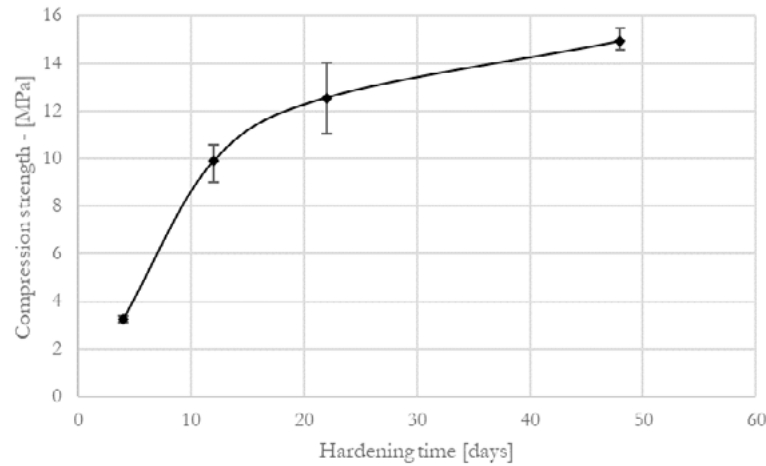


Figure 3: Compressive strength of cylindrical samples BPC3.1-12. over dry hardening times at 50°C (corresponding to step 8 in Table 2). The error bars show maximum and minimum values. The connecting line has been smoothened.

The drying characteristics are expected to be geometry dependent, as well as reliant on initial water content, ambient temperature and humidity. Other than the thermoplastic hardening, dry hardening is expected to not conclude, but rather to approximate asymptotically to an upper bound, which is dependent on the ambient humidity. Therefore, varying water contents through differing binder to aggregate compositions, possibly show divergent hardening times. This, however is up to date not experimentally verified.

3.1.2 Density

Characterizing density and shrinkage is useful to evaluate the material on its suitability for constructional 3D printing by limiting self-weight and shrinkage cracking. For sample batches BPC1, BPC2, BPC3, and BPC4 (cf. Table 1); volume, weight and length have been measured before testing and after drying. Respectively calculated density values can be seen in Figure 4. The mean values range from 1.6g/cm³ to 1.4g/cm³ for varying binder contents. Densities generally decrease with a decrease in aggregate shares in the mix.

The material's density is scattered around a value of about 1.5 g/cm³. The composite is therefore lighter than cementitious mortar, which is here assumed with the typical value of 2.2 g/cm³. The mixing ratios influences the material's density only marginally for a binder content of 10%-20% (BPC1, BPC2, BPC3). A content of 25%, however, causes a large density loss of 10%. Due to the comparably high density of the used sand (2.6 g/cm³), low density binder (1.3 g/cm³), and the continuous change of mixing ratios (10%, 15%, 20%, 25% binder content) throughout the tests, a linear decrease of density could have been expected. Contrary, the non-linear appearing measurements of Figure 4 let suppose, that the pore content for samples with a binder content of over 20% increases substantially, i.e. its density decreases.

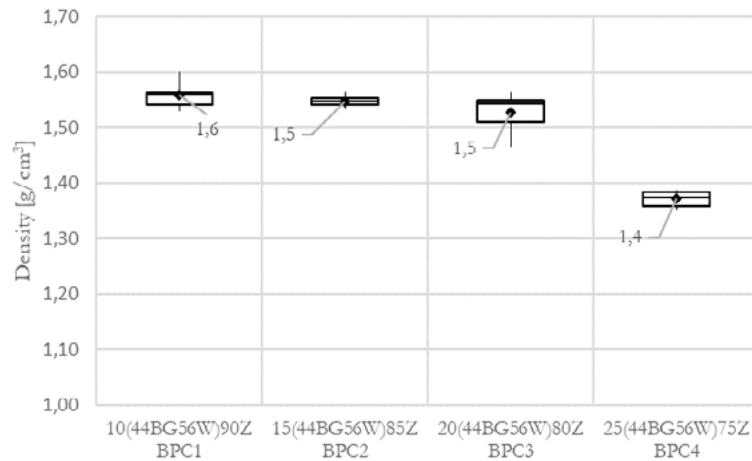


Figure 4: Density of sample batches with varying binder contents. Whiskers show maximum and minimum value of the data set; boxes define upper, middle and lower quartile; the marker shows mean values. Each boxplot is substantiated with a data point quantity of six measurements.

3.1.3 Shrinkage

The densities tendency is reversely reflected by shrinkage ratios in Figure 5. The continuous increase of the data set ranges from 0.3% to 2% and increases for higher binder contents. Therefore, shrinkage appears to be directly interlinked to the materials composition, or rather to the binder's water content. The results suggest that the evaporation of water causes the material to shrink.

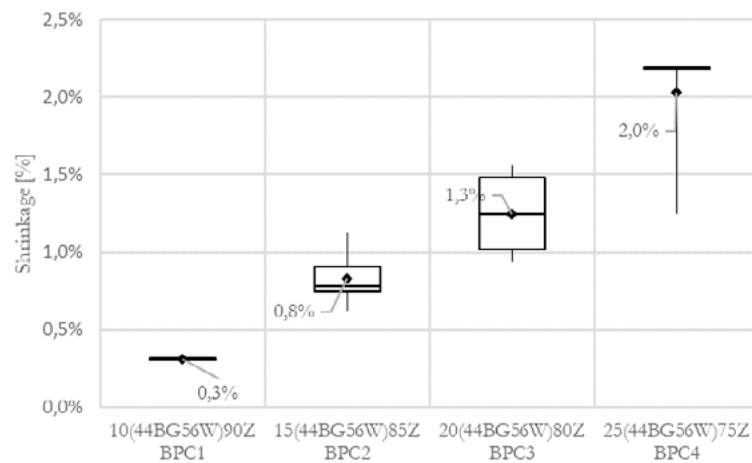


Figure 5: Shrinkage of sample batches with varying binder contents. Whiskers show maximum and minimum value of the data set; boxes define upper, middle and lower quartile; the markers show mean values. Each boxplot is substantiated with a data point quantity of six measurements.

3.1.4 Strength of BPC

The composite's properties are expected to be strongly dependant on the material's composition. Therefore, the dependencies on varying binder-contents were measured to determine performance peaks of flexural and compressive strength. Six prisms (Figure 2-b) for each composition were casted with a binder content of 10%, 15%, 20% and 25% (BPC1-4) and a W/GG-ratio by weight of 1.25. Corresponding mixtures can be found in Table 1, a dry-hardening duration of 21 days was chosen for all samples. Figure 6 and 7 show the obtained results for flexural and compressive strengths.

Flexural strength: As shown in Figure 6, batch BPC2 had the highest flexural strength, i.e. the batch with a binder content of 15%. When lowering the binder content to 10% (Batch BPC1), the flexural strength

was more than halved. Increasing the binder content to 20% and 25%, i.e. BPC3 and BPC4, resulted in a decreased flexural strength, though not as significant as for the prisms with 10% binder.

Compressive Strength: The compressive strength for the prisms are shown in Figure 7. A tendency to a maximum mean compressive strength of batch BPC3 can be identified as a peak performance value. However, the upper error bar for batch BPC3 has a relatively large magnitude and is decisive for an increased mean value, being higher than middle and upper quartile. Therefore, a difference between batch BPC2 and BPC3 can not be concluded. A major drop in strength is located between BPC3 and BPC4.

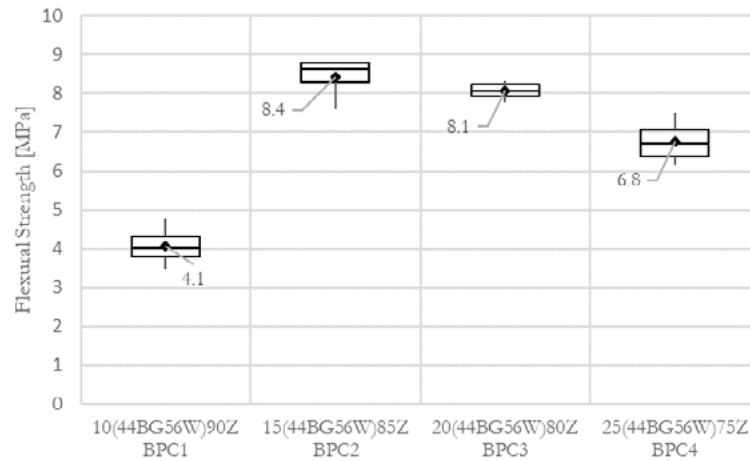


Figure 6: Flexural strength of prism samples with varying binder contents. Whiskers show maximum and minimum value of the data set; boxes define upper, middle and lower quartile; the marker shows mean values.

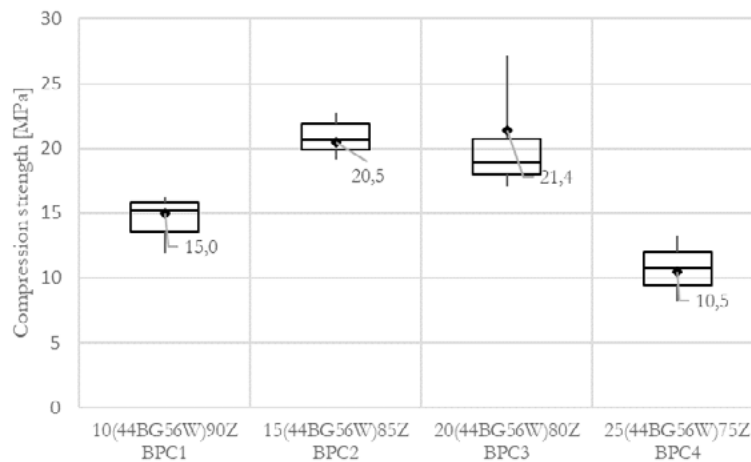


Figure 7: Compressive strength testing of prism samples with varying binder contents. Whiskers show maximum and minimum value of the data set; boxes define upper, middle and lower quartile; markers show mean values.

Both, flexural and compressive strength suggest a performance peak between 15% and 20% binder content. The peaking of strength in this range, and the subsequent decrease for higher binder contents can potentially be explained with: 1) an increase of porosity due to the higher binder content and therefore decrease in density and strength (see Figure 4), or 2) an incomplete or not comparable dry-hardening process between varying binder contents as described in Section 3.1.1.

Even though in similar range, flexural- and compressive strength propose diverging mean performance peaks in the margin of 15%-20%. The boxplots however do show similar order for both stresses in Figure 6 and 7. The correlation of mean flexural- and compressive strength was therefore evaluated to determine

the consequences of an increase of binder content in the mixture. The results are shown in Figure 8. It appears that the two properties react differently on the composition change. A consistent ratio in strength could therefore be excluded. A general observed trend is that higher binder contents cause an increase in relative flexural strength. Contrary, low binder contents lay the performance's focus on the compressive strength. The maximum ratio in Figure 8 has a magnitude of 65% for a binder content of 25% (BPC4). The indicated performance peaks for BPC2 and BPC3 show a strength ratio of around 40%. In all cases, the ratio of flexural- to compressive strength surpasses the performance of conventional cementitious concrete, which is around 10%, as a rule of thumb.

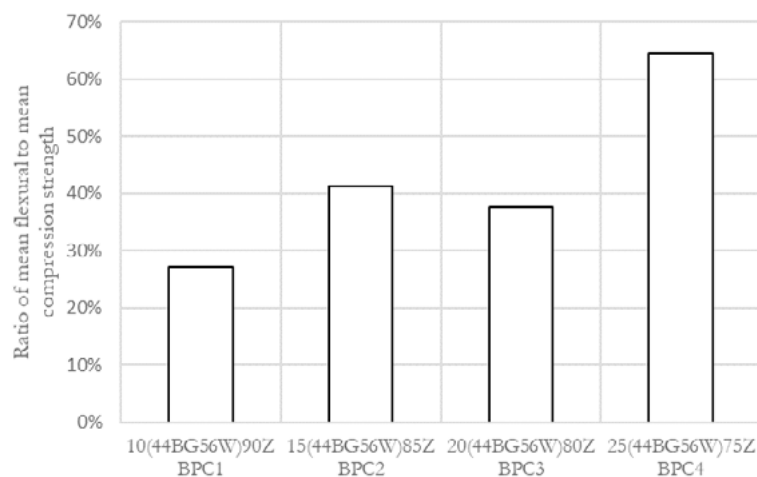


Figure 8: Ratio of flexural strength to compressive strength for varying binder contents. Mean values of measured strengths as in Figure 6 and 7 were used.

3.2 Discussion

The BPC's properties were tested to assess the materials suitability for constructional 3D-printing. In the following, the results are brought into context, i.e. 'suitable'- and 'to be further advanced' properties are listed and compared.

Suitable properties of BPC for constructional 3D-printing:

Printability of BPC: Primary advantage of BPC for constructional 3D-printing is the easy controllable thermoplastic hardening and thickening of the material. The in Section 2.2 and 3.1.1 discussed thermoplasticity shows, that the material increases rapidly in viscosity only by the exposure to room temperature. During an envisaged printing process, the material itself would therefore not only rely on the thixotropic build-up of the composite material, as for 3D-printing with cementitious concrete [16]. By the ability of controlling the thermoplasticity to a high degree, and increasing the early age strength of the matrix, the thinness of layers could be increased and potential early age moment failure of the built up prevented. More slender constructions and higher degree of freedom in terms of overhanging prints, could possibly be realised. This is also supported by the material's low density and high relative flexural strength, as described in Section 3.1.4, which can increase the early age moment resistance and lower the dead load added to the system under construction.

Composite strength: As proposed in Section 3.1.4, BPC shows generally a strength in the order of magnitude of cementitious concrete, though not comparable with high performance printing concretes [12]. One of the biggest challenges of constructional 3D-printing is the integration of reinforcement [3]. The printing process prevents the placing of extensive steel reinforcement and limits the freedom of shape

for cementitious concrete substantially due to the lack of flexural strength in cementitious materials. With a high ratio of flexural- to compressive strength of BPC, as described in Section 3.1.4, the BPC material could deliver a filament that could render building components loaded in flexure and thereby diminish the need for reinforcement.

Structural integrity of prints: Assuming a layer-by-layer 3D-printing process for the constructional use of the material, the integrity of the meso-scale structure is at risk by possibly exceeded shrinkage limits or detachment of layers through lacking interface adhesion [17]. Shrinkage, as evaluated in Section 3.1.3, can be controlled by editing the binder content. Possibly, fibre reinforcement could be added to limit shrinkage cracking. The found shrinkage ratios of 0.3% to 2% is therefore evaluated as suitable for constructional 3D-printing. The bone glue has furthermore been traditionally used for carpentry constructions and instrument making and adheres well to itself. It is therefore expected, that the contact surface of a printed layer bonds well to precedent layers. This, however needs to be experimentally verified in further work.

- *Sustainability:* The substitution of high cement contents and extensive admixtures in constructional 3D-printing filaments with biologically based binders such as bone glue could have a positive impact on the sustainability account of the method. This is due to lower production temperatures of bone glue in comparison to cement, and avoidance of CO₂-emissions under the calcination of limestone.

BPC properties, crucial to be further advanced:

- *Durability:* BPC has, due to its organic compounds and hygroscopic behaviour, a high risk of fast deterioration. During the testing, some of the samples, especially for binder contents over 20%, showed moulding attack.
- *Fire resistance:* The thermoplastic properties of the material are expected to be beneficial for the 3D-printing process but disadvantageous for its fire-resistance. The fireproofing of the material is crucial for further development.
- *Hygroscopic properties:* As described in Section 3.1.1, the water content is decisive for the structural strength of the material. Removing the water contents, hardens the material. The process can also be reversed, i.e. exposure of the hardened material to water softens its strength, which is critical for the use as structural material.

An overview of the above described can be found in Table 4.

Table 4: In sum – advantageous properties in comparison to ongoing advancements

Properties of BPC, suitable for constructional 3D-printing	Properties of BPC, crucial to be advanced
Thermoplasticity	Durability
Flexural- /compressive strength	Fire resistance
Low density	Water resistance
Self-adhesion	
Shrinkage	

4. Conclusions

A composite of a biopolymer binding material (bone glue – a bio-gel produced from the meat industry's waste) in conjunction with mineral aggregates was evaluated on its suitability as a filament for constructional 3D-printing of concrete. The findings show structural strengths in the order of magnitude of conventional concrete, i.e. flexural strength of 8 MPa and compressive strength of 21 MPa, and suggest therefore the

composite's usability as a structural building material. A density of around 1.5 g/cm³, easy controllable thermoplastic hardening characteristics, and a high moment resistance through high flexural- to compressive strength ratios of up to 65%, propose furthermore the benefit for additive manufacturing processes. Low induced dead loads, early-age material strength and high moment resistance, could diminish the need for reinforcement integration of 3D-printed structures, and enable higher degrees of freedom in terms of overhanging and thin geometries. The results suggest the suitability of bone glue as a binding material for concrete and the use in constructional 3D printing, linked with further research and development work for the composite's durability, fire- and water resistance.

5. Acknowledgment

The presented research work in this paper has been financed by Ingeniør Kaptajn Aage Nielsens Familiefond, grant (00023307) from VILLUM FONDEN (VILLUM Experiment), and DTU's Department for Civil Engineering. We thank our lab-personnel for technical advice and assistance.

6. References

- [1] Y. W. D. Tay, B. Panda, S. C. Paul, N. A. Noor Mohamed, M. J. Tan, and K. F. Leong, "3D printing trends in building and construction industry: a review," *Virtual Phys. Prototyp.*, vol. 12, no. 3, pp. 261–276, 2017.
- [2] N. Labonnote, A. Rönquist, B. Manum, and P. Rüther, "Additive construction: State-of-the-art, challenges and opportunities," *Autom. Constr.*, vol. 72, pp. 347–366, 2016.
- [3] F. Bos, R. Wolfs, Z. Ahmed, and T. Salet, "Additive manufacturing of concrete in construction: potentials and challenges of 3D concrete printing," *Virtual Phys. Prototyp.*, vol. 11, no. 3, pp. 209–225, 2016.
- [4] S. Ren and S. Galjaard, "Topology Optimisation for Steel Structural Design with Additive Manufacturing Shibo," in *Modelling Behavior*, 2015, pp. 35–36.
- [5] "MX3D Bridge." [Online]. Available: <https://mx3d.com/projects/bridge-2/>. [Accessed: 26-Apr-2019].
- [6] A. Menges, "BUGA Fibre Pavilion 2019 | Institute for Computational Design and Construction," 2018. [Online]. Available: <https://icd.uni-stuttgart.de/?p=22271>. [Accessed: 26-Apr-2019].
- [7] S. J. Keating, J. C. Leland, L. Cai, and N. Oxman, "Toward site-specific and self-sufficient robotic fabrication on architectural scales," *Sci. Robot.*, vol. 2, no. 5, 2017.
- [8] G. Pasquarelli, W. Sharples, C. Sharples, and R. Caillouet, "Additive Manufacturing Revolutionizes Lightweight Gridshells," 2017.
- [9] L. Mogas-Soldevila and N. Oxman, "Water-based engineering & fabrication: Large-scale additive manufacturing of biomaterials," *Mater. Res. Soc. Symp. Proc.*, vol. 1800, pp. 46–53, 2015.
- [10] I. Perkins and M. Skitmore, "Three-dimensional printing in the construction industry: A review," *Int. J. Constr. Manag.*, vol. 15, no. 1, pp. 1–9, 2015.
- [11] D. Marchon, S. Kawashima, H. Bessaies-Bey, S. Mantellato, and S. Ng, "Hydration and rheology control of concrete for digital fabrication: Potential admixtures and cement chemistry," *Cem. Concr. Res.*, vol. 112, no. December 2017, pp. 96–110, 2018.
- [12] T. T. Le, S. A. Austin, S. Lim, R. A. Buswell, A. G. F. Gibb, and T. Thorpe, "Mix design and fresh properties for high-performance printing concrete," *Mater. Struct. Constr.*, vol. 45, no. 8, pp. 1221–1232,

2012.

[13] Y. Zhang, Y. Zhang, W. She, L. Yang, G. Liu, and Y. Yang, “Rheological and harden properties of the high-thixotropy 3D printing concrete,” *Constr. Build. Mater.*, vol. 201, pp. 278–285, 2019.

[14] “More than Tools | Dictum.” [Online]. Available: <https://www.dictum.com/en/>. [Accessed: 23-Apr-2019].

[15] DS/En 196-1, “Metoder til prøvning af cement – Del 1: Styrkebestemmelse Methods of testing cement – Part 1: Determination of strength,” 2016.

[16] R. J. M. Wolfs, F. P. Bos, and T. A. M. Salet, “Early age mechanical behaviour of 3D printed concrete: Numerical modelling and experimental testing,” *Cem. Concr. Res.*, vol. 106, no. May 2017, pp. 103–116, 2018.

[17] Y. W. D. Tay, G. H. A. Ting, Y. Qian, B. Panda, L. He, and M. J. Tan, “Time gap effect on bond strength of 3D-printed concrete,” *Virtual Phys. Prototyp.*, vol. 14, no. 1, pp. 104–113, 2019.

A silica aerogel synthesized from olivine and its application as a photocatalytic support

Y.X. Chen ^{1,2}, Y. Hendrix ¹, K. Schollbach¹, H.J.H Brouwers ^{1,2}

¹Department of the Built Environment, Eindhoven University of Technology

P.O. Box 513, 5600 MB Eindhoven, The Netherlands

²State Key Laboratory of Silicate Materials for Architectures, Wuhan University of Technology, Wuhan 430070, PR China

Abstract:

Air purification is an important topic for public health and one of the solutions is to apply photocatalysis. It has been shown that the photocatalytic activity increases when the photocatalyst is supported on a silica network with a large surface area like silica aerogels. Silica aerogels are an ultralight and porous inorganic material consisting of 90~99% air voids inside a porous silica network structure. The inter-connected pore structure and the pore size are advantageous for the silica aerogel to function as a catalyst support or absorbent. However, silica aerogel is currently mainly produced with organic silica precursors and via supercritical drying, which is an energy intensive production route. Therefore, it is of interest to lower the production cost and reduce the energy input to produce silica aerogel with a lower CO₂ footprint. In this study, silica aerogel was first synthesized from olivine via ambient pressure drying and was applied as a support to load photocatalytic anatase crystals. The aerogel production steps include sol-gel synthesis, ion-exchange, surface modification and ambient pressure drying. The produced silica aerogel obtained a high specific surface area (694 m²/g) and pore volume (2.99 cm³/g), with a uniform pore size distribution and mesoporous structure. Titania was loaded onto the prepared silica aerogel through the precipitation method. Titanium (IV) isopropoxide was used to slowly form titania in a dispersion with the silica aerogel. This method was used to precipitate titania inside the mesopores of the silica aerogel to obtain a great spread of the titania around and inside the aerogel for a high photocatalytic activity. The resulting samples were tested by measuring their conversion efficiency to oxidize nitric oxide under UV-light irradiation, nitrogen physisorption and FTIR. The prepared silica aerogel with titania crystals showed a photocatalytic activity of 99.6%, showing to be a promising photocatalysts for air purification.

Keywords: Silica aerogel, Titanium oxide, Photocatalytic support, NO oxidation

1. Introduction

Silica aerogel is an ultra-light inorganic material that contain above 90% porosity filled with air. Silica aerogel obtain ultra-low density (0.03-0.2 g/cm³), high specific surface area (500-900 m²/g) and ultra-high porosity (90-99%). Due to these properties of aerogel, many researchers have synthesized different kinds of silica aerogels and applied them as thermal insulation materials [1, 2], catalytic supports [3, 4], absorbent of pollutants [5] and drug carrier materials [6]. However, the industrial silica aerogels are mostly produced from organic silica sources like tetrathoxysilane (TEOS) and methyltrimethoxysilane (MTMS), through supercritical drying [7]. These processes are energy intensive and obtain a high carbon footprint

[8]. Therefore, a sustainable and low energy consumption method to produce silica aerogel would be a more desirable way to produce silica aerogel.

In the last few years, researchers developed several methods to produce silica aerogel from alternative silica sources, like kaolin [9] and fly ash [10]. However, all these methods include a calcination process that can increase the carbon footprint and energy consumption. Recently a novel nano-silica was produced from olivine at low temperatures (50-90 °C) [11, 12]. Olivine silica is produced by the dissolution of olivine in acid and shows advantages in terms of lower CO₂ footprint, energy consumption and costs [13]. In this research, olivine silica is prepared at 50 °C and obtains a silica purity higher than 99% with SSA_{BET} between 100 to 400 m²/g, indicating a fast reaction with sodium hydroxide solution and a pure water glass formation. Thus, olivine silica has great potential to be a sustainable silica source in the production of silica aerogel while the total energy consumption is lower. In terms of drying procedure, ambient pressure drying was applied in this study due to the lower pressure and temperature that used compared to supercritical drying [7]. This drying method includes a surface modification process that transforms the surface –OH group on silica gel surface to –CH₃ group with TMCS and heptane as an agent. Therefore, with a ‘spring back’ effect the silica gel can re-expand the volume under ambient pressure drying and lower the density and increase the porosity of the final silica aerogel.

Due to the large pore volume and porosity of silica aerogel, it is promising to apply silica aerogel as a catalyst support to load a catalyst like photocatalytic titania. The crystal size of well-prepared anatase crystals can be smaller than the majority of the pore sizes in the silica aerogel (10~20 nm) [14]. Therefore, it is possible to apply the aerogel as a catalyst support to make a great spread of the titania on and inside the aerogel for a high photocatalytic activity. Therefore, in this research, silica aerogel was first synthesized from olivine via ambient pressure drying. Then the as-prepared silica aerogel was applied as a photocatalytic support to load titania and the photocatalytic efficiency was measured. Furthermore Fourier-transform infrared spectroscopy (FTIR) and nitrogen physisorption were used to analyze the microstructure of the resulting silica aerogel-TiO₂ composite.

2. Methodology

2.1 Materials

Olivine used in this research was from Norway supplied by Eurogrit (GL70). Table 1 lists the oxides composition of GL70 measured by X-ray fluorescence (XRF). The loss on ignition and the olivine content are also shown in Table 1.

Table 1: Composition of GL-70 from Norway and olivine silica

Composition	MgO	Fe ₂ O ₃	SiO ₂	Cr ₂ O ₃	Al ₂ O ₃	NiO	MnO	CaO	LOI*	Olivine
GL-70	49.3	7.32	41.4	0.31	0.46	0.32	0.09	0.15	0.59	88.9
Olivine nano-silica	0.03	0.02	99.8	-	-	-	-	0.03	-	-

*Loss on ignition

-Not detected

Sodium hydroxide pellets (NaOH, VWR), Ethanol absolute (CH₃CH₂OH, 100%, VWR), n-Heptane (C₇H₁₆, Analytic grade, Biosolve), Ammonia solution (NH₃·H₂O, 5N, Sigma-Aldrich), Trimethylchlorosilane (C₃H₉SiCl, □ 99%, Sigma-Aldrich) and Amberlyst 15 hydrogen form (Strongly acidic cation exchange resin, Sigma-Aldrich) were used to prepare silica aerogel from olivine GL-70. Olivine silica was prepared

according to our previous research [15] and its chemical composition is shown in Table 1. Titanium (IV) isopropoxide 97% (Sigma-Aldrich) was used as the precursor to produce the titania monomer. Commercial titania P25 was used as a reference to compare the performance of titania-aerogel composite sample.

2.2 Methods

2.2.1 Preparation of silica aerogel

The primary procedures for the preparation of silica aerogel via ambient pressure drying include network strengthening, solvent exchange and surface modification. For the solvent exchange, different kinds of alcohols and alkanes with low surface tension are believed to be the best options. The surface tension of the pore liquid can be reduced through stepwise solvent exchange and hence prevent capillary pressure from damaging the network of silica aerogel during ambient pressure drying. For the surface modification, the hydroxyl groups of the aerogel can be replaced by non-polar silyl groups through the use of trimethylchlorosilane (TMCS) and n-heptane as solvent. When drying a hydrophobic gel, the skeleton of the silica network is barely influenced by the surface tension of water, thus avoiding the collapse of the pores of the aerogel. Furthermore, the ‘spring back’ effect further lowers the density of the silica aerogel due to inert $-\text{CH}_3$ groups attaching on the surface of the gel. During the full evaporation of the pore liquid, the aerogel can bounce back and increase the volume of the aerogel. The schematic process of the projected silica aerogel production is presented in Fig. 1.

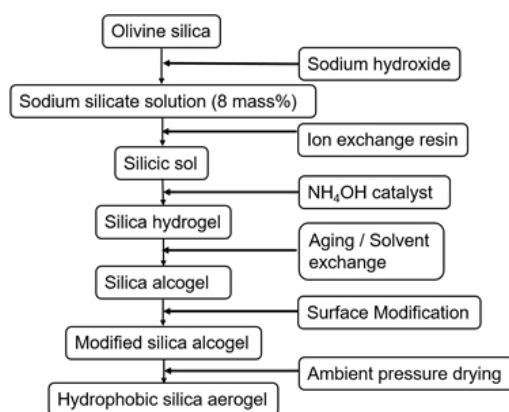


Figure 1: Schematic process of silica aerogel production from olivine silica

2.2.2 Preparation of titania-silica aerogel composite

The silica aerogel was first dried at 500 °C overnight to remove the $-\text{CH}_3$ groups on the surface of silica. Subsequently, 1 g of silica aerogel was weighed and then milled with a mortar. Then silica aerogel was dispersed in a 500 ml ethanol absolute solution and the pH was adjusted to 3~4 by adding small amounts of sulfuric acid. The molar ratio of titania and silica aerogel was kept at 1:1, which was determined according to our previous study to be a proper amount. Afterwards, 4.16 g TP (Titanium isopropoxide) was added into the solution quickly to avoid any contact with moist air. Then water was slowly added during 12 hours until the water content of the dispersion medium reached 2.5 vol%. After the synthesis of the composite, the resulting sample was filtered and washed 4 times with distilled water. Lastly, the sample was dried overnight at 105 °C and then calcined at 300 °C for 3 hours.

2.2.3 Characterization methods

The resulting photocatalytic properties of silica aerogel-titania composites were evaluated by testing their photocatalytic conversion of NO under UV-light using the ISO 22197-1 standard for comparative purpose. The setup for these measurements is shown in Fig. 2.

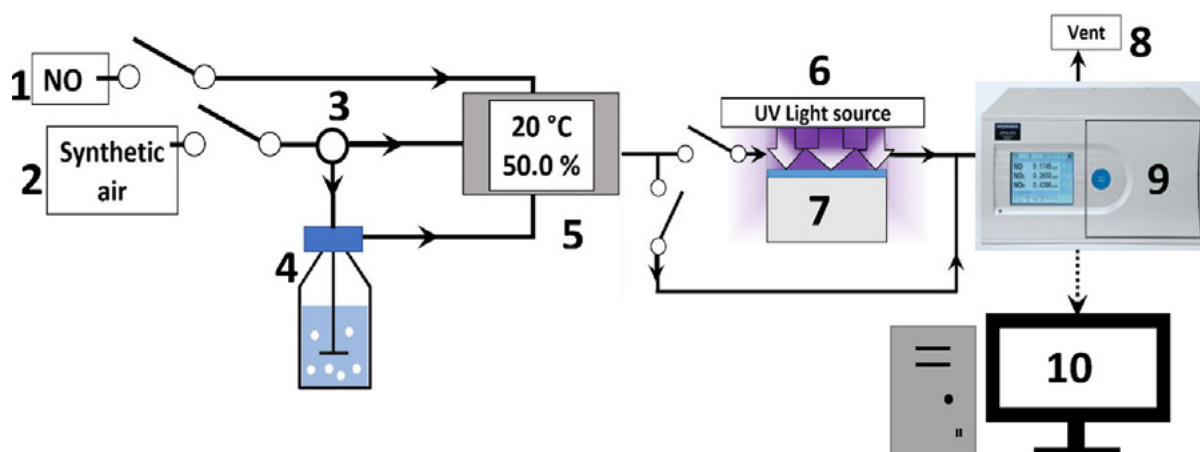


Fig. 2 Schematic view of the PCO measurement setup: 1) NO gas source, 2) synthetic air source, 3) valve, 4) bottle containing water, 5) humidity and temperature sensor, 6) light source, 7) reactor, 8) air vent, 9) NO_x detector and 10) computer to control inflow of gasses and data collection. (Permission from [14])

Chemical bonds in the silica aerogel were detected by Fourier-transform infrared spectroscopy (FTIR), which was performed with a Varian 3100 instrument with the wavenumbers ranging from 4000 to 400 cm⁻¹ at a resolution of 2 cm⁻¹. Nitrogen physisorption was performed with a Tristar II equipment at 77 K using liquid nitrogen to determine the specific surface area using the BET theory and pore size distribution using the BJH theory. For microstructure analysis, transmission electron microscopy (TEM) was performed using a Tecnai 20 microscope, operated at 200 kV.

3. Results and discussion

3.1 Properties of olivine silica aerogel

The density and porosity of the prepared silica aerogel is shown in Table 2. All the silica aerogel obtained a porosity beyond 93.6% and density below 0.134 g/cm³. It can be observed that 48 hours aging slightly increased the particle density of the silica aerogel. The reason behind this is that a longer aging time means a higher degree of poly-condensation between colloidal particles and hence a denser silica gel microstructure. The strength of the silica network increased, and could more easily resist the pressure caused by evaporation of the solvent, but with the sacrifice of an increase in density and decrease in porosity. Also, excessive aging reduces the permeability of the silica gel and make it difficult for the solvent exchange process to work properly. Therefore, a suitable aging time of 36 hours is suggested in this study.

The pH of the silicic acid can also influence the density of the produced silica aerogel by changing the hydrolysis and condensation rates of the silicic sol. When the pH of the silicic sol is 4.5, the silica monomer concentration increases too fast and forms silicate nuclei rather than cross linking silica networks, leading to an increase in density. It is observed that a pH of 5.5 can balance the hydrolysis rate and condensation rates, which means condensation immediately follows hydrolysis of silicate and a uniform nanoporous structure can be formed. The silicate monomer concentration is low and favours to grow and form cross-linking silica particles. Therefore, the strength of the gel would increase and less shrinkage happened, leading to a lower density and higher porosity of silica aerogel. The specific surface area and pore size distribution of the silica aerogel (pH 5.5, A36) is shown in Fig. 3. It can be seen from Fig. 3 (a) that the isotherm of the aerogel shows a typical type IV isotherm with an obvious hysteresis. The hysteresis is caused by the narrow pore size distribution with most of the pores being around 8 nm as shown in Fig. 3 (b). The specific surface area and pore volume of the aerogel is 694 m²/g and 2.99 cm³/g, respectively. After calcination at 500 °C for 4 hours, the SSA of silica aerogel rises to 920 m²/g and pore volume to 5.30 cm³/g. The reason behind

this result is that the calcination process makes the aerogel expand its pore size and coarsens the backbone of silica particles. The silica aerogel after heating to 500 °C has a larger pore size, which is around 18 nm, indicating a different pore structure and silica network. Also, the amount of absorbed nitrogen increases at a high relatively pressure, indicating a greater SSA and bigger pore size as well. These properties are suitable for silica aerogel function as a catalytic support with the aim of a better spread of titania both around and inside the pores of silica aerogel.

Table 2: Particle density and porosity of olivine silica aerogel.

Density (g/cm ³) / Porosity (%)	pH 4.5	pH 5.2	pH 5.5	pH 5.9
A36	0.134/93.6	0.124/94.1	0.0972/95.4	0.110/94.8
A48	0.138/93.8	0.128/94.3	0.105/95.0	0.125/94.0

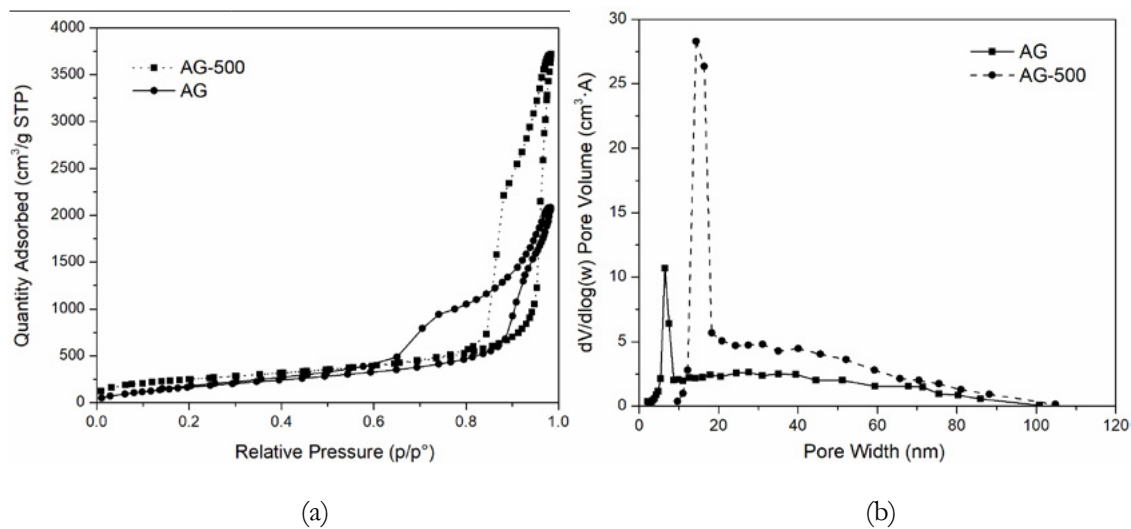


Figure 3: Pysisorption isotherm (a) and pore size distribution (b) of olivine silica aerogel before and after 500 °C calcination using BET and BJH methods

3.2 Microstructure of titania-silica aerogel composite

The pysisorption isotherm and pore size distribution before and after incorporation of titania are shown in Fig.4. The hysteresis loop of the silica aerogel-titania composite is quite small compared to the pure silica aerogel, indicating a smaller pore size of the composite samples, as shown in Fig. 4 (b). The pore size shrank to 10 nm and pore size distribution is broader than the sole silica aerogel. Moreover, the pore volume decreased significantly, which reduced from 4.99 cm³/g to 1.77 cm³/g. Therefore, it can be inferred from the nitrogen pysisorption results that titania crystals are inside the pores of silica aerogel which makes the pore volume decrease significantly.

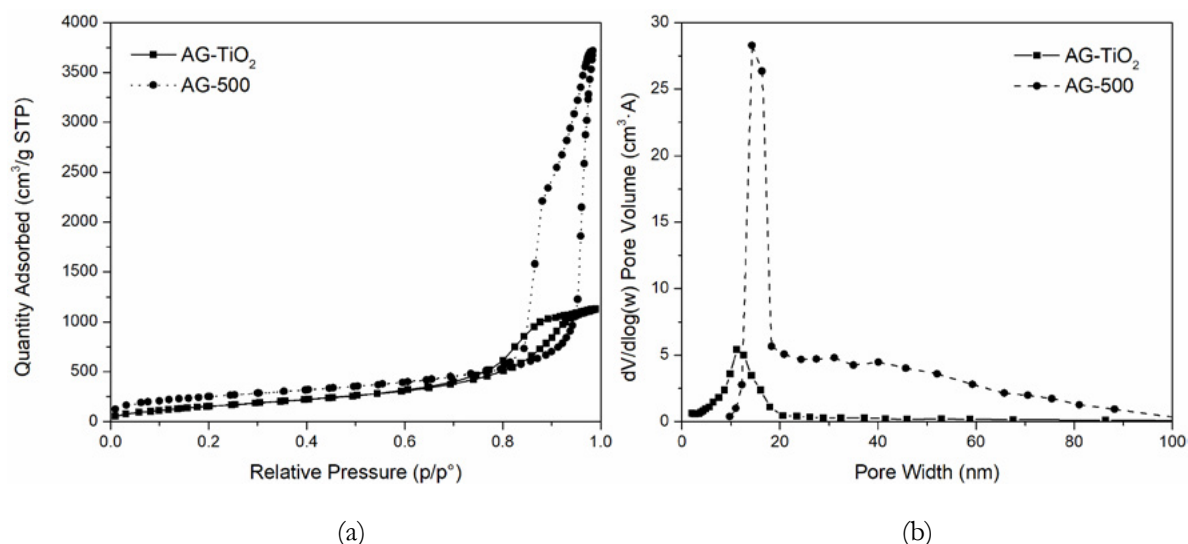


Figure 4: Physisorption isotherm (a) and pore size distribution (b) of silica aerogel after incorporation of titania

The FTIR spectra (Fig. 5) shows the $-\text{CH}_3$ groups are grafted on the surface of the original silica aerogel. After 500 °C heat treatment, the $-\text{CH}_3$ groups disappear and $-\text{OH}$ groups are visible, which may be due to the moisture in the atmosphere forming the silanol bond. With the incorporation of titania, the Si-O-Ti bond is visible at 960 cm^{-1} , indicating a good chemical combination between silica aerogel and titania. The reason behind this is that the pH around 3-4 of the reacting solution leads to opposite charge between the aerogel and formed titania. Moreover, the pH value is lowered to 3~4 for the sake of a slower hydrolysis reaction of TP. According to a model proposed from [14], the ratio between the Ti-O-Si bond and Si-O-Si bond is around 0.059, indicating a moderate bonding between these two materials.

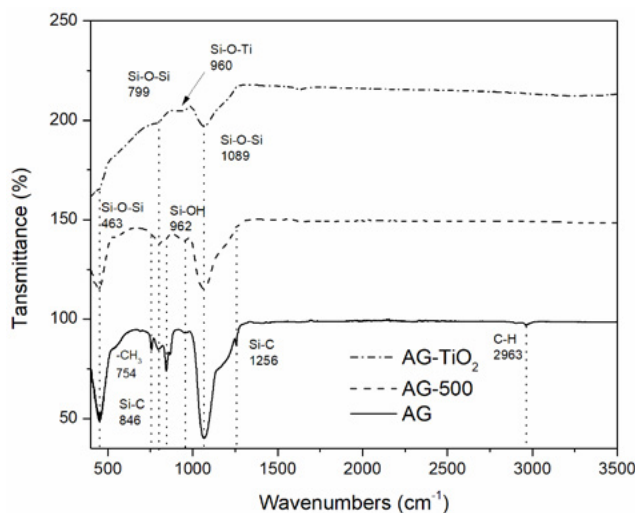


Figure 5: FTIR spectra of silica aerogel and composite sample

3.3 PCO efficiency of the titania-silica composite

The degradation of the NO_x gasses is shown in Fig. 6. While the degradation of NO is 99.6%, it is almost the same as that of the coating using P25, the degradation of NO_x (which is the combination of NO and the intermediate NO_2) is higher with the silica aerogel composite. The overall conversion on the composite of NO_x is 93.6%, while only 57.8% for the reference P25. The high conversion of NO and NO_x is due to the titania forming inside and around the silica aerogel, which fills the pores and as a result, some of the titania being spread evenly. This is confirmed by the nitrogen adsorption and FTIR test in

the previous section. Therefore, the silica aerogel-titania composite is a promising photocatalyst and needs further research.

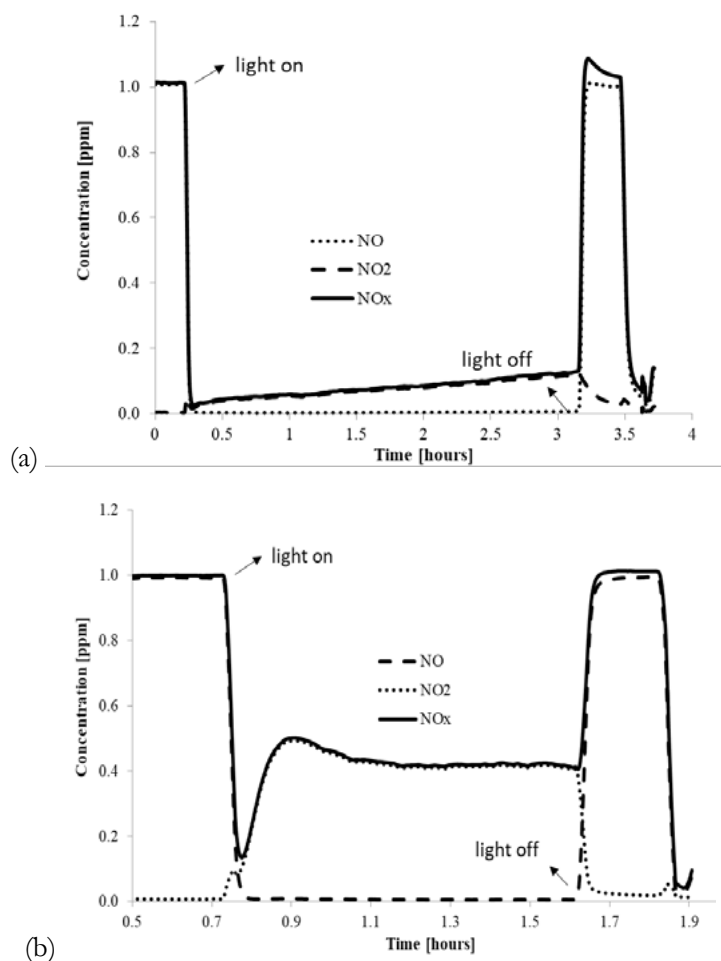


Figure 6: Concentration of NO, NO₂ and NO_x in time, showing degradation due to conversion by titania. (a) Silica aerogel-titania composite (b) P25

4. Conclusions

Silica aerogel has been synthesized from olivine via ambient pressure drying at a low temperature. The produced silica aerogel obtained high SSA of 694 m²/g and 2.99 cm³/g. Calcination at 500 °C increased the SSA (920 m²/g) and pore volume (5.3 cm³/g) significantly. Titania was loaded into the silica aerogel using a precipitation method. The prepared silica aerogel-titania composite shows a greater conversion efficiency (99.6% for NO and 99.3% for NO_x) than the reference sample P25.

5. Acknowledgment

This research was supported by the Department of the Built Environment at Eindhoven University of Technology and China Scholarship Council (201706950053). Ing. A.C.A. Delsing is acknowledged for the experimental support on analytical analysis.

6. Reference

- [1] M. Koebel, A. Rigacci, P. Achard, Aerogel-based thermal superinsulation: an overview, J Sol-Gel Sci Techn, 63 (2012) 315-339.
- [2] A.M. Papadopoulos, State of the art in thermal insulation materials and aims for future developments,

Energy and Buildings, 37 (2005) 77-86.

[3] J.E. Amonette, J. Matyáš, Functionalized silica aerogels for gas-phase purification, sensing, and catalysis: A review, *Microporous and Mesoporous Materials*, 250 (2017) 100-119.

[4] H. Maleki, N. Hüsing, Current status, opportunities and challenges in catalytic and photocatalytic applications of aerogels: Environmental protection aspects, *Applied Catalysis B: Environmental*, 221 (2018) 530-555.

[5] H. Maleki, Recent advances in aerogels for environmental remediation applications: A review, *Chem Eng J*, 300 (2016) 98-118.

[6] H. Maleki, L. Duraes, C.A. Garcia-Gonzalez, P. Del Gaudio, A. Portugal, M. Mahmoudi, Synthesis and biomedical applications of aerogels: Possibilities and challenges, *Advances in colloid and interface science*, 236 (2016) 1-27.

[7] M.A. Aegerter, N. Leventis, M.M. Koebel, *Aerogel handbooks*, Springer, New York, 2011.

[8] J. Fricke, Aerogels-Recent progress in production techniques and novel applications, *J Sol-Gel Sci Techn*, 13 (1998) 299.

[9] W. Hu, M. Li, W. Chen, N. Zhang, B. Li, M. Wang, Z. Zhao, Preparation of hydrophobic silica aerogel with kaolin dried at ambient pressure, *Colloids and Surfaces A: Physicochemical and Engineering Aspects*, 501 (2016) 83-91.

[10] F. Shi, J. Liu, K. Song, Z. Wang, Cost-effective synthesis of silica aerogels from fly ash via ambient pressure drying, *Journal of Non-Crystalline Solids*, 356 (2010) 2241-2246.

[11] A. Lazaro, G. Quercia, H.J.H. Brouwers, J.W. Geus, Synthesis of a Green Nano-Silica Material Using Beneficiated Waste Dunites and Its Application in Concrete, *World Journal of Nano Science and Engineering*, 03 (2013) 41-51.

[12] A. Lazaro, L. Benac-Vegas, H.J.H. Brouwers, J.W. Geus, J. Bastida, The kinetics of the olivine dissolution under the extreme conditions of nano-silica production, *Applied Geochemistry*, 52 (2015) 1-15.

[13] A. Lazaro, H.J.H. Brouwers, G. Quercia, J.W. Geus, The properties of amorphous nano-silica synthesized by the dissolution of olivine, *Chem Eng J*, 211-212 (2012) 112-121.

[14] Y. Hendrix, A. Lazaro, Q.L. Yu, H.J.H. Brouwers, Influence of synthesis conditions on the properties of photocatalytic titania-silica composites, *Journal of Photochemistry & Photobiology A: Chemistry*, 371 (2019) 25-32.

[15] A. Lazaro, nanosilica production at low temperatures from the dissolution of olivine, Eindhoven University of Technology, Eindhoven, 2013.

The influence of cellulose-based micro and nanomaterials on early-age properties of cement grouts

H. Karimi¹, Q.L. Yu¹, H.J.H. Brouwers¹

¹ Department of the Built Environment, Eindhoven University of Technology, P.O. Box 513, 5600 MB Eindhoven, the Netherlands.

Abstract

This study investigates the use of different cellulose micro and nanofibers in cement pastes and examines the early-age properties of cement pastes in terms of rheology, shrinkage deformation, and hydration kinetics, compared to two commercially available viscosity-modifying admixtures. The results show that for a constant water to binder ratio, cellulose-based materials are capable of adjusting flowability in terms of yield stress and dynamic viscosity similar to commercially-available viscosity-modifying admixtures. In addition, cellulose-based materials do not affect the hydration kinetics at the studied low dosages. Their effect on volume change depends on their morphology and fineness.

Keywords: cement grout, cellulose nanofiber, cellulose microfiber, shrinkage, hydration.

1. Introduction

Cement grouts are currently being used in a wide variety of applications such as post-tensioning, anchorage sealing, and injection grouting. Different types of chemical admixtures can be added to cement grouts to improve or control their mechanical properties. For example, high range water reducers (HRWRs) are utilized to improve the flowability and viscosity modifying admixtures (VMAs) are applied to control that of cement grouts. Since the incorporation of admixtures into cement grouts increases the production costs, many efforts are made to find new sources and obtain cheaper VMAs. Cellulose is a sustainable material which is the most abundant of all naturally occurring organic compounds, constituting the largest natural resource available to man [1]. Cellulose microfibers (CMF) and cellulose nanofibers (CNF) are capable of modifying the rheology of cement grouts and may be considered as an interesting resource to produce VMA [2,3]. Hence, this study aims to investigate the viscosity-modifying performance and early-age impact of these materials in cement grouts.

Cellulose can be extracted from plants, wood, cotton, hemp, etc. [4]. It can also be synthesized by tunicates, bacteria, and algae [4,5]. Cellulose microfibrils can be mass-produced with the thickness of 2-10 nm and the length of 100-200 nm, while cellulose nanofibers have diameters of down to 15 nm [6,7]. A few chemical and mechanical extraction methods for cellulose-based materials (CMs) in addition to CMs' classification based on the morphology and crystallinity have been introduced [8]. Cellulose-based materials (CMs) can have very different properties including, for instance, tensile strength, elongation at break and Young's modulus depending on their source [9]. Pure crystalline nano-cellulose has exceptional mechanical properties with Young's modulus estimated at 150 GPa and theoretical tensile strength of 7.5-7.7 GPa which is much higher than that of steel wire or aramid fibre [8]. Moreover, nano-cellulose has a good chemical resistance and heat stability allowing high-temperature applications (lower than 200 °C) [10].

Despite a few researches on applying CMs in cement and concrete have been reported [2,3], there is little information on the effect of CMs on the early-age properties, especially as a viscosity modifying admixture (VMA), in cement composites.

Viscosity Modifying Admixtures (VMAs) increase the passing ability and stability of concrete mixtures at lower levels of cementitious materials [11]. They enhance the rheological properties of cement-based materials in the plastic state to reduce the risk of segregation and washout [12]. In other words, VMAs work to mimic the effect of higher fines - substituting polymer interaction or ultra-fine particle interaction to achieve the cohesive effect made by much higher levels of cementitious materials [11]. They are often used as pumping aids since they can lubricate mixtures and decrease the needed pumping pressure [13]. Studies on the changes caused by the incorporation of VMAs in cementitious composites cover a broad scope of topics including, but not limited to: compatibility [14], washout [15], interfering with hydration [14], capillary pore structure [14], excessive air entrainment capacity [16], plastic shrinkage cracking susceptibility [16] and robustness [17,18]. Despite the many advantages of VMAs, they may increase the concrete production cost [19]. Since cellulose is the most abundant natural product on our planet, it could provide a sustainable route to produce VMAs. In order for a CM (CMF or CNF) to be regarded as a useful additive to modify the early-age behaviour of cement grouts, it should be compatible with the other admixtures incorporated, especially the HRWR. Further, to be regarded as a VMA, it should be able to modify the flow behaviour of cement grout. Since CMs absorb part of free water available in the mixtures, they may change autogenous shrinkage behaviour of cement grouts. Also, since some wood-based materials release sugar and deteriorate hydration the effect of CMs on hydration kinetics should be investigated. This study aims to investigate these effects of CMs on the fresh characteristics of cement grouts regarding flowability, shrinkage, and hydration kinetics at early age. The yield stress and viscosity are studied as a function of the shear rate and compared with that of the commercially-available VMAs, either natural, such as diutan gum, or synthetic, such as high-molecular-weight synthetic copolymers.

2. Methodology

2.1 Materials

Ordinary Portland Cement CEM I 52.5 R, provided by ENCI (The Netherlands), in combination with a polycarboxylic ether based high-range water reducer admixture (HRWRA) were used in proportioning cement grouts. Neat cement grout was made without adding VMA and was referred to as the reference mixture (REF) throughout this study. The mixtures were made using two types of CMFs (CMF1 and CMF2), three types of CNFs (CNF1 to CNF3), and two different commercially available VMAs, diutan gum (COM1) and a synthetic copolymer (COM2). The difference between different CMFs and CNFs was in the mechanical energy used in their manufacturing. The dosages of HRWR, cellulose micro and nanofibers, and diutan gum were calculated as their solid ratio by the weight of binder and kept constant at 0.35%, 0.08%, 0.08%, and 0.08%, respectively. CMF and CNF were stabilized in a slurry with a solid content of 1%. The synthetic copolymer was in liquid form and was used at the maximum suggested dosage by the manufacturer, which was 1% of binder.

2.2 Methods

All the mixtures were prepared using a high shear mixer. The mixing procedure started with placing all the mixing water, HRWR, and VMA in the double-wall mixing bowl connected to a bath thermostat and mixing at 800 rpm for 1 min. Then the cement was added to the liquid while mixing at 800 rpm in 30 s. After mixing at the same speed for 30 s, the mixer was stopped and scraped with a spatula for 30 s. The mixer was restarted at 2000 rpm, and the material was mixed for another 2 min. After stopping the mixer for 30 s and scraping the bowl for 30 s again, the mixing was continued at the same speed for 1 min. Fresh

cement grouts were then placed in the rheometer to study the flow behaviour. The rheology of the mixtures was characterized using an Anton Paar 300 rheometer equipped with a water bath unit and Peltier Plate temperature control system. Serrated parallel plate-plate geometry covered with waterproof sandpaper grit 180 with 1 mm spacing was used in the flow curve tests. The temperature was kept steady at 23 °C in all the experiments. All the samples were tested 7 min after cement comes into contact with water. Hydration kinetics were measured by a TAM Air isothermal calorimeter according to the ASTM C1679 [20]. All the samples were mixed externally and transferred into glass ampoules and sealed. The sealed vials were then inserted into isothermal calorimeter and kept there for seven days. Autogenous shrinkage tests were carried out according to the ASTM C1698 [21]. Three replicate specimens were used for each batch. The length of samples was first measured at the time of final setting, and all the measurements were specified by the date of the first contact between cement and water.

3. Results and discussion

3.1 Rheology

The effect of the additives on the flow behaviour of cement grouts is shown in Figure 1. As listed in Table 1, the different flow curves could be well-described with the Bingham model (Equation 1) ($R^2 > 0.985$):

$$\sigma = \sigma_D + \eta \dot{\gamma} \quad (1)$$

with σ the shear stress, σ_D the dynamic yield stress, η the viscosity and $\dot{\gamma}$ the shear rate. Neat cement grout curve (REF) has the lowest viscosity and yield stress among all the mixtures. The mixture modified by diutan gum (COM 1) shows high viscosity and yield stress. However, CNF2 is able to increase the viscosity more than the diutan gum at lower yield stress. The synthetic copolymer's effect on the yield stress and viscosity is very similar to CNF 1. Different cellulose-based materials cover a wide variety of rheology modifying effects and are able to mimic the properties of commercially available VMAs, either synthetic (e.g. synthetic copolymer in COM 2), or in natural form (e.g. diutan gum in COM1). Hence, cellulose-based materials can be designed and manufactured to incorporate different viscosity-modifying effects in cement grouts. While they can be designed to increase viscosity even more than diutan gum, at similar dosages (CNF 2 vs. COM 1), they can also be manufactured to change the thickness similar to synthetic commercial copolymers. Although modifying a synthetic copolymer to change its effect on the rheology of cement grouts is somewhat complicated, the structure of cellulose may allow producers to manufacture cellulose based VMAs with a broad range of modifying effects (CNF1 to CNF 3 or CMF1 to CMF2).

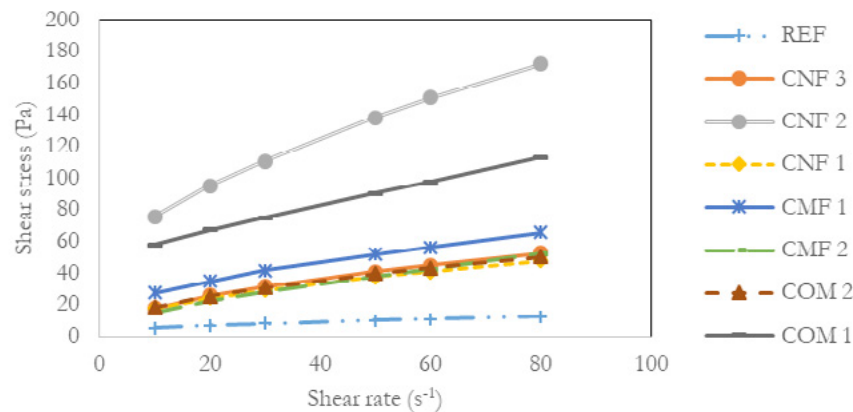


Figure 1: Influence of different cellulose-based materials on the rheology of cement grouts.

Table 1: Parameters of the Bingham flow model

Mixture	σ_D	η	R^2
REF	4.4817	0.1016	0.9873
CMF1	23.9091	0.5355	0.9925
CMF2	11.0521	0.5246	0.9958
CNF1	15.4877	0.4183	0.9873
CNF2	66.9335	1.3653	0.9902
CNF3	15.1874	0.4880	0.9858
COM1	51.1060	0.7800	0.9993
COM2	15.9725	0.4481	0.9878

3.2 Autogenous shrinkage

The effect of different CNFs on the autogenous shrinkage of the cement grouts is shown in Figure 2. The results imply that adding CNF to cement grouts increases the autogenous shrinkage, depending on the structure and morphology of CMs. This effect might be attributed to the fact that the CMs absorb a fraction of free water available in the mixture and decrease water to cement ratio, hence increasing the autogenous shrinkage. It can also be observed that different CMs with different routes (CNF1 to CNF3) may result in different volume changes.

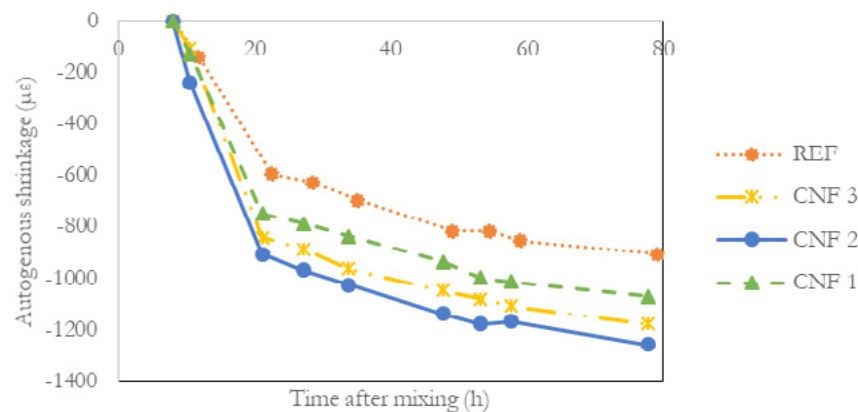


Figure 2. Linear autogenous shrinkage of cement grouts with and without CMs

Figure 3 compares the effect of the size of CM (CNF vs. CMF2) on linear autogenous shrinkage. The dosage of superplasticizer in Figure 3 is twice as much as that in Figure 2. Specimens incorporating CMF2 tend to draw more free water from the mixtures and shrink more than the ones proportioned with CNF at the similar dosages. The difference in water absorption might also be attributed to the differences in morphology of CMFs and CNFs. The mechanical milling process changes morphology and converts cellulose clusters to single fibres, hence altering shrinkage susceptibility.

3.3 Hydration kinetics

The effects of different cellulose nanofibers (CNF) and cellulose microfibers (CMF) are shown in Figure 4. Studies have shown that some wood-based pulp may deteriorate hydration kinetics due to water-soluble sugars [22,23]. However, isothermal calorimetry test results show that using CMs has a negligible effect on the peak height and the time required to reach the early rate peak. Therefore, hydration kinetics is not

affected by the addition of cellulose-based materials at the very low dosages of the admixtures incorporated in this study (0.08 % of cement).

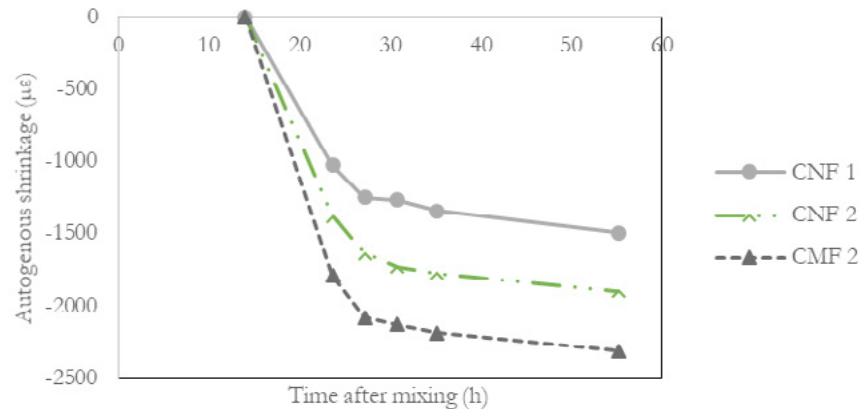


Figure 3. Linear autogenous shrinkage of cement grouts with CMF or CNF

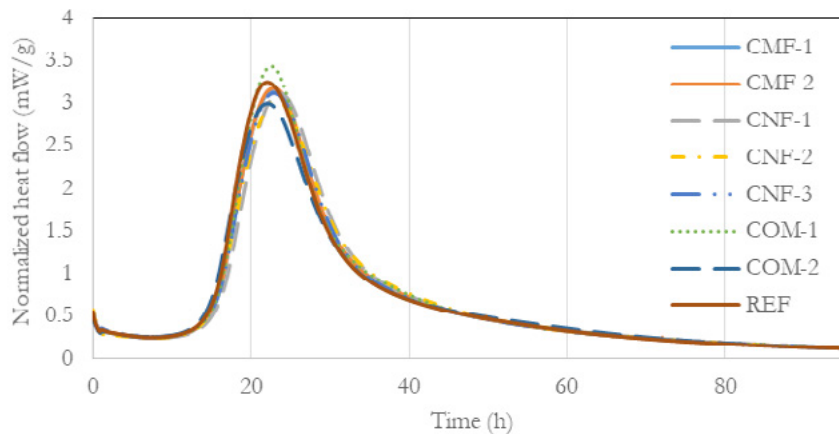


Figure 4: Isothermal calorimetry test results of different CMFs and CNFs

4. Conclusions

In the present research, the effects of two different types of cellulose-based materials (CMs) in micro and nano form on the viscosity of cement grouts and associated hydration and shrinkage are investigated. Two commercially available viscosity modifying admixtures, namely diutan gum and a synthetic copolymer, are used as references. Based on the properties assessed and the results obtained, the following conclusions can be drawn:

- Cellulose based materials, either cellulose microfiber or cellulose nanofiber, modify the rheology of cement grouts, and their modifying capacity is comparable to diutan gum or synthetic copolymers. Depending on their structure, they can adjust viscosity in different levels based on their structure.
- Various types of cellulose-based material affect linear shrinkage deformation differently, based on their morphology and structure.
- Application of CMF or CNF at low dosages (0.08% of cement) does not influence the hydration kinetics.

5. Acknowledgment

This research is a cooperation with Sappi Nederland Services BV. Dr. L. Xu and Dr. M. Jennekens are thanked for initiating the collaboration, and Dr. R. Cardinaels, Ir. R. Claessen, Dr. L. Tufano and Dr. L. Xu are thanked for the fruitful discussions throughout the project.

6. References

- [1] N.P. Kutscha, J.R. Gray, TB41: The Potential of Lignin Research, Maine Agric. For. Exp. Stn. Tech. Bull. 41 (1970). http://digitalcommons.library.umaine.edu/aes_techbulletin.
- [2] X. Sun, Q. Wu, S. Lee, Y. Qing, Y. Wu, Cellulose Nanofibers as a Modifier for Rheology, Curing and Mechanical Performance of Oil Well Cement, *Sci. Rep.* 6 (2016) 31654. doi:10.1038/srep31654.
- [3] X. Sun, Q. Wu, J. Zhang, Y. Qing, Y. Wu, S. Lee, Rheology, curing temperature and mechanical performance of oil well cement: Combined effect of cellulose nanofibers and graphene nano-platelets, *Mater. Des.* 114 (2017) 92–101. doi:10.1016/j.matdes.2016.10.050.
- [4] J.H. Kim, B.S. Shim, H.S. Kim, Y.J. Lee, S.K. Min, D. Jang, Z. Abas, J. Kim, Review of nanocellulose for sustainable future materials, *Int. J. Precis. Eng. Manuf. - Green Technol.* 2 (2015) 197–213. doi:10.1007/s40684-015-0024-9.
- [5] N. Lavoine, I. Desloges, A. Dufresne, J. Bras, Microfibrillated cellulose - Its barrier properties and applications in cellulosic materials: A review, *Carbohydr. Polym.* 90 (2012) 735–764. doi:10.1016/j.carbpol.2012.05.026.
- [6] X.Y. Jin, C.W. He, X.R. Liu, X.J. Yan, Q.Z. Yu, Effect of Cellulose Crystal Content on the Mechanical Property of Nano-Crystalline Cellulose/Lignin Composite Fibrous Film, *Key Eng. Mater.* 727 (2017) 527–531. doi:10.4028/www.scientific.net/KEM.727.527.
- [7] S. Boufi, I. González, M. Delgado-Aguilar, Q. Tarrès, P. Mutjé, Nanofibrillated cellulose as an additive in papermaking process, in: *Cellul. Nanofibre Compos. Prod. Prop. Appl.*, 2017: pp. 153–173. doi:10.1016/B978-0-08-100957-4.00007-3.
- [8] R.J. Moon, A. Martini, J. Nairn, J. Simonsen, J. Youngblood, Cellulose nanomaterials review: structure, properties and nanocomposites, *Chem. Soc. Rev.* 40 (2011) 3941. doi:10.1039/c0cs00108b.
- [9] A.N. Nakagaito, H. Yano, Novel high-strength biocomposites based on microfibrillated cellulose having nano-order-unit web-like network structure, *Appl. Phys. A.* 80 (2005) 155–159. doi:10.1007/s00339-003-2225-2.
- [10] J. George, S. S. N, Cellulose nanocrystals: synthesis, functional properties, and applications, *Nanotechnol. Sci. Appl.* Volume 8 (2015) 45. doi:10.2147/NSA.S64386.
- [11] ACI Committee 212, ACI 212.3R-16 Report on Chemical Admixtures for concrete, Farmington Hills, 2016.
- [12] ACI Committee 237, Report on Chemical Admixtures for Concrete, 2016.
- [13] ACI Committee 237, ACI 237R-07 Self-Consolidating Concrete, American Concrete Institute, Farmington Hills, 2007.
- [14] K.H. Khayat, Effects of antiwashout admixtures on properties of hardened concrete, *ACI Mater. J.* 93 (1996) 134–146. doi:10.14359/1412.

-
- [15] K.H. Khayat, Viscosity-enhancing admixtures for cement-based materials — An overview, *Cem. Concr. Compos.* 20 (1998) 171–188. doi:10.1016/S0958-9465(98)80006-1.
 - [16] K.H. Khayat, K. H. Khayat, Workability, Testing, and Performance of Self-Consolidating Concrete, *ACI Mater. J.* 96 (1999). doi:10.14359/632.
 - [17] M. Sakata, N., Maruyama, K., and Minami, Basic properties and effects of welan gum on self-consolidating concrete, *Prod. Methods Work. Concr. Proc. Conf. RILEM, E&FN Spon.* (1996).
 - [18] O. Berke, N.S., Cornman, C.R., Jeknavorian, A.A., Knight, G.F., Wallevik, The effective use of superplasticizers and viscosity-modifying agents in self-consolidating concrete, *First North Am. Conf. Des. Use Self-Consolidating Concr. Chicago, ACBM.* (2002) 173–178.
 - [19] M. Lachemi, K.M.A. Hossain, V. Lambros, N. Bouzoubaâ, Development of Cost-Effective Self-Consolidating Concrete Incorporating Fly Ash, Slag Cement, or Viscosity-Modifying Admixtures, *ACI Mater. J.* 100 (2003) 419–425. doi:10.14359/12818.
 - [20] ASTM Committee C09.48, ASTM C1679-14: Standard Practice for Measuring Hydration Kinetics of Hydraulic Cementitious Mixtures Using Isothermal Calorimetry, West Conshohocken, 2014. doi:10.1520/C1679-14.
 - [21] ASTM Committee C09.68, ASTM C1698 - 09(2014) Standard Test Method for Autogenous Strain of Cement Paste and Mortar, West Conshohocken, 2014. doi:10.1520/C1698-09R14.
 - [22] K. Bilba, M.A. Arsene, A. Ouensanga, Sugar cane bagasse fibre reinforced cement composites. Part I. Influence of the botanical components of bagasse on the setting of bagasse/cement composite, *Cem. Concr. Compos.* 25 (2003) 91–96. doi:10.1016/S0958-9465(02)00003-3.
 - [23] O. Onuaguluchi, N. Banthia, Plant-based natural fibre reinforced cement composites: A review, *Cem. Concr. Compos.* 68 (2016) 96–108. doi:10.1016/j.cemconcomp.2016.02.014.

The recycling potential of waste wood into wood-wool/cement composite

F. Berger¹, F. Gauvin¹, and H.J.H. Brouwers¹

¹ Department of the Built Environment, Eindhoven University of Technology, P. O. Box 513, 5600 MB Eindhoven, The Netherlands.

Abstract

Nowadays, the recycling potential of waste wood is still limited and in a resource cascading approach, recycling waste wood in cement composite materials, such as wood wool cement board (WWCB), appears as a promising solution. The quality of the waste wood is the main factor leading to the instability of the final product and can affect the mechanical proprieties or the wood cement compatibility. However, the possibility to recycle waste wood as spruce replacement for WWCB manufacture needs more investigation in order to assess the impact of waste wood on the mechanical performances of the final product but also to characterize the behavior of hazardous substances embodied in a cement matrix. This paper addresses the characterization of two types of waste wood, from pallets and demolition waste and their influence on the manufacturing process, mechanical proprieties and the chemical compatibility when used in WWCB. A comprehensive approach is provided to define the influence of waste wood on the hydration reaction of the cement and the chemical and physical proprieties of the composite are assessed by isothermal calorimetry, leaching measurement and microscopy. Finally, the mechanical proprieties of WWCB are tested for different waste wood content in order to define the best wood/waste wood ratio and thereby confirming the possibility to reuse waste wood in fiber/cement composite for building applications.

Keywords: Circular economy; natural fibers; treated wood; cement composite; leaching; mechanical testing;

1. Introduction

Nowadays, waste wood represents an important economic and environmental issue. Recently, studies estimate that 50 million cubic meters of waste wood is generated each year in the European Union [1]. Currently, the recycling potential of waste wood is still low, mainly caused by a lack of sustainable reusing or recycling applications [2,3]. In fact, the main part of waste wood can be treated by different ways (e.g. heat, chemical or mechanical treatment) and this involves a large amount of preservative-treated wood which contains organic and inorganic contaminants [4,5]. Those contaminants represent a real issue in waste management which can conduct to health and environmental issues during the end of life of wood [6]. Waste wood is subject to two different approaches in terms of waste management according to policy targets: It can be reused as materials in the *circular economy* or as energy recovery (e.g. Renewable Energy Directives). However, several environmental assessments show contradictory results about these two options because of the presence of contaminants in wood products [7]. The EU encourages the « resources cascading » approaches in order to promote the circular economy. This dynamic is described in the *Waste Framework Directive* (2008/98/EC) by the European Parliament, which helps to determine the future reuse of waste (Figure 1).

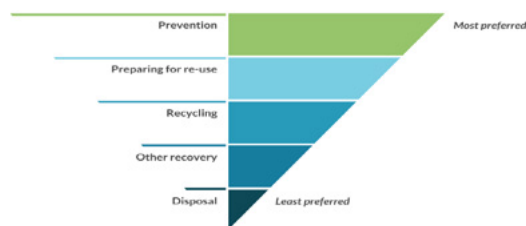


Figure 1: Circular economy diagram showing the different recycling options

In a resource cascading approach, various options are possible. But in order to use wood without losing its value (i.e mechanical properties), this current study focuses on the possibility to find sustainable applications in order to recycle waste wood into wood wool, in order to reinforce wood-cement composites, such as Wood Wool Cement Board (WWCB) (Figure 2). In these applications, the waste wood is turned into fibers and can be used in state-of-the-art materials.



Figure 2: Wood wool cement board (WWCB) manufactured with spruce wool

WWCBs are an example of wood-cement composites. They are made of wood which can be spruce (softwood) or poplar (hardwood), as well as a binder which is commonly ordinary Portland cement (OPC) or white cement (WC). These binders are known to guarantee the mechanical and physical properties of the final product [8]. Since 1940, WWCBs are commonly used in Europe and Asia, thanks to their good resistance to decay and insect but also for their good thermal and acoustical insulating properties and low density (300-500 kg/m³) [9]. Nowadays, the wood used for the manufacture of WWCB comes from forest harvesting and industrial wood products [2]. Replacing spruce by waste wood can lead to environmental issues because waste wood is mixed with different types of waste (raw wood, processed wood) and various treatments and contaminations can be found. Moreover, the presence of contaminants can disturb the wood cement compatibility and also limit the potential range of application due to leaching and the toxicity of waste wood [10–14]. Heterogeneity of waste wood is also a critical factor. As shown in several studies, depending on the wood species, its hygroscopic behavior, cement compatibility and effect on cement hydration can be significantly different due to the carbohydrate and saccharides contents in the fibers but also because of the different morphologies of the wood fibers. [15,16].

Countless types of waste wood can be used, but among the potential candidates, the wood from pallets is one of the most interesting because it is generally only heat-treated for environmental and recycling reasons leading to a clean wood resource for biomass or reuse applications. Moreover, wood from construction

and demolition wastes is also very interesting because of its great availability. However, several types of treatments are used, as shown by the UK Waste and Resources Action Program. Indeed, 74% of waste wood which comes from construction and building site are treated [17]. During the past 40 years, *Chromated copper arsenate* (CCA), *Penta* and *Creosote* are the three most used preservative treatments for wood products. Furthermore, the use of CCA treatment was the main preservative for housing or decking applications in order to prevent or delay decay caused by fungi or termites, especially in Australia, New Zealand, and the United States [5][11]. Therefore, a huge amount of CCA treated wood still remains in service worldwide and will be concerned with disposal and recycling applications. This fact implies a real recycling potential for these upcoming waste into composite materials.

In this study, the mechanical and chemical properties of the two waste wood samples provided by Nedvang (Pallets and C&D) are studied in order to compare them with conventional spruce wood, used as a reference. The wood-cement compatibility is assessed as well as the leaching behavior of the waste woods by various methods, such as pH measurement, isothermal calorimetry and scanning electron microscopy (SEM). Then, wood fibers are processed and studied (mechanical behavior, microstructure). Thereafter, the mechanical, physical and leaching properties of WWCB manufactured with different percentage of waste wood (every 10% until 100%) are compared to conventional and commercial WWCBs.

2. Methodology

2.1 Materials

In this study, the spruce wood is taken as reference in the form of Excelsior wood wool (or also called *fiber* in this study) and is provided by Knauf insulation (NL). These fibers are conventionally used for the industrial manufacture of WWCB. The studied waste woods are provided by Nedvang (NL) and come from pallets and construction & demolition sites, respectively. The binder applied in the study is CEM I 52.5 R white (PC) provided by ENCI (NL).

2.2 Methods

2.2.1 Scanning electron microscopy

Microstructure analysis of the waste wood fiber is performed by Scanning Electron Microscopy (SEM, Phenom pro-X) with a back-scattering electron detector (5 kV). The waste wood fiber has been coated with a 20 nm gold layer before the microscopy. The moisture content of the waste wood has been limited by drying the material in an oven at 60° C, for 2 h prior to analysis.

2.2.2 Leachates characterization

The leaching of waste wood is studied by using the TCLP extraction methods to obtain the leachate solution. The samples are reduced to a particle size of less than 1 cm. Subsequently, the leachate is prepared according to the TCLP standard, the waste was added to a determined extraction fluid and mixed during 18h at 30 rpm at room temperature. Thereafter, the solution is filtrated through a 0,6 to 0,8 µm glass fiber filter. The leachate obtained is analyzed by inductively coupled plasma mass spectrometry (ICP-MS) in order to measure the concentration of heavy metal and other potential contaminants rejected by the wood.

2.2.3 Isothermal calorimetry

The hydration kinetics is studied by isothermal calorimetry with a TAM Air Isothermal calorimeter set at a constant temperature of 20 °C during 72h. The wood samples and the binder were first well mixed in an ampoule before the water was added. After addition of water, the mixture was mixed for 3 min before being loaded in the calorimeter. The heat evolution rate data were calibrated by subtracting the heat evolution of

ampoules with water as a baseline.

2.2.4 Mechanical properties of the wood fibers

Mechanical properties of wood strands are measured by using an Instron 5967 bench equipped with a 2530-100 N load cell and 2710-111 wedge grip with rubber jaw faces. Tensile tests are conducted in displacement control with a crosshead speed of 5 mm/min. More than 15 samples for each condition are tested. Tensile strength (cN/tex) and Young's modulus (N/tex) are measured as a function of the linear density of the fiber (tex) by measuring the length and the weight of each fiber prior to analysis.

2.2.5 Manufacture of the composites

In order to evaluate the mechanical performances of the composite according to different Waste wood/spruce wood ratios (called *W/S ratio* in this study), WWCBs are manufactured with 10 different chosen ratios (0.1 to 1), named PW/S0.1 to PW/S1.0 for pallets wood. In this study, the manufacture of the composites is based on the dry method, usually applied in the WWCB production. The final product is placed into a mold 30 x 60 cm and pressed for 24 h, using a mechanical press. Successively, the sample is cured in a plastic sheet for 7 days and then left drying at ambient conditions for another 3 days. In order to achieve the same moisture content before testing, the boards are dried in the oven for 2 h at 50 °C.

2.2.6 Mechanical performances of the composites

The bending strength is measured at 10 days by a three-point flexural test (Instron 5967) on a sample with dimensions of 5 x 20 x 1.5 cm, using a testing speed of 5 mm/min, and a support span of 15 cm. Three samples of each W/S ratio are tested. As reference values, the dimensional stability has to be satisfied, by a maximum thickness of 15 mm and a minimum bending strength of 1.7 MPa, according to the BS EN 12089, *Thermal insulating products for building applications* standard.

2.2.7 Thermal conductivity measurement

Thermal conductivity is measured on WWCB by a heat transfer analyzer *ISOMET 2104*. As a reference, commercial WWCB with a thickness between 15 and 30 mm have a thermal conductivity range of 0.08-0.11 W.m⁻¹.K⁻¹ according to the BS EN 12089, *Thermal insulating products for building applications* standard.

3. Results and discussion

3.1 Waste wood characterization

In order to characterize the two streams of wood, microscopy and isothermal calorimetry are performed. These two methods allow controlling the potential compatibility (i.e. mechanical and chemical) between the wood and the cement in WWCB.

The micrographs in Figure 3 shows the surface of spruce (in the form of fiber) and pallet wood (waste strands). These two kinds of wood are closed to each other and depict the same microstructure and surface aspect. Tubular cell walls are visible for both types of wood and the lumens (white arrows) have the same shape and almost the same size, with around 7µm for the pallets wood and 5µm for the spruce. Additional cell walls are visible with the waste wood (black arrows) indicating some heterogeneity. In addition, the pallet wood shows no noticeable signs of contaminants at its surface. Moreover, as compared to the reference, the surface of the waste wood seems to have less wax and lignin. These observations indicate a potential good wood/cement compatibility. The very similar structure also indicates that the manufacture of WWCB with waste wood from pallet would be not problematic because similar pore size means the same water demand and same cement coating during the process.

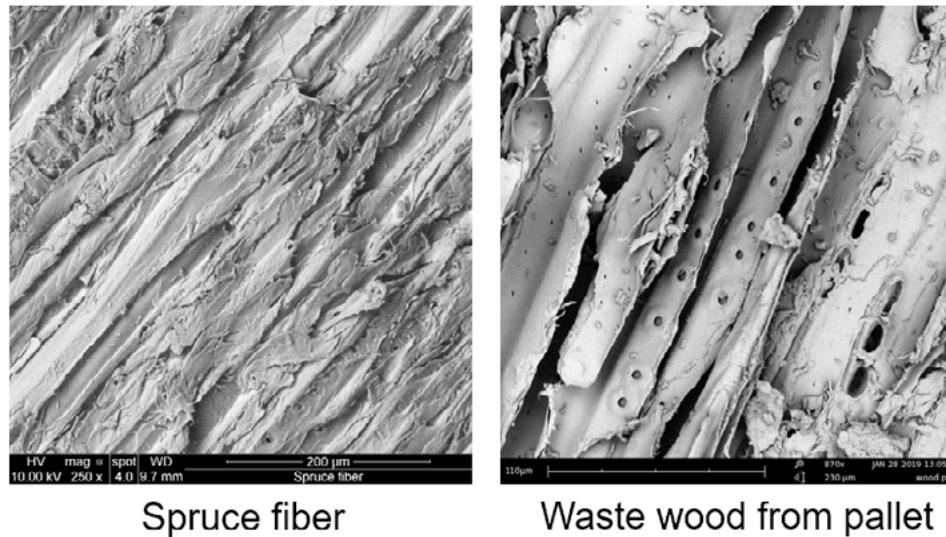


Figure 3: SEM microscopy of waste wood from pallet and spruce fiber, which is used in WWCB manufacture

However, waste wood from construction and demolition (C&D) sites seems more problematic, even if its structure remains quite close to the spruce because its cell walls and its surface show the presence of contaminants (Figure 4). These particles can be heavy metals such as chromium or inorganics substances that have been mixed with the waste woods. These substances can disturb the manufacturing process by delaying the hydration reaction of the cement, reducing the wood cement compatibility or limiting the range of applications due to health and environmental issues involved by the leachates.

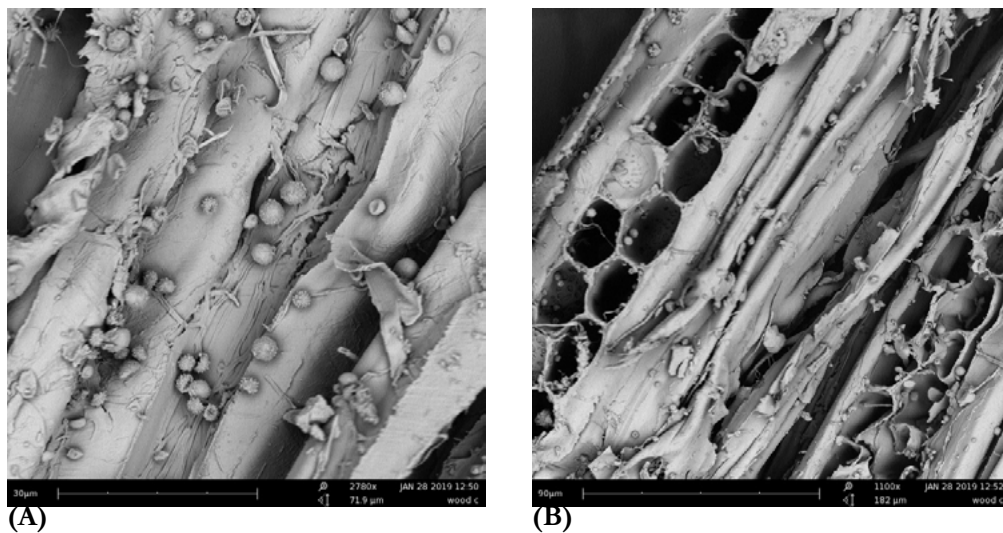


Figure 4: SEM microscopy of C&D wood

3.2 Compatibility with cement

Results of the calorimetry of the three kinds of wood are depicted in Figure 5, showing the chemical compatibility between the wood and the cement.

From the results, the two types of waste wood (building and pallets) are really close to each other. As compared to the reference, the hydration peaks have been delayed by 1.5h due to the presence of the waste wood. A probable hypothesis is that the waste wood is slightly degraded, especially at its surface,

as it can be seen by SEM (i.e. lack of matrix at the surface of the wood). The hemicellulose degradation creates monosaccharides and polysaccharides that are mixed in the cement paste and can delay the cement hydration. However, this retardation is not very important and indicates that both kinds of waste wood have a low sugar content and will not affect the manufacturing process nor the final proprieties of the WWCB. In addition, the maximum released heat is 20% lower in the presence of wood inside the cement paste. This decrease does not have a significant impact on the reaction as it remains low and also it can be explained by the presence of sugars involved by waste woods.

From these results, it appears that both types of waste wood have good chemical compatibility with cement. Moreover, the waste wood from pallets is surprisingly close to the spruce fiber and would be a perfect candidate to replace it due to its similar microstructure. Therefore, in this study, only waste wood from pallets is be turned into fibers and used in WWCB.

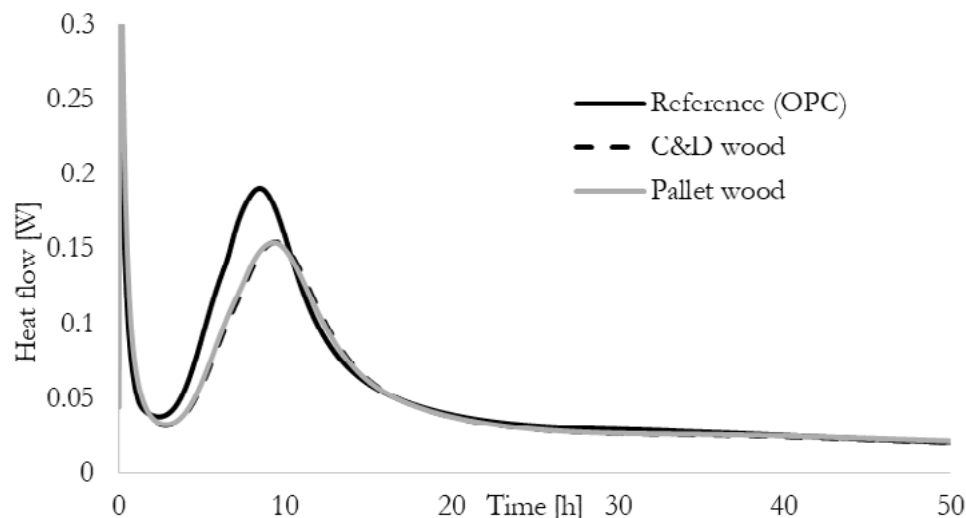


Figure 5: Isothermal calorimetry of the 2 wood streams as compared to the reference (i.e. white cement), showing the effects of the waste woods on the cement hydration

3.3 Pallet wood fiber manufacture

Fibers made of pallets are manufactured in the TU/e BPS laboratory using thin layers of pallet cut with a ribbon saw and then turned into fibers with a wood plane. Figure 6 depicts the process, which resulted in wood wool with very similar aspect than regular wood wool manufactured from spruce (Figure 6-C).

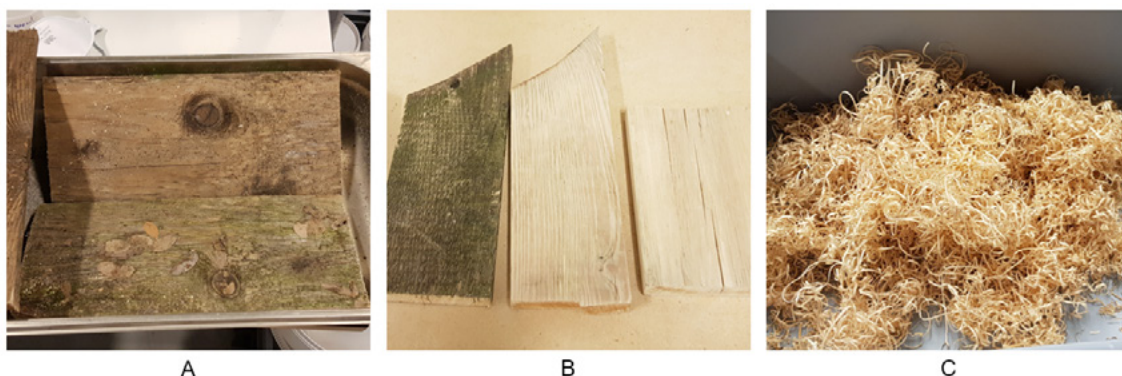


Figure 6: Pallet wood fiber manufacture. A: Pallet is cut into pieces, washed; B: wood is sanded and dried; wood is cut into 10-15 cm fibers.

3.4 Mechanical properties of wood fibers

The tensile test of fibers highlights the variation of the mechanical properties between the pallet wood and the spruce in the form of fibers. These results average 30 tests on each type of wood fibers and are displayed in Figure 7 and Table 1.

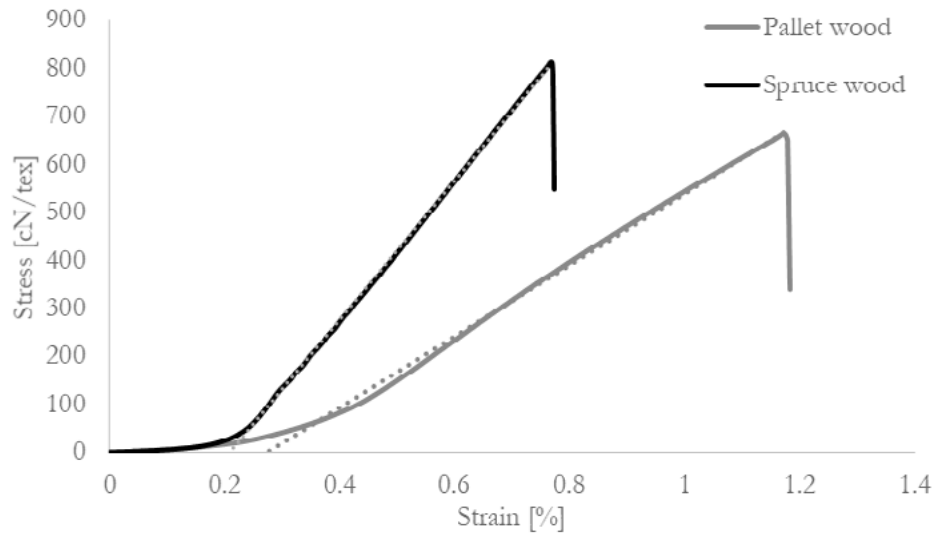


Figure 7: Average stress/strain curve of the two types of fibers

Table 1: Summary of the mean results

Sample	Modulus [cN/tex]	Tensile strain [cN/tex]
Pallet fibers	770	812
Spruce fibers	1332	663

The tensile strength of the pallet fibers is slightly lower than the spruce one, with a decrease of approximately 20%. On the other hand, the modulus of elasticity is almost 50% lower. Many phenomena can affect the mechanical behavior of the fiber (e.g. external degradation, differences in morphology or composition...) but here, SEM characterization has shown that spruce and pallet woods are very similar.

First of all, it is unlikely that the pallet wood is degraded. SEM characterization has shown very clean wood and isothermal calorimetry has shown almost no impact on cement. If the wood would have been degraded, the tensile strength of the fiber would have been critically affected since the degradation would have affected the wood structure. Here, only the modulus of elasticity of the pallet wood is significantly different and this propriety is directly related to the cellulosic fibrils within the structure of the wood. Therefore, the difference between the two types of wood can be explained by an internal degradation of the cellulose but also by the orientation of the cellulose fibrils depending on the cutting axis of the fibers. The first hypothesis is very unlikely, because the isothermal calorimetry shows no real difference between the two types of wood, and degradation of the cellulose would also indicate a major hemicellulose degradation, thereby inducing a critical amount of polysaccharide in the system.

A more probable explanation would be that these differences can be related to the manufacturing process or the morphology of the fibers. The spruce fibers are made thanks to an industrial process, using wood logs whereas the pallet fibers have been made differently because the conventional process is not applicable for a recycled material due to the variation in terms of shape and size. The industrial process is specially

developed to obtain the greatest mechanical proprieties for each fiber, following the cell walls of the wood, with an optimum orientation of the cellulose fibrils.

SEM microscopy of the pallet wood fiber (Figure 8) confirms these observations. It does not show matrix degradation and reinforce the fact that the microstructure of both wood sample is the same (as compared to Figure 4). However, the structure of the wood (following the black arrow in A) is slightly tilted as compared to the cutting direction (in the box), which can explain the low modulus of elasticity. Therefore, the anisotropy of wood causes the differences in Young's modulus. But this significant decrease is not very problematic in the composite strength because WWCBs are tested in flexural mode, and the rigidity of the boards are not a requirement in the existing standards.

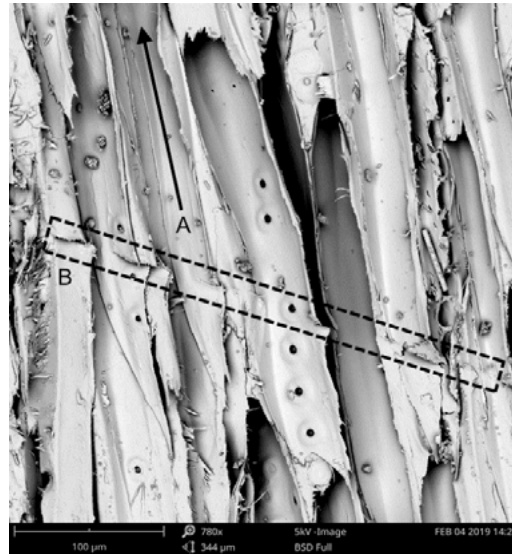


Figure 8: SEM microscopy wood fiber made of pallet. The cell direction is indicated with the black arrow (A). The cutting direction is indicated in B, with scratching marks.

3.5 Mechanical properties of WWCB

Flexural strength of WWCB containing 10 to 100% of pallet wood fibers (as replacement of spruce) are measured, as well as the density of these boards. Results are shown in Figure 9.

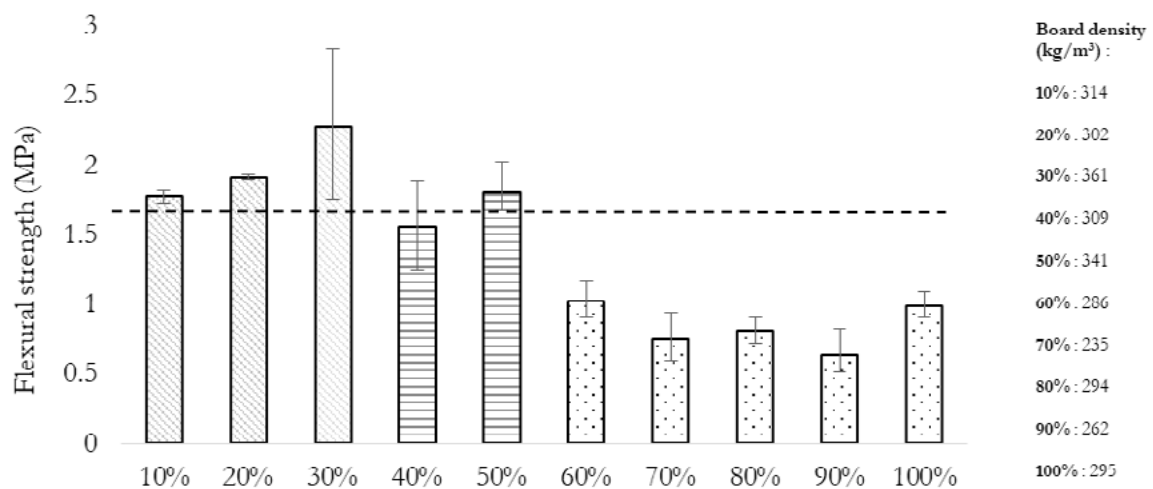


Figure 9: Flexural strength of WWCB containing 10 to 100% of waste wood (mixed with spruce wood). The dashed black line is set at 1.7 MPa, which is the acceptable limit for boards

In average, WWCB made industrially with spruce have a flexural strength of 2 MPa, for low-density range

(300-400 kg/m³). When waste wood is added to spruce in WWCB, results can be regrouped in three groups.

Between 10 and 30% of waste wood (light grey dashed lines), WWCBs are always above the acceptable limit since all tested specimens have a flexural strength above 1.7 MPa. An important standard deviation is visible for the PW/S0.3 board but only because some specimens have shown extraordinary results (probably because of the good cement/fiber dispersion).

When more than 30% of waste wood is added to spruce (dark grey, horizontal lines), results are acceptable. PW/S0.4 averages a flexural strength of 1.7 MPa and PW/S0.5 is always slightly above the limit. It proves that up to 50% of spruce can be replaced with waste wood, without causing issues.

However, above 50% of waste wood (black dots), the flexural strength of WWCBs significantly decrease, with average values from 1 to 0.6 MPa. Increasing the weight fraction of waste wood also leads to a decrease in the density of the boards. This phenomenon is explained by the expansion of boards after compression during the manufacturing process: Boards with more than 50% of wood are 1 to 2 cm bigger than boards made with more than 50% of spruce wood. As it was explained before, pallet wood fibers are very heterogeneous, and the fiber orientation is not optimal. It means that some fibers have the tendency of being curled as compared to spruce wood fibers which are always straight (see Figure 10).

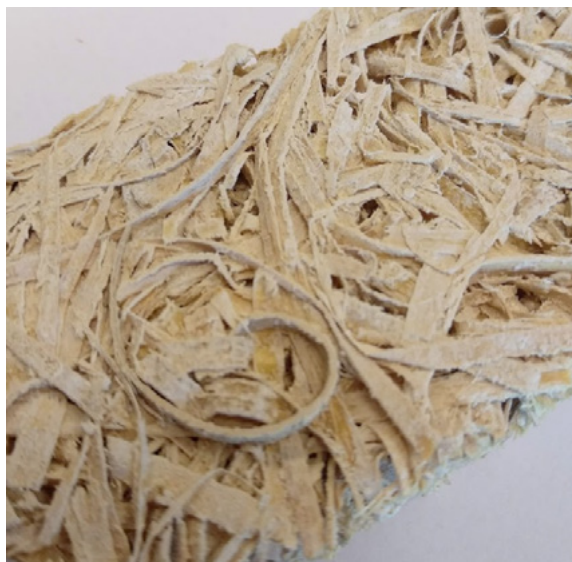


Figure 10: WWCB made of 100% of waste wood. In the red box, a fiber is curled, explaining the higher porosity of WWCBs containing a high fraction of waste wood

3.6 Thermal properties of WWCB

Thermal conductivity of WWCB containing 10 to 100% of pallet wood fibers (as replacement of spruce) are measured and the average results are shown in Figure 11. The first observation is that the thermal conductivity of all the manufactured boards is way below the acceptable limit (0.11 W.m⁻¹.K⁻¹), which can be explained by the low density of all the boards, due to the selected recipe design.

Moreover, the differences in the thermal conductivity are mostly due to the density difference, as Figure 11 shows some correlation between these two properties. Since the microstructure of the two kinds of wood is very close, only the porosity and the macrostructure of the composite can explain this phenomenon. Besides, it is also noticeable that using a higher fraction of waste wood help to decrease the thermal conductivity because of the higher porosity formed by the curled-fibers in the structure, as shown in Figure 10.

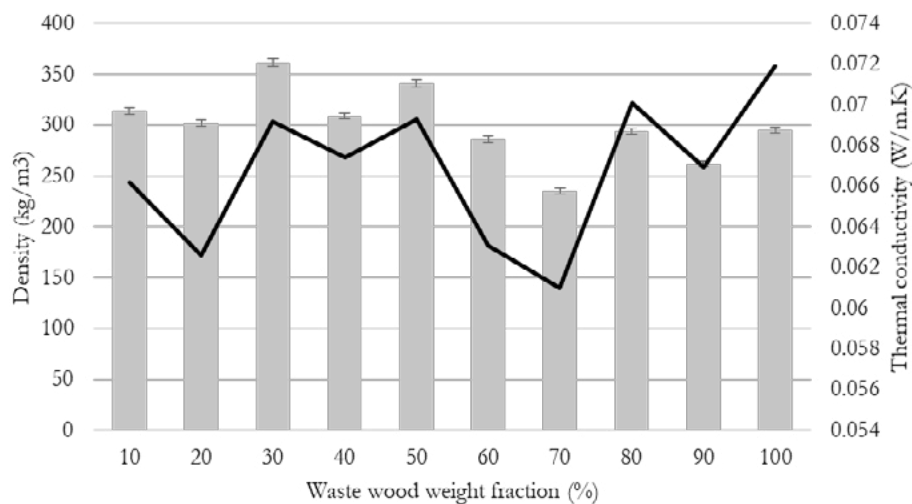


Figure 11: Average thermal conductivity of WWCB as well as the boards' density

3.7 Environmental assessment

Leaching analysis of the waste wood is performed on its leachate and the results are shown in Table 2, showing heavy metal contaminants as well as some alkali and earth alkali. From the EU 2009/894/EC legislation, when recycled wood is used in wood-based materials, some elements such as arsenic, lead or copper should not exceed a limit value, indicated in the table.

Here, leaching values of all elements are far below the limit, which means that the wood can be used freely in WWCB. Moreover, these values are measured prior to manufacture meaning that the concentration of the WWCB leachate would be even lower, due to the complexation of some element with cement.

Table 2: Element concentration (mg/L) in waste wood leachate.

Element concentration (mg/L)	As	Al	Ba	Cd	Co	Cr	Cu	Fe	Li
	0.031	0.200	0.163	-	-	0.022	0.115	0.085	0.021
Limit values from EU 2009/894/EC	25	-	-	50	40	25	40	-	-
Element concentration (mg/L)	Ni	Pb	Sr	Ti	Zn	Na	K	Mg	Ca
	-	0.057	0.218	0.007	0.971	100	50	30	100
Limit values from EU 2009/894/EC	100	90	-	-	-	-	-	-	-

4. Conclusions

In this study, waste wood has been used in order to replace conventional spruce wood in wood wool cement boards (WWCB), composite that can be used for ceilings or walls. Following the experimental results, the following conclusions have been drawn:

- Wood from pallets is an excellent candidate for WWCB because its structure is very similar to the spruce industrially used in the manufacture of these composites. On the other hand, using wood from construction and demolition sites is more challenging, because this wood is more heterogeneous (i.e. more than one type of wood is used in this kind of application) and can be contaminated.
- Waste wood is quite compatible with white cement, which is used in the production of WWCB. Measured by isothermal calorimetry, the effect of waste wood on cement is not significant. Moreover, the environmental assessment made on waste wood shows no traces of contaminants in wood, paving the way for its usage in composites.

- Making wood fibers from waste material is challenging because the conventional industrial process is not designed for waste wood. Yet, in this study, an alternative method has been used, turning successfully pallet wood into fibers, with microstructure and mechanical properties very close to spruce wood. The only noticeable issue is the difficult control of the anisotropy of the wood, leading to fibers not always oriented in the right direction (alongside the cell walls of the wood).
- WWCBs have been made mixing 10 to 100% of waste wood fibers with spruce fibers. Results show that up to 50% of waste wood, boards are above the acceptable limit (1.7 MPa). Above 50% of waste wood, flexural strength and density of the boards decrease significantly. Thermal properties of these boards are always acceptable, with very good values below 0.08 W.m⁻¹.K⁻¹.

In conclusion, waste wood from pallet can be a good option to replace spruce in WWCB. So far, its replacement level is successful until 50%. Above this limit, the fiber morphology is too heterogeneous to guarantee a good reinforcement. Better process or another source of wood can be evaluated in the future, as well as another kind of *green* binder, in order to create a more sustainable composite for building applications.

5. Acknowledgment

The authors would like to acknowledge the financial support provided by M2i (Materials innovation institute). For the material support, the authors would like to acknowledge Nedvang (The Netherlands), Knauf Insulation (The Netherlands) and ENCI (the Netherlands).

6. References

- [1] F.C. Bergeron, Energy and climate impact assessment of waste wood recovery in Switzerland, Biomass and Bioenergy. 94 (2016) 245–257. doi:10.1016/J.BIOMBIOE.2016.09.009.
- [2] M.H. Ramage, H. Burrige, M. Busse-Wicher, G. Fereday, T. Reynolds, D.U. Shah, G. Wu, L. Yu, P. Fleming, D. Densley-Tingley, J. Allwood, P. Dupree, P.F. Linden, O. Scherman, The wood from the trees: The use of timber in construction, Renew. Sustain. Energy Rev. 68 (2017) 333–359. doi:10.1016/J.RSER.2016.09.107.
- [3] M. Humar, J. Jermer, R. Peek, Regulations in the European Union with Emphasis on Germany, Sweden and Slovenia, Environ. Impacts Treat. Wood. (2006) 37–57. doi:10.1201/9781420006216.ch3.
- [4] E.-H. Pommer, Wood, Preservation, in: Ullmann's Encycl. Ind. Chem., Wiley-VCH Verlag GmbH & Co. KGaA, Weinheim, Germany, 2000. doi:10.1002/14356007.a28_357.
- [5] C.C. Felton, R.C. Groot, The recycling potential of preservative-treated wood., For. Prod. J. 46 (1996) 37–46.
- [6] M.I. Shahidul, M.L. Malcolm, M.S.J. Hashmi, M.H. Alhaji, Waste Resources Recycling in Achieving Economic and Environmental Sustainability: Review on Wood Waste Industry, Ref. Modul. Mater. Sci. Mater. Eng. (2018). doi:10.1016/B978-0-12-803581-8.11275-5.
- [7] G. Faraca, D. Tonini, T.F. Astrup, Dynamic accounting of greenhouse gas emissions from cascading utilisation of wood waste, Sci. Total Environ. 651 (2019) 2689–2700. doi:10.1016/J.SCITOTENV.2018.10.136.
- [8] K. Kochova, K. Schollbach, H.J.H. Brouwers, Use of alternative fibres in Wood Wool cement boards and their influence on cement hydration, in: 19th Int. Conf. Build. Mater., Ibausil, 2015: pp. 2–1375. <https://pure.tue.nl/ws/files/3889104/935776505712757.pdf>.

-
- [9] F.C. Jorge, C. Pereira, J.M.F. Ferreira, Wood-cement composites: A review, *Holz Als Roh - Und Werkst.* 62 (2004) 370–377. doi:10.1007/s00107-004-0501-2.
- [10] J.A. Hingston, C.D. Collins, R.J. Murphy, J.N. Lester, Leaching of chromated copper arsenate wood preservatives: A review, *Environ. Pollut.* 111 (2001) 53–66. doi:10.1016/S0269-7491(00)00030-0.
- [11] A. Mohajerani, J. Vajna, R. Ellcock, Chromated copper arsenate timber: A review of products, leachate studies and recycling, *J. Clean. Prod.* 179 (2018) 292–307. doi:10.1016/j.jclepro.2018.01.111.
- [12] R.W. Wolfe, A. Gjinolli, Cement-Bonded Wood Composites as an Engineering Material, (1997) 84–91. <https://www.fpl.fs.fed.us/documnts/pdf1997/wolfe97a.pdf> (accessed February 20, 2019).
- [13] T. Townsend, T. Tolaymat, H. Solo-Gabriele, B. Dubey, K. Stook, L. Wadanambi, Leaching of CCA-treated wood: implications for waste disposal, *J. Hazard. Mater.* 114 (2004) 75–91. doi:10.1016/J.JHAZMAT.2004.06.025.
- [14] A. Quiroga, V. Marzocchi, I. Rintoul, Influence of wood treatments on mechanical properties of wood-cement composites and of *Populus Euroamericana* wood fibers, *Compos. Part B Eng.* 84 (2016) 25–32. doi:10.1016/j.compositesb.2015.08.069.
- [15] K. Kochova, K. Schollbach, F. Gauvin, H.J.H. Brouwers, Effect of saccharides on the hydration of ordinary Portland cement, *Constr. Build. Mater.* 150 (2017) 268–275. doi:10.1016/j.conbuildmat.2017.05.149.
- [16] G.C.H. Doudart De La Grée, Q.L. Yu, H.J.H. Brouwers, THE EFFECT OF GLUCOSE ON THE HYDRATION KINETICS OF ORDINARY PORTLAND CEMENT, in: *First Int. Conf. Bio-Based Build. Mater.*, Clermont-Ferrand, 2015: pp. 126–132.
- [17] Composition of wood waste from construction & demolition (C & D) sites, (2009).
- [18] & C. Schmidt, R., Marsh, R., Balatinecz, J. J., Increased wood-cement compatibility of chromate-treated wood, 44 (1994) 5–9.

Mechanical properties and shrinkages of coir fibers reinforced light-weight aggregate concrete

X.X. Zhang, F. Gauvin, H.J.H. Brouwers

Department of the Built Environment, Eindhoven University of Technology, P. O. Box 513, 5600 MB Eindhoven, the Netherlands.

Abstract

Natural fibers (NFs) from agricultural wastes have been increasingly used as reinforcements in cement-based materials to replace synthetic fibers thanks to their advantages, for instant, low cost, light weight and considerably mechanical properties. The present research aims to investigate the effects of different contents of saturated coir fibers on the mechanical properties and drying and autogenous shrinkages of cement-based lightweight aggregate concrete (LWAC). The concrete is designed by adopting the modified Andreasen and Andersen (A&A) particle packing model to achieve a more compacted matrix. LWAs made of waste glass are applied to develop a greener concrete. Three dosages of coir fibers, 0.5%, 1.5%, and 3%, are added by weight of the concrete. The results show that the compressive strength, flexural strength and toughness of LWAC are enhanced with added coir fibers. A low content of coir fibers such as 0.5% is benefit for achieving favourable compressive and flexural strength of concrete meanwhile higher contents of coir fibers such as 1.5% and 3% is in favour of obtaining good flexural toughness. The drying shrinkage of LWAC is slightly increased by adding coir fibers, while the autogenous shrinkage decreases significantly. Concrete with 3 wt.% coir fibers exhibits an expansion deformation, which indicates the internal curing effects of saturated coir fibers.

Keywords: Coir fibers, reinforcement, shrinkage, internal curing

1. Introduction

Due to the requirement for high-rise, long-span or functional buildings, lightweight aggregate concrete (LWAC) has attracted increasing attention because of its unique advantages, for example, lower density, larger specific strength and superior thermal insulation [1–8]. However, LWAC also has drawbacks such as low flexural strength and poor fracture toughness which have restricted its wider applications [9–11]. These defects could be usually compensated by adding fibers such as steel or synthetic fibers [12,13]. Nevertheless, even though these fibers are found to positively influence the properties of LWAC, some correlatively negative effects should be addressed. For example, both the steel and synthetic fibers have both high material and energy consumption, and can lead to a substantial environmental footprint in their production processes [14]. Moreover, synthetic fibers can cause health risks (e.g. skin irritations or respiratory diseases) during the manufacturing and bring environmental burden due to difficulty in disposing [15]. Additionally, the cost of some fibers like carbon fibers is not economical [16]. Moreover, steel fibers significantly increase the density of LWAC, especially when their fraction exceeds 1vol.% [17].

Unlike artificial fibers, natural fibers (NFs) are eco-friendly, renewable, recyclable and disposable [18,19], and have other advantages such as their low cost, light weight and good mechanical properties [20–22]. Brittle

materials reinforced with natural fibers exhibit equivalent mechanical performance as with synthetic fibers [23–25]. Thus, NFs are a good candidate to replace synthetic fibers to reinforce concrete with economic and environment benefits. Furthermore, due to the compatibility of NFs and LWAC, both have relatively light-weight and low mechanical properties, therefore, NFs are especially suitable for reinforcing LWAC. Among the various available NFs, coir fibers extracted from the waste coconut husks is abundant, with approximately 500,000 tons of coir fibers produced annually worldwide [26]. As compared to the most used NFs such as flax or bamboo, coir fibers possess a comparable specific tensile strength and have a higher toughness and flexibility [27]. Moreover, coir fibers can preserve good mechanical properties under aggressive conditions [28]. Some studies have been carried out to investigate the reinforcing effect of various contents and lengths of coir fibers on the mechanical performance of concrete. The results show that coir fibers significantly enhance the flexural strength, toughness and impact resistance of concrete [29,30] and their optimum content ranges from 1% - 3 wt.% (about 2% - 12 vol.%) with length of 2 - 5 cm, respectively [31,32].

However, because coir fibers are hydrophilic and thus their high moisture absorption can cause competitive water absorption with cement, thereby consequently affecting the available water amount for cement hydration [33,34]. Saturated fibers can be used to take advantage of this feature, thus extra water can be entrained in cement system for internal curing [35]. Nevertheless, only several presented studies are related to the internal curing effect of macro saturated fibers [35,36]. Accordingly, the objective of this study is to investigate the reinforcement effects of saturated coir fibers in concrete. The concrete is designed by adopting the modified Andreasen and Andersen (A&A) particle packing model to achieve a more compacted matrix and LWAs made of waste glass are applied to develop a greener concrete. The influence of saturated coir fibers with various contents on the mechanical properties and drying and autogenous shrinkages of cement composites are analysed. In addition, the internal curing effect of saturated coir fibers are investigated.

2. Methodology

2.1 Materials

The cement used is Ordinary Portland Cement (OPC) CEM I 52.5 R, supplied by Heidelberg Cement (The Netherlands). The chemical compositions and particle size distributions (PSDs) of cement are determined by X-ray fluorescence (XRF) and laser particle size analyzer (LPSA), shown in Table 1 and Figure 1, respectively.

The lightweight aggregates presented in Figure 2 are produced from recycled glass, supplied by Liaver Company (Germany). The chemical compositions and particle size distributions of LWAs are provided by the supplier, listed in Table 1 and Fig. 1. The physical properties of LWAs are presented in Table 2, obtained from the research of Yu et al. [37]. These LWAs have encapsulated cellular structures inside but a closed external shell outside, resulting in their low water absorption. The SEM graphs of LWAs microstructure are shown in Figure 3.

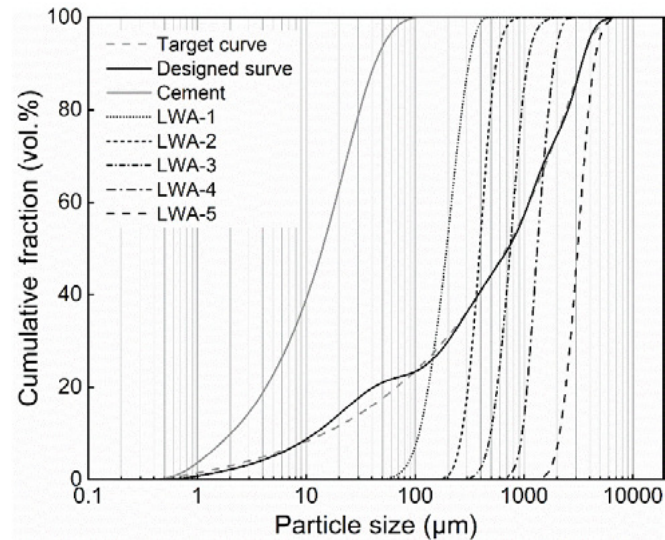


Figure 1: Particle size distributions (PSD) of the raw materials, the target curve and the resulting integral grading curve of the mixture.

Table 1. Chemical compositions of the cement and LWAs

Substances	Cement (mass %)	LWAs (mass %)
CaO	64.60	64.68 ± 2
SiO ₂	20.08	71 ± 2
Al ₂ O ₃	4.98	2 ± 0.3
Fe ₂ O ₃	3.24	0.5 ± 0.2
K ₂ O	0.53	1 ± 0.2
Na ₂ O	0.27	13 ± 1
SO ₃	3.13	-
MgO	1.98	2 ± 1
TiO ₂	0.30	-
Mn ₃ O ₄	0.10	-
P ₂ O ₅	0.74	-
Cl	0.05	<0.01



Figure 2: Appearance of lightweight aggregates (LWAs): expanded waste glass

Coir fibers are provided by the Wageningen University & Research (The Netherlands), shown in Figure 4. The chemical compositions of CFs are analyzed by a high performance anion exchange chromatography (HPAEC), given in Table 3. The bulk density is measured as the mass of coir fibers divided by their total bulk volume, and the specific density is tested by a Helium pycnometer (AccuPyc II 1340 Micromeritics). The bulk density and specific density of coir fibers are shown in Table 4.

Table 2. Physical properties of LWAs [37]

Materials size range	Bulk density	Specific density	Crushing resistance
(mm)	(kg/m ³)	(kg/m ³)	(N/mm ²)
LWA-1: 0.1-0.3	450	810	>3.5
LWA-2: 0.25-0.5	300	540	>2.9
LWA-3: 0.5-1.0	350	450	>2.6
LWA-4: 1.0-2.0	220	350	>2.4
LWA-5: 2.0-4.0	190	310	>2.2

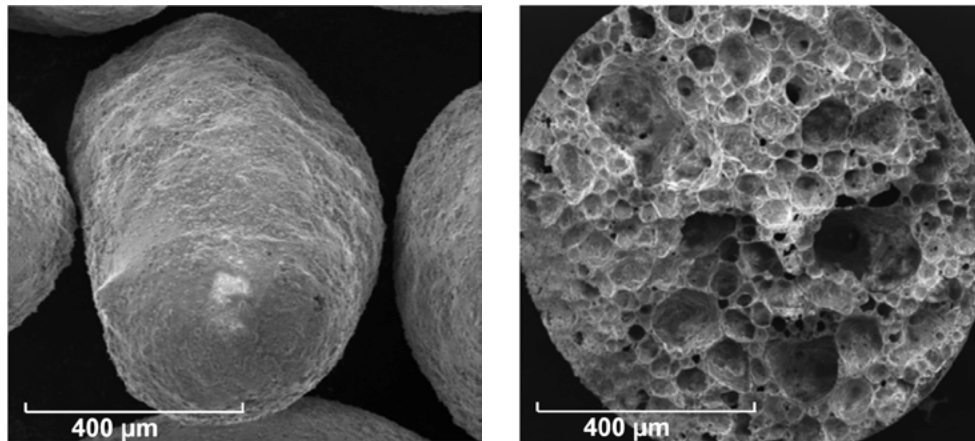


Figure 3: Microstructure of LWAs



Figure 4: Appearance of coir fibers

Table 3. Chemical compositions of coir fibers

Substances	Coir fibers (mass %)
Cellulose	36.6 ± 0.15
Hemicellulose	37.0 ± 0.15
Lignin	22.2 ± 0.05
Ash	1.9 ± 0.04
Extractive	5.7 ± 0.05

Table 4. Physical properties of coir fibers

Density (kg/m ³)	Coir fibers
Bulk density	69.8
Specific density	1539.6

2.2 Methods

2.2.1 Mixture design and mixing procedures

The mix proportions of LWAC are presented in Table 5. The mixtures of the LWAC are designed by applying the modified Andreasen and Andersen (A&A) packing model to optimize the granular packing of all solid materials [38]:

$$P(D) = \frac{D^q - D_{min}^q}{D_{max}^q - D_{min}^q} \quad (1)$$

where P(D) is the fraction of total solid materials with particle sizes lower than D (μm). D_{min} and D_{max} are the smallest and largest particle sizes (μm), which are 0.4 and 4000 μm, respectively. q is the distribution modulus, and a larger q results in a coarser mixture. In order to achieve a targeted strength as well as a low density of LWAC, a relatively large q is chosen as 0.35 for all mixtures. The PSDs of the target curve and the resulting integral grading curve (designed curve) of the mixture are shown in Figure 1.

Table 5. Mix proportions of LWAC (unit: kg/m³)

No.	C	LWA-1	LWA-2	LWA-3	LWA-4	LWA-5	W	SP	Coir fibers (wt.%)
F0 (Ref)	526.7	85.1	32.3	41.2	43.9	60.9	210.7	0.8	0.0%
F0.5	524.1	84.6	32.1	41.0	43.7	60.6	209.6	1.0	0.5%
F1.5	518.8	83.8	31.8	40.6	43.3	60.0	207.5	2.3	1.5%
F1.5-Ca	518.8	83.8	31.8	40.6	43.3	60.0	207.5	2.3	1.5%
F1.5-Si	518.8	83.8	31.8	40.6	43.3	60.0	207.5	2.3	1.5%
F3	510.9	82.5	31.3	40.0	42.6	59.1	204.4	4.1	3.0%

To avoid segregating without deteriorating the workability of the mixes, a water/cement ratio is fixed at 0.4. The dosages of coir fibers are 0.5%, 1.5%, and 3%, respectively, by weight of the concrete (including cement and LWAs). Meanwhile, a polycarboxylic ether based superplasticizer (SP) is adopted to adjust the workability of concrete, and all slumps of concrete are controlled under about 140 mm. According to the adopted fiber contents, the amounts of SP are 0.2%, 0.45%, 0.8% by weight of the cement to remedy the workability loss caused by adding fibers. For the reference mixture without fibers, the SP amount is used as 0.15%.

The mixing procedures are carried out as described below. Cement and LWAs are firstly put in a mixer for dry mixing about 1 min. Then around 75% water is gradually added and mixed with the cement and LWAs for about 2 min, meanwhile coir fibers are consistently fed. Subsequently, the remaining water mixed with SP is added and mixed for an additional 2 min. The fresh concrete are poured into the molds and vibrated for about 1 min with a vibration table, then its surface is covered with a plastic film. After the first 24 h, the samples are demolded and cured in a climate chamber at a temperature of 20 °C and a relative humidity of 95%, following EN 12390-2:2000.

2.2.2 Compressive properties

The compressive strength is measured under load control by an Autamax 5 Automatic tester, following EN 196-1. The loading speed used is 2400 N/s. Samples with a dimension of 40 x 40 x 40 mm³ are tested at the

ages of 3, 7 and 28 days. In total, six samples are measured at each age to obtain the average compressive strength.

2.2.3 Flexural properties

The flexural properties are measured under three-points bending combined with displacement control with an Instron 5967 universal testing machine, following the EN 196-1. The span support adopted is 100mm and the mid-span deflection rate applied is 0.5 mm/min. Samples with a dimension of 160 x 40 x 40 mm³ are tested at the ages of 3, 7 and 28 days. At least three samples are measured at each age for calculating the average flexural strength.

The flexural strength can be determined from the ultimate load:

$$\sigma = \frac{3FL}{2bh^2} \quad (3)$$

where F is the ultimate concentrated load, L is the span length; b and h are the width and height of samples.

The flexural toughness, expressing the energy absorption capacity of a material, can be calculated from the area under the load-deflection curves:

$$T_f = \int_0^{\delta_u} F(\delta) d\delta \quad (4)$$

where δ_u is the maximum deflection, generally about 10 mm in this study.

2.2.4 Drying and autogenous shrinkage

Both the drying and autogenous shrinkage tests are conducted on samples of 160 x 40 x 40 mm³. After 24 h sealed curing, the specimens are demolded for shrinkage tests and additionally, the specimens for autogenous shrinkage test are immediately sealed with a hydrophobic plastic film to avoid moisture loss. The zero-time of measurement is defined as the demolding time for both shrinkages. The initial length of all samples is straightway measured by a dial gauge, then the followed length is measured once per working day until 28 days and three times a week until 56 days. Totally, three specimens are tested to obtain the average values of the two shrinkages.

3. Results and discussion

3.1 Compressive strength

The compressive strength of LWAC is shown in Figure 5. The compressive strength of LWAC slightly increases by adding coir fibers, while decreases with the increased coir fiber content. The 28-day compressive strength of the reference sample is 19.0 MPa and those of mixtures with 0.5% and 1.5% coir fibers are 21.6 MPa and 19.8 MPa, respectively, corresponding to an approximately 14%, and 5% increase. This is because of the bridging effect of coir fibers. Coir fibers retard the cracks propagation and bridge the matrix from rupture under compression, thus a larger force are required for concrete failure [39]. However, when the coir content further increases to 3%, no improvement is observed in compressive strength. The explanations seem to be related to the mixing procedure, the porous structure of fibers and the introduced ITZs between fibers and matrix. More fibers tend to cause fiber agglomeration during mixing thus has a negative effect on the compaction and homogeneity of mixture [40], leading to reduced bonding between fibers and matrix, and increased flaws in the mixture. In addition, due to the cellular structure of coir fibers, a higher fiber content leads to larger porosity in the mixture. Moreover, more weak ITZs are introduced which are easily subject to failure. Finally, the combined action from these factors deteriorates the compressive strength of the mixture.

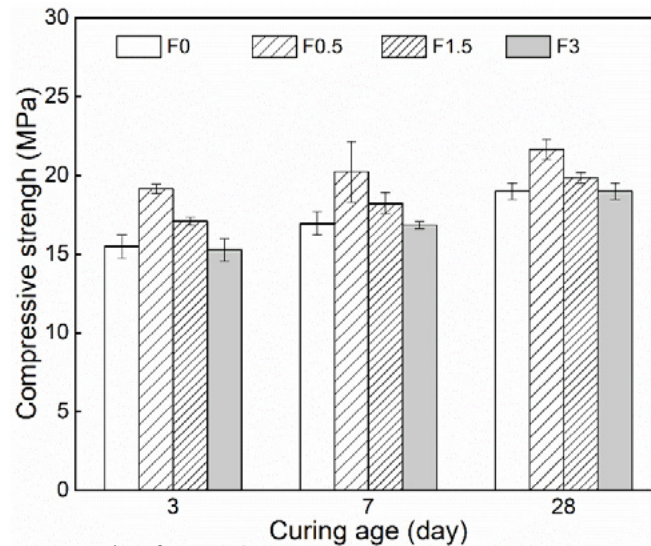


Figure 5: Compressive strength of LWAC

3.1 Flexural properties

The load–deflection curves are shown in Figure 6. The initial cracking strength significantly increases with improved fiber contents. After the initial cracking, a sharp drop in loads in all samples can be seen because of the reduced load-bearing capacities. Usually, a lower drop of loads occurs in the samples with a higher fiber content, while in the reference samples, the stress drops to zero directly. This is because of more active fibers, allowing improved tolerance to stress, thus higher residual strengths can be observed [41].

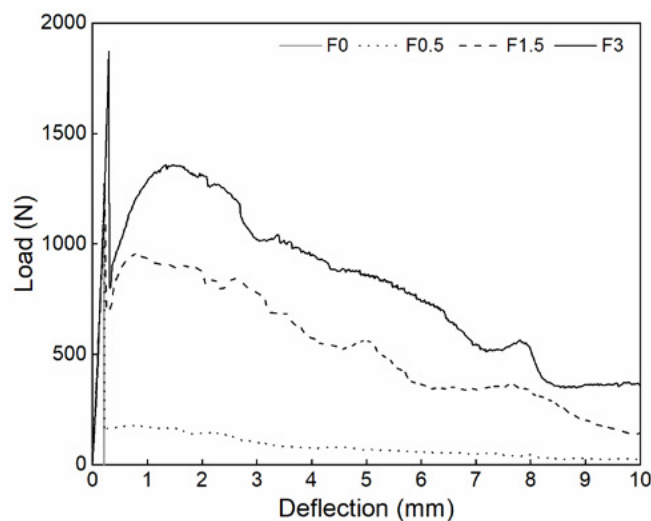


Figure 6: Average load–deflection curve of LWAC

The flexural strength of LWAC is shown in Figure 7. The flexural strength of LWAC significantly increases with an increased fiber content. The highest 28-day flexural strength of samples with 3% fibers is about 4 MPa, indicating an increase of about 70% as compared to the reference samples (2.6 MPa). The main explanation can be that a load applied can be transferred to coir fibers which are more tolerant to tension than cement matrix [42], and more fibers can bear a higher tensile stress for cement resulting in a higher flexural strength. The flexural strength of the samples with 1.5% fibers shows a negligible improvement compared to 0.5% fibers, since fibers can introduce additional defects into the matrix.

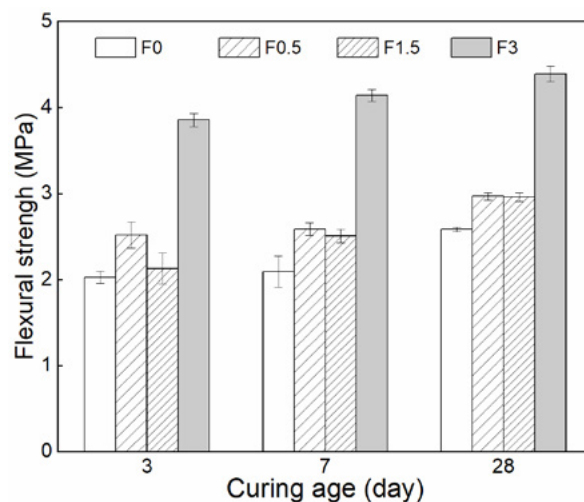


Figure 7: Flexural strength of LWAC

The flexural toughness of each mixtures is shown in Figure 8. The toughness is obviously enhanced by increasing the amount of fibers. The toughness of the sample with 3% fibers shows about 8 times increase than the reference sample. This is because the cracks extending acquires stretching, debonding and breaking of fibers [41,43], during which generates a considerable energy loss, contributing to increased fracture toughness.

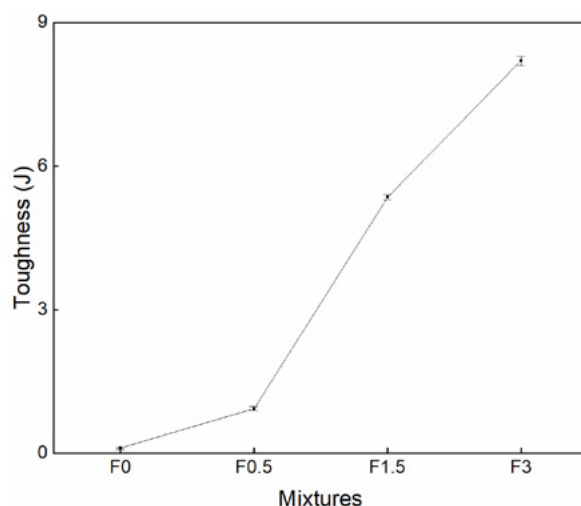


Figure 8: Flexural toughness curve of LWAC

3.2 Drying and autogenous shrinkages

Figure 9 shows the drying shrinkage development of concrete with coir fibers within 56 days. The drying shrinkage increases rapidly within the first two weeks, after which the growth of the shrinkage slows down since less water loss occurs in the later age. Moreover, the drying shrinkage notably rises by the increased fiber content. This behaviour can be firstly explained by the increased water introduced by more coir fibers in the system, which results in a higher amount of evaporated water loss, thus causing larger desiccative deformation. Another explanation is that coir fibers enlarge the porosity in the matrix and increase the connectivity of pores [44,45], which accelerates the drying process and consequently increases the drying shrinkage.

Figure 10 shows the autogenous shrinkage development in coir fibers reinforced concrete within 56 days. Most of the autogenous shrinkage is developed within the first week and then its intensity appears to

reduce because of subdued cement hydration. Coir fibers seem to result in a reduction in the autogenous shrinkage, and the increasing amount of fibers significantly decreases the autogenous shrinkage. This performance is due to the higher quantity of coir fibers contributing to sufficient internal curing water, which compensates for cement internal self-desiccation caused by chemical hydration [46]. As a result, a lower capillary pressure is induced, and thus less autogenous shrinkage is observable. Another reason is that fibers can sustain tensile strain and restrain cracking introduced by drying, and thus decrease the autogenous shrinkage of concrete. When the fiber content is set to 3%, the concrete exhibits a rapid expansion during the first day and continues showing a slight expansion during the whole period, therefore, the autogenous shrinkage of concrete is completely eliminated. This expansion is mostly because of the higher crystallization stress resulting from the increasing level of the oversaturated portlandite in solution caused by fiber leachates [47,48], which can entirely overwhelm the effect of self-desiccation resulting in almost no autogenous shrinkage. Therefore, when plenty of coir fibers are used, sufficient water can be introduced for internal curing in the cementitious matrix.

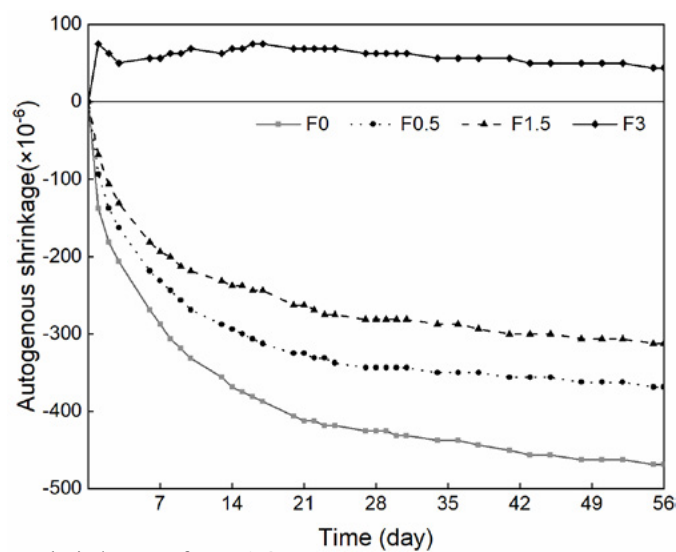


Figure 10: Autogenous shrinkage of LWAC

4. Conclusions

This paper presents the influences of coir fibers on the mechanical properties and shrinkages of cement-based LWAC. Based on the results obtained, the following conclusions can be drawn:

- The compressive strength of LWAC increases slightly by adding fibers but shows no improvement when the fiber fraction increases up to 3 %. This is caused by the porous structure of fibers and the more weak interfaces introduced by fibers.
- Both flexural strength and toughness increase significantly by increasing the fiber contents. It is resulting from the bridging effect of fibers, and more fibers in composite requires larger force and energy to develop cracks and to debond and break fibers.
- The drying shrinkage of concrete increases by increasing the coir fiber content. This is because of the extra water introduced by saturated fibers and improved connectivity of pores caused by porous fibers, resulting in accelerated drying process.
- The autogenous shrinkage markedly decreases as increasing fiber dosage. It is due to sufficient preserved water in fibers, providing internal curing for cement.
- When a sufficient content of coir fibers (i.e. in this study: 3 wt.%) is applied, fibers can be used for

internal curing.

5. Acknowledgment

This research was carried out under the fund of China Scholarship Council and Eindhoven University of Technology.

6. Reference

- [1] M. Davraz, M. Koru, A.E. Akdağ, The effect of physical properties on thermal conductivity of lightweight aggregate, *Procedia Earth Planet. Sci.* 15 (2015) 85–92.
- [2] H. Uysal, R. Demirboga, R. Şahin, R. Gül, The effects of different cement dosages, slumps, and pumice aggregate ratios on the thermal conductivity and density of concrete, *Cem. Concr. Res.* 34 (2004) 845–848.
- [3] M.E. Dilli, H.N. Atahan, C. Şengül, A comparison of strength and elastic properties between conventional and lightweight structural concretes designed with expanded clay aggregates, *Constr. Build. Mater.* 101 (2015) 260–267.
- [4] H.K. Kim, J.H. Jeon, H.K. Lee, Workability, and mechanical, acoustic and thermal properties of lightweight aggregate concrete with a high volume of entrained air, *Constr. Build. Mater.* 29 (2012) 193–200.
- [5] O. Sengul, S. Azizi, F. Karaosmanoglu, M.A. Tasdemir, Effect of expanded perlite on the mechanical properties and thermal conductivity of lightweight concrete, *Energy Build.* 43 (2011) 671–676.
- [6] O. Ünal, T. Uygunoğlu, A. Yildiz, Investigation of properties of low-strength lightweight concrete for thermal insulation, *Build. Environ.* 42 (2007) 584–590.
- [7] C. Tasdemir, O. Sengul, M.A. Tasdemir, A comparative study on the thermal conductivities and mechanical properties of lightweight concretes, *Energy Build.* 151 (2017) 469–475.
- [8] R. Demirboğa, Thermal conductivity and compressive strength of concrete incorporation with mineral admixtures, *Build. Environ.* 42 (2007) 2467–2471.
- [9] M.H. Zhang, L. Li, P. Paramasivam, Flexural toughness and impact resistance of steel-fibre-reinforced lightweight concrete, *Mag. Concr. Res.* 56 (2004) 251–262.
- [10] G. Zi, S. Kim, J. Choi, S. Hino, K. Yamaguchi, Influence of fiber reinforcement on strength and toughness of all-lightweight concrete, *Constr. Build. Mater.* 69 (2014) 381–389.
- [11] M. Chen, D. Law, M. Zhao, M. Zhao, J. Li, An experimental study on strength and toughness of steel fiber reinforced expanded-shale lightweight concrete, *Constr. Build. Mater.* 183 (2018) 493–501.
- [12] J. Li, J. Niu, C. Wan, X. Liu, Z. Jin, Comparison of flexural property between high performance polypropylene fiber reinforced lightweight aggregate concrete and steel fiber reinforced lightweight aggregate concrete, *Constr. Build. Mater.* 157 (2017) 729–736.
- [13] B. Chen, J. Liu, Contribution of hybrid fibers on the properties of the high-strength lightweight concrete having good workability, *Cem. Concr. Res.* 35 (2005) 913–917.
- [14] M.A. Aziz, P. Paramasivam, S.L. Lee, Prospects for natural fibre reinforced concretes in construction, *Int. J. Cem. Compos. Light. Concr.* 3 (1981) 123–132.

-
- [15] A.I. Al-mosawi, Natural Fiber as a substitute to Synthetic Fiber in Polymer Composites: A review, *Res. J. Eng. Sci.* 2(3) (2013) 46–53.
 - [16] S. Das, Life cycle assessment of carbon fiber-reinforced polymer composites, *Int. J. Life Cycle Assess.* 16 (2011) 268–282.
 - [17] S. Guler, The effect of polyamide fibers on the strength and toughness properties of structural lightweight aggregate concrete, *Constr. Build. Mater.* 173 (2018) 394–402.
 - [18] A.K. Mohanty, M. Misra, G. Hinrichsen, Biofibres, biodegradable polymers and biocomposites: An overview, *Macromol. Mater. Eng.* 276–277 (2000) 1–24.
 - [19] R. Dungani, M. Karina, Subyakto, A. Sulaeman, D. Hermawan, A. Hadiyane, Agricultural waste fibers towards sustainability and advanced utilization: A review, *Asian J. Plant Sci.* 15 (2016) 42–55.
 - [20] L.Y. Mwaikambo, Review of the history, properties and application of plant fibres, *African J. Sci. Technol.* 7 (2006) 120–133.
 - [21] A. Kicińska-Jakubowska, E. Bogacz, M. Zimniewska, Review of natural fibers. Part I-vegetable fibers, *J. Nat. Fibers.* 9 (2012) 150–167.
 - [22] R. wood Chang Hong, A Review on natural fibre-based Composites-Part I: structure, processing and properties of vegetable fibres, *J. Nat. Fibers.* 1 (2004) 37–41.
 - [23] S. Mukhopadhyay, S. Khatana, A review on the use of fibers in reinforced cementitious concrete, *J. Ind. Text.* 45 (2015) 239–264.
 - [24] C.A. Juarez, G. Fajardo, S. Monroy, A. Duran-Herrera, P. Valdez, C. Magniont, Comparative study between natural and PVA fibers to reduce plastic shrinkage cracking in cement-based composite, *Constr. Build. Mater.* 91 (2015) 164–170.
 - [25] P. Wambua, J. Ivens, I. Verpoest, Natural fibres: Can they replace glass in fibre reinforced plastics?, *Compos. Sci. Technol.* 63 (2003) 1259–1264.
 - [26] <http://www.naturalfibres2009.org/en/fibres/coir.html>, (n.d.).
 - [27] A. Komuraiah, N.S. Kumar, B.D. Prasad, Chemical composition of natural fibers and its influence on their mechanical properties, *Mech. Compos. Mater.* 50 (2014) 359–376.
 - [28] T.H. Nam, S. Ogihara, N.H. Tung, S. Kobayashi, Effect of alkali treatment on interfacial and mechanical properties of coir fiber reinforced poly(butylene succinate) biodegradable composites, *Compos. Part B Eng.* 42 (2011) 1648–1656.
 - [29] C. Hwang, V. Tran, J. Hong, Y. Hsieh, Effects of short coconut fiber on the mechanical properties, plastic cracking behavior, and impact resistance of cementitious composites, *Constr. Build. Mater.* 127 (2016) 984–992.
 - [30] M. Ali, A. Liu, H. Sou, N. Chouw, Mechanical and dynamic properties of coconut fibre reinforced concrete, *Constr. Build. Mater.* 30 (2012) 814–825.
 - [31] Z. Li, L. Wang, X. Wang, Flexural characteristics of coir fiber reinforced cementitious composites, *Fibers Polym.* 7 (2006) 286–294.
 - [32] V.M. John, M.A. Cincotto, C. Sjöström, V. Agopyan, C.T.A. Oliveira, Durability of slag mortar

reinforced with coconut fibre, *Cem. Concr. Compos.* 27 (2005) 565–574.

[33] B. Taallah, A. Guettala, The mechanical and physical properties of compressed earth block stabilized with lime and filled with untreated and alkali-treated date palm fibers, *Constr. Build. Mater.* 104 (2016) 52–62.

[34] V. Caprai, F. Gauvin, K. Schollbach, H.J.H. Brouwers, Influence of the spruce strands hygroscopic behaviour on the performances of wood-cement composites, *Constr. Build. Mater.* 166 (2018) 522–530.

[35] P. Jongvisuttisun, J. Leisen, K.E. Kurtis, Key mechanisms controlling internal curing performance of natural fibers, *Cem. Concr. Res.* 107 (2018) 206–220.

[36] V. Zanjani Zadeh, C.P. Bobko, Nano-mechanical properties of internally cured kenaf fiber reinforced concrete using nanoindentation, *Cem. Concr. Compos.* 52 (2014) 9–17.

[37] Q.L. Yu, P. Spiesz, H.J.H. Brouwers, Ultra-lightweight concrete: Conceptual design and performance evaluation, *Cem. Concr. Compos.* 61 (2015) 18–28.

[38] H.J.H. Brouwers, Packing fraction of particles with lognormal size distribution, 052211 (2014) 1–12.

[39] S. Yin, R. Tuladhar, F. Shi, M. Combe, T. Collister, N. Sivakugan, Use of macro plastic fibres in concrete : A review, *Constr. Build. Mater.* 93 (2015) 180–188.

[40] A.M. Brandt, Fibre reinforced cement-based (FRC) composites after over 40 years of development in building and civil engineering, *Compos. Struct.* 86 (2008) 3–9.

[41] H. Unwerstty, Models of fiber debonding and pullout in brittle composites with friction, *Mechanics Mater.* 9 (1990) 139–163.

[42] C.X. Qian, P. Stroeven, Development of hybrid polypropylene-steel fibre-reinforced concrete, *Cem. Concr. Res.* 30 (2000) 63–69.

[43] C. Marotzke, L. Qiao, Interfacial crack propagation arising in siger-fiber pull-out tests, *Compos. Sci. Technol.* 57 (1997) 887–897.

[44] L.C. Roma, L.S. Martello, H. Savastano, Evaluation of mechanical, physical and thermal performance of cement-based tiles reinforced with vegetable fibers, *Constr. Build. Mater.* 22 (2008) 668–674.

[45] F. de A. Silva, R.D.T. Filho, J. de A.M. Filho, E. de M.R. Fairbairn, Physical and mechanical properties of durable sisal fiber-cement composites, *Constr. Build. Mater.* 24 (2010) 777–785.

[46] D.P. Bentz, O.M. Jensen, Mitigation strategies for autogenous shrinkage cracking, *Cem. Concr. Compos.* 26 (2004) 677–685.

[47] O.M. Jensen, P.F. Hansen, Water-entrained cement-based materials II. Experimental observation, *Cem. Concr. Res.* 32 (2002) 973–978.

[48] O.M. Jensen, P.F. Hansen, Water-entrained cement-based materials I. Principles and theoretical background, *Cem. Concr. Res.* 31 (2001) 647–654.

Super-hydrophobic magnesium oxychloride cement (MOC): from structural control to self-cleaning property evaluation

Z.Y. Qu^{1,2*}, F.Z. Wang¹, Q.L. Yu², H.J.H. Brouwers^{1,2}

¹State Key Laboratory of Silicate Materials for Architectures, Wuhan University of Technology, Wuhan 430070, PR China

²Department of the Built Environment, Eindhoven University of Technology, P.O. Box 513, 5600 MB Eindhoven,

Abstract

We report our study on designing a super hydrophobic magnesium oxychloride cement (MOC), applying a facile method involving immersion in a fluoroalkylsilane (FAS) -ethanol solution. We evaluate the super hydrophobicity and self-cleaning property of the new material and correlate them with the structural characteristics of the raw materials. The phase compositions, microstructure, compressive strength, water resistance and wetting behaviour are studied in detail by using X-Ray diffraction (XRD), scanning electron microscopy (SEM), a water contact angle measurement instrument, and mechanical testing. We observe a very high water contact angle of the as-prepared MOC up to about $152\pm1^\circ$, and we explain the derivation of water contact angle with the Cassie-Baxter model. The experiments using rolling off dust on the super hydrophobic surface present excellent self-cleaning ability. Moreover, the super hydrophobic surface presents excellent UV-durability, indicating a promising potential for outdoor application..

Keywords: Magnesium oxychloride cement, super hydrophobic, UV-durable, water-resistance, self-cleaning.

1. Introduction

Magnesium oxychloride cement (MOC) is a promising material thanks to its excellent materials properties such as fast setting, high mechanical strength, good resistance to abrasion and fire [1–5]. The behavior of MOC is mainly regulated by the composition and microstructure of the hydration products, produced through neutralization-hydrolysis-crystallization process in the ternary system of $\text{MgO-MgCl}_2\text{-H}_2\text{O}$ [2,6]. $\text{Mg}(\text{OH})_2\cdot\text{MgCl}_2\cdot 8\text{H}_2\text{O}$, or widely recognized as Phase 5 (P5), has been commonly recognized as the most desirable reaction product in MOC-based composites, as it is believed that the Phase 5 crystals can provide the best mechanical properties [3,5,6].

However, when exposed to water, Phase 5 will be easily decomposed to $\text{Mg}(\text{OH})_2$ that leads to a poor water resistance, which seriously restricts its outdoor applications. Preventing the water penetration by generating super-hydrophobic surfaces has already led to various new hybrid materials with astonishing properties [10–12]. A surface can be described as super hydrophobic if the contact angle (CA) of water on this surface is larger than 150° [13,14]. The best known example of super hydrophobic surface is the lotus leaf, on which water easily rolls off, leaving little or no residue and carrying away surface contamination, showing excellent self-cleaning properties [10,15]. Scanning electron microscopy (SEM) analysis shows that the surface of lotus leaves possesses protruding nubs of 20–40 μm apart each covered with a smaller

scale rough of epicuticular wax crystalloids [12]. This wax only consists of $-C-H$ and $-C-O$ group, which are the origin of the super hydrophobicity and self-cleaning property of the lotus leaf. Since Tsujii et al. first fabricated biomimetic surfaces in the mid-1990s, numerous smart and efficient methods for attaining rough surfaces to prepare super hydrophobic surface have been reported [12,16–18]. In summary, there are two main kinds of surface microstructures to prepare super hydrophobic surface: one is the hierarchical micro- and nanostructure like the lotus leaf and the other one is the unitary micro-line structure like the ramee leaf [19–22].

Considering the complexity of the preparation of micro-, nano-, and lotus-type micro-/ nanocomposite structures, unitary micro-line structure provides a facile solution to prepare super hydrophobic surfaces [13,23]. Ogawa et al. prepared super hydrophobic film-coated nano-fibrous membranes based on the inspiration of self-cleaning silver ragwort leaves [23]. After the modification with fluoroalkylsilane (FAS), the surface of the nano-fibrous membrane presented super hydrophobicity with the highest water contact angle of 162° and the lowest water-roll angle of 2° [23]. Li et al. reported a simple solution-immersion method to fabricate a super hydrophobic surface on a cellulose-based material (i.e. cotton fabric or paper) [24]. The surface morphology of the fabric provided ideal roughness for trapping the air to build a super hydrophobic surface [24]. Jiang et al. prepared $Cu(OH)_2$ nano-needle arrays presenting little contact-angle hysteresis, even under certain hydrostatic pressures, by a facile chemical-base deposition method [25]. The average length of the needles is $5\text{ }\mu\text{m}$ and the average diameter of the nano-needle is 300 nm [25]. The above results also inspired us to prepare super-hydrophobic and self-cleaning surface by taking advantages of the native needle structure of MOC. Until now, research about construction of superhydrophobic surface on MOC is still limited.

We aim to propose a novel and facile method for the fabrication of super hydrophobic surface on MOC by applying the unique needle-like structure Phase 5 of MOC. The compressive strength and water resistance of the MOC samples are studied. The phase composition and microstructural properties were determined by using X-ray diffraction (XRD) and scanning electron microscopy (SEM). The water-repellence ability was evaluated by performing the water contact angle and water sliding angle tests. As UV-durability property is crucial for practical outdoor use, which mainly depends on the surface chemical composition and surface structures, UV-durability of the as prepared surface was also examined. The results show that the designed super MOC surface possesses a super hydrophobic property, together with an excellent water-repellence and self-cleaning ability.

2. Methodology

2.1 Materials

We use the following raw materials to prepare the MOC cement paste: light-burnt magnesia powder (MgO), magnesium chloride hexahydrate ($MgCl_2 \cdot 6H_2O$), and tap water. Triethoxy-1H,1H,2H,2H-tridecafluoro-n-octylsilane (FAS) and Ethanol is used to prepare a FAS-ethanol solution. The MOC samples are prepared by mixing MgO and the $MgCl_2 \cdot 6H_2O$ solution (see Table 1). Based on the mixed recipe, the samples are designated as MOC-510 (Mixture 1), MOC-68 (Mixture 2) and MOC-610 (Mixture 3). The samples are prepared following EN 196-1 [26] and cast in cubic moulds with dimensions of $40 \times 40 \times 40\text{ mm}^3$ to determine the compressive strength. For the preparation of superhydrophobic MOC, after 48 hours' curing in the air, the MOC products are then placed in a FAS ethanol solution (5%) for 24 hours at room temperature and then dried for 1 hour.

2.2 Methods

The XRD analysis is performed by using a Bruker D8 advance powder X-ray diffractometer with a Cu tube

(20 kV, 30 mA) with a scanning range from 5° to 65° (2θ), applying a step 0.02° and 0.2 s/step measuring time. A contact angle meter DataPhysics SCA20 (DataPhysics Germany) is used to measure the static water contact angle and sliding angle with 10 µl water drop at the ambient temperature. The morphologies of the MOC are observed using a field emission scanning electron microscopy (FESEM) of Quanta 450 (FEI USA). The UV durability test under different environmental conditions is performed in a homemade set-up. MOC boards with the dimension of 20 cm × 10 cm × 5 cm are prepared for the UV durability test which fit the size of our reactor. The UVA light intensity E is kept constant at 14 W/m² which is close to outdoor conditions during the summer [27].

3. Results and discussion

The XRD patterns of the MOCs show that the mineralogical phases consist of major Phase 5, minor Mg(OH)₂ and unreacted MgO and MgCO₃ (Fig. 1). As the Phase 5 is the most favourable crystalline phase [3,6], the molar ratio of MgO/MgCl₂ is desired to be higher than 5 and the molar ratio of H₂O/ MgCl₂ is in the range of 6-15. The MgCO₃ is from the carbonation during the preparation process. It can be found that MOC-510 exhibits the weakest characteristic peaks of unreacted MgO in the paste matrices, because of the lower molar ratio of MgO/MgCl₂.

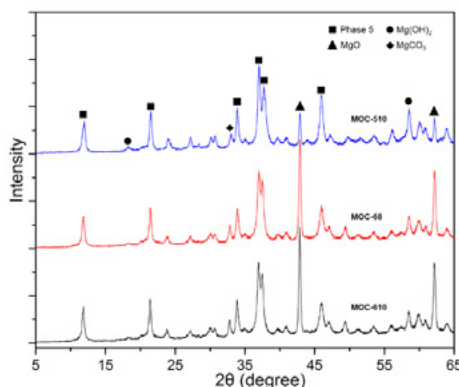


Fig. 1. XRD patterns of the MOCs at 28 days.

The SEM images (Fig. 2) show that all the samples present a composite structure consisting of needle-like Phase 5 and gel-like Phase 5.

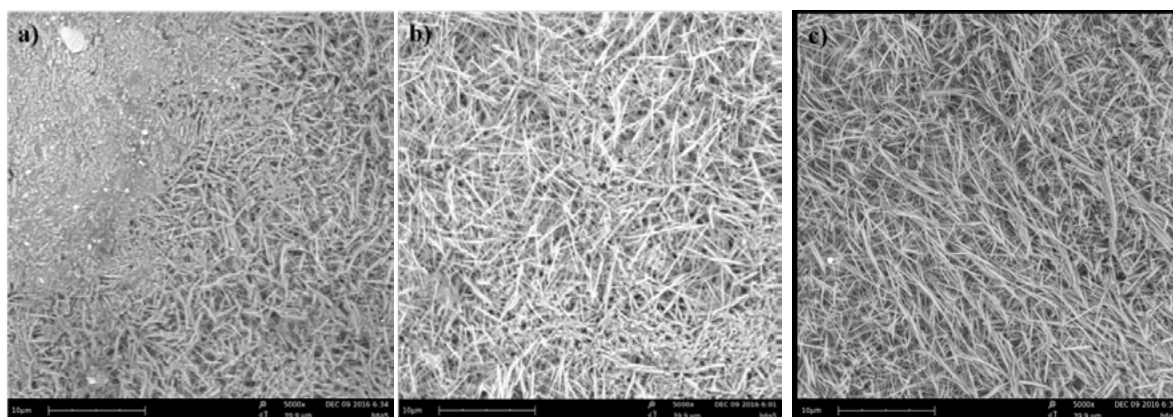


Fig. 2. SEM images of paste matrices of: (a) MOC-510, (b) MOC-68, (c) MOC-610.

It can be seen that MOC-510 presents more gel-like Phase 5 compared to the other two samples. This can be attributed to the smaller amount of MgO in the reaction system. As stated in [3] and [6], MgO could act as a role of reaction seeds, which in turn increase the reaction sites in the MOC hydrated process. So

less MgO seeds would increase the possibility of group growth of the MOC, which leads to more gel-like Phase 5. MOC-610 exhibits more needle-like Phase 5 than MOC-68 as shown in Fig. 2b and Fig. 2c, which is attributed to the lower MgCl₂ concentration in MOC-610.

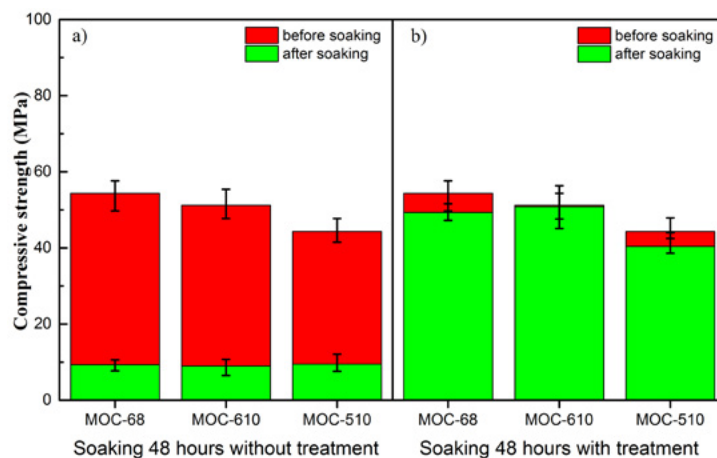


Fig. 3. Comparison between compressive strength of the MOCs before and after 48 hours' soaking: a) without FAS treatment and b) with FAS treatment.

The water resistance improvement of MOC after super hydrophobic modification can be seen from the compressive strength changes after soaking the samples for 48 hours (see Fig. 3). The retention of compressive strengths of unmodified MOC-68, MOC-610 and MOC-510 are only 17.1%, 17.6% and 21.4%, respectively, caused by the decomposition of the hydration products into Mg(OH)₂ [6][30]. It should be noted that the compressive strength retention of MOC-510 is higher than the other two samples, attributed to its more gel-like Phase 5. Owing to the super hydrophobicity, all of the MOC samples have a much higher compressive strength retention than the unmodified samples. The compressive strength retentions of MOC 68, MOC-610 and MOC-510 after soaking 48 hours are 91.3%, 99% and 91.2%, respectively, indicating the hydrophobic treatment is highly effective to improve the water resistance of MOC.

All unmodified MOC samples present high hydrophilic property and the water drop penetrate inside the MOC sample very quickly and no water contact angles were able to be tested. After FAS modification, as shown in Fig. 4a, the MOC-510 has a water contact angle about 130°, indicating a hydrophobic property [12,13]. After the increase of the MgO content, the CA of the MOC-610 increased to about 152°, indicating that the MOC surface becomes super hydrophobic. On the contrary, the water repellence of MOC-68 decreases and the CA decreases to about 143° after decreasing the amount of MgO. The change of the surface microstructures (Fig. 2(a–c)) was responsible for the increase of CA. This can be explained by the ideal Young equation [27,31,32] and the Cassie-Baxter equation [33,34]. A rougher surface will lead to a larger contact angle and more hydrophobic behaviour [33,34]. When gel-like Phase 5 is generated among the needle-like structure, it will fill in the interspace that in turn decreases the air amount for air trapping. This can be used to explain the decrease of super hydrophobic ability from MOC-610 to MOC-510 as the amount gel-like Phase 5 increases.

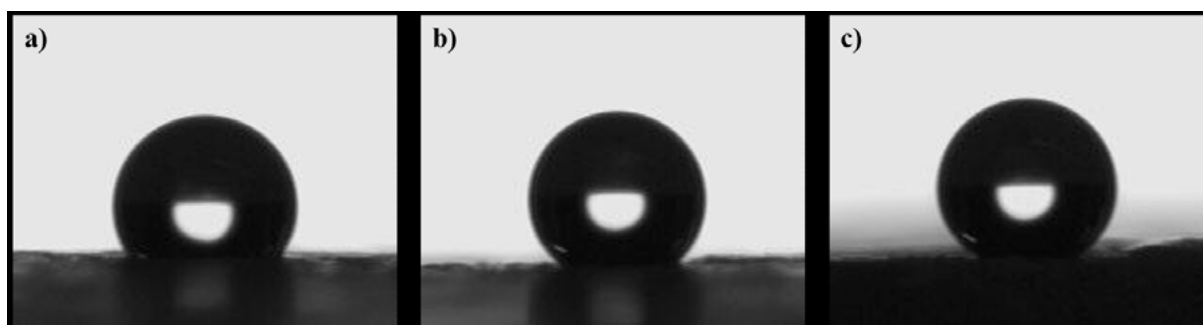


Fig. 4. Water contact angle of: (a) the MOC-510, $130^{\circ} \pm 1^{\circ}$. (b) the MOC-68, $143^{\circ} \pm 1^{\circ}$. (c) the MOC-610, $152^{\circ} \pm 1^{\circ}$.

Barthlott et al. reported that water droplets can roll off from the lotus leaves and remove the dust particles [35]. As MOC products are often used for a decorative purpose (e.g. decoration boards), it will be very meaningful for MOC possessing the self-cleaning ability. Fig. 5a shows the results of rolling water on the super hydrophobic MOC surface (MOC-610). UV-resistivity is crucial for practical outdoor applications, which mainly depends on the surface chemical composition and surface structures [36–38]. The static contact angle and sliding angle as a function of UV-irradiation time are presented in Fig. 5c. It is shown that after 7 days' UV irradiation, the surface still exhibits a contact angle of 152.1° and a sliding angle of 8° at 25°C and 50% humidity and a contact angle of 152.8° and a sliding angle of 9° at higher temperature. Even under a higher humidity, the MOC surface presents a contact angle of 152.3° and a sliding angle of 8° , suggesting a superior UV-durability. This can be attributed to both the properties of the MOC and the low surface energy of FAS.

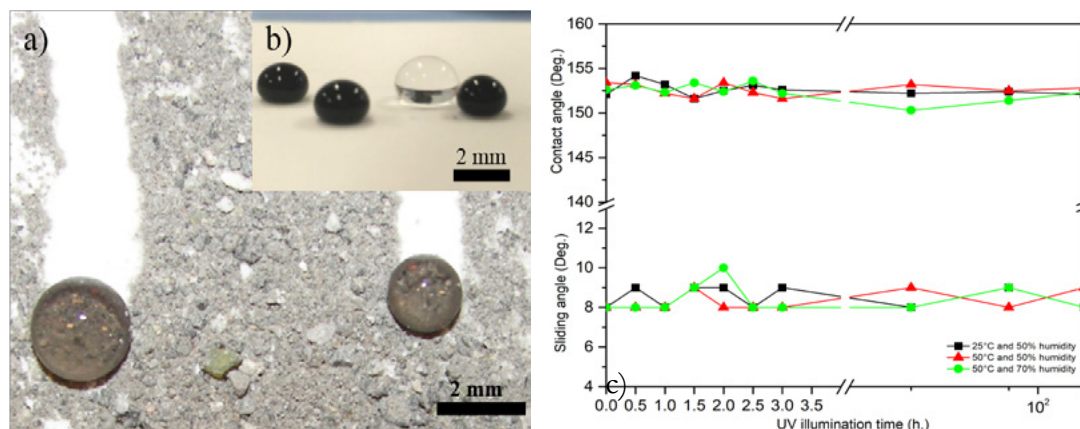


Fig. 5. Assessment of the hydrophobicity and self-cleaning ability by: (a) the rolling of particles, and (b) blue ink and water drops on the sample surface; and (c) Contact angle and sliding angle of MOC-68 samples over UV-irradiation time under different environmental conditions.

4. Conclusions

A super hydrophobic MOC surface with excellent self-cleaning ability is fabricated applying a facile solution immersion method with FAS. The influences of the molar ratio on the microstructures, compressive strength, water resistance and hydrophobic performance are investigated. The self-cleaning ability and UV-durability are characterized. Through the control of the MgO/MgCl_2 and $\text{H}_2\text{O}/\text{MgCl}_2$ molar ratios, MOC samples with different microstructures are acquired. From the XRD and SEM results, it can be concluded that MOC-510 exhibits a higher amount of gel-like Phase 5 and MOC-610 presents a higher amount of nano-needle like Phase 5. The hydrophobic treatment improves the water resistance of the MOC samples. The compressive strength retentions after 48 hours' water soaking of MOC-510, MOC-68 and MOC-610 are only 17.1%, 17.6% and 21.4%, respectively, before the modification by FAS. However,

the compressive strength retentions increase to 91.3%, 99% and 91.2%, respectively, after the hydrophobic treatment. Owing to the large amount of nano-needle like Phase 5 structures, MOC-610 is found to be the optimum recipe for the super hydrophobic surface fabrication, having a water contact angle of $152^{\circ} \pm 1^{\circ}$. The prepared super hydrophobic surface presents an excellent self-cleaning ability. Moreover, the super hydrophobic MOC surface is highly durable under UV irradiation.

5. Acknowledgment

The authors would like to acknowledge the financial support by STW-foundation and the EPSRC-NSFC Joint Research Project (No. 51461135005) for funding this research. Mrs. A.C.A. Delsing in the lab of Building Physics and Services at Eindhoven University of Technology is acknowledged for providing experimental support on the SEM analysis.

6. References

- [1] B. Xu, H. Ma, C. Hu, S. Yang, Z. Li, Influence of curing regimes on mechanical properties of magnesium oxychloride cement-based composites, *Constr. Build. Mater.* 102 (2016) 613–619.
- [2] D. Dehua, Z. Chuanmei, The formation mechanism of the hydrate phases in magnesium oxychloride cement, *Cem. Concr. Res.* 29 (1999) 1365–1371.
- [3] Z. Li, C.K. Chau, Influence of molar ratios on properties of magnesium oxychloride cement, *Cem. Concr. Res.* 37 (2007) 866–870.
- [4] Z. Liu, M. Balonis, J. Huang, A. Sha, G. Sant, The influence of composition and temperature on hydrated phase assemblages in magnesium oxychloride cements, *J. Am. Ceram. Soc.* 100 (2017) 3246–3261.
- [5] Z. Liu, S. Wang, J. Huang, Z. Wei, B. Guan, J. Fang, Experimental investigation on the properties and microstructure of magnesium oxychloride cement prepared with caustic magnesite and dolomite, *Constr. Build. Mater.* 85 (2015) 247–255.
- [6] Y. Li, Z. Li, H. Pei, H. Yu, The influence of FeSO_4 and KH_2PO_4 on the performance of magnesium oxychloride cement, *Constr. Build. Mater.* 102 (2016) 233–238.
- [7] C.K. Chau, J. Chan, Z. Li, Influences of fly ash on magnesium oxychloride mortar, *Cem. Concr. Compos.* 31 (2009) 250–254.
- [8] D. Deng, The mechanism for soluble phosphates to improve the water resistance of magnesium oxychloride cement, *Cem. Concr. Res.* 33 (2003) 1311–1317.
- [9] C. Li, H. Yu, Influence of fly ash and silica fume on water-resistant property of magnesium oxychloride cement, *J. Wuhan Univ. Technol. Sci. Ed.* 25 (2010) 721–724.
- [10] S. Grumbein, D. Minev, M. Tallawi, K. Boettcher, F. Prade, F. Pfeiffer, C.U. Grosse, O. Lieleg, Hydrophobic Properties of Biofilm-Enriched Hybrid Mortar, *Adv. Mater.* 28 (2016) 8138–8143.
- [11] P.A. Levkin, F. Svec, J.M.J. Fréchet, Porous polymer coatings: a versatile approach to superhydrophobic surfaces, *Adv. Funct. Mater.* 19 (2009) 1993–1998.
- [12] Z. Guo, W. Liu, B.-L. Su, Superhydrophobic surfaces: from natural to biomimetic to functional, *J. Colloid Interface Sci.* 353 (2011) 335–355.
- [13] L. Jiang, Y. Zhao, J. Zhai, A lotus-leaf-like superhydrophobic surface: a porous microsphere/nanofiber composite film prepared by electrohydrodynamics, *Angew. Chemie.* 116 (2004) 4438–4441.

- [14] H.Y. Erbil, A.L. Demirel, Y. Avci, O. Mert, Transformation of a simple plastic into a superhydrophobic surface, *Science* (80-.). 299 (2003) 1377–1380.
- [15] A.V. Rao, M.M. Kulkarni, S.D. Bhagat, Transport of liquids using superhydrophobic aerogels, *J. Colloid Interface Sci.* 285 (2005) 413–418.
- [16] E. Celia, T. Darmanin, E.T. de Givenchy, S. Amigoni, F. Guittard, Recent advances in designing superhydrophobic surfaces, *J. Colloid Interface Sci.* 402 (2013) 1–18.
- [17] M. Horgnies, J.J. Chen, Superhydrophobic concrete surfaces with integrated microtexture, *Cem. Concr. Compos.* 52 (2014) 81–90.
- [18] I. Flores-Vivian, V. Hejazi, M.I. Kozhukhova, M. Nosonovsky, K. Sobolev, Self-assembling particle-siloxane coatings for superhydrophobic concrete, *ACS Appl. Mater. Interfaces.* 5 (2013) 13284–13294.
- [19] Z. Guo, W. Liu, Biomimic from the superhydrophobic plant leaves in nature: Binary structure and unitary structure, *Plant Sci.* 172 (2007) 1103–1112.
- [20] M. Nosonovsky, B. Bhushan, Biomimetic superhydrophobic surfaces: multiscale approach, *Nano Lett.* 7 (2007) 2633–2637.
- [21] J.-Y. Shiu, C.-W. Kuo, P. Chen, C.-Y. Mou, Fabrication of tunable superhydrophobic surfaces by nanosphere lithography, *Chem. Mater.* 16 (2004) 561–564.
- [22] J.B. Boreyko, C.-H. Chen, Self-propelled dropwise condensate on superhydrophobic surfaces, *Phys. Rev. Lett.* 103 (2009) 184501.
- [23] T. Ogawa, B. Ding, Y. Sone, S. Shiratori, Super-hydrophobic surfaces of layer-by-layer structured film-coated electrospun nanofibrous membranes, *Nanotechnology.* 18 (2007) 165607.
- [24] S. Li, S. Zhang, X. Wang, Fabrication of superhydrophobic cellulose-based materials through a solution-immersion process, *Langmuir.* 24 (2008) 5585–5590.
- [25] X. Yao, Q. Chen, L. Xu, Q. Li, Y. Song, X. Gao, D. Quéré, L. Jiang, Bioinspired ribbed nanoneedles with robust superhydrophobicity, *Adv. Funct. Mater.* 20 (2010) 656–662.
- [26] T.S. EN, 196-1, *Methods Test. Cem.* 1 (2006).
- [27] X. Zhang, F. Shi, J. Niu, Y. Jiang, Z. Wang, Superhydrophobic surfaces: from structural control to functional application, *J. Mater. Chem.* 18 (2008) 621–633.
- [28] D. Dehua, Z. Chuanmei, The effect of aluminate minerals on the phases in magnesium oxychloride cement, *Cem. Concr. Res.* 26 (1996) 1203–1211.
- [29] Y. Li, H. Yu, L. Zheng, J. Wen, C. Wu, Y. Tan, Compressive strength of fly ash magnesium oxychloride cement containing granite wastes, *Constr. Build. Mater.* 38 (2013) 1–7.
- [30] J.J. Beaudoin, V.S. Ramachandran, Strength development in magnesium oxychloride and other cements, *Cem. Concr. Res.* 5 (1975) 617–630.
- [31] W. Li, A. Amirfazli, Hierarchical structures for natural superhydrophobic surfaces, *Soft Matter.* 4 (2008) 462–466.
- [32] F. Dong, M. Zhang, W.-W. Tang, Y. Wang, Formation and mechanism of superhydrophobic/hydrophobic surfaces made from amphiphiles through droplet-mediated evaporation-induced self-assembly,

J. Phys. Chem. B. 119 (2015) 5321–5327.

[33] A. Marmur, Wetting on hydrophobic rough surfaces: to be heterogeneous or not to be?, *Langmuir*. 19 (2003) 8343–8348.

[34] A. Marmur, The lotus effect: superhydrophobicity and metastability, *Langmuir*. 20 (2004) 3517–3519.

[35] C. Neinhuis, W. Barthlott, Characterization and distribution of water-repellent, self-cleaning plant surfaces, *Ann. Bot.* 79 (1997) 667–677.

[36] N. Wang, D. Xiong, Y. Deng, Y. Shi, K. Wang, Mechanically robust superhydrophobic steel surface with anti-icing, UV-durability, and corrosion resistance properties, *ACS Appl. Mater. Interfaces*. 7 (2015) 6260–6272.

[37] M. Manca, A. Cannavale, L. De Marco, A.S. Arico, R. Cingolani, G. Gigli, Durable superhydrophobic and antireflective surfaces by trimethylsilanized silica nanoparticles-based sol–gel processing, *Langmuir*. 25 (2009) 6357–6362.

[38] T. Verho, C. Bower, P. Andrew, S. Franssila, O. Ikkala, R.H.A. Ras, Mechanically durable superhydrophobic surfaces, *Adv. Mater.* 23 (2011) 673–678.

[39] M. Miwa, A. Nakajima, A. Fujishima, K. Hashimoto, T. Watanabe, Effects of the surface roughness on sliding angles of water droplets on superhydrophobic surfaces, *Langmuir*. 16 (2000) 5754–5760.

[40] R. Furstner, W. Barthlott, C. Neinhuis, P. Walzel, Wetting and self-cleaning properties of artificial superhydrophobic surfaces, *Langmuir*. 21 (2005) 956–961.

Durability of photocatalytic mortars

A.M. Kaja¹, H.J.H. Brouwers¹, Q.L. Yu¹

¹Department of the Built Environment, Eindhoven, University of Technology Eindhoven, 5600 MB, the Netherlands.

Abstract

Photocatalytic technology attracts great attention due to the increasing need to improve air quality, especially in highly polluted urban areas. Concrete is found to be an excellent substrate for photocatalytic processes due to its high availability and exposure of large surfaces to solar irradiation. The presence of semiconductors in the concrete surface layer induces the oxidation of air pollutants. For example, NO and NO₂ can be photocatalytically oxidized to nitrates, which are later removed from the concrete surface with rainwater. Among the available semiconductors, titania is the most commonly used. TiO₂ nanoparticles can be either coated on the concrete surface or intermixed with cement in concrete surface layer. Simple coating, however, does not result in sufficient durability. On the other hand, even if titania is intermixed with cement, some durability aspects like carbonation cannot be avoided. This study aims to evaluate the impact of carbonation on the photocatalytic efficiency of white cement-based photocatalytic mortars doped with three types of titania photocatalysts (Aeroxide TiO₂ P25, KRONOcLean 7000 carbon doped titania, and one home-synthesized composite photocatalyst consisting of 85% of SiO₂ and 15% of TiO₂). The study revealed that the oxidation of the pollutants by photocatalytic mortars dramatically depends on the type of photocatalyst. Silica-titania composite exhibits equally high performance as P25 providing the alternative route for the costs reduction during the manufacture of photocatalytic concrete. Upon carbonation, a drastic decrease of photocatalytic efficiency occurs regardless of the type of photocatalysts used. This effect is intensified when photocatalyst forms agglomerates. The selectivity of the photocatalytic reaction is also lowered after carbonation.

Keywords: Photocatalytic mortar, carbonation, photocatalytic efficiency, selectivity.

Self-cleaning and air purification performance of Portland cement paste with low dosage of nanodispersed TiO₂ coatings

Z. Wang^{1,2*}, F. Gauvin², P. Feng¹, H.J.H. Brouwers², Q.L. Yu²

¹ School of Materials Science and Engineering, Southeast University, Nanjing 211189, China, Email: z.wang3@tue.nl

² Department of the Built Environment, Eindhoven University of Technology, P.O. Box 513, 5600 MB Eindhoven, The Netherlands

Abstract

In this study, a stable and nano dispersed anatase TiO₂ hydrosol was synthesized by hydrolysis of titanium isopropoxide at low temperatures. The self-cleaning and depollution performance of Portland cement paste at early age with TiO₂ hydrosols were investigated with different dosages. According to the results, the average hydraulic diameter of TiO₂ particles in aqueous solution was about 19 nm and the zeta potential was higher than +30 mV, which indicating this nanodispersed TiO₂ hydrosol can be easily dispersed in water evenly without producing agglomeration. The self-cleaning and air purification properties of TiO₂ hydrosols coated cement paste were evaluated by the photodegradation of Rhodamine B (RB) and NO_x under the UV light over different irradiating time after 7 days of hydration. The RB colour change rates of cement samples coated TiO₂ hydrosol tested by spectrometer was more than 90% after 2640 min UV irradiation, which was 1.5 times as higher than that of cement paste coated with P25 at the same dosage and test conditions. The NO conversion (>97%) of TiO₂ hydrosol coatings and P25 coatings were similar at the lower dosage, while the TiO₂ hydrosol coatings presented better NO conversion effect than P25 at higher surface concentration. These differences may relate to the better dispersion and greater specific surface area of TiO₂ nano particles in the form of hydrosols. Due to the high self-cleaning, air purification and solar reflectance of TiO₂ hydrosol coatings on the surface of Portland cement paste, the nano dispersed TiO₂ hydrosols provide a low cost, low-energy consumption, high efficient and convenient choice to form the protective and self-cleaning layer on the surface of concrete structures.

Keywords: Nano dispersed TiO₂ hydrosol, Air purification performance, Self-cleaning coatings, Portland cementitious materials

1. Introduction

Cementitious materials in buildings are directly and continuously exposed to many atmospheric and organic pollutants, microorganisms under different weather conditions. Colour, the main index of aesthetic properties of buildings, has to give a pleasant appearance that should give to the public an adequate perception of the quality and maintenance. The main cause of colour change on the surface of cementitious materials is the reduction in initial solar reflectivity, mainly from atmospheric aerosol pollutants such as nitrogen oxides, carbon-based materials and volatile organic compounds [1,2]. Titanium-based photocatalysis has proven to be a promising technology for the efficient degradation of a range of organic compounds and some

inorganic compounds (NO_x and SO_2), in busy canyon streets, road tunnels, urban environments, etc [3]. In addition, the combination of TiO_2 and cement-based products have some synergistic advantages because the reaction product can be adsorbed on the surface and then washed away by rain [4]. Furthermore, when TiO_2 is activated by solar photons, holes diffuse to the surface and react with water molecules adsorbed on the surface to generate hydroxyl radicals, thereby increasing the number of hydroxyl groups on the surface of TiO_2 during irradiation [5]. Therefore, during irradiation, the contact angle of the surface of TiO_2 with water molecules is gradually close to zero. This phenomenon is called light-induced super-hydrophilicity, which present as the self-cleaning performance of the TiO_2 coated surfaces. Thus, TiO_2 could be used to increase the life cycle of cement-based materials while it could also substantially decrease the concentration of some air pollutants and enhance the self-cleaning property.

In most of the studies [6–9], the commercially available nano TiO_2 powder (Degussa P-25) was studied either as concrete coatings to improve its photocatalytic activity. The inherent agglomeration and very poor dispersity of nano TiO_2 powders in aqueous system caused by the calcination in synthetic process maybe the biggest holdback in making photocatalytic and self-cleaning cement-based materials. The nanodispersed TiO_2 hydrosols are usually synthesized by the sol–gel process of titanium alkoxide precursors [10–12], where the solvent is water, in large excess with respect to the alkoxide [13–19]. The acids are used as peptizator and produce a colloidal suspension containing TiO_2 particles with size ranges from 15 to 100 nm. This route is a cheap and low-energy consumption method to obtain anatase and well-dispersed nano TiO_2 particles. Moreover, the good dispersity of nano TiO_2 particles in coatings is the critical point of self-cleaning and photocatalytic performances, because the photodegrading reactions between pollutants and coatings occur on the surface of TiO_2 particles and the stable dispersion of nano TiO_2 particles in coatings can provide more reaction areas because of the greater specific surface areas [20]. In nano dispersed TiO_2 hydrosol can be considered as the water was divided by the nano TiO_2 particles evenly. According to the definition of specific surface area, which is the surface area of an object per unit volume (or per mass), the surface area of TiO_2 particles (for example the particle size is 10 nm and mass content is 1% of hydrosol) in 1 g hydrosol is more than $1 \times 10^5 \text{ m}^2/\text{g}$. Compared with the specific surface area of the P25 powders (about $50 \text{ g}/\text{m}^2$), the specific surface area of nano TiO_2 in hydrosol is super huge that indicates the surge of surface energy, and the surface characteristics of the system, such as adsorption, double-layer effect, and chemical reaction performance become more prominent.

In this study, the self-cleaning and photocatalytic performance of cement paste with anatase and well dispersed TiO_2 hydrosols coatings synthesized at low temperatures were studied at 7 days age. The commercial nano powder P25 suspension was selected as the reference coating. The self-cleaning properties and photocatalytic performance enhancement of TiO_2 hydrosol was also discussed via optical analysis.

2. Materials and experimental

2.1 Materials

Titanium tetra-isopropoxide (TTIP, 97.0%) was purchased from Sigma-Aldrich. Acetic acid glacial (99.6%), absolute ethanol (99.9%), were purchased from VWR Chemicals. Deionized water ($18.2 \text{ M}\Omega\cdot\text{cm}$) was used throughout the preparation process of TiO_2 hydrosol. The method anatase TiO_2 hydrosols was referred from literatures [21][14], and the different synthesis temperatures were carried out. The synthesis was as follows: TTIP was dissolved in absolute ethanol with the TTIP/ethanol molar ratio of 2.44, and then the solution was stirred for 30 min at different temperatures (50°C and 40°C). Then, the obtained solution was added dropwise of the speed $0.01 \text{ mL}/\text{s}$ into a mixture containing acetic acid and deionized water with the molar ratio of 0.175. After that, the suspension was continually stirred for 48 h at 50°C or 40°C , and then aged for at least 72 h at room temperature to produce a translucent sol.

In preparing cement paste, CEM I 52.5R cement and tap water were used and the water to cement ratio was 0.4. The samples were wet-mixed for four minutes before moulded in 40 mm× 40 mm× 40 mm moulds and 100 mm× 200 mm× 5 mm, and then the samples were covered with plastic sheets. After 1 day curing (20 °C/60% RH), the samples were demoulded and cured in ambient until test ages.

2.2 Methods

2.2.1 Particle size and zeta potential

The particle size distribution and zeta potential of TiO₂ hydrosol were tested by the Zetasizer NanoSeries (Malvern Panalytical) at 25 °C. In these tests, the initial hydrosol was diluted 100 times in distilled water. The TiO₂ hydrosol samples were tested three times by Zetasizer Nano Series by using a process called Dynamic Light scattering (DLS). The Zetasizer Nano Series calculated the zeta potential by determining the electrophoretic mobility and then applying the Henry equation.

2.2.2 XRD pattern analysis

The phase composition of TiO₂ hydrosol dried at 105 °C were investigated by comparing X-ray diffraction (XRD) pattern (Bruker D4 PHASER, Philips, The Netherlands) with a Co tube (40 kV, 40mA). A typical run was made with a step size of 0.02°/min and a dwell time of 0.5s.

2.2.3 UV-VIS absorbance and UV-VIS-NIR reflectance

The UV-VIS absorbance spectrum of TiO₂ hydrosol and P25 suspension samples was measured by the UV-VIS-NIR spectrophotometer (Perkin Elmer Lambda 750), the tested range was 250 nm to 800 nm, 1 nm per second. For the reflectance test of cement paste coated with different coatings, the TiO₂ hydrosol and P25 suspension coatings with the solid content of 1.54% were applied on the surface of paste samples after 28 days hydration. Due to the Beer–Lambert law, the samples content should lower than 0.01M and the absorbance should below 1.0, in this test the P25 suspension sample was diluted down to 0.02 % and the TiO₂ hydrosol sample was diluted down to 1.0 % by distilled water.

2.2.4 Self-cleaning performance

The self-cleaning performance of the cubic coated cement paste was evaluated by colorimetric analysis of the degradation of the organic dye Rhodamine B (RB). Before tests, the paste top surfaces were polished by SiC sand papers to obtain relative smooth surface with the roughness in the range of 10 to 14 micrometres. Each surface area of paste samples was stained by painting 600 uL of 0.1 mM RB aqueous solution. Then the samples were kept overnight in dark box at room temperature for drying. For each coated sample, 9 points were considered for the colorimetric tests and each point was tested for 4 times. The samples were exposed to a UV lamp (10±0.05 W/m²) to simulate UV light in natural conditions, monitoring the discoloration of the stains.

The reflected colour measurements were taken directly on the surface of each points on each sample at different illumination with a spectrometer USB4000 Oceanoptics, which optimized for the 380- 780 nm wavelength range and analysed mathematically to yield colorimetric quantities like xyz, RGB or L*a*b*. In this study, the percentage of discoloration (R_t) was expressed with the coordinate of the dominant colour of dye a*, value of the CIE Lab colour space for RB [22,23][24], according to Eq. (1).

$$R_t(\%) = \frac{a_0^* - a_t^*}{a_0^*} \times 100 \quad (1)$$

Where, a_0^* the value of a* at time 0 before irradiation, a_t^* its value after t minutes irradiation.

2.2.5 Air purification performance

The air purification experiments [8,9,25,26] of coated cement paste were carried out in a homemade reactor designed in accordance with standard ISO 22197-1. The experimental setup consisted of a planar reactor cell, an UVA light source, a chemiluminescent NO_x analyser, and a gas supply. The main operating conditions of the system were as follows: the wavelength of UV light resource was 300-400 nm, the irradiance flux on the surface of cement paste samples was $10 \pm 0.05 \text{ W/m}^2$, the pollutant source concentration was 1.0 ppm, the NO flow and air flow were 60 mL/min and 2.94 L/min, and the total gas flow was 3.0 L/min, the relative humidity in the reactor was $50 \pm 1\%$. The concentration of TiO₂ particles in two coatings were 1.54 g/m² and 3.08 g/m². Before the test the top surfaces of cement paste panels were pre-prepared by the same method as shown in Section 2.2.4. The amount of NO_x converted in the reactor is calculated following:

$$NO_x \text{ Conversion}(\%) = \frac{[C_{NO_x}]_{in} - [C_{NO_x}]_{out}}{[C_{NO_x}]_{in}} \times 100 \quad (2)$$

Where $[C_{NO_x}]_{in}$ is the initial concentration [ppm], measured by taking the average value of the first 5 min of the experiment, before turning on the light. The outlet concentration $[C_{NO_x}]_{out}$ is measured by taking the average value of the last 5 min of the irradiation period [ppm].

The amount of NO converted in the PCO reactor is calculated following:

$$NO \text{ Conversion}(\%) = \frac{[C_{NO}]_{in} - [C_{NO}]_{out}}{[C_{NO}]_{in}} \times 100 \quad (3)$$

Where $[C_{NO}]_{in}$ is the initial concentration [ppm], measured by taking the average value of the first 5 min of the experiment, before turning on the light. The outlet concentration $[C_{NO}]_{out}$ is measured by taking the average value of the last 5 min of the irradiation period [ppm].

3. Results and discussions

3.1 Effects of synthesis temperatures on the dispersity of TiO₂ hydrosols

The average particle size and Zeta potential values were showed in the Table 1. The average particle size (of intensity) of TiO₂ hydrosol samples at 40 °C and 50 °C was 19 nm and 38 nm respectively. The zeta potential of TiO₂ hydrosol synthesized at 40 °C and 50 °C were 43 mV and 39 mV, which meant that the dispersion of hydrosols in distilled water was stable. These results indicated that the synthesis temperature had a great influence on the particle size of TiO₂ in hydrosols, while the influence on the zeta potential of TiO₂ hydrosols was limited.

Table 1 The average particle size and zeta potential of TiO₂ hydrosols

Synthesis temperatures	Size±SD (d. nm)	%Intensity	Z-average ±SD (d. nm)	Polydispersity Index	Zeta potential	Conductivity (mS/cm)
50 □	38±16	100	35±13	0.14	39	0.12
40 □	19±6	100	17±6	0.11	43	0.11

3.2 Crystal form of TiO₂ hydrosols

The diffraction angle 2θ of (101) crystal plane of anatase TiO₂ crystal was 29.4°, the (004) crystal plane was 44.2° and the (200) (105) and (204) crystal planes were 56.4°, 63.5° and 74.3°. As it can be seen in Figure 1, the TiO₂ particles in hydrosol synthesized at 40 °C and 50 °C showed all the typical diffraction peaks of anatase TiO₂ that indicating the synthesized TiO₂ particles in TiO₂ hydrosol was pure anatase TiO₂ crystal. Since the TiO₂ hydrosol synthesized at lower temperature presented smaller particle size, dispersity and same crystal form, the following charactering tests were focused on the comparison between TiO₂ hydrosol synthesized at 40 °C and P25 suspension.

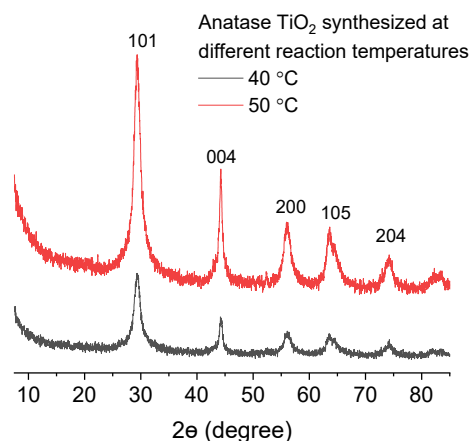


Figure 1 XRD pattern of TiO_2 hydrosols dried at 105 °C

3.3 UV-VIS absorbance of TiO_2 hydrosol

The visual observation of colour changes, as well as UV-VIS absorbance of both TiO_2 hydrosol and P25 suspension are shown in Figure 2. As it can be seen from Figure 2, TiO_2 hydrosol was transparent, while the P25 suspension sample with the same mass content was pure white and non-transparent. In the Figure 2, the light absorbance of TiO_2 hydrosol in the 250-300 nm range is higher than P25 suspension. In general, the P25 powder was made of 20% rutile crystal and 80% anatase crystals, and in theory, the absorption band edge was near 380 nm for anatase and 300 nm for rutile [27]. As seen from Figure 2, the absorbance of light at 400 to 800 nm of P25 suspension is the result of the light scattering phenomenon caused by the big particles of P25 in aqueous solution. As a result, the nano particles in TiO_2 hydrosol were more stable than in P25 suspension.

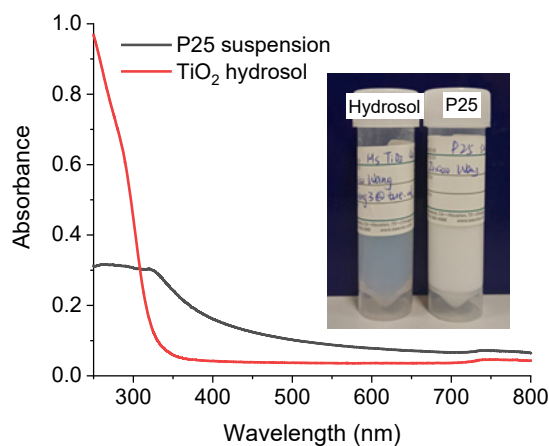


Figure 2 The UV-VIS absorbance spectrums of TiO_2 hydrosol and P25 suspension

3.4 Self-cleaning performance

In Figure 3, the percentage of colour change for RB of cement paste at 7 days age with coatings is presented. The colour change of blank cement sample was around zero after 24 h irradiation, which meant the blank cement at early age present barely no self-cleaning performance. The R_t values of cement paste coated TiO_2 hydrosol with the dosage of 0.77, 1.54 and 3.08 g/m^2 after 24 h irradiation were 85.88%, 91.71% and 94.65% respectively, while the R_t of cement paste coated P25 with the dosage of 1.54 g/m^2 after 24

h irradiation was only 64.88%. In the TiO_2 hydrosol coated samples, the colour change of RB trended to stable after two hours irradiation, while it needed at least 6 hours irradiation to obtain a stable colour change in the P25 coated sample. These results indicated that the self-cleaning performance of cement paste coated 1.54 g/m^2 TiO_2 as the form of hydrosol coatings is much better than that of P25 suspension coatings.

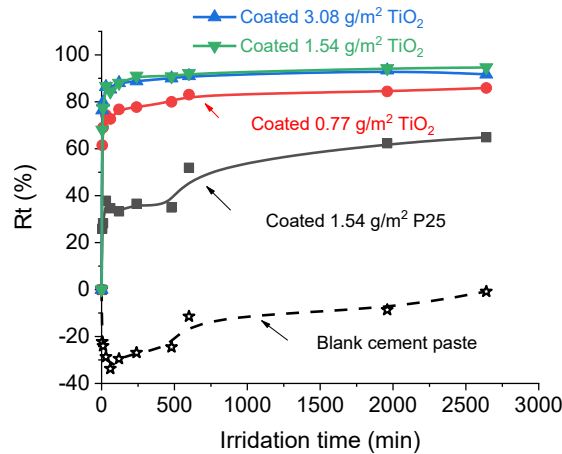


Figure3 Percentage of colour change for RB of cement paste with different coatings after 7 days hydration

3.5 NO_x degradation performance

Figure 4 shows the degradation process of NO_x of cement paste panels at 7 days age. Table 2 presents the conservation values of NO and NO_x of panels. In overall, the cement coated with these two coatings presented very high conversation of NO and NO_x regardless the coating dosage. However, the conversations of NO and NO_x increased along with the dosage of TiO_2 hydrosol coated panels, while the conversations of NO and NO_x decreased with the dosage of P25 coated panels. These results might relate to the poor dispersity and high agglomeration of TiO_2 nano particles in P25 suspension coating with higher dosages. To verify this speculate, the reflectance analysis of cement paste with and without coatings were carried out, this results are discussed in Section 3.6.

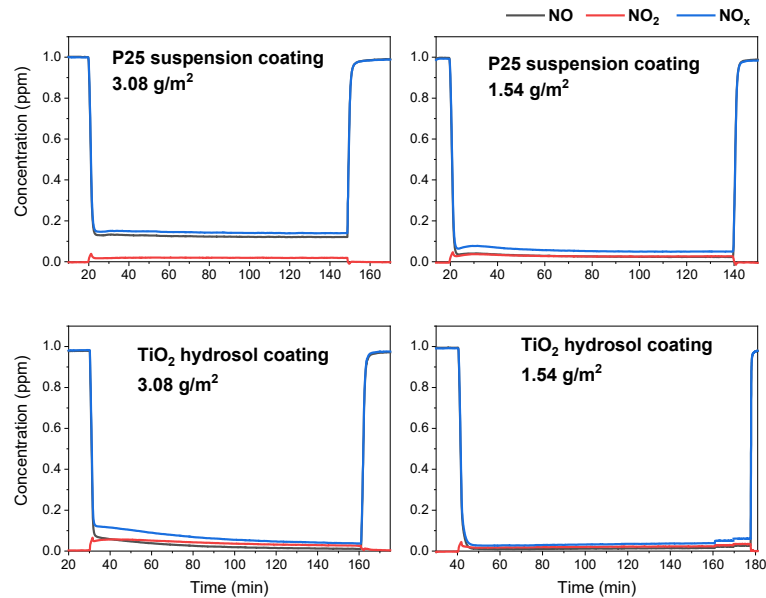
Table 2 The conversion rate of NO and NO_x of cement panels with two coatings

Coatings	Dosage (g/m^2)	Conversion rate (%)	
		NO	NO_x
TiO_2 hydrosol	3.08	98.88	96.14
	1.54	97.36	93.85
P25 suspension	3.08	87.92	86.01
	1.54	97.66	94.97

3.6 Reflectance of cement paste with coatings

Figure 5 presents the reflectance spectra in the range of 200 nm to 2500 nm of cement paste samples at 28 days age. From Figure 5, it can be seen that after being coated by TiO_2 , the reflectance of cement paste samples is significantly increased, especially in the range of VIS (400 to 800nm), NIR (800 to 1000 nm) and SWIR (1000 to 2500nm). These results indicate that the cement paste could also obtain certain solar reflectance from the TiO_2 hydrosol coatings, especially in the range of SWIR. The high reflectance of cement paste coated with P25 suspension in the range of visible light also revealed that the P25 coating was whiter than TiO_2 hydrosol coating, which means that the significant agglomeration of nano TiO_2 particles

in P25 coating. These results supported speculates mentioned in the Section 3.5, showing that the greater agglomeration of TiO_2 particles in P25 suspension was the main reason of the relatively poor performance of air purification in higher surface concentration of coating. Moreover, the better dispersity led to the higher specific surface area of TiO_2 in TiO_2 hydrosol coating, which means that the greater inaction surface areas between TiO_2 and pollutant molecules and better self-cleaning and air purification performance of cement paste with TiO_2 hydrosol coating.



+

Figure4 NO, NO₂ and NO_x concentration graphs of cement panel samples coated TiO₂ hydrosol and P25 suspension coatings

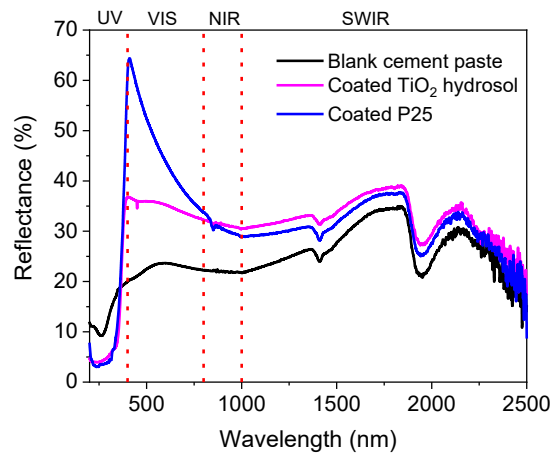


Figure 5 Reflectance of cement paste with different TiO_2 coatings

4. Conclusions

1. In this work, the nano dispersed anatase TiO_2 hydrosol was synthesized by an easy and lower energy consumption method. As compared to the P25 powder suspension, the TiO_2 hydrosol presented much better dispersity and stability in aqueous solution according to the results of particles size, zeta potential test and analysis of UV absorbance.

2. The self-cleaning performance of cement paste sample coated by TiO₂ hydrosol after 24 hour UV irradiation was increased with the surface concentration of TiO₂ hydrosol, and the self-cleaning performance of TiO₂ hydrosol with a surface concentration of 1.54 g/m² was 91.71% which was 1.41 times more efficient than P25 coating. The NO and NO_x conversion rates of these two coatings with the surface concentration of 1.54 g/m² were higher than 95%.
3. The poor dispersity and high agglomeration of TiO₂ particle in P25 suspension coating led the worse air purification ability of cement panel with higher surface concentration of coating. And the higher reflectance of cement paste with P25 coating in the range of visible light indicated the whiter colour of the coating, which proofed the greater agglomeration of TiO₂ particles in P25 coating. The high self-cleaning and air purification performance of cement paste with TiO₂ hydrosol coating was because of the high dispersity and greater specific surface areas of nano particles in coating.

5. Acknowledgments

The authors appreciate the financial supports from the National Natural Science Foundation of China under the contract No. U170620242, the China Scholarship Council (No. 201806090146) and Eindhoven University of Technology (TU/e). The authors gratefully acknowledge M.Sc. Bin Meng (Building Performance group of TU/e) for his help in processing data of self-cleaning performance characterization, and Prof. Albert Schenning and M.Sc. Xinglong Pan (Stimuli-responsive Functional Materials & Devices group of TU/e) for their supports and advices in the discussion of the spectrum analysis.

6. References

- [1] P. Berdahl, H. Akbari, L.S. Rose, Aging of reflective roofs: soot deposition, *Appl. Opt.* 41 (2002) 2355. doi:10.1364/AO.41.002355.
- [2] M. Sleiman, T.W. Kirchstetter, P. Berdahl, H.E. Gilbert, S. Quelen, L. Marlot, C. V. Preble, S. Chen, A. Montalbano, O. Rosseler, H. Akbari, R. Levinson, H. Destailats, Soiling of building envelope surfaces and its effect on solar reflectance - Part II: Development of an accelerated aging method for roofing materials, *Sol. Energy Mater. Sol. Cells.* 122 (2014) 271–281. doi:10.1016/j.solmat.2013.11.028.
- [3] J. Chen, C. sun Poon, Photocatalytic construction and building materials: From fundamentals to applications, *Build. Environ.* 44 (2009) 1899–1906. doi:10.1016/j.buildenv.2009.01.002.
- [4] E. Boonen, A. Beeldens, Photocatalytic roads: From lab tests to real scale applications, *Eur. Transp. Res. Rev.* 5 (2013) 79–89. doi:10.1007/s12544-012-0085-6.
- [5] R. Wang, K. Hashimoto, A. Fujishima, M. Chikuni, E. Kojima, A. Kitamura, M. Shimohigoshi, T. Watanabe, Photogeneration of highly amphiphilic TiO₂ surfaces, *Adv. Mater.* 10 (1998) 135–138. doi:10.1002/(SICI)1521-4095(199801)10:2<135::AID-ADMA135>3.0.CO;2-M.
- [6] Y. Hendrix, A. Lazaro, Q.L. Yu, H.J.H. Brouwers, Influence of synthesis conditions on the properties of photocatalytic titania-silica composites, *J. Photochem. Photobiol. A Chem.* 371 (2019) 25–32. doi:10.1016/j.jphotochem.2018.10.040.
- [7] C. Giosuè, Q.L. Yu, M.L. Ruello, F. Tittarelli, H.J.H. Brouwers, Effect of pore structure on the performance of photocatalytic lightweight lime-based finishing mortar, *Constr. Build. Mater.* 171 (2018) 232–242. doi:10.1016/j.conbuildmat.2018.03.106.
- [8] S. Lorencik, Q.L. Yu, H.J.H. Brouwers, Design and performance evaluation of the functional coating for air purification under indoor conditions, *Appl. Catal. B Environ.* 168–169 (2015) 77–86. doi:10.1016/j.

apcatb.2014.12.012.

- [9] E. Luévano-Hipólito, A. Martínez-De La Cruz, E. López-Cuellar, Q.L. Yu, H.J.H. Brouwers, Synthesis, characterization and photocatalytic activity of WO₃/TiO₂ for NO removal under UV and visible light irradiation, *Mater. Chem. Phys.* 148 (2014) 208–213. doi:10.1016/j.matchemphys.2014.07.034.
- [10] Y. Wang, Y. He, Q. Lai, M. Fan, Review of the progress in preparing nano TiO₂: An important environmental engineering material, *J. Environ. Sci. (China)*. 26 (2014) 2139–2177. doi:10.1016/j.jes.2014.09.023.
- [11] M. Malekshahi Byranvand, A.N. Kharat, L. Fatholahi, Z. Malekshahi Beiranvand, A review on synthesis of nano-TiO₂ via different methods, *J. Nanostructures*. 3 (2013) 1–9. http://jns.kashanu.ac.ir/article_5436_20d28461e8600e7c915eab3d24924117.pdf.
- [12] R. Vijayalakshmi, V. Rajendran, Synthesis and characterization of nano-TiO₂ via different methods, *Arch. Appl. Sci. Res.* 4 (2012) 1183–1190. doi:10.11648/j.nano.20140201.11.
- [13] O.B. Pavlova-Verevkin, S.N. Chvalun, E.D. Politova, V. V. Nazarov, L.A. Ozerina, A.N. Ozerin, Study of the stable nanocrystalline TiO₂ hydrosol and its fractions, *J. Sol-Gel Sci. Technol.* 35 (2005) 91–97. doi:10.1007/s10971-005-1311-7.
- [14] P. Alphonse, A. Varghese, C. Tendero, Stable hydrosols for TiO₂ coatings, *J. Sol-Gel Sci. Technol.* 56 (2010) 250–263. doi:10.1007/s10971-010-2301-y.
- [15] E. Burunkaya, M. Akarsu, H. Erdem Çamurlu, Ö. Kesmez, Z. Yeşil, M. Asiltürk, E. Arpaç, Production of stable hydrosols of crystalline TiO₂ nanoparticles synthesized at relatively low temperatures in diverse media, *Appl. Surf. Sci.* 265 (2013) 317–323. doi:10.1016/j.apsusc.2012.11.003.
- [16] X. Ding, S. Pan, C. Lu, H. Guan, X. Yu, Y. Tong, Hydrophobic photocatalytic composite coatings based on nano-TiO₂ hydrosol and aminopropyl terminated polydimethylsiloxane prepared by a facile approach, *Mater. Lett.* 228 (2018) 5–8. doi:10.1016/j.matlet.2018.05.103.
- [17] J.X. Yu, R.A. Chi, J. Guo, Desorption and photodegradation of methylene blue from modified sugarcane bagasse surface by acid TiO₂ hydrosol, *Appl. Surf. Sci.* 258 (2012) 4085–4090. doi:10.1016/j.apsusc.2011.12.106.
- [18] E. Ghenne, F. Dumont, C. Buess-Herman, Stability of TiO₂ hydrosols synthesized by hydrolysis of titanium tetraethoxide, *Colloids Surfaces A Physicochem. Eng. Asp.* 131 (1998) 63–67.
- [19] M.M. Soderzhinova, D. V. Tarasova, F.K. Chibirova, Aging of titania hydrosols prepared via ultrasonic processing, *Inorg. Mater.* 52 (2016) 470–475. doi:10.1134/S0020168516050162.
- [20] S. Singh, T. Shi, R. Duffin, C. Albrecht, D. van Berlo, D. Höhr, B. Fubini, G. Martra, I. Fenoglio, P.J.A. Borm, R.P.F. Schins, Endocytosis, oxidative stress and IL-8 expression in human lung epithelial cells upon treatment with fine and ultrafine TiO₂: Role of the specific surface area and of surface methylation of the particles, *Toxicol. Appl. Pharmacol.* 222 (2007) 141–151. doi:10.1016/j.taap.2007.05.001.
- [21] L. Yang, A. Hakki, F. Wang, D.E. Macphee, Photocatalyst efficiencies in concrete technology: The effect of photocatalyst placement, *Appl. Catal. B Environ.* 222 (2018) 200–208. doi:10.1016/j.apcatb.2017.10.013.
- [22] M.V. Diamanti, R. Paolini, M. Rossini, A.B. Aslan, M. Zinzi, T. Poli, M.P. Pedferri, Long term self-cleaning and photocatalytic performance of anatase added mortars exposed to the urban environment, *Constr. Build. Mater.* 96 (2015) 270–278. doi:10.1016/j.conbuildmat.2015.08.028.

- [23] M. V. Diamanti, B. Del Curto, M. Ormellese, M.P. Pedferri, Photocatalytic and self-cleaning activity of colored mortars containing TiO_2 , *Constr. Build. Mater.* 46 (2013) 167–174. doi:10.1016/j.conbuildmat.2013.04.038.
- [24] E. Jimenez-Relinque, J.R. Rodriguez-Garcia, A. Castillo, M. Castellote, Characteristics and efficiency of photocatalytic cementitious materials: Type of binder, roughness and microstructure, *Cem. Concr. Res.* 71 (2015) 124–131. doi:10.1016/j.cemconres.2015.02.003.
- [25] E. Luévano-Hipólito, A.M. la Cruz, Q.L. Yu, H.J.H. Brouwers, Precipitation synthesis of WO_3 for NO_x removal using PEG as template, *Ceram. Int.* 40 (2014) 12123–12128. doi:10.1016/j.ceramint.2014.04.052.
- [26] F. Gauvin, V. Caprai, Q.L. Yu, H.J.H. Brouwers, Effect of the morphology and pore structure of porous building materials on photocatalytic oxidation of air pollutants, *Appl. Catal. B Environ.* 227 (2018) 123–131. doi:10.1016/j.apcatb.2018.01.029.
- [27] E. Jimenez-Relinque, I. Llorente, M. Castellote, TiO_2 cement-based materials: Understanding optical properties and electronic band structure of complex matrices, *Catal. Today.* 287 (2017) 203–209. doi:10.1016/j.cattod.2016.11.015.

Innovative production technologies and applications in the field of Wood Cement Products

E.J.B. van Elten,

Eltomation BV, Barneveld, The Netherlands

Abstract

This paper describes the further development of advanced production technologies for the manufacture of various types of Wood Cement Boards and the wide range of applications of these boards.

Due to the increasing awareness for healthy and comfortable living conditions with reduced energy costs, the demand for various types of Wood Cement Boards has grown significantly over the last years. In Western Europe this growth is furthermore supported by the increasing need for “acoustic performance” in public buildings and private homes. As a result, the demand for automated production lines for these acoustic and energy-saving boards has also increased.

Eltomation BV, The Netherlands, being a major player in the supply of turnkey Wood-Cement Board Plants, has further developed its advanced production technologies to meet this increasing demand. Although the basis for acoustic Wood Wool Cement Boards lies within Western Europe, an increasing demand for these acoustic and energy-saving boards is being developed in countries such as Russia. In addition, special solutions are being developed to meet the high demand for Affordable & Sustainable Housing in various regions of Africa and elsewhere. This paper provides a general overview of the various Wood Cement Boards on the market and the new technologies being developed to meet the increasing demand for thermal insulation, fire-resistance, acoustic performance and sustainability.

Keywords: Wood Wool Cement Boards, Advanced Production Technology, Energy Saving & Acoustic Applications.

1. Introduction

Eltomation BV of Barneveld, The Netherlands, is specialized in the development and supply of turn-key plants and equipment for the production of various Wood Cement Boards. The family-owned company, active in this specific field for over 60 years, is regarded as a specialist in the production technologies for these Wood-based Mineral Bonded Boards.

The main product produced in these plants is the so-called low-density Wood Wool Cement Board (WWCB). Other Wood-Cement Products include the medium-density Wood Strand Cement Boards (WSCB - EltoBoard) and the Prefab Large WWC Wall Elements. Where the above listed products are based on using long wood wool (excelsior) as raw material, another product for which Eltomation has provided plant solutions is the so-called Cement Bonded Particle Board (CBPB), which high-density (fire-retardant) product is based on using small wood particles as raw material.

Our European clients include renowned producers such as Knauf Insulation (their WWCB products being known under the brand name Heraklith) with multiple plants throughout Europe, Trolldtekt A/S – Denmark,

Fibrolith Dämmstoffe GmbH – Germany (part of Soprema Group), Celenit S.p.A – Italy, Träullit AB – Sweden and others. Annual production volume of WWCB is in the range of 16-18 Million square meters, serving mainly the (fire-retardant) acoustic ceiling market. This demand is still rapidly increasing.

During the last decade an increased interest for durable, environmentally friendly and energy-saving building materials has come from the new Russian and Chinese markets. During these recent years a total of 7 additional full-size Wood Wool Cement Board Plants have been supplied to clients in Russia and China for serving the local markets with these fire-resistant, energy-saving products. In addition, these new Russian WWCB Plants also produce large quantities of fine-fibre acoustic ceiling panels for export to the large ready market in Western Europe.

2. Overview of main Wood Cement Products

In general the following Wood Cement Boards (and Large Elements) are considered to be the main Wood-Cement Board products which are on the market today:

1. Wood Wool Cement Board (WWCB);
2. Large WWC Wall Elements;
3. Wood Strand Cement Board (WSCB/ EltoBoard);
4. Wood Residue Cement Board (WRCB);
5. Cement Bonded Particle Board (CBPB).

This paper will mainly deal with the production technology for the first three mentioned product types. Each of these 3 product types require small diameter logs (mostly soft wood species such as pine, spruce, poplar, eucalyptus, etc.) as raw material, to enable the production of long and thin wood wool or wood strands. WRCB and CBPB are not made from wood wool but from wood chips, respectively small wood particles, thereby having different properties and applications.

3. Properties of Wood Wool Cement Board

Of the above described main Wood Cement Products, Wood Wool Cement Board (WWCB) is by far the most common product with a significant annual production volume. To ensure its excellent properties in view of thermal insulation and sound absorption, WWCB is produced at a low density of only approx. 350-460 kg/m³. These densities are subject to the board thickness and specific application.

The main features of WWCB are:

- Excellent acoustic performance
- High fire resistance (both as B1 and A2 class)
- Wet and dry rot resistance
- Freeze-thaw resistance
- Termite and vermin resistance
- High thermal insulation (energy-saving)

For increased thermal insulation, WWCB can optionally be produced as a (2 or) 3 layer sandwich board with a core of EPS/Polystyrene, Rockwool or PU-foam. This product is referred to as “Composite WWCB”. A

main application of such Composite WWCB panel is e.g. acoustic ceilings in open parking garages, where the floor of the apartments or store above the parking house not only needs the required fire-safety, but also a high thermal insulation.



Figure 1 - Standard (white cement) WWC Board WWCB

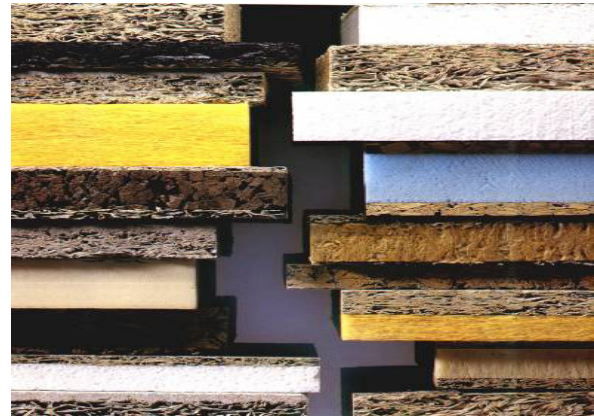


Figure 2 – Various types of Composite

4. Applications of Wood Wool Cement Board

Standard applications of WWCB include:

- Acoustic ceiling applications (being the vast majority of the market demand);
- Reinforced Roofing boards (mainly applied in Scandinavia, where heavy snow-loads apply);
- In addition, specialty applications include:
- Insulation board for external walls (and floors), referred to as “permanent shuttering” board;
- General board for insulation / renovation / fire protection purposes.



Figure 3 - Acoustic ceiling panels in public building



Figure 4 - Reinforced Roofing Boards



Figure 5 - Permanent Shuttering Boards



Figure 6 – WWCB for renovation projects

Nowadays there is a fast growing application of WWCB in Decorative & Acoustic Applications on walls in offices, bars & restaurants, stores, theatres, etc., mainly due to the good acoustic performances and nice and modern appearance. These boards are typically applied in various decorative shapes or patterns and/or as a mix of various matching colours. Major players in this field are the companies BAUX from Sweden and Troldekt, Denmark.



Figure 7 – Decorative WWCB (Troldekt)



Figure 8 – Decorative WWCB (Träullit/BAUX, Sweden)

5. Production Technology for WWCB

The modern WWCB Plants supplied to the market nowadays combine the need for high-capacity production and minimal labour requirement with consistent high-quality boards. A high percentage of the output will find its way to the acoustic ceiling market. These boards require not only the needed fire-resistance (in either standard B1 or special non-combustible A2 Class) but also have a high standard for visible appearance. This has resulted in an increasing market for special ceiling panels, produced with fine wood wool of minimal width, such as 1,5 mm or only 1,0 mm in width (where standard WWCB is commonly produced with a wood wool width of 2,5 mm or 3,0 mm) and using white cement as binder.

The high-speed production of the fine-fibre wood wool is realized by means of a special-developed Rotating Wood Wool Machine (the so-called “Eltomatic CVS-16”). Such Eltomatic replaces a series of up to 8 of the previously known reciprocating crankshaft driven wood wool planing machines, which are no longer used in modern WWCB production plants due to safety and CE regulations. In the last decades over 30 modern Eltomats have been installed in WWCB plants worldwide, either as part of a new turn-key plant or simply replacing the old wood wool machines as part of a modernisation (in combination with safety-issues and labour savings).

Where the vast majority of the WWCB Plants use standard Portland Cement as a binder (increasingly white cement replacing the previously common grey cement), a few lines are based on using Magnesite as binder

(where these boards are mainly applied indoors), however the majority is based on having cement as binder. Optionally, these acoustic boards are profiled/bevelled and/or spray-painted in the desired colour.

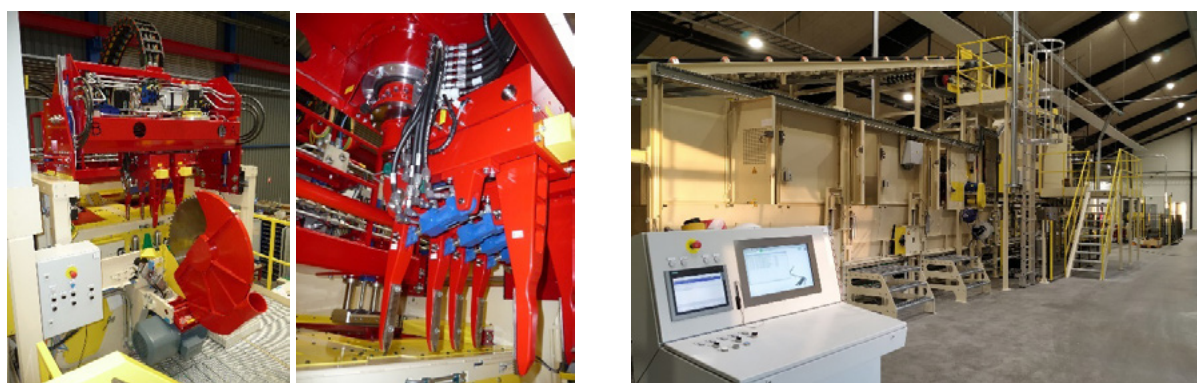
WWC-Boards are typically produced as 60 cm (optionally 2') in width and having a range in length from 240 – 300 cm (optionally 8'- 10'). Thicknesses of solid WWCB range from 15 to 100 mm, where the majority will be in the 15-35 mm range. For applications with a higher thermal insulation (or further increased fire-resistance), the WWCB panel can be combined with a layer/core of insulating material, such as EPS/XPS, rockwool or PU-foam. These so-called (2- or 3-layer) Composite WWCB Panels are nowadays produced at a thickness of up to 250 mm, subject to application and required R-value. Where in the old days the Composite sheet was added to the fresh WWCB in the main production line, this procedure is nowadays mainly done by gluing such Composite Sheet to a ready WWCB Panel in the Finishing Area.

For acoustic ceiling panels, boards are usually cut into 120 cm length (standard for the European market), where the standard in the USA is mainly based on 60 x 60 cm (or 2'x 2'). Nowadays WWCB is produced in accordance with EN 13168 (replacing the former DIN 1101).

After forming of the fresh mixture, the boards initially cure for 24 hours (up to 48 hours) in the moulds, before being demoulded. The demoulded boards are automatically stacked onto pallets for further curing in the Second Setting Area for say 10-15 days. As a final step all boards pass through an automatic Board Dryer to bring the moisture content of each board down to the desired approx. 12% (ATRO), which provides the required long-term stability of the board. As a final step each board may pass through a Board Thickness Calibrator, before (optionally) being spray-painted in the desired colour. An increasing volume is produced as a “natural-look” panel (non-painted), based on having white cement as a binder.

The capacity of a standard WWCB Plant is nowadays up to 4.100 m² boards per shift (based on 25 mm board thickness) with a production line speed of the main line of up to 20 m/min. (resulting in average one board being produced per 7 seconds). Each WWCB Producer determines whether he wishes the line to be operational on either a 1, 2 or even 3 shifts per day. Modern WWCB Plants are able to produce up to 3 Million square meters of boards on an annual basis.

With the integration of modern electronic control systems, the lines are not only more automated but also provide a more accurate formed board in view of even distribution, weight and visual appearance. Only a handful of supervisors are required to operate such line, supported when needed by direct on-line support from the Eltomation office in Barneveld, Holland.



Figures 7, 8 - Eltomatic Rotating Wood Wool Machine Figure 9 – Double Forming Station at WWCB Plant (cap.: 3.000 kg/hr.)

6. Wood Strand Cement Board (WSCB – EltoBoard)

The production of medium-density Wood Strand Cement Board (WSCB – EltoBoard) is accomplished on

a standard WWCB Plant to which a special hydraulic EltoBoard Press has been added at the end of the line. The Press will receive a full stack of filled moulds and will compress the fresh wood-cement mat to a much higher density. To ensure and maintain sufficient pressure during initial curing, the pressed stack of full moulds is secured in a so-called Press Package, consisting of a heavy-duty Top- and Bottom Frame, secured by Tension Arms. The Package is secured under pressure during the initial 24 hours of curing, where after the Press Package is again opened in the same EltoBoard Press, to allow further processing, such as demoulding, further curing, final trimming, etc.

This extra procedure results in a medium density board with structural strength (bending strength of up to approx. 20 MPa). Board dimensions are typically 60 cm wide and 240-300 cm long. Board thicknesses range from 8 to 25 mm.

Producing these medium-density Wood Cement Boards on such WWCB Plant, provides a big advantage to the End-user, by now having the flexibility to produce both low-density WWCB and medium-density Wood Strand Cement Boards on one plant, allowing a wider range of products from one plant location.

Wood Strand Cement Board is commercially being produced in Russia (OOO Building Innovations) and Japan (Takemura Co.).



Figure 10 - WSCB Plant with EltoBoard Press Figure 11 - WSCB applied in walls, floors and roof
(Takemura, Japan)

7. Large WWC Wall Element Building System - introduction

During the last decade, a new revolutionary prefab building system has been developed by the company Träullit AB in Sweden, being one of Eltomation's long-term clients.

Utilising the excellent properties of WWCB in view of thermal insulation, weather-, fire, insect- and rot-resistance, the company decided to produce WWCB in much larger dimensions (referred to as "Large WWC Elements"), enabling fast and efficient prefab construction of homes, schools, offices, etc. These large wall elements are made out of uniform (although light-weight) WWC with dimensions of up to 6 m (optionally 20') in length, 2,7 - 3 m (approx. 9' - 10') in wall height and up to 40 -50 cm (approx. 1' - 4" to 1' - 8") thickness, subject to the local climatic conditions.

In addition to the excellent thermal insulation ($U = 0,19 \text{ W/m}^2 \text{ }^\circ\text{C}$ at 40 cm wall thickness), these elements also provide a high thermal storage capacity ($250 \text{ kJ/m}^2 \text{ }^\circ\text{C}$), which contributes to excellent living conditions in these homes.



Figure 16 – Collage of Large Element System: Production, Installation and a Finished Large Element House.

8. Construction with Large WWC Wall Elements

Due to the low weight of the wall elements, a truck/trailer can be loaded with up to 12-16 Elements (subject to wall thickness), allowing for very efficient transport. The elements are loaded into open containers, or onto special drop-off frames, which are commonly used in the concrete element business, so the full load can be dropped-off at the building site (and when possible an empty container/rack is picked-up for return to the plant).



Figures 17, 18 - Ready Elements are loaded into open containers, or onto special drop-off frames. Elements are lifted from the transport frame by a small crane (by making use of the two hoisting straps embedded in each Element). A small team of 3 workers can in this way place all Elements of a typical medium-size one-story house in one day.



Figures 19, 20, 21 - Ready Elements are efficiently placed on the ready concrete slab

For one- and two-story housing, as commonly applied in Sweden, the Large Wall Element System receives its load-bearing properties by means of the reinforced concrete beams, which are freshly poured on-site, by filling up the U-shaped cavities between 2 lined-up Elements. In addition to these vertical “pillars”, each Element is provided with a horizontal running U-shaped groove (“Ring-beam”) at the crest of each Element. Both the vertical cavities and horizontal U-shaped groove are reinforced with steel bars and are cast on-site. The large wall element itself has a compression resistance of 27 kN per running metre. A possible bending down of the concrete beam is prevented by the large wall element that works together with the concrete ring beam. However, the architects designing these houses are used to put the load-bearing property of the Element to zero, so purely calculating the concrete ring-beam and vertical supports to carry the full load.



Figure 22 - Open Ring-beam Figure 23 - Pouring of concrete

Figure 24 - Anchors in ring beam for floor support

Some of the main technical properties of the Large WWC Wall Element are listed in the Table A below, based on the standard 40 cm wall thickness, as applied in most projects executed in Sweden.

Table A – Main Technical Specifications of the Large WWC Element.

Träullit Large Wall Element, Thickness 400 mm Technical Data	
U-value	0,19 W/m ² K
Fire rating	REI360 (6 hours)
Heat storage capacity	250 kJ/m ² °C
Critical RH (preliminary tests)	90 %
Air permeability	20 m ³ /mhPa
Load carrying strength	27 kN per running metre of wall
Density	Approx. 360 kg/m ³

Although the listed thermal insulation of $U=0,19$ ($R=5,2 \text{ m}^2\text{K/W}$) is sufficient for most projects, such as houses, schools, etc. in Sweden, certain applications (such as a so-called “Artic House Project”) may require an even higher thermal insulation. For such projects it will be possible to make the Elements of a thickness of 50 cm and even up to 60 cm. Such 60 cm thick wall will provide for a R-value of up to 10.

From the Table A above, one can see the excellent Heat Storage Capacity ($250 \text{ kJ/m}^2 \text{ °C}$) of this material, which may be one of the most important features for a comfortable living condition in the house. The heat of the day is stored in the walls, to be only gradually be released during the night. Another figure, which comes to mind is the very high fire-rating of REI 360. Extensive tests have been performed at the SP

Technical Research Institute in Sweden, where a test Element was made subject to flames of 1200 degrees centigrade on one side during an extended period of 360 minutes (6 hours) under load. During this period the temperature on the other side of the element only came to 45 degrees Celsius and the overall Element remained intact. After the 6 hours testing period was successfully reached, the load was steadily increased up to 67 kN/m, which caused initial cracks in the test element.

The various pictures displayed in this paper show the construction of houses, schools, etc. in Sweden, where the Elements are shipped to the building site as cut-to-size Element, however without any base stucco, which is applied only once all Elements are put in place. Also openings for electrical fittings are afterwards milled into the wall. Eltomation's new fully-automated Large Element Line is provided with a CNC Centre, which not only provides the proper sizing of each Element (including cut-outs for window openings, etc.), but will also provide all such openings for cables and piping in the plant, allowing certain components and fittings to be pre-mounted in the factory. As a final step the client may choose to already apply a base stucco in the plant and mount window-frames, where possible.

These additional steps will contribute to a higher efficiency in providing the Elements on full pre-fab basis, thereby further reducing labour on the building site and an overall quicker delivery of the finished house.



Figures 25, 26 - two-story villa under construction (Träullit, Sweden)





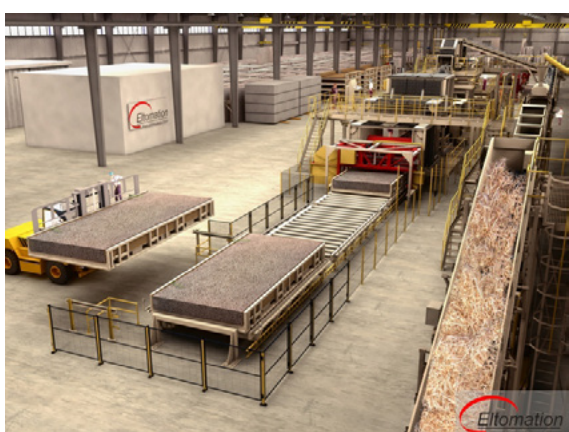
Figures 27, 28, 29, 30 – Construction of a highly insulated day-care centre in Sweden, utilising Large Elements for the outer walls and Reinforced Roofing Boards for the roof (Träullit, Sweden)



Figures 31, 32, 32 – Affordable & Sustainable Housing for Africa (and other regions worldwide)

9. Production Line for Large WWC Wall Elements

During the first years of production of the large WWC wall elements, Träullit, Sweden has further optimised its product using semi-automated production facilities, such as for forming, demoulding, storage, cutting/finishing, etc. In order to meet the demand for a fully-automated production of these Large Elements at considerably higher plant capacity, Eltomation has in recent years developed a production line for the fully-automated production of such large elements at high capacity and reduced labour requirements.



Figures 33, 34 - Impression fully- automated Large Element Line

The first such fully-automated Large Element Line, was supplied to a client in Yixing, Jiangsu Province, PR of China. Plant capacities of such Large Element Line are up to 24-30 Elements per shift (subject to wall thickness), allowing construction of up to 1500 housing units per year. Contracts for the supply of similar Large Elements Lines to clients in Western Europe and Russia are expected to be secured during 2019.

Typical dimensions for these large elements are 6 m length x 2,8 m wall height. The wall thickness will standard be based on 30 - 50 cm, subject to the climatic conditions. Per each plant location and intended range of applications, the maximum wall thickness will be optimised (say up to 30 cm for a potential project in central Africa and up to 50 cm for a project in Northern Europe. Also the maximum wall height will be optimised to the local market demand (typically ranging from 2,7 to 3,0 m). To secure a flexible production range, the Large Element Line can produce various wall thicknesses, which can be secured by laying in a dummy-bottom plate in the large form. For example by adding a 15 cm dummy bottom in a 40 cm high form, also Elements of 25 cm thickness can be produced on the same line.

The fresh mat of material is formed continuously in the slow-moving large forms, which pass underneath the Double Forming Station in an uninterrupted flow. Each Element is formed in 2 subsequent layers (say of 20 cm thickness each, allowing the line to have hoisting straps or reinforcements to be inserted in between the 2 fresh layers of wood-cement mixture material. The continuous mat is hereafter cut into the desired (6 m) lengths by the separating saw, which moves at the same speed of the forms, while making the cut between 2 forms. The individual full forms are stacked for initial curing of the fresh mixture in the forms for approx. 48 hours. After this curing period the cured Element is released from the Form by means of a hydraulic Turing Table, where after each form is returned to the Forming Line. The Element is transferred to a CNC Milling & Cutting Station to be processed to the proper dimensions, including creating openings for window frames, electrical conduits, etc. As a final step the Producer may insert the window frames and apply a base stucco/plaster to both sides of the ready Elements. These steps contribute to an efficient Prefab Building technology, greatly reducing the on-site activities and virtually eliminating on-site construction waste. This all results in a very fast construction time, which benefits not only the contractor but also the new home owner.



Figure 35 - Finished Element from CNC operation



Figure 36 – Elements ready for shipment

The capacity of the Large Wall Element Line is designed to be approx. 500 m³ of finished product per day (based on a 3 shift production). For typical 40 cm thick Wall Elements, this results in a capacity of up to 23 Elements per shift (subject to complexity), allowing a capacity of Elements for up to 1500 housing units per year. For the market for Affordable & Sustainable Housing Units for countries in e.g. Africa, based on a typical 25-30 cm wall thickness and say 55-60 m² single story housing unit, such Large Element Line may have an output of Wall Elements for up to 2500 housing units per year. Such Large Element Line may be supported by a Wood Wool Cement Board (WWCB) Plant, for the production of all partitioning walls (typically 100 mm thickness), Reinforced Roofing Boards (typically 75 mm thickness) and optional acoustic ceiling panels. Such combined Large Element Line and WWCB Plant will allow all such main building materials to come from one plant location, utilising the local available small diameter plantation wood. Other interesting markets for the prefab Large Elements are currently being developed, such as for Sound

Barriers along highways and railroad tracks.

10. Durability and Sustainability

WWCB, WSCB and Large WWC Elements are produced from only natural materials, such as FSC-certified small diameter Spruce (optionally Pine or Poplar), mixed with Portland Cement. To this mixture water and a small percentage of salt-solution is added for the proper binding.

Both scientific tests, initiated by customers of Eltomation, as well as open air application of WWCB have shown that WWCB is unaffected by over 70 years of open air exposure to the elements (even in countries with a high number of freeze-thaw cycles, such as Sweden). This property is further improved when the WWCB is stuccoed as is customary done for applications where the material is exposed to the elements.

At the end of the life cycle the WWC material can be fully recycled. The leading WWCB producer Trolldtekt has already obtained a Cradle-to-Cradle Silver Certificate for its WWCB production process. Currently test are being conducted to have the trimming waste from production be ground to form basic ingredients for new cement production. In this respect, WWCB is one of the few building products with a neutral Life Cycle Analyses (LCA). WWCB meets the most stringent international environmental norms and certifications, such as the Danish Indoor Climate Labelling, the Finnish M1 Low-Emission Classification, UK's 'Allergy Friendly Product Award' and Healthy Indoor Climate Certificate.

11. Conclusion

Although Wood Wool Cement Boards (WWCB) have been on the European market for some 100 years, it has seen a sharp increase in sales and applications over the last decade, with annual production volumes growing towards the 20 Million square meters annually. Reasons for this re-birth of WWCB are the steadily increasing volumes for decorative acoustic ceiling panels with fine-fiber boards, produced with white cement. Leading countries in this field are Denmark, Germany and Holland. One specific sector seeing an increased demand is the Agro-sector where special lightweight WWCB is applied in (pig) stables to act as a filter for the clean air flow through the ceiling in such stables. Producers in Austria and Germany also benefit from the market increase for fire-resistant applications in (indoor) parking garages, where new European fire-safety norms apply. In addition, new markets for fully-automated WWCB Plants have been developed in countries such as Russia and China, where consumers, architects and builders have discovered the benefits of this sustainable and energy-saving product in a wide range of applications. As a result of the above, Eltomation BV, The Netherlands has further developed its range of semi-automatic and fully-automatic plants for the production of various types of Wood Cement Products, to meet this market demand. In general, the Wood Cement Products described in this paper, although being a niche product in the huge building materials market, still has a bright future ahead.

12. Acknowledgement

The author wishes to express his gratitude to the management of Träullit AB, Sweden and Trolldtekt A/S, Denmark for the technical support provided and the courtesy of making use of the technical data in Table A and some of the pictures used in this paper. Additional pictures of WWCB applications are courtesy of Träullit / BAUX, Sweden and Celenit, Italy.

13. References

1. G. J. (Gerry) van Elten, Eltomation BV, The Netherlands. 2004. History, present and future of Wood Cement Products. 9th International Inorganic Bonded Composite Materials Conference. Vancouver, Canada, 2004. Proceedings published by IIBCC.
2. E. J. (Bert) van Elten, Eltomation BV, The Netherlands. 2010. New Developments in the field of

Wood Cement Products, applications and production technologies. 12th International Inorganic Bonded Composite Materials Conference. Aalborg, Denmark, 2010. Proceedings published by IIBCC.

Sponsored by:

